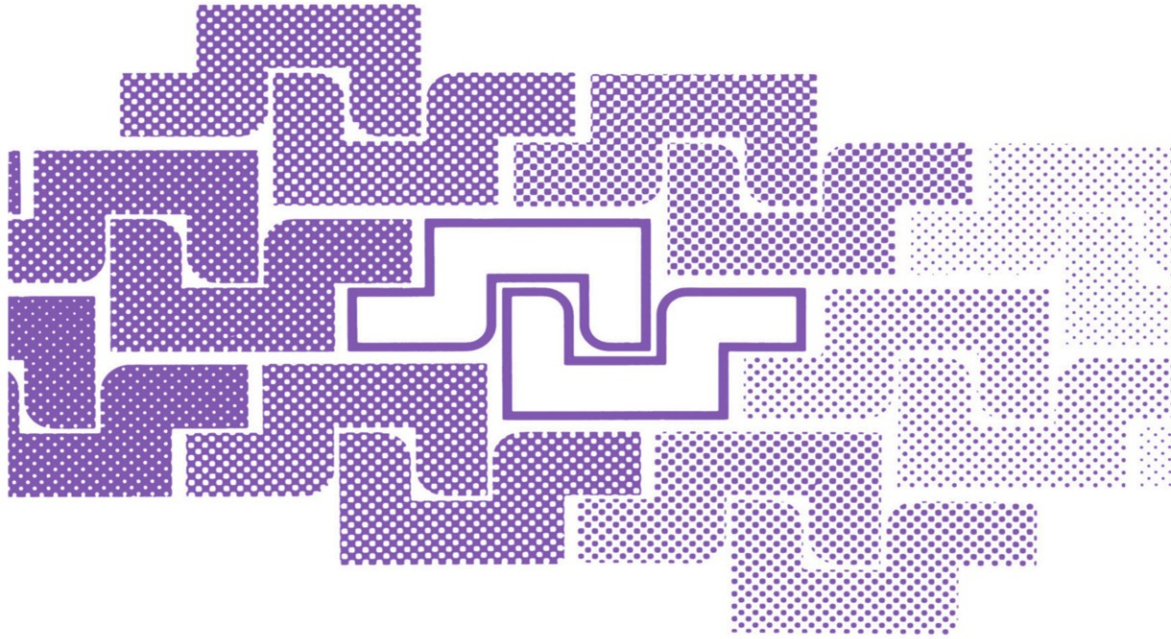

Timing Neutron Stars

Edited by

H. Ögelman and E. P. J. van den Heuvel

NATO ASI Series

Series C: Mathematical and Physical Sciences - Vol. 262

Timing Neutron Stars

NATO ASI Series

Advanced Science Institutes Series

A Series presenting the results of activities sponsored by the NATO Science Committee, which aims at the dissemination of advanced scientific and technological knowledge, with a view to strengthening links between scientific communities.

The Series is published by an international board of publishers in conjunction with the NATO Scientific Affairs Division

A Life Sciences	Plenum Publishing Corporation
B Physics	London and New York
C Mathematical and Physical Sciences	Kluwer Academic Publishers
D Behavioural and Social Sciences	Dordrecht, Boston and London
E Applied Sciences	
F Computer and Systems Sciences	Springer-Verlag
G Ecological Sciences	Berlin, Heidelberg, New York, London,
H Cell Biology	Paris and Tokyo

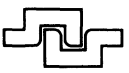

Series C: Mathematical and Physical Sciences - Vol. 262

Timing Neutron Stars

edited by

H. Ögelman

Max-Planck Institute for Extraterrestrial Physics,
Garching, F.R.G.

and

E. P. J. van den Heuvel

Astronomical Institute and Center for High-Energy Astrophysics,
University of Amsterdam, Amsterdam, The Netherlands

Kluwer Academic Publishers

Dordrecht / Boston / London

Published in cooperation with NATO Scientific Affairs Division

Proceedings of the NATO Advanced Study Institute on
Timing Neutron Stars
Çeşme, İzmir, Turkey
4–15 April 1988

Library of Congress Cataloging in Publication Data

Timing neutron stars : proceedings of the NATO Advanced Study Institute held in Çeşme, Izmir, Turkey, 4-15 April 1988 / edited by H. Ögelman and E.P.J. van den Heuvel.
p. cm. -- (NATO ASI series. Series C, Mathematical and physical sciences ; vol. 262)
Includes index.

1. Neutron stars--Congresses. I. Ögelman, H. II. Heuvel, Edward Peter Jacobus van den, 1940- . III. Series: NATO ASI series. Series C, Mathematical and physical sciences ; no. 262.
QB843.N4T55 1989
523.8--dc19 88-34265

ISBN-13: 978-94-010-7519-0 e-ISBN-13: 978-94-009-2273-0
DOI: 10.1007/978-94-009-2273-0

Published by Kluwer Academic Publishers,
P.O. Box 17, 3300 AA Dordrecht, The Netherlands.

Kluwer Academic Publishers incorporates the publishing programmes of
D. Reidel, Martinus Nijhoff, Dr W. Junk and MTP Press.

Sold and distributed in the U.S.A. and Canada
by Kluwer Academic Publishers,
101 Philip Drive, Norwell, MA 02061, U.S.A.

In all other countries, sold and distributed
by Kluwer Academic Publishers Group,
P.O. Box 322, 3300 AH Dordrecht, The Netherlands.

TABLE OF CONTENTS

III. INTERNAL STRUCTURE OF NEUTRON STARS

IV. BIRTH AND EVOLUTION OF NEUTRON STARS

V. MAGNETOSPHERES, ACCRETION PROCESSES AND COLUMNS

PREFACE

The idea for organizing an Advanced Study Institute devoted largely to neutron star timing arose independently in three places, at Istanbul, Garching and Amsterdam; when we became aware of each other's ideas we decided to join forces. The choice of a place for the Institute, in Turkey, appealed much to us all, and it was then quickly decided that Çeşme would be an excellent spot.

When the preparations for the Institute started, early in 1987, we could not have guessed how *timely* the subject actually was. Of course, the recently discovered QPO phenomena in accreting neutron stars and half a dozen binary and millisecond radio pulsars known at the time formed one of the basic motivations for organizing this Institute. But none of us could have guessed that later in 1987 we were to witness the wonderful discovery of the binary and millisecond radio pulsars in globular clusters and, - as if Nature wished to give us a special present for this Institute- the discovery in March 1988 of a millisecond pulsar in an eclipsing binary system, the first eclipsing radio pulsar ever found, and the second fastest in the sky! The discussion of this pulsar, its formation and fate was one of the highlights of this meeting, especially since its discoverers were among the participants of the Institute and could provide us with first-hand information.

In all wavelength domains, from radio waves to X- and gamma-rays, the time structure of the signals from neutron stars contains a wealth of physical information about these objects, their interiors and magnetospheres. Without exaggeration, it can be said that timing is the most powerful and universal tool in the study of neutron star physics; major advances in our understanding of neutron stars including their discovery have come through the investigation of their temporal structure. A few examples suffice to illustrate this:
- Measurement of radio pulsar spin-down rates yields the strength of neutron star magnetic fields and, through the braking index, provides valuable information on the magnetospheric processes that produce the pulsed radiation.
- Observation of the time structure of glitches from radio pulsars yields valuable information about the superfluid neutron star core and about the coupling between this core and the solid crust.
- Doppler tracking of binary X-ray pulsars and their companions and radio pulsars is our only way to obtain quantitative information on neutron star masses, while the spin-up of X-ray pulsars teaches us much about the mass transfer and accretion processes.
- The extreme stability of the pulse periods of radio pulsars allows one to use pulsars in binary systems as probes to testing general relativity to unprecedented accuracy. The detection of gravitational-wave-induced decrease of the orbital period of the Hulse-Taylor binary pulsar PSR 1913+16 is the prime example, convincingly demonstrating the existence of gravitational radiation as predicted by Einstein's general relativity theory.
- A new dimension of accuracy was added to timing, by the discovery of the 1.55 millisecond pulsar in 1982. The few "standard" general and special relativistic

corrections to pulse arrival times that always had to be applied to account for the motion of the Earth in its elliptical orbit around the Sun, turned out to be insufficient in this case. An entire series of additional relativistic solar system clock correction terms had to be added, to do full justice to this pulsars's intinsic clock accuracy. This pulsar now has turned out to be the most stable clock available to man!
- In the X-ray domain, timing of X-ray burst sources and of QPO has added new dimensions to the study of the underlying objects and of the accretion processes taking place close to the neutron star surface - eventhough, as yet, we do not have a full understanding of QPO.

We have attempted to have good mix of theory and observation as well as tutorial and current research aspect in the lectures, and thanks to the lecturers, we feel that we have come close to achieving this goal.

This Institute could not have been possible without the grant of the NATO Advanced Study Institute Program; we thank the committe for their generous support. We also thank the Turkish Scientific and Technical Council, TÜBİTAK, for being cooperative and helpful in the extension of the grant to local participants. Two of our collegues, Ali Alpar and Jan van Paradijs deserve special thanks for helping us in all phases of the organisation as well as in editing of the proceedings. The excellent support of the local organizing committee was crucial in the success of the Institute. We thank Joachim Trümper for helping support the Institute by making possible a sizeable participation from the Max-Planck Institute. The management of the Altın Yunus Hotel provided several free rooms for some of the non-NATO participants for which we are grateful. We thank Mrs. W. Frankenhuizen for taking care of a large fraction of the pre-conference organisation, Nedim Ögelman for typing parts of the manuscript, and Andreas Langmeier for preparing the subject and object index.

H. Ögelman, Garching
E.P.J van den Heuvel, Amsterdam
September 1988

LIST OF PARTICIPANTS

Ayvur Akalın	Ankara Üniv., Turkey
Can Akan	Ege Üniv., Turkey
Murat Alev	Orta Doğu Teknik Üniv., Turkey
Ali Alpar	TÜBİTAK, Turkey
Lorella Angelini	ESTEC, The Netherlands
Herald Atmanspacher	MPE, F.R.Germany
Donald Backer	Berkeley, U,S.A.
Matthew Bailes	Mount Stromlo, Australia
Altan Baykal	Orta Doğu Teknik Üniv., Turkey
James Biggs	NRAL, United Kingdom
Giovanni Bignami	CNR Milano, Italy
David Blair	Univ. of West. Australia, Australia
Hale Bradt	MIT, U.S.A.
Lino Buccheri	CNR Palermo, Italy
Maria C. Busetta	CNR Palermo, Italy
Hugo Burm	Univ. of Amsterdam, The Netherlands
Serhat Çakır	Orta Doğu Teknik Üniv., Turkey
Hülya Çalışkan	İstanbul Üniv., Turkey
Ramon Canal	Univ. de Barcelona, Spain
Patrizia Caraveo	CNR Milano, Italy
Marcello Carollo	CNR Palermo, Italy
Rikkat Çelikel	Orta Doğu Teknik Üniv., Turkey
K.S. Cheng	Univ. of Wollongong, Australia
Hong-Yee Chiu	GSFC, U.S.A.
Robin Corbet	ISAS, Japan
Jacqueline Cote	Univ. of Amsterdam, The Netherlands
Stefan Cronjaeger	MPE, F.R.Germany
Eugene Damen	Univ. of Amsterdam, The Netherlands
Osman Demircan	Ankara Üniv., Turkey
Valentin Demmel	MPE, F.R.Germany
Ethem Derman	Ankara Üniv., Turkey
Rachel Dewey	JPL, U.S.A.
Fehmi Ekmekci	Ankara Üniv., Turkey
Nihal Ercan	Boğaziçi Üniv., Turkey
Akif Esendemir	Orta Doğu Teknik Üniv., Turkey
Hasan Esenoğlu	Marmara Üniv., Turkey
Serdar Evren	Ege Üniv., Turkey
Roger Foster	Berkeley, U,S.A.
Andrew Fruchter	Princeton Univ., U.S.A.
Jack Fry	Univ. of Wisconsin, U.S.A.
Michael Garcia	SAO, U.S.A.

Ahmet Giz	İstanbul Tek. Üniv., Turkey
Fatma Gök	Orta Doğu Teknik Üniv., Turkey
Necdet Güdür	Ege Üniv., Turkey
Serap Güngör	İstanbul Üniv., Turkey
Gülşen Gürbüz	İstanbul Tek. Üniv., Turkey
Avadis Hacınlıyan	İstanbul Tek. Üniv., Turkey
Paul Harrison	NRAL, United Kingdom
Günther Hasinger	MPE, F.R.Germany
David Helfand	Columbia Univ., U.S.A.
Wim Hermsen	Lab. f. Space Res., The Netherlands
Heinz Herold	Univ. of Tübingen, F.R.Germany
Ed van den Heuvel	Univ. of Amsterdam, The Netherlands
Cafer İbanoğlu	Ege Üniv., Turkey
Ocker de Jager	Univ. Potchefstroom, Rep. of S. Africa
Seval Karahaliloğlu	Ankara Üniv., Turkey
Varol Keskin	Ege Üniv., Turkey
Shunji Kitamoto	Osaka Univ., Japan
Nilgun Kızıloğlu	Orta Doğu Teknik Üniv., Turkey
Ümit Kızıloğlu	Orta Doğu Teknik Üniv., Turkey
Michiel van der Klis	ESTEC, The Netherlands
Lydie Koch-Miramond	SACLAY, France
Lucien Kuiper	SRON, The Netherlands
Ping-Wai Kwok	Whipple Observatory, U.S.A.
Nick Kylafis	Univ. of Crete, Greece
Fred Lamb	Univ. of Illinois, U.S.A.
Füsun Limboz	İstanbul Üniv., Turkey
Jeff McClintock	SAO, U.S.A.
Jonathan McKenna	NRAL, United Kingdom
Thomas Maile	Univ. of Tübingen, F.R.Germany
Apostolos Mastichiadis	MPE, F.R.Germany
John Mattox	MPE, F.R.Germany
Fotis Mavromatakis	Univ. of Crete, Greece
Hans Mayer-Hasselwander	MPE, F.R.Germany
Teresa Mineo	CNR Palermo, Italy
Corinna von Montigny	MPE, F.R.Germany
Gregor Morfill	MPE, F.R.Germany
Ewald Müller	MPA, F.R.Germany
Zekeriya Müyesseroğlu	Ankara Üniv., Turkey
Hakkı Ögelman	MPE, F.R.Germany
Serdar Öğüt	Orta Doğu Teknik Üniv., Turkey
Canan Oral	Boğaziçi Üniv., Turkey
Michal Ostrowski	Uniw. Jagiellonski, Poland
Mehmet Özel	GSFC, U.S.A.
Türker Özkan	İstanbul Üniv., Turkey
Arvind Parmar	ESTEC, The Netherlands

Frits Paerels	Univ. of Utrecht, The Netherlands
Jan van Paradijs	Univ. of Amsterdam, The Netherlands
Emmanuel Paschos	Univ. Dortmund, F.R.Germany
David Pines	Univ. of Illinois, U.S.A.
Christ Raubenheimer	Univ. Potchefstroom, Rep. of S. Africa
Andreas Rebetzky	MPE, F.R.Germany
Leonidas Resvanis	Univ. of Athens, Greece
Roger Romani	Berkeley, U.S.A.
Mal Ruderman	Columbia Univ., U.S.A.
Jim Sauls	Northwestern Univ., U.S.A.
Norbert Schulz	MPE, F.R.Germany
Selim Selam	Ankara Üniv., Turkey
Jacob Shaham	Columbia Univ., U.S.A.
Graham Smith	NRAL, United Kingdom
Yıldırım Taner	Orta Doğu Teknik Üniv., Turkey
Joseph Taylor	Princeton Univ., U.S.A.
Zeynel Tunca	Ege Üniv., Turkey
Keith Turver	Univ. of Durham, United Kingdom
Joseph Ventura	Univ. of Crete, Greece
Frank Verbunt	MPE, F.R.Germany
Wolfgang Voges	MPE, F.R.Germany
Ralph Wijers	Univ. of Amsterdam, The Netherlands
Kiriaki Xilouri	Univ. of Crete, Greece
Sophia Yancopoulos	Columbia Univ., U.S.A.
Ilhami Yeğingil	Çukurova Üniv., Turkey
Jean in t'Zand	Lab. f. Space Res., The Netherlands
Tomaz Zwitter	SISSA/ISAS, Italy

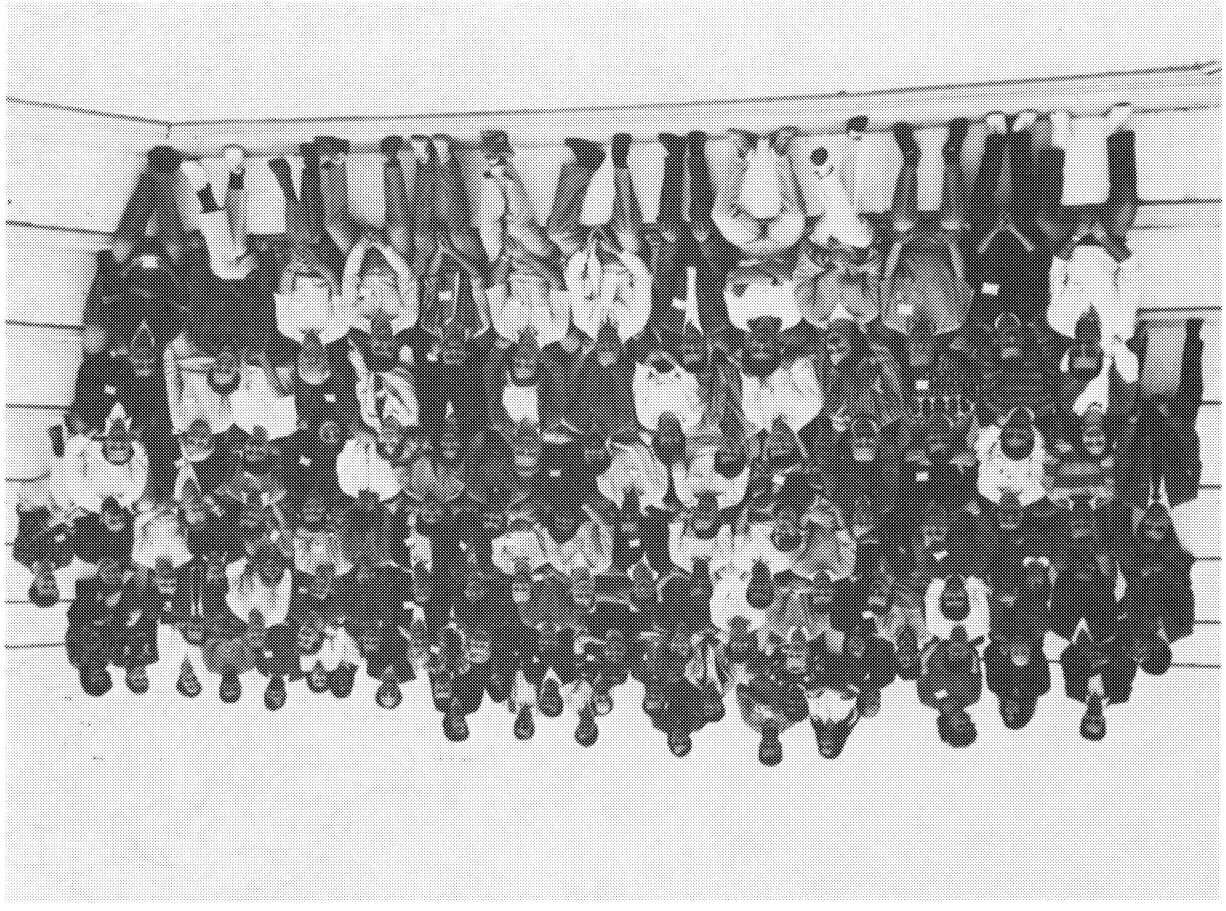

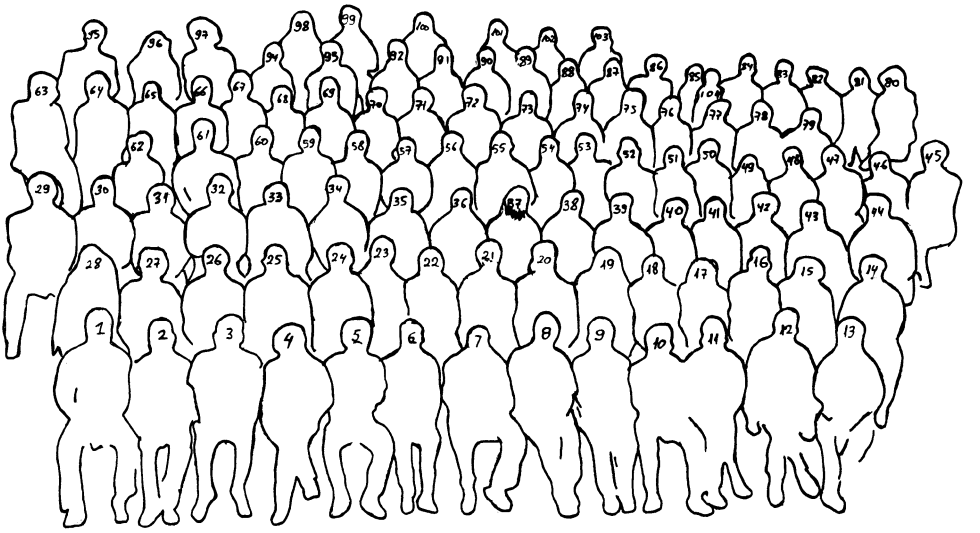

Photograph reference list

1. Varol Keskin
2. Z. Müyessiroğlu
3. Hong-Ye Chiu
4. Ethem Derman
5. Selami Selam
6. Fehmi Ekmekçi
7. David Pines
8. Don Backer
9. Matthew Bailes
10. Nick Kylafis
11. Graham Smith
12. Joe Taylor
13. Ali Alpar
14. Hakkı Ögelman
15. Lydie Koch-Miramond
16. Hasan Esenoğlu
17. Hülya Çalışkan
18. Serap Güngör
19. Ayvur Akalın
20. Jacob Shaham
21. Jim Sauls
22. Rachel Dewey
23. Roger Foster
24. Roger Romani
25. Can Akan
26. Zeynel Tunca
27. C. Sezer
28. Seval Karahaliloğlu
29. Cafer Ibanoğlu
30. H. Mayer-Hasselwander
31. Günther Hasinger
32. Wim Hermsen
33. Ed van den Heuvel
34. Robin Corbet
35. Keith Turver
36. Christ Raubenheimer
37. David Blair
38. Türker Özkan
39. Füsun Limboz
40. Canan Oral
41. Frank Verbunt
42. Tomaz Zwitter
43. Ralph Wijers
44. Norbert Schulz
45. Jonathan McKenna
46. Nilgün Kızıloğlu
47. Andrew Fruchter
48. Nihal Ercan
49. Jacqueline Cote
50. Jean in't Zand
51 Lorella Angelini
52. Ping-Wai-Kwok
53. Shunji Kitamoto
54. Andreas Rebetzky
55. Thomas Maile
56. Valentin Demmel
57. Harald Atmanspacher
58. Murat Alev
59. Frits Paerels
60. Apostolos Mastichiadis
61. Fotis Mavromatakis
62. Rikkat Çelikel
63. Z. Eker
64. Ilhami Yeğingil
65. Ümit Kızıloğlu
66. Serdar Ögüt
67. Yıldırım Taner
68. Fatma Gök
69. Stefan Cronjaeger
70. Corinna von Montigny
71. Paul Harrison
72. James Biggs
73. Hugo Burm
74. Jeff McClintock
75. Jan van Paradijs
76. Michiel van der Klis
77. Eugene Damen
78. Lucien Kuiper
79. Necdet Güdür
80. Teresa Mineo
81. Marcella Carollo
82. Patrizia Caraveo
83. Giovanni Bignami
84. Wolfgang Voges
85. Sophia Güvener
86. Joseph Ventura
87. Heinz Herold
88. Xiluri Kiriaki
89. Akif Esendemir
90. Fred Lamb
91. Mel Ruderman
92. K.S. Cheng
93. Serhat Çakır
94. Altan Baykal
95. Mike Garcia
96. Sophia Yancopoulos
97. John Mattox
98. Gülşen Gürbüz
99. Ahmet Giz
100. Gregor Morfill
101. Ocker de Jager
102. Lino Buccheri
103. Maria C. Busetta
104. Lea Ventura

I. TIMING NEUTRON STARS: GENERAL TECHNIQUES AND APPLICATIONS

PULSAR TIMING

D. C. Backer
Astronomy Department and
Radio Astronomy Laboratory
University of California
Berkeley, CA 94720
USA

ABSTRACT An introduction to the methods of measurement of radio pulse arrival times and some recent results.

1. INTRODUCTION

Following the discovery of pulsars in 1967 a number of extensive pulse timing programs were initiated. The first wave of timing included efforts at Arecibo Observatory, Jodrell Bank, Parkes, the University of Massachusetts, and the Jet Propulsion Laboratory.

In the past several years a number of new programs have been initiated. In these proceedings you will find reports about many of these programs. The excitement in the new efforts is divided between deeper investigations of the neutron star structure in young pulsars, and the use of old, yet short period pulsars as celestial clocks to conduct fundamental physics experiments.

My goal is to introduce the experimental methods of pulsar timing. I will conclude with a few results from recent work. Taylor's contribution in these proceedings continues this topic with particular attention on the celestial clock topic.

2. TIME OF ARRIVAL MEASUREMENT

2.1. Signal Averaging

The primary data recorded in most timing observations is a series of average pulse profiles with the averaging interval in the range between 1 and 20 minutes. Each profile is the result of folding the data samples modulo the apparent pulse period. Time resolutions range from 0.0002 (*e.g.*, Downs and Reichley 1983) to 0.015 (*e.g.*, Davis *et al.* 1985) periods. The data are often sampled synchronously with the apparent period so that folding is simply modulo a fixed number of samples, *e.g.*, 1024. In other cases hardware constrains the sampling interval to asynchronous values. Folding this data requires computation of the pulse phase with respect to the first sample, depositing the sample in the correct pulse phase averaging 'bin', and incrementing a counter that keeps track of the additions in each bin for subsequent normalization.

The apparent period is predicted from previous estimates of the pulsar parameters and an ephemeris of the earth's motion (see section 6). The precision required is such that the smearing of the pulse during the multi-minute averaging interval is significantly less than the arrival-time estimation error expected for each profile.

The reading of the observatory time standard at the time of the first sample of each profile is recorded. The estimation of the arrival time of the first pulse following this time is discussed in

H. Ögelman and E. P. J. van den Heuvel (eds.), Timing Neutron Stars, 3–16.

section 2.4. In some observations each profile is started at a fixed phase within the apparent pulse period. In other cases observations begin at a fixed time such as an even 10s, or even at a random time.

2.2. Differential Dispersion Removal

Dispersion of pulsar signals by thermal electrons in the interstellar, and interplanetary, media must be removed from the observed bandwidth of radio signals to obtain a desired resolution. Alternatively the bandwidth could be reduced to limit dispersion, but this reduces sensitivity as discussed in the next section. The time smearing that results from a given bandwidth b at a given radio frequency ν_o for a given column density of electrons, or dispersion measure DM, is

$$\Delta t = 8.3\ \mu s \frac{DM(\text{pc cm}^{-3}) b(\text{MHz})}{\nu_o^3(\text{GHz})}$$

For example, if $DM = 35$, $b = 1$, and $\nu_o = 1.4$, then $\delta t = 100 \mu s$. If we want 128 bins per period, then these parameters would limit observations to periods in excess of 12.8 ms. Hankins and Rickett (1975) discuss signal processing techniques for improving resolution by dispersion removal.

An approach that allows high time resolution and wide total bandwidth uses a multi-bandwidth receiver. Many narrow channels defined by a bank of filters are sampled and synchronously averaged as described above. The relative dispersion between these channels is removed with respect to a fiducial channel in post-observing analysis. The center frequency of the fiducial channel becomes the effective frequency of the observation. The center of the band is recommended. Rawley (1986) constructed a bank of signal averagers that allow each filter bank output to be independently averaged for precise removal of dispersion.

At Berkeley we have developed an alternative approach which uses a digital correlator for the multichannel analyzer. The output of the correlator is synchronously averaged just as with the filter-bank approach. In post-processing we fourier transform the pulse-phase resolved correlation functions into the frequency domain before dispersion removal. The digital correlator has the advantages of bandwidth agility and stability. Figure 1 illustrates the steps involved in this approach to pulsar timing. The digital correlator technique has been implemented both in our digital signal processor which is devoted to pulsar research, and at Arecibo in their general purpose, 40-MHz correlator.

Alternatively the dispersion may be removed in real-time by a hardware device. Orsten (1970) and Boriakoff (1973) describe devices that operate on a bucket-brigade principle. These devices are limited by their individual filter response times; Δt cannot be reduced below $1/2b$. Further effort at reducing the effects of dispersion requires processing of pre-detection data. The differential dispersion can be treated as a filter, and the inverse filter can be applied to the data. This is regularly done in chirped radar systems for chirps that are considerably less than those imposed by the interstellar medium. The inverse filter approach has been implemented both in software (Hankins 1971) and more recently in hardware using a surface acoustic wave filter (Hall, Hamilton and McCulloch 1985) and using a integrated circuit transversal filter (Hankins, Stinebring and Rawley 1987).

The dispersion can also be removed from a narrow band of signals by sweeping the local oscillator synchronously with pulse path in the frequency-time domain. This technique converts radio frequency into pulse phase. McCulloch, Taylor and Weisberg (1979) implemented this technique using a digital correlator. Biraud (1987 personal communication) in France is developing a similar system for millisecond pulsar timing.

2.3. Sensitivity

The sensitivity of a pulsar timing observation is dependent on both telescope and receiver parameters as well as pulsar parameters. The standard equation for the radiometer sensitivity is:

$$\Delta S(\text{Jy}) = F \frac{(T_r + T_s + T_b)}{(N_p N_s b \tau)^{0.5}} \frac{k}{A_g \eta},$$

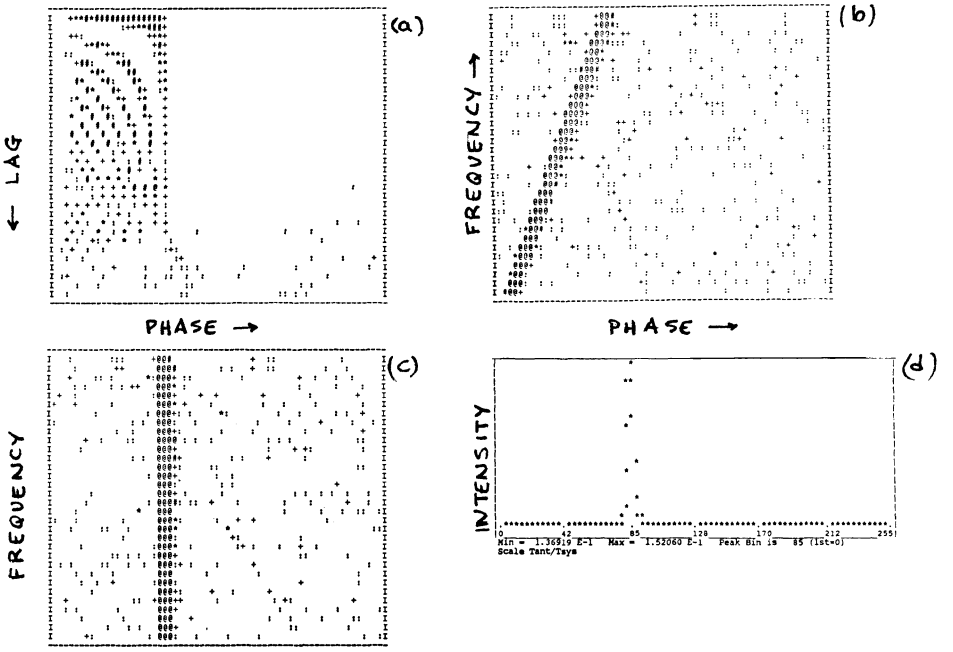

Figure 1 Data analysis for pulsar timing of PSR 1933+16 with the Berkeley correlator at NRAO Green Bank 300ft: (a) phase-resolved, time-averaged correlation function; (b) data after delay-radio frequency transform; (c) dispersion removed; (d) profile from average over radio frequency.

where F = clipping factor (1.2); T_r = receiver temperature (1-50K); T_s = spillover and scattering temperature(10-35K); T_b = background temperatures (1.7K sec(elev) + (1-10K) $\nu^{-2.7}$ + 2.7K); N_p = number of polarizations (2); N_s = number of spectral channels of width b (64); τ = integration time (250s); A_g = geometric area of telescope ($10^4 m^2$); η = aperture efficiency (0.5). The parameters suggested above lead to values of ΔS in the range from 0.1 mJy to 1.0 mJy.

Pulsar flux densities are normally quoted in terms of the equivalent continuum flux density $< S >$. The arrival-time error is roughly equal to the pulse width W divided by the signal-to-noise ratio of the pulse peak detection when optimally sampled. The pulse peak is then $< S > P/W$, where P is the pulse period. The signal-to-noise ratio uses the radiometer equation above with the integration time reduced by W/P. The resulting arrival-time error is:

$$\Delta t = \frac{W^{1.5} \Delta S}{P^{0.5} < S >} .$$

The strong dependence of δt on W is reduced when the resolution of an observation is dispersion limited owing to the dependence of δS on the channel bandwidth which is determined by the resolution.

2.4. Time-of-Arrival Estimation

The next step in the analysis of timing data is estimation of the pulse arrival time within the averaged and dedispersed profile, typically an array of 64-1024 numbers. This step is usually accomplished by cross-correlation of the observed profile with a template profile. Estimation of the maximum of the cross-correlation function using a polynomial fitting algorithm gives the delay offset of the profile with respect to the template. This procedure is equivalent to a Chi-squared minimization between

the template model and the observation, and is an example of the matched filter approach to signal estimation. The template is formed iteratively from the observations themselves. A delta function or triangle template can be used to make the initial period estimates; then the period estimate can be used to accurately phase individual observations to create a nearly noise-free template. Alternatively the pulse waveform can be modeled by a set of components; this is particularly useful for profiles that depend strongly on radio frequency owing to interstellar scattering (Rankin *et al.* 1970 and section 5.1 below).

An equivalent approach is to work with phases of the fourier components of the pulse profile. The phases, when corrected for the structure phase by subtracting the corresponding template phase, can be weighted and averaged to estimate the arrival time. Although this approach is equivalent to the cross-correlation technique (Backer 1985), there are some operational advantages (Rawley 1986).

The time offset determined in the analysis discussed above is then added to the start time of the first sample to obtain the observatory, or topocentric, arrival time. The offset between the first sample and some fiducial mark on the template profile must be added for accuracy and specificity. It is advisable to add an offset of an integral number of periods equal to about half the integration time to refer the observation to the midpoint just as the frequency was referred to the middle of the band.

2.5. Pulse Profile Stability

The discussion in the preceeding sections ignores the fact that pulsar emission is very erratic from one pulse to the next. Many time scales of variations exist (see summary in Manchester and Taylor 1977). The average pulse profile reaches a stable, reproducible form when the average extends over hundreds of pulse periods. This stability is essential for measurement of the stellar rotation with precisions reaching 0.001 periods or less. The reproducibility of the pulse profile patterns in each pulsar require a stable system of currents that are responsible for the radio emission.

Several authors have investigated the how the individual pulses approach the stable profile that is used in timing stellar rotations (Helfand, Manchester and Taylor 1975, Downs and Krause-Polstorff 1986). Figure 2 demonstrates the rapid decrease with averaging time of the mean-square deviation of pulse averages from the ensemble average.

3. 'TIME' CORRECTION

3.1. Atomic Time and Terrestrial Time

Our observatory arrival time are ultimately referred to a terrestrial standard atomic time. The atomic time standard is defined by

'The second is the duration of 9,192,631,770 periods of the radiation corresponding to the transition between two hyperfine levels of the ground state of the Cesium-133 atom.' (13th CGPM 1967).

Guinot (1988) has recently summarized the development of International Atomic time (TAI). This standard is an ensemble average of the individual realizations of atomic time (AT) at standards laboratories around the globe. The weights given to each vary according to an assessment of their stabilities. Some laboratories operate a bank of commercial Cesium clocks and take the ensemble average to define their local AT scale. Adjustments are made based on comparison with TAI. Other laboratories have in addition to a cesium clock bank a primary standard so that they can realize the standard given in the above definition to within a measurable tolerance.

The comparison between the scales at various standards laboratories requires a correction for relativistic effects (Ashby and Allan 1979). The reduction is to mean sea level of the equipotential geoid. The proposed nomenclature for this scale is evolving from Terrestrial Dynamic Time (TDT) to simply Terrestrial Time (TT) (Guinot and Seidelman 1988).

3.2. Time Transfer

The comparison of atomic time scales between standards laboratories and the use of an atomic time at a remote site requires a system of time transfer. There are a number of systems for time transfer.

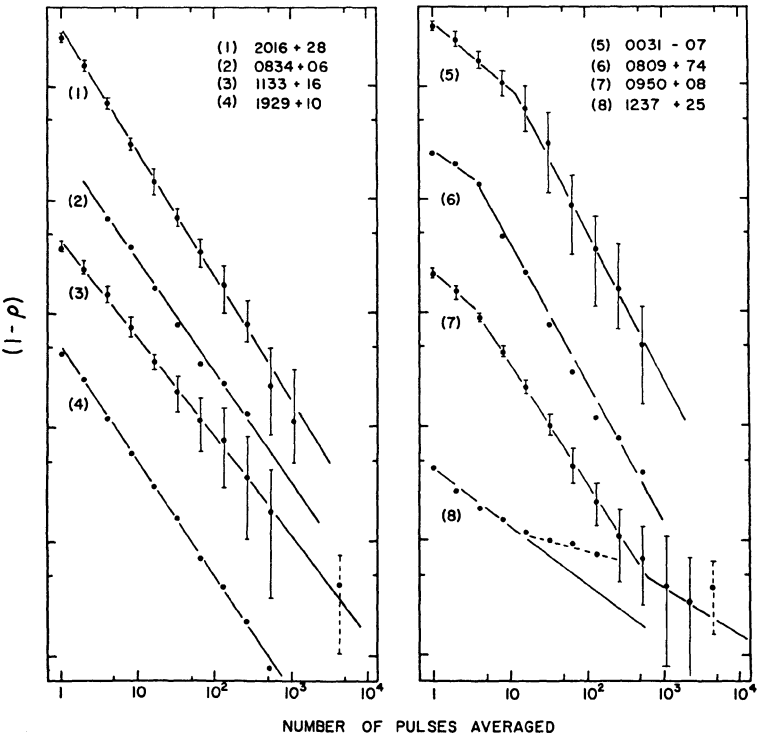

Figure 2 Stabilization of profile with increasing integration time (from Helfand *et al.* 1975).

Each has a different accuracy or other limitation. These systems are discussed in NBS Monograph 140 (1974).

In the US millisecond-level time transfer is done using HF transmissions of WWV from Ft. Collins, CO, and WWVH from Hawaii at 2.5, 5, 10, 15 and 25 MHz. Signals propagate by line of sight and by reflection off the ionosphere over distances of 1000's of kilometers.

The US Navy maintains cesium standards at the transmission sites of the LOng RAnge Navigation C system (LORAN C) around the globe. These signals at 100 kHz propagate up to 1500 km as surface waves and provide microsecond level time transfer.

The most recent development in time transfer is the Global Positioning Satellite system (Allan *et al.* 1985). These US DoD navigation satellites have cesium clocks on board. The orbital period of the satellites is about 24 hours, and the plan is for a web of 18 satellites circling the globe. The time information from these clocks is transmitted at frequencies near 1.5 GHz. The epochs and rates of the individual cesium clocks are monitored at the standards laboratories so that a extrapolated correction can be sent up to the satellites for transmission. Time is transferred at the level of 100 ns by this means. If a given satellite is observed by two parties simultaneously, then time can be transferred from one site to the other at the level of 10 ns. This 'common-view' technique requires precise application of relativistic principles (Allan, Weiss and Ashby 1985).

3.3. Barycentric Time

The time scale kept by an earth-based clock does not flow uniformly with respect to an external observer owing to the combined effects of gravitational redshift and time dilation. The elliptical

orbit of the earth leads to a variation of the epoch of an earth clock with respect to an external observer with an amplitude of 1.6 ms and a period of one year. The corresponding variation that results from the moon pulling the earth in and out of the solar potential has an amplitude of 0.5 μs and a period of about 29 days.

Barycentric Dynamical Time (TDB) is defined to remove these periodic variations that result from relativity (USNO 1984, Chandler 1985, Backer and Hellings 1986). The time scale that results is that of a clock in a circular orbit about the sun at one astronomical unit. This definition is chosen so that TDB runs at nearly the same rate as TDT, and has only small deviations in epoch, *i.e.*, much less than 1.6 ms. For the pulsar timing analysis a cleaner definition would be to define a time scale that removes the solar system effects completely (Backer and Hellings 1986). TDB effectively does this since the difference between TDB and a true clock at rest in the barycenter of the solar system is a uniform rate which can be absorbed into the definition of the second.

Operationally the conversion from TDT to TDB is done by an ephemeris for time similar to the ephemeris for position that will be discussed in the next section. There is no conceptual difficulty is this process – it is a straightforward application of the equivalence principle and special relativity that can be performed with adequate precision for pulsar observations. The differential rate that includes the effects of all solar system masses and motions is first integrated to give the difference between the true barycentric clock and TDT. Then a linear term that represents the mean rate is removed to leave the periodic terms. The interval over which the linear term is removed is presently a matter of choice: 100 years (Hellings 1985) or 59 years which is near twice Saturn's period and five times Jupiter's (Chandler 1985). Fairhead (1987) has developed an analytic approach applicable over a few thousand years.

3.4. Stability

Observations of PSR 1937+21 now rival the stability of atomic clocks over intervals of a year or more – 10^{-14} or 0.3μs over one year (Allan, Ashby and backer 1985; Rawley *et al.* 1987). This topic will be discussed at further length in the lecture by Taylor. The stability of atomic time scales will not limit the timing of an array of millisecond pulsars since they can be compared to each other. This is discussed below in section 8.

4. 'SPACE' CORRECTION

4.1. Earth Ephemerides

After correcting the pulse arrival time to TDB we next want to correct it to an inertial frame, the solar system barycenter. Two ingredients are required – the celestial coordinates of the source and the instantaneous location of the telescope. The dot product between the unit vector to the source and the telescope position is then added to the arrival time to obtain the barycentric arrival time. Two groups, one at the Harvard-Smithsonian Center for Astrophysics and one at the Jet Propulsion Laboratory, provide ephemerides of the earth's position, and velocity that can be used for this correction.

The correction from the earth's center to the telescope requires the telescope's geocentric coordinates and a simple model of the earth's motion. This correction is identical to the delay calculated in VLBI observations although orders of magnitude less precision is required. If observations from different observatories are to be compared at the microsecond level, then one must specify both the fiducial point on the pulse and the reference point at the telescope. The telescope reference point used in VLBI is the intersection of the axes (Thompson *et al.* 1986; p. 95).

4.2. Radio Astrometry

The space correction requires precise coordinates of the pulsar. These are derived in the parameter fitting process discussed below. The coordinate frame is inertial since the ephemeris of the earth's motion is given in an inertial reference frame. The common reference frame of radio interferometry, B1950.0–B for Besselian, is not inertial. The terms of elliptical aberration (USNO 1984) are required

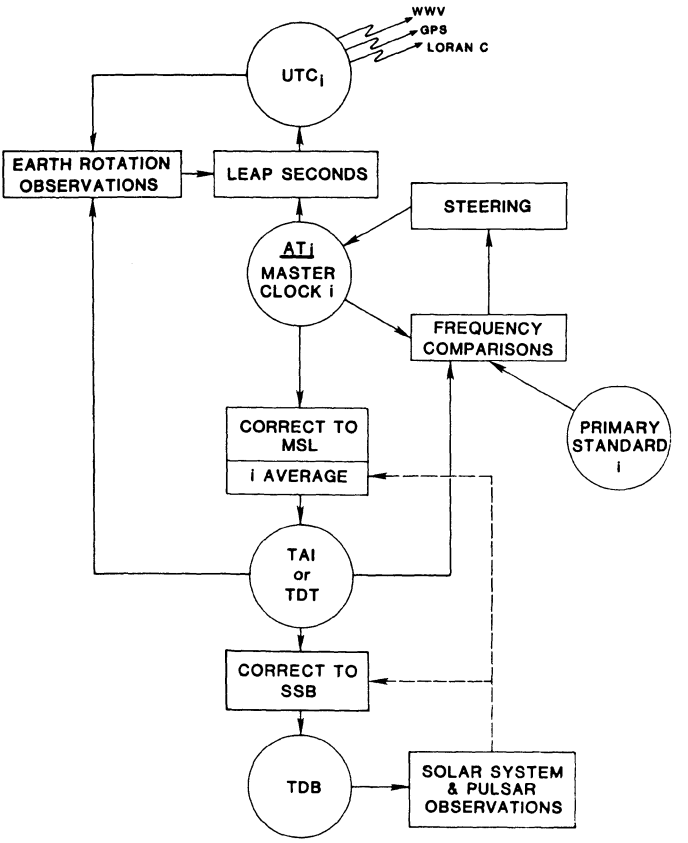

Figure 3 Connection between time scales (from Backer and Hellings 1986).

to transform between the two systems. The choice for future precision efforts is to work in the J2000 system, J for Julian, which is allows a unified approach with both pulsar timing and radio interferometry.

4.3. Stability

The accuracy of the earth ephemeris is difficult to estimate since one is interested in the extrapolation of a many parameter fit to the earth's motion. The Earth-Mars distance was measured with a precision of 25 ns during the lifetime of the Viking mission. This data is fundamental to the development of the Earth ephemeris, and residuals to fits to the data provide an estimate of the accuracy of ephemeris. Reasenberg *et al.* (1979) show residuals that have a rms of about 75 ns over a 14-month interval. The ephemeris correction stability is discussed by Hellings and by Chandler in Allan, Ashby and Backer (1985).

5. 'PROPAGATION' CORRECTION

5.1. Plasma Dispersion and Turbulence

Pulsar signals are dispersed by the column density of electrons between the pulsar and the earth.

$$t_d = 0.00415\text{s}\ \nu(\text{GHz})^{-2} DM(\text{pc cm}^{-3})$$

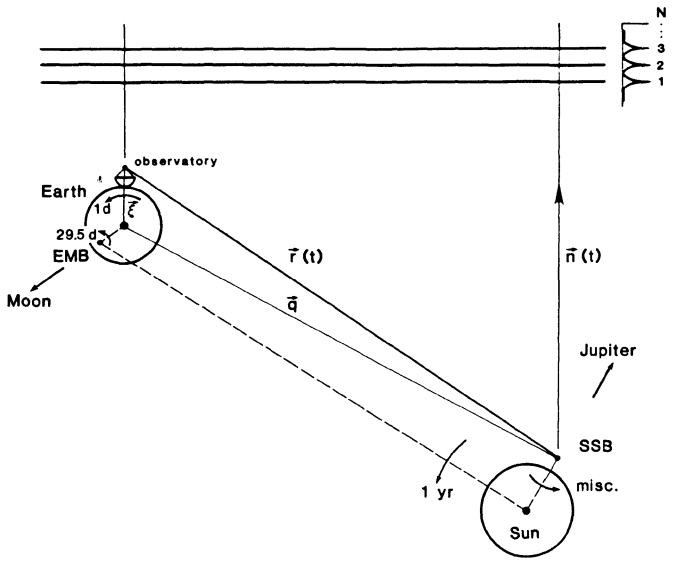

Figure 4 Space correction of telescope arrival time to the solar system barycenter (from Backer and Hellings 1986).

Furthermore turbulence in this plasma leads to diffractive and refractive propagation effects. Measurements over multiple radio frequencies, *e.g.*, 400 MHz, 700 MHz and 1400 MHz, can be used to determine the instantaneous column density of electrons so that the pulse arrival time can be extrapolated to infinite frequency. The observing frequency is the observatory value corrected by the doppler shift of the moving earth. Propagation delays in the solar wind can be significant; the column density from 1 e cm^{-3} over 1 AU leads to a delay of 0.5 μs at 1.4 GHz. Foster and Cordes discuss the removal of the effects of propagation in a turbulent medium later in this proceedings.

5.2. Relativistic Delay

The photons from a pulsar also suffer a relativistic delay as they traverse the solar potential. The additional delay is 135 μs when the signal passes by the limb of the sun compared to an observation six months later. The delay falls logarithmically with

$$c\Delta t = \frac{GM}{c^2} \ln(1 + \cos\theta)^{-1}$$

where θ is the heliocentric angle between the pulsar and the earth. In a globular cluster there are sizeable delays from passing the nearest stars, but the effects are small and monotonic, and cannot be distinguished from a period derivative.

6. PULSAR PARAMETER ESTIMATION

6.1. Least-Squares Analysis of Residuals

A set of observations must be treated in stages of slowly increasing data length to determine the pulse parameters. At each stage one uses the minimum number of parameters to model the arrival times without period ambiguity and within the experimental errors. Fractional period phase residuals from the model are analyzed in a least-squares fitting procedure to determine improved model parameters. In some cases one must start with estimates of the period from separate observations.

6.2. Rotation Model

The simplest model for a rotating neutron star consists of an initial phase, a period and a period derivative. In a few cases a second derivative can be determined. The model for the phase residuals is a simple power series:

$$\phi(t) = \phi_0 + \Omega\, t + \dot{\Omega}\, t^2/2 + \ddot{\Omega}\, t^3/6,$$

where Ω is the rotation frequency. The detection of a second derivative allows an estimate of the 'braking index' n, $\dot{\Omega}^2/\Omega\ddot{\Omega}$. The braking index is 2.5-2.8 for the three pulsar with measured values of $\ddot{\Omega}$; the most recent determination is by Manchester, Durdin and Newton (1985). An index of 3.0 obtains if the decelaration torque is pure magnetic dipole radiation.

6.3. Astrometric Parameters

The celestial coordinates of a pulsar are required to do the space correction. The 'lever arm' of the space correction is 1 AU, or 500 s. If microsecond precision is required, then the celestial coordinates must be known or determined with a precision of 2 nanoradians, or 0.4 milliarcsec. This is sufficient to measure a proper motion of 2 km s^{-1} at a distance of 1 kpc in one year. Four parameters are then required to specify the pulsar's celestial position: an initial right ascension and declination, and a proper motion in right ascension and declination.

The precision that is possible with millisecond pulsars can only be matched by the precision in the solar system ephemerides that incorporate modern radar measurements of planetary orbits (Rawley, Taylor and Davis 1988). Radio interferometry has only reached a precision of around 5 nanoradians, for a limited number of strong, compact quasars, although recently the resolution has been pushed to 0.3 nanoradians with VLBI measurements at 100 GHz.

The comparison between positions derived from timing and interferometer measurements has led to some puzzles (Fomalont *et al.* 1984; Backer *et al.* 1985; Bartel *et al.* 1985). Part of the problem is that the pulsar positions are corrupted by low-frequency timing noise. Part of the problem may result from the use of the out-of-date B1950.0 conventions in radio interferometry that include old constants for precession and nutation. Rawley, Taylor and Davis (1988) question the inertial character of the CfA ephemeris. More work needs to be done within the modern J2000 system and using the most stable pulsars to clear up this issue.

6.4. Dispersion Measure

Observations with multiple frequencies allow a solution for the dispersion measure by fitting for a quadratic arrival time with radio frequency. Care must be taken in obtaining the true dispersion when the pulse shape changes with radio frequency.

7. ROTATION NOISE

7.1. Spectral Decomposition

The phase residuals after a model fit for the parameters discussed above are not always consistent with white noise from measurement errors. In many cases the pulsar's spin displays instabilities. The deviations of phase from the model are often no more than 0.1 rotation periods. The spectrum of these instabilities, $\delta t/t$, can be characterized by a power-law index (Thompson *et al.* 1986, section 9.4). If the torque on the star varied randomly on a short time scale, then the phase residual spectrum would have a slope of -2. Other processes have been discussed with flatter slopes. Figure 5 displays timing residuals from Cordes and Downs (1985) for PSRs 1237+25 and 1929+10 that are characterized by power spectrum indices of 2 (white phase noise) and 0 (white frequency noise), respectively.

7.2. Activity Parameter

In cases such as PSR 1929+10 mentioned above there is insufficient data to determine a reliable spectrum. Cordes and Downs (1985) have introduced the concept of an activity parameter–a single

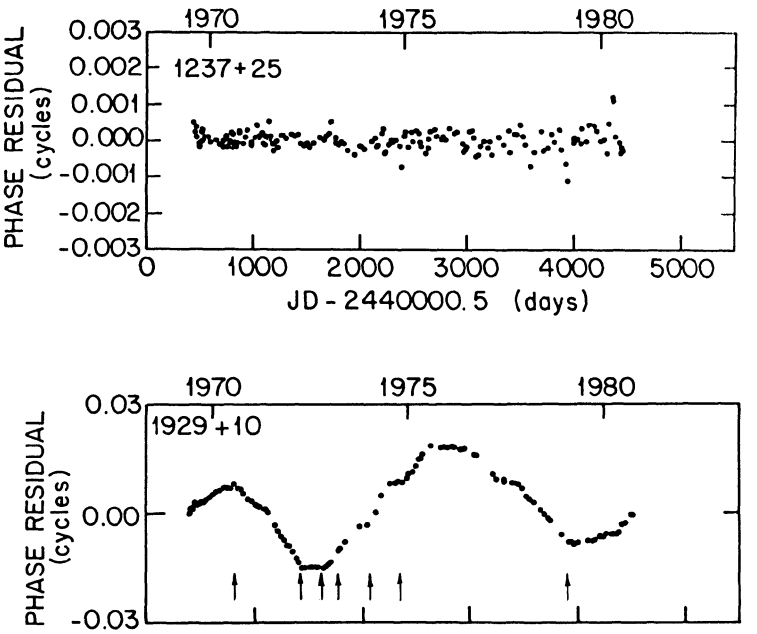

Figure 5 Timing residuals for two pulsars (from Cordes and Downs 1985).

variance statistic that takes the logarithm of the ratio between the intrinsic timing noise residual (σ, in seconds) for any object and the corresponding statistic, determined over the same time interval, for the Crab pulsar.

$$\text{Activity } A = \log_{10}\left[\frac{\sigma_{TN}(\text{star}, t)}{\sigma_{TN}(\text{Crab}, t)}\right],$$

$$\sigma_{TN}(\text{Crab}, t) = 6.8\text{ms}\left(\frac{t}{1000\text{ d}}\right)$$

Cordes and Downs demonstrate a correlation between A and the period derivative $\dot{P}$.

7.3. Glitches

The most dramatic discrepancies between the model and the observations occur when suden changes in the period and period derivative–glitches–occur. These are now seen in 5 pulsars: 0355+54 (Lyne 1987; 0531+21, the Crab; 0833-45, Vela; 0525+21; 1951+32, CTB80 (below). McKenna also reports several new pulsars with glitches in this proceedings. The magnitude of the changes range are $10^{-6 \text{ to } -9}$ in $\delta P/P$ and $10^{-1 \text{ to } -3}$ in $\delta\dot{P}/\dot{P}$. Smaller less dramatic glitches also occur (see Fig. 5: arrows in PSR 1929+10 data indicate small discontinuities in phase). The analysis and interpretation of these events in the life of some neutron stars is beyond the scope of this introductory lecture, but is discussed elsewhere in these proceedings.

8. RECENT RESULTS

8.1. PSR 1951+32 in CTB80

We began timing the pulsar found in the radio nebula CTB80 shortly after its discovery, or uncovery, in July 1987 (Kulkarni *et al.* 1988; Fruchter *et al.* 1988). Observations are continuing at the Arecibo

Observatory with the time shared between 430 MHz and 1400 MHz. A new timing system with the 40-MHz correlator was developed. The data were sparsely sampled in 1987 and more frequently sampled in 1988. At the time of the NATO ASI we knew that the rotation of the CTB80 star was not stable. Either it had one of the highest activity parameters of all pulsars, or it had undergone a glitch. Figure 6 demonstrates now that there was a glitch with a magnitude of 4×10^{-9} in $\delta P/P$. A full account of this event and the recovery of the star will be presented elsewhere by Foster, Backer and Wolszczan. The hopes that the star would be sufficiently stable to determine a proper motion from timing have been dropped.

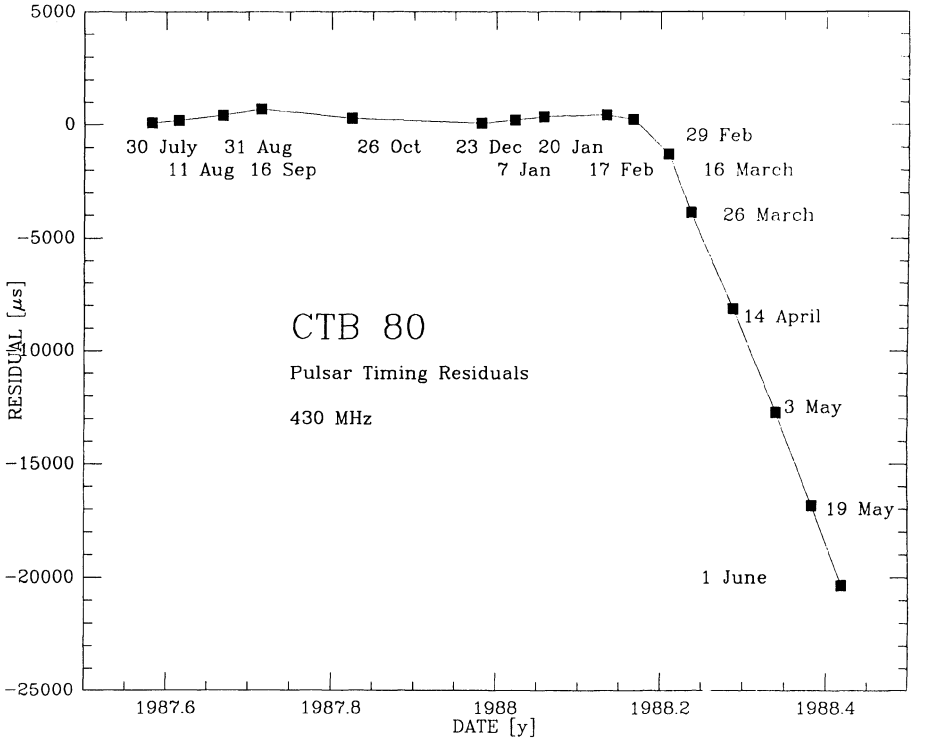

Figure 6 Residuals from timing PSR 1951+32 at Arecibo by Foster, Backer and Wolszczan. Fit was performed on data up to 17 February 1988.

8.2. The Globular Cluster Pulsars

In late 1986 we learned about the strong polarization of the point source in the globular cluster M28 (Erickson *et al.* 1987). This set in motion an effort to combine data from one of the largest radio telescopes, at Jodrell Bank, with the largest capacity data analysis procedure, that of Middleditch at Los Alamos. A 3.1-ms second pulsar was found (Middleditch *et al.* 1987). In the year following this uncovery, many globular cluster pulsar searches have been conducted. There are now a total of 5 pulsars in 4 globular clusters. These are: 0021-72A in 47TUC (P=4.479 ms)–Ables *et al.* 1988; 0021-72B in 47TUC (P=6.127 ms)–Ables *et al.* 1988; 1620-26 in M4 (P=11.076 ms)–Lyne *et al.* 1988; 1821-24 in M28 (P=3.054 ms)–Lyne *et al.* 1987; and 2127+11 in M15 (P=110.665)–Wolszczan *et al.* 1988. These neutron stars are concentrated within one core radius of the cluster centers, which is similar to the Xray objects (Grindlay *et al.* 1983). Verbunt discusses these pulsars in more detail in these proceedings.

The first period derivative of a globular cluster pulsar has been determined by Foster *et al.* (1988). The value for PSR 1821-24 leads to a spindown age of only 30 My. This is surprisingly short given the nominal age of clusters, and the likely age of the millisecond pulsars. The authors dismiss the influence of a gravitational encounter as the dominant source of the period derivative; an acceleration leads to a period derivative of aP/c.

8.3. The Pulsar Timing Array

The globular cluster millisecond pulsars have provided us with objects distributed across the sky. The timing observations of this array of pulsars can be used to solve for the uncertainties in both atomic time and in the location of the earth. The time term has a monopole signature on the sky–all timing residuals are affected by a constant. The space term has a dipole signature–there is an instantaneous vector error in the assumed earth position and therefore a dipole-like correlation in the barycentric correction. Pulsar timing array data can be used to look for a stochastic background of gravitational wave radiation (Detweiler 1979). This background will have a quadrupole correlation that can be detected in the timing array data without the limitation of the time and space uncertainties. Romani discusses this measurement further in these proceedings. We have started a Pulsar Timing Array experiment using the fully steerable 140-ft telescope at NRAO Green Bank. The first results from this are displayed in Figure 6. With improved hardware and longer time spans we expect the Pulsar Timing Array data to reach a level of 10^{-8} in the energy density of gravitational radiation relative to the closure density.

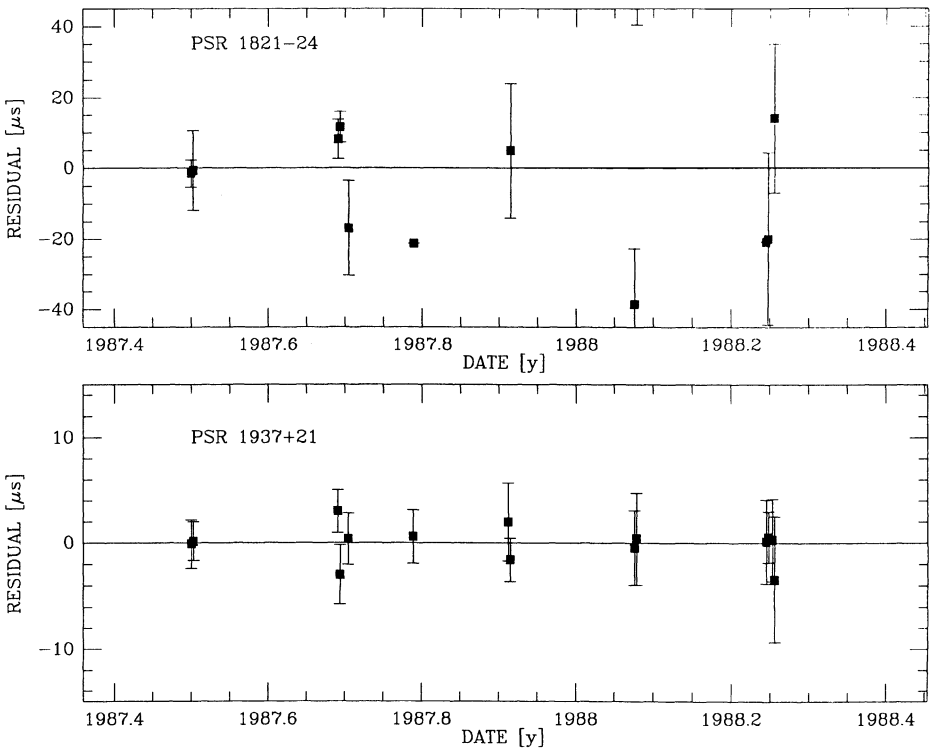

Figure 7 Residuals for two pulsars in Pulsar Timing Array experiment at the NRAO 140ft telescope.

ACKNOWLEDGEMENTS

The author wishes to thank the organizers for their support, and acknowledges the support of NSF grant AST-8719094.

REFERENCES

Ables, J. G., Jacka, C. E., McConnell, D., Hamilton, P. A., McCulloch, P. M., and Hall, P. J. 1988, *IAU Circ. No.* 4602.

Allan, D. W., Weiss, M. A., and Ashby, N. 1985, *Science*, **228**, 69.

Allan *et al.* 1985, *IEEE Trans. Instr. Meas.*, **34**,118.

Allan, D. W., Ashby, N., and Backer, D. C. 1985, NBS Time and Frequency Division Special Publication.

Ashby, N., and Allan, D. W. 1979, *Radio Sci.*, **14**, 649.

Backer, D. C. 1985, in Allan, Ashby and Backer (1985).

Backer, D. C. and Hellings, R. W. 1986, *Ann. Rev. Astron. Ap.*, **24**, 537.

Backer, D. C., Fomalont, E. B., Goss, M. M., Taylor, J. H., and Weisberg, J. M. 1985, *Astron. J.*, **90**, 2275.

Bartel, N., Ratner, M. I., Shapiro, I. I., Capallo, R. J., Rogers, A. E. E., and Whitney, A. R. 1985, *Astron. J.*, **90**, 318.

Biraud, F. 1988, personal communication.

Boriakoff, V. 1973, Ph. D. Thesis, Cornell University, Ithaca.

Chandler, J. F. 1985, see Allan, Ashby and Backer (1985).

Cordes, J. M., and Downs, G. A. 1985, *Ap. J. Suppl.*, **59**, 343.

Detweiler, S. 1979, *Ap. J.*, **234**, 1100.

Downs, G. S., and Reichley, P. E. 1983, *Ap. J. Suppl.*, **53**, 169.

Downs, G. S., and Krause-Polstorff, J. 1986, *Ap. J. Suppl.*, **62**, 81.

Davis, M. M., Taylor, J. H., Weisberg, J. M., and Backer, D. C. 1985, *Nature*, **315**, 547.

Erickson, W. C., Mahoney, M. J., Becker, R. H., and Helfand, D. J. 1987, *Ap. J. Lett.*, **314**, L45.

Fairhead, L. 1987, personal communication.

Fomalont, E. B., Goss, W. M., Lyne, A. G., and Manchester, R. N. 1984, *M.N.R.A.S.*, **210**, 113.

Foster, R. S., Backer, D. C., Taylor, J. H., and Goss, W. M. 1988, *Ap. J. Lett.*, **326**, L13..

Fruchter, A. S., Taylor, J. H., Backer, D. C., Clifton, T. R., Foster, R. S., and Wolszczan, A. 1988, *Nature*, **331**, 53.

Grindlay, J. E., Hertz, P., Steiner, J. E., Murray, S. S., and Lightman, Ap. J. Lett. 1984, *Ap. J.*, **282**, L13.

Guinot, B. 1988, *Astron. Ap.*, **192**, 370.

Guinot, B., and Seidelman, P. K. 1988, *Astron. Ap.*, in press.

Hall, P. J., Hamilton, P. A., and McCulloch, P. M. 1982, *J. E. E. E. Austr.*, **2**, 150.

Hankins, T. H. 1971, *Ap. J.*, **169**, 487.

Hankins, T. H., and Rickett, B. J. 1975, *Methods in Comp. Phys.*, **14**, 55.

Hankins, T. H., Stinebring, D. R., and Rawley, L. A. 1987, *Ap. J.*, **315**, 149.

Helfand, D. T., Manchester, R. N., and Taylor, J. H. 1975, *Ap. J.*, **198**, 661.

Hellings, R. W. 1985, see Allan, Ashby and Backer (1985).

Kulkarni, S. R., Clifton, T. R., Backer, D. C., Foster, R. S., Fruchter, A. S., and Taylor, J. H. 1988, *Nature*, **331**, 50.

Lyne, A. G. 1987, *Nature*, **326**, 569.

Lyne, A. G., Brinklow, A., Middleditch, J., Kulkarni, S. R., Backer, D. C. , and Clifton, T. R. 1987, *Nature*, **328**, 399.

Lyne, A. G., Biggs, J. D., Brinklow, A., Ashworth, M., and McKenna, J. 1988, *Nature*, **332**, 45.

Manchester, R. N., and Taylor, J. H. 1977, *Pulsars*, [W. H. Freeman : San Francisco].

Manchester, R. N., Durdin, J. M., and Newton, L. M. 1985, *Nature*, **313**, 374.

McCulloch, P. M., Taylor, J. H., and Weisberg, J. M. 1979, *Ap. J. Lett.*, **227**, L133.

Middleditch, J., Lyne, A. G., Brinklow, A., Backer, D. C., Clifton, T. R., and Kulkarni, S. R. 1987 *IAU Circ. No. 4401.*

National Bureau of Standards 1974, *Monograph No. 140.*

Orsten, G. S. F. 1970, *Rev. Sci. Instru.*, **41-7**, 957.

Rankin, J. M., Comella, J. M., Craft, H. D., Richards, D. W., Campbell, D. B., and Counselman, C. C. 1970, *Ap. J.*, **162**, 707.

Rawley, L. A. 1986, Ph. D. Thesis, Princeton University, Princeton.

Rawley, L. A., Taylor, J. H., and Davis, M. M. 1988, *Ap. J.*, **326**, 947.

Rawley, L. A., Taylor, J. H., Davis, M. M., and Allan, D. W. 1987, *Science*, **238**, 761.

Reasenberg, *et al.* 1979, *Ap. J. Lett.*, **234**, L219.

Thompson, A. R., Moran, J. M., and Swenson, G. W. 1986 *Interferometry and Synthesis in Radio Astronomy*, [Wiley : NY].

U.S. Naval Observatory 1984, *The Astronomical Almanac.*

Wolszczan, A. S., Middleditch, J., Kulkarni, S. R., Backer, D. C., and Fruchter, A. S. 1988, *IAU Circ. No.* 4552.

TIMING BINARY AND MILLISECOND PULSARS

J. H. Taylor
Joseph Henry Laboratories and Physics Department,
Princeton University,
Princeton, NJ 08544 USA

ABSTRACT. This tutorial lecture outlines the essentials of making and analyzing timing observations of binary and millisecond pulsars. Many of the necessary procedures are, of course, similar to those used for slow, single pulsars. However, achieving the best attainable timing accuracy for millisecond pulsars requires much tighter tolerances on observing and data-processing procedures, and the presence of orbital motion qualitatively complicates both data acquisition and analysis. In return for adequate diligence in these matters, an observer gains access to a much richer set of measurables than are available for ordinary pulsars. Binary pulsars provide the only experimental handles on the masses of non-accreting neutron stars, and the parameters of their orbits and characteristics of their companion stars provide unique clues on the origin and evolution of the systems. In the most favorable circumstances, significant tests of fundamental physical laws are even possible. Timing data on millisecond pulsars turns out to be valuable for other reasons as well: because they are extremely stable clocks, these objects provide exquisite tools for a wide range of studies in fundamental astrometry, cosmology, gravitation physics, and metrology.

Don Backer has already given us a sound primer on radio pulsar timing techniques (Backer 1989). To review briefly, I will remind you that a typical observing procedure uses a setup like the one diagrammed in Figure 1, used by my colleagues and me at Arecibo Observatory over the past several years (Rawley, Taylor, Davis, & Allan 1987; Rawley, Taylor, & Davis 1988). Incoming signals from the telescope are amplified, converted to intermediate frequency, and passed through a "filter bank" spectrometer which analyzes the total accepted bandwidth into channels narrow enough that the observed pulse widths are not dominated by dispersive smearing. Synchronous signal averaging is used to accumulate estimates of a pulsar's average waveform in each of the spectral channels, using electronics under control of a small computer and accurately synchronized with the Observatory's time and frequency

H. Ögelman and E. P. J. van den Heuvel (eds.), Timing Neutron Stars, 17–26.

standard. A programmable synthesizer, whose output frequency is updated once a second in a phase continuous manner, compensates for variable Doppler shifts due to motions of the pulsar and the observatory. Integrated pulsar waveforms are recorded once every few minutes, together with appropriate time tags.

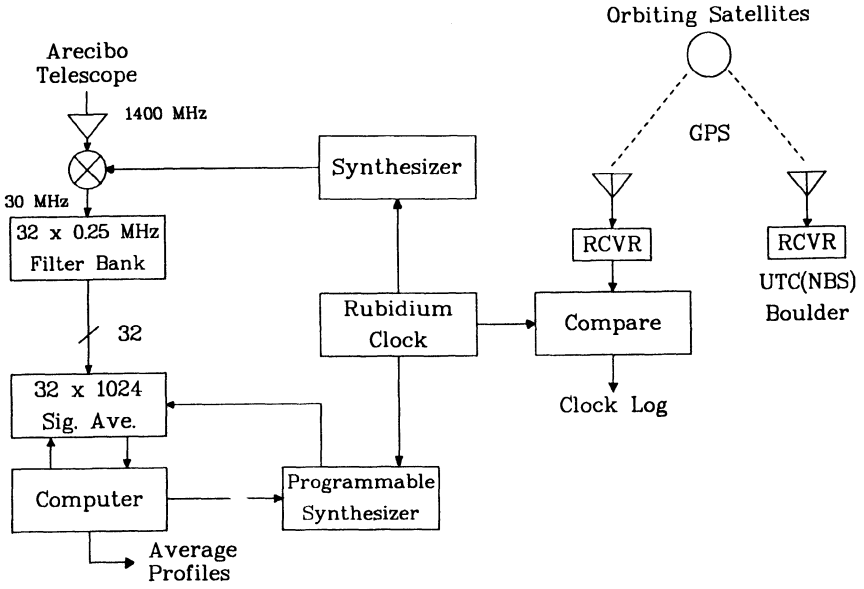

Figure 1: Block diagram of a pulsar timing system used for binary and millisecond pulsars at Arecibo Observatory.

Analysis of recorded profiles usually follows a series of steps similar to those listed in cookbook Recipe 1 on the next page. The first step after observing involves "template matching" to determine the phase of each recorded profile relative to the start of its integration. This process can be carried out by cross-correlation in the time domain, or by an equivalent procedure in the Fourier transform domain. There may be reasons of operational convenience to prefer one of these methods over the other; more importantly, there are significant reasons to prefer the Fourier transform approach when the signal-to-noise ratio is high and the achievable timing uncertainty is much smaller than the interval at which the waveform has been sampled (Rawley 1986). (These conditions are true, for example, in our observations of the millisecond pulsar 1937+21 at Arecibo.) After a phase offset has been determined, the corresponding time delay is added to the start time of the integration to yield a topocentric time of arrival, or TOA.

Recipe 1. Pulsar timing observations and analysis.

1. Observe average profiles at known UTCs.
2. Determine topocentric TOA's by template matching.
3. If necessary: remove dispersive delays, sum channels.
4. Apply clock corrections to yield TDT.
5. Transform to TDB at solar system barycenter.
6. Bootstrap a timing model (see Recipe 2 or 3).
7. Repeat from step (1) as often as possible.

$\Downarrow$

8. Output: α, δ, ϕ_0, P, $\dot{P}$; possibly also μ_α, μ_δ, $\ddot{P}$, and orbital parameters.

For a given pulsar, the optimum template or "standard profile" for use in the matching procedure is a high signal-to-noise version of the profile, generally observed with the same equipment but over a longer integration time. For pulsars too weak to give adequate signal-to-noise ratio in a single filter bank channel, the data in all channels can be summed (after shifting phases to account for the different dispersion delays at each frequency) and a single equivalent TOA determined.

An accurate time transfer system, using signals from satellites in the Global Positioning System, allows us to express all TOA's in terms of Coordinated Universal Time as maintained and distributed by the US National Bureau of Standards, or in terms of any of a number of other high-precision atomic time standards kept at national timekeeping laboratories around the world. An appropriately weighted average of these standards represents the best currently available approximation to an ideal implementation of terrestrial dynamical time, or TDT, and is the reference standard of choice for the most exacting observations.

A model capable of predicting pulse arrival times is most conveniently formulated in an inertial reference frame, for which the solar system barycenter is an adequate approximation. The necessary general relativistic transformation from TDT to barycentric dynamical time, or TDB, must be done with care (see Backer & Hellings 1986). The transformation depends on accurate knowledge of the pulsar's celestial coordinates, α and δ, and unambiguous numbering of the received pulses requires good knowledge of the pulsar period P and spin-down rate, $\dot{P}$. Since these quantities may be poorly known at the beginning—they are, after all, among the parameters one is trying to measure—the process necessarily requires an iterative "bootstrap" approach like that outlined in Recipe 2.

Recipe 2. Bootstrap procedure for timing single pulsars.

1. Collect data at various intervals—say 2 m, 10 m, 2 h, 1 d, 10 d, 3 mo, ...
2. Obtain least-squares estimates of P, α, δ, $\dot{P}$ (or a subset).
3. Inspect residuals for non-random appearance ($\Rightarrow$ evidence of mis-numbering of pulses across gaps in data).
4. Repeat, possibly adding or subtracting integers in the pulse numbering scheme, until *you've got it!*

One of the principal reasons that pulsar timing data can yield so much information is that the rotation phase of a non-accreting neutron star can be measured to within a small fraction of a turn, and predicted with similar accuracies over intervals as long as years. Therefore phase-coherent solutions are possible, spanning many years of observations and perhaps 10^8–10^{11} rotations of the neutron star. In such solutions the integer pulse number corresponding to each observed TOA is determined unambiguously.

When timing observations are begun for a new pulsar, the bootstrap procedure to reach the desirable phase-connected state of affairs is facilitated if data are collected at various intervals in rough geometric progression, with increments no more than a factor of 10 (see Recipe 2). The largest gaps between available TOA's will then be small enough that one should be able to extrapolate across them without pulse numbering ambiguities, or at worst with only a small range of integer values permitted. A least-squares solution can then be carried out to determine improved values of P and, when enough data are available, also α, δ, and $\dot{P}$. A plot of the post-fit residuals from the solution gives a clear indication of whether the pulses have been numbered correctly. Some trial and error may be required, but the correct solution is easily recognized when attained.

Three examples of post-fit residual plots are illustrated in Figure 2. These observations, made with the NRAO 92 m telescope at Green Bank by Dewey *et al.* (1988), were concentrated in nine observing sessions between January 1985 and May 1987. Each observing session lasted several days, and each of about 75 pulsars was observed for 5 to 10 two-minute integrations on one or more days in a session. Thus the data set for a given pulsar generally consists of TOA's with spacings of 2–20 minutes, 1–4 days, 15 days, and several months to 2.3 years. The residuals in the examples amount to a few milliperiods or less, and appear to be essentially random. Solutions like these typically determine P to 11 or 12 significant figures, $\dot{P}$ to an uncertainty $\sim 10^{-18}$, and the pulsar coordinates to within about 0.1″.

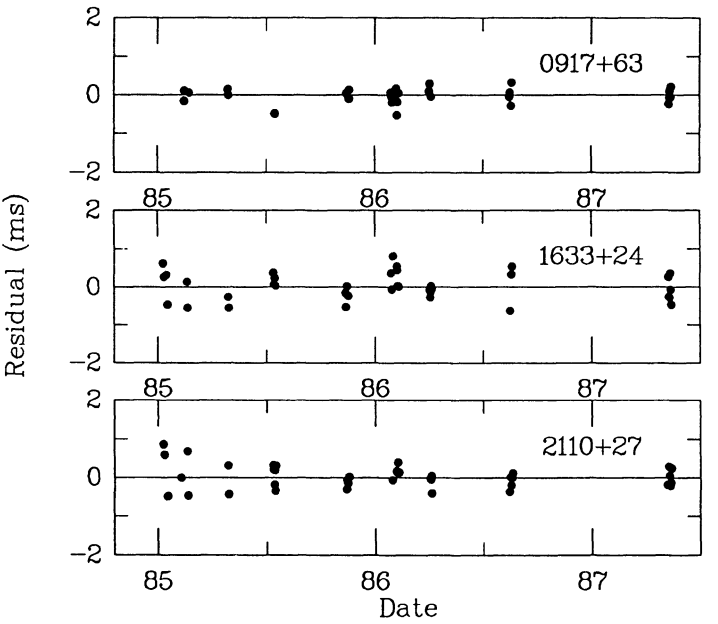

Figure 2: Plots of the post-fit residuals for timing observations of three pulsars (after Dewey *et al.* 1988). For clarity only a single datum is plotted for each observing day.

For binary pulsars the procedure is similar in concept, but a number of additional parameters are involved, including five elements of a Keplerian orbit and possibly observable general relativistic effects as well. In formulating the timing model an additional relativistic transformation is required, dependent on the orbital parameters, to convert from TDB to proper time at the pulsar. Since the orbital parameters are not known (even approximately) at the outset, the bootstrap procedure to attain a phase connected solution is usually much more difficult than with single pulsars.

A workable scheme that my colleagues and I have used to obtain phase connected solutions for 8 binary pulsars is summarized in Recipe 3. When initial timing observations suggest that the period of a pulsar is variable, we proceed to collect as many TOA's as possible. The data are separated into blocks no longer than $\sim$ 20 m and periods are computed for each block, reduced to the solar system barycenter. In principle a plot of these periods as a function of time should trace out the orbiting pulsar's velocity curve. In practice, however, the data are likely to be coarsely and irregularly sampled, and recognizing the orbital period may be very difficult.

An algorithm for determining the orbital period in such circumstances is out-

Recipe 3. Bootstrap procedure for timing binary pulsars.

1. Collect data: get TOA's and pulsar periods P_i at many epochs.
2. Determine approximate orbital period, P_b (see Recipe 4).
3. Incoherent solution: use P_i's to obtain least-squares estimates of P, $a_1 \sin i$, e, T_0, P_b, ω.
4. Phase-connected solution: use TOA's to obtain least-squares estimates of P, $a_1 \sin i$, e, T_0, P_b, ω, α, δ, $\dot{P}$, and possibly relativistic parameters.

lined in Recipe 4. Its equations contain nothing about Kepler's laws or the expected shapes of orbital velocity curves; the procedure works simply by seeking the smoothest possible dependence of observed period on computed orbital phase, consistent with the observations. When an approximate orbital period has been found, we use the (P_i, t_i) pairs to carry out a least-squares solution for the orbital elements (step 3, Recipe 3). Since there is no attempt to "connect phase" between the various independent measurements, pulse numbering ambiguities are not an issue. The orbital elements determined from this solution are then used as input values for a phase connected solution, which yields optimized estimates for all of the interesting parameters.

Recipe 4. Algorithm for finding a binary pulsar's orbital period, P_b.

1. Obtain solar-system barycentric periods P_i at many epochs t_i.
2. Set trial P_b to minimum reasonable value.
3. Compute orbital phases, $\phi_i = \mathrm{mod}(t_i/P_b, 1.0)$.
4. Sort list of (P_i, t_i, ϕ_i) triplets in order of increasing ϕ.
5. Compute $s^2 = \sum (P_j - P_{j-1})^2$, omitting any terms for which $\phi_j - \phi_{j-1} > 0.1$. ($j$ is the index after sorting).
6. Increment $P_b := [1/P_b - 0.1/(t_{max} - t_{min})]^{-1}$.
7. Repeat from (3) until maximum reasonable P_b is reached.
8. Choose the P_b that yielded the smallest normalized s^2.

The most complete and well documented model for analyzing binary pulsar timing data is that of Damour & Deruelle (1986), based on a highly accurate solution they developed for the general relativistic two-body problem. In addition to the

usual parameters for single pulsars and five Keplerian orbital parameters, my implementation of their model includes as many as six "post-Keplerian" parameters. As an example of its use, Table 1 presents the latest list of measured orbital parameters of the PSR 1913+16 system. Further details may be found in Weisberg & Taylor (1984) and references therein.

Table 1. Orbital parameters of PSR 1913+16.

Keplerian orbital elements	
Projected semimajor axis	$a_p \sin i = 2.341769(24)$ light sec
Eccentricity	$e = 0.6171311(14)$
Orbital Period	$P_b = 27906.981644(12)$ s
Longitude of periastron	$\omega_0 = 178.86372(29)$ deg
Julian ephemeris date of periastron, and reference time for P_b and ω_0	$T_0 = 2442321.4332075(9)$
Post-Keplerian parameters	
Mean rate of periastron advance	$\langle \dot{\omega}_0 \rangle = 4.22660(10)$ deg y^{-1}
Gravitational redshift and time dilation	$\gamma = 4.302(24)$ ms
Orbital period derivative	$\dot{P}_b = (-2.40 \pm 0.04) \times 10^{-12}$ s s^{-1}

Timing observations of binary pulsars have provided information that has been extremely useful in delimiting the range of possible evolutionary schemes for pulsars and neutron stars. I'll have no time in this lecture to discuss these matters further; some of the important ideas have already been outlined for us by Ed van den Heuvel (1989), and I have no doubt we'll be hearing more about them over the next few days. For a more detailed summary of results and some very recent work, see Taylor (1987) and Taylor & Dewey (1988).

In the remainder of this talk I will deal with some special issues relevant to timing millisecond pulsars. For these objects it is possible to measure TOA's with observational uncertainties well under a microsecond; consequently, to avoid contaminating good data by sloppy handling, and to extract the maximum possible information content, one must take extraordinary care in the data analysis. As an example of the quality of data obtainable, and to illustrate one particular type of observational problem that must be dealt with, Figure 3 illustrates post-fit residuals for the data on PSR 1937+21 that we have been acquiring at Arecibo Observatory since October 1984.

Both portions of Figure 3 are based on exactly the same data, analyzed in

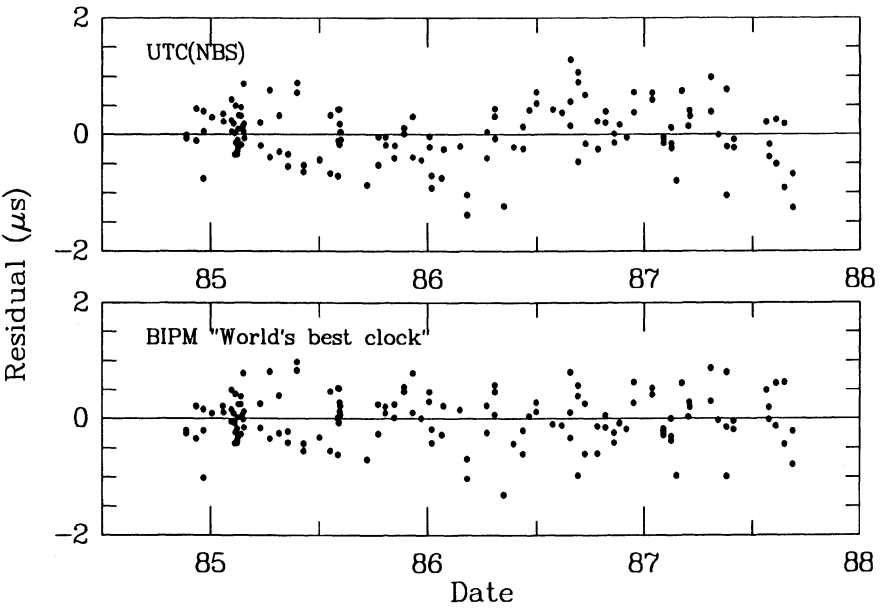

Figure 3: Post-fit arrival time residuals for PSR 1937+21 relative to UTC(NBS) (top) and to the BIPM "World's best clock" (bottom).

exactly the same way, except for using different time standards. For the upper portion of the Figure we used UTC(NBS), the version of Coordinated Universal Time distributed by the US National Bureau of Standards. This time scale, believed to be stable to within a few parts in 10^{14} over timescales of a year or so, is apparently not quite stable enough to serve as an adequate reference for this experiment. Neither, incidentally, is *any other* of the independent time standards maintained at timekeeping laboratories around the world. Some are a bit worse, and one or two appear to us to be a bit better—especially the one maintained by the Physikalisch-Technische Bundesanstalt in the Federal Republic of Germany—at least within our limited experience since late 1984. Significantly, we think, most of the slow, systematic wandering of the PSR 1937+21 residuals in the top panel of Figure 3 disappears when we use a weighted mean of of the world's best clocks (computed by the Bureau International de Poids et Measures in Paris) as the reference standard. Residuals from a such fit are shown in the lower panel of Figure 3.

People in the time-and-frequency business assure me that they have not been not standing still, and that better reference standards will be available Real Soon Now. In the meantime, we astronomers should not overlook the possibility of cre-

ing our own time standard by comparing TOA's from a number of millisecond pulsars. At present the next best pulsar with a substantial quantity of accumulated timing data is PSR 1855+09, which shows random residuals of about 2 μs rms after 2.3 years. Unfortunately, timing measurements with uncertainties in the sub-microsecond range have not yet been achieved for any pulsar besides PSR 1937+21—except for the very recently discovered PSR 1957+20, which Andy Fruchter will speak about shortly.

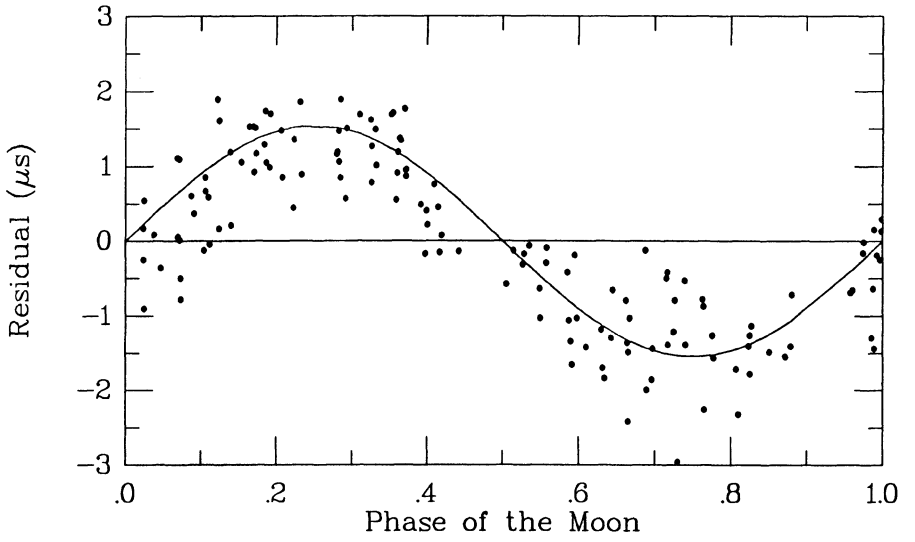

Figure 4: Post-fit arrival time residuals for PSR 1937+21, for a solution in which the monthly changes in gravitational redshift of terrestrial clocks was intentionally ignored. The smooth curve illustrates the omitted term in the time transformation.

I have already mentioned that in order to model the expected TOA's of any pulsar with the accuracies implicit in Figure 3, extraordinary care is required in the analysis procedure. An example of what can go wrong when a small effect is ignored is presented in Figure 4. For this solution we intentionally omitted the monthly cycle in the relativistic transformation from TDT to TDB. (All clocks on Earth run slightly slower when the Moon is full, because the Earth is deeper in the solar gravitational potential; furthermore, the magnitude of the Earth's total velocity changes with lunar phase, causing changes in time dilation.) In Figure 4 the residuals resulting from this omission are plotted as a function of phase of the moon, together with a curve corresponding to the omitted term. Interestingly, one can use this effect to perform Einstein's gravitational redshift test of the equivalence

principle. For the ratio of observed to expected monthly redshift effect, we obtain 1.04 ± 0.06 (Gelfand 1988).

There is little doubt that further examples of binary and millisecond pulsars will be found, and that timing observations of them—as well as continued timing observations of those already known—will continue to pay very worthwhile dividends.

REFERENCES

Backer, D. C. 1989, this volume.

Backer, D. C., & Hellings, R. W. 1986, *Ann. Rev. Astron. Astrophys.*, **24**, 537.

Damour, T., & Deruelle, N. 1986, *Ann. Inst. H. Poincaré (Physique Théorique)*, **44**, 263.

Dewey, R. J., Taylor, J. H., Maguire, C. M., & Stokes, G. H. 1988, *Astrophys. J.*, in press.

Gelfand, B. Y. 1988, unpublished Princeton University "Junior Paper."

Rawley, L. A. 1986, Princeton University Ph.D. thesis.

Rawley, L. A., Taylor, J. H., & Davis, M. M. 1988, *Astrophys. J.*, **326**, 947.

Rawley, L. A., Taylor, J. H., Davis, M. M., & Allen 1987, *Science*, **238**, 761.

Taylor, J. H., 1987, *The Origin and Evolution of Neutron Stars,* ed. D. J. Helfand and J.-H. Huang, Dordrecht: Reidel, p. 383.

Taylor, J. H., & Dewey, R. J., *Astrophys. J.*, in press.

van den Heuvel, E. P. J. 1989, this volume.

Weisberg, J. M., & Taylor, J. H. 1984, *Phys. Rev. Letters*, **52**, 1348.

FOURIER TECHNIQUES IN X-RAY TIMING

M. van der Klis,
EXOSAT Observatory,
Space Science Department of ESA,
ESTEC, Postbus 299,
2200 AG Noordwijk,
The Netherlands

ABSTRACT. Basic principles of Fourier techniques often used in X-ray time series analysis are reviewed. The relation between the discrete Fourier transform and the continuous Fourier transform is discussed to introduce the concepts of windowing and aliasing. The relation is derived between the power spectrum and the signal variance, including corrections for binning and dead time. The statistical properties of a noise power spectrum are discussed and related to the problems of detection (and setting upper limits) of broad and narrow features in the power spectrum. A "dependent trial" method is discussed to search power spectra consistently for many different types of signal simultaneously. Methods are compared to detect a sinusoidal signal, a case that is relevant in the context of X-ray pulsars.

1. INTRODUCTION

Fourier techniques are widely used in science and engineering, but problems of terminology and differing conventions hamper the flow of information between the various branches. Even within the field of neutron-star timing, radio-, X-ray and high-energy gamma-ray astronomers sometimes have difficulties to compare the techniques they routinely apply.

In the present paper an attempt will be made to explore some of the techniques that are commonly used in timing studies of neutron stars, and that refer to the detection of signals against a background of noise, in the language of the X-ray astronomer.

The regime that I will nearly exclusively be referring to is that of equidistantly binned timing data, the background noise of which is dominated by counting statistics. If there are gaps in the data, they are far apart, and the data are not "sparse"

H. Ögelman and E. P. J. van den Heuvel (eds.), Timing Neutron Stars, 27–69.

in the sense that nearly all time bins are empty. This kind of data is eminently suited to analysis with Fast Fourier Transform (FFT) techniques, and the discussed methods will all be based on these techniques. Emphasis will be on the statistics of the detection of weak signals rather than on the characterization of signal shapes, with a special discussion of the basic problem of detecting a strictly periodic signal with a sinusoidal shape. While the discussion is specially geared towards photon counting data such as produced by, for example, an X-ray proportional counter, many of the techniques discussed are also applicable in other regimes.

Section 2 contains a general introduction to the Fourier transform and introduces the power spectrum. Section 3 deals with the problem of detecting a signal in the presence of noise. In Section 4 it is discussed how to quantify the power of the signal and how to estimate its variance using the power spectrum. Section 5 discusses how to search a power spectrum by making use of the basic properties of power spectral statistics only, using "independent trials". At the end of this section there is a summary in "recipe" form of how to simply search a power spectrum for a weak signal. In Section 6, a detailed discussion is given of the specific case of detecting a sinusoidal signal. The subject of Section 7, finally, is a method of searching power spectra for various types of signal simultaneously. The methods discussed in Sections 6 and 7 have in common that because higher demands are made on the tests performed on the power spectrum than in Section 5, the test statistics are no longer simple (in particular, "dependent trials" are considered) and have to be evaluated by simulations.

The present exposition owes much to the paper by Leahy *et al.* (1983). Some of the material discussed is also contained in Chapter 2 of the review about quasi-periodic oscillations by Lewin, van Paradijs and van der Klis (1988), hereafter Paper 1.

2. THE FOURIER TRANSFORM

2.1. Introduction

In this section (2.1) the Fourier transform is introduced in very general terms. We do not yet worry about summation indices and the like; such details are filled in in the following sections.

A Fourier transform gives a decomposition of a signal, say, $x(t)$, into sine waves. At any given frequency ω, one can find a set of values (a, ϕ) or (A, B) such that the sinusoid $a\cos(\omega t - \phi) = A\cos\omega t + B\sin\omega t$ best fits the data $x(t)$[1]. Do this for a sufficient number of different frequencies ω_j, then the signal can be written as

[1] (a, ϕ) and (A, B) are, of course, related by $a = \sqrt{A^2 + B^2}$ and $\tan\phi = B/A$

$$x(t) = \frac{1}{N}\sum_j a_j \cos(\omega_j t - \phi_j) = \frac{1}{N}\sum_j (A_j \cos\omega_j t + B_j \sin\omega_j t)\,. \tag{2.1}$$

The Fourier coefficients A_j and B_j can be straightforwardly computed as

$$\begin{aligned} A_j &= \sum_k x_k \cos\omega_j t_k \\ B_j &= \sum_k x_k \sin\omega_j t_k, \end{aligned} \tag{2.2}$$

where $x_k = x(t_k)$. It can be seen from Eq. 2.2 that A_j and B_j are simply the **correlation** of the signal x_k with a sine or cosine wave of frequency ω_j: if there is a good correlation then the corresponding Fourier coefficient is high and gives a large contribution to the sum in Eq. 2.1 which reconstructs the signal out of sine waves.

For easier handling of the two numbers ((A, B) or (a, ϕ)) which one obtains at each frequency, it is possible to represent the Fourier transform in terms of complex numbers:

$$a_j = \sum_k x_k e^{i\omega_j t_k} \tag{2.3a}$$

$$x_k = \frac{1}{N}\sum_j a_j e^{-i\omega_j t_k}, \tag{2.3b}$$

where $i^2 = -1$. The complex numbers a_j are called the **(complex) Fourier amplitudes**; together they form the Fourier transform of the x_k. Inversely, the x_k form the **inverse Fourier transform** of the a_j. Writing a_j as $|a_j|e^{i\phi_j}$, we see (Eq. 2.3*b*) that the signal x_k is now decomposed into functions of the form $a_j e^{-i\omega_j t_k} = |a_j|e^{-i(\omega_j t_k - \phi_j)} = |a_j|\big(\cos(\omega_j t_k - \phi_j) - i\sin(\omega_j t_k - \phi_j)\big)$, having a non-zero imaginary component. This is nothing to worry about: in this representation both positive and negative frequencies are considered, with $\omega_{-j} = -\omega_j$, and if the x_k are real numbers then one sees from Eq. 2.3*a* that $a_{-j} = a_j^*$ (the asterisk indicating the complex conjugate), so that the imaginary terms at j and $-j$ (*i.e.*, at ω_j and ω_{-j}) cancel out and the end result in the summation (2.3*b*) is $(2/N)|a_j|\cos(\omega_j t_k - \phi_j)$, strictly real.

2.2. The Discrete Fourier Transform

We now get a bit more specific and define our signal as a series of N numbers x_k ($k = 0, \ldots, N-1$); in the applications discussed in this article, x_k will always stand for the number of photons detected in bin k. The discrete Fourier transform a_j ($j = -N/2, \ldots, N/2-1$) decomposes this signal into N sine waves. The following expressions describe the signal-transform pair:

$$a_j = \sum_{k=0}^{N-1} x_k e^{2\pi i j k/N} \qquad j = -\frac{N}{2}, \ldots, \frac{N}{2} - 1 \tag{2.4a}$$

$$x_k = \frac{1}{N} \sum_{j=-N/2}^{N/2-1} a_j e^{-2\pi i j k/N} \qquad k = 0, \ldots, N-1. \tag{2.4b}$$

If, as before, the signal is an equidistant time series of length T, so that x_k refers to a time $t_k \equiv kT/N$, then the transform is an equidistant "frequency series", and a_j refers to a frequency $\omega_j \equiv 2\pi\nu_j = 2\pi j/T$. The time step is $\delta t = T/N$; the frequency step is $\delta\nu = 1/T$, and substituting $2\pi jk/N = \omega_j t_k$, we find back Eq. 2.3.

It is a matter of taste where one puts the factor $1/N$ in Eq. 2.4; definitions where this factor appears in Eq. 2.4*a*, or where both sums are preceded by a factor $1/\sqrt{N}$ are also possible and do, in fact, occur in literature.

Note that the number (N) of input values x_k equals the number of output values a_j; if the x_k are uncorrelated, then the a_j are as well. The discrete Fourier transform gives a complete description of the discrete signal; the highest frequency needed for this complete description is $\nu_{N/2} = \frac{1}{2}N/T$. This frequency, equal to half the "sampling" frequency defined by the spacing of the x_k, is called the **Nyquist frequency**. An oscillation at $\nu_{N/2}$ corresponds to an alternating "up-down" signal in the x_k. Note that $a_{-N/2} = \sum_k x_k e^{-\pi i k} = \sum_k x_k (-1)^k = a_{N/2}$; it does not matter whether one puts the Nyquist frequency at the positive end or the negative end of the Fourier transform. At zero frequency, the result of Eq. 2.4*a* is just the total number of photons detected; $a_0 = \sum_k x_k \equiv N_{\rm ph}$.

2.2.1. The Fast Fourier Transform. The fast Fourier transform (FFT) is a computer algorithm to efficiently compute the discrete Fourier transform. Often, but not always, the data is constrained by these algorithms to have a number of bins N equal to a power of 2. See, *e.g.*, Press *et al.* (1986) for an exposition of the functioning and sample computer codes of FFT algorithms.

2.3. The Continuous Fourier Transform

The continuous Fourier transform decomposes an infinitely extended continuous function $x(t)$ $(-\infty < t < \infty)$ into an infinite number of sine waves:

$$a(\nu) = \int_{-\infty}^{\infty} x(t) e^{2\pi\nu i t}\, dt \qquad -\infty < \nu < \infty \tag{2.5a}$$

$$x(t) = \int_{-\infty}^{\infty} a(\nu) e^{-2\pi\nu i t}\, d\nu \qquad -\infty < t < \infty. \tag{2.5b}$$

When doing analytical calculations, the continuous Fourier transform has a number of pleasing properties (for example, the continuous Fourier transform of a sine wave is a delta function; this is not in general true for the discrete Fourier transform, see Fig. 6.1*a*). Therefore, theoretical predictions of the shape of the Fourier transform of a signal are usually in terms of the continuous Fourier transform.

Unfortunately, in the real world the data are not infinitely extended nor continuous, and one might well ask what is the relation of Eq. 2.5 with the discrete Fourier transform of a discretely sampled **section** of $x(t)$. This question will be adressed in Section 2.5.

2.4. The Power Spectrum

A result known as Parseval's theorem states:

$$\sum_{k=0}^{N-1} |x_k|^2 = \frac{1}{N} \sum_{j=-N/2}^{N/2-1} |a_j|^2. \tag{2.6}$$

This implies that there is a relation between the summed squared modulus of the Fourier amplitudes and the total variance of the data: $\mathrm{Var}(x_k) \equiv \sum_k (x_k - \overline{x})^2 = \sum_k x_k^2 - \frac{1}{N}\left(\sum_k x_k\right)^2 = \frac{1}{N}\sum_j |a_j|^2 - \frac{1}{N}a_0^2$, so that

$$\mathrm{Var}(x_k) = \frac{1}{N} \sum_{\substack{j=-N/2 \\ j\neq 0}}^{N/2-1} |a_j|^2. \tag{2.7}$$

Adopting the normalization used by Leahy *et al.* (1983), we will define the **power spectrum** as

$$P_j \equiv \frac{2}{N_{ph}} |a_j|^2 \qquad j = 0, \ldots, \frac{N}{2}, \tag{2.8}$$

where N_{ph} is again the total number of photons $\sum x_k = a_0$ and a_j is given by Eq. 2.4*a*. Using once more the result that for real data $|a_j| = |a_{-j}|$ and taking

account of the fact that the term at the Nyquist frequency occurs only once in Eq. 2.7, we find for the expression for the total variance in terms of the P_j:

$$\mathrm{Var}(x_k) = \frac{N_{ph}}{N}\left(\sum_{j=1}^{N/2-1} P_j + \tfrac{1}{2}P_{N/2}\right). \tag{2.9}$$

Note the differences in the indexing of a_j and P_j. Computer implementations of the FFT usually employ a storage scheme that is different again (Fig. 2.1).

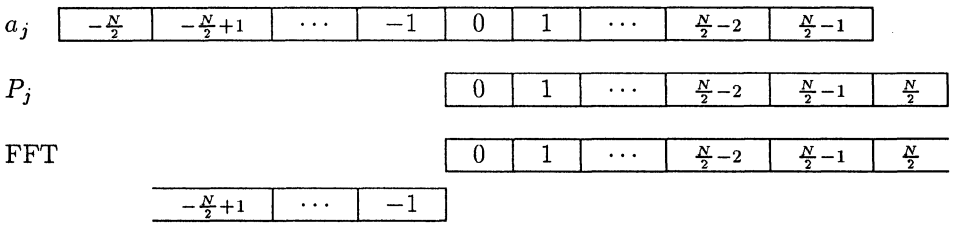

Fig. 2.1. *Storage schemes. The FFT scheme may differ between implementations — in this example bin* $-\frac{N}{2}+1$ *follows bin* $\frac{N}{2}$.

Often the variance is expressed in terms of the fractional root-mean-square (rms) variation in the x_k:

$$r \equiv \frac{\sqrt{\frac{1}{N}\mathrm{Var}(x_k)}}{\overline{x}} = \sqrt{\frac{\sum_{j=1}^{N/2-1} P_j + \frac{1}{2}P_{N/2}}{N_{\mathrm{ph}}}}. \tag{2.10}$$

Sometimes r is expressed in terms of a percentage, and is then also called the "percentage rms variation". A sinusoidal signal at the Fourier frequency ν_j (see Section 4 for the more general case) $x_k = A\sin(2\pi\nu_j t_k)$ will cause a spike at ν_j in the power spectrum with

$$P_{j,\mathrm{sine}} = \frac{1}{2}\frac{N^2}{N_{\mathrm{ph}}}A^2. \tag{2.11}$$

The reason for choosing this apparently rather awkward normalization for the powers lies in the statistical properties of the noise power spectrum, to be described in Section 3.

If the data consist of the sum of a number of independent signals: $x_k \equiv y_k + z_k$, then the so-called superposition theorem ("the transform of the sum is the sum of the transforms") says that if b_j and c_j are the Fourier transforms of y_k and z_k,

respectively, then the Fourier transform of x_k is $a_j = b_j + c_j$. This means, that a similar superposition principle does **not** apply to power spectra:

$$|a_j|^2 = |b_j + c_j|^2 = |b_j|^2 + |c_j|^2 + \text{cross terms.} \tag{2.12}$$

However, if one of the two signals summed consists of random uncorrelated noise, then the cross-terms will tend to average out to zero.

2.5. The Relation between the Discrete and the Continuous Fourier Transform

The answer to the question posed in Section 2.3 about the relation between the discrete and the continuous Fourier transform can be obtained by making use of one of the powerful theorems of Fourier analysis, the convolution theorem. This theorem states, that the Fourier transform of the product of two functions is the **convolution** of the Fourier transforms of these two functions. So, if $a(\nu)$ is the continuous Fourier transform of $x(t)$ and $b(\nu)$ that of $y(t)$ then the continuous Fourier transform of $x(t)y(t)$ is $a(\nu) * b(\nu) \equiv \int_{-\infty}^{\infty} a(\nu')b(\nu - \nu')d\nu'$: "the transform of the product is the convolution of the transforms". The inverse is also true ("the transform of the convolution is the product of the transforms"), and in the case of the discrete Fourier transform analogous theorems apply.

Now suppose that $a(\nu)$ $(-\infty < \nu < \infty)$ is the continuous Fourier transform of the infinitely extended continuous function $x(t)$ $(-\infty < t < \infty)$. Suppose, furthermore, that x_k $(k = 0, \ldots, N-1)$ is a finite discrete time series defined as $x_k = x(t_k)$, where $t_k = kT/N$, *i.e.*, x_k is a discretely sampled section of $x(t)$. Then we see (Fig. 2.2*a*) that the relation of $x(t)$ with x_k is given by a **double multiplication**: $x(t)$ has been multiplied with a "window function"

$$w(t) = \begin{cases} 1, & 0 \le t < T \\ 0, & \text{otherwise,} \end{cases} \tag{2.13}$$

and with a "sampling function"

$$i(t) = \sum_{k=-\infty}^{\infty} \delta\left(t - \frac{kT}{N}\right), \tag{2.14}$$

where $\delta(t)$ is the Dirac delta function.

Consequently, the relation of $a(\nu)$ with a_j is given by a **double convolution**(Fig. 2.2*b*): $a(\nu)$ must be convolved with the Fourier transforms of both the window function and the sampling function.

Because (to be consistent with Eq. 2.4) we have chosen the window function to be asymmetric around $t = 0$, the "window transform" $W(\nu)$ turns out to be

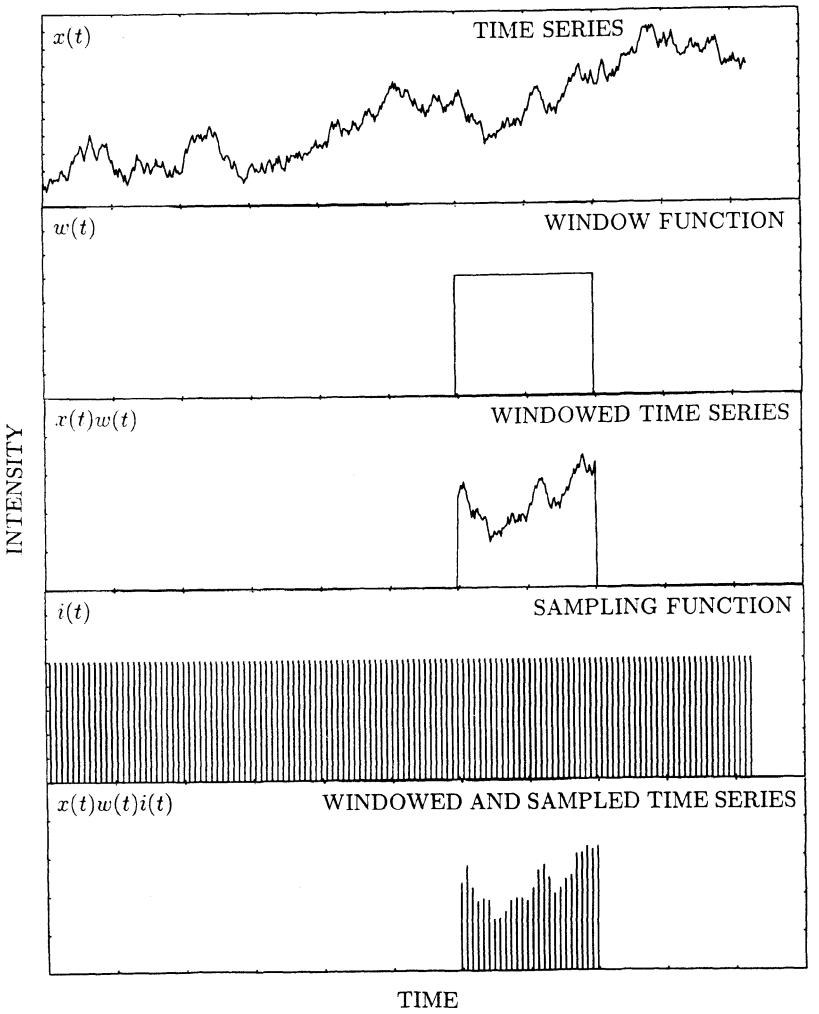

Fig. 2.2. *a) Obtaining the discrete time series x_k as a discretely sampled section of $x(t)$ involves a double multiplication.*

complex. To understand what is going on, it is sufficient to consider the power spectrum of $W(\nu)$:

$$|W(\nu)|^2 \equiv \left| \int_{-\infty}^{\infty} w(t) e^{2\pi\nu i t} \, dt \right|^2 = \left| \frac{\sin \pi\nu T}{\pi\nu} \right|^2 . \tag{2.15}$$

For a symmetric $w(t)$ we would have $W(\nu) = \sin(\pi\nu T)/\pi\nu$. The Fourier transform

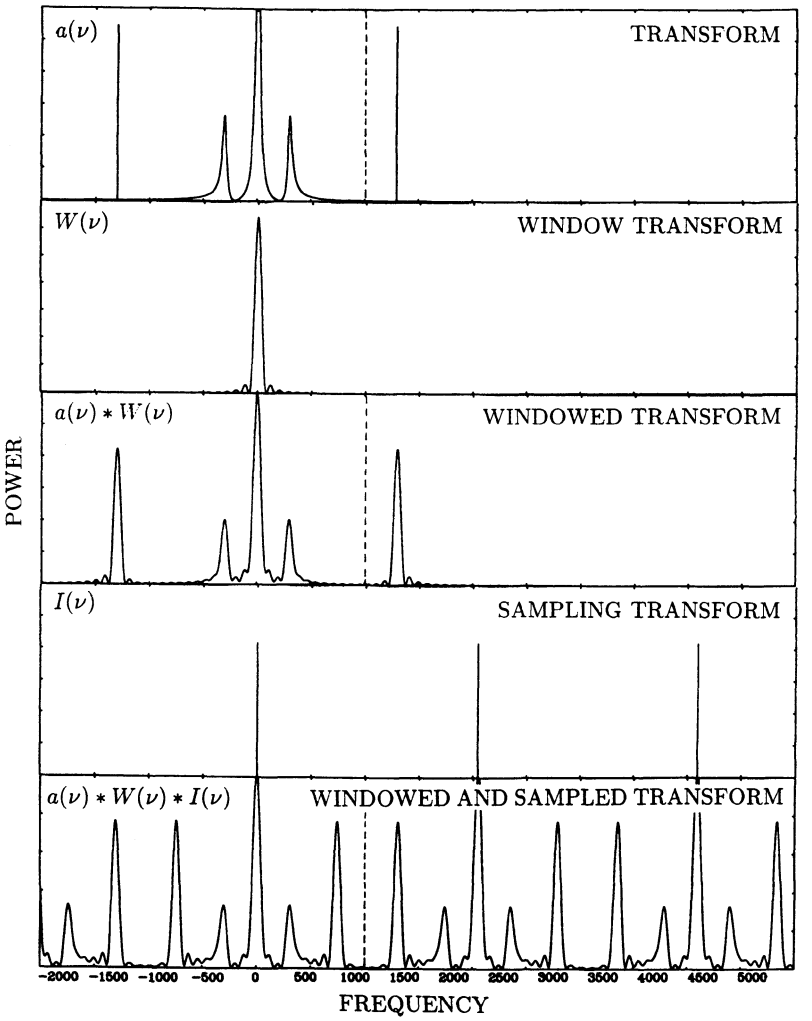

Fig. 2.2. *b) The discrete Fourier transform a_j of x_k is obtained out of the continuous Fourier transform $a(\nu)$ by a double convolution. The figure shows the power spectra corresponding to the various Fourier transforms. Vertical dashed lines indicate the Nyquist frequency.*

of an infinitely extended periodic series of delta functions such as the sampling function $i(t)$ is again an infinite periodic series of delta functions:

$$I(\nu) \equiv \int_{-\infty}^{\infty} i(t) e^{2\pi\nu i t}\, dt = \frac{N}{T} \sum_{\ell=-\infty}^{\infty} \delta\left(\nu - \ell \frac{N}{T}\right). \tag{2.16}$$

The functions $w(t)$ and $i(t)$ and the power spectra corresponding to $W(\nu)$ and $I(\nu)$ are plotted in Fig. 2.2.

The convolution of $a(\nu)$ with $W(\nu)$ causes all features in $a(\nu)$ to become wider; in particular, a delta function can be seen in Fig. 2.2 to change into shifted version of $W(\nu)$; a peak of finite width with side lobes. The convolution of an arbitrary function with a delta function at ν_0 is a shifted version of the original function: $f(\nu) * \delta(\nu - \nu_0) = f(\nu - \nu_0)$. Therefore, the convolution of $a(\nu)$ with $I(\nu)$, which is a series of delta functions with spacing N/T results in a convolved function $a(\nu) * I(\nu)$ that repeats every N/T frequency units.

For a real signal $x(t)$ we have, as before, $a(-\nu) = a(\nu)^*$, so that $|a(\nu)|^2 = |a(-\nu)|^2$: the power spectrum is symmetric around $\nu = 0$. The final result is that the power spectrum of the convolved function $|a(\nu) * I(\nu)|^2$ is reflected around the Nyquist frequency $\nu_{N/2} = \frac{1}{2}N/T$. This causes features with a frequency exceeding the Nyquist frequency by ν_x (so, located at $\nu = \nu_{N/2} + \nu_x$) to **also** appear at a frequency $\nu_{N/2} - \nu_x$, a phenomenon known as **aliasing**; the reflected feature is called the **alias** of the original one.

Using Eqs. 2.13 and 2.14 it is straightforward to show that the discrete Fourier amplitudes a_j are the values at the Fourier frequencies $\nu_j \equiv j/T$ of the windowed and aliased continuous Fourier transform $a_{WI}(\nu)$

$$a_{WI}(\nu) \equiv a(\nu) * W(\nu) * I(\nu) = \int_{-\infty}^{\infty} x(t)w(t)i(t)e^{2\pi i\nu t}\,dt$$

$$= \int_{-\infty}^{\infty} x(t) \sum_{k=0}^{N-1} \delta\left(t - \frac{kT}{N}\right) e^{2\pi i\nu t}\,dt = \sum_{k=0}^{N-1} x\left(\frac{kT}{N}\right) e^{2\pi i\nu kT/N},$$

so that $a_{WI}(j/T) = a_j$. Explicitly performing the convolution of $a(\nu)$ with $I(\nu)$ we finally have:

$$a_j = a_{WI}(j/T) = a_W(j/T) * I(j/T) = \frac{N}{T} \sum_{\ell=-\infty}^{\infty} a_W\left(\nu_j - \ell\frac{N}{T}\right), \qquad (2.17)$$

where we have used Eq. 2.16 and where $\nu_j = j/T$ and $a_W(\nu) \equiv a(\nu) * W(\nu)$.

To summarize, the transition from the continuous Fourier transform to the discrete Fourier transform involves two operations: windowing, a convolution with the function $W(\nu)$, which is essentially a peak with a width $\delta\nu = 1/T$ plus sidelobes, and aliasing, a reflection of features above the Nyquist frequency back into the range $(0, \nu_{N/2})$. Windowing is caused by the finite extent, aliasing by the discrete sampling of the data.

In practice, aliasing is not so much of a problem as one might fear, as the data are not really discretely sampled at intervals $\delta t = T/N$, but rather binned into time bins with a width δt. This is equivalent to **convolving** the data with the "binning window"

$$b(t) = \begin{cases} N/T, & -\frac{T}{2N} < t < \frac{T}{2N} \\ 0, & \text{otherwise} \end{cases} \tag{2.18}$$

before the discrete sampling. Applying the "inverse" convolution theorem, we see that the effect of this on the Fourier transform will be that $a(\nu)$ is **multiplied** with the transform of $b(t)$:

$$B(\nu) = \frac{\sin \pi \nu T/N}{\pi \nu T/N}. \tag{2.19}$$

This function drops from a value of 1 at $\nu = 0$ to 0 at $\nu = N/T$; halfway, at the Nyquist frequency it has a value of $2/\pi$, so that the effect of this multiplication is a considerable repression of the high-frequency features that could be aliased back into the frequency range $(0, \nu_{N/2})$. This is understandable; the effect of the binning is nothing else than averaging the time series over the bin width T/N so that variations with a frequency close to N/T are largely averaged out.

The problems caused by the windowing can be more serious; the "leakage" caused by the finite width of the central peak of $W(\nu)$ and by its side lobes can strongly distort steep power spectra (they become less steep, *e.g.*, Deeter, 1983) and, as we will see later on, it can spread out delta functions over the entire power spectrum.

2.6. Literature

The "handy cookbook" of time series analysis has yet to be written. A good standard reference that covers a large amount of information but is not always easy to follow is Jenkins and Watts (1968). Much easier are the texts by Bloomfield (1976) and Bracewell (1965). A very clear exposition of some basic principles of Fourier analysis stressing intuition rather than mathematics can be found in Press *et al.* (1986).

3. POWER SPECTRAL STATISTICS

3.1. Introduction

The process of detecting something in a power spectrum against a background of noise has several steps. The first thing we need to know is the **probability distribution** of the "noise powers" $P_{j,\text{noise}}$ in a power spectrum of data consisting

only of noise. If one or more of the powers P_j in the observed power spectrum differ significantly from the values expected from noise, then we may conclude that we have detected a "source signal", which is the term I shall use to indicate intrinsic variability in the x_k other than due to background noise.

To quantify the power of the source signal, *i.e.*, to determine what the "signal powers" $P_{j,\mathrm{signal}}$ of the source signal would have been in the absence of noise (or to determine their upper limit), we must consider the **interaction between the noise and the signal powers**.

This quantitative knowledge about the $P_{j,\mathrm{signal}}$ can be directly converted into a statement about the variance (or the rms variation) of the source signal. To say something about other properties of the source signal we need to consider the **expected shape** of the signal power spectrum. The optimal way to detect a given signal will also depend on this expected shape.

In this section, we will consider the first of these steps, signal detection, and consequently we must consider the probability distribution of the noise powers. The problem of quantifying the signal power will be discussed in Section 4. For the interaction between the noise and signal powers, we will follow convention by making the following very simple assumption

$$P_j = P_{j,\mathrm{noise}} + P_{j,\mathrm{signal}}. \tag{3.1}$$

Note that this is an approximation; as we have seen (Section 2.4), if it would be true that $a_j = a_{j,\mathrm{noise}} + a_{j,\mathrm{signal}}$, and if the noise is random uncorrelated noise, then Eq. 3.1 is probably valid. However, for a photon counting signal, the properties of the (*e.g.*, Poissonian) counting noise will in general change with the count rate. As long as the amplitudes of the source signal are small with respect to those of the noise, so that the source signal can be seen as a small disturbance of the noise, Eq. 3.1 will be approximately correct.

3.2. The Probability Distribution of the Noise Powers

For a wide range of types of noise, the noise powers $P_{j,\mathrm{noise}}$ follow[2] the χ^2 (chi-squared) distribution with 2 degrees of freedom (dof). The proof of this χ^2 property of the noise powers proceeds approximately as follows (see *e.g.*, Jenkins and Watts, 1968):

The noise power $P_{j,\mathrm{noise}} = A^2_{j,\mathrm{noise}} + B^2_{j,\mathrm{noise}}$, where A_j and B_j are given by Eq. 2.2; A_j and B_j are both linear combinations of the x_k. Therefore, if the x_k follow the normal distribution, then the A_j and B_j do as well, so that P_j, by

[2] With the exception of the power at the Nyquist frequency which follows the χ^2 distribution with 1 dof.

definition, is distributed according to the χ^2 distribution with 2 dof. If the x_k follow some other probability distribution, for example the Poisson distribution, then it follows from the central limit theorem that for "certain" conditions on this other distribution the A_j and B_j will still be approximately normally distributed (for large N), so that the χ^2 property for the P_j still approximately holds.

While this "proof" may seem somewhat unsatisfactory, the conditions for the central limit theorem to be applicable not being spelled out, in practice one finds that noise powers are nearly always χ^2 distributed, not only for Poisson noise, but also for many other types of noise. We shall see examples of this later on in this section.

The normalization of the power spectrum defined by Eq. 2.8 is chosen such, that if the noise in the photon counting data x_k is pure Poissonian counting noise, then the distribution of the $P_{j,\mathrm{noise}}$ is exactly given by the χ^2 distribution with 2 dof, so that the probability to exceed a certain threshold power level $P_{\mathrm{threshold}}$ is given by

$$\mathrm{Prob}(P_{j,\mathrm{noise}} > P_{\mathrm{threshold}}) = Q(P_{\mathrm{threshold}}|2) \qquad (j = 1, N/2 - 1), \tag{3.2}$$

where the integral probability of the χ^2 distribution is defined as

$$Q(\chi^2|\upsilon) \equiv \left[2^{\upsilon/2}\Gamma\left(\frac{\upsilon}{2}\right)\right]^{-1} \int_{\chi^2}^{\infty} t^{\frac{\upsilon}{2}-1} e^{-\frac{t}{2}}\, dt, \tag{3.3}$$

where υ is the number of dof.

Because the $P_{j,\mathrm{noise}}$ follow this distribution, the power spectrum is very noisy; the standard deviation of the noise powers is equal to their mean value: $\sigma_{P_j} = \langle P_j \rangle = 2$. This noisy character of the power spectrum can not be improved by increasing the length T of the data or taking a coarser time step δt; this just changes the number of powers.

Two more or less equivalent methods are often used to decrease the large variance of the $P_{j,\mathrm{noise}}$. One is to rebin the power spectrum, averaging W consecutive frequency bins; the other to divide the data up into M equal segments, transform these segments each individually and then average the resulting M power spectra, each normalized according to Eq. 2.8, where N_{ph} is now the number of photons **in one transform**. Both methods of power spectrum compression, of course, degrade the frequency resolution.

As the time required to calculate the Fourier transform of N data points using an FFT algorithm is proportional to $N \log N$, there is a computational advantage in the second method; the time saving factor is about $1 + \log M / \log N$. In many cases, considerable additional time savings result from the smaller array sizes that need to be handled by the computer. For a variable source, a further advantage of the

second method is that cutting up the data into smaller segments allows one to study variations in the power spectra as a function of, *e.g.*, source intensity by selectively averaging power spectra obtained within certain source intensity intervals and that it allows the construction of two-dimensional images showing the time evolution of the power spectrum. These techniques have proven particularly useful in the detection of transient QPO phenomena. The first method, on the other hand, has the advantage of producing a power spectrum that extends to lower frequencies (the lowest measurable frequency being $1/T$). It is possible to combine both methods; each power in the final spectrum will then be the average of MW original powers.

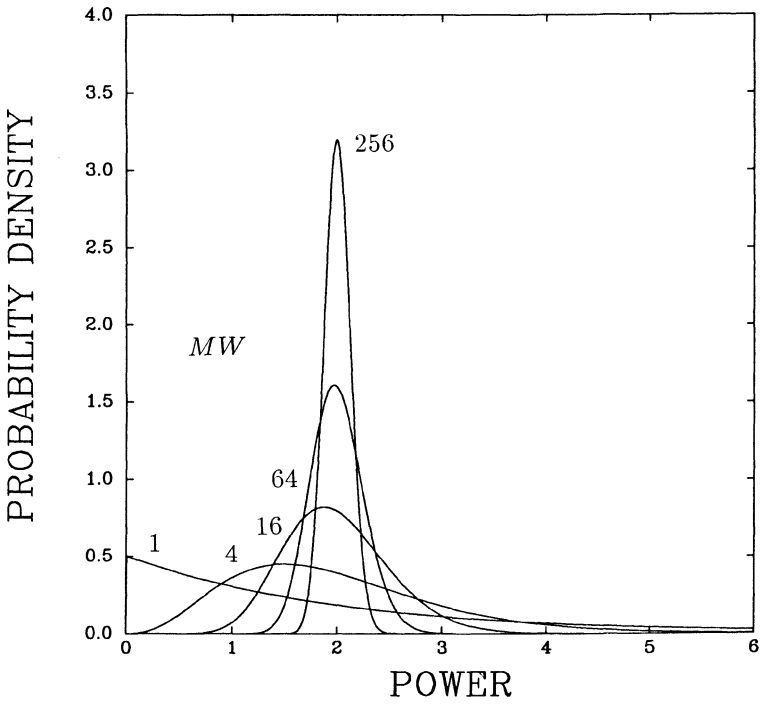

Fig. 3.1. *The probability distribution of average noise powers for different values of the number of powers MW averaged.*

Because of the additive properties of the χ^2 distribution, the sum of MW powers is distributed according to the χ^2 distribution with $2MW$ dof, so that the powers in the averaged spectrum will be distributed according to a χ^2 distribution with $2MW$ dof scaled by a factor $1/MW$. The mean of this distribution is 2, its variance is $4/MW$, and its standard deviation $2/\sqrt{MW}$ so that for large MW the

spectrum becomes much less noisy. The probability for a given power $P_{j,\mathrm{noise}}$ in the averaged spectrum to exceed a $P_{\mathrm{threshold}}$ is given by

$$\mathrm{Prob}(P_{j,\mathrm{noise}} > P_{\mathrm{threshold}}) = Q(MWP_{\mathrm{threshold}}|2MW), \tag{3.4}$$

where $Q(\chi^2|\upsilon)$ is again given by Eq. 3.3. For large MW, this distribution tends asymptotically to a normal distribution (see Fig. 3.1) with a mean of 2 and standard deviation $2/\sqrt{MW}$:

$$\lim_{MW\to\infty} \mathrm{Prob}(P_{j,\mathrm{noise}} > P_{\mathrm{threshold}}) = Q_{\mathrm{Gauss}}\left(\frac{P_{\mathrm{threshold}} - 2}{2/\sqrt{MW}}\right), \tag{3.5}$$

where the integral probability of the normal distribution is

$$Q_{\mathrm{Gauss}}(x) \equiv \frac{1}{\sqrt{2\pi}} \int_x^\infty e^{-t^2/2} dt. \tag{3.6}$$

So, a considerable simplification can be obtained by averaging large numbers of powers, empirically determining mean and standard deviation of the averaged power spectrum to account for non-Poissonian noise in the x_k (see Section 3.4), and then using Gaussian statistics. In the following, we will, unless otherwise stated, assume the more general case described by Eq. 3.4.

3.3. The Detection Level - the Number of Trials

Assuming the χ^2 property for the noise powers (Eq. 3.4), we can now determine how large a power must be to constitute a significant excess above the noise.

Define the $(1-\epsilon)$ confidence detection level P_{detect} as the power level that has only the small probability ϵ to be exceeded by a noise power. So, if there is a power P_j that exceeds P_{detect} then there is a large probability $(1-\epsilon)$ that P_j is not purely due to noise, but also contains signal power (Eq. 3.1).

A crucial consideration, occasionally overlooked, is the number of different P_j values, known as the **number of trials** N_{trial} that one wishes to compare with P_{detect}. N_{trial} can be equal to the total number of powers in the power spectrum, or less than that if only a certain frequency range in the spectrum is considered. The probability to exceed P_{detect} by noise should have the small value ϵ for all powers in the frequency range of interest **together**, so that the chance **per trial** should have the much smaller value of about[3] $\epsilon/N_{\mathrm{trial}}$. So, the detection level P_{detect} is given by

[3] The exact expression can be obtained by setting the joint probability for N_{trial} values of P_j **not** to exceed P_{detect} equal to $1-\epsilon$, which gives a chance to exceed P_{detect} per trial of $1-(1-\epsilon)^{(1/N_{\mathrm{trial}})}$, nearly equal to $\epsilon/N_{\mathrm{trial}}$ for $\epsilon \ll 1$.

$$\frac{\epsilon}{N_{\rm trial}} = Q(MWP_{\rm detect}|2MW) \tag{3.7}$$

In Fig. 3.2, $P_{\rm detect}$ is plotted as a function of $N_{\rm trial}$ for various values of MW and for confidence levels of 90% ($\epsilon = 0.1$) and 99% ($\epsilon = 0.01$). Note that although $P_{\rm detect}$ increases with the number of trials $N_{\rm trial}$, the increase is relatively slow.

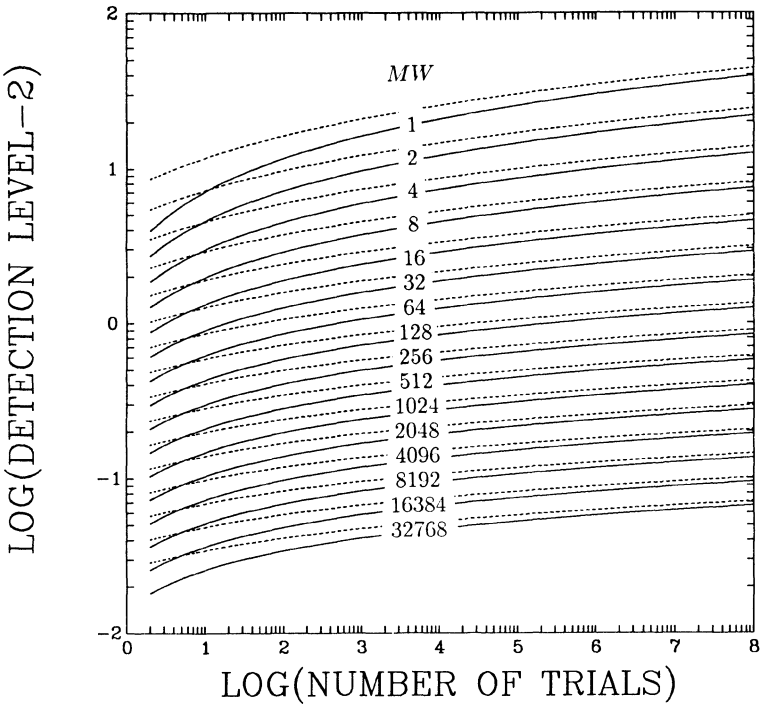

Fig. 3.2. *90% (drawn) and 99% (dashed) confidence detection levels (minus 2) as a function of the number of trials. The number of independent powers, MW, averaged together due to rebinning of the power spectra by a factor W and averaging M different power spectra increases by a factor of 2 in consecutive curves. The trials are assumed to be independent, so no overlaps between the W-bin averages are allowed. As an example, for a power spectrum produced by averaging together 2 "raw" power spectra of 4096 bins each and binning up the resulting spectrum by a factor of 4 to produce a 1024-bin average spectrum the 90% confidence detection level can be read from the curve $MW = 8$ at $N_{\rm trial} = 1024$ to be 5.8.*

3.4. Non-Poissonian Noise

For various reasons the noise in the x_k can differ from purely Poissonian counting noise. The consequence of this is that the $P_{j,\mathrm{noise}}$ are no longer distributed according to Eq. 3.4; in general, correlations introduced by the noise process between the x_k will introduce correlations between the $P_{j,\mathrm{noise}}$, so that the noise power spectrum will not even be flat any more. However, as we have seen in Section 3.2, under "certain" conditions one still expects the noise powers to follow a χ^2 distribution with 2 dof. Even if this is the case, the normalization will be different from that implied by Eq. 3.4 and will in general depend on j.

3.4.1. Dead Time

One reason why noise in the x_k can be non-Poissonian is the occurrence of various instrumental effects summarized under the name "dead time". Various types of dead time exist, all of which considered here have in common that the instrument is unable to detect a photon for a given short interval of time τ_{dead} after a photon has been detected; τ_{dead} may be constant, or depend itself on various instrumental parameters.

The case where τ_{dead} is constant is typical for an X-ray proportional-counter dead time. If the incident count rate is λ and the detected count rate μ, then during an observation of length T the total dead time will be $\mu T \tau_{\mathrm{dead}}$, so that ("incident = detected + missed") $\lambda T = \mu T + \mu T \tau_{\mathrm{dead}} \lambda$, or

$$\mu = \frac{\lambda}{1 + \tau_{\mathrm{dead}} \lambda}. \tag{3.8}$$

This type of dead time introduces a correlation between the x_k: if a photon has been detected in bin k, then there is a certain probability that the dead time interval associated with this photon extends into the next bin $k+1$, and therefore the average chance to detect a photon in bin $k+1$ will be diminuished. This then means that the average chance in bin $k+2$ will be slightly higher, *etc.*, so that the final result is that a quasi-periodic oscillation is introduced into the x_k with a frequency equal to the Nyquist frequency. Consequently, the noise power spectrum will rise towards $\nu_{N/2}$. This constant τ_{dead} process has been simulated by Weisskopf (1985). The result of these simulations is that the expectation value of the noise power spectrum (normalized according to Eq. 2.8, where $N_{\mathrm{ph}} = \mu T$) becomes:

$$\langle P_{j,\mathrm{noise}} \rangle = 2\,(1 - \mu\tau_{\mathrm{dead}})^2 \left[1 + 2 \left(\frac{\mu\tau_{\mathrm{dead}}}{1 - \mu\tau_{\mathrm{dead}}} \right) \left(\frac{\tau_{\mathrm{dead}}}{T/N} \right) \sin^2 \frac{\pi j}{N} \right]. \tag{3.9}$$

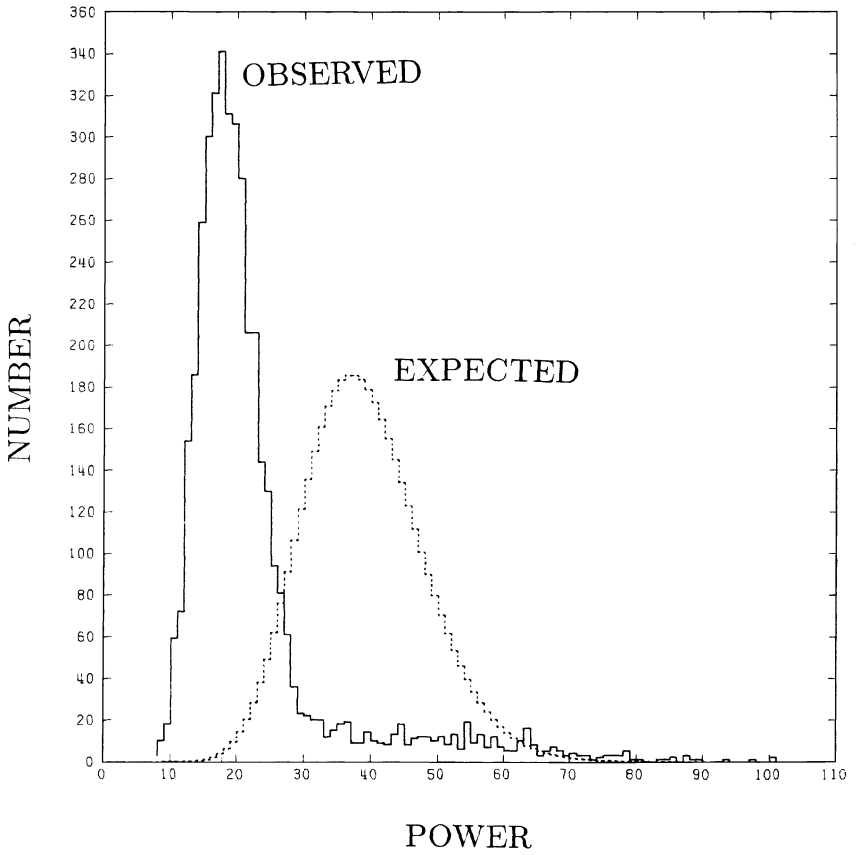

Fig. 3.3. *The complicated dead time process of the EXOSAT ME (see Andrews and Stella 1985, Tennant 1987) strongly modifies the probability distribution of the noise powers (drawn) with respect to that expected for a Poisson noise process. After scaling the distribution with the mean noise power, however, the match with the expected χ^2 distribution (dashed) is good. (Simulated QPO data; sum of 20 power spectra.)*

The amplitude of the frequency-dependent component in the noise power spectrum is seen to be proportional to both the ratio of total dead time to total live time and the ratio of $\tau_{\rm dead}$ to the duration of a time bin T/N.

Another simple type of dead-time process is that where the instrument can only detect at most one photon per instrumental "sample" cycle, which has a duration $\tau_{\rm sample}$. So, in this case $\tau_{\rm dead}$ is variable and lasts from the time a photon is detected until the end of the sample. If the arrival times of the incident photons are Poisson

distributed, then the chance that no photon arrives during $\tau_{\rm sample}$ is $e^{-\tau_{\rm sample}\lambda}$, so that the chance that a photon is detected is $1 - e^{-\tau_{\rm sample}\lambda}$, so

$$\mu = \frac{1 - e^{-\tau_{\rm sample}\lambda}}{\tau_{\rm sample}}. \tag{3.10}$$

If each bin x_k contains $N_{\rm sample}$ samples, then the number of counts in x_k is the number of "successes" among $N_{\rm sample}$ trials, where the chance of success is $p = 1 - e^{-\tau_{\rm sample}\lambda}$. This means that the x_k follow (by definition) the binomial rather than the Poisson distribution, with mean $N_{\rm sample}$ and standard deviation $\sqrt{p(1-p)N_{\rm sample}}$. Note that in this case no correlations are introduced between the x_k. With Eq. 2.9 for the total variance in the x_k and noting that $N_{\rm ph} = \sum x_k = pNN_{\rm sample}$ it can be derived that the average noise power will be

$$\langle P_{j,\rm noise} \rangle = 2e^{\tau_{\rm sample}\lambda} = 2(1 - \mu\tau_{\rm sample}), \tag{3.11}$$

as compared to 2 in the case of Poisson noise.

In practice, dead-time processes are often much more complex than in the two examples above. In particular, there may be an interaction between dead-time processes in different instrumental channels (see Paper 1). However, usually one finds that the χ^2 property of the noise powers is at least approximately preserved (Fig. 3.3).

3.4.2. Intrinsic Noise

It is very common for the source signal itself to consist (partly) of noise. Such intrinsic noise signals can contain very useful information about the source and are worthwhile to try and detect over the background noise caused by, *e.g.*, counting statistics; examples are red noise and QPO. However, in many cases one wishes to consider such an intrinsic noise component as background against which to detect another source signal component. In such cases it is of particular importance to test empirically the probability distribution of the noise powers.

For example, a theoretical description of red noise as the integral of white noise (*e.g.*, Deeter and Boynton 1982) suggests that the χ^2 property of the noise powers will apply for red noise. However, although any observed power spectrum that rises towards lower frequencies is often called a red noise spectrum, the underlying source variability is not specified by this power spectral property (it is not even necessarily a noise process) and the χ^2 property can not be guaranteed.

Again, in practice one usually finds that also for noise in the source signal the noise power distribution closely matches a χ^2 distribution scaled to the local average power (Figs. 3.4, 3.5).

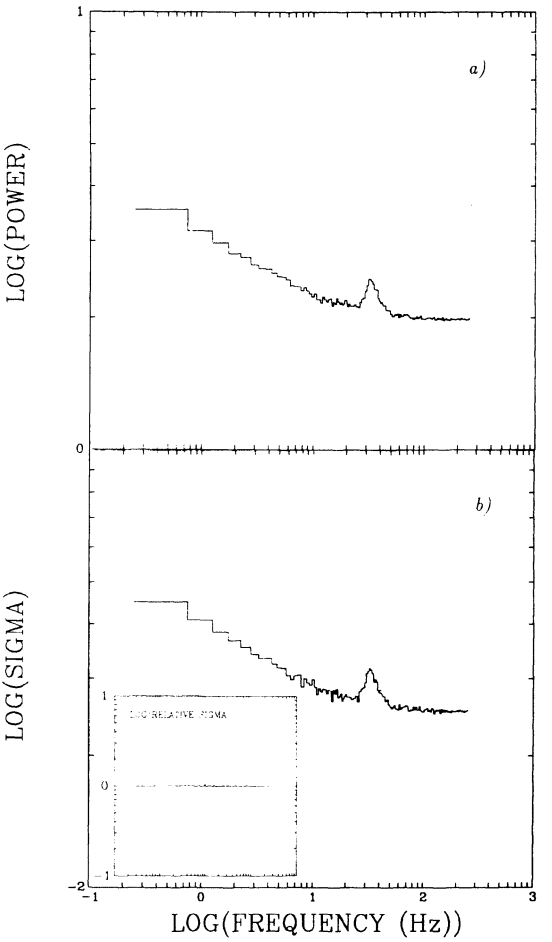

Fig. 3.4. *a) An average of 6166 power spectra of EXOSAT ME data on the source GX 5-1 showing red noise and QPO (quasi-periodic oscillations). b) The standard deviation of the 6166 power values averaged in each frequency bin. Inset: the ratio of b) to a). Standard deviation equals mean power as expected for* χ^2 *distributed powers.*

It is stressed that it is **essential** when looking for weak source signals to take into account the (likely) presence of intrinsic noise. In particular it is completely wrong to use the normalization of the noise power distribution valid for Poisson statistics (Eq. 3.4) when trying to detect something against a background of red noise. Note that red noise can be present even if the quality of the data is not

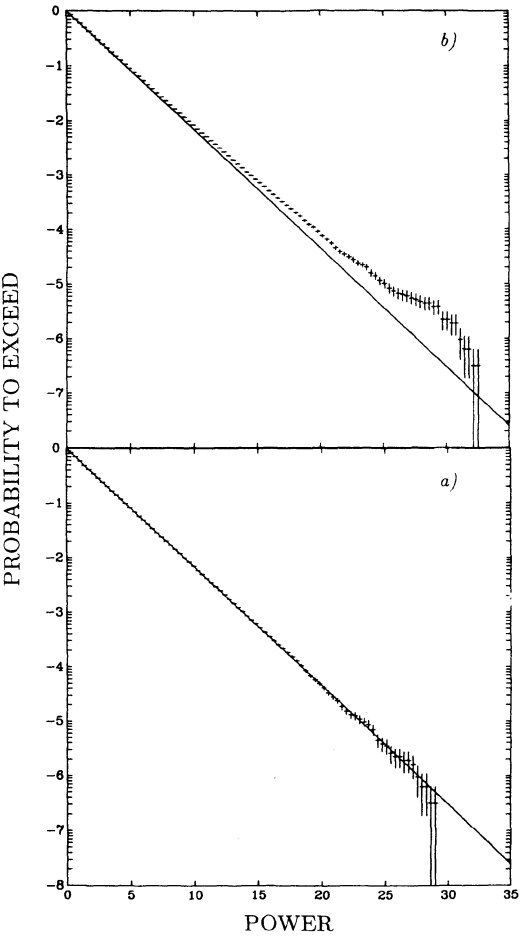

Fig. 3.5. *a) Integral distribution of all individual powers in the 6166 power spectra of Fig. 3.4a (crosses). Strong deviations from a χ^2 distribution (drawn line) due to QPO and red noise are visible. b) Distribution of the same powers as in a), after dividing each individual power spectrum by the average spectrum of Fig. 3.4a. The match to the χ^2 distribution is very close now. Small residual wiggles are due to the intrinsic variations of the shape of the QPO/red noise power spectrum as a function of source intensity.*

sufficient to clearly see the slope in the power spectrum [4].

If the χ^2 property is expected to apply then a correct procedure would for

[4] "Scrambling" techniques where the time order of the x_k is randomized are

example be to **divide** the power spectrum by some average red noise shape (*e.g.*, a best-fit power law) in order to bring all noise powers back to one χ^2 distribution and then evaluate the significance of any excess. Obviously, the uncertainties in the description of the shape of the noise spectrum itself should also be taken in into account in such an analysis.

4. THE SIGNAL POWER

4.1. Introduction

Any quantitative statement one can make about the signal power $P_{j,\mathrm{signal}}$ will be a statement of a probability based on the probability distribution of the noise powers $P_{j,\mathrm{noise}}$, because the only thing one knows for sure is the total power P_j which is (Eq. 3.1) equal to the signal power contaminated with an unknown amount of noise power. In Section 4.2 we will consider this process of quantifying the signal power. In Section 4.3 it will be discussed how to convert a statement about $P_{j,\mathrm{signal}}$ into a statement about the rms variation in the source signal. It is reiterated at this point that to say anything else about the source signal, *e.g.*, about the amplitude of a sine wave, is an entirely different problem for which we need to model the shape of the signal power spectrum. For a sinusoid signal, this problem will be touched upon in Section 6.

4.2. Quantifying the Signal Power

4.2.1. Detected Signal Power. Supposing that we have a detection, *i.e.*, for given j it is true that $P_j > P_{\mathrm{detect}}$, then we ask what is the probable value of the signal power $P_{j,\mathrm{signal}}$ at j.

Determine a "limiting noise power level" $P_{\mathrm{noiselimit}}$ that has only a small probability ϵ' to be exceeded in one trial:

$$\epsilon' = Q(MWP_{\mathrm{noiselimit}}|2MW). \tag{4.1}$$

Then, with confidence $(1 - \epsilon')$ we can say that for given j $P_{j,\mathrm{noise}} < P_{\mathrm{noiselimit}}$. Because according to Eq. 3.1 $P_{j,\mathrm{signal}} = P_j - P_{j,\mathrm{noise}}$, this implies that

$$P_{j,\mathrm{signal}} > P_j - P_{\mathrm{noiselimit}} \qquad (1 - \epsilon') \text{ confidence.} \tag{4.2}$$

---

sometimes used to evaluate the probability to produce a certain feature in the power spectrum by chance given the distribution of the x_k. These techniques are incorrect when red noise is present, as the scrambling destroys the correlations in the x_k underlying the red noise and artificially converts the red noise into white noise.

Note that a slightly misleading statement about this case occurs in Paper 1 (in the text after Eq. 2.13).

4.2.2. Upper Limit to the Signal Power. If no significant power level has been attained by any of the P_j, then it is useful to determine an upper limit to the signal power. The $(1-\delta)$ confidence upper limit P_{UL} to the signal power is defined as the power level for which with $(1-\delta)$ confidence $P_{j,\mathrm{signal}} < P_{\mathrm{UL}}$ irrespective of where (at which j) in the frequency range of interest this signal power may have occured.

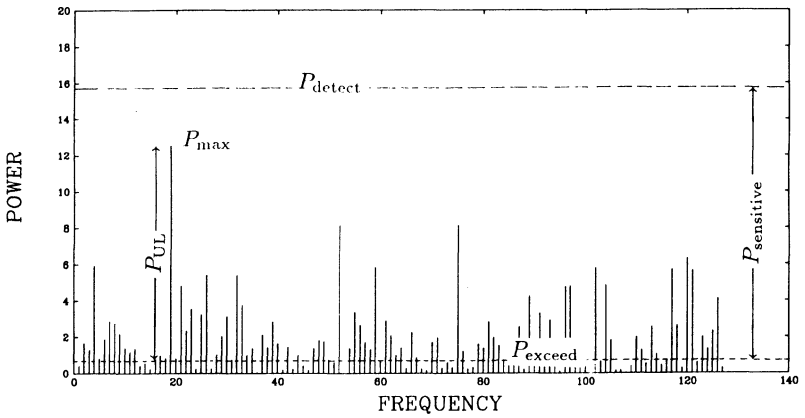

Fig. 4.1. *Relations between the detection level* P_{detect}, *the "usually exceeded" level* P_{exceed}, *the maximum observed power* P_{max}, *the upper limit* P_{UL} *and the sensitivity level* $P_{\mathrm{sensitive}}$ *(see text).*

To determine P_{UL} we define a power level P_{exceed} that has the large probability $(1-\delta)$ to be exceeded by a given individual $P_{j,\mathrm{noise}}$:

$$1-\delta = Q(MWP_{\mathrm{exceed}}|2MW). \tag{4.3}$$

So, a fraction of approximately $(1-\delta)$ of all powers considered will exceed P_{exceed} in the absence of a source signal. We now find the largest actually observed power P_{max} in the frequency range of interest, and write

$$P_{\mathrm{UL}} = P_{\mathrm{max}} - P_{\mathrm{exceed}}. \tag{4.4}$$

If for some j there would have been a signal power in the power spectrum with $P_{j,\mathrm{signal}} > P_{\mathrm{UL}}$, then for that j with $(1-\delta)$ confidence P_j would have exceeded $P_{\mathrm{max}} = P_{\mathrm{UL}} + P_{\mathrm{exceed}}$ (Eq. 3.1). As we know that for all j it is true that $P_j \leq P_{\mathrm{max}}$,

we can say with $(1-\delta)$ confidence that indeed for all j $P_{j,\text{signal}} \leq P_{\text{UL}}$. Note that the number of trials N_{trial} does not enter into the calculation of P_{UL}, as one reasons in terms of one hypothetical undetected signal power $P_{j,\text{signal}}$ at **given** j.

4.2.3. Sensitivity to Signal Power. It is sometimes useful to predict the capabilities of a planned experiment in terms of its sensitivity to signal power. The sensitivity level $P_{\text{sensitive}}$ can be calculated on the basis of the (expected) probability distribution of the noise power as

$$P_{\text{sensitive}} = P_{\text{detect}} - P_{\text{exceed}}, \tag{4.5}$$

where P_{detect} and P_{exceed} are defined in Eqs. 3.7 and 4.3, respectively. If there occurs a $P_{j,\text{signal}}$ somewhere in the power spectrum that exceeds $P_{\text{sensitive}}$ then with $(1-\delta)$ confidence it will be detected (at the $(1-\epsilon)$ confidence level associated with P_{detect}). Note that $P_{\text{sensitive}}$ is not the same as P_{UL}; in fact, $P_{\text{sensitive}}$ is in a sense the upper limit to P_{UL} (see Fig. 4.1).

4.3. The rms Variation in the Source Signal

Assuming that the signal power spectrum has been properly separated out from the total power spectrum using the methods described in Section 4.2, we can convert the signal power into the rms variation r of the source signal in the x_k using the expression

$$r = \sqrt{\frac{W \sum_j P_{j,\text{signal}}}{N_{\text{ph}}}}. \tag{4.6}$$

(*c.f.* Eq. 2.10), where P_j is an MW times averaged power and where N_{ph} is the number of photons per transform.

We shall consider two effects that may cause a difference between the value of r obtained in this way and the actual value R applicable to the signal $x(t)$ as emitted by the source. As we have seen in Section 2.5, the binning of the data causes the power spectrum to be suppressed preferably towards the higher frequencies. The correction factor by which r should be multiplied is

$$\left(\frac{R}{r}\right)_{\text{binning}} = \beta = \frac{\pi \overline{\nu} T/N}{\sin \pi \overline{\nu} T/N}, \tag{4.7}$$

(*c.f.* Eq. 2.19), where $\overline{\nu}$ is some appropriate average over the signal feature in the power spectrum.

The second effect is our old friend dead time (see also Section 3.4.1). Provided that the variations in the signal of interest are slow with respect to the dead time

process, the way in which dead time changes the signal is completely described by the instrument-dependent relation between λ and μ, the incident and detected count rates. Examples of such relations are given in Eqs. 3.8 and 3.10; any relation, either theoretical or empirical, can be used.

Expressing the relation as the dead time attenuation factor $f(\lambda) \equiv \mu/\lambda$, one finds that a small change $\delta\lambda$ in the incident rate causes a change $\delta\mu$ in the observed rate given by

$$\frac{\delta\mu}{\mu} = \left(1 + \frac{\lambda}{f}\frac{df}{d\lambda}\right)\frac{\delta\lambda}{\lambda}. \tag{4.8}$$

From this expression we can derive the dead time correction factor

$$\left(\frac{R}{r}\right)_{\text{dead time}} = \alpha = \frac{|\delta\lambda|/\lambda}{|\delta\mu|/\mu} = \left(\left|1 + \frac{\lambda}{f}\frac{df}{d\lambda}\right|\right)^{-1}. \tag{4.9}$$

See Paper 1 for a discussion of the case of dead-time interaction between several instrumental channels.

One minor pitfall remains to be considered, being the practice of describing the signal power spectrum $P_{j,\text{signal}}$ in terms of a function $P_{\text{signal}}(\nu)$ defined such that $P_{\text{signal}}(\nu_j) \equiv P_{j,\text{signal}}$. When integrating this function one should note that $\int P_{\text{signal}}(\nu)\,d\nu = \frac{W}{T}\sum P_{j,\text{signal}}$. Defining the **excess power** in the power spectrum due to the signal as $P_{\text{excess}} \equiv W\sum P_{j,\text{signal}} = T\int P_{\text{signal}}(\nu)\,d\nu$, we finally have for the fractional rms variation in the signal corrected for binning and dead time

$$R = \alpha\beta\sqrt{\frac{P_{\text{excess}}}{N_{\text{ph}}}} = \left|1 + \frac{\lambda}{f}\frac{df}{d\lambda}\right|^{-1}\frac{\pi\overline{\nu}\delta t}{\sin\pi\overline{\nu}\delta t}\sqrt{\frac{\int P_{\text{signal}}(\nu)\,d\nu}{I}}, \tag{4.10}$$

where $I = N_{\text{ph}}/T$ is the count rate, $\overline{\nu}$ the average frequency of the signal feature in the power spectrum, $\delta t = T/N$ the duration of a time bin, and the sum and the integral run over all frequencies where the signal causes a non-negligible power (a power at the the Nyquist frequency should enter with a factor $\frac{1}{2}$, see Eq. 2.10).

5. OPTIMAL DETECTION - INDEPENDENT TRIALS

5.1. Introduction

When deriving the detection level from the noise power distribution in Section 3.3, we implicitely assumed that the trials (*i.e.*, the powers to be tested against the detection level) would all have the same statistical properties, and that they would be statistically independent. In particular, MW was assumed to be equal for all trials and no overlaps were allowed between the averages of W bins. This

approach is not necessarily optimal for all signal shapes, but it has the enormous advantage that the statistical properties of any power excess that is found can easily be evaluated analytically from the known distribution of the noise powers. In this section, we develop the possibilities of this method to its limit by considering the optimal value of the number of bins to average, given the expected signal. In Section 5.4 the method as it has been developed in the previous sections is summarized in a step-by-step style. In Sections 6 and 7, we shall abandon the constraints that the trials should be equal and independent.

5.2. Detecting a Narrow Feature

The detection of a narrow feature in the power spectrum (defined as a feature in which all power is concentrated in one frequency bin) is a fundamental problem because the continuous Fourier transform of a strictly periodic signal consists of one or more delta functions (see, however, Section 4.5 for the case of the discrete Fourier transform). If the signal power of a narrow feature in a full frequency-resolution power spectrum is P_{signal}, then it will drop to $P_{\text{signal}}/(MW)$ after the frequency resolution has been degraded by a factor MW by one of the methods described in Section 3. For the method of averaging W adjacent bins this is immediately obvious; for the method involving division of the data into M equal segments, this can be seen by using Eq. 2.9 (and assuming that the signal remains the same through the observation).

The detection level also drops when the frequency resolution is degraded, both because the probability distribution of the noise powers in the average power spectrum becomes narrower and because the number of trials decreases by a factor MW. In addition, the narrower noise distribution causes P_{exceed} to increase. However, in the final analysis the sensitivity level $P_{\text{sensitive}}$ (Eq. 4.5) always drops more slowly than $1/MW$ (Fig. 5.1), so that the conclusion is that for detecting a narrow feature in the power spectrum the highest sensitivity is reached for the maximum possible frequency resolution, *i.e.*, by choosing $MW = 1$. Note that we have not specified what the source signal should be in order for the signal power spectrum to be narrow; as we shall see, the discrete Fourier transform of even a strictly periodic sinusoidal signal does not approximate a delta function very well.

5.3. Detecting a Broad Feature

Similar reasoning as in Section 5.2 shows that also for a feature of finite width $\Delta\nu$ the signal power **summed** over all frequency bins in the feature will drop proportionally to $1/MW$ when the frequency resolution of the power spectrum is degraded. However, as long as the width of the feature exceeds the frequency resolution: $\Delta\nu > MW/T_{\text{obs}}$, where $T_{\text{obs}} = MT$ is the total length of the observation, the

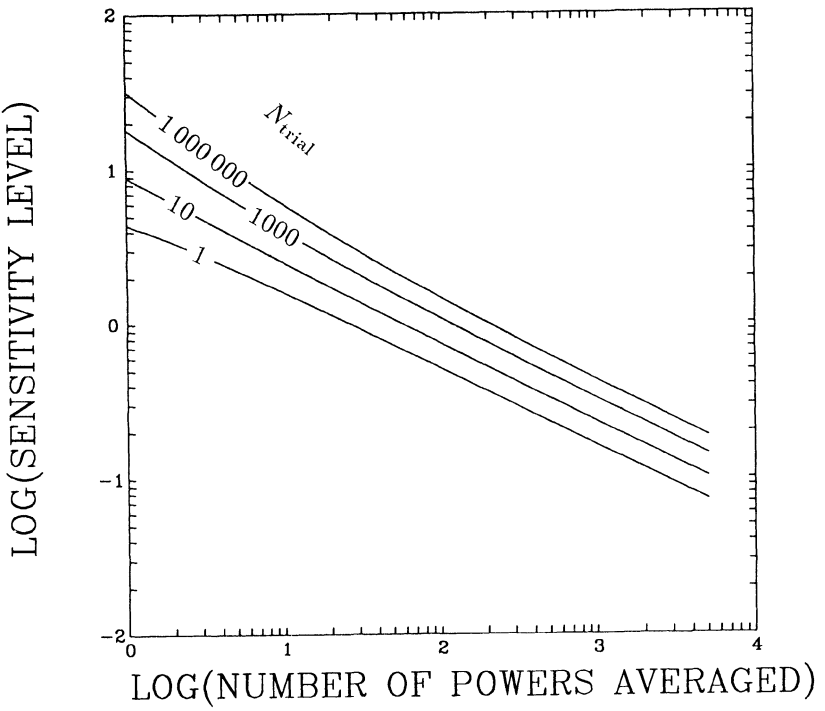

Fig. 5.1. *The sensitivity level as a function of the number of powers averaged (MW) for various numbers of trials. The sensitivity level always decreases more slowly than* $1/MW$.

signal power in one frequency bin within the feature will remain constant (strictly speaking, for a feature with a rectangular profile, and ignoring edge effects), because the number of bins in the feature $\Delta\nu/(MW/T_{\rm obs})$ is also inversely proportional to MW. Because $P_{\rm sensitive}$ drops as a function of MW, this implies that the sensitivity to the feature increases with MW. When $(MW/T_{\rm obs}) > \Delta\nu$, we recover the case of Section 5.2, and the sensitivity begins to drop. So, the optimal value of MW is that which **just** concentrates all power in one bin: $T_{\rm obs}\Delta\nu$.

The above argument ignores the alignment between the feature and the frequency bins; for $MW = T_{\rm obs}\Delta\nu$ one is lucky when all power is in one bin; more likely is a situation where the power is distributed over 2 bins. It is possible to devise tests which take into account various possible alignments and which are optimized for specific shapes of the broad feature; some examples of this will be considered in

Sections 6 and 7.

5.4. Summary: Power Spectral Searches Made Easy

In this section we collect all previous results into a "how to" recipe of testing the power spectrum for a weak signal using equal statistically independent trials.

1. Determine the M and W (Section 3.2). The optimal choice for MW is that which approximately matches the expected width of the power spectral feature one desires to detect, $T_{\rm obs}\Delta\nu$ (Sections 5.2 and 5.3), but gaps in the data or the desire to see the time evolution of the power spectrum may dictate M.
2. Calculate the M power spectra normalized according to Eqs. 2.8 and 2.4*a*. Note that x_k is the number of photons in bin k and $N_{\rm ph}$ the number of photons in **one** power spectrum, $\sum_k x_k$.
3. Average the M power spectra.
4. Think about the noise power distribution (Sections 3.2 and 3.4). Does the noise power spectrum seem to be flat? Is its mean level 2.0? If so, the noise is probably dominated by Poissonian counting statistics – go to step 5. If not, find out why not. Try to determine whether the χ^2 property applies (Section 3.4). If you are satisfied that it does, you can divide the power spectrum by some mean noise power spectral shape and go on step 5. Otherwise, find out what **is** the distribution of the noise powers and determine the detection level accordingly.
5. Determine the detection level (Eq. 3.7, Fig. 3.1).
6. Check the average spectrum for powers exceeding the detection level.
7. Quantify the signal power in terms of a detection (Section 4.2.1) or an upper limit (Section 4.2.2).
8. If necessary, multiply back in the noise power shape you may have divided out in step 4.
9. Convert the signal power into the relative rms variation of the source signal, correcting for the effects of binning and dead time (Section 4.3).
10. To say more about the signal, you need to model its power spectrum. For a sinusoidal signal, see Section 6.

6. DETECTING A SINUSOIDAL SOURCE SIGNAL

6.1. Introduction

When searching for an X-ray pulsar, the first assumption that is made is often that the pulse shape is sinusoidal – and for many X-ray pulsars, of course, this is not a bad assumption. In this section, we first derive the shape of the discrete power spectrum of a sinusoidal signal of arbitrary frequency and phase, and then consider

in some detail how to optimize a power spectral search towards detecting a weak sinusoidal signal. We allow the possibility of dependent trials, which means that detection levels have to be determined by simulations. Throughout this section, we ignore the binning and dead time corrections (Section 4.3).

6.2. The Power Spectrum of a Sinusoidal Signal

The continuous Fourier transform of a sinusoidal signal is a delta function.

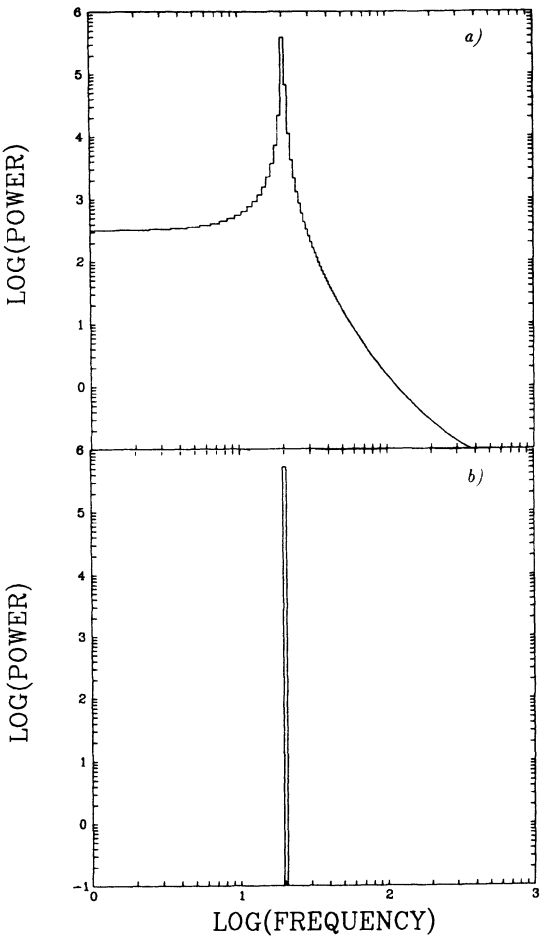

Fig. 6.1. *a) The discrete power spectrum of a sinusoid with an arbitrary frequency. b) Same, with frequency equal to a Fourier frequency.*

However, if one calculates the FFT of some arbitrary sinusoid the result, more likely than not, will be something similar to Fig. 6.1*a*. The reason that this power spectrum does not look very much like a delta function is of course that is was calculated from a discrete Fourier transform. As discussed in Section 2.5, windowing causes a strong distortion of the Fourier transform. (The reason that the spectrum in Fig. 6.1*a* does not look very much like the window transform $W(\nu)$ of Section 2.5 either is that the frequency resolution of a discrete Fourier transform is equal to the width of the side lobes of $W(\nu)$, namely, $1/T$). Only when the frequency ν_{sine} of the sinusoid is equal to one of the Fourier frequencies $\nu_j = j/T$ will all power be concentrated in one bin of the discrete Fourier transform (Fig. 6.1*b*).

The discrete power spectrum of a sinusoidal signal

$$x_k = A\cos(\omega_{\text{sine}} t_k + \phi) \tag{6.1}$$

can be calculated directly from Eq. 2.4*a* by making use of the result

$$\sum_{k=0}^{N-1} e^{i\alpha k} = e^{\frac{1}{2}(N-1)i\alpha} \frac{\sin \frac{1}{2}N\alpha}{\sin \frac{1}{2}\alpha} \tag{6.2}$$

(*e.g.*, Bloomfield 1976). The result of this calculation is

$$|a_j|^2 = \tfrac{1}{4}A^2N^2 \left(\frac{\sin \pi x}{\pi x}\right)^2 \left[\left(\frac{\pi x/N}{\sin \pi x/N}\right)^2 + \left(\frac{\pi x/N}{\sin[\pi(2j+x)/N]}\right)^2 + \right.$$
$$\left. + 2\left(\frac{\pi x/N}{\sin \pi x/N}\right)\left(\frac{\pi x/N}{\sin[\pi(2j+x)/N]}\right)\cos\left[(N-1)\left(2\pi(j+x)/N\right) + 2\phi\right]\right], \tag{6.3}$$

where $x = (\nu_{\text{sine}} - \nu_j)T$, the frequency offset of the sinusoid frequency from frequency bin j in units of the Fourier frequency step $1/T$. The dependence of this expression on the phase ϕ of the sinusoid is small except for j close to 0 or $N/2$ (Fig. 6.2). The function describing the signal power at ν_j as a function of x is of course closely related to $|W(\nu)|^2$ (Eq. 2.15). For $x/N \ll 1$ and $0 \ll j/N \ll \frac{1}{2}$, *i.e.*, for frequency bins close to ν_{sine} and not too close to either zero or the Nyquist frequency, expression (6.3) reduces to

$$|a_j|^2 \approx \tfrac{1}{4}A^2N^2 \left(\frac{\sin \pi x}{\pi x}\right)^2. \tag{6.4}$$

This function, normalized to 1 at $x = 0$ is shown as the drawn curve in in Fig. 6.2*b*.

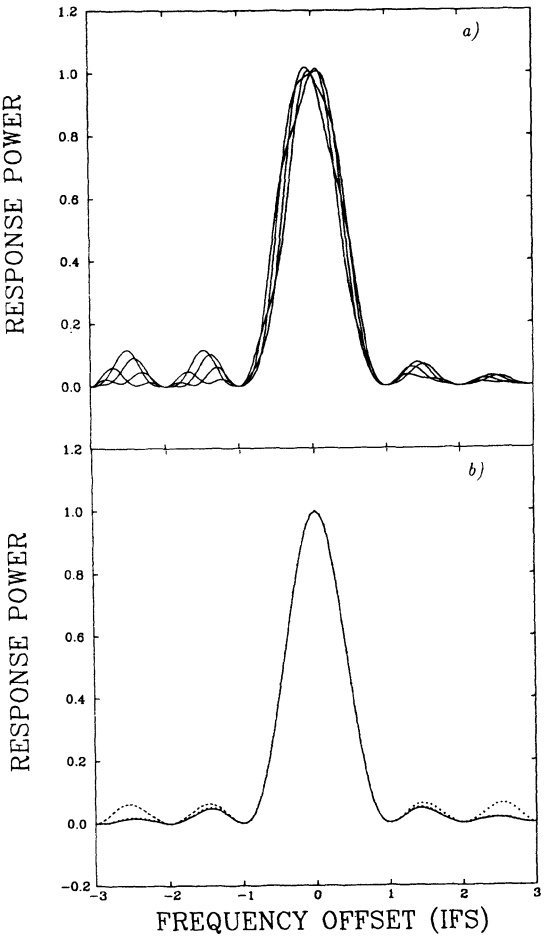

Fig. 6.2. *Response power at ν_j to a sinusoidal signal as a function of $\nu_{\text{sine}} - \nu_j$ in units of the independent Fourier frequency step (IFS). Calculations are for $N = 1024$. a) $j = 2$. Curves are for various phases of the sinusoid. b) Phase-averaged curves. Drawn: $j = 200$; dashed: $j = 2$; dotted: $j = 510$.*

6.3. Single-Power Response

The highest power in the signal power spectrum will be obtained at the Fourier frequency ν_j closest to ν_{sine}. Normalized to a power of 1 for $\nu_{\text{sine}} \equiv \nu_j \quad (x = 0)$, this power varies between 0.405 and 1, with an average value of 0.773 (Fig. 6.5, drawn curve). In the following we will use the term "input power" for the power that

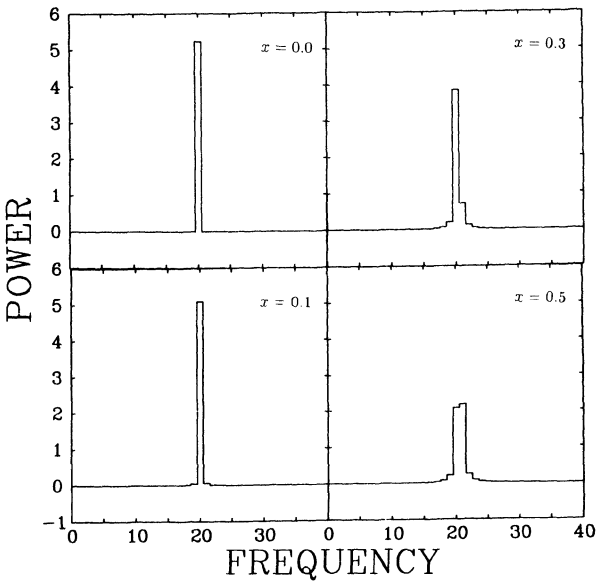

Fig. 6.3. *Discrete power spectra of a sinusoidal signal with frequency offsets from the nearest Fourier frequency as indicated. Nearly all power is in all cases concentrated in the two bins closest to* $\nu_{\rm sine}$.

would have been caused by the sinusoidal signal if $\nu_j = \nu_{\rm sine}$; the "response power" is the power that is actually produced in the signal power spectrum. The "response function" is the response power divided by the input power as a function of x, and the "response" is the highest response power in the power spectrum divided by the input power. So, the drawn curve in Fig. 6.2*b* is a response function. For this curve, the input power is 1, the response power depends on x and is between 1 and 0 and the response depends on x and is between 1 and 0.405. This "ripple" in the response to a sinusoidal signal implies that we can not exactly predict the highest response power for a sinusoidal signal of given input power and arbitrary frequency: the best we can do is calculate the probability distribution of the response.

This fact should in principle be taken into account when interpreting a power spectrum in terms of the properties of a sinusoidal source signal. For example, to set an upper limit to the amplitude A of the signal when no significant power has been detected, one should take into account that A depends not only on P_j, but also on x, ϕ and, mostly via the binning factor, on j. The canonical method

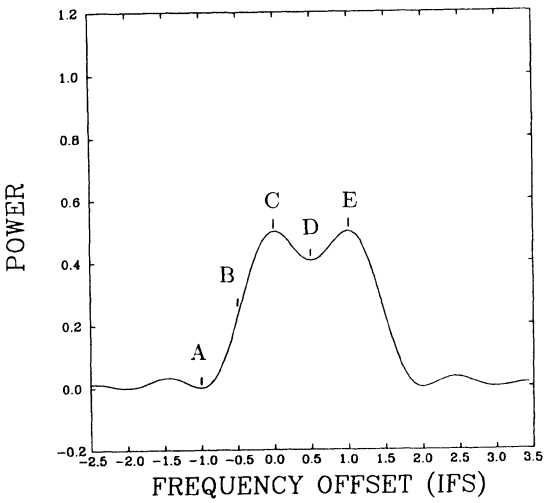

Fig. 6.4. *Averaged response power in two adjacent bins j and $j+1$ as a function of the frequency offset x of the sinusoidal signal from bin j.*

is to first determine an upper limit to $P_{j,\mathrm{signal}}$ using the noise power distribution (Section 4.2.2), and then convert this into an upper limit to A by using the average value (0.773) of the response. However, a signal with an amplitude considerably larger than the upper limit A_{UL} obtained in this way can easily be hidden in the data if its frequency happens to be close to halfway two Fourier frequencies. If there is a $P_{j,\mathrm{signal}}$ somewhere in the spectrum that actually reaches the limiting level P_{UL}, then there is a probability of ~44% that $A > A_{\mathrm{UL}}$. The factor by which A can exceed A_{UL} is at most 1.4, which would in most circumstances probably not be considered a large error. A better way of obtaining A_{UL} would be to consider the bivariate probability function of A in its dependence on $P_{j,\mathrm{noise}}$ and x, (the dependence on ϕ is weak, and that on j is usually kept).

6.4. Optimal Detection of a Sinusoidal Signal

The ripple in the single-power response to a sinusoidal signal will cause one to preferably miss signals with a frequency halfway between two Fourier frequencies.

Inspection of Fig. 6.3 shows that in this case ($x = 0.5$) nearly all power in the signal is divided between the two adjacent bins – power loss to frequency bins further out is relatively small. This suggests taking two-bin averages as a method to diminuish the ripple. Note that degrading the frequency resolution by dividing the data into M segments (Section 3.2) will not diminuish the ripple at all, but will instead lead to a loss of sensitivity similar to that discussed in Section 5.2.

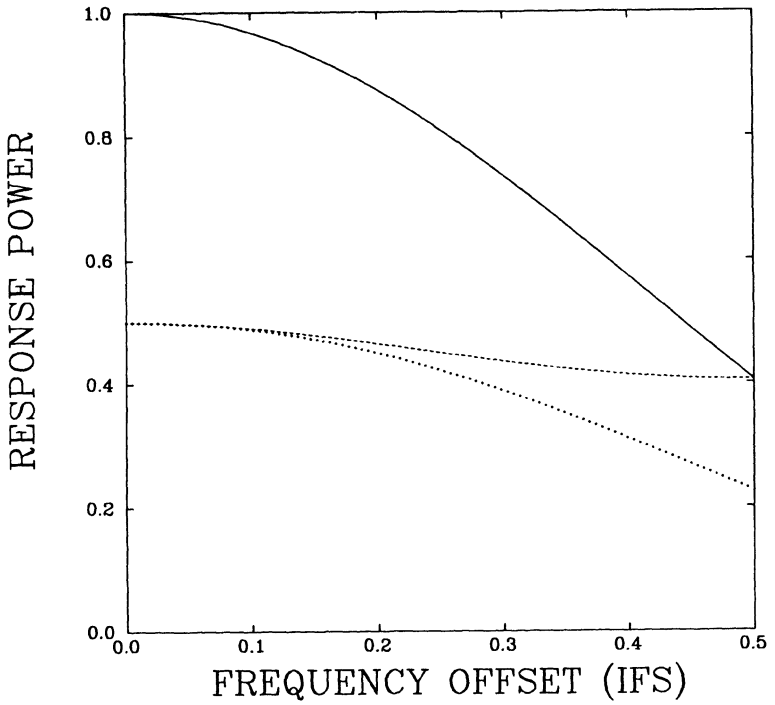

Fig. 6.5. *Comparison of the responses of the single-bin (drawn), two-bin running average (dashed) and two-bin no-overlap (dashed and dotted) schemes.*

Fig. 6.4 shows the average power in two adjacent bins as a function of x. To take full advantage of the flat part (C-E) of the two-bin response, it is necessary to consider **overlapping** averages ($\frac{1}{2}(|a_j|^2 + |a_{j+1}|^2)$; $\frac{1}{2}(|a_{j+1}|^2 + |a_{j+2}|^2)$; ...), otherwise in 50% of the cases the signal would still be in between bins (section B-C of the response). This means that the number of trials will nearly be equal to the single-bin case. In Fig. 6.5 the response of this 2-bin average, 1-bin overlap scheme (to be indicated henceforth as (2,1)) is compared to the single-bin (1,0) approach. The (2,0) response is also indicated. The (2,1) response is a factor 2 lower than the (1,0) one at $x = 0$, but the corresponding detection level is also much lower, the noise having been averaged over two bins. The (2,1) response varies between 0.5 and 0.405 with an average of 0.451.

Because of the overlap between the (2,1) trials, the chance to exceed a certain power level by noise can not be straightforwardly estimated analytically. One can perform simulations of many noise power spectra to determine the chance to exceed a certain power level by noise somewhere in the power spectrum as a function of

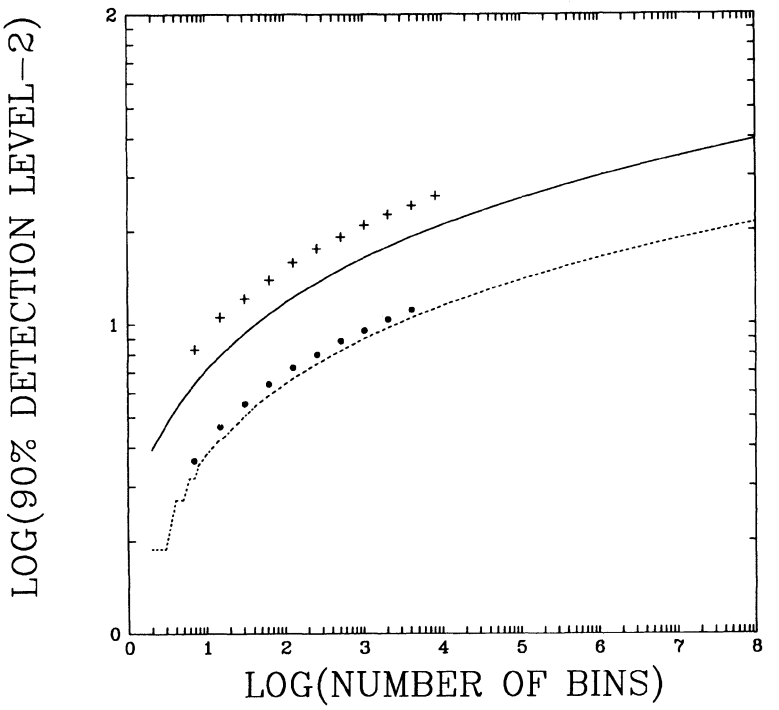

Fig. 6.6. *90% confidence detection levels as a function of the number of frequency bins in the power spectrum for the (1,0) (drawn) and (2,0) (dashed) schemes as determined from Eq. 3.7 (MW = 1), and the (2,1) (filled circles) and B&IB (crosses) schemes as determined from simulations of noise power spectra. Each point corresponds to 10^4 simulated power spectra; error bars are smaller than the points.*

the number of bins in the power spectrum. Results of simulations of this type are given in Fig. 6.6 in terms of the 90% confidence detection level (filled circles). It can be seen that the detection level is scarcely higher than for (2,0) sampling of the power spectrum (dashed curve), despite the twice higher number of trials. The reason for this is the large dependence of the extra trials in the (2,1) scheme with those already in the (2,0) scheme.

Another method of decreasing the ripple, used in pulsar radio astronomy (Backer 1988, priv. comm.) is "interbinning". In this method (Cullers *et al.* 1984), an extra frequency bin is created **in between** each two Fourier frequencies by calculating the difference of the adjacent complex Fourier amplitudes. One calculates the "interbin amplitude"

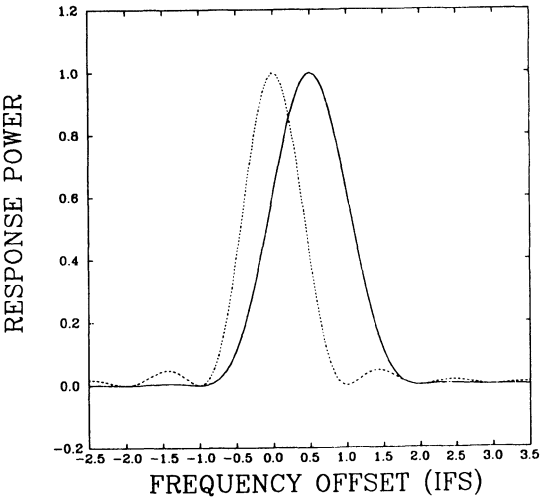

Fig. 6.7. *Interbin response power at $j+\frac{1}{2}$ for an input power of 1 (drawn) compared to response power at j (dashed) as function of the frequency offset x. The interbin reponse has its maximum at $x = \frac{1}{2}$.*

$$a_{j+\frac{1}{2}} = \frac{\pi}{4}(a_j - a_{j+1}). \tag{6.5}$$

The response function of this "filter" is

$$\left(\frac{\pi}{4}\frac{\cos(\pi(x-\frac{1}{2}))}{\pi x(1-x)}\right)^2 \tag{6.6}$$

This function is plotted in Fig. 6.7 together with the response function of one of the adjacent bins. The interbin response function is seen to be wider; its normalization is such that the response is 1 when ν_{sine} is exactly in between Fourier frequencies. The ripple in the response of bins and interbins (henceforth B&IB) together is even less than that in the (2,1) scheme: it varies between 1 and 0.857 with an average of 0.951. The number of trials in the B&IB scheme is twice that in the (1,0) or (2,1) schemes. Again the detection levels of the B&IB scheme must be determined with the help of simulations. In Fig. 6.6 some preliminary results are given (crosses). Note that the choice of one single detection level for bins and interbins together is not necessarily optimal, as the noise distributions of bins and interbins are different. In fact, the reason that the detection levels of the B&IB system are seen to be considerably higher than those corresponding to single-bin trials (1,0), is not so much the twice higher number of trials but the fact that the

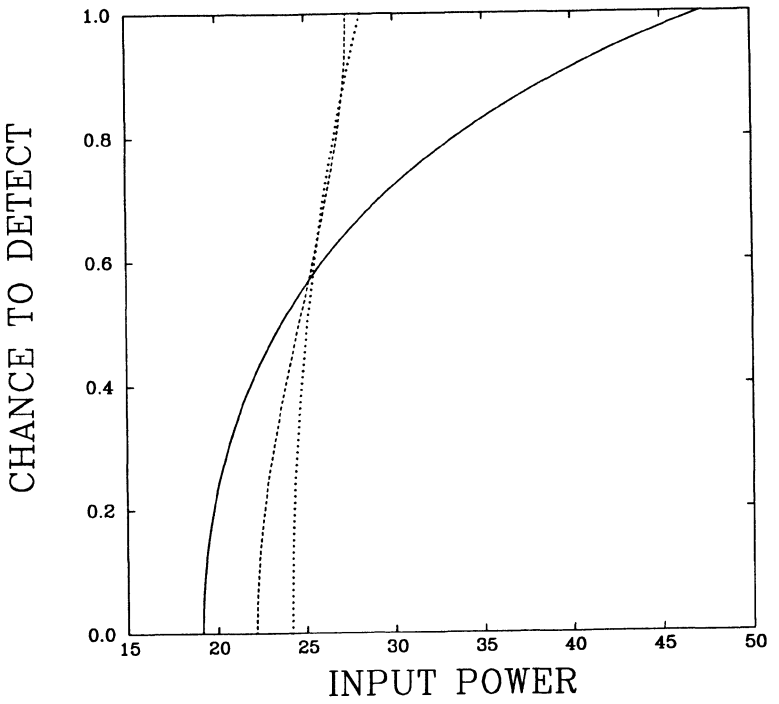

Fig. 6.8. *Comparison of the probability to detect (at the 90% confidence level) a sinusoidal signal of arbitrary frequency as a function of its input power for the single-power (drawn), 2-bin running average (dashed) and bin/interbin (dotted) methods. In this example, N = 8192 (4095 bins in the power spectrum). For input powers between 19.1 and 47.2, the average chance to detect the signal is 73, 80 and 77%, respectively.*

average noise level in the interbins is higher than in the bins by a factor ~1.23.

Knowing the detection levels (Fig. 6.6) and the probability distributions of the response to a sinusoidal signal that can be derived from the response functions (Figs. 6.5 and 6.7), one can estimate the probability to detect a sinusoidal signal of given amplitude in the various schemes ((1,0),(2,1),B&IB) as a function of the number of bins in the power spectrum. Fig. 6.8 displays the probability to detect the signal as a function of the input power for a power spectrum containing 4095 bins (the Nyquist frequency was excluded), where the phase-averaged response functions were used, and where the approximation was made that $P_j = P_{j,\mathrm{signal}} + 2$ rather than folding in the noise power distribution; given the large signal powers considered this is probably not a serious approximation. It is seen that the curves of the (2,1)

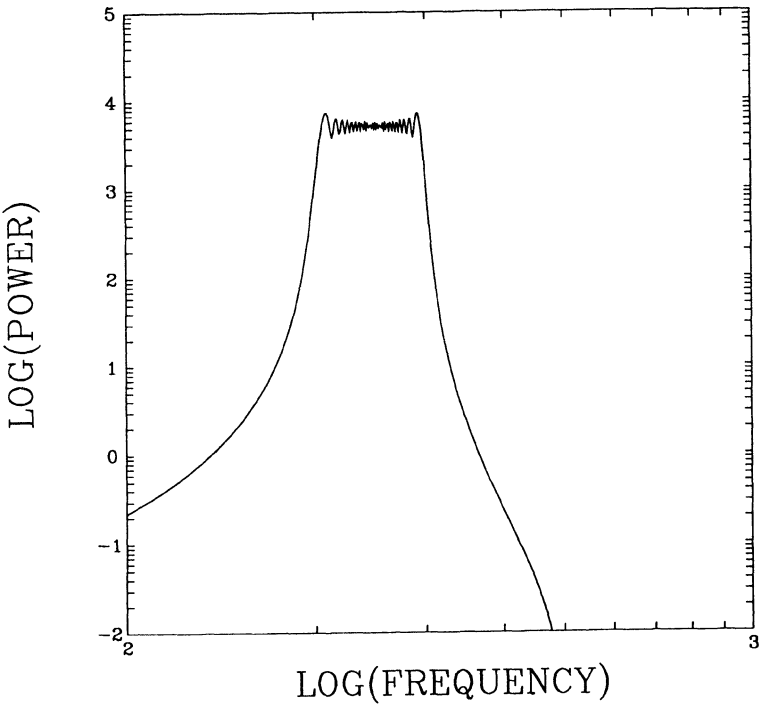

Fig. 6.9. *Power spectrum of a sinusoidal signal with a constant frequency derivative. The sinusoid frequency changes by 100 Fourier frequency steps during the observation.*

(dashed) and B&IB (dotted) schemes are quite similar and much steeper than that of the (1,0) scheme (drawn). The latter method has some probability to detect weak signals which are always missed by the former two, but signals always detected by the (2,1) and B&IB schemes will sometimes be missed by the (1,0) scheme.

When the input power is arbitrary, the methods can be compared by determining the average chance to detect a signal over the entire range of input powers where the three methods give different chances to detect the signal (for very high input powers the chance to detect is 1 for all methods, for very low ones, 0). The results of the preliminary simulations presented here seem to indicate that the differences between the methods are small, that the (2,1) method is best and the (1,0) method worst, with the B&IB method intermediate. However, the differences are sufficiently small for the approximations of the simulations to become relevant.

In any case it seems clear, that even for strictly periodic sinusoidal signals the single-bin approach is not always optimal. If there is any intrinsic broadening of

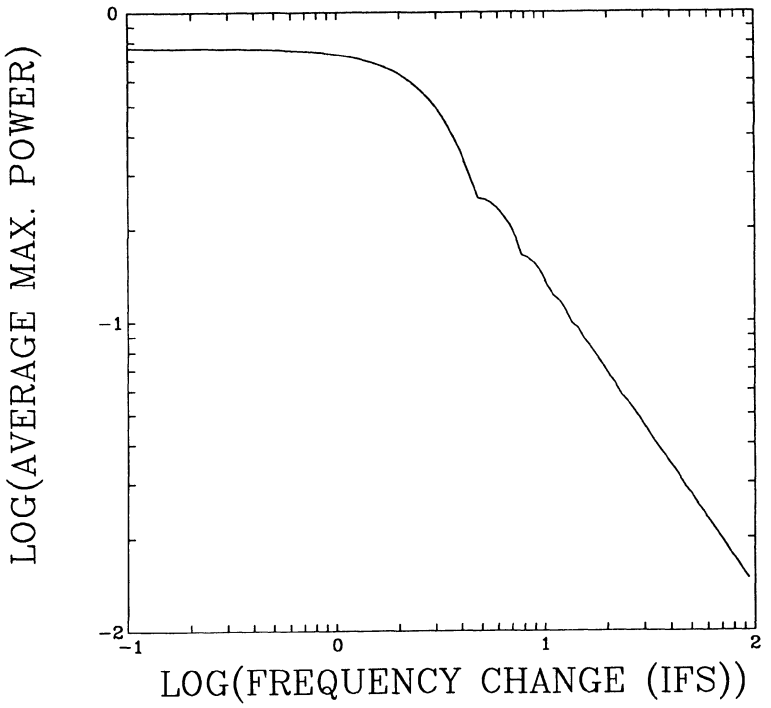

Fig. 6.10. *Highest power in a power spectrum of a sinusoidal signal with a constant $\dot{\nu}$ as a function of $\dot{\nu}T^2$.*

the signal, then the frequency resolution should certainly be degraded to optimize the search.

6.5. Sinusoidal Signal with Varying Frequency

The shape of the power spectrum in the case of a sinusoidal signal with a constant frequency derivative $\dot{\nu}$ is mainly determined by the number of bins in the power spectrum that the frequency changes during the observation ($\dot{\nu}T^2$). In general, the power spectral peak will have a width equal to this; the power will be more or less equally spread out over the peak (Fig. 6.9).

Averaging over all possible phases of the sinusoid and the over the initial frequency offset x one finds that the highest power in the power spectrum drops rapidly for $\dot{\nu}T^2 > 2$ (Fig. 6.10). As we have seen in Section 5.3, the frequency resolution of the power spectrum should be degraded to match the width of the peak for optimal sensitivity.

Another type of frequency variations that is encountered in practice is that caused by orbital motion. In this case, the frequency will change periodically with an amplitude $\nu_0 K/c$ (where ν_0 is the rest frequency, K the velocity amplitude of the orbital motion and c light speed) and a period equal to the orbital period $P_{\rm orb}$. If the observation is much shorter than the orbital period: $T \ll P_{\rm orb}$, then we approximately recover the previous case with $\dot{\nu} \approx \nu_0 (K/c)(2\pi/P_{\rm orb}) \cos \Phi_{\rm orb}$, where $\Phi_{\rm orb}$ is the orbital phase.

If on the other hand $T \gtrsim P_{\rm orb}$ then the power spectrum gets quite complicated, a central peak at ν_0 being accompanied by many side lobes with a separation $1/P_{\rm orb}$. Often, one tries to deal with the complexities of this situation by cutting up the observation into M segments and demanding that the change of frequency caused by the orbital motion is less than one frequency bin in any individual power spectrum. This implies

$$T < \sqrt{\frac{cP_{\rm orb}}{2\pi K \nu_0}}. \tag{6.7}$$

However, this condition does not prevent the power spectral peak from moving from one bin to the next in successive power spectra, so that a broad peak in the average spectrum in any case results.

An in principle very powerful method to deal with variable-frequency signals is "precorrecting": correcting the arrival times of the data for different assumed binary orbital parameters or frequency derivatives in the hope to recover a constant-frequency signal. A large gain in sensitivity can in principle be attained with this method. However, often the number of different sets of parameters one needs to try is prohibitive.

7. COMPREHENSIVE POWER SPECTRAL SEARCHES

In the previous sections we have considered how to optimize power spectral searches to finding specific features of known width. Often, the signal(s) one is looking for are not sufficiently closely constrained to predict the width of the feature in the power spectrum, or one wishes to look for source variability in general. In that case, one needs to perform a search of the power spectrum that is sensitive to narrow as well as broad features.

A reasonable approach seems to search the power spectrum several times, using different values of W. The trials in these searches will obviously be strongly interdependent, so that the detection levels will again have to be determined using simulations, and should take into account the total number of trials in the entire search. The degree of interdependence of the trials, and therefore the detection levels, will depend on the particular **search scheme** that is employed, and in particular, on the values of W and on the overlap between the trials. As different

values of W will occur in a search, the distribution of the noise powers will differ between the trials. It seems reasonable, therefore, to choose the detection level different for each value of W, in such a way that the *a priori* chance ϵ_{scheme} **in one trial** to exceed the detection level is equal for all trials in the entire search. Instead of one detection level P_{detect}, there will now be several different ones $P_{\text{detect},W}$ corresponding to the different values of W that occur. These detection levels are given by

$$\epsilon_{\text{scheme}} = Q(MWP_{\text{detect},W}|2MW). \tag{7.1}$$

Note that the number of times the detection levels are actually exceeded in the search of a pure noise spectrum is **not** equal to $\epsilon_{\text{scheme}}N_{\text{trial}}$ because of the strong interdependence of the trials. Therefore, ϵ_{scheme} can not be simply related to the required confidence level of detection, but has to be determined from simulations of the search scheme. ϵ_{scheme} is just a compact way of summarizing the different detection levels $P_{\text{detect},W}$ applicable to the particular search scheme employed.

In Fig. 7.1 ϵ_{scheme} corresponding to a 90% confidence detection level is plotted for two different search schemes *vs.* the number of independent powers in the power spectrum. In both schemes the values chosen for W were (1,2,4,8,...,$N/2$). In one scheme (indicated by filled circles) a 50% overlap between trials of the same width was used; in this scheme $N_{\text{trial}} \approx 3N/2$, (the number of powers in the spectrum, or the number of trials in a (1,0) scheme is $N/2$). In the other scheme (crosses) no overlap was allowed; in this scheme $N_{\text{trial}} \approx N$.

The values of ϵ_{scheme} in Fig. 7.1 were determined from simulations of many noise power spectra by assuming, for each power spectrum, a series of different values of ϵ_{scheme}, calculating for each value of ϵ_{scheme} the detection levels $P_{\text{detect},W}$ corresponding to each value of W using Eq. 7.1, and then testing the power spectrum for averaged powers exceeding these levels. The value of ϵ_{scheme} corresponding to a 90% confidence detection was then determined as that value for which only 10% of the spectra showed an excess over a $P_{\text{detect},W}$.

The way in which one would employ in practice the results of such simulations would be to use the ϵ_{scheme} obtained by simulations of the appropriate search scheme to calculate the various $P_{\text{detect},W}$ values with Eq. 7.1, and then test the spectrum, following the search scheme, against these detection levels. An excess would have well-defined statistical properties (it would constitute a detection at the required confidence level), contrary to the method where likely-looking excesses are selected by eye from plots of the power spectrum and tested *a posteriori* for significance using rules-of-thumb. A method such as described here has the further advantage that it is sensitive to "everything". It is of course somewhat less sensitive to a specific signal than a specialized test.

Once the simulation process has been set up, search schemes of this kind can

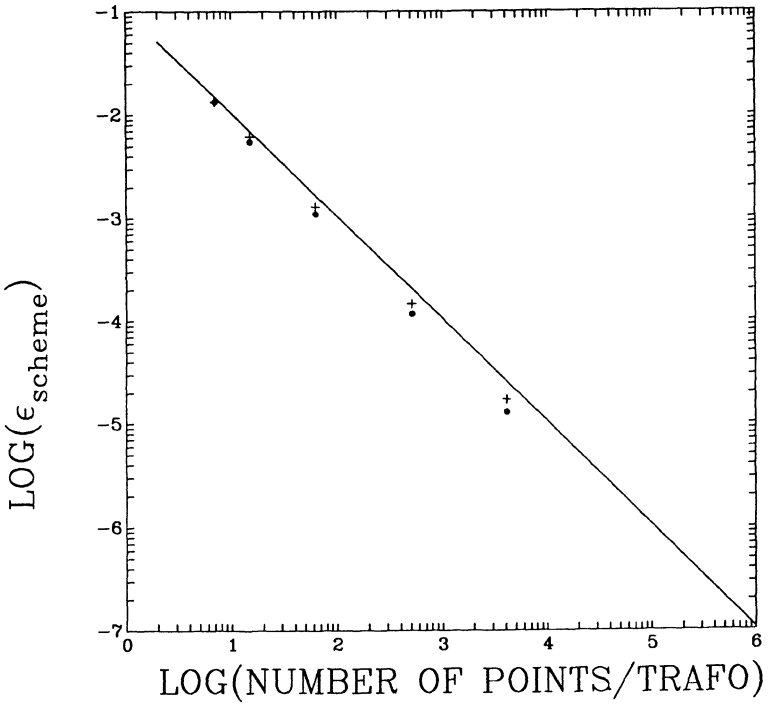

Fig. 7.1. *The a priori chance to exceed the detection level in one trial, from which one must calculate the detection levels as a function of W to obtain an effective 90% confidence detection level. Two "dependent sample" schemes (symbols) and the (1,0) scheme (curve) are illustrated. See text for a description of the dependent sample schemes. Each point corresponds to 10^4 simulated power spectra. Error bars are smaller than the points.*

easily be extended to include searches where W itself depends on j (for example, because the features searched for have a known $\Delta\nu/\nu$) or where searches are performed of two-dimensional arrays of power spectra (for example when searching dynamic power spectra for transient phenomena).

ACKNOWLEDGEMENTS

This paper benefitted from stimulating discussions with many of the participants of this ASI, notably Don Backer and Ocke de Jager, and with Luigi Stella.

REFERENCES

Andrews, D., Stella, L., 1985, *EXOSAT Express* **10**, 35.

Bloomfield, P., 1976, *Fourier Analysis of Time Series: an Introduction*, (John Wiley & Sons – New York).

Bracewell, R., 1965, *The Fourier Transform and its Applications*, (McGraw-Hill).

Deeter, J.E., 1983, *Astrophys. J.* **281**, 482.

Cullers, D.K., Oliver, B.M., Day, J.R. and Olsen, E.T., 1984, *NASA Tech. Paper* **2244**, 49.

Deeter, J.E., and Boynton, P.E., 1982, *Astrophys. J.* **261**, 337.

Jenkins, G.M. and Watts, D.G., 1968, *Spectral Analysis and its Applications*, (Holden-Day – Oakland).

Leahy, D.A., Darbro, W., Elsner, R.F., Weisskopf, M.C., Sutherland, P.G., Kahn, S. and Grindlay, J.E., 1983, *Astrophys. J.* **266**, 160.

Lewin, W.H.G., van Paradijs, J. and van der Klis, M., 1988, *Space Science Reviews*, in press (Paper 1).

Press, W.H., Flannery, B.P., Teukolsky, S.A. and Vetterling, W.T., 1986, *Numerical Recipes*, (Cambridge University Press).

Tennant, A.F., 1987, *MNRAS* **226**, 963.

Weisskopf, M.C., 1985, talk presented at Workshop *Time Variability in X-Ray and Gamma-Ray Sources*, Taos NM, USA.

DETERMINISTIC CHAOS IN ACCRETING NEUTRON STAR SYSTEMS

G.E. MORFILL, H. ATMANSPACHER, V. DEMMEL, H. SCHEINGRABER, AND W. VOGES

Max-Planck-Institut für Physik und Astrophysik
Institut für extraterrestrische Physik
D-8046 Garching, FRG

Abstract:
This review contains a brief introduction to the terminology of deterministic chaos, and a summary of important properties and definitions of strange attractors. A method is described how to reconstruct the attractor from experimental data. Using synthetic data, the specific problems associated with the reconstruction are examined. As an observational example, analysis of data from the accreting neutron star system Her X-1 is described. Finally, we discuss the physical interpretation of these observations, the possible implications for the description of the system from a general point of view, the specific implication for the pulse shape and pulse to pulse variations, and possible approaches towards a better understanding of both accretion disc and accretion column.

Introduction to the theory of deterministic chaos:

A given physical system can be regular, e.g. it can be stationary, periodic, doubly periodic etc., it can be stochastic which implies a description with probability distributions, or it can be chaotic. Chaotic systems are described by a set of coupled nonlinear differential or difference equations, which can be solved numerically, the solution describing a trajectory in phase space. A general property of these systems is the exponential divergence of initially nearby trajectories. This means that a given trajectory may only be predicted for a finite time interval, corresponding to the correlation time of the system. In this sense, chaotic systems occupy the regime between regular (correlation time $\rightarrow \infty$) and stochastic (correlation time $\rightarrow 0$) systems, and it seems plausible that they will be difficult to differentiate from the latter. Further information on these concepts can be found in Atmanspacher and Scheingraber (1987).

The one clear distinguishing feature is that stochastic systems eventually occupy all the available phase space as $t \rightarrow \infty$, whereas chaotic systems are confined to a subregion of the available phase space. In order to distinguish between these two situations in practice, which means limited data sets, new techniques have been

H. Ögelman and E. P. J. van den Heuvel (eds.), Timing Neutron Stars, 71–93.

developed. These techniques allow us to characterise chaotic systems, to quantify their complexity, to differentiate them from other systems and to identify them.

In the present context we consider continuous systems which may be described by a set of first order differential equations:

$$\dot{\mathbf{x}}(t) = \mathbf{F}(\mathbf{x}(t), \mu) \tag{1}$$

where the vector $\mathbf{x}$ is

$$\mathbf{x}(t) = (x_1(t), x_2(t), ..., x_n(t)) \tag{2}$$

The equations are autonomous ($\mathbf{F}$ is not explicitly a function of t) nonlinearly coupled, and there exists at least one external control parameter, μ. This implies that the system is open to interactions with the surroundings; e.g. forcing and dissipation.

The temporal evolution of the uncertainty in one variable, say δx_i, is governed by

$$\frac{d}{dt}\left(\delta x_i\right) = \sum_{j=1}^{n} \frac{\partial F_i}{\partial x_j} \delta x_j \tag{3}$$

and the Jacobian $D\mathbf{F}$ can be evaluated once (1) is specified. For a given $\mathbf{x}$, the object is to determine the eigenvalues of the matrix $D\mathbf{F}$, $\Lambda_i(t)$. Note that by choosing a local coordinate sytem, so that $(\delta x_1 \mathbf{e}_1) \times \dot{\mathbf{x}}(t) = 0$, $\Lambda_1 = 0$ in all cases. Here $\mathbf{e}_1$ is the unit vector in the direction of x_1. This yields, provided the matrix can be diagonalised

$$\frac{d}{dt}(\delta x_i) = \Lambda_i \delta x_i \tag{4}$$

i.e. the uncertainty grows or declines exponentially depending on the sign of Λ_i. If the uncertainty grows exponentially, then according to our earlier description, neighbouring trajectories in phase space diverge and the system is chaotic. Since Λ_i is a function of t, and therefore a "local" quantity, we have not adequately described the evolution of the system on a temporal average ($t \to \infty$). This is done by defining the Ljapunov exponent

$$\lambda = \lim_{t \to \infty} \frac{1}{t} \int_0^t \Lambda(t')dt' \tag{5}$$

It has the dimension $(\text{time})^{-1}$, is a specific property of the system and, if positive and finite, defines deterministic chaos.

The local solution of (4) is

$$\delta x_i(t) = \delta x_i(0)\ exp\left\{\int_0^t \Lambda_i(t')dt'\right\} \tag{6}$$

and using the Ljapunov exponent (5), the average evolution of the uncertainty δx_i is given by

$$\delta x_i(t) = \delta x_i(0)\ exp\left\{\lambda_i t\right\} \tag{7}$$

For a multidimensional vector $\mathbf{x} = (x_1, ..., x_n)$, we may define an uncertainty volume as a measure of that subset of phase space ascribed to a solution of (1),

$$\delta V(t) = \prod_{i=1}^{n} \delta x_i(t) \tag{8}$$

which becomes, using (7)

$$\delta V(t) = V(0)\ exp\left\{\sum_{i=1}^{n} \lambda_i(t)\right\} \tag{9}$$

For a non-diverging uncertainty volume (confinement), we have the two cases

$$\sum_{i=1}^{n} \lambda_i = 0 \tag{10}$$

(conservative system) and

$$\sum_{i=1}^{n} \lambda_i < 0 \tag{11}$$

which defines a dissipative system. In contrast, for a stochastic system in the sense mentioned above we have

$$\sum_{i=1}^{n} \lambda_i > 0 \tag{12}$$

If condition (11) is satisfied, the evolution of the corresponding dissipative system in the limit $t \to \infty$ takes place on an attractor. We can now classify some types of attractors, see table 1, remembering that by choice of the local coordinate system we may always identify $\lambda_i(\| \dot{\mathbf{x}}) = 0$.

Tab. 1 : Classification of attractors

n	Ljapunov exponents			Attractor
1	$\lambda_1 < 0$			fixed point
2	$\lambda_1 = 0,$	$\lambda_2 < 0$		limit cycle (1-torus)
3	$\lambda_1 = 0,$	$\lambda_2 < 0,$	$\lambda_3 < 0$	limit cylce (1-torus)
	$\lambda_1 = 0,$	$\lambda_2 = 0,$	$\lambda_3 < 0$	2-torus
	$\lambda_1 = 0,$	$\lambda_2 > 0,$	$\lambda_3 < 0$	strange attractor

There is one more case, where the system develops towards a fixed point, for $n = 3$, all $\lambda_i < 0$. As a necessary condition for a strange attractor, it is required that $n \geq 3$, i.e. at least three nonlinearly coupled differential equations.

Another quantity which is useful in this context is the Kolmogorov entropy. Under certain preconditions (Pesin 1977) it is given by the sum of the positive Ljapunov exponents

$$K = \sum_{i=1}^{n} \lambda_i H(\lambda_i) \tag{13}$$

where H is the Heavyside function.

It has the dimension $(\text{sec})^{-1}$, $K > 0$ implies at least one positive Ljapunov exponent and therefore a chaotic system. From an information theoretical viewpoint, K can be considered as the rate of production of information, and K^{-1} is a measure of the time for which the system is still predictable to a reasonable degree.

The Ljapunov exponent λ_i and the Kolmogorov entropy K are dynamical invariants of the system. The geometrical structure of the attractor for the system in its asymptotic limit $t \to \infty$ (where initial transients have been damped out) are also of interest. The relation between K and the correlation time suggests a simple analysis of the clustering of points in phase space using spatial two – point or multi – point correlation approaches.

The two – point correlation function for a quantity $\varrho(x)$ is

$$c^{(2)}(r) = < \varrho(x)\varrho(x - r) > \tag{14}$$

where r is the running variable, and angular brackets denote averages. The integral two – point correlation function is

$$C^{(2)}(r) = \int_0^r c^{(2)}(r')d^n r' \tag{15}$$

for an n – dimensional array.

Motivated by a number of empirical examples, it has turned out that a simple scaling assumption

$$C^{(2)}(r) \propto r^{D^{(2)}} \tag{16}$$

gives a reasonable description of many systems. In general, the scaling index $D^{(2)}$ is a non – integer number determined by:

$$D^{(2)} = \lim_{r \to 0} \frac{\log C^{(2)}(r)}{\log r} \tag{17}$$

This correlation dimension alludes to the complexity of the attractor. It is a metric invariant of the system and can be related to system properties as will be described below. The variable r may be viewed as a geometrical length scale, defining the resolution with which we are investigating the attractor.

If the attractor of the system is self – similar, i.e. geometrically reproduces itself on increasingly finer levels ad infinitum, then relationship (16) yields non – integer $D^{(2)}$ in most investigated cases.

Topologically, deterministic chaos and strange attractors are often associated with self – similar structures and fractal dimensions. Regular processes have integral dimensions (0 = fixed point, 1 = periodic, 2 = doubly periodic).

In addition to the correlation dimension $D^{(2)}$, the analysis can be generalised to multi – point correlations $C^{(q)}$ and generalised dimensions $D^{(q)}$. The dimension $D^{(0)}$ is termed Hausdorff, or fractal dimension, $D^{(1)}$ is the information dimension, and generally

$$D^{(q)} \leq D^{(q-1)} \tag{18}$$

If an analysis of an experimental data set provides a non – integer correlation dimension $D^{(2)}$, then the following information has been extracted:

1) The system is chaotic (strange attractor)

2) A sufficient number, n, of differential equations needed to describe the system is given by the next integral number greater than $D^{(2)}$. From our preceeding discussion we had $n \geq 3$, which implies $D^{(2)} \geq 2$.

3) The characteristic time scale K^{-1} for the chaotic processes is $\Delta t \ll K^{-1} \ll T$, where Δt is the minimum resolution of the data, T the total length of the record.

There may, of course, be some confusion from an overlap due to pure stochastic effects (e.g. photon statistics), but this can in principle, be recognised in the analysis.

Reconstruction of the attractor from data: theory

The statement of the problem is the following:

We have a data record from our astrophysical object. This is generally a time series of light intensities or photon counts. The experiment cannot be reproduced, the data set is unique. So we have to assume that the data record is representative of the system: it must truly define the extent and structure of the attractor. A second and third data set of similar quality should therefore produce similar results, unless the system undergoes significant evolutionary or topological changes (e.g. outbursts, obscuration effects etc.).

The time signal we have received generally integrates over the object, which usually is not spatially resolved. We may, however, identify major emission regions based on timing analysis (e.g. pulsed emissions), spectral information (e.g. polar cap emission as opposed to disc emission, doppler shift), correlated observations with other complementary instruments etc.

The signal contains information about microscopic processes (e.g. photon production, absorption, resonances) and macroscopic processes (e.g. radiation transfer, matter flow, instabilities, torques, precession). In the case of accreting neutron stars and pulsars, we suspect that the macroscopic processes might exhibit a chaotic component, if at all, and that the microscopic signatures probably will not.

It is our conviction that it is a valuable additional information to know whether astrophysical systems are chaotic or not, and if they are, what the characteristic time scale and the degree of complexity is. Otherwise we would be throwing away information which goes beyond that which is obtained from Fourier analysis. In addition, theorists might be guided into new approaches and even new phenomena may be discovered as a result.

On the other hand, as will become apparent later, the reconstruction techniques cannot be regarded as black boxes, a good deal of detailed analysis is necessary, test runs with artificial data sets have to be performed in order to get confidence in the results. Obtaining a dimension $D^{(q)}$ is a very long way away from producing a physically convincing model – it is, however, a constraint. Clearly only low order systems are tractable and will, naturally, elicit most attention.

(Thus the solution of the *Final Question*, which apparently requires dimension $n = 42$ (D. Adams, *The Hitchhikers Guide to the Galaxy*) is securely beyond the scope of present modelling.)

From a practical point of view, we now briefly describe the method, which we have used to analyse data records with respect to their possible chaotic content (Takens 1981, Grassberger and Procaccia, 1983a). The method is based on using a given data set of equally spaced points to construct an artificial phase space of d dimensions.

The data are represented as d shifted time series.

$$
\begin{aligned}
&x(t_1), ..., x(t_N) \\
&x(t_1 + \Delta t), ..., x(t_N + \Delta t) \\
&x(t_1 + 2\Delta t), ..., x(t_N + 2\Delta t) \\
&\vdots \\
&x(t_1 + (d-1)\Delta t) ..., x(t_N + (d-1)\Delta t)
\end{aligned}
\tag{19}
$$

Thus $x_i = \{x(t_i), x(t_i + \Delta t), ...x(t_i + (d-1)\Delta t)\}$ is a d – dimensional vector, defining a point in a d – dimensional space.

In this way, the attractor is "reconstructed" from a time series of data coming from a single variable (e.g. X – ray flux). The real attractor, which gave rise to the particular data sequence, is completely embedded in the artificial d – dimensional phase space, if $d \to \infty$. The procedure is then to determine $|\mathbf{x}_i - \mathbf{x}_j|$ for $d = 1$, and to calculate the correlation integral $C^{(q)}_{d=1}(r)$. Next, the dimension of the artificial phase space is incremented, and $C^{(q)}_{d=2}(r)$ is calculated etc. until the artifical phase space dimension is believed to be sufficiently large. Usually $d \approx 2n + 1$ is adequate (Takens 1981). This can, in principle, be done for any multipoint correlation, q (see Pawelzik and Schuster 1987, Atmanspacher et al. 1988).

For the mathematical proof of the embedding theorem the data were assumed to be free of noise, the sampling interval is arbitrarily small, and the values of the data are known to infinite precision (Takens 1981). These prerequisites clearly cannot be fulfilled by real physical measurements, but for successfully reconstructing attractors one always has to try hard to come as close as possible to these conditions. If the attractor is sufficiently embedded, the slopes of the correlation integrals converge such that

$$
D^{(q)} = \lim_{r \to 0} \lim_{d \to \infty} \frac{\log C^{(q)}_d(r)}{\log r} \tag{20}
$$

Different orders q of the correlations signify local substructure in phase space, i.e. a different scaling of regions of different point densities.

In practice, the limits given in (20) cannot be obtained, of course. This is not necessary, anyway. For practical applications very high dimensions, n, are not tractable. We have found that an embedding dimension, $d \approx 2n + 1 \approx 20$ provides reasonable results in many cases of low – dimensional chaos. The unavoidable random noise present in the data shows up in the correlation integral $C^{(q)}_d(r)$ as a gradient increasing with increasing embedding dimension. These random processes are superimposed on any chaotic processes and occupy regions of small r. Hence plotting the slope of $C^{(q)}_d(r)$ for given d as a function of r helps in disentangling these two components, provided the stochastic part is not overwhelmingly large. In this case it may mask the chaotic signature.

In principle, the analysis can be carried further to obtain the Kolmogorov entropy and the spectrum of scaling indices. We shall not describe this here, the reader is referred to the original literature (Grassberger and Procaccia 1983b, Halsey et al. 1986, Pawelzik and Schuster 1987).

Reconstruction of the attractor from data: tests

We have already mentioned that a real system will certainly have stochastic fluctuations superimposed on the chaotic signature. Stochastic effects could be due to real random variations in flow patterns, due to integrating the system spatially over many uncorrelated fluctuating emission centres because it cannot be resolved, due to photon counting statistics etc. This should make the extraction of information about the system even more complicated, since it is obviously hard, a priori, to differentiate between two superimposed irregular signals. In practice, this only works if either the power in the random signal is sufficiently low, or if the two can be separated by different time (length) scales. These general considerations apply also to the situation where regular signals are extracted from a "noisy" data set – the difference occurs in the meaning of "sufficient" in both instances.

Next, we have drawn the analogy with the geometrical representation and the presentation of the data in phase space (or the projection onto a given plane in phase space – a so called Poincaré section). It is intuitively obvious, that the projection of the data in phase space has to be important; e.g. a periodic signal is represented by a closed curve in phase space, however, if the time resolution of our measurements were by chance to coincide with the signal period, we would obtain a fixed point based on the available information – and we would be wrong. The same applies, in principle, to chaotic attractors. One may obtain better or poorer representations of the system in phase space and an important part of the problem is to optimise this.

We illustrate some of these points with a simple example: a sine – wave with superimposed random fluctuations. We know that the dimension $D^{(2)}$ of this system is 1.

In Fig. 1 we plot the slope of $\log_2 C_d^{(2)}$ as a function of $\log_2 r$ for dimensions of the artificial phase space $d = 1$ to 10. (Notice that in common with standard practice, with respect to underlying probability theoretical concepts and the relation to information theory, the log to base 2 is plotted. For readers interested in information theoretical discussions please consult Shannon and Weaver 1962, Balatoni and Renyi 1976). As can be seen, $d = 1$ is not sufficient to encompass the attractor, whereas for $d > 1$ a clear plateau at the expected value unit develops. This plateau broadens as the value for d is increased, however, there are deviations at small r's associated with the fact that a finite data set with finite resolution is used. The hump for large r's is a geometric effect depending on the distance norm used in the calculation of the correlation integral. This effect is most pronounced in cases where the attractor is a circle (sphere, hypersphere and so on). This system contained no random noise.

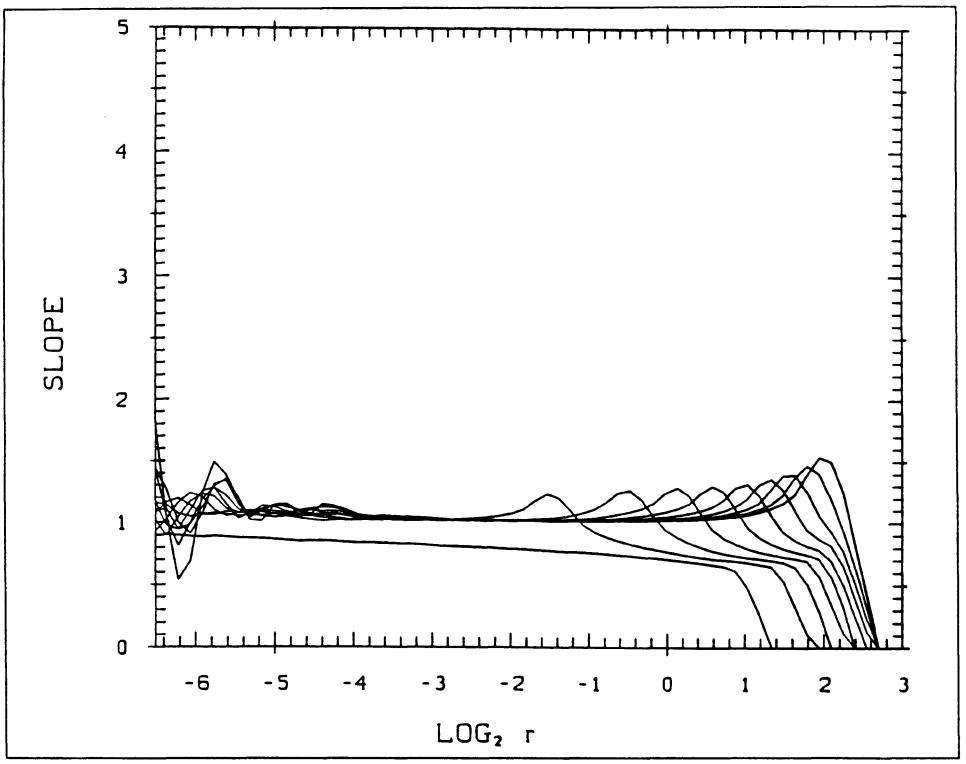

Figure 1: Slope of the correlation integral $(\log_2 C_d^{(2)}(r)/\log_2 r)$ vs. $\log_2 r$ for a simple sinusoidal function without noise. The time resolution is about 430 points per period, the shift Δt is 10 times the time resolution and the number of points is 2000. The dimension d of the artificial phase space is varied from $d = 1$ to $d = 10$.

To illustrate projection effects and the optimisation of the phase space representation, we show Fig. 2. The left panel is a phase space representation of the signal $x(t)$ plotted vs. $x(t + l\tau)$ for a fixed ratio of the period and the time resolution τ. The upper graph has $l = 3$, i.e. is a fine resolution map, the middle one is a little coarser, with $l = 10$, and the bottom one is coarser still, $l = 33$. The right panel gives the slope of $\log_2 C_{10}^{(2)}(r)$ plotted as a function of $\log_2 r$. The expected value of unit is found in all cases, however, the upper graph shows that the projection is not optimal as witnessed by the step in the slope of $C_{10}^{(2)}$ at large r. The lower graph (the one with the best projection) has a more pronounced hump than the middle one.

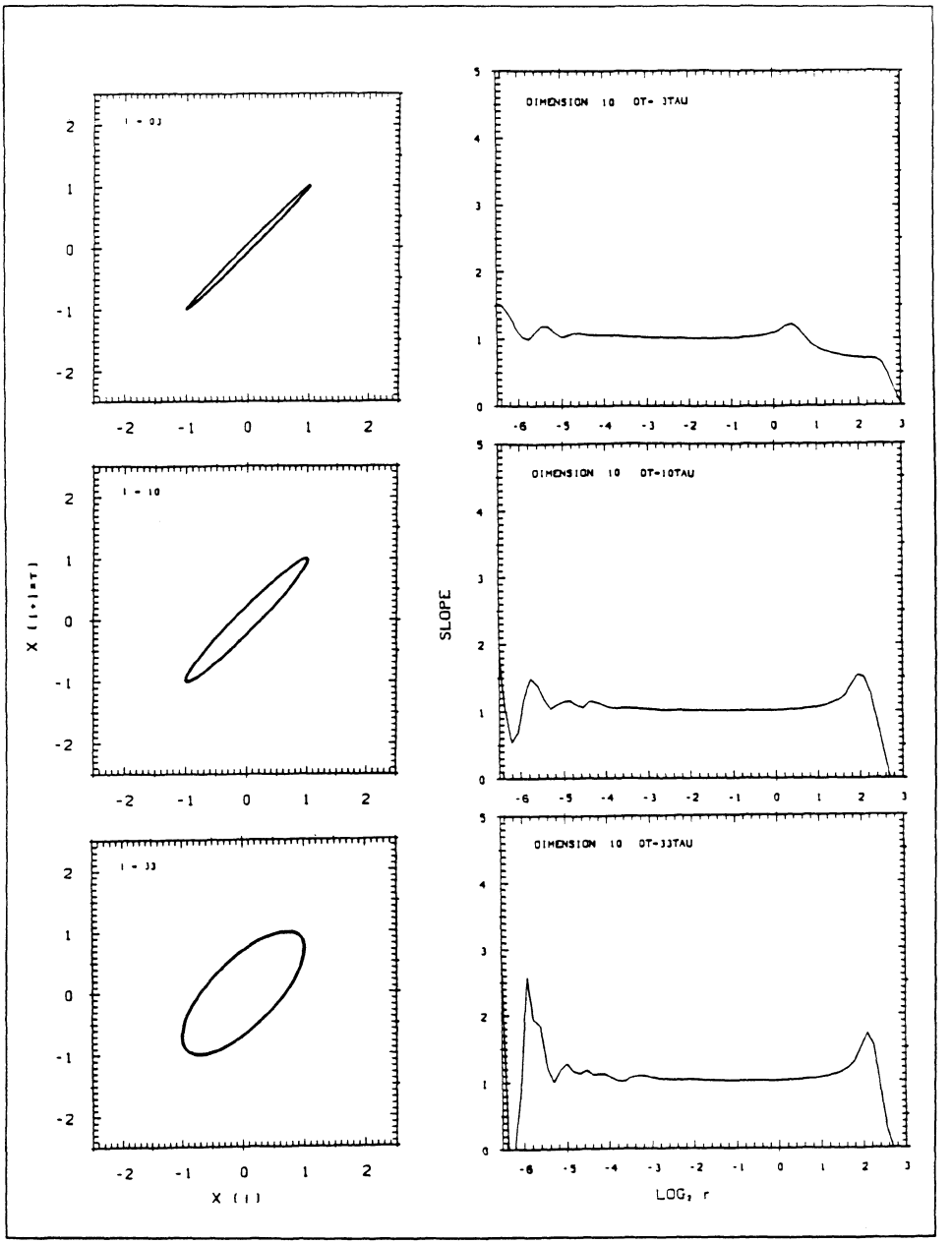

Figure 2: Two dimensional phase portraits $x_i(t)$ vs. $x_i(t + \Delta l\tau)$ for $l = 3, 10, 33$ (left column), and corresponding slopes of the correlation integral $C_{10}^{(2)}(r)$ vs. $\log_2 r$ (right column) of the sinusoidal function from fig. 1.

When noise is added to the signal, the data points become randomly scattered around the original attractor. Since the noise is completely uncorrelated, this component tends to occupy the whole phase space. The slope of $\log_2 C_d^{(2)}$ of this random component increases with increasing dimension d of the embedding artificial phase space as already mentioned before. When the noise component is small, we expect this effect to occur at small r, but depending on the noise level, it might still blanket the underlying regular or chaotic signal. The effect of noise on the sine – wave is shown in Figs. 3 and 4. In Fig. 3 we have plotted the slope of $\log_2 C_{10}^{(2)}(r)$ as a function of $\log_2 r$ with 6% (compared with the wave amplitude) noise. We clearly see the expected result. At small r, the slope increase rapidly trying to approach the maximum dimension of $d = 10$. At large r we see the slope 1 from the sine – wave plus the hump noted earlier. When the noise level is increased to 20% of the signal amplitude we have the result shown in Fig. 4. The noise effects have become noticeable at larger r. In Fig. 3 the cut – off was at $\log_2 r \approx -2$.

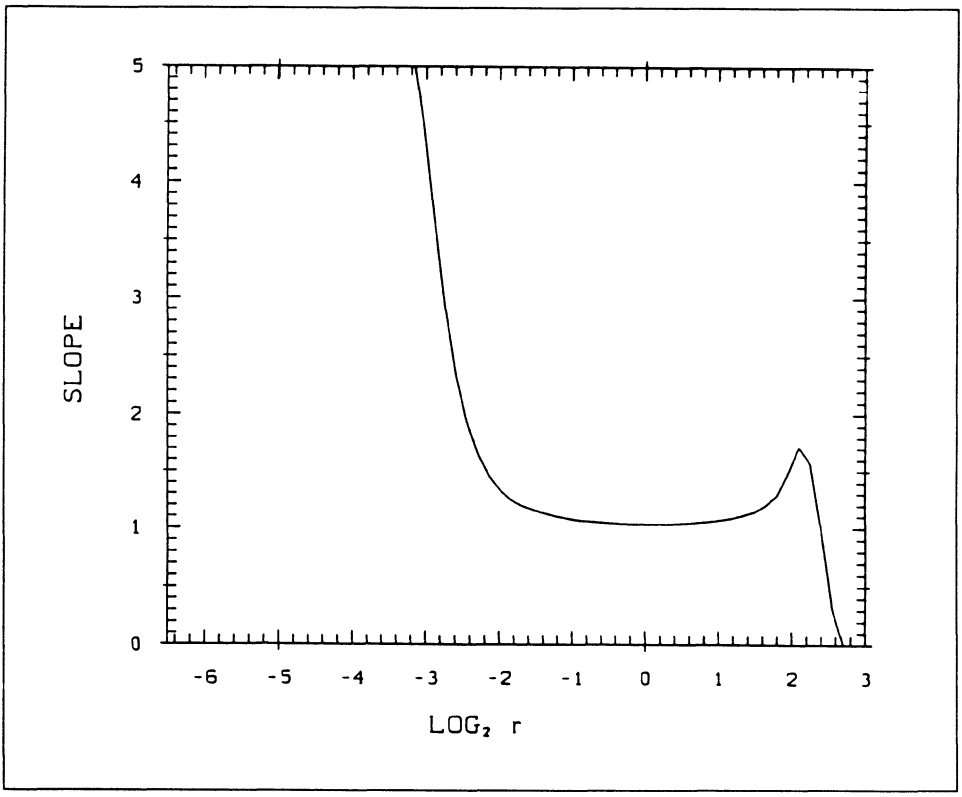

Figure 3: Slope of the correlation integral vs. $\log_2 r$ for the sinusoidal function but with 6% noise. One clearly can recognise the steepening at small r's due to the stochastic noise.

In Fig. 4 the cut – off occurs at $\log_2 r \approx 0$. In addition the slope does not reach the plateau of unity, as it should. Superposition of noise and of the hump leave too little space in r to allow this. In principle, analysing a longer time series should help here, provided that the resolution of the measurement is good enough to increase not only the number of points but also to increase the information with respect to the attractor.

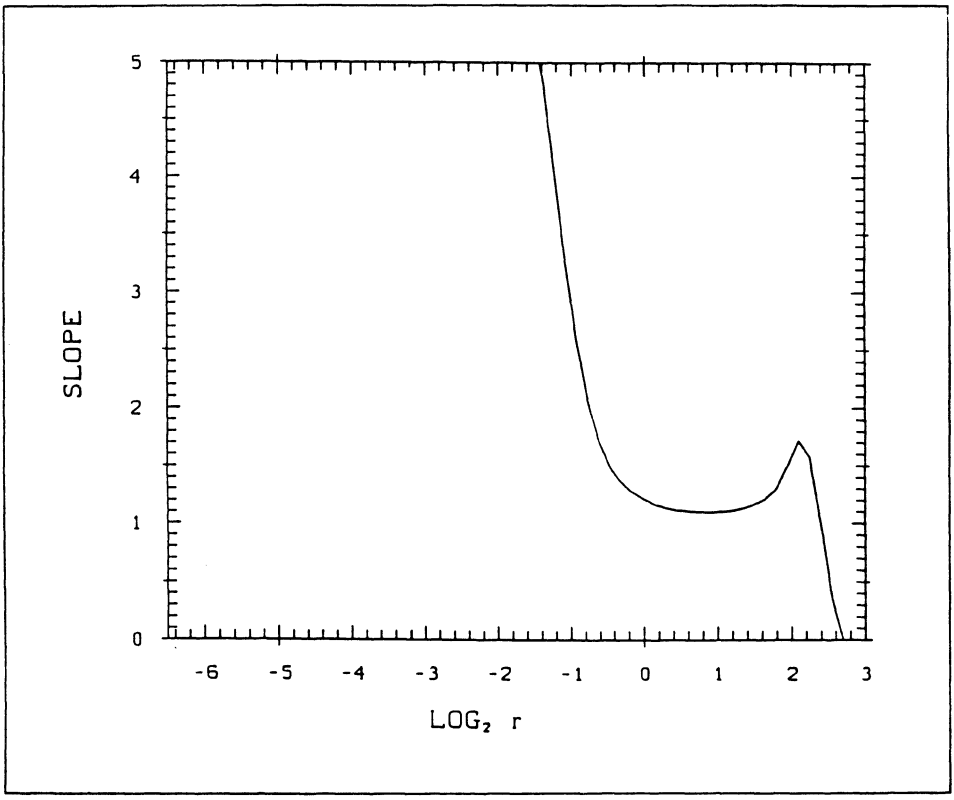

Figure 4: Same as fig. 3 but with 20% noise. The linear scaling range is now reduced so much that the slope did not reach the value one anymore.

Similar studies have been performed using known chaotic attractors and signal time series attained from them, with superimposed noise etc. As a summary of our tests we conclude the following:

1) Under certain conditions the qth order attractor dimension $D^{(q)}$ can be calculated from a time series measurement of one observable, and with that the minimum degrees of freedom required to adequately describe the system responsible for the signal.

2) The best representation in phase space must be found, that means an appropriate Δt has to be determined. This could be a very difficult problem and in some cases it may only work by trial and error.

3) Chaotic processes are associated with a certain time scale K^{-1}, which is a system property. This must be considered when a signal is analysed. Good guesses for this time scale can be obtained from autocorrelation analysis or a physical input.

4) Careful pre – scanning of the data using standard time series analysis methods (e.g. Fourier, autocorrelation, power spectra) is an indispensable prerequisite for a successful chaos analysis.

5) No black – box fool – proof algorithm exists so far, that can be applied to any time sequence of data.

Reconstruction of the attractor from data: Her X-1

Her X-1 is an X – ray binary system, one partner is a neutron star, the other, HZ – Herculis, is a $\approx 2\ M_{\odot}$ star (Liller 1972, Bahcall and Bahcall 1972, Middleditch and Nelson 1976). The rotation period of the neutron star is 1.24 sec, the orbit period of the system around its common centre of mass is 1.7 days and there is also a rough 35-day periodicity observed. The magnetic field of the neutron star is $\approx 5 \times 10^{12}$ Gauß (Trümper et al. 1978).

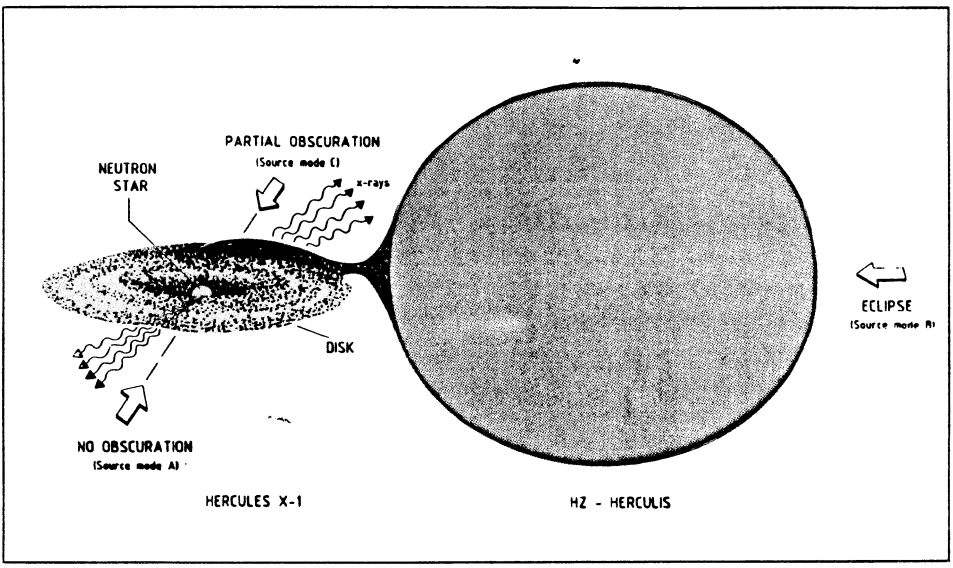

Figure 5: Schematic diagram of the Her X-1 system showing the optical companion, the accretion disc and the different viewing geometries described in the text.

Fig. 5 shows the binary system, approximately drawn to scale, as it has been derived from the available data. HZ– Herculis fills its roche lobe completely, mass

is drawn over to the neutron star and forms an accretion disc. The strong magnetic field of Her X-1 prevents the disc from reaching the neutron star surface, it is believed that matter is channelled along the field lines and impacts on the polar caps. The nonalignment of rotation and magnetic dipole axes leads to the regular periodic pulsing observed. Also shown in Fig. 5 are the three principal observation sequences for the object: eclipse, when the neutron star disappears behind its companion; no obscuration, when the neutron star is fully visible and partial obscuration, when the neutron star is viewed through portions of the accretion disc.

Voges et al. (1987) made the first analysis of X – ray data from an astrophysical object, which was designed to reconstruct the attractor and check for the possible occurrence of deterministic chaos. The object was Her X-1. One of the data sets used in this analysis is shown in Fig. 6. It is the unobscured source mode data, averaged in 770 msec bins, taken from EXOSAT observations made on June 11th, 1984.

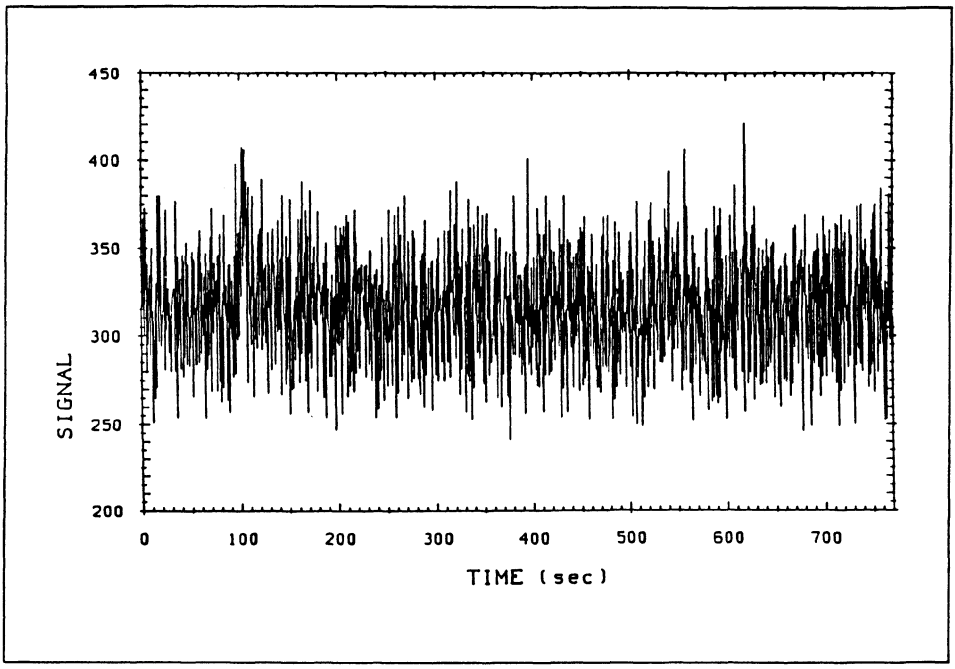

Figure 6: Section of the temporal evolution of the X – ray count rate from Her X-1 in the unobscured mode. The time series contain 1000 points with a temporal resolution of 770 msec.

Various phase space projections of this data are shown in Fig. 7, taking consecutive, every third, tenth and thirtieth point in the sequence. Inspection shows very little difference in the phase space projections.

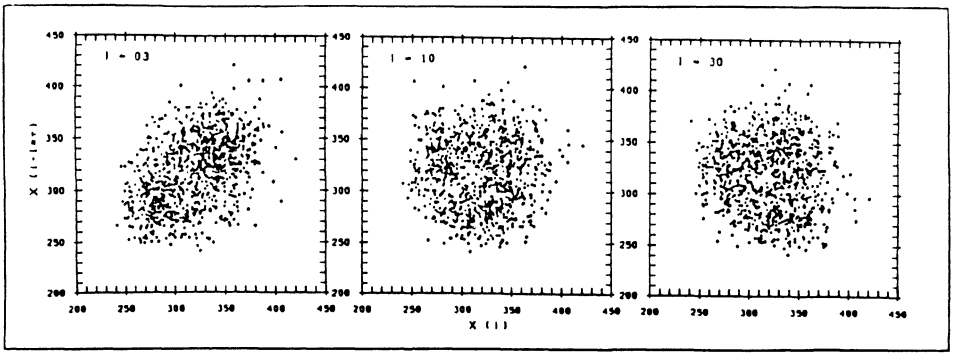

Figure 7: Two dimensional phase portraits of the Her X-1 measured time series $x(t)$ vs. $x(t + l\tau)$ for delay times of 3, 10, and 30 τ. The projection does not change very much with the delay time.

The analysis of $D_d^{(q)}(r)$ used the consecutive data point projection. This is shown in Fig. 8 for the two – point correlation function (i.e. actually shown is the slope of the correlation integral) for artificial phase space dimension d ranging from 1 to 20. The stochastic component is clearly discernible and dominates for $\log_2 r$ smaller than 7.0. Above this we note that the slope develops a plateau for embedding dimensions $d \geq 7$. The attractor is completely embedded in the chosen artificial phase space range $d \leq 20$. The value of the plateau level is about 2.4, a fractal greater than 2! This strongly suggests that a low order chaotic process is operating, which determines irregular fluctuations in the signal. The most likely degrees of freedom associated with this process is 3, i.e. a system of three nonlinear coupled first order ordinary differential equations should suffice to describe the process. From our earlier theoretical discussion, it follows that this is also the minimum necessary to obtain chaos in continuous dissipative systems.

There is more information, however. The choice of the time scale, τ, for binning the data points ($\tau = 770$ msec) also allows us to determine the characteristic time scale of the process, K^{-1} which is a few τ. Data which was binned in much more highly resolved smaller time segments ($\tau < 70$ msec) was dominated by stochastic noise (e.g. photon statistics, background events etc.) and reduced in signal depth, so that no clear chaotic signature was discernible. Data averaged over a significantly longer time step ($\tau \geq 7$ sec) did not suffer from the background random noise problem, but was beset with presumably real stochastic variations in the accretion flow. In any case, chaotic behaviour again was not found, giving a clue about the value of K associated with the chaotic process. These results could be reproduced for other data sets measured on different occasions.

As a test of the results, similar analyses were performed while Her X-1 was in eclipse. Pure random noise was observed, identical within the range of statistical uncertainties with a pure background, off source, observation. For further details the reader is referred to Voges et al. 1987, Atmanspacher et al. 1988 and the contribution by Atmanspacher et al. in this volume.

Even without a theoretical interpretation of the meaning of this chaotic signal and

the underlying processes involved, the mere fact that a chaotic behaviour has been identified in this binary X-ray source, with a time scale K^{-1} of the order of a few rotation periods of the neutron star, is an important result.

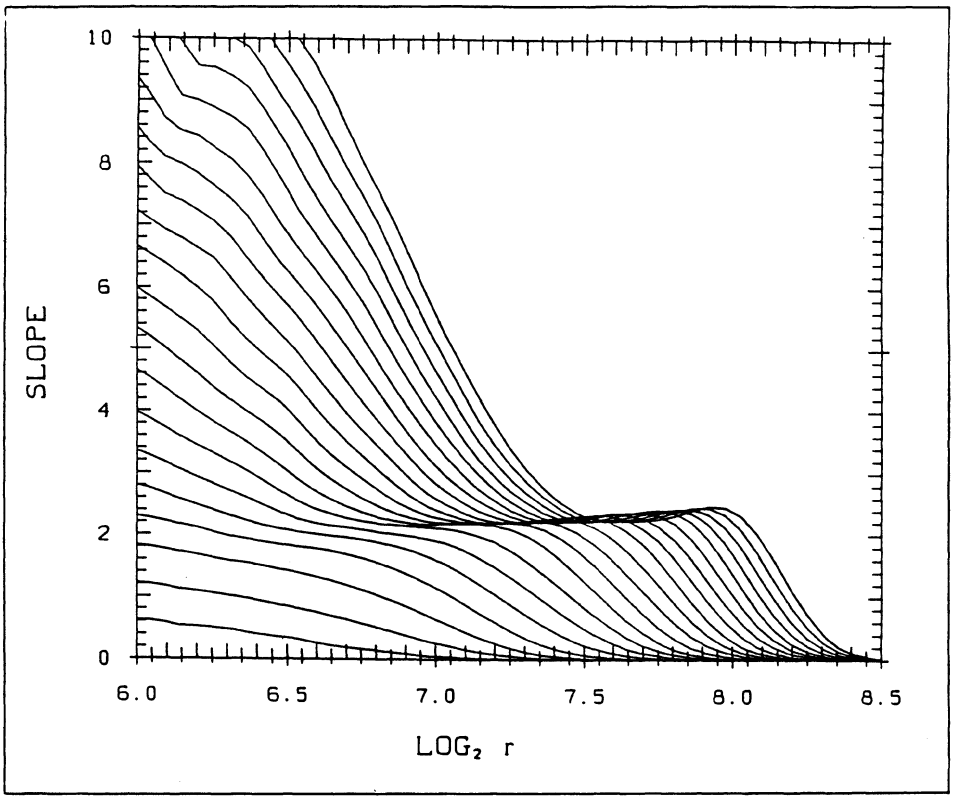

Figure 8: Plot of the slope $(\log_2 C_d^{(2)}(r)/\log_2 r)$ vs. $\log_2 r$ for the X – ray count rate from Her X-1 for embedding dimensions d from $d = 1$ to $d = 20$. At small r's the influence of the noise increases the slope with increasing embedding dimension while the plateau stays constant (slope $\approx$ 2.4) for $d > 7$.

Physical interpretation: general remarks

There are two major challenges for theorists in this context of deterministic chaos in dynamical systems: firstly there is the question how best to derive invariant properties of the strange attractors from a limited data set and secondly there is the inverse problem, i.e. the reconstruction of the fractal geometry and the dynamics of the system, given these properties. The latter may also be regarded as the physical interpretation of the analysis of the data.

In general, if an astrophysical system is analysed and found to be chaotic, we should be able to manipulate the governing equations which describe the system in such a

way that the source of the chaotic behaviour is clearly recognisable and can be understood theoretically. It would be strange indeed if we had no notion whatsoever about the governing equations, so we will exclude this complete state of ignorance from our discussion. For low order chaos this manipulation effectively implies considerable simplification in the mathematics coupled with a clearer understanding of the physics. In this sense a chaos analysis and its physical interpretation are not only useful extensions of the usual data analysis – the outcome could have much more far reaching consequences.

The dynamical systems of interest here are accreting neutron stars. This implies that we are dealing with a problem in radiation (magneto)hydrodynamics. The principal transport equations involved are the conservation laws and the radiative transfer equation. These are supplemented by another set of equations governing the behaviour of the physical processes. The former are partial differential equations, radiative transfer often being described in the diffusion approximation. If the system is optically thin, source effects are simply transmitted directly, including the signatures of possible chaotic effects. If the system is optically thick, radiation pressure may become dynamically important and a multi – fluid description is appropriate. The interaction between the radiation fluid and the gas may itself create new instabilities and/or chaotic behaviour (see e.g. the discussion in Demmel et al., this issue).

Methods how to manipulate and reduce these equations have been developed, although it must be stated that these methods are not universal, and so far have been applied only to singular situations. The two general concepts that have emerged are "mode reduction" and "hierarchies of equations" (Campbell 1987). The most celebrated example of mode reduction is the set of "Lorenz equations" (Lorenz 1963).

Use of mode reduction assumes that in e.g. a fluid flow problem only a few modes are important, so that the effective phase space dimension is much smaller than the full dimension of the equations. The mode reduction should ideally be advanced to a level, where the number of degrees of freedom of the reduced set of equations are just sufficient to describe the essential features of the dynamical system. The remaining modes can be related to e.g. persistent features in the flow such as convective motions. For instance, one can develop the spatial dependence in terms of Fourier modes with time dependent amplitude, retain only a few terms of the Fourier series, and thus obtain a system of coupled nonlinear ordinary differential equations. Information regarding the number of modes which have to be kept comes from the analysis of the data and the derived values of $D^{(2)}$ and n. We caution, however, against the indiscriminate use of such techniques, each attempt at mode reduction should be checked, where possible, by suitable reanalysis of the data.

The hierarchy of equations method again is very problem specific, although the basic concept is clear. The idea is to describe the dynamical system by approximate partial differential equations, reducing these e.g. via inertial manifold or more heuristic methods to a set of coupled ordinary differential equations which may then, if possible, be reduced further to the simplest example of a given universality class.

Physical interpretation: Her X-1

It has been known for some time that the photon emission from Her X-1 exhibits strong pulse to pulse variations which cannot be explained by photon statistics alone (see e.g. Morfill et al. 1984). In order to test whether the chaotic behaviour perhaps reflects this pulse to pulse variability or whether it is related to a pulse phase dependent process, the data were averaged over the neutron star rotation period and multiples thereof, and $D^{(2)}(r)$ was calculated using the techniques described earlier.

If we only had a periodic signal, with period τ_{sys}, then as mentioned earlier, by choosing $\tau = N\tau_{sys}$ with N an integer, we would (somewhat) pathologically reduce the system to a fixed point with overlying random noise.

If, however, the integrated intensity over the pulse profile is variable because a deterministic, but chaotic, process is operating, then this should show up over the random noise, as it did in Fig. 8. The result of this analysis was quite enlightening, even if partially expected: the chaotic signature disappeared.

The measurements can be understood in the following ways:

1) The pulse consists of at least three components of the form:

$$L_i = A_i(t)B_i(\phi) + \delta L_i \tag{21}$$

where $B_i(\phi)$ are fixed functions of phase angle and where δL_i is the random noise. To quantify the stability of the pulse phase dependence (ϕ) of the components, we note that $B_i(\phi)$ could be variable over a time scale very much longer than the length of the data record – i.e. we cannot preclude variations on time scales of the orbital period or even the 35 day cycle. The amplitudes of the components are, however, time dependent and linked by a set of equations of the type (1). Since $\phi = 2\pi\frac{t}{\tau_{sys}}$, ϕ is in principle a function of t. Equation (21) is simply an expression removing the periodic part of the signal from the irregular part. This is the purpose of introducing ϕ as an independent parameter.

The total signal strength is

$$L = \sum_i L_i \tag{22}$$

and the long term average is

$$\bar{L} = \sum_i < A_i(t)B_i(\phi) > = \sum_i < A_i(t) > \bar{B}_i \tag{23}$$

with $\bar{B}_i = const.$, by definition. The random part averages to zero, of course.

Averaging over ϕ also implies averaging over time segments of duration τ_{sys}, the rotation period of the neutron star. This is written as

$$< L_i >_\phi = < A_i >_\phi \bar{B}_i + < \delta L_i >_\phi \tag{24}$$

$$< L >_\phi = \sum_i < L_i >_\phi \tag{25}$$

with $< A_i >_\phi$ varying from one ϕ – averaged point to the next.

If the difference

$$\left| < L >_\phi - \bar{L} \right| < \sum_i < \delta L_i >_\phi \tag{26}$$

then the data points may be too noisy and extraction of a chaotic signal may be impossible.

2) The positioning of the components in phase ϕ may vary from pulse to pulse, i.e. the $B_i(\phi)$ are not fixed functions, however, the $A_i(t)$ are correlated such that $A_i/A_j = const.$. Phase averaging would then always remove any chaotic signature. In a phase dependent sampling, however, the chaotic signature should become apparent, provided the $B_i(\phi)$ are of the form

$$\frac{d\mathbf{B}}{d\phi} = \mathbf{F}\left(\mathbf{B}(\phi), \mu\right) \tag{27}$$

Further data analysis is needed to differentiate between these possibilities and to then pinpoint the process responsible for the chaotic signal. Clearly, the next task is to check on this pulse phase question, and to see if there is any corroborating evidence. A Fourier analysis of the data should yield simply a large number of modes in order to describe the time variable signal of a limited data set "adequately". This has been done, and the number of modes required is indeed large, about 10 (Õgelman 1988).

Furthermore, we can perform a superposed epoch analysis and determine the pulse shape as a function of phase, ϕ. If there is some obvious structure, then our notion of a phase dependent process receives independent support. Fig. 9, taken from Kahabka (1987) shows the pulse structure observed (left panel) and a decomposition into its various components (right panel): a constant background, a sinusoidal variation, a main pulse and an interpulse. The fits to the main pulse and interpulse were Gaussian curves, and it was concluded that the main pulse was quite complicated, consisting of a Gaussian centre and two wing pulses (see the right panel), also Gaussian.

The interpretation of the interpulse is that we are seeing the less favoured other polar cap. The signal is weak during this phase of the cycle and statistically probably not too important. The sinusoidal component was interpreted as scattered radiation from distributed plasma in the magnetosphere and surrounding the magnetopause. The phase and modulation for this component are the same, within

the limits of observational uncertainty, as those of the soft (< 1 keV) X – ray pulse profile, which supports this interpretation (Kahabka 1987).

Scattered radiation is, of course, derived from the main source, it is seen with a delay time typically $3l\tau_{opt}/c$ where l is the size of the scattering region and τ_{opt} is the optical depth. Since scattering is a random process, source signatures are damped out if $\tau_{opt} \ll 1.$. For Her X-1, l is the size of the magnetosphere ($\approx 2 \times 10^8$ cm), giving a delay time of 20 τ_{opt} msec.

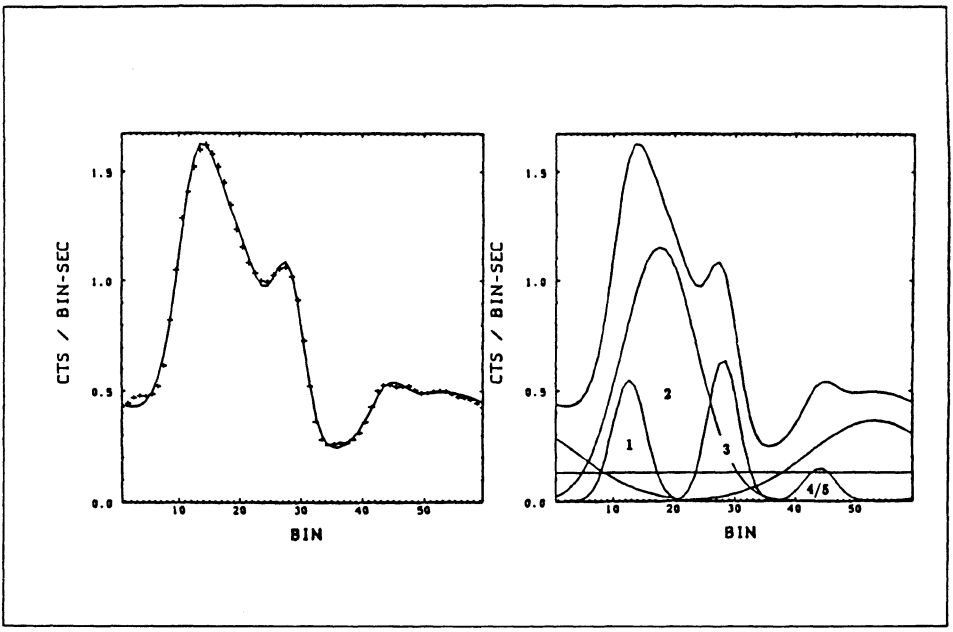

Figure 9: Pulse structure of Her X-1, taken on May 5th 1984 in the energy range 1.9 - 3.9 keV. The left panel shows the observations together with the multi – component fit which is detailed in the right panel. The main pulse (components 1 to 3) and the other features are described in the text (from Kahabka, 1987).

The main pulse, with its substructure, is explained in the following way (Kahabka 1987, see also Kaminker et al. 1982):

The main pulse, based on its energy spectral behaviour can be interpreted as the p – component, pointing along the magnetic field and being determined by the ordinary polarisation mode.

The wing pulses are asymmetric with respect to the main pulse ($\approx 10°$) and, again based on energy spectral characteristics, are interpreted as the s – component, which is predominantly determined by the extraordinary polarisation mode. Pulse maxima for this component are expected at $\approx 40°$, observations show 30° and 50°

for the two wing pulses, i.e. an asymmetry. The s – component depends on the vacuum parameter, V, the p – component does not. V is defined as

$$V = \frac{1}{60\pi n_e} \left(\frac{mc}{\hbar}\right)^3 \left(\frac{\hbar\omega_B}{mc^2}\right)^4 \tag{28}$$

where n_e is the electron density, m the electron mass and ω_B is the cyclotron frequency. Increasing V (e.g. by decreasing the electron density) reduces the s – component.

The plasma densities inferred for the polar cap by Kahabka (1987) are of the order 4×10^{22} cm^{-3}, which gives a vacuum parameter $V \simeq 23$.

It is known that the pulse form varies during the 35-day cycle. The most obvious change is seen in the relative intensities of the main pulse and interpulse, however, there are also clear phase variations which are of the order 40°. Pulse to pulse variations beyond the statistical uncertainty can also be established (e.g. Morfill et al. 1988), however, statistical limitations do not allow quantitative statements about phase variations of the individual components.

Regarding possible causes of such variations there are a number of options, which have to be investigated in detail in conjunction with further specialised analysis of the data and, possibly, new instruments. Amongst these are variable accretion torques, neutron star precession, atmospheric density and scale height variations as a function of heat transport in the neutron star, bending of field lines in regions of very high mass accretion through the plasma pressure, variable geometry of the hot spots etc. coupled to the problem of ray tracing.

It is too early yet to pinpoint any one cause as being responsible for the signatures seen in the data. At present we have identified the chaotic signal, its correlation time and the degrees of freedom associated with the process(es) responsible. We have further identified two possible ways of understanding this in terms of time and phase dependent processes. We now have the task of analysing the data in such a way that we may be able to differentiate between these two possible ways. This appears feasible. In this way steady progress is achieved in restricting the diversity of options and finally understanding the causes of the chaotic behaviour.

Summary:

In this paper we reviewed the pertinent aspects of the theory of deterministic chaos, how to identify chaotic systems, quantify them (their complexity), reconstruct the attractor, and determine the degrees of freedom of the system from a single time series of data points. We discussed problems associated with superposition of random noise, signal depth, time resolution and projection in phase space, using a simple example. We then proceeded to the actual motivation for the whole study: the fact that an accreting neutron star system, Her X-1, has been identified as a chaotic system. The data were briefly discussed and then the physical interpretation – firstly, some general remarks how low order deterministic chaos may be viewed in terms of dominant modes of a (in principle) much more complex system

and the ensuing mathematical simplifications, and secondly, direct interpretation of the Her X-1 results in terms of the complexity of the pulse form.

Finally, we want to point out once more, as has been done in several places in the main text, that no fool – proof algorithm exists as yet with which a chaos analysis can be performed from a given set of data efficiently. The chaos investigation has to be preceeded and supported by a Fourier analysis and by an analysis of the effects of different phase space projections. Furthermore, although considerable progress has been made in manipulating a set of governing equations so that the chaotic element is extracted (e.g. mode reduction), these efforts still remain singular and are not of general application. However, determination of the dimensionality, hence the degrees of freedom, and thus e.g. the number of modes, does provide an important guide for certain mathematical reduction, and hence, hopefully, to greater insight and deeper understanding of the system. It is our conviction that especially for astrophysical objects this source of information should therefore be investigated routinely.

References:

1. H. Atmanspacher and H. Scheingraber, *Found. Phys.* **17**, 939 (1987), and further references therein
2. J. B. Pesin, *Russ. Math. Survey* **32**, 455 (1977) (*Usp. Math. Nauk* **32**, 55 (1977))
3. F. Takens, in *Dynamical Systems and Turbulence, Lecture Notes in Mathematics* **898**, eds. D. A. Rand and L. S. Young (Springer, Berlin, 1981), p.366
4. P. Grassberger and I. Procaccia, *Phys. Rev. Lett.* **50**, 346 (1983)
5. K. Pawelzik and H. G. Schuster, *Phys. Rev.* **A 35**, 481 (1987)
6. H. Atmanspacher, H. Scheingraber, and W. Voges, *Phys. Rev.* **A 37**, 1314 (1988)
7. P. Grassberger and I. Procaccia, *Phys. Rev.* **A 28**, 2591 (1983)
8. T. C. Halsey, M. H. Jensen, L. P. Kadanoff, I. Procaccia, and B. I. Shraiman, *Phys. Rev.* **A 33**, 1141 (1986)
9. C. E. Shannon and C. Weaver, *The Mathematical Theory of Communication* (Univ. of Illinois Press, 1962)
10. J. Balatoni and A. Renyi, in *Selected Papers of A. Renyi, Vol.1*, (Akademie Budapest, 1976), p.588
11. W. Voges, H. Atmanspacher, and H. Scheingraber, *Ap. J.* **320**, 794 (1987)
12. H. Atmanspacher, H. Scheingraber, and W. Voges, this volume
13. D. Campbell, *Nucl. Phys. B Suppl.* **2**, 541 (1987)
14. E. N. Lorenz, *J. Atmos. Sci.* **20**, 130 (1963)

15. J.N. Bahcall, N.A. Bahcall,*IAU Circ.(1972)*,Nos. 2427 and 2428.

16. P. Kahabka, *Der 35-Tage-Zyklus von Hercules X-1*, PhD-Thesis, München 1987

17. W. Liller,*IAU Circ. (1972)*,Nos. 2415 and 2427.

18. H. Ögelman, *Astron. Astrophys.* **172**, 79 (1987)

19. J. Middleditch and J. Nelson, *Ap. J.* **208**, 567 (1976)

20. J. Trümper, W. Pietsch, C. Reppin, W. Voges, R. Staubert, E. Kendziorra *Ap. J.*, 219(1978)L105 (Letters)

21. A.D. Kaminker, G.G. Pavlov, and Yu.A. Shibanov, *Ap. Space Sci.* **86**, 249 (1982)

DETECTION AND DESCRIPTION OF PERIODICITIES IN SPARSE DATA. SUGGESTED SOLUTIONS TO SOME BASIC PROBLEMS.

R. Buccheri [1], O.C. De Jager [2]

[1] Istituto di Fisica Cosmica e Applicazioni dell'Informatica, Consiglio Nazionale delle Ricerche, Palermo, Italy

[2] Potchefstroom University for CHE, Department of Physics, Potchefstroom, South Africa

ABSTRACT. We discuss some of the basic steps of the analysis for the detection and description of short periodicities in the photon counting regime (typical of gamma-ray astronomy), focusing the attention to those aspects where a certain degree of subjectivity by the analyst may lead to erroneous conclusions. As a statistical test for the detection of the periodic signal, the use of the H_m-test is suggested in all exploratory cases when information on the expected light curve shape is lacking. The bin free kernel density estimator (KDE) and cluster analysis are used for the description of intensities, the location and significance of structures on the light curve and are proposed as alternatives to the histogram technique which is easy to use, but since the construction of the histogram is largely based on subjective considerations, it may lead to wrong interpretations especially in the case of weak signal and low counting statistics.

1. INTRODUCTION

The analysis for the detection of periodicities in the arrival times of gamma-ray photons started about 20 years ago in the context of the search for pulsed gamma-ray emission from radio pulsars as observed in the TeV region (Charman et al., 1968; Fazio et al., 1968) or with instrumentation on board of stratospheric balloons (Vasseur et al., 1970). The method used was the application of Pearson's test (see for example Eadie et al., 1971) to the phase histogram derived after binning of the residual phases obtained by folding the measured times with the period suggested by the radio observations. This method of analysis has revealed to be not very accurate due to several reasons. First of all there is a high degree of subjectivity in the choice of the number of histogram bins and of the zero phase of the histogram. The number of histogram bins has a very precise meaning in terms of selection of the signal shape; in particular, choosing few bins implies a search for broad light curve shapes whereas the use of many bins is implicitly connected with the presence of narrow or complex structures. In addition to this, the final choice for the presentation of the results was made, in many cases, a posteriori by selecting the best-looking histogram thus implying an erroneous interpretation about the reality of the periodic signature. The binning process itself, on the other hand, may lead to a consistent loss of power in the case of low counting statistics (De Jager, 1987) which is the normal case in high energy gamma-ray astronomy with balloon or satellite experiments in the 100 MeV region or EAS experiments. Another not negligible reason is the assumption very often made in the past that Pearson's test statistic follows the χ^2 probability distribution with M-1 degrees of freedom, M being the chosen number of bins. In the reality the χ^2 distribution can be reliably used for Pearson's test only in the case of goodness-of-fit tests; when looking

H. Ögelman and E. P. J. van den Heuvel (eds.), Timing Neutron Stars, 95–111

for deviation from uniformity (in our case of the distribution of the residual phases) we are actually using the tail of Pearson's test statistic which, in the case of low sample sizes, deviates from the χ^2 distribution. As a consequence of the misuse of Pearson's test statistic, a number of claims for significant detections has been made in the past, claims that have had serious difficulties to be confirmed by independent experiments. Viceversa, we can immagine that the use of Pearson's test in several cases may have been inadequate to put into evidence real periodicities because of its reduced power due to the binning process and/or to the wrong choice about the number of bins.

The situation has improved in the last ten years when several groups started to invest time and effort in the study and formalization of the reliable statistical procedures needed in a search for periodicities in the photon arrival times as measured in a gamma-ray experiment. As a result of this effort a set of procedures have been derived with the test statistics having received particular attention. In spite of these efforts the process of search still contains several points of indetermination to which this paper aims to dedicate some attention in order to suggest some solutions. We will concentrate ourselves to a large region of low values of the period investigated ($P << \tau$, τ being the inverse count rate), where the Fourier spectrum is flat, for a better handling of the probability distribution of the test to use. Concerning the analysis we will give special emphasis to the process of testing the distribution of residual phases against the presence of a periodicity in the data and suggest the use of a new statistical test (the H_m-test) which is very powerful when no information is available on the structure of the signal. Also we will discuss the recent achievements about the description of the structure itself once a positive detection has been made. It will be reported that the KDE and cluster techniques for the representation of the pulsar light curve give at the moment the best way for a qualitative and quantitative estimate of the widths and intensities of the peaks contributing to the pulsed signal.

2. STEPS TO FOLLOW FOR PERIODICITY SEARCHES.

Fig. 1 shows the general flow of operations in the analysis for the search of periodicities in gamma-ray astronomy (reproduced from Maccarone and Buccheri, 1988). A first discussion on the analysis steps is given by Buccheri, 1987. The round boxes are critical points of the analysis where some external decision by the analyst is requested, the decision implying generally a certain degree of subjectivity. We will discuss them after the rectangular boxes which refer to standard processing of the data making use of software packages implemented for a particular experiment or for a well defined calculation method.

2.1 Standard operations

The preprocessing includes all the operations needed to be performed on the raw data for the derivation of photon arrival times, generally expressed in Julian Days and referred to the Solar System Barycentre in order to eliminate the modulation due to the earth orbit around the sun and to the motion of the observatory site (e. g. the satellite).

The folding procedure is generally needed in photon counting statistics in order to derive the residual phase distribution which will be successively tested against the presence of periodicity. This step is not necessary if the analysis is performed by using Fast Fourier Trasform procedures. We will not consider this case because the FFT analysis is generally not convenient in gamma-ray astronomy due to several reasons: a) impossibility to use oversampling which may be decisive for the detection of weak signals; b) difficulty in summing the power of more harmonics of the signal preventing the detection of complex structures

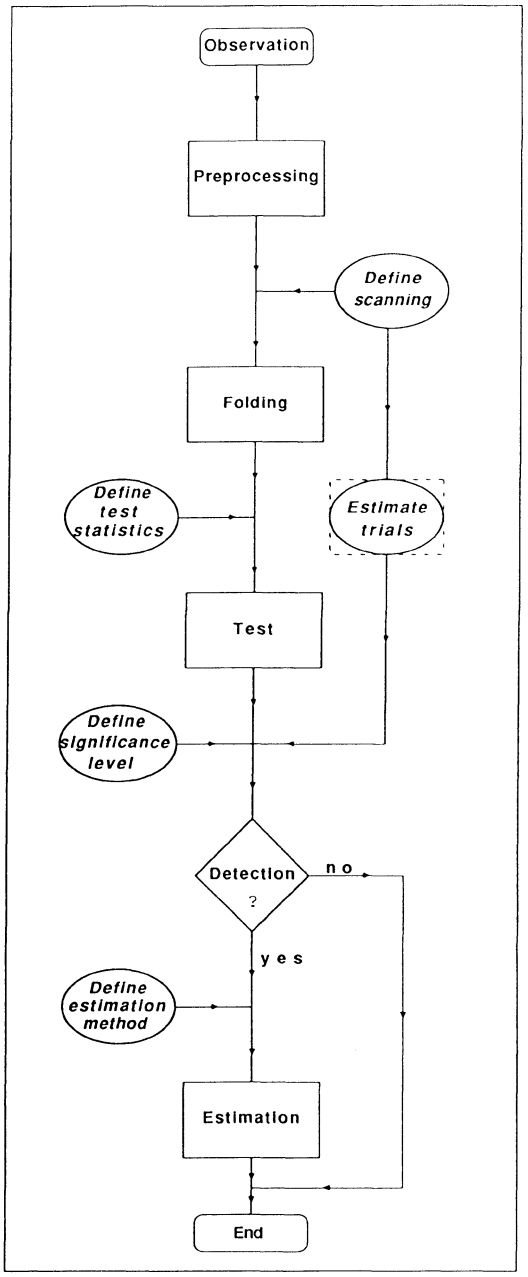

Fig.1

General flow of operations in the analysis for search of periodicity in Gamma-Ray Astronomy (from Maccarone & Buccheri, 1988)

(unless very strong) and c) loss of resolution in the times due to the binning. Considering, on the other hand, that FFT procedures are optimized concerning the computer time of analysis, they may be useful at the condition that i) the numer of arrival times to process is very large; ii) the signal expected has a quite strong power in its fundamental frequency and iii) no information at all exists on the interval of investigation of the period (purely exploratory cases). In the general cases typical of gamma-ray astronomy, the folding procedure is applied for all the trial periods within the interval investigated, which gives rise to a set of residual phase distributions, one per trial period. Each of these distributions will be tested against the presence of periodicity and the final decision on the positivity of the detection must make use of all the (independent) trial period investigated. Since the significance level for the acceptance of a pulsed signal (and therefore the sensitivity of the search) decreases with the number of trials, care must be taken in the predefinition of the scanning interval.

The process of testing the distribution of residual phases implies the a priori choice of a test statistic; in the traditional use the null hypothesis is the absence of any pulsed signal and the alternative hypothesis is the presence of a periodicity in the data. The pulsed signal is considered as detected when the value of the test statistic exceeds a predefined significance level α (see below); this operation implies a probability α to claim a positive detection when no signal is present (type I error) and, viceversa, a probability β to claim a negative result in the presence of a periodic signal (type II error). The value $1 - \beta$, giving the probability to accept as positive a detection when a periodic signal is truely present, is referred to as the *power* of the test used. In the following we will mainly refer to the so called Z^2_n-test defined as

$$Z^2_n = (2/N) \sum_{k,1}^{n} \left(\sum_{i,1}^{N} \cos(2\pi k\phi_i)\right)^2 + \left(\sum_{i,1}^{N} \sin(2\pi k\phi_i)\right)^2 \qquad (1)$$

where N is the total number of selected arrival times and ϕ_i, (i = 1 to N) are the residual phases derived after the folding process. In the particular case of n = 1 the Z^2_n-test reduces to the Rayleigh test (see Mardia, 1972). In the asymptotic case (N > 100) and in the absence of a periodic signal, the probability distribution of Z_n^2 closely follows the χ^2 distribution with 2n degrees of freedom. Fig. 2 shows the cumulative probability distributions of the χ^2_{2n} random variable and Z^2_n statistic in comparison with that of Pearson's test with m=2n+1 bins for n = 1 and 10 and N = 10, 50 and 200.

The Z^2_n-test, depending on the chosen number of harmonics n, is sensitive to any kind of light curve shape and, being described by a χ^2_{2n} probability distribution down to sample sizes $N \cong$ 50, is very easy to handle. Fig.3 shows the probability distribution of Z^2_n (for n = 2, 5 and 10) in the absence of any signal compared with the same distribution when a periodic signal with a gaussian spread is present. The FWHM of the gaussian was taken as 10% and 20% respectively. The power of the test for the detection of such signals is shown in the figure at a significance level α = 0.01. An additional study of the power of the Z^2_n-test can be found in Protheroe (1988).

A review of the test statistics used in periodicity searches is contained in De Jager, 1987 where the relative powers are also shown. All of these tests have the (positive) characteristics to be independent from the relative distances between the arrival times under analysis and are then independent of the phase location of the signal peak. The y-test, used in Harwit et al. (1987) does not show this advantage and the power of the test is varying with the phase location of the peak (see fig. 4), the reason being implicit in the definition of the test as the sum

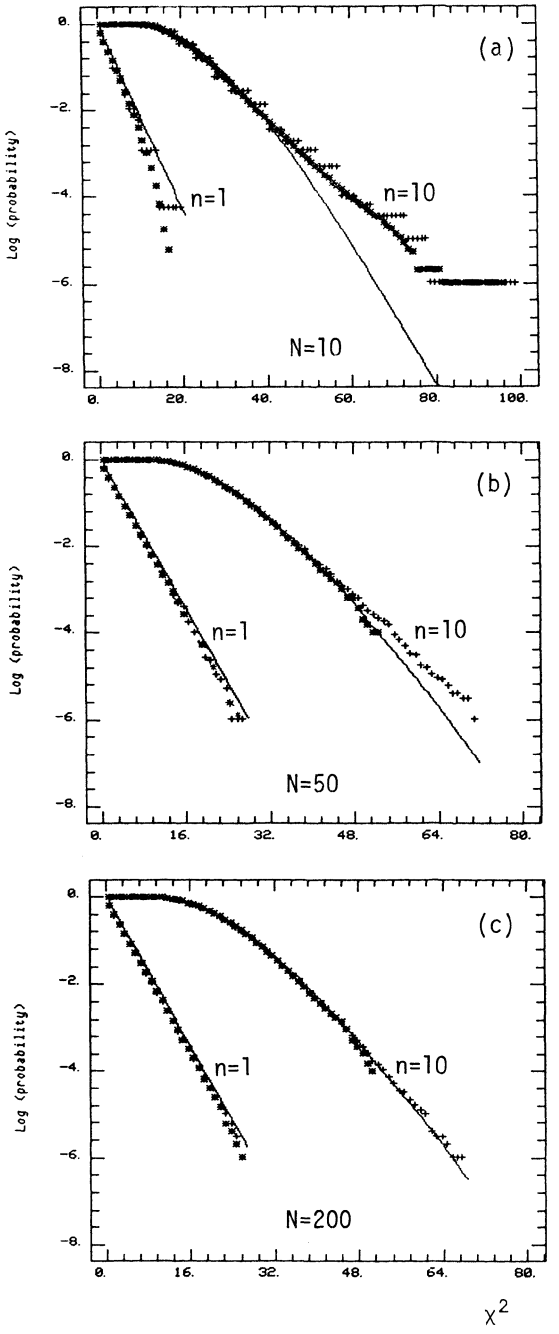

Fig. 2

Cumulative probability distribution of χ^2 (continuous line) compared with Z^2_n (asterisks) and Pearson's test statistics (crosses). Figs. a), b) and c) refer to sample sizes N = 10, 50 and 200 resp. The comparison is made in the cases of n = 1 (2 d.o.f. for χ^2 and 3 bins for Pearson's test) and n = 10 (20 d.o.f. for χ^2 and 21 bins for Pearson's test).

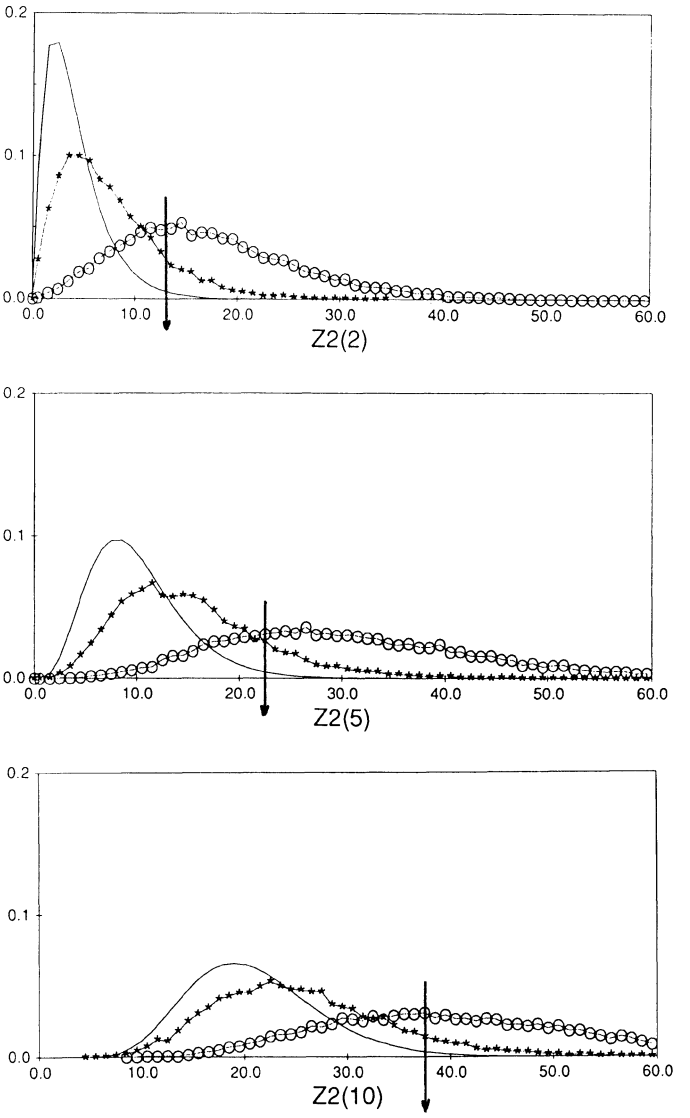

Fig. 3 - Probability density distributions of Z^2_n for n = 2 (fig.a), 5 (fig.b) and 10 (fig.c) in the absence of a signal (continuous line), compared with the same distributions in the presence of a periodic signal (asterisks for a 10% signal strength and circles for a 20% signal strength). Arrows indicate 0.01 confidence level.

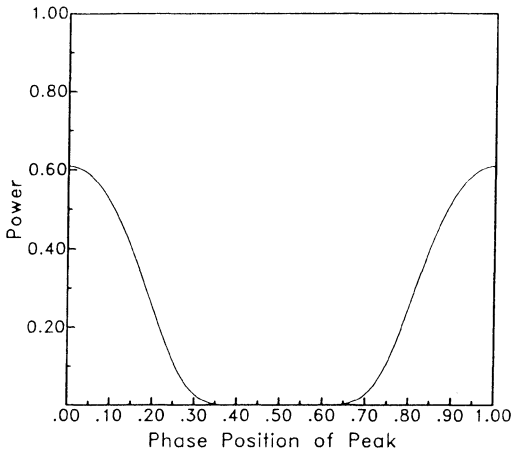

Fig. 4

Power of the y-test as a function of the phase position of the peak.

of the squares of the residual phases. Fig. 5 shows the probability distribution of the y-test in the absence of a signal (a), compared with the same distribution in the presence of a pulsating signal consisting in a gaussian peak located at zero phase (b) or at phase 0.5 (c). In these conditions identical gaussian shapes located at different phases may have a very high or very low chance to be detected, depending on the (casual) distance between the phase of the peak and the phase of the first detected arrival time, to which all the phases are usually referred. Similar problems may be found in the Q-test quoted by Fischer (1987).

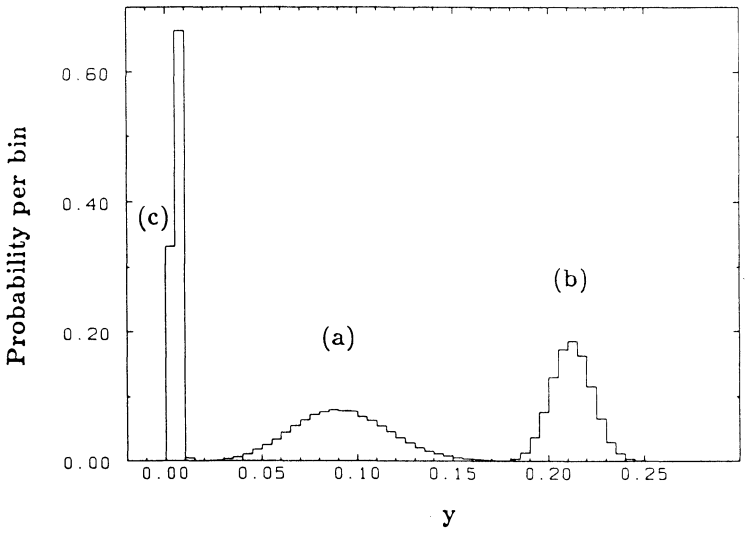

Fig. 5 - Probability density distribution of the y-test: (a) in the absence of any signal ; (b) in the presence of a gaussian peak located at zero phase; (c) in the presence of a gaussian peak located at phase 0.5 (reproduced from Buccheri and Ogelman, 1988).

Parameter estimation consists in our case in the evaluation of the pulsation period (and period derivative) together with its accuracy and in the description of the pulsed signal topology for positively detected signals.

Concerning the period and its accuracy as a result of a detection, a generally accepted method of estimation does not exist. It is true that the error on the estimated period is related to an independent Fourier spacing (IFS) which equals a frequency interval T^{-1} (where T is the total observation time) and a phase analysis at the true frequency $\pm$ T^{-1} will result in uniformly distributed phases. However, to assume that the error equals one IFS leads to a very conservative confidence interval. Another method used in the literature is a (gaussian) fit to the experimental curve describing the behaviour of Z^2_n versus the period investigated; we consider this method too optimistic in the determination of the accuracy to be attached to the period and will propose below a different evaluation procedure.

For what concerns the evaluation of the topological characteristics of the detected pulsation the traditional analysis is done selecting by eye the regions of the phase histogram where an increase of the signal over the background appears. In the following we will discuss some alternatives to this technique.

2.2 Decision problems and suggested solutions

Definition of the scanning interval. The definition of the search interval of the parameter values to investigate (period, period derivative, coordinates,...) depends on the previous knowledge on the parameters themselves; it is very large in the case of exploratory experiments (where no knowledge at all exists on the parameter values) but reduces to only one value in confirmatory cases, when the parameters are well known. The intermediate cases in which some information exist (from other experiments or from theoretical expectations) are the most usual; the typical intermediate case is the search for pulsation in the 100 MeV gamma-ray emission from a radio pulsar in an interval of period values derived by extrapolating parameters measured in the radio range at an epoch which is a few years apart from the epoch of gamma-ray observations. Considering that gamma-ray observations in the 100 MeV range are usually few weeks long, require the parameters to be known to a high accuracy. However, several unpredictable events (glitches, period noise,...) may cause the true pulsar period to be shifted out of the predicted interval. The search range in period should therefore be carefully selected. This subjective choice is left to the experience of the analyst. The decision is generallly made on the basis of two competing aspects which is difficult to quantify: a too small interval may result in the exclusion of the real period whereas a too large interval will result in a decrease in the sensitivity due to the inclusion of too many trial periods (Buccheri, Özel, Sacco, 1987). The solution to this problem is the most precise determination (where possible) of the scanning interval; in the case of searches for pulsed gamma-ray emission a from radio pulsar, simultaneous gamma-radio measurements of the pulsar parameters change the case from exploratory to confirmatory and may solve the problem; this is the plan for radio pulsar investigation by the Compton telescope COMPTEL, on board the Gamma Ray Observatory satellite (GRO) (Buccheri et al. 1987).

Estimate of the independent trials. For a correct evaluation of the statistical significance of a detection it is essential to quantify with care the number of independent trial periods investigated in a search. The probability for chance occurrence to be assigned to the maximum value Z_{max} of the used statistical test in a search through k independent trial periods is given by the formula

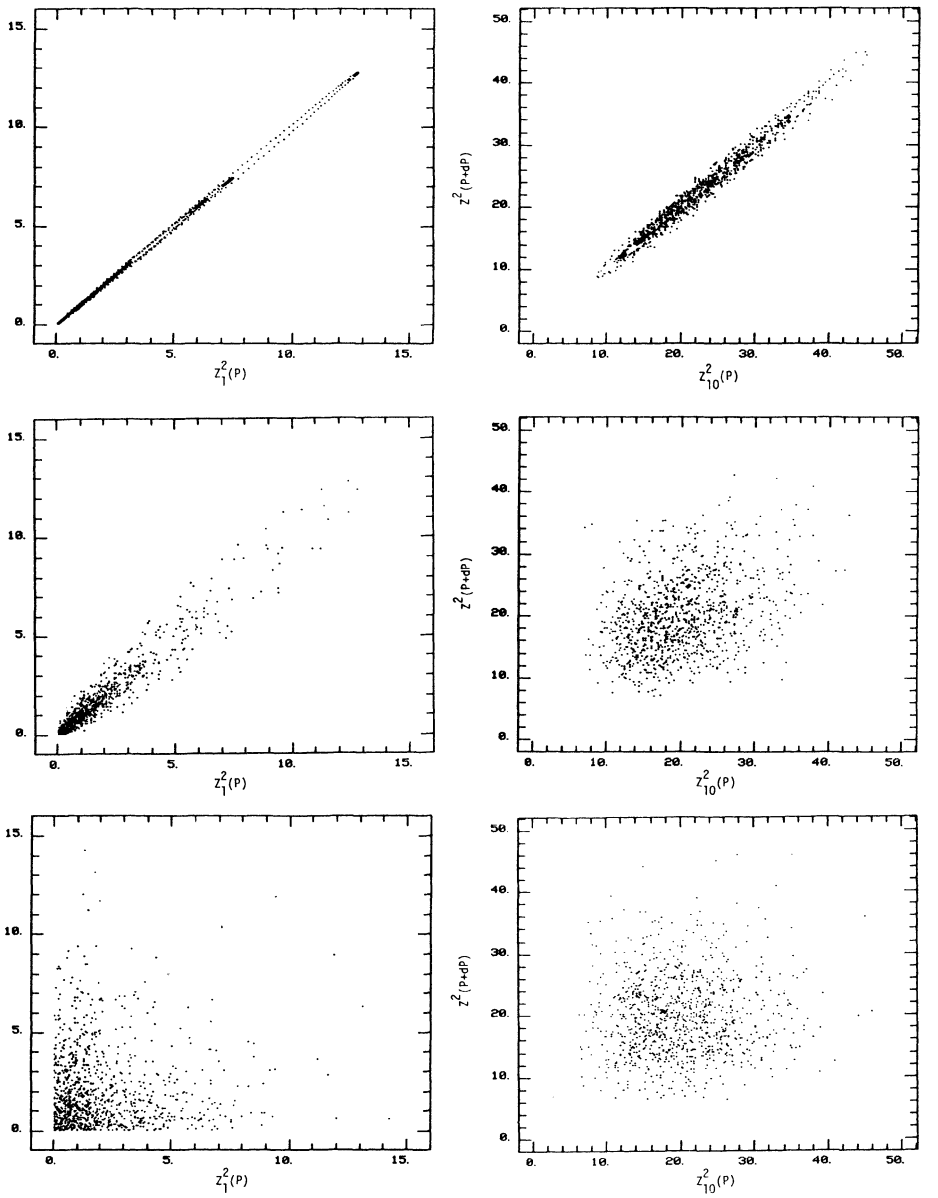

Fig. 6 - Correlation between adjacent values of Z^2_n for uniformly distributed arrival times in a search with period steps separated by 0.01, 0.1 and 1 IFS (from up to low respectively). Left figures refer to n = 1, right figures refer to n = 10.

$$p = 1 - (1 - p_{max})^{k} \qquad (2)$$

where p_{max} is the probability to get Z_{max} in a single trial. Little is known how to determine k in the case of oversampling (i.e. when the distance between trial periods is less than one IFS). Oversampling is fairly often adopted in gamma-ray astronomy where the signal expected is near the visibility threshold and therefore we will dedicate some attention to it. Two extreme attitudes are used in the literature for the calculation of eq. 2. A conservative one is to use all the trials as if they were independent; as a result of this attitude, weak signals may be missed. An optimistic attitude is to consider for k only the number of IFS's present in the search interval with the result to overestimate the significance of an effect and possibly claim a positive detection when it is not true. An analytical method to derive the effective number of independent trials in the case of oversampling is not yet available in the general case. Fig. 6 shows a scatter plot of values of Z^2_n for three different values of the step used in a period search for n =1 and 10; for step distances larger than or equal to one IFS, the test statistics are uncorrelated, but the correlation increases when the step distances decrease to zero. The immediate consequence of this correlation is that in case of oversampling the effective number of independent trials is between the total trials and the number of IFS contained in the search interval. When only the latter are used (i.e. k in eq. 2 equals the total number of IFS included in the search interval) the probability p for chance occurrence must be multiplied by a factor r of underestimation which can be derived by Montecarlo simulation for each specific case. Furthermore, r will also be a function of Z_{max}. Fig. 7 (De Jager, 1987) shows this factor for Z^2_{10} and Z_1^2 in the case of 0.05 IFS step distance. Although this procedure of simulation cannot be considered as a solution to the general problem of the evaluation of the effective independent trials in a search with oversampling, it gives a way to make a reasonable estimate of the significance of a detection.

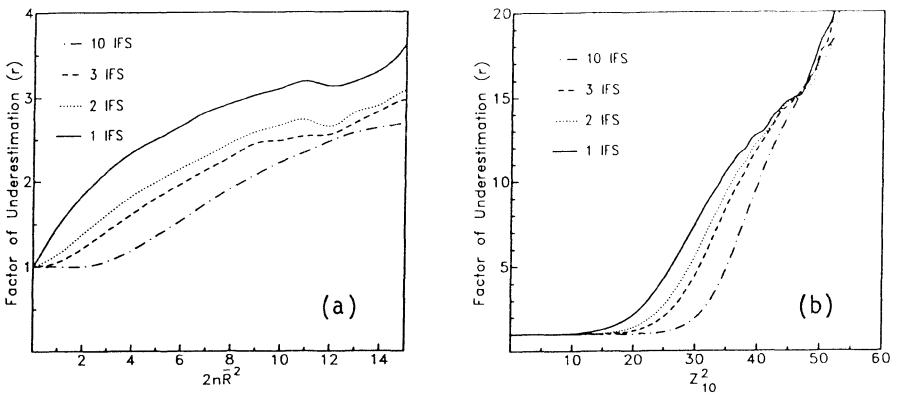

Fig. 7 - Factor by which to multiply eq. 2 in order to take oversampling into account. The four cases refer to 20 trials within 10, 3, 2 and 1 IFS. The two figures refer to Z^2_1 (a) and Z^2_{10} (b) (reproduced from De Jager, 1987)

Definition of the significance level. The definition of the significance level at which to accept a detection as positive, depends generally on the personal taste of the analyst, some being satisfied that a chance probability of 1% is low enough to exclude an improbable statistical fluctuation. If one takes into account that, willing or not, one is always led to unconsciously optimize the selection criteria in function of the desired positive detection (by trying different energy and acceptance angle selections and different statistical tests for example) and having always an eye to the possibility that the selected arrival times are almost never uniformly distributed along the observation duration (thus implying the presence of systematic deviations of the probability distributions with respect to the theoretical expectation) a more conservative probability threshold for positive detection should be used. The latter problem can be solved to a certain extent by deriving the probability distribution of the test statistic from the data base itself by sampling more than $1/p_{max}$ periods around the expected period, each having a spacing of T^{-1} (see for ex. North et al., 1987). In the case of binary systems with large orbital periods (e.g. Vela X-1) one can quantify the change in the probability distribution due to non-uniform orbital coverage (see Protheroe, 1984, for the treatment of PeV data). Depending on the situation this can also be done by using bootstrap procedures (see Raubenheimer et al., 1988, for TeV data).

Definition of the test statistics. The examples of fig. 8 illustrate how the probability for chance occurrence, as calculated using the probability distributions of Z^2_1 (Rayleigh) and Z^2_{10}, varies in function of the trial period when a signal is present. Fig. 8a refers to the presence of a gaussian peak, 0.3 FWHM, containing 0.134 of the total counts, fig. 8b is related to a much narrower gaussian peak (only 5% FWHM) containing 0.09 of the total counts. The abscissa describes the distance from the true period in units of IFS. It is striking to note that, at the true period, the Rayleigh test may accept as positive the broad signal of fig. 8a (99.7 % confidence level) but may miss the narrow shape (only 99 % c.l.); viceversa the Z^2_{10}-test definitely accepts as positive the narrow shape (99.9999% c.l.) but rejects the broad shape (93 % c.l.).

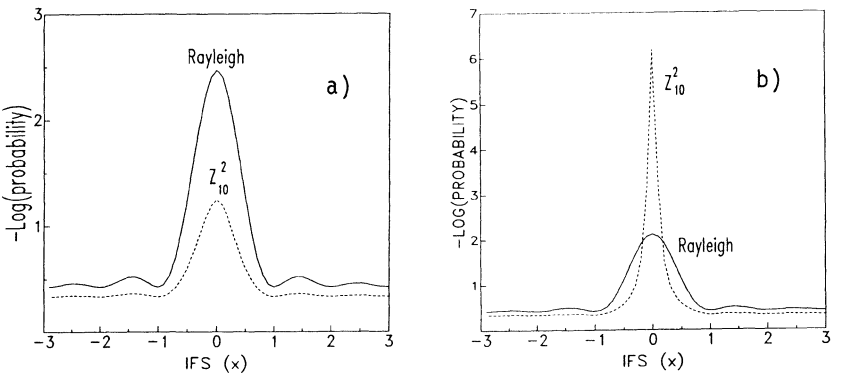

Fig. 8 - Probability for chance occurrence versus the period (in IFS units) in a search using Z^2_1 and Z^2_{10} to detect a periodic signal. In fig. 8a the signal has a broad shape (30% FWHM) and a strength of 13.4%; in fig. 8b the peak is narrow (5% FWHM) and has a strength of 9% (reproduced from De Jager, 1987).

It has to be stressed here that the use of Pearson's test with 21 bins would behave approximately as the Z^2_{10} (with further reduced sensitivity as illustrated in fig.2) and is therefore useless for weak signals with broad shapes, at variance with what suggested by Leahy (1987). It is clear that the acceptance as positive or the rejection as negative in the case of weak signals is strongly dependent on the chosen test statistic. In a confirmatory case where the shape of the searched signal is known a priori (from theoretical assumptions or from other experiments) a harmonic analysis of it will define the exact number of harmonics to use in the Z^2_n-test to apply. In the general exploratory case, when the information on the shape is scarse, there is a consistent risk to miss a signal by using an incorrect value of n.

A solution to this problem is the H_m-test, first suggested by De Jager (1987). The underlying idea is the use of Z^2_n with n unknown a priori but is optimally estimated from the data, giving m as the estimate. The definition of the test and an estimate of the probability distribution is given in De Jager (1987); a more complete treatment with the derivation of a much improved (in simplicity and effectiveness) distribution is given in De Jager et al., 1988. We recall here that the statistical variable related to the H_m-test is given by

$$H_m = Z^2_m - 4m + 4 \qquad (3)$$

as derived from the "Hart rule" (Hart, 1985) which determines the optimal number of harmonics in a periodic signal. The probability distribution of the H_m statistic has now a simple exponential form $\exp(-bH_m)$ where b is given in fig 9a for variour values of the sample size; for large sample sizes (N > 100) b can be approximated by 0.4. For strong signals (H_m > 25) the distribution of the statistic flattens out and the exponential term must be multiplied by a factor of underestimation as given in fig. 9b.

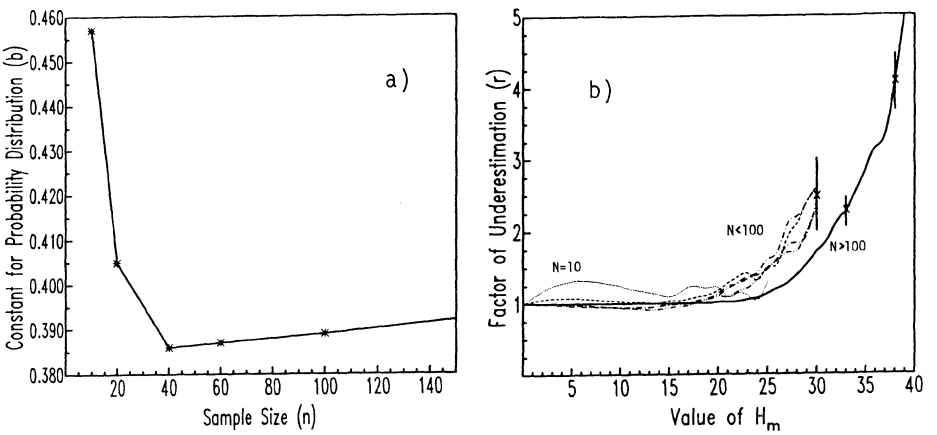

Fig. 9 - Parameters of the probability distribution related to the H_m-test statistic: a) gives the constant b as a function of the sample size; b) a factor by which to multiply the simple exponential term in case of strong signal and low sample sizes. In the latter case the errors (1 s) are indicated by the bars (reproduced from De Jager et al., 1988).

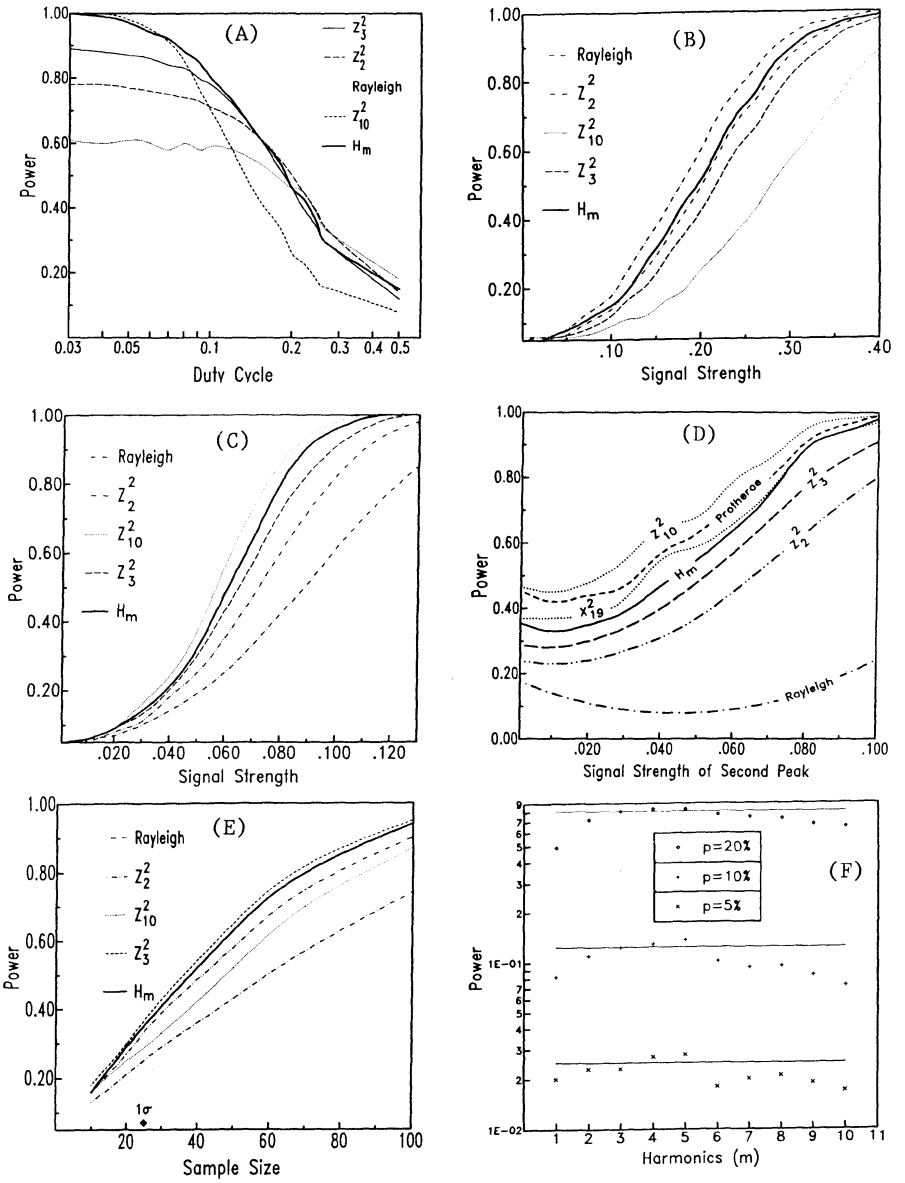

Fig. 10 - Power of H_m compared with Z^2_n for various values of n versus a) duty cycle; b) signal strength (sinusoidal signal); c) signal strength (gaussian peak with FWHM= 5%); d) signal strength of the second peak in a Vela-like light curve with fixed first peak shape; e) sample size (gaussian peak with FWHM= 10%); f) harmonics n for a single gaussian peak with FWHM= 10% and various signal strengths (H_m is indicated by the solid line).

Figs. 10a to 10f show the power of the H_m-test as compared with Z^2_n as a function of a) the harmonics n for various values of the signal strength, b) the duty cycle (FWHM) in the case of a gaussian peak, c) the sample size, d) the signal strength of a sinusoidal signal and e) a narrow gaussian peak and f) the strength of the second peak of a Vela-like double peaked structure. In all cases the power of the H_m-test is comparable with the power of the Z^2_n-test which proves the importance to use this test when a priori information on the structure of the signal is not available.

Definition of the estimation method. Fig. 11 (De Jager, 1987) shows that in the case of a narrow shape the randomization of the phase distribution occurs for an error on the period consistently less than one IFS. Extensive Montecarlo simulations for two extreme cases (a sinusoidal shape and a narrow gaussian peak, 0.1 FWHM) were used to estimate the standard deviation on the period corresponding to the maximum value of the used statistical test. These are given in fig. 12 in function of the signal strenght expressed in sigmas over the background. As expected, the accuracy is better for narrower shapes and improves with the signal intensity. In any case it can assume values which are small with respect to the IFS. The various curves refer to different choices of the number of harmonics n in Z^2_n; the one to choose in a specific case must be derived after a harmonic analysis of the detected period.

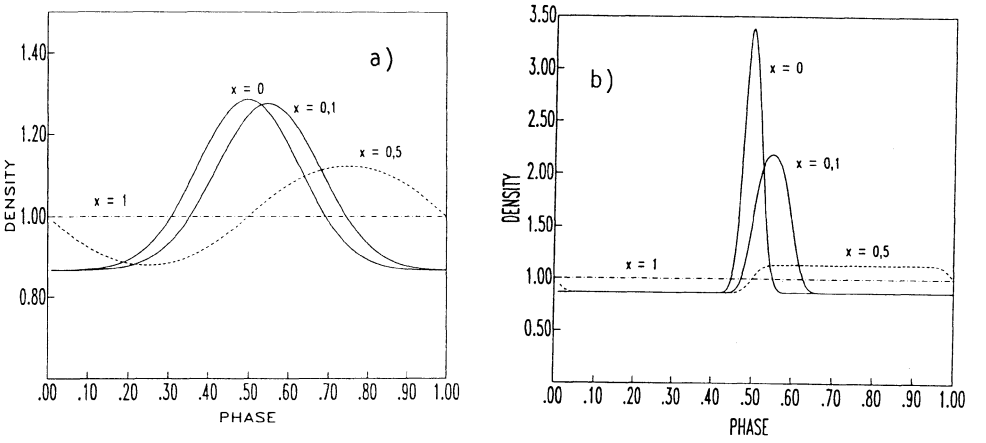

Fig. 11 - The average appearance of a light curve when a wrong value of period is used (x is the displacement from the true period in units of IFS). a) for a broad light curve with 30% FWHM and b) for a narrow peak (FWHM=5%).

Fig. 12 - The expected error (1 σ standard deviation) on the period estimated from the periodogram as a function of the contribution of the periodic signal to the DC excess. The period is that value at which the test statistic obtains its maximum. This is illustrated for a sinusoidal signal (a) and for a gaussian peak with 10% FWHM.

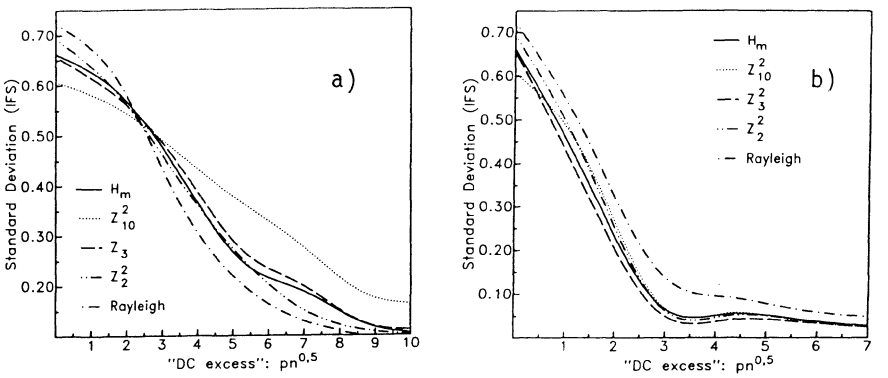

De Jager et al. (1986) have shown how to apply the Kernel Density Estimate procedures to the evaluation of the topological characteristics of a pulsar light curve. The derivation of the optimal smoothing parameter by minimizing the Mean Integrated Squared Error (MISE) between the KDE and the true unknown light curve, leads to a continuous function describing the radiation intensity. The KDE is aimed at a reduction of the bias- a characteristics not shared by the traditional histogram technique. It also converges with probability one to the true unknown phase density for large N and it smooths down unwanted fluctuations not present in the parent density distribution. However, weak but real microstructures may also be smoothed out in the process. To overcome this difficulty, Buccheri et al. (1988) introduced a new method (complementary to KDE) based on the adaptive cluster technique, which allows the identification of clusters at a very small scales down to the experimental resolution limit. Fig. 13 shows the light curve of the Vela pulsar at energies above 100 MeV (data from the COS-B satellite, first observation of 1975) as derived using the KDE and cluster technique and compared with that obtainable with the traditional histogram technique. These methods are strongly suggested for use in gamma-ray astronomy with the KDE being more useful in the case of broad peaks and the cluster method for the investigation of microstructures.

Acknowledgements. The authors thank B.C.Raubenheimer for discussions and M.Busetta for help with the software.

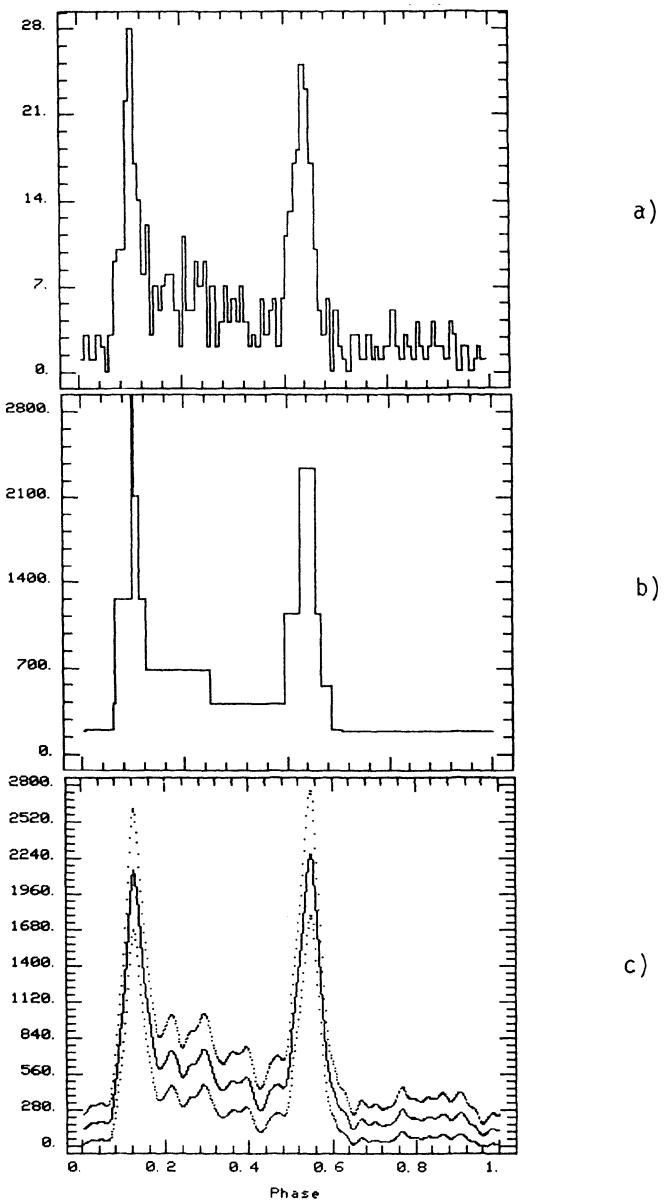

Fig. 13 - Light curve of the Vela pulsar above 100 MeV as observed by COS-B from Sept. 17 to Oct. 7, 1975, by the following estimators: a) histogram with 100 bins; b) cluster analysis (0.05 probability threshold) and c) Kernel Density Estimator (with 2 σ confidence bands).

3. REFERENCES.

- Buccheri R.
Int. Workshop on 'Actual problems of gamma-ray astronomy in the light of the planned experiments', Odessa, 1987
- Buccheri R. & Ögelman H.
Nature, **331**, no. 6154, 309-310, 1988
- Buccheri R. et al.
Int. Colloquium on "Coordination of observational projects", Strasbourg, 1987
- Buccheri R., Özel M.E., Sacco B.
Astron. Astrophys., **175**, 353, 1987
- Buccheri R., Di Gesu' V., Maccarone M.C., Sacco B.
Astronomy and Astrophys. , in the press
- Charman W.N., Jelley J.W., Orman P.R., Drever R.W.P., Mc Breen B.
Nature, **220**, 565, 1968
- De Jager O.C.
PhD Thesis, University of Potchefstroom, South Africa, 1987
- De Jager O.C., Swanepoel J.W.H. and Raubenheimer B.C.
Astron. Astrophys., 170, 187-196, 1986
- De Jager O.C., Buccheri R., Swanepoel J.W.H., Raubenheimer B.C.
In preparation for Astronomy and Astrophysics
- Eadie W.T., Drijard D., James F.E., Roos M., Sadoulet B.: "Statistical Methods in Experimental Physics", Amsterdam, 1971
- Fazio G.G., Helmken H.F., Rieke G.H., Weekes T.C.
Nature **220**, 892, 1968
- Fischer D.
Astron. Astrophys., 186, L11-L13, 1987
- Hart J.D.
Jou. Stat. Comput., 21, 95, 1985
- Harwit M., Bierman P.L., Meyer H., Wassermann I.M.
Nature, 328, 503, 1987
- Leahy D.A.
Astron. Astrophys., **180**, 275, 1987
- Maccarone M.C. and Buccheri R.
XII IMACS World Congress on Scientific Computation, Paris, 1988
- Mardia K.V.: "Statistics of directional data",
New York, Academid Press, 1972
- North A.R., Raubenheimer B.C., De Jager O.C., van Tonder A.J., van Urk G.
Nature, **326**, 567, 1987
- Protheroe R.J.
Proc. Astron. Soc. Australia, 1988, in press
- Protheroe R.J. et al.
Ap. J., **280**, L47, 1984
- Raubenheimer B.C., De Jager O.C., North A.R., Nel H.I.
Ap. J., 1988 (in press)
- Vasseur J. et al.
Nature 226, 534, 1970

TIMING A MILLISECOND PULSAR ARRAY

Roger W. Romani
Astronomy Department
University of California
Berkeley, CA 94720, USA

ABSTRACT. Pulse arrival times for millisecond pulsars show remarkable predictability over periods of years; in particular, dominant sources of long-term deviation from timing models for PSR1937+21 seem to be uncertainties in the terrestrial time, as established by atomic clocks, and small departures from the expected ephemerides of earth motion. It is shown that present limits on additional sources of perturbations, such as those generated by a background of gravitational waves, can be improved by timing an ensemble of pulsars in concord. Such analyses would also provide measurements of the clock and ephemeris corrections and could be used to characterize any gravity wave perturbations.

1. INTRODUCTION

For conventional pulsars, measurements of the pulse arrival time at the milliperiod level (Backer, these proceedings) allow one to examine perturbations on the scale of the several year observation span with accuracies of $\sim \Delta T/T_{obs} \sim 10^{-11}$. In view of this precision Mulholland (1971) suggested that ephemeris errors might eventually contribute to the arrival time uncertainty and Detweiler (1979) showed how the lowest amplitude pulsar timing residuals could be used to limit a hypothetical background of cosmological gravitational radiation. The later argument is surprisingly strong– the energy density in low frequency gravity waves of amplitude h is $\rho_{GW} \sim \dot{h}^2/(16\pi G)$ which for waves of period near T_{obs} and a Hubble constant of H gives a background bound (in units of the critical density for closure) of $\Omega_{GW}(T_{obs}) \lesssim \delta T^2/(H^2 T_{obs}^4)$. With existing data it was found that $\Omega_{GW} \lesssim 10^{-3}$ for T_{obs} ~3-10 years (Hellings and Downs 1983, Romani and Taylor 1983); timing noise due to intrinsic instability in the pulsar rotation was found to be the limiting factor in these analyses. Millisecond pulsar (MSP) timing (Taylor, these proceedings) has made these measurements substantially more powerful, as here $\sim$ milliperiod accuracies in arrival time determination correspond to sub-microsecond timing residuals. Nominally, then, one would expect the bounds on the energy density of any perturbations such as a gravity wave background to improve as the mean square timing residual R_{rms}^2, *i.e.* by $\sim$ 6 orders of magnitude for observations over a comparable interval.

2. ARRIVAL TIME NOISE SOURCES

The noise contributing to departures from the timing model fall broadly into two categories: those peculiar to the individual pulsar or it's signal propagation path to the Earth receiver, and those effects common to all pulsar arrival times which produced correlated residuals. We discuss briefly

H. Ögelman and E. P. J. van den Heuvel (eds.), Timing Neutron Stars, 113–117.

the noise sources believed to be important in the present timing of PSR1937+21.

For an individual pulsar, finite signal-to-noise at the receiver and additional uncertainties in measuring the pulsar phase will give a fundamental random error per epoch, σ. With current measurement procedures, such noise at $\sigma \sim 0.3\mu$s apparently dominates the PSR 1937 timing residuals up to periods $\sim 10^7$s. After averaging over the observation epoch $10^7\tau_7$s, this ~white noise contributes a mean squared residual of $\bar{R}^2 \sim 0.013\tau_7^{-1}\mu s^2$. In propagating through the interstellar medium, the pulsar signal will suffer variable dispersion delays and refraction due to electron density fluctuations along the ray path. The fluctuating dispersion produces a mean square residual $\bar{R}^2 \sim 1.5C_{-4}\lambda_m^2 D_{kpc}(v_7\tau_7)^2\mu s^2$ (*cf.* Armstrong 1984, Romani, *et al.* 1986) where C_{-4} characterizes the strength of the scattering, the observation wavelength is $\lambda_m$meters, the pulsar distance is D_{kpc} and the effective velocity of the medium is $10^7 v_7$cm s^{-1}; with parameters appropriate to 1937 at 1400MHz this is $\bar{R}^2 \sim 0.015\tau_7^2\mu s^2$. Note that this variance will continue to grow only until $v_7\tau_7$ exceeds the (unknown) outer scale of the ISM perturbations. Moreover, simultaneous observations at 2380MHz allow the removal of much of this excess delay (Rawley, *et al.* 1988), and 70d averages leave residual errors of $\sim 0.2\mu$s which are thereafter approximately white in nature. Intrinsic fluctuations in the pulsar rotation must eventually be an additional source of noise at some level. If, as in many pulsars, this takes the form of a random walk in frequency of strength $10^{-28}S_{FN}$Hz^{2}s^{-1} for a P_{ms}ms spin period the resulting residual grows as $\bar{R}^2 \sim 3 \times 10^{-5} S_{FN} P_{ms}^2 \tau_7^3 \mu s^2$. Present observations show $S_{FN} < 1$, however in view of MSP evolutionary histories, it would not be surprising if S_{FN} were substantially less than those of the quietest measured 'normal' PSRs, *i.e.* ~ 0.1.

All pulsars whose arrival time is determined at a given epoch will suffer additional common errors. The terrestrial clock used as a reference will show frequency noise on the longest time scales and thus introduce additional residuals of $\bar{R}^2 \sim 10^{-2}\sigma_{y,-14}^2(10^7)\tau_7^3\mu s^2$ where the fractional frequency stability is $10^{-14}\bar{\sigma}_{y,-14}$ at 10^7s. Errors in the Earth ephemerides produce significant correlated residuals for observation spans $\gtrsim 10^7$s: although these will have a complicated frequency structure and are of uncertain magnitude, the resulting residual should grow as roughly $\bar{R}^2 \sim 10^{-3}\tau_7^2\mu s^2$.

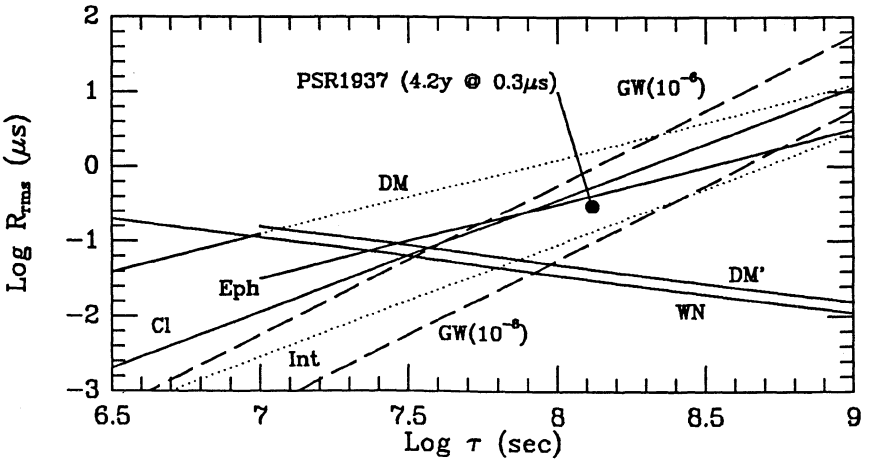

Figure 1. Rms arrival time residuals appropriate to PSR1937 as a function of observation span for ISM propagation (DM, DM'), pulse measurement (WN), clock (Cl), and ephemeris (Eph) errors. Also shown are the observed rms daily residual and contributions due to hypothetical gravity wave backgrounds (dashed lines) and pulsar activity (Int).

Finally, a hypothetical cosmological gravity wave background of energy density per logarithmic frequency interval Ω_{GW} times the closure value can produce arrival time perturbations, giving

$\bar{R}^2 \sim 33\Omega_{GW}\tau_7^4\mu s^2$. Buffeting of the Earth will produce a correlated signal, perturbations at the pulsars will in general be independent (two MSP in a single globular cluster could however show correlated signals with a lag proportional to their seperation). The various noise sources describes above are displayed at levels appropriate to the present timing of PSR1937. The lines DM and DM' show the dispersion-induced arrival time fluctuations at 1400 MHz before and after correction, the dotted line INT is intrinsic frequency noise at a level $S_{FN} = 10^{-29}$. The rms residuals contributed by a hypothetical Gravity wave background are indicated for $\Omega_G W = 10^{-6}$, 10^{-8}. The solid point is the rms daily residual observed during 4.2 years of timing (Rawley, *et al.* 1988). Since fitting the pulsar model subtracts some of the noise power (Blandford *et al.* 1984), the actual noise down to frequencies $1/\tau$ will be slightly higher.

3. REMOVAL OF CLOCK AND EPHEMERIS ERRORS

After subtraction of contributions due to known dispersion measure variations, Figure 1 shows that clock errors and ephemeris uncertainties will increasingly dominate the timing residuals for periods $\gtrsim$1 year. Thus the timing residual will grow upwards along the corresponding solid lines. Limits on Ω_{GW} (dashed lines) would still improve, albeit slowly. However, clock and dipole errors peculiar to the Earth observatory can be accounted for by timing several pulsars in parallel. A clock correction would appear as a 'monopole' term $C(t)$ common to all pulsars on the sky, while at any instant, errors in the Earth ephemeris will leave a small unmodeled velocity– the timing residuals would thus show a varying derivative (which can be thought of as a redshift) of $(\delta t_1 - \delta t_2)/(t_1 - t_2) = D(t) f_i(\theta_d, \phi_d)$ where f_i gives the component of the dipole velocity along pulsar i. Monitoring these variations would provide improved long-term time standards and better estimates of the barycentric motion.

A gravity wave of strain amplitude h passing the Earth will also produce an anomalous residual in a pulsar at (θ_i, ϕ_i) corresponding to a Doppler shift

$$z_i(t) = h(t)1/2(1 - \cos\gamma_{iW})\sin(2\alpha) = h(t)g_i(\theta_i, \phi_i; \theta_W, \phi_W, \varphi_W)$$

where the wave is incident from (θ_W, ϕ_W) at angle γ_{iW} to the pulsar and α gives the angle of projection of the wave's principle polarization vector along φ_W. Inasfar as the gravity wave signal in the collection of pulsars is non-degenerate with the other corrections, modeling the clock and ephemeris errors can improve bounds on Ω_{GW}, as well.

The rate of change of the residual (*i.e.* Doppler shift) seen for pulsar i due to the perturbations above will be

$$z_i(t) = S_i(t) + C(t) + D(t)f_i + h(t)g_i + \tilde{h}_i(t)\tilde{g}_i$$

where S_i is the individual error and $\tilde{h}_i$, $\tilde{g}_i$ refer to gravitational waves buffeting pulsar i. After performing a least squares fit to extract the clock corrections we would have a new set of residuals $z_i'(t) = z_i(t) - (\sum_m z_m(t)/\sigma_m^2)/(\sum_m \sigma_m^{-2})$ where σ_m is the rms individual noise associated with pulsar m, and the clock corrections will be determined to an accuracy $\sim (\sum_m \sigma_m^{-2})^{-1/2}$. Simultaneous fitting of the ephemeris term gives a more complicated expression.

To separate these various fluctuations it is clearly desirable to have a number of accurate pulsar clocks distributed across the sky. Intrinsic timing noise has not been identified for any 'reprocessed' pulsar, so the inverse of the arrival time signal-to-noise(*cf.* Backer, these proceedings) provides an observing system-independent estimate of the 'timability'. This residual noise level will scale as S_{1400}/W_{ms}, where S_{1400} is the flux at 1400MHz and W_{ms} is the pulse width in ms. The positions of several reprocessed pulsars, with a symbol proportional to the log of this timability, are shown in Figure 2, along with the line of the galactic plane and the declination range accessible to Arecibo observatory. Although detection and timing of fast pulsars will be easiest in the Arecibo dec range, the need for substantial angular separations in the timing array encourages searches in the anti-center and southern hemisphere– the recently discovered MSPs in the globular clusters M4, M28 and 47Tuc are important in this regard.

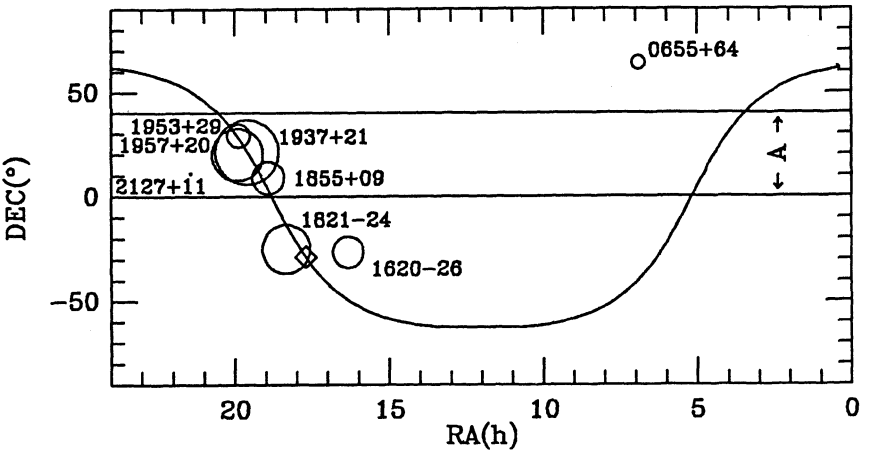

Figure 2. Positions of several 'reprocessed' pulsars with symbols scaled by the log of the estimated pulse arrival time sensitivity. The galactic plane and the Arecibo declination range are indicated.

4. LIMITS ON STOCHASTIC BACKGROUNDS OF GRAVITY WAVES

Although the gravity wave signal is partly quadrupolar in nature, in fitting out the clock and dipole terms as above we have absorbed some potential gravity wave power; as in the case of the temporal transfer function estimated by Blandford, *et al.* it is important to take account of this filter when converting a observed residual variance to a limit on the gravity wave spectrum.

The correlation among residuals allows us to form such a limit, although not knowing the direction and polarization of the gravity waves, the signal from the various 'baselines' formed by pulsar pairs (i, j) must be averaged up incoherently. Accordingly, a bound on the autocorrelation function of the spectrum will be provided by

$$\langle \chi(\tau) \rangle = \left\langle \sum \alpha_{ij} z_i'(t) z_j'(t+\tau) / \sum \alpha_{ij} G_{ij} \right\rangle$$

where G_{ij} describes the average response of the pulsar pair i, j to a passing gravity wave and the weightings α_{ij} are chosen such that the variance

$$\langle \chi^2(\tau) \rangle = \left\langle \sum \alpha_{ij}\alpha_{kl} z_i'(t) z_j'(t+\tau) z_k'(t) z_l'(t+\tau) / \left(\sum \alpha_{ij} G_{ij} \right)^2 \right\rangle$$

is minimized. When clock and dipole errors are not removed $G_{ij} = (g_{ij} + \delta_{ij}/6)$, where the second term is omitted if only the gravity waves perturbing the Earth are to be measured and g_{ij} is the average of $g_i g_j$ over all wave directions and polarizations. The expression for G_{ij} after extraction of $C(t)$ and/or $D(t)$ will have additional terms, so the resulting α_{ij} will differ, as well. Since $h^2(\tau) \lesssim \chi(\tau)$ this provides an minimum bound on the background energy density for an array of pulsars i. Note that the α_{ij} will be functions of the individual noises $\sigma_i(\tau)$ and will vary as a function of lag, especially if the σ_i are red in nature. Moreover, the transmission function for the gravity wave signal will, in general, be decreased by fitting other parameters, so unless the noise removed by the fit is larger than this decrease in transmission, the limit on $h^2(\tau)$ will not improve. For instance, removal of 'clock' terms from collinear pulsars would also absorb all Earth passing gravity wave signals.

As an example consider an array composed of PSRs 1937, 1957 and 1821 timed for a period such that the relative arrival time accuracies are (1:3:5) and the clock errors introduce additional residuals of 10 in these units (*i.e.* $\sim$ 3-10y at present sensitivities). If only the local (Earth-crossing) component of the gravity wave background is considered, then after selecting the optimum α_{ij} as above, the rms value for χ will be reduced below that estimated from 1937 alone by a factor of 2.2 when monopole clock corrections are not fitted out; the rms χ is, however, 2.1 times larger when the clock is previously fit. If the distant (pulsar crossing) gravity waves are considered, as well, then the limits improve by 2.5 (no fit) and degrade by 1.4 (clock fitted), respectively. However, with larger relative contribution of clock errors (slightly longer observation spans) gravity wave background limits should always be lower with clock error removal, and will improve rapidly with observation span relative to the single pulsar values. In addition, improved timing relative to 1937 or the discovery of other accurate pulsars at large angles would allow more complete separation of the clock, ephemeris and gravity wave residuals.

The techniques for improving limits on cosmological backgrounds of gravity waves suggested above can produce bounds quite significant for several popular cosmologies. In particular, present limits from 1937 timing alone, $\Omega_{GW} < 1.5 \times 10^{-2} \Omega_{\gamma}$ for waves of frequency $0.23 \lesssim f \lesssim 0.63 \mathrm{yr}^{-1}$ (Rawley *et al.* 1987), already place rather tight constraints on theories of cosmic string-induced galaxy formation (Vilenkin 1981, Romani 1988). Even modest improvements obtainable from timing an array of PSRs over short periods would produce strong violations of the backgrounds predicted by most forms of these theories. On a more speculative note, improved pulsar timing might eventually reach sensitivities for which gravity wave perturbations (which are certainly present at a minimum level associated with primordial fluctuations) are significant and contribute to the timing noise. It is also possible that exotic astrophysical sources might generate detectable waves at late times. For instance $\sim$ 10y of 1μs white noise residuals would give a strain sensitivity of $\sim 10^{-15}$— a $10^9 M_{\odot}$, 3 year period black hole binary anywhere within the Hubble volume could then be detected with a signal-to-noise of $\sim$ 10. (For one such object to be present today, one could require that 10^{-3} of all massive galaxies would suffer mergers and coalescence of such central black holes.) In this case the positive identification of the gravity wave signal could be obtained via the correlated 'local' residuals between several pulsars timed at this level of accuracy. Since the signals would now be detected coherently on the several baselines, simulation shows that the timing experiment would then operate as a gravity wave 'telescope', locating such sources to $\sim$ 10arcmin accuracy and providing measurements of the wave amplitude and polarization; alternatively, the array would put rather strong limits on their occurrence.

REFERENCES

Armstrong, J.W. 1984, *Nature*, **307**, 527.
Blandford, R., Narayan, R., and Romani, R.W. 1984, *J. Astrophys. Ast.*, **5**, 369.
Detweiler, S. 1979, *Ap.J.*, **234**, 1100.
Hellings, R.W. and Downs, G.S. 1983, *Ap.J.*, **265**, L39.
Hogan, C.J. and Rees, M.J. 1984, *Nature*, **311**, 109.
Mulholland, J.D. 1971, *Ap.J.*, **165**, 105.
Rawley, L.A., Taylor, J.H., Davis, M.M., and Allan, D.W. 1987, *Science*, **238**, 761.
Romani, R.W. and Taylor, J.H. 1983, *Ap.J.*, **265**, L35.
Romani, R.W., Narayan, R., and Blandford, R.D. 1986, *Mon.Not. R. astr. Soc.*, **220**, 19.
Romani, R.W. 1988, *Phys. Lett. B*, submitted.
Vilenkin, A. 1981, *Phys. Lett.*, **107B**, 47.

THE SCALING OF RADIO PULSAR TIMING NOISE WITH SPIN PARAMETERS

Rachel J. Dewey[1] and James M. Cordes
Center for Radiophysics and Space Research
Cornell University
Ithaca, NY 14853
USA

ABSTRACT. Measurements of pulsar timing noise are now available for 39 pulsars, and upper limits for 18 other pulsars. We investigate the relation of timing noise to pulsar period and period derivative using a method that incorporates the upper limits. We confirm previous findings that timing activity, as conventionally quantified, depends strongly on period derivative but only weakly (if at all) on period. We also find that the scatter around our best fit to P and $\dot{P}$ is considerably larger the measurement error, suggesting that other variables must play a significant role in timing activity. At this point we find no need to treat millisecond pulsars as a separate population in timing noise studies, though this may become necessary if the limits on the timing activity of such pulsars continue to decrease.

KEYWORDS: pulsars - stars: neutron

1. INTRODUCTION:

Radio pulsars are, in general, very good clocks: some appear to be as good or better than the best clocks on earth (see papers by Backer and Talyor in this volume). Others, however, are not nearly as good and most pulsars with periods longer than 10 ms show deviations from a simple secular slowdown. These deviations appear as sizable "glitches" in period P and period derivative $\dot{P}$ and/or as lower level timing noise *i.e.* small random fluctuations in pulsar arrival times. Timing noise reflects small scale changes in the pulsar's rotation rate which are believed to be tied directly to the the interior dynamics of the neutron star or to processes in its magnetoshpere. Pulsar timing behavior can therefore be used as a probe of neturon star physics (*e.g.* Alpar *et al.* 1984ab, Alpar, Nandkumar and Pines 1985, 1986, Cheng 1987ab; see also Alpar, Cheng, Pines, Shaham and Sauls in this volume).

In this paper we investigate the correlation of timing activity to pulsar period and period derivative. These quantities describe the basic rotational behavior of pulsars and are expected to be intimately connected with timing activity. In addition they correlate strongly with other neutron star properties (*e.g.* age and magnetic field) on which timing activity may depend. Therefore, even if timing activity cannot be completely described by P and $\dot{P}$, its dependence on these quantities should provide useful information about the underlying neutron star physics.

[1] Present address: Jet Propulsion Laboratory, 4800 Oak Grove Drive, Pasadena, CA 91109 USA

H. Ögelman and E. P. J. van den Heuvel (eds.), Timing Neutron Stars, 119–124.

2. DATA AND METHODS USED

Studies of pulse arrival times (*e.g.* Cordes and Downs 1985, Cordes and Helfand 1980) show that the level of timing noise varies strongly from pulsar to pulsar as does its detailed behavior. Rotational phase deviations can be described as superpositions of small discontinuities in phase, frequency, or frequency derivative and the rms phase residual after a second order polynomial fit (used to remove the secular spindown) is the simplest measure of timing noise. Following Cordes and Helfand (1980), we define an "activity parameter"

$$A = \log\left[\frac{\sigma(2,T)}{\sigma_{Crab}(2,T)}\right]$$

which relates $\sigma(2,T)$, the rms residual over a time span T after a second order fit, to the same quantity for the Crab pulsar over the same length of time. Since the timing noise of the Crab has been idenitified as frequency noise, $\sigma_{Crab}(2,T)$ can be scaled from the value measured over 1628 days:

$$\sigma_{Crab}(2,T) = \sigma_{Crab}(2,1628)\left(\frac{T_{days}}{1628}\right)^{3/2} \approx (12ms)\left(\frac{T_{days}}{1628}\right)^{3/2}.$$

Note that the rms timing noise is defined in *temporal* units. In the analysis below this choice of units affects the way in which A scales with P and $\dot{P}$; we also consider the scaling which results when the rms timing noise is expressed in phase units.

We used as our data set the activity parameters compiled by Cordes and Downs (1985), with improved data for PSRs 1937+21 and 1913+16 from Rawley (1986). We also included data for three recently discovered pulsars, PSRs 1855+09 and 1953+29 for which good upper limits on the timing noise are available (Rawley 1986) and PSR2334+61 which shows measurable timing noise (Dewey *et al.* 1988). Figure 1 shows the activity parameters of these pulsars plotted against period and period derivative.

For a number of the most interesting pulsars, and for a considerable range in $\dot{P}$, only upper limits on A are available and it is useful to incorporate these into the analysis of timing noise. To do this we use the parameterized maximum likelihood method described by Avni *et al.* 1980. Similar methods are discussed by Schmitt (1985) and Feigelson and Nelson (1985). We assume that timing activity depends on P, $\dot{P}$ and on some "hidden variables", such as mass or temperature, on which we have no direct information. These hidden variables produce scatter around any relation between A, P and $\dot{P}$. We assume that the *mean* activity parameter scales with $\log P$ and $\log \dot{P}$ as

$$\bar{A} = \alpha \log P + \beta \log \dot{P} + \gamma$$

where P is measured in seconds, $\dot{P}$ in units of $10^{-15}\,\mathrm{s\,s^{-1}}$, and where α, β and γ are unknown constants. Individual values of A are assumed to be gaussianly scattered about the mean with standard deviation δ that, for tractability, is considered independent of both of P and $\dot{P}$. Our analysis shows no evidence to contradict this last assumption.

For a given underlying distribution described by $\alpha, \beta, \gamma, \delta$, the probability p_i that the i^{th} pulsar with period P_i and period derivative $\dot{P}_i$ has a measured activity parameter A_i is

$$p_i(\alpha,\beta,\gamma,\delta) = \frac{1}{\delta\sqrt{2\pi}} e^{[A_i - \bar{A}(P_i,\dot{P}_i)]^2/2\delta^2} \Delta A_i \quad .$$

where ΔA_i is the uncertainty in the measurement of A_i. The probability of observing an upper limit A_i is

$$p_i(\alpha,\beta,\gamma,\delta) = \frac{1}{\delta\sqrt{2\pi}} \int_{-\infty}^{A_i} e^{[x - \bar{A}(P_i,\dot{P}_i)]^2/2\delta^2} dx \quad .$$

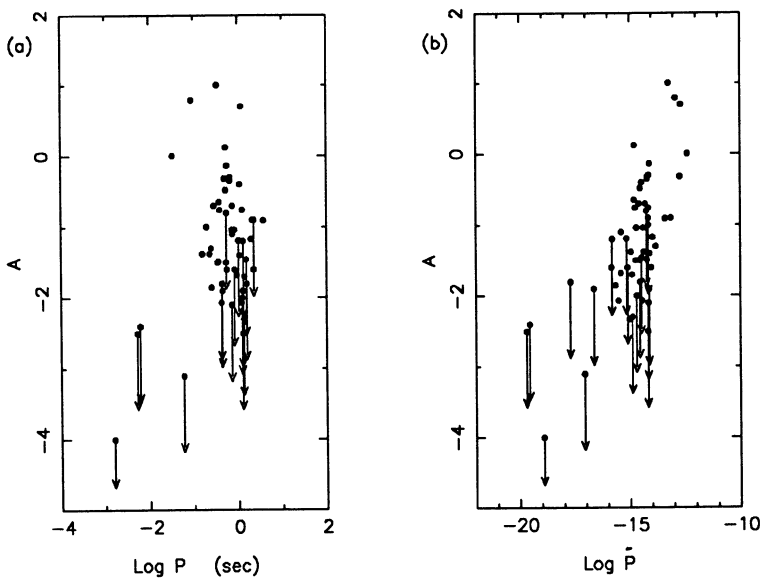

Figure 1 The activity parameters which make up our data set plotted against pulsar period (a) and period derivative (b).

The probability of obtaining the total observed set of A_i for N pulsars is:

$$p_{tot}(\alpha, \beta, \gamma, \sigma) = \prod_{i=1}^{N} p_i(\alpha, \beta, \gamma, \delta) \quad ,$$

where p_i is given by whichever of the above equations is appropriate. By maximizing p_{tot} with respect to $\alpha, \beta, \gamma, \delta$, we obtain the underlying distribution (given our choice of underlying functional form) most likely to result in the N observed values of A. The maximization was done numerically, assuming $\Delta A = 0.2$ for all pulsars for which a value (rather than an upper limit) for A was determined. The values which maximized p_{tot} were $\alpha = -0.4$, $\beta = 0.8$, $\gamma = -1.8$, $\delta = 0.75$.

3. GOODNESS OF FIT AND ERROR ESTIMATES

The method just described gives a "best fit" to the data, but does not quantify the goodness of fit. If the fit is good the probability, p_{max}, of the maximized solution should be similar to the optimum value obtained if the input data are replaced with random numbers drawn from the best fit underlying functional form. We found this to be true. If the assumed form of the underlying distribution is in error a fit to subsets of the data, such as pulsars with large P, or pulsars with small $\dot{P}$, should result in different solutions for α, β, and γ and smaller values of δ. Fits to such subsets did not result in smaller values of δ, and within the uncertainties (which were large for some subsets) did not result in different solutions for α, β or γ. Finally,

if the basic underlying model is good and A indeed depends more strongly on P and $\dot{P}$ than on any of the hidden variables, the scatter around $\bar{A}$ should be significantly smaller than the total range of A. Since values of A range from -4.0 to 1.0 and $\delta = 0.75$, we find this to be true.

We used two methods to estimate the uncertainties in our solution. Avni *et al.* (1980) show that the 95% confidence level is equivalent to the surface in $\alpha, \beta, \gamma, \delta$ space where

$$\frac{p_{tot}(\alpha, \beta, \gamma, \delta)}{p_{max}} = e^{-4} \quad .$$

This method has the disadvantage that it does not provide any information about the overall goodness of fit. Schmitt (1985) suggests obtaining error estimates by generating pseudo input data from the best fit underlying distribution and looking at the scatter obtained in numerous trials. This allows a comparison of the values of p_{max} obtained from pseudo data with that obtained from the actual data, as described above. We found that the two methods produce similar error estimates. Our final results are:

$$\alpha = -0.4 \pm 0.8$$

$$\beta = +0.8 \pm 0.4$$

$$\gamma = -1.8 \pm 0.4$$

$$\delta = +0.75 \pm 0.2 \quad .$$

Since the rotational dynamics of neutron stars are naturally quantified using $\Omega = 1/P$, and $\dot{\Omega}$, it is useful to define an alternative function for the mean activity parameter in terms of these variables:

$$\bar{A} = \alpha' \log \Omega + \beta' \log |\dot{\Omega}| + \gamma' \quad .$$

It may be shown that $\alpha' = -(\alpha + 2\beta)$ and $\beta' = \beta$. Another 'rescaling' results if, instead of expressing phase deviations in time units, a new activity parameter A_ϕ is defined in terms of dimensionless phase deviations:

$$A_\phi \equiv A + \log P_{Crab} - \log P \quad .$$

If A_ϕ scales as

$$\bar{A}_\phi = \alpha'' \log P + \beta'' \log \dot{P} + \gamma'',$$

then $\alpha'' = \alpha - 1$ and $\beta'' = \beta$.

Figure 2a shows the regions of the α, β plane allowed by our solutions and Figure 2b shows the value of $\bar{A}$ predicted by our best fit solution plotted against measured values of A. The upper limit on the activity parameter for PSR1937+21 ($A \leq -4.0$) lies slightly below the predicted value ($\bar{A} = -3.8$), though well within the expected scatter. This suggests that 1937+21 may begin to show meausurable timing activity in the next few years. The limits on A for the two other millisecond pulsars in our sample (1855+09 and 1953+29) lie well above the predictions for $\bar{A}$.

4. CONCLUSIONS

A number of conclusions can be safely drawn from our results. First, and most importantly, it is possible at present to treat all pulsars as a single population with regard to timing activity. This may cease to be true if the upper limits on A for the millisecond pulsars (and PSR1913+16) decrease significantly (more than one unit in A). Such a decrease requires at least an order of

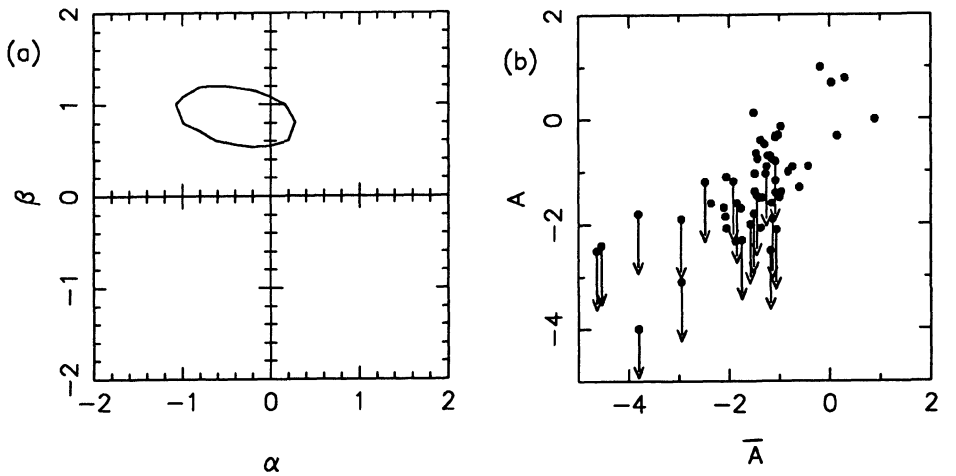

FIGURE 2 (a) The regions of the α, β plane allowed by our solution and (b) observed values of A plotted against values of $\bar{A}$ obtained from our best fit model.

magnitude increase in timing accuracy or an additional seven to ten years of data at current accuracies. Second, when timing activity is measured in temporal units, the dependence of A on only $\dot{P}$ and hidden variables is allowed by the data, while dependence on only $\dot{\Omega}$ and hidden variables is not. If phase units are used, the data allow a dependence of A_ϕ on $\dot{\Omega}$ alone but not on $\dot{P}$ alone. Finally, for values of $\dot{P} > 10^{-16}\,\mathrm{s\,s^{-1}}$, A depends more strongly on $\dot{P}$ than on any of the hidden variables (for lower values of $\dot{P}$ only upper limits on A are available and so the true scatter in the data is unknown). However, the scatter ($\delta = 0.75$) around our best fit model is considerably larger than the measurement uncertainty, signifying that variables other than P and $\dot{P}$ play a substantial role in determining a pulsar's level of timing activity.

This research was supported by the NSF through grant AST 85-205030 to Cornell University and by the National Astronomy and Ionosphere Center, operated by Cornell University under contract with the NSF. A portion of the research described in this paper was carried out by the Jet Propulsion Laboratory, California Institute of Technology under contract with the National Aeronautics and Space Administration.

REFERENCES

Alpar, M. A., Anderson, P. W., Pines, D. and Shaham, J. 1984a, *Ap. J.* **276**, 325.
————. 1984b, *Ap. J.* **278**, 791.
Alpar, M. A., Nandkumar, R. and Pines, D. 1985, *Ap. J.* **288**, 191.
————. 1986, *Ap. J.* **311**, 197.
Avni, Y., Soltan, A., Tananbaum, H. and Zamorani, G. 1980, *Ap. J.* **238**, 800.
Cheng, K. S. 1987a, *Ap. J.* **321**, 799.

————. 1987b, *Ap. J.* **321**, 805.
Cordes, J. M. and Helfand, D. J. 1980, *Ap. J.* **239**, 640.
Cordes, J. M. and Downs, G. S. 1985, *Ap. J. Suppl.* **59**, 343.
Dewey, R. J., Taylor, J. H., Maguire, C. M. and Stokes, G. H. 1988, *Ap. J.* , .in press/
Feigelson, E. D. and Nelson, P. I. 1985, *Ap. J.* **293**, 192.
Rawley, L. A. 1986, unpublished Ph.D. thesis, Princeton University, Princeton, NJ.
Schmitt, J. H. M. 1985, *Ap. J.* **293**, 178.

SIMULATION OF INTERSTELLAR SCATTERING EFFECTS ON PULSAR TIMING

Roger S. Foster[1] and James M. Cordes[2]
[1]Astronomy Department, University of California, Berkeley, CA 94720 USA
[2]Astronomy Department, Cornell University, Ithaca, NY 14853 USA

ABSTRACT. A computer simulation has been devised to study the effects of interstellar scattering on pulsar pulse times-of-arrival using a one-dimensional power-law phase screen. The motivation for this study is to understand the limits on pulsar timing imposed by interstellar scattering (ISS). For a given model of the electron density spectrum, multi-frequency timing observations may be able to remove the plasma propagation effects. Removal of these effects is necessary to obtain sub-microsecond timing estimation of pulsar proper motion, parallactic distance, and other effects. In this paper we present some of our preliminary results.

1. INTRODUCTION

Pulse times-of-arrival are perturbed by delays associated with the low wavenumber (refractive) electron density variations in the interstellar medium (e.g. Armstrong 1984; Blandford, Narayan, and Romani 1984; Cordes, Pidwerbetsky, and Lovelace 1986). We use a one-dimensional phase screen to simulate the effects of a varying electron column density along different lines of sight. The electron density spectrum can be modelled as a power spectrum

$$P_{\delta n_e}(q) = {C_N}^2 q^{-\alpha}, \qquad q_0 \leq q \leq q_1, \tag{1}$$

where q is the fluctuation frequency, q_0 and q_1 are the low frequency and high frequency cut-offs respectively, ${C_N}^2$ measures the amplitude of the power spectrum, and α is the spectral index. Cordes *et al.* (1988) show, from three years of timing observations on PSR 1937+214, that diffractive scintillation parameters (time scale and bandwidth) scale with frequency in a manner consistent with a Kolmogorov turbulent spectrum. A Kolmogorov spectrum in the one-dimensional case corresponds to a power spectrum with $\alpha = 8/3$.

As a function of position along the screen, the phase can be directly related to the changing electron column density (dispersion measure) fluctuations as follows:

$$\phi(x) = -\lambda r_e \int_0^{\Delta z} dz' \delta n_e(x) = -8.4 \times 10^5 \lambda \Delta DM, \tag{2}$$

where r_e is the classical electron radius, λ is the observing wavelength in cm, $\delta n_e(x)$ is the amplitude of the electron density fluctuations, Δz is the screen thickness, and ΔDM is the dispersion measure fluctuation in pc cm^{-3}. The refraction angle produced by the screen is proportional to the derivative of the phase across the screen:

$$\theta_r(x) = k^{-1} \frac{\partial \phi(x)}{\partial x}, \tag{3}$$

where k is the wavenumber.

The phase screen $\phi(x)$ produces three major time delay terms that can be observed in pulsar timing analysis. The dispersion measure delay is proportional to the phase divided by the frequency, $\sim \phi(x)/\omega$. The geometrical delay, $\sim D{\theta_r}^2/2c$ depends on the increased path-length a wave travels

H. Ögelman and E. P. J. van den Heuvel (eds.), Timing Neutron Stars, 125–129.

after refractive bending. Finally, the angle-of-arrival fluctuations introduce errors in estimating the times of arrival at the solar system barycenter, manifested as an additional refractive delay term. This ISS barycentric correction error for a source in the ecliptic plane is $\sim (AU\theta_r/c)\cos\Omega t$, where Ω is the orbital frequency of the earth around the sun. In the simple single cloud model these three delays scale as λ^2, λ^4, and λ^2 respectively. For the case of a Kolmogorov power spectrum these delays scale as λ^2, $\lambda^{49/15}$, and $\lambda^{49/30}$.

TABLE I

Time of Arrival Variations

Term	Single cloud	Kolmogorov spectrum	PSR 1937 @ 1 GHz (τ in months)
DM variation	λ^2	λ^2	$0.4\,\tau^{5/6}\ \mu s$ ($\tau_{sat} \approx 10^4$ yr)
Geometric time delay	λ^4	$\lambda^{49/15}$	$0.1\,\tau\ \mu s$ ($\tau_{sat} \approx 2.3$ months)
ISS 'barycentric error'	λ^2	$\lambda^{49/30}$	$0.2\,\tau\cos(\Omega t)\ \mu s$ ($\tau_{sat} \approx 1.9$ months)

Other frequency dependent delays that contribute at the sub-microsecond level, including variability of the diffraction smearing time, imperfect polarization calibration, and pulse phase jitter. These additional delays have been explicitly neglected in this simulation, but are effectively included in the white noise background. Table I lists the various delay terms, the wavelength dependence of each term, and the amplitude of the term scaled for PSR 1937+21 at an observing frequency of 1 GHz. These terms scale with time τ up to a saturation scale. Different phase screens have been used in the simulations, but most of the work was done using a standard Kolmogorov power-law screen.

2. MODEL

The simulation model is based on a spherical wave radiating from a pulsar at distance D. A one-dimensional phase screen is generated by multiplying a white noise spectrum by a power law and taking its Fourier transform. The phase screen is then normalized to produce the appropriate dispersion measure variation for a given scintillation bandwidth at 1 GHz. The screen propagates perpendicular to the observer at a velocity V_{scr} and distance $D/2$. The screen has explicitly mapped structure covering scales from $\sim 10^{12}$ cm to $\sim 10^{16}$ cm. Length scales between 10^9 cm to 10^{12} cm are reached by scaling laws. The 10^{16} cm outer scale is arbitrary, and equals the size of the computed phase screen. Each point on the phase screen maps to a unique point on the ground using a ray-optics code. The mapping from the ground back to the screen may be multi-valued, however. Every point on the ground has an accumulated intensity and average angle-of-arrival.

The resulting data scale with frequency according to the observational input parameters, the power spectrum slope, and the assumed scintillation bandwidth. The arrival times of the wavefronts are adjusted to topocentric arrival times from barycentric arrival times assuming a circular earth orbit. After fitting the data for standard pulsar spin parameters (P, $\dot{P}$, $\ddot{P}$), proper motion and

distance, residuals are output for further analysis. The assumed parameters for the PSR 1937+21 system used in the simulation are given by Rawley *et al.* (1987, 1988). The timing accuracy was (optimistically) assumed to be $\sim$ 100 nanoseconds for most runs. Table II list the scaling of the various terms used in the simulation.

TABLE II

Scaling Laws Used in Code

Term		Scaling Relationship	Description
Scintillation Bandwidth	$\Delta\nu$	$\nu^{2(\alpha+1)/(\alpha-1)}$	set to $\sim$ 3 x 10^5 Hz for PSR 1937+21 @ 1 GHz
Diffraction angle	θ_d	$2(c/\pi D\Delta\nu)^{1/2}$	using spherical wave geometry
Fresnel Scale	R_f	$(\lambda D/4\pi)^{1/2}$	assuming a 1-D screen at distance D/2
Diffraction scale	b_d	$1/k\theta_d$	
Refraction scale	l_r	R_f^2/b_d	
Multi-path scale	R_{mp}	$D\theta_d/2$	where D/2 is the screen distance
Bin size	b	V_{scr}	bin size is in units of screen velocity times seconds per day
rms phase amplitude	ϕ_{rms}	$(b/b_d)^{(\alpha-1)/2}$	root-mean-square phase fluctuations used to normalize screen

3. RESULTS

Assuming a Kolmogorov power law spectrum for the electron turbulence and an observing frequency of 1 GHz, a four-year simulation for one particular phase screen produces ISS barycentric correction errors of $\sim$ 0.5 μs, geometrical delays of $\sim$ 0.3 μs, and dispersion measure delays of about 4 μs. These terms plus the final fits are shown in figure 1. Simulations at lower frequencies yield results that scale according to the wavelength dependences given above and in Foster and Cordes (1988). Looking at the best-fit residual data, the derived proper motion is determined to better than 50 percent of the true value, while the distance estimate has no statistical significance.

Comparison of the simulated data and the observed data from PSR 1937+214 (Cordes *et al.* 1988) has not been completed. Assuming that the electron density power spectrum really does obey a Kolmogorov power law then it may be possible to remove the effects of a phase screen by fitting

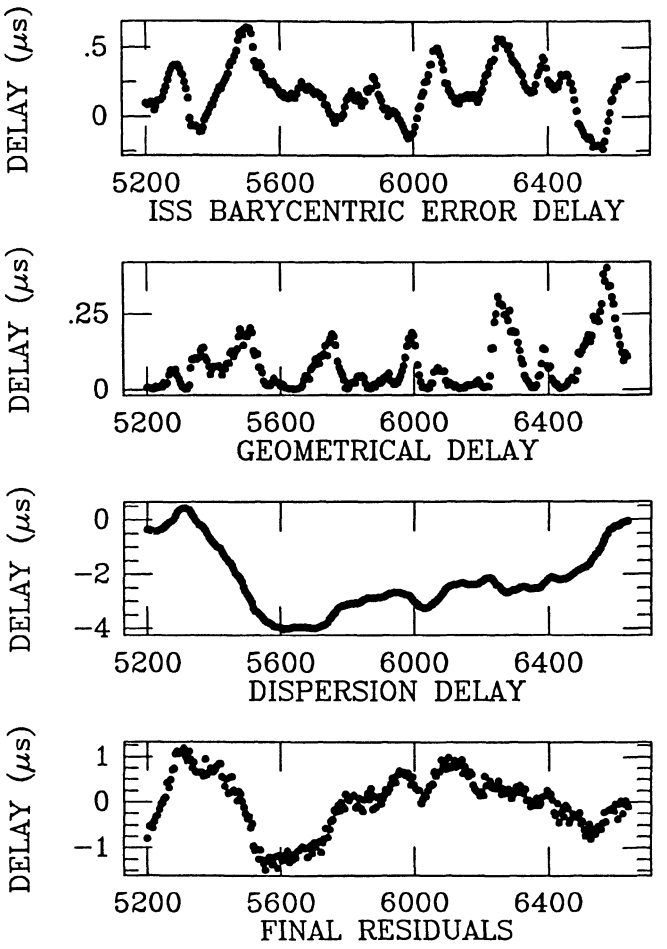

FIGURE 1

1 GHz

Simulated timing residuals at 1 GHz as a function of observation date. Panels show the ISS barycentric correction term, geometrical delay, dispersion delay, and post-fit residuals.

multi-frequency data to the appropriate frequency dependent functions. Clearly, if high precision timing is the primary goal then higher frequency observations reduce the dependence on removing the effects of a phase screen. Lower frequency observations though, can be utilized to probe the electron column density turbulent spectrum. With the appropriate measurements, removal of the dispersion measure and refractive delays may be performed. The ultimate precision of delay removal is uncertain, as it depends on the form of electron density variations for scales much larger than those probed with scintillation observations. Although pulsar scintillations show consistency with a Kolmogorov spectrum, ample evidence exists (Fiedler *et al.* 1987; Cordes and Wolszczan 1986) that discrete electron density clumps exist that are probably distinct from any Kolmogorov process. Removal of the effects caused by clumps will require observations at several to many frequencies.

4. CONCLUSIONS

Dispersion measure and geometrical delay terms cannot be separated by single frequency observations. Multiple frequency observations could help separate the various frequency dependent terms. The ISS barycentric correction term is not separable from the dispersion measure fluctuations because they both scale as $\sim \lambda^2$. At observing frequencies near 1 GHz, dispersion measure and ISS barycentric correction errors dominate for a Kolmogorov spectrum and four years of simulated data. Near 500 MHz the geometrical term becomes more important.

High precision timing data require very frequent regular sampling over intervals much less than the refraction time scale. A good distance estimate from the parallax term requires sampling at intervals of less than one month. Angle-of-arrival and dispersion measure fluctuations may be evident on time scales of days. Long-term high precision timing of multiple pulsars along different lines of sight can place constraints on the likelihood of observing extreme scattering events of the kind reported by Fiedler *et al.* (1987). Well sampled data also place constraints on the electron density spectrum that exists in the interstellar medium.

The authors gratefully acknowledge helpful discussions with R. Romani and D. Backer. Particular mention is given to D. Backer for his suggestion to consider the ISS barycentric correction error effect on pulsar timing.

References

Armstrong, J. W. 1984, *Nature*, **307**, 527.

Blandford, R. D., Narayan, R., and Romani, R. 1984, *J. Astr. Ap.*, **5**, 369.

Cordes, J. M. and Wolszczan 1986 *Ap. J. Letters*, **307**, L27.

Cordes, J. M., Pidwerbetsky, A., and Lovelace, R. V. E. 1986 *Ap. J.*, **310**, 737.

Cordes, J. M., Wolszczan, A., Dewey, R. J., Blaskiewicz, M., and Stinebring, D. R. 1988 in preparation.

Fiedler, R., Dennison, B., Johnston, K., Hewish, A. 1987 *Nature*, **326**, 675.

Foster, R. S. and Cordes, J. M. 1988 *American Institute of Physics Proceedings on Radio Wave Scattering in the Interstellar Medium*, to be published.

Rawley, L. A., Taylor, J. H., Davis, M. M., and Allan, D. W. 1987, *Science*, **238**, 761.

Rawley, L. A., Taylor, J. H., Davis, M. M. 1988, *Ap. J.*, **326**, 947.

II. OBSERVING NEUTRON STARS: RADIO - X-RAYS - GAMMA-RAYS

THE RADIO EMISSION FROM PULSARS

F. Graham Smith
University of Manchester
Nuffield Radio Astronomy Laboratories
Jodrell Bank
Macclesfield
Cheshire SK11 9DL, UK

The location and the geometry of the radio emission from pulsars follow a simple pattern: the excitation and mechanism of the radiation are complex and less easily understood. The simple geometry may even be obscured behind the mass of detail imposed by the variety and variability of the observed characteristics of the radiation.

1. GEOMETRY

I start with the simplest model, in which the radio emission originates in limited regions over the polar caps, forming two opposite radial beams.

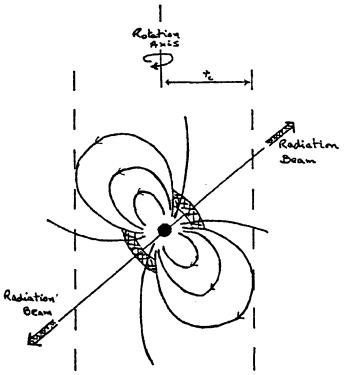

Figure 1. The magnetic field structure of a pulsar, showing the two radio emitting regions. The light cylinder radius $r_c = c\omega^{-1}$, where ω is the angular velocity.

Depending on the position of the observer, one or both of these beams may cross his line of sight to the pulsar; the width and shape of the pulse then depend on the angular width of the emitted beam and on the way in which the beam crosses the line of sight.

H. Ögelman and E. P. J. van den Heuvel (eds.), Timing Neutron Stars, 133–141.

The two youngest pulsars, Crab and Vela, conform to this model but radiate in addition another double beam from optical to gamma-ray energies. The Crab Pulsar also radiates in the radio spectrum in these high photon energy beams: its typical radio emission, analogous to that of all other radio pulsars, is only in its so-called precursor pulse. The high photon energy beams are radiated from further out in the co-rotating magnetosphere, from locations defined by the edges of the polar caps but about nine-tenths of the radial distance to the velocity-of-light cylinder (Smith et al. 1988).

Although the pulses from a typical pulsar are very variable, the integrated profiles constructed by superposing some hundreds of pulses are stable. They vary greatly in shape and width, but could be characterised by a small number of simple components each of order 2^{o} wide spread over about 10^{o} of rotation. These individual components

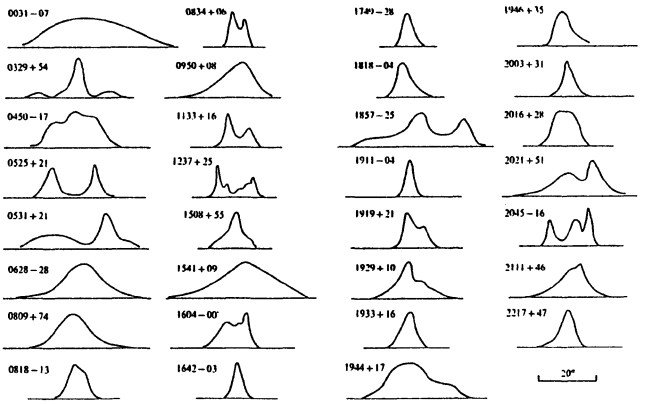

Figure 2. Integrated profiles of thirty-one pulsars, on a single scale of rotational longitude. (Jodrell Bank; 408 MHz)

originate in discrete regions within the polar cap, indicating that there is a stable pattern of excitation which varies across the cap.

The integrated profile of most pulsars is recognisably similar over a wide range of radio frequencies, often showing the same pattern of discrete components. The overall width, however, is frequency dependent, especially below 1 GHz, where the width varies as $\nu^{-\frac{1}{4}}$. This frequency dependence is simply interpreted as lower radio frequencies originating from larger radial distances.

Some integrated profiles are very wide: these correspond to close alignments between the magnetic polar axis, the rotation axis and the line of sight. For PSR 0826-34 the beam remains within the line of sight for almost the complete pulse period, while for PSR 0950+08 the beam occupies about half the period. In the latter case, the radiation is seen to be concentrated at the outer edges of the beam, and one edge is stronger than the other.

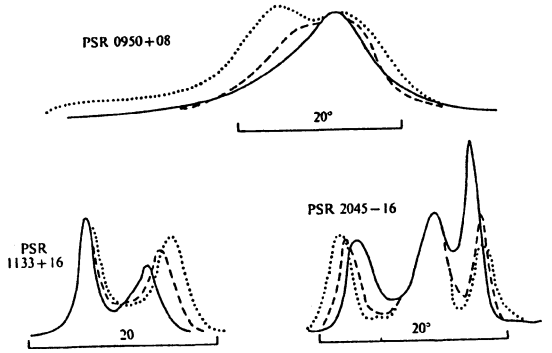

Figure 3. Profiles at three frequencies: ——, 610 MHz; ----. 240 MHz; ····, 150 MHz. (After Lyne, Smith & Graham, 1971).

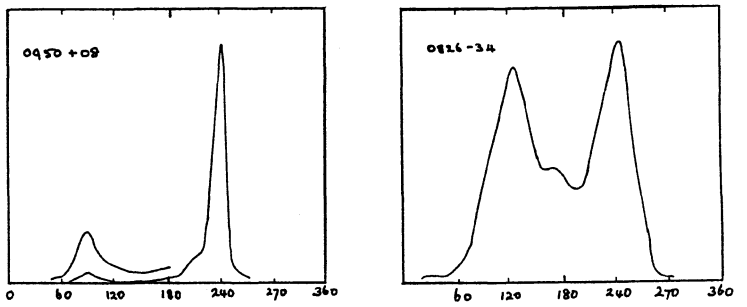

Figure 4. Integrated profiles of two pulsars with wide profiles

Some integrated profiles are doubles in which the two pulses correspond to the two poles: here the polar axis is perpendicular to the rotation axis, and the observer is close to the equatorial plane.

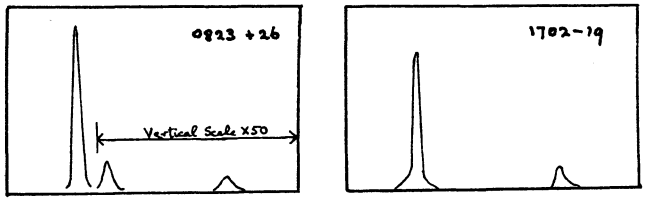

Figure 5. Integrated profiles of two pulsars with interpulses

These geometrical effects combine with the inherent variety of excitation across the polar cap to produce a chaotic range of integrated pulse shape and width. The chaos has been reduced to order by Rankin (1983) and by Lyne and Manchester (1988). The key is the recognition of partial profiles, in which part of the polar cap is not observed: these are recognised by the pattern of linear polarisation, and their proper width can then be deduced. Lyne and Manchester show that this width depends on the orientations of the polar and rotation axes. The bipolar pulsars give the minimum observed width; other orientations give wider widths.

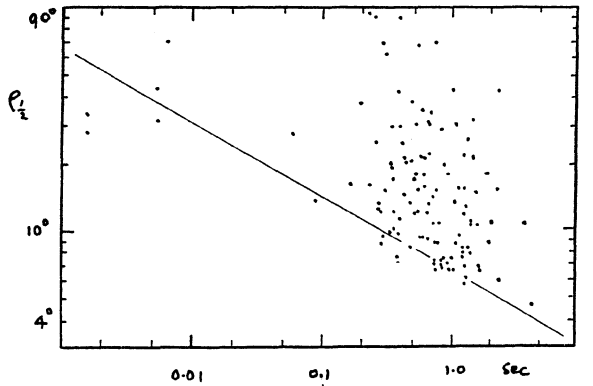

Figure 6. Corrected angular beamwidths (shown as the angular half-width $\rho_{\frac{1}{2}}$) as a function of period P.

The minimum deduced widths $\rho_{\frac{1}{2}}$, as shown in Fig.6 as angular half-widths for 408 MHz, follow a simple law:

$$\rho_{\frac{1}{2}} = 6.5^{\circ}\ P_{\text{sec}}^{-1/3}$$

The larger values correspond to different orientations. Their distribution enabled Lyne and Manchester to point out a weak tendency towards alignment of the magnetic and rotation axes in older pulsars.

2. EXCITATION AND THE RADIATION MECHANISM

We have already seen that the polar cap is not a uniform source of radiation. The discrete components of a typical profile originate in discrete locations, which seem to be randomly distributed over the polar cap. These components may switch on and off, giving the phenomonon of moding.

Moding occurs simultaneously at all radio frequencies: it is regarded as a change in excitation which follows along a connecting magnetic field line. An extreme form of moding is nulling, in which all components switch off simultaneously. Modes and nulls may persist for any time from a single pulsar period up to several hours.

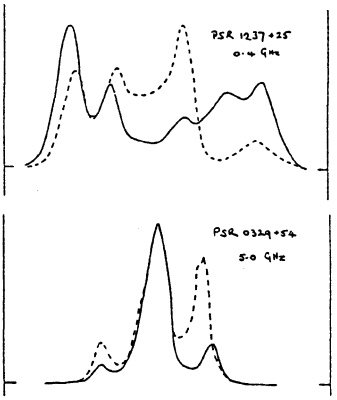

Figure 7. Two different modes for the pulsars PSR 1237+25 and PSR 0329+54

The polarisation in the integrated profile follows a simple typical pattern, showing none of the complicated components of the intensity profile itself.

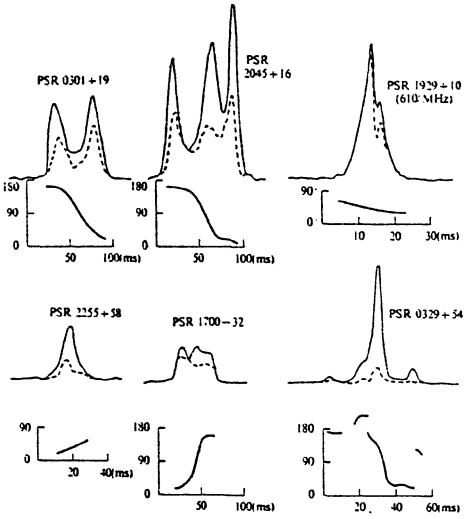

Figure 8. Polarisation in integration profiles of six pulsars. The broken line represents the linearly polarised component, and the graphs below the profiles show the position angle. (Jodrell Bank recordings at 408 MHz and 610 MHz).

The linear component shows the typical S-shaped sweep, covering up to 180°. The total swept range, and the rate of sweep, provide the

essential beam geometry as investigated by Lyne and Manchester. A circularly polarised component is often observed in integrated profiles when the line of sight cuts close to the centre of the polar cap: typically a simple switch is observed between the two hands of circular. The linear polarisation is often very high, approaching 100%. The circular polarisation reaches 50% in the bipolar pulsar PSR 1720-19; surprisingly it has the same hand for the two opposite poles.

3. INDIVIDUAL PULSES

The repeatability of the integrated profiles is in contrast to the variability of the individual pulses.

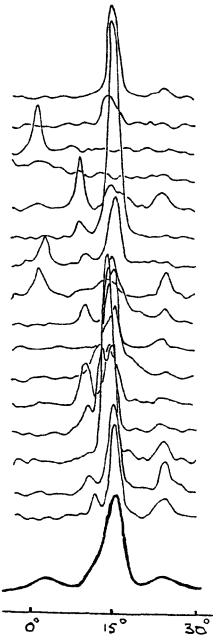

Figure 9. A sequence of individual pulses of PSR 0329+54, and the integrated profile

This variability is at least partly attributable to change in excitation affecting a wide range of radio frequencies simultaneously. Some individual pulses have a very fine structure, known as micro-structure; This is often quasi-periodic, repeating at intervals of order 1 millisecond. Microstructure is also seen simultaneously over a considerable range of frequencies, and is therefore regarded as a variation in excitation common to a particular field line.

Individual pulses are commonly very highly polarised, occasionally practically 100% polarised.

An organised pulse-to-pulse variation which is observed mainly in older pulsars is the phenomenon of drifting.

Here an identifiable pulse component is seen in successive pulses at a progresively earlier or later pulse phase. Again, this is regarded

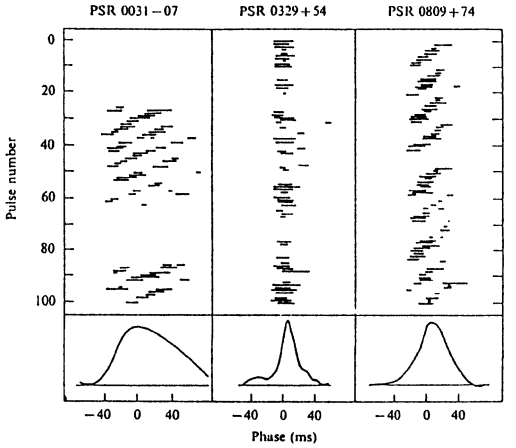

Figure 10. Drifting and nulling. Each horizontal line is centred on the expected arrival time, with time increasing downwards and to the right. The positions of each sub-pulse are shown. PSR 0031-07 and PSR 0809+74 are typical negative drifters. PSR 0031-07 shows large null periods, missing about twenty pulses. (After Taylor & Huguenin, 1971).

as a variation in excitation. Activity of some kind circulates around the magnetic pole. Two or more excited regions can be seen as they move into and cross the observable region of the polar cap.

Drifting and nulling are interconnected. When pulses restart after a short null, the drifting has apparently continued through the nulling interval, but at a modified rate.

4. INTENSITY AND SPECTRUM

The overall radio spectrum is very steep. It is well fitted by a power law, with a change of index in the region of 1 GHz and often with a low frequency cut-off. The centre of the polar cap has a steeper spectrum than the outer regions.

The intensity is very high, corresponding to impossibly high brightness temperatures. Both the high intensity and the narrow bandwidth of radiation from a particular location indicate that the radiation is coherent.

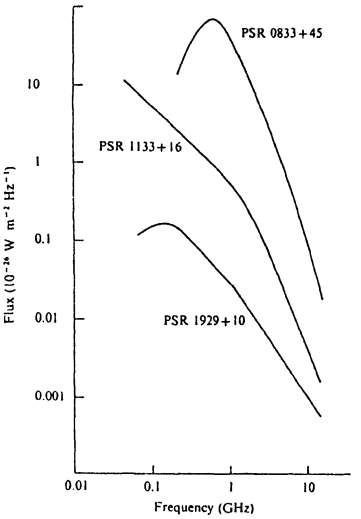

Figure 11. Typical radio frequency spectra of pulsars. The spectra are generally curved, and often show a low frequency cut-off.

5. INTERPRETATION

The geometry of the emitting regions is determined by the polar magnetic field, and the emission is directed along the field lines. If we locate the edges of the integrated profile on the limiting field lines, i.e. those lines which just close on the velocity of light cylinder, we can find the height of emission from simple geometry. If the limiting field line is inclined to the magnetic axis by angle δ_a as it crosses the surface at radius a, its inclination δ at radius r is given by

$$\frac{\sin\delta^2}{\sin\delta_a} = \frac{r}{a}$$

Since $\delta_a = \left(\frac{\Omega a}{c}\right)^{\frac{1}{2}}$ where Ω is angular velocity, for a pulsar with a=15 km we have an angular beam width for a source on the surface

$$2\,\delta_a = 2^o\, P_{sec}^{-\frac{1}{2}}$$

The observed beamwidth at 408 MHz is $13^o\, P_{sec}^{-1/3}$. We deduce that the source is at radius r ≈ 40 a for a pulsar with P = 1 sec, and at radius r ≈ 20 a for P = 10 millisec. At other frequencies these heights vary as $\nu^{-\frac{1}{2}}$

This height probably does not scale exactly down to the shortest periods, where it would place the radio source far out in the magnetosphere beyond the velocity of light cylinder. In these pulsars we may have to take account of relativistic beaming.

The radiation frequency is associated with radius; the beamwidth and polarisation are determined by the magnetic field lines. It is reasonable to associate the radio frequency with magnetic field strength. The gyro frequency for electrons with relativistic factor Γ is

$$\omega = \frac{eH}{\Gamma mc}$$

At r = 40a, H ≈ 10^7 gauss. Hence we need $\Gamma \sim 10^2$ to 10^3, which is reasonable. The radius-to-frequency mapping needs $\Gamma \propto r^{-1}$.

Coherence probably falls with decreasing wavelength, giving the steep spectrum. We therefore expect the enhancement in brightness temperature to be due to particle concentrations within linear distances of the order of one wavelength, i.e. in bunches of order one metre in size.

The radiation mechanism is presumably similar to gyro radiation, in a stream moving towards the observer along the curved field lines. It is boosted by coherence which varies across the source and which may differ for different polarisations. A warning against simple models is provided by the common phenomenon of orthogonal polarization, in which the position angle switches by about 90° either within a pulse or randomly in successive pulses. As with other switching phenomena it seems that this is to be associated with changes in excitation rather than with propagation conditions outside the source.

Nulling itself does not mean that a stream of particles has been cut off. Fillipenko and Radhakrishnan (1982) suggest that the stream may continue, but without the bunching that is essential for radio emission.

6. CONCLUSION

We now understand the geometry of the radio emission, but not very much of the physical processes of excitation and radiation.

REFERENCES

Fillipenko, A.V. & Radhakrishnan, 1982. Astrophys.J. 263, 828
Lyne, A.G. & Manchester, R.N., 1988. Mon.Not.R.astr.Soc. in press
Rankin, J.M., 1983. Astrophys.J. 275, 333.
Smith, F.G. et al., 1988. to be published
Taylor, J.H. & Huguenin, G.R., 1971. Astrophys.J. 167, 273
Lyne, A.G., Smith, F.G. & Graham, D.A., 1971. Mon.Not.R.astr.Soc. 153, 337.

A Timing Analysis of the Clifton and Lyne Pulsars

Jonathan McKenna
University of Manchester
Nuffield Radio Astronomy Laboratories
Jodrell Bank
Macclesfield , Cheshire, SK11 9DL U.K.

ABSTRACT. Utilising standard procedures, timing studies of the 40 pulsars discovered in the Jodrell Bank 1400MHz Survey have been undertaken. The results include the first measurement of the pulsars' period derivatives which then permit a determination of their characteristic ages. On average, the pulsars are about one order of magnitude younger than the rest of the known pulsar population. Despite this, none of them, with the possible exception of PSR 1822-14, is associated with a known supernova remnant. Although confirming that previous searches missed some younger, faster pulsars, the results presented here do not preclude the possibility that pulsars are "injected" into the population with a period of about 0.5s (Narayan,1987). Finally, "glitches" have been observed in two of the pulsars. That seen in 1823-13 has $\Delta P/P \simeq -2.5 \times 10^{-6}$ making it one of the largest glitches yet seen. The glitch in 1737-30 has $\Delta P/P = -4.2 \times 10^{-7}$ and $\Delta \dot{P}/\dot{P} = 2.6 \times 10^{-3}$.

1. INTRODUCTION

In this paper, I intend to show how the timing of radio pulsars can impinge upon many areas of neutron star astronomy. In particular, we shall see that timing studies can reveal about the birth, evolution and interior of neutron stars.

First, however, it might be appropriate to make a few general remarks about pulsar timing as done at Jodrell Bank. The techniques employed to collect, reduce and analyse data are very similar to those used by other groups (Backer, 1989; Taylor, 1989). One possibly important difference is the use at Jodrell of the JPL planetary ephemeris (Standish 1982), as opposed to the MIT ephemeris more commonly used. Tests are, however, currently underway to ensure that no major discrepancies exist in results obtained from the different pulsar timing programs.

In total, about 130 pulsars are observed regularly at Jodrell Bank. This means that for each pulsar two or three observations separated by a few days are made about every three months. Timing is undertaken primarily at 408 MHz, 610 MHz, 1420 MHz and 1667 MHz and we have the use of four fully-steerable telescopes. One of these, the 12.5m dish,

H. Ögelman and E. P. J. van den Heuvel (eds.), Timing Neutron Stars, 143–152.

follows the Crab pulsar for as long as it is above the horizon.

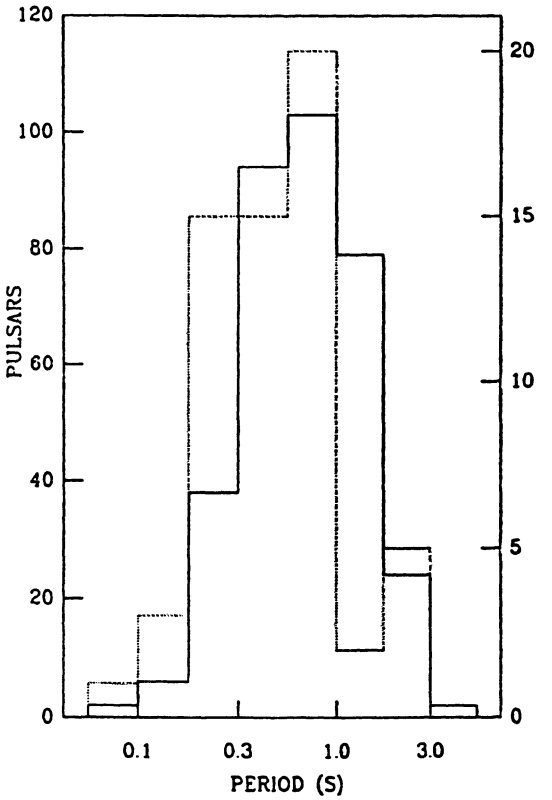

Figure 1. A histogram showing the distribution of periods for (a) all pulsars discovered in previous major surveys (solid line and left-hand scale) and (b) the Clifton and Lyne pulsars (dotted line and right-hand scale).

2. THE JODRELL BANK 1400 MHz SURVEY

The particular sample of pulsars under consideration here were discovered in the Jodrell Bank 1400 MHz Survey of 1983/4 (Clifton,1985; Clifton and Lyne, 1986; Clifton et al, 1987). Essentially, this survey was an attempt to find young, fast, Crab-like pulsars by mitigating certain selection effects which had biased previous surveys against such objects. The main features employed to this end were a high observing frequency, 1400 MHz, and a high sampling rate of 500 Hz. The concomitant reductions in pulse broadening due to scintillation, dispersion and sampling were calculated to allow increased sensitivity towards shorter period pulsars. The high observing frequency also

reduced the relative strength of the galactic background, thus permitting a low galactic latitude search for young pulsars.

The survey found forty new pulsars, thirty of which, it is estimated, would not have been detected in previous surveys. Figure 1 shows that the survey was successful in finding faster pulsars; it is clear that the average period of these pulsars is somewhat shorter than that of the rest of the known population. To ascertain whether or not the Clifton and Lyne pulsars (as these objects are widely known) are young pulsars requires a knowledge of their period derivatives. These only became available after timing observations were made over a number of months.

3. THE TIMING ANALYSIS

The observations of the pulsars were carried out between August 1985 and January 1988 during which time an average of 30 separate observations were obtained for each pulsar. The standard methods of data analysis (Manchester and Taylor, 1977 ; Backer and Hellings,1985) were used to solve for six parameters - period, period derivative, dispersion measure, position and epoch. In most cases, this was the first determination of the pulsar's period derivative. Unique fits were obtained for 34 of the 40 pulsars and the results are given in Tables I and II.

4. THE IMPLICATIONS OF PERIOD DERIVATIVE

The determination of a pulsar's period derivative allows us to estimate both its magnetic field and its age.

4.1. Magnetic Field

An approximation to a pulsar's magnetic field strength can be made if we assume the pulsar to be an oblique rotator (Pacini, 1967). It can then be shown that the surface magnetic dipole strength, B, is given by

$$B \simeq 3.2 \times 10^{19} (P\dot{P})^{\frac{1}{2}} \qquad (1)$$

where B is measured in gauss, P in seconds and $\dot{P}$ in ss^{-1}. Thus the magnetic fields of the Clifton and Lyne pulsars are shown in Table I. Note that PSR1737-30 has the second highest field in the known pulsar population.

4.2. Characteristic Age

A pulsar's "characteristic age", τ_c, is defined as,

$$\tau_c = \frac{P}{2\dot{P}} \qquad (2)$$

TABLE I

Periods , period derivatives , characteristic ages and magnetic fields of the Clifton and Lyne pulsars

PSR	PER seconds	PDOT E-15 ss	AGE E+03 yr	B E+12 g
1735-32	.76849876730(3)	0.800(3)	15000	0.79
1736-29	.32288076515(1)	7.851(1)	650	1.6
1736-31	.52943755808(1)	18.406(3)	460	3.2
*1737-30	.60657976231(4)	466.31(3)	21	17
1750-24	.5283332229(1)	14.07(1)	590	2.8
1753-24	.67047989826(2)	0.284(1)	37000	0.44
1800-21	.133588492866(1)	134.0951(3)	16	4.3
1804-20	.9184064710(1)	17.09(1)	850	4.0
1806-21	.70241276657(2)	3.819(2)	2900	1.7
1809-173	1.20536193373(4)	19.118(4)	1000	4.9
1809-175	.538340252(1)	1.5(1)	5700	0.91
1813-17	.782326(4)			
1815-14	.29148820999(1)	2.035(1)	2300	0.78
1817-13	.9214587178(1)	4.502(3)	3200	2.1
1819-14	.21477093439(3)	0.45(2)	7600	0.31
1820-11	.279822(6)			
1821-11	.43575827169(2)	3.576(2)	1900	1.3
1822-14	.27918201531(1)	22.6781(3)	200	2.5
1823-11	2.0931352637(3)	4.89(3)	6800	3.6
1823-13	.101440656830(3)	75.217(1)	21	2.8
1824-09	.2457569048(1)	1.48(1)	2600	0.61
1828-10	.40502972520(3)	60.035(2)	110	5.0
1829-10	.330354(4)			
1829-08	.64727924004(1)	63.8912(2)	160	6.5
1830-08	.085281651607(1)	9.1618(1)	150	0.89
1832-06	.30583(1)			
1834-04	.35423614431(4)	1.79(2)	3100	0.81
1834-06	1.9058085410(4)	0.79(3)	38000	1.2
1838-04	.186145156242(1)	6.3877(1)	460	1.1
1839-04	1.8399442066(1)	.50(1)	58000	0.97
1841-04	.99102572826(4)	3.918(3)	4000	2.0
1841-05	.255697129412(4)	9.7016(4)	420	1.6
1842-02	.5077185070(3)	15.11(3)	530	2.8
1842-04	.1622506			
1849+00	2.1802			
1855+02	.41581416756(1)	40.2849(3)	160	4.1
1859+07	.64399810043(4)	1.578(4)	6500	1.0
1903+07	.6480389969(1)	4.94(1)	2100	1.8
1904+06	.267274526144(3)	2.1356(1)	2000	0.76
2000+32	.69673832884(3)	104.792(3)	110	8.6

Notes.(1) Periods quoted are for MJD 47000 except for PSR 1737-30 (*) where epoch is MJD 47075 .
(2) The formal error in the last quoted figure is given in brackets .

TABLE II

Positions and dispersion measures
of the Clifton and Lyne pulsars

PSR	RA h m s	DEC ° ′ ″	DM $cm^{-3}pc$
1735-32	17'35'38.65(2)	-32'10'11(1)	52(3)
1736-29	17'36'23.57(1)	-29'01'48(1)	136(1)
1736-31	17'36'09.76(1)	-31'29'39(1)	601(2)
1737-30	17'37'21.27(1)	-30'14'27(1)	152.3(1)
1750-24	17'50'26.2(1)	-24'56'46(30)	657(6)
1753-24	17'53'53.54(1)	-24'35'29(8)	365(2)
1800-21	18'00'51.137(4)	-21'37'15(3)	234.2(3)
1804-20	18'05'07.0(1)	-20'58'30(14)	608(8)
1806-21	18'06'14.70(1)	-21'09'35(4)	379(2)
1809-173	18'09'12.64(2)	-17'19'16(2)	252(2)
1809-175	18'09'38(1)	-17:30(6)	630(20)
1813-17	18'13'04(26)	-17:30(6)	490(30)
1815-14	18'15'32.9(1)	-14'23'51(6)	626(2)
1817-13	18'17'29.7(1)	-13'47'38(4)	784(5)
1819-14	18'20'05.6(1)	-14'01'51(7)	605(3)
1820-11	18'20'37(24)	-11'12(6)	430(50)
1821-11	18'21'42.47(2)	-11'20'25(1)	597(3)
1822-14	18'22'11.64(1)	-14'48'36(1)	349(3)
1823-11	18'23'18.1(1)	-11'33'30(3)	327(11)
1823-13	18'23'23.312	-13'36'34.77	230(1)
1824-09	18'24'24.5(1)	-09'58'10(5)	442(7)
1828-10	18'28'01.20(3)	-11'01'27(2)	170(5)
1829-10	18'29'28(24)	-10'26(6)	440(40)
1829-08	18'29'53.416(4)	-08'29'20.2(2)	300(1)
1830-08	18'30'56.696(3)	-08'29'51.2(2)	411.2(5)
1832-06	18'32'32(24)	-06'46(6)	'10(40)
1834-04	18'34'12.3(1)	-04'38'59(3)	7(2)
1834-06	18'34'33.0(1)	-06'55'41(4)	3(8)
1838-04	18'38'26.771(2)	-04'28'11.9(1)	327(1)
1839-04	18'39'48.15(3)	-04'02'59(1)	190(7)
1841-04	18'41'54.44(2)	-04'36'20(1)	127(3)
1841-05	18'41'24.82(1)	-05'41'38.9(?	416(1)
1842-02	18'42'10.5(1)	-02'47'20(′	372(33)
1842-04	18'42'36(24)	-04'35(6)	280(30)
1849+00	18'49'54.3(1)	00'28'20(	680(60)
1855+02	18'55'12.35(1)	02'08'36.4(3)	506(1)
1859+07	18'59'14.20(3)	07'11'56(1)	261(5)
1903+07	19'03'28.0(1)	07'04'45(1)	295(11)
1904+06	19'04'08.93(1)	06'36'21.2(1)	473(1)
2000+32	20'00'07.07(2)	32'08'53.3(3)	139(2)

Note. The formal error in the last quoted figure is given in parentheses.

Given eqn (1), this is a reasonable approximation to the pulsar's true age if its magnetic field remains constant and if it is born spinning very fast. Calculating these characteristic ages for the Clifton and Lyne pulsars provides the second test of the survey's effectiveness. The results, shown in histogram form in figure 2, indicate that, on average, these pulsars are one order of magnitude younger than the rest of the known population. This then confirms the success of the survey.

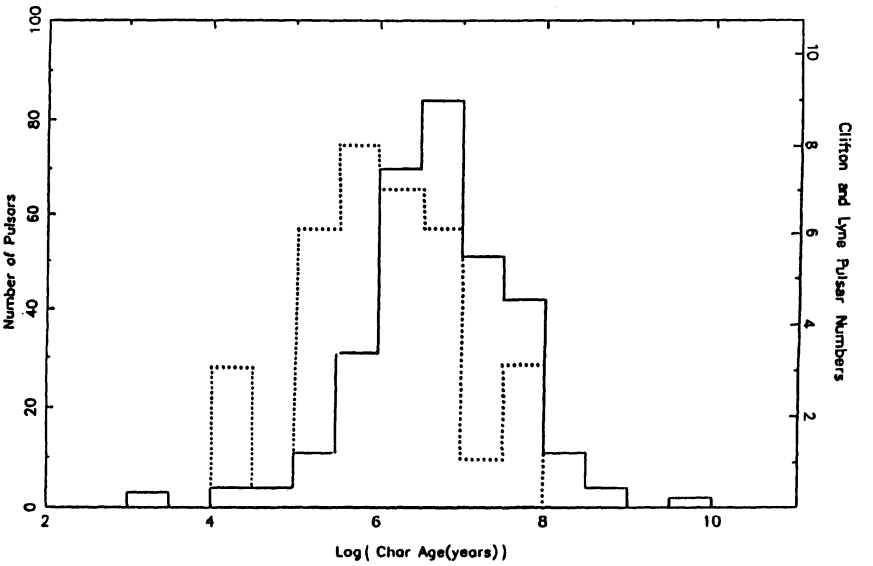

Figure 2. A histogram showing the distribution of characteristic ages for (a) all pulsars discovered in previous major surveys (solid line and left-hand scale) and (b) the Clifton and Lyne pulsars (dotted line and right-hand scale)

5. PULSAR-SUPERNOVA REMNANT ASSOCIATIONS

Of the 40 pulsars, three - 1822-14, 1838-04 and 1904+06 - lie within the boundaries of a known supernova remnant (hereafter SNR). PSRs 1838-04 and 1904+06 have characteristic ages of 0.46 Myr and 2.0 Myr respectively, and since it is unlikely that recognisable SNR morphology would last longer than 0.2 Myr (Caswell and Lerche, 1979), these associations must be considered purely coincidental.

Pulsar 1822-14 lies within an area of complex radio morphology; the object with which it is associated, G16.85-1.05, is an extended HII region seen in front of a strongly polarised remnant (Reich et al.,

1986). With a characteristic age of 0.2 Myr, this pulsar might still have an extent SNR but it is more likely that this is just a chance association. Given the size of G16.85-1.05, two or three of the Clifton and Lyne pulsars might be expected to be positionally coincident with a SNR while not being causally connected. Hence further study is required before any association of PSR 1822-14 with G16.85-1.05 can be corroborated.

Another approach to this problem is to inpsect the eight pulsars with characteristic ages less than 0.2 Myr. Knowing both their dispersion measure (distance) and period derivative (age), we can calculate the transverse velocities they would require to have moved from the centre of the nearest known SNR to their present position. Five of these pulsars - 1737-30, 1800-21, 1823-13, 1828-10 and 1855+02 - would need velocities far in excess of 400 kms^{-1}, the maximum observed pulsar velocity (Lyne, Anderson and Salter, 1982). Consequently, we can be certain these pulsars are not associated with any known SNRs. This is a negative test since the comparative speeds of pulsars and supernova shells suggest that pulsars ought to be found within their SNRs. Hence, although they would not require unrealistic velocities, the other three pulsars - 1829-08, 1830-08 and 2000+32 - are unlikely to be connected with their nearest SNRs. Thus, it would seem improbable that any of the Clifton and Lyne pulsars is associated with a known supernova remnant.

6. THE CASE FOR PULSAR INJECTION

The standard theory of pulsar birth envisages a pulsar with a period of about 10 ms born in a supernova explosion. However, this has been challenged by Vivekanand and Narayan (1981) whose model-independent analysis of 210 pulsars led them to suggest that pulsars are injected into the population with periods as high as 0.5 seconds. This was questioned by Lyne, Manchester and Taylor (1985) who argued that the previous analysis had neglected those selection effects which discriminate against the faster pulsars. They also showed that pulsar statistics could be adequately explained using the accepted model of pulsar birth and the luminosity relation $L \propto B^2$.

As this timing analysis has revealed, many fast, young pulsars have been missed by previous surveys and this seems to confirm the criticism by Lyne et al of injection. However, more recent studies by Narayan (1987) have allowed for the aforesaid selection effects and, using a luminosity model $L \propto \dot{P}^{1/3}/P$, the evidence for injection is said to increase. However, an alternative analysis of pulsar statistics (Stollman 1987), which utilises a slightly different luminosity model, does not require pulsar injection. It would seem then that a resolution of the controversy awaits a definitive luminosity model,

7. PULSAR GLITCHES

These timing studies have revealed that two of the youngest pulsars

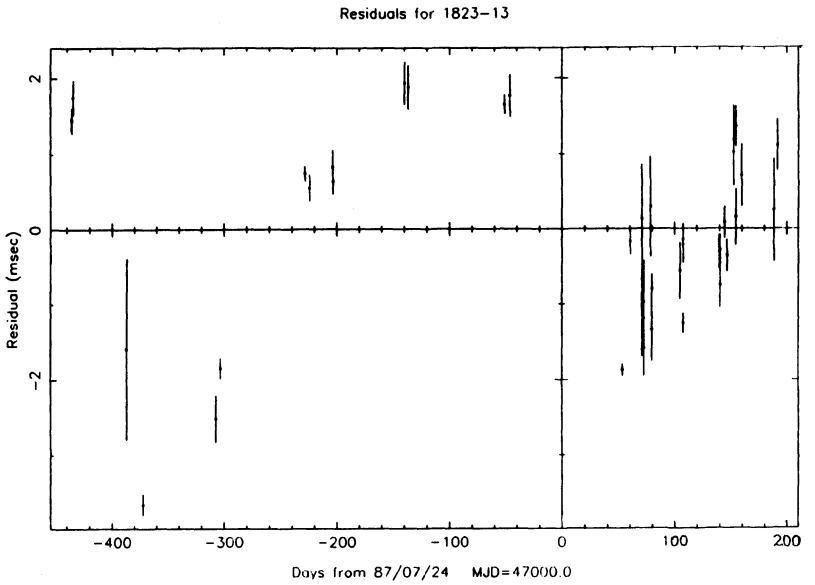

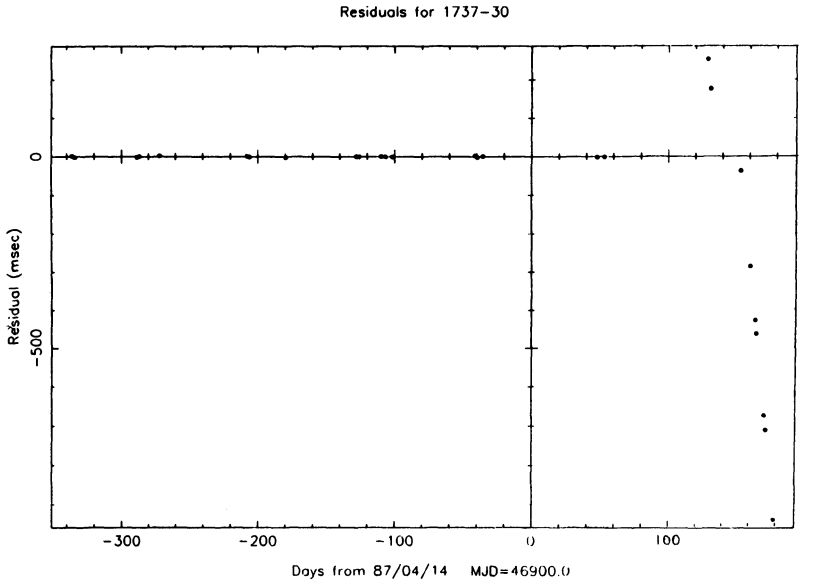

Figure 3a (top). Post-glitch residuals for PSR 1823-13 after fitting for P, $\dot{P}$ and $\ddot{P}$. The apparent quartic variation is due to the underlying exponential recovery from the glitch. Figure 3b(bottom). Residuals before and after the glitch in PSR 1737-30

have recently undergone sudden spin-up events or "glitches". PSR 1823-13 glitched between January 19 1986 and May 14 1986. The fractional change in period was

$$-2.2\times10^{-6} \geq \frac{\Delta P}{P} \geq -2.7\times10^{-6}$$

which makes this one of the largest glitches yet observed. The relative scarcity of pre-glitch data for the pulsar has prevented a precise determination of the fractional change in period derivative but this could be as high as 6%, i.e.,

$$\frac{\Delta\dot{P}}{\dot{P}} \leq 0.06$$

The other pulsar to have glitched is PSR 1737-30. Unfortunately, but not surprisingly, this glitch also occured in a large gap in our data between June 7 1987 and August 21 1987. The glitch parameters in this case were

$$\frac{\Delta P}{P} \simeq -4.2\times10^{-7} \qquad \frac{\Delta\dot{P}}{\dot{P}} \simeq 2.6\times10^{-3}$$

There is some evidence for an exponential recovery from both these glitches. In figure 3a, we see the post-glitch residuals of PSR 1823-13 after a fit has been made for period, period derivative and period second derivative. There is clearly a quartic variation in the residuals almost certainly due to the unfitted fourth-order term in an exponential. Figure 3b shows the timing residuals for PSR 1737-30 and they depict a classical glitch behaviour (see, eg. Lyne 1987). At the time of writing, however, the parameters of the exponential recovery were undetermined, partly as a result of period ambiguities. However, further investigation of the post-glitch data should yield the recovery timescales and so further elucidate the behaviour of neutron stars' superfluid interiors.

8. FUTURE WORK

We have seen how observations taken from August 1985 to January 1988 have led to improved values for the parameters of the Clifton and Lyne pulsars. These results have permitted some investigation of pulsar-supernova remnant associations and the problem of pulsar injection.

The collection of further timing data will allow us to determine the period derivatives of those six pulsars still without good timing solutions. Eventually, a quantitative study of timing noise will also be possible. It is quite likely that more glitches will come to light and the study of these, and the two already seen, will provide further information on the superfluid interior of a neutron star.

9. Acknowledgements

The author would like to thank Dr. A.G. Lyne for his guidance and useful discussions, Dr. A.W. Jones, whose preliminary work was invaluable, and Drs. T.R. Clifton and D. Frail for a number of helpful VLA positicns.

References

Backer, D.C. and Hellings, R.W., 1986. Ann.Rev.Astron.Astrophys. 24, 537
Backer, D.C., 1989. This volume
Caswell,J.L., and Lerche, I.,1979. Mon.Not.R.astr.Soc., 187, 201
Clifton, T.R. 1985. PhD.Thesis, University of Manchester
Clifton,T.R. and Lyne, A.G., 1986. Nature, 320, 43
Clifton, T.R., Jones, A.W. and Lyne,A.G., 1987. 'The Origin and Evolution of Neutron Stars' Proc.IAU Symp.No.125 (eds.D.J. Helfand and J.H.Huang). D.Reidel Publishing Co.
Lyne, A.G.,Anderson,B. and Salter,M.J., 1982. Nature, 301, 503
Lyne, A.G., Manchester,R.N. and Taylor, J.H., 1985 Mon.Not.R.astr.Soc., 213, 613
Lyne, A.G., 1987. Nature, 326, 569
Manchester, R.N. and Taylor, J.H., 1977. 'Pulsars', W.H.Freeman, San Fransisco.
Narayan, R., 1987. Astrophys.J., 319, 162
Pacini,F., 1967. Nature, 304, 421
Standish, E.M., 1982. Astron.Astrophys., 114, 297
Stollman, G.M. 1987 Astron.Astrophys., 178, 143
Taylor, J.H., 1989. This volume
Vivekanand,M. and Narayan,R., 1981. J.Astrophys.Astr., 2, 315

SLOWDOWN RATE AND OSCILLATIONS IN THE CRAB PULSAR

F. Graham Smith
University of Manchester
Nuffield Radio Astronomy Laboratories
Jodrell Bank
Macclesfield, Cheshire SK11 9DL U.K.

Continuous monitoring of arrival times from 1982, as reported by Lyne, Smith and Pritchard (1988), has provided a complete record over more than 5 x 10^9 pulsar rotations. One well-defined glitch occurred on 22 Aug 1986 (Lyne and Pritchard 1987); the total amplitude of the phase deviation was 3 milliseconds, and the overall effect was minor compared with the normal slowdown and with the major oscillation which is discussed in this paper.

We have included data from 1969 to 1987 in an analysis of the pulsar slowdown rate $\dot{\nu}$. Fig.1 shows the almost linear variation of ν, with a small step at the major glitch of 1975 (Gullahorn et al. 1977). Fig.2 shows the same data on an expanded scale after the removal of a single value of $\ddot{\nu}$. A small curvature can now be seen in addition to the 1975 step. This curvature is fitted within 10% by the value of the next derivative, $\dddot{\nu}$, found from the usual power-law spin down. If the timing behaviour is correctly expressed by

$$\dot{\nu} \propto -\nu^n$$

then the index n is found from

$$n = \frac{\nu\,\ddot{\nu}}{\dot{\nu}^2}$$

Our observations give n = 2.509±0.001.

The third derivative is expected to be given by

$$\dddot{\nu} = \frac{n(2n-1)\dot{\nu}^3}{\nu^2} = -0.615 \times 10^{-30}\ s^{-4}.$$

Fig.3 shows the data corrected for this value. No other trends are discernable, and it is concluded that the power-law is a good overall representation of the slowdown.

The data from 1982 onwards provide a phase-connected record which can be used to measure deviations from the smooth slowdown behaviour. These timing residuals are shown in Fig.4. The conspicuous feature is a quasi-sinusoidal oscillation with a period of about 20 months and a peak-to-peak amplitude approaching one complete pulse rotation. It is

H. Ögelman and E. P. J. van den Heuvel (eds.), Timing Neutron Stars, 153–156.

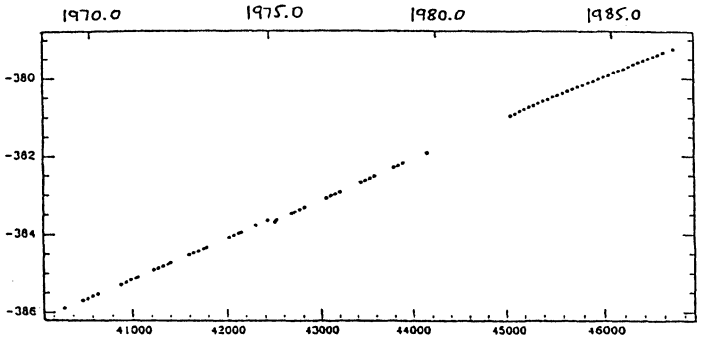

Figure 1

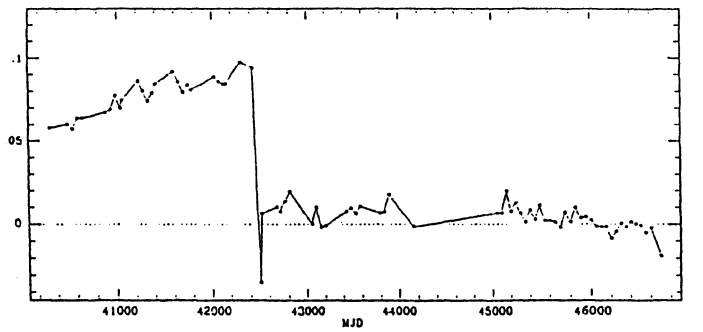

Figure 2

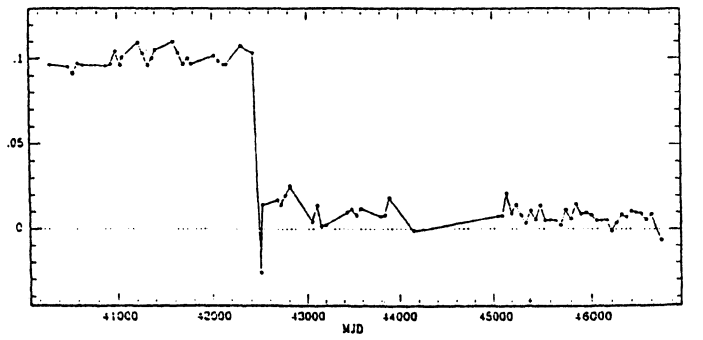

Figure 3

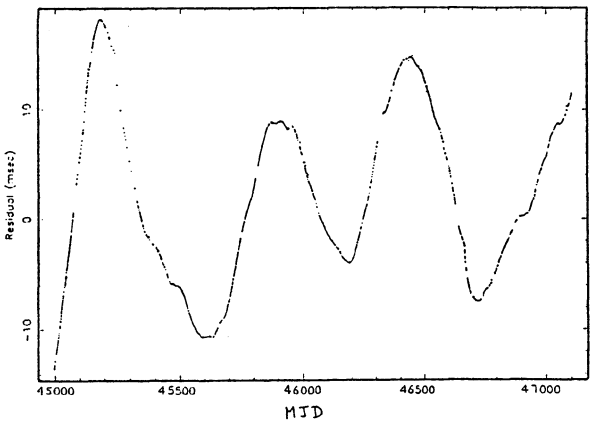

Figure 4. Timing residuals for the Crab Pulsar, showing the quasi-periodic oscillation remaining after removing the first three derivatives of the frequency ν.

a low-Q oscillation, but it is obviously different from the red noise behaviour which has been used to describe shorter data sets. The period and amplitude of the oscillation, as they appear in our analysis, are unrelated to the total length of our data set.

The oscillation may be due to some form of precession, or to an internal oscillation which does not involve a movement of the spin axis. If it is due to precession, it must involve a slow periodic change in the angle between the magnetic dipole and the spin axis, resulting in a modulation of spin-down rate of order 1 part in 10^9.

Internal oscillation may be some form of Tkachenko oscillation of the superfluid vortex lattice (Tkachenko, 1966; Ruderman 1970). The superfluid vortices have an area density proportional to angular velocity, and their lattice structure is maintained by elastic forces as in a crystalline solid. A torsional oscillation of the vortices inside a superfluid sphere with radius 12 km has a period of 20 months, if the vortex density corresponds to a period P=1 second. The oscillation period varies as (vortex density)$^{-\frac{1}{2}}$, i.e. $P^{\frac{1}{2}}$, so that for the Crab Pulsar the observed period is five times too long. Furthermore, only part of the superfluid can be involved, since the core is rigidly attached to the dipole magnetic field.

It may be significant that the amplitude of the oscillation is less than half a rotation of the pulsar, whereas a variation in slowdown due to a change in the angle of the magnetic axis in some form of precession might produce a very much larger or much smaller effect. If the oscillation is internal, it may be appropriate to consider it as an oscillation in the proportion of vortices which are pinned to the crust. This proportion evidently can change, as seen in the 1975 glitch which resulted in a long-term change in slowdown rate; there is as yet no explanation for an oscillatory change in numbers of pinned vortices.

A combination of the two explanations may be appropriate; the period may be that of a precession, and the effects may be due to a consequent reorganisation of the interior vortices.

REFERENCES

Gullahorn, G.E., Isaacman, R., Rankin, J.M. & Payne, R.R., 1977. Astr.J. 82, 309.
Lyne, A.G. & Pritchard, R.S., 1987. Mon.Not.R.astr.Soc., 229, 223.
Lyne, A.G., Smith, F.G. & Pritchard, 1988. Mon.Not.R.astr.Soc. in press.

A SEARCH FOR MILLISECOND PULSARS IN GLOBULAR CLUSTERS

J. D. Biggs, A. G. Lyne and A. Brinklow
University of Manchester
Nuffield Radio Astronomy Laboratories
Jodrell Bank
Macclesfield
Cheshire SK11 9DL, United Kingdom

ABSTRACT. We present details of a search for millisecond pulsars in 24 globular clusters. One new pulsar, PSR 1620–26, has been detected in a wide binary system in the core of the globular cluster M4. Upper limits to pulsed emission are given for the other 23 globular clusters. A future software enhancement should considerably improve the sensitivity of the search and reveal any weak pulsars that reside in the globular clusters we have observed.

INTRODUCTION

Millisecond pulsars are neutron stars that are thought to have attained their rapid rotation rate during an episode of mass transfer from a low-mass giant companion. The study of millisecond pulsars provides information concerning many aspects of pulsar-neutron star astrophysics, binary stellar evolution and the mass transfer process. Observations of millisecond pulsars have applications in many other scientific disciplines ranging from time standards to general relativity (Backer 1987).

In 1987 May, radio pulses were detected from the first pulsar to be found in a globular cluster; namely PSR 1821-24 in the globular cluster M28 (Lyne *et al.* 1987). This discovery provided support for the suggestion that the cores of globular clusters were favourable environments for millisecond pulsar formation owing to their high stellar densities and attendant high binary formation rate (Fabian *et al.* 1983). Information on the evolution of millisecond pulsars in globular clusters and their probable relation to low-mass x-ray binaries will be obtained from further discoveries of such pulsars. Also, the proper motion of globular clusters may be determined from timing observations of the millisecond pulsars they contain (Romani, Kulkarni & Blandford 1987).

Here we report on a search for radio pulses from pulsars in globular clusters. So far we have detected one millisecond pulsar, PSR 1620-26, in a wide, low-mass binary system in the core of the globular cluster M4 (Lyne *et al.* 1988).

H. Ögelman and E. P. J. van den Heuvel (eds.), Timing Neutron Stars, 157–162.

OBSERVATIONS

Observations were made from 1987 June 19 to 23 using the 76-m Lovell telescope at Jodrell Bank, England. The observation parameters are given in Table 1. Pulse searches are favoured at 610 MHz because the reduction in adverse effects (such as galactic background radiation and dispersion) outweighs the characteristic decrease in pulsar radio luminosity at higher observing frequencies. The receiver was sensitive to both senses of circular polarisation and these were combined after square law detection to form the total intensity. The total intensity from each channel of the filter bank was sampled and recorded with 1-bit precision every 300 μs. A loss in sensitivity of about 20% results from the 1-bit digitisation as compared with multi-bit sampling, but it also maximises the duration of data recorded on a given storage medium.

Table 1: Observation and analysis parameters.

Observation frequency	610 MHz
Beamwidth	30 arcmin
Bandwidth	32 channels × 125 kHz
Sample interval, τ_{samp}	300 μs
Receiver temperature, T_{rec}	55 K
Observation duration	75 min ($\approx 14 \times 2^{20}$ time samples)
Maximum frequency, $f_{Nyquist}$	1666.7 Hz
Dispersion measure when smearing = τ_{samp}, DM_0	65 pc cm^{-3}
Observation duration for each analysis	315 s (2^{20} time samples)
Elapsed cpu time for each analysis	120 s

Off-line analysis was performed on the University of Manchester Regional Computing Centre Cyber 205 supercomputer. The analysis algorithm searched for periodicities using a two-dimensional fast Fourier transform (Ashworth & Lyne 1988) and has the parameters given in Table 1. The five periodicities with highest signal-to-noise ratio (S/N) were output after incoherent summation of each of 1, 2, 4, 8 and 16 harmonics, for approximately 50 values of dispersion measure (DM). Analyses were conducted on data sets of length 2^{20} time samples (× 32 frequency channels). About 14 independent analyses were performed on each source and the outputs from all of these were searched for coincidence in frequency and DM. Searching for coincidences has the effect of reducing the S/N threshold at which a detection is deemed significant. The data were also analysed after averaging the input time samples. This increased the sensitivity of the pulse search at the expense of increasing the minimum detectable pulsar period and reducing the number of independent analyses per source.

The globular clusters observed were chosen from among those visible from Jodrell Bank that were either:

1) close, R_o (heliocentric distance) < 5 kpc, or
2) dense, ρ_o (core density) > $10^4 M_\odot pc^{-3}$.

The globular clusters that had been observed by Hamilton, Helfand & Becker (1985) were not included since the sensitivity of their survey was slightly better than that described here and they detected no significant sources other than the one in M28. Table 2 shows the sources observed and their relevant properties.

Table 2: Globular clusters observed at 610 MHz. Most of the parameters are from Webbink (1985).

name			l (°)	b (°)	R_o (kpc)	$\log\rho_o$[a]	T_{sky} (K)	S_{min} (mJy)
0443+313	Pal 2		170.5	−09.1	13.6	5.1	12	4.6
0522−245	NGC 1904	M 79	227.2	−29.4	13.0	4.2	5	4.5
1516+022	NGC 5904	M 5	003.9	+46.8	7.6	4.1	11	4.5
1620−264	NGC 6121	M 4	351.0	+16.0	2.1	3.9	19	5.5
1714−237	NGC 6325		001.0	+08.0	6.2	4.3	31	5.9
1716−184	NGC 6333	M 9	005.5	+10.7	7.5	4.1	23	5.3
1720−263	NGC 6355		359.6	+05.4	7.1	4.4	48	7.2
1725−050	NGC 6366		018.4	+16.0	4.0	2.4	20	5.1
1730−333	Lil 1		354.8	−00.2	7.9	6.1	146	13.8
1745−247	Ter 5		003.8	+01.7	7.1	6.4	94	10.3
1746−203	NGC 6440		007.7	+03.8	7.1	5.7	53	7.4
1747−312	Ter 6	HP 5	358.6	−02.2	12.8	5.0	111	11.3
1759−089	NGC 6517		019.2	+06.8	6.1	5.4	43	6.7
1801−300	NGC 6528		001.1	−04.2	6.8	5.0	60	7.9
1802−075	NGC 6539		020.8	+06.8	3.1	4.2	38	6.4
1804−250	NGC 6544		005.8	−02.2	2.6	4.7	92	10.1
1820−303	NGC 6624		002.8	−07.9	8.0	5.3	32	6.1
1827−255	NGC 6638		007.9	−07.2	6.7	4.4	38	6.4
1828−235	NGC 6642		009.8	−06.4	5.5	5.2	44	6.7
1852−227	NGC 6717	Pal 9	012.9	−10.9	7.8	5.1	22	5.3
1908+009	NGC 6760		036.1	−03.9	4.1	4.3	41	6.6
2003−220	NGC 6864	M 75	020.3	−25.7	18.5	4.7	10	4.8
2127+119	NGC 7078	M 15	065.0	−27.3	9.7	5.3	9	4.4
2130−010	NGC 7089	M 2	053.4	−35.8	11.9	4.0	8	4.3

[a] ρ_o units are $M_\odot$ pc^{-3}.

The minimum detectable flux density (S_{min}) in a pulsar survey is given by

$$S_{min} = \beta S_o \left[\frac{T_{rec} + T_{sky}(l,b) + T_{sp}(\text{elevation})}{T_o}\right] \left[\frac{PW_e}{W(P - W_e)}\right]^{\frac{1}{2}}. \quad (1)$$

This equation is discussed more fully by Stokes *et al.* (1986), Narayan (1987) and references therein, and only an outline is given below. The first term of equation (1) is composed of a factor β (> 1) which is related to losses in the system and the S/N threshold for positive detection, and S_o is the rms fluctuation of the system. The second term of equation (1) is a factor related to the noise contribution from the receiver, galactic background and spillover as compared to the average noise. The third term of equation (1) takes into account the pulse duty cycle and effects that tend to broaden the pulse to width W_e from its intrinsic width (W). Figure 1 shows the typical variation of S_{min} as a function of pulse period and DM for varying time-sample averages.

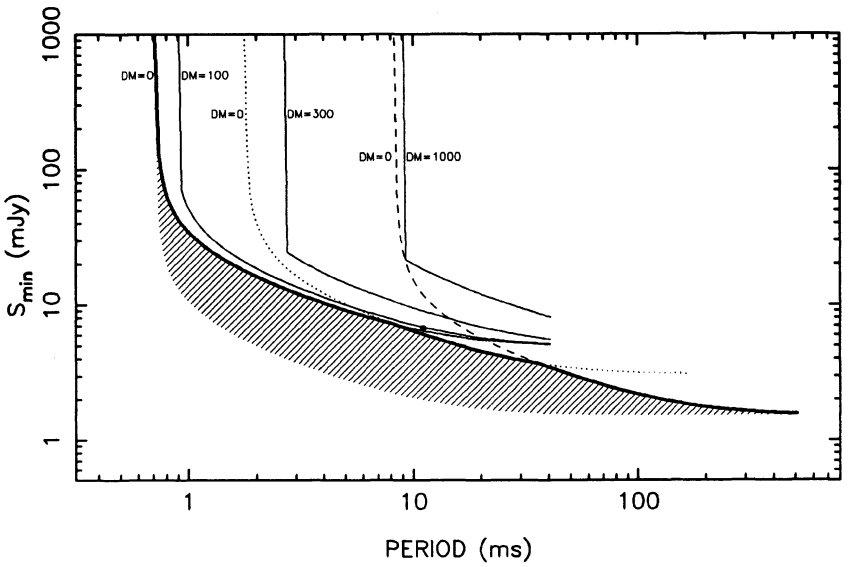

Figure 1. Minimum detectable flux density plotted as a function of pulse period in the direction of the globular cluster M4 and assuming a duty cycle of 5%. The thin lines are S_{min} without time sample averaging for DM = 0, 100, 300 and 1000 pc cm^{-3}. The dotted and dashed lines are S_{min} after averaging 3 and 14 time samples, respectively. The thick line is the locus of S_{min} for all the analyses with DM = 0 pc cm^{-3}. The filled circle corresponds to the detection parameters for PSR 1620-26. The shaded region is the parameter space accessible after a future software upgrade.

Calibration was effected by observing known pulsars such as PSR 0531+21 and PSR 1937+21 firstly with the millisecond pulsar search system and shortly after with the normal timing system. The S/N and average flux density of the calibration pulsar was determined from the periodicity search analysis and the integrated pulse profile output during the timing observation, respectively.

RESULTS AND DISCUSSION

To date, only one pulsar has been discovered; PSR 1620-26 in a wide, low-mass binary system in the core of the globular cluster M4 (Lyne *et al.* 1988). Its current measured parameters are given in Table 3. PSR 1620-26 probably followed a low-mass x-ray binary evolution (van den Heuvel 1984) and its current companion is most probably the only companion it has had and hence is the star from which matter was transferred in order for it to be spun up. Its surface magnetic field is unknown since $\dot{P}$ has yet to be determined, however, proposals for spinup suggest that it lies between 4×10^8 G and 8×10^9 G (Lyne *et al.* 1988 and references therein).

Table 3: Measured Parameters of the PSR 1620-26 system.

Pulsar period	11075.75μs
Dispersion measure	62.876 pc cm^{-3}
Right ascension (1950.0)	$16^h20^m34^s.14$
Declination (1950.0)	$-26°24'58''.0$
Flux density (408 MHz)	$\sim$ 15 mJy
Projected semi-major axis, $a \sin i$	64.808 light s
Orbital period, P_b	191.440 days
Mass function, $f(m_p, m_c)$	0.007 $M_\odot$
Eccentricity, e	0.025
Longitude of periastron, ω	117.135°
Time of periastron	47192.72 MJD
Projected orbital velocity	$\sim$ 7 km s^{-1}

Upper limits to pulsed emission from the globular clusters observed are given in Table 2. The S_{min} values are determined from the 14 independent analyses without time sample averaging as illustrated in Fig. 1. S_{min} is smallest ($\approx$ 4 mJy) far from the galactic plane and increases toward the galactic plane as does the background temperature. The average S_{min} in Table 2 compares well with other recent surveys by Manchester, D'Amico & Tuohy (1985) and Clifton & Lyne (1986) when account is taken of the different observing frequencies. Averaging 14 time samples reduces S_{min} quoted in Table 2 by about a factor of 3 as shown in Fig. 1. The weak pulsar recently discovered in the globular cluster M15 (Wolszczan *et al.* 1988) was not detected in this survey, even when averaging was employed, and this implies it has a spectral index $\gtrsim$ -1.5.

A planned software upgrade will enable a search for periodicities using the whole data set in one analysis. This should facilitate the detection of any weak, fast rotating pulsars to which the present analysis is insensitive (see Fig. 1). If the luminosity function of millisecond pulsars is similar to that of the more numerous, slowly rotating, radio pulsars, the future improvement in sensitivity should result in the discovery of some more millisecond pulsars in the present sample of globular clusters.

ACKNOWLEDGEMENTS

We would like to thank Mike Ashworth for development and support of the Cyber 205 software, Paul Harrison for assistance with the observations and Jonathan McKenna for the results of timing observations for PSR 1620-26.

REFERENCES

Ashworth, M. & Lyne, A. G., 1988. *Parallel Comput.*, **6**, 217.
Backer, D. C., 1987. In: *IAU Symposium No. 125: The Origin and Evolution of Neutron Stars*, p. 13, eds. Helfand, D. J. & Huang, J. H., Reidel, Dordrecht.
Clifton, T. R. & Lyne, A. G., 1986. *Nature*, **320**, 43.
Fabian, A. C., Pringle, J. E., Verbunt, F. & Wade, R. A., 1983. *Nature*, **301**, 222.
Hamilton, T. T., Helfand, D. J. & Becker, R. H., 1985. *Astr. J.*, **90**, 606.

Lyne, A. G., Brinklow, A., Middleditch, J., Kulkarni, S. R., Backer, D. C. & Clifton, T. R., 1987. *Nature*, **328**, 399.
Lyne, A. G., Biggs, J. D., Brinklow, A., Ashworth, M. & McKenna, J., 1988. *Nature*, **332**, 45.
Manchester, R. N., D'Amico, N. & Tuohy, I. R., 1985. *Mon. Not. R. astr. Soc.*, **212**, 975.
Narayan, R., 1987. *Astrophys. J.*, **319**, 162.
Romani, R. W., Kulkarni, S. R. & Blandford, R. D., 1987. *Nature*, **329**, 309.
Stokes, G. H., Segelstein, D. J., Taylor, J. H. & Dewey, R. J., 1986. *Astrophys. J.*, **311**, 694.
van den Heuvel, E. P. J., 1984. *J. Astrophys. Astr.*, **5**, 209.
Webbink, R. F., 1985. In: *IAU Symposium No. 113: Dynamics of Star Clusters*, p. 541, eds. Goodman, J. & Hut, P., Reidel, Dordrecht.
Wolszczan, A., Middleditch, J. M., Kulkarni, S. R., Backer, D. C. & Fruchter, A. S., 1988. *IAU Circ., No. 4552.*

A MILLISECOND PULSAR IN AN ECLIPSING BINARY

A. S. Fruchter, D. R. Stinebring and J. H. Taylor
Joseph Henry Laboratories and Physics Department
Princeton University
Princeton NJ 08544

ABSTRACT. We report the discovery of a remarkable pulsar with period 1.6 ms, moving in a nearly circular 9.17 hour orbit around a low mass companion star. At an observing frequency of 430 MHz, the pulsar, PSR 1957+20, is eclipsed once each orbit for about 50 minutes. For a few minutes before an eclipse becomes complete, and for more than 20 minutes after the signal reappears, the pulses are delayed by as much as several hundred microseconds—presumably as a result of propagation through plasma surrounding the companion. The pulsar's orbit about the system barycenter has a radius of 0.089 light seconds projected onto the line of sight. The observed orbital period and size, together with the fact that eclipses occur, imply a surprisingly low companion mass, only a few percent the mass of the sun. The eclipsing mass extends well beyond the Roche lobe of the companion, and appears to possess a comet-like tail, strongly suggesting that the pulsar is evaporating its companion.

The new pulsar was discovered in the course of a general survey for millisecond pulsars being carried out with the 305 m telescope of the Arecibo Observatory, which I will describe in detail in a later talk during this meeting. The signal from PSR 1957+20 was first observed in October 1986, during some of the earliest observations of the search, but re-observation of the accumulated list of candidate pulsars was not begun until March 1988. The existence of PSR 1957+20 was confirmed on 3 March 1988; observations over the next several days showed its period to be variable at a level corresponding to orbital velocities of ± 5 km s^{-1}. These observations also revealed the presence of a strong interpulse. On 5 March, at approximately 1330 UT, the signal disappeared abruptly for no apparent reason. As I will explain later, we now realize that the pulsar went into eclipse behind its companion star.

Additional observations were made for about 2.5 hours per day on 9 additional days between 9 and 28 March. These measurements made use of two data acquisition systems explicitly designed for timing millisecond pulsars[1,2]. The newest system, used for most of the observations, coherently de-disperses the signals received in two

H. Ögelman and E. P. J. van den Heuvel (eds.), Timing Neutron Stars, 163–168.

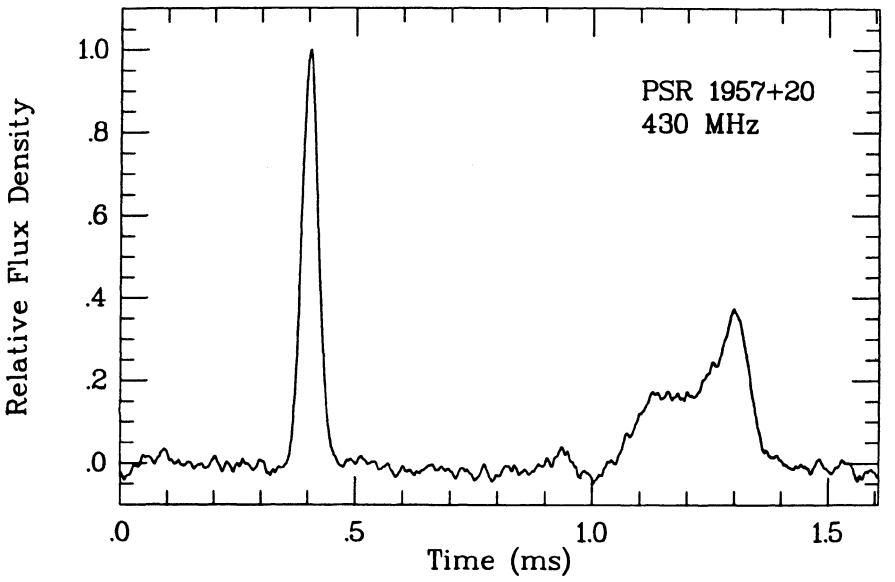

Figure 1: Integrated profile of PSR 1957+20 at 430 MHz. Instrumental smoothing amounts to about 15 μs, mostly a result of drifting pulse phase during the integration caused by imperfect knowledge of the period.

0.4 MHz passbands centered at 427 and 430 MHz. After square-law detection, these signals are sampled, integrated synchronously with the topocentric pulsar period, and recorded approximately once a minute. The sum of 20 of these integrated profiles is plotted in Figure 1, illustrating the main pulse of width 39 μs and a much wider interpulse separated by about half a period.

Using the process of template fitting described by Joe Taylor in the previous talk, an equivalent pulse arrival time was determined for each integration. Analyzed in short segments of about 5 min duration, the arrival times (reduced to the solar system barycenter) yield periods which, when folded modulo the 9.17 hour orbital period, comprise the velocity curve illustrated in the second figure. A linearized least-squares fit to the period data yielded the pulsar and orbital parameters shown in Table 1. A "phase connected" solution to the observed pulse arrival times, with no pulse numbering ambiguities between observing days, should be achievable soon and will provide much more accurate pulsar and orbital parameters.

The entire orbit has now been observed. Good observations exist on five different

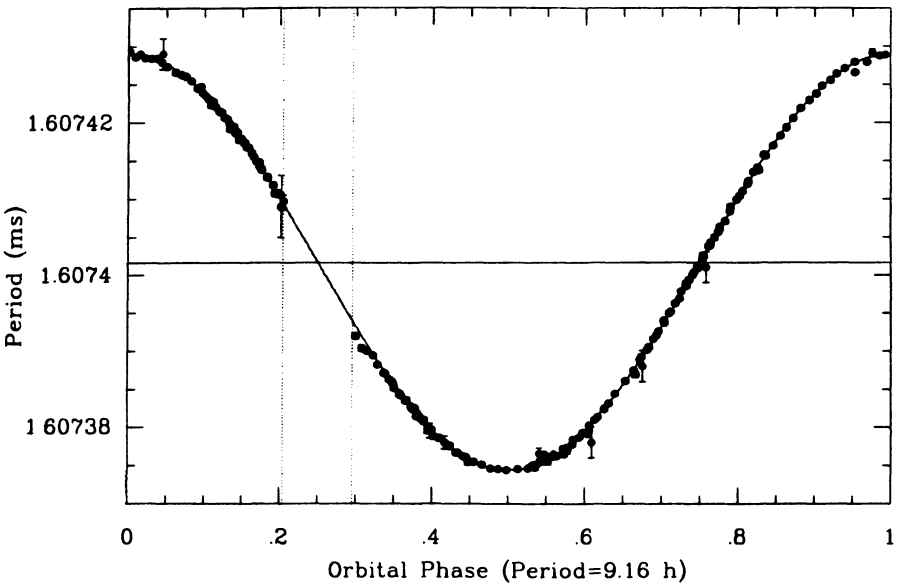

Figure 2: Orbital velocity curve of PSR 1957+20. The pulsar is eclipsed by its companion between phases 0.21–0.29. Points with visible error bars were taken using the pulsar survey system; all other points were obtained with the data acquisition system designed for timing millisecond pulsars.

TABLE 1. Parameters of the PSR 1957+20 system

Right Ascension (1950.0)	$19^h\ 57^m\ 10^s \pm 20^s$
Declination (1950.0)	$\delta = +20°\ 40' \pm\ 5'$
Pulsar period	$P = 1607.40171 \pm\ 0.00003\ \mu$s
Dispersion Measure	$DM = 29.13 \pm\ 0.01$ cm^{-3} pc
Flux Density at 430 MHz	$S = 25 \pm\ 10$ mJy
Projected semi-major axis	$a_1 \sin i = 0.08923 \pm\ 0.00007$ light s
Eccentricity	$e < 0.001$
Orbital period	$P_b = 33001.9 \pm\ 0.5$ s
Time of ascending node	$T_0 = 2447245.08471 \pm\ 0.00004$ JED

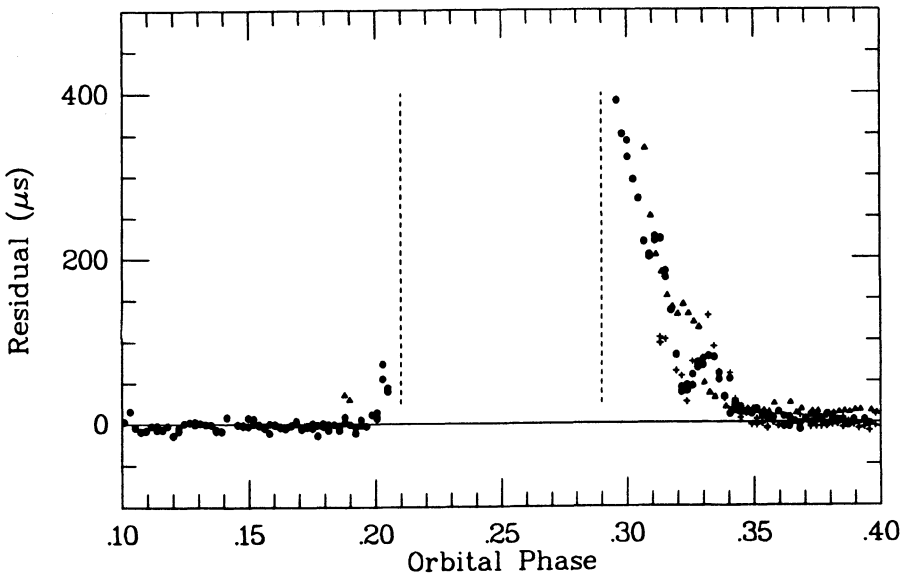

Figure 3: Excess group delays in the pulsar signal at 430 MHz relative to a model based on our best-fit parameters, plotted as a function of orbital phase near the center of eclipse. Different symbols correspond to different observing days.

days for all or part of the region $0.15 < \phi < 0.35$, where orbital phase ϕ is measured from the time of the ascending node. On all of these days the pulsar signal has disappeared completely between the orbital phases 0.21 and 0.29. At $\phi = 0.25$ the pulsar is at its greatest distance from Earth, and closest to being directly behind the companion star. We, therefore, believe that the intervals of missing signal are the result of eclipses by a surprisingly large, though very low mass, companion.

During the few minutes immediately before eclipse, and for about 20 minutes after the eclipse, the pulsar signal is delayed by as much as 400 μs relative to arrival times predicted from a model fitted to parts of the orbit farther from eclipse. These effects are illustrated in Figure 3, which shows that although the eclipse interval is very nearly symmetric about $\phi = 0.25$, the magnitude and duration of the excess signal delays are far from symmetric, and appear to change significantly from orbit to orbit.

The excess delays are probably the result of propagation in ionized gas surrounding the companion. The maximum delay, just after the pulsar has emerged from eclipse, corresponds to an increase in dispersion measure of about 0.017 cm^{-3} pc, or

equivalently an electron column density of 5×10^{16} cm^{-2}. Unfortunately, our two frequency channels at 427 and 430 MHz are too closely spaced to reliably determine the frequency dependence of the effect. Away from eclipse the dispersion measure to the pulsar is found to be 29.13 ± 0.01 cm^{-3} pc.

The orbital parameters listed in Table 1 correspond to a pulsar mass function

$$\left(\frac{2\pi}{P_b}\right)^2 \frac{(a_1 \sin i)^3}{G} = \frac{(m_2 \sin i)^3}{(m_1 + m_2)^2} = (5.20 \pm 0.01) \times 10^{-6}\ M_\odot\ ,$$

where G is the gravitational constant, m_1 and m_2 are the masses of the pulsar and companion and i is the inclination between the plane of the orbit and the plane of the sky. The observed eclipses suggest that $\sin i$ is not much less than 1.0, and thus for a pulsar mass $m_1 \approx 1.4\ M_\odot$ the companion mass must be near the minimum possible mass of $0.022\ M_\odot$. Even without the observation of eclipses, the *a priori* probability of finding $\sin i < 0.4$, and hence $m_2 > 0.055$, is less than 10%. A pulsar mass of $1.4\ M_\odot$ further implies that the ratio m_1/m_2 is around 60, and that the radius of the companion's orbit is near $2.4\ R_\odot$. As the eclipse lasts for about 10% of an orbit, we find that the opaque portion of the companion star must be at least $1.5\ R_\odot$ across.

The radius of the Roche lobe of the companion is only $\sim 0.3\ R_\odot$, so most of the volume occupied by the eclipsing body lies well outside it. We suggest that the eclipsing plasma may be a stellar wind powered by the ~ 100 solar luminosities of energy that would be emitted by the pulsar were it to spin down at a rate comparable to other millisecond pulsars. (For a detailed account of the mechanisms by which the pulsar could heat its companion, see talks by M. Rudermann and J. Shaham in this volume, and references contained therein). The slow decrease of plasma density on the trailing side of eclipse might then be interpreted as a comet-like tail spewing off the companion.

It is exciting to speculate that we are witnessing the evaporation of the companion by the pulsar. While it is difficult to reconstruct the density of the plasma without knowing the geometry of the object, the rapid variation in the observed column density suggests a scale size perhaps as small as 0.1 light s, and thus a plasma density exceeding 10^6 cm^{-3} in the transparent region. If the plasma concentration continues to rise steeply in the region that is now obscured, and if the wind reaches velocities comparable to the companion's orbital velocity, it seems possible that the companion will disappear in much less than 10^9 years, leaving behind an isolated millisecond pulsar. We expect that in the near future radio observations at higher frequencies, and perhaps spectroscopy of the wind, will allow us to determine whether there is any truth to this fascinating possibility.

We thank G. Berman, M. Davis, J. Hagen, T. Hankins, P. Perillat, and M. Ryba for essential contributions to the observational work, and B. Paczynski and C. Thompson for valuable discussions concerning binary evolution. This work was made possible

by the excellent facilities of the National Astronomy and Ionosphere Center and the John von Neumann National Supercomputer Center, and was supported by grants from the US National Science Foundation and the National Bureau of Standards. A. S. F. is supported by a John von Neumann Fellowship.

References

1. Rawley, L. A., Taylor, J. H., Davis, M. M., and Allen, D. W. *Science*, **238**, 761 (1987).

2. Hankins, T. H., Stinebring, D. R., and Rawley, L. A. *Ap. J.*, **315**, 149 (1987).

X-RAY OBSERVATIONS OF ACCRETING NEUTRON STARS

HAKKI ÖGELMAN
Max Planck Institut für Extraterrestrische Physik
D-8046, Garching bei München
Federal Republic of Germany

ABSTRACT. The class of accreting neutron stars that are in close binary systems is reviewed. Basic physical parameters related to their X-ray emission are summarized. The highlights of the accretion process from leaving the companion star to landing on the neutron star are considered. Recent revival of the neutron star free precession interpretation of the long-term cycles is discussed.

1. Introduction

The first X-ray source outside the solar system was discovered back in 1962 by Giacconi *et al.* (1962) during a short, 5 minute rocket exposure of a detector consisting of $\sim$20 cm^2 area Geiger counters. This source, Sco X-1, turned out to be an accreting binary neutron star, the class of objects I want to discuss in this review.

It is interesting to note that one of the scientific motivations for starting X-ray astronomy was to detect thermal radiation from cooling neutron stars in the X-ray energy band. Since neutron stars are the remains of the central cores of massive stars that have consumed all possible internal energy sources, it was logical to assume that they would be cooling from the moment they were born. The hope was to detect youngish neutron stars with surface temperatures around a few million degrees. The newly discovered X-ray source did not fit the cooling scheme; the temperature was about a factor ten higher hence the luminosity about 10^4 higher than expected. While scientists were pondering over the nature of this new class of X-ray objects, neutron stars were discovered as pulsars (Hewish *et al.* 1968). In retrospect, it is obvious that during the collapse to a neutron star, the original magnetic field and the rotation rate of the progenitor star would be amplified by approximately the square of the initial to final radius ratio ($\simeq 10^{10}$), and that such objects should be capable of generating periodic electromagnetic signals as they spin. These ideas were already being expressed in the literature, prior to the discovery of pulsars (Hoyle *et al.* 1964, Woltjer 1964, Tsuruta and Cameron 1966, Wheeler 1966, Pacini 1967).

H. Ögelman and E. P. J. van den Heuvel (eds.), Timing Neutron Stars, 169–189.

Meanwhile, the strong X-ray sources, discovered 5 years before the pulsars, were also being considered as neutron stars; Shklovskii (1967) suggested that Sco X-1 was a neutron star in a close binary system accreting mass from its companion and converting the gravitational energy gained by the infalling gas to X-rays emitted from the surface. However, several years were to pass before the observations with the *UHURU* satellite showed the existence of pulsing X-ray sources which were unmistakably interpreted as rotating, accreting neutron stars. In effect, it was the *timing* aspect of the measurements that again was the clinching argument of the neutron star signature.

In this review of the X-ray observations of accreting neutron stars, I will attempt to summarize the general status and the outstanding problems of the field. I will give in section 2 a brief overview of the basic physics underlying their X-ray emission. Section 3 contains a short summary of binary physics related to accreting neutron stars. In section 4, I discuss the statistics of their properties including classification according to their companion masses, orbital and rotational period distributions. Section 5 contains a discussion of the various phases of the mass transport from the companion to the neutron star surface. The resulting accretion torques leading to spin-up/down are summarized in section 6. In section 7, the free-precession of the neutron star is discussed as a possible mechanism underlying the long-term cycles observed in several systems. Evolution of single and binary neutron stars are covered by van den Heuvel in this volume and hence are not discussed in this review. More detailed treatment of some of these topics can be found in related articles in this volume.

2. The Basic Physics

The limiting mass of a neutron star was estimated by Landau (1932) more than half a century ago. The argument went approximately as follows (see Shapiro and Teukolsky 1983 for a more complete discussion): Consider the neutron star to be a ball of radius R containing N neutrons (with total mass $M = Nm_n$). The Fermi energy E_F of the neutrons in the relativistic regime is determined by their number density as

$$E_F \sim \frac{\hbar c N^{1/3}}{R} \tag{1}$$

the gravitational energy as

$$E_G \sim -\frac{GMm_n}{R} = -\frac{GNm_n^2}{R} \tag{2}$$

making the total energy

$$E = E_F + E_G = \frac{N^{1/3}}{R}\left[\hbar c - Gm_n^2 N^{2/3}\right] \tag{3}$$

The stability of eqn. 3 to radial perturbations depend on the sign of the term in brackets: If it is positive (meaning small N), the energy decreases as R gets large,

and when the fermions become nonrelativistic stability can be achieved at a finite value of R (i.e a white dwarf). If the term is negative (meaning large N) minimum energy is achieved as R approaches 0, meaning gravitational collapse. We can also achieve stability when the term in brackets is 0; this condition gives us roughly the maximum mass of the neutron star

$$N_{max} \sim \left[\frac{\hbar c}{G m_n^2}\right]^{3/2} \sim 10^{57} \tag{4}$$

corresponding to about 1 $M_\odot$. The radius at this maximum mass can be determined only after an equation of state is adopted; typically this value turns out to be about 10 km.

Knowing that a neutron star should have the mass and radius estimated as above (M_{ns}=1 $M_\odot$, R_{ns}=10 km) we can proceed to derive the scales of physical parameters associated with accretion:

What would happen to a mass m dropped from ∞ to its surface? The kinetic energy gained E_k can be estimated as

$$E_k = \frac{G M_{ns} m}{R_{ns}} = 0.15 mc^2 \tag{5}$$

and its velocity

$$\beta = \frac{v}{c} = \left[1 - \frac{1}{(1 + \frac{E_k}{mc^2})^2}\right]^{\frac{1}{2}} = 0.49 \tag{6}$$

If we assume that the mass m is an atom with its associated electrons then we can consider the radiation of the electrons with the above velocity when they impinge on a target, i.e. the surface of the neutron star. The typical bremsstrahlung photons emitted will have an endpoint energy of 75 keV and and $1/E_\gamma$ differential photon number spectrum. Due to the gravitational red shift, the photons will soften by about 15% by the time they arrive at ∞. These energies imply that if the neutron star accretes mass and if this mass strikes the surface and emits bremsstrahlung radiation we should be seeing the bulk of the emitted energy in the hard X-ray region. Thus the discovery of accreting binary neutron stars in the X-ray band is a natural consequence of the mass and radius of the neutron star.

The emerging luminosity of an accreting neutron star can be simply calculated from a given mass accretion rate $\dot{M}$ as the product of $\dot{M}$ times the energy dissipated per unit mass as given in eqn.5

$$L = \frac{G M_{ns} \dot{M}}{R_{ns}} = 0.15 \dot{M} c^2 \tag{7}$$

There is a *maximum limit to the luminosity of an accreting neutron star* called the *Eddington Luminosity.* Consider a hydrogen atom falling under the gravitational potential of the neutron star while at the same time it is being illuminated by the luminosity from the neutron star. The outcoming photons will interact with the

electron of the atom and exert radiation pressure on it in a direction opposite to the gravitational pull. Any force on the electron will also be exerted on the proton since they are strongly bound by electrostatic forces. The same argument holds for ionized plasmas since no internal electric field can be maintained in conducting plasmas. When the luminosity is sufficiently high the gravitational force on the atom is balanced by the radiation force and accretion stops. This limiting luminosity is called the Eddington luminosity L_{Edd}. We can proceed to derive this limit by considering that the radiation pressure at a distance r from the neutron star is

$$P_r = \frac{L}{4\pi r^2 c} \tag{8}$$

The force is P_r times the effective cross section of the electron, the Thomson cross section σ_0 given by

$$\sigma_0 = \frac{8\pi}{3}\left(\frac{e^2}{mc^2}\right)^2 = 6.6 \times 10^{-25}\text{cm}^2 \tag{9}$$

Balancing the radiation and gravitational forces gives

$$\frac{L_{Edd}\sigma_0}{4\pi r^2 c} = \frac{GM_{ns}m_H}{r^2} \tag{10}$$

which yields

$$L_{Edd} = \frac{4\pi G M_{ns} m_H c}{\sigma_0} = 1.3 \times 10^{38}\frac{M_{ns}}{M_\odot}\ \text{erg s}^{-1} \tag{11}$$

If we assume that all this luminosity comes from accretion of mass we can estimate the Eddington mass accretion rate as

$$\dot{M}_{Edd} = \frac{4\pi m_H R_{ns} c}{\sigma_0} = 6 \times 10^{17}\text{gm s}^{-1} = 10^{-8}\frac{M_{ns}}{M_\odot}\ M_\odot\ \text{yr}^{-1} \tag{12}$$

The effective blackbody temperature of a neutron star emitting at Eddington luminosity can also be estimated from the Stefan-Boltzman relationship

$$T = \left[\frac{L_{Edd}}{4\pi\sigma {R_{ns}}^2}\right]^{\frac{1}{4}} \simeq 2 \times 10^7\ K \tag{13}$$

This temperature corresponds to a peak intensity around photon energies of 5 keV which again falls in the X-ray band.

Many of the bright X-ray sources like Sco X-1, indeed have the typical values of *Luminosity* and *Temperature* as estimated above close to the Eddington limits.

The spectral characteristics of the X-ray emitting neutron stars have been extensively studied and found to have different properties. It has been generally possible to fit the observations with some combinations of blackbody, thermal bremsstrahlung and power-law models. In Figure 1, I show the comparative shapes

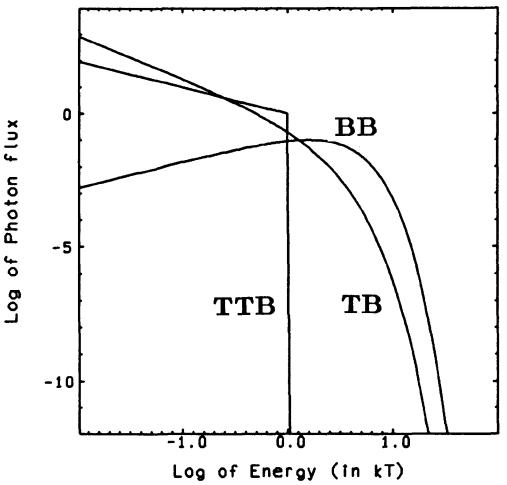

Figure 1: Energy spectrum of various possible processes that can contribute to the X-ray spectrum of accretion powered neutron stars: TTB - thin target bremsstrahlung; TB - thermal bremsstrahlung; BB - blackbody. The photon energy is in units of kT; for the thin target bremsstrahlung, the electron energy is assumed to be kT.

of thin target bremsstrahlung of monoenergetic electrons, thermal bremsstrahlung of a spectrum of thermal electrons and a blackbody spectrum as discussed in this section. In real measurements, the additional effects of the strong magnetic fields on the opacity can be also observed and used to determine the field strengths (e.g. Trümper *et al.* 1978; Voges *et al.* 1982).

3. Some Binary Physics

I have already mentioned that an X-ray emitting neutron star derives its luminosity through the mass accreted from its binary companion. At least half of the stars we observe are in binary pairs, hence it is not surprising that some neutron stars are also in such systems. The parameters that specify a binary system are the masses of the two stars M_{ns}, and M_c(companion mass), the semi-major axis a, and the eccentricity of the orbit e. There are two additional parameters that specify the orientation of the orbit with respect to the observer, the inclination angle i of the orbital plane and ω the longitude of the periastron in the plane of the orbit. Detailed information exists in a number of books on orbital motion (see e.g. Kopal 1978, Roy 1982).

Kepler's third law relates the the orbital period P_{orb} to a and the total mass of the system

$$G(M_{ns} + M_c) = 4\pi^2 \frac{a^3}{P_{orb}^2} \tag{14}$$

For the sake of simplicity, here I discuss circular orbits only ($e = 0$) which appears to be valid for most accreting neutron stars. If we define the mass ratio $q \equiv M_{ns}/M_c$, the distances from the center of mass a_{ns} and a_c are also related as $a_c/a_{ns} = q$.

The most readily observable parameter in an X-ray binary is the orbital period P_{orb}. If the neutron star shows pulsations (i.e. a rotation period) then we can also measure $a_{ns} \sin i$. Together these quantities give us the mass function $f(M)$ of the system

$$f(M) = 4\pi^2 \frac{(a_{ns} \sin i)^3}{G P_{orb}^2} = \frac{M_c \sin^3 i}{(1+q)^2} \tag{15}$$

If in addition, the companion star is identified we may be able to measure the amplitude of the companion star's velocity variations K_c and infer q through the relationship

$$q = \frac{K_c P_{orb}}{2\pi a_{ns} \sin i} \tag{16}$$

The factor $\sin i$ is still not determined and it scales the mass with it's 3rd power. Possible observations of eclipses, together with stellar models can restrict the ranges of $\sin i$ so as to allow reasonable mass determinations.

In the case of accreting X-ray binaries an additional physical assumption is that the companion star has a radius close to a critical radius called the *radius of the Roche lobe*. This radius is can be calculated simply by examining the motion of a test mass in a coordinate system rotating with the angular velocity of the binary system (see Rose 1977). Choosing a coordinate system with its origin on the center of mass and x-axis going through the two stars, z-axis along the rotation axis Ω we can express the potential V felt by the test particle as

$$V = -\frac{GM_{ns}}{[(x - x_{ns})^2 + y^2]^{\frac{1}{2}}} - \frac{GM_c}{[(x - x_c)^2 + y^2]^{\frac{1}{2}}} - \frac{G(M_{ns} + M_c)(x^2 + y^2)}{2(x_{ns} + x_c)^3} \tag{17}$$

The first two terms in the above equation are the gravitational potentials of the neutron and companion star respectively, the third term is the centrifugal potential $-\frac{1}{2}\Omega^2(x^2 + y^2)$ rewritten in terms of the Kepler's law (eqn 14). The additional relationships

$$|x_{ns}| M_{ns} = |x_c| M_c, \text{ and } |x_{ns}| + |x_c| = a \tag{18}$$

can be used to reduce eqn. 17. further. Figure 2 shows the plots of potential derived from eqn. 17 in the $x-z$ plane for increasing values of y starting with 0; the parameters $M_{ns} = 1.4\ M_\odot$, $M_c = 2.2\ M_\odot$ and $P_{orb} = 1.7$ days (appropriate for Her X-1) were used. The curves are symmetric for negative values of y. The Lagrangian points L_1, L_2, L_3, and L_4 where the potential has a maxima are indicated (there is a symmetric counterpart of L_4 for the negative y values. A test particle arriving at L_2 ,L_3, L_4, and L_5 will leave the system. On the other hand, a particle on the atmosphere of the companion at L_1 will fall in to the gravitational well of the

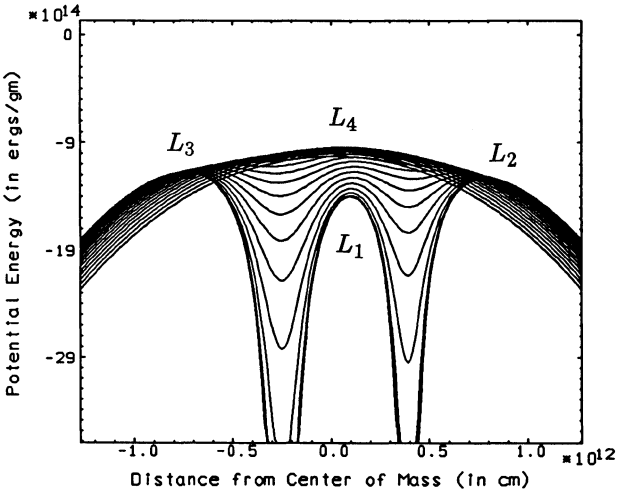

Figure 2: Plots of potential derived from eqn. 17 in the $x - z$ plane for increasing values of y starting with 0; the parameters $M_{ns} = 1.4\ M_\odot$, $M_c = 2.2\ M_\odot$ and $P_{orb} = 1.7$ days (appropriate for Her X-1) were used. The companion star is on the left. The curves are symmetric for negative values of y. The Lagrangian points L_1, L_2, L_3, and L_4 where the potential has maxima are indicated. The potential going through L_1 is called the critical Roche potential.

neutron star and lead to X-ray emission. The potential around the companion going through this point is called the critical Roche potential, and defines the Roche lobe.

The radius of the Roche lobe R_L is calculated by equating its volume to $\frac{4}{3}\pi R_L^3$. Numerical calculations of Eggleton(1983) give the following expression for R_L.

$$\frac{R_L}{a} = \frac{0.49}{0.6 + q^{2/3} ln(1 + q^{-1/3})} \tag{19}$$

When we observe an X-ray emitting neutron star in a binary system, we assume that the companion star is filling its Roche lobe and we can use the above approximate relationships for the radius to separation ratio R_c/a of the companion. Using various stellar mass-radius relationships it is then possible to take one further step in the complete specification of the binary system parameters.

4. Statistics of their Properties

Presently there exist $\sim 10^2$ observed bright X-ray sources estimated to be binary systems with accreting neutron stars. About half of them have measured binary periods; the X-ray luminosity lies in the 10^{34} to several times 10^{38} erg s^{-1} luminosity range. In about 30 of these sources, the rotation period of the neutron star has been detected. Table 1 is a summary of these X-ray pulsars.

Table 1. **List of confirmed and unconfirmed X-ray pulsars as of May 1988.**

Name	Rot.Per. (sec)	Orb.Per. ($days$)	$a_x \sin i$ ($lt-sec$)	f(M) $M_\odot$	L_x $ergs^{-1}$	ecc.
[2]$1E1024-57$	0.061					
[3]$A0538-66$	0.069	16.7			8×10^{38}	0.4
[1]$SMC\ X-1$	0.714	3.89	53.46	10.8	5×10^{38}	$<.007$
[1]$Her\ X-1$	1.24	1.70	13.18	0.9	1×10^{37}	$<.003$
[4]$H0850-42$	1.78				1×10^{37}	
[1]$4U0115+63$	3.61	24.3	140.13	5	3×10^{37}	.34
[5]$V0332+53$	4.38	34.25	48	.1	4×10^{35}	.31
[1]$Cen\ X-3$	4.84	2.09	39.79	15.5	5×10^{37}	$<.0008$
[6]$1E1048.1$	6.44					
[7]$1E2259+59$	6.98	.03?	$<.2$?		2×10^{35}	
[1]$4U1627-67$	7.68	.03			3×10^{37}	
[8]$2S1553-54$	9.30	30.6	164	5		.09
[1]$LMC\ X-4$	13.5	1.41	26	15	7×10^{38}	$<.02$
[1]$2S1417-67$	17.6					
[9]$GPS1840+01$	29.5					
[1]$OAO1653-40$	38.2				1×10^{37}	
[10]$EXO2030$	41.8					
[11]$CepX-4$?	66					
[12]$4U1700-37$	67.4?	3.4			3×10^{36}	
[1]$A0535+26$	104	111	500	20	2×10^{37}	.3
[1]$GX\ 1+4$	122				4×10^{37}	
[1]$4U1230-61$	191					
[1]$GX\ 304-1$	272	133	500		5×10^{35}	
[1]$4U0900-40$	283	8.96	112	20	2×10^{36}	.09
[1]$4U1145-61$	292	188	600		3×10^{35}	
[1]$1E1145.1$	297				3×10^{36}	
[1]$A1118-61$	405					
[13]$GPS1722-36$	414					
[14]$4U1907+09$	438	8.38	80	9	5×10^{35}	.22
[1]$4U1538-52$	529	3.73	55	13		
[1]$GX\ 301-2$	696	41.5	367	31	1×10^{36}	
[1]$4U0352+30$	835	580			4×10^{33}	

Discovery references:

[1]The discoveries are referenced in Rappaport & Joss 1983. [2]Caraveo *et al.*, this volume. [3]Skinner *et al.* , 1982. [4]Wood & Norris, IAU Circ. 5859, 1984. [5]Stella & White, IAU Circ. 3902, 1983. [6]Seward *et al.* , 1986. [7]Fahlman & Gregory 1983. [8]Kelley, Ayaslı and Rappaport, IAU Circ. 3667, 1982. [9]Ginga Team, IAU Circ. 4598, 1988. [10]Parmar *et al.* , IAU Circ. 4066, 1985 [11]Ginga Team, IAU Circ. 4577, 1988. [12]Murakami *et al.* , 1984. [13]Ginga Team, IAU Circ. 4530, 1988. [14]Tenma Team, IAU Circ. 3882, 1983.

Since we suspect that the neutron stars in all these binary systems more or less have similar properties, an obvious sub-divisions of the accreting systems can be made on the basis of the companion mass M_c. Indeed, a closer look at the galactic X-ray binaries reveals that they are divided into two main categories: massive X-ray binaries with companion masses $M_c \gtrsim 10\ M_\odot$ (*HMXRB*), and the low mass systems (*LMXRB*) with $M_c \lesssim 2\ M_\odot$. Roughly, similar amount of sources belong to each category. Inbetween these categories, extending into the *HMXRB* category, there are the B emission star companions. These systems generally show transient X-ray emission owing either to their elliptic orbits or the transient shell ejection fom the B star. A further possible subdivision in the *LMXRB* may be made for $M_c \sim M_\odot$ (young-population *LMXRB*) and $M_c \ll M_\odot$ (old-population *LMXRB*) (van den Heuvel 1983). A sizeable fraction of *LMXRB* s show X-ray bursts with seconds to minutes duration interpreted as thermonuclear flashes on the neutron star surface. It has been also recognized that a high fraction of the low-mass systems occur in globular clusters (see Lewin and Joss 1983; Parmar and White 1988 for reviews). The expected X-ray lifetimes for the high-mass and the low-mass systems are $\sim 10^4 - 10^5$ and $\sim 10^8 - 10^9$ years respectively (Savonije 1983). Considering that we see about equal numbers in both categories, the formation rate of high mass X-ray binaries must be about 10^4 times more. If we further take into account the smaller number of massive stars, the formation probability of an X-ray binary must be a factor $\sim 10^6$ more in high mass systems in comparison to the low mass ones.

Figure 3 is the countrate profile during an early rocket flight, back in 1973 where three different sources were observed in sequence (Rothschild 1977). The two classes mentioned above, and a black hole candidate Cyg X-1 are seen with their characteristic intensity fluctuations: Her X-1, although at the low mass end of the massive X-ray binary category, showing the typical periodic time profile due to its 1.24 s rotation; Cyg X-2, a low mass X-ray binary showing low frequency quasi periodic oscillations; and Cyg X-1, showing bursts of millisecond shot-noise type fluctuations.

The massive X-ray binaries show a galactic disk distribution with an average galactic height of $\sim$ 70 pc, reminiscent of OB stars; low-mass systems are more concentrated toward the galactic center and have an average height of $\sim$ 500 pc, reflecting an older population (White 1987).

Figure 4 shows the orbital period distribution of X-ray binaries in both high- and low-mass systems. With the exception of few, most of the low-mass systems lie on the shorter side of 1 day orbital period and the high-mass systems on the longer side. There is a good reason for this. As can be seen from Keplers law, eqn. 14, the ratio of a^3/P^2 is fixed for a given M_c(assuming that $M_{ns} \sim 1.4 M_\odot$). Equation 19 (or 20) fixes also the Roche lobe radius to separation ratio. The radius R_c of the companion star should be less than the Roche lobe radius $R_c \lesssim R_L$ (otherwise mass transfer would be too fast). If we further express R_c as a function of M_c through the mass-radius relationship for main-sequence stars (since most of a star's lifetime is spent on the main-sequence) as $R_c/R_\odot \simeq (M_c/M_\odot)^{3/4}$ we can get the following approximate expression that gives the minimum period that can accomodate a

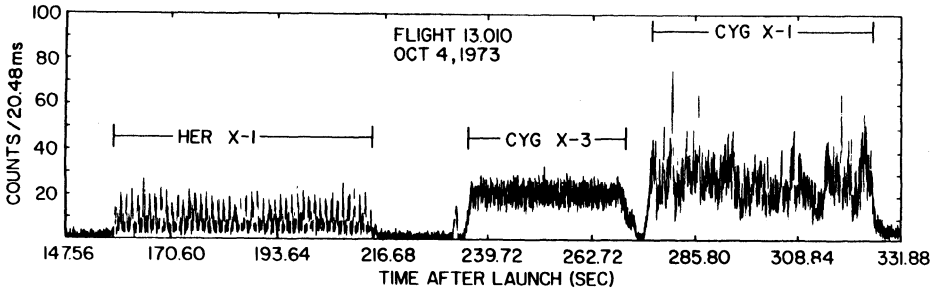

Figure 3: Counting rate of a GSFC X-ray detector rocket payload on October 4, 1973 where three different class of X-ray sources are detected in sequence (from Rothschild 1977).

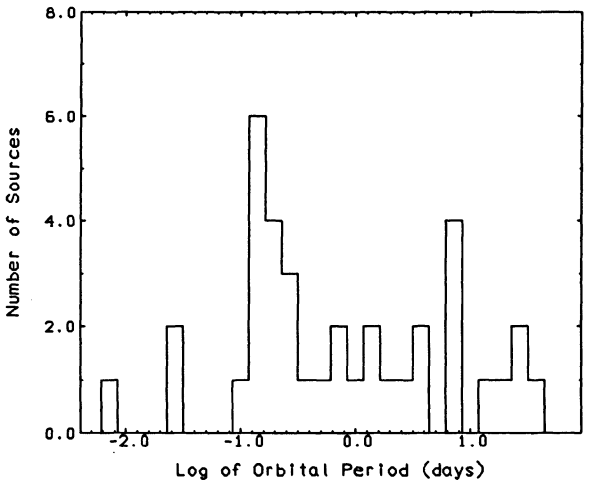

Figure 4: Orbital period distribution of accreting neutron stars.

main-sequence companion star of mass M_c

$$P(in\ days) \gtrsim \frac{{M_c}^{5/8}}{(1+\frac{M_{ns}}{M_c})^{1/2}}(1.60+0.84\ log\ \frac{M_{ns}}{M_c})^{-3/2} \qquad (20)$$

(all masses are in $M_\odot$). For example, an 8 $M_\odot$ star has to have a period of more than one day in order to fit inside its Roche lobe radius. Or conversely, as in Figure 4, we can conclude that the binary systems with periods less than one day have to be less massive than 8 $M_\odot$ if they are on the main-sequence; if they have evolved off the main-sequence, they have to be even less massive. Similar calculations for degenerate dwarfs can be made using different mass-radius relationships.

The rotation periods of the neutron stars in accreting systems are listed in Table 1 and plotted in Figure 5. Compared to radio pulsars, the accreting neutron stars appear to have considerably longer periods. The mean period of the observed accreting neutron stars is $\sim$ 160 s in comparison to the mean period of $\sim$ 0.8 s for single radio pulsars. Assuming that binary and single neutron stars are born with similar periods, this implies that considerable external accretion torques are exerted on a binary neutron star throughout its lifetime in order to slow it down to the observed values. Assuming a moment of inertia of 10^{45} gm cm^2, we can conclude that about 10^{46} gm cm^2 s^{-1} worth of angular momentum must have been extracted from the system before it became an X-ray binary. In fact, it has been noticed that neutron stars have to slow down in order to reduce their dipole radiation pressure and allow accretion to start (Illarionov and Sunyaev 1975; see Henrichs 1983 for a review). It is interesting that most of the observed present period changes of the X-ray pulsars are in the sense of a slow spin-up superimposed with considerable noise. In section 6 I discuss the general features of accretion torques.

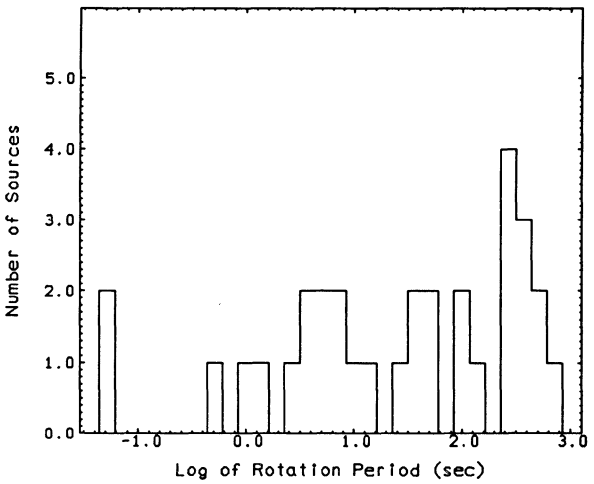

Figure 5: Rotation period distribution of accreting neutron stars.

5. From the Companion onto the Neutron Star Surface

In this section I will review some of the standard arguments that follow the path of the accreting material from the atmosphere of the companion to the surface of the neutron star.

5.1 LEAVING THE COMPANION

I have already mentioned the Roche lobe geometry in section 3. If the companion

star is filling its Roche lobe the material should flow out of the Lagrangian point L_1 into the Roche lobe of the neutron star; this type of mass transfer is called *Roche lobe overflow*. The rate of mass transfer through L_1 has been calculated by a number of authors (for a review see Savonije 1983). If the companion star's envelope is radiative, it is estimated that the peak mass-transfer rates would be of the order of (Paczynski 1971)

$$\dot{M}_c \sim \frac{RL}{GM_c} \sim 3 \times 10^{-8} \frac{R_c}{R_\odot} \frac{L_c}{L_\odot} \frac{M_\odot}{M_c} \; M_\odot \; \mathrm{yr}^{-1} \tag{21}$$

If the companion star has a convective envelope, the mass transfer is ecpected to proceed in a more violent way as soon as the Roche lobe is filled. The problem of determining the time history of Roche lobe overflow type mass-transfer is a complicated one involving the angular momentum transfer within the binary system and from the system. It is generally estimated that massive-systems in Roche lobe filling geometry have typical lifetimes of 10^5 years before the mass-tranfer rate exceeds the Eddington limit given in eqn. 12.

In the case of low-mass systems, the conventional picture is that processes such as orbital gravitational radiation (e.g. Rappaport *et al.* 1982; Paczynski and Sienkiewicz 1981 and references therein) or rotational braking by a magnetic stellar wind (e.g. Verbunt and Zwaan 1981) keeps driving the two stars closer while the mass-transfer from the less massive companion to the neutron star keeps driving the two stars apart. Presumably these two processes keep the system in a steady mass-transfer state throughout the evolutionary timescale of the companion at a rate $\sim 10^{-8}\ M_\odot\ \mathrm{yr}^{-1}$. Thus, these X-ray binaries can be luminous X-ray sources for 10^8 years or more.

In the case the companion star does not fill its Roche lobe, a fraction of a strong wind may also end up on the neutron star leading to X-ray emission. Such strong winds ($\sim 10^{-6} - 10^{-4}\ M_\odot\ \mathrm{yr}^{-1}$) are only expected in massive stars. A first order estimate for the fraction of the wind that is accreted is given by a simple argument (Bondi and Hoyle 1944). One assumes that all the wind material that arrives within a radius R_{acc} from the neutron star is accreted if the kinetic energy of the wind with respect to the neutron star is less than the gravitational energy at that radius; i.e.

$$R_{acc} \lesssim \frac{2GM_{ns}}{v_{rel}^2} \tag{22}$$

where v_{rel} is the relative velocity of the wind with respect to the neutron star. Consequently, the accretion rate onto the neutron star can be estimated as the geometrical cross section of this radius at the separation distance a

$$\dot{M}_{acc} \simeq \dot{M}_c \left(\frac{GM_{ns}}{av_{rel}^2}\right)^2 \tag{23}$$

There are several *HMXRB* where wind accretion may be the responsible mechanism for X-ray emission. For example in the case of Vela X-1 (4U 0900-40), with $v_{rel} \sim 900\ \mathrm{km\ s}^{-1}$, $a = 3.6 \times 10^{12}$ cm, eqn. 23 requires that $\sim 4 \times 10^{-5}$ of the wind is

captured. Its X-ray luminosity of 10^{36} erg s^{-1} implies that $\dot{M}_{acc} \sim 10^{-10}\ M_\odot\ \mathrm{yr}^{-1}$ and $\dot{M}_c \sim 3 \times 10^{-6}\ M_\odot\ \mathrm{yr}^{-1}$; a wind mass-loss rate that the $\sim 20\ M_\odot$ companion is capable of providing.

5.2 FORMING AN ACCRETION DISK

In the case of Roche lobe overflow, it is likely that the material will have sufficient angular momentum to prevent it from falling directly onto the neutron star. The velocities at the Lagrangian point are expected to be in random directions having velocities of the order of the internal velocities of the gas i.e. the sound speed. These velocities times the distance of the Lagrangian point from the neutron star gives the typical specific angular momentum of the flowing gas (angular momentum per unit mass) which is nominally higher than the specific angular momentum of a Keplerian orbit near the neutron star. If these particles behaved as non-interacting particles, their angular momentum would force them to settle in stable orbits around the neutron star and no accretion would take place. However, if we turn on some energy dissipating interactions (i.e. viscosity) then velocities perpendicular to the orbital plane are reduced and elliptical orbits become circularized and we end up with a flat disk. The gas in this disk moves in almost Keplerian orbits with azimuthal velocities

$$v_\phi = (GM_{ns})^{1/2} r^{-1/2} \tag{24}$$

The gas has to also move in the radial direction slowly in order to provide the mass acretion rate to the neutron star at its center

$$v_r(r) = -\frac{\dot{M}}{4\pi r^2 \rho(r)} \tag{25}$$

while angular momentum has to flow out radially since the specific angular momentum j_K of a Keplerian orbit goes like

$$j_K(r) = (GM_{ns})^{1/2} r^{1/2} \tag{26}$$

There has been extensive literature on disk modelling in close binaries starting some 20 years back (see Pringle 1981 and references therein). In the case of accreting neutron star binaries it is believed that all low-mass systems and a major fraction of the high-mass systems accrete via a disk. In many cases, the disk obscures the direct emission from the neutron star and complicates the measurements pertaining to the processes happening in the close vicinity of the neutron star. Absence of periodic modulation in most *LMXRB* s is blamed on the existence of a disk that extends very close to the neutron star surface.

5.3 ACCRETION ONTO THE NEUTRON STAR

As we know from radio pulsars, neutron stars have strong magnetic fields of the order of 10^{12} gauss near the surface (dipole moments $\mu = B_s R_s^3 \sim 10^{30}$ gauss-cm^3).

In the case of accreting neutron stars, electron-cyclotron reasonances have been observed for Her X-1 indicating the existence of a field in the $2-5\times10^{12}$ gauss range near the surface (Trümper *et al.* 1978). These fields play a very important role in determining how the material coming down in the disk (or wind) gets eventually onto the neutron star.

The first step in calculating the approximate scale of the magnetospheric radius r_m (also called the Alfvén radius) is to balance the magnetic pressure with the ram pressure of the infalling material at this radius (Davidson and Ostriker 1973; Lamb *et al.* 1973):

$$\frac{\mu^2}{8\pi r_m^6} \simeq \rho(r_m) v_r^2(r_m) \tag{27}$$

where the radial velocity v_r is assumed to be a fraction of the free-fall (or Keplerian) velocity at r_m

$$v_r(r_m) \lesssim \left(\frac{GM_{ns}}{r_m}\right)^{1/2} \tag{28}$$

After expressing the density in terms of $\dot{M}$ by the use of the continuity equation (eqn. 25) we can write

$$r_m \sim \mu^{4/7}(GM_{ns})^{-1/7}\dot{M}^{-2/7}$$

$$\sim 2\times10^8 \text{ cm } \mu_{30}^{4/7}\left(\frac{M_{ns}}{1.4M_\odot}\right)^{-1/7}\left(\frac{\dot{M}}{10^{-8}M_\odot \text{ yr}^{-1}}\right)^{-2/7} \tag{29}$$

The wind accretion case gives a similar magnetospheric scale since the magnetic pressure goes up very steeply with decreasing r.

The interaction of the accretion disk or a wind with the magnetosphere of a rotating magnetic neutron star is a complex phenomenon despite the surprising success of the above ideas. In the next section I will outline some of the current ideas and their experimental checks through the observed period changes in accreting neutron stars.

6. Accretion Torques

The simple model outlined in the previous section assumes that the plasma approaches the neutron star all the way to the magnetospheric radius without knowing anything about the neutron star except its gravitational attraction. And all of a sudden it finds itself in the grasp of the neutron star's magnetic field and starts co-rotating with it. Effectively the plasma switches from one state to the other in an infinetely thin region. If we continue with this logic, the rate of angular momentum carried in by the accreted material $\dot{J}$ (or the torque $N = I\dot{\Omega}$) can be obtained by multiplying $\dot{M}$ with the specific angular momentum $j_K(r_m)$ as given in eqn. 26.

Since angular momentum is only added, in this simplified picture, the neutron star would only spin-up. The timescale of spin-up τ can be obtained as:

$$\tau = \frac{\Omega}{\dot{\Omega}} = \Omega I \mu^{-2/7} (GM_{ns})^{-3/7} \dot{M}^{-6/7} \tag{30}$$

This relationship can also be expressed in terms of the X-ray luminosity L_x via eqn. 7. With typical parameters ($\mu = 10^{30}$ gauss-cm^3, $M_{ns} = M_\odot$, $R_{ns} = 10^6$ cm, $L_x = 10^{38} - 10^{37}$ erg s^{-1}), the value of τ in the above equation is in the range 10^3 to 10^4 years. If we assume all the neutron stars have about the same moment of inertia (I), mass and radius then the measured $\Omega/\dot{\Omega}$ should scale as $\Omega L_x^{-6/7}$. The early measurements indeed showed that this was generally true although spin-down episodes also existed (see Rappaport and Joss 1983). Another consequence of the simple picture is that the neutron star should approach an *equilibrium period* P_{eq}, when its period is equal to the Keplerian period at the magnetospheric radius r_m i.e.

$$r_m = (GM_{ns})^{1/3} (\frac{P_{eq}}{2\pi})^{2/3} \tag{31}$$

Using eqns. 7 and 29 the above relationship becomes

$$P_{eq} \simeq 2\pi \mu^{6/7} (GM_{ns})^{-2/7} R_{ns}^{-3/7} L_x^{-3/7} \tag{32}$$

Again, with typical parameters the equilibrium periods expected range around a few seconds. At this period the accretion should stop since the the centrifugal force at r_m equals the gravitational attraction and the material should not be able to flow in.

There has been further theoretical work that improves the simple picture by taking into account the disk magnetosphere interaction (Ghosh and Lamb 1978, 1979a, 1979b; Anzer and Börner 1980, 1983; Wang, 1987). Continuing observations reveal that almost all accreting neutron stars with known spin periods do show spin-down phases indicating that short-term torque fluctuations dominate the long-term trends. The spin fluctuations have been extensively studied in Vela X-1 (4U0900-40) (Boynton *et al.* 1984). They find that a white noise in $\dot{\Omega}$ leading to a random walk in Ω provides an acceptable model of the pulse timing fluctuations. In such a model, the rms deviation of Ω, $< \delta\Omega >_{rms}$ from its value at $t = 0$, can be expressed in terms of the elapsed time t and the equivalent strength of the noise S as $< \delta\Omega >_{rms} \simeq (St)^{1/2}$. For Vela X-1, the measured noise strength is $S = 6.4 \times 10^{-19}$ rad^2 s^{-3}. Effectively, on the timescale of few days, the torque can be $\sim 10^5$ times more than that expected from eqn. 30, and have positive and negative values equally likely. Vela X-1 is possibly a wind accreting source (see section 5.1) and hence may have a reason for showing both spin-up and spin-down. However Her X-1, a source with strong observational evidence for a disk, also shows $\pm \dot{P}$ values. Figure 6 shows the period history of this source.

A similar torque noise analysis for Her X-1 also shows that the white torque noise can account for these variations; the corresponding noise strength S is about

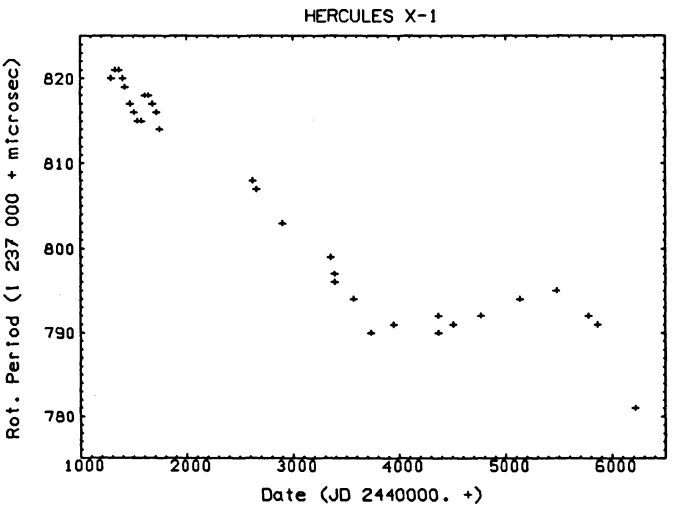

Figure 6: Rotation period of Her X-1 as a function of time.

8×10^{-18} rad^2 s^{-3} (Boynton, 1981). Assuming that all pulsars that show $\dot{P}$ fluctuations can be explained by white torque noise, I have estimated the magnitude of their noise strength S by a crude procedure where the first and last Ω measurements are connected with a straight line and the maximum deviation from this line $\Delta\Omega$ yields

$$S \sim \frac{2(\Delta\Omega)^2}{\Delta t} \tag{33}$$

where Δt is the time interval between the first and last measurement. Figure 7 shows a plot of S versus the X-ray luminosity for 11 X-ray pulsars. It is apparent that sources with higher L_x (or $\dot{M}$) also have larger torque noise strength. A better theoretical understanding of this behaviour and hence the accretion torques is yet to come.

7. Long Periods: Precession?

While the rotation frequencies and binary periods of accreting neutron stars have been readily identified, a third type of *long-timescale periodicity* that exists in some X-ray binaries has not found a convergent interpretation (see Priedhorsky and Holt 1987 for a review of long-term cycles in X-ray sources). Two X-ray pulsars, Her X-1 and LMC X-4 have intensity variations with periodicities of 35 and 30.4 days respectively; there are some half a dozen more neutron stars in massive systems that are possible candidates for long-term variations. The source SS433, shows a precessing relativistic jet at a period of 164 days; it is a black hole candidate although the possibility of being a neutron star is not excluded. Another black hole candidate, Cyg X-1, shows intensity variations at 294 day period. Long-period

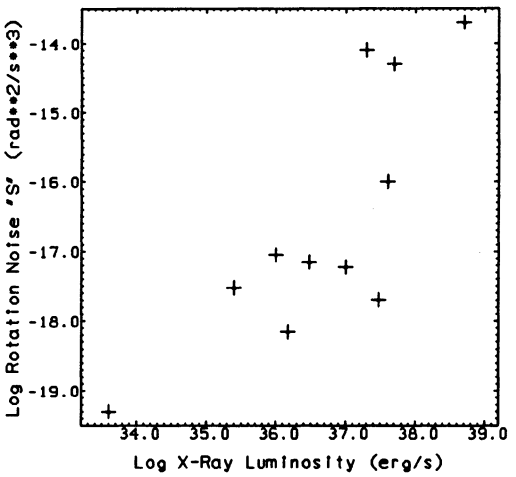

Figure 7: Rotation noise strength S as a function of X-ray luminosity for 11 pulsars (in increasing luminosity order: 4U0352+30, 4U1145-61, GX 301-2, 4U0900-40, 1E1145.1, Her X-1, A0535+26, 4U1627-67, GX 1+4, Cen X-3, SMC X-1).

cycles have also been observed in several low-mass systems. These are generally interpreted as variations in mass transfer rates. The Be/neutron star systems that constitute about half of the massive systems also show long-term cycles. Some of these systems are in wide, eccentric orbits and it is speculated that the periodicity results from enhanced mass transfer during periastron passage.

The most extensively studied system showing this long-term periodicity is the Her X-1/HZ Her X-ray binary, initially discovered by Tananbaum *et al.* (1972). A variety of mechanisms has been proposed to explain this 35 day cycle (Katz 1973; Brecher 1972; Pines, Pethick, and Lamb 1973; Roberts 1974; Lamb *et al.* 1975; Petterson 1975, 1977; Meyer and Meyer-Hofmeister 1984). A disk that periodically occults the X-ray source is assumed in most of the models to explain the details of the X-ray and optical light curves of the system. The three major choices for the clock mechanism under current discussion are: a) a clock mechanism that is provided from the outer part; i.e. the precession of HZ Her (Roberts 1974; Petterson 1975, 1977); b) a mechanism that resides in the properties of the disk itself either in the form of long wavelength azimuthal perturbations that grow into a tilted structure (Boynton, Crosa, and Deeter 1980), or self excited nonlinear mass flow oscillations (Meyer, and Meyer-Hofmeister 1984); c) A centrally located clock mechanism that originates from the precession of the neutron star, Her X-1 (Brecher 1972; Pines, Pethick, and Lamb 1973; Lamb *et al.* 1975; Trümper *et al.* 1986). Due to the imprecise nature of the turnons and the large amplitude of phase excursions Boynton, Crosa, and Deeter (1980) have argued that the origin of the 35 day clock cannot reside in more precise mechanisms such as the precession of HZ Her or Her X-1. Trümper et al. (1986), on the other hand, have presented clear evidence for

changes of 1.24 s pulse profiles throughout the 35 day cycle that fits a precessing neutron star picture thus making this model viable again. The precession model was further developed by Kahabka (1987) using a pulse decomposition method in which the pulse profiles are fitted with a physical beaming model initially developed by Kaminker *et al.* (1982, 1983) where the angular dependence of the emerging radiation in an atmosphere with strong magnetic field has been investigated. With this beaming model it was possible to associate with each pulse profile a theoretical shape parameterized with the viewing geometry of a dipole field. Thus, it was possible to determine the precession parameters: the angle between the figure axis of the neutron star and its rotation axis as $10° - 25°$; the angle between the figure axis and the dipole axis as $65° - 75°$. A recent analysis of the HEAO-1 A-4 low-energy detector data from Her X-1 has shown that the relative intensity of the two poles can also change rapidly during the main-on state (Soong *et al.* 1987), thus casting doubt on the determination of precession parameters based on relative intensity of the two poles of the neutron star. However, the pulse shape decomposition analysis of Kahabka (1987) still shows that the beam profile model fits to the precession parameters are valid.

One previous objection to the precession model, the inaccuracy of the clock mechanism, has further been examined by Ögelman (1987), and concluded that, in addition to the poor quality clock models with white period noise, an alternative possibility exists which implies that the intrinsic clock is good and that the turnon phase fluctuations can be modelled with white phase noise plus an integrating filter with about 1.5 to 7 year timescale which may originate in the timescales of the mass transfer process from HZ Her.

The implications of neutron star precession on the dynamics of the superfluid interior of the neutron star has been re-examined by Alpar and Ögelman (1987). They find that the superfluid interior of the star has steady states in which the interior follows the crust's precession. The steady state of the core superfluid is determined by the internal torque on it which is linear in the lag between the rotation rates of the superfluid and the crust. Furthermore, the pinned crust superfluid also takes part in the precession through vortex creep. The constraint of absolute pinning which, as shown by Shaham (1977) would change the precession frequency drastically, is never operative because a steady state exists in the regime where the creep rate is linear in the lag between the pinned superfluid and the crust. Using the current understanding of the neutron star interior based on observations of radio pulsars, they show that the torques necessary to make up for the dissipation do not exceed those available in the Her X-1/ HZ Her binary system.

Pines (1987) has shown that the precession of Her X-1 can be used to constrain the neutron matter equation of state. Effectively, the current observed oblateness $\epsilon \sim \Omega_{prec}/\Omega_{rot} \sim 4 \times 10^{-7}$ can be related to the maximum period P_o^{max} at which the crust has solidified. A stiff equation of state gives $P_o^{max} \sim 20$ ms, in contrast to a very soft equation of state where $P_o^{max} \sim 1.5$ ms. In view of our understanding of initial birth periods of pulsars which should not be as short as 1.5 ms, the very soft equations of state are unlikely to be valid if Her X-1 is precessing at the 35-day period. To be able to study nuclear forces through X-ray observations of astrophysical objects is a fine example of the progress of scientific understanding

through the advances in very different fields.

ACKNOWLEDEMENTS: I acknowledge my collegues at the MPE X-ray group for many helpful discussions. I thank Konrad Dennerl for carefully going over this manuscript, correcting my errors, and making suggestions for improving its readability.

REFERENCES:

Alpar, A., and Ögelman, H.: 1987, *Astron. Astrophys.* **185**, 196.

Anzer, U. and Börner, G.: 1980, *Astron. Astrophys.* **83**, 133.

Anzer, U. and Börner, G.: 1983, *Astron. Astrophys.* **122**, 73.

Bondi, H. and Hoyle, F.: 1944, *Mon. Not. R. astr. Soc.* **104**, 273.

Boynton, P.E., Crosa, L.M., and Deeter, J.E.: 1980, *Astrophys. J.* **237**, 169.

Boynton, P.E.: 1981, in *Pulsars, IAU Symposium No. 95*, eds. W. Sieber and R. Wielebinski (Reidel, Dordrecht), p. 279

Boynton, P.E. *et al.* : 1984, *Astrophys. J. (Letters)* **283**, L53.

Brecher, K.: 1972, *Nature,* **239**, 325.

Davidson, K. and Ostriker, J.P.: 1973, *Astrophys. J.* **179**, 585.

Eggleton, P.P.: 1983, *Astrophys. J.* **268**, 368.

Fahlman, G.G. and Gregory, P.C.: 1983, in *Supernova Remnants and their X-ray Emission, IAU Symposium No. 101*, eds. J. Danziger and P. Gorenstein, (Reidel, Dordrecht), p. 445

Ghosh, P. and Lamb, F.K.: 1978, *Astrophys. J.* **223**, L83.

Ghosh, P. and Lamb, F.K.: 1979a, *Astrophys. J.* **232**, 259.

Ghosh, P. and Lamb, F.K.: 1979b, *Astrophys. J.* **234**, 296.

Giacconi, R., Gursky, H., Paolini, F.R. and Rossi, B.B: 1962, *Phys. Rev. Lett.* **9**, 439.

Henrichs, H.F.: 1983, in *Accretion Driven Stellar X-Ray Sources*, eds. W.H.G. Lewin and E.P.J. van den Heuvel (Cambridge University Press, Cambridge), p. 393.

Hewish, A., Bell, S.J., Pilkington, J.D.H., Scott, P.F., and Collins, R.A.: 1968, *Nature,* **217**, 709.

Hoyle, F., Narlikar, J.V., and Wheeler, J.A.: 1964, *Nature,* **203**, 914.

Illarionov, A.F. and Sunyaev, R.A.: 1975, *Astron. Astrophys.* **39**, 185.

Kahabka, P.: 1987, MPE report 204.

Kaminker, A.D., Pavlov, G.G., and Shibanov. Y.A.: 1982, *Ap. Space Sci.* **86**, 249.

Kaminker, A.D., Pavlov, G.G., and Shibanov. Y.A.: 1983, *Ap. Space Sci.* **91**, 167.

Katz, J.I.: 1973, *Nature Pys. Sci.*,**246**, 87.

Kopal, Z.: 1978, *Dynamics of Close Binary Systems*, Reidel.

Lamb, F.K., Pethick, C.J. and Pines, D.: 1973, *Astrophys. J.* **184**, 271.

Lamb, D.Q., Lamb, F.K., Pines, D., and Shaham, J.: 1975, *Astrophys. J. (Letters)* **198**, L21.

Landau, L.D.: 1932, *Phys. Z. Sowjetunion*, **1**,285.

Lewin, W.H.G, Joss, P.C.: 1983, in *Accretion Driven Stellar X-Ray Sources*, eds. W.H.G. Lewin and E.P.J. van den Heuvel (Cambridge University Press, Cambridge), p. 41.

Meyer, F., and Meyer-Hofmeister, E.: 1984, *Astron. Astrophys.* **140**, L35.

Murakami, T., Kawai, N., Makishima, K. and Mitani, K.: 1984, *Publ. Astron. Soc. Japan* **36**, 691.

Ögelman, H.: 1987, *Astron. Astrophys.* **172**, 79.

Pacini, F.: 1967, *Nature,* **216**, 567.

Paczynski, B.: 1971, *Ann. Rev. Astr. Astrophys.* **9**, 183.

Paczynski, B. and Sienkiewicz,R.: 1981, *Astrophys. J. (Letters)* **248**, L27.

Parmar, A.N. and White, N.E.: 1988, *EXOSAT* Preprint No 72, to appear in *X-Ray Astronomy with EXOSAT*, Ed. R. Pallavicini and N.E. White, **Journal of the Italian Astr. Soc.**

Petterson, J.A.: 1975, *Astrophys. J. (Letters)* **201**, L61

Petterson, J.A.: 1977, *Astrophys. J.* **218**, 783

Pines, D., Pethick, C.J., and Lamb, F.K.: 1973, *Astrophys. J.* **184**, 271.

Pines, D.: 1987, *in High Energy Phenomena Around Collapsed Stars*, ed. F. Pacini (Reidel, Dordrecht), p. 193.

Priedhorsky, W.C. and Holt, S.S.: 1987, *Space Sci. Rev.* **45**, 269.

Pringle, J.E.: 1981, *Ann. Rev. Astr. Astrophys.* **19**, 137.

Rappaport, S., Joss, P.C. and Webbink, R.F.: 1982, *Astrophys. J.* **254**, 616.

Rappaport, S.A. and Joss, P.C.: 1983, in *Accretion Driven Stellar X-Ray Sources*, eds. W.H.G. Lewin and E.P.J. van den Heuvel (Cambridge University Press, Cambridge), p. 1.

Roberts, J.W.: 1974 *Astrophys. J.* **187**, 575.

Rose, W.K.: 1977, *Recognition of Compact Objects*, eds. H. Ögelman and R. Rothschild, NASA SP-421, p. 55

Rothschild, R.: 1977, *Recognition of Compact Objects*, eds. H. Ögelman and R. Rothschild, NASA SP-421, p. 125

Roy, A.E.: 1982, *Orbital Motion*, Adam Hilger, Bristol

Savonije, G.J.: 1983, in *Accretion Driven Stellar X-Ray Sources*, eds. W.H.G. Lewin and E.P.J. van den Heuvel (Cambridege University Press), p. 343.

Seward, F.D., Charles, P.A. and Smale, A.P.: 1986, *Astrophys. J.* **305**, 814.

Shaham, J.: 1977, *Astrophys. J.* **214**, 251

Shapiro,S.L. and Teukolsky, S.A.: 1983, *Black Holes, White Dwarfs, and Neutron Stars*, John Wiley & Sons (New York), p. 64.

Shklovskii, I.S.: 1967, *Astron. Zhur.*, **44**, 930.

Skinner, G.K., Bedford, D.K., Elsner, R.F., Leaky, D., Weisskopf, M.C. and Grindlay, J.: 1982, *Nature,* **297**, 568.

Soong, Y., Gruber, D.E., and Rothschild, R.E.: 1987, *Astrophys. J. (Letters)* **319**, L77.

Tananbaum, H., Gursky, H., Kellog, E.M., Levinson, R., Schreier, E., and Giacconi, R.: 1972, *Astrophys. J. (Letters)* **174**, L143.

Tsuruta, S., and Cameron, A.G.W.: 1966, *Nature,* **211**, 356.

Trümper, J., Pietsch, W., Reppin, C., Voges, W., Staubert, R., Kendziorra, E.: 1978, *Astrophys. J. (Letters)* **219**, L105.

Trümper, J., Kahabka, P., Ögelman, H., Pietsch, W., and Voges, W.: 1986, *Astrophys. J. (Letters)* **300**, L63.

van den Heuvel, E.P.J.: 1983, in *Accretion Driven Stellar X-Ray Sources*, eds. W.H.G. Lewin and E.P.J. van den Heuvel (Cambridge University Press, Cambridge), p. 303.

Verbunt, F. and Zwaan, C.: 1981, *Astron. Astrophys.* **100**, L7.

Voges, W., J., Pietsch, W., Reppin, C., Trümper, J., Kendziorra, E., Staubert, R.: 1982, *Astrophys. J.* **263**, 803.

Wang, Y.-M.: 1987, *Astron. Astrophys.* **183**, 257.

Wheeler, J.A.: 1966, *Ann. Rev. Astr. Astrophys.* **4**, 393.

White, N.E.: 1987, in *The Origin and Evolution of Neutron Stars*, eds. D.J. Helfand and J.-H. Huang, Reidel, p. 135.

Woltjer, L.: 1964, *Astrophys. J.* **140**, 1309.

GALACTIC POPULATIONS OF X-RAY BINARIES

Jan van Paradijs
Astronomical Institute "Anton Pannekoek",
University of Amsterdam

Abstract

The Galaxy contains two major groups of accretion-driven stellar X-ray sources, the high-mass and the low-mass X-ray binaries. In this paper the properties of these two types of sources are briefly described, with some emphasis on optical observations. The differences between their properties are likely related to a large difference in the magnetic fields of the neutron stars in these objects. A brief discussion is given of the evidence that magnetic fields of neutron stars decay.

Introduction

The properties of the spectra of the first two optically identified X-ray sources, Sco X-1 [57] and Cyg X-2 [15] led to early speculation that their X-ray luminosity is generated by accretion onto a compact star in a mass-transfer binary star. In the case of Sco X-1 the spectrum was found to be similar to those of old novae and U Gem type stars, which were known to be binary stars, in particular through the work of Crawford and Kraft [11,24] in the 1950s and '60s. The optical spectrum of Cyg X-2 was found to be composite, showing the signatures of both an F-type giant and a component of much higher excitation; Cyg X-2 also showed significant radial-velocity variations. However, the single most important characteristic of a binary star, i.e. an orbital periodicity, was not found in either system until many years later, in spite of substantial effort (see e.g. [19,25] for discussions of early optical observations of X-ray sources, and references).

The idea that the bright galactic X-ray sources are binary stars gained immediate acceptance with the discovery [58] of the eclipsing binary X-ray pulsar Centaurus X-3, which showed persuasively that in this system the X rays are generated by accretion onto a strongly magnetized neutron star rotating at the observed 4.8 s pulse period. The properties of the X-ray orbit showed that the mass-transferring companion star is very massive ($> 10\ M_\odot$), a result which was later confirmed by the optical identification of this source with an O-type giant star

H. Ögelman and E. P. J. van den Heuvel (eds.), Timing Neutron Stars, 191–207.

[26]. The discovery that Cen X-3 is an X-ray binary star was soon followed by more observations of eclipsing X-ray sources, some of them pulsating, and the identification of these X-ray sources with early-type stars (see e.g. [36, 49, 80]). In addition, a general framework for the origin and evolution of a massive X-ray binary, as a rather normal episode in the life of a massive close binary star with successive stages of mass transfer between the two components, was readily accepted [70]. Thus, within a few years the existence of a galactic population of high-mass X-ray binaries (HMXB) was well established.

The clustering of bright X-ray sources within ~30° of the direction of the galactic center without a strong background of unresolved sources showed already quite early that there is a group of sources located in the central regions of the Galaxy [55,59]. It was therefore suspected that apart from the above-described HMXB there is a class of low-mass X-ray binaries (see e.g. [56]), but proof for this basic idea was hard to obtain. Apart from the difficulty of finding orbital periods, the apparent heterogeneity of the properties of low-mass X-ray binaries (LMXB) probably played a role. Compared to the HMXB the first handful of systems now classified as LMXB (Her X-1, Cyg X-3, Sco X-1, Cir X-1) show rather more diversity than similarity in their properties. As a result, the establishment of two broad groups of galactic X-ray sources has come slowly, and along various roads: only at the end of the 1970's it became clear that with respect to their sky distributions, X-ray spectral characteristics, optical properties, and types of X-ray variability, the LMXB are distinct from the HMXB as a group with "family traits" (see e.g. [31]). The LMXB comprise the globular cluster X-ray sources, X-ray bursters, soft X-ray transients, and the bright galactic bulge X-ray sources (most of which have recently been found to be QPO sources; see [35] for a review).

In this paper I briefly describe the main properties of the HMXB and LMXB, with some emphasis on optical observations, and show how the differences between these two groups of X-ray sources may be linked to a difference in the strength of the magnetic fields of the neutron stars they harbour. Within the limits of these conference proceedings I cannot strive for completeness. For background information on various topics related to X-ray binaries the interested reader is advised to consult individual chapters in [12, 13, 14, 33, 34, 41, 46, 51, 60]. References on optically identified individual sources can be found in [3, 76].

Optical counterparts

The optical counterparts of HMXB have normal early-type spectra, in the sense that they can be MK-classified without particular difficulty, on the basis of ratios of spectral line strengths. Some disturbance of the spectrum, indicative of anisotropic gas flow near the primary may show up as variable emission/absorption components, particularly in Hα,β, He II λ4686, and the CIII-NIII λ4640 complex. However, when the latter two lines are strongly in emission (see e.g. [18]) this is likely due to a very early spectral type (Of characteristics) of the primary, and not to the presence of the X-ray source.

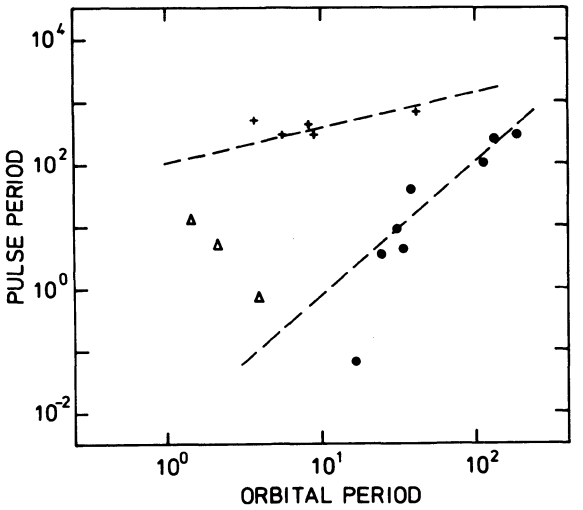

Fig. 1: Relation between pulse period and orbital period for three types of high-mass X-ray binaries: Be/X-ray sources (filled circles), non-Be wind-driven X-ray sources (crosses), and non-Be/X-ray sources driven by Roche-lobe overflow (triangles). See refs 7, 8, 82.

The reason that the X-ray source does not seem to affect the spectral properties of the primary much, is that the bolometric luminosity of the latter generally exceeds the X-ray luminosity, often by a large margin (see [76]).

With respect to the spectral types of the optical counterparts the HMXB can be subdivided into two subgroups, as follows.

(i) The spectral type is earlier than B2, and the luminosity class is I to III, i.e. the primary star has evolved off the main sequence. These stars are filling, or close to filling their Roche lobes, as is apparent from the amplitudes of their optical light curves (see below).

(ii) The primary is a B-emission (Be) star, located in the Hertzsprung-Russell diagram rather close to the main sequence. The orbits of these Be/X-ray binaries are eccentric, and their periods tend to be long. The primaries underfill their Roche lobes.

As first suggested in [38] the mass transfer in these two groups is

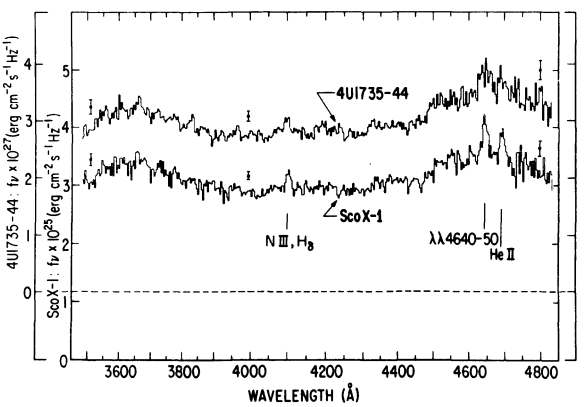

Fig. 2: Optical spectra of the low-mass X-ray binaries Sco X-1 and 4U/MXB 1735-44 (a burst source). The similarity of these spectra is striking (ref. 42).

driven by different mechanisms. In the first group mass is transferred via a strong stellar wind (in a few short-lived sources Roche-lobe overflow is important). In the Be/X-ray binaries the mass transfer is related to the anisotropic (often highly variable) shedding of mass as observed in all Be stars, which is believed to be the result of their rapid rotation [61]. This inferred difference in mass transfer mechanism is supported by the different relations between orbital period and X-ray pulse period (first pointed out in [7, 8] for these two groups of sources (see e.g. the discussion in [72]).

Most Be/X-ray binaries are highly variable, or transient. In some of them recurrent outbursts have been observed, which reflect the varying accretion rate onto the neutron star as it moves in its eccentric orbit through regions of varying density around the Be star. In addition, a more sudden turning on and off of the accretion can occur when the wind density becomes too low for the neutron star magnetosphere to be within the corotation radius, so that accretion becomes centrifugally inhibited [65]. However, in many cases outbursts have been observed which are not related to the orbit of the Be/X-ray binary, but are due to a sudden enhancement of the mass loss of the Be star (for recent reviews of various aspects of Be stars see [62]).

The optical counterparts of LMXB are rather faint stars. Their spectra show a few characteristic emission lines, particularly Hα,β, HeII λ4686, and CIII/NIII λ4640, superposed on a flat (in frequency) continuum. These spectra, which definitely are not those of normal stars, are dominated by the emission from an acretion disk around a neutron star, which radiates mainly through reprocessing of incident X rays into optical/UV photons. In very few cases the signature of a companion star can be discerned.

It appears that the optical properties of LMXB are rather uniform,

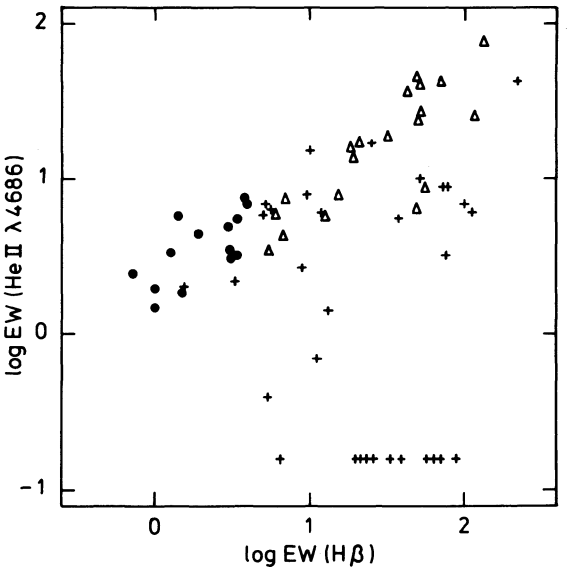

Fig. 3: Relation between the equivalent widths of the HeII 4686 line and H-beta. Low-mass X-ray binaries are indicated by filled dots, magnetic cataclysmic variables by triangles, and non-magnetic cataclysmic variables by crosses (adapted from ref. 77).

and can be well described by average values [76]. The colour indices B-V and U-B (reddening-corrected) have average values of 0.0 ± 0.3, and -0.9 ± 0.2, respectively (errors are one sigma standard deviations), close to those expected for a flat continuum (F_ν = constant). The distribution of the ratio of X-ray to optical luminosity is rather sharply peaked. Expressed in terms of an "optical/X-ray colour index" B_0 +2.5 log $F_X(\mu Jy)$, the peak occurs at 21.5, corresponding to a ratio of fluxes emitted in X rays (2-11 keV) and in optical light (3000-7000 A) of ~350.

Absolute visual magnitudes have been estimated for optical counterparts of X-ray burst sources and some soft X-ray transients, for which a reasonable distance determination can be made. These absolute magnitudes (average value M_V = 1.0) scatter over a remarkably small interval of ± 1 magnitude [76]. This small scatter may be related to a rather small range in orbital periods of the systems used in this average. If the relative shape of the accretion disk (in particular its angular thickness as seen from the neutron star) is assumed to be independent of the orbital period then the X-ray irradiated accretion disk will (for the same X-ray luminosity) be hotter as the orbital period decreases since they are then smaller [T^4 (:) a^{-2} (:) $P^{-4/3}$]. A relatively larger fraction of its emission will then be in the UV (i.e. the bolometric correction increases).

It is of some interest to compare the optical properties of LMXB with the closely related cataclysmic variables (CVs), which are different in that the accreting compact star is not a neutron star but a white dwarf. The spectra of CVs bear a general resemblance to those of LMXB, showing emission lines superposed on a continuum. However, in general the equivalent widths of these lines in LMXB spectra, in particular that of Hβ, are much smaller than those in CV spectra [77] (see Fig. 3). Since the absolute magnitudes of LMXB and CV differ by values ranging between ~3.5 mag (for nova-like variables, and dwarf novae in outburst) and at least 6 mag (for dwarf novae in quiescence) the luminosities in Hβ are substantially higher in the LMXB than in CV. In general, the equivalent width of HeII λ4686 varies somewhat less

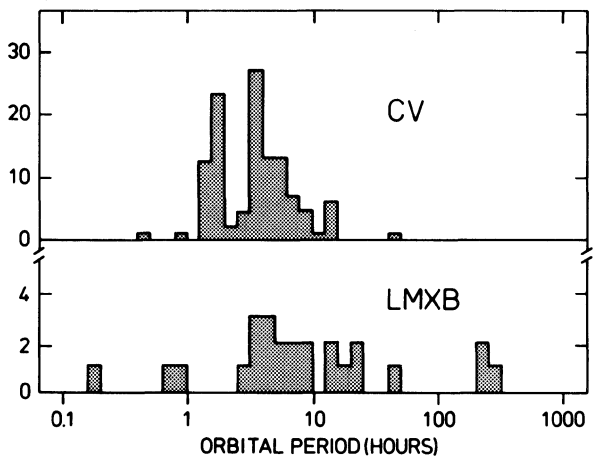

Fig. 4: Distributions of orbital periods for low-mass X-ray binaries and cataclysmic variables. Data have been taken from refs 47 and 53, except that we have not included LMC X-2 (for which recent observations give no evidence for a 6.4 h period), and have included the 15.1 h period system Cen X-4 (ref. 5).

between the LMXB and CV (except the AM Her systems); this suggests that in the LMXB the luminosity in this line is enhanced by X-ray reprocessing by a similar factor as the continuum flux.

The orbital-period distributions of CV and LMXB (see Fig. 4) are different. Compared to the CV there is a relatively larger fraction of LMXB with periods above about half a day; this may partly reflect the fact that CV systems with long orbital periods may be classified as symbiotic stars. Also, there are no LMXB in the period range between 1 and 2 hours (i.e. below the period gap), which is well populated by the CV. This is perhaps the result of evaporation of the companion stars by the large luminosity from the rapidly rotating neutron star (spun up by accretion torques), which becomes active as the mass transfer stops when the system has reached the upper edge of the period gap [54, 73].

Optical light curves of HMXB and LMXB

Regular optical brightness variations at the orbital period have been observed for many HMXB and LMXB.

In almost all HMXB an important contribution to the orbital optical light curve is due to a double-wave modulation with generally equal maxima and two somewhat different minima. This so-called ellipsoidal variation is the result of the tidal and rotational distortion of the companion star, and a non-uniform surface brightness distribution ("gravity darkening"), often described by Von Zeipel's theorem. The maxima in the light curve occur at quadratures of the system, the deepest minimum at inferior conjunction of the X-ray source. The amplitude of these ellipsoidal light curves is mainly determined by the mass ratio $q = M_{opt}/M_X$, the inclination angle i of the orbital plane, and a dimensionless potential parameter Ω, which measures how far the companion star fills its Roche lobe.

Superposed on the regular orbital brightness variations significant irregularity is observed; consequently observations over many orbital cycles are required to obtain a fair estimate of the average light curve that hopefully contains information on the geometry of the primary.

In some systems (e.g. Cen X-3, SMC X-1) the presence of the X-ray source is noticeable through the heating by X rays of the hemisphere of the companion star facing the X-ray source. This leads to a brightening of that side of the star and therefore a filling-in of the deepest minimum of the purely ellipsoidal light curve.

A further complication in the light curve arises when an accretion disk is present, which: (i) provides an additional source of light; (ii) can give rise to mutual eclipses with the companion ; (iii) shields a fraction of the companion star from X rays. Since those HMXB in which mass transfer occurs through Roche-lobe overflow (and which therefore have an accretion disk) are also the most luminous X ray sources, the effects of X-ray heating and of the presence of the acretion disk tend to be present together.

In Fig. 5 we show some examples of optical light curves of HMXB, illustrating the above mentioned effects. For detailed description of the light curves of HMXB, and discussions of the limitations and

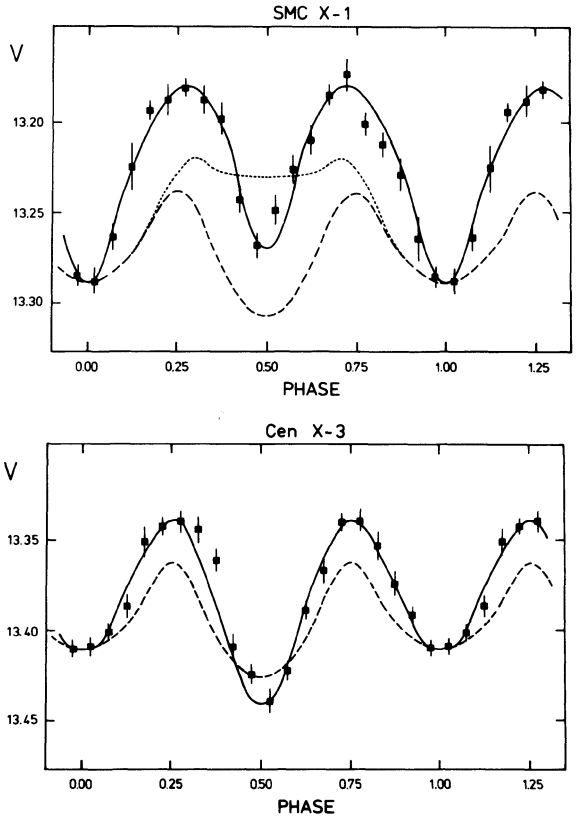

Fig. 5: Optical light curves for the high-mass X-ray binaries SMC X-1 and Cen X-3. Observed data are indicated by squares. In both cases the dashed line indicates the expected purely ellipsoidal light curve. The dotted line for SMC X-1 shows the effect of X-ray heating of the companion star. The solid curves indicate the theoretical curves which include ellipsoidal variations, X-ray heating, and the effects of an accretion disk (see ref. 68).

underlying assumptions, we refer to [68, 86].

Optical counterparts of LMXB are generally faint, with apparent visual magnitudes V > 17 in the majority of cases. With notorious exceptions (e.g. Sco X-1 [85]) orbital variations of the optical brightness are not too difficult to detect, particularly since the use of CCD photometers has become commonplace. As a result orbital light curves have now been determined for many optically identified LMXB.

As mentioned above, the optical emission of LMXB comes mainly from X-ray reprocessing in matter in the binary system. Orbital light variations are therefore due to deviations from axial symmetry of the reprocessing matter. This asymmetry is mainly provided by the companion star, whose "polar caps" are not shielded from X rays by the disk, and therefore are heated (see below).

The orbital light curves of LMXB show "family characteristics"; their amplitude is correlated with the inclination, i, of the orbital plane (see Fig. 6) , and also their shape seems to change with i in a characteristic way.

For low inclination angles (as apparent from the lack of X-ray eclipses and X-ray "dips", see [47]) the light curves are approximately sinusoidal (see Fig. 7), with an amplitude of a few tenths of a

magnitude. For systems with somewhat higher inclination angles (as evident from the presence of periodic dips in the X-ray intensity curve, but absence of X-ray eclipses) the amplitude of this sinusoidal light curve increases to ~0.5 mag (e.g. X1755-338). For systems with the highest inclinations the amplitude reaches about 1.5 mag. For these

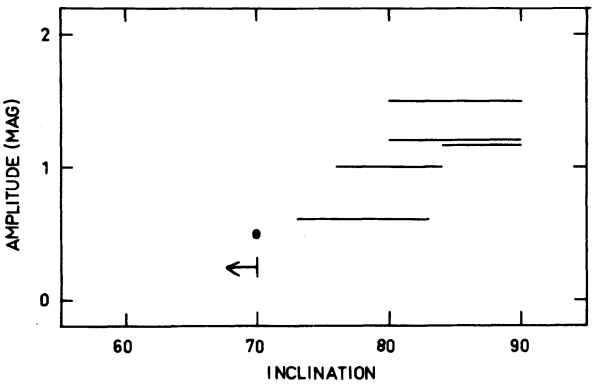

Fig. 6: Relation between orbital inclination and amplitude of the optical light curve for low-mass X-ray binaries. Data have been taken from ref. 39. Systems which show X-ray eclipses are represented by horizontal lines which indicate the allowed range of inclination. Three sources which show X-ray dips, but not eclipses, are assumed to have i = 70°. Sources which do not show eclipses or dips are likely to have smaller inclinations. Systems in which the companion star contributes significantly to the optical brightness have not been included in this Figure.

systems the optical light curve can be decomposed into the sine wave that is also observed for systems at lower inclinations, and a rather sharp cusp superposed on the minimum of the sine wave (see Fig. 7). From a comparison of the phases of the optical and X-ray intensity curves it appears that the cusp (and therefore the minimum of the sine wave component) occurs at superior conjunction of the X-ray source. This indicates that the cusp in the optical light curve is due to the eclipse of the luminous accretion disk. The relative phasing in the non-eclipsing system X1755-338 of the sinusoidal optical light curve, and the X-ray dips, confirm that this picture is valid also for the lower-inclination systems. The correlation of the amplitude of the sinusoidal component with inclination angle is likely due to the fact that as the inclination angle decreases the average brightness of the accretion diskincreases (larger projection factor, less self shielding), and the relative importance of the variable component (due to eclipses of the disk and the heating of the companion star) decreases.

Galactic distributions of optically identified HMXB and LMXB

The sky distributions of the optically identified HMXB and LMXB are shown in Fig. 8. The HMXB are distributed along the galactic plane, with

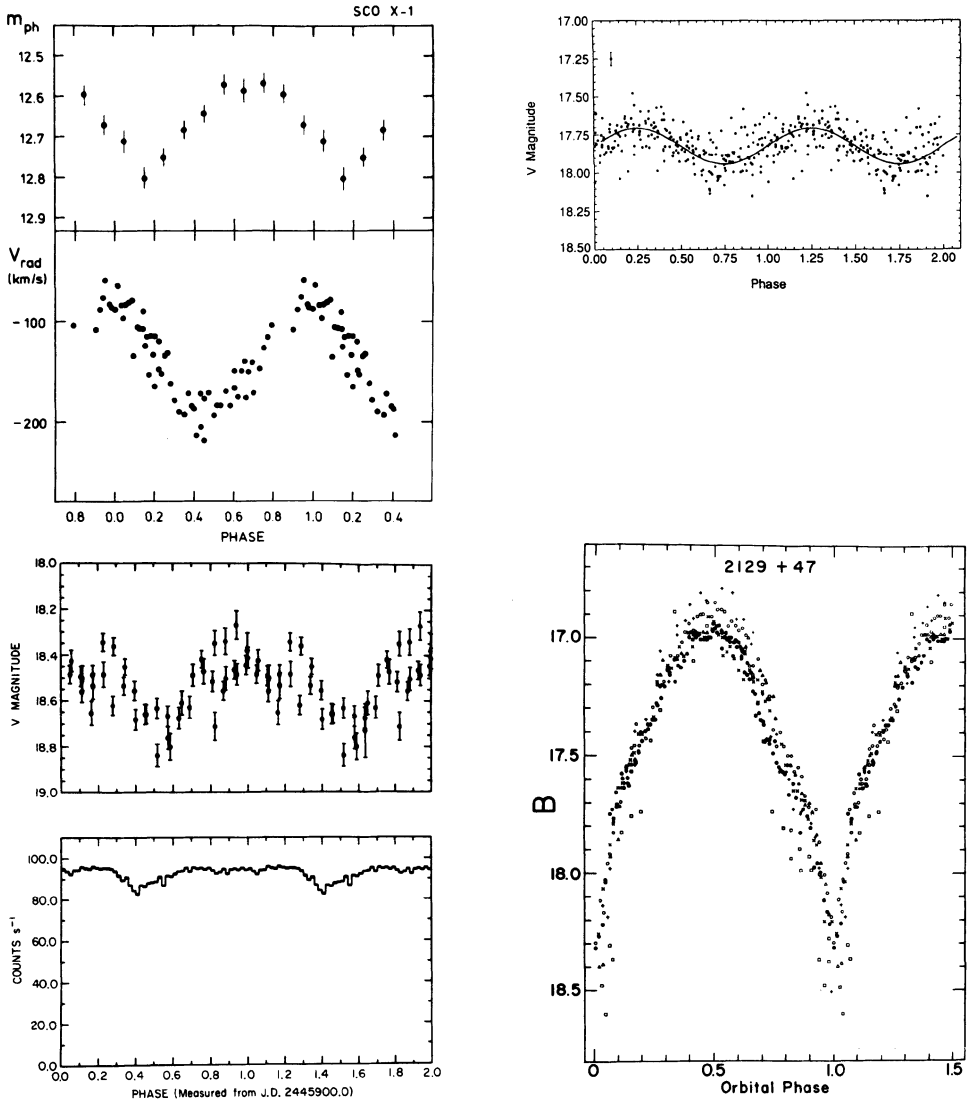

Fig. 7: Optical light curves for the low-inclination LMXB Sco X-1 (ref. 85) and 4U/MXB 1636-53 (ref. 63), the X-ray dipper X1755-338 (ref. 40), and the X-ray eclipsing system 4U2129+47 (ref. 43). In the case of Sco X-1 the radial-velocity curve (ref. 10) of the accretion disk shows that maximum light is reached when the X-ray source is in inferior conjunction. The X-ray intensity curve of the X-ray dipper X1755-338 suggests a similar phase relation for the optical maximum for this source.

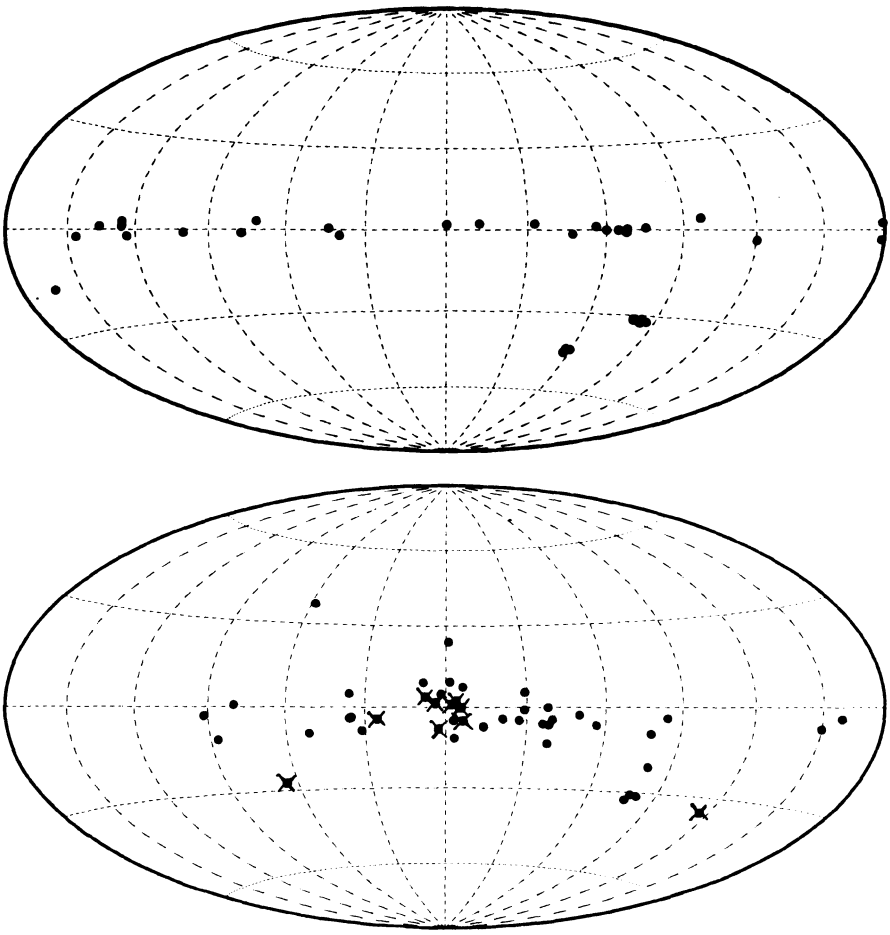

Fig. 8: Sky maps (in galactic corrdinates) of the optically identified high-mass X-ray binaries (top panel) and low-mass X-ray binaries (bottom panel); the latter also contains the globular-cluster X-ray sources (indicated by crossed square boxes).

a narrow latitude distribution ($\langle b^{II} \rangle = -0.5 \pm 3.9°$; if we leave out the very nearby high-latitude system X Per we find $0.2 \pm 1.9°$). The optical counterparts of LMXB have a much wider latitude distribution ($\langle b^{II} \rangle = -1.6 \pm 10.7°$), and are also more concentrated in the general direction of the galactic center.

These distributions fit the idea that the HMXB and LMXB are parts of a very young galactic population of massive stars (population I), and of a much older population (population II, and old disk poulation), respectively.

A recent detailed analysis [75] of the kinematic properties of the optically identified HMXB indicates that these objects are runaway stars; this is perhaps the result of asymmetries of the supernova explosions in which the (now) acreting neutron stars were formed [75].

The radial velocities of the LMXB optical counterparts support their membership of an old galactic population [9].

X-ray variability: pulsations and bursts

Almost all HMXB show X-ray pulsations, which indicates that the accreting compact stars in these systems are strongly magnetized neutron stars (for a review of various aspects of X-ray pulsars see e.g. [22, 52]). Strong magnetic fields (a few 10^{12} G) have also been inferred from the presence of cyclotron lines in the hard X-ray spectra of some X-ray pulsars (see [23], for a review of this subject).

Observed pulse periods range over a factor $\sim 10^4$, between 69 msec (for the LMC transient A0538-66) to 835 s in the Be/X-ray system X Per. From a survey of X-ray pulsars with HEAO-1 White et al. [84] found a correlation between the pulse profile and the X-ray luminosity; their result are supported by recent EXOSAT observations of the transient source EXO 2030+475 which cover a large range in luminosity [48].

Pulse-arrival time measurements for pulsating HMXB, in combination with radial-velocity observations of their massive companions, have provided invaluable information on the masses of neutron stars (see [22, 52] for a review). In Fig. 9 our present knowledge on neutron-star

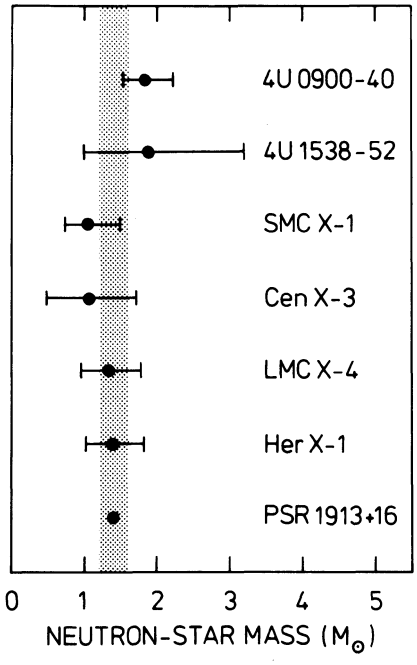

Fig. 9:
Summary of our present knowledge of neutron star masses from observations of binary X-ray pulsars and the binary radio pulsar PSR 1913+16. This Figure is an update from ref. 22, using more recent data from refs 50 and 82.

masses is summarized. These results are consistent with a standard neutron star mass between 1.2 and 1.6 $M_\odot$; however, mass differences of more than 0.5 $M_\odot$ cannot at present be excluded. The limiting factor in the accuracy of neutron star masses are the optical radial-velocity data (which so far have mainly been based on photographic and image-tube observations). Significant progress in this area in the form of much improved error ranges for these masses, and an extension of the sample of observed neutron stars, appears definitely possible with presently available CCD spectrographs.

X-ray pulsations occur only rarely in LMXB. This suggests that the magnetic fields of the neutron stars in these systems are much weaker than of those in HMXB. (The alternative that the magnetic and rotational axes of the neutron stars are aligned, is discussed below).

On the other hand, many LMXB emit X-ray bursts, which are the result of thermonuclear flashes in accreted matter on the surface of a neutron star (for reviews of X-ray bursts see [32, 78].

Not a single source is known that shows both pulsations and bursts. Apparently, the presence of a strong magnetic field suppresses the instability of the nuclear reactions that gives rise to bursts (as expected from models for thermonuclear flashes, see e.g. [21]). This mutual exclusion of bursts and pulsations indicates that it is a weaker magnetic field, and not only alignment of the field axis, which distinguishes the neutron stars in LMXB from those of HMXB.

The radiation observed during an X-ray burst originates directly from the surface of the neutron star (with possibly some modification

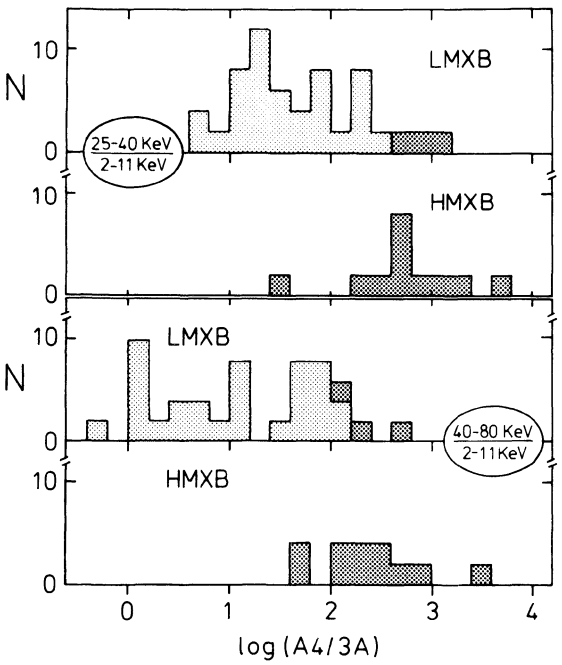

Fig. 10: Distributions of the ratios of count rates, as observed with the HEAO-1 A4 experiment (ref. 30) in the 25-40 keV and 40-80 keV bands, to that observed with Ariel 5 in the 2-11 keV band (refs 44, 81), shown separately for the high-mass and low-mass X-ray binaries. X-ray pulsars are indicated by a darker shade.

due to e.g. Compton scattering in intervening hot plasma). Because of this, time-resolved spectral studies of bursts provide an observational method to study the properties of neutron stars, in particular their mass-radius relation. The main problem in this area appears to be the interpretation of X-ray burst spectra in terms of atmospheric models (see [78] for a recent discussion of this topic).

X-ray spectra

The X-ray spectra of HMXB (most of which are pulsars) are generally much harder than those of LMXB [20, 45, 67, 83]. This distinction is present for both the steady and transient X-ray sources [6]. As is illustrated in Fig. 10 the difference in spectral hardness persists into the hard X-ray energy range, up to $\sim 10^2$ keV. From this Figure it appears that the average difference in spectral hardness, as measured by the ratio of the count rates observed with the A4 experiment on HEAO-1 [30] and with the SSI on Ariel-5 [44, 81], is about a factor 10.

It is remarkable that the few LMXB which show pulsations (GX 1+4, Her X-1, and 1627-673) have X-ray spectra which are as hard as those of HMXB (almost all of which are, likewise, pulsars). This result strongly suggests that the division into hard and soft X-ray spectra is related to a difference in the geometry of the accretion flow. For neutron-star magnetic fields of the order of 10^{12} G, and sub-Eddington accretion rates, the accretion flow is dominated by the magnetic field within a relatively large distance (of the order of 10^3 km) from the neutron star (magnetospheric radius, see e.g. [17]); a large fraction of the inflowing matter reaches the neutron star via an accretion column on a relatively small area (near the polar caps). For magnetic fields $< 10^9$ G the magnetospheric radius becomes comparable to the radius of the neutron star; one then expects that the accreting material is distributed over a larger fraction of the neutron star surface.

It should be noted that alignment of the magnetic and rotational axis of the neutron star may also lead to the disappearance of pulsations, even for fields of 10^{12} G. However, since the magnetospheric radius will not be much affected by this alignment one does not expect the accretion flow within $\sim 10^3$ km of the neutron star to be much affected by the alignment; it is therefore unlikely that alignment alone can explain the systematic difference in the hardness of the X-ray spectra of pulsating and non-pulsating sources. Thus, the differences in these X-ray spectra support the inference, from the distribution of pulsars and bursters among the HMXB and LMXB, that the magnetic fields of the neutron stars in LMXB are systematically weaker than those of the neutron stars in HMXB.

In many LMXB a correlation has been observed between the X-ray intensity and the hardness of the X-ray spectrum (see [35] for references). In addition to this so-called normal-branch (NB) spectral state a number of LMXB have, at times, been observed in a different state, in which the X-ray spectrum is relatively hard (but still much softer than the X-ray spectra of pulsars), and does not change much with

source intensity (horizontal branch: HB). These different spectral states are correlated with different fast-variability behaviour, with high-frequency intensity-dependent QPO occurring in the HB state, and low-frequency QPO (~5 Hz, independent of source intensity) occurring in the NB state [74]. Recently, a third spectral state (the "flaring branch" in the spectral hardnesss vs. intensity diagram) has been distinguished, which also is correlated with QPO behaviour [16]. The origin of the different spectral states, and the connection to the QPO properties is presently unknown.

For reviews of QPO in LMXB with emphasis on observations and data analysis we refer to [35] and the contributions of Hasinger and of Van der Klis to the present volume. For a recent review with emphasis on models for QPO see [29].

Magnetic field decay ?

The strong correlation between X-ray pulsars and HMXB on the one hand, and between X-ray bursters and LMXB on the other hand, and, in addition, the striking correlated difference in the persistent X-ray spectra of HMXB and LMXB (except for the LMXB pulsars), persuasively argues for a systematic difference in the magnetic field strengths of the neutron stars in these two groups of X-ray sources.

There are two possible ways to understand this difference. In the first place the magnetic fields of the (generally old) neutron stars in LMXB may be much weaker than those of the (young) neutron stars in HMXB, because they have always been very weak. This difference might be related to a difference in the formation mechanism of neutron stars in HMXB and LMXB, viz. via the normal evolution of a massive star, and via the accretion-induced collapse of a white dwarf, respectively (see e.g. [4]). With respect to the latter process it is of interest to note that for two of the three (old) LMXB which show pulsations (Her X-1, GX 1+4) the accretion lifetime can be calculated from the system parameters; these lifetimes of both systems turn out to be very short (of the order of 10^7 years) compared to a typical accretion lifetime of a LMXB (of the order of 10^9 years). This coincidence strongly suggests that in these LMXB pulsars the neutron star magnetic field is high because the neutron star was formed recently through accretion-induced collapse of a white dwarf during the same stage of accretion in which we observe the system now as a source of X rays.

As discussed in more detail in [64] the above idea is hard to reconcile with : (i) observed periods and period derivatives of new-born radio pulsars; (ii) the observed weak magnetic fields of the binary radio pulsars PSR 1913+16 and PSR 0655+64, which are late stages in the evolution of massive binary stars (see e.g. [69]); (iii) the statistics of CV's and LMXB in globular clusters [79].

It appears that the simplest description of the properties of LMXB vis a vis the HMXB is provided by the assumption that the magnetic fields of all neutron stars decay. This is in agreement with a simple interpretation of kinematic data of new-born radio pulsars [37]. We note that these kinematic data (and data on pulse profiles) have been been

interpreted as evidence for alignment of the rotational axis of the neutron star with the magnetic axis [2]; (see also the contribution of Blair to this Volume). However, this interpretation does not exclude that decay takes place.

It is possible that decay of a magnetic field takes place only in accreting neutron stars. As shown in [66] one cannot distinguish between spontaneous decay, and decay as a consequence of accretion; in particular the inferred B fields of neutron stars correlate well with the total amount of accreted material.

Observations of millisecond radio pulsars in binaries provide good evidence that the decay of the field of neutron stars does not continue indefinitely. From the colours of the optical counterpart of PSR 0655+64 (a white dwarf) Kulkarni [27] estimated that the (cooling-) age of this system is $\sim 2\ 10^9$ years, yet the magnetic field of the neutron star (as inferred from its period derivative) is a few 10^{10} Gauss. A similar conclusion follows from the observed number of millisecond pulsars in binaries which descended from LMXB [1, 71] (see also [28]). These results indicate that when the magnetic field has decayed to a value of the order of 10^{9-10} G (this value may be different for different sources) the decay time increases substantially (from $\sim 10^7$ to more than 10^9 years).

References

[1] Bhattacharya, D. & Srinivasan, G. 1986: Current Sci. **55,** 327.
[2] Blair, D.G. & Candy, B.N. 1988: preprint.
[3] Bradt, H.V. & McClintock, J.E. 1983: Ann. Rev. Astr. Aph. **21,** 13.
[4] Chanmugan, G. & Brecher, K. 1987: Nature **329,** 696.
[5] Chevalier, C. et al. 1988: Astr. Aph. (in press).
[6] Cominsky, L. et al. 1978: Aph. J. **224,** 46.
[7] Corbet, R.H.D. 1984: Astron. Aph. **141,** 91.
[8] Corbet, R.H.D. 1986: in ref. [62], p. 63.
[9] Cowley, A.P. et al. 1987: Aph. J. **320,** 296.
[10] Crampton, D. et al. 1976: Aph. J. **207,** 907.
[11] Crawford J.A. & Kraft R.P. 1956: Aph. J. **123,** 44.
[12] Eggleton, P.P. & Pringle, J.E. 1985: "Interacting Binaries", NATO ASI Series C, Vol. 150 (Reidel).
[13] Filip ov, L. & White, N.E. (eds) 1988: Proc. COSPAR/IAU Symposium "The Physics of Compact Objects: Theory versus Observations", Sofia, July 1987, (Pergamon Press).
[14] Frank, J., King, A.R. & Raine, D.J. 1985: "Accretion Power in Astrophysics", (Cambridge Univ. Press).
[15] Giacconi R. et al. 1966: Aph. J. (Lett.) **148,** L129.
[16] Hasinger, G. 1988: in ref. [13] (in press).
[17] Henrichs, H.F. 1983: in ref. [33], p. 393.
[18] Hensberge, G., Van den Heuvel, E.P.J. & Paes de Barros, M. 1973: Astron. Aph. **29,** 69
[19] Hiltner W.A. & Mook D.E. 1970: Ann. Rev. Astron. Aph. **8,** 139.
[20] Jones, C. 1977: Aph. J. **214,** 856.
[21] Joss, P.C. & Li, F.K. 1980: Aph. J. **238,** 287.

[22] Joss, P.C. & Rappaport, S.A. 1984: Ann. Rev. Astron. Aph. **24**, 537.
[23] Kirk, J. & Truemper, J. 1983: in ref. [33], p. 261.
[24] Kraft, R.P. 1962: Aph. J. **135**, 408.
[25] Kraft, R.P. 1973: I.A.U. Symposium **55**, 36.
[26] Krzeminski, W. 1974: Aph. J. (Lett.) **192**, L135.
[27] Kulkarni, S. 1986: Aph. J. (Lett.) **306**, L85.
[28] Kulkarni, S. & Narayan, R. 1988: Aph. J. (in press).
[29] Lamb, F.K. 1988: in ref. [13]
[30] Levine A.M. et al. 1984: Aph. J. Suppl. **54**, 581.
[31] Lewin, W.H.G. & Clark, G.W. 1980: Ann. New York Ac. Sci. **336**, 451.
[32] Lewin, W.H.G. & Joss, P.C. 1983: in ref [33], p. 41.
[33] Lewin, W.H.G. & Van den Heuvel, E.P.J. (eds), 1983: "Accretion-driven Stellar X-ray Sources", Cambridge Univ. Press.
[34] Lewin, W.H.G., Truemper, J. & Brinkmann, W. (eds) 1986: "The Evolution of Galactic X-ray Binaries", NATO ASI Series C, Vol. 167 (Reidel).
[35] Lewin, W.H.G., Van Paradijs, J. & Van der Klis, M. 1988: Space Sci. Rev. (in press)
[36] Liller, W. 1973: Aph. J. (Lett.) **184**, L23.
[37] Lyne, A.G. et al. 1982: M.N.R.A.S. **213**, 613.
[38] Maraschi, L., Treves A. & Van den Heuvel, E.P.J. 1975: Nature **259**, 292.
[39] Mason, K.O. 1986: in ref. [41], p. 29.
[40] Mason, K.O., Parmar, A.N. & White, N.E. 1985: M.N.R.A.S. **216**, 1033.
[41] Mason, K.O., Watson, M.G. & White, N.E. (eds) 1986: "The Physics of Accretion onto Compact Objects" Lecture Notes in Physics, Vol. 266, (Springer).
[42] McClintock, J.E., Canizares, C.R. & Backman, D.E. 1978: Aph. J. **223**, L75.
[43] McClintock, J.E., Remillard, R.A. & Margon, B. 1981: Aph. J. **243**, 900.
[44] McHardy, I.M., et al. 1981: M.N.R.A.S. **193**, 893.
[45] Ostriker, J. 1977: Annals New York Acad. Sci. **302**, 229.
[46] Pallavicini, R. & White, N.E. (eds) 1988: "X-ray Astronomy with EXOSAT" (Memorie della Societa' Astronomica Italiana), in press.
[47] Parmar, A.N. & White, N.E. 1988: in ref. [46].
[48] Parmar, A.N. et al. 1988: Aph. J. (in press).
[49] Penny, A.J. et al. 1973: M.N.R.A.S. **163**, 7P.
[50] Pietsch, W. et al. 1984: Space Sci. Rev. **40**, 371.
[51] Pringle, J.E. & Wade, R.A. (eds) 1985: "Interacting Binary Stars", (Cambridge University Press).
[52] Rappaport, S. & Joss, P.C. 1983: in ref. [33], p. 1.
[53] Ritter, H. 1987: Astr. Aph. Suppl. **70**, 335.
[54] Ruderman, M.A. et al. 1988: Aph. J. (in press)
[55] Ryter, C. 1970: Astr. Aph. **9**, 288.
[56] Salpeter, E.E. 1973: I.A.U. Symposium **55**, 135.
[57] Sandage A. et al. 1966: Aph. J. **146**, 316.
[58] Schreier E. et al. 1972: Aph. J. (Lett.) **172**, L112.
[59] Setti, G. & Woltjer, L. 1970: Aph. Space Sci. **9**, 185.
[60] Shapiro, S.L. & Teukolsky, S.A. 1983: "Black Holes, White Dwarfs and Neutron Stars", (John Wiley and Sons).

[61] Slettebak, A. 1987: in ref. [62], p. 24.
[62] Slettebak, A. & Snow, T.P. (eds) 1987: "Physics of Be Stars", (Cambridge Univ. Press).
[63] Smale, A.P. & Mukai, K. 1988: M.N.R.A.S. (in press).
[64] Srinivasan, G. et al. 1988: in preparation.
[65] Stella, L., White, N.E. & Rosner, R. 1986: Aph. J. **308**, 669.
[66] Taam, R.E. & Van den Heuvel, E.P.J. 1986: Aph. J. **305**, 235.
[67] Tananbaum, H. 1973: I.A.U. Symposium **55**, 9.
[68] Tjemkes, S., Zuiderwijk, E.J. & Van Paradijs, J. 1986: Astr. Aph. **154**, 77.
[69] Van den Heuvel, E.P.J. 1984: J. Aph. Astron. **5**, 209.
[70] Van den Heuvel, E.P.J. & Heise, J. 1972: Nature Phys. Sci. 239, 67.
[71] Van den Heuvel, E.P.J., Van Paradijs, J. & Taam, R.E. 1986: Nature **322**, 153.
[72] Van den Heuvel, E.P.J. & Rappaport, S. 1987: in ref. [62], p. 291.
[73] Van den Heuvel, E.P.J. & Van Paradijs, J. 1988: preprint
[74] Van der Klis, M. et al. 1987: Aph. J. (Lett.) **313**, L19.
[75] Van Oyen, J. 1988: submitted to Astr. Aph.
[76] Van Paradijs, J. 1983: in ref. [33], p. 189.
[77] Van Paradijs, J. & Verbunt, F. 1984, A.I.P. Conf. Proc. Vol. 115, p. 49.
[78] Van Paradijs, J. & Lewin, W.H.G. 1988: in ref. [46]
[79] Verbunt, F. & Meylan, G. 1988: Astr. Aph. (in press).
[80] Vidal, N.V. 1973: Aph. J. (Lett.) **182**, L77.
[81] Warwick R.S. et al. 1981: M.N.R.A.S. **193**, 865.
[82] Weisberg, J.M. & Taylor, J.H. 1984: in "Millisecond Pulsars", S.D. Reynolds & D.R. Stinebring (eds), p. 317.
[83] White, N.E. & Marshall, F.E. 1984: Aph. J. **281**, 354.
[84] White, N.E., Swank, J.H. & Holt, S.S. 1984: Aph. J. **270**, 711.
[85] Wright, E.L., Gottlieb, W. & Liller, W. 1975: Aph. J. **200**, 171.
[86] Zuiderwijk, E.J. 1979: Ph. D. Thesis, Univ. Amsterdam

TRANSIENT X-RAY SOURCES WITH LATE-TYPE COMPANIONS

Jeffrey McClintock
Harvard-Smithsonian Center for Astrophysics
60 Garden Street
Cambridge, Massachusetts 02138, U.S.A.

ABSTRACT. In a few short-period ($P \lesssim 1$ day) X-ray binaries it is possible to observe the late-type secondary. Two examples are the X-ray novae Cen X-4 and A0620-00. Optical studies have shown that the degenerate star in the former has the mass expected for a neutron star, whereas the compact object in the latter is considerably more massive and is a likely black hole. Another binary, 4U2129+47, which was a persistent X-ray source for at least several years, has been in an X-ray "off" state since mid 1983. Its optical appearance and behavior in the off state are wholly unexpected and puzzling given the compelling model that was developed earlier when the source was X-ray active. A fourth transient source discussed here, EXO 0748-676, is a 3.8-hour eclipsing binary, which has provided a fresh look at the properties of neutron-star shell flashes and accretion-disk coronae.

1. INTRODUCTION

About a quarter of the well-studied Low-Mass X-ray Binaries (LMXBs) are transient sources ($I_{max}/I_{min} > 100$) that undergo month-long to decade-long periods of X-ray quiescence (Bradt and McClintock 1983). Best known are the X-ray novae, or soft (spectrum) X-ray transients, which brighten to a maximum X-ray/optical intensity in a few days and then fade on a timescale of weeks to months.

During quiescence the X-ray luminosity of X-ray novae is thousands to millions of times less than during outburst; correspondingly, the optical intensity, which during outburst is due to reprocessed X-rays, dims by five magnitudes or more. Consequently, in a few favorable cases, it is possible to observe the late-type secondary directly. This is fortunate, since star light contains important and interpretable information, as I will illustrate by discussing two X-ray novae, Cen X-4 and A0620-00. For a broad review of the properties of X-ray novae see White et al. (1984) and van Paradijs and Verbunt (1984).

A few LMXB have transient episodes that are distinctly unlike those of the

H. Ögelman and E. P. J. van den Heuvel (eds.), Timing Neutron Stars, 209–218.

eruptive X-ray novae. For example, the large optical modulation of HZ Her/Her X-1 almost ceased for several years in the 1950's (as determined from an inspection of archival plates); presumably the X-ray source, Her X-1, was inactive then also (Jones et al. 1973). Another example is the (formerly) persistent source 4U2129+47. Its X-ray emission turned off in mid 1983 and since then the source has remained dormant. Recent studies of its quiescent optical counterpart, V1727 Cygni, have yielded surprising results, which are difficult to reconcile with earlier (X-ray on-state) models of this supposedly well-characterized system. This intriguing puzzle is outlined in Section 3.

The fourth and final transient discussed here is the 3.8-hour eclipsing, "dipping", bursting, coronal source EXO0748-676 (Parmar et al. 1986), which displays a wider range of phenomona than any other X-ray binary. It has proved, however, to be more than a freak: because it is a transient, it has provided important new data on how type I bursts and scattering coronae are affected by changes in luminosity.

It is probable that the transient nature of EXO0748-676 is more akin to that of 4U2129+47 than to an eruptive nova like A0620-00 (Parmar et al. 1986). In any case, the causes of alternating cycles of activity and quiescence in LMXB are poorly understood and are not considered here (see Hameury et al. 1986, and references therein).

2. X-RAY NOVAE: CEN X-4 AND A0620-00

In most X-ray active LMXB the light from the accretion disk overwhelms the feeble light of the late-type secondary. Consequently, because almost nothing definite is known about the properties of X-ray illuminated disks, most optical studies of active LMXBs have been rather unrewarding.

Fortunately, there are a few nearby X-ray novae (d~1 kpc) with relatively luminous secondaries ($M_v \sim 8$), which are bright enough for quiescent-state spectroscopic study. In particular, recent optical studies of the K-dwarf secondaries of two soft transients — A0620-00 and Cen X-4 — have yielded precise and insightful results. The absorption-line radial velocity data imply strongly that A0620-00 is a black hole (McClintock and Remillard 1986), whereas Cen X-4, which is a type I burst source, has the mass expected for a neutron star (Fig. 1; Cowley et al. 1988). For both systems the optical light curves are dominated by tidal (ellipsoidal) effects of the primary on the secondary (Fig. 1; Chevalier et al. 1988; McClintock and Remillard 1986), a process that can be modeled. Further study of these light curves, combined with measurements of the rotational widths of the K-star absorption lines, should provide useful information on the system parameters (orbital inclination and mass ratio) and further constrain the masses of the compact objects.

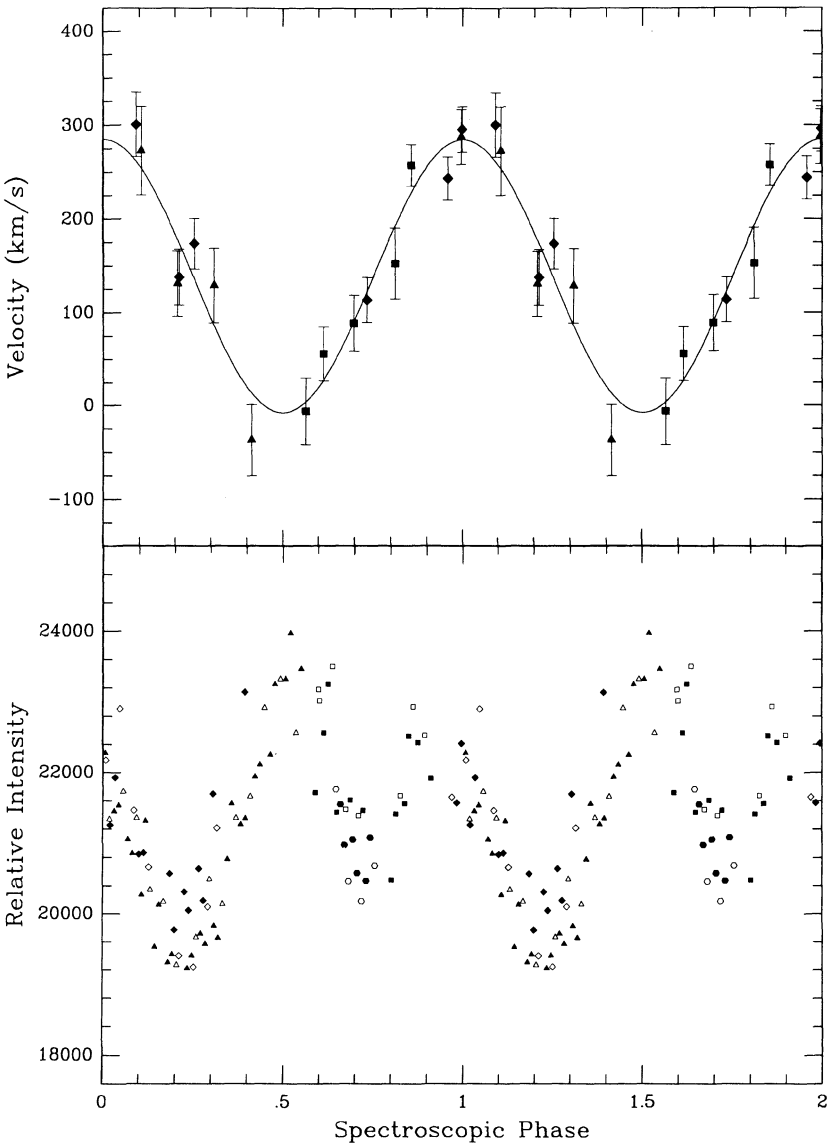

Figure 1. Simultaneous spectroscopic and photometric data for Cen X-4 obtained at CTIO on 24-27 April 1987 (McClintock and Remillard 1988). The different symbol shapes represent different observing nights. (Top) Radial velocities of the K-dwarf secondary vs. orbital phase (P_{orb} = 15.098 hours). The velocity semi-amplitude is 146±12 km s^{-1}. (Bottom) Folded CCD light curve of Cen X-4. The solid symbols are I-band data and the open symbols are V-band data, which have been scaled to match the mean intensity in the I band.

It is highly probable that both K stars fill their respective Roche lobes, even in quiescence. This is strongly implied by the sizable modution of the ellipsoidal light curves (Bochkarev et al. 1979). Moreover, a full Roche lobe is required to explain the bright, quiescent-state accretion disks, which are present in both systems: the luminous disks ($M_v \sim 8$) shine due to viscous heating, and their optical luminosities imply a mass transfer rate $\sim 10^{-12}$ $M_\odot$ yr^{-1}. Such a rate is consistent with the quiescent X-ray luminosity of Cen X-4 ($1 - 4 \times 10^{33}$erg s^{-1}; van Paradijs et al. 1987). In the case of A0620-00, however, no quiescent X-ray emission is detected ($L_x < 10^{32}$ erg s^{-1}), which seemed to me (McClintock 1986) inconsistent with the inferred rate of mass transfer. This puzzle was solved recently by de Kool (1988) who argues as follows: the effective X-ray temperature of an inner accretion disk scales as $\dot{M}^{1/4}$; consequently, the kT$\sim$ 1 keV X-ray spectrum of A0620-00 in outburst ($\dot{M} \sim 10^{-8}$ $M_\odot$ yr^{-1}) cools to become an 0.1 keV EUV spectrum in quiescence ($\dot{M} \sim 10^{-12}$ $M_\odot$ yr^{-1}), which is difficult to detect (with $E_{B-V} \approx 0.39$ mag and $N_H \sim 3 \times 10^{21}$ cm^{-2}).

Of course, one expects the Cen X-4 disk spectrum to be similarly softened in passing from outburst to quiescence. However, the outburst spectrum of Cen X-4 is much harder than that of A0620-00 (5 keV vs. 1 keV), and therefore should still be observable in quiescence at X-ray energies as a soft component. In addition, the quiescent mass-transfer rate should generate a relatively hard spectral component at the neutron star magnetosphere or at the boundary layer between the neutron star and the disk. No comparable source of emission will be present in A0620-00 if, as expected, its surface is a black-hole event horizon.

A cartoon sketch to scale of A0620-00 and Cen X-4 are shown in Figure 2. The longer orbital period of Cen X-4 (15.1h vs. 7.8h) compensates for the greater mass of A0620-00 to make the two systems about the same size. As shown, a main-sequence K dwarf (represented by the cross-hatched circle) essentially fills its Roche lobe in A0620-00 (a conclusion that is independent of the assumed orbital inclination). Based on evolutionary models of A0620-00, it appears probable that its secondary began life as a dwarf star, and has been affected little by the subsequent evolution of the binary system, including the black-hole collapse of its massive companion (Eggleton and Verbunt 1986; de Kool et al. 1987).

On the other hand, Cen X-4's secondary, which almost certainly fills its Roche lobe (see above), has a density that is only a tenth that of a main-sequence K dwarf, and it therefore appears to be in a peculiar evolutionary state. Cen X-4's neutron-star primary was probably formed by the accretion-induced collapse of a white dwarf (Chevalier et al. 1988, and references therein).

Cen X-4's large systemic velocity suggests that it is an old, halo-population object (Cowley et al. 1988), whereas, A0620-00 may belong to the disk population. Thus, despite similarities (spectral type and the occurrence of nova eruptions), it appears probable that Cen X-4 and A0620-00 had very different origins.

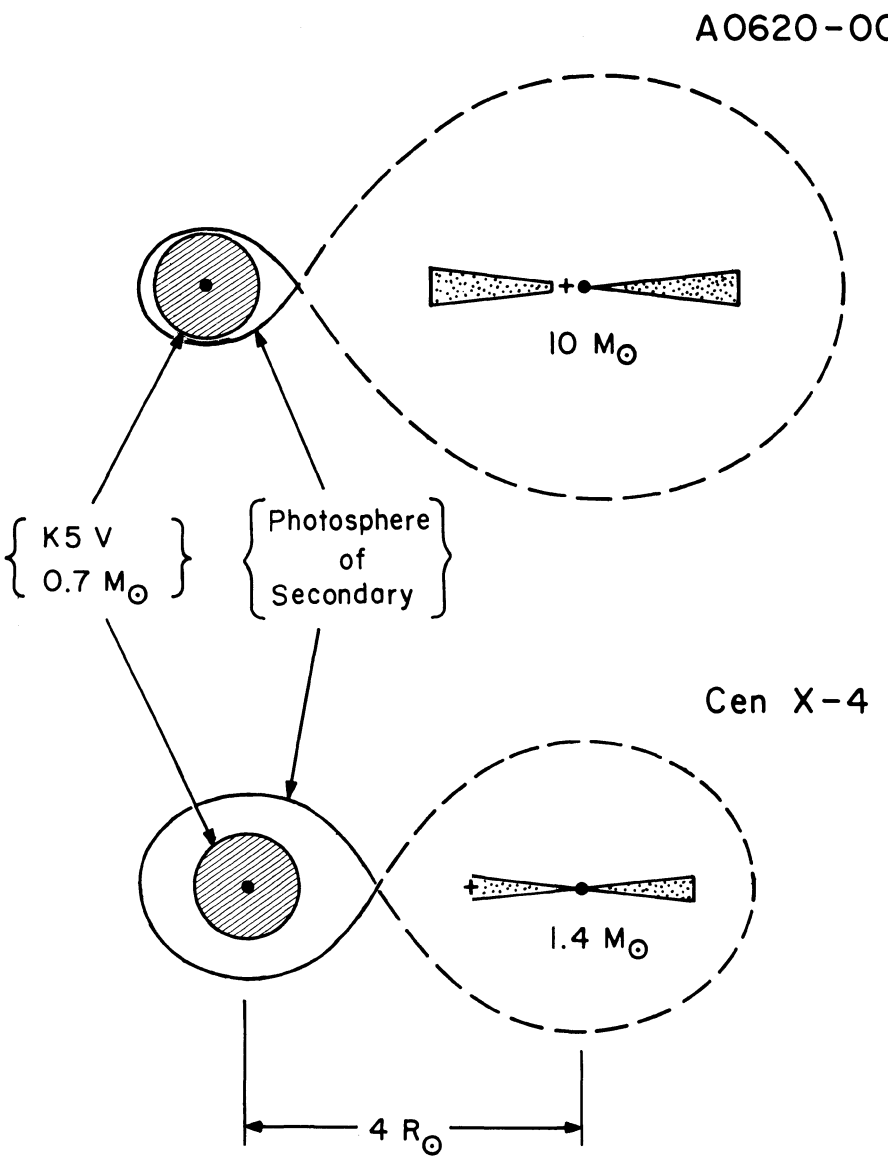

Figure 2. A sketch to scale of plausible models for two X-ray novae. The view is in the orbital plane. The critical Roche lobe is a figure eight, the sytem center of mass is marked by a "+" symbol, and an accretion disk whose size is not known is represented by a stippled region centered on each compact star. For both systems it is assumed that the orbital inclination is 45^0 and the mass of the secondary is 0.7 $M_\odot$.

3. THE PUZZLING OFF-STATE OF 4U2129+47=V1727 CYGNI

The star V1727 Cygni, the optical counterpart of the X-ray source 4U2129+47, displayed pronounced photometric variations with a period of 5.2 hours from the time of its discovery in 1979 until some time in 1983 (Thorstensen et al. 1979; McClintock et al. 1981). The light curve was very similar to that of Her X-1/HZ Her; the color was bluest at maximum light, which showed that the modulation arose from the X-ray heated face of the companion star. The large amplitude of the modulation ($\Delta m_B \approx 1.5$ mag) established that the plane of the orbit is highly inclined to the plane of the sky ($i > 60^0$).

Partial X-ray eclipses, which occurred at the phase expected from the optical ephemeris, were discovered in X-ray data obtained in mid 1980 (McClintock et al. 1982). The gradualness of the eclipse and the energy-independent shape of the X-ray light curves were interpreted as due to the partial eclipse of an extended X-ray source — an accretion disk corona (White and Holt 1982; McClintock et al. 1982). In this model, the system is viewed nearly edge on ($i \approx 80^0$), the compact X-ray source itself is hidden from us by the accretion disk, and we observe only those (relatively few) X-rays that are Compton scattered toward us by the corona above the disk. Recently, in a search of archival Einstein Observatory data, Garcia and Grindlay (1987) found a type I X-ray burst, which showed conclusively that the compact object is a neutron star; moreover, the properties of the burst also supported the accretion-disk corona model.

Thus, during the X-ray active state, observations pointed to a model with a secondary of radius 0.6 $R_\odot$ (determined by the 5.2-hour period) orbiting a neutron star. The X-ray eclipses and large optical modulation showed plainly that the inclination of the orbit is close to edge on. In short, 4U2129+47 appeared to be a well-understood LMXB.

In the fall of 1983, X-ray observations by Pietsch et al. (1986) revealed that the X-ray source had gone into an "off" state; the source was not detected and had become more than 100 times fainter than it was in June 1980. Pietsch et al. also reported that the optical counterpart was in a low intensity state and was no longer strongly modulated at the orbital period.

Extensive CCD photometric data were obtained by Thorstensen et al. (1988). They found no photometric modulation: at the binary period their 99 percent confidence limit on the amplitude of a sinusoidal modulation is 0.012 mag in the V band. No eclipse was detected, despite extensive coverage at the expected phase. The magnitude (V=17.88±0.03) and color (B-V=0.93±0.05) in the quiescent state are comparable to but slightly fainter and redder than the magnitude and colors observed at minimum light during the X-ray active state (McClintock et al. 1981). The spectrum of the quiescent star resembles a late F type with Balmer lines, G Band and (possibly interstellar) absorption lines. No sizable radial velocity amplitude ($K_{opt} < 20$ km s^{-1}) is observed at the orbital period (Garcia 1988).

The complete absence of optical modulation in quiescence is a great surprise: previous (on-state) models predicted a large ellipsoidal modulation (due to the tidal deformation of the secondary), an effect that was observed for HZ Her during the 1950's off-state mentioned above (Jones et al. 1973). The limit on the modulation of V1727 Cygni in quiescence is about a factor of 20 less than the predicted value. Similarly, the radial velocity amplitude of the secondary was expected to be $\sim$ 200 km s^{-1}, whereas the observed amplitude is less than a tenth of this value. Finally, the colors of the quiescent counterpart are much too blue and the spectral type is too early to be consistent with a late K or M type secondary, which was predicted as a consequence of the short orbital period.

The observations of V1727 Cygni in quiescence present a serious challenge to previous models of the system. Thorstensen et al. attempt a reconciliation by considering a half-dozen possibilities: light from an accretion disk? A low-mass neutron star? Low metallicity? An underfilled Roche lobe? A grossly abnormal secondary? A third star? They conclude that none of the alternatives are entirely satisfactory, although a very low metallicity system with a somewhat underfilled Roche lobe may be consistent with all of the observations. Another possibility is that the quiescent X-ray star itself has faded below visibility and one is now observing another star along the line of sight. The probability of an unrelated interloper is small (10^{-3}), but the system might more plausibly be triple.

4. A REMARKABLE X-RAY SOURCE: EXO0748-676

EXO0748-676 is a transient X-ray burst source that is abruptly eclipsed by its companion for 8.3 minutes during its 3.82-hour orbital cycle (Parmar et al. 1986). It displays irregular, periodic dips in X-ray intensity; these are presumably caused by obscuration of the X-ray source by a "splash" region where the accretion stream strikes the disk. Also seen in EXO0748-676 is a residual X-ray emission during eclipse, which may be due to X-rays scattered into our line of sight by an accretion disk corona. All the above-mentioned phenomona are apparent in a simple plot of count rate vs. time (see Fig. 1 in Parmar et al. 1986).

Bursts, eclipses, coronal scattering, and so on, have all been observed in other LMXB. Because EXO0748-676 is a transient, however, Parmar et al. were able to study how two of these phenomona — type I bursts and X-ray emission during eclipse — are affected by gross changes in X-ray luminosity.

X-ray emission during eclipse. The X-ray eclipse is not total. There is a residual emission that is linearly correlated with the average strength of the uneclipsed intensity observed during the intervals preceding and following the eclipses (see Fig. 4 in Parmar et al. 1986). The 2-6 keV flux in eclipse is a constant fraction ($\approx$ 4%) of the uneclipsed flux. Parmar et al. attribute this residual emission to

scattering of the eclipsed, compact source by an accretion disc corona. This is plausible; there is strong evidence for the presence of such coronae in other LMXB (see Section 3). It is surprising, however, that an order-of-magnitude increase in the uneclipsed source intensity of EXO0748-676 leads to only an order-of-magnitude increase in the eclipsed intensity. One might have expected the scattered component to increase faster than linearly, since the corona, which is powered by the central source, should grow in size and opacity as the source luminosity rises. This apparent constancy of the corona with changes in X-ray luminosity may prove to be a valuable input to models of accretion disk coronae.

Type I bursts. Gottwald et al. (1986,1987) observed and analyzed about three-dozen type I bursts from EXO0748-676. They found that the burst properties are a strong function of the persistent emission. For example, the ratio (α) of the total persistent energy emitted between bursts to the energy emitted in the following burst decreased by about an order of magnitude as the strength of the persistent flux decreased by a factor of 5. This result is contrary to the predictions of nuclear flash models with stable hydrogen burning, and Gottwald et al. (1986) suggest that it may be due to the flashes changing from helium-dominated at high accretion rates to hydrogen-triggered, helium-hydrogen flashes at low accretion rates. This suggestion was first made by Fujimoto et al. 1981. The apparent blackbody radius during the burst decline was also correlated with the persistent flux and decreased from about 9 km to 4 km (for a fixed temperature of 1.6 keV) as the persistent emission decreased by a factor of 5.

Especially interesting was the detection of several bursts with very short ($\sim$10 minute) recurrence times—so-called "double bursts"—which are not well accounted for by the thermonuclear flash model. The double bursts occurred during periods of low accretion rate and, in so short an inter-burst interval, it is not possible to accrete sufficient material to fuel a flash. Gottwald et al.'s analysis of these bursts suggests that they are due to fuel that is not completely consumed during the first burst, but which is somehow ignited 10 or so minutes later in a second burst. These results support a model proposed by Fujimoto et al. (1987) to explain the occurrence of double bursts in 4U1636-53.

5. CONCLUSION

Observations of transient sources in quiescence provide opportunities for a qualitative increase in our knowledge of LMXBs: Direct optical observations of the secondaries in A0620-00 and Cen X-4 have yielded valuable dynamical data and strong constraints on evolutionary scenarios; the findings from recent optical observations of 4U2129+47, a supposedly well-understood system, are surprising and puzzling, and should lead us eventually to new insights. Finally, the study

of EXO0748-676 in an X-ray active state has given us new information on the properties of scattering coronae and thermonuclear shell flashes.

I thank John Raymond for stimulating discussions on accretion disks and Ronald Remillard, my collaborator, for discussions and for his considerable help in preparing this paper. I am also grateful for financial support from the Research Opportunities Fund of the Smithsonian Institution.

REFERENCES

Bochkarev, N.G., Karitskaya, E.A., and Shakura, N.I. 1979, *Soviet Astron.*, **23**, 8.

Bradt, H.V.D. and McClintock, J.E. 1983, *Ann. Rev. Astron. Astrophys.*, **21**, 13.

Chevalier, C., Ilovaisky, S.A., van Paradijs, J., Pedersen, H., and van der Klis, M. 1988, to appear in *Astron. Astrophys.*

Cowley, A.P., Hutchings, J.B., Schmidtke, P.C., Hartwick, F.D.A., Crampton, D., and Thompson, I.B. 1988, to appear in *Ap.J.*

de Kool, M. 1988, to appear in *Ap.J. (Letters).*

de Kool, M. van den Heuvel, E.P.J., and Pylyser, E. 1987, *Astron. Astrophys.*, **183**, 47.

Eggleton, P.P. and Verbunt, F. 1986, *MNRAS*, **220**, 13P.

Fujimoto, M.Y., Hanawa, T., and Miyaji, S. 1981, *Ap.J.*, **246**, 267.

Fujimoto, M.Y., Sztajno, M., Lewin, W.H.G., and van Paradijs, J. 1987, *Ap.J.*, **319**, 902.

Garcia, M.R. 1988, private communication.

Garcia, M.R. and Grindlay, J.E. 1987, *Ap.J.*, **313**, L59.

Gottwald, M., Haberl, F., Parmar, A.N., and White, N.E. 1986, *Ap.J.*, **308**, 213.

Gottwald, M., Haberl, F., Parmar, A.N., and White, N.E. 1987, *Ap.J.*, **323**, 575.

Hameury, J.M., King, A.R., and Lasota, J.P. 1986, *Astron. Astrophys.*, **162**, 71.

Jones, C.A., Forman, W., and Liller, W. 1973, *Ap.J. (Letters)*, **182**, L109.

McClintock, J.E. 1986, in *Lecture Notes in Physics: The Physics of Accretion onto Compact Objects*, eds. K.O. Mason, M.G. Watson, and N.E. White (Berlin: Springer-Verlag) p.211.

McClintock, J.E., London, R.A., Bond, H.E., and Grauer, A.D. 1982, *Ap.J.*, **258**, 245.

McClintock, J.E. and Remillard, R.A. 1986, *Ap.J.*, **308**, 110.

McClintock, J.E. and Remillard, R.A. 1988, in preparation.

McClintock, J.E., Remillard, R.A., and Margon, B. 1981, *Ap.J.*, **243**, 900.

Parmar, A.N., White, N.E., Giommi, P., and Gottwald, M. 1986, *Ap.J.*, **308**, 199.

Pietsch, W., Steinle, H., Gottwald, M., and Graser, U. 1986, *Astron. Astrophys.*, **157**, 23.

Thorstensen, J.R., Brownsberger, K.R., Mook, D.E., Remillard, R.A., McClintock, J.E., Koo, D.C., and Charles, P.A. 1988, to appear in *Ap.J.*

Thorstensen, J., Charles, P., Bowyer, S., Briel, U.G., Doxsey, R., Griffiths, R.E., and Schwartz, D.A. 1979, *Ap.J. (Letters)*, **233**, L57.

van Paradijs, J. and Verbunt, F. 1984, in *High Energy Transients in Astrophysics*, ed. S.E. Woosley (New York: AIP), p49.

van Paradijs, J., Verbunt, F., Shafer, R.A., and Arnaud, K.A. 1987, *Astron. Astrophys.*, **182**, 47.

White, N.E. and Holt, S.S. 1982, *Ap.J.*, **257**, 318.

White, N.E., Kaluzienski, J.L., and Swank, J.H. 1984, in *High Energy Transients in Astrophysics*, ed. S.E. Woosley (New York: AIP), p31.

Chaotic dynamics in the X-ray variability of Her X-1

H. ATMANSPACHER, H. SCHEINGRABER, AND W. VOGES

Max-Planck-Institut für extraterrestrische Physik, 8046 Garching, FRG

1. Introduction

In addition to its fundamental implications on the foundations of statistical physics, the concept of deterministic chaos in dynamical systems has provided considerable impact concerning the experimental characterization of dynamical systems. There exist different methods to derive invariants of such systems from measured time series (for an overview, see Ref.1). The determination of these invariants is possible, if only one single variable of a generally complex system is accessible by observation. This issue underlines the particular importance for astrophysical systems, for which the only observable variable is the electromagnetic radiation.

In the present contribution we report results obtained from one of the mentioned procedures introduced by Grassberger and Procaccia[2] and described elsewhere in this volume.[3] In brief, this method allows for a determination of the dimension of the reconstructed attractor representing the investigated process. A non – integer dimension indicates chaotic behavior.

The attractor dimension is of specific interest since it gives a lower bound for the number of degrees of freedom of the system. It provides the mathematical justification to model the system with the corresponding low number of variables.[1] Since it is an appropriate measure for the complexity of a system, the attractor dimension can also serve as a classifying criterion for different dynamical systems of similar type. (For instance, it would be interesting to investigate and compare the attractors of white dwarfs, neutron stars, and black hole candidates[5] as different compact objects.)

This article describes the attractor analysis based on the X – ray luminosity from the neutron star Her X-1. In the following sections we present the observational material (2), discuss some methodical details (3), and summarize the obtained results (4).

---

[1] For an example of a successful application of this idea we refer to the discovery of low – dimensional chaos in multimode laser systems. Here, the attractor analysis has led to the prediction of unexpected microphysical mode coupling mechanisms which could be verified by its additional effects on the behavior of the laser system.[4]

H. Ögelman and E. P. J. van den Heuvel (eds.), Timing Neutron Stars, 219–224.

We proceed without an elementary introduction into the applied method, for which we refer to Refs.1-3.

2. Observational material

The neutron star Her X-1 and its visible companion HZ Her form a low mass X-ray binary system showing several specific features. Her X-1 is surrounded by an accretion disk consisting of gaseous matter flowing in from HZ Her. The strong surface magnetic field of $\approx 4 \times 10^{12}$ Gauss causes a channeling of the accreted matter onto the polar regions of Her X-1. The gravitational energy of the decelerated matter is mainly converted into X-ray radiation.

The emitted X-ray radiation as observed by the EXOSAT satellite shows three different periods of regular temporal variability: (i) the 1.24 sec rotaion period of the neutron star, (ii) the 1.7 day orbital period of the system, and (iii) the 35 day period ascribed to a warping accretion disk. The geometry of the system is illustrated in Fig.1.

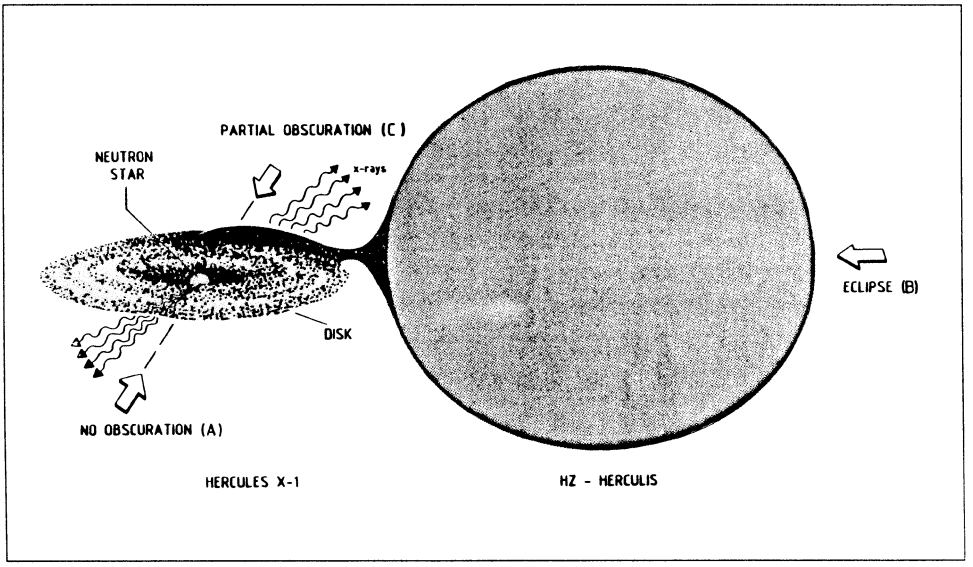

Figure 1: The geometrical configuration of the binary system HZ Her / Her X-1. The different source modes (A) - (C) are indicated as described in the text.

In addition to the regular periodic behavior, irregular (erratic) temporal variabilities have been found on each of the periodic time scales. In order to distinguish this irregular behavior in different geometrical configurations we define the following source modes (see also Fig.1):
(A) Unobscured phase: the X-ray radiation is observed without any obscuration effects due to the accretion disk or due to HZ Her and its atmosphere. The unobscured radiation amounts to slightly above 400 counts/sec and shows small intensity variations.

(B) Totally obscured phase (eclipse): the X-ray source is shaded by HZ Her and the count rate is reduced to less than 300 counts/sec.
(C) Partially obscured phase (absorption dips): strong intensity variations of a typical duration of some hours. The count rates cover the range between (A) and (B).
(D) Background: in the off – source observation mode, the X-ray signal shows irregular temporal variations around an average count rate comparable to the eclipse mode.

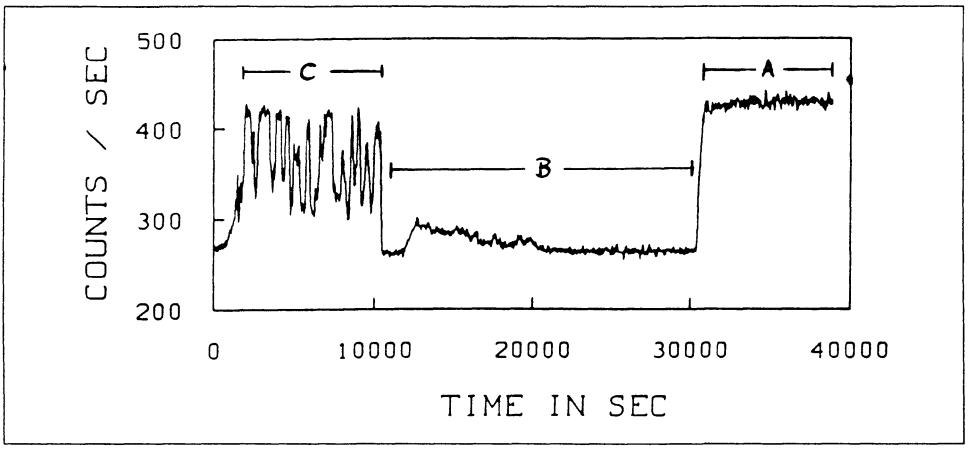

Figure 2: EXOSAT count rates of the ME X-ray radiation from Her X-1 as a function of time. The different source modes (A) - (C) are indicated. The increased intensity during eclipse is due to solar activity.

An X-ray luminosity time series containing source modes (A) - (C) is shown in Fig.2. The data have been acquired in the EXOSAT PULS mode during a main – on state of the 35 day period of the system at April 5, 1984 (for further details see Ref.6). A much better impression of the temporal variablity in the individual modes can be achieved on a spread time axis. In Fig.3 count rates for modes (A) and (B) per 770 msec are plotted over a time interval of 770 sec. In both time series, some long time variability of the signal can be recognized in addition to the erratic short time variations. However, it seems extremely difficult to state any significant difference between both types of irregular behavior. As it will be shown in the following section, a clearcut difference can be obtained from an attractor analysis.

3. Methodical details

The attractor analysis according to the procedure of Grassberger and Procaccia requires a careful pre – investigation of the system in terms of conventional methods like correlation functions and power spectra. Subsequently one has to determine the crucial parameters for the attractor analysis, namely: (i) the optimum temporal resolution τ of the time series, (ii) the time delay Δt for the reconstruction of the attractor in an artificial phase space, and (iii) a sufficient number N of data points per time series.

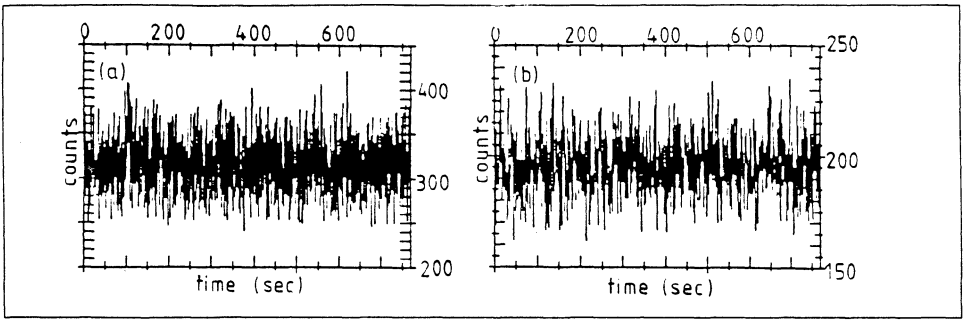

Figure 3: Temporal evolution of the X-ray count rates from Her X-1 in modes (A) and (B). Both time series consist of 1000 data points with a temporal resolution of 770 msec.

The temporal correlation of the signal has a direct consequence for the value of τ. In order to achieve a sufficiently dense covering of the attractor, a number of some ten data points per correlation period is usually required. Too few data points per correlation period would simulate an uncorrelated (random) behavior. On the other hand, a very high temporal resolution often results in low count rates so that counting statistics may dominate the signal which then appears to be random. For the unobscured source mode (A), Her X-1 provides a correlation period of roughly 10 sec. The effects mentioned above appear for $\tau > 1$ sec and $\tau < 150$ msec, resp. A value of ≈ 770 msec has eventually been chosen.[2]

For a proper choice of Δt we refer to a suggestion of Fraser and Swinney.[7] Obviously, Δt must not correspond to an eigenperiod of the system, since in this case the artificial phase space would necessarily be one – dimensional. For the Her X-1 analysis the results were basically independent of Δt between τ and 10τ.

A criterion for a sufficient number N of data points has been proposed recently.[8] The idea is to check whether an increase in N causes an improved representation of the entire attractor in the artificial phase space. As a result, $N = 1000$ turned out to be an adequate number of data points.

The determination of the attractor dimension from the time series shown in Figs.3a and b is shown in Figs.4 (mode (A)) and 5 (mode (B)). While Fig.5 clearly represents random behavior, Fig.4 shows a deterministic component indicated by the plateau in the slope plot 4c. The constant slope corresponds to an attractor dimension of ≈ 2.35, whereas the random behavior in the eclipse mode can of course not be associated with any attractor.[3]

The fact that τ is not too different from the 1.24 sec rotation period of Her X-1

[2]The EXOSAT data acquisition time binning is 9.67 msec. Longer time bins are simply achievable by integration.

[3]It seems worth to emphasize that the slope plot 4c nicely illustrates a basic feature of this type of analysis. It decomposes the dynamics of the system into its random and its deterministic contribution. The different types of behavior in Figs.4 and 5 allow for a clear distinction between the time series shown in Figs. 3a and b.

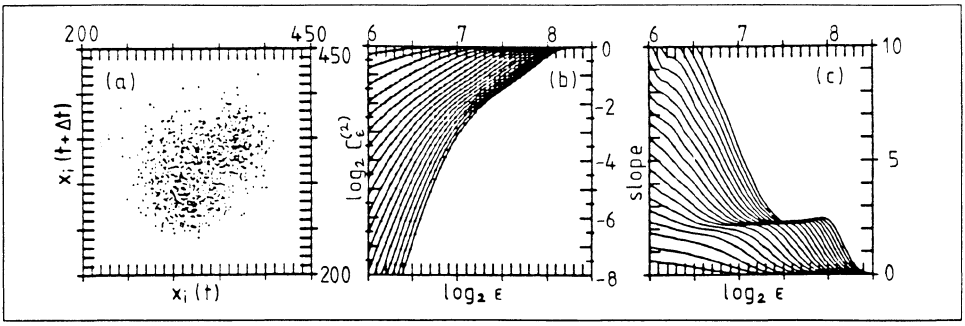

Figure 4: Attractor analysis of the time series shown in Fig.3a representing X-ray count rates from Her X-1 in mode (A). a) Two – dimensional phase protrait of the measured time series vs the first delay series ($\Delta t = \tau$); b) correlation integral $C_\epsilon^{(2)}$ according to Grassberger and Procaccia c) plot of the slope ($\log C_\epsilon^{(2)} / \log \epsilon$ vs $\log \epsilon$. Dimensions of the artificial phase space are shown from $d = 1$ to 20, $N = 1000$, $\tau = 770$ msec.

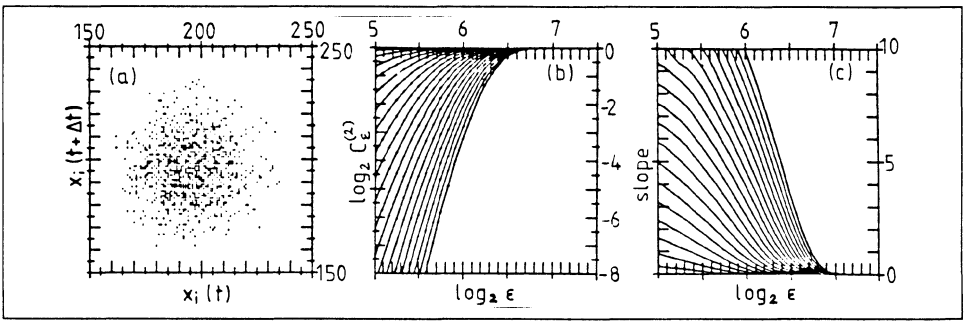

Figure 5: Attractor analysis of the time series shown in Fig.3a representing X-ray count rates from Her X-1 in mode (B). a) - c) as in Fig.4. The lacking plateau in 5c indicates that there is no attractor, but purely random behavior.

might suggest the influence of some sort of beat phenomenon on the analysis. In order to check the relevance of the obtained result in this respect, an analysis of a time series with a subtracted average 1.24 sec pulse profile has been performed. In this case the signal turned out to be much too noisy to provide a deterministic component. The pulse – corrected signal will be further investigated by methods which are less sensitive to high noise levels.[9]

4. Results

A detailed description of the analyzed time series and the calculated dimensions can be found elsewhere.[6,8] The main results are the following:

In the unobscured mode (A) the reconstructed attractor reveals a dimension of $D \approx 2.35$ for different time series and different data acquisition modes. This low dimension indicates a fairly low number of variables required to model the dynamical process accounting for the irregular X-ray variations. Corresponding attempts

have been started.[10]

For the eclipse data (B) and the X-ray background (D) there is no deterministic component of the irregular signal. The motion of the system in the artificial phase space is purely random.

During the absorption dips (mode (C)) we obtained a correlation period of $\approx$ 200 sec and an optimum integrated resolution of $\approx$ 5 sec. On this time scale, the mode (A) behavior appears to be random, so that a separate attractor analysis is possible for mode (C). The investigation of different time series provided dimensions in the range between 8 and 10. The corresponding attractor can be ascribed to the turbulent dynamics of density inhomogeneities in the accretion disk as the origin of the partial obscurations.

In summary, the analysis of the irregular X-ray variability of Her X-1 in terms of attractor dimensions provides basic information about the underlying dynamical processes. Apart from its capability to distinguish random from deterministic components of the system, the complexity of the deterministic contribution can be quantified. Since it provides a lower bound for the number of variables of the system, the attractor dimension should be considered as a tool supporting the search for theoretical models of the dynamics of the system.

REFERENCES

1. H. Atmanspacher, H. Scheingraber, and W. Voges, in *Data analysis in astronomy III*, eds. V. Di Gesu and L. Scarsi (Plenum Press, New York, 1988)
2. P. Grassberger and I. Procaccia, *Phys. Rev. Lett.* **50**, 346 (1983)
3. G. Morfill *et al.*, this volume
4. H. Atmanspacher and H. Scheingraber, *Phys. Rev.* **A 34**, 253 (1986); H. Atmanspacher, H. Scheingraber, and V. M. Baev *Phys. Rev.* **A 35**, 142 (1987); Yu. M. Ajvasjan *et al.*, *Appl. Phys. B*, in press
5. S. Miyamoto and S. Kitamoto, this volume
6. W. Voges, H. Atmanspacher, and H. Scheingraber, *Ap. J.* **320**, 794 (1987)
7. A. M. Fraser and H. L. Swinney, *Phys. Rev.* **A 33**, 1134 (1986)
8. H. Atmanspacher, H. Scheingraber, and W. Voges, *Phys. Rev.* **A 37**, 1314 (1988)
9. D. S. Broomhead and G. P. King, *Physica* **20 D**, 217 (1986)
10. V. Demmel, G. Morfill, and H. Atmanspacher, *Mitt. Astron. Ges.* **68**, 251 (1987), see also this volume

THE X-RAY SOURCE IN THE CORE OF 47 TUCANAE *

M. Aurière
Observatoire du Pic du Midi
F - 65200 Bagnères-de-Bigorre

L. Koch-Miramond **
Centre d'Etudes Nucléaires de Saclay
DPhG/SAp
F - 91191 Gif sur Yvette CEDEX

S. Ortolani
Osservatorio Astronomico di Padova
Vicolo dell'Osservatorio, 5
I - 35122 PADOVA

ABSTRACT - We present new data on the X-ray source lying in the core of 47 Tuc that is the brightest of the dim globular cluster X-ray sources. From the recalibrated IPC Einstein satellite data the X-ray spectrum was obtained (thermal bremsstrahlung with $kT = 2^{+4}_{-1}$ keV and no intrinsic absorption). X-ray variability is present at time scales of days, hours and tens of minutes. In addition we have discovered transient periodic pulsations at period 120.200 s. Rapid periodic pulsations at period 4.580 s are also marginally present.
We present the results of a CCD and image tube optical search for a faint blue variable object in the X-ray source field. The limiting magnitude U = 17 ($M_U \sim 3.6$) is reached. A possibly UV and variable object stands out in our U CCD frames.
We then discuss the nature of the X-ray source : cataclysmic variable or transient low mass X-ray binary.

1. INTRODUCTION.

The Einstein survey of 71 globular clusters gives a bimodal luminosity function (Hertz and Grindlay, 1983 a, b). The source X0021.8-7221 which lies at 0.36 core radius from the centre of 47 Tuc is the brightest of the "dim" sources, but still 10-100 times fainter than the faintest of the low mass X-ray binaries (LMXB) observed outside or inside globular clusters (Verbunt et al, 1984). Its nature is then unclear.
The accurate position provided by 5 HRI observations permits a sensitive search for the optical counterpart though the object is located in the overcrowded core of the cluster.
In this paper we present new spectral and variability X-ray data, we give the result of a high angular resolution optical investigation of the X-ray field and discuss the nature of the object (see Aurière et al, 1988, for a more detailed presentation).

* The optical data are based on observations collected at the European Southern Observatory, La Silla, Chile.

** Presenter of this paper.

H. Ögelman and E. P. J. van den Heuvel (eds.), Timing Neutron Stars, 225–241.

Table 1 - IPC spectral fitting parameters, fluxes and luminosities of X 0021.8-7221 in the 0.2-4keV energy range

Model Spectrum	$\chi^2_{min/dof}$ (1)	kT (keV) or α index (2)	N_H ($10^{19}cm^{-2}$) (2)	f_x observed (erg	f_x emitted cm^{-2} s^{-1})	L_x erg s^{-1} (3)
Th. Brems.	2.6/9	$2.0^{+4.0}_{-1.0}$	18^{+13}_{-16}	$2.5\ 10^{-12}$	$2.8\ 10^{-12}$	$7.0\ 10^{33}$
Pow. law	2.4/9	2.1 ± 1.0	31^{+44}_{-20}	$2.7\ 10^{-12}$	$3.5\ 10^{-12}$	$8.7\ 10^{33}$

(1) χ^2_{min} : minimum χ^2 (not reduced) ; dof : degrees of freedom = number of IPC channels used in the fit - 2 fit parameters.

(2) kT = spectral fit parameter for thermal bremsstrahlung spectrum ;

α = logarithmic slope for power law energy spectrum $S(\nu) \propto \nu^{\alpha}$.

The uncertainties on kT (or α) and N_H are 90 percent confidence limits, they correspond to $\chi^2_{min} + 4.6$ (Avni, 1976).

(3) Distance = 4.6 kpc

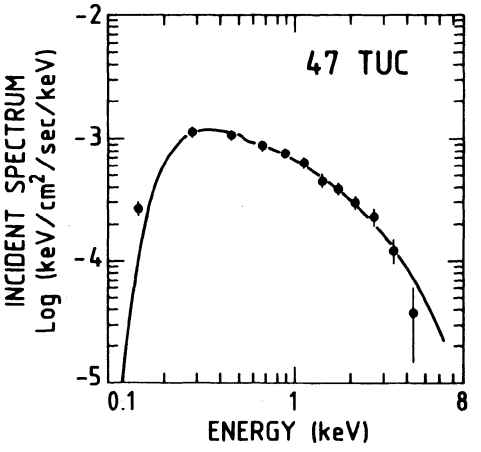

Figure 1 :
The incident energy spectrum of X 0021.8-7221 as deduced from the EINSTEIN IPC data. The error bars are 1σ. The histogram is the predicted distribution for a thermal bremsstrahlung spectrum with temperature kT = 2 keV and an absorbing column density $N_H = 1.8\ 10^{20}cm^{-2}$.

2. THE EINSTEIN X-RAY DATA ON 47 TUC REVISITED.

2.1. Spectral parameters :

The Einstein IPC data were obtained during a 16240.7s exposure lasting from 19 to 22 November, 1979, the observatory axis pointing 10.5 arcmin. North of the centre of 47 Tuc. In the 44 arc min diameter circle corresponding to the angular diameter of the cluster, 3 X-ray sources are detected above 4 , the brightest one, detected at 31.7 X0021.8-7221 is the core source discovered by Hertz and Grindlay (1983b) and precisely located at 0.36 core radius from the cluster centre by Grindlay et al. (1984). A highly significant spectral fit is obtained (Koch-Miramond and Aurière, 1987). Table 1 shows the parameters of the best fits : either a thin thermal bremsstrahlung spectrum with kT = 2 keV and $N_H = 1.8\ 10^{20} cm^{-2}$ or a power law energy spectrum with index 2.1 and $N_H = 3.1\ 10^{20} cm^{-2}$ (reduced $\chi^2 = 0.28$ in both cases). No acceptable fit was obtained with black body spectra. The former best value of N_H corresponds to that deduced from the visual absorption, $A_V = 0.04$ mag., to the cluster. Figure 1 shows the incident spectrum together with the predicted distribution of the best spectral fit for thermal bremsstrahlung. The 90 percent confidence limits on kT and N_H corresponding to $\chi^2_{min} + 4.6$ (Avni, 1976) are $1 < kT < 6$ keV and $2\ 10^{19} < N_H < 3.1\ 10^{20} cm^{-2}$.

Note that $kT \geq 10$ keV cannot be completely excluded due to the very limited energy range of the Einstein IPC and to the shape of the chisquare grid : nevertheless a very soft spectrum (kT a few tens eV) is excluded.

We conclude that the core source in 47 Tuc has a low temperature spectrum ($kT \approx 2$ keV) with little or no intrinsic cut-off and no very soft spectral component.

We then deduce the fluxes (observed and emitted) and the luminosities in the 0.2 - 4 keV energy range. As shown in Table 1 a luminosity approaching 10^{34} erg s^{-1} is found.

2.2. Brightness variability :

i) Long term variations :

We have used the spectral parameters determined above to calculate the ratio of the fluxes given by the two Einstein instruments IPC and HRI in their common bandwith 0.5 - 2.5 keV. We then have corrected the fluxes obtained with the IPC in order to compare them with the HRI fluxes, using the above ratio and the same spectral parameters (assumed to remain constant with time). This correction factor remains smaller than the statistical errors when kT varies within the 90 percent confidence limits defined above. The last column of Table 2 gives the calculated fluxes and figure 2 shows their variation versus time. There is evidence for a long term variability of the source, amounting to a factor 2.5 to 3 in 2.6 days and to a factor 2 in 12 h.

We have searched for shorter term variability of the source with the simple variability test using χ^2 applied to the photon arrival times in the IPC (Harnden et al, 1984). As shown in Table 3 evidence of variability is obtained for bin sizes 987s and 1780s, the probability being 0.5 percent that the source is constant at these time scales.

The source was observed at maximum brightness during the HRI observations, $L_X = 2\ 10^{34}$ erg s^{-1}. During the IPC observations the source was in a lower state lasting at least 2 days, $L_x = (7 \pm 1)\ 10^{33}$ erg s^{-1}.

Table 2 - X0021.8-7221 in 47 TUC :
observations with the Einstein observatory

Instrument/ Sequence	Date (1979)	Middle observ. time	Effective obs. time s	Count Rate x 1000 s^{-1}	Calculated fluxes erg cm^{-2} s^{-1}
HRI / 658 *	21 April	1h31m	1640	71 ± 7.7	$5.3\ 10^{-12}$
HRI / 4858	18 Nov.	19h14m	838	81 ± 12	$6.1\ 10^{-12}$
HRI / 4857	19 Nov.	7h05m	1513	85 ± 10	$6.4\ 10^{-12}$
HRI / 4855 **	19 Nov.	15h12m	1989	65 ± 7	$4.9\ 10^{-12}$
HRI / 4856	19 Nov.	18h25m	1882	56 ± 7	$4.2\ 10^{-12}$
IPC / 4969 A	19 Nov.	20 h47m	4774	119 ± 5	$2.9\ 10^{-12}$
IPC / 4969 B	20 Nov.	6h14m	4828	101 ± 5	$2.4\ 10^{-12}$
IPC / 4969 C	21 Nov.	23h00	7208	90 ± 6	$2.2\ 10^{-12}$

* 47 TUC is on axis for sequence 658 and offset by ~ 8 arcmin in a different direction for each of the 4 other HRI sequences.

** The x-ray source is split into two equal sources separated by 15 arcsec and located in two adjacent 12x12 arcsec detection cells ; we have summed the corresponding counts.

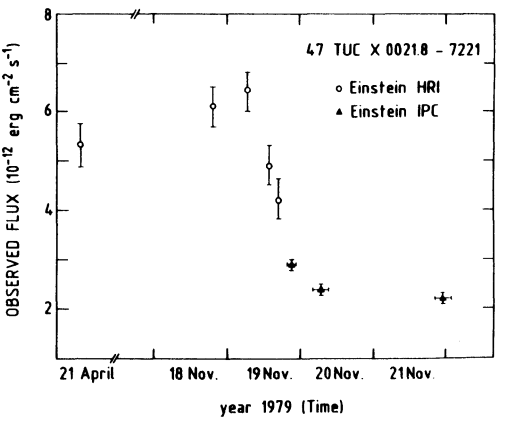

Figure 2 :
The X-ray flux of X 0021.8-7221 versus time in the Einstein energy band 0.2-4 keV. Five HRI and 3 IPC flux measurements with 1σ error bars are shown. Intercalibration of the two measurements is explained in the text.

Table 3 - Search for variability of X 0021.8-7221
in the photon arrival times (Einstein IPC)

	Observation time	Effective obs. time s	Photons used	Bin size s	Reduced χ^2	Dof	Probabil. (3)	Variabil. (4)
	Nov. 1979							
Start	19, 19h.68	4774.4	568	800	1.54	8	0.2	-
Stop	19, 21h.90			1600	0.7	4	0.6	-
Start	20, 3h.56	4828.2	489	987	3.2	7	0.005	Yes
Stop	20, 8h.49			1780	3.9	5	0.005	Yes
(1)	20, 5h.83	1679.4	139	336	1.2	4	0.3	-
(2)	20, 8h.26	409.5	63	90	2.2	4	0.07	Possible
Start	21, 20h.52	7208.6	651	1084	0.96	12	0.5	-
Stop	22, 1h.48			1872	1.95	6	0.07	Possible

Einstein IPC, sequence number 4969

(1) Zooming on interval where counting rate is 11 σ above mean value on Nov. 20.

(2) Zooming on interval where counting rate is 7 σ below mean value on Nov. 20.

(3) Probability for getting χ^2 or greater from random data.

(4) Probability less than 1 percent is the adopted criterion for variability. "Possible" means that there is some evidence for variability (probability that source is constant is less than 10 percent).

Table 4 - Parameters of the frequency analysis of X 0021.8 - 7221
with a Fast Fourier Transform algorithm

IPC Segment	Total Elapsed time s	Minimum frequency Hz	Maximum frequency Hz	Period range s
A	7928	$1.26\ 10^{-4}$	2.06	0.48 - 7928
B1	8393	$1.19\ 10^{-4}$	1.95	0.51 - 8393
B2	1679	$5.94\ 10^{-4}$	9.76	0.10 - 1679
C	13394	$7.46\ 10^{-5}$	1.22	0.81 - 13394

Figure 3 :

The distribution of bins versus power in all bins from period 0.6 s up to 2640 s for 597 photons from the source and 590 background photons. The histogram represents the experimental data and the straight line the theoretically expected distribution. The arrow shows the bin with signal at period 120.123 s.

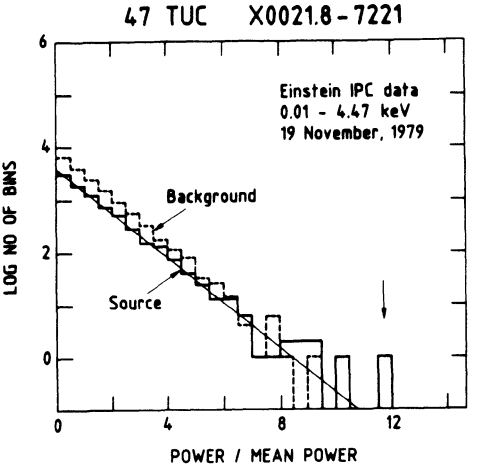

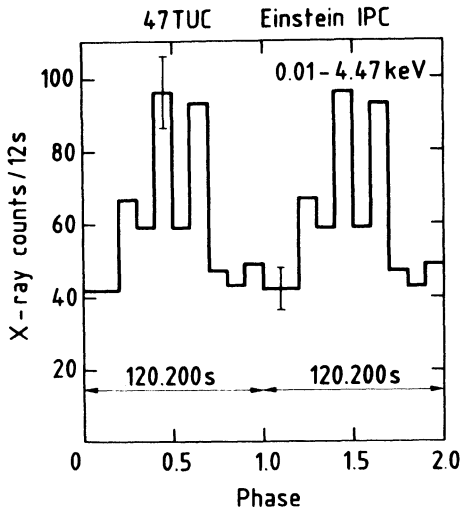

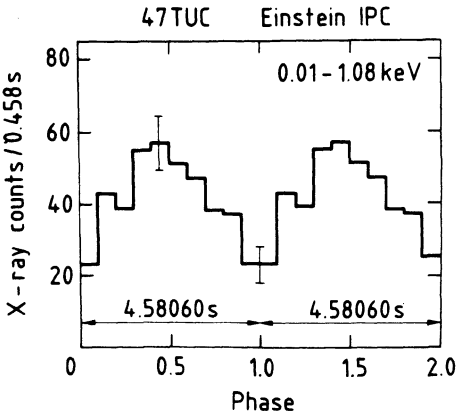

Figure 4 :

X-ray light curve of X 0021.8-7221 during segment A of the IPC observation, on 19 November, 1979, when the decreasing luminosity of the source was $L_X \sim 8\ 10^{33}$erg s^{-1}. The data in the 0.01-4.47 keV range have been folded modulo 120.200 s in 12.02 s channels. The 1 σ statistical error bars are shown. The phase 0. has been chosen in the middle of the lower plateau. The peak to peak modulation is 52 $\pm$ 14 percent.

Figure 5 :

X-ray light curve of X 0021.8-7221 during segment C of the IPC observation on 21 November, 1979, when $L_X \sim 6.10^{33}$ erg s^{-1}. Low energy data (0.01 - 1.08 keV) folded modulo 4.5806 s in 0.458 s channels. The 1 σ statistical error bars are shown. The peak modulation is 58 $\pm$ 14 percent.

ii) Periodic oscillations :

A frequency analysis using a Fast Fourier Transform (FFT) algorithm was done on 4 segments of the IPC observation which started on 19 November, 1979, finished on 22 November, 1979 (see Table 3) and on a background file containing 1732 counts registered in a 6.6 arcmin radius circle at the centre of the same IPC field where no sources are detected. For each segment the broad energy range of the IPC (0.01 - 4.47 keV), its soft part (0.01 - 1.08 keV) and hard part (1.08 - 4.47 keV) were analysed separately. The data in each segment are divided in 32768 time bins, producing 16384 evenly spaced frequency samples starting with f min = 1/T (T total elapsed time in each segment) and finishing with f max = 16384/T. In Table 4 we list for each segment the total elapsed time, the minimum and maximum frequencies and the corresponding period range in the FFT search. In the Fourier spectrum of segment A, a frequency peak with amplitude 3.45 is present, the probability being 99.1 percent that the source is not steady at the corresponding period P_1 = 120.123 s. Figure 3 demonstrates that the distribution of power within the various frequency bins follows the expected exponential law for random fluctuations (Middleditch and Nelson, 1973) except for the peak at 120.123 s. Another frequency peak, corresponding to a period P_2 = 4.580 s, appears in the Fourier spectrum with a probability of 92.5 percent in the low energy data of segment C, but its harmonics 2, 3 and 4 are also present with smaller probabilities in the low and high energy data of all segments.

These frequency peaks and their harmonics are not present in the Fourier spectrum of the background as shown by figure 3 for segment A.

We have then folded the 597 photons collected during the 7928 s of the first segment in 10 or 20 bins in the period range 119.8 s to 120.3 s with 0.01 s steps. The best (reduced χ^2 = 5.96 for 9 degrees of freedom is obtained for a period P = 120.200 s. The corresponding light curve is shown in figure 4 with the 1σ statistical error bars. Taking into account the number of independant frequency bins used in this analysis we obtain a probability of 5 10^{-5} that this light curve could be produced by chance. The peak to peak modulation of the X-ray flux is 52 $\pm$ 14 percent. The double peaked shape of the light curve is still present at the same phase when we fold an uninterrupted data set in segment A (duration 2335 s, 284 photons) or when we change the binning of the data. The level of confidence associated with the light curve is higher than that of the Fourier peak, due to the non-sinusoidal modulation of the X-ray flux.

We have then folded the 413 low energy photons collected during the 13393 s of segment C, in 10 bins, in the period range 4.575 to 4.595 s with 0.0002 s steps. The best (reduced) χ^2, 4.49 for 9 degrees of freedom, is obtained for the period P_2 = 4.58060 s (the fundamental detected in the Fourier analysis). The corresponding light curve with the 1 σ statistical error bars is shown in figure 5 ; it has a probability of 1.5 percent of being random. The peak to peak modulation of the X-ray flux is 58 $\pm$ 14 percent.

We conclude that the X-ray core source in 47 Tuc shows variability at days, hours and tens of minutes time scales. In addition transient periodic oscillations at period 120.200 s lasting for 2.2 h were present on 19 Nov. 1979 and rapid periodic oscillations at period 4.580 s were marginally present two days later and probably during the entire observation. The upper limits of the coherence are found to be 10^{-6}s/s and 10^{-8}s/s respectively for these 2 periods.

Owing to the recent discovery of two millisecond binary pulsars in 47 Tuc

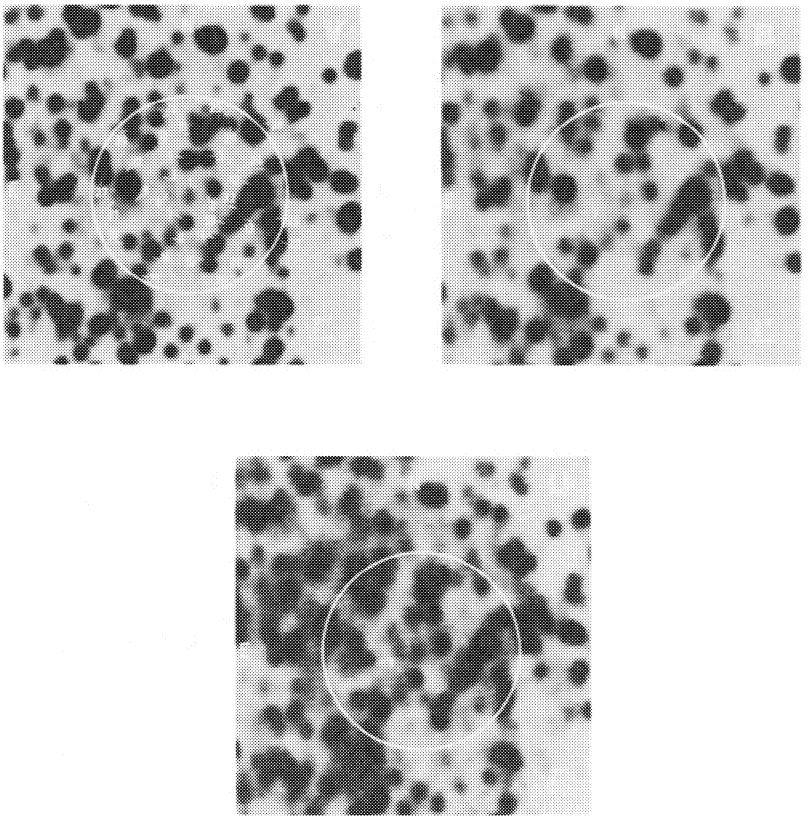

Figure 6 :
The investigated field around the HRI Einstein position for the core X-ray source in 47 Tuc.
The V, B, U images are from 20 s, 1 min, 10 min exposures obtained with the GEC CCD at ESO La Silla 2.2 m telescope. The observations are listed in table 5 and the photometry for identified stars is given in table 6. Star 9 is the bluest object in the field and could be a hot object.
The drawn circle is 7 arcsec radius and centred on star 1. Our best estimate for the centre of the error circle (used in table 6) is however located between star 1 and star 6. North is up. East is left.

(Ables et al. 1988) we have searched for a modulation of the X-ray flux of X0021.8-7221 at the orbital period, 1924.3 +_ 0.3 s, of the pulsar PSR0021-72A. No signigicant peak appears at the corresponding frequency in the Fourier spectrum. The same negative result was obtained for X0022.5-7229, a source lying at ~ 27 core radii from the centre of 47 Tuc and detected at 7 σ level by the IPC.

3. SEARCH FOR THE OPTICAL COUNTERPART.

As for the corresponding galactic objects a faint blue variable object is expected (Bradt and McClintock, 1983). The error box for its position is small (Grindlay et al. 1984) but is located in the core of the cluster, at ~10 arcsec from the centre. The good point is that 47 Tuc is a nearby object with a high metallicity : 1) fainter absolute meagnitudes might be reached ; 2) its horizontal branch does not contain blue stars and only two RR Lyrae variables are catalogued (Sawyer Hogg, 1973). Every hot or faint variable star in the error box region should then be an interesting object.

3.1. The error circle :

Grindlay et al (1984) give the position of the X-ray source in 47 Tuc with a 1σ precision of 0.9 arcsec. Nevertheless, the optical identification of the M 15 X-ray source (Aurière et al. 1984), with M 15 : AC 211, a star located about 3 arcsec from the HRI Einstein position, suggests taking this last value as the uncertainty for the 47 Tuc source position. As we did not do astrometry in 47 TUC, we used the field chart of Fig.1 in Grindlay et al (1984) in order to find the centre of the error circle : the star alignment procedure we had to use adds an uncertainty of ~ 4 arcsec. Finally we traced an error circle of 7 arcsec.

3.2. Observations and photometry :

Our optical investigation is based upon 3 sets of data obtained at ESO (La Silla) : a series of UBV frames taken with a UV coated GEC CCD camera at the 2.2 m telescope (Aurière, 1986) ; UBV image tube photographs obtained at the 1.5 m Danish telescope with an instrumentation specially designed for the study of cores of globular clusters (Aurière and Cordoni, 1981) ; a series of B and V frames obtained with a RCA CCD at the 1.5 m Danish telescope. The GEC set obtained in excellent seeing conditions is the deepest one. The RCA set was mainly used for calibration purposes. Table 5 gives the journal of observations. 33 stars were resolved in the error circle defined above. Figure 6 shows the corresponding field from the GEC CCD data (with 385x576 pixels 22μ square in size, each representing 0.26 arcsec on the sky). The relative photometry in the U,B,V filters was obtained on the July 1987 GEC CCD series using the DAOPHOT and ALLSTAR packages (Stetson, 1987). The magnitude calibration was obtained from Landolt (1983) standard stars for the B and V. As for the U, we used the U-B aperture photometry of Da Costa (1979) combined with our B photometry. The uncertainty in the final zero point calibration is about 0.03 mag. both in B and V and 0.1 mag. in U. The complete photometric procedure used to reduce our CCD data is described in Aurière and Ortolani (1987).

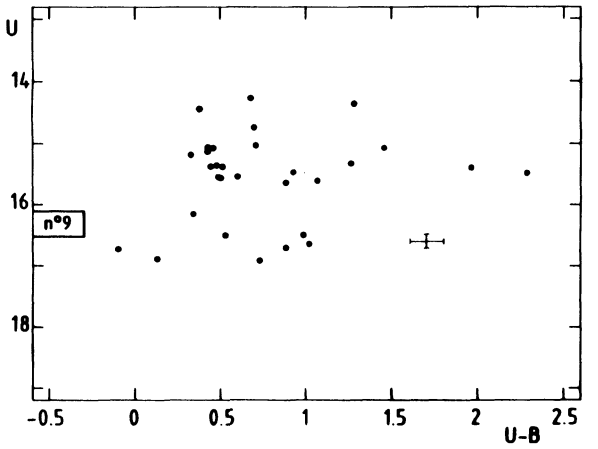

Figure 7 :

U/U-B colour magnitude diagram for 31 stars resolved in the error circle for 47 Tuc X-ray source. The possible locus for the blue star 9 is shown. The large cross shows a typical interval error of 0.1 mag. (in both magnitude and colour) due essentially to background determination.

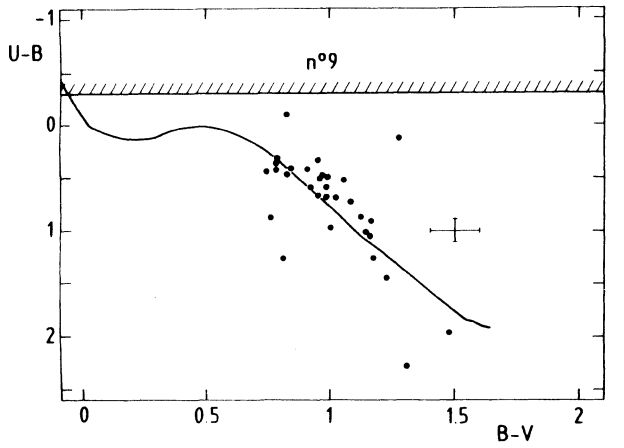

Figure 8 :

U-B/B-V two colours diagram for 31 stars resolved in the position error circle of the 47 Tuc X-ray source. The possible locus for the blue star 9 is shown. The solid line shows a population I relation reddened with E (B-V) = 0.04. The large cross shows a typical internal error of 0.1 mag (on both colours) due essentially to background determination.

3.3. Results :

Table 6 presents positions and photometry for the 33 stars resolved in the error circle. NUM is the star number marked on Fig 6 ; the X and Y define the star position in CCD pixel coordinates ; R_X is the distance in arcsec between the star and our best estimate of the X-ray source position in the field ; next columns give the classical UBV magnitudes and colours when available. Fig. 7 and Fig. 8 show the corresponding U/U-B colour magnitude and U-B/B-V colour-colour diagrams. These diagrams are the best suited for having hot objects stand out. Bars give our 1σ estimate of $\pm$ 0.1 mag. both in magnitude and colour. Star 9 appears of great interest. It stands out on the 3 U images obtained in July 1986, in good seeing conditions (U = 16.3 $\pm$ 0.2). This star is nevertheless almost invisible on our B and V frames (Fig. 6) and measurements appear to be almost impossible : if we impose the star position, it is found fainter than the limiting magnitude of the frames ; if the position is free, we find B = 16.8 and V = 16.4 but the star position moves by 0.6 arsec and 0.3 arsec respectively, with respect to the U position. One has to consider that star 9 is 1.2 arsec from a red giant (star 17). The contamination by star 17 is not troublesome in U (U = 15.4, FWHM = 1 arcsec) but is worse in B (B = 13.4) and in V, though seeing is better (FWHM = 0.8 arcsec but V ~ 12 and star 17 is slightly saturated). We then only got a lower limit for the B magnitude of star 9. We estimated B > 16.8 since this number is the magnitude of the two faintest stars well resolved in the field, star 6 and star 31 (which is only 1.7 arcsec from star 17) as well as the value found for star 9 (using ALLSTAR) when the position is free.

With U = 16.3 $\pm$ 0.2 we conclude that U - B $\leq$ - 0.3. The locus for star 9 is then plotted on Fig. 7 and Fig. 8 which show that this object is unusually blue for 47 Tuc. A typical star of 47 Tuc at the level U = 16.3 would have U - B~0.5 which gives B~15.8 and should have been easily measurable at the position of star 9.

Star 9 has the U-B colour of a hot object. Nevertheless, there is another possibility due to the tremendous crowding conditions : it could be a blend of several stars unresolved in U and somewhat diluted in B and V in the wings of the red giant star 17. We tested this hypothesis and concluded that would neither change significantly the present U magnitude nor the fact that star 9 is undetectable in B at present position : this may imply that star 9 has a marked negative U-B index. Only excellent angular resolution B observations will solve this problem.

The main conclusions of our optical investigation are :

- Under subarcsecond seeing conditions it is possible to resolve and measure stars down to U = 17 (V~16) in the field of the X-ray source in 47 Tuc. Taking $(m-M)_V$ = 13.4 and small absorption (Hesser et al., 1987) give M_U~3.6.

- We have not detected flaring stars down to this magnitude level, on our small sample of frames under consideration (Table 5).

- The bluest object observed in the present investigation, star 9, appears too UV to be a normal 47 Tuc star. It could be a hot star but we cannot discard the possibility of an observational bias due to blending of several objects in this overcrowded region. Star 9 stands out only on our best series of 3 U frames

Table 5 Journal of optical observations of 47 Tuc

Date	Instrument	FWHM	Band/Exp.time
1984-10-31	1.5 m + I.T.	about 1"	U/ 4 m x 2
1984-10-31	1.5 m + I.T.	about 1"	U/ 2 m x 2
1984-10-31	1.5 m + I.T.	about 1"	B/ 2 s x 1
1984-10-31	1.5 m + I.T.	about 0"8	V/ 1 s x 1
1985-06-25	1.5 m + RCA	1"3	B/15 s x 2
1985-06-25	1.5 m + RCA	1"3	V/30 s x 3
1986-01-01	2.2 m + GEC	1"4	U/ 2 m x 1
1986-01-01	2.2 m + GEC	1"1	B/30 s x 1
1986-01-01	2.2 m + GEC	1"	V/20 s x 1
1986-07-26	2.2 m + GEC	1"	U/ 2 m x 2
1986-07-26	2.2 m + GEC	1"	U/10 m x 1
1986-07-26	2.2 m + GEC	1"	B/30 s x 2
1986-07-26	2.2 m + GEC	0"8	V/20 s x 1

Table 6 - Positions and photometry for stars in the position error circle of the 47 Tuc X-ray source X0021.8-7221

NUM	X(1)	Y(1)	R_X(2)	U	B	V	B-V	U-B
1	232.25	256.25	0.65	16.15	15.81	14.86	0.95	0.34
2	239.08	254.23	2.43	15.13	14.71	13.87	0.84	0.42
3	237.17	246.55	3.05	15.37	14.86	13.90	0.95	0.51
4	231.91	246.95	2.34	15.60	14.54	13.38	1.16	1.06
5	225.45	250.80	1.70	16.90	16.17	15.09	1.08	0.73
6	227.30	255.38	0.64	16.73	16.83	16.01	0.82	-0.10
7	231.59	263.16	1.95	15.54	15.05	14.08	0.97	0.49
8	227.14	267.19	3.00	16.64	15.62	14.48	1.14	1.02
9	218.87	257.93	2.85	16.30				
10	221.06	242.49	4.09	15.36	14.89	14.07	0.82	0.47
11	235.22	239.62	4.39	14.28	13.61	12.66	0.95	0.67
12	251.26	255.81	5.52	14.34	13.07	12.26	0.81	1.27
13	246.08	262.00	4.48	15.07	14.61	13.87	0.74	0.45
14	239.67	269.15	4.27	15.46	14.54	13.38	1.16	
15	237.90	274.18	5.16	15.07	14.65	13.74	0.91	0.42
16	221.91	270.91	4.37	14.75	14.06	13.08	0.98	0.69
17	215.44	253.54	3.73	15.40	13.44	11.96	1.48	1.96
18	215.80	268.51	4.85	15.55	15.05	14.06	0.98	0.50
19	218.55	276.61	6.07	15.53	14.93	14.01	0.91	0.60
20	245.99	276.48	6.75		16.67	15.55	1.12	
21	249.10	270.59	6.25	16.70	15.82	14.70	1.12	0.88
22	256.58	267.76	7.54	15.07	13.62	12.39	1.22	1.45
23	254.81	262.56	6.66	15.32	14.06	12.89	1.17	1.26
24	255.61	248.12	6.93	15.52	14.92	13.94	0.98	0.60
25	239.93	236.46	5.62	15.18	14.86	14.08	0.78	0.32
26	223.01	236.30	5.31	15.37	14.93	14.15	0.78	0.44
27	208.15	250.93	5.70	14.44	14.07	13.28	0.78	0.37
28	250.04	238.96	6.77	15.47	13.19	11.88	1.31	2.28
29	244.08	237.50	5.97	16.48	15.95	14.90	1.05	0.53
30	216.23	240.01	5.35	16.50	15.52	14.52	1.00	0.98
31	212.89	259.61	4.45	16.89	16.76	15.48	1.27	0.13
32	249.00	259.00	4.97	15.02	14.32	13.30	1.02	0.70
33	244.00	264.00	4.22	15.62	14.74	13.98	0.76	0.88

(1) Coordinates of the star in pixel (1 pixel = 0.26 arcsec)

(2) Distance in arcsec between the star and the X-ray source position.

obtained in July 1986. In particular, it appears to be about 0.6 mag. fainter on image tube photographs obtained in excellent seeing on October 31, 1984. Since different instrumentation was used, this observation is unsufficient to prove variability.

Thus, star 9, 2.8 arcsec from the centre of our large error circle (7 arcsec radius) for the X-ray source position is a possibly hot and variable object ; it is only a weak candidate for the optical counterpart due to the difficulty of the measurements. To go on with this optical investigation, will require :

- better resolved B and V images of the field. The use of DISCO at the 2.2 m of ESO (Maaswinkel et al., 1987) should improve the present situation.

- additional U CCD images in good seeing conditions in order to confirm variability of star 9.

- accurate astrometry in the core of 47 Tuc in order to reduce the error box radius.

4. POSSIBLE NATURE OF THE X-RAY SOURCE IN 47 Tuc.

4.1. The luminosity :

The location of this source in the core of 47 Tuc suggests that it is a cluster member. The distance is thus well determined and the luminosity can be accurately derived : $L_X \sim 7\ 10^{33} - 2\ 10^{34}$ erg/s in the 0.2 - 4 keV energy range (see section 2). The most massive evolving stars in 47 Tuc are about 0.8 $m_\odot$ and a massive X-ray binary is then excluded. However, the above luminosity is 10 to 100 times lower than the luminosity of the faintest low mass X-ray binary (excluding quiescent soft transients) observed in or out of globular clusters (Verbunt et al. 1984) : the 47 Tuc X-ray source is then naturally classified in the dim globular cluster (G.C.) X-ray sources. Nevertheless, its luminosity is 4 times larger than that of the brightest of the cataclysmic variables (C.V) observed (up to now) in the galaxy (Cordova and Mason, 1983 : Patterson and Raymond, 1985). Now, Exosat observations of ω Cen (Verbunt et al. 1986 ; Koch-Miramond and Aurière, 1987) have shown two sources, HGA and HGD at the level $L_X = 10^{33}$erg/s. IPC spectra and two Exosat observations (Koch-Miramond and Aurière, 1987) suggest that this luminosity is real and not due to soft spectra. The rather large distance of these sources from the cluster centre (at about 5 core radii) and their variability properties are rather in favour of cataclysmic variables. Bright C.V. are thus likely to exist in globular clusters. Though being 4 times brighter than the most luminous C.V. in the galaxy (GK Per, Cordova and Mason, 1983) or HGA or HGD in ω Cen, the X-ray source in 47 Tuc could be a C.V. since it is fainter than the theoretical luminosity upper limit for accretion on a low mass white dwarf (Kylafis and Lamb, 1979, 1982). Nevertheless it should have been observed in outburst during the two Einstein HRI observations seven months apart, a rather unlikely hypothesis.

The place of soft X-ray transients in the evolution of LMXRB is beginning to be well understood (Hameury et al. 1987). Nevertheless, the quiescent phase is badly known because generally the X-ray flux is so faint that it is

unmeasurable. Two unambiguous detections of soft X-ray transient in quiescence have been recently reported however : Aquila X-1 with Einstein (Czerny et al. 1987) ; Cen X-4 with Exosat (van Paradijs et al. 1987). The sources were detected respectively at the 10^{34}erg/s and 2-4 10^{33}erg/s luminosity level. Transient LMXRB are also found in at least two globular clusters : bursts were detected in Terzan 5 with Hakucho (Inoue et al. 1984) while Einstein observations gave only an upper limit equal to $10^{34.5}$erg/s (Hertz and Grindlay 1983b) ; Liller 1 contains the transient rapid burster. The case of NGC 6440 can also be tentatively related to these objects : a bright transient source was observed (Markert et al. 1975 ; Forman et al. 1976) ; later, a weak source (8500 times fainter) was detected with the Einstein IPC (at the level $L_X \sim 10^{32.8}$erg/s (Hertz and Grindlay 1983b). These observations of NGC 6440 led Hertz and Grindlay, 1983b, to suggest that some of the dim G.C.X.R.S. could be transient LMXRB.

An interesting object also in our context is the transient low mass X-ray binary EXO 0748-676 (Parmar et al., 1986). It was detected on IPC Einstein observations at the level $L_X \sim 10^{34}$erg/s for an assumed distance of 10kpc. The nature of this low state is unclear : it could correspond to an intrinsic low level X-ray source or alternatively be due to hiding of the central source by the accretion disk (as EXO 0748-676 is observed at high inclination).

With respect to our 47 Tuc investigation, we have to remark that the only galactic X-ray sources which have a similar luminosity $L_X \sim 10^{34}$erg/s are the LMXRB Aquila X-1 in quiescence and EXO 0748-676.

4.2. The spectral data :

No very soft component was detected in the X-ray spectrum of the 47 Tuc source (see section 2) contrary to the case of U Gem in outburst (Cordova and Mason, 1983).

As to soft X-ray transients in quiescence in Aquila X-1 a good fit is obtained with a thermal bremsstrahlung with $kT \sim 2.7$ keV, (Czerny et al, 1987) very similar to what we obtain for 47 Tuc. In the model of Hameury et al. (1986) for S.X.R.T. however, the quiescent Xray flux has a harder composition (more than a few keV).

In conclusion, the spectrum obtained for the 47 Tuc X-ray source does not show characteristic features of either C.V. or LMXRB but is compatible with both hypotheses.

4.3. Periodic pulsations :

Periodic oscillations similar to those discovered in the 47 Tuc X-ray source (section 2.2) are observed in all sub-classes of C.V. (Cordova and Mason, 1983). Periods and degrees of coherence in the same range that we have obtained are seen in the optical and soft X-rays (0.1-0.5 keV) light curves of SS Cyg, U Gem, Am Her and 2A0311-227. This latter object and AE Agr, TT Ari and YZ Cnc also show rapid pulsations at higher (greater than 0.5 keV) X-ray energies at periods ranging from 9 sec to 4 min. These oscillations may last for a few cycles or be quasi-periodic or even coherent in many cataclysmic

binaries.

Two LMXRB are known to show periodic X-ray pulsations (Joss and Rappaport 1984) : X 1626-67 and X2259 + 586 ; Her X 1 and GX 1+4 may be related also to this class of objects (Taam and van den Heuvel, 1986). Nevertheless, in the case of these X-ray pulsars, transient behaviour, multiple periods and strong modulations are not expected for the pulsations.

The periodic pulsations discovered in the X-ray data of 47 Tuc are thus a strong argument in favour of a C.V. However, since it is now believed that some LMXRB can evolve to X-ray pulsar then to rapid radio pulsar (Taam and van den Heuvel, 1986 ; Verbunt 1988) one cannot rule out completely that a LMXRB could present the periodic pulsations observed in 47 Tuc.

4.4. Optical survey :

C.V. in outburst are about $M_V \sim 3$ in the galaxy (Warner, 1976). Taking (m-M)v = 13.4 (Hesser et al., 1987) gives V = 16.4 and $U \sim 16$ for a blue object. Scaling the optical flux for the brightest galactic C.V., SS Cyg and GK Per in outburst, (Cordova and Mason, 1983) to the relative Einstein IPC X-ray flux gives V = 15.2 and 16.8 respectively. Thus, a bright C.V. in outburst in 47 Tuc could be detectable with our optical survey. On the other hand, a quiescent C.V. at the time of the optical observations should be much fainter ($Mv \sim 7$) and out of reach for our survey.

In the case of LMXRB observed at high inclination we could expect the ratio $L_X/Lopt < 1$. If we normalize the M 15 X-ray flux to the 47 Tuc X-ray flux, assume the same spectrum for both optical counterparts and $L_X/Lopt = 1$ (as in the case of 2S0921-630), we find $U \sim 16$ for 47 Tuc. Such an object is within reach of our optical survey.

At quiescence, the optical spectrum of a soft X-ray transient is expected to be dominated by the secondary object i.e. a faint main sequence star. In Cen X-4, one K7V star is observed with $M_V > + 7.8$ (Chevalier et al. 1988) and in Aquila X - 1 one KO V star is observed, with $M_V \sim 5.9$ and $U - B > - 0.1$ (Charles et al. 1980). Such objects which are typical of what is expected in this case, are obviously out of reach of our optical investigations.

Thus, if an optical counterpart for the 47 Tuc X-ray source was confirmed, it should prove that it is a C.V. or a LMXRB observed at high inclination.

5. CONCLUSION.

The periodic X-ray pulsations presented by X0021.8-7221 in 47 Tuc strongly suggest that it is a C.V. However, its position in the core and its luminosity would be better fitted by a soft X-ray transient in quiescence.

The confirmation of a detected optical counterpart should rule out the soft X-ray transient hypothesis. On the other hand, the properties of star 9 of our optical survey, if confirmed, are quite compatible with what is expected for a C.V. New high angular resolution observations of the central region of 47 Tuc are thus urgently needed.

Acknowledgments.

The authors gratefully acknowledge the support received from the Einstein Observatory data analysis team. We are particularly grateful to D. Harris and C. Stern for patiently and efficiently running the F.F.T. and FOLD programs for us. We would like to thank F. Seward for his help during analysis, J. Grindlay and R. Rocchia for stimulating conversations, R. Buonanno for doing ROMAFOT analysis on our field and P. Stetson for making ALLSTAR available to us. The optical part of this work was done while M.A. and S.O. were visiting the ESO scientific group in Garching.

References

Ables J.G. et al. 1988, IAU circular N°4602

Aurière, M. : 1986, in ESO-OHP Workshop on "The Optimization of the Use of CCD Detectors in Astronomy", J.P. Baluteau and S. D'Odorico Editors, p. 223.

Aurière, M.; Cordoni,J.P. : 1981, Astron. Astrophys. Suppl.46 ,347

Aurière M., Koch-Miramond L., Ortolani S. 1988, Astron. Astrophys., in press

Aurière, M. Le Fèvre, O., Terzan, A. : 1984, Astron. Astrophys. 138, 415.

Aurière, M., Ortoloni, S. : 1987, submitted to Astron. Astrophys., ESO preprint n° 553.

Avni, Y. : 1976, Astrophys. J. 210, 6242

Bradt, H.V.D., McClintock, J.E. : 1983, Annn. Rev. Astron. Astrophys. 21, 13.

Charles, P.A. et al. 1980, Astrophys. J. 237,154

Charles, P.A., Jones, D.C., Naylor, T. : 1986,Nature 323,417

Chevalier, C., Ilovaisky, S.A., van Paradijs, J., Pedersen, H., van der Klis, M. : 1988, preprint.

Cordova, F.A., Mason, K.O. : 1983, in "Accretion-driven stellar X-ray sources" W.H.G. Lewin and E.P.J. van den Heuvel editors, 147.

Cordova, P.A., Mason, K.O. : 1984, Mon. Not. R. astr. Soc. 206, 879

Czerny, M., Czerny, B., Grindlay, J.E. : 1987, Astrophys. J. 312, 122.

Da Costa, G.S. : 1979, Astron. J. 84, 505

Forman, W., Jones, C., Tananbaum, H. : 1976, Astrophys. J. 207, L25.

Grindlay, J.E., Hertz, P., Steiner, J.E., Murray, G.S., Lightman, A.P.: 1984, Astrophys. J., 282,L13

Hameury, J.M., King, A.R., Lasota, J.P. : 1986, Astron. Astrophys. 162, 71.

Hameury, J.M., King. A.R., Lasota, J.P. : 1987, Astron. Astrophys. 171, 140

Harnden, F.R., Fabricant, D.G., Harris, D.E. and Schwarz, J.: 1984, Smithsonian Astr. Obs. special report 393

Hertz, P., Grindlay, J.E. : 1983a, Astrophys. 267, L83

Hertz, P., Grindlay, J.E. : 1983b, Astrophys. J. 275, 105.

Hertz, P., Wood, K.S. : 1985, Astrophys. J. 290, 171.

Hesser, J.E., Harris, W.E., Vandenberg, Don A., Allwright, J.W.B., Shott, P. Stetson, P.B. : 1987, Pub. Astron. Soc. P. 99,739.

Inoue, H. et al. : 1984, Pub. Astr. Soc. Japan 36,855

Joss, P.C., Rappaport, S.A. : 1984, Ann. Rev. Astron. Astrophys. 22,537.

Koch-Miramond, L., Aurière, M. : 1987, Astron. Astrophys. 183,1

Kylafis, N.D., Lamb, D.Q. : 1979, Ap.J. 228,L105

Kylafis, N.D., Lamb, D.Q. : 1982, Ap.J. suppl. 48,239

Landolt, A.U. : 1983, Astron. J. 88,439

Maaswinkel, F., D'Odorico, S., Huster, G., Bortoletto, F. : 1987, The ESO Messenger 48, 51.

Markert, T.H., Backman, D.E., Canizares, C.R., Clark, G.W., Levine, A.M. : 1975; Nature 257, 32.

Mason, K.O., Branduardi-Raymont, G., Cordova, F.A., Corbet, R.H.D.: 1987, Mon. Not. R. astr. Soc. 226, 423.

Middleditch J., Nelson J. 1973, Astrophys. Lett. 14, 129

Ogelman, H., Beuermann, K., Krautter, J. : 1984, Astrophys. J. 287 , L 31

Parmar, A.N., White, N.E., Giommi, P., Gottwald M. : 1986, Astrophys. J. 308, 199.

Patterson, J., Raymond, J.C.: 1985, Astrophys. J. 292,535 and 550

Sawyer Hogg, H. : 1973, "A third catalogue of Variable Stars in Globular Clusters" Publ. of the David Dunlap Observatory University of Toronto, vol. 3, n°6

Stetson, P.B.: 1987, Pub. Soc. Astron. Pac. 99, 191.

Taam,, R.E., van den Heuvel, E.P.J. :1986, Astrophys. J. 305, 235.

Van Paradijs, J., Verbunt, F., Shafer, R.A., Arnaud, K.A. : 1987, Astron. Astrophys. 182, 47.

Verbunt, F. : 1988, to be published in "The physics of compact objects : theory vs. observation" eds N.E. White and L. Filipov Pergamon Press.

Verbunt F., Shafer R., Jansen F., Arnaud K., van Paradijs J., 1986 Astron. Astrophys. 168, 169

Verbunt, F., van Paradijs, J., Elson, R. : 1984, Mon. Not. R. astr. Soc. 210, 899.

Warner, B. : 1976, in UAI Symposium 73 "Structure and Evolution of Close Binary systems", P. Eggleton, S. Mitton, J. Whelan editors, p. 85.

A New 60-msec X-Ray Pulsar and Its Massive Early-Type Companion(★)

Patrizia A. Caraveo, Giovanni F. Bignami and Andrea Goldwurm(*)

Istituto di Fisica Cosmica del C.N.R. Milano ITALY

(*)Univ. of Southampton, Physics Dept. U.K.

ABSTRACT

Einstein Observatory IPC and HRI observations of a serendipitous, variable, X-ray source in the galactic plane in Carina are presented. Timing analysis shows the source to have a periodicity P ~ 60 msec. The optical identification with the 12.7 mag Wack 2134 star, suggested by the positional coincidence, is confirmed by spectroscopic observations done at ESO La Silla. The star appears to be probably of O5 type. The X-ray and optical data suggest the discovery of a new binary system where a hot massive star loses mass to a spinning neutron star, which would then be the fastest X-ray binary pulsar to date.

(★)Based on Observation Collected at the European Southern Observatory, La Silla, Chile

INTRODUCTION

The X-ray investigations of the region of the Galactic plane around l = 284 , b = 0 with the Imaging Proportional Counter (IPC) of the Einstein Satellite (Giacconi et al, 1979) was originally conceived as a search for soft X-ray counterparts of the COS-B galactic gamma-ray source 2CG 284-00 (see Bignami and Hermsen, 1983). The X-ray coverage (discussed in Goldwurm et al.,1987, hereafter Pap.I) yielded three serendipitous sources: 1E1021.5-5720 a weak source of probable stellar origin, 1E1022.2-5730 an extended source coincident with RCW49, and 1E1024.0-5732, a relatively bright, variable point source tentatively identified in Pap I with Wack 2134, an $m_v \sim 12.7$ *mag* early-type star.

In what follows, we shall present a detailed analysis of the reprocessed Einstein Observatory observations of this source, as well as results of a first set of optical observations carried out at ESO - La Silla which confirm the X-ray source identification and suggest the system to be of the massive type containing a young massive star and the fastest X-ray pulsar to date. The properties of this new system will be briefly discussed also in view of its distance and absolute luminosity.

THE X-RAY DATA

Our soft X-ray data were collected during two IPC observations performed on 1979 July 13 (1700 sec exposure time) and on 1980 July 8 (7600 sec exposure time) and an HRI observation of 7000 sec performed on 1980 July 10. The count-rate of 1E1024.0-5732 varied significantly between the two reprocessed IPC observations. Discovered as a $3.6\ x10^{-2}$ count/sec serendipitous source, 1E1024.0-5732 yielded one year later a total of 450 photons at a rate of $(5.92 \pm 0.02)\ x10^{-2}$ counts/sec, or 70% higher that the 1979 rate. However, no significant variability was present during the > 2 hour observation. Inspection of the POSS plates at the IPC position readily excluded the possibility of the source being due to coronal emission from a field star. With an f_x/f_{opt} of $5x10^{-2}$ it could possibly be linked to the emission line star Wack 2134 (as suggested by Hertz and Grindlay (1984) and in Pap I) marginally compatible with the IPC error circle. The source was

H. Ögelman and E. P. J. van den Heuvel (eds.), Timing Neutron Stars, 243–249.

subsequently detected with the HRI, albeit at a meagre $6x10^{-3}$ counts/sec. Direct comparison between the IPC and HRI fluxes on July 1980 is difficult, due to the obvious presence of heavy interstellar absorption for this source at l = 284.5 deg and b = -0.23 deg and to the HRI greater response to lower energy photons. Because of its weak flux and of its off-centre location in the HRI field, the source was positioned with an 8″ uncertainty (instead of the more usual ~4″) at α = 10h 24m 4.35sec, δ = -57 33′ 22.7″. This is compatible with the position of Wack 2134 (α = 10h 24m 5.4sec, δ = -57 33′ 24.0″), and by itself renders the identification virtually certain.
As for the source X-ray spectral properties, and the subsequent absolute flux and absorbing column determination, Table 1 shows how the IPC counts are distributed in energy, for the nominal value of the instrumental gain. It is apparent that 1E1024.0-5732 is well visible only in 7 energy channels, thus making any spectral fitting procedure very difficult and uncertain. Only general remarks can be made: while the low energy channels are empty because of the heavy interstellar absorption, the lack of photons for E > 3.5 KeV is significant and suggests a relatively steep source spectrum. On the other hand, uncertainty in the instrument's gain also plays a role because of the off-axis position of the source in the IPC field. Power law-,bremsstrahlung-, and black-body-type fits were tried on the data with no definite conclusion because of the limited number of channels available for the fitting as well as uncertainties on N_H and gain. As a result the source flux could be anywhere between the extreme cases of (1) several 10^{-10} erg/cm^2 sec for a pure exponential fit with $N_H = 6x10^{22}$ and kT = .16 KeV and (2) few 10^{-11} erg/cm^2 sec for a black body fit with $N_H = 2x10^{22}$ and kT = .25 KeV or for a power law fit with $N_H = 6x10^{22}$ and index 3.3.
Photon arrival time analysis was performed on this source for the 1980 (long) IPC observation. Barycentrized arrival times of events within a circle of 15 pixels of the maximum and with energies between .5 and 3.5 KeV were used. The FFT power spectrum gave the highest power in the run for P = 0.0606928 sec. The 337 photon arrival times were then folded around such suggested period, covering the range from 60.6925 to 60.6932 msec with < 30 independent steps of $\sim 310^{-8}$ sec. A reduced χ^2 (9 d.o.f.) of 6.57 was obtained for period 60.69272 ± 0.00006 msec, for the light curve shown in fig. 1 . The chance occurence probability of such light curve is negligible ($< 10^{-7}$), even when the scanning steps are taken into account. A necessary check on the temporal behaviour of an equivalent number of background photons showed a completely flat distribution. Finally, for the period value shown in fig.1, the a posteriori check was performed of decreasing the acceptance radius for the source photons: while decreasing statistics, this improves the signal to noise ratio. Accordingly, the χ^2 value was seen to reach 7.3 for a radius of 10 pixels (231 photons), with a light curve similar to that in fig. 1. Periodicity was also searched for in the 1979 observation with negative result, in itself inconclusive owing to the limited number (~40) of available photons.
In view of the general source characteristics, and in particular of its looking like an X-ray binary, it would be reasonable to search for a period derivative. As mentioned, the few hundred source photons were collected during a total instrument active time of 7600 sec, while the total elapsed time during the measurement was 15,000 sec . This means that any $\dot{P} > 10^{-11}$ sec/sec. would have destroyed the photon coherence over the observation. This value thus represents a firm upper limit to the system period derivative,if supposed constant during the observation. Breaking down the observation to search independently for periodicity in separate data sets appeared hopeless, since the $\dot{P}$ value required to show a significant difference in period value between the sets (of less than 100 photons each) would be higher than the upper limit quoted above.

OPTICAL OBSERVATIONS

The region of the sky containing 1E1024.0-5732 was observed on Jan. 30, 1987 with the ESO Faint Object Spectrograph and Camera (Dekker and D'Odorico, 1985) at the 3.6m La Silla telescope. Fig. 2 shows a 10 sec CCD image of the field taken through a V filter, after dark current substraction an flat fielding on dome sunlight. The pixel length is 0.675 arcsecs, and the seeing was measured at 1.8″. Both the IPC and HRI error boxes are shown, the latter being somewhat wider than usual (8″ radius) as mentioned. Down to the plate limit of > 20 mag., only two objects are seen to be compatible with the HRI (and IPC) position: Wack 2134 ($m_v = 12.67$) on the eastern side, and a fainter star ($m_v = 15.75$) on the west. The region of the sky, on the galactic plane at the Carina longitudes, is very crowded, in spite of the heavy absorption. A chance coin-

cidence is thus probable, even in the HRI error box. Spectra were obtained for all objects brighter than $m_v \sim 16$ in the IPC/HRI error boxes, using the EFOSC Multiple Objects Spectrograph (MOS), with the resolution of 6 A per CCD pixel. While the spectra of the other stars show no peculiarities, the spectrum of Wack 2134 deserves attention. The general shape of the spectrum, shown in Fig 3, is obviously affected by heavy interstellar absorption, and the B-V value derived from continuum integration is 1.48.

As for spectral lines, first of all one notes the presence of interstellar absorption features, such as λ = 6284 A, a blend between 6212 and 6164 A, λ = 5890 A (NaD), possibly λ = 5780/5797 A, and λ = 4430 A. Unfortunately, for most of these interstellar absorption lines the precise determination of the equivalent widths presents serious problems : 6284 may be saturated and may need a correction for telluric O_2, the region around 6200 is a blend impossible to disentangle, the NaD and other lines around 5700-5900 are contaminated by the star's emission. On the other hand, a good E.W. determination for 4430 is possible, yielding a value of $\sim$4.0 A, or, according to the calibration of Herbing (1975), an $E_{(B-V)} = 1.9$, and thus $A_v \sim 6.3$ (Herbst, 1975).

As to the star's emission lines, the very strong feature at 4686 can certainly be attributed to HeII emission, one of the characteristics of X-ray binaries, and in this case a further basis for the identification with the X-ray source. A possible weak NIII (or CIII) at 4640, the possible but weak presence of HeI at 5876, and the very weak Pickering HeII lines all favour a spectral type earlier than about O5. The very strong Hα emission (the basis for the Wackerling classification, 1969) has a width of $>$40 A, very large and possibly due to electron scattering, or otherwise corresponding to a Doppler width of $>$ 2000 Km/sec, and broader emission wings cannot be ruled out. On the other hand, the Balmer decrement is high ($H_{\beta,\gamma,\delta,\varepsilon}$ barely visible, with a possible double-peaked structure in H_β) and in itself would rule against a strong light contribution from an accretion disc. Finally, we note that the strong emission feature at 5804 A can be attributed to CIV, but, although CIV emission is frequently present in Wolf-Rayet stars, Wack 2134 does not show the line pattern typical of WR's. Thus, a W-R classification for Wack 2134 remains somewhat of an open question.

In summary, it appears tempting to classify Wack 2134 as an early O type, at least on the basis of the present spectrum, although one should of course use caution when dealing with a star so heavily reddened and anyway coupled with a strong X-ray emitter which could perturb its atmosphere. A classification of this type would also favour a stellar-wind accretion on to the spinning neutron star (see the Hα width?) and be consistent with absence of light from an accretion disc, which is seldom formed in these systems or which, if present, should be fainter than the star. All O-type stars have B-V of $\sim$-0.32, yielding and $E_{(B-V)}$ of 1.8 in nice agreement with value derived from the IS lines E.W.'s, in spite of the big uncertainty involved in the $E_{(B-V)}$ determination from IS lines.

CONCLUSIONS

The X-ray and optical data presented above definitely support the association of 1E 1024.0-5732 with Wack 2134. This can best be interpreted with the discovery of a new X-ray binary, characterized by a rapidly spinning neutron star accreting from an O (W-R ?) type primary. Of course, no direct evidence of the binary nature of the system is present in the data given above, since, for example, only one optical spectrum is available. Moreover, no orbital modulation could be observed in the X-ray period; on the other hand our upper limit on a $\dot{P}$ for the system is certainly not very restrictive, owing to the short observation and limited photon statistics. One can note that the strong variation observed between the two IPC data sets and the absence of pulsation in the low flux observation (in itself not significant due to the limited counts) could be consistent with the pattern of recurrent outbursts of emission as, e.g. in the case of A0538-66 (Skinner et al 82). The latter is a system in the LMC in which a rapidly spinning neutron star (P $\sim$ 69 msecs) is in an eccentric orbit around a massive B star and accretion only occurs near periastron. The problem with 1E1024.0-5732 is that its luminosity is highly uncertain, due to the heavy interstellar absorption. If the $A_v \sim 6.3$ value deduced both from the star colors and from the interstellar lines in the spectrum is to be trusted, the dereddened apparent magnitude of Wack 2134 is $m_v \sim 6.4$, while the M_v of an early O-type is -6, insensitive to the luminosity class (e.g. Allen, 1973). Since, anyway,

hot stars much brighter than $M_v = -6$ do not exist, the corresponding distance modulus of ~ 12, or 3 kpc, is, in a sense, an upper limit for the distance of 1E 1024.0-5732. In this Carina region of the galactic plane, 2 mag of absorption per kiloparsec are probably acceptable, also considering the presence of molecular clouds at least close to the line of sight. Obviously, a better determination of A_v is crucial for this star. However, taking 3 kpc as the distance value the X-ray data are compatible with a luminosity range, from 10^{34} *ergs/* sec to 10^{36} *ergs/* sec (0.5 – 3.5 *KeV*). This ample X-ray luminosity range, coupled with the uncertainty in the optical A_v determination, renders very difficult to extract, from the observed f_x/f_{opt} of $5x10^{-2}$, a meaningful L_x/L_{opt}, which could be in the range 10^{-4} – 10^{-2}, in agreement with the MXRB data compilation of, e.g., van Paradijs,1983.

In summary, the system 1E1024.0-5732/Wack 2134 is probably a new X-ray binary of the rarely observed type including a fast spinner and a massive early-type star, most likely losing mass through stellar wind accretion on the neutron star companion. It is, at the time of writing, the fastest X-ray (binary) pulsar in the sky, and it obviously deserves further X-ray and optical observations, firstly directed to the search for an orbital law of the system.

Acknowledgements This work was partially supported by the PSN of the Italian CNR and by NATO grant RG 86/0120. A.G. acknowledges receipt of an Angelo della Riccia Fellowship.

REFERENCES

Allen C.W. 1973 Astrophysical Quantities, 3rd edn. The Athlone press London
Bignami, G. F. and Hermsen, W. 1983 Ann. Rev. Astr. Astrophys. 21, 675
Dekker H. and D'Odorico S. 1985 ESO Operating Manual N.4
Giacconi, R. et al. 1979 Ap.J. 230, 540
Goldwurm, A., Caraveo, P.A. and Bignami G.F. 1987 Ap.J. 322,349
Herbing, G.H. 1975 Ap. J. 196,129
Herbst, W. 1975 Astron. J. 80,498
Hertz, P. and Grindlay, J.E. 1984 Ap.J. 278,137
van Paradijs J. 1983 in"Accretion Driven X-Ray Sources" p.189 eds Lewin, W.H.G. &van den Heuvel ,E.P.J. Cambridge University press
Skinner, G.K., Bedford, D.K., Elsner, R.F., Leahy, D., Weisskopf, M.C., Grindaly, J. 1982 Nature 297,568
Wackerling, L.R. 1969 Mem. R.A.S., 73,153

TABLE 1

Energies (keV)	Net Counts
0.03- 0.16	-4.5± 5.9
0.16- 0.32	9.1± 6.4
0.32- 0.55	8.9± 6.1
0.55- 0.80	20.5± 7.7
0.80- 1.07	36.8± 8.8
1.07- 1.38	58.2± 8.8
1.38- 1.72	57.7± 8.2
1.72- 2.13	42.2± 7.8
2.13- 2.68	36.4± 6.6
2.68- 3.47	18.9± 6.9
3.47- 4.44	7.3± 6.5
4.44- 5.81	1.0± 5.6
5.81- 7.95	2.9± 6.8
7.95-10.65	-8.4± 6.9

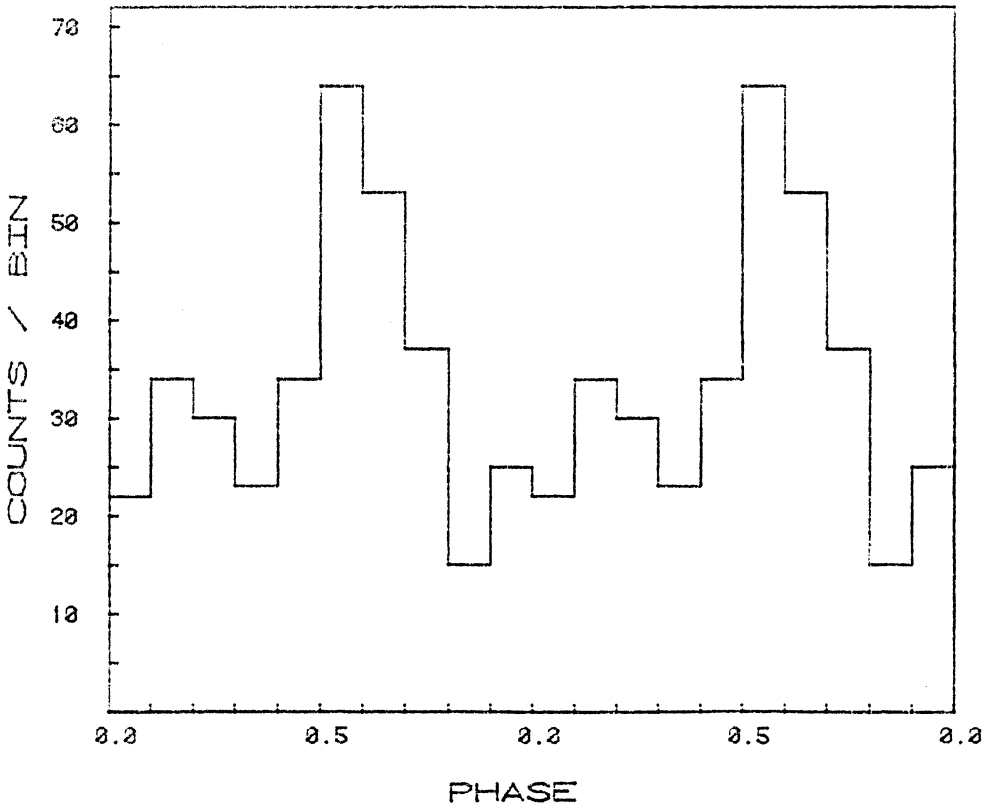

Figure 1 Light curve of 1E 1024.0-5732 for the 1980 IPC observation. Photon arrival times are folded modulo P = 60.69272 msec. The reduced χ^2 (9 d.o.f.) is 6.57. The pulsed fraction of the source is seen to be ~ 50%.

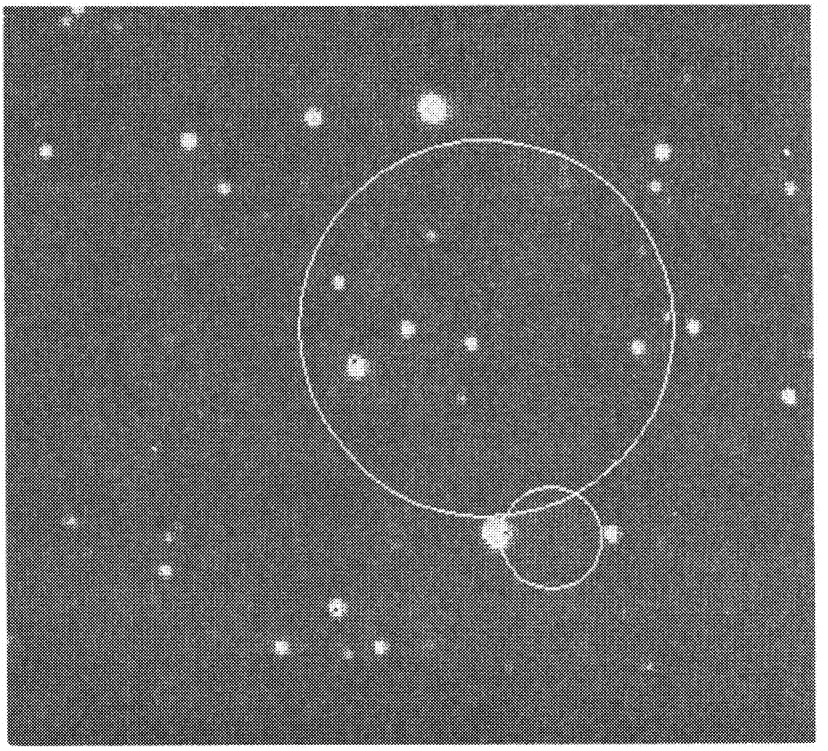

Figure 2 The field of 1E1024.0-5732 shown as a V-filter, 10-sec exposure taken with the EFOSC at the ESO 3.6m at La Silla. The IPC (30″ radius) and the HRI (8″ radius) error circles are shown. The candidate counterpart, Wack 2134 of $m_v = 12.67$ is on the eastern side of the HRI error box. North at top, East at left.

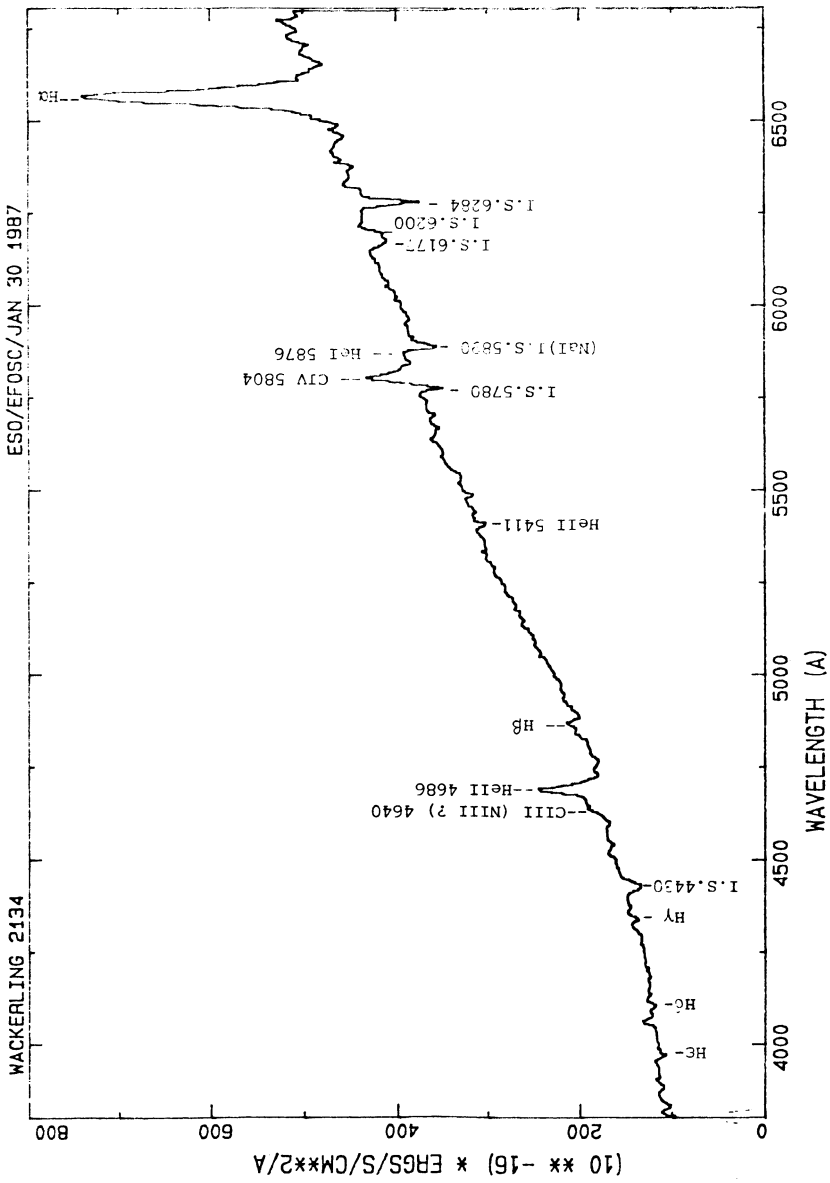

Figure 3 Optical spectrum of Wack 2134, taken at the 3.6 m ESO La Silla. Resolution is 6 A. Heavy interstellar reddening and absorption feature are apparent over the star spectrum, probably of O5 type (see text)

Non-Planckian behaviour of burst spectra: dependence of the blackbody radius on the duration of bursts

E. M. F. Damen
Astronomical Institute 'Anton Pannekoek'
Roetersstraat 15
1018 WB Amsterdam
The Netherlands

ABSTRACT
From a statistical study of X-ray bursts observed with EXOSAT from 4U/MXB 1636-53 and EXO 0748-67, we find a strong correlation between the burst duration and the blackbody temperature of the burst source, as measured at 10% of the Eddington flux. In view of the evidence that the burst duration depends on the chemical composition of the bursting layers, this correlation suggests that deviations of burst spectra from a Planck curve depend on the chemical composition of the bursting layers.

1. INTRODUCTION

The spectra of X-ray bursts can be described reasonably well by a blackbody model. However, the emission from atmospheres, dominated by electron scattering (as is the case for neutron star surface layers during bursts), is expected to deviate substantially from that of a blackbody [1, 23]. Detailed knowledge of these deviations is essential in attempts to determine the mass-radius relation of neutron stars from burst observations [21, 25]. Several authors have published numerical models of radiative-equilibrium neutron-star atmospheres, considering inelastic electron scattering and free-free and bound-free absorption processes [4, 5, 12, 15, 16, 19].

Observations of bursts from 4U/MXB 1636-53 and 4U 1608-52 [17] and EXO 0748-676 [9] have shown that bursts from a single source sometimes show different blackbody radii at the same color temperature. For 0748-676 a correlation of the blackbody radius with the persistent emission has been found [9].

We here report some results of a time-resolved spectral analysis of all X-ray bursts observed with EXOSAT from 1636-53 and 0748-676, emphasizing deviations from a blackbody. We find a strong correlation between the duration of the burst and the blackbody temperature, as measured at a fixed flux level (i.e. the blackbody radius). Possible consequences of these results for the determination of the mass-radius relation of neutron stars are discussed.

H. Ögelman and E. P. J. van den Heuvel (eds.), Timing Neutron Stars, 251–256.

2. OBSERVATIONS AND ANALYSIS METHOD

EXOSAT observations of the low-mass X-ray binaries 4U/MXB 1636-53 and EXO 0748-676 lasted in total ~180 hours, and ~14 hours, respectively. 60 X-ray bursts were recorded from 1636-53, and 35 from 0748-676. Two bursts from 0748-676 occurred during X-ray eclipse, and have been excluded from our analysis. Several bursts have been analyzed and described before [9, 10, 14, 20, 22]. Using an adapted version of an EXOSAT data analysis package developed at the Space Research Laboratory in Leiden, we (re-)analyzed all bursts in a uniform way.

In this analysis, we fitted burst spectra, after subtraction of background and persistent emission, with a blackbody model, including a low-energy cut off. This fit yields a color temperature kT_c, and a bolometric flux F_{bol}. Details on the analysis method are described in [2].

3. RESULTS

Fig. 1 gives the data of three representative bursts from 1636-53 in a log F_{bol} vs log kT_c diagram, comparable to a Hertzsprung-Russell diagram. Data points from the rising parts of the bursts have been excluded from this diagram, since they have large uncertainties in kT_c. Typical errors at several flux levels are indicated on the left part of the diagram. This diagram clearly shows that the cooling tracks can differ from burst to burst, and that bursts do not exactly behave like a cooling blackbody with a fixed radius (the latter would have a cooling track with a slope of value 4, as

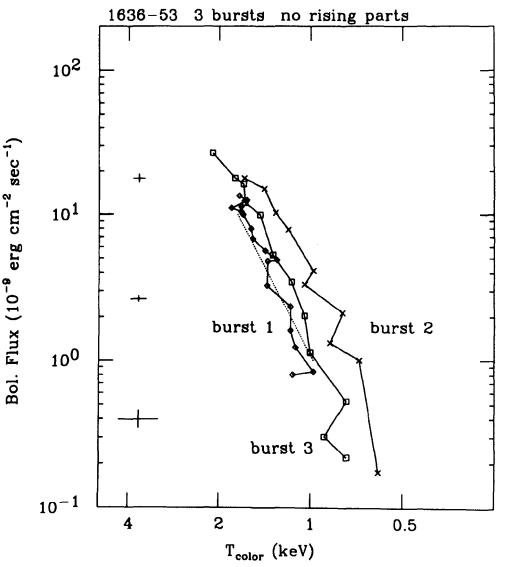

Fig. 1: Diagram of bolometric flux vs fitted color temperature of three different bursts from 1636-53. Clearly, the position and slope of cooling tracks can differ for bursts from a single source. The dashed line is a theoretical cooling track for a blackbody with a radius of 10 km at a distance of 10 kpc.

indicated by the dashed line). The difference in temperature at the same flux level is equivalent to a difference in blackbody radius, according to the relation:

$$4\pi d^2 F_{bol} = 4\pi R_{bb}^2 \sigma T_c^4$$

Here d is the source distance, F_{bol} the observed bolometric flux, R_{bb} the blackbody radius, and T_c the fitted color temperature.

To analyze the differences between bursts in a more quantitative way, we made lineair least-square fits to the data points in the HR-diagram for each burst separately. We limited these fits to the part of the cooling track that is approximately straight for all bursts and centered the fits at the 10% Eddington flux level of the sources (the Eddington flux, F_{edd}, equals the observed average maximum flux of bursts showing radius expansion, and has the value 6.3 x 10^{-8} and 4.0 x 10^{-8} erg cm^{-2} s^{-1} for 1636-53 and 0748-676, respectively) The results are expressed in the fit parameters: the slope of the fit Σ and the value of kT_c at 10% of the Eddington flux, $kT_{0.1}$.

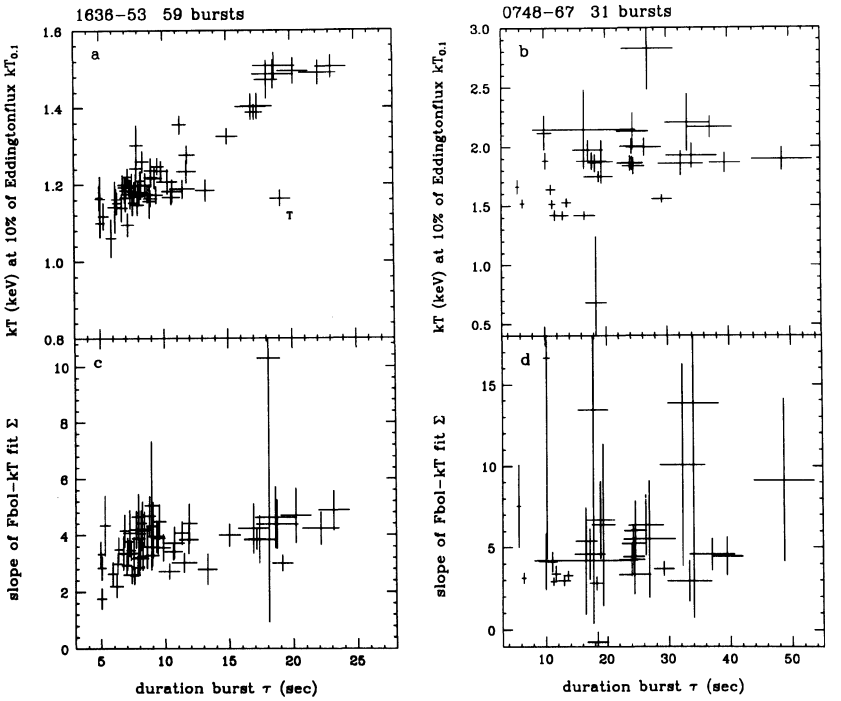

Fig. 2: (a) and (b): relation between the duration of bursts and the fitted color temperature at 10% of the Eddington flux in the burst for 1636-53 (a) and 0748-676 (b); (c) and (d): relation between the duration of bursts and the slope of the cooling track in the HR-diagram for 1636-53 (c) and 0748-676 (d). See text for more details.

We searched for possible correlations of the fit parameters with other burst properties, and found that the duration of the bursts τ (defined as the ratio of total burst fluence over peak flux, E_b/F_{max}) is correlated with $kT_{0.1}$. This correlation is displayed in Figs. 2a and 2b for 1636-53 and 0748-676, respectively. The correlation is very strong in the case of 1636-53, and weaker (but definitely present) in 0748-676. The point designated with "T" in Fig. 2a is the triple burst [24], which shows three peaks in its bolometric flux profile, probably caused by multiple release of energy. Because of this, the burst has a relatively long duration but a "normal" cooling track, shifting it to the right in the diagram.

Figs. 2c and 2d show Σ as a function of τ for 1636-53, and 0748-676, respectively. For 1636-53, there is a clear correlation between these two parameters: the average value of the slope increases from ~2.5 for bursts with $\tau \lesssim 7$ sec to ~4 for bursts with $\tau \gtrsim 15$ sec. The latter value ($\Sigma = 4$) equals the value expected for Planckian spectra. In the case of 0748-676, interpretation of the results is difficult, due to large error bars on the data points, caused by the fact that most of the fits in the HR-diagram are done on only few points (but always more than two). Fig. 2d shows no correlation between Σ and τ, as in 1636-53. The average value of Σ for all data points for 0748-676 is ~5.5, which drops to ~4.5 if we exclude the points with large error bars.

4. DISCUSSION AND CONCLUSION

Possible explanations for the correlation of $kT_{0.1}$ with τ are: (i) variable anisotropy of the burst radiation; (ii) variation in the size of the radiating area, and (iii) non-Planckian burst spectra. We will discuss each explanation separately:

i) It is likely that the burst radiation is not isotropic (e.g. [6, 11]). However, the question is whether the anisotropy is constant throughout a burst, and has the same value in every burst. The small scatter around the relation between maximum burst flux and waiting time for 1636-53 [14], and the presence of a gap in the distribution of burst peak fluxes for 1636-53 (related to a difference in Eddington limits for hydrogen-rich and hydrogen-poor meterial, see [27]), indicates that major variations of the anisotropy probably do not occur.

ii) The same arguments as above hold for this explanation. A variable radiating area would increase the scatter in a diagram of maximum burst flux vs waiting time, and would smear the flux gap.

iii) Apart from the above arguments, the fact that the variations in $kT_{0.1}$ are correlated with the duration of the bursts indicates that they are intrinsic to the burst, and not caused by geometric effects outside the neutron star. The most likely cause of the variation in $kT_{0.1}$ is a variable deviation of burst spectra from a Planckian function.

There is evidence that the burst duration is determined by the chemical composition of the flashing layer (see e.g. [7, 26] and references therein). Bursts which are due to helium flashes in a hydrogen-rich environment, last longer than pure helium bursts, due to

the relatively long time scales involved in proton capture processes. The shift of position in the HR-diagram of the cooling tracks of long bursts, relative to those of short burst, is in qualitative agreement with theoretical cooling tracks of hydrogen-rich and hydrogen-poor bursts [3]. Our results therefore suggest that it is the variation in composition of the flashing layer that changes the burst spectrum. For this relation to exist there must be mixing between the flashing layer and the neutron star atmosphere during bursts. Note however, that the variation in $kT_{0.1}$ is much larger than can be expected on the basis of these models [3].

The dependence of the burst spectra on the composition of the atmosphere must be taken into account in determinations of the mass-radius relation of neutron stars from observations of X-ray bursts. To illustrate this, we show in fig. 3 mass-radius relations for the neutron star in 1636-53, based on two bursts from this source. The curves shown are the results of calculations using a method described in [21], without applying any correction for differences between color temperature and effective temperature.

Our results show that detailed information on model-atmosphere parameters (such as chemical composition) is needed before information of neutron star properties can be inferred from an interpretation of X-ray burst spectra.

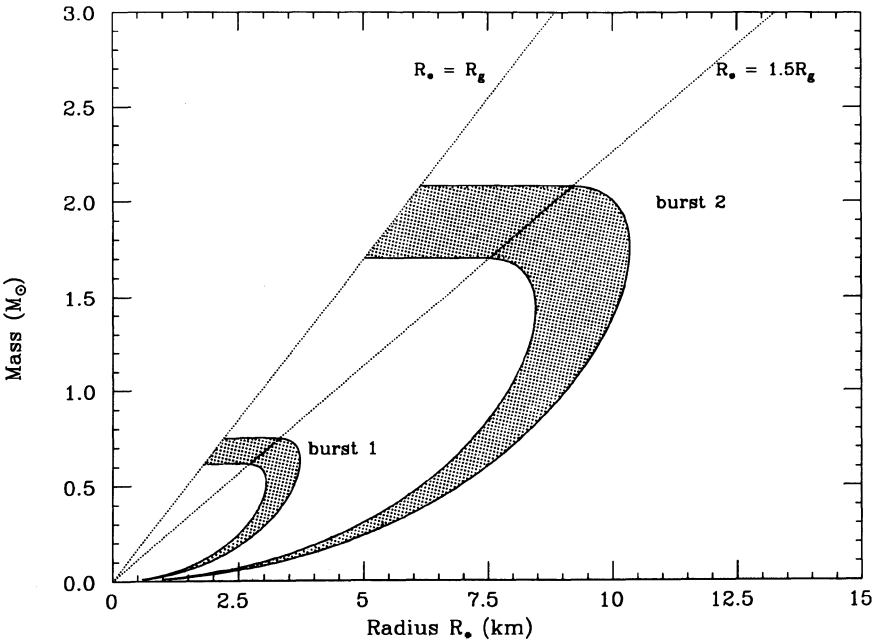

Fig. 3: Mass-radius relation of the neutron star in 1636-53, based on data from a long burst and a short burst (burst 1 and 2, see fig. 1). Curves are 1 sigma uncertainty contours, arising from errors on color temperature.

ACKNOWLEDGEMENTS
ED is supported by the Netherlands Organisation for the Advancement of Research NWO/ASTRON under contract no. 782-371-019.

REFERENCES

[1] Czerny, M., Sztajno, M., 1983. Act. Astron., **33**, 213
[2] Damen, E., Jansen, F., Penninx, W., Oosterbroek, T., van Paradijs, J., Lewin, W., 1988. Mon. Not. R. astr. Soc., submitted
[3] Ebisuzaki, T., Nakamura, N., 1988. Astrophys. J., **328**, 251
[4] Ebisuzaki, T., Nomoto, K., 1986. Astrophys. J., **305**, L67
[5] Foster, A. J., Ross, R. R., Fabian, A. C., 1986. Mon. Not. R. astr. Soc., **221**, 409
[6] Fujimoto, M., Y., 1988. Astrophys. J., **324**, 995
[7] Fujimoto, M. Y., Hanawa, T., Miyaji, S., 1981. Astrophys. J., **247**, 267
[8] Gorenstein, P., 1975. Astrophys. J., **198**, 95
[9] Gottwald, M., Haberl, F., Parmar, A. N., White, N., 1986, Astrophys. J., **308**, 213
[10] Gottwald, M., Haberl, F., Parmar, A. N., White, N., 1987. Astrophys. J., **323**, 575
[11] Lapidus, I. I., Syunyaev, R. A., 1985. Mon. Not. R. astr. Soc., **217**, 291
[12] Lapidus, I. I., Syunyaev, R. A., Titarchuk, L. G., 1986. Sov. Astron. Lett., **12**, 383
[13] Lawrence, A., Cominsky, L., Engelke, C., Jernigan, G., Lewin, W., Matsuoka, M., Mitsuda, K., Oda, M., Ohashi, T., Pedersen, H., van Paradijs, J., 1983. Astrophys. J., **271**, 793
[14] Lewin, W., Penninx, W., van Paradijs, J., Damen, E., Sztajno, M., Trümper, J., van der Klis, M., 1987. Astrophys. J., **319**, 893
[15] London, R., Taam, R., Howard, W., 1984. Astrophys. J., **287**, L27
[16] London, R., Taam, R., Howard, W., 1986, Astrophys. J., **306**, 170
[17] Matsuoka, M., 1987. In: The Evolution of Galactic X-ray Binaries, Rottach-Egern 1985, p.301, eds Trümper, J., Lewin, W.
[18] Schmidtke, P. C., Cowley, A. P., 1987. Astronom. J., **92**, 374
[19] Syunyaev, R., Titarchuk, L., 1986. Sov. Astron. Lett., **12**, 359
[20] Sztajno, M., van Paradijs, J., Lewin, W., Trümper, J., Stollman, G., Pietsch, W., van der Klis, M., 1985. Astrophys. J., **299**, 487
[21] Sztajno, M., Fujimoto, M., van Paradijs, J., Vacca, W., Lewin, W., Penninx, W., Trümper, J., 1987. Mon. Not. R. astr. Soc., **226**, 39
[22] Turner, M., Breedon, L., 1984. Mon. Not. R. astr. Soc., **208**, 29P
[23] van Paradijs, J., 1982. Astr. Astrophys., **107**, 51
[24] van Paradijs, J., Sztajno, M., Lewin, W., Trümper, J., Vacca, W. D., van der Klis, M., 1986. Mon. Not. R. astr. Soc., **221**, 617
[25] van Paradijs, J., Lewin, W., 1987. Astr. Astrophys., **172**, L20
[26] van Paradijs, J., Penninx, W., Lewin, W., 1988. Mon. Not. R. astr. Soc., submitted.
[27] Sugimoto, D., Ebisuzaki, T., Hanawa, T., 1984. Publ. Astron. Soc. Japan, **36**, 839

X-RAY SPECTRAL VARIABILITY OF LOW-MASS X-RAY BINARIES

Michael R. Garcia
Harvard-Smithsonian Center for Astrophysics
60 Garden Street
Cambridge, MA. 02138, USA

ABSTRACT. We report on a study of the x-ray spectral variability of 37 low-mass x-ray binaries (LMXRB). The sample studied consists of all LMXRB which were detected with the EINSTEIN Monitor Proportional Counter (MPC) at greater than 10 c s^{-1} . The spectral variability has been studied through the use of Hardness-Intensity Diagrams (HID). The brighter sources often show complicated HID which contain 'loops', while the HID of the less bright, bursting sources are much simpler. We speculate on the cause of the 'loops' in the HID, and point out that observations of bursts in the brighter sources may help to determine the cause of the loops. The spectral variations of some of the bursters indicates that Compton scattering mechanisms dominate their x-ray emission. It is shown that the brighter sources may have a higher level of radio emission than the bursting sources, indicating that additional energy generation mechanisms are operating in the brighter sources.

1. INTRODUCTION

Studies of the variability of the X-ray flux in LMXRB have proven to be among the most effective methods for advancing our understanding of these sources Parsignault and Grindlay (1978) studied the spectral and temporal variation of 20 LMXRB with data from the ANS satellite. Their main conclusion was that the sources could be grouped into two classes showing markedly different spectral and temporal behavior. An important distinction between the two classes is that the class 1 (brighter) sources show positive correlations of hardness ratio (HR, defined as the ratio of counts in a high energy band to those in a lower energy band) with intensity, while the class 2 (weaker, and bursting) sources show either no correlations or negatively correlated HR variations. Similarly, Ponman (1982) studied the spectral variations of 15 LMXRB with data from the Ariel 5 RMC, and concluded that the sources can be grouped into 'super-critical' (brighter) and 'sub-critical' (bursting) classes. Van Paradijs and Lewin (1986) point out that these two classification schemes divide the sources into nearly identical groups, and that the underlying discriminator appears to be luminosity — the bursting

H. Ögelman and E. P. J. van den Heuvel (eds.), Timing Neutron Stars, 257–266.

sources have X-ray luminosities (L_X) $\sim 10^{37}$ erg s^{-1}, and the brighter sources have $L_X \sim 10^{38}$ erg s^{-1}.

Using data from the Tenma GSPC, Mitsuda (1984) was able to explain why the spectra of LMXRB typically harden with increasing counting rate. The spectra cannot be represented by a simple one component model, but are adequately described by a two component model consisting of a soft and a hard component. The harder component is more variable, therefore producing the positive correlation of HR and intensity typically seen.

The more complicated looping seen in the HID of some sources, initially in Cyg X-2 (Branduardi *et al.* 1980) and GX5-1 (Mitsuda 1984) remains largely unexplained. The similarity of this behavior to that expected for cataclysmic variables (CV, Kylafis and Lamb 1982) lead Branduardi *et al.* to suggest that Cyg X-2 was a CV system. Subsequent measurements of the source luminosity (Cowley, Crampton and Hutchings 1979, McClintock *et al.* 1984) and the discovery of bursts (Kahn and Grindlay 1984) show that it is a LMXRB, not a CV. The observational picture has advanced since these initial discoveries, in that we now know these loops are relatively common in the brightest sources (Hasinger 1987, Schulz and Hasinger 1987, Garcia 1987, Schulz, Hasinger and Trumper 1988). However, an understanding of the cause of these loops still eludes us. We suggest a possible cause of this looping behavior in the next section.

We have undertaken this study because the larger number of sources observed with MPC allows us to expand upon the previous studies. The results we have obtained are similar to those found by Schulz, Hasinger and Truemper (1988) in their study of the EXOSAT data. Additionally, the number of radio fluxes measured for LMXRB is now large enough to allow us to search for correlations between the radio flux and HID of the sources.

2. OBSERVATIONS

The sample includes 157 separate observations of 37 sources, with exposure times ranging from $\sim$ 1,000 to $\sim$ 70,000 seconds. Due to space limitations, the HID are shown here for only a few of the more interesting sources. The observations are often interrupted by earth block or SAA entry, rendering a continuous pointing into a series of snapshots of the source. A good example is the HR distribution seen in GX5-1 (Figure 1): it would appear to be a set of disjoint points, but observations of this source by other researchers, and observations of similar sources presented here (i.e., GX340+0, Figure 1) assure us that the points can be connected in a smooth fashion.

Two hardness ratios have been used: a soft hardness ratio, defined as the ratio of the source counts in the 3.5–7.0 keV/1.2–2.4 keV bandpasses, and a hard hardness ratio, defined as the source counts in the 10.2–20.0 keV/3.5–7.0 keV bandpasses. These values are plotted vs. total 1.2–20.0 keV counting rate, producing the HID

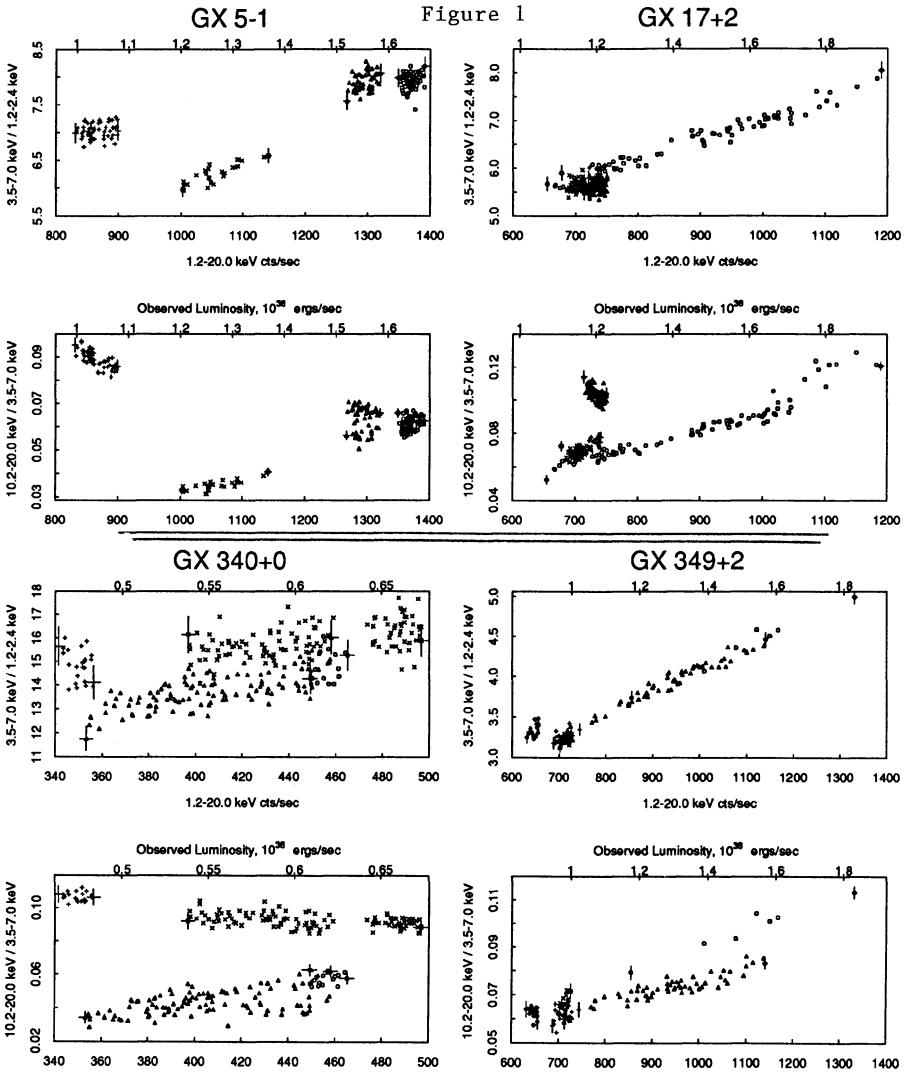

Figure 1

The HID are shown for four of the brighter sources; GX5-1, GX17+2, GX349+2, and GX340+0. In each case the 'soft' HID is presented above the 'hard' HID, and typical errors in the HR are shown. The top axis is luminosity in units of 10^{38} erg s^{-1}. Loops in the upper right of the hard HID are evident in GX5-1, GX17+2, and GX340+0, while a loop is visible in the lower left in the hard HID of GX349+2. In order to calculate the luminosities we have assumed that GX5-1, GX340+0, and GX349+2 are at the galactic center, which we take to be 7.0 kpc distant (Ebisuzaki, Hanawa, and Sugimoto 1984). We have assumed GX17+2 is at the 7.5 kpc distance derived from its burst luminosity (Ebisuzaki, Hanawa, and Sugimoto 1984).

for each source. The use of two somewhat independent energy bands for the hardness ratios allows both an investigation of the spectral changes over the entire 1–20 keV range, and a determination of the sensitivity of the HID to the chosen energy bands. The source counts are summed in 51.2 second blocks (= 20 readouts) in order to improve the statistical accuracy.

2.1 The Brighter Sources

A few of the more interesting HID are shown in Figure 1. These HID appear different from those presented by Schulz and Hasinger (1987) in that they are interrupted by gaps due to earth block and SAA entrance. However, we know from the continuous EXOSAT observations (Schulz and Hasinger 1987) that the sources move smoothly along these HID. The HID in three of the sources in Figure 1 (GX5-1, GX17+2, and GX340+0) show two distinct regions, one at higher, nearly constant hardness ratio (the Horizontal Branch or HB); and a second at lower, varying hardness ratio (the Normal Branch or NB). The branches meet to form a loop in the upper right of the HID. The fourth source in Figure 1 (GX349+2) has a HID nearly identical to that of Sco X-1 as seen with EXOSAT (Priedhorsky *et al.* 1986). Both of these sources have a loop in the HID at the lower left. A close

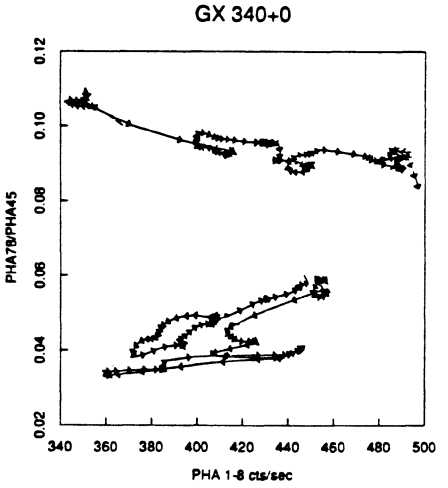

Figure 2:
This HID of GX340+0 has been further smoothed (in time) in order to show the source variations more clearly. What appears to be a single normal branch in Figure 1 is seen here (in the lower part of this diagram) to be two branches which connect at the lower left, one at nearly constant HR, and the other with HR increasing with counting rate. If this latter branch is extended it would meet the HB in the upper right. These three branches for a Z-like curve in the HID.

look at the HID for GX340+0 (Figure 2) shows that a single source can show both loops in the upper right and lower left, therefore forming a Z-like structure in the HID. The observation of this Z-like structure in GX340+0, and also in Cyg X-2, Sco X-1, GX17+2 (Schulz, Hasinger, and Truemper 1988) suggests that all sources form this Z, but we often observe only one section of it. As the loops on the upper right of the HID appear more common, we will concentrate on the interpretation of them in what follows.

As was mentioned earlier, the cause of these loops is not known. Currently, even the direction in which the mass transfer rate ($\dot{M}$) varies as the source moves along the HID is not known. However, it is tempting to assume that $\dot{M}$ varies monotonically along the loop, as the sources always move smoothly along the HID, never jumping directly from one branch to another. Assuming that the variation is monotonic, then the x-ray luminosity and $\dot{M}$ must be anti-correlated along one (or two) of the branches. We suggest that it may be possible to determine the variation of $\dot{M}$ through the observations of x-ray bursts which infrequently occur in these sources.

Several bursts, at least one of which has been identified as a Type 1 burst (Sztajno *et al.* 1985), have been seen to occur in GX17+2. Two of these bursts occurred when the source was at the lowest count rate section of the normal branch (Kahn and Grindlay 1984, Sztajno *et al.* 1985), and the third occurred when the source was at an intermediate count rate but still on the normal branch. If the steady state models of type 1 x-ray bursts are applicable (Ayasli and Joss 1982) then the occurrence of bursts on the normal branch implies that $\dot{M}$ must have temporarily fallen below the level above which nuclear burning proceeds smoothly ($\sim 5\times10^{-7}$ $M_\odot$/year). This implies that $\dot{M}$ must be lowest at the bottom of the NB, must increase up the NB and increase further as the source moves to the left along the HB of the HID. The mass transfer rate and x-ray luminosity would then be anti-correlated along the horizontal branch. This presents a problem for magnetospheric 'beat-frequency' models of Quasi-Periodic Oscillations (QPO; Alpar and Shaham 1985, Lamb *et al.* 1985), as they are based on the assumption that $\dot{M}$ and the x-ray luminosity are correlated on the HB (which is where the rapid QPO occur).

We tentatively suggest that the loop in the upper right of the HID occurs when $\dot{M}$ reaches the value corresponding to Eddington limited accretion. Given the uncertainties in the distances to these sources, the luminosity at the upper right corner the HID is consistent with that expected for Eddington limited accretion onto a 1.4 $M_\odot$ neutron star (see Figure 1). The further increase in mass transfer rate along the HB may therefore naturally lead to a decrease in the observed X-ray luminosity if the mass which cannot accrete blocks our view of the central source. This picture bears some similarities to the models for QPO on the HB by van der Klis *et al.* (1987) and Boyle, Fabian and Guilbert (1986), which postulate that intermittent obscuration of the central source causes the QPO. However, these models do not assume the mass transfer rate to be above Eddington on the HB.

We must point out two problems with the above picture. The first is a lack of statistics (we have considered only 3 bursts from GX17+2) and the second is the uncertain applicability of the steady-state model for x-ray bursts. The statistics on the number of relevant bursts can be improved by analysis of additional observations of GX17+2 (Tawara *et al.* 1984) or by analysis of observations of other bright LMXRB which occasionally burst (i.e., Cir X-1, 4U1820-30, and 4U1705-44). As the luminosity, and by inference $\dot{M}$, of the bright LMXRB can vary by large factors, the steady state model of x-ray bursts may not be applicable. However, application of the non-steady state model of x-ray bursts (Fushiki and Lamb 1987) should allow us to determine if the steady state model is correct in predicting that $\dot{M}$ is lower on the HB.

2.2 The Bursters.

In Figure 3 the HID for four of the less luminous sources are shown. It is immediately apparent that these HID are much simpler than those in Figure 1. Note that the statistics are still good enough that the looping behavior seen in the brighter sources could be seen here if it existed. In general, most of these sources show positive correlations of the HR with luminosity, in agreement with previous work. A few sources, most notably 4U1636-536 (Breedon *et al.* 1986) and in 4U1735-44 (Smale *et al.* 1986) have previously been seen to show negative correlations, which have been interpreted as being due to Compton cooling. The four sources show in Figure 3 show this unusual negative correlation of HR with intensity.

The negative correlation is most pronounced in the hard HID. At lower energies the typical positive correlation is still seen. This sort of spectral variation requires that the spectrum must inflect — that is, the count rate must increase at medium energies, and at the same time drop at the highest and lowest energies. In addition, a simpler behavior, that is only a drop in the count rate at high energies, is also seen at times (i.e., in some of the observations of 4U1636-536 shown in Figure 3).

These rather complex variations can be produced with a remarkably simple model — one of a source whose emission is dominated by Compton scattering processes. By fitting models to the observed spectrum we can determine the Compton parameter y, the gas temperature kT, and the electron scattering optical depth τ_{es}. The variations seen in GX3+1 can be interpreted as due to an increase in y and a decrease in kT. The behavior of 4U1636-536, GX339-4, and 4U1630-472 can be modeled with (at times) a simple drop in kT with y nearly fixed, and at other times as a drop in both kT and y. The gas temperature for these sources is found to range from 1 to 3 kev, the Compton parameter from 0.5 to 5, and the electron scattering depth from 5 to 20. By requiring that other emission mechanisms — most importantly thermal bremsstrahlung — do not contribute substantially to the X-ray flux, we can set limits on the size and density of the emitting region (c.f.

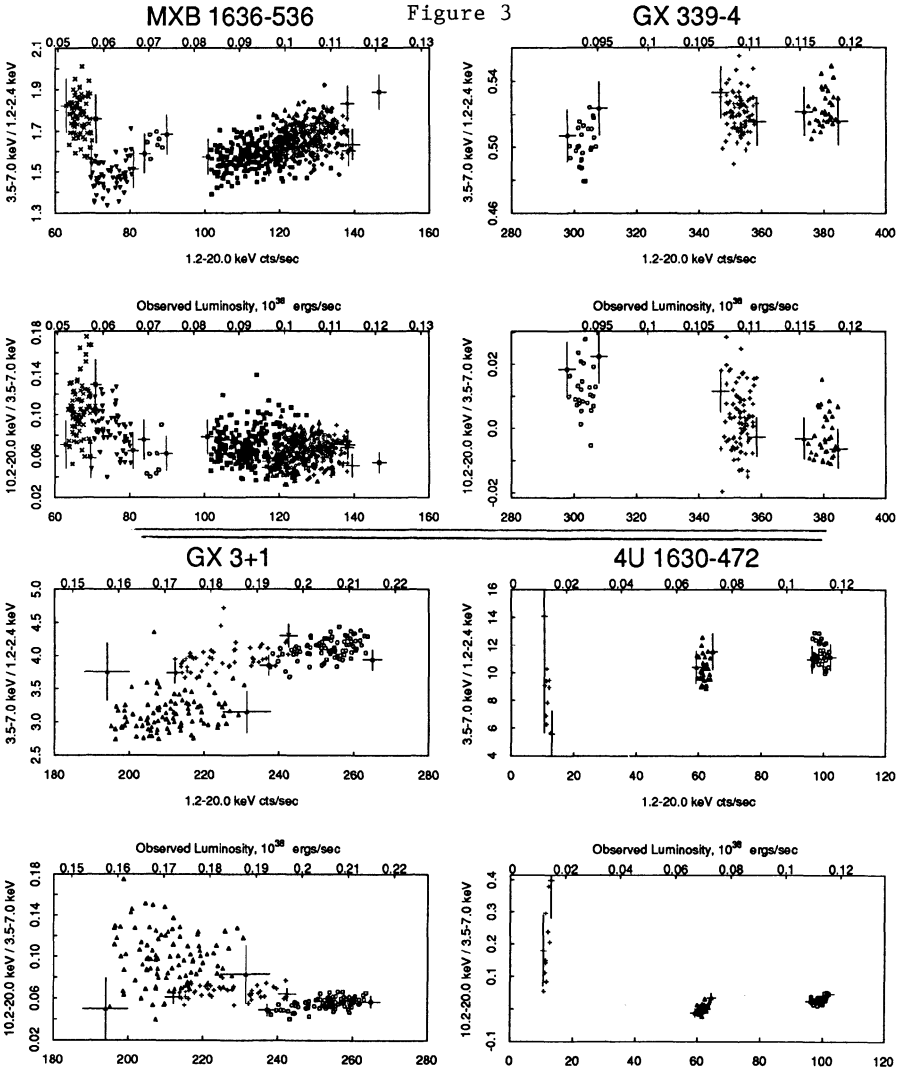

Figure 3

The HID are shown for four of the less bright, or bursting sources; 4U1636-53, GX339-4, 4U1630-47, GX3+1. In each case the 'soft' HID is presented above the 'hard' HID, and typical errors in the HR are shown. These HID are clearly simpler than those shown in Figure 1. While GX3+1 is usually not considered a bursting source, it did burst and was at a lower than average luminosity during the MPC observations. The distances used for the luminosity calculations are: 4U1636-53, 6.1 kpc; GX3+1, 5.9 kpc (Ebisuzaki, Hanawa and Sugimoto 1984); 4U1630-472, 7.0 kpc (assumed to be at the galactic center); GX339-4, 4.0 kpc (Maejima *et al.*1984, Doxsey *et al.*1979, Grindlay 1979).

Breedon *et al.* 1986). When this is done, we find that the scale height must be larger than the thermal scale height of gas near the neutron star, implying that the material is outflowing in a wind, or (perhaps more likely) that it is above the accretion disk.

It is curious that the timescale on which these negative correlations are seen to occur is rather long. Within individual several thousand second observations (for example of GX3+1) the HR is correlated with intensity, but when the three observation of GX3+1 are considered together (they are separated by 1 week and 1 year) the HR is seen to be negatively correlated with intensity. The observed timescale for what we assume to be Compton cooling is therefore very long compared to the timescale for Compton cooling of the corona surrounding a neutron star (Guilbert, Fabian and Ross 1982). It would seem that the temperature of the gas is regulated by mechanisms which change only on long timescales — and therefore it is not regulated by Compton heating and cooling mechanisms.

3. RADIO EMISSION.

Where radio emission from LMXRB has been well studied, most notably in Cyg X-2, GX13+1, and Sco X-1, the emission is non-thermal and most likely due to synchrotron emission from relativistic electrons. By studying the radio emission and its relation to other source properties we may learn what mechanisms generate the relativistic electrons necessary to power the synchrotron sources.

We wish to ask the question 'is there any difference in the radio emission of the brightest and less bright LMXRB?' Obviously they are different in their x-ray spectral behavior as we have just seen that the brighter ones show loops in the HIDs and also QPOs, which the less bright ones do not show. The brightest ones are also often detected at radio wavelengths — Figure 4 shows the ratio of the radio to x-ray flux (F_r/F_x) for these brightest sources and also for the less bright sources. The edge on system 4U1916-05 has anomalously high F_r/F_x (presumably because it has anomalously low F_x), and so has been excluded.

Using the method of detection and bounds (Avni *et al.* 1980) we can construct the most likely luminosity function of F_r/F_x for the bright sources, and then ask what is the probability of drawing each of the upper limits measured for the less bright x-ray sources from this luminosity function. This probability is 1.4%, indicating that the ratio of radio to x-ray flux is substantially higher in the brighter sources.

This enhanced radio emission may relate to the presence of QPO in these sources. If the magnetospheric models of QPO are correct in their prediction that the neutron stars in the bright sources have weak but non-negligible magnetic fields, then shearing of this magnetic field at the Alfen radius may generate the relativistic particles necessary to power the synchrotron radio source. Such an explanation for the radio emission of Sco X-1 has previously been suggested (Priedhorsky 1986).

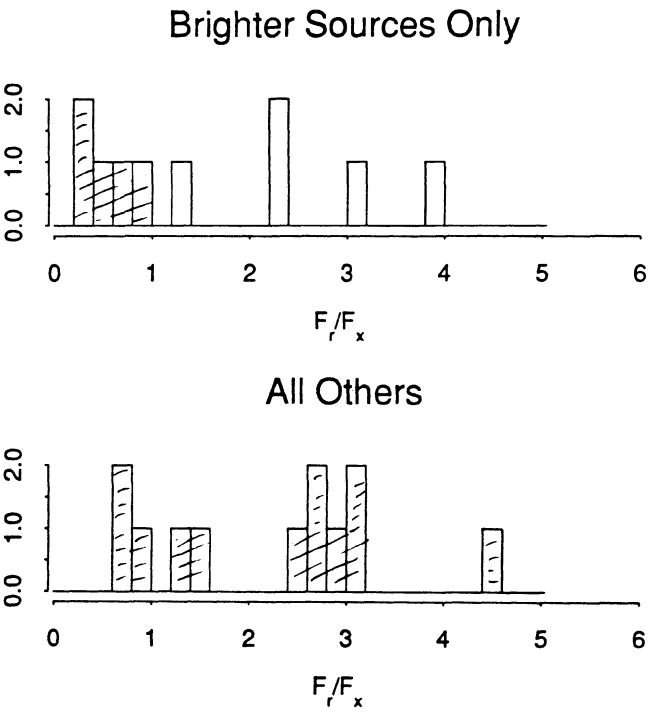

Figure 4:
Histograms of the ratio of radio to x-ray flux for the brighter and less-bright sources are shown. Hashed areas indicate upper limits. The radio flux measurements have been taken from the literature, predominately from Geldzahler (1983) and Grindlay and Seaquist (1984). The x-ray flux is that measured with the MPC.

REFERENCES.

Alpar, M.A., and Shaham, J. 1985, *NATURE* **316**, 239.
Avni, Y., Soltan, A., Tananbaum, H., and Zamorani, G., 1980, *Ap.J*, **238**, 800.
Ayasli, A., and Joss, P.C., 1982, *Ap.J.*, **256**, 637.
Breedon, L.M., Turner, M.J.L, King, A.R., and Courvoisier, T.J-L., 1986 *M.N.R.A.S.*, **218**, 487.
Boyle, C.B., Fabian, A.C., Guilbert, P.W., 1986 *Nature* **319**, 648.
Branduardi, G., Kylafis, N.D., Lamb, D.Q., Mason, K.O., 1980 *Ap.J.* **235**, L153.
Cowley, A.P., Crampton, D., and Hutchings, J.B., 1979 *Ap.J.* **231**, 539.
Doxsey, R., Grindlay, J.E., Griffiths, R., Bradt, H. , Johnston, M., Leach, R., Schwartz, D, and Schwartz, J., 1979 *Ap.J.* **228**, L67.
Ebisuzaki, T. Hanawa, T., and Sugimoto, D., 1984 *P.A.S.J.* **36**, 511.
Fushiki, I., and Lamb, D., 1987 *Ap.J.* **323**, L55.
Garcia, M.R., 1987, Ph.D. Thesis, Harvard University.
Geldzahler, B.J., 1983, *Ap.J.* **264**, L49.
Grindlay, J.E., and Seaquist, E.R, 1986, *Ap.J.* **310** 172.
Grindlay, J.E, 1979 *Ap.J. (Letters)* **232**, L33.
Guilbert, P.W., Fabian, A.C., and Ross, R.R., 1982 *MNRAS* **199** 763.
Hasinger, G. 1987 *Astr. Ap.* **186**, 153.
Kahn, S.M., and Grindlay, J.E., 1984, *Ap.J.* **281**, 826.
Kylafis, N.D., and Lamb, D.Q. 1982, *Ap.J.* **48**, L239.
Lamb, F.K, Shibazaki, N., Alpar, M.A., and Shaham, J., 1985, *NATURE* **317**, 681.
Maejima, Y., Makishima, M., Matsuoka, M., Ogawara, Y., Oda, M., Tawara, Y., and Doi, K., 1984, *Ap. J.* **285**, 712.
McClintock, J.E., Petro, L.D., Hammerschlag-Hansberge, G., Proffitt, C.R., and Remillard, R.A., 1984, *Ap.J.* **282**, 119.
Mitsuda, K., 1984, *X-ray Emission from Accreting Low Mass Binary X-ray Sources*, Ph.D. Thesis, University of Tokyo.
Parsignault, D.R., and Grindlay, J.E., 1978 *Ap.J.* **225**, 970.
Ponman, T., 1982, *MNRAS* **201**, 769.
Priedhorsky, W. 1986, *Ap. J. Lett*, **306**, L97.
Priedhorsky, W., Hasinger, G., Lewin, W. H. G., Middleditch J., Parmar, A., Stella, L., and White, N. 1986, *Ap. J. (Lett.)*, **306**, L91.
Schulz, N., and Hasinger, G. 1987, poster paper presented at *The Physics of Accretion onto Compact Objects*, ed. K.O. Mason, M.G. Watson, and N.E. White, (Springer-Verlag:Berlin)
Schulz, N., Hasinger, G., and Truemper, J. 1988, submitted to *Astr. Ap.*
Smale, A.P. , Corbet, R.H.D, Charles, P.A., Menzies, J.W., and Mack, P., 1986 *MNRAS* **223**, 207.
Sztajno, M., Trumper, J., Zimmerman, H., and Langmeier, A., 1985, *Adv. Space. Res.*, **5**, # 3, 113.
Tawara, Y., *et al.*, 1984, *Ap. J.* , **276**, L41.
van Paradijs, J. and Lewin, W.H.G., 1986, in *The Evolution of Galactic X-ray Binaries*, ed. J. Truemper, W.H.G. Lewin, and W. Brinkmann, (Reidel:Boston) p. 187.
van der Klis, M., Stella, L., White, N., Jansen, F., and Parmar, A.N., 1987 *Ap.J.* **316**, 411.

FRACTAL AND CHAOTIC TIME VARIATION IN CYGNUS X-1

S. Kitamoto and S. Miyamoto
Department of Physics, Faculty of Science,
Osaka University
1-1, Machikaneyama-cho, Toyonaka, Osaka, 560, Japan

ABSTRACT. The large area proportional counters onboard Ginga enabled us to investigate detailed time variability of a black hole candidate; Cyg X-1. Complex cross spectrum analysis between the fluxes in two different energy X-ray bands of Cyg X-1 indicates that the delay time of the high energy X-rays (15.8-24.4 keV) with respect to the low energy X-rays (1.2-5.7 keV) strongly depends on the frequency. The delay time of the high energy X-rays is about 2 msec at the period of about 0.01 sec and it increases almost linearly to several sec at the period of around 300 sec. Furthermore, it becomes negative at periods of several tens sec. Power spectral density analysis and variation function analysis show the larger time variation of the high energy X-rays compared to the soft X-rays, in the shorter time scale less than about 10 msec. These results can not be explained by the inverse Compton scattering model of Cyg X-1, which has been considered to be the mechanism that produces the high energy X-rays.

1. INTRODUCTION

Cyg X-1 is one of the black hole candidates. One of the characteristics of this source is the rapid and chaotic time variation in its intensity (e.g. Oda, 1977; Liang and Nolan, 1984). The origin, however, is not yet known. The power spectral density function (hereafter power spectrum) of this source is roughly 1/f noise between 10^{-1} Hz and greater than 10^{1} Hz (Nolan, 1981). Such 1/f power spectrum extended wide frequency range is unique in the galactic X-ray sources. The power law shape of the power spectrum means that the time variation has no characteristic time scale, or in other word, the time variation is self similar for the change of the time scale. It is interesting to study that to how much frequency the 1/f power spectrum extend.

For the X-ray energy spectrum of Cyg X-1, there is a model that high energy X-rays from Cyg X-1 are the result of inverse Compton scattering of low energy photons by a high temperature plasma situated at the central part of the accretion disk (Shapiro et al. 1976; Katz, 1976; Sunyaev and Trumper, 1979). If this inverse Compton scattering model is correct, high energy X-rays are expected to be delayed with respect to the low energy X-rays due to

H. Ögelman and E. P. J. van den Heuvel (eds.), Timing Neutron Stars, 267–275.

the scattering. To confirm this, several people (Brinkman et al. 1978; Weisskopf et al. 1975; Priedhorsky et al. 1979; Nolan et al. 1981; Page et al. 1981; Page, 1985) searched for the delay time using cross correlation methods. Page et al.(1981) found a high energy X-ray lag time of 7.5 msec between X-rays of 3-40 keV and 1-3 keV during the high state. Page (1985) also reported a hard X-ray lag time of about 6 msec between 5-14 keV and 2-5 keV X-rays in the low state. These lag times are very important to test the inverse Compton model and to estimate the size of the hot plasma. However, Ogawara et al. (1977) reported that the high energy X-rays in the range 10-25 keV have a larger variation in the time range less than about 5 msec than the low energy X-rays. This result is hardly explained by the inverse Compton model like that proposed by Sunyaev and Trumper (1979). Therefore, the reinvestigation of the short time variability and the hard X-ray delay time are important to test the inverse Compton model.

In this paper, we report the result of the analysis of good statistical data obtained with the large area proportional counters onboard Ginga. The power spectrum analysis will be described in section 3. The amount of the short time variability will be presented in section 4. In section 5, the high energy time delay will be shown. Discussion about the inverse Compton model will be in section 6.

2.OBSERVATION

Observations were made from August 5, 1987 to August 8, 1987 by large **area proportional counters** (Turner et al. 1988) onboard Ginga (Makino, 1987). On August 5, the observation was made with high time resolution (PC) mode to investigate short time variability of Cyg X-1. The observed energy ranges (time resolutions) were 1.2-5.7 keV (1 msec), 5.7-24.4 keV (2 msec), 1.2-15.7 keV (1 msec), and 15.8-24.4 keV (2 msec). The effective area of each energy bands was 2000 cm^2. On August 6 to 8, the observations were made in the MPC-3 mode, which had twelve energy channels for 1.2-37 keV, and the time resolution of 8 msec. The effective area was 4000 cm^2.

This report is based on the PC mode observations on August 5 and the MPC-3 mode observations on August 6. Data observed after August 7 are not included in this analysis, because these include data of the absorption dip phenomena, which are known to occur frequently at orbital phase of 0.9-1.0 in Cyg X-1 (e.g. Kitamoto et al. 1984). The orbital phase on August 5 and 6 are 0.6 and 0.8, respectively. During the observation, Cyg X-1 was in its low state.

3.POWER SPECTRUM

Figure 1 shows the power spectra of the data obtained on August 5, in the energy range 1.2-5.8 keV and 15.7-24.4 keV as a function of the period, over the period range from 4 msec to 64 sec. The contributions of the Poisson noise are removed. Both power spectra show clear bend at around 8 sec period. In the longer period region, the power spectra are approximately flat. However, in the

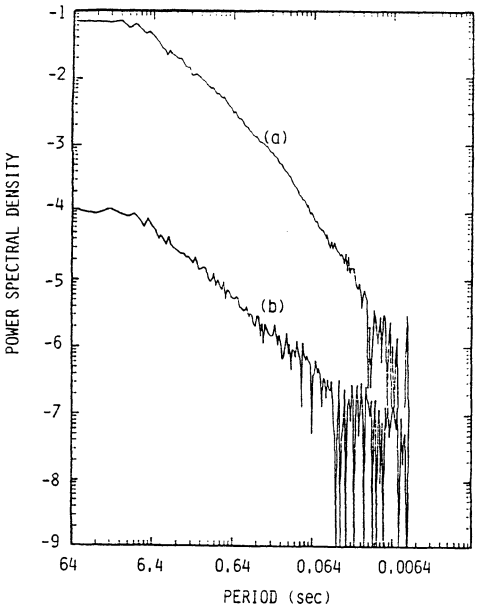

Figure 1. Power spectra of the data obtained on August 5, in the energy range 1.2-5.8 keV (a) and 15.7-24.4 keV (b) over the period range from 4 msec to 64 sec.

shorter period region, one can see a difference between the two power spectra. The power spectrum of high energy band appears to follow a power law with an exponent of about -1.1 ± 0.2. On the other hand, the low energy band shows more steep exponent and a small bend at a period of around 0.1 sec. The exponent in the range between periods 6 sec and 0.1 sec is about -1.15 ± 0.15, and that in the range less than 0.1 sec is about -1.9 ± 0.1. The power spectra of the data on August 6 also show similar dependence on the period.

4.VARIATION FUNCTION

To investigate the amount of the variation and the characteristic time scale of the variation, the variation function introduced by Ogawara et al.(1977) is useful. The variation function is defined as

$$\eta(\Delta T) = (\sigma^2 - \langle D \rangle)^{1/2} / (\langle D \rangle - B),$$

where <D> is the mean value of the time sequence data with ΔT bin, B is the background count for ΔT bin, and σ is the standard deviation of the time sequence data. The variation function is a function of the time bin width, ΔT, and it is recognized as a ratio of the standard deviation of the source flux minus the contribution of the Poisson statistics noise to the source flux. The variation function on the time bin width ΔT contains all the longer time scale variation than ΔT. Therefore, the variation function will exhibit a significant slope over time ranges corresponding to the characteristic time scale involved in the variability.

Figure 2 shows the variation functions of the 4 energy bands in the time range between 2 msec and 40 sec. For times longer than about 20 msec, higher energy bands have smaller variation, but in the range shorter than about 10 msec, the highest energy band has the largest variation. This is consistent to the result of the power spectrum analysis, where the power spectrum of the high energy band, in the small period range, has a small exponent in contrast with the large exponent of that of the low energy band.

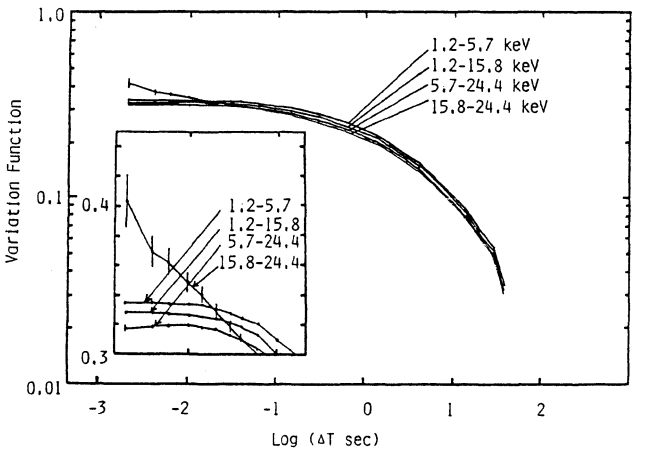

Figure 2. Variation functions of 4 energy bands in the range between 2 msec and 40 sec.

5.TIME DELAY IN HIGH ENERGY X-RAYS

To get the delay time between various energy bands, first, cross correlation functions are calculated between the energy bands of 1.2-5.7 keV and 15.8-24.4 keV with 2 msec bin. We find an asymmetric cross correlation, where the high energy X-ray delay direction has larger fall time. In other word, high energy X-rays are delayed. However, the displacement of the correlation peak is consistent with 0, and its upper limit is less than 5 msec. Therefore, the displacement of the correlation peak is not a good parameter to represent the time delay of the high energy X-rays. The fall times are also not good parameters, because the shape of the cross correlation is not exactly an exponential shape.

Therefore, we use the cross spectrum analysis, which was applied to investigate the time delays between different energy bands of the QPO sources by van der Klis et al.(1987). The time lag calculated from cross spectrum of 15.8-24.4 keV band from 1.2-5.7 keV band of the data obtained in August 5 are shown in figure 3. The hard X-ray delay time between 1.2-5.7 keV and 15.8-24.4 keV X-rays is about 2 msec at the period of about 0.01 sec, and it increases almost linearly up to several sec at the periods of around 300 sec. However, in the period region around 50 sec, soft X-ray lags appear.

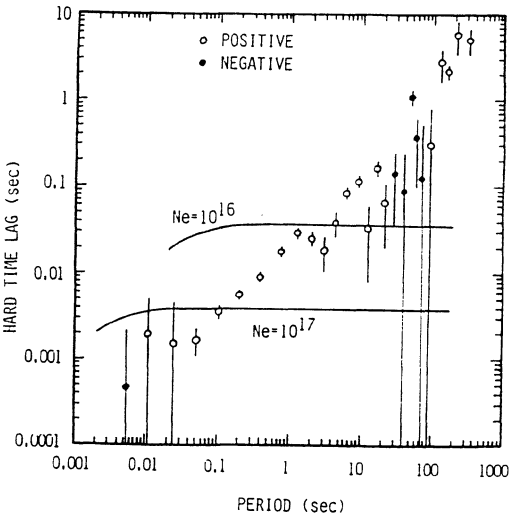

Figure 3. The phase dependent delay time of the hard X-rays (15.8-24.4 keV) from the soft X-rays (1.2-5.7 keV) of PC mode (August 5) data. Filled circles are those of negative values (soft X-ray lag). The expected delay time, from the inverse Compton model, between X-rays of energies of 3.5 keV and 20 keV are also shown, where we assumed that τ_{es}=5, kT=27 keV, N_e was 10^{16} and 10^{17} cm^{-3} and the initial photon energy was assumed to be 100 eV. The parameters except for N_e are those proposed by Sunyaev and Trumper(1979).

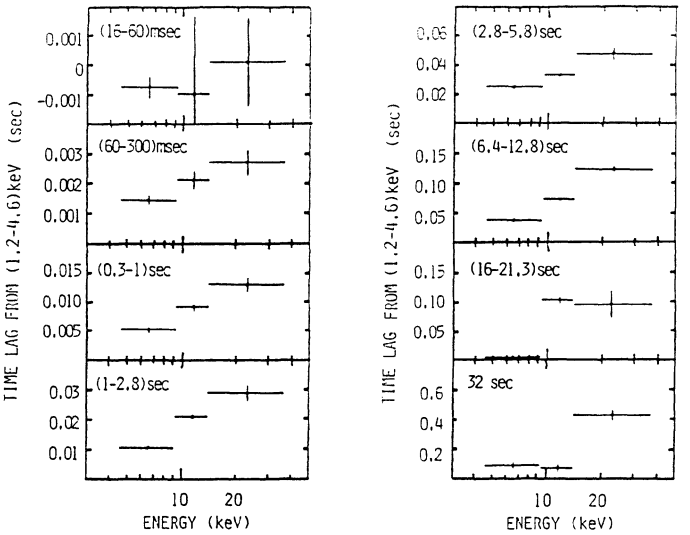

Figure 4. The energy dependence of the hard X-ray lag time. The data on August 6 (MPC-3 mode) were used. The lag times are averaged over the certain period band, shown in the figures.

To check the energy dependence of the hard X-ray lag time, using the data from August 6, the lag times of three energy bands relative to the energy band 1.2- 4.6 keV, are shown in figure 4. The time lag occurs over the complete energy band of the observation, in the range from several tens m sec to about tens sec. In other word, the higher the X-ray energy is, the larger the lag time is, in that period range.

6.DISCUSSION

The power spectrum of the high energy band shows a bend at about 8 sec period and follows a power law with an exponent of about -1.0, in higher frequency region. These results are similar to those reported by Nolan et al.(1981), although the frequency of the bend is slightly different. Nolan et al.(1981) reported that the bend is at a period of about 20 sec, in the energy range between 11 kev and 137 keV. Therefore, the difference between the bend frequencies may be due to the energy differences.

However, in low energy band, the power spectrum is steeper than that of high energy band. Furthermore, it shows a knee at around 0.1 sec period. This result means that Cyg X-1 has a characteristic time scale around 0.1 sec, in the low energy X-ray production mechanism, as well as the time scale of about 8 sec as observed at high energies.

We must address the question of how we are able to obtain such

time scales. The knee of the power spectrum of an exponential shot noise process occurs at several times the period of the decay time. However, a shot noise process with constant exponential decay time results in a power spectrum with f^{-2} dependence which is not observed, Therefore we need to consider more sophisticated shot noise models, for example, a bimodial distribution of shot time scale, etc.(Meekins et al.1984). Indeed, if we introduce the two type of the shot, with the decay time of 2 sec and 0.1 sec, we can simulate the power spectrum observed in the low energy band. But, since this model only explains the shape of it, the consistency to other observational results and the physical meanings of this shot model should be studied, in future work.

In the variation function analysis, we reconfirm the result reported by Ogawara et al.(1977), where the variability of the high energy X-ray band, on the time scale less than about 5 msec, is larger than that of the low energy band. This result is inconsistent with standard inverse Compton model (Shapiro et al. 1976; Katz, 1976; Sunyaev and Trumper, 1979), excepting special cases, for example, where a hot plasma varies in its size, density or temperature, on the time scale of m sec. In this case, the size of this plasma should be less than about 10^8 cm.

The frequency dependent hard X-ray lag time is also hard to explain by the inverse Compton model, though the energy dependence of the lag time favors this model. Sunyaev and Titarchuk (1980) and Payne (1980) analytically computed the radiation transfer in the plasma. Assuming a spherical hot plasma of a temperature T, Payne(1980) derived the time after an instantaneous input of soft photons of energy E_0 to reach maximum intensity, at a given energy E. Using their result, we can derive the difference time, t_{diff}, between the maximum fluxes of the energy E_1 and E_2 as,

$$t_{diff} \sim (1/2)((9/4)+(4\alpha/y)^{-1/2} (\ln(E_1/E_2))/((kT/m_ec^2)N_e\sigma c),$$

where α is the geometry dependent factor with a value of few, m_e is the mass of electron, N_e is the electron number density, σ is the Thomson scattering cross section, and $y=(4kT/m_ec^2)\tau^2$, where τ is the electron scattering optical depth. After flux maximum is reached, it decreases exponentially with an energy independent decay time constant of $\sim 3R\sigma_{es}/(\pi^2 c)$, where R is the radius of the hot plasma. As this decay time constant is independent of the X-ray energy, the delay time between X-rays of different energy bands is mainly determined by t_{diff} value given above. Thus it is expected that the delay time is similar in value for all frequencies (period). We simulated the dependence of the delay time on the frequency using Payne's result and found that the delay time is really almost constant with frequencies as shown in figure 3.

Thus the observed large dependence of the delay time on frequencies should be due to mechanisms other than the inverse Compton scattering, for instance, the temperature evolution of the shot process.

It is possible that the delay time of 2 msec at periods less than 0.1 sec is due to the inverse Compton scattering. In this case, however, the optical depth of the hot plasma should be less than about 1. Otherwise, the large part of the high energy X-rays

are produced by the scattering in the hot plasma, which do not remember the initial delay time relationship because of the various path lengths and the various energy exchange rates.

The soft X-ray lag appeared around several tens periods might occur when the X-ray emitting plasma is cooling down. Some reverse wave from the inner part of the disk to the outer part may cause the soft X-ray lag. The period, where soft X-ray lag occurs, may relate to the scale of a special disk region.

7.CONCLUSION

We studied the short term variation in Cyg X-1. The power spectrum indicates that Cyg X-1 has a characteristic time scale around 0.1 sec in the low energy X-ray production mechanism, as well as the time scale of about 8 sec as observed at high energies.

Power spectral density analysis and variation function analysis show the larger time variation of the high energy X-rays compared to the soft X-rays, in the shorter time scale less than about 10 msec. Complex cross spectrum analysis between the fluxes in two different energy X-ray bands of Cyg X-1 indicates that the delay time of the high energy X-rays (15.8-24.4 keV) with respect to the low energy X-rays (1.2-5.7 keV) strongly depends on the frequency. The delay time of the high energy X-rays is about 2 msec at the period of about 0.01 sec and it increases almost linearly to several sec at the period of around 300 sec. Furthermore, it becomes negative at periods of several tens sec. These results can not be explained by the inverse Compton scattering model of Cyg X-1.

Authors wish to thank all the members of the Ginga team. They also wish to acknowledge Miss Seiko Mizobuchi for her help to make the simulation calculation of the delay time. They also thank Dr. D. Roussel-Dupre of Los Alamos National Laboratory for her valuable comments.

REFERENCES

Brinkman, A.C., Parsignault, D.R., Schreier, E., Gursky, H., Kellogg, E.M., Tananbaum, H., and Giacconi, R., 1974, Astrophys. J., **188**, 603.

Katz, J.I., 1976, Astrophys. J., **206**, 910.

Kitamoto, S., Miyamoto, S., Tanaka, Y., Ohashi, T., Kondo, Y., Tawara, Y., and Nakagawa, M., 1984, Publ. Astron. Soc. Japan, **36**, 731.

Liang, E.P., and Nolan, P.L., 1984, Space Sci. Rev., **38**, 353.

Makino, M., and Astro-C Team, 1987, Astrophys. Lett. Communications, **25**, 223.

Meekins, J.F., Wood, K.S., Hedler, R.L., Byram, E.T., Yentis, D.J., Chubb, T.A., and Friedman, H., 1984, Astrophys. J., **278**, 288.

Nolan, P.L., Gruber, D.E., Matteson, J.L., Peterson, L.E., Rothschild, R.E., Doty, J.P., Levine, A.M., Lewin, W.H.G., and Primini, F.A., 1981, Astrophys. J., **246**, 494.

Oda, M., 1977, Space Sci. Rev., **20**, 757.

Ogawara, Y., Doi, K., Matsuoka, M., Miyamoto, S., and Oda, M., 1977, Nature, **270**, 154.
Page, C.G., 1985, Space Sci. Rev., **40**,387.
Page, C.G., Bennetts, A.J., and Ricketts, M.J, 1981, Space Sci. Rev., **30**, 369.
Payne, D.G., 1980, Astrophys. J. **237**, 951.
Priedhorsky, W., Garmire, G.P., Rothschild, R., Boldt, E., Serlemitsos, P., and Holt, S., 1979, Astrophys. J., **233**, 350.
Shapiro, S., Lightman, A.P., and Eardley, D.M., 1976, Astrophys. J., **204**, 187.
Sunyaev, R.A., and Trumper, J., 1979, Nature, **279**, 506.
Sunyaev, R.A., and Titarchuk, L.G., 1980, Astron. Astrophys., **86**, 121.
Turner, M.J.L. et al. 1988, Publ. Astron. Soc. Japan, in preparation.
van der Klis, M., Hasinger, G., Stella, L., Langmeier, A., van Paradijs, J., and Lewin, W.H.G., 1987, Astrophys. J., Letters, **319**, L13.
Weisskopf, M.C., Kahn, S.M., and Sutherland, P.G., 1975, Astrophys. J., Letters, **199**, L147.

ANALYSIS OF THE OPTICAL ORBITAL LIGHTCURVE OF THE BLACK HOLE CANDIDATE LMC X-3

L. M. Kuiper
Laboratory for Space Research Leiden
P.O. Box 9504
2300 RA Leiden
The Netherlands

ABSTRACT. The optical orbital lightcurve of the X-ray binary LMC X-3 is used to determine relevant system parameters, especially the mass of the compact object. The used model comprises:
- ellipsoidal variations.
- X-ray heating of the companion star.
- effects of the presence of an accretion disk.

Within the framework of this model it is found that the mass of the compact object in this system is in the range: $(4.5 - 6.5)(d/50\ \mathrm{kpc})M_{\odot}$. Also the effects of varying the mass function, the geometry of the X-ray emitting region and the accretion disk filling factor on the lower limit of the mass of the compact object have been investigated. We conclude that the compact object in this system is likely a black hole.

1. INTRODUCTION

The X-ray source LMC X-3 has been discovered during a survey with the UHURU-satellite (1). From its optical identification (2) it turned out that the optical companion (the primary) is a B3V star with

$$K_{opt} = 235 \pm 11 \text{ km/s and } P_{orb} = 1^{d}.7$$

The corresponding mass function for the compact object in this system,

$$f_x\,(m_x, q_x, i) = m_x \cdot \sin^3 i/(1+1/q_x)^2 = 2.3\ M_{\odot},$$

suggests that this source is a good candidate for a black hole with a mass in the stellar range ($q_x = m_x/m_{opt}$ is the mass ratio, i is the inclination angle). The X-ray source does not exhibit eclipses and does not pulsate. So, unfortunately, we are not dealing with a pulsar in an orbit around a companion, in which case we could determine the mass ratio q_x and, in the case of eclipses, also the inclination angle i.

Recently a good-quality optical orbital lightcurve has become available (3) which in principle incorporates the necessary information. The optical orbital lightcurve (in the symmetric folding

H. Ögelman and E. P. J. van den Heuvel (eds.), Timing Neutron Stars, 277–282.

case), derived from measurements contemporary to EXOSAT X-ray observations, has the following characteristics (cf. (3)):

A00 = 0.157 (5) (amplitude at phase 0.0)
A05 = 0.147 (6) (amplitude at phase 0.5)

Orbital phase 0.0 is defined when the compact object is behind the optical companion seen by a distant observer. The double wave shape of the lightcurve indicates a significant contribution of ellipsoidal variations. The near equality of both amplitudes and the large X-ray flux/ optical flux ratio, F_x/F_{opt} = 50 - 100, suggests that X-ray shielding by a thick accretion disk is important (4).

In order to determine q_x, i we studied the optical orbital lightcurve using a theoretical model comprising:

- the rotationally and tidally distorted primary and its inhomogeneous flux distribution.
- X-ray heating of the primary.
- the presence of an accretion disk.

The model parameters needed as input for our lightcurve synthesis program are chosen to be consistent with all observational properties of LMC X-3. The requirement that the theoretical lightcurves match the observational one (especially the amplitudes) can be translated into a constrain on the compact object mass.

In section 2 an outline is given of the model and the choice of the model parameters. In section 3 the results are presented and, finally, the conclusions of this study are given in section 4. For a more detailed description I refer to (14).

2. THE MODEL AND MODEL PARAMETERS

2.1. The model

The shape of the optical companion is that of a tidally and rotationally distorted star, determined by the potential parameter

$$\Omega = \Omega_{crit} = \Omega_{crit}\ (q_x)$$

where the subscript crit means critical Roche-lobe. The flux of each surface element of the primary in absence of X-ray heating is given by Von Zeipels theorem:

$$F_{rad} \propto g_{eff} \qquad \text{with} \quad g_{eff} = \left| \nabla \Omega_{crit} \right|$$

Furthermore, the accretion disk is considered to be a flat cylinder with the upper- and lower plane symmetric and parallel to the orbital plane, radiating uniformly and isotropically like a blackbody with mean effective temperature T_d. The cylinder is described by a radius, r_d, and thickness, γ , expressed as follows:

$$r_d = \alpha . r_1 \ (q_x), \quad \gamma = \arctan (H_D/r_d),$$

in which H_D is the height above the orbital plane. Both, H_D and r_d are in unit semi-major axis a; α is the disk Roche-lobe filling factor and r_1 (q_x) is the mean radius of the Roche-lobe (13).

Primary elements which are visible from the compact object can be X-ray heated. A fraction ($1 - \eta_x$) of the infalling X-ray radiation is absorbed and re-emitted as lower energy fotons (i.e. deep heating approximation (5)). For the X-ray albedo η_x I took:

$$0.3 < \eta_x < 0.5 \qquad \text{(cf. (6), (7))}.$$

In this study I will consider two types of geometries of the X-ray emitting region near the compact object.

- spherical emitting region.
- flat emitting region, expected to be important in the case of a black hole accretion disk.

The effects of an accretion disk can be summarized as follows:

- it acts as an additional lightsource.
- it casts an X-ray shadow on the primary.
- possible occurence of mutual eclipses.

The flux calculation is carried out each 1/20 th orbital phase and consists in adding the flux contributions from both primary and accretion disk elements which are visible from a distant observer (taking into account possible mutual eclipses).

2.2. The model parameters

The input parameters for a lightcurve calculation are:

- the bolometric luminosity of the primary L_{opt}
- the mass of the primary m_{opt}
- the mass ratio q_x
- the inclination angle i
- the X-ray albedo η_x
- the disk thickness γ
- the mean disk effective temperature T_D
- the X-ray luminosity L_x
- the disk Roche-lobe filling factor α
- the choice of the geometry of the X-ray emitting region.

m_x, q_x and i are related by the mass function f_x (m_x, q_x, i).
The parameters γ, η_x and α are "free" within reasonable ranges:

$$0° < \gamma < 20°; \ 0.3 < \eta_x < 0.5; \ 0.8 < \alpha < 1 \text{ (cf. 8)}.$$

The other parameters are constrained by observations.

The mass of a Roche-lobe filling primary can be determined using Keplers' formula and a formula derived by Paczynski (9) appropriate for $q_x > 1$ ($q_{opt} < 1$):

$$m_{opt} = 4.\pi^2.3^4.R_{opt}{}^3/(2^3.G.P_{orb}{}^2),$$

with G the gravitational constant, R_{opt} the mean primary radius, and P_{orb} the orbital period.
R_{opt} can be determined from its absolute magnitude (needed is the apparent visual magnitude V_o = 17.32 and distance d = 40/50/60 kpc) and a relation between surface brightness and intrinsic coluor index B-V (10). So, for each assumed distance we get different m_{opt} ranges. For fixed m_{opt} and chosen inclination i the mass function determines q_x. The bolometric luminosity L_{opt} is determined using:

$$L_{opt} = 4.\pi.R_{opt}^2.\sigma.T_{eff}^4$$

Required are V_o, d, spectral type, Bolometric correction B.C (T_{eff}) and the assumption of Roche-lobe filling. The X-ray luminosity L_x follows from the measured X-ray flux and distance d. The mean disk temperature can be determined from the known ratio:

$$L_{disk}/L_{opt} = 10^{0.4(V_{opt}-V_{disk})},$$

with V_{opt} = 17.32 and V_{disk} = 17.60.

Each model can be represented in a (log q_x, i)-diagram (see fig. 1).

3. RESULTS

For given d, f_x (m_x, q_x, i), γ , η_x, α and X-ray emitting region geometry one can calculate along a m_{opt} = const. track in the log q_x, i)-diagram the inclination at which the calculated amplitudes A00 and A05 match the observed ones. Repeating this procedure with different m_{opt} values and connecting the different streches for each m_{opt} one obtains a "solution box", where both A00 and A05 match the observed values.
Doing so for different γ one obtains a band of solution boxes in the (log q_x, i)-diagram (see fig. 2). Then this procedure can be repeated for different η_x, d, α and X-ray emitting region geometry.

4. CONCLUSIONS

All the performed calculations indicate, that the inclination is limited between 65°-70°, and that in the case of a spherically X-ray emitting region, α = 1 and f_x (m_x, q_x, i)=2.3 M_O, the compact object mass m_x can be expressed in the following manner:

$$m_x = (4.5 - 6.5)(d/50 \text{ kpc}) M_\odot.$$

A combination of varying the mass function, X-ray emitting region geometry and disk Roche-lobe filling factor in such a way to push m_x to the lowest possible value leads to the following lower limit for m_x.

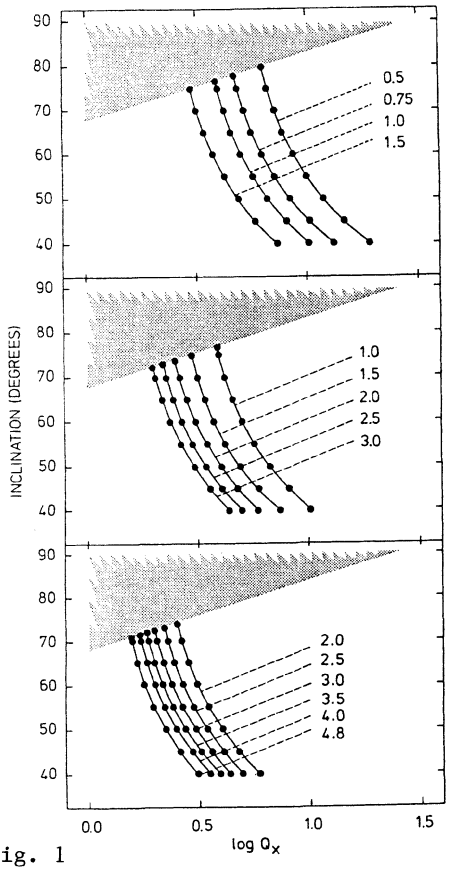

Fig. 1

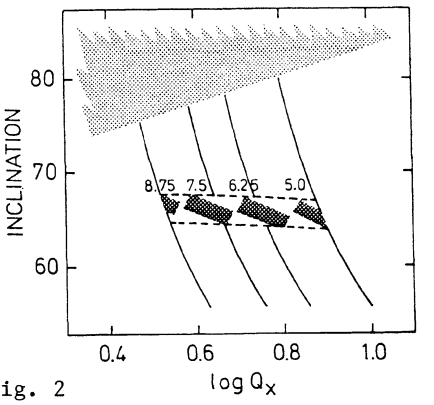

Fig. 2

Fig. 1: Three (log q_X, i) diagrams, for distances of 40 kpc (upper panel), 50 kpc (middle panel), and 60 kpc (lower panel), indicating combinations of system parameters for which light curves have been calculated. The points representing the model parameters are located along lines M_{opt} = constant (the value of M_{opt} is indicated for each drawn line). In these diagrams it has been assumed that the mass functions f_X (m_X, q_X, i) = 2.3 $M_\odot$. The grey areas indicate parameter regimes that are excluded by the observed lack of X-ray eclipses.

Fig. 2: Solution boxes in the (log q_X, i) diagram as a function of γ (thickness of the accretion disk). This figure is for spherical X-ray emission, f_X (m_X, q_X, i) = 2.3 $M_\odot$, d = 40 kpc, η_X = 0.3, α = 1. It appears that, approximately independent of γ, the inclination angle is limited between 64° and 67°. The corresponding limits on M_X are 3.8 and 5.3 $M_\odot$.

$m_x = 3.15\ M_\odot$ for $f_x = 2.0\ M_\odot$ $(1\text{-}\sigma)$.

$m_x = 2.8\ M_\odot$ for $f_x = 1.7\ M_\odot$ $(2\text{-}\sigma)$.

This lower limit for m_x is too high for realistic neutron star models (11) and much higher than the observed masses of neutron stars in X-ray binaries (12). So the compact object in LMC X-3 is likely a black hole.

The most uncertain factors in this conclusion is the uncertainty in the distance to the LMC cloud, the uncertainty in the mass function and the separation of the long-term variations from orbital variations (3). So improvement in this field is needed to rule out other possibilities and requires much observational work.

REFERENCES

1. Leong, C., Kellogg, E., Gursky, H., Tananbaum, H. & Giacconi, R.: 1971, Astrophys. J. (Letters) **170** , L67.
2. Cowley, A.P., Crampton, D., Hutchings, J.B. Remillard, R. & Penfold, J.E.: 1983, Astrophys. J. **272** , 118.
3. Van Paradijs, J., Van der Klis, M., Augusteijn, T., Charles, P.A., Corbet, R.H.D., Ilovaisky, S.A., Maraschi, L., Motch, C., Pakull, M., Smale, A.P., Treves, A. & Van Amerongen, S.: 1987, Astron. Astrophys. **184** , 201.
4. Van der Klis, M., Clausen, J.V., Jensen, K., Tjemkes, S. & Van Paradijs, J.: 1985, Astron. Astrophys. **151** , 322.
5. Tjemkes, S.A., Zuiderwijk, E.J. & Van Paradijs, J.: 1986, Astron. Astrophys. **154** , 77.
6. London, R., MacCray, R. & Auer, L.H.: 1981, Astrophys. J. **243** , 970.
7. Milgrom, M. & Salpeter, E.E.: 1975, Astrophys. J. **196** , 583.
8. Paczynski, B.: 1977, Astrophys. J. **216** , 822.
9. Paczynski, B.: 1971, Ann. Rev. Astron. Astrophys. **9** , 183.
10. Popper, D.M.: 1980, Ann. Rev. Astron. Astrophys. **18** , 115.
11. Arnett, W.D. & Bowers, R.L.: 1977, Astrophys. J. Suppl. **33** , 415.
12. Rappaport, S. & Joss, P.C.: 1983, in "Accretion-driven Stellar X-ray Sources", ed. W.H.G. Lewin & E.P.J. van den Heuvel (Cambridge University Press), p. 1.
13. Eggleton, P.P.: 1983, Astrophys. J. **268** , 368
14. Kuiper, L.M., Van Paradijs, J., Van der Klis, M.: 1988, Astron. Astroph. in press.

The Luminosity Dependence of the Pulse Period and Profile of the Transient X-ray Pulsar EXO 2030+375

A. N. Parmar, N. E. White, and L. Stella
EXOSAT Observatory,
Astrophysics Division,
Space Science Department of ESA,
ESTEC, Noordwijk, The Netherlands.

SUMMARY

Using the *EXOSAT Observatory* we have discovered a new, transient, X-ray pulsar, EXO 2030+375 and followed its evolution through two outbursts. During the first outburst the 1–20 keV intensity declined by a factor $\gtrsim 2500$ from a discovery value comparable to that of the Crab Nebula. Cyclic variations in the 42 s pulse period give a likely orbital period in the range 44.3–48.6 day and an eccentricity of ~ 0.4. We have measured, for the first time, the dependence of the pulse period time derivative, $\dot{P}_s$, on luminosity, L, for an individual pulsar. At high and intermediate luminosities we find that $-\dot{P}_s \propto L^{1.08-1.35}$. This observed dependence is significantly steeper than that predicted by simple accretion torque theory where $-\dot{P}_s \propto L^{0.86}$. At low luminosites the determination of this relation is complicated by the interplay between secular and orbital period changes and we await an independent determination of the orbital elements that will allow these effects to be separated.

We observed marked luminosity dependent changes in pulse profile. At high luminosities the pulse profile consisted of a smooth asymmetric main pulse separated by $\sim 180°$ in phase from a small inter-pulse. As the luminosity decreased the relative strength of the two pulses reversed, with the inter-pulse becoming the dominant pulse. These changes are consistent with the dominant beaming mechanism changing from a fan beam at high luminosities to a pencil beam at low luminosities.

During the second outburst, in 1985 October, the light curve was dominated by a series of flares that recurred quasi-periodically every 3.96 hr. The origin of these flares is unclear, but their discovery demonstrates that another clock can give rise to regular outbursts from OB star X-ray binary systems.

I. INTRODUCTION

There are now ~ 30 known accreting X-ray pulsars. Until recently, the only way to investigate the dependence of their properties over a wide range of luminosity was by comparative studies of different systems (e.g., Rappaport and Joss 1977; Mason 1977; White, Swank, and Holt 1983). Such studies, while useful, suffer from the effects of comparing systems with different magnetic field strengths and geometries as well as from the large uncertainties in distance determinations. Observations of an individual X-ray pulsar over a wide luminosity range, such as observed from the transient systems, provide a much better way to study the dependence of the pulse period, profile, and spectrum on luminosity. However, it has been difficult to 'catch' a transient pulsar close to its

H. Ögelman and E. P. J. van den Heuvel (eds.), Timing Neutron Stars, 283–293.

maximum luminosity and monitor its decay over the following weeks or months, and consequently previous studies have not been over a sufficiently large range in luminosity to significantly constrain pulsar emission models (e.g., Fishman and Watts 1977; Ricker *et al.* 1976; Elsner, Ghosh, and Lamb 1980; White, Swank, and Holt 1983).

We report on *EXOSAT* observations of a previously uncatalogued, 42 s, transient, X-ray pulsar, EXO 2030+375 that underwent two outbursts between 1985 May and November (Parmar *et al.* 1985). During the first outburst the intensity decayed by a factor $\gtrsim 2500$ from a value comparable to the Crab Nebula to undetectable levels in the medium energy instrument (ME; Turner, Smith, and Zimmermann 1981). During the second outburst the phase-averaged 1–10 keV light curve was dominated by a series of regular flares that repeated every 3.96 hr. The method of discovery, overall X-ray spectrum, and luminosity dependence of the pulse period are discussed in Parmar *et al.* (1988) while the luminosity dependence of the pulse profile is presented in Parmar, White, and Stella (1988). The properties of the optical counterpart are discussed in Motch and Janot-Pacheco (1987); Coe *et al.* (1988) and Janot-Pacheco, Motch, and Pakull (1988).

II. DISCOVERY AND OBSERVATIONS

A total of 14 *EXOSAT* observations of EXO 2030+375 were made between 1985 May and November. Figure 1 shows the average 1–10 keV count rate detected in the ME for each observation. Initially the ME count rate from each observation declined linearly from a maximum of 1080 counts s^{-1} on 1985 May 18 to 120 counts s^{-1} on 1985 July 10. The decline then continued at a slower rate until 1985 August 13 when the ME count rate reached 12 counts s^{-1}. Pulsations were detected in all these observations. During the next observation, on 1985 August 25, only a faint 0.29 ± 0.04 counts s^{-1} source was detected by the ME. The upper limit to any pulsations in this observation is larger than the observed count rate so it is not clear whether this emission is coming from EXO 2030+375 or from another source within the 45′ FWHM field of view of the ME. This rapid decrease in luminosity (by a factor ~ 30 in 12 days) may be caused by the centrifugal inhibition of accretion when the magnetospheric radius exceeds the corotation radius (cf. Stella, White, and Rosner 1986).

No further observations of EXO 2030+375 were made until 1985 October 28 when EXO 2030+375 was again observed to be active. A subsequent 23 hr duration *EXOSAT* observation on 1985 October 30–31 showed the source to be undergoing quasi-periodic flares, each lasting between 1.3–2.3 hr and repeating every 3.96 ± 0.04 hr. A total of six flares were observed (Fig. 2). During each flare the ME counting rate increased rapidly from a quiescent level of 25 counts s^{-1} to a peak of 150 counts s^{-1} and then returned in an exponential fashion to the quiescent level. On several occasions a precursor was seen, where the count rate increased by $\sim 15\%$ for about 15 minutes prior to the main rise. During the flare decays there was significant variability in X-ray intensity with five of the flares showing evidence for quasi-periodic oscillations with periods of 900–1200 s and peak-to-peak amplitudes of $\sim 30\%$.

The recurrence interval of the flares of 3.96 hr appears unrelated to the much longer orbital period of the system and demonstrates that another clock can give regular outbursts from OB star X-ray binaries. In addition, the detection of regular flaring on a timescale unconnected with the orbital period means that regular flaring can no longer be regarded as necessarily indicating an underlying orbital period. Possible origins for the flaring activity include periodic mass ejection from the companion star and magnetospheric instabilities (cf. Parmar *et al.* 1988).

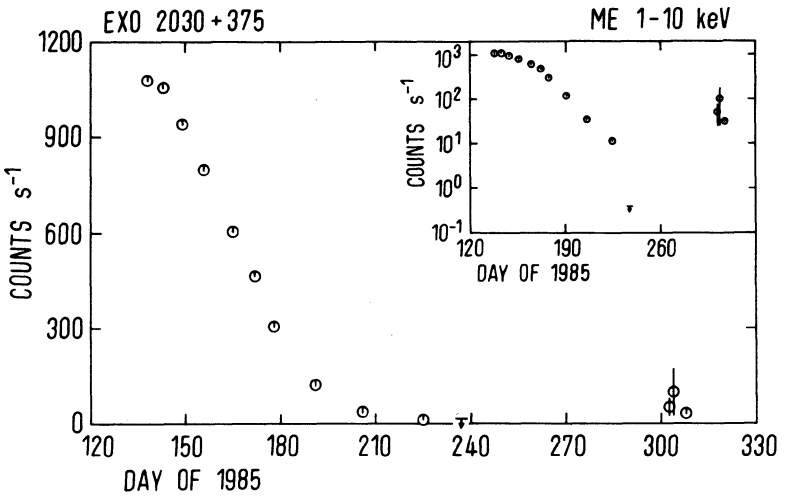

Fig. 1 The 1–10 keV count rate of EXO 2030+375 measured with the ME. Each point represents the average of an entire *EXOSAT* observation. The insert panel shows the same data plotted with a logarithmic count rate axis.

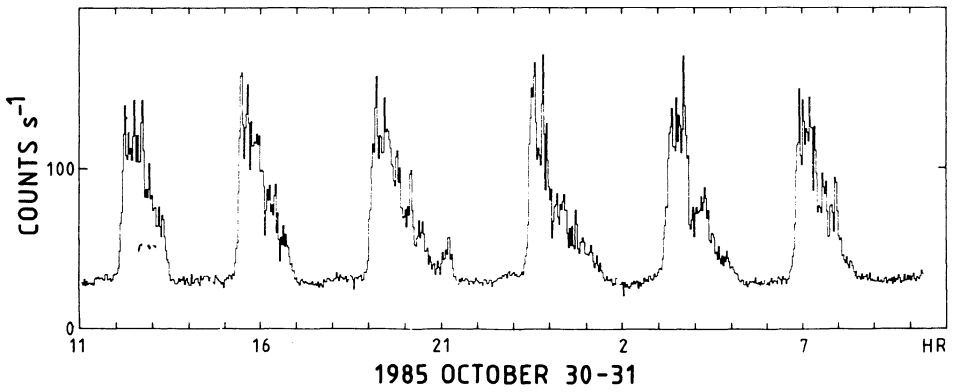

Fig. 2 The light curve of the 1985 October 30–31 observation of EXO 2030+375. The time resolution of the plot is 155 s, showing the quasi-periodic flaring activity discussed in the text.

III. PULSE PERIOD VARIATIONS

a) The orbital Period

During the first outburst the pulse period decreased from a value of 41.83264 s on 1985 May 18 to 41.7341 s on 1985 August 13. The decrease was not linear, but rather showed local reversals

between some observations that did not correspond to related changes in luminosity (Fig. 3; upper panel). When an accretion disk mediates the flow towards a magnetised neutron star a torque will be applied at the radius at which the accreting material is forced to corotate with the magnetosphere (Pringle and Rees 1972; Davidson and Ostriker 1973; Lamb, Pethick, and Pines 1973; Mason 1977; Rappaport and Joss 1977). For a neutron star of mass $1.4M_{\odot}$ and radius 10^6 cm, according to simple accretion theory, this torque will cause the neutron star spin period to change according to:

$$-\dot{P}_s \approx 1.9 \times 10^{-5} \mu_{30}^{2/7} P_s^2 L_{37}^{6/7} \quad \text{s} \quad \text{yr}^{-1} \tag{1}$$

where L_{37} is the luminosity in units of 10^{37} erg $\text{s}^{-1}$and μ_{30} the neutron star's magnetic moment in units of 10^{30} G cm^3. The observed variations in pulse period were modelled by a function of the form:

$$P_s = P_0 + \dot{P}_s t + \frac{1}{2}\ddot{P}_s t^2 + \text{F}(P_{orb}, a_x \sin i, e, w, \tau) \tag{2}$$

where P_0 is the pulse period on 1985 May 18.0, t is the time elapsed since that date and F represents the effect of a Keplerian orbital motion with orbital period P_{orb}, projected semi-major axis $a_x \sin i$, eccentricity e, longitude of periastron w, and time of periastron passage τ.

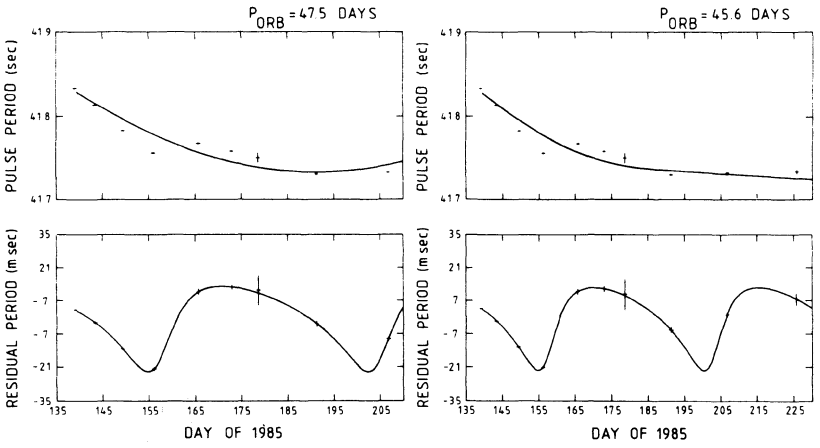

Fig. 3 The measured pulse periods with the best-fit long-term trends (upper panels) derived using models I and III (47.5 and 45.6 day orbital periods) indicated as solid lines. The secular and orbital period changes derived using model II are very similar to those of model III and are not shown. The pulse period residuals are shown in the lower panel along with the fit to the orbital motion.

During the first eight period measurements the luminosity decreased linearly by a factor of ~ 8. This linear decline simplifies the orbital fitting since differentiating equation (1) indicates that the

expected change in $\ddot{P}_s$ should be independent of time since $\ddot{P}_s$ is only weakly dependent on L and P_s only changes by a negligable amount. Thus, there is no need to include a $\dddot{P}_s$ term in equation (2). However, restricting the fit to these eight pulse periods does not provide a unique orbital solution because of the interplay between the secular and orbital terms in equation (2), and only a lower limit to P_{orb} is obtained of > 26.2 days. Including in the fit the ninth period measurement (1985 July 25), does give a unique solution with $P_{orb} = 47.5 \pm 1.1$ days and $e = 0.38 \pm 0.09$ (model I). Including the tenth period measurement of the first outburst (1985 August 13) does not give an acceptable fit for any orbital period, with a minimum χ^2 of 99 for 2 dof for $P_{orb} = 44.9$ days. This poor fit is consistent with accretion theory since by 1985 August 13 $\dot{L}_{37}$ had deviated considerably from the earlier linear relation (cf. Fig. 1).

An acceptable fit to all the pulse period measurements made during the first outburst can be obtained if equation (2) is modified by the addition of a $\frac{1}{3}\ddot{P}_s t^3$ term (model II). This gives a χ^2 of 0.01 for 1 dof with an orbital period of $45.9 \pm^{1.8}_{1.3}$ day and eccentricity $0.45 \pm^{0.15}_{0.20}$. The overall variation in $\dot{P}_s$ with time is similar to that given by model I until 1985 June 27 with the spin-up timescale increasing from 30 yr to 133 yr. After this the two models diverge with the spin-up timescale in this model decreasing after reaching a maximum of 800 yr on 1985 July 25 to 290 yr on 1985 August 13.

As a further estimate of the uncertainties involved in determining $\dot{P}_s$ as a function of time in conjunction with the orbital elements we have considered whether the observed pulse period measurements can be fit to equation (2), but with a constant $\dot{P}_s$ after a time t_0 (model III). The small $\dot{L}$ observed towards the end of the first outburst indicates that $\ddot{P}_s$ should be small during this interval and forcing $\dot{P}_s$ to be constant represents a useful limiting case. This fit gives a χ^2 of 0.1 for 1 dof with $P_{orb} = 45.6 \pm 1.3$ days and $e = 0.39 \pm 0.08$. The best-fit value of t_0 corresponds to 1985 July 4 with an uncertainty of ± 4 days. This time agrees closely with the end of the linear decline in luminosity (cf. Fig. 1).

In summary, we find that three different approaches to modelling the secular period changes give formally acceptable fits to the observed pulse periods. The derived orbital periods of 47.5 ± 1.1 days, $45.9 \pm^{1.8}_{1.3}$ days, and 45.6 ± 1.3 days are all, within the uncertainties, consistent with each other. Model I excludes the last data point, but this does not allow this model to be excluded since it is possible that between 1985 July 25 and August 13 the luminosity of EXO 2030+375 may have changed in an unexpected way, so causing an anomalous change in spin period. The major difference between the secular spin-period changes predicted by the three models occur at luminosities $\lesssim 10^{37}$ erg s^{-1}. Below this luminosity in model I the period derivative reverses sign, in model II it increases again, and in model III it remains constant.

b) The Dependence of the Change in Pulse Period on Luminosity

The dependence of the secular period change, $\dot{P}_s$, on luminosity is convolved with the orbital solution because the magnitude of the orbital Doppler effect is comparable to the secular change (cf. Fig. 3). In Figure 4 the region bounded by the allowed values of $-\dot{P}_s$ is plotted against luminosity for all three models. The dependence between the two appears to be approximately linear. The uncertainties in the deconvolution of the orbital effects from the intrinsic pulse period changes at low luminosity are evident from the increased area which allows a turn-up, turn-down or a flattening. There is also a turn-up for the highest luminosity point which may be related to a modification of the accretion process as the luminosity may be close to Eddington (cf. Basko and Sunyaev 1976). Each set of corrected pulse periods were fit to a function of the form: $-\dot{P}_s \propto L^m$. An acceptable fit cannot be obtained if all the derived $\dot{P}_s$ values are included. Excluding the two lowest luminosity measurements

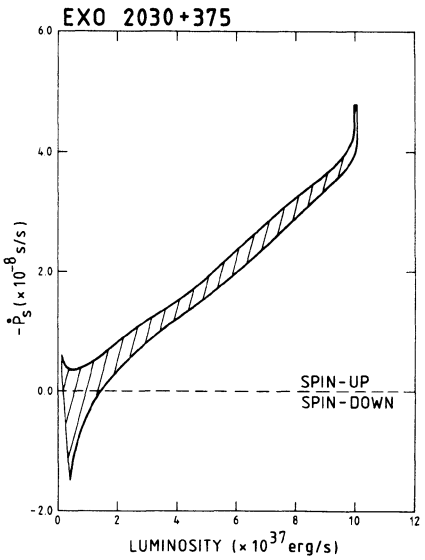

Fig. 4 The values of $-\dot{P}_s$ for each of the orbital solutions (enclosed by the hatched area) plotted against luminosity (in units of 10^{37} erg s^{-1}) for an assumed distance of 5 kpc.

from the fit gives acceptable fits with m in the range 1.08–1.35. This is significantly steeper than the $-\dot{P}_s \propto L^{0.86}$ relation predicted by the simplest version of accretion torque theory.

c) The Ghosh and Lamb Accretion Torque Model

The observed variations in $\dot{P}_s$ are inconsistent with the predictions of simple accretion torque theory. A more detailed consideration of the interaction of a neutron star's magnetosphere with an accretion disk has shown that the dependence of $-\dot{P}_s$ on luminosity can be substantially different from the simple model. This deviation is most pronounced when the co-rotation radius, r_c, approaches the magnetospheric radius, r_m. In this regime the details of the interaction of the inner disk with the magnetosphere become important. Two different models for this interaction have been proposed. The simplest model is that the disk is perfectly diamagnetic such that surface currents exclude the stellar field. The regions of the disk outside $r_c \sim r_m$ may be responsible for a centrifugal wind which will carry away angular momentum and cause a reduction in the $\dot{P}_s$ (Anzer and Börner 1983; Arons *et al.* 1984). Alternatively, Ghosh and Lamb (1979) and Wang (1987) suggest that the field is not complelety excluded and that partial threading of the disk can exert a significant spin-down torque when $r_m \sim r_c$. Only the latter models have been developed in sufficient detail to allow a comparison with observations.

In the Ghosh and Lamb (1979) model the torque exerted on the neutron star will cause the pulse period to change according to:

$$-\dot{P}_s \approx 4.3 \times 10^{-5} \mu_{30}^{2/7} n(\omega_s) P_s^2 L_{37}^{6/7} \quad \text{s yr}^{-1} \tag{3}$$

where the *fastness parameter*, ω_s, is the ratio of the stellar angular velocity and the Keplerian angular velocity at the magnetospheric boundary (cf. Elsner and Lamb 1976). The function $n(\omega_s)$,

introduced by Ghosh and Lamb (1979) parameterizes the different dependence of the torque from that given by simple accretion theory. When $\omega_s \ll 1$ then $n(\omega_s) \sim 1.4$ and the neutron star experiences a strong spin-up torque, as in the unmodified case. For increasing values of ω_s, $n(\omega_s)$ decreases until it reaches zero at a critical *fastness*, ω_c, where the spin-up and spin-down torques are equal. When $\omega_s > \omega_c$ the pulsar spins-down because $n(\omega_s) < 0$.

Equation (3) provides an alternative way of accounting for the secular pulse period changes during the outburst. The value of $n(\omega_s)$ depends on both μ_{30} and L_{37} (cf. Ghosh and Lamb 1979) and provides a means of estimating μ_{30} and the distance to EXO 2030+375 by examining the variation of $\dot{P}_s$ with luminosity. This was done by substituting the secular period change terms in equation (2) by equation (3) and allowing the orbital terms to vary as before in the fit. The luminosity between each measurement was assumed to be that given by a cubic-spline interpolation. When the revised equation (2) was fit to the first nine period measurements, an orbital solution with a period of 46.6 ± 1.1 day was obtained with a χ^2 of 0.1 for 1 dof. The best-fitting distance and magnetic moment are (5.3 ± 0.3) kpc and $(2.0 \pm 0.4) \times 10^{31}$ G cm^3 respectively. Including the tenth period measurement (1985 August 13) in the fit does not give an acceptable solution for any orbital period. The minimum χ^2 of 20.0 for 2 dof corresponds to $P_{orb} = 45.5$ days, a magnetic moment of 1.1×10^{31} G cm^3, and a distance of 5.0 kpc. This variation in magnetic moment may either result from limitations associated with the Ghosh and Lamb (1979) model, or it is possible that between the 1985 July 25 and August 13 observations the luminosity of EXO 2030+375 varied in an unexpected way. Nonetheless, the fact that this model gives a reasonable fit for all but the final period measurement is encouraging. Assuming that the range of best-fit values obtained using different numbers of period measurements gives an indication of the likely uncertainties, we obtain a magnetic moment of $1.1\text{–}2.4 \times 10^{31}$ G cm^3 and a distance 5.0–5.6 kpc.

IV. THE LUMINOSITY DEPENDENCE OF THE PULSE PROFILE

Figure 5 shows, for the first outburst, the average 1–10 keV pulse profile for each of the 10 observations where pulsations were detected. At the maximum observed 1–20 keV luminosity of 1.0×10^{38} erg s^{-1} (assuming a distance of 5kpc; see Parmar *et al.* 1988) the 1–10 keV pulse profile shows a smooth asymmetric light curve with two local minima on the trailing edge. The second of the minima is a distinctive notch that becomes both sharper and deeper as the luminosity declines. This notch has been arbitrarily used to define $\Phi = 0$. The other minimum also becomes more distinct at lower luminosities such that the pulse maximum at $\Phi \sim 0.6$ becomes much more symmetric. The notch at $\Phi = 0$ is clearly present in all but the 1985 July 25 and August 13 profiles. For these two observations the phase was determined by aligning the single pulses seen at $\Phi \sim 0.3$ with the narrow pulse seen on 1985 July 10. This seems a reasonable procedure given the similarity in overall shape of the pulses and the evidence for a small feature resembling a notch at $\Phi \sim 0$ in the 1985 July 25 profile. As the luminosity decreased from the maximum an inter-pulse located at $\Phi \sim 0.3$ appeared and became stronger, until by 1985 July 10, when the 1–20 keV luminosity had fallen to 1.2×10^{36} erg s^{-1}, the inter-pulse and the pulse at $\Phi \sim 0.6$ were of approximately equal strength. This trend continued until by 1985 August 13 the pulse at $\Phi \sim 0.7\text{–}0.1$ had almost entirely disappeared, and the profile became dominated by what had previously been an inter-pulse. The modulation amplitude of the profile of $\sim 80\%$ (peak-to-peak) was approximately the same during all observations. Examination of the folded light curves obtained during the 1985 October 30–31 observation, when the source was flaring, shows that the same luminosity dependence of the pulse profile was present.

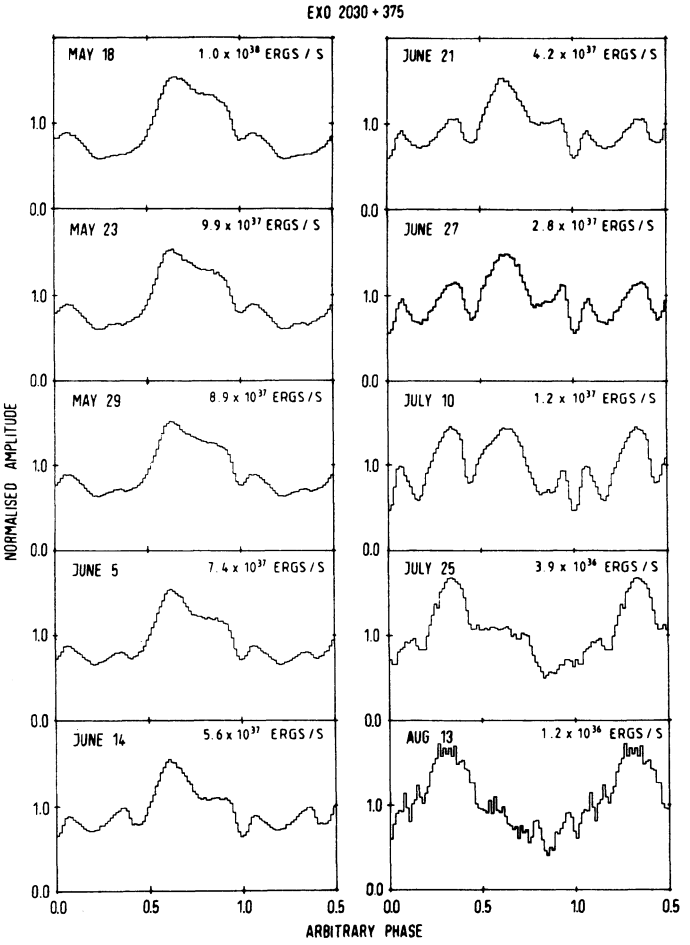

Fig. 5 The folded 1–10 keV ME light curves of EXO 2030+375 showing the evolution of the pulse profile as the first outburst decayed.

The luminosity dependence of the pulse profile of EXO 2030+375 is the first to be found, primarily because no other pulsar had been systematically studied over a factor $\sim$ 100 range in luminosity. These observations provide a new avenue for understanding the basic properties of the emission region in X-ray pulsars by comparing the dependence of models on the mass accretion rate with the observations. The observation of the same dependence on luminosity of the pulse profile on timescales of hours (during the flares) rather than weeks (during the first outburst) rules out geometric effects resulting from e.g., a precessing neutron star, and suggests that either the basic beaming mechanism switched from a fan to a pencil configuration (or *vice versa*), or that a different

magnetic pole became active.

To investigate the possibility that the luminosity dependence of the pulse profile can be explained as the beaming direction switching from a fan to a pencil configuration we compared the observed pulse profile to that expected from a neutron star emitting simple fan and pencil beams. Wang and Welter (1981) were the first to attempt such a comparison for X-ray pulsars. The above change in beam shape is expected if the emission region changes from a cylindrical 'pillbox' at high luminosities to a thin 'slab' at low luminosities (Nagel 1981*a*, *b*; Basko and Sunyaev 1975; Wang and Frank 1981; Mészáros *et al.* 1983).

We have used a geometric model similar to that used by Wang and Welter (1981), but including a simple relativistic correction. A dipole magnetic field was assumed, with each magnetic polar cap subtending an angular size of 20° from the center of the neutron star. Both a pencil and a fan-beam were included with the relative strength of the two beams, R_{F-P}, a free parameter. The relative strength of the total emission from each of the two poles, R_{2-1}, was also a free parameter, but the relative strength of the pencil to the fan-beam was assumed to be the same for both poles. Each fan-beam was assumed to be emitted by a uniformly emitting column of height 5×10^4 cm located above the cap and to be axially symmetric. The dependence of the beam emissivity on the angle from the magnetic axis was assumed to be exponential with maxima parallel and perpendicular to the magnetic axis for the pencil and fan beams, respectively. The effect of gravitional bending of the beams was approximated by assuming a deflection angle at infinity of 23.8° for a beam emitted parallel to the horizon (no adjustment was made for column height). This value is one half of the deflection angle of a beam with a turning point 10^6 cm from the center of a $1.4M_\odot$ mass object. For simplicity, we have assumed that the gravitational bending varies as $\sin\alpha$, where α is the angle between emitted radiation and the perpendicular to the neutron star surface. Occultation of the beams by the neutron star surface was included.

Figure 6 (upper panel) shows the best-fit model pulse profile overlayed on the observed pulse profile of 1985 May 18, which was used from comparison purposes. The overall profile is reproduced in a qualitative sense, with the fan-beam dominating. A pencil-beam fails to reproduce the broadness of the pulse, although this could be adjusted by including the angular dependence of the beam in the fitting procedure. However, in either case the two minima on the trailing edge of the pulse and its asymmetry are not present in the model, suggesting a more complex approach to be necessary. The next step was to introduce an asymmetry. For simplicity we chose to offset the magnetic axis from the rotation axis, although probably the same effects can be obtained by introducing an axial asymmetry in the fan-beam. The beams were assumed to be generated perpendicular and parallel to the magnetic field lines. This means that the emitting columns are no longer perpendicular to the neutron star surface. Asymmetric profiles then arise because the occultation of the beams by the neutron star's surface and the gravitational bending of the beams are no longer axially symmetric. Figure 6 (lower panel) shows the model profile most similar to that observed on 1985 May 18. The best-fit polar cap positions correspond to an angle subtended with the center of the neutron star of 105°. The relative intensities of the beams were $R_{F-P} = 7.5$, $R_{2-1} = 0.73$ and $I_{DC} = 0.45$; i.e the fan-beam dominates and the overall emission from one pole is 37% higher. As might be expected the fit is still far from acceptable, however the overall model profile gives a much better qualitative representation of the pulse profile.

To see if this simple model can account for the observed luminosity dependence of the pulse profile each of the profiles shown in Figure 5 was fit to the model profiles in a similar way to the 1985 May 18 pulse profile. The polar cap positions were allowed to vary, although the inclination angle was fixed

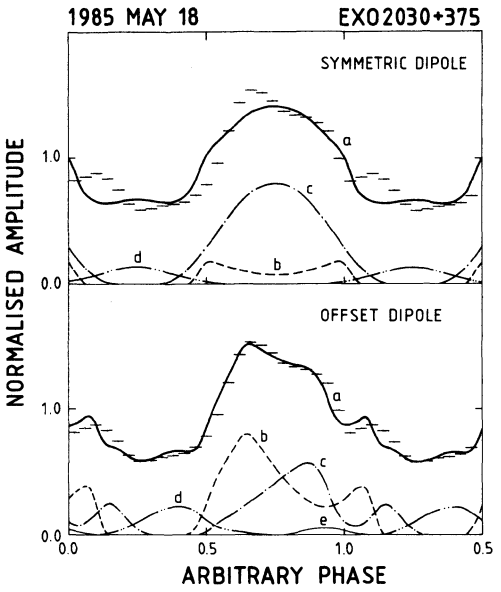

Fig. 6 Best fit model pulse profiles are shown as continuous lines (a) overlayed on the pulse profile of the 1985 May 18 observation. In the upper panel the magnetic poles are constrained to be located 180° apart on the neutron star surface. In the lower panel the observed asymmetry is modelled by allowing the positions of both polar caps to be free parameters in the fitting. The individual contributions from the fan beams are labelled as (b) and (c) and from the pencil beams as (d) and (e).

at -25°. The model and observed profiles show reasonable agreement at high and low luminosities. However, the fits to the profiles observed between 1985 June 14 and July 10 are significantly worse, with marked deviations from the observed profiles. During this interval two changes in observed profile occured that are not well modelled; the broad asymmetric peak at $\Phi \sim 0.6$ becomes narrower and the notch, located at $\Phi = 0.0$ more prominent. These may result from other changes such as a variable fan-beam angular dependence, changes in the height of the column or polar cap size. Given the number of possible free parameters and combinations we did not consider it worthwhile to pursue the fitting procedure any further. The standard deviation in best-fit positions are $\approx 20°$ and $\approx 15°$ for the two poles. This small dispersion in derived positions suggests the model is self-consistent at different luminosities. The dependence of the observed profile on luminosity is modelled primarily by a change from a pencil to fan-beam (a decrease in R_{F-P}) with the pencil-beam becoming a factor ≈ 10 more intense than the fan-beam. In addition the relative contribution of the two poles to the total changed by a factor of ≈ 10 (an increase in R_{2-1}).

V. CONCLUSIONS

These observations illustrate the importance of observing transient X-ray pulsars over a large range in luminosity. They also illustrate the importance of making a sufficient number of observations

to allow the secular and orbital pulse period changes to be disentangled. The results reported here can be improved upon simply by obtaining a better determination of the orbital elements of EXO 2030+375. If this source is detected to be once again active then we strongly urge it be observed in sufficient detail for the orbit to be measured. This will allow a reexamination of the *EXOSAT* data presented here and a much more accurate determination of the secular period changes.

REFERENCES

Anzer, U. and Börner, G. 1983, *Astr. Ap.*, **122**, 73.

Arons, J., Burnard, D. J., Klein, R. I., McKee, C. F., Purdritz, R. E., and Lea, S. M. 1984, *AIP Conference Proceedings*, **115**, 215.

Basko, M. M., and Sunyaev, R. A. 1975, *Astr. Ap.*, **42**, 311.

Basko, M. M., and Sunyaev, R. A. 1976, *M.N.R.A.S.*, **175**, 395.

Coe, M. J. Payne, B. J., Longmore, A. J., and Hanson, C. G. 1988, *M.N.R.A.S.*, submitted.

Davidson, K., Ostriker, J. P. 1973, *Ap. J.*, **179**, 585.

Elsner, R. F., Ghosh, P., and Lamb, F. K. 1980, *Ap. J. (Letters)*, **241**, L155.

Elsner, R. F., and Lamb, F. K. 1976, *Nature*, **262**, 356.

Fishman, G. J., and Watts, J. W. 1977, *Ap. J.*, **212**, 211.

Ghosh, P., and Lamb, F. K. 1979, *Ap. J.*, **234**, 296.

Janot-Pacheco, E., Motch, C., and Pakull, M. W. 1988, *Astr. Ap.*, in press.

Lamb, F. K., Pethick, C. J., and Pines, D. 1973, *Ap. J.*, **184**, 271.

Mason, K. O. 1977, *M.N.R.A.S.*, **178**, 81p.

Mészáros, P. Harding, A., Kirk, J. G., Galloway, D. J. 1983, *Ap. J. (Letters)*, **266**, L33.

Motch, C., and Janot-Pacheco, E. 1987, *Astr. Ap.*, **182**, L55.

Nagel, W. 1981*a*, *Ap. J.*, **251**, 278.

Nagel, W. 1981*b*, *Ap. J.*, **251**, 288.

Parmar, A. N., Stella, L., Ferri, P., and White, N. E. 1985, *IAU Circ.*, 4066.

Parmar, A. N., White, N. E., and Stella, L. 1988, *Ap. J.*, in press.

Parmar, A. N., White, N. E., Stella, L., Izzo, C., Ferri, P. 1988, *Ap. J.*, in press.

Pringle, J. E., and Rees, M. J. 1972, *Astr. and Ap.*, **21**, 1.

Rappaport, S., and Joss, P. C. 1977, *Nature*, **266**, 683.

Ricker, G. R., Scheepmaker, A., Ballintine, J. E., Doty, J. P., Kriss, G. A., Ryckman, S. G., and Lewin, W. H. G. 1976, *Ap. J., (Letters)*, **204**, L73.

Stella, L., White, N. E., and Rosner, R. 1986, *Ap. J.*, **308**, 669.

Turner, M. J. L., Smith, A., and Zimmermann, H. U. 1981, *Space Sci. Rev.*, **30**, 512.

Wang, Y.-M. 1987, *Astr. Ap.*, **183**, 257.

Wang, Y.-M., and Frank, J., 1981, *Astr. Ap.*, **93**, 255.

Wang, Y.-M., and Welter, G. L. 1981, *Astr. Ap.*, **102**, 97.

White, N. E., Swank, J. H., and Holt, S. S. 1983, *Ap. J.*, **270**, 711.

SPECTRAL CLASSIFICTION OF BRIGHT LMXBs WITH COLOR-COLOR DIAGRAMS

N.S. SCHULZ, G. HASINGER AND J. TRÜMPER
Max Planck Institut für Extraterrestrische Physik
D-8046, Garching bei München
Federal Republic of Germany

ABSTRACT. This article describes the spectral variations of bright low-mass X-ray binaries (LMXBs). A large set of observations monitored with the European X-Ray Observatory EXOSAT are analysed and plotted into color-color and hardness-intensity diagrams. Correlations are compared with spectral branches observed in the bright source Cyg X-2 and then classified into three spectral states, a horizontal, a normal and a flaring branch state. A spectral parametrisation demonstrated that the observed color-color data correspond to very similar spectral parameters. The parametrisation can further be used to correct color-color data for interstellar absorption. The deabsorped data indicate, that the energy spectra as well as the observed spectral variability of bright LMXBs are of common nature.

1. Introduction

Low-Mass X-Ray Binaries (LMXBs) show spectral variations as a function of source intensity. Within a study of X-ray sources with similar properties to Sco X-1 using Ariel V and Copernicus data Mason et al. (1976) computed a hardness ratio and showed, that there is a positive correlation between spectral shape and flux intensity. These Sco X-1 type correlations in the 'hardness-intensity diagram' (HID) have been found in several sources (see also Parsignault and Grindley 1978). Recent observations with the Japanese X-ray satellite TENMA also demonstrated such a correlation (Makishima and Mitsuda 1985).

Branduardi et al. (1979) first reported two different spectral modes in observations of Cyg X-2, documented by two different correlations between spectral hardness and intensity. Shibazaki and Mitsuda (1984) found a similar behaviour in GX 5-1. On the 'horizontal' branch the hardness ratio changes very little with source intensity, while on the 'normal' branch the hardness ratio is positively correlated with intensity. EXOSAT observations of Cyg X-2 confirmed this bimodal

H. Ögelman and E. P. J. van den Heuvel (eds.), Timing Neutron Stars, 295–304.

behaviour (Hasinger 1987b). More recent observations of Sco X-1, on the other hand, have revealed also two branches (Priedhorsky et. al. 1986), however, both with positive correlation between hardness and intensity but with different slopes connected at the lower left side of the HID. The comparison between these two sources led to the conclusion that LMXB in general can be found on three different branches, the horizontal, normal and flaring branch, forming a Z-shaped color-color correlation profile (Hasinger 1987a; Hasinger, Priedhorsky and Middleditch, 1988). Indications for three different spectral branches have also been found in Einstein MPC data of GX 340+0 (M. Garcia, this volume).

The European X-ray satellite EXOSAT made extensive observations of LMXBs with observation periods of sometimes up to several days. In this article we present EXOSAT spectral data of bright LMXBs. The data were plotted into HIDs and color-color diagrams. Similar variation patterns will be discussed and classified as far as possible. We then parametrisize the color-color data using a simple two component model, which enables us to correct the color-color data for interstellar absorption. A more detailed analysis of this subject is presented in a recent publication by the authors (Schulz, Hasinger and Trümper 1988).

2. Spectral Variations

2.1 Hardness Ratios (Colors)

22 observations of ten bright LMXBs, including Cyg X-2, Sco X-1 and eight bright galactic bulge sources carried out with the Medium Energy Experiment onboard the European X-ray Observatory EXOSAT are analysed. Each observation has been cut into samples of 100-200 sec, the countrates of each sample were corrected for deadtime and background and normalized to 8 observing detectors. We then integrated an 1-20 keV energy spectrum for each sample and divided it into three broad energy bands: CHN1 = 1-3 keV, CHN2 = 3-6 keV and CHN3 = 6-20 keV. Two spectral hardness ratios (colors) are defined by the ratios of the fluxes in these energy bands: SR = CHN2 / CHN1 is the soft hardness ratio (soft color) and HR = CHN3 / CHN2 is the hard hardness ratio (hard color). The data are then plotted into hard hardness-intensity diagrams (HIDs) and hard hardness-soft hardness diagrams (color-color diagrams).

2.2 Observed Spectral Branches

Figure 1a-j and 2a-j show a set of color-color diagrams and HIDs for the ten bright LMXBs. The abscissa of the color-color diagrams is defined by the soft hardness ratio SR, the ordinate by the hard hardness ratio HR. In the HIDs the abscissa represents total source count rates (1-20 keV), the ordinate again the hard hardness ratio. Different observations of one source are marked with different symbols.

In figure 1a we plotted color-color correlation data of Cyg X-2. Within two different observation periods three differently correlated data strings could be observed. The flat data string corresponds to the 'horizontal' spectral branch (HB), which at its highest soft ratio turns into a steep positively correlated data string,

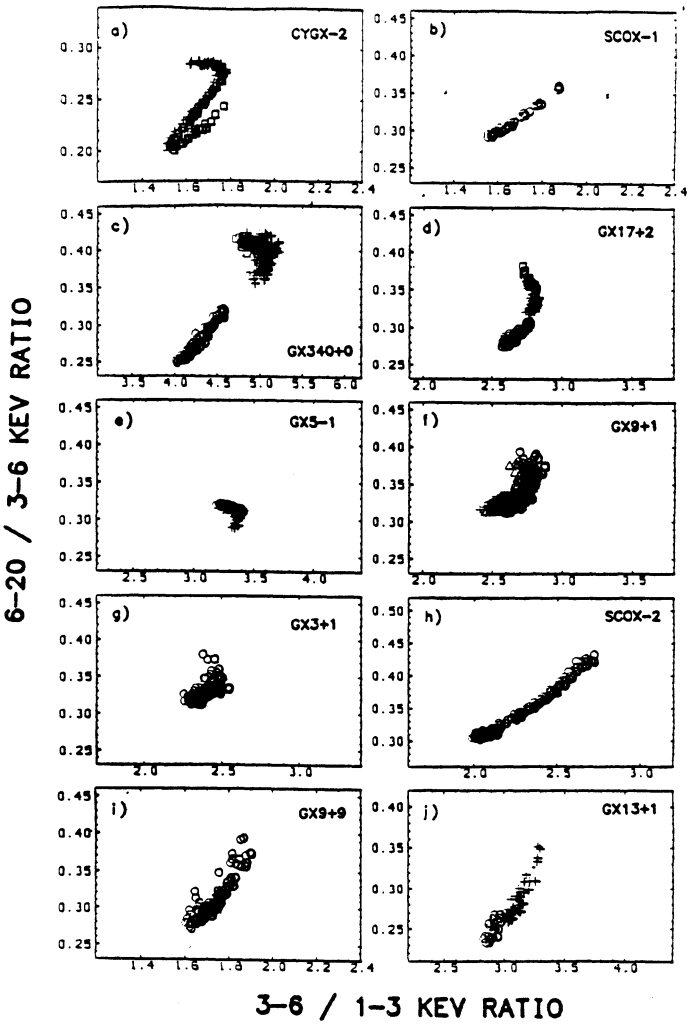

Figure 1: Color-color diagrams of ten bright LMXBs

the 'normal' spectral branch (NB). At the lowest soft ratio of the NB the correlation changes again and turns into another positively correlated data string of flatter slope called the 'flaring' branch (FB). We call the turnover from the HB to the NB at *high* soft ratio the 'hard' apex and the turnover from the NB to the FB at *low* soft ratio the 'soft' apex. The HID in fig. 2a also indicates three distinct spectral branches correponding to HB, NB and FB. The HB and NB are clearly recognicable, the FB intensity, however, shows rather erratic behaviour. The sum of all

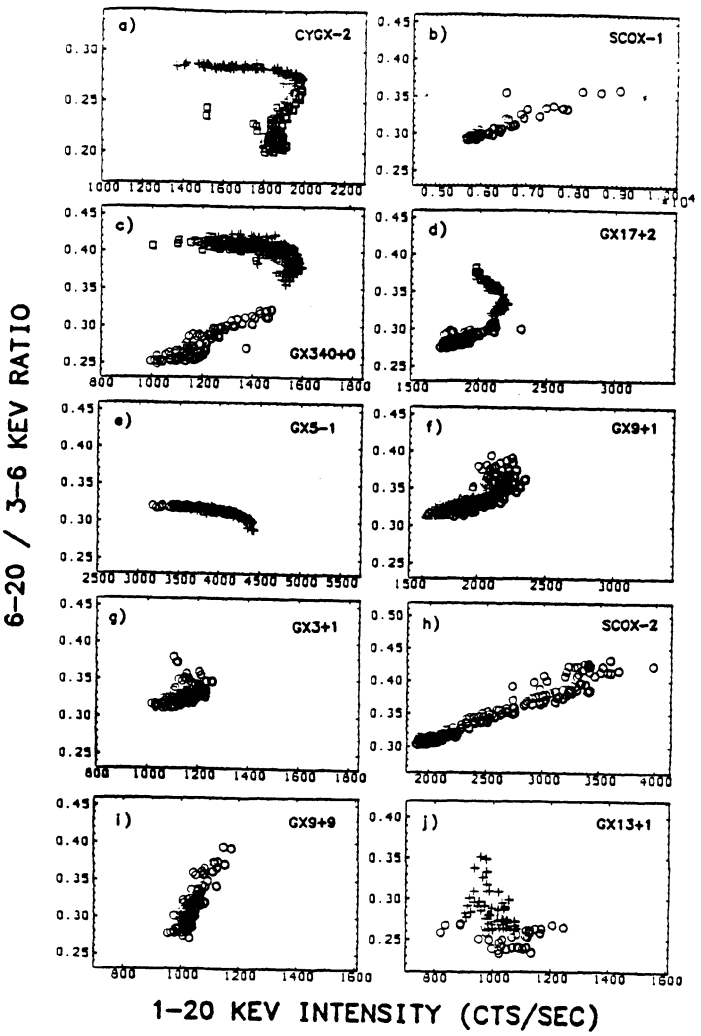

Figure 2: HIDs of ten bright LMXBs corresponding to the color-color diagrams in figure 1

spectral branches then leads to a Z-shaped color-color correlation pattern.

Color-color data of Sco X-1 are shown in figure 1b and 2b. The diagrams indicate a single positively correlated spectral branch, which could represent either a NB or a FB. A renalysis of the same data with slightly different colors showed, that this correlation clearly corresponds to a FB with a soft apex to the NB (Schulz, Hasinger and Trümper 1988). Hasinger, Priedhorsky and Middleditch (1988) re-

cently reported on a horizontal branch in a different data set. Thus Sco X-1 has also a Z-shaped color-color correlation pattern similar to Cyg X-2.

GX 340+0 (v.Paradijs et al. 1988), GX 17+2 (Langmeier 1988) and GX 5-1 (v.d.Klis et al 1985) (figures 1c-e and 2c-e) show a bimodal type of correlation including HB-NB transitions with a hard apex. The bimodal behaviour of GX 340+0 is only marginally present in the color-color diagram, however clearly seen in the HID. Hasinger and van der Klis (1988) recently reported on a flaring branch in GX 17+2.

The color-color data of GX 9+1 and GX 3+1 (see fig 1f,g and 2f,g) show positive correlation accompanied by higher source intrinsic scatter of the data. At high soft ratio both sources show a larger data spread. In GX 3+1 this can be interpreted as the turnover into HB behaviour, which would be similar to the behaviour found by Lewin et al. 1987 in an analysis of different data. In the case of GX 9+1 such an interpretation has still to be confirmed.

Sco X-2 (fig. 1h and 2h) shows a clearly positively correlated spectral branch. There is, similar to Sco X-1, a data accumulation at low soft ratios. A reanalysis with optimized energy bands like it was done for Sco X-1 also clarified this correlation as FB-behaviour in addition to a transition at low soft ratios into a NB (Schulz, Hasinger and Trümper 1988).

The sources GX 9+9 and GX 13+1 (fig. 1i,j and 2i,j) show positively correlated color-color data with no indication of a change in correlation. The HID of GX 13+1, however, shows a bifurcation, which does not match the observations in other sources. It is also different to the bifurcation found by Stella et al. 1985.

2.3 Spectral Classification

Table I summarizes all the spectral branches which have been identified up to now within individual sources. Three sources, namely Cyg X-2, Sco X-1 and GX 17+2 show a chracteristic Z-shaped pattern of horizontal, normal and flaring branch. In GX 340+0, GX 5-1, GX 3+1 and Sco X-2 two distinct spectral branches have been observed, which could be identified as HB-NB transition behaviour in GX 340+0, GX 5-1 and GX 3+1 and as NB-FB transition in Sco X-2. Spectral variability in GX 9+1, GX 9+9 and GX 13+1 remains rather unclear within this classification scheme. It is however interesting to note, that the latter sources also did not show quasiperiodic oscillations, which otherwise are a rather common phenomenon in bright sources.

3. Spectral Parameters from the Color-Color Diagram

The color-color diagrams of the bright sources indicate large similarities of spectral variations with Cyg X-2. Thus we use this source as a template for the parametrisation of the color-color diagram. For parametrisation we use a simple two component model, which fits the source spectrum of Cyg X-2 reasonably well. This model consisted of a blackbody and a thermal bremsstrahlungs component. As a reference spectrum a source spectrum at the hard apex of the color-color profile of Cyg X-2 was accumulated and fitted with the model spectrum.

Source	HB	NB	FB
Cyg X-2	X	X	X
Sco X-1	X	X	X
GX 340+0	X	X	
GX 17+2	X	X	X
GX 5-1	X	X	
GX 9+1		X?	
GX 3+1	X	X	
GX 349+2		X	X
GX 9+9		X?	X?
GX 13+1		X?	X?

Table I: Spectral Branches in Bright Sources.

3.1 Simulations

The two component spectrum is characterized by four parameters, the blackbody flux and temperature and the thermal bremsstrahlungs flux and temperature. In addition the effect of interstellar absorption. has to be added. In the following we measure fluxes only in terms of the blackbody flux contribution to total. The fitted photon spectrum at the hard apex of Cyg X-2 showed a thermal bremstrahlungs temperature of 6.5±0.4 keV, a blackbody temperature of 1.25±0.08 keV and a blackbody contribution of 25%, The interstellar absorption was fixed at 3×10^{21} atoms/cm^2.

We then simulated three sets of color-color data. Each of this set represents the variation of one parameter leaving the others fixed. The blackbody temperature was fixed to 1.30 keV, which corresponds to the observed value in the hard apex spectrum of Cyg X-2. This leads to a threedimensional grid of simulated data. In order to simplify the representation of this grid in the color-color diagram we formed parameter 'tracks'. Those 'tracks' are the projection of the variation of *one* parameter into the color-color plane: the *IBB-track* represents the blackbody flux contribution, the *NH-track* variations of interstellar absorption and the *TTH-track* variations of thermal bremstrahlungs temperature.

3.2 Spectral Parameters and Color-Color Data

The results from the simulation allows to convert the colors into spectral numbers with some accuracy. The color-color diagram in figure 3 shows ~90% contour

lines of the color-color data presented in figure 1 together with the simulated two component data grid: Dotted contours are identified horizontal branches, the solid contours are normal branches, the hatched contours are flaring branches and the blank ones represent unclear correlations. The parameter grid consists of IBB-tracks (dashed lines) and NH-tracks (thin lines) at five different thermal bremsstrahlungs temperatures (4.0, 6.0, 8.0, 12.0 and 20.0 keV) and TTH-tracks (thick lines) at four different interstellar column densities (0.0, 10.0, 25.0 and 50.0×10^{21} atoms/cm^2). The arrows point in direction of parameter increase.

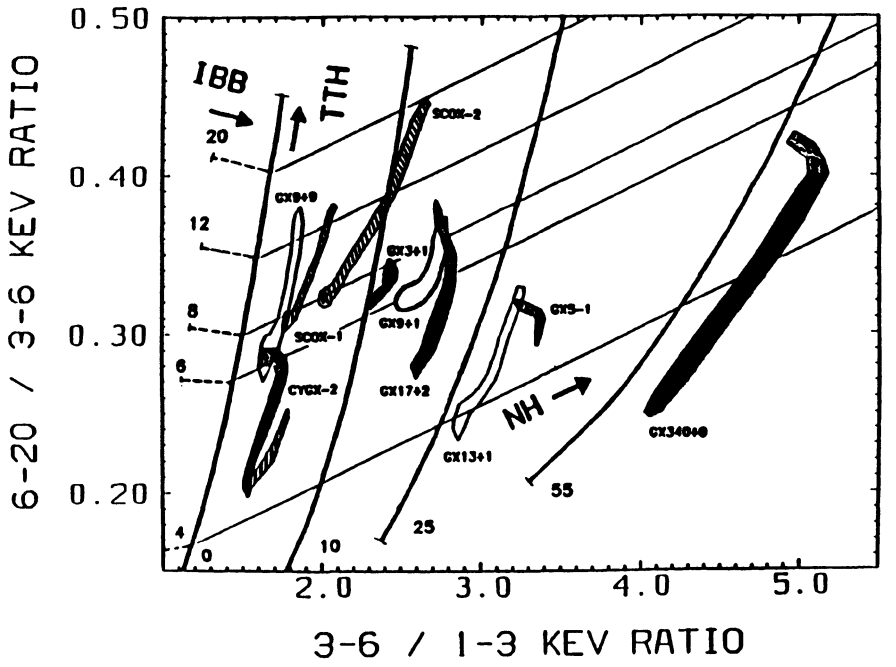

Figure 3: Color-color diagram of bright LMXBs with simulated spectral parameter tracks

It can be observed that most of the observed normal branch color-color data fit the slope of the TTH-track indicating that spectral variability in the normal branch can be reasonably well described by the thermal bremsstrahlungs variation. This should also be the case in GX 9+9 and GX 13+1. The temperature range covered by all color-color data accounts for 3.0-20.0 keV for the thermal bremsstrahlungs component at 1.30 keV blackbody temperature and does not change significantly for blackbody temperatures between 1.0 and 1.6 keV. The slopes of the horizontal branches fit reasonably well to the IBB-tracks. In Figure 3 these IBB-tracks show variations in blackbody contribution from zero to 30%. Their length is comparable to the observedd horizontal branches in Cyg X-2, GX 5-1 and GX 340+0. Flaring

branches do not fit well to any of the included tracks, indicating a more complex behaviour.

3.3 Interstellar Absorption

In addition to the instrinsic similarities of the color-color data, figure 3 clearly shows that the position of the data contours differ considerably in soft ratio. While sources like Cyg X-2, Sco X-1 and GX 9+9 have low soft ratios of approximately 1.5, there are some sources, i.e GX 13+1, GX 5-1 and GX 340+0, which have values from 3.0 up to 5.0. From the simulation it became clear, that the only parameter that can be responsible for such an effect is the NH-value. This is demonstrated in figure 3 by the NH-tracks, which point from the lower left to the upper right of the diagram. Thus we interprete the observed the different positions of the color-color data of each individual source along the soft ratio scale in terms of different interstellar absorption column densities for each source. Note also, that at very high NH-values the slope of the TTH-tracks flattens.

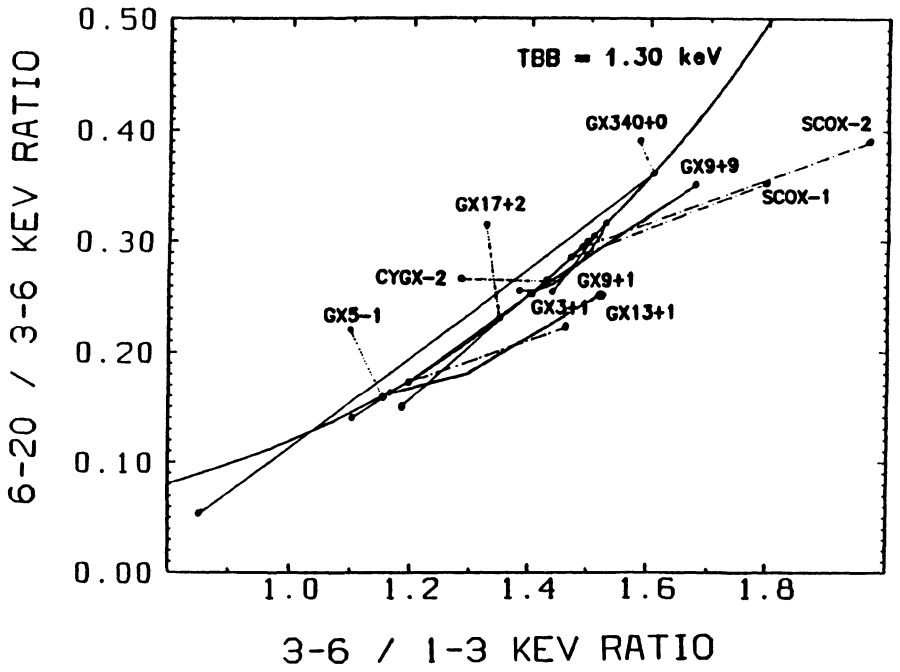

Figure 4: Color-color diagram of 'de-absorbed' color-color data

Using this information it should be possible to 'de-absorb' the color-color data of each individual source along the NH-track to predict the unabsorbed profile. Thus we shifted all data contours (for sources at very high soft ratios the flattening

of the contour slopes has also to be considered) along the NH-tracks from the right of the diagram to the position of the TTH-track at zero NH at the very left of the diagram. The result of this shift is shown in figure 4. For illustration purpose the profiles were now marked with lines connecting the extrema of each spectral branch, the dotted, solid and dash-dotted lines correspond to the HB, NB and FB, respectively. The shifted color-color data now pile up along a the plotted TTH-track showing strong overlaps. Normal branches fit this line almost perfectly (they hardly can be distinguished from the TTH-track), horizontal branches stick out to the left side of the track under different angles, the flaring branches stick out to the right side.

This 'de-absorption' poses an important result in the analysis of the spectral variability of LMXB energy spectra. It shows, that energy spectra *and* the observed spectral variability of bright LMXBs may be consistent with a simple spectral parametrisation.

4. Conclusion

Color-color diagrams and HIDs are a useful tool to describe the spectral variability of LMXB energy spectra. They show, that bright LMXBs can be found in at least three different spectral states, a horizontal branch, a normal and a flaring branch state. Up to now three sources could be observed in all three states and four in at least two of these states. Thus it seems, that this threefold spectral behaviour is a general property of bright sources and that it is only a matter of observation time in order to observe all bright LMXB in all three states.

Horizontal, normal and flaring branch are connected forming an overall variability pattern that looks like a twisted Z. This Z has two characteristic transition regions, the hard apex, where the spectra change from horizontal to normal branch variability, and the soft apex, where spectra change from normal to flaring branch variability. The fact that there is no jumping from one branch to another shows, that the overall spectral variability is rather continuous, although hard and soft apex imply a very drastic change in spectral behaviour. It is not clear yet on which timescales a single source can be typically found in one specific spectral state. We know however, that the souces spend a considerable amount of time in the hard and soft apex region (see also v.Paradijs et al. 1988, Priedhorsky et al. 1986).

The parametrisation of the color-color diagram in terms of a combination of a blackbody and a thermal bremsstrahlungs spectrum turned out to be a good mathematical description of the observed spectral variability. It indicated, that not only the energy spectra are of common nature in these source but they also quantitatively show very similar observables, i.e temperatures, emission radii etc.. It indicated further, that each spectral branch is dominated by the variation of a certain observable in all of these sources. Thus it is highly probable, that spectral branches as well as hard and soft apex in bright LMXBs are formed by common intrinsic processes of rather physical significance.

References

Branduardi, G.; Kyaflis, N.D.; Lamb, D.Q.; Mason, K.O.: 1980, *Astrophys. J. (Letters)* **235**, L153.

Hasinger, G.: 1987b in *The Origin and Evolution of Neutron Stars*, eds. D.J. Helfand and J.-H. Huang, p.333.

Hasinger, G.; Priedhorsky, W. and Middleditch, J.: 1988, submitted to *Astrophys. J.* .

Hasinger, G. and van der Klis, M: 1988 (in preparation).

van der Klis, M.; Jansen, F.; van Paradijs, J.; Lewin, W.G.H.; van den Heuvel, E.P.J.; Trümper, J.E.; Sztajno, M.: 1985, *Nature* **316**, 225.

Langmeier, A.: Universität München,Thesis 1988.

Lewin, W.H.G.; van Paradijs, J.; Hasinger, G.; Penninx, W.H., Langmeier, A.; van der Klis, M.; Jansen, F.; Basinska, E.M.; Sztajno, M. Trümper, J.: 1987 *Mon. Not. R. astr. Soc.* **226**, 383.

Makishima, K. and Mitsuda, K.: 1985, *Japan-US. Seminar on Galactic and Extragalactic Compact X-Ray Sources*, eds. Y. Tanaka and W.H.G. Lewin, p.127, ISAS.

Mason, K.O.; Charles, P.A.; White, N.E; Culhane, J.L.; Sanford, P.W.; Strong, K.T.: 1976 *Mon. Not. R. astr. Soc.* **177**, 513.

van Paradijs, J.; Hasinger G.; Lewin W.H.G.; van der Klis, M.; Sztajno, M.; Schulz, N.; Jansen, F.: 1988 *Mon. Not. R. astr. Soc.* **231**, 379.

Parsignault, D.R. and Grindlay, J.E : 1978, *Astrophys. J.* **225**, 970.

Priedhorsky, W.; Hasinger, G.; Lewin, W.G.H.; Middleditch, J.; Parmar, A.; Stella, L.; White, N.E.: 1986, *Astrophys. J. (Letters)* **306**, L91.

Schulz, N.S.; Hasinger, G.; Trümper, J.: 1988, *Astron. Astrophys.* (submitted).

Shibazaki, N. and Mitsuda, K.: 1984 in *High Energy Transients in Astrophysics*, ed. S.E. Woosley, American Institute of Physics, New York, p.49.

Stella L.; White, N.E; Taylor, B.G.: Proc. ESA Workshop: *Recent Results on Cataclysmic Variables*, Bamberg 1985 (ESA SP-236), p.125.

X-RAYS FROM A POSSIBLE PULSAR IN SUPERNOVA 1987A

APOSTOLOS MASTICHIADIS
Max Planck Institut für Extraterrestrische Physik
D-8046, Garching bei München
Federal Republic of Germany

ABSTRACT. We report on Monte-Carlo calculations of the emergence of X- and γ-rays from the envelope of the supernova 1987A. Assuming that there exists an X-ray emitting pulsar at the centre, we discuss the possibilities of observing its radiation and find that if the pulsar is about as luminous as the present-day Crab, it may be possible to detect the breakout at $\sim$ 20 months. The pulsar should emerge first in the 6–16 keV band covered by *GINGA*. About six months later it would appear in the 20–45 keV band of *MIR-HEXE*. Because the optical depth of the envelope at breakout is still substantial ($\sim$ 4), we do not expect pulses to be detected straightaway. Our conclusions are based on a simple homogeneous model for the envelope and do not depend on whether or not ^{56}Co is mixed into the outer layers. The time at which a pulsar of higher luminosity would emerge can be obtained from a simple scaling of our results.

1. Introduction

The observed absorption in the Balmer lines class the supernova 1987A as type II; the identification of the presupernova star, the neutrino flux detected at the time of the explosion, the evolution of the optical light-curve and the observations of emission of X-rays and soft γ–rays confirm this classification. Therefore, it is expected that a neutron star lies at the centre of the remnant. Any observation of such a star would arouse great interest since the properties of very young neutron stars are largely unknown.

The prospects of making such an observation depend, however, not only on the properties of the star, but also on those of the material enshrouding it. This material absorbs and scatters radiation from the neutron star. In addition, because of the decay of ^{56}Ni and ^{56}Co nuclei left over from the explosion, it produces a substantial luminosity itself, which may mask the radiation of the imbedded star.

At present, the observed intensity and decay rate of the optical light curve together with the photon flux in the range 10–1000 keV can be described by a model in which the 847 and 1238 keV γ–ray lines from the decay of .07 $M_\odot$ of ^{56}Co are losing energy to the 10–15 $M_\odot$ envelope by means of Compton scattering

H. Ögelman and E. P. J. van den Heuvel (eds.), Timing Neutron Stars, 305–315.

(e.g., Pinto and Woosley 1988). Equipped with a satisfactory description of the expanding remnant, it becomes possible to investigate the emergence of radiation from the imbedded neutron star. Young pulsars, such as that present in the Crab Nebula, emit a large amount of energy in the form of either energetic particles or low frequency electromagnetic waves. Eventually, such a pulsar positioned at the centre of SN1987A would be expected to have a strong effect on the dynamics of the envelope (Rees 1970, Ostriker 1987, Pacini 1987) by blowing out a cavity around itself. However, energy in this form remains inaccessible to *direct* observation unless strong inhomogeneities (holes) are present (Rees 1987). A significant fraction may, nevertheless, be deposited in the envelope and contribute to the optical light curve. On the other hand, substantial pulsed X-ray emission is expected from a young pulsar of the Crab type, and could penetrate the envelope once the optical depth to Thomson scattering has decreased to a few. To investigate this possibility, we have developed and used a Monte-Carlo code which simulates the down-Comptonization and absorption of energetic photons in the envelope of SN1987A. The code is similar to that developed by Ambwani and Sutherland (1988), and used by McCray *et al.* (1987), and Woosley *et al.* (1987). It is based on the algorithm described by Pozdnyakov *et al.* (1983), the only innovation being the introduction of certain variance reduction techniques which enable us to compute accurately the spectrum in the range 6–20 keV.

In section 2 a brief description of the code is given. In section 3 we apply this code to models of the ejecta and show that it successfully describes the optical, X-ray and γ-ray observations. Subsequently, we apply the same code to an envelope with no radioactive energy input but, instead, containing at its centre an X-ray emitting pulsar similar to that in the Crab Nebula. In section 4 we discuss the implications of these calculations for future measurements which may detect the imbedded pulsar. This paper is a somehow more extended version of Mastichiadis, Ögelman and Kirk (1988).

2. The Monte-Carlo code

In order to calculate the emergent photon spectrum and to take a good resolution of the iron line we have adopted the following procedure: We draw a photon that is given a weight $w(1) = 1$ and an energy E_1 and it is assumed that it is emitted from some initial radius r_1 at some random direction n_1. We calculate the optical depth $\tau(E_1)$ to the boundary and we allow a part $wes(1) = w(1)e^{-\tau(E_1)}$ to escape. This part is put into the emergent spectrum while the remaining fraction is forced to interact. For this purpose it is given a free path l such that $l <$ distance to the boundary (see Pozdnyakov, Sobol ans Sunyaev 1983). At the point of interaction we split the photon anew into a part $wabs(E_1)$ that goes into photoabsorption and a part that goes to the other processes (i.e., Compton and coherent scattering and pair production). This branching is taken by multiplying the incoming weight of the photon with the ratio of the photoabsorption cross section to the total cross-section involved. A part of the fraction that goes into photoabsorption will eventually radiate the 6.4 keV Fe Ka line and we treat this possibility as follows: We force the photon in the line to be emitted and we give it a weight $wf(1) = .34 * fFe * wabs(1)$ where fFe is the fraction of the photoabsorption that is due to iron and the factor

.34 is the line's yield for emission.

On the other hand we choose randomly between the other three processes (according to the ratios of their respective cross-section to the total one) and once this is done we find the end product of the particular process. The new photon is given a weight $w(2)$ which is that of the incoming photon. Once again we assume that a fraction escapes (which is scored in the spectrum) and we follow the already described procedure for the fraction that remains. We continue doing so until the weight of the photon has fallen below some small number ϵ. Assume now that this occurs after m interactions of the original photon. This means that this photon has contributed m inputs to the spectrum with weights $wes(1), wes(2), ..., wes(m)$, and $m-1$ emissions with weights $wfe(1), ..., wfe(m-1)$ in the Fe Ka line. So we return to the respective photoabsorption points $r(1), ..., r(m-1)$ and we assume that a 6.4 keV photon is emitted each time with the appropriate weight. We follow the same procedure as before only that this time each part that goes to photoabsorption is assumed to contribute to the optical lightcurve. With this technique we are able calculate the shape of the iron line with large resolution.

For the end product(s) of the various processes we have assumed that if a Compton scattering occured, the photon changed both its energy and direction. If the scattering was coherent, the photon was assumed to change its direction but not its energy. Finally pair production was assumed to give two 511-keV photons created from the annihilation of the produced electron-positron pair (not a very good assumption, especially if the pair producing photon is of high energy, which implies that the produced particles are also created with high energies and one needs to follow their cooling that involves ionization losses and bremsstrahlung (and thus additional photons) before annihilation). Nevertheless, for Thomson optical depths $\lesssim 20$ that are of interest here, pair production is not that important (its cross section remains way below the Thomson cross section) and a detailed treatment of the pair cooling would not change the overall spectrum.

3. The ejecta and pulsar models

The assumptions which we make in order to compute the spectrum and time dependence of the radiation emitted by the expanding supernova envelope are essentially the same as those contained in previous papers in this field (McCray *et al.* 1987, Chan and Lingenfelter 1987, Gehrels *et al.* 1987, Xu *et al.* 1988, Woosley *et al.* 1988, Kumagai *et al.* 1988). About one month after the explosion event, the light curve of the supernova is powered by the radioactive decay of ^{56}Co. (Before this, the decay of ^{56}Ni plays a role.) The luminosity of the cobalt is taken to be $L(t) = L_0 \exp(-t/114d)$ with $L_0 = 1.8.10^{42}$ erg s^{-1} . If the envelope is very optically thick, this energy, which is released mainly in the form of γ-rays in six nuclear lines, is given up in Compton scattering events with electrons in the envelope, which can be regarded as cold for this purpose. Eventually, when a photon has been degraded into an X–ray photon of energy less than about 20 keV, the small amount of remaining energy disappears in a single photoabsorption event. The energetic electrons that accompany the down-Comptonization process will lose their energy predominantly by ionization and thus will not radiate more X-rays.

As time proceeds, the envelope expands and its optical depth decreases. We as-

sume a homologous expansion and scale it such that the optical depth (to Thomson scattering) as a function of time is $\tau(t) = \tau_1(t/yr)^{-2}$ where τ_1 is the optical depth at age one year. At an optical depth of about 20, it becomes possible for photons to escape the envelope before undergoing absorption. Since these photons must still suffer many Compton scatterings, they appear as X-rays, as predicted by McCray *et al.* (1987). Thus the flux of X-rays emerging in a given band increases with time initially. Two effects then come into play which cause the X-ray flux to reach a maximum and subsequently decline. In the first place, the number of photons injected per second decreases as the ^{56}Co decays away. The second effect is more complex, but can be understood as follows (*cf.* Sutherland, *et al.* 1988): the typical emergent, down-scattered photons from ^{56}Co decay have an energy $\epsilon_f = mc^2/\tau^2$. If we consider photons of energy ϵ and define τ_{cr} as the optical depth at which $\epsilon_f = \epsilon$, then as long as $\tau > \tau_{cr}$ (and thus $\epsilon_f < \epsilon$), the flux of photons in the energy band around ϵ keeps increasing with decreasing τ. This rate of increase dominates the steady decline due to the decay of ^{56}Co. However, the flux at the energy of interest reaches a maximum at that time for which $\tau = \tau_{cr}$ and starts dropping thereafter, because when $\epsilon_f > \epsilon$, most of the photons do not suffer enough Compton scatterings to reach ϵ. As a result, the maximum flux is reached sooner for the soft X-rays than the hard ones. Eventually, when the envelope is optically thin, the γ–rays emerge unimpeded without producing an X–ray flux.

In the calculations presented here we assume the envelope to be an expanding sphere of uniform density and homogeneous composition with metal abundance $Z = Z_\odot$. We have varied the ^{56}Co distribution in two extreme ranges; all at the center and 95% mixed. Several groups have come to the conclusion that the observations of soft X–rays and γ–ray lines are not consistent with a realistic model of the envelope unless a certain amount of ^{56}Co is assumed to be mixed into the outer layers (Pinto and Woosley 1988, Ebisuzaki and Shibazaki 1988a,b, Kumagai *et al.* 1988). We find that in the extreme range of mixing we have considered the X-ray continuum and γ–ray line observations can be easily accommodated (see Kumagai *et al.* 1988 for a discussion on the effects of mixing). We do find, however, that the pulsar breakout occurs at epochs where the effects of ^{56}Co mixing have become unimportant.

Figure 1 shows the emergent spectrum (solid histogram) from such an envelope at four different epochs, assuming the optical depth at one year to be $\tau_1 = 10$. The spectrum clearly shows the six γ–ray lines as well as the prominent iron fluorescence line at 6.4 keV. As can be seen in Figure 1, our code gives particularly good spectral resolution at the point where the photoabsorption of X–rays becomes important i.e., at photon energies of less than about 20 keV, so that the shape of the iron line is accurately portrayed.

In addition to the spectrum to be expected from the envelope alone, Figure 1 also displays the spectrum to be expected from a pulsar alone (dots), assuming that the envelope contains no ^{56}Co. Because our calculations do not consider complications such as the degree of ionization of the envelope, the output photon fluxes are linearly related to the input photon fluxes and thus the results of the pulsar calculations can be simply scaled according to the assumed pulsar luminosity and added to the results of the cobalt calculations. In Figure 1 we assumed the

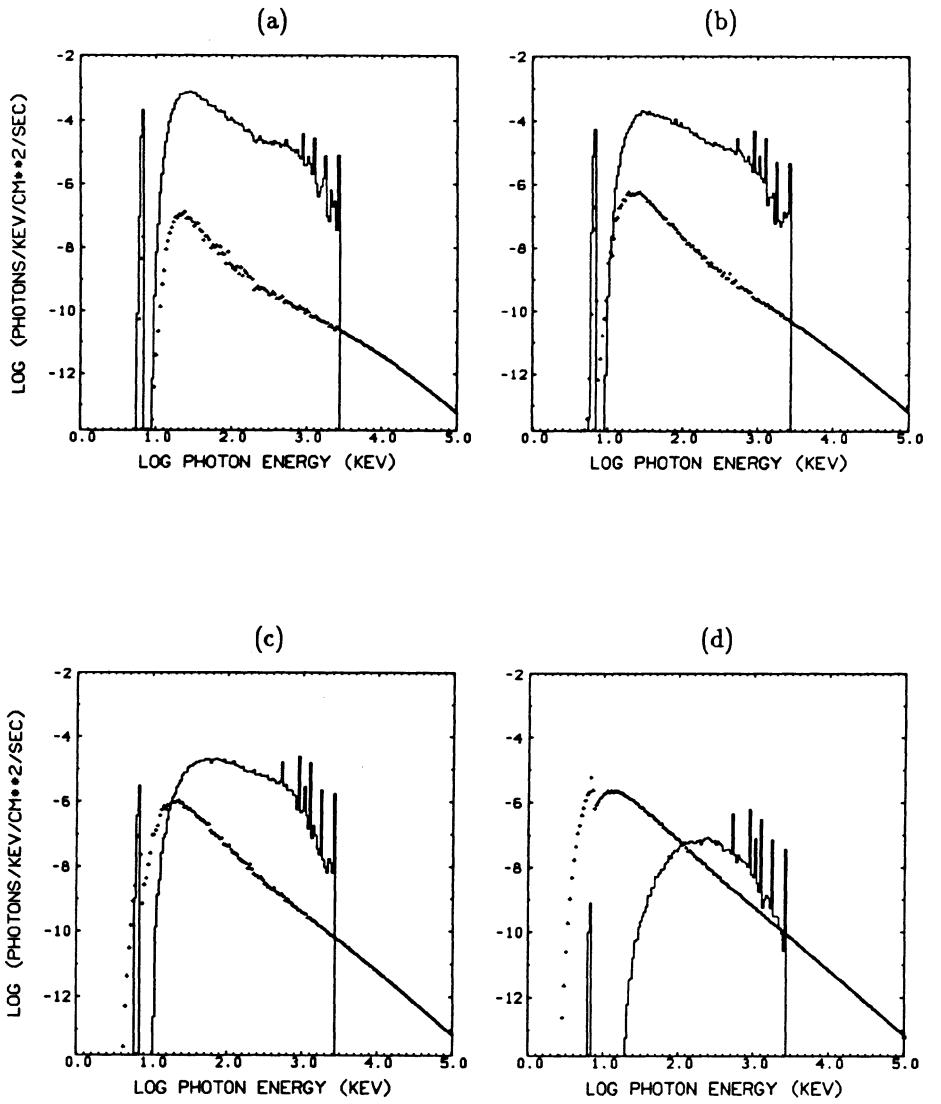

Figure 1: A comparison of the evolution of the ^{56}Co *decay spectrum (histogram) and the pulsar spectrum (dots) for various times t after the explosion: (a)* $t = 12$ *months (*τ*=10); (b)* $t = 17$ *months (*τ*=5); (c)* $t = 22$ *months (*τ*=3); (d)* $t = 38$ *months (*τ*=1). The* ^{56}Co *luminosity is assumed to come from* $.07M_{\odot}$ *of that element produced at the SN explosion. The pulsar is scaled to a Crab-like spectrum and luminosity (*E^{-2} *spectrum with* $10^{36} erg\ s^{-1}$ *per energy decade). For the ejecta we assume that the optical depth at age one year is 10 and the metallicity is solar.*

hypothetical pulsar to have a luminosity equal to that of the Crab pulsar, assumed for our purposes to possess an E^{-2} spectrum between 1 keV and 1 GeV with a luminosity of 10^{36}erg s^{-1} per energy decade.

The effect of the decreasing optical depth as the envelope expands is quite different in the pulsar case. The input spectrum is modified mainly in the 10–1000 keV region. For energies below 10 keV, photoabsorption by heavy elements removes essentially all injected photons, whereas for energies above 1 MeV, electron scattering (Compton scattering) enters the Klein-Nishina regime in which the cross-section decreases significantly. The only other opacity present is that of pair production which is, however, only a small fraction of the Thomson opacity, so that for optical depths smaller than about 10, the spectral shape of the input radiation remains virtually unaffected. In short, the injected pulsar spectrum is modified less and less as τ decreases and the emergent photon flux at each energy always increases with time.

Adding the "cobalt" and "pulsar" curves in Figure 1, shows that for a pulsar imbedded in Supernova 1987A, we expect the first X-ray signature to appear in the window between the photoabsorbtion cut-off and the energy to which the γ-ray line photons are down-Comptonized i.e., around 10–20 keV.

Figure 2 combines the Monte-Carlo derived lightcurves of the ^{56}Co and the pulsar in the ranges 6–16 keV, 16–26 keV (the ranges reported for *GINGA* satellite results), and 20-45 keV (the soft component of the *MIR-HEXE* X-ray telescope). As before, the pulsar is scaled to a luminosity of 1 Crab; other input luminosities can be derived simply by scaling these curves. In order to investigate the effects of mixing the ^{56}Co into the outer layers we considered two extreme cases, one without mixing and the other with 95% mixing (i.e., with the ^{56}Co homogeneously distributed within a radius equal to 95% of the outer radius of the envelope). The results of these two calculations are shown in Figure 2 connected by a vertical line in each energy bin used. Mixing can be seen to be important for high optical depths ($\tau > 10$), but it does not affect the pulsar breakout. For epochs earlier than those depicted, the effects of mixing are even more pronounced and easily accommodate the soft X-ray observations reported by *GINGA*. In Figure 2a we again assume the ejecta to be a homogeneous expanding sphere with metal abundance $Z = Z_\odot$ and the Thomson optical depth of the ejecta after a year to be $\tau_1 = 10$. A Crab-like pulsar should appear 21 months after the explosion in the 6–16 keV band, 2 months later in the 16–26 keV and 3 months after that in the 20–45 keV band, i.e., it will be almost half a year between the detections by *GINGA* and *MIR-HEXE*. If we were to assume a 10 times more luminous pulsar, the outbreak would occur 2 months earlier in each of the three bands. Figure 2b shows the same quantities but for $Z = 0.25Z_\odot$. Photoabsorption is reduced, resulting in an increased flux, especially in the soft band. However, the effects of metallicity are the same on both the ^{56}Co spectrum and the pulsar spectrum so that the pulsar appears at around the same time as in Figure 2a.

Figure 3 shows the effects of the mass of the envelope on the pulsar breakout. Here the mass was scaled so that the optical depth to be (a) 10 and (b) 20 in one year. The metallicity was assumed to be $Z = 0.25Z_\odot$ and the assumptions about mixing were the same as before. The results are shown only for the range 6-16

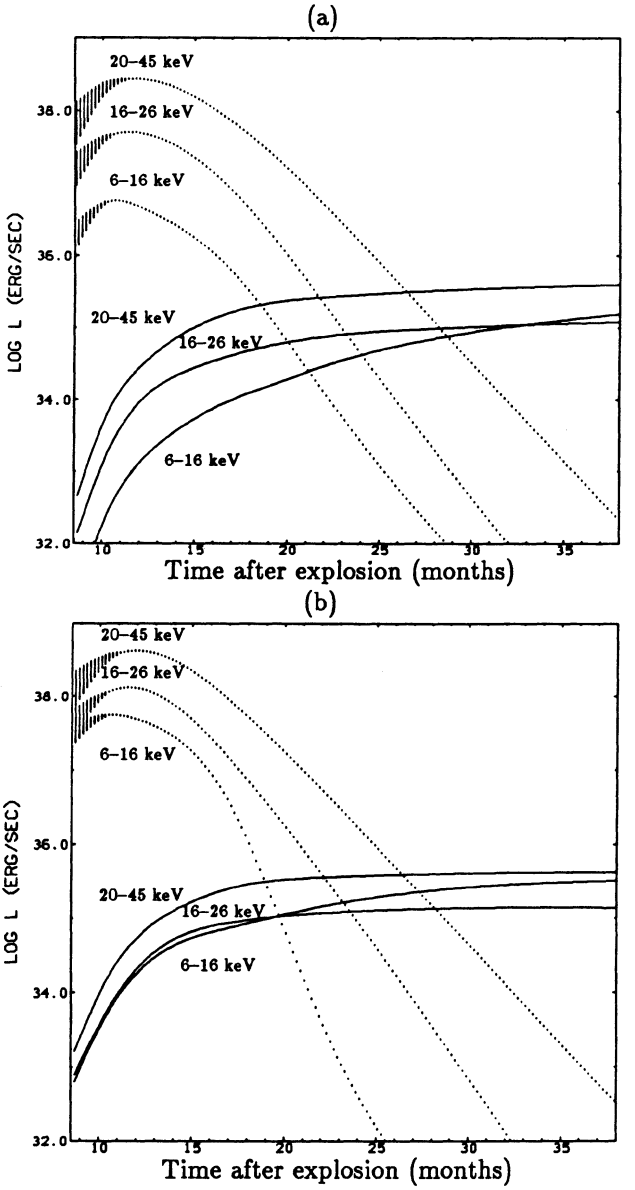

Figure 2: The effects of the metallicity on the calculated lightcurves for three energy bands: 6–16 keV, 16–26 keV (both GINGA) and 20–45 keV (MIR-HEXE) for metallicity: (a) $Z = Z_{\odot}$ and (b) $Z = 0.25Z_{\odot}$. Dotted lines represent the X-rays from ^{56}Co decay, whereas solid lines show the X-rays from the pulsar. The ejecta are assumed to have an optical depth of 10 at age one year.

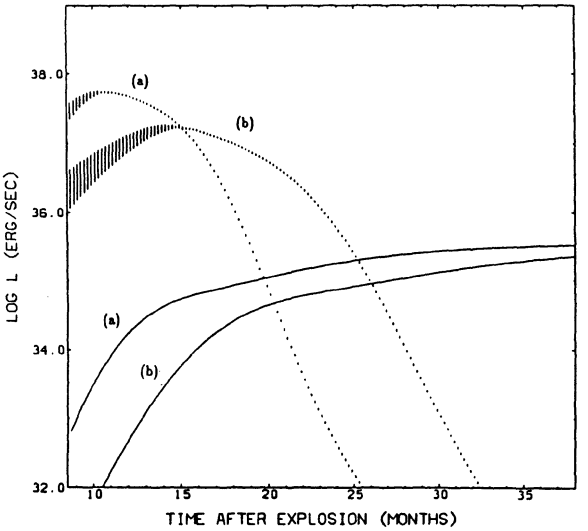

Figure 3: The effects of the total mass of the ejecta (expressed by the Thomson optical depth in one year τ_1) on the calculated lightcurves for the 6-16 keV energy band: (a) $\tau_1 = 10$ and (b) $\tau_1 = 20$. The dotted line represents the X-rays from ^{56}Co decay, whereas the solid line shows the X-rays from the pulsar. The ejecta are assumed to have a metallicity $Z = 0.25 Z_\odot$.

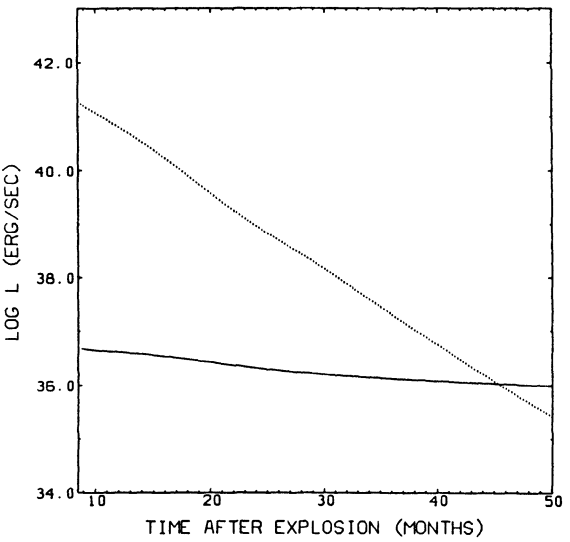

Figure 4: Calculated optical lightcurves for optical depth in one year equal 10. The dotted line represents the lightcurve from the decay of ^{56}Co, whereas the solid line shows the pulsar lightcurve.

keV, but they are qualitatively the same for the other energy bands. The pulsar breakout is not delayed by more than 6 months.

Finally, Figure 4 shows the *optical* lightcurves expected from such a scenario. The only parameter that is important in this case is the optical depth that was assumed to be 10 in one year. The pulsar will start dominating the ^{56}Co almost 3.5 years after the explosion, i.e., more than a year after its breakout in the soft X-rays. The main reason for that is that the ^{56}Co optical lightcurve falls less steeply with time than the X-ray one.

4. Discussion

Using a Monte-Carlo code which simulates the Comptonization of energetic photons, we have shown that the emerging spectrum of an imbedded Crab-like pulsar in Supernova 1987A will first start dominating over the ^{56}Co decay produced spectrum in the energy region just above the photoabsorbtion cut-off (~10–20 keV). This is due to the facts that: a) the ^{56}Co decay induced spectra gets depleted faster from the low energy side due to the decrease of optical depth as a function of time; b) the rate of injection of photons by ^{56}Co decays exponentially with time; c) the pulsar spectrum is relatively unaffected in the $E \geq 10$ keV region when $\tau \lesssim 5$, and is probably steady on the timescales discussed. These results are largely independentof the pulsar's spectral index or its high energy cut-off. The only important assumption here is that the pulsar is an X-ray emitter.

The breakout energy of ~10 keV is determined by the photoelectric absorption, which in turn is determined primarily by the amount of heavy elements in the ejecta, as can be seen in Figure 2. Effectively, there are two properties of the envelope which influence the conclusions reached in here: the metallicity of the ejecta (fig.2) and the total mass of the ejecta (fig.3), which is reflected in the assumed value of τ_1 (the optical depth at age one year), and the metallicity of the ejecta. As for the other important parameters: the total amount of ^{56}Co is fairly accurately determined from the optical light curve as .07 $M_\odot$ (e.g., Danziger 1988); the degree to which ^{56}Co is mixed into the outer layers, whilst important at early times, has lost its effect at the time we predict the pulsar radiation will breakout (see Figure 2). We find that the present *GINGA* and *MIR-HEXE* data (Dotani *et al.* 1987, Sunyaev *et al.* 1987) favour a model in which either a high optical depth at one year $\tau_1 \sim 20$ is combined with a low metallicity $Z \lesssim 0.25 Z_\odot$, or a lower optical depth $\tau_1 \sim 10$ with a high metallicity. On the other hand, the recent departure of the optical light curve from the exponential decay of timescale 114 days (Danziger 1988) implies that the optical depth at 13 months was less than or of the order of 10. Our calculations indicate that the fraction of the energy input by radioactive decay which emerges as X-rays and γ-rays varies between 0.1 for an unmixed envelope to 0.25 for 95% mixing, assuming an optical depth $\tau = 10$ (fig.4). Clearly an accurate determination of the structure of the envelope must await further observations.

Perhaps the biggest unknowns in these calculations are the luminosity and the spectral characteristics of the pulsar, which we have simply assumed to be Crab-like. How realistic is this assumption? The few pulsars we can directly associate with young ($\sim 10^3$ yr) supernova remnants are the Crab pulsar itself, PSR 0540-69 in the LMC, and PSR 1509-58. These pulsars have periods of 33, 50 and 150 milliseconds respectively. The Crab and PSR 0540-69 are copious emitters of pulsed

X-rays whereas PSR 1509-58 is about a factor of 100 less luminous in this band. The typical conversion efficiency of rotational energy loss to X-rays is of the order of $10^{-3} - 10^{-2}$ (Seward 1985). So that if the pulsar in Supernova 1987A rotates at the supposed birth period of the Crab ($\sim$ 17ms see Ostriker 1987) its luminosity should be more than an order of magnitude greater than the present-day Crab.

The most pessimistic scenario for an X-ray observation of a pulsar in Supernova 1987A is that of Chevalier and Emmering (1986) and Narayan (1987), who have argued that the present period *vs.* period derivative distribution of radio pulsars favours periods at birth in the range .1 to 1 second. If this is indeed the case for the pulsar in Supernova 1987A, we may never see any pulsar radiation from it. However, even then, after several years, when the envelope has thinned out to $\tau \lesssim 1$, we should be able to observe the soft X-ray photons from the hot surface of the cooling neutron star. If standard cooling theories are correct (Nomoto and Tsuruta 1987), we estimate that an X-ray telescope such as *ROSAT* should be able to observe the neutron star in Supernova 1987A.

On the other hand, an optimistic extrapolation of a Crab-like pulsar back to its state at birth yields much higher luminosities than those presently observed from the Crab. If the X-ray luminosity scales like $(\text{period})^{-10}$, as has been suggested by Pacini (1971), we may already have begun to observe X-rays which originated on its surface! However, the good agreement of the optical light curve with the exponential decay rate of ^{56}Co indicates that the pulsar cannot be pumping more than about 10^{40} erg s^{-1} into the envelope. Whatever the reader's favourite prejudice, the pulsar spectrum presented here can simply be scaled up and down according to the desired luminosity, provided that the photon spectrum remains a power-law with index -2.

Are the available instruments sensitive enough to detect a Crab-like pulsar in Supernova 1987A when it starts dominating the radiation from the ejecta? In the X-ray range, *GINGA* and *MIR-HEXE* satellites are probably at the borderline of unpulsed detection. However as τ decreases to values around 1, the chance of detecting an unscattered photon becomes significant, enabling the detection of pulsed radiation from the stellar surface. Thus, the sensitivity for detecting a Crab-like pulsar increases. For example, the LMC pulsar PSR 0540-69 happens to lie in the same field of view as Supernova 1987A and is easily detected by *GINGA* (Dotani *et al.* 1988).

In the γ–ray energy range above a few MeV, calculations indicate that the pulsar spectrum emerges almost unaffected by the ejecta once $\tau \lesssim 10$. However, to observe this we must wait until 1990's, when the instruments on board the *GRO* satellite should be able to detect the pulsar if it is several times more luminous than Crab.

ACKNOWLEDGMENTS: The author gratefully acknowledges the substantial help of H. Ögelman and J. Kirk. Discussions with H. Böhringer, G. Hasinger, N. Kylafis, J. Trümper and J. Ventura were of great assistance.

REFERENCES

Ambwani, K. & Sutherland, P.G.: 1988 *Astrophys. J.* **325**, 820
Chan, K.W. & Lingenfelter, R.E.: 1987 *Astrophys. J. (Letters)* **318**, L51

Chevalier, R.A. & Emmering, R.T. 1986 *Astrophys. J.* **304**, 140
Danziger, I.J.: 1988 to appear in *Proceedings of the 20th. Yamada Conference*, Tokyo, March 1988
Dotani, T. *et al.*: 1987, *Nature* **330**, 230
Dotani, T. *et al.*: 1988, poster paper, Int. Symp. on the Physics of Neutron Stars and Black Holes, Tokyo.
Ebisuzaki, T. & Shibazaki, N.: 1988a *Astrophys. J. (Letters)* **327**, L5
Ebisuzaki, T. & Shibazaki, N.: 1988b *Astrophys. J. (Letters)* **327**, L9
Gehrels, N., MacCallum, C.J. & Levanthal, M.: 1987 *Astrophys. J. (Letters)* **318**, L51
Kumagai, S., Itoh, M., Shigeyama, T., Nomoto, K. & Nishimura, J.: 1988, *Astron. and Astrophys.* **197**, L7
McCray, R.A., Shull, J.M. & Sutherland, P.G.: 1987 *Astrophys. J. (Letters)* **317**, L73
Mastichiadis, A., Ögelman, H. & Kirk, J.G.: 1988, *Astron. and Astrophys.* **201**, L19
Matz, S.M., Share, G.H., Leising, M.D., Chupp, E.L., Vestrand, W.T., Purcell, W.R., Strickman, M.S. & Reppin., C.: 1988, *Nature* **331**, 416
Narayan, R.: 1987, *Astrophys. J.* **319**, 162
Nomoto, K. & Tsuruta, S.: 1987, *Astrophys. J.* **312**, 711
Ostriker, J.P.: 1987, *Nature* **327**, 287
Pacini, F.: 1971, *Astrophys. J. (Letters)* **163**, L17
Pacini, F.: 1987, in the *Proceedings of the ESO Workshop on SN 1987A*, ed: I.J. Danziger, page 565
Pinto, P.A. & Woosley, S.A.: *Astrophys. J.* , in press
Pozdnyakov, L.A., Sobol, I.M. & Sunyaev, R.A.: 1983, *Soviet Sci. Rev., Ap. and Space Phys.*, **2**, 189 (New York: Harwood)
Rees, M.J.: 1970, *Astrophys. Letters* **6**, 55
Rees, M.J.: 1987, *Nature* **328**, 207
Seward, F.D.: 1985, *Comments Astrophys.*, **11**, 15
Sunyaev, R.A. *et al.*: 1987, *Nature* **330**, 227
Sutherland, P.G., Xu, Y., McCray, R.A. & Ross, R.R.: 1987, in *Proceedings of IAU Colloquium No. 108*
Woosley, S.A., Pinto, P.A. & Ensman, L.: 1988 *Astrophys. J.* **324**, 446
Xu, Y., Sutherland, P., McCray, R.: 1988 & Ross, R.R. *Astrophys. J.* **327**, 197

X-RAY OBSERVATIONS OF SN1987A WITH A CODED MASK IMAGING SPECTROMETER

J.J.M. in 't Zand, R. Jager, J. Heise, A.C. Brinkman
Space Research Laboratory, Utrecht, The Netherlands.

R.A. Sunyaev, M.R. Gilfanov, N. Yu. Pappe, E.M. Churazov,
N.S. Yamburenko
Space Research Institute, USSR Academy of Sciences, Moscow, USSR.

G.K. Skinner, O. Al-Emam, T.G. Patterson, A.P. Willmore
Department of Space Research, University of Birmingham, Edgbaston,
Birmingham B15 2TT, UK.

ABSTRACT - During June-August 1987 observations of SN1987A were performed by COMIS-TTM, the coded mask imaging spectrometer aboard the KVANT-module, which is attached to the MIR space station. Summed images of the LMC-field with a total integration time of 37000 sec during August 1987 were processed in two energy-bands: 2-10 and 10-20 keV.

In the 3-7 keV range a 3σ upper limit of 2×10^{-4} phot.cm^{-2}.s^{-1}.keV^{-1} was determined, for a flat spectrum. For 10-20 keV a 3σ upper limit was obtained of 1×10^{-4} phot.cm^{-2}.s^{-1}.keV^{-1}.

Compared with the result found by the Ginga-team on Sep. 3rd (Dotani et al., 1987) the low energy upper limit found with COMIS-TTM is a factor 3 lower, indicating possibly strong X-ray flux variation.

1. INTRODUCTION

X-ray emission from a region containing the supernova SN1987A was independently discovered from the results of the ROENTGEN Observatory (Sunyaev et al., 1987) in the range 20-300 keV and the GINGA satellite (Dotani et al., 1987) in the range 4-30 keV.

The ROENTGEN Observatory (Brinkman et al., Smith, Reppin et al., 1985) consists of four complementary X-ray instruments, as part of the KVANT module attached to the MIR space station. One of these is the Coded Mask Imaging Spectrometer COMIS-TTM, built by the Space Research Laboratory Utrecht and the Department of Space Research of the University of Birmingham. This paper is concerned with the analysis of the results of the COMIS detector. The instrument is sensitive in the range 2-30 keV and therefore coincides with the X-ray range observed with the GINGA satellite.

H. Ögelman and E. P. J. van den Heuvel (eds.), Timing Neutron Stars, 317–323.

2. INSTRUMENTAL CHARACTERISTICS

2.1 Description

Figure 1 shows a schematic drawing of COMIS-TTM. The camera consists of a gas filled proportional counter (Mels et al., 1988) with a mask in front at some distance which casts shadows of sky sources on the detector. The mask consists of opaque and transparent elements of 1 square mm which are distributed in a pseudo-random pattern of size 255 by 257 mm (see e.g. Skinner, 1984). Each sky source in the total FOV (= Field Of View) of 16 by 16 degrees casts a shadow of the mask on a certain part of the detector, depending on the sky-position of that source. The detector is sensitive to photons with energies between 2 and 32 keV, whereby Figure 2 shows the calculated sensitivity curve of COMIS-TTM for normal incidence. For off-axis sources the detector will only be partly illuminated causing the sensitivity-function to have a pyramidical shape over the reconstructed sky image with a FWHM of 7.8x7.8 degrees. The total range of 2-32 keV is subdivided in 31 channels. The detector position resolution is 0.5 mm for most photon energies. The energy resolution of the detector ranges from 19% at 6 keV to 13% at 23 keV. The time resolution is 1 sec for low intensity sources and 0.1 sec for strong sources. For monitoring purposes the detector is illuminated by five radioactive calibration sources: four Fe55 sources and one Cd109 source. For the reconstruction of the sky images it is important to note that the detector window is supported against the gas pressure of the detector by a window support structure. For further detector characteristics: see Table I.

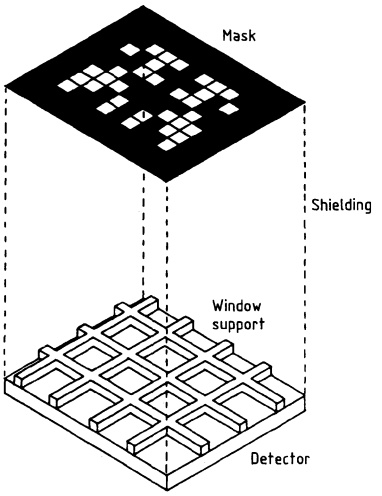

Figure 1. Schematic drawing COMIS (from Hammersley, 1986)

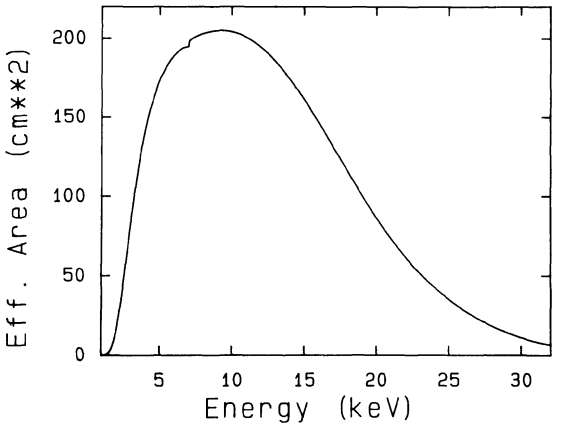

Figure 2. Calculated effective area of COMIS vs. photon energy for normal incidence.

TABLE I: Characteristics of COMIS-TTM.

Energy-range	2-32 keV
Field of View	7.8 x 7.8 degrees FWHM
Mask area = Detector area	25 x 25 cm^2
Mask-detector separation	184 cm
Window material	200 μm Be
Gas	95% Xe, 5% CO_2 at 1.1 atm.
Angular resolution	2 arcminutes
Mask transparency	50%
Mask element size	1.0 x 1.0 mm^2
Detector pixel size	0.375 x 0.375 mm^2

2.2 In flight performance

The detector imaging performance is as expected and will be discussed later. The spectral performance is somewhat less than expected. Consequently spectral diagnostics are more elaborate: corrections have to be made which are dependant on background countrate. As a consequence only observations at relatively low background rates are useful.

3. RECONSTRUCTING SKY IMAGES

Detector images consist of mask-shadows of one or more sources superimposed on a diffuse X-ray background level. To obtain a sky image the detector image has to be decoded. For a thorough description of reconstruction-methods we refer to Hammersley (1987). Here we give a short resume of the method we followed.

After choosing a time interval and an energy range the detector image is binned into 1 by 1 mm pixels conform the dimension of the mask elements. Then this image is correlated with the mask pattern in the following way:

$$C(i,j) = \sum_{k,l} D(k,l) * M(k+i,l+j)$$

where D is the detector image, M represents the mask pattern and equals 1 if the element (k+i,l+j) is open and $-t_k/(1-t_k)$ if that element is closed, with t_k the transparency of that part of the mask which is used for the reconstruction of sky-element (i,j). t_k varies within 4% of the mean value of 0.50 for the FWHM of the FOV. The advantage of the use of this so called t_k-correlation over the normal correlation (M=1 for open and 0 for closed elements) is that the average countrate at empty reconstructed sky parts will become zero.

After this correlation images can show a strong regular structure that is caused by the window support structure. This structure is

eliminated by processing the detector-images beforehand: at the known positions beneath the support structure the countrates are set to the mean of the whole detector. An additional cleaning is necessary when strong sky sources are present towards the sides of the FOV. These cast shadows of the support structure on the detector, giving still rise to regular structures in the image after the previous reprocessing is done. This can be avoided by redefining the width of the support bars to such an extent that shadows of the off-axis sources will be beneath the widened support structure. In the case of the observations of SN1987A, discussed hereafter, the support structure was widened by a factor 2.5, to eliminate the shadow-effect of the off-axis source LMC X-2. A disadvantage of this processing is that counts will be lost that are under the widened support structure. For the SN1987A-observations this amounts to a loss of 25%. On the other hand weak sources will be easier distinguishable after the regular structure has been eliminated.

It is also possible to make reconstructed sky images utilizing the 0.375 square mm size of the detector-pixels. Before correlation the mask pattern is then subdivided into 0.375 by 0.375 mm^2 bins. Sky images of strong sources in detector-resolution clearly show the PSF (= Point Spread Function). Checks on the PSF with observations of the sources Cyg X-1, Her X-1 and LMC X-1 confirm the preflight predictions satisfactorily. By determination of the center of the observed PSF it is possible to find the sky-position of the source with an accuracy which depends on the number of accumulated counts and which amounts to 0.8 arcminutes in the worst case.

4. OBSERVATIONS ON SN1987A

4.1 Observation characteristics / summing of images

COMIS-TTM observed SN1987A in three periods: 10-12 June, 16 July and 10-23 August 1987. The total integration time was 41000 sec. The FOV of each session was centered roughly around SN1987A and included sources as LMC X-1, X-2, X-3, X-4 and the pulsar 0540-693. Because most integration time, 37000 sec, was obtained in the August period we will concentrate here on these observations.

About 50 images were taken from this period, each having a slightly different orientation towards the sky. Before the images could be added each session had to be shifted and rotated to a reference. The shift and rotation parameters were calculated from the positions of LMC X-1 and X-2, which were prominent in all images.

4.2 Results

Summations were made in 2 energy bands: 2-10 keV and 10-20 keV. Figure 3 shows a 3-dimensional plot of the sum in the lower energy band. Clearly visible are the strong sources in the FOV: LMC X-1, X-2, X-3 and X-4. Figure 4 is a contour map of a 1.5 x 1.5 degrees part of Fig.3, cross correlated with the PSF in detector resolution and including LMC X-1, the pulsar 0540-693 and the position of SN1987A.

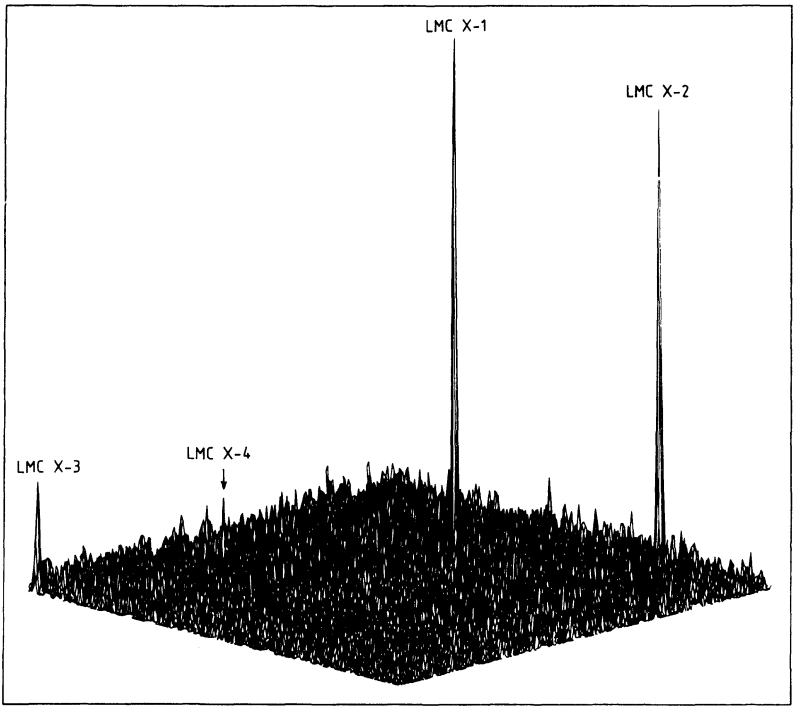

Figure 3. 7.8x7.8 degrees part of the summed image in 2-10 keV in 10-23 August, including the sources LMC X-1, X-2, X-3 and X-4. The total integration time is 37000 sec.

Because COMIS-TTM has not observed the Crab-nebula yet, the supernova remnant 0540-693, observed with a significance of 5σ, has been used as a calibration-source, being a Crab-like 1 mCrab (2-32 keV) strong remnant containing a 50 ms X-ray pulsar (Seward et al., 1984). As can be seen the optically determined position of the supernova (McNaught, 1987) coincides with a 3σ peak within a distance of 2 arcmins from the peak-position. The 3σ peak does not coincide within 0.8 arcmin with the position of SN1987A as would be expected if the peak originated from SN1987A. Therefore an upper limit is derived of 2.0×10^{-4} phot.cm^{-2}.s^{-1}.keV^{-1} ($3s$) in the energy-range 3-7 keV.

Upper limits in 10-20 keV and for the other two observation periods, expressed in phot.cm^{-2}.s^{-1}.keV^{-1} using a flat energy spectrum as well as a Crab like spectrum in 2-32 keV, are given in Table II.

4.3 Comparison with other observations

Dotani et al. (1987) observed a two component spectrum of SN1987A:

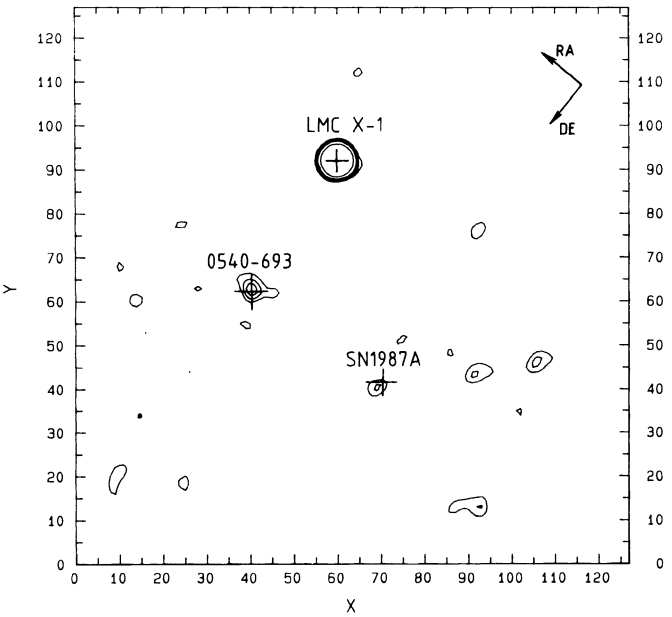

Figure 4. 1.5 by 1.5 degrees part of Fig.3, cross correlated with the in-flight determined PSF, in a contour map. Contour levels are given for 2, 3, 4, 5 and 10 σ. The crosses indicate previously determined positions of the sources. Coordinates are pixel indices.

a soft X-ray power-law spectrum up to ~12 keV and a hard tail. If one extrapolates their spectrum from 4 to 3 keV it results in a flux of 6 x 10^{-4} phot.cm^{-2}.s^{-1}.keV^{-1} (3-7 keV) on September 3rd. This is a factor 3 higher than our 3σ upper limit, which is averaged over the period 10-23 August. A possible explanation for this discrepancy is a rather fast variation in the X-ray lightcurve.

The 10-20 keV results are reasonably in agreement with those found by the Ginga team (1 x 10^{-4} phot.cm^{-2}.s^{-1}.keV^{-1} detection) and those found by examining the data from the other three ROENTGEN-telescopes (Sunyaev et al., 1987).

TABLE II: Photon upper limits of SN1987A in phot.cm^{-2}.s^{-1}.keV^{-1} for a flat spectrum. The last column contains Crab-spectrum upper limits, expressed in mCrab. Upper limits are 3σ-values.

	chs.4-14 (3-7 keV)	chs.20-27 (10-20 keV)	Crab-spectrum
june	: < 4.5 x 10^{-4}	< 2.2 x 10^{-4}	< 1.2 mCrab
july	: < 2.3 x 10^{-3}	< 1.1 x 10^{-3}	< 6.0 mCrab
august	: < 2.0 x 10^{-4}	< 1.0 x 10^{-4}	< 0.6 mCrab

5. SUMMARY AND DISCUSSION

The summed image observed with the COMIS-TTM instrument of a region of 7.8x7.8 degrees of the Large Magellanic Cloud clearly exhibits 5 sources, resolved with a position resolution of typically 2 arcmin. These are LMC X-1, X-2, X-3, X-4 and the pulsar 0540-693. This last (weak) source has been used for calibration. A region of 1.5x1.5 degrees around SN1987A shows in addition three small peaks exceeding the 3σ limit of the noise in the background, consistent with statistical expectation. One of these coincides within 2 arcmin with the position of SN1987A, but it is located too far away to assign this peak with enough certainty to SN1987A. Thus an upper limit of 2×10^{-4} phot.cm^{-2}.s^{-1}.keV^{-1} was derived in 3-7 keV, a factor 3 lower than the X-ray flux observed by GINGA from SN1987A a few days later.

Possible origins of the X-ray emission include 1) thermal emission from a hot plasma compressed and heated by the supernova shock wave, 2) Compton scattered gamma radiation from the radio active decay of ^{60}Co and 3) X-ray radiation from a young fast pulsar. These mechanisms are further discussed in Sunyaev et al. (1987).

6. REFERENCES

Brinkman, A.C. et al., Smith, A., Reppin, C. et al.: 1985, *Non Thermal and Very High Temperature Phenomena in X-Ray Astronomy*, eds. G.C. Perola and M. Salvati, Instituto Astronomico, Universitá "La Sapienza", Roma, p.261-282.

Dotani, T. et al.: 1987, *Nature*, **330**, 230.

Hammersley, A.P.: 1986, *The Reconstruction of Coded Mask Data under Conditions Realistic to X-ray Astronomy Observations*, Ph.D. Thesis, Department of Space Research, University of Birmingham.

McNaught, R.H.: 1987, *IAU Circ.*, nr. 4316.

Mels, W.A. et al.: 1988, *Nucl.Inst.Meth.*, accepted.

Seward, F.D. et al.: 1984, *Ap.J.*, **255**, L19.

Skinner, G.K.: 1984, *Nucl.Inst.Meth.*, **221**, 33.

Sunyaev, R.A. et al. : 1987A, *Nature*, **330**, 227.

SS433: A BLACK HOLE CANDIDATE?

Tomaž Zwitter & Massimo Calvani
International School for Advanced Studies
Strada Costiera 11 - 34014 Trieste, Italy

Abstract. Stewart *et al.* (1987) recently derived limits on the masses and dimensions of the components of the SS433 binary system. In this paper we show how their limits can be improved by using a better Roche lobe geometry and taking account of the fact that the accretion disk in this system, which is geometrically thick according to optical observations (Wagner 1986), may occupy a considerable fraction of the Roche lobe of the compact object. Our results are based on the minimum amount of information from X–ray and optical observations. We find that the mass of the compact object is $\approx 10 M_{\odot}$ and that the length of the X–ray jet is $L_j \approx 1.4 \times 10^{12}$ *cm*.

1. Assumptions and constraints

In this article we use the following assumptions defining the geometry of the system:

(1) All of the 2–10 keV band photons come from that part of each jet between the exit from the disk funnel and the end of the X–ray jet (which has length L_j).
(2) The jets are exactly oppositely aligned. The axis of their precession cone is perpendicular to the orbital plane of the system. The cone opening angle α is 19°.8 and the system inclination angle i is 78°.2 (Margon 1984). The precession is retrograde (Leibowitz 1984).
(3) The rotation axis of the star is nearly perpendicular to the orbital plane. The star co–rotates with the orbital motion (Leibowitz 1984) and so the usual Roche–lobe geometry is valid.
(4) The star fills its critical lobe.
(5) The size and shape of the disk is arbitrary (we shall comment on this later) but the optically thick part of it is inside the disk's critical lobe.

We use the following constraints obtained from the measurements by WTS and Stewart *et al.* (1987, hereafter STW):

(a) Only the X–ray jet pointing towards the observer was seen at the particular precessional phase of their measurements; the red–shifted jet was obscured by the disk (WTS).
(b) At the times of measurements 2 and 3 (Table 1) the jet was partly eclipsed by the star. Therefore the partial eclipse lasted at least from the beginning of measurement 2 to the end of measurement 3.

H. Ögelman and E. P. J. van den Heuvel (eds.), Timing Neutron Stars, 325–328.

(c) The system showed some X-ray brightness during all measurements (Table 1). Therefore, if the blue-shifted jet was totally eclipsed, it happened between the end of measurement 2 and the beginning of 3.

	JD (mid-exp)	13-day orbital phase (beg-exp)	(end-exp)	eclipse
1	2,445,965.219	0.7538	0.7644	no
2	68.042	0.9705	0.9793	partial
3	69.010	0.0393	0.0587	partial
4	70.667	0.1685	0.1827	no

Table 1: EXOSAT observations (adapted from STW).

Fig. 1 shows clearly what the constraints are on L_j and the mass ratio $q = M_x/M_\star$. The limits which we get are more stringent than those obtained by STW, which are also shown in Fig. 1 for comparison (dotted lines). Using the orbital ephemeris (Kemp *et al.* 1986) we get as allowed ranges (dashed triangle in Fig. 1):

$$0.295 < q < 0.65 \quad , \quad 0.207 < L_j < 0.35 \tag{1a}$$

while if we use only time differences between the measurements (solid line triangle in Fig. 1) we get:

$$0.245 < q < 1.39 \quad , \quad 0.084 < L_j < 0.42. \tag{1b}$$

In order to translate the relative sizes and mass ratios into absolute values we use the mass function $f(M) = M_\star^3/(M_\star + M_x)^2 = 10.6 M_\odot$ (Crampton and Hutchings 1981; Margon 1984) derived from HeII λ4686 emission line velocities. Using eq. (1a) we get:

$$5.2 M_\odot < M_x < 18.8 M_\odot \quad , \quad 17.7 M_\odot < M_\star < 28.9 M_\odot \tag{2a}$$

$$4.6 \times 10^{12}\ cm < A < 5.9 \times 10^{12}\ cm \quad , \quad 1.2 \times 10^{12}\ cm < L_j < 2.1 \times 10^{12}\ cm$$

while the more conservative limit from eq. (1b) gives:

$$4.0 M_\odot < M_x < 84 M_\odot \quad , \quad 16.4 M_\odot < M_\star < 61 M_\odot. \tag{2b}$$

$$4.4 \times 10^{12}\ cm < A < 8.6 \times 10^{12}\ cm \quad , \quad 7.1 \times 10^{11}\ cm < L_j < 3.6 \times 10^{12}\ cm$$

Note that the mass function is calculated using $K = 195 \pm 19$ km/s. However, if one allows the possibility of $K = 157$ km/s, instead of the average value as in eq. (2), the most conservative limit on M_x turns out to be $2.1 M_\odot$.

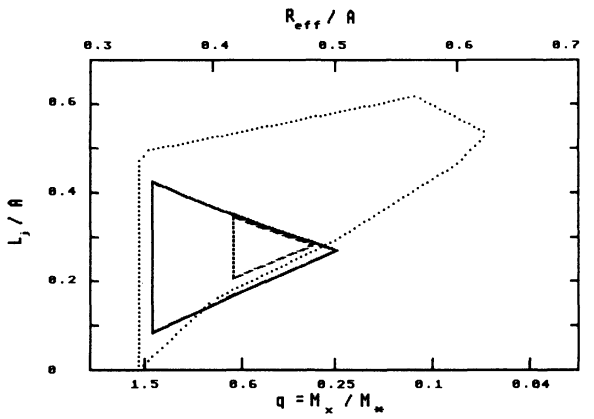

Fig. 1. Constraints on the length L_j of the X-ray emitting jets and the mass ratio q for the SS433 system (see text). The effective radius of the Roche-lobe of the normal star is given for reference. The binary separation is denoted by A.

2. Discussion and conclusions

The main result of this paper is the determination of allowed ranges of mass and dimension of the system components *without* any assumption on the disk shape: the values which we have derived for L_j and q are therefore the least stringent ones. One could of course choose a particular geometry for the disk shape (as in WTS); on the other hand, we know that the disk is geometrically thick (Wagner 1986; the thickness ratio is > 0.7 and the sizes of the star and the disk are comparable; see also Anderson *et al.* 1983) and therefore we believe that our results would not change much if we did this.

The lower mass limit for the compact object is, of course, the most interesting result. Causality arguments alone (Shapiro and Teukolsky 1983, p. 264) imply that such a massive compact object should be a black hole.

An approach similar to ours was used for the optical part of the spectrum by Leibowitz *et al.* (1984); their results indicate that $0.43 < q$. Using $10.6M_\odot$ for the mass function one then gets $9.4M_\odot < M_x$. This range of masses overlaps with ours.

We conclude that the compact object in SS433 is very probably a black hole whose mass is of the order of $M_x = 10M_\odot$. In this case the mass of the normal star is $23M_\odot$; the separation between the centers of mass is then one third of the astronomical unit and the effective radius of the star is 45 per cent of the separation. The maximum length of the jets is $L_j = 1.5 \times 10^{12} cm$. This implies a mass flow rate of $10^{-6}M_\odot\ y^{-1}$ and a kinematic luminosity in the jets of $2 \times 10^{39}\ ergs\ s^{-1}$ (WTS; Ögelman 1986; Spencer 1984; Sarazin *et al.* 1980). Such an enormous kinematic luminosity requires an even larger radiative luminosity (see however Katz 1986); the accretion rate in the system is therefore supercritical and this implies, on theoretical grounds (Calvani and Nobili 1981), that the accretion disk must be geometrically thick, in agreement with the observations (Wagner 1986; Antokhina and Cherepashchuk 1985).

Supercritical accretion onto a black hole seems therefore to be the best explanation for this most unusual astronomical phenomenon.

References

Anderson S. F., Margon B. & Grandi S. A., 1983. *Astrophys. J.*, **269**, 605.
Antokhina E. A. & Cherepashchuk A. M., 1985. *Sov Astron. Lett*, **11**, 4.
Calvani M. & Nobili L., 1981. *Astrophys. Space Sci.*, **79**, 387.
Crampton D. & Hutchings J. B., 1981. *Astrophys. J.*, **251**, 604.
Katz J., I., 1986. *Comments Astrophys.*, **11**, 201.
Kemp J. C., Henson G. D., Kraus D. J., Carroll L. C., Beardsley I. S., Takagishi K., Jugaku J., Matsuoka M., Leibowitz E. M., Mazeh T. & Mendelson H., 1986. *Astrophys. J.*, **305**, 805.
Leibowitz E. M., 1984. *Mon. Not. Roy. Astron. Soc.*, **210**, 279.
Leibowitz E. M., Mazeh T., & Mendelson H., 1984. *Nature*, **307**, 341.
Margon B., 1984. *Ann Rev. Astron. Astrophys.*, **22**, 507.
Ögelman H., 1986. Invited talk at *Erice School: Neutron stars, Agn's and Jets.*
Sarazin C. L., Begelman M. C. & Hatchett S. P., 1980. *Astrophys. J. Lett.*, **238**, L129.
Shapiro S. L. & Teukolsky S. A., 1983. *Black holes, white dwarfs and neutron stars*, John Wiley ed.
Spencer R. E., 1984. *Mon. Not. Roy. Astron. Soc.*, **209**, 869.
Stewart G. C., Watson M. G., Matsuoka M., Brinkmann W., Jugaku J., Takagishi K., Omodaka T., Kemp J. C., Kenson G. D., Kraus D. J., Mazeh T. & Leibowitz E. M., 1987. *Mon. Not. Roy. Astron. Soc.*, **228**, 293 (STW).
Wagner R. M., 1986. *Astrophys. J.* , **308**, 152.
Watson M. G., Stewart G. C., Brinkmann W. & King A. R., 1986. *Mon. Not. Roy. Astron. Soc.*, **222**, 261 (WTS).

SOLITARY NEUTRON STARS AS GAMMA-RAY SOURCES

M. Ruderman*
Department of Physics and
Columbia Astrophysics Laboratory
Columbia University
New York, NY 10027

ABSTRACT. Very high energy particle accelerators exist in the outer magnetospheres of some rapidly spinning solitary radiopulsars. The production of $e^{\pm}$ pairs and γ-rays associated with these accelerators evolves as the pulsar spins down. Expected evolution proceeds from a weak γ-ray source to a stronger Crab-like pulsar, then to a Vela-like pulsar, to a much stronger Cos B source, and, after several $\cdot 10^4$ years, to an extinct aligned Vela-like neutron star whose further spin-down is quenched. The latter can be reignited to be a transient Gamma Ray Burst source by various "match-like" phenomena. Reasons are given for the different evolution of canonical radiopulsars. Outer magnetosphere accelerators in millisecond pulsars and around magnetized neutron stars with accretion disks are also considered.

1. Introduction

Most observed pointlike sources of MeV–GeV cosmic γ-rays are still unidentified. These may be mainly solitary neutron stars as are several of the identified sources. Galactic starlike γ-ray sources include the following:

1) Accreting X-ray pulsars. These are certain strong magnetic field relatively slowly spinning, neutron stars in binaries (Massive X-ray Binaries) which seem to be sources of TeV γ-rays (cf. Turver 1989; de Jager 1989).

2) The Galactic Center Region source. This energetic radiation (e.g. Riegler *et al.* 1985) have been interpreted as MeV γ-ray emission from several Low Mass X-ray Binaries (Kluzniak *et al.* 1988).

3) Rapidly spinning radiopulsars. The young rapidly spinning Crab and Vela pulsars are strong MeV–GeV γ-ray sources. These and other short period radiopulsars seem also to have been observed as TeV γ-ray sources. Among all of these only the Crab pulsar is also a strong X-ray source; for Vela $L_x < 10^{-2} L_\gamma$. (cf. Turver 1989; de Jager 1989)

4) Unidentified Cos B sources. About 20 otherwise unidentified strong point-like sources of $10^2 - 10^3$ MeV γ-rays have been observed in our Galaxy (e.g. Bignami 1987). Their γ-ray luminosity is in the range $(0.4 - 5) \cdot 10^{36}$erg s^{-1}. They have not been observed in X-rays, implying $L_X \lesssim 10^{-3} L_\gamma$.

5) Gamma Ray Burst sources (GRB's). During their brief transient bursts these can be the brightest γ-ray sources in the sky (e.g. Liang and Petrosian 1986). A small subset, which we shall not consider further, consists of repeaters with a soft spectrum that does not seem to extend above an MeV. The others have spectra observed, so far, in the range $10^{-2} - 10^2$ MeV. The bursts last between 10^{-2} and 10^2s. GRB's have been observed at the rate of 2 to 3 per week but do not appear to repeat from the same source during observations extending over a decade. The bursts seem to originate from

* Research supported in part by NSF grant AST-86-02381

H. Ögelman and E. P. J. van den Heuvel (eds.), Timing Neutron Stars, 329–341.

an isotropic distribution of sources. If these GRB sources are in the Galactic disk there must be at least 10^5 of them. Are the GRB sources neutron stars? The case for such an interpretation is largely circumstantial but, nevertheless, rather persuasive. a) There are submillisecond structures in some bursts suggesting a radiating source size $\lesssim 10^7$ cm. b) A 450 KeV bump often claimed in the photon spectrum can be interpreted as $e^+ - e^-$ annihilation γ-rays gravitationally redshifted by propagation out from the neutron star surface. c) The 10^5 needed sources exceeds the population of most potential Galactic source populations except for the $10^8 - 10^9$ neutron stars. d) If not neutron stars what else can they be? (e.g. Paczinski and Gordon 1987 for another answer). If GRB sources are indeed neutron stars, are these in accreting binaries where the companion is necessary for the source or solitary? The total number of neutron stars in accreting binaries may possibly be as large as the needed 10^5. However, only that small subset of neutron star binaries in which accretion is too small to give an observed X-ray source, but large enough to power large bursts every decade or so (neutron star accretion rate $\sim 10^{-15} M_\odot \mathrm{yr}^{-1}$), is a potential GRB source population. This narrowly defined subset is expected to be too small to contain the needed 10^5 sources. If the 10^5 GRB neutron stars are part of the population of 10^8 solitary ones, the typical age of a GRB neutron star cannot be much less than 10^7 yrs.

We shall review in this paper some general features of a model for the γ-ray sources in the radiopulsars of family 3), how they evolve, and how they may, in the future, develop into the γ-ray sources of families 4) and 5). (Ruderman and Cheng 1988, hereafter RC; Ruderman 1987b). The γ-raly spectra of these three families is sketched in Fig. 1. For γ-ray energies above one MeV there is a qualitative similarity among them. At much lower energies only the Crab maintains a luminosity comparable to that in γ-rays and we turn first to that special source.

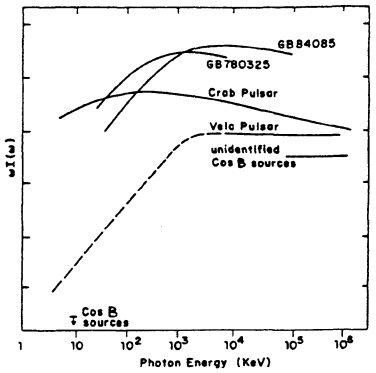

Figure 1. Spectra of two hard spectrum GRB's, GB 780325 and GB 780325 (Share *et al.* 1986, Epstein 1987), the Crab pulsar, the Vela pulsar, and unidentified Cos B sources. The dotted extrapolation of Vela's X-ray spectrum is the theoretical one of Cheng, Ho, and Ruderman (1986b) based upon synchrotron radiation from e^-/e^+ which do not survive in Vela's outer magnetosphere long enough to lose all of their energy. A much more steeply decreasing X-ray spectrum is not achievable in such models and a less steep one would exceed measured upper bounds. The designated X-ray Cos B upper bound assumes $L_x \lesssim 10^{-3} L_\gamma$ as the criterion for no X-ray detection. (The spectral intensity scale is arbitrary.)

2. Outer Magnetosphere Plasma Gaps and Crab Pulsar Radiation

About 10^{-3} of the spin-down energy of the Crab pulsar is radiated into two subpulses whose arrival times are energy independent over a photon energy range extending from optical to above 10^{12} eV (e.g. Dowthwaite *et al.* 1984). The rest seems to be emitted in a 10^{39}erg s^{-1} TeV wind which sustains the surrounding nebula's emission and accelerated expansion (Kennel and Coroniti 1984;

Ruderman 1987b). Since $e^{\pm}$ are produced by γ-rays it seems simplest to suppose that there is a particular region near the neutron star which is the source of both the observed γ-rays and the huge $e^{\pm}$ flux. Because that region must allow the escape of 10^{12} eV γ-rays the local magnetic field ($\vec{B}$) cannot greatly exceed 10^6 G. The region cannot be too far from the star or the γ-rays from it will not find sufficient target photons (or B) on which to conver to $e^{\pm}$ pairs. These two constraints suggest a strong particle accelerating region near the "light cylinder" at $r \sim c\Omega^{-1} \sim 10^8$ cm in which there is a large electric field ($\vec{E}$) component along $\vec{B}$ to accelerate e^-/e^+ to energies enough to account for the pulsar's double pulsed energetic photon spectrum and $e^{\pm}$ production.

A region within a pulsar's light cylinder with a large steady $\vec{E} \cdot \vec{B}$ which accelerates e^-/e^+ to ultrarelativistic energies can exist only where there is almost no magnetospheric plasma, instead of the canonical one of net charge density $\vec{\Omega} \cdot \vec{B}/2\pi c$ needed to keep $\vec{E} \cdot \vec{B} \sim 0$ in the rest of the corotating magnetosphere. Such a charge deficient region ("gap") in the outer magnetosphere is a common feature of a variety of models and is an expected consequence of assumed magnetospheric current flow patterns (Cheng, Ho, and Ruderman 1986 a and b, hereafter CHR I and II). We shall use the model of CHR I, II for further analysis but expect the general features of the evolution which results to be more robust than model details. Because of charge separated current flow a stable outer magnetosphere gap forms and expands in the regions indicated in Fig. 2.

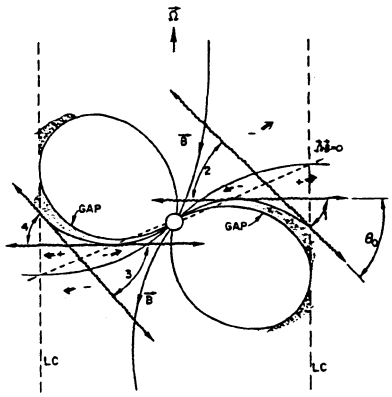

Figure 2. Outer gap accelerator regions in the CHR I, II model. The charge deficient regions in which $\vec{E} \cdot \vec{B} \neq 0$ are shaded. Most of the γ-ray production comes from synchrotron radiation and inverse Compton scattering at the gap boundary. Two fan beams of longitudinal width $\theta_0 \sim \pi/2$ would be observable. Crossed γ-ray beams fill the rest of the magnetosphere with pairs from $\gamma + \gamma \rightarrow e^+ + e^-$. A very small fraction of the e^-/e^+ are reversed by weak $\vec{E} \cdot \vec{B}$ to keep $\vec{E} \cdot \vec{B} \sim 0$ everywhere except in the accelerator gaps. The dotted line on which $\vec{\Omega} \cdot \vec{B}$ vanishes separates regions in which net current is carried by e^- moving in and e^+ moving out, the needed source coming from the $e^{\pm}$ production. A pair of possible secondary gaps is also indicated (but these may be quenched by primary gap powered pair production).

When such a gap begins to grow, the accelerating $\vec{E} \cdot \vec{B}$ in it also increases until the resulting e^-/e^+ accelerator becomes strong enough to support so much $e^{\pm}$ production that the supply of pair plasma quenches further gap growth. For the Crab pulsar this is the result of a series of processes (CHR II):

a) An $e^{\pm}$ pair produced in the gap is instantly separated by the large $\vec{E} \cdot \vec{B}$ there which accelerates the e^- and e^+ in opposite directions. Because of magnetic field line curvature each lepton radiates multi-GeV curvature γ-rays.

b) These are converted into $e^{\pm}$ pars in collisions with keV X-rays [from d) below]. Pairs created in the gap repeat process a).

c) Pairs created beyond the gap boundary lose their energy to synchrotron radiation

(optical to MeV) and to higher energy γ-rays from Compton scattering on the same X-ray flux responsible for the pair creation.

d) The X-ray flux from the synchrotron radiaiton of c) is that which initially caused the curvature radiation γ-rays of a) to materialize and the inverse Compton scattering of the pairs in e). Since the entire series of processes is powered by the extremely energetic e^- and e^+ of a) moving in opposite directions within the gap, all of the resulting fluxes of photons and $e^\pm$ pairs are also oppositely directed. The pairs and γ-rays moving in one direction then interact mainly with the X-rays moving oppositely.

e) A third generation of $e^\pm$ pairs comes from partial materialization of the crossed γ-ray beams from c).

The above processes a) - d) "bootstrap" the creation of an $e^\pm$ plasma until enough is produced to form a gap boundary layer which quenches further growth. The calculated spectral shape from $1-10^9$ eV which results from them fits the crab pulsar observations in Fig. 1. Some 10^{13} eV emission (not shown) is expected from inverse Compton scattering of gap e^-/e^+ on optical photons in the gap from process c) and from the synchrotron radiation by the $e^\pm$ pairs these ultra high energy γ-rays make beyond the gap boundary. (Radiation reaction limits gap e^-/e^+ to about 10^{13} eV. Higher energies would be given to protons whch traverse the entire 10^{15} Volt gap potential drop. These 10^{15} eV protons can make π°-mesons in collisions with the soft X-ray photons from the Crab pulsar, but 10^{15} eV γ-rays from π°-decay could escape without conversion to $e^\pm$ by the magnetospheric B only if the π° is made well beyond the pulsar light cylinder. Nebula matter is another possible target for π° production).

3. From the Crab to the Vela Pulsar

Observations of the Crab and Vela pulsars imply that these spinning neutron stars differ only in their spin periods: the Crab has a period $P \sim 3 \times 10^{-2}$s while for Vela $P \sim 9 \times 10^{-2}$s. Both pulsars appear to have the same dipole field strengths (surface dipole $B_s \sim 4 \times 10^{12} G$) and an almost identical double subpulse structure which suggests very similar relative orentations between their spins and magnetic dipoles and probably also with the line of sight to us. It seems very plausible, therefore, that in less than 10^4 years, when the Crab pulsar's spin will have slowed to that of Vela, its observed energetic radiation will have evolved into that seen today from Vela. This implies certain large changes must occur as the neutron star spin slows by a factor of three:

1) The Crab and Vela energetic radiation spectra are similar at photon energies above 1 MeV as shown in the spectra of Fig. 1. From the Crab the emitted power is somewhat greater in X-rays and remains strong down to optical frequencies. In Vela's spectrum, however, there is a sharp break at around one MeV and a very great relative intensity suppression at all lower photon energies.

2) The fraction of the total spindown power of the Crab which is radiated as energetic radiation ($\sim 10^{-3}$ if the radiated beams are much more greatly extended in latitude than in longitude as in Fig. 2) is only 10^{-1} that from the more slowly spinning Vela.

Both of these features have a natural explanation in the outergap accelerator model.

The series of mechanisms which limit the growth of an outer magnetosphere gap in the Crab pulsar are not nearly so efficient in the Vela pulsar. The synchrotron X-rays of 2c), necessary for the $e^\pm$ conversion of curvature γ-rays from the gap, are greatly suppressed in Vela. This is because the time it takes for a relativistic e^-/e^+ to synchrotron radiate down to a particular characteristic frequency is proportional to B^{-3}. Since Vela has about the same dipole moment as the Crab, but spins 3 times less rapidly, the local outer magnetosphere B is smaller by $3^3 = 27$. This is enough to suppress strong

X-ray synchrotron radiation since the radiating pairs will leave the magnetosphere, either directly or after reflection if spiralling inward along converging magnetic field lines, before such radiation is strong. Vela seems to limit its outer magnetosphere gap growth by mechanisms rather different from those of the Crab, and the gap grows to almost 1/3 the available oute rmagnetosphere volume before this is accomplished. The calculated spectrum in CHR II is consistent with that of Fig. 1.

Because of the strong synchrotron X-ray emission from the Crab pulsar's outer magnetosphere, $e^{\pm}$ production there can utilize more efficient mechanisms than those available for Vela. These Crab mechanisms become dominant for $P < 5 \times 10^{-2}$s (CHR II, following Eq. 4.23). In this faster spin regime (CHR II Eq. 4.19 and/or 6.7)

$$L_\gamma \sim \left(\frac{P}{3 \times 10^{-2}\text{s}}\right) 10^{36}\text{erg s}^{-1}. \tag{1}$$

We note that for pulsars spinning more rapidly than the Crab but which are otherwise identical, Eq. (1) predicts that their L_γ should be less. This is because in the larger outer magnetosphere magnetic fields of faster spinning pulsars it becomes easier to make $e^{\pm}$ pairs. The calculated evolution of γ-ray luminosities as a function of pulsar periods up to that of Vela is shown in Fig. 3. As a Vela pulsar slows to a period somewhat greater than 9×10^{-2}s, calculation of its expected L_γ indicates a change from one which diminishes with the decreasing spin-down power to one which increases sharply until almost all of the pulsar's spin-down power is being radiated away as energetic γ-rays. We turn next to that stage of the pulsar's evolution.

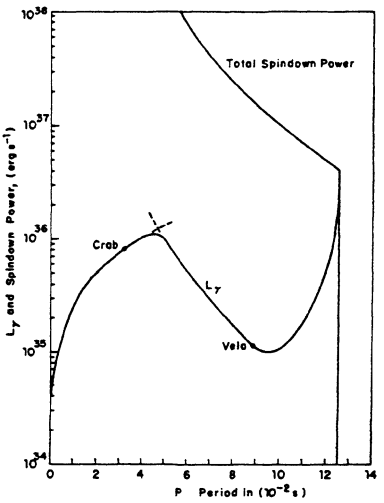

Figure 3. Evolution of calculated γ-ray luminosity (L_γ) and total pulsar spin-down power as a function of pulsar period when $P \lesssim 9 \times 10^{-2}$s. The estimated evolution of L_γ for periods in the interval P(Vela) – $1.4P$(Vela), after which L_γ is strongly quenched, is based upon the discussion in Sects. 3 and 4. The total spin-down power is assumed to be 7×10^{38}erg s^{-1} for the present Crab (from the radiation and accelerated expansion of the surrounding nebula and to be proportional to P^{-4}.

4. Future Evolution of Vela to a Stronger Cos B Source

Key mechanisms in the symbiotic complex which sustains the $e^{\pm}$ pair production needed for Vela's outer magnetospheric current flow include $\gamma + \gamma \rightarrow e^- + e^+$ by crossing radiation beams which contain the observed γ-ray flux. Pair production from such crossed beam photon collisions is largest for photon center of mass energies between the threshold $2mc^2 \sim 10^6$ eV and several MeV. As a young pulsar's spin slows to around that of Vela, L_γ remains a fixed fraction ($\sim 10^{-2}$) of the pulsar's total spin-down power (cf. Fig. 3). However, as the spectral break exceeds several MeV,

the number of γ-rays in the beams with energies in the most effective range to make $e^{\pm}$ pairs greatly decreases. Moreover the suppression of the lower end of the γ-ray spectrum leaves many fewer γ-ray photons in the beams. Because the spectral break rises so sharply with increasing pulsar period, a very much larger fraction of the pulsar's spin-down power must then be devoted to sustaining the needed outer magnetospheric pair production and thus to the γ-rays associated with it. In Vela the outer magnetosphere accelerator already occupies around 1/3 the total open field line volume. As P increses even very modestly, that fraction must grow very considerably in order to maintain required outer magnetospher $e^{\pm}$ production until, finally, all of the avialable volume is used for the accelerator. Then most of the pulsar's spin-down power will be dissipated in γ-rays produced near the pulsar light cylinder. For $P \sim 10^{-1}$s the consequent upper bound to the pulsar's γ-ray luminosity is

$$L_{\gamma} \sim I\Omega\dot{\Omega} \sim 5 \times 10^{36} \text{erg s}^{-1} \tag{2}$$

It has been estimated (RC) that this maximum L_{γ} will be achieved for Vela when its period reaches $P \sim 0.13$ s, as is indicated by the vertical drop at that P in Fig. 3. In the interval between $P = P(\text{Vela}) \sim 9 \times 10^{-2}$s and $P \sim 0.13$s, the pulsar γ-ray luminosity could almost reach that of Eq. (3.1) as indicated in Fig. 2. The radiated hard γ-ray spectrum would be expected to remain that of Fig. 1 which can be approximated by a flux spectrum $N(\omega) \sim \omega^{-2}$ at the higher energy and of tis range (CHR II, Eq. 5.13). The number of such luminous "post-Vela" γ-ray sources is the number of Vela-like pulsars whose periods lie between that of Vela and one a factor 1.4 greater. For a nominal birthrate of pulsars in this family of one per 10^2 years the total Vela-like Galactic population in this period interval would be 40, a large fraction of which could have L_{γ} approaching that of Eq. (2). The population, the γ-ray luminosity and spectrum, and the Vela-like suppression of X-ray emission are consistent with those of the 20 "unidentified" Cos B sources. It is tempting to suggest that the latter may consist of such post-Vela neutron stars with rising L_{γ} and $P \sim 10^{-1}$s.

We turn next to the evolution of these γ-ray pulsars when their outer magnetospheres can no longer sustain the large $e^{\pm}$ production rates needed to sustain strong magnetospheric current flow.

5. Terminal Alignment of Post-Vela Gamma-ray Pulsars

In the very luminous γ-ray emission phase of Sect. 4. the charge open field line accelerator region of the outer magnetosphere had to grow with increasing P until it occupied such a large region that L_{γ} approached the entire spin-down power of the pulsar. That growth was necessary to sustain needed large $e^{\pm}$ creation rates there. When P lengthens still further the accelerator, already at its maximum relative volume, can no longer sustain the needed steady copious $e^{\pm}$ production. As a result we expect that a very large part of the magnetosphere current flow between the polar cap and the light cylinder will also be quenched. A great suppression of current flow through the polar cap would give a corresponding reduction its spin-down torque from $\vec{J} \times \vec{B}$ inside the neutron star beneath the cap. Then any large further spin-down of the neutron star would have to be accomplished through the Maxwell torque from the radiation of the star's spinning non-aligned magnetic dipole moment. If the neutron star is approximated by a rigid sphere or, more realistically, as a spinning fluid whose shape is always axially symmetric about its spin axis, then that torque would not only spin-down a Vela-like star in about 10^4 years, it would also, on that same time scale, align its magnetic moment with $\vec{\Omega}$ (Davis and Goldstein 1970; Michel and Goldwire 1970) and thus quench the Maxwell spin-down torque. Long lived solid crust deformations and neutron superfluid vortex pinning may complicate estimates of alignment timescale (Goldreich 1970) but crustal relaxation mechanisms would ultimately allow alignment. If such relaxation is within 10^4 years, then the range of final periods for the family of aligning post-Vela γ-ray pulsars is $P \sim (1-2) \times 10^{-1}$s if the current flow through the stellar magnetosphere is largely quenched (RC). [Proposed models for the magnetospheres of such aligned neutron stars have been given by Krause-Polstorff and Michel (1985 a and b). According to Michel (1986) a very small departure from exact alignment would result in enough magnetic dipole radiation for radiation pressure to prevent much ambient matter

from being pulled to the star despite the net electric charge on the star plus magnetosphere in these models.] Because they no longer spin-down, the expected number of solitary aligned rapidly spinning ($P \sim 1 - 2 \times 10^{-1}$s) former γ-ray pulsars in the Galaxy could be of order the birthrate of Vela-like pulsars ($\sim 10^{-2}$yr) times the age of the Galaxy. In Sect. 7 we consider the ways in which among these 10^8 stars many may still be transient sources of X-ray and γ-ray emission. However, we first turn to the crucial question of why canonical radiopulsars survive unaligned for well over 10^6 years.

6. Postponing Alignment in Conventional Radiopulsars

The evolutionary scenario of Sect. 5 is certainly very different from that which describes the evolution of conventional radiopulsars. These pulsars have periods in the range $3 \times 10^{-1} < P < 3$s, and are much older than 10^4 years. There is almost certainly considerable open-field-line current flow through their polar caps which is the source of RF radiation. Most significantly, typical 10^6 year old radiopulsars are not yet aligned and are spinning down canonically. How and why does their evolution differ so strikingly from that proposed here for Vela-like γ-ray pulsars?

One possibility is, of course, frozen crustal deformations which do not relax for 10^6 yrs in canonical pulsars. Another is variations in polar cap local magnetic field geometry whose consequences we now discuss.

We note that the current flow maintained through the creation of $e^{\pm}$ pairs in a pulsar outer magnetosphere could also be accomplished if co-moving $e^{\pm}$ pairs (or e^- –positive ion pairs) were made elsewhere, transported into the needed "creation" region, and then separated there by a weak local $\vec{E} \cdot \vec{B}$. When e^- subsequently moves in a direction opposite to that of its positively charged consort it is electrodynamically as if a pair were created where the separation begins. Pair creation (as opposed to pair separation) can much more easily be sustained above a pulsar's polar cap where $B \sim 10^{12}G$ than in a much weaker outer magentosphere field. Possible Pair transport before separation from that production area to special charge deficient regions in the outer magnetosphere is then a critical issue. We consider first a non-aligned pure dipole field as in Fig.4. There are several arguments and models for expected $e^{\pm}$ production above the polar cap on upward curving (toward $\vec{\Omega}$) $\vec{B}$-field lines (Arons and Scharlemann 1979; Jones 1986). In all of them e^-/e^+ accelerated by $\vec{E} \cdot \vec{B} \neq 0$ give curvature γ-rays which materialize to $e^{\pm}$ pairs in the strong B above the polar cap. This copious outflowing $e^{\pm}$ plasma then shorts out almost all $\vec{E} \cdot \vec{B}$ in the regions along $\vec{B}$ through which it subsequently passes. A small remanant $\vec{E} \cdot \vec{B}$ need reverse only that very small fraction of $e^-(e^+)$ needed to maintain that net local charge density $\sim \vec{\Omega} \cdot \vec{B}/2\pi c$ along the flow which keeps $\vec{E} \cdot \vec{B} \sim 0$. The curvature γ-rays which create the outflowing $e^{\pm}$ plasma are radiated from primary e^-/e^+ which have characteristic energies along $\vec{B}$ of about 10^{12} eV. Their curvature γ-rays are emitted almost tangent to the local $\vec{B}$ and do not materialize on downward curving open field lines. Outflowing $e^{\pm}$ pairs do not reach the critical outer magnetosphere region beyond the $\vec{\Omega} \cdot \vec{B} = 0$ "null surface" of Fig. 2 which the CHR model gives as the seat of outer magnetosphere $e^{\pm}$ creation and γ-ray emission. However, if the polar cap $\vec{B}$ field is more complicated than pure dipole, then γ-rays created on only a certain portion of polar cap open field lines may, nevertheless, be capable of creating $e^{\pm}$ pairs on all polar cap field lines as suggested by Jones (1987) and shown in Fig. 5. Such pulsars do not need real pair production in the region beyond the null surface to sustain full current flow through their polar caps to their light cylinders. They would not be strong γ-ray sources (except for those γ-rays made above their polar caps which escape before materializing as pairs). They would not align when $P \sim 10^{-1}$s and could remain as observable radiopulsars until polar cap $e^{\pm}$ pair production begins to be quenched. Only then, when P approaches the radiopulsar "death line," would the still fully effective Maxwell torque be expected to begin aligning the pulsar. [Evidence for such aligning at this stage in the evolution of conventional radiopulsars has been summarized by Blair and Candy (1987) and Blair (1989)].

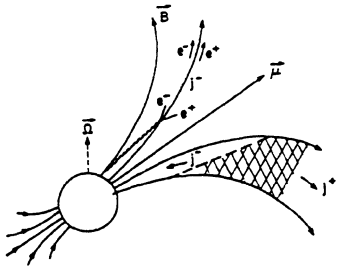

Figure 4. Dipole field structure, polar cap current (j) and $e^{\pm}$ flow from expected pair production above a polar cap. The cross-hatched region is that in which outer magnetosphere pair production would be needed to sustain the current flow. The neutron magnetic dipole moment is $\vec{\mu}$ and its spin is $\vec{\Omega}$.

Because the Vela and Crab pulsars give strong evidence for outer magnetosphere creation of γ-rays and $e^{\pm}$ pairs they could be assigned to the family of radiopulsars whose polar cap magnetic field structure is closer to that of Fig. 4 than to that of Fig. 5: they establish $e^{\pm}$ creation and accelerator systems in their outer magnetospheres to maintain full global magnetosphere current flows. It is also possible, however, that these young still relatively hot neutron stars do not yet produce any $e^{\pm}$ pairs on upward curving open field lines above their polar caps. These pulsars may strip enough partially ionized atoms from their polar caps, as these ions are accelerated through the hot thermal X-rays emitted from the polar cap surface, that newly stripped ion-electron pairs could play the same role as $e^{\pm}$ paris in quenching $\vec{E} \cdot \vec{B}$ on upward curving field lines. There would be no similar creation of such ion-electron pairs on downward curving ones. Such young pulsars should then produce $e^{\pm}$ pairs and γ-rays on the downward curving open field lines in their outer magnetospheres. Only when the polar caps cooled would $e^{\pm}$ creation above them take over the role previously played by the creation and separation of ion-electron pairs. At that time continued life as a non-aligned radiopulsar or aligned latent pulsar/GRB source may be determined by the resemblence of the polar cap magnetic field structure to that of Fig. 4 or to that of Fig. 5.

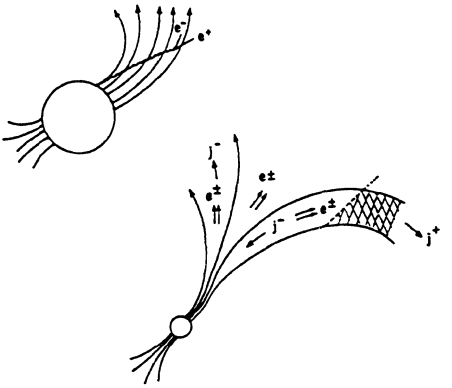

Figure 5. Alteration from Fig. 4 in the flow of $e^{\pm}$ pairs produced above a polar cap when the $\vec{B}$ field has a multipole structure such that all open field lines near the cap curve upward. In this case $e^{\pm}$ production and outflow occurs on all open field lines including those which reached the cross-hatched region. Pair separation there can replace the pair production otherwise needed in that region.

7. Transient Emission from Latent Aligned Post-Vela Pulsars: Gamma-ray Burst Sources

If the magnetic field of strongly magnetized neutron stars decays substantially after 10^7 years, then only 10^5 of the solitary aligned rapidly spinning neutron stars in the Galaxy are still Vela-like. If strong dipole fields survive longer this population would be increased proportionately. It has been proposed (Ruderman 1987 a; RC) that members of this large population of aligned latent pulsars can be re-ignited during certain brief transient events (e.g. a modest flux of soft X-rays passing through their outer magnetospheres). Their temporary emissions would then resemble those of the Vela family of Sects. 4 and 5, except that the alignment of the pulsar dipole would greatly diminish strong modulation at the pulsar spin period. A possible 10^5 population is not inconsistent with the minimum number of distinct GRB sources discussed in Sect. 1. A GRB spectrum resembling that of Vela is suggested by Fig. 1. A key feature of a Vela-like model is that the main source for L_γ is the outer magnetosphere, far enough from the stellar surface that reprocessing of γ-rays into X-rays by stellar surface γ-ray absorption does not give an (unobserved) $L_x/L_\gamma > 3 \times 10^{-2}$. A standard candle for energetic radiation up to 1 MeV of $L_{x,\gamma} \sim 10^{36}$erg s^{-1} suggested by Eq. (2) is compared to observed GRB time integrated fluences in Fig. 6. These data do not conflict with the possibility that most GRB's are temporarily reignited Velas.

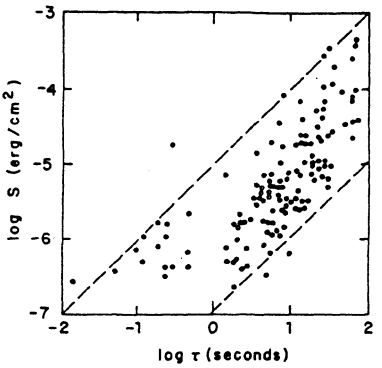

Figure 6. Gamma-Ray Burst fluence S (time integrated intensity) as a function of burst duration time from Konus experiment data (Mazets *et al.* 1981) which measured mainly X-rays of energy < 1 MeV. The two diagonals give the fluence of 10^{36}erg s^{-1} sources at 10^{-2} and 10^3 light year distances (after Liang and Petrosian 1986).

Among many claimed but controversial GRB spectral features is an occasional (10^{-1} of GRB's) bump at photon energies near 450 KeV which contains over 10^{-2} of $L_{\gamma,x}$. If this feature is interpreted as a 510 KeV γ-ray from $e^+ + e \rightarrow \gamma + \gamma$ gravitationally red-shifted on escaping from the neutron star surface, a 10^{36}erg s^{-1} GRB source must put about $10^{40}\, e^{\pm}$s^{-1} onto the stellar surface. According to CHR II the Vela pulsar should be creating $e^{\pm}$ pairs at the rate $\dot{N}_{\pm} \sim 10^{36}$s^{-1} and the Crab pulsar at a rate $\sim 10^{39}$s^{-1} mainly from crossed beam $\gamma + \gamma \rightarrow e^- + e^+$ in their outer magnetospheres (CHR II p. 536). A similar estimate for reignited latent Vela-like pulsars with L_γ of Eq. (4.2) gives $\dot{N}_{\pm} \sim 10^{40}$s^{-1}. Those $e^{\pm}$ pairs which are created moving out of the magnetosphere along open field lines will escape. A comparable flux will be created moving inward along converging field lines. Most of these may be reflected and also escape. Some can synchrotron radiate rapidly enough to avoid such reflection and reach the neutron star surface where $e^{\pm}$ will annihilate with emission of a γ-ray pair. An unknown fraction would be created on closed field lines on which all e^+ would suffer the same fate. If, in either of the above ways, a substantial fraction of $\dot{N}_{\pm}$ reach the stellar surface, red-shifted e^+ annihilation γ-rays with the claimed observed intensity would be emitted.

8. Possible Matches for Reigniting Latent Post-Vela Gamma-ray Pulsars

The first observations of GRB's were very quickly followed by a large number of suggested models in which neutron stars were the sources. Examples (e.g. see Taam 1987) included neutron stars in binaries with occasional nuclear explosions of accreted material or accretion instabilities. Models with solitary neutron star sources involked cometary or asteroidal impacts, internal structure readjustments, surface magnetic field reconnection and flares, and explosions from interstellar matter accretion. A scaled down version of any of these could serve simply as a "match" which injects enough soft X-rays or plasma into the partially charge depleted outer magnetosphere of a latent γ-ray pulsar to reignite, temporarily, outer magnetosphere $e^{\pm}$ production and the γ-ray/X-ray emission associated with it. The match need supply only a modest power, just enough to support closing of the outer magnetospheric current circuit where it was opened by a charge deficient void, and allow the former pulsar to radiate again at nearly its full spin-down power.

Quasiperiodic surface explosions of accreted interstellar matter may be the most plausible match candidate for igniting a solitary latent γ-ray pulsar. That accretion mass flow down onto the stellar polar cap should, however, not continually spin-down the neutron star prior to the transient explosion. It has been estimated (RC) that a polar cap X-ray burst from runaway nuclear burning of accreted interstellar matter may be repeated at intervals of order 10^2 yrs. The relatively weak match with $\hat{L}_x \sim 10^{34}$erg s^{-1} could stay lit for up to 10^2 s. and supply enough soft X-rays to keep a latent outer gap active with an $L_\gamma \sim 10^2 \hat{L}_x$.

9. Evolution in a Millisecond Gamma-ray Pulsar Family

The magnetospheres of low magnetic field millisecond pulsars are qualitatively similar to the outer magnetosphere of Vela. the maximum potential drop from charge depletion which can be realized along $\vec{B}$ and the maximum current flow are both proportional to $B_s P^{-2}$; the maximum luminosity $L \propto B_s^2 P^{-4}$. The position of the spectral break in the γ-ray/X-ray spectrum is proportional to $B_s^{-3} P^7$. These quantities are compared for Vela and the millisecond pulsar PSR 1937 in Table 1. The γ-ray luminosity of the millisecond pulsar is expected to be much less than that from Vela despite the similarity in total spin-down power (CHRII p. 529). The millisecond pulsars may be expected to contain the same two subfamilies as those of the Vela-like pulsars of Sect. 6, one of which "soon" aligns. That millisecond pulsar family may also go through an evolution which passes through Cos B sources and ends as GRB sources. However, with the same spin-down power as a Vela-like pulsar the millisecond pulsar will stretch the duration of the Cos B evolutionary phase by the ratio of its spin energy to that of Vela, $(9 \times 10^{-2}/1.5 \times 10^{-3})^2 \sim 4 \times 10^3$. Therefore the formation rate of millisecond pulsars need be only 3×10^{-4} that of Vela-like pulsars for them to be a significant part of, and perhaps even most of, the Cos B sources. Such a birthrate does not conflict with the observed population of millisecond radiopulsars. If millisecond pulsars are almost 10^{-1} of all radiopulsars (Taylor 1987) and each survives as a radiopulsar for $10^8 - 10^{10}$ years, then they could constitute $10^{-2} - 10^{-4}$ of all neutron stars. If their aligned latent millisecond pulsar cousins are similarly abundant they would have a birthrate $10^{02} - 10^{-4}$ that of Vela-like pulsars and evolve into $10^4 - 10^6$ potential GRB sources.

	ΔV_{max} (volts)	J_{max} (amps)	Spectral break (MeV)
Vela	5×10^{15}	2×10^{14}	1
PSR 1937	2×10^{15}	1×10^{14}	0.1

Table 1. The maximum potential drop (ΔV_{max}), current (J_{max}), and spectral break energy in the outermagnetosphere of the Vela pulsar and those obtained by scaling them to the millisecond pulsar PSR 1937 as discussed in Sect. 9.

10. Accelerator Gaps Around Neutron Stars with Accretion Disks

The model outer magnetosphere accelerator gaps and the γ-rays they power are a consequence of the inability of the neutron star's distant environment to corotate with its magnetosphere. For a solitary star this environment is the universe beyond its light cylinder. For a neutron star connected by its magnetic field to an accretion disk whose inner regions rotate more rapidly than the star similar gaps can exist. An example of such a gap is sketched in Fig. 7. Parts of the neutron star magnetosphere directly connected to it corotate with the star. These parts of the magnetosphere directly connected to the differentially rotating disk (with inner angular frequencies $\Omega_d > \Omega_*$) corotate with that part of the disk to which they are connected. Separating these two parts of the magnetosphere and enclosing the "null surface" cone on which $\vec{\Omega} \cdot \vec{B} = 0$ is an empty gap. Everywhere above (below) that surface in the magnetosphere there are only positive ions (electrons) on which the total force ($\vec{F}$) from electric field, gravitational pull, and centrifugal acceleration satisfies $\vec{F} \cdot \vec{B} = 0$. The potential drop across the gap from 3 to 4 in Fig. 7 is

$$\Delta V_{34} = \int_1^2 [\Omega_d(r) - \Omega^*] \, r dr/c \tag{3}$$

which can be comparable to that achieved from the Crab and Vela pulsar outer magnetosphere gaps. The kinds of radiation which come from the disk-star gaps are, however, very different from those discussed earlier because these gaps are usually imbedded in an intense flux of accretion powered X-rays. Details will be given elsewhere (Cheng and Ruderman 1988).

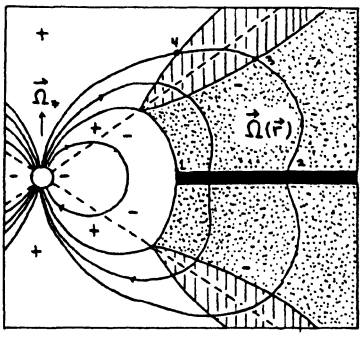

Figure 7. Charge separated magnetosphere structure around a spinning neutron star with an aligned magnetic moment and accretion disk. The disk is presumed to rotate more rapidly (at least near its inner edge) than the star. The dashed line designates the "null surface" on which $\vec{\Omega} \cdot \vec{B} = 0$. Above (below) it all magnetosphere charge is +(−). The white areas corotate with the star with angular frequency $\vec{\Omega}_*$. In the dotted area negative charge corotates with that part of the disk to which it is connected by $\vec{B}$. The vertical striped area is empty "gap" in which charged particles can be accelerated along $\vec{B}$. Where the magnetosphere charge density does not vanish all forces on it are perpendicular to $\vec{B}$.

This research was supported in part by NSF grant AST-86-02381

References

Arons, J. and Scharlemann, E. 1979, *Ap.J*, **231**, 854.

Bignami, G. 1987 in *High Energy Phenomena around Collapsed Stars*, F. Pacini, ed. NATO ASI; Cargese 1985 (Reidel).

Blair, D. and Candy, B. 1987 in 13^{th} *Texas Symposium on Relativistic Astrophysics – 1986*, ed. M. Ulmer (Singapore: World Scientific).

Blair, D. 1989, these proceedings.

Cheng, K.S. and Ruderman, M. 1988, "Particle Accelerators Around Accreting Neutron Stars" to be published.

Cheng, K., Ho, C., and Ruderman M. 1986a *Ap.J*, **300**, 495 (CHR I).

Cheng, K., Ho, C., and Ruderman, M. 1986b *Ap.J.*, **300**, 522 (CHR II).

Davis, L. and Goldstein, M., 1970 *Ap. J.*, **5**, 21.

Dowthwaite *et al.* 1984 *Ap.J.*, **286**, L35.

Epstein, R, 1988, "Gamma Ray Bursts and Glitching Neutron Stars," in *Physics Reports*, in press.

Goldreich, P. 1970 *Ap.J.*, **160**, L11.

de Jager, O. 1989, these porceedings.

Jones, P. 1986 *M.N.R.A.S.*, **222**, 577.

Jones, P. 1987, Oxford preprint.

Kennel, C. and Coroniti, F. 1984 *Ap.J.*, **283**, 710.

Kluzniak, W., Ruderman, M., Shaham, J. and Tavani, M. 1988 "Low Energy Galactic Center Gamma Rays from Low Mass X-ray Binaries," submitted to *Nature*.

Paczinski, B. and Gordon 1987, *Ap.J. (Letters)*.

Krause-Polstorff, J. and Michel, F.C. 1985a *M.N.R.A.S.*, **144**, 72.

Krause-Polstorff, J. and Michel, F.C. 1985b *M.N.R.A.S.*, **213**, 43.

Liang, E. and Petrosian, V. 1986, eds. *Gamma Ray Bursts*, AIP Conf. Proc. 141.

Mazets, E., and Golenetskii, S. 1981, *Astrophys. and Space Phys. Rev*, **1**, 205.

Michel, F.C. and Goldwire, H. 1970, *Ap.J.*, **5**, L21.

Reigler, G., Ling, J., Mahoney, W., Wheaton, W., and Jacobson, A. 1985 *Ap.J.*, **294**, L13.

Ruderman, M., and Cheng, K.S. 1988, "Evolution of A Short Period Gamma-Ray Pulsar Family: Crab, Vela, Cos B Source, Gamma-Ray Burst Source," *Ap.J.*, in press.

Ruderman, M. 1987a in 13^{th} *Texas Symposium on Relativistic Astrophysics – 1986*, ed. M. Ulmer, p. 448, (Singapore: World Scientific).

Ruderman, M. 1987b in *High Energy Phenomena Around Collapsed Stars; Cargese 1985*, ed. F. Pacini, p. 145 (Dordrecht: Reidel).

Share, G., Matz, S., Messina, D., Nolan, P., Chupp, E., Forrest, D., and Cooper, J., 1986 preprint.

Taam, R. 1987 in 13^{th} *Texas Symposium on Relativistic Astrophysics – 1986*, ed. M. Ulmer, p. 546 (Singapore: World Scientific).

Taylor, J., 1987 in 13^{th} *Texas Symposium on Relativistic Astrophysics – 1986*, ed. M. Ulmer, p. 546 (Singapore: World Scientific).

Turver, K. 1989, these proceedings.

Balloon observation of the Crab pulsar in the energy range 0.2-6 MeV

B. Agrinier (1), E.Costa (3), G.Gerardi (4,7), C.Gouiffes (1), P. Mandrou (2), J.L. Masnou (5), E. Massaro (6), T. Mineo (4), M. Niel (2), B. Sacco (4), M. Salvati (8), L.Scarsi (4).

(1) Service d' Astrophysique, CEN Saclay, France
(2) CESR, Université P. Sabatier, Toulouse, France
(3) Istituto di Astrofisica Spaziale, CNR-Frascati, Italy
(4) Istituto di Fisica Cosmica ed Applicazioni dell'Informatica, CNR-Palermo, Italy
(5) Observatoire de Paris, Meudon, France
(6) Istituto Astronomico, Università "La Sapienza", Roma, Italy
(7) Istituto di Fisica, Università Palermo, Italy
(8) Osservatorio Astronomico di Arcetri, Firenze, Italy

Abstract

The paper presents the results of an observation of the PSR0531+21 in the low energy gamma ray range, made on 11th July 1986, during the balloon flight of the F. I. GA. R. O. experiment.
The pulsar light curves in two energy bands are shown and a comparison with others in different energy ranges is made.
The phase-averaged spectrum between 0.2 and 6 MeV is found to be compatible with a power law of spectral index 2.2.

Introduction

The Crab pulsar (PSR0531+21) is one of the most extensively studied sources from radio frequencies to gamma rays. There are, however, only few data in the low energy gamma ray range because of the rather poor value of the signal to noise ratio usually obtainable in normal experimental conditions.
In the present work we briefly describe the results of an observation in the energy range 0.2 - 6 MeV of the Crab pulsar carried out on July 11th 86 with the F. I. GA. R. O. (French Italian GAmma Ray Observatory) balloon borne experiment. This is a wide field detector (Agnetta et al. 85) specifically designed to observe sources with a well established time signature, like pulsars. It is composed of nine modules of NaI crystal scintillator with a total geometric area of 3600 cm^2, and a thickness of 5 cm. The effective area is equal to the geometrical one up to 0.3 MeV and

H. Ögelman and E. P. J. van den Heuvel (eds.), Timing Neutron Stars, 343–346.

goes down to 2000 cm^2 at 4 MeV; the energy resolution is 16% at 0.6 MeV and the time resolution is 20 μs. The gain control is implemented by a tagged source (Na^{22}) at 0.511 MeV.

The principal detector is shielded from the environmental background by twelve NaI modules around the sides and by four blocks of plastic scintillator on the bottom. Charged particles coming from the top are anticoincided by a thin plastic scintillator blanket (0.5 cm) covering the experiment. In order to reduce furtherly the high energy background, each module of the principal detector is in anticoincidence with each one of its neighbours.

The observation of the Crab pulsar was made during a trans-mediterranean balloon flight at an altitude corresponding to a residual atmosphere of 4 mbar . The average count rate at the ceiling was about 1350 counts/sec., implying a telemetry dead time of 10%. The duration of the observation was about three hours.

The PSR0531+21 light curve

In order to compute the Crab light curve the photon arrival times were reduced to the Solar system barycentre and then folded with the pulsar's period, taking also into account the variation due to its first derivative; the pulsar ephemeris has been kindly provided by A.G. Lyne (Jodrell Bank) . The resulting phase values were binned in the 50 channels histogram showed in fig.1a.

The well known double peak structure is here clearly evident with the second peak at a separation of 0.39 from the first one. Moreover the light curve shows unexpected features at phases 0.2, 0.45 and 0.58, each one with a statistical significance of about 3 standard deviations. The first one is mainly apparent above 0.42 MeV (fig. 1c), while the two others are visible over the full energy range (fig. 1b,1c).

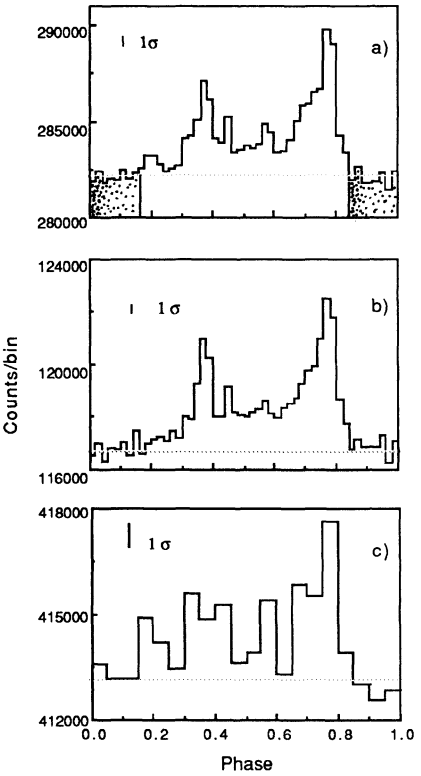

Figure 1. Crab light curve: a) 0.2 - 6 MeV, b) 0.2 - 0.42 MeV, c) 0.42 - 6 MeV.

A comparison of our light curve with some others in different energy ranges is shown in fig .2. The first peak is dominant over the second one from the optical frequencies up to the soft X rays (fig. 2a,b). Above 20 keV this picture changes and the relative importance of the two peaks is inverted. Such effect, well evident in the hard X-ray energy range (fig. 2c), is definitively confirmed in our experiment (fig. 2d). The peak ratio inverts again at higher energies as shown in fig. 2e by the COS-B results at E>50 MeV, where the first peak is again the dominant feature.

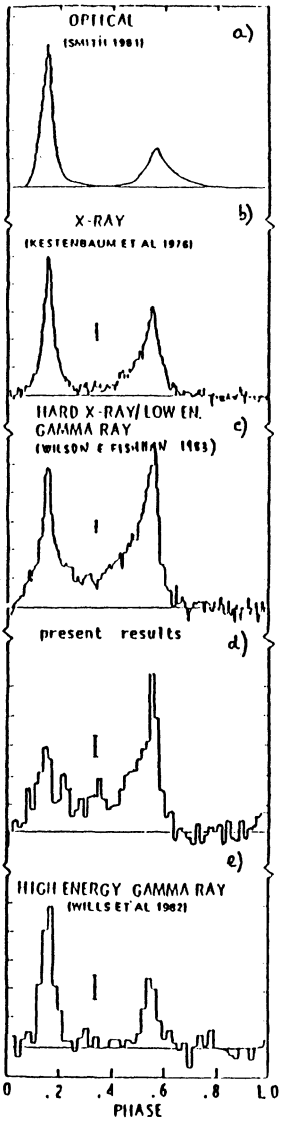

Figure 2. Crab light curves relative to different energy ranges: a) 2.1 - 4.1 eV; b) 0.6 - 23 keV; c) 45 - 360 keV; d) 0.2 - 6 MeV; e) 50 -3000 MeV.

The spectrum.

The background phase region was defined as the largest phase interval where the counts can be fitted with a constant. This corresponds to the intervals [0 - 0.15] and [0.85 - 1] (see fig. 1a). The background counts, weighted for the relative phase width, was subtracted from the "on pulse" counts corresponding to phases from 0.15 to 0.85, and the raw spectrum was fitted with a power law in energy convolved with the response matrix of the instrument including the atmospheric absorption. The best fitting spectrum was:

$$N(E) = No * (E)^{-\alpha}$$

where:

$No = (6.39 \pm 0.25) * 10^{-4}$ ph. $cm^{-2}\ s^{-1} MeV^{-1}$

$\alpha = 2.24 \pm 0.20$

in a good agreement with that in the energy range 50-500 keV, given by Mahoney et al. (84).

A preliminary analysis of the dependence of the spectral index on the phase indicates that the spectrum does not flatten from the first to the second peak, at variance with the results of Knight (82) and Hasinger (82),

that give an interpeak's spectrum between 0.02 and 0.2 MeV harder than those of the two peaks. This difference in the spectral shape of the interpeak component with respect to the peaks suggests that these emissions are not originating from the same region of the magnetosphere, or that are not due to the same physical process.

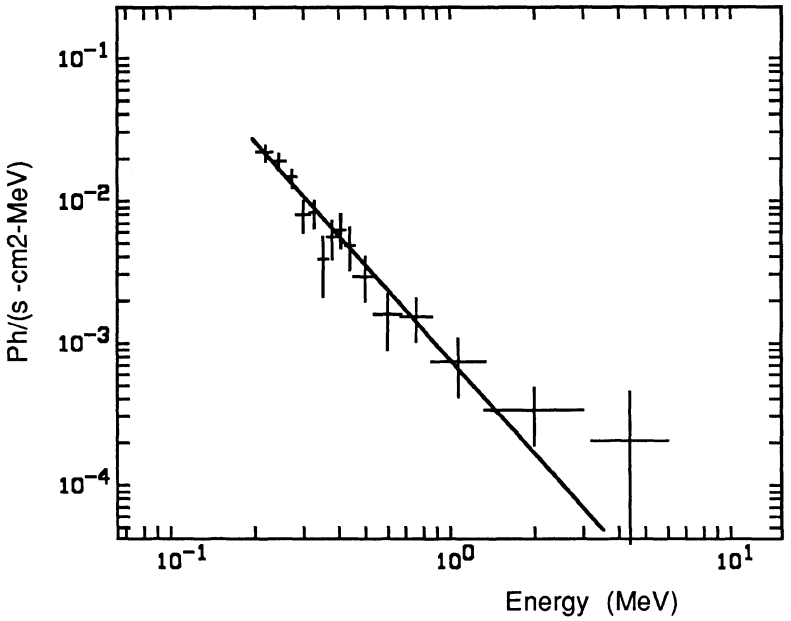

Figure 3: Crab pulsar spectrum in the energy range 0.2-6 MeV.

We thank A.G. Lyne and R.S. Pritchard who provided to us at the time of the flight the up to date Jodrell Bank Crab pulsar timing radio results.

References

Agnetta G. et al. Proc. of 19th Int. Cosmic Ray Conf. ,La Jolla, USA, august 11-23,1985.

Graser U. and Shonfelder V. , 1982, Ap. J., **263**, 677.

Hasinger G. et al. Proc in Accreting Neutron Stars, Brinkman and Trumper (eds.), Garching: MPE-177, 1982

Kestenbaum H.L., Ku W., Novick R. and Wolff R.S., 1976, Ap. J. (Letters), **203**, L57.

Knight, F.K. , Ap. J., 1982, **260**, 538

Mahoney W. A., Ling J.C.and Jacobson A.S., Ap.J., 1984, **278**,784

Smith F.G., 1981, in IAU Symposium 95,Pulsar, ed. W. Sieber and R. Wielebinski (Dordrecht: Reidel), 221.

Wills R.D. et al. 1982, Nature , **296**, 723.

Wilson R.B. and Fishman G.J. Ap. J. ,1983, **269**, 273.

PRODUCTION SITES AND MECHANISMS OF DISCRETE GAMMA-RAY COMPONENTS OF THE VELA AND CRAB LIGHT CURVES

W. HERMSEN[1], I.A. GRENIER[2,3]
[1] *Laboratory for Space Research Leiden, P.O. Box 9504, 2300 RA Leiden, The Netherlands*
[2] *Service d'Astrophysique, Centre d'Etude Nucleaires de Saclay, France*
[3] *Centre d'Etude Spatiale des Rayonnements, Toulouse, France*

ABSTRACT. New results on the temporal and spectral characteristics of the high-energy (50 MeV to 5 GeV) gamma-ray emission from the Vela pulsar have become available from an new analysis of COS-B data. The total pulsed flux is found to exhibit long-term variability. Five discrete emission regions within the pulsar lightcurve have been identified, with the spectral characteristics and long-term behaviour being different. These characteristics differ significantly from those reported earlier for the gamma-ray emission from the Crab pulsar. The identification of the different components in the Vela gamma-ray lightcurve and different components, noted earlier, in the Crab X-ray lightcurve supports the idea that several source regions exist in different parts of the pulsars magnetospheres. The different spectral characteristics of these components indicate that different generating processes exist in each source. Geometrical pulsar models have been proposed (e.g. Morini *et al.*. 1983; Smith *et al.*1986) which could explain many of these features.

1. Introduction

The only radio pulsars detected in high-energy gamma-rays so far are the young pulsars Crab and Vela. Recently, Clear *et al.*(1987) presented detailed results on the Crab pulsar using the final COS-B database; now also detailed results are available for the Vela pulsar (Grenier *et al.*1988). Prior to these new results, the experimental status on the latter can be summarized as follows: Tümer *et al.*(1984) at 0.3–30 MeV, Thompson *et al.*(1977) above 35 MeV and Bennett *et al.*(1977) at 50 MeV – 5 GeV all report a similar Vela lightcurve structure which is characterised by two sharp peaks separated by 0.42 in phase and bracketing the optical pulses. An extrapolation to X-ray energies of the COS-B spectrum of Kanbach *et al.*(1980) lies several orders of magnitide above the reported upper limits, while at TeV energies the flux values reported by Bhat *et al.*(1980) clearly require a break in the spectrum. Earlier results from COS-B data by Bennett *et al.*(1977) and Kanbach et al. (1980) indicate a possible break in the spectrum at a few hundred MeV, but the level of significance of these results is low. The next section summarizes the latest results on the Vela pulsar in the 50 MeV to 5 GeV energy range (Grenier *et al.*1988). In section 3 gamma-ray, hard-X-ray (Hasinger 1984) and some radio characteristics of the Vela and Crab pulsars are compared, followed in section 4 by a discussion of the implications for some pulsar models.

H. Ögelman and E. P. J. van den Heuvel (eds.), Timing Neutron Stars, 347–356.

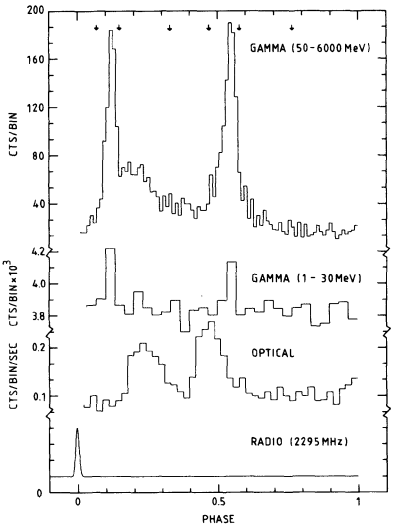

Table I. Intervals of the Vela lightcurve.

Region	Phase interval
Peak 1	0.07 - 0.15
Interpulse-1	0.15 - 0.33
Interpulse-2	0.33 - 0.47
Peak 2	0.47 - 0.58
Trailer	0.58 - 0.77
Background	0.77 - 0.07

Figure 1. The lightcurve from PSR 0833-45 at radio (Buccheri *et al.*1978), optical (Manchester *et al.*1980), soft energy gamma-rays (Tümer *et al.*1984) and high energy gamma-rays (final COS-B). The arrows indicate the position of the selected phase boundaries.

2. Temporal and Spectral Characteristics of the Vela Gamma-ray Pulsar

Grenier *et al.*(1988) analysed all final data on the Vela pulsar collected with the COS-B satellite, which had Vela within its field-of-view during 10 observation periods between October 1975 and June 1981. The total COS-B gamma-ray lightcurve together with the radio and optical ones are given in Figure 1. Part of the analysis was concerned with the characteristics of the total pulsed emission, and in part the temporal and spectral characteristics of separate phase intervals of the lightcurve (see Figure 1 and Table I) were studied in detail, exploiting the good exposure obtained during 5 of the observation periods. The findings by Grenier, Hermsen and Clear will be summarized in this section, for details on the method and the statistical calculations the readers are referred to the full paper.

2.1 *Steady Emission.* The background region of the lightcurve has been analysed for possible steady emission from Vela above the diffuse galactic emission. For the total energy range 50 MeV–5 GeV no evidence was found for steady emission from Vela; the 95 % confidence upper limit is 1.15 x 10^{-6} photons/cm^2 s.

2.2 *Spectrum total pulsed flux.* The spectrum of the whole emission derived independently at energies above and below 300 MeV and using all observations is:

$$F(50\ \text{MeV} \leq E \leq 300\ \text{MeV}) = (2.74 \pm 0.21)10^{-4} E_{\text{MeV}}^{-1.72\pm0.07} \text{ph cm}^{-2}\text{s}^{-1}\text{MeV}^{-1}$$

$$F(300\ \text{MeV} \leq E \leq 5000\ \text{MeV}) = (2.71 \pm 0.04)10^{-3} E_{\text{MeV}}^{-2.12\pm0.07} \text{ph cm}^{-2}\text{s}^{-1}\text{MeV}^{-1}$$

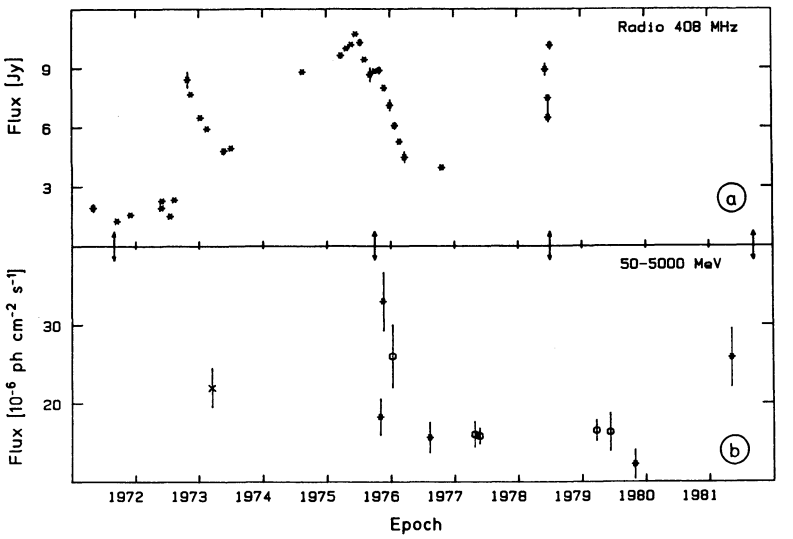

Figure 2. Comparison between the evolution of the radio flux (a) at 408 MHz (McAdam, 1981) and the high energy gamma ray flux (b) for the Vela pulsar. Gamma-ray data points:* COS-B likelihood analysis; o COS-B "saturation method"; × SAS-2 (Thompson *et al.*1977). The epochs of the pulsar glitches are indicated.

The significant difference between the high and low energy spectral indices clearly shows that the time averaged Vela pulsed spectrum from 50 to 5000 MeV cannot be described by a single power law. At least two are required and in this representation the good connection between the two spectra at 300 MeV strongly supports the choice of 300 MeV as the energy of the break.

2.3 *Long-term variability total pulsed flux.* Figure 2b presents the evidence for a striking long-term variability of the Vela gamma-ray flux. To study the energy dependence of this variability, the evolution of the pulsed flux for the energy ranges 50–300 MeV and 300–5000 MeV have been evaluated. The main contribution to the flux variability is clearly due to the low energy emission. The different evolutions of the flux from the two energy ranges denote a distortion of the Vela spectrum from one epoch to the next. The observed fluctuation in the spectral ratios (the ratio of low to high energy flux) has a probability of 10^{-10} of being due to a random effect.

2.4 *Spectra for different phase intervals.* Figure 3a shows the time averaged spectral index as a function of phase. The probability that the emission may be best represented by a homogeneous spectrum over all phases is 10^{-4}. Analysis of the spectral characteristics of the high energy emission (E>300 MeV) shows that there is no significant variation in its spectral index with phase, giving a phase averaged value of 2.12 ± 0.07. In contrast, the spectral index of the low energy emission shows evidence for phase dependence (chance probability 5 10^{-3}). It was concluded from the change in the spectral index at low energies (from the first peak to interpulse-2, 4.5σ, and interpulse-2 to the second peak, 3.6σ and

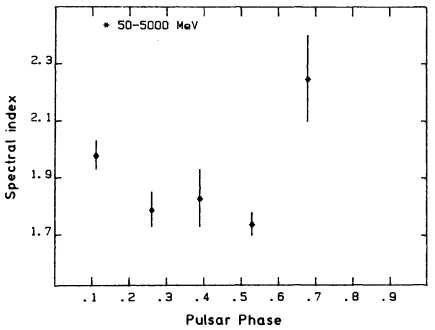

Figure 3. Time-averaged pulsed spectral index as a function of phase for a one-power-law fit over total energy range.

from the softness of the first peak and trailer over the entire energy range, that 5 separate phase components exist in the Vela gamma-ray lightcurve.

2.5 *Flux variability for separate phase components.* The evolution of the flux from each of the phase components for each observation and for both high and low energy ranges had also been studied. The long-term variability is obvious and the relative amplitude of the variability is significantly larger for the two interpulse emissions. Furthermore, the flux variations in the separate energy intervals are different resulting in spectral distortions (probability levels are given in Grenier *et al.*1988). To illustrate their long term evolution, the energy spectra giving the maximum likelihood fits to the data for each observation are displayed in Figure 4. Good agreement is observed between the low and high energy fits at approximately 300 MeV for most phase components. The two power law representation is therefore a good approximation to the real spectra (for the trailer, the poor statistics make interpretation of the results rather difficult). The actual position of the break or bend in the real spectrum will vary somewhat in energy following the apparent long term variability.

2.6 *Total PSR0833-45 Spectrum.* The two-power-law fit time-averaged spectrum of the whole pulsed emission has been plotted in Figure 5 together with the data recorded at other wavelengths in order to show the full energy distribution of the Vela pulsed radiation over the entire electromagnetic spectrum. Over this spectrum, the pulsar reaches its maximum luminosity in the MeV–GeV domain.

2.7 *Long-term time variabilty of PSR0833-45; Gamma vs. radio.* The flux evaluation presented in Figure 2b demonstrates the gamma-ray variability of the pulsar over several years. A large discontinuity in the pulsar rotational parameters, a so-called glitch, occurred sometime between September 25 and October 15, indicated in Figure 2 (Manchester *et al.*1976), while the COS-B gamma-ray observations started on October 20. This could indicate a relation between the gamma-ray flux with an exponential risetime of $\sim$ 11 days and decay time of $\sim$ 140 days, and the glitch event. However, the recurrence of such a phenomenon may be questioned. A further glitch occurred in July 1978 (Downs *et al.*1978) when no COS-B data were taken from the source (see Figure 2). According to the time

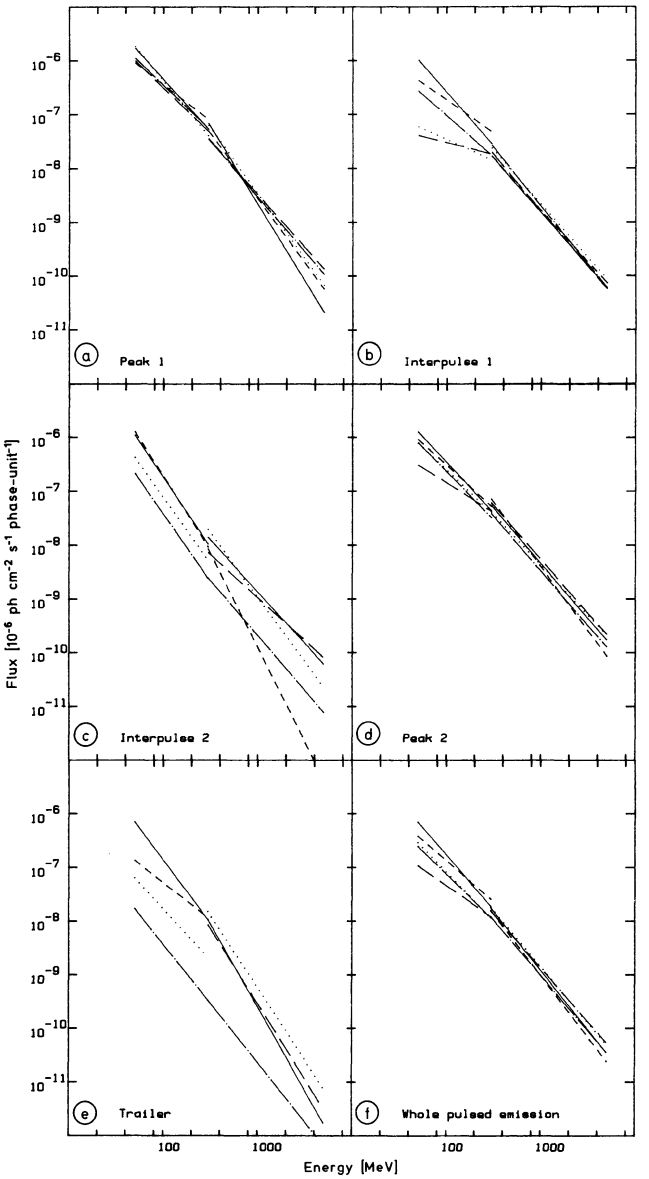

Figure 4. Differential pulsed gamma-ray spectra (50–5000 MeV) from Vela for 5 phase intervals and the total phase averaged emission. The power law spectra giving the maximum likelihood fits are shown for the 50–300 MeV and 300–5000 MeV energy ranges, respectively, for each observation; period 2 ....., period 3 —, period 12–.–.–, period 45 – –, period 59 - - - .

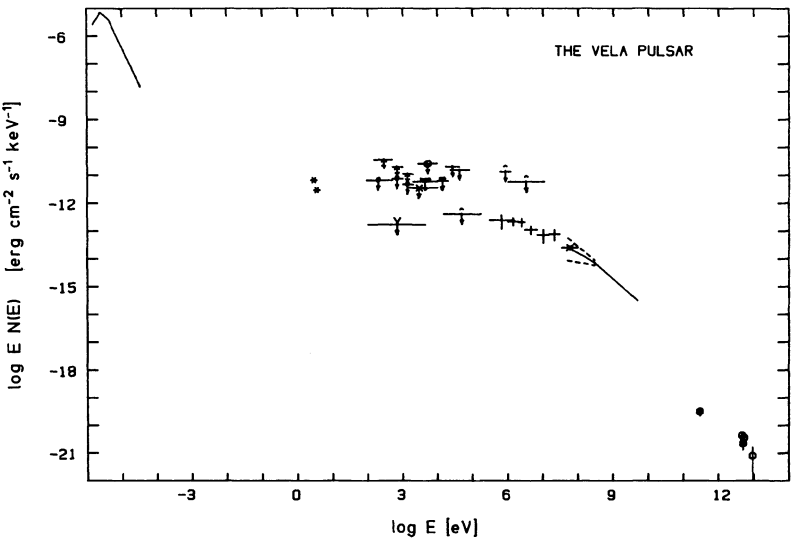

Figure 5. Total energy spectrum from the radio up to the very high energy gamma-ray domain. The upper limits (3σ) displayed in the X-ray range are calculated for an assumed duty cycle of 0.2 similar to the optical one. The broken lines indicate the extremities in the variabilities measured by COS-B between 50 and 300 MeV. For references on the data points see Grenier *et al.*(1988).

scales quoted above, a coincident gamma-ray flux increase could have happened without being noticed in later COS-B observations. What is surprising, is the high gamma-ray flux recorded in April and May 1981 when no glitch was reported. Such an event occurred five months later, in October 1981 (Gorenstein *et al.*1981), when Vela was not in the field-of-view. Thus, the gamma-ray enhancement is recurrent but it does not necessarily follow a glitch event. For this reason, it is not possible to draw any firm conclusion from the COS-B data on the relationship between the gamma-ray variability and the glitch phenomenon.

The Vela pulsed radio flux is not stable either. As shown in Figure 2a, three large irregularities were recorded at 408 MHz between 1971 and August 1978 when the observations at the Molonglo Observatory were stopped (McAdam, 1981). These secular changes could not be explained by the interstellar scintillation, nor do they appear to be related to the glitches. Their rather regular aspect over the years suggested that such fluctuations are caused by a precession in the beam angle with respect to our line of sight (McAdam, 1981). Despite the minimal overlap of the radio and the gamma-ray data, one could conclude that the two variation patterns are not strongly correlated. Therefore, the precession effect proposed for the radio evolution is not supported by the gamma-ray data, since in this case it would not explain the stability of the first peak while the other phase components all vary. No other clues to the origin of the long-term variability can be found from the pulsed emission at other wavelengths. In the optical band, the 24th magnitude Vela object is too faint to provide so far precise information on possible apparent magnitude changes.

3. Crab versus Vela Characteristics

The detailed gamma-ray results on the Vela pulsar, presented in the previous section, can be compared with the COS-B results from a detailed analysis of the high-energy gamma-ray emission from the Crab pulsar (Clear *et al.*1987). First, it is reminded, that the Crab pulsar is the only pulsar seen to emit pulsed radiation over a range of $\sim$ 20 decades in frequency, while the Vela pulsar is only detected in the radio, optical and gamma-ray domain. Futhermore, it was found that the Crab pulsar reaches its maximum luminosity in the hard X-ray range till soft gamma-ray range, while the Vela pulsar reaches its maximum luminosity in the few-hundred-MeV range. The relatively low X-ray emissivity of the Vela pulsar is in clear contrast to that of the Crab pulsar. In the high-energy gamma-ray domain (50 MeV to about 5 GeV) the spectrum of the Crab pulsar emission can be represented by a single power law of index 2.00 ± 0.10 and no systematic variations of spectral index with pulsar phase have been noted (three components in the Crab light curve were compared: first peak, interregion and second peak). However, at the neighbouring hard X-ray energies (some tens of keV up to $\sim$1 MeV) the situation is different: the spectral index varies with phase such that the softest spectrum is found for the first peak and the hardest spectrum for the interregion (Knight, 1982; Hasinger 1984). The differences with the spectrum of the Vela pulsar emission are evident: the Vela gamma-ray spectrum cannot be represented by a single power law and the spectrum varies significantly with pulsar phase, while X-rays have not been detected.

The striking similarity between the appearances of the two gamma-ray lightcurves, both dominated by two peaks separated in phase by about 0.42, holds only for the gamma-ray range. The Vela lightcurves have been shown in Figure 1; in the case of the Crab the two peaks in the lightcurves in the optical, X-ray and gamma-ray (up to a few GeV) domains are coincident to within the timing errors, and coincide with the main radio pulse and interpulse. In the latter domain below 1 GHz there is also a separate component, known as the 'precursor' (Rankin et al. 1970); this is similar in shape, spectrum and polarization to the radio pulse of Vela. However, the Crab and Vela gamma-ray lightcurves differ in detail. Particularly, the appearance of the structure in the interregion is different. In the case of Vela, the interpulse-1 emission which is roughly coincident in phase with the first optical peak, shows up as a significant structure in the total interregion. For the total Crab lightcurve the statistics are insufficient to reach a conclusion on possible structure in the gamma-ray interregion emission. But, at hard X-ray energies the enhanced interpulse emission can be attributed to extended wings of the two pulses (Hasinger *et al.*1984). Furthermore, the relative contributions of the Crab interpulse emission and the second pulse reach a maximum in the hard X-ray range: the ratio of pulse-2 plus interregion emission over pulse-1 emission, (P2+I)/P1, increases from 0.5 in the optical domain, $\sim$1 at 1 keV up to $\sim$3 at 100 keV - 1 MeV, (Hasinger 1984, 1985), after which the ratio decreases sharply at the soft gamma-rays and COS-B energies to an average of $\sim$0.7 (Clear *et al.*1987).

Finally in Chapter 2 strong flux and spectral long-term variability of the Vela gamma-ray emission was evidenced; in the case of the Crab long-term variability has been noted, at a 3σ significance level, and the flux ratio (P2+I)/P1 varied roughly between 0.5 and 1.2 (3σ), (Clear *et al.*1987). At hard X-ray energies the Crab lightcurve shape appeared to be stable so far (e.g. Hasinger *et al.*1984). Particularly remarkable is the strong variability in the Vela interpulse emission. Furthermore, the Vela pulsar showed long-term variability in its

radio emission. Other radio pulsars have proved to be variable sources as well, but usually on a much shorter time-scale. In the Crab case, after a continuous weakening of the 74 MHz pulsed emission was observed between 1971 and 1975, its radio flux remained steady over the next six years (Rickett and Seiradakis, 1982), as did its optical and X-ray flux (Knight, 1982). Hence, in the long-term, the Vela and Crab pulsars do behave differently and the large variability observed from Vela, both in radio and gamma-rays, looks unusual compared to the measured behaviour of all other pulsars.

4. Implications for some Pulsar Models.

Various models have been proposed to explain how pulsed radiation can be produced at different wavelenghts within a pulsar magnetosphere. Many agree on the existence of accelerating regions called "gaps", which arise from a local charge depletion and provide the primary population of ultra relativistic particles streaming along the magnetic field lines. However, the models disagree on the location of the active regions (e.g. polar gaps, outer gaps etc.), on the type of physical processes and on the sequences of processes which convert primary particles into pulsed radiation. In Grenier *et al.*(1988) the implications of the new Vela results on some models for the Vela pulsar are discussed; here the discussion is limited to the outer-gap model of Cheng *et al.*(1986) and to a geometrical model which has been evaluated by Morini (1983) for the Vela pulsar and further by Smith (1986) for the Crab and Vela pulsars together.

In the frame-work of the outer gap model of Cheng *et al.*(1986), primary photons and secondary pairs are produced, respectively, by inverse Compton scattering and collisions with a tertiary population of soft synchrotron photons (mainly IR) which illuminate the outer magnestosphere. The predicted pulsed spectrum is in good agreement with the total Vela spectrum. In the gamma-ray domain, the spectral shape agrees with the data of Tümer *et al.*(1984) and with the time averaged COS-B spectrum up to 3 GeV where their model induces a break which is, however, not seen in the COS-B data. Cheng *et al.*argue that their model can reproduce the different gamma-ray and optical phase separations between the peaks; the tertiary optical photons being emitted somewhat closer to the star (about half way) than the secondary gamma-rays. However, with the outer gap model it seems difficult to explain the existence of the two gamma-ray interpulse components. Because of their position, they should also originate from a part of the gap closer to the star then the section responsible for the main peaks. It is then difficult to conceive how the inner part of the same gap may be subject to a significant long term variability while the outer part remains comparatively stable. Furthermore, since in this framework the two main peaks are produced by two symmetrical outer gaps, it is difficult to explain the different spectra. Finally, the spectral shape predicted by the outer gap model is not consistent with that of the two interpulse spectra.

Morini and Smith evaluated a scheme in which the magnetic dipole is assumed to be orthogonal to the rotation axis and the two main gamma-ray pulses are produced in the two sets of the terminal field lines above the same pole and close to the light cylinder. The Vela radio pulse and the Crab precursor are produced at the opposite pole. This scheme assumes that the photons are emitted along the field lines, and shows that the arrival phases of the photons depend on the radii, between the star surface and the light cylinder, at which they are created. They show that the differences in the spectra between

the two Vela gamma-ray peaks may come from the phase reconstruction. Only those photons created near the leading terminal field lines close to the light cylinder contribute to the first peak. On the other hand, "outer" photons from the trailing side may combine with photons from the same field lines deeper in the magnetosphere and also with photons from the polar cap region to produce the second peak with its harder gamma-ray spectrum. Furthermore, the geometrical patern indicates that for Vela the optical pulses are produced in the open magnetosphere above the pole, at a distance which is about half the light cylinder radius, and that the gamma-ray interpulses originate along the same lines at a slightly higher altitude. The mixing in interpulse-2 of photons created well inside the magnetosphere and near the polar cap could again explain the spectral differences with interpulse-1. Morini calculates spectra for the two main peaks, assuming that relativistic particles produce synchro-Compton emission near the light cylinder (for the first peak and part of the second) and gamma-rays near the polar cap by inverse Compton scattering of the thermal X-rays from the hot surface (for the rest of the second peak). These spectra are consistent with the COS-B Vela results, but strongly underestimate the intensity of the second peak for energies below 50 MeV. The synchronisation of the pulses in the Crab lightcurve from the optical to the gamma-ray range indicates that they are all emitted close to the light cylinder along the outer gap (Smith, 1986). Also, the similarity of the gamma-ray spectra of the two peaks, indicates that for the Crab the geometry of the magnetic field lines is somewhat different, excluding a significant contribution in the second peak from regions deeper into the magnetosphere. On the other hand, Hasinger (1984, 1985) uses the same geometrical model to explain the hard X-ray characteristics of the Crab lightcurve components. The total first pulse and part of the second pulse are due to synchrotron radiation, while the interpulse emission and a significant fraction of the second pulse are due to curvature radiation emitted by the particles moving along the curved field lines from the neutron star to the light cylinder. For the Crab, one can assume an average field line curvature of 10^8 cm, and particles with Lorentz factors between 400 and 5×10^6, as derived from the synchrotron radiation, are expected to emit curvature radiation up to $\sim$30 MeV, consistent with the measured enhanced hard X-ray emission in the interpulse and second pulse, and the weaker intensity of the gamma-ray interpulse emission.

The recent study by Caraveo *et al.*(1987) of possible polarisation of the Vela gamma-ray emission using COS-B data, also suggests that the peak and interpulse emissions originate in different parts of the magnetosphere. Their result, if confirmed, indicates a high degree of linear polarisation for the gamma-rays coming from the entire interpulse, while the effect is much weaker for the second peak and not observed in the first peak. In the scheme proposed by Smith, a highly polarised gamma-ray component deep in the open magnetosphere, created from synchrotron radiation or surviving selective absorption processes (Caraveo *et al.*1987), would be consistent with the present observations.

The long-term variability of the Vela gamma-ray lightcurve also implies different source locations for the highly variable interpulse emissions and for the relatively stable main peaks. In the model presented by Smith, the various evolutions observed for the different gamma-ray components in the Vela lightcurve would signify that the region sensitive to the variability is the open magnetosphere in the polar region, while the conditions along the last open field lines in the outer magnetosphere would be more steady. This agrees with the steadiness of the Crab pulsar emission at all wavelengths.

For Vela, the details of the radio pulse profile and polarisation involve a source located close to the star cap (Krishnamohan and Downs, 1983). Therefore, the variability observed

in radio supports the idea that the conditions in the inner magnetosphere may change in the long-term. The same conclusion is reached when considering that the largest contribution to the variability in the gamma-ray domain comes from the low energy part, provided that in the cascade of photons the softer originate from deeper into the magnetosphere.

5. Conclusion

The qualitative discussion of the new aspects of the gamma-ray emission from the Vela pulsar (long-term, phase-dependent flux and spectral variability, and possible phase dependent polarization; Grenier *et al.*1988, Caraveo *et al.*1987, respectively), and of the X-ray emission from the Crab (phase-dependent spectra; Hasinger, 1984) in these geometrical models proposed by Morini and Smith suggests that the origin of the interpulses exists above one of the poles, deep in the magnetosphere or at medium latitudes, with the sources of the peaks lying close to the co-rotating magnetosphere and to the light cylinder. Now the main problem remains: what process at or near the star surface causes these long-term variabilities which apparently lose their significance while propagating further out into magnetosphere.

References

Bennett, K. *et al.*: 1977, *Astron. Astrophys.* **61**, 279.
Bhat, P.N. *et al.*: 1980, *Astron. Astrophys.* **81**, L3.
Buccheri, R. *et al.*: 1978, *Astron. Astrophys.* **69**, 141
Caraveo, P.A., Bignami, G.F., Mitrofanov, I., Vacanti, G.: 1987, *Astrophys. J.*, in press
Cheng, K.S., Ho, C., Ruderman, M.: 1986, *Astrophys. J.* **300**, 522.
Clear, J. *et al.*: 1987, *Astron. Astrophys.* **174**, 85
Downs, G.S., Manchester, R.N., Newton, L.M.: 1978, *IAU Circ.*, 3274
Gorenstein, M.V., Shapiro, I.I., Rogers, A.E.E., Cohen, N.L.: 1981, *IAU Circ.*, 3644
Grenier, I.A., Hermsen, W., Clear, J.: 1988, *Astron. Astrophys*, in press.
Hasinger, G.: 1984, Ph.D. Thesis, Ludwig-Maximilians-Universität, München.
Hasinger, G.: 1985, in *The Crab Nebula and Related Supernova Remnants*, p. 47, ed. Kafatos and Henry, Cambridge Univ. Press.
Hasinger, G. *et al.*: 1984, *Advances in Space Research 3* **Vol 10-11**, 63
Kanbach, G. *et al.*: 1980, *Astron. Astrophys.* **90**, 163
Knight, F.K.: 1982, *Astrophys. J.* **260**, 538
Krishnamohan, S., Downs, G.S.: 1983, *Astrophys. J.* **65**, 372
Manchester, R.N., Goss, W.M., Hamilton, P.A.: 1976, *Nature* **259**, 291
Manchester, R.N. *et al.*: 1980, *Mon. Not. R. Astr. Soc.* **190**, 9P
McAdam, W.B.: 1981, *Proc. Astr. Soc. Austr.* **4**, 219
Morini, M.: 1983, *Mon. Not. R. Astr. Soc.* **202**, 495
Rankin, J.M. *et al.*: 1970, *Astrophys. J.* **162**, 707
Rickett, B,J., Seiradakis, J.H.: 1982, *Astrophys. J.* **256**, 612
Smith, F.G: 1986, *Mon. Not. R. Astr. Soc.* **219**, 729
Thompson, D.J. *et al.*: 1977, *Astrophys. J. Letters* **214**, L17
Tümer, O.T. *et al.*: 1984, *Nature* **310**, 214

NEW TIME SIGNATURES IN NEUTRON STARS AND PULSE-HEIGHT VARIABILITY IN CRAB

M. E. Özel
NASA/Goddard Space Flight Center
Laboratory for High Energy Astrophysics
Greenbelt, MD 20771 U.S.A.

Abstract: Accumulating evidence for new time scales other than the spin and orbital periods in several single and binary systems involving neutron stars are noted and the pulse height variability observed in Crab pulsar is discussed.

1. Introduction

Accumulating high ($\geq$100 MeV) and very high (> TeV) energy gamma ray data from several neutron star (single and binary) systems are indicative of new time scales not well understood yet. Among them are: (1) the periodicities very near the established Neutron Star (NS) spin periods, in the range of seconds, as in Her X-1 (Lamb et al., 1987, Resvanis et al., 1988); (2) burst-like emission of high energy gamma rays at TeV energies with durations of minutes, tens of minutes or longer as in 4U0115+63, Her X-1, Vela X-1, Cyg X-3 and Crab Pulsar (Gibson et al., 1982; Chadwick et al., 1985; Lamb and Weeks, 1986; Bhat et al., 1987; North et al. 1987; Resvanis et al., 1988); (3) a longer time-scale repetition near an established binary period as in Cyg X-3 with its 4.95 hr anamolous period (Molnar et al., 1984) different than the established 4.8 hr orbital X-ray period and (4) still longer term variabilities, for example, the variability of gamma ray intensity of individual peaks in double-peak NS light curves as in Crab pulsar (Wills et al., 1982, see also below). For some effects, an explanation is usually formulated in terms of subtle details of already complex and not fully understood double star-accretion disk geometries if the system is a binary (see Lamb and Weeks 1987 and references therein). One should also note that some of the reported 'effects' may and do need further confirmations.

As is apparent, the relatively 'cleaner' and 'well behaving' Crab also posess new time scales for which adequate and satisfactory explanations are not yet developed. Below will be summarized the accumulating evidence for the variability in the ratio of

H. Ögelman and E. P. J. van den Heuvel (eds.), Timing Neutron Stars, 357–362.

secondary to main pulses of the Crab Pulsar, also called the pulse-height-ratio (PHR) variability and its possible 'explanation' as an effect arising from the free precessional , motion of the NS.

2. Pulse-height-ratio variability in Crab Pulsar

During the 7-year lifetime of the COS-B satellite which was sensitive to gamma rays in the range of energies 70 MeV to 5 GeV, the Crab Pulsar was observed 6 times, about 1 month duration each (Mayer-Hasselwander, 1985). Early observations revealed that (Wills et al., 1982) the intensity of peaks in the gamma ray light curves obtained varies considerably from one observation to the other and as a measure of this variability, the intensity ratio of the second pulse to the first pulse, R, at a mean epoch t, defined as

$$R(t) = P2 \; / \; P1 \qquad (1)$$

where P2 and P1 are the intensity (practically the number) of gamma rays in the second and first puses, was proposed. This definition had the advantage of being a ratio, where uncertainties in instrumental sensitivity, sky background and some other factors that may enter absolute flux variation estimations cancel.

With the inclusion of all observations by COS-B, the variation in R(t) at $\geq$ 70 MeV is found significant at a level of

$$p < 0.0008 \qquad (2)$$

when tested against a constant 'mean' value throughout the observations (Ozel and Mayer-Hasselwander, 1985). More recent and comprehensive work by COS-B Caravan Collaboration (Clear et al., 1987) confirms these earlier findings together with indications for some other subtle effects which will not be discussed here. In Fig. 1, the PHR parameter R(t) is shown at the available epochs including reports other than COS-B for the photon energies above several tens of MeV or higher, superposed with a best fit periodic sine function of the type

$$R(t) = A \; \mathrm{Sin} \; [2\pi(t - to)/P_r] + B \; . \qquad (3)$$

Using the data points from COS-B and SAS-2 (Kniffen et al., 1974) observations, a best fit to (3) is obtained for a period value of

$$P_r = 4160 \pm 40 \text{ days} \qquad (4)$$

together with

$$A=0.5, \; B=0.7, \; to=8739.5 \; (=1973.6) \qquad (5)$$

PRODUCTION SITES AND MECHANISMS OF DISCRETE GAMMA-RAY COMPONENTS OF THE VELA AND CRAB LIGHT CURVES

W. HERMSEN[1], I.A. GRENIER[2,3]
[1] *Laboratory for Space Research Leiden, P.O. Box 9504, 2300 RA Leiden, The Netherlands*
[2] *Service d'Astrophysique, Centre d'Etude Nucleaires de Saclay, France*
[3] *Centre d'Etude Spatiale des Rayonnements, Toulouse, France*

ABSTRACT. New results on the temporal and spectral characteristics of the high-energy (50 MeV to 5 GeV) gamma-ray emission from the Vela pulsar have become available from an new analysis of COS-B data. The total pulsed flux is found to exhibit long-term variability. Five discrete emission regions within the pulsar lightcurve have been identified, with the spectral characteristics and long-term behaviour being different. These characteristics differ significantly from those reported earlier for the gamma-ray emission from the Crab pulsar. The identification of the different components in the Vela gamma-ray lightcurve and different components, noted earlier, in the Crab X-ray lightcurve supports the idea that several source regions exist in different parts of the pulsars magnetospheres. The different spectral characteristics of these components indicate that different generating processes exist in each source. Geometrical pulsar models have been proposed (e.g. Morini *et al.*. 1983; Smith *et al.*1986) which could explain many of these features.

1. Introduction

The only radio pulsars detected in high-energy gamma-rays so far are the young pulsars Crab and Vela. Recently, Clear *et al.*(1987) presented detailed results on the Crab pulsar using the final COS-B database; now also detailed results are available for the Vela pulsar (Grenier *et al.*1988). Prior to these new results, the experimental status on the latter can be summarized as follows: Tümer *et al.*(1984) at 0.3–30 MeV, Thompson *et al.*(1977) above 35 MeV and Bennett *et al.*(1977) at 50 MeV – 5 GeV all report a similar Vela lightcurve structure which is characterised by two sharp peaks separated by 0.42 in phase and bracketing the optical pulses. An extrapolation to X-ray energies of the COS-B spectrum of Kanbach *et al.*(1980) lies several orders of magnitide above the reported upper limits, while at TeV energies the flux values reported by Bhat *et al.*(1980) clearly require a break in the spectrum. Earlier results from COS-B data by Bennett *et al.*(1977) and Kanbach et al. (1980) indicate a possible break in the spectrum at a few hundred MeV, but the level of significance of these results is low. The next section summarizes the latest results on the Vela pulsar in the 50 MeV to 5 GeV energy range (Grenier *et al.*1988). In section 3 gamma-ray, hard-X-ray (Hasinger 1984) and some radio characteristics of the Vela and Crab pulsars are compared, followed in section 4 by a discussion of the implications for some pulsar models.

H. Ögelman and E. P. J. van den Heuvel (eds.), Timing Neutron Stars, 347–356.

corresponding to a precession period of

$$P_g = (2\pi/w)\, C/(C-A). \qquad (10)$$

We may identify $P_g = P_r$ and the implied flattening (also called the dynamical ellipticity) for the neutron star becomes

$$(C-A)/C = (2\pi/w)/P_r \cong 10^{-10} \qquad (11)$$

Interestingly, this is also about the order of magnitude for NS moment of inertia readjustment scales discussed to explain the Crab pulsar glitches (Shapiro and Teukolsky, 1983):

$$\Delta P/P \simeq \Delta I/I \cong 10^{-9} \qquad (12)$$

On the other hand, the reported medium duration periodicity at 430 MHz (Richards et al., 1970)

$$P_n = 77 \pm 7 \text{ days} \qquad (13)$$

may also find a natural explanation in the context of present model as an ondulation (nutation) period, since P_n looks like an integer divider for P_r:

$$P_r/P_n = 54.0 \qquad (14)$$

4. Conclusions

The emerging picture is that Crab Pulsar may be the long sought and suspected freely precessing (and probably nutating) body probably under its own gyroscopic torque with a small flattening caused by its fast rotation and the nonalignment of body and rotation axes. Forthcoming observations by the gamma ray detectors onboard Gamma-1 (Akimov et al., 1985) and Gamma Ray Observatory (Thompson et al., 1987) will provide more light for the proposed model and the true nature of observed PHR variability (see Fig. 1). An extrapolation back to 1971.294 observations of Parlier et al. (1973) by a balloon instrument for $\geq$ 20 MeV gamma rays seems to be in good agreement with the proposed periodicity model (3), although its statistical significance is low due to the large error in the estimated R(t) value.

One problem with the present 'simple' picture is the assertion that, without an efficient feeding mechanism, this type of precessive motion should be damped out in time scales less than ~ 1000 years (Alpar and Ogelman, 1987). It could be that, the initial misalignment in Crab at its birth may still be the effective cause in keeping the precession alive. Actually several wobble excitation mechanisms for radio pulsars are proposed and discussed in the literature (Goldreich, 1970, Henriksen et al., 1972, Alpar and Ogelman, 1987). Without viable examples to test

the ideas it has been rather difficult to converge on a concensus on the nature and extent of NS precessional motion however. Even having a closeby testing ground may sometimes not be enough for a true understanding. For example, long observed Chandler wobble of the Earth is still in debate for a fully satisfactory explanation after about a century of its first recognition (Stacey, 1977, Pines and Shaham, 1973 and references therin).

The periodic PHR variability effect is probably masked in X-rays (up to MeV energies) due to the onset of a new, plasma-dominated radiation contributing heavily and preferentially to the second pulse as is proposed and discussed in detail by Hasinger et al. (1984) and Hasinger (1985) in order to explain the observed X-ray spectral differences between P1 and P2 and the spectral dependence of PHR in X-ray energies. It looks worthwhile and timely (it has been 20 years since the discovery of the first pulsar) to search for similar long-term effects in optical and radio frequencies in order to understand the connection between the PHR variability and NS precession as well as the extent of proposed radiation component causing the masking of the effect at X-ray energies.

References

Akimov et al., 1985, Proc. 19th ICRC, paper OG 9.2-10.
Alpar, A., Ogelman H., 1987, MPE preprint.
Brecher, K., 1972, Nature, 239, 325.
Bhat et al., 1984, Adv. in Space Sci., 3, 10.
Chadwick et al., 1984, Astron. Astrophys., 151, L1.
Clear et al., 1987, Astron. Astrophys., 174, 85.
Gibson et al., 1982, Nature, 296, 833.
Goldreich, P., 1970, Ap. J., 960, L11.
Hasinger, G., et al., 1984, Adv. in Space Res. 3, Vol 10-11, p. 63.
Hasinger, G., 1985, in "The Crab Nebula & Related SNRs", (ed. Kafatos & Henry), Cambridge Univ. Press, p. 47.
Henriksen, R., Feldman, P., Chau, W., 1972, Ap. J., 172, 717.
Kniffen et al., 1974, Nature, 251, 397.
Lamb, R. C., et al., 1987, Proc. 20th ICRC, Moscow, 1, 244.
Lamb, R. C., Weeks, T. C., 1986, Astrophys. Lett., 25, 73.
Lamb, R. C., Weeks, T. C., 1987, Science, 238, 1483.
Mayer-Hasselwander, H., (on behalf of Caravan Collaboration), 1985, 'Explanatory Suppl. for COS-B Final Data Base', ESA preprint.
North et al., 1987, Nature, 326, 567.
Ozel, M. E., Mayer-Hasselwander, H., 1984, in Proc. of "Data Analysis in Astronomy", p. 181 (ed., di Gesu et al., Plenum Press).
Parlier et al., 1973, Nature, 242, 117.
Pines, D., Shaham, J., 1973, Nature, 245, 77.
Pines, D., Shaham, J., 1974, Nature, 248, 483.

Pines, D., Shaham, J., Ruderman, M., 1974, in "Physics of Dense Matter", (IAU Symposium, ed., C. Hansen), p. 189.
Resvanis et al., 1988, 'VHE gamma rays from Her X-1', preprint.
Richards et al., 1970, Ap. J. Lett., 160, L1.
Shapiro, S., Teukulsky, S., 1983, "Physics of Compact Objects", p. 297 (John Wiley).
Stacey, S., 1977, "Physics of the Earth", John Wiley.
Truemper, J., et al., 1986, Ap. J. Lett., 300, L63.
Thompson, D. J., et al., 1987, IEEE Trans. Nuc. Sci., NS-34, 36.
Wills et al., 1982, Nature, 296, 723.

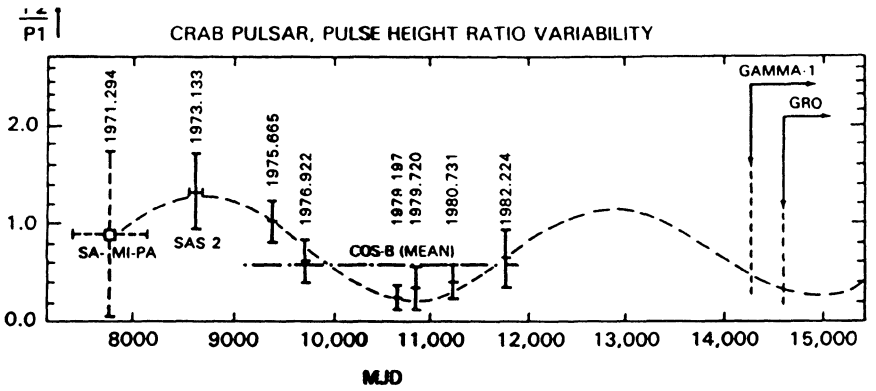

Fig. 1: Variability of PHR in Crab Pulsar gamma ray emission since 1971 (after Ozel and Mayer-Hasselwander, 1985). The broken sine curve is the best fit to data discussed in the text.

SEARCH FOR LINEAR POLARIZATION IN HIGH-ENERGY γ-RAY SOURCES

G.F. Bignami, P.A. Caraveo
Istituto di Fisica Cosmica del C.N.R.,Milano,ITALY

I. Mitrofanov
Institute for Space Research, Academy of Sciences, Moscow, USSR

G. Vacanti
Iowa State University, Ames, IOWA, U.S.A.

ABSTRACT

The azimuthal distribution of planes containing e^+/e^- pairs from high-energy photon materialization is reminiscent, through a quadrupole anisotropy, of the degree and position angle of linear polarization of the incident photons. Data from the COS-B spark chamber are used in a search for such an effect in > 50 MeV photons from bright sources, such as Vela, Crab, Geminga and a reference galactic plane region in Cygnus. Only for the Vela pulsar a low-chance-probability effect is found apparently implying a high (~ 100%) degree of linear polarization for the Vela photons. This has important implications on the physics of the production mechanisms as well as of their geometry.

INTRODUCTION

A property like linear polarization would be very useful in understanding the nature of the high-energy γ-ray sources discovered by the COS-B mission. Certainly, polarization is a common property of radio pulsars (e.g. Rankin 1983a,b, and Taylor and Stinebring 1986, for a recent review). For instance, PSR0833-45 is the one showing the highest percentage (~ 100% at 4.8 GHz) of linear polarization, and PSR0531 + 21 too shows very significant polarization in both the radio and the optical. The detailed properties of radio pulsar linear polarization are often complex, and include such features as rotation of the polarization position angle, presence of orthogonal modes, etc. However, it is well possible that all such features be explained starting from the basic fact that the radiating particles have acceleration components parallel and perpendicular to the magnetic field and radiate their transversal energy due to the magneto-bremsstrahlung mechanism (see, e.g. Bjornsson 1984; Taylor and Stinebring 1986). In this case, it is not inconceivable that, irrespective of possible different light curve morphologies, also the pulsed high-energy γ-rays be polarized.

The basic idea on how to search for polarization in high-energy γ-rays from cosmic sources has been proposed by Kozlenkov and Mitrofanov (1985, and references therein; hereafter KM), and is based on the expected effect of quadrupole modulation of the azimuthal distribution of the planes containing the e^+/e^- pairs produced in the γ-ray interactions. This anisotropy of the pair plane orientations is due to the linear polarization of the incoming photons (Maximon and Olsen 1961).

In a system with the z-axis along the wave-vector K of the incident gammas, the azimuthal distribution $\Phi(\varphi)$ of the e^+/e^- pairs has a quadrupole-like anisotropy with amplitude and direction determined, respectively, by the degree of polarization and by the polarization position angle of the incident radiation. Such a distribution can be written as:

$$(1) \qquad \Phi(\varphi) = \frac{N_t}{2\pi}\{1 + RP\cos[2(\varphi - \varphi_0)]\}$$

H. Ögelman and E. P. J. van den Heuvel (eds.), Timing Neutron Stars, 363–368.

where φ_0 is the polarization position angle, P is the degree (between 0 and 1) of linear polarization, N_t is the total number of observed photons, and R is a numerical factor which depends on the intrinsic asymmetry ratio in the process physics and on the detection characteristics. In the ultrarelativistic case ($E_\gamma >> m_e c^2$), and allowing for screening (KM), a value of $0.14 < R < 0.2$ is obtained, considering also the COS-B detection requirements. This is consistent with the higher values proposed by Maximon and Olsen(1961).

The quadrupole asymmetry of the effect allows for the use of a simple method (KM) for its determination: for Nt observed events, let N1 and N2 (with (N1 + N2 = Nt)), be the two numbers of observed events corresponding to two intervals of the observed azimuth angle ($\varphi, \varphi + \pi/2$) and ($\varphi + \pi/2$, $\varphi + \pi$); and let $S(\varphi)$ be the quadruple deviation function

$$(2) \qquad S(\varphi) = \frac{[N_1(\varphi) - N_2(\varphi)]^2}{N_1(\varphi) + N_2(\varphi)}$$

Because of the theoretical law (1), the deviation function should have a well-pronounced sinusoidal-like shape:

$$(3) \qquad S(\varphi) = \frac{4N_t R^2 P^2}{\pi^2} \sin^2[2(\varphi - \varphi_0)]$$

Using the function (2) one may then check the presence of quadrupole modulation in the data: for the effect to be real, $S(\varphi)$ should take the shape (3). In this case, from the minimum, $S(\varphi) = 0$ of (3), one can derive the position angle, while from the maximum, $S(\varphi) = S^*$, one can estimate the degree of linear polarization:

$$(4) \qquad P = \frac{\pi}{2R} \sqrt{\frac{S^*}{N_t}}$$

Even for a totally polarized radiation (P = 1), the amplitude of the expected azimuthal modulation is rather small (< 20%), and several factors conspire to "blur" the effect, the most important of which is certainly the limitation on Nt, the available statistics. Accordingly, one may estimate the Nt necessary for measuring a 100% polarization using $S(\varphi)$ to estimate the probability that the observed azimuthal modulation result from a statistical fluctuation. For a constant phase angle, the value S can be considered as the number of standard deviations of the random variable N1 (or N2) from the expectation value for the case of zero polarization, in the assumption that its dispersion equals (N1 + N2)/2. The probability of such deviation gives the probability of the zero hypothesis. Following this method, for $E_\gamma > 50$ MeV , Nt is about 2,000 events, so that, it appears worthwile to perform a search for the polarization effect in the COS-B data, also because for the first time in the history of γ-ray astronomy, an acceptable photon number is available for a few sources.

DATA ANALYSIS AND RESULTS

During its ~7 year lifetime, COS-B performed 65 pointed observations of > 1 month each (Mayer-Hasselwander et al. 1985); we have used the data of periods referring to the brightest observed sources. The reconstructed arrival directions for Crab and Vela were within 10 deg of the source for $50 < E_\gamma < 150$, 7 deg for $150 < E_\gamma < 300$ and 5 deg for $E_\gamma > 300$ MeV, while for Geminga and the Cygnus Region only events with arrival direction within 5 deg from the source position were selected. From the azimuthal $\Phi(\varphi)$ distribution of the event planes one can then estimate the amplitude and phase of their quadrupole modulation using the deviation function $S(\varphi)$ for the numbers of events N1 and N2 as described earlier. For the determination of the position angle of the effect it is necessary to vary the starting azimuth value in steps of 2 deg, so that 45 steps are necessary to cover the $\pi/2$ interval of the $S(\varphi)$ function. Such steps are of course taken into account in the final evaluation of the event probability.

Fig.1 (curve a) shows $S(\varphi)$ for the 2526 events from the 2CG263-02 source, or the sum of all the COS-B events satisfying our selection from the Vela pulsar region. For comparison, curve b shows

the same distribution for data from another region of the sky, that of Cygnus, probably dominated by diffuse emission and for which no polarization is expected. Specifically, 3109 photons were selected from a region of 5 deg radius centered at l = 80 deg, b = 0 deg. The two curves are very different: while for curve a the suggestion exists of a well-ordered modulation of the azimuthal dependence of the event planes, curve b does not show any effect, proving that the observed anisotropy for the Vela data cannot be due to some systematics of the spacecraft. To evaluate the statistical significance of the effect, a Montecarlo simulation was performed. The maximum value of the deviation function (S(φ)) was computed for 300,000 random 2500-event distributions, each going through the 45 steps phase coverage cycle. The Montecarlo results thus give the chance occurence probability for a given S value for the Vela data. Such a probability is shown in Fig.1. From curve a, it is seen that azimuthal anisotropy for the Vela data has a chance occurrence probability $\sim 1.5 \times 10^{-4}$. As a further check, we have constructed the same type of distribution but with the event plane azimuths not corrected for the satellite spin, i.e. in the sky of the spark chamber rather than in the true one. No deviation from the random expectations was observed for the Vela or Cygnus data, nor any sign of sinusoidal modulation is present. Therefore, the low chance probability effect is also not due to some systematics of the spacecraft.

Another COS-B source investigated was 2CG185-5, the Crab. As in the case of Vela, we consider all class 22 events with the usual source distance selection, yielding 1533 photons over 6 observing period. Curve (a) of Fig.2 shows the result for this "total" Crab emission: no significant evidence is apparent for a modulation. On the same Figure, curve (b) shows the distribution for the Geminga (2CG195 + 5) data, referring to 1204 photons with the usual selections and coming from 5 observing periods, most of which were in common with the Crab. Here too no significant modulation is present.

PULSAR PHASE ANALYSIS

Considering, as mentioned earlier, the high degree of linear polarization in radio photons from pulsars in general and for the Vela pulsar in particular (up to $\sim 100\%$), it seems natural to approach the azimuthal anisotropy suggested by the data as due to linear polarization of the incoming γ-rays. In this case, according to the predictions of the effect as outlined above, eq. (4), the value of $S^* = 20$ (Fig.1, curve a) implies $RP = 0.14$, or a very high degree of polarization (bigger than 50%, and up to 100%, depending on the uncertainty on R) for the high-energy γ-rays from the Vela source. One must now, of course, remember that the majority of the COS-B γ-rays from 2CG263-02 are in fact pulsed at the period of PSR0833-45 (see,e.g., Kanbach et al. 1980), and it seems worthwhile to investigate the effect in the various region of the pulsars light curve (or phase diagram), even with necessarily reduced statistics. The 2526 photons from Vela were than divided in 4 phase intervals

(1) First pulse	: containing	584	photons
(2) Second pulse	: containing	666	photons
(3) Interpulse	: containing	791	photons
(4) Background	: containing	485	photons

Accordingly, curves (1) to (3) of Fig. 3 show the usual S(φ) distributions for the corresponding intervals, while curve (4) shows the total "pulsed", or (1) + (2) + (3) and curve (5) shows the "background" emission, as defined above.

The severe limitation introduced in statistics by such a breakdown renders any firm conclusion from Fig. 3 very difficult; it looks, however, as if the interpulse (plus may-be the II pulse) region is the one contributing most to the possible polarization. It would also appear that the S^* values of the interpulse and total pulsed radiation require RP to approach its maximum value, or a $\sim 100\%$ polarized radiation.

As to the value of the polarization P.A., bearing in mind the $\pi/2$ periodicity of the S(φ) function, from Fig. 1 (curve a) and Fig. 3 (curve (4)) one finds $\sim 130 \pm 15$ deg. A comparison appears natural with the polarization results in the radio region, where, it should be remembered, the light curve shape is completely different, featuring only one short peak not in phase with the γ-ray peaks, but rather in a γ-ray "background" region . The classic result of Radhakrishnan and Cooke (1969) shows a significant P.A. shift (90 deg) centered at 120 deg or 154 deg, depending on the

frequency, within the 4 msec peak. Our data would seem to support a picture very different from that at radio frequencies, considering also the high percentage value requested to interpret the observed anisotropy as linear polarization: the P.A. of the polarization plane either swings of a relatively small value (< 30 deg) or remains constant over a big interval of the pulsar phase (= interpulse + II pulse, or 44% of the phase).

Going back to Fig. 3, since the interpulse data are the ones that, taken singly, would seem to suggest some non-random behaviour in spite of the limited statistics, it appears interesting to look at the raw azimuth distribution of the 791 event planes. This is shown in Fig. 4, with the full π azimuth range covered in 10 deg bins. It makes sense to use the run test on such a distribution, to gauge its regularity of shape vis a vis the expectations. As apparent (and expected), the depth of modulation is shallow, but the data can indeed be divided in two separated 9-bin families, yielding a chance probability of $4x10^{-5}$ (Beyer 1968). Note that this is a one-shot test, with the initial azimuth fixed and no steps performed.

A similar pulsar phase analysis, albeit in the context of worse statistics, can be tried for the Crab data. The total 1533 events were divided in phase corresponding to I peak, II peak and background (see Wills et al. 1982). As could be expected from the result for the total events, no significant deviation from random expectations is observed for the Crab data subsets. One must also take into account the nebular emission (see e.g. Clear et al. 1987), concurring in this case to blur a possible pulsar signal, expecially at low energies, where a lot of the Crab events are. In any case, it would appear that a much better statistics is necessary for a meaningful investigation.

CONCLUSIONS

The method outlined above has shown that, in spite of obvious difficulties, it is meaningful to search for polarization in high-energy γ-ray data in the COS-B spark chamber data. A rather significant anisotropy has been found for 2500 selected events from the Vela pulsar, and has been shown not to be present in other strong sources or in the Cygnus region of the galactic plane. With the proviso of the poor statistics and of other experimental limitations discussed, a linear polarization of the incoming photons appears as the natural explanation for this finding which has important implications on the emission mechanisms responsible for the pulsed emission (see Caraveo et al. 1988) Unfortunately, not much more can be done now to improve the significance of and confirm the experimental result of the COS-B data. This task, for both the Vela and Crab pulsars as well as for other sources, rests with the next generation of γ-ray telescopes.

REFERENCES

Beyer W.H. 1968, Handbook of Probability and Statistics CRC,p.414
Bjornsson, C-I. 1984, Ap. J., 277,367
Caraveo, P.A., Bignami, G.F., Mitrofanov, I, Vacanti, G. 1988, Ap. J. 327,203
Clear, J., Bennett, K., Buccheri, R., Grenier, I.A., Hermsen, W., Mayer-Hasselwander, H.A., and Sacco, B. 1987, Astron. Ap., 174, 85
Kanbach, G., Bennett, K., Bignami, G.F., Buccheri, R., Caraveo, P., D'Amico, N., Hermsen, W., Lichti, G.G., Masnou, J.L., Mayer-Hasselwander, H.A., Paul, J.A., Sacco, B., Swanenburg, B.N., and Wills, R.D. 1980, Astron. Ap., 90, 163
Kozlenkov, A.A., and Mitrofanov, I.G. 1985, Sov. Astron., 29, 159
Maximon, L.C., and Olsen, H. 1962, Phys. Rev., 126, 310
Mayer-Hasselwander, H.A., Bennett, K., Bignami, G.F., Bloemen, J.B.G.M., Buccheri, R., Caraveo, P.A., Hermsen, W., Kanbach, G., Lebrun, F., Paul, J.A., Sacco, B., and Strong, A.W. 1985, Proc. 19th Int. Cosmic Rays Conf., la Jolla, 3, 383
Radhakrishnan, V., and Cooke, D.J. 1969, Ap. Letters, 3, 225
Rankin, J.M. 1983(a), Ap. J., 274, 333
Rankin, J.M. 1983(b), Ap. J., 274, 359
Taylor, J.H., and Stinebring, D.R. 1986, An. Rev. Astron. Ap., 24, 285
Wills, R.D., Bennett, K., Bignami, G.F., Buccheri, R., Caraveo, P.A., Hermsen, W., Kanbach, G., Masnou, J.L., Mayer-Hasselwander, H.A., Paul, J.A., and Sacco, B. 1981, Nature, 296, 723

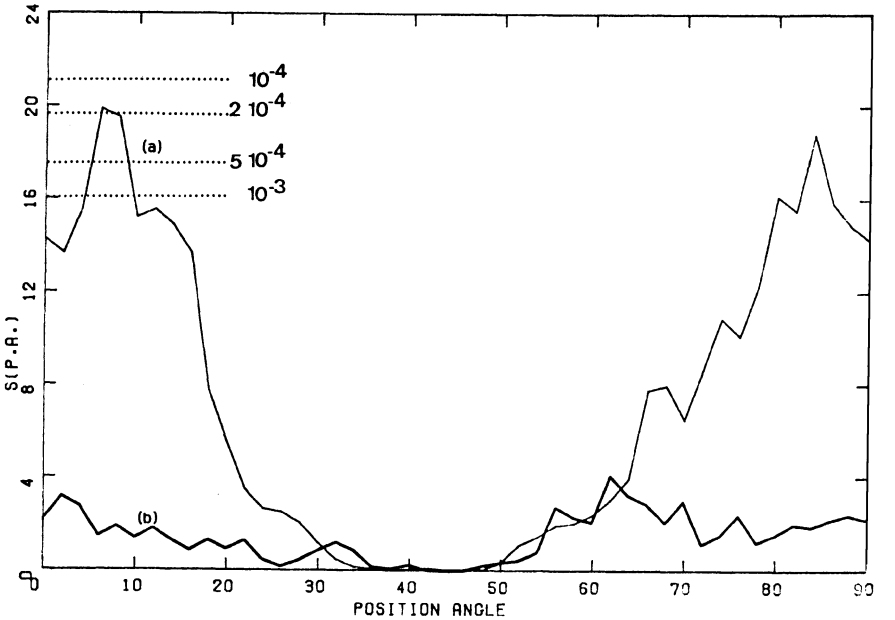

Fig.1 Curve (a) : deviation function S(φ) for the 2526 photons from Vela. Following its definition, the numerical values of S are equivalent to a chi-square value with one degree of freedom. Overall chance occurence probability levels are also shown, according to Montecarlo simulations (see text). Curve (b): as above, but for 3109 photons from the Cygnus Region of the galactic plane (l = 80 deg, b = 0 deg).

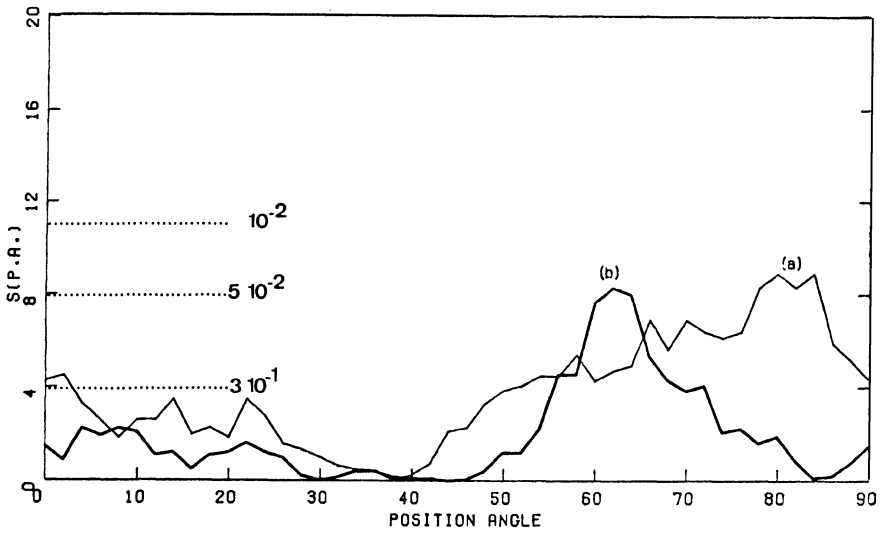

Fig.2 Curve (a) S(φ) for 1533 photons from the Crab.
Curve (b) as above, for 1204 photons from Geminga. Units as in Fig.1. The overall chance occurrence probability levels shown are derived from Montecarlo simulations for 1500 events.

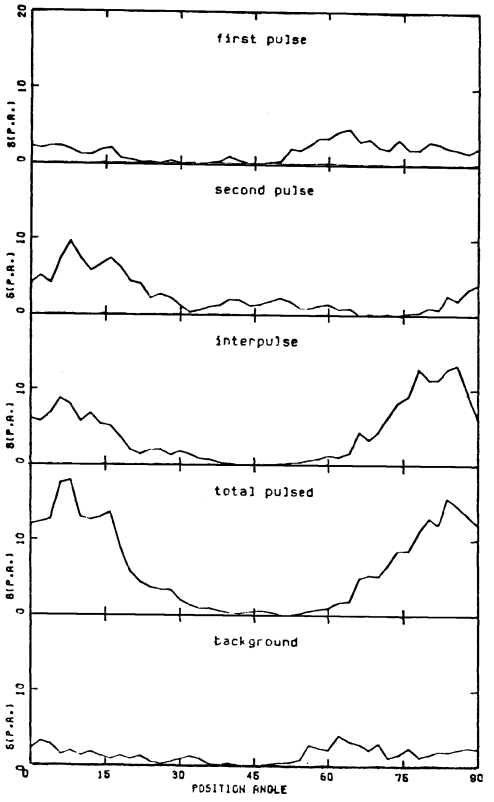

Fig.3 Deviation functions for different intervals of PSR0833-45 light curve (see text for exact definition). The "total pulsed" is the sum of I pulse, II pulse and interpulse distributions.

Fig.4 Raw data distribution: pair plane orientation histogram (N(P.A.)) for the PSR0833-45 interpulse data (791 photons).

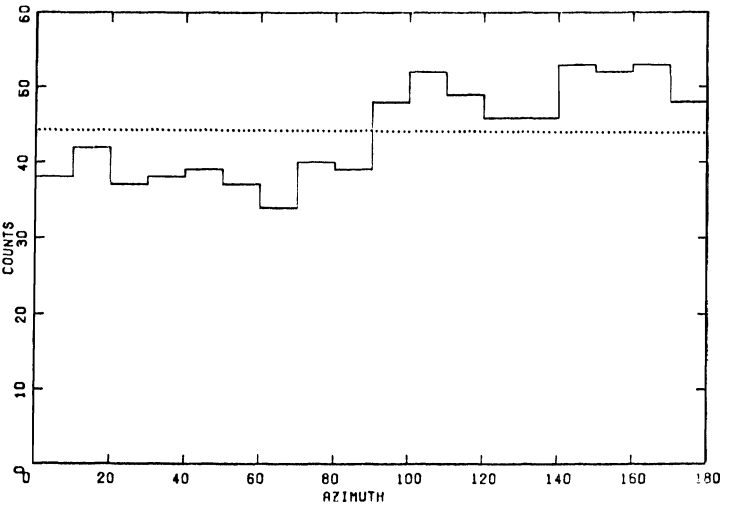

VHE GAMMA RAY EMISSION FROM CENTAURUS X-3

A. Carraminana, P. M. Chadwick, N. A. Dipper, E. W. Lincoln,
V. G. Mannings, T. J. L. McComb, K. J. Orford, S. M. Rayner,
K. E. Turver and D. G. Williams
Department of Physics
University of Durham
Durham DH1 3LE
UK

ABSTRACT. The high mass X-ray binary Centaurus X-3 has been observed using the Narrabri 250 GeV gamma ray telescope and the observations show evidence for pulsed VHE gamma ray emission, significant at the 4.2 SD level. The detected gamma ray signal in the total dataset comprises a broad pulse at precisely the contemporary X-ray period. The VHE emission is strongest for a few hours around the ascending node in the 2.1 d binary orbit. The time averaged energy flux in VHE gamma rays (> 250 GeV) is estimated to be ~ 10^{36} erg s^{-1} with a peak luminosity of 3×10^{36} erg s^{-1}.

1. INTRODUCTION

Centaurus X-3 is a high mass binary X-ray pulsar located at a distance of 8 kpc and which has many interesting features. It has a 4.8 s pulsation (Giacconi et al (1971)) and is in a system showing eclipses every 2.1 d (Schreier et al (1972)) together with variations in X-ray intensity on a time scale of months (Baity et al (1974)). The extensive X-ray observations show a changing pulse period which at times spins up due to accretion from a Keplerian disc, but at other times shows a spin down. Overall there is evidence for a long term spin up with a period derivative of about 1.1×10^{-10} s/s. This is confirmed by the recent GINGA observation which measured a period in mid-1987 of 4.8230 +/- 0.0002 s (Makino et al (1987)).

We present evidence for the emission of 250 GeV gamma rays by the Cen X-3 system which has been obtained with the new Narrabri atmospheric Cerenkov gamma ray telescope during observations taken between 1987 January and 1988 January. They include measurements which have greater scope for demonstrating the reality of the VHE signal than was the case with our earlier Dugway observations of Northern hemisphere objects.

H. Ögelman and E. P. J. van den Heuvel (eds.), Timing Neutron Stars, 369–374.

2. THE GAMMA RAY TELESCOPE

The observations were made with the University of Durham Mk III gamma ray telescope situated at Narrabri, NSW, Australia (30^{o} 29' S, 149^{o} 39' E, alt 210 m above sea level) (Chadwick (1987)). The telescope has a threshold of 250 GeV in the zenith. The telescope is of conventional design and comprises three light collectors made of high reflectivity aluminium, each of area 11.4 m^2, on a single computer controlled alt-azimuth mount. Each light collector is viewed by a cluster of 7 fast 40 mm dia photocathode PMTs (type RCA 8575). The 21 PMTs are arranged to provide 7 light detecting channels, each one comprising a triple mirror-PMT combination. One of the channels views the object and the others monitor the surrounding region of sky at equal angular offsets of 2^{o}, providing comprehensive monitoring of the background. The geometrical aperture of each channel is 0.9^{o} full width, the smallest value reasonable on the basis of our experience with a range of earlier telescopes.

Two modes of operation of the telescope have been employed in the Cen X-3 observations. Most of the data were taken in the tracking mode when the central PMT system followed the source. In this case the complete encirclement of the central "on-source" channel with 6 "guard ring" channels gave maximum rejection of nucleon induced events characterised by the simultaneous response of the central channel and an off-source channel. The second mode of operation involves the mechanical chopping of the signal by movement in azimuth of the whole telescope by 2 spatial deg every 2 min. This ensures that the central channel and another located in the same horizontal plane alternately observe the source and a background sky region. Here all the advantages of the well established chopping procedure, which provides two independent interleaved datasets, are available, e.g. the appearance of the gamma ray signal in the on-source channels, and its absence in the same channels when off source.

3. VHE GAMMA RAY DATA

Observations were made for a total of 100 hrs on 34 nights between 1987 January 28 and 1988 January 25. An observing log showing number of events recorded in measurements at various intervals in orbital phase is given in Table I. Although no data are available at phase 0.4 - 0.5 and 0.9 - 1.0 , the remainder of the 2.1 d orbit has been sampled. Note that data taken in 1988 January were taken in the chopping mode and have comprehensive information which are able to demonstrate the validity of the claimed effects.

4. PULSE TIMING ANALYSIS

The results from X-ray measurements of the period of the pulsar in Cen X-3 suggest a long term spin up of the pulsar as shown in Figure 1. These data and in particular the near contemporaneous measurement by

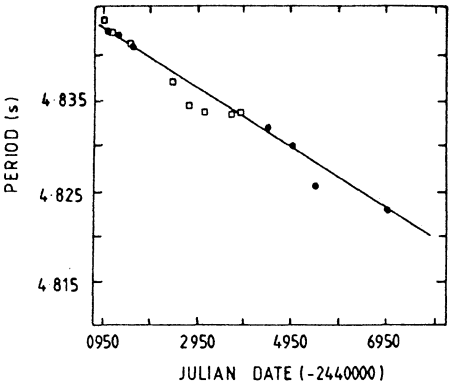

Figure 1. The measured variation of the period of the X-rays from Cen X-3 (from a compilation of Nagase et al (1984), the latest point being from Makino et al (1987)).

ORBITAL PHASE	NO. OF DAYS	TOTAL NO. OF EVENTS	SIGNAL STRENGTH %	CHI SQUARE PROBABILITY
0.0 - 0.1	4	23970	1.1	4.7×10^{-1}
0.1 - 0.2	5	26970	1.3	3.3×10^{-1}
0.2 - 0.3	6	27355	1.1	4.2×10^{-1}
0.3 - 0.4	1	5411	2.4	4.2×10^{-2}
0.4 - 0.5	-	-	-	-
0.5 - 0.6	4	23201	0.7	6.3×10^{-1}
0.6 - 0.7	7	34204	1.1	5.0×10^{-1}
0.7 - 0.8	6	33687	2.3	3.2×10^{-6}
0.8 - 0.9	1	2684	3.5	3.7×10^{-2}
0.9 - 1.0	-	-	-	-
TOTALS	34	177482	1.5	1.4×10^{-3}

Table 1. An observing log of the orbital phases of Cen X-3, showing the number of occasions the phase region was observed and the total number of events detected.

the GINGA satellite indicate a period of 4.8230 +/- 0.0002 s for mid-June 1987. For a dataset of 2.5 hrs duration, which is typical of our data on an individual night, the independent sampling interval is 0.0025 s. The effect of the secular change in period over 6 months is about 1/2 of this amount.

The time of arrival of each Cerenkov light flash was recorded in Coordinated Universal Time (UTC) to an absolute accuracy of better than 1 ms and a resolution of 1 s. The time for each event has been converted from UTC to Barycentre Corrected Julian Ephemeris Time using the JPL solar system ephemeris and the position of the X-ray pulsar. A further correction to allow for the orbital motion of the X-ray pulsar has been made by adjusting the times to the focus of the binary orbit according to the X-ray measurements (Kelley et al (1983)).

An analysis of all the data (177482 events after selection to reject off source candidates using the "guard ring" channels) involving a periodicity test using the Rayleigh test has been made. Since the data span more than a year and difficulties arise if attempts are made to hold phase with an uncertain period derivative, data have been tested night by night and the probabilities for the appropriate X-ray period have been combined with equal weights. The test gives a average signal strength of 1.5 +/- 0.5% for all counts and corresponds to a chance probability of 0.0014 for periodicity at

the X-ray pulsar period. In Table 1 we show the the average signal strengths and the chance probabilities for periodicity at the X-ray period in our data divided into 10% wide intervals of the 2.1 d orbit. There is no indication of any significant pulsed VHE gamma ray emission at any phase other than the interval 0.7 - 0.8 for which the chance probability is 2×10^{-6} (overall chance probability 2×10^{-5} allowing for pre-selection of data in 10 orbital phase bands). Within the phase band 0.7 - 0.8 the data arise from measurements on 6 nights and the pulsed signal strength on these individual nights is plotted as a function of orbital phase in Figure 2. The significant emission is confined to the 4 nights (1987 April 29, May 20, May 22 and 1988 Jan 21) in the phase range 0.73 - 0.77. The peak emission at phase 0.75 is 3.7 +/- 0.9% of the cosmic ray background, corresponding to a flux of 250 GeV gamma rays of 3×10^{-10} cm^{-2} s^{-1} and source luminosity of 3×10^{36} ergs s^{-1}.

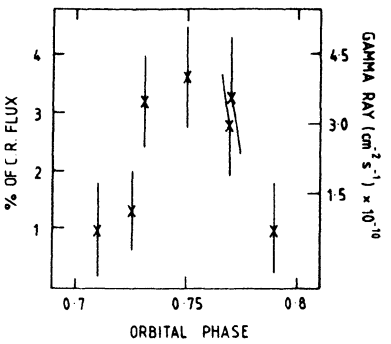

Figure 2. The strength of the VHE gamma ray signal on individual observations at phases in the range 0.7 to 0.8 of the 2.1 d orbit.

MODE	SIGNAL STRENGTH %	CHANCE PROBABILITY
(a)	3.7	6.4×10^{-4}
(b)	1.7	1.0×10^{-1}
(c)	1.5	1.0×10^{-1}

Table 2. Chance probabilities of periodicity in data taken on 1988 Jan 21 at phase 0.75 of Cen X-3: (a) on-source data, taken by one of two alternating central channels, (b) off-source data, taken by the alternate central channel, (c) off-source data taken by a channel which did not observe the source.

5. VALIDATION OF DATA

The data for one of the observations showing strong emission, (3.7% on 1988 Jan 21), were obtained with the telescope in the chopping mode. Observing conditions were not ideal and the data were suitable for pulsar analysis but interpretation of the on/off source count rates

was precluded. Nevertheless, validation tests were possible to demonstrate the genuine nature of the gamma ray signal. For example, the signal strengths and chance probabilities for the data from the two chopped channels have been evaluated. These indicate that the periodicity is confined to those times when the source is in the FOV of the on-source channel. The enhancements to the signal from employing the coincidence "guard ring" technique also suggest that the signal is genuine. For example, the strength of the signal in the data for the 4 nights referred to above, selected on the basis of an unguarded central detector (essentially the case for a normal single channel telescope) is 2.0 +/- 0.8%. This increases to 3.2 +/- 0.9% if the events having accompanying off axis "guard ring" responses are rejected.

6. DISCUSSION

The existence of VHE emission from several binary X-ray pulsars points to a production mechanism with inherently wide beaming, or a beam direction which varies with orbital position. Direct emission of VHE gamma rays from the pulsar magnetosphere as is the case for young fast pulsars seems unlikely; strong accretion flows and a luminous pulsar are not easily reconciled. The model of Cheng, Ho and Ruderman (1986) does not seem capable in such a slow pulsar of providing powerful magnetospheric gaps as emission sites. A model which could readily explain VHE emission from a pulsar magnetosphere directly, that of Cohen and Mustafa (1987), requires a vacuum-field at the polar regions, just where the accretion flow would be funneled. Also, it predicts an exceedingly narrow beam, requiring a large neutron star precession amplitude for pulsations to be observed. This contradicts the present result which shows an apparent link between VHE emission and the orbit. The VHE emission therefore may originate outside the magnetosphere. This could arise due to a number of effects; for example, to ion acceleration by the pulsar interacting with the accretion disc or wake or the companion's envelope as suggested by Eichler and Vestrand (1984). Alternatively, it could be due to electron acceleration in the electrical potential generated by the differentially-rotating accretion disc and the pulsar field (Chanmungan and Brecher (1985)).

The presence of pulses in the VHE emission places two restrictions on the latter model. First, the size of the emission region must be much smaller than the radius of the accretion disc (4.8 lt-s). Second, the pulsar spin axis must possess a significant angle with respect to the disc, since the generated potential is proportional to the magnetic field component perpendicular to the disc. The size of the emission region must be less than ~ 1 lt-s and is probably located just outside the Alfven radius. The exact position of the Alfven surface depends on a number of unknown parameters - including the pulsar magnetic field strength and the accretion rate. However, since the pulsar is spinning up, the Alfven radius must be less than the co-rotation radius and < ~0.8 lt-s from the pulsar. On a

simple model, the sign of the electric field will change at the co-rotation radius, giving the possibility that the outer disc region may possess a large potential sufficient to accelerate ions to provide PeV emission. The inner part of the disc, between the Alfven radius and the co-rotation radius, may accelerate ions and produce pulsed VHE emission; the details of the particle acceleration and photon emission remain to be worked out. For this model, the confinement of the VHE emission to a small part of the orbit suggests a beaming geometry which is orbital phase dependent. This could be due to the fact that the accretion disc just outside the magnetosphere will be tilted out of the orbital plane and into the equatorial plane of the pulsar. Such a model could predict further that the VHE emission may be sporadic, correlating with but preceding X-ray emission. (This is due to the dependence of both emissions on the rate of accretion of material on to the magnetosphere). In this case the VHE emission may show some evidence of other periodicities. Quasi-periodic X-ray emission is most easily explained by the "beat frequency model" of Alpar and Shaham (1985) arising from clumps of material passing through the inner accretion disc at orbital rates slightly different from the pulsar's. Such clumps (Ghosh and Lamb (1979)), possibly formed by the interaction of a pulsar magnetic field highly-inclined to the disc plane, could cause locally enhanced VHE emission for short intervals, and perhaps at periods slightly shorter than the pulsar period.

ACKNOWLEDGEMENTS

We are grateful to the Science and Engineering Research Council for the support of the project and to the University of Sydney for the lease of the Narrabri site. The telescope was designed and constructed with the assistance of the staff of the Physics Department and the efforts of Mr. P. Cottle, Mrs. S. E. Hilton and Mr. K. Tindale are gratefully acknowledged.

REFERENCES

Alpar, M.A. and Shaham, J.: 1985, Nature, 316, 239.
Baity, W.A. et al.: 1974, Astrophys. J., 187, 341.
Chanmungan, G. and Brecher, K.: 1985, Nature, 313, 767.
Chadwick, P.M.: 1987, Ph.D. Thesis, University of Durham.
Cohen, J.M. and Mustafa, E.: 1987, Astrophys. J., 319, 930.
Cheng, K.S., Ho, C. and Ruderman, M.: 1986, Astrophys. J., 300, 500.
Eichler, D. and Vestrand, W.T.: 1984, Nature, 307, 613.
Ghosh, P. and Lamb, F.K.: 1979, Astrophys. J., 232, 259.
Giacconi, R. et al.: 1971, Astrophys. J. (Letters), 167, L67.
Kelley, R.L. et al.: 1983, Astrophys. J., 268, 790.
Makino, F. et al.: 1987, IAU Circ. No. 4459.
Nagase, F. et al.: 1984, Publ. Astron. Soc. Japan, 36, 667.
Schreier, E. et al.: 1972, Astrophys. J. (Letters), 172, L79.

Observation of TeV Gamma-rays from the Crab Nebula and PSR 0531

P.W.Kwok[1], M.F.Cawley[2], D.J.Fegan[3], K.G.Gibbs[1], A.M.Hillas[4], R.C.Lamb[5], D.A.Lewis[5], D.Macomb[5], N.A.Porter[3], P.T.Reynolds[3], G.Vacanti[5], T.C.Weekes[1]

1. Whipple Observatory, Harvard-Smithsonian Center for Astrophysics, P.O. Box 97, Amado, Arizona 85645-0097, USA
2. Physics Department, St, Patrick's College, Maynooth, Ireland
3. Physics Department, University College, Dublin, Ireland
4. Physics Department, University of Leeds, Leeds, LS2 9JT, England
5. Physics Department, Iowa State University, Ames, Iowa 50011, USA

Abstract The Whipple Observatory 10 m Reflector operating as a 37-pixel camera has been used to observe the Crab Nebula in TeV gamma rays. Using gamma-ray image selection a detection is reported at the 9.0 sigma level; this corresponds to a flux of 1.8 x 10^{-11} photons-cm^{-2}-s^{-1} above 0.7 TeV. Less than 25% of the observed flux is pulsed at the period of PSR 0531. An upper limit (95% confidence level) for the pulsed flux is 4.5 x 10^{-12} photons-cm^{-2}-s^{-1}.

Introduction

The Crab Nebula and pulsar have been intensively studied at all wavelengths including energies accessible with ground-based gamma-ray telescopes. Using a refined version of the atmospheric Cherenkov technique we here report the detection of steady flux of gamma-rays above 0.7 TeV from the Crab Nebula at a high level of statistical significance. The flux is in agreement with that reported previously by Fazio et al. [1] in 1969-72 and in an earlier (1983-5) observation by Cawley et al. [2] with this same technique. The periodicity search suggests a broad light curve, but with low statistical significance.

Atmospheric Cherenkov Imaging.

The atmospheric Cherenkov imaging technique offers the possibility of improved angular discrimination as well as increased angular resolution with a single optical reflector. The basic idea is to record the image of the Cherenkov light of each air shower, and to use the image information to reject background showers.

In 1983 a 37-element camera was installed at the focal plane of the 10 m optical reflector at the Whipple Observatory giving a 3.5° full field of view [3].

The tracking ON/OFF technique was employed for the reported observation. The candidate source was tracked to within $\pm$ 0.1° of the optic axis for 28 sidereal minutes throughout the ON scan. Then, in two minutes the reflector was slewed to point to a

H. Ögelman and E. P. J. van den Heuvel (eds.), Timing Neutron Stars, 375–382.

position 30 minutes later in right ascension; this, the OFF scan, was continued for 28 minutes during which the same range of zenith and azimuth angles were followed. This sequence of ON/OFF pairs was repeated as long as the skies were excellent (no clouds) and the zenith angle z was less than 55°. The majority of the observations were taken at $z < 30°$.

Calibration files were taken at the beginning and end of each night so that the data files could be later flat-fielded. Preliminary data analysis consisted of three processes; (1) image normalisation and editing; (2) shower image parameterization; (3) candidate gamma-ray event selection. These images could then be used to look for an excess from the source direction or to search for periodicity in the data stream.

Differentiation between gamma-ray shower images coming from a discrete source on the optic axis of the camera and from hadronic showers coming from random directions rests on two distinct factors: (a) inherent differences in shower size and/or shape between the two types of shower; (b) differences between the image orientation based on the point of origin i.e. discrete source on-axis or isotropic background.

The relatively poor resolution of this camera and the high data rate did not justify very sophisicated image analysis routines. Simple moment-fitting routines were found to be most effective [4]. To a first approximation the images are elliptical; if the major and minor axis is determined, then two parameters are easily defined: the Width along the minor axis and the Length along the major axis. The angle that the major axis makes with respect to the center of the field of view (also the source direction) is the impact parameter in angular space and is called here the Miss parameter.

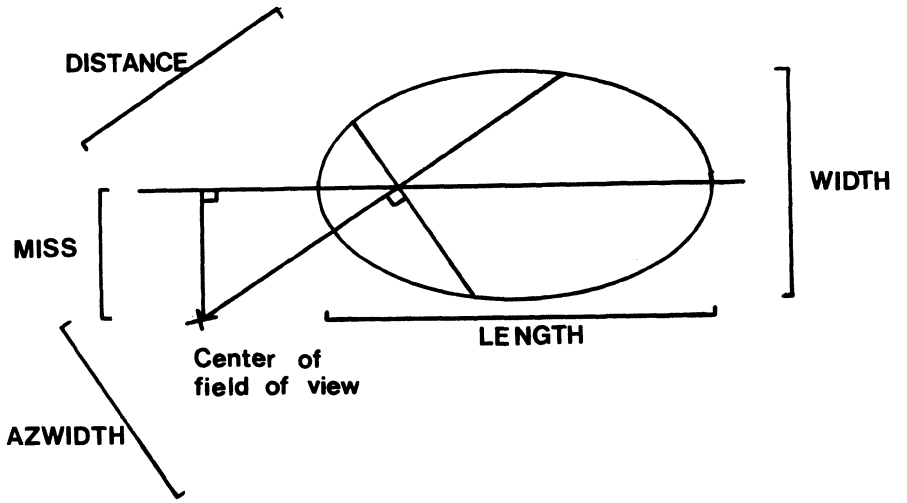

Figure 1 Image parameters

A single parameter can be defined which combines the discrimination expected from size/shape and orientation criteria. This parameter, Azwidth, is the width along the radius passing through the shower image centroid. This is really a combination of the discrimination achieved by Width and Miss and hence should be more effective than either acting alone.

Monte Carlo simulations of the response of the Whipple Observatory camera to both gamma-ray and proton showers [4] showed that any one of these four parameters (as well as two other quasi-independent parameters) could be used as an effective discriminator. In each case a gamma-ray domain is defined with a cut-off value which determines the range of parameter values where there is the maximum acceptance of gamma rays combined with the minimum contamination by background cosmic rays.

Some confidence in the simulations comes from a comparison of the measured parameters of the background cosmic ray events with those predicted by the simulations. For this analysis we have used values predicted by the simulations which were made prior to the observations; hence no optimisation is involved and no extra degrees of freedom must be accounted for.

Results

The data-base upon which the analysis is based is composed of 210 pairs of ON/OFF observations in the direction of the Crab Nebula taken between December, 1986 and February, 1988. A preliminary examination of the data-base (but prior to any comparison of the ON/OFF raw data totals) led to the rejection of 35 pairs for various reasons e.g. unequal lengths of scans, electronic problems, dramatic changes in minute-to-minute rates suggesting weather changes, etc.

For the complete data-base in 175 ON/OFF pairs before image cut, there is an excess of 1210 raw events (+1.12 sigma using the statistic of Li and Ma [5], Table I). This is not significant but is consistent with the result of Fazio et al. [1] in which 3.0 sigma excess was seen in 150 hours of observation.

We have then applied the parameterization routines to each image and sorted the image according to the prescription outlined above. The results are summarised in Table I.

Table I Result Summary 1986-88, 175 ON/OFF pairs

Parameter	ON	OFF	% All	Diff.	% OFF	Sigma
All	653,099	651,889	100.0	+1,210	0.19	+1.12
Azwidth	9,104	7,933	1.2	+1,171	14.76	+8.97
Width	43,152	41,613	6.4	+1,539	3.70	+5.29
Miss	91,746	90,641	13.9	+1,105	1.22	+2.59

We note that: (a) the percentage of events that pass the discrimination threshold is on average 1.2 % , in agreement with the simulations; (b) there is an excess of events in the ON source data of order 15 % of the excess; (c) the effect is consistent with the difference in the All ON/OFF; (d) the cumulative total excess has a statistical significance of 9.0 sigma; this is a level not previously encountered in VHE or UHE gamma-ray astronomy.

The data is internally consistent with the detection of a flux of gamma rays. We check that (a) the net excess that is seen in Azwidth is seen also in two other independent parameters that are the basis of this selection: Width and Miss, thus demonstrating that both shape and orientation are helping to select gamma rays (Table I); (b) the excess is seen in the other parameter cuts also; in particular we see the effect when we use the cut combination outlined by Hillas [4]; (c) if the effect was noise-generated, it would be more apparent in the events that were just above threshold; division of the data by total digital counts recorded does not show that the effect is dominated by the smallest events; (d) selection into the gamma-ray domain is less efficient at larger zenith angles ; division of the data-base by zenith angle shows that the technique is most sensitive close to the zenith; (e) the effect of the star, Zeta Tau, is shown to have no bias on the data selection; (f) the order of observations (ON before OFF) is shown to have no systematic effect.

Earlier Observations

A total of 70 acceptable ON/OFF pairs of observation of the Crab Nebula were made using the same technique but with an early version of the camera [3]. The results of a preliminary empirical analysis [2] and a more detail analysis [6] (Table II) using the published discrimination factors were encouraging, although the statistical significance is not high.

As there were significant differences between this data-set and the 1986-88 data-set, we have chosen to treat them separately. In particular, (a) the camera trigger was different with the majority of the data taken with any one of the inner seven tubes firing; (b) the camera electronics were custom-built and subject to drifts not seen in the improved camera; (c) the influence of the star, Zeta Tau, was treated differently.

Table II Result Summary 1983-85, 70 ON/OFF pairs

Parameter	ON	OFF	% All	Diff.	% OFF	Sigma
All	255,711	255,310	100.0	+401	0.16	+0.58
Azwidth	896	797	0.3	+99	12.42	+2.41
Width	3,370	3,277	1.3	+93	2.84	+1.14
Miss	56,835	56,189	22.0	+646	1.15	+1.92

Based on the excess seen with the Azwidth selection (99 events in (28 x 70) minutes of observation), we estimate that the effect is compatible with a flux $1.47 \pm 0.28 \times 10^{-11}$ photons-cm^{-2}-s^{-1} with the gamma-ray energy threshold 0.6 TeV [6].

Variation with Time

Previous observations of emission from the Crab Nebula had given some indication of variability, possibly associated with glitches in the pulsar period [1]. To search for variability on a monthly timescale the data has been analysed by dark period. Using Azwidth as discriminator the results are shown in Figure 2. We conclude that our measurements are consistent with a steady flux over the epoch 1986-88. Within the limitations of the earlier measurement (1983-85), there is no evidence for variability over that larger timescale. As we shall see in later section, the flux and energy derived are also consistent with the measurement made in 1969-72. There was one large glitch in the pulsar period between 1983 and 1988 (August, 1986) but no gamma-ray observations were made until four months later; no effect was noted so the possible association with this phenomenon is still problematic.

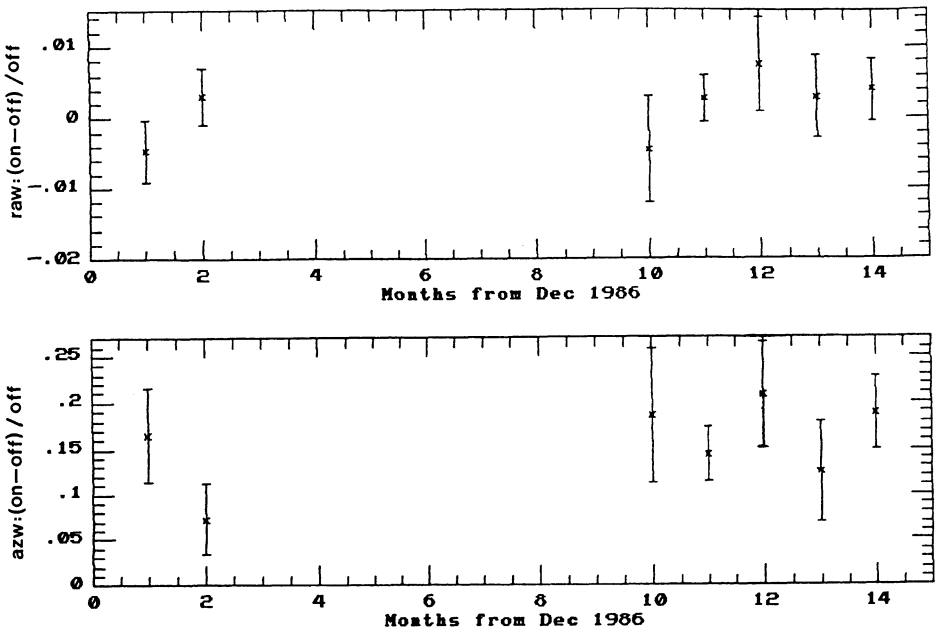

Figure 2. Variation of the unselected (raw) data and Azwidth selected data with dark run; expressed as ratio of (ON-OFF)/OFF counts.

Periodicity Analysis

The angular resolution of the technique at these energies is not sufficient to distinguish emission coming from the Nebula from that from the pulsar. The latter should be pulsed with the characteristic pulsar period and can be separated by the steady unpulsed emission from the former.

The database for analysis consists of all the ON runs used in the dc analysis plus some ON and tracking scans with non-optimum weather conditions. A total of 214 runs for ~102h of observation was available.

The arrival time of each events was recorded with a resolution of 1 microsecond. The Coordinated Universal Time (UTC) is maintained to an accuracy of 0.5 ms by a WWVB receiver. During the second season of observations(1987/8) a Rubidium clock was added to the timing system. Accuracy of the absolute time is maintained to < 100 microseconds. The arrival times in the lab frame were corrected for known clock drifts and then barycentered with MIT (PEP311) ephemeris [7]. Absolute phases were then computed by folding the time series with the pulsar's radio ephemeris [8].

The Azwidth parameter was used as before to reject almost 98% of the background data. The remaining 11,276 events were folded in the light curve shown in Figure 3. There is suggestion for a board light curve but this is not supported by strong statistical significance. The result contrasts with the narrow peak light curve claimed by Dowthwatite et al.[9]. We estimated 25% of the observed flux are pulsed with upper limit (95% confidence level) 4.5 x 10^{-12} photons-cm^{-2}-s^{-1}.

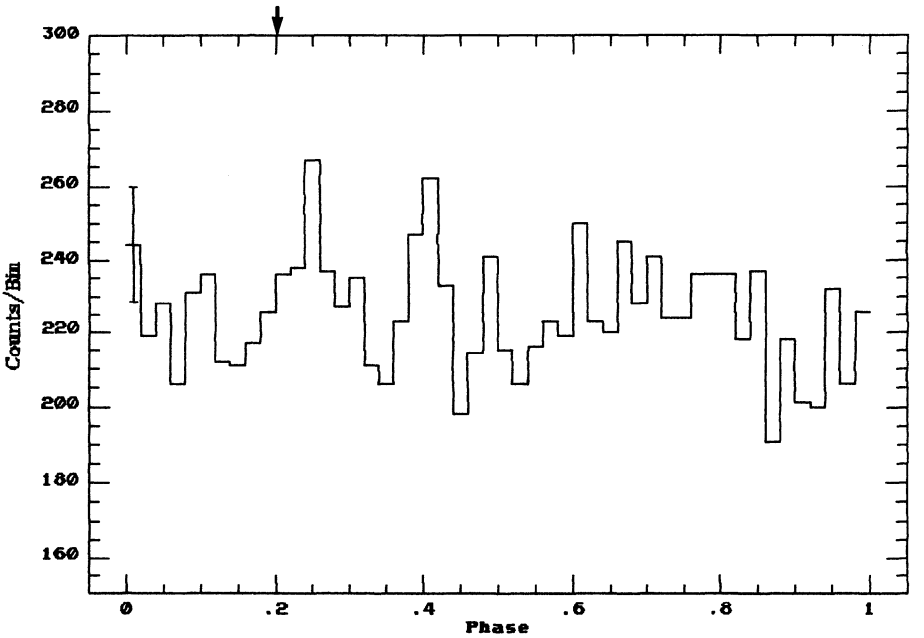

Figure 3. Selected Azwidth data light curve of the Crab Pulsar. Arrow indicates the radio main pulse position.

Energy and Flux

Monte Carlo simulations of the response of this telescope to a gamma-ray source spectrum assume a power law with differential exponent of -2.25 [4]. The collection area and energy threshold vary with zenith angle; to derive a flux we use the net excess observed with the Azwidth discriminator for $z < 30°$ (1043 events in 116x28 minutes). We derive a flux of 1.8×10^{-11} photons-cm^{-2}-s^{-1} for photons of energy greater 0.7 TeV. Further simulations are required to refine these values (whose uncertainty is greater than the small formal statistical errors); we estimate an uncertainty of order of a factor of 1.5 in both values.

Discussion

The detection of a flux of TeV gamma-rays from the Crab Nebula is further evidence for the Compton-synchrotron model of photon acceleration within the system [10,11,12]. To date this extended gamma-ray spectrum has not been detected at any other energy. At lower energies (100 MeV) a non-pulsed component has been detected but its steep spectrum [13] is not compatible with a Compton-synchrotron nebular origin and it is most likely that this is an unpulsed component of the pulsar. The extrapolated flux (Figure 4) falls a factor of ten below the flux reported here.

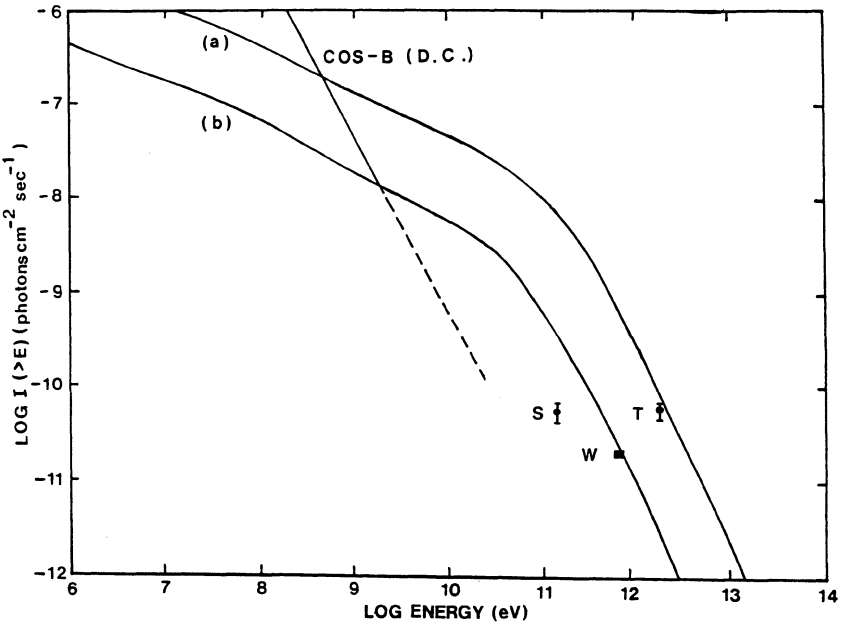

Figure 4. Compton-scattered spectrum of Crab Nebula for two values of magnetic field: (a) 10^{-4} gauss; (b) 3×10^{-4} gauss [11]. Extrapolated flux from COS-B measurements are shown [13] and measured points at TeV energies (S = Smithsonian [1]; T = Tien shan [15]; W = this work).

Although there is always more than statistical uncertainty in the energy thresholds and collection areas assumed for air shower systems, there is at least qualitative agreement between the flux reported here and that reported by Fazio et al. [1]. This measurement is in agreement of the value of the magnetic field derived from the earlier measurement [14]. This implies an ambient field close to the equipartition value of 6×10^{-4} gauss or a field that falls off radially from a value of 1×10^{-3} gauss at a radius of 0.1 pc from the pulsar. Although there was some suggestion of variability in the earlier data, both data sets are compatible with steady emission.

The existence of a steady source of TeV gamma rays has important consequences for the development of the field. For years this has been hampered by the absence of a standard candle which would act as a calibrator and a test for new techniques. Although weaker than ideal, the Crab Nebula appears to have the stability necessary for this role. It will be of interest therefore to compare the results from other experiments when they devote some time to the study of the steady emission from this source.

We are grateful to Kevin Harris for technical support in all aspects of the project. We are also grateful for assistance at various times from John Clear, Kevin MacKeown, Vic Stenger, Peter Gorham, and David Liebing. We acknowledge the support of U.S. Department of Energy, the Smithsonian Scholarly Studies Fund, and the National Board of Science and Technology of Ireland. A.M.H. and T.C.W. acknowledge the support of a NATO grant.

References

[1] Fazio et al., Astrophys. J. Lett., 175, L117 (1972)
[2] Cawley et al., Proc. 20th Int. Cosmic Ray Conf., La Jolla, 1, 131 (1985)
[3] Cawley et al., Proc. 20th Int. Cosmic Ray Conf., La Jolla, 3, 453 (1985)
[4] Hillas, A.M., Proc. 20th Int. Cosmic Ray Conf., La Jolla, 3, 445 (1985)
[5] Li, T.P. and Ma, Y.Q., Astrophys. J., 272, 317 (1983)
[6] Gibbs, K.: PhD. Dissertation, Univ. of Arizona, (unpublished), (1987)
[7] Ash, M.E. et al., Astron. J., 72, 338 (1967)
[8] Lyne, A.G. and Pritchard, R.S., Private Communication (1988)
[9] Dowthwaite et al., Astrophys. J. lett., 286, L35 (1984)
[10] Gould, R.J., Phys. Rev. Lett., 15, 511 (1965)
[11] Rieke, G.H. and Weekes, T.C., Astrophys. J. 15 577 (1969)
[12] Grindlay, J.E. and Hoffman, J.A., Astrophys. Lett. 8, L209 (1971)
[13] Clear et al., Astron. Astrophys., 175, 85 (1987)
[14] Grindlay, J.E., Proc. Gamma Ray Symposium, Goddard Space Flight Center, 84 (1976)
[15] Mukanov, J.B., Izv, Krimskol Astrophys. Obs. 67, 55 (1983)

PSR1509-58: A POSSIBLE OUTER GAP GAMMA RAY SOURCE

H.I. Nel, O.C. de Jager, B.C. Raubenheimer and A.R. North
Department of Physics
Potchefstroom University for CHE
Potchefstroom 2520
South Africa

Abstract: New results are presented which confirm the original detection of PSR 1509-58 as a source of TeV γ-radiation[1]. We confirm the triple peaked light curve at a confidence level of 99.91%. With this result the total significance of radiation from this source, as measured over two years became 1.1×10^{-5}. The data also indicate that the source is not radiating steadily, but goes through periods of radiation lasting ~ 10 days. and similar periods with no radiation. It was observed that the amplitude of the three peaks varies with time and a fourth peak appeared occasionally. It is shown that this behaviour is allowed by the outer gap model[7] provided that the pulsar has a free precession with a small amplitude and a period of the order of days.

1. Introduction

The young radio pulsar PSR 1509-58 (hereafter called MSH) in the supernova remnant MSH 15-52, was identified as a steady, pulsed source of TeV γ-rays, emitting mainly in the third harmonic of the known radio period at 150 ms[1]. This pulsar has the largest known period derivative of all known pulsars and together with Crab[2], Vela[3], PSR 1937+214[4] and PSR 1802-23[5] it forms a small group of isolated pulsars reported to radiate TeV γ-rays.

The detection is based on observations with the Potchefstroom TeV γ-ray telescope[6] which uses the atmospheric Cerenkov technique to investigate the possible existence of such very high energy γ-ray sources. MSH was observed from 10 to 21 June 1985 on 11 occasions in the tracking mode. A total of 37 334 Cerenkov events were registered over 20.9 hours of observations (hereafter called Observation A). Since the form of the TeV light curve was unknown, the H_M-test[1] was applied. It indicated a strong deviation from uniformity with a confidence level of 99.92% when the effects of a search within an independent Fourier spacing (IFS) and the initial uncertainty of the TeV γ-ray light curve were taken into account. Indications were found that this pulsar emits TeV γ-rays in a steady periodic mode over the 11 days of observations. The (3.6 ± 0.8) % signal

H. Ögelman and E. P. J. van den Heuvel (eds.), Timing Neutron Stars, 383–388.

strength leads to a TeV γ-ray luminosity of $\sim 3 \times 10^{34}$ erg.s^{-1} which corresponds well with the predicted TeV γ-ray luminosity when the outer gap model[7] is applied. The light curve shows three peaks and a harmonic analysis indicated that most of the power is concentrated in the third harmonic. It was shown[1] that the outer gap model[7] allows for up to four peaks to be visible in the TeV γ-ray range (see Section 4).

2. Further observations and confirmation

From 10 to 20 July 1985, 29 drift scans of 36 minutes duration each (up to four per night) were done through the position Cir X. As the positions of MSH and Cir X-1 differ only by 1.68° in right ascension and 1.97° in declination, we saw the possibility of searching for MSH in this data. This is made possible by the 2.2° field of view of our telescope. Depending on the assumed lateral distribution of Cerenkov light and the assumed aperture function an estimated 8-30 % of the MSH emission will be seen in a drift scan through Cir X-1. Selecting the 10 minutes around nearest approach between Cir X-1 and MSH resulted in 10 981 events over 4.8 h of observations (hereafter called Observation B).

Between 29 April and 28 June 1987 a further 27 observations with an average duration of 3 h were done in the tracking mode on MSH. A total of 274 981 events were registered during the 81.1 h of observations (hereafter called Observation C).

All the arrival times were transformed to the Solar System barycentre using the PEP 740R ephemeris[8]. The arrival times were then folded to produce the phases of the events modulo the pulsar period using an ephemeris[9,10], which is applicable up to March 1988, thus including all three observation periods.

As the analysis of the 1985 data showed that most of the power was in the third harmonic, we tested the hypothesis of uniformity against the hypothesis of emission in the third harmonic at the predicted radio period by using the test statistic $2nR^2_3$, where the general form is given by

$$2nR^2_\ell = (2/n)[(\sum_{i=1}^{n} \cos\ell\theta_i)^2 + (\sum_{i=1}^{n} \sin\ell\theta_i)^2]$$

where θ_i is the phases of the n events. Here nR^2_ℓ is the Rayleigh power of the ℓth harmonic. The analysis was conducted on a night to night basis to see if a signal was present over short time intervals. The probabilities of the individual nights were then combined[11]. Since no conclusion on the coherency from night to night is possible, this technique is called an incoherent analysis. This resulted in a chance probability for uniformity of 7.6×10^{-3} and 1.2×10^{-2} for Observations B and C respectively. These two independent sets of data thus confirm the original detection at a combined confidence level of 99.91%. Combination of these two detections with the original detection therefore rejects the hypothesis of uniformity of the data at the radio period at the 1.1×10^{-5} level.

To see whether the aforementioned effect peaked at or near the radio frequency, a periodic analysis in frequency was conducted over 660 μHz around the radio frequency using the incoherent technique. For Observation A the effect at the radio period is 5.4×10^{-5} while the corresponding

effect for Observations A, B and C (i.e. all the data) is 1.0×10^{-6} (Figure 1). Furthermore the results (Figure 1) illustrate that the main peak is shifted by 4.2μHz with respect to the radio frequency. However it has a FWHM of 35μHz, indicating that the effect is associable with the radio emission.

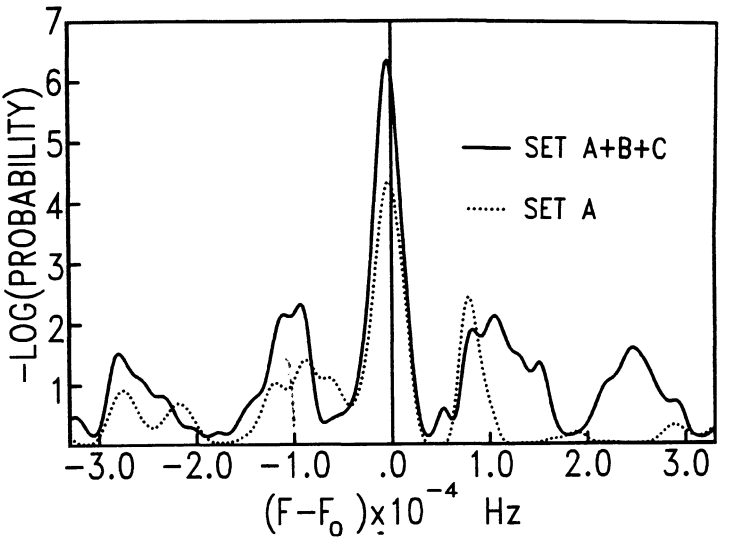

Figure 1: The incoherent combination of the Rayleigh powers at the third harmonic for Observation A and for the combination of Observations A, B and C as a function of the difference between the tested frequency F and the known radio frequency F_0.

3. Variability of the signal

The original detection inferred a steady pulsed signal over a period of 11 days. The new data covered four additional dark moon periods. To see whether the signal was indeed steady, the signal strength of each of the 49 nights were calculated, assuming emission only in the third harmonic. In this case the signal strength p is given by:

$$p = 2[(nR^2{}_3-1)/(n-1)]^{\frac{1}{2}} \pm [2/n]^{\frac{1}{2}}$$

where n is the number of events. During 53% of the nights a non-zero signal was seen. A runs test[13] on the five sets of signal strengths (Observations A and B and 3 dark moon periods during Observation C) indicates that the emission of three of the dark moon periods may be associated with a constant signal. During one dark moon period in 1987 the source did not show emission over at least 12 days, while Observation B indicates an enhancement of the signal lasting ~ 7 days. We therefore conclude that MSH may be switching from an on- to an off-state over time scales of ~ 10 days.

4. Interpretation of the light curves

An investigation of the light curves on a night to night basis shows an interesting behaviour as illustrated in Figure 2. The triple peaked structure (which gives rise to the strong third harmonic contribution) is evident on 13, 18 and 21 June 1985. The average peak separations are not 0.33, but 0.27, 0.3 and 0.43 respectively. Thus there seems to be space for a fourth peak between peaks 3 and 1. Such a peak was indeed seen on 16 June when peaks 1 and 3 seemed to be absent.

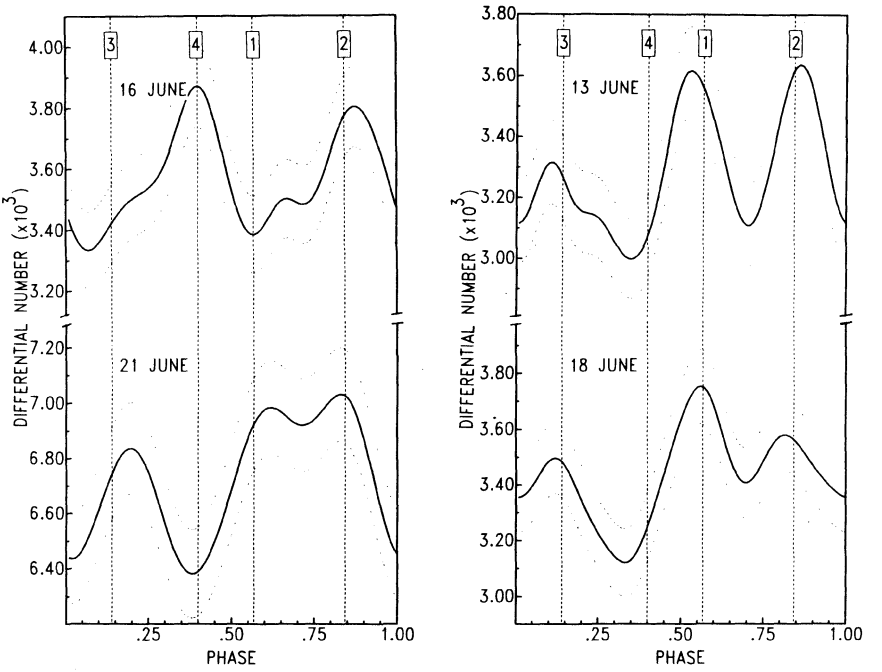

Figure 2 : Four representative light curves for PSR 1509-58 (using the Kernel Density Estimator technique with 1σ confidence bands), folded with the correct radio parameters, but not matched with the radio pulse. The vertical dashed lines indicate the average peak positions for the four observations. The peaks are numbered according to the outer gaps in Figure 3.

During fifteen nights the signal strength was large enough to warrant a further investigation of the light curves: Nine showed triple peaks, five showed double peaks (like 16 June) and there is one example where all four peaks were observed. A basic question is whether the fourth harmonic alone is significant in all the data: Adding the Rayleigh powers for the fourth harmonic incoherently, one obtains a confidence level of 98.2%.

The outer gap model for energetic radiation[7] allows the observation of four peaks on the light curve, provided that the angle between the magnetic axis **M** and the spin axis Ω is not too large[14]. If this angle is large, only two beams can be observed (e.g. Crab and Vela). Any outer gap (see Figure 3) lies on the last closed magnetic field line between the $\Omega.\mathbf{B} = 0$ null surface and the light cylinder and is the site for the production of two oppositely directed γ-ray beams, of which only one will reach the observer, depending on the orientation of the line of sight with respect to Ω . An observer at A or B will see gaps 3, 4, 1 and 2 in chronological order as the pulsar rotates. However, beam 4 passes closest to the neutron star surface and part of the TeV beam may be absorbed due to (1) magnetic pair production and (2) absorption on keV X-ray photons (if the latter are produced close to the polar cap), leaving only three of the four peaks visible. In general one can see four peaks, but the relative amplitudes may differ. Furthermore, due to the geometry of radiation and relativistic effects near the light cylinder, one cannot expect the interpeak separation to be exactly 0.25 as was observed. If there is a small amplitude free precession of the pulsar (with an amplitude which is approximately equal to the angle between A and B), peak 4 may become visible as the line of sight changes from A to B. Furthermore, the observer will also start to see different parts of the other outer gaps and spectral and/or intensity changes along any gap will result in the amplification or quenching of the corresponding peak on the TeV light curve, especially when the signal strength is low.

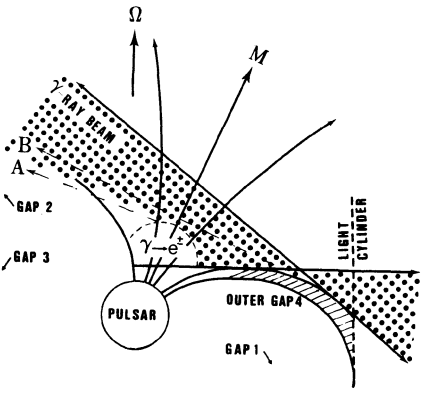

Figure 3. The outer gap model: showing outer gap 4 and the two corresponding oppositely directed TeV γ-ray beams. Any observer will see only one of the two beams from this gap. The other three gaps are also shown.

5. Conclusions

TeV γ-rays from the isolated radio pulsar PSR 1509-58 was initially detected in 1985 using the H_m test for uniformity. Nearly all the Fourier power was concentrated in the third harmonic. Using this new information, the Rayleigh power for the third harmonic was used to confirm the emission of γ-rays from this pulsar in subsequent observations during 1985 and 1987 giving a significance for this source which is now at the 1.1×10^{-5} level. The outer gap model can account for the observed luminosity and the fact that up to four beams may be visible. The observed dominant triple peak is indicative of the absorption of the fourth beam's TeV γ-rays by the strong B field (and possibly keV X-rays) close to the polar cap. However,

lower energy (E_γ < 1TeV) photons may pass through unabsorbed since the energy threshold for magnetic pair production for PSR1509-58 is about 1TeV. The occasional occurrence of the fourth peak may be indicative of a small amplitude free precession of the pulsar with a period of the order of days. Further TeV observations are necessary to confirm the results and interpretations presented here.

Acknowledgements

OCDJ and BCR wishes to thank K.S. Cheng for useful discussions and suggestions. G. van Urk, A.J. van Tonder and B. Visser are thanked for their assistance with the measurements.

References

1. De Jager, O.C. et al, **Astrophys. J., 329,** in press, (1988)
2. Dowthwaite, J.C. et al, **Astrophys. J., 286**, L35 (1984)
3. Bhat, P.N. et al, **Astron. Astrophys., 178,** 242 (1987)
4. Chadwick, P.M. et al, **Proceedings of NATO Advanced Research Workshop**, Durham (UK) (1986)
5. Raubenheimer, B.C. et al, **Astrophys. J., 307**, L43 (1986)
6. De Jager, H.I. et al, **South African J. Phys., 9**, 107 (1986)
7. Cheng, K.S. et al, **Astrophys. J., 300**, 500 (1986)
8. Chandler, J.F., private communication (1985)
9. Manchester, R.N. et al, **Nature, 313**, 374 (1985)
10. Manchester, R.N. and Siegman B.C, private communication (1988)
11. Eadie, A.T. et al, **Statistical Methods in Experimental Physics,** (Amsterdam: North Holland) (1972)
12. Mardia, K.V., **Statistics of directional data**, (New York. Acedemic Press) (1972)
13. Swed, F.S. and Eisenhart, C., **Ann. Math. Statist., 14**, 66 (1943)
14. Cheng, K.S., Private communication (1988)

THE ORIGIN OF HIGH-ENERGY RADIATION FROM THE CRAB PULSAR

F. Graham Smith
University of Manchester
Nuffield Radio Astronomy Laboratories,
Jodrell Bank, Macclesfield, Cheshire SK11 9DL UK

The spectrum of the double pulse from the Crab Pulsar is continuous from infra-red to very high energy gamma rays. Over this range the pulse shape (Fig.1) is almost unchanged, and we can assume that the radiation is from the same source. Radio emission is also observed from this double source, but the shape of the radio pulse is different. The radio spectrum is unconnected with the infrared, and the radio emission must be coherent.

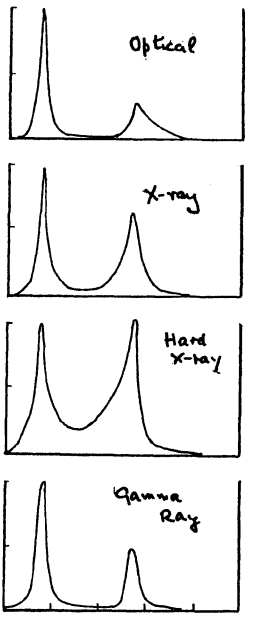

Figure 1. Pulse profiles for the Crab Pulsar

H. Ögelman and E. P. J. van den Heuvel (eds.), Timing Neutron Stars, 389–392.

The high-energy (optical to gamma) spectrum can be fitted by curvature radiation from particles streaming out along magnetic field lines. The problem is to identify the regions in which this emission occurs. Observations of linear polarisation at optical wavelengths provide a solution.

The observations have been described by Smith et al. (1988). They are presented in Fig.2 as a plot of the linear Stokes parameters throughout the double pulse. For most of the pulse cycle, including the lowest intensity of about 1% immediately before the main pulse, there is a high degree of linear polarisation, approaching 50%, at a constant position angle. This background polarised component is identified as a triangular point in Fig.2.

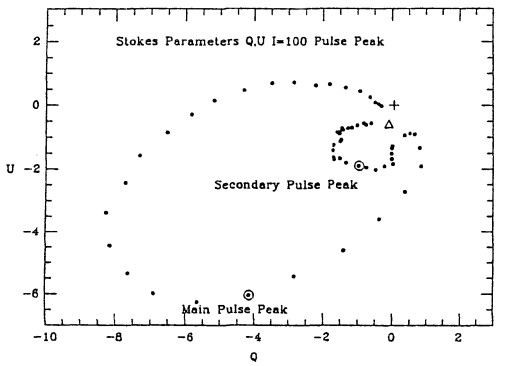

Figure 2. Linear Stokes Parameters Q,U through the cycle of the Crab Pulsar

The polarized component, and the position angle, of the two pulse components vary practically identically. The swing of position angle is about 90° (seen as a 180° swing in the plot of Stokes parameters); successive time markers on the two tracks show that the rates of swing are almost identical.

Any model of the source of optical radiation, and by implication of the whole high energy spectrum, must therefore contain two geometrically identical sources. The source of the radiation must in any case be at a large radial distance from the pulsar, so that gamma rays can emerge without loss in the magnetosphere by pair creation. It follows that the magnetic field is dipolar, or in any case symmetrical, leading us to expect a spacing of 0.5 cycle instead of 0.4 cycle between the pulses. We will see that this is explained by light travel time in a model where the radiation is emitted at distances approaching the velocity of light cylinder.

A further constraint on the model is set by the observed phase of the radio precursor, which is probably emitted in a radial direction from above a magnetic pole. An analysis of expected arrival phase for high-energy sources located on the boundary between the closed and open field lines of an orthogonal rotator (Smith 1986) showed that the

phase of the radio could only be fitted to a model in which the emitting regions were near the velocity of light cylinder.

The present observation of close similarity between the two pulses appears to rule out models in which they represent radiation from the leading and trailing edges of a single polar region. They can, however, be the leading edges of the two polar caps. The asymmetry which leads to the spacing of 0.4 cycle is obtained in a model suggested by Smith (1971), as shown in Fig.3.

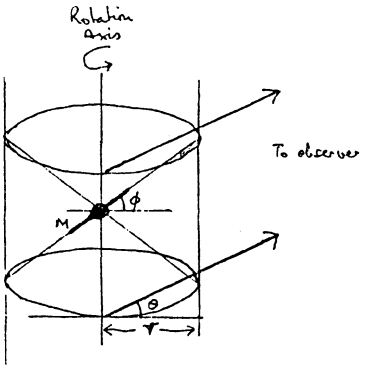

Figure 3. Two sources of radiation near the light cylinder. The difference in light travel time is $2r\tan\phi\ \sin\theta$.

In this model the high-energy radiation is emitted from a radial distance about 0.9 of the velocity of light cylinder, and is visible over a wide latitude range, as it is in a wide fan beam. The magnetic dipole is aligned about 60^{o} from the spin axis, and the observer's line of sight is also about 60^{o} from the spin axis. The departure from 0.5 phase interval is due to light travel time difference between two sources seen under nearly identical conditions.

CURVATURE RADIATION FROM MAGNETOSPHERIC GAPS

The emitting regions are identified with the outer magnetospheric gaps described by Cheng, Ho and Ruderman (1986). The particle flux, and the energy carried outwards, may be estimated by identifying the radiation as curvature radiation from electrons (or positrons) flowing outward along the field lines. The emitted radiation is Doppler shifted upwards in frequency, due to the rotation, by a factor 4.4. Allowing for this shift, the main parameters are:

Electron energies range from 5×10^{9} eV to 2.5×10^{13} eV.

Power spectrum $N(E) \propto E^{-\gamma}$, where $\gamma = 4$ at high energy and 1 at infrared.

Most of the energy flux is carried by particles with energy 5×10^9 eV to 5×10^{10} eV.

Total energy flux is 10^{38} erg sec^{-1} (of total available from spin-down = 10^{38} erg sec^{-1}; total required to power the Nebula = 10^{38} erg sec^{-1}).

The mechanism for radio emission from these high-energy regions is unknown.

If this model is correct, any high-energy radiation from other short-period pulsars may be expected to be in a wide fan-beam, giving a good chance of detection.

REFERENCES

Cheng, K.S., Ho, C. & Ruderman, M.A., 1986. Astrophys.J., 300, 500.
Smith, F.G., 1971. Nature Phys.Sci., 231, 191.
Smith, F.G., 1986. Mon.Not.R.astr.Soc., 219, 729.
Smith, F.G., Jones, D.H.P., Dick, J.B. & Pike, C.D., 1988. Mon.Not.R.astr.Soc., in press.

FUTURE U.S. X-RAY PROGRAMS RELATED TO TIMING NEUTRON STARS

Hale V. Bradt* and Jean H. Swank**

*Room 37-581, M.I.T., Cambridge MA 02139 USA
**Code 666, GSFC, NASA, Greenbelt MD 20771 USA

ABSTRACT. The timing capabilities of future U.S. x-ray astronomy satellite experiments that are adapted to timing studies of neutron-stars are presented. The X-ray Timing Explorer (XTE) is specifically designed for such studies. As a non-focusing and large-aperture (0.6 m^2) instrument, it is best suited to the study of the brightest $\gtrsim 10^3$ celestial x-ray sources. It features a continous low-background 2 - 200 keV response and flexible response to temporal phenomena by virtue of its all sky monitor and rapid maneuverability. It will carry out detailed energy-resolved studies of phenomena close to neutron stars (e.g. QPO's) because of its sub-milliscond timing (to 5 μs), its high telemetry rates (to 256 kbs), and the high-throughput of its data system (to $\gtrsim 2 \times 10^5$ c s^{-1}). Two AXAF focal-plane experiments (the high-resolution camera and the CCD Imager) are also described. The Japanese mission ASTRO-D, a moderate-resolution collecting system with substantial timing capability, is also presented. There is strong U.S. participation in the ASTR0-D program which is scheduled for a 1993 laumch. The imaging/collecting systems are best suited for faint-source timing or moderate to high resolution spectral studies at energies up to ~10 keV.

1. INTRODUCTION

The primary future US timing mission is the X-ray Timing Explorer (XTE). However, in principle, any x-ray astronomy mission carries out timing observations. The pervasive variability over wide ranges of time scales of most classes of x-ray sources means that any observation of an x-ray source is potentially a timing measurement that can be compared to earlier or later measurements. The time constants of interest for neutron stars include the free-fall time for matter close to a neutron star (~100 μs), the minimum expected spin period of a neutron star (~1.5 ms), typical spin periods (0.1 - 1000 s) , the orbital periods of neutron-star binary systems (10^3 s to 10^2 d), and the decay times of some x-ray novae (months). Preceding a description of the XTE mission and the science topics it will address, we choose to describe briefly several other instruments with significant timing capabilities, namely two experiments on the Advanced X-ray Astrophysics Facility (AXAF), and the Japanese-U.S. Mission ASTRO-D.

H. Ögelman and E. P. J. van den Heuvel (eds.), Timing Neutron Stars, 393–405.

2. AXAF INSTRUMENTS

The AXAF is a focusing high angular resolution (~0.5") system with a geometrical aperture of 1500 cm^2. It will probably carry 4 focal plane instruments. The two imaging systems described here have capability for relatively short time scale studies of neutron stars. The other two (Bragg Crystal Spectrometer and Calorimeter Spectrometer) are appropriate for studies of systems on longer time scales. Objective grating systems on AXAF may also be used in conjunction with the imaging systems to study temporal variability of spectral features at $E/\Delta E \sim 2000$ at 1/4 keV and ~100 at 8 keV. The current launch date is mid 1996.

2.1 High Resolution Camera (HRC)

The HRC is the successor to the High-resolution imager (HRI) on the Einstein satellite. It will have substantially improved capabilities in the areas of quantum efficiency, detector size, background rate, and intrinsic energy resolution. Its basic parameters are given in Table I and Figure 1. It consists of a CsI-coated multichannel plate. The counting rates are expected to be 20-40 times those of the HRI on Einstein or 5-10 times those of the Einstein IPC. The counting rate from 1/10 the Crab nebula is ~ 500 c s^{-1} Every event will be timed to 16 μs. Its sensitivity to time variable phenomena is indicated in Figure 2. The instrument will be developed at the Harvard-Smithsonian Center for Astrophysics; principal investigator S. Murray.

The HRC is a powerful tool for intrinsic timing/imaging studies of faint deep-space objects, e.g. temporal variability of active galactic nuclei and searches for pulsars in young supernova remnants and in M31. Also, the HRC may be used in conjunction with the gratings to carry out important timing studies of spectral features of x-ray binaries, e.g. orbital variations of Fe-line emission and absorption edges.

TABLE I
High-Resolution Camera on AXAF

Detector:	CsI-coated microchannel plate
Energy Range	0.1 - 8 keV
Energy resolution	100% at 1 keV
Effective Area	~300 cm^2 at 2 keV
Field of View	32' × 32'
Resolution	0.5" on axis
Readout time	16 μs (all events)
Maximum rate	375 c/s (telemetry limit); 1000 c/s (instantaneous)
Expected rates	5 - 10 times IPC on Einstein
Crab nebula rate	$\sim 5 \times 10^3$ c/s

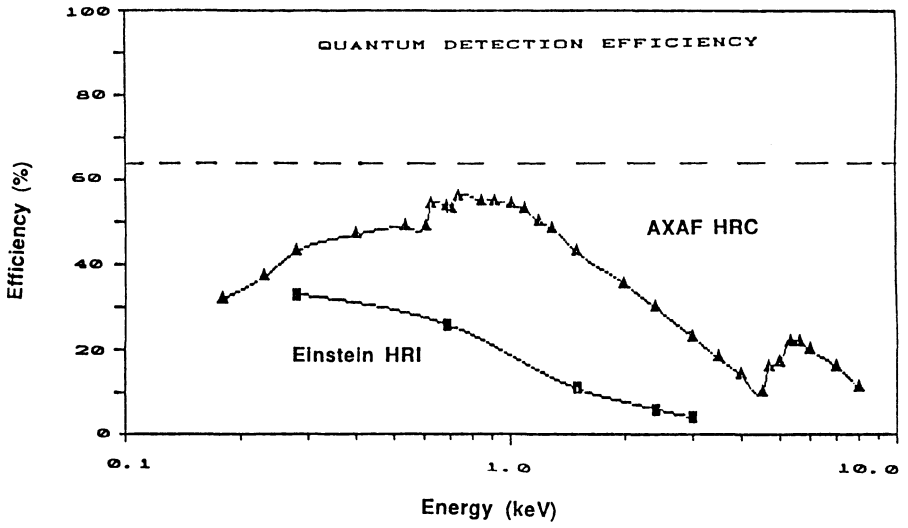

Figure 1: Comparison of the quantum detection efficiencies of the AXAF HRC and the Einstein HRI detectors. The dashed line represents the geometrical efficiency of the HRC. (from S. Murray, pvt comm.)

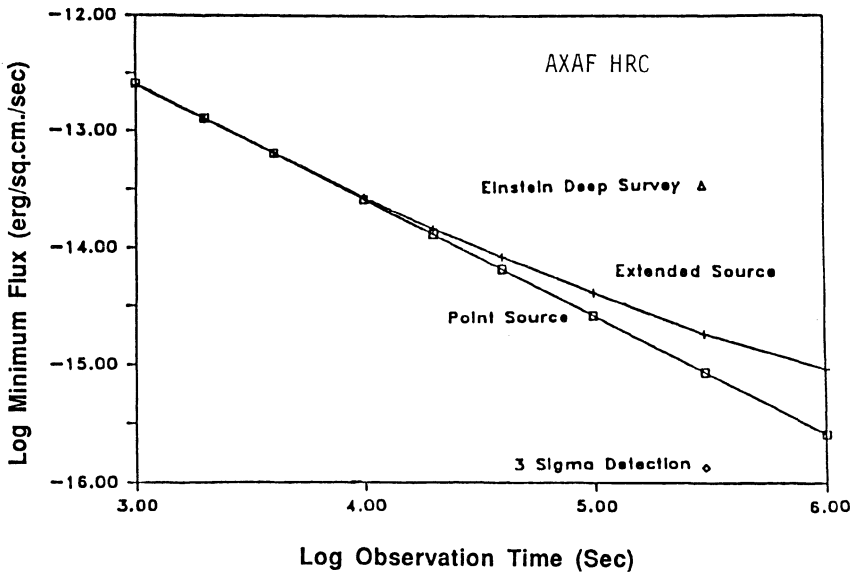

Figure 2: Sensitivity for a 5 sigma measurement with the HRC. A power law spectrum of photon index 1.4 and $N_H = 3 \times 10^{20}$ cm^{-2} was adopted. The minimum flux indicated is for the energy band 0.2 - 8 keV. 1.0 microCrab nebula corresponds to ~4 $\times 10^{-14}$ erg s^{-1} cm^{-2}. The Einstein deep survey is indicated for comparison.

1.2 AXAF CCD Imaging Spectroscopy (ACIS)

This instrument brings single-photon CCD detection to x-ray astronomy with excellent imaging and intrinsic energy resolution (~125 eV at 6 keV) and high efficiency to and beyond 6 keV (Fig. 3). The CCD design will be optimized for low energies by thinning the SiO_2 protective overcoat to 0.05 μm and for high energies by a thickening of the Si epitaxial layer to 40 μm. The basic characteristics of ACIS are given in Table II. The attainable time resolution is limited by the readout time of ~ 10 s for the full field. However if the source location in the field is known, a single strip can be read out in 100 μs. Bright-source studies are limited by the requirement that each pixel contain ≤ 1 detected photon per readout. Sources of intensity ~1/5 Crab (~1000 c/s) could be studied easily in the 'strip' mode. The instrument is being provided by Penn State University, JPL, and M.I.T.; principal investigator G. Garmire; deputy PI G. Ricker.

The ACIS instrument is ideal for studies of the temporal variabilty of spectral features such as the Fe lines in neutron-star binaries, with energy resolution far exceeding that of traditional proportional counters. Its excellent high-energy response is well matched to Fe-line studies at ~ 6-7 keV and for pulsar searches in absorbed regions of M31. Pulse profiles of pulsars as a function of energy can be studied over large ranges of accretion rates in order to determine accretion geometries and beaming patterns.

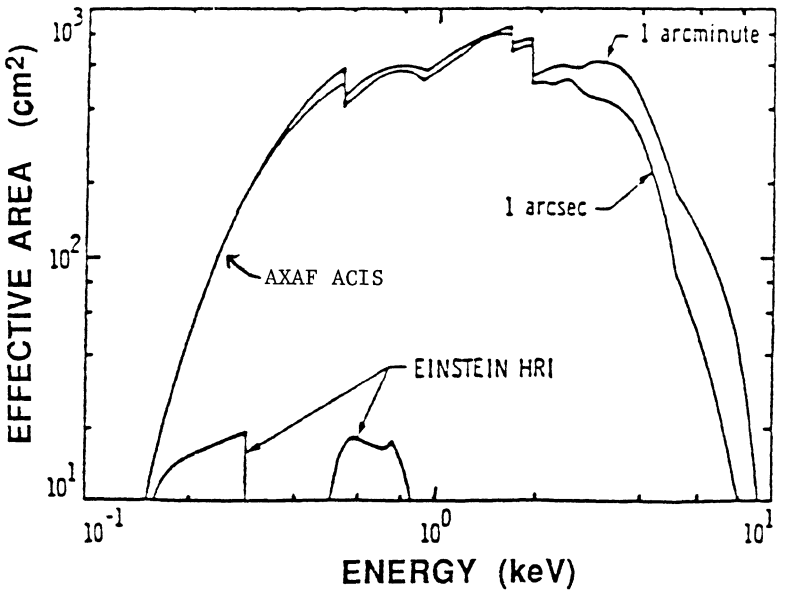

Figure 3. Effective area of AXAF/ACIS. The Einstein HRI is shown for comparison. (from G. Ricker, pvt. comm.) The sensitivity improves with integration over a large number of pixels (e.g. 1 arcmin) at high energies because of photon scattering in the system.

TABLE II
CCD Imager / spectrometer on AXAF (ACIS)

Detector:	CCD; single photon detection
Energy range	0.3 - 8 keV
Energy Resolution	2% at 6 keV
	6% at 1 keV
Effective Area	400 - 600 cm^2 at 3 keV
Field of View	18' × 12'
Angular Resolution	~ 0.5"
Readout time	10 s (entire field)
	100 μs (one strip)
Maximum rate	~1/5 Crab ≈ 1000 c/s

3. ASTRO-D (JAPAN-U.S.)

The next Japanese x-ray astronomy mission (following GINGA, now in orbit) will consist of a set of 4 conical foil assemblies of modest angular resolution (~1') and large collecting area (Fig. 4) over a range of 0.4 to 10 keV. Two of the assemblies will have imaging gas scintillation proportional counters (IGSPC) at the foci, and the other two will have single-photon detecting CCD's.

The basic parameters of the systems are given in Table III for the current preliminary design. The conical mirror assemblies are being developed at GSFC (P. Serlemitsos) and the CCD detector system at MIT (G. Ricker); both groups will work as part of instrument teams consisting of Japanese and American scientists and engineers. The Japanese will provide the IGSPC systems, the on-board data system and spacecraft, and the overall direction of the program. A strong guest program for American (and possibly other) observers will follow the 1993 launch. The project leader is Y. Tanaka.

The major thrust of this mission will be high throughput spectroscopic studies where imaging requirements are modest, e.g. spectral features in QSO, supernova, and galactic sources. The net effective area (all 4 detection systems) will be ~500 cm^2 in the 4 - 8 keV region. The total counting rate for the Crab nebula (over all energies and all detectors) is roughly estimated to be about 5000 c s^{-1}. Searches for pulsars in M31, the study of variability of accretion rates in distant binary systems, and the discovery and study of neutron stars in SNR are all important timing objectives. ASTRO-D could be the instrument that discovers, as an x-ray pulsar, the expected underlying neutron star in SN1987A .

TABLE III
ASTRO-D Parameters (Preliminary)

Mirror Assemblies	
Number	4
Angular resolution	1' (half power radius)
Effective Area (4 mirrors)	~ 1000 cm^2 at < 2 keV ~ 600 cm^2 at 2 - 7 keV
Imaging Gas Scintillation Proportional Counters	
Number of units	2
Net effective area (2 units)	250 cm^2 at 3 keV
Window	~37 μm Be window
Energy range	1 - 12 keV
Energy resolution	8% at 6 keV
Spatial resolution	1 mm (ang. resolution ~1')
CCD Assemblies	
Number units	2
Effective area (2 units)	~200 cm^2 at 3 keV
Energy range	0.3 - 10 keV
Energy resolution	2% at 6 keV, 6% at 1 keV
Telemetry	32 kb/s for 4 orbits per day 4 kb/s for 11 orbits

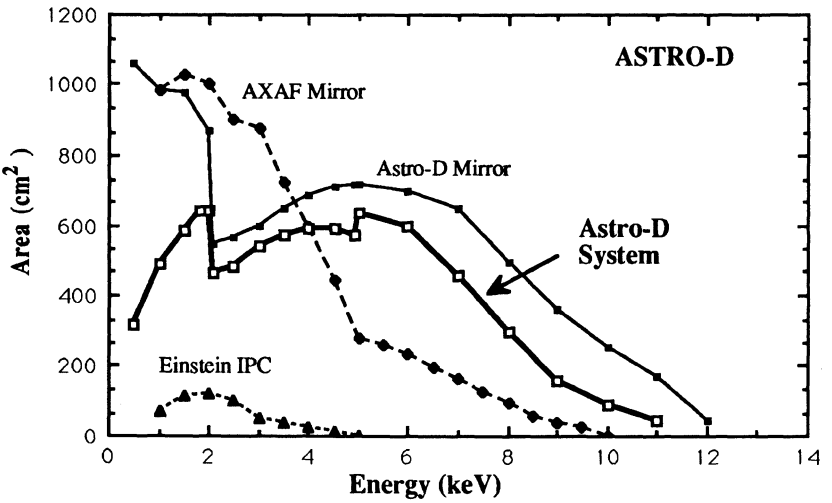

Figure 4: Approximate areas of the ASTRO-D mirror and the ASTRO-D mirror/detector system versus energy (current design). The effective system area (dark curve) is the approximate total of all 4 focal plane instruments. The effective areas of the AXAF Mirror and of the Einstein IPC are shown for comparison. (Adapted from data provided by Y. Tanaka, P. Serlemitsos, and G. Ricker.)

4. THE X-RAY TIMING EXPLORER (XTE)

The X-ray Timing Explorer, scheduled for launch in early 1994, is directed toward timing studies of compact objects (galactic and extragalactic). It will carry 3 instruments, a large-area proportional-counter array (PCA), a high-energy crystal scintillation experiment (HEXTE), and an all-sky monitor (ASM). The instruments and their fields of view are shown schematically in Fig. 5, and the effective areas as a function of energy are shown in Fig. 6. The essential parameters of XTE are given in Table IV. XTE will be carried on the Explorer Platform for at least 2 years beginning in early 1994. The observing time will be devoted 100% to Users (Guests). The mission scientist is J. Swank.

The mission has been previously described by McClintock and Levine (1984); it has since been reduced in aperture by about 30% to reduce costs and to make it compatible with a Delta vehicle should the shuttle become unavailable. The science potential of the XTE and the Japanese Ginga missions has been discussed by Epstein, Lamb and Priedhorsky (1985).

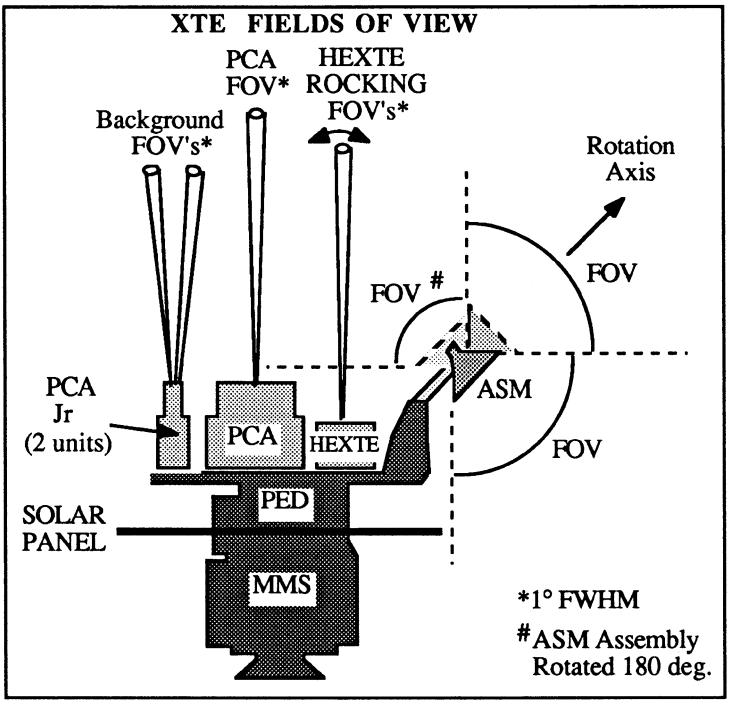

Figure 5. Schematic view of XTE showing the fields of view of the Proportional Counter Array (PCA), the High-Energy X-ray Timing Experiment (HEXTE), the All-Sky Monitor (ASM), and elements of the Explorer Platform, e.g., the Multi-Mission Spacecraft (MMS) and the Payload Equipment Deck (PED).

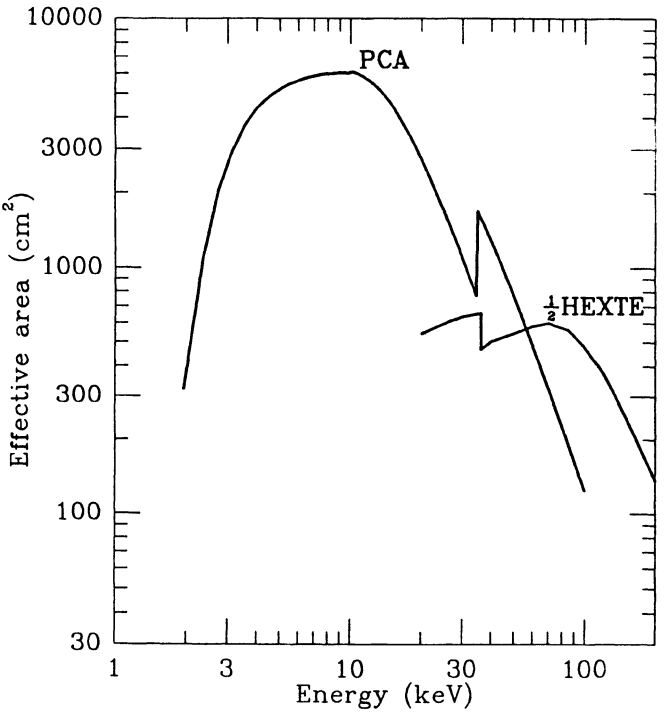

Figure 6. Effective Area of the PCA and of 1/2 of the HEXTE. The two HEXTE assemblies each rock on and off the source so that only 1/2 the area is on the target source at a given time.

4.1 The Explorer Platform

The Explorer Platform is, in essence, the same spacecraft (MMS) that carries the Solar Maximum mission. It is highly maneuverable (6°/min) and can point the PCA/HEXTE to any point on the sky on any day of the year, if the PCA-sun angle is > 30°. It will provide, via tape dumps through TDRSS, an average telemetry rate of 26 kbs for the scientific instruments and 256 kbs for up to 30-min a day. Neither XTE nor the Platform carries expendables that would artificially limit the lifetime. XTE will be preceeded on the Platform by the Extreme Ultraviolet Explorer (EUVE). XTE will be carried into orbit on the shuttle, the Platform/EUVE will be captured and placed in the shuttle bay, XTE will be exchanged with EUVE in the bay, and then the Platform/XTE will be deployed. The orbit will, of necessity, be a low-earth orbit at altitude ~ 550 km at 28° inclination. The XTE mission would terminate when another experiment replaces it on the Platform.

4.2 The Proportional Counter Array (PCA)

The proportional counter array consists of 5 large detectors with a total area of 6250 cm^2. Each detector will be a large version of the HEAO-1 HED detectors that featured low-background through efficient anti-coincidence schemes including side and rear chambers

TABLE IV
X-Ray Timing Explorer Parameters and Features

POINTED INSTRUMENTS

6250 cm^2; Xe Proportional Counters; 2 - 60 keV; 'PCA'; GSFC
HEAO-A2 type; low background.
1600 cm^2; NaI/CsI; 15 - 200 keV; 'HEXTE'; UCSD
Chops on-off source continuously; low background

PARAMETERS OF POINTED INSTRUMENTS

Net Area	3000 cm^2 at 3 keV 6000 cm^2 at 10 keV 1200 cm^2 at 50 keV (NaI); 800 cm^2 at 50 keV (Xe) 1100 cm^2 at 100 keV 300 cm^2 at 200 keV
Field of View	1^o FWHM circular; PCA and HEXTE coaligned
Energy Resolution	18% at 6 keV (Xe) 18% at 60 keV (NaI)
Sensitivity*	0.1 mCrab 2-10 keV (minutes); limit of source confusion 1 mCrab 90 - 110 keV (3σ; 10^5 s)
Time Resolution	5 μs
Background	2 mCrab 2-10 keV 100 mCrab (1×10^{-4} cts cm^{-2} s^{-1} keV^{-1}) at 100 keV
Telemetry	24 kbs continuous; 256 kbs ~30 min/day
Flight Data System(MIT) (for PCA/ASM)	Flexible binning criteria (microprocessor-driven) Pulsar folding and high time resolution burst searches Simultaneous binning with different criteria Real-time sub-ms resolution FFT's High throughput, $>2 \times 10^5$ ct s^{-1}

ALL-SKY MONITOR ('ASM'; MIT)

Energy Range	2-10 keV; 3 energy channels
Net Area	90 cm^2 net
Positional Resolution	0.2^o x 2^o (Positions to 3' x 30')
Scan time	90 min; 80% of the sky per orbit
Sensitivity	30 mCrab in 90 min; 10 mCrab in 1 day
Dissemination	Routine analyses carried out immediately to assess need for pointed studies, i.e. a S/C maneuver. Results placed in public domain (computer access) to aid community in proposal writing, optical observations, etc.

SPACECRAFT and OPERATIONS

Maneuverability	6^o/min; precise to < 0.1 deg.; aspect to 0.01 deg. . 85% of sky accessible (includes anti-sun pointing for coordinated observations)
Response to Transients	Few hours after detection

USER (GUEST) PROGRAM

PCA/HEXTE	100% of time competitively assigned. (PI's also compete) Single object, class studies, or contingency (i.e. transients) proposals allowed Observing at SOC or at PI institutions (with less support) Remote observing from observer's home institution possible Multi-wavelength coordinated observations encouraged
ASM	Proposals for specialized analyses possible

* 1 mCrab ≈ 1.06 μJy at 5 keV

and a propane top layer. The two windows (the front one and the one separating the propane and xenon chambers) are each 25-μm Mylar. The xenon is 3.6 cm thick at 1.0 atmosphere. The PCA is effective over the range 2-60 keV with 18% energy resolution at 6 keV and 256-channel pulse height discrimination. The 1° FOV (FWHM) yields a source confusion limit at ~0.1 mCrab. The PCA is being provided by GSFC; principal investigator S. Holt.

The Crab nebula will yield 8700 c s^{-1} (2-10 keV) and 1200 c s^{-1} (10-30 keV) in the PCA. The backgrounds in these 2 bands are respectively 20 and 24 c s^{-1}, corresponding to 2 and 20 mCrab respectively. With these backgrounds, an AGN source of intensity 1.3 mCrab (2 - 10 keV) and energy index 0.7 will be detected at $>2\ \sigma$ in only 1 s at 2 - 10 keV and at 3σ in 10 s at 10-30 keV. Monitored anticoincidence rates will yield the background reliably to at least 10% of its value. Two counters of similar construction, but with area of only 300 cm^2 each and with offset fields of view, will be used to continuously monitor the background in order to refine and confirm the background model.

The microprocessor-driven flight data system for the PCA can handle high throughputs to $\gtrsim 2 \times 10^5$ c s^{-1} (Sco X-1 yields 160,000 c s^{-1}) and can time events to 5 μs. The data stream can be binned simultaneously in several modes each of which can be chosen arbitrarily for optimum tradeoffs of timing and spectral information. The binned data can be preprocessed prior to being telemetered. Burst searches at high time resolution, pulse folding, and on-line FFT's and autocorrelations with time resolutions to 10 μs are features of the system in the current design. The data system, which will also be used for the ASM, is being provided by MIT.

4.3 The High-Energy X-ray Timing Experiment (HEXTE)

The HEXTE experiment consists of two rocking clusters of NaI/CsI phoswich detectors which cover the energy range 15 - 200 keV. Each cluster contains 4 detectors; the total area of the entire system is 1600 cm^2 The clusters (or the collimators) will be continuously rocked on and off source for background subtraction. An automatic gain control feature further refines the background knowledge. The field of view is 1° FWHM and is coaligned with the PCA when on target. The HEXTE flight data system will provide the following modes: binned, event encoded, pulsar fold, flare catcher, and an optimum high-speed code. The telemetry rate for HEXTE will be at least 3 kbs. The instrument will be provided by UCSD; principal investigator R. Rothschild.

The Crab nebula will yield 170 c s^{-1} (15-30 keV) and 130 c s^{-1} (>30 keV) in 1 cluster (1/2 HEXTE). The background in these energy bands will be ~6 and ~29 c s^{-1} respectively. At 100 keV, the background is about 100 mCrab (1×10^{-4} cts cm^{-2} s^{-1} keV^{-1}). In the 90-110 keV band, the limiting sensitivity is expected to be about 1 mCrab (1×10^{-6} cts cm^{-2} s^{-1} keV^{-1}) or 1% of the instrument background. This sensitivity can be reached at 3σ in 10^5 s.

4.4 The All Sky Monitor (ASM)

The ASM consists of 3 'scanning shadow cameras' (SSC) on one rotating boom with a total net effective area of 90 cm^2. Each SSC is a one-dimensional 'Dicke camera' consisting of a 1-dimensional mask and a 1-dimensional imaging proportional counter. A weak-source detection provides a single line of position of $0.2^\circ \times 90^\circ$. Two of the units view perpendicular to the rotation axis and serve as 'crossed slat collimators'; the third unit

views along the axis of rotation and serves in part as a 'rotation modulation collimator'. The crossed slats provide a positional resolution of $0.2^o \times 2^o$ for a weak source and $3' \times 30'$ for a bright source. A spacecraft maneuver could reduce this to $3' \times 3'$. The ASM will be provided by MIT; principal investigator H. Bradt.

The sky will be scanned once every 90 min, and 80% of the sky will be surveyed to a depth of 30 mCrab (about 50 sources). Frequent spacecraft maneuvers will insure that 100% of the sky is surveyed each day. In one day, the limiting sensitivity becomes ~10 mCrab. The instrument is sensitive to 2 - 10 keV x rays which will be telemetered in 3 channels. The intensities derived from the data will immediately be made available to the duty scientist and to the community in general (via computer bulletin board). The results will make possible rapid acquisition by the PCA/HEXTE of sources when they undergo a change of state, e.g. to the horizontal branch or a transient.

4.5 Science Objectives of XTE

XTE is expected to carry out pioneering studies in the following measurement domains: sub-ms timing and in rapid response to temporal phenomena. In addition it will forge substantial new ground in spectral studies to ~200 keV, in the facilitation of multiwavelength observations, and in long-term very-sensitive monitoring of temporal phenomena (sampling with the PCA).

The principal scientific objectives and expected results of XTE are given here. The results reflect directly specific experiments. Each makes use of XTE's particular combinations of strengths. Most but not all pertain to neutron star timing.

Nature of the X-ray source in active galactic nuclei. XTE studies of quasars, Seyfert galaxies and BL Lac objects will determine conditions in the innermost regions of AGN by (1) bounding the total x-ray luminosity, (2) searching for a characteristic frequency by obtaining the PDS spectrum to $\lesssim$ 200s, and (3) exploring the very-low-frequency variations (days to years). XTE will also determine if AGN are the major contribution to the diffuse background through measurement of their spectra to > 100 keV.

Structure of accreting neutron stars. XTE results will improve substantially the constraints on models of the internal structure of neutron stars through measurements of rotation-rate changes in accretion-driven x-ray pulsars.

Behavior of matter close to a stellar black hole. XTE will determine the character of the millisecond variability (aperiodic and quasi-periodic). This will provide strong diagnostics of the innermost regions of accreting black holes, including possibly (quasi-)periodicities from relativistic matter in the innermost orbits.

The Nature of Quasi-Periodic Oscillators in Accreting Systems. XTE will search for millisecond coherent pulsing in low-mass x-ray binary systems (LMXB) strongly suggested by quasi-periodic oscillations (QPO) in the detected flux. If successful, this will provide direct evidence for magnetic-field decay in neutron stars and will prove unequivocally that these systems are the precursors of millisecond radio pulsars. XTE will also determine directly the processes and geometries of the formation of the x-ray spectrum in LMXB through studies of phase lags (as a function of energy) of QPO.

X-ray transient studies of accretion torques, compact-star masses, and stellar winds. XTE will use the changing accretion-flow rate in 'hard' pulsing transients to determine, with minimal ambiguity, the accretion torques, magnetic fields, and pulse-beaming geometries in high-mass x-ray binaries. XTE will also detect and identify 10 to 20 'soft' x-ray transients that will lead to strong lower limits for the masses of the compact objects. This could strengthen greatly the case for stellar black holes.

The magnetic fields of neutron stars and white dwarfs . XTE will determine white-dwarf magnetic fields and the temperatures and geometries of accretion shocks in magnetic cataclysmic variables through phase resolved x-ray spectral measurments to $\gtrsim$ 30 keV. XTE will also measure the directions and strengths of magnetic fields of neutron stars and obtain the plasma conditions in them through studies of cyclotron features to ~150 keV.

Nature of x-ray emission from the galactic plane. XTE will map the structure and temporal variability of the galactic 'ridge' with 1-deg^2 and 1-day resolutions with the objective of elucidating the nature of the x-ray emission. Newly discovered (in x-rays) pulsing Be-star systems will yield stellar-wind parameters.

Search for a neutron star in SN 1987A . XTE will search for pulsing x-rays from SN1987A that may be visible only above ~20 keV in 1994-6. Discovery would demonstrate that a black hole was not formed in the collapse. Follow-on pulse-timing studies would address fundamental physical issues, specifically the evolution of the progenitor from a search for binary motion, the magnetic dipole moment of the pulsar from the braking index, and the structure of the neutron star from glitch studies.

Studies of new prototype objects. Discoveries of objects that extend or modify the characteristics of an x-ray class are still forthcoming from the ongoing identification of x-ray sources in the HEAO-1 LASS catalog (Wood et al. 1984), the all-sky survey that underlies the XTE mission. The numbers of sources in each class of identified 'bright' hard x-ray emitters (e.g. BL Lac objects, LMXB) remains modest , from a few to ~100 (e.g., Bradt et al 1988). Thus newly identified objects frequently are found to have have unusual properties. These objects often become prototypes of new subclasses worthy of study at all wavelengths, e.g. by XTE. ROSAT identifications will further infuse new science into the XTE program. We stress that the population characteristics of the ~10^3 brightest x-ray sources in the sky are not yet fully known and that XTE will make a substantial contribution to their definition.

5. ACKNOWLEDGMENTS

The authors are grateful to the numerous XTE, AXAF, and ASTRO-D team members whose ideas are incorporated herein, especially S. Holt, K. Jahoda, A. Levine, S. Murray, G. Ricker, R. Rothschild, P. Serlemitsos, and Y. Tanaka. In addition, we are grateful to many colleagues, including the above, who have contributed to recent discussions about the scientific contributions that XTE could make in the context of our current knowledge. We particularly thank F. Lamb, J. McClintock, and R. Mushotzky for their efforts in this regard. Our contributions to this work are supported by NASA.

6. REFERENCES

Bradt , H., Remillard, R., Tuohy, I., Buckley, D., Brissenden, R., Schwartz, D., Roberts, W. 1988 *Proceedings of the International Symposium on The Physics of Neutron Stars and Black Holes*, Tokyo, Feb. 1988. In press

Epstein, R., Lamb, F., and Priedhorsky, W. in *Astrophysics of Time Variability in X-Ray and Gamma-Ray Sources, Proceedings of the Taos Workshop , Los Alamos Science* , No. 13, 1986)

McClintock, J.A. and Levine, A. M. 1984, in *High Energy Transients in Astrophysics,* ed. S. Woosley, Am. Inst. of Phys. NY, p. 642.

Wood, K., Meekins, J., Yentis, D., Smathers, H., McNutt, D., Bleach, R., Byram, E., Chubb, T., Friedman, H. 1984 *Ap. J. Suppl.* **56**, 507.

FUTURE EUROPEAN PROGRAMS IN X-RAY ASTRONOMY

Günther Hasinger and Joachim Trümper
Max-Planck-Institut für extraterrestrische Physik
D-8046 Garching bei München
Federal Republic of Germany

Abstract.

The properties of the major European X-ray telescopes of the future are summarized here with particular emphasis on the German X-ray satellite ROSAT which is the next mission to be launched.

1. Introduction

About 26 years ago Sco X-1, the first cosmic X-ray source, has been discovered by Giacconi and collaborators (1962). Since then X-ray astronomy has become an integral part of astrophysics, taking an equal role with astronomy in other wavebands in the exploration of our universe. Although many exciting results have been achieved with sounding rocket and high-altitude balloon payloads, satellite missions have played the most important role in X-ray astronomy in the last 15 years.

Table 1: X-ray Satellites of the Past

Satellite	Country	Launch	Instrumentation
UHURU	USA	1970	collimated counters
ARIEL-V	UK	1971	collimated counters
ANS	USA/NL	1974	collimated counters
SAS-3	USA	1975	coll. counters, parabolic collectors
OSO-8	USA	1975	collimated counters
HEAO-1	USA	1977	collimated counters
Einstein	USA	1978	imaging telescope (IPC,HRI,SSS,FPCS,OGS) + collimated counter (MPC)
Hakucho	J	1979	collimated counters
Tenma	J	1983	collimated counters (GSPC)
EXOSAT	ESA	1983	collimated counters + GSPC + imaging telescope (PSD,CMA,OGS,filters)

H. Ögelman and E. P. J. van den Heuvel (eds.), Timing Neutron Stars, 407–418.

Table 1 lists the major X-ray satellites of the past, starting with the milestone UHURU which performed the first all-sky survey in X-rays, and ending with ESA's X-ray observatory EXOSAT which at present is still keeping us busy with exciting results. A total of ten X-ray satellites is listed in the sixteen years between 1970 and 1986. The main type of instrumentation on these payloads were collimated proportional or scintillation counters. Only the Einstein and EXOSAT satellites were carrying imaging X-ray telescopes.

Table 2 lists the present and future X-ray satellite programs. It starts with the Japanese Ginga satellite, carrying the largest array of proportional counters ever flown, and the X-ray payload on the QUANT astrophysical module which is docked to the Sovjet space station MIR. Both of these instruments are currently active and produce exciting results. One example is the discovery of X-rays from SN1978a last fall, almost simultaneously from both instruments (Dotani et al., 1987, Sunyaev et al., 1987).

The list continues with the missions of the near and further future. The tentative launch dates are also given. A clear evolution in instrumentation becomes obvious from table 2: almost all future X-ray and XUV satellites will be equipped with imaging telescopes. Various kinds of focal plane instrumentations are also indicated. Also a trend to more and more multinational projects is evident. The major European telescopes will be briefly discussed here.

Table 2: X-ray Satellites of the Present and Future

Satellite	Country	Launch	Instrumentation
Ginga	J/UK	1987	collimated counters
QUANT/MIR	USSR/NL/ UK/G/ESTEC	1987	coded mask + coll. counter + GSPC
ROSAT	G/USA/UK	1990	XRT: imaging telesc. (PSPC, HRI) WFC: imaging telesc. (CMA, filters)
EUVE	USA	1991/2	imaging telescope (CMA, filters)
XTE*	USA	1991/2	collimated counters
SAX*	I/NL/ESTEC	1992	coll. counters, imag. telesc. (IGSPC)
Spectrum-X*	USSR/DK/ UK/G/I	1993	XPECT: 2 imag. telescopes (SSD) JET-X: 2 imag. telescopes (CCD)
Astro-D	J/USA	1993	imag. telesc. (IGSPC, CCD)
SPEKTROSAT*	G	1994	imag. telesc. (OGS, PSPC, HRI)
AXAF*	USA	1996	imag. telesc. (CCD, HRC, OGS, FPCS, Calorim.)
XMM	ESA	1998	3 im. telesc. (CCD, IGSPC, RG)

* project not finally approved

2. ROSAT

The main scientific objective of the ROSAT mission (Trümper, 1983) is to perform the first all-sky survey with an imaging X-ray telescope and the first all-sky survey in the XUV waveband. The X-ray all-sky survey will be several orders of magnitude more sensitive than previous surveys. About 100000 new X-ray sources, comprising almost every class of astronomical objects from nearby ordinary stars to the most distant quasars, are expected to be discovered. The XUV survey enters an almost unexplored domaine. After completion of the sky survey (1/2 year) the instruments will be used for detailed pointed observations of selected targets. The pointed mode, compared to the Einstein telescope, provides substantially improved sensitivity as well as angular and spectral resolution. It will be exclusively open to guest observers.

Table 3: Characteristics of the ROSAT XRT

Mirror System	
material	Zerodur, gold coated
outer diameter	83 cm
inner diameter	37 cm
geometrical area	1141 cm^2
focal length	240 cm
mean grazing angle	2^o
on axis resolution	3.5 arcsec (HEW)
PSPC	
size	8 cm x 8 cm
gas filling	argon,xenon,methane
background rejection	99.5 %
energy resolution at 1keV	40 % FWHM
Telescope with PSPC	
field of view	2^o diameter
energy range	0.1 - 2 keV
effective area at 1 keV	420 cm^2
0.28 keV	470 cm^2
on-axis angular resolution at 1 keV	25 arcsec FWHM
0.28 keV	1 arcmin FWHM
Telescope with HRI	
field of view	36 arcmin diameter
on-axis angular resolution	7 arcsec HEW

2.1 Instrumentation

The main instrument of the ROSAT observatory is the X-ray telescope (XRT) with a fourfold nested Wolter type I mirror system of 83 cm diameter and three different focal-plane detectors. The design, construction and performance of the X-ray mirror system is described by Aschenbach (1988). The focal plane assembly consists of a caroussel carrying two position-sensitive proportional counters (PSPC), built by MPE (Briel and Pfeffermann, 1986) and a 'high-resolution imager' (HRI), provided by SAO (Henry et al., 1977). The PSPCs have an angular resolution of about 25" and a spectral resolution of about 40 % at 1 keV. The HRI is a channelplate detector with an angular resolution of a few arcsec but no energy resolution. A detailed description of the XRT focal plane instrumentation is given by Pfeffermann et al., (1987). Table 3 summarizes the main characteristics of the ROSAT XRT.

The second instrument aboard ROSAT, the British Wide-Field Camera, is a smaller telescope for the extreme ultraviolet (XUV). It consists of a three-fold nested Wolter-Schwarzschild type I system of 58 cm diameter and 53 cm focal length. Two identical microchannelplate detectors and several thin filters can be moved into the focus. Table 4 summarizes the main WFC characteristics.

Table 4: Characteristics of the ROSAT WFC

Mirror System	
outer diameter	57.6 cm
focal length	52.5 cm
field of view	5^o diameter
energy range	0.21 - 041 keV (60 - 300 Å)
on-axis angular resolution	1 arcmin rms radius
average angular resolution	2 arcmin rms radius
filter bandpasses: Lexan	60-170 Å
Be/Lexan	112-190 Å
Al/Lexan	170-300 Å

2.2 Spacecraft and Mission

Figure 1 gives a schematic overview of the present configuration of the ROSAT spacecraft and its major components. The two telescopes, XRT and WFC, are coaligned and each one possesses its own taperecorder and star tracker(s). The two XRT star trackers have a field of view of roughly $4.5^o \cdot 6^o$ and can locate stars down to 6.5th magnitude with an accuracy of about 1 arcsec. A three-fold solar array, buffered by batteries, provides electrical power. ROSAT is three-axis stabilized using four momentum wheels which are almost continuously unloaded by three magnetic torquers. Four gyroscopes as well as the XRT star trackers, magnetometers and sun sensors are used as attitude sensors. The attitude accuracy

and stability are expected to be better than 1 arcmin and 5arcsec/sec, respectively. The post-facto pointing accuracy will be several arcsec. A fiducial-light system is continuously monitoring small thermal motions between star trackers and X-ray telescope.

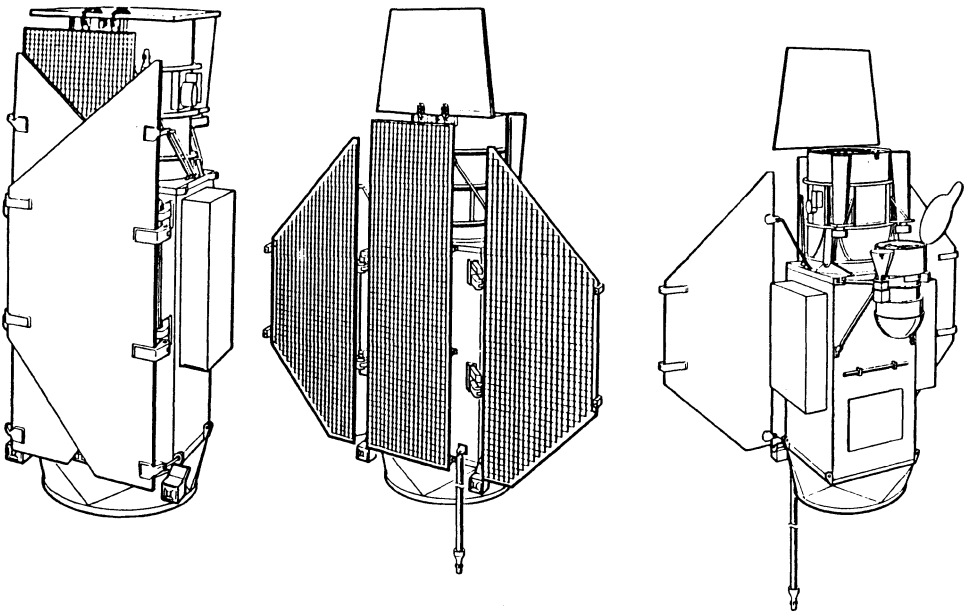

Figure 1: Schematic overview of the ROSAT spacecraft

The flight model of ROSAT is currently being integrated at Dornier Systems, and we are looking forward to the final tests and calibrations. ROSAT is presently scheduled for launch from Cape Kennedy with a Delta II rocket in February 1990 into a 580 km circular orbit with 57^o inclination. Its design lifetime is 1.5 years, enough for 1/2 year of all-sky survey and one year of pointed phase. In principle the lifetime of the orbit and instrumental consumables (counter gas, batteries) should allow a much longer operation.

2.3 Prospects of ROSAT Observations

During the survey the sky is covered by continously scanning great circles perpendicular to the earth-sun line, all great circles are meeting at the ecliptic poles. The full sky will be surveyed in one half year, yielding exposure times of ~600 s at the ecliptic equator and ~40000 s at the ecliptic poles. ROSAT will achieve a sensitivity over the whole sky which is similar to the serendipitous Medium Sensitivity Survey of the Einstein satellite (Gioia et al., 1984) which, however, only covered about 100 square degrees. The survey will therefore vastly enlarge the existing samples of different classes of sources and open space for truly new discoveries. This will

allow the detection of roughly 100000 new X-ray sources, the majority of which will be extragalactic objects: Seyfert galaxies, quasars and several thousand clusters of galaxies. The largest population of galactic objects should comprise a few ten thousand ordinary stars with coronal emission.

The second part of the mission is devoted to pointed observations of selected targets. For the study of emission from stellar coronae the wide spectral range of the XRT and WFC, providing in total about ten energy channels will be of special importance. Investigations of supernova remnants and clusters of galaxies will profit from the low intrinsic background of the XRT. Depending on the neutron star cooling curves, the thermal radiation of several tens of nearby radio pulsars, of special interest for the theme of *this* conference, will be observable in pointed observations (Hartner et al., 1988). As a special example we want to discuss in some detail the ROSAT 'deep surveys', very long pointed exposures (50000 s - 400000 s) of as yet empty fields in the sky. These will give a glimpse of the faintest X-ray sources ever observed ($2 - 5 \cdot 10^{-15} erg/cm^2 s$). These observations should resolve a fair fraction of the diffuse extragalactic X-ray background - if it is made up by point sources. Extended optical work on the designated fields is already in progress. We expect optical counterparts of the X-ray sources as faint as 25 magnitude. The combined X-ray/optical data set should allow an almost complete optical identification of the detected objects, the remaining unidentified X-ray error boxes can finally be searched with the Hubble Space Telescope.

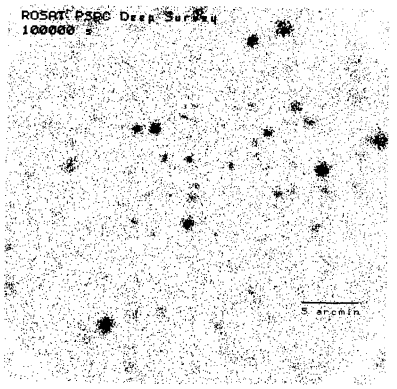

Figure 2a (left): Simulated image of a ROSAT deep survey observation with the PSPC in the focal plane. In 100000 seconds a total of 60-100 sources can be detected. At the sensitivity limit about 50-70 percent of the diffuse extragalactic background can be resolved. Figure 2b (right): Same field as in fig. 1 but now observed with the HRI in 400000 seconds. Positional accuracy of $\sim$ 2 arcsec can be reached.

The ROSAT X-ray data will be automatically analysed in the Rosat Scientific Data Center (Zimmermann et al., 1986). The results of this 'standard analysis' will be distributed to the guest investigators. At the same time guest investigators

will be provided with a portable software system for a more detailed interactive analysis. This system is based on MIDAS and runs on work stations under UNIX or VMS. Similar data services will be provided by the US and UK ROSAT data centers.

The algorithms to detect and analyse X-ray sources in ROSAT images are outlined by Hasinger (1985) and Cruddace, Hasinger and Schmitt (1987). In order to be able to predict the sensitivity and scientific thrust of different types of observations and in order to test and optimize the analysis algorithms extensive simulations of various types of observations have been carried out. A catalcgue of sources is created extrapolating known logN/logS functions (see e.g. Schmidt and Green, 1986). Properties of the individual sources like spectrum, extent or time-variability as well as the interstellar absorption column density can be chosen. The resulting artificial 'sky' is then observed with the telescope either in survey or pointed mode. Every single photon that is emitted from the sources is followed by ray tracing through a realistic model of the mirror system and detector. The resulting data, stored in the ROSAT telemetry format are then treated just like flight data and analysed using the automatic search procedures. The last step to derive the properties of the X-ray source uses a maximum-likelihood algorithm which treats every individual photon seperately (Cruddace, Hasinger and Schmidt, 1987).

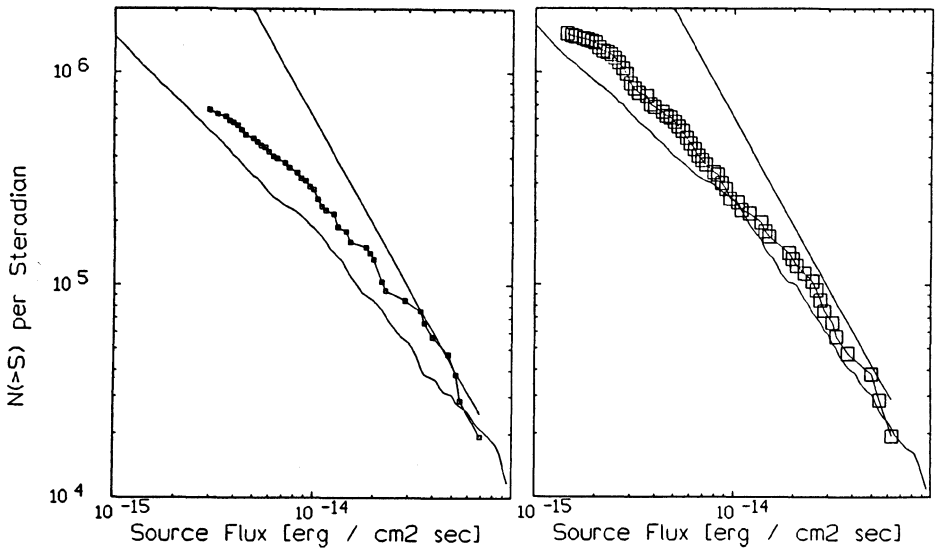

Figure 3: LogN/LogS distributions for the simulated PSPC (3a) and HRI (3b) fields. See text.

Figure 2a shows a simulated image of a PSPC deep-survey observation of 100000 seconds. The simulation contains quasars, active galactic nuclei, clusters of galaxies and normal stars. A total of ~60 sources is detectable here. For a good fraction of those it will be possible to measure the X-ray spectrum. Figure 2b shows the

same field as observed with the HRI for 400000 seconds, giving a positional accuracy of $\sim$ 2 arcsec. The results of searching the PSPC and HRI fields with the ROSAT standard analysis software are displayed in figure 3a and b, respectively. The squares represent the measured logN/logS distribution. The nearby solid line is obtained for the input artificial sky. The straight line to the right represents a power law extrapolation of the Einstein Medium Sensitivity Survey results (Gioia et al., 1984). Sources a factor of 10 and 20 fainter than the limiting flux of the Einstein deep surveys (Giacconi et al., 1979) can be detected with the PSPC and HRI, respectively.

3. SPEKTROSAT

The planned ROSAT follow-up mission is dedicated to X-ray spectroscopy. SPEKTROSAT will be an almost identical copy of the ROSAT satellite with one main additional element: a transmission grating. An adaptation of the focal plane instrumentation to the requirements of the grating (e.g. curved, larger detector) has to be considered. In addition, another type of add-on instrument could be accomodated where ROSAT is housing the WFC now.

The spectrometer design is described by Predehl and Bräuninger (1986). Depending on the choice of focal plane detector SPEKTROSAT can reach a maximum resolving power of a few 100 in the wavelength range below $\sim$ 150 – 200 Å. Compared to the objective grating spectrometer on Einstein and EXOSAT it will be more sensitive by a factor of 30 to 100. Figure 4 shows the expected X-ray spectrum from a 10000 s observation of Capella (Predehl and Bräuninger, 1986).

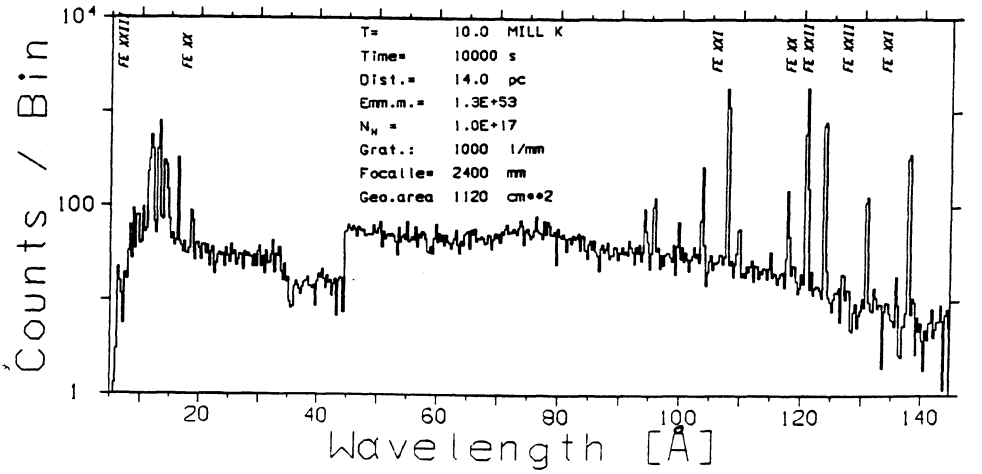

Figure 4: Simulated spectrum of the star Capella as expected to be measured with SPEKTROSAT

4. Medium-Energy X-ray Mirrors

All of the X-ray instruments discussed so far (Einstein, EXOSAT and ROSAT) have relatively soft response, their effective area drops rather rapidly above 2-4 keV. A major scientific objective of a whole new family of X-ray telescopes of the 1990s is to extend the sensitivity of imaging optics to higher energies. Especially the iron line complex, which may give unprecedented diagnostic power, will be covered. Simultaneously larger and larger collecting areas are aimed for. Figure 5 shows a comparison of the effective areas of X-ray mirrors from various missions. In table 5 the prospected characteristics of several medium-energy X-ray mirrors are compared.

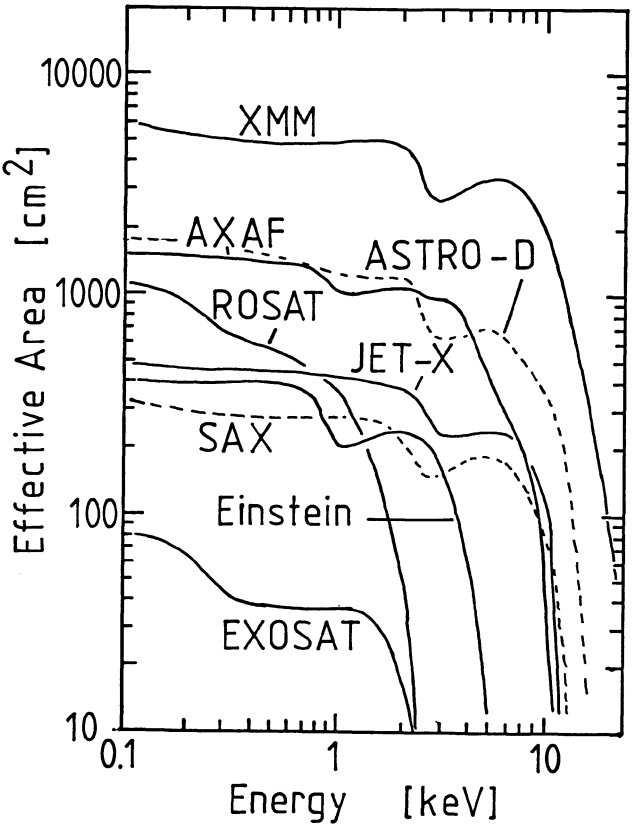

Figure 5: Comparison of effective areas of various X-ray mirrors

4.1 SAX

The Italian X-ray programme SAX (Satellito di Astronomia X) is a broadband ob-

Table 5: Characteristics of various X-ray telescopes

Experiment	SAX	JET-X	Astro-D	AXAF	XMM
Mirror Type	Concentrator	Wolter	Thin Foil	Wolter	Wolter
Energy Range (keV)	0.1-10	0.2-10	0.3-10	0.1-10	0.3-10
Angular Resolution (")	60	≤ 30	≤ 120	0.5	≤ 30
Effective Area at 2 keV (cm^2)	200	320	1300	1100	6000
Effective Area at 8 keV (cm^2)	125	140	500	145	2650
Spectral Resolution	2-15	10-70	10-70	10-1000	10-500
Orbit	low	high	low	low	high
Launch Year	1992	1993	1993	1996	1998

servatory which, in addition to an X-ray spectrometer with imaging concentrators carries several collimated counters including a coded mask wide-field camera. The spectrometer characteristics are described in table 5, imaging gas scintillation proportional counters (IGSPCs) are used as focal plane instruments. A seperate GSPC (320 cm^2) covers the energy range 3-120 keV, a phoswich scintillation counter (680 cm^2) the energy range 15-200 keV. The latter two instruments have collimators of 1.0^o and 1.5^o FWHM, respectively. An additional Wide-Field Camera (300 cm^2) with a field of view of 27^ox27^o can locate sources with an accuracy of 5 arcmin in the energy range 2-30 keV. SAX will be launched into a low-earth orbit.

4.2 Spectrum-X / JET-X

The USSR plans to launch two satellite missions for X-ray and gamma-ray astronomy in the first half of the 1990s. Besides other instruments the X-ray mission, called 'Spectrum-X', will carry two sets of imaging X-ray telescopes: XPECT (Denmark) will consist of two sets of multi-nested thin foil reflectors (similar to the Astro-D mirrors; see table 5) of ~8 m focal length with solid-state detectors in the focus. JET-X (the 'Joint European X-ray Telescope') consists of two parallel Wolter type-I telescopes with a focal length of 3.6 m, each having a butted array of CCDs in the focus. The telescopes are built in collaboration with institutes from the UK, Western Germany, Italy and ESTEC. Spectrum-X will be launched into a highly eccentric 4-day orbit that will allow long, uninterrupted observations.

4.3 XMM

XMM, the European X-ray Multi Mirror Mission, is the second cornerstone of the ESA science programme Horizon-2000 with a planned launch date just before the end of this millenium. The scientific payload consists of three highly nested Wolter type-I telescopes (58 shells per mirror system) with butted arrays of CCDs in their

focal planes. In addition reflection gratings provide high spectral resolution at soft X-rays. XMM will be launched into a highly eccentric 24-hour orbit.

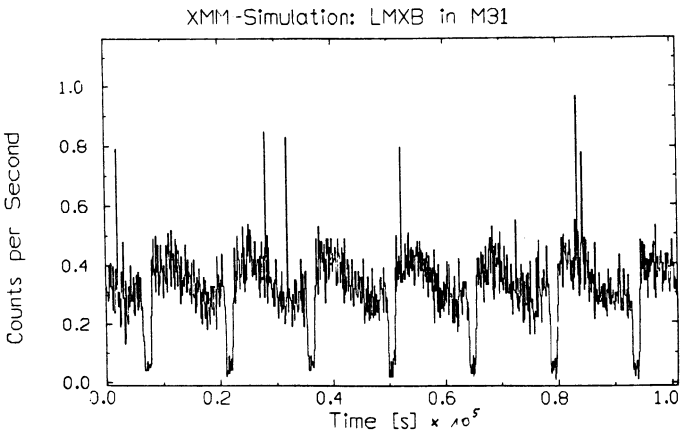

Figure 6: Simulated light curve of a LMXB in M31 observed with XMM

The scientific thrust of XMM is described in detail in the 'Mission-Science Report' (ESA SP-1097). Here we want to illustrate the unique capabilities of the high-throughput telescopes for the study of neutron star binaries in nearby galaxies. In a single observation of e.g. the Andromeda Nebula XMM can study the whole population of X-ray binaries in this galaxy. It can detect the time variability from X-ray pulsars, X-ray bursters and other sources and obtain high quality spectra in reasonable observing times. Figure 6 shows the simulated lightcurve one of the fainter low-mass X-ray binaries in M31, as observed through the three XMM telescopes in 10^5 seconds. One can clearly see eclipses, a 40 % orbital modulation and several bursts.

This way the knowledge about neutron stars in our Galaxy that has been accumulated over the past two decades by UHURU, Ariel-V, SAS-3, HEAO-1, Tenma, EXOSAT and Ginga can be extended and compared to complete and homogeneous samples of neutron stars in nearby galaxies.

Acknowledgements

Dr. B. Aschenbach is thanked for his inputs for table 1 and 2. We are grateful to Dr. F. Nagase for supplying the information about Astro-D.

References

Aschenbach, B., 1988, 31st SPIE symp., San Diego, Aug. 1987

Briel, U.G. and Pfeffermann, E., 1986, *Nucl. Inst. and Meth.*, **A242**, 376.

Cruddace, R.G., Hasinger, G., Schmitt, J.H.M.M. 1987 in: *Astronomy from Large Databases*, Murtagh and Heck eds., ESO Conference Proceedings No. 28, p.

177.

Dotani, T., et al., 1987 *Nature* **330**, 230.

Giacconi, R., Gursky, H., Paolini, F.R. and Rossi, B.B. 1962 *Phys. Rev. Letters* **9**, 439.

Giacconi, R. et al., 1979, *Astrophys. J. (Letters)* **234**, L1.

Gioia I.M., Maccacaro, T., Schild, R.E., Stocke, J.T., Liebert, J.W., Danziger, I.J., Kunth, D. and Lub, J. 1984 *Astrophys. J.* **283**, 495.

Hartner et al., 1988 (in. prep.)

Hasinger, G., 1985 *Bull. d' Information du Centre de Donnees Stellaires* **28**, 87.

Pfeffermann, E., Briel, U.G., Hippmann, H., Kettenring, G., Metzner, G., Predehl, P., Reger, G., Stephan, K.H., Zombeck, M.V., Chappel, J., and Murray, S.S., 1986, SPIE **733**, 519.

Predehl, P. and Bräuninger, H. 1986 SPIE /bf 733, 203.

Schmidt, M. and Green, R.F. 1986, *Astrophys. J.* **305**, 68.

Sunyaev, R. et al., 1987 *Nature* **330**, 237.

Trümper J., 1983, *Adv. Space. Res.* **2**, 241.

Zimmermann, H.U., Gruber, R., Hasinger, G., Paul, J., Schmitt, J. and Voges, W., 1986, in: *Data Analysis and Astronomy II*, Gesu et al., eds., Plenum Press, New York, p. 155.

PROSPECTS FOR PULSAR SEARCHES WITH THE GAMMA RAY OBSERVATORY GRO

R. Buccheri [1] , V. Schönfelder [2]

[1] Istituto di Fisica Cosmica e Applicazioni dell'Informatica,
Consiglio Nazionale delle Ricerche, Palermo, Italy

[2] Max Planck Institut fur Extraterrestrische Physik,
Garching bei Munchen, FRG

ABSTRACT. We use the existing data on about 300 radio pulsars to estimate their detectability by the gamma-ray detectors EGRET and COMPTEL on board the Gamma Ray Observatory satellite. If a luminosity $L \sim BP^{-2}$ is assumed, as predicted by the polar cap model, EGRET should detect about 30 pulsars and COMPTEL about 7 above 3 σ statistical significance if they have the same light curve shape as the Crab pulsar. Furthermore, the summed signals from several other pulsars should be detected both by EGRET and COMPTEL above 3 σ. Finally it is shown that possible pulsation from Geminga can be extracted directly from the EGRET data and, if detected, can serve as input for a positive detection in the COMPTEL data.

1. INTRODUCTION

The number of pulsars detected up to now in the radio band is near to 450. The most of them have been discovered in the course of systematic surveys carried out at the radio telescopes of Arecibo, Jodrell Bank and Molonglo. Such a large sample size should appear, in principle, high enough to allow a complete and exhaustive study of the physical characteristics of these objects. As a matter of fact, detailed studies are available on various aspects of the pulsar phenomenology like timing noise, glitches, polarization, structures of the light curve shape (at large and small scale) etc... In spite of this wealth of information, a generally accepted physical model on how the known fundamental processes mix together to produce the observed radiation does not exist. There may be several reasons for this difficulty.

First of all the pulsars known are a biased sample of the parent pulsar population; the technology available in the main surveys priviledged the detection of old, long period pulsars presumably in a similar stage of their evolution. The need for improving the search sensitivity with respect to short periods was felt only recently, after the discovery of millisecond pulsars (Backer et al., 1982; Boriakoff et al., 1983), objects that may have been spun-up by a companion star following an accretion phase. These discoveries triggered new surveys of the sky searching for fast and superfast pulsars culminated in the recent discovery of other millisecond pulsars in globular clusters and in other fast, relatively young, pulsars (Lyne et al., 1987; Lyne et al., 1988, Kulkarni et al., 1988). The analysis of the millisecond pulsars' behaviour will certainly help in the comprehension of the underlying physical mechanisms which produce the measured pulsation, however, being (or having been) members of a binary system, additional processes other than in the case of isolated pulsars may have a more important role.

A second, not negligible reason, is the severe lack of information on the pulsar behaviour in the gamma-ray energy range where the only two pulsars detected up to now (PSR0531+21, the

H. Ögelman and E. P. J. van den Heuvel (eds.), Timing Neutron Stars, 419–428.

Crab pulsar and PSR0833-45, the Vela pulsar) show to convey the most of their energy release, several orders of magnitude more than in the radio band. The limiting detection threshold of past gamma-ray missions (around 10^{-6} ph/cm^{2}s above 100 MeV) may have favoured this situation. However, the detectors of the new generation which are foreseen to fly on board of the future gamma-ray satellite missions, seem to be able to undertake the necessary step further with the detection of numerous gamma-ray pulsars. In this paper we aim to quantitatively estimate the information obtainable on gamma-ray pulsars by the high energy gamma-ray experiments on board the Gamma Ray Observatory satellite (EGRET and COMPTEL) to be launched in 1990.

2. DETECTABILITY OF GAMMA PULSED RADIATION FROM RADIO PULSARS

Two young radio pulsars, PSR0531+21 (Crab) and PSR0833-45 (Vela), are known to emit pulsed gamma radiation above 1 MeV. The structure of the emission is the same for both objects with two main peaks separated by 0.4 in phase and some bridge emission between them (Clear et al., 1987; Grenier et al., 1988). For other radio pulsars extensive searches have only produced upper limits on their possible gamma-ray emission (Buccheri et al., 1983; Graser & Schönfelder, 1983; Thompson et al., 1983).

The gamma-ray flux from a pulsar can be estimated by assuming that its intrinsic luminosity is a predictable fraction μ of the rotational energy loss i.e.

$$L_\gamma = \eta \dot{E} = -\eta I \omega \dot{\omega} = 4\pi^2 \eta I \dot{P}/P^3 \qquad \text{ergs/s} \qquad (1)$$

where I is the moment of inertia of the neutron star, P is the pulsar period and $\dot{P}$ its time derivative. From eq. 1 the pulsed flux at the earth can be derived at a given energy range and for a given beaming factor β :

$$\phi = (L_\gamma/E_\gamma) / (4\pi\beta d^2) \qquad \text{ph / cm}^2\,\text{s} \qquad (2)$$

where $E\gamma$ is the average photon energy in the given range, d is the pulsar distance and β is a function of the pulsar duty cycle δ.

The detectability of the pulsed gamma-ray flux, as predicted by eq. 2, is a function of the experiment sensitivity and of the background (i.e. diffuse galactic and extragalactic radiation as well as instrumental background radiation) and depends on the method used for the analysis of the timing data. We base our predictions on the application of a Z_m^2-test on the residual phase distribution obtained by folding the gamma-ray photon arrival times with the pulsar period and period derivative as derived in the radio band. In this case the statistical significance of a pulsed signal, expressed in terms of standard deviations above the mean value $\langle Z_m^2 \rangle = 2m$ expected in the case of uniformly distributed arrival times, is given by (Buccheri et al., 1983):

$$n_\sigma = R^2\, C(m,\delta)\, (\phi\, S\, T)^2 / (\phi\, S\, T + B) \qquad (3)$$

where S and T are the sensitive area and the effective duration of the experiment, R is the fraction of source photons within an optimal acceptance region defined by the angular resolution of the experiment, B is the number of background photons within the same region and C is a parameter depending on the duty cycle δ of the pulsar and on the number of harmonics m

chosen for the analysis. The background B includes galactic (B_g), extragalactic (B_e) and instrumental (B_i) components besides the possible unpulsed radiation (B_s) from the pulsar.

Our predictions on the detectability of a pulsed gamma-ray signal from radio pulsars is based on the assumption that the shape of the signal is the same for all pulsars and equal to that of the Crab (and Vela); we assume also that no known phase relation exists between the radio and gamma-ray light curve, this being the main reason for the choice of Z^2_m. According to these assumption, β has been calculated by considering two peaks of phase width 0.075, as measured for the Crab and Vela pulsars in the COS-B case. The relation between δ and β, as described in Buccheri (1981) for this case, results in β=0.185. The value of m follows from the assumed width of the pulsar duty cycle and is $m = 1/(2\delta) = 7$ with a corresponding value for C $=(1-\delta)/(2\delta m) = 1.13$. The canonical value of 10^{45} g cm^3 has, furthermore, been used for the moment of inertia I.

For a better understanding of the final results it must, however, be taken into account that, in the general case of weak signals, n_σ depends on the square of (η/β) meaning that our predictions are subject to large fluctuations due to possible variations in the values of η and β.

Independently of the validity of the assumptions and of the adequacy of the experiment sensitivity, however, the chance to detect a pulsed signal is based on the availability of very accurate pulsar parameters (period, period derivative, coordinates and distance) to be determined in the course of simultaneous gamma-radio observations (Buccheri et al., 1987). This will enable the derivation of the correct distribution of the residual phases to be tested against the presence of the pulsed signal.

Many different models are presently in competition to explain the pulsed radiation from the pulsar magnetosphere. A common feature of almost all models is the existence of gaps, arising from a local charge depletion, which are able to accelerate particles to relativistic velocities along the magnetic field lines. The location of these gaps and the sequence of the physical processes giving rise to the observed pulsed radiation are under debate. For the estimate of the fraction η (the conversion efficiency from rotational energy loss into gamma rays) we have based on the polar cap model of Ruderman & Sutherland (1975) according to which the accelerating potential drop (gap) is located just on the surface of the neutron star, in the polar cap region. In this condition a gamma-ray luminosity L proportional to BP^{-2} is expected from the curvature radiation of relativistic particles accelerated along the magnetic field lines of intensity B, if the attenuation due to pair production and consequent secondary emission is neglected (Harding, 1981). The result is a conversion efficiency given by (Schönfelder, 1985)

$$\eta = A\, P\, \tau^{0.5} \qquad (4)$$

where τ is the timing age $P/(2\dot{P})$ of the pulsar and the constant A can be derived by normalization, using the measured values of η in the cases of Crab and Vela. It is not clear at which age the potential drop across the polar cap is not anymore sufficiently high to inject charged particles to the open magnetosphere. According to Ruderman & Sutherland the accelerating activity continues until the condition $P > (10\, B_{12})^{1/2}$ s is reached. For sake of simplicity and to mantain the conversion efficiency within reasonable limits, we will assume that the eq. 4 is always valid with the limitation that η cannot be higher than 0.5, condition assured up to ages of about $5\ 10^6$ years where P is well below $(10\, B_{12})^{1/2}$ s.

The extension of eq. 4 to millisecond pulsars must, however, be considered with caution expecially in the case of binary systems where, due to the possible presence of accretion activity, the use of $P/(2\dot{P})$ as a pulsar age may result in error.

3. PREDICTION ON VISIBILITY OF GAMMA-RAY PULSARS BY GRO

Table I gives the observational characteristics of the high energy gamma-ray experiment EGRET on board the Gamma Ray Observatory (GRO) relevant for our analysis (Fichtel et al., 1983) and the assumptions used for the estimate of the background. In order to optimize the signal-to-noise ratio, we have applied our analysis to photon energies greater than 100 MeV (average photon energy E =220 MeV for a E^{-2} spectrum). In this energy range, the 70% of the photons from a point source are detected within an acceptance cone of 2.4 degrees (Thompson, 1986). The background photons within this cone amount to about 70 of extragalactic origin and 1620, 430 and 20 of galactic origin from respectively the galactic center region, the anticenter and the high latitude regions (Thompson, 1986). The pulsed gamma-ray flux from the Crab and Vela pulsars above 100 MeV is 2.86 10^{-6} and 1.00 10^{-5} ph/cm^2 s respectively (Clear et al., 1987; Grenier et al., 1988) resulting in a conversion efficiency of 1.90 10^{-4} and 2.75 10^{-3} respectively. Fig.1 shows the value of η expected for this energy range on the basis of eq. 4; the value A = 2.1 10^{-4} was derived by a fit through the Crab and Vela data.

S=1800 cm^2 ; T=5.44 10^5 s; R=0.7;
B_e=70; B_i=0; B_s=0;
B_g= 1620 for b < 5 , l < 60 and l > 300
B_g= 430 for b < 5 , 60 < l < 300
B_g = 20 for b > 5

Table I - EGRET experimental parameters and expected values for the galactic and extragalactic diffuse emission used for our predictions.

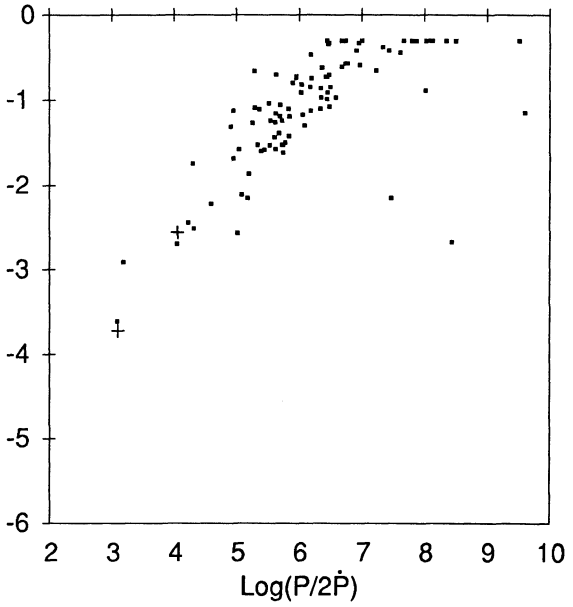

Fig.1 - Log of conversion efficiency η from rotational energy loss $\dot{E}$ to gamma rays for the pulsars of our catalogue, as given by eq.4 in the EGRET case. The two crosses give the measured values of log η for Crab and Vela.

The value of n_σ as given by eq. 3 was computed in the case of 287 pulsars for which the parameters are available from radio observations. As a result, 31 pulsars are expected to be visible at more than 3 σ with 13 showing more than 30 σ. If the observation duration is extended to 30 days (instead of the standard 2 weeks) the number of pulsars observable above 3 σ increases to 43. The list of expected positive detections with significances above 3 σ in two weeks observing time is given in Table II.

		P (s)	d (pc)	$\phi_{>100\ MeV}$ (10^7 ph/cm^2 s)	
$n_\sigma > 1000$					
	0531+21	0.033	2000	36.4 *	C
	0833-45	0.089	500	71.5 *	C
	0950+08	0.253	85	22.2 *	C
	0959-54	1.437	60	49.5 *	C
	1929+10	0.227	75	75.7 *	C
$100 < n_\sigma < 1000$					
	0656+14	0.385	400	8.24 *	C
	1133+16	1.188	150	2.53	
$10 < n_\sigma < 100$					
	0450+55	0.341	450	1.63	
	0740+28	0.167	1500	1.14	
	0906-17	0.402	510	0.53	
	0919+06	0.431	1000	0.56	
	1055-52	0.197	920	1.39	
	1451-68	0.263	230	1.88	
	1855+09	0.005	340	4.31	C
	1951+32	0.039	2500	2.13 *	
$3 < n_\sigma < 10$					
	0149-16	0.833	440	0.30	
	0203-40	0.631	470	0.42	
	0355+54	0.156	1600	0.56	
	0823+26	0.531	710	0.29	
	0834+06	1.274	430	0.42	
	0905-51	0.254	860	0.61	
	1001-47	0.307	1600	0.46	
	1508+55	0.740	730	0.28	
	1706-16	0.653	810	0.31	
	1822-09	0.769	560	1.46	
	1953+29	0.006	2700	0.69	
	2021+51	0.529	680	0.42	
	2045-16	1.962	380	0.26	
	2327-20	1.644	290	0.32	

Table II - List of pulsars expected to be detected by EGRET. Pulsars marked with asterisk are the only expected if η is the same for all pulsars and equal to η_{Vela}. Pulsars labelled with C are individually detectable by COMPTEL if eq.4 is valid.

Pulsars 0959+08, 0959-54 and 1929+10 are expected to be detected at significance levels 1629 σ's, 3355 σ's and 4437 σ's respectively under our assumptions. If we scale them to the COS-B case by using the experimental parameters of that case (sensitive area, useful time,

background,...) we find that COS-B should have detected them at 9, 17 and 33 σ's respectively. Since the significance in terms of number of σ's depends on ther square of luminosity and beaming (see eq. 3), the negative result by COS-B (Buccheri et al., 1983) can be explained if these pulsars have a slightly larger duty cycle and/or a slighly smaller conversion efficiency than assumed by us.

Fig. 2 shows the distribution of the pulsar fluxes, expected under the assumptions done. The fluxes above about 0.25×10^{-7} (less than 1% of Crab) are all individually detectable above 3 σ statistical significance. The m pulsars with fluxes between .25 10^{-7} and .87 10-10 ph/cm^2 s have signals too weak to be detected individually; their individual signals $n_{\sigma i}$, however, can be combined by the relation $g_\sigma = \Sigma\, n_{\sigma i} / \sqrt{m}$ to give a global significance $g_\sigma > 3\ \sigma$ (Buccheri et al., 1983). The detection of such a global signal would be an important test for the validity of the assumptions discussed above.

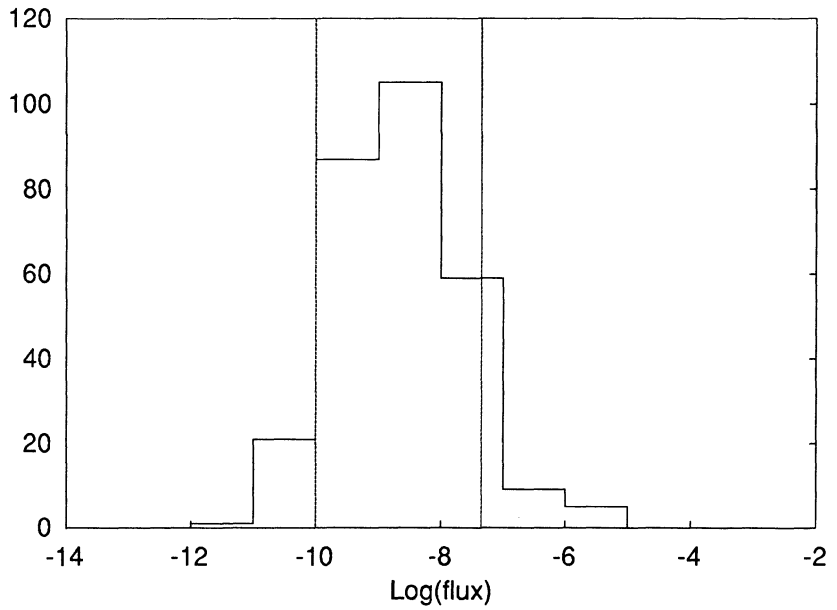

Fig.2 - Distribution of pulsar fluxes at the earth above 100 MeV as expected on the basis of our assumptions on η and on the duty cycle. The pulsars with fluxes larger than .25 10^{-7} ph/cm^2 s are all individually detectable by EGRET above 3 σ. A global signal at 3 σ level is furthermore expected by summing al the individually undetectable signals from the pulsars with fluxes between .25 10^{-7} and .87 10^{-10} ph/cm^2 s .

Fig. 3 shows the value of the conversion efficiency η needed in order to detect the pulsars at 3 σ level, independently of any a priori model on the emission precess. The plot refers to only 69 pulsars for which the computed value for η does not exceed 0.5. The measured values for

Crab and Vela are also shown; it is seen that if the value of η measured for Vela ($2.75\ 10^{-3}$) is typical for all pulsars, EGRET should still see 8 pulsars above 3 σ (those marked with * in table II plus PSR1509-58 for which the polar cap models predicts a small conversion efficiency).

Let us now estimate the visibility of pulsed signals by the Compton telescope COMPTEL aboard GRO, coaxial with EGRET. We use again eq. 4 for the estimate of the conversion efficiency but deriving the constant $A = 2.7\ 10^{-4}$ through a fit of the existing data on η in the COMPTEL energy range (1-30 MeV where $\eta_{Crab} = 4.55\ 10^{-4}$ and $\eta_{Vela} = 1.88\ 10^{-3}$).

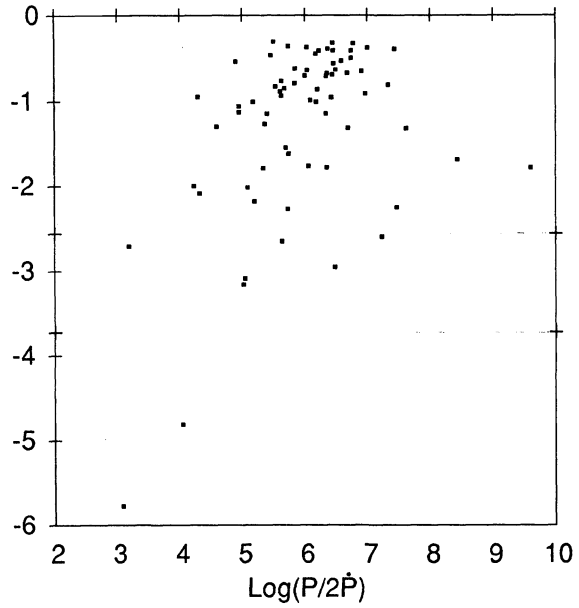

Fig.3 - Value of the conversion efficiency η requested for the pulsars of our catalogue become detectable by EGRET above3 σ; 69 of them have $\eta < 0.5$ and 8 have $\eta < \eta_{Vela}$.

If η_{Crab} is typical, no pulsars (besides Crab and Vela) will be detected by EGRET.

The optimal acceptance region has been chosen in a 4 x 4 square degrees centered on the pulsar direction; in this region, which contains the 80% of the photons from a point source, the total estimated background is 110000 photons, practically independent of its position in the galaxy. To derive our predictions we take $S = 30\ cm^2$ (Schönfelder et al., 1984) and assume the same observing duration $T=5.44\ 10^5$ s as for EGRET. The result is a set of 7 pulsars individually detectable above the 3 σ level as shown in table II (pulsars labelled with C).

The instrument sensitivity of COMPTEL is not such that any global signal can be detected with this analysis. However, if the search in the COMPTEL data can be driven by the positive results obtained by EGRET, the sensitivity can be much improved using the knowledge on the phase position of the pulsed signal. In these conditions, in fact, instead of using the Z_m^2 analysis one can test directly the phase interval predicted by EGRET using for the significance of the signal

$$n_\sigma = (R\phi ST)/\ (2\delta B) \qquad (5)$$

more powerful than eq. 3 for weak signals. Fig. 4 shows the distribution of the pulsar fluxes expected in the COMPTEL energy range assuming an increase with age of the conversion efficiency. Fluxes down to 4 10^{-5} ph/cm^{2}s (less than 10% of the Crab) are individually visible. The region below this value and down to 3 10^{-6} ph/cm^{2}s, includes the pulsars individually detected by EGRET and whose global signal can be detected by COMPTEL above 4 σ using eq. 5.

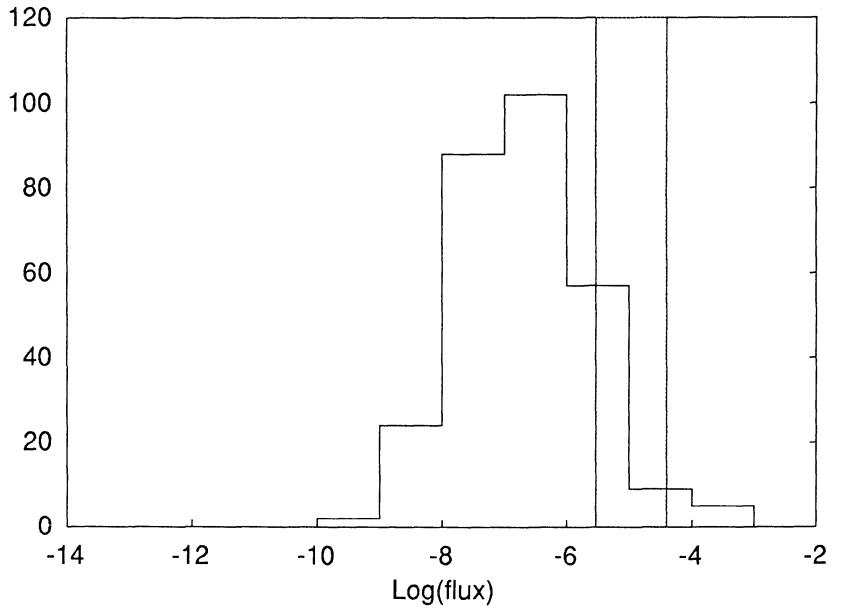

Fig.4 - Distribution of pulsar fluxes at the earth expected between 1 and 30 MeV on the basis of our assumptions on η and on the duty cycle. The 7 pulsars with fluxes above 4 10^{-5} ph/cm^{2}s are individually detectable by COMPTEL above 3 σ. A global signal at 4σ level is furthermore expected in COMPTEL by summing the signals from the pulsars individually detected by EGRET (fluxes between 4 10^{-5} and 3 10^{-6} ph/cm^{2}s).

4. SEARCH OF PERIODICITY IN THE GRO DATA FROM GEMINGA

As it was stressed above, the detection of a pulsed signal in the gamma-ray data depends very critically on the knowledge of the pulsation parameters as derived by (simultaneous) radio observations. Without this knowledge one should perform the test of eq. 3 on the phase distributions derived by folding the photon arrival times with different sets of pulsar parameters, thus reducing drastically the significance of the test. However, for sufficiently strong signals, the test can still be applied with success provided that all the trial periods tested are taken into account.

The sensitivity of a search using Z^2_1 (the Rayleigh test) has been studied by Buccheri et al. (1987); according to them the minimum fraction of the total collected photons needed to be detected in a pulsed signal is given by

$$f_{min} = \sqrt{-(1+\ln(S_0/M))/NC} \qquad (6)$$

where S_0 is the detection threshold in terms of probability for chance occurrence, M is the number of trial periods investigated, N the total number of collected photons and C is defined as in eq. 3.

Let us apply eq. 6 to verify the feasibility of a search for a pulsating signal in the data from 2CG195+04 (Geminga) as will be observed by EGRET. The flux of Geminga above 100 MeV is 4.8 10^{-6} ph/cm^{2}s, resulting in 3300 source photons detected within 2.4 degrees to be added to the 500 background photons within the same acceptance cone. The number of independent trial period needed to test for a full investigation down to a period of 100 ms = 0.1 s is T/0.1 = 1.2 10^7 (T is here the full observing time of 2 weeks). We will use $M=10^9$ in order to take into account the ivestigation of period derivatives up to 10^{-12} s/s and some oversampling in order to assure a uniform search sensitivity. With this choice, the value of f_{min} for detecting at 99.9% c.l. a broad pulse shape with C = 0.3 is 0.153 i.e. 581 photons (17.6% of the total source counts). A successfull search for periodicity in the gamma-ray emission from Geminga is therefore possible with the EGRET data. The application of the eq. 6 to the COMPTEL data reveils that the search sensitivity is too low for a successful detection. However, if a positive detection is made by EGRET, the period found can be tested successfully in the COMPTEL data provided that the pulsed Geminga is not weaker than 0.2 of the Crab pulsar in the 1 to 30 MeV energy range. This can easily be verified by using eq. 6 with N = 110000 and M =1 and considering that the expected counts from the Crab in the acceptance region are about 6500.

REFERENCES

- Backer D.C., Kulkarni S.R., Davis M.M., Goss W.M.
  Nature, 300, 615, 1982
- Boriakoff V., Buccheri R., Fauci F.
  Nature, 304, 417, 1983
- Buccheri R.
  IAU Symp. n. 95 "Pulsars",
  eds. W.Sieber & R.Wielebinski, 241, 1981
- Buccheri R. et al.
  Astron. Astrophys., 128, 245, 1983
- Buccheri R., Özel M.E., Sacco B.
  Astron. Astrophys., 175, 353, 1987
- Buccheri R. et al.
  Proc. of Int. Coll. on Coordination of Observational
  Projects, Strasbourg, 1987
- Clear J., Bennett K., Buccheri R., Grenier I.A., Hermsen W., Mayer-Hasselwander H.A. and Sacco B.
  Astron. Astrophys., 174, 85, 1987
- Fichtel C.E. et al.
  Proc. of 18th ICRC, Vol. 8, p.19, 1983
- Graser U. & Schönfelder V.

Astrophys. J., 273, 681, 1983
- Grenier I.A., Hermsen W. & Clear J.
Astron. Astrophys., 1988, in press
- Harding A.K.
Astrophys. J., 245, 267, 1981
- Kulkarni S.R., Clifton T.R., Backer D.C., Foster R.S., Fruchter A.S., Taylor J.H.
Nature, in press
- Lyne A.G., Brinklow A., Middletitch J., Kulkarni S.R., Backer D.C., Clifton T.R.
Nature, 328, 399, 1987
- Lyne A.G., Biggs J.D., Brinklow A., Ashworth M., McKenna J.
Nature, 332, 45, 1988
- Ruderman M.A. & Sutherland P.G.
Astrophys. J., 196, 51, 1975
- Schönfelder V.
Naturwissenschaften 72, 133, 1985
- Schönfelder V. et al.
IEEE Trans. on Nucl. Sci., NS-31, 766, 1984
- Thompson D.J., Bertsch D.L., Hartman R.C., Hunter S.D.
Astron. Astrophys., 127, 220, 1983
- Thompson D.J.
Nucl. Instr. & Meths. in Phys. Res., A251, 390, 1986

III. INTERNAL STRUCTURE OF NEUTRON STARS

INSIDE NEUTRON STARS

M. ALI ALPAR
Physics Department, Research Institute for Basic Sciences
P.O. Box 74, 41470 Gebze-Kocaeli Turkey

1. Introduction

Neutron stars present a fascinating interface between condensed matter physics and astrophysics. They are the most compact **observable** objects in the universe. The only configuration that is even more collapsed than the neutron star, the black hole, is not observable in terms of the state of the matter it contains - according to the famous no hair theorems it has only three observable properties: mass, angular momentum, and charge. Neutron stars thus contain the most extreme observable states of condensed matter, and in the largest quantities: to mention one aspect, we are dealing with bulk superfluid, of a solar mass, at nuclear matter density and rotating with a period typically less than a second. This fantastic compactness is the endpoint, after going through the full history of stellar evolution and exhausting all other possible states of matter that can withstand gravitational collapse. The compactness and condensed state of a neutron star is in turn responsible for its current astrophysical properties. In particular, the rapid rotation rates are tenable only by objects of such high density as neutron stars. The processes that render the rapid rotation observable, namely the radio beams from a pulsar magnetosphere or the X-ray beams from the accretion process on to a neutron star in a binary are also direct consequences of the intense gravitational and magnetic fields characteristic of the collapsed neutron star.

Table 1 quantifies the compactness of a neutron star through a comparison of its properties with those of the sun. Most notably, the average density of a neutron star is higher than nuclear matter density. Outside neutron stars, such high densities exist only in atomic nuclei. Observed rotation rates, which are as high as 4000 rad s^{-1}, can be supported only at such high densities. The temperatures quoted are high in comparison to those of the sun, but at the high densities and pressures of the neutron star interior, all the physical energy scales of condensed matter are much larger than kT. The Fermi energy of the neutrons, for example, is of the order of 30

H. Ögelman and E. P. J. van den Heuvel (eds.), Timing Neutron Stars, 431–440.

Table I

Comparison of a neutron star with the sun

	Neutron Star	Sun
Mass	$\sim 1\ M_\odot$	$1\ M_\odot$
Radius	$\sim 10^6$ cm	7×10^{10} cm
Mean density	$\sim 5 \times 10^{14}$ gm cm^{-3}	1.4 gm cm^{-3}
Rotation period	1.5 ms $\lesssim P \lesssim$ several s	25 days
Surface magnetic field	$\sim 10^9 - 10^{12}$ gauss	$1 - 2$ gauss
Surface temperature	$\lesssim 10^7$ °K	6000 °K
Central temperature	$\sim 10^8 - 10^{10}$ °K	1.5×10^7 °K

MeV. The cyclotron energy $\hbar\omega_c$, the Debye energy of the crust lattice, $\hbar\omega_D$, and the superfluid gap Δ are all large compared to the temperature, except in very young neutron stars. Neutron stars are thus effectively at absolute zero temperature - they cool the largest quantities of the most extremely condensed matter, to the deepest temperatures. This talk will discuss aspects of the extreme regimes in the neutron star interior. This is not a survey of the interior. Particular regions of the star will be chosen for the interesting open problems presented by the extreme states of condensed matter. The bearing of existing or future astrophysical observations on these problems and the guidance that theoretical modelling of the interior provides to the interpretation of the observations will be pointed out. Fig. 1 shows a cross section through a model neutron star. Different layers of the crust and the core of the star are labeled with the state of matter they contain. We start with the outermost layers of the crust where the strong magnetic field plays a dominant role in the properties of the matter.

2. Matter In A Strong Magnetic Field

Near the surface of a neutron star, at the lowest densities, the properties of matter will be dominated by the magnetic field (Hernquist 1985). This arises because the magnetic field distinguishes between the electron quantum states in directions transverse to the field and the states in the direction of the field. The anisotropy introduced by the magnetic field fundamentally alters the equation of state at low densities, while with increasing density, the effect becomes unimportant and the state of matter will change gradually to that of isotropic degenerate matter. The neutron star crust near the surface consists of a crystal lattice of iron-like nuclei. To illustrate some basic points we shall approximate the electrons in this lattice as free electrons.

When there is no magnetic field, a degenerate, non-relativistic electron gas at T=0 is characterized by a Fermi energy.

$$\varepsilon_F^o = \frac{\hbar^2 k_F^2}{2m_e} \tag{1}$$

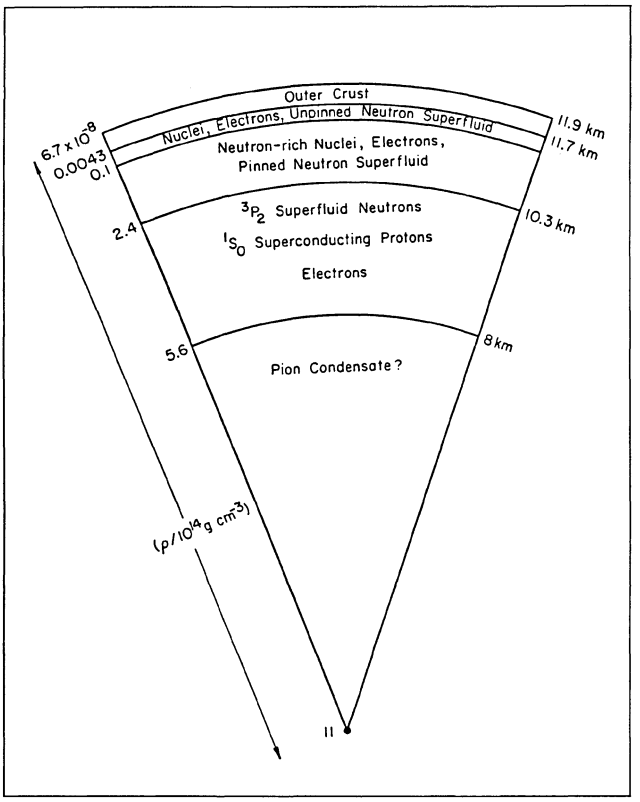

Figure 1: Cross section of a 1.4 $M_\odot$ neutron star model.

where the Fermi wavenumber k_F is related to the electron density n_e by

$$k_F = (3\pi^2\, n_e)^{1/3} \tag{2}$$

All free electron states with $|\vec{k}| \leq k_F$ are occupied. The density of states in $\vec{k}$ space is, isotropically, $2/(2\pi)^3$, giving a total of n_e electrons per unit volume in real space.

In a magnetic field, electrons perform circular (oscillatory) motion in the plane perpendicular to $\vec{B}$. Their energy is then quantized as

$$\varepsilon_\perp = \hbar\omega_c\,(n + \frac{1}{2}) \tag{3}$$

where $\omega_c = eB/mc$ is the cyclotron frequency, and $n = 0, 1, 2, \ldots$ Motion parallel to the field is in plane wave states, with wavenumber $k_\parallel$ quantized as

$$k_\parallel = n_\parallel \frac{2\pi}{L} \tag{4}$$

where $n_{\|}$ is an integer and L the length of the system in the direction of $\vec{B}$. The possible energy levels are thus:

$$\varepsilon = (n + \frac{1}{2})\,\hbar\omega_c \pm \frac{1}{2}\hbar\omega_c + \frac{\hbar^2 k_{\|}^2}{2m} = n'\hbar\omega_c + \frac{\hbar^2 k_{\|}^2}{2m} \tag{5}$$

where the second term is the energy of the two possible states of the electron spin. All the **Landau levels** except $n' = 0$ are two-fold degenerate. The number of distinct cyclotron sites is $A/\Delta A$ if the transverse area of the system is A. ΔA is found by using the uncertainty relation and relating the spacing of $\vec{k}$ in the transverse plane to the transverse energy spacing:

$$\frac{1}{\Delta A} = 2\pi k_{\perp}\Delta k_{\perp} = \frac{2m}{\hbar^2}\,\hbar\omega_c = \frac{2\pi B}{\Phi_o} \tag{6}$$

where $\Phi_o \equiv hc/2e$ is the flux quantum.

Now we consider N electrons in an arbitrary box of length L along $\vec{B}$ and transverse area A. At zero temperature, all available electron states up to a Fermi energy ε_F will be occupied. For each Landau level n', the maximum longitudial energy available is $\varepsilon_F - n'\hbar\omega_c$, so that states with $k_{\|}$ between

$$\pm\,(2m/\hbar^2)^{1/2}\,(\varepsilon_F - n'\hbar\omega_c)^{1/2}$$

are occupied. Thus the counting of states gives:

$$N = \frac{A}{\Delta A}\frac{1}{(2\pi/L)}\{\,2(\frac{2m\varepsilon_F}{\hbar^2})^{1/2} + 4(\frac{2m}{\hbar^2})^{1/2}_{n'=1}(\varepsilon_F - n'\hbar\omega_c)^{1/2}\theta(\varepsilon_F - n'\hbar\omega_c)\}$$

$$n_e = \frac{B}{\Phi_o}\{\,2(\frac{2m\varepsilon_F}{\hbar^2})^{1/2} + 4(\frac{2m}{\hbar^2})^{1/2}_{n'=1}(\varepsilon_F - n'\hbar\omega_c)^{1/2}\theta(\varepsilon_F - n'\hbar\omega_c)\} \tag{7}$$

The first term counts the longitudinal states for $n' = 0$. This is simply,

$$(A/\Delta A)\;(2k_{\|}^{max}\;(n'=0)\;/\;(2\pi/L)$$

counting from $-k_{\|}^{max}$ to $+k_{\|}$. Other terms in the sum have an extra factor of 2 because of the double degeneracy for $n' \geq 1$. The sum has a finite number of terms, for $n'\hbar\omega_c < \varepsilon_F$. This expression can be generalized to finite temperature, with a chemical potential $\mu(T) \neq \varepsilon_F$ (Hernquist 1985). The basic point is that, as the density increases there are discontinuous changes in the equation of state and other thermodynamic relations at each density that requires the opening up of a new Landau level. Equation (7) is illustrated in Fig. 2.

With increasing density, as more and more Landau levels become occupied, the equation of state rapidly approaches the familiar non-magnetic case. Let us examine the extreme magnetic case, with only $n' = 0$ occupied. This will happen

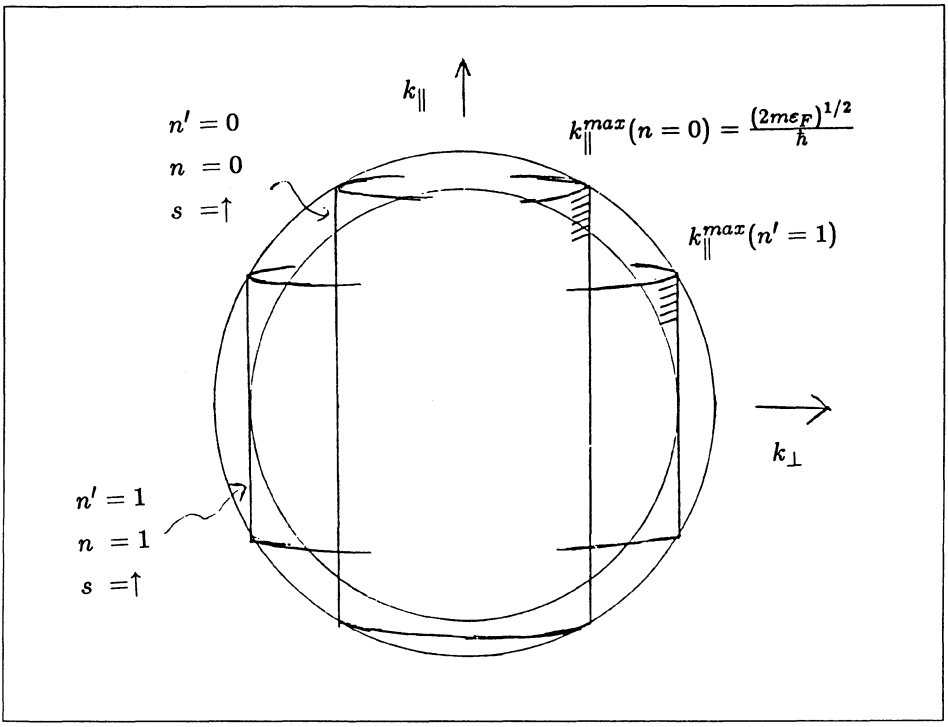

Figure 2: The filling of the Landau levels. Only the up spin ($\vec{s} \parallel \vec{B}$) case is shown. The inner sphere is the Fermi sueface, $\hbar^2 k_\parallel^2/2m + \varepsilon_\perp + \varepsilon_s = \varepsilon_F$. The outer sphere is $\hbar^2 k_\parallel^2/2m + \varepsilon_\perp = \varepsilon_F - \varepsilon_s$; for the up spin case $\varepsilon_s = -1/2\ \hbar\omega_c$. The notches on the Landau cylinders denote the quantized $k_\parallel$ levels.

below the density at which $\varepsilon_F^o = \hbar\omega_c$, the non-magnetic Fermi energy is of the order of the energy required to occupy the next Landau level. This density is

$$\rho_o = \mu_e B_{12}^{3/2}\ 10^4\ gm/cm^3 \tag{8}$$

where $\mu_e \sim 2$ is the number of nucleons per electron. At lower densities, only the first Landau level is populated, so that

$$n_e = \frac{2B}{\Phi_o}\left(\frac{2m\varepsilon_F}{\hbar^2}\right)^{1/2} \equiv \frac{2B}{\Phi_o}\, k_\parallel \tag{9}$$

Using the thermodynamic definition for pressure, $P = -\frac{\partial E}{\partial V}|_N$, we obtain

$$P = \frac{2\hbar^2}{3m}\left(\frac{\Phi_o}{2\pi B}\right)^2 n_e^3 \tag{10}$$

which differs radically from the equation of state $P \propto n_e^{5/3}$, for nonrelativistic degnerate electrons when $B = 0$. The equation of state in the extreme magnetic case will make the neutron star surface terminate rather abruptly: integrating the equation of hydrostatic equilibrium from $\rho = \rho_{cr}$ out to $\rho = 0$, $P = 0$, one finds a thickness $\delta r \cong 0.1\ cm\ B_{12}/g_{14}$ for the outermost surface layer (g_{14} is the surface gravity in units of $10^{14}\ cm/sec^2$), while with the non-magnetic equation of state, $\delta r \cong 50 cm/g_{14}$ from $\rho = \rho_o$ out to the surface. Along with changing the structure of the outermost surface layers so drastically the magnetic field must also alter transport processes. The rates of various processes that effect the transport coefficients can be approached using the Golden Rule:

$$\tau^{-1} = \frac{2\pi}{\hbar}\Sigma_f \frac{dN}{d\varepsilon_f} |V_{i\to f}|^2 \tag{11}$$

The density of final states at the Fermi surface, $\frac{dN}{d\varepsilon}|_{\varepsilon=\varepsilon_F}$ is enhanced as $(\rho_o/\rho)^{4/3}$ in the magnetic case. On the other hand the matrix elements $|V_{i\to f}|$ are restricted to transitions between the states $k_\parallel^{max}$ and $-k_\parallel^{max}$. The calculation of the various processes poses a set of interesting open problems, which must also take account of the anisotropy introduced by the direction of the magnetic field. A particularly interesting problem is the thermal conductivity and the calculation of the surface temperature which will be a function of angular position from the magnetic axis. The relation between the temperature of the neutron star interior and the surface luminosity is determined predominantly by the thermal conductivity on a "sensitivity strip" which typically lies at densities $\sim 10^6\ gm/cm^{-3}$, much deeper in the crust than the magnetic surface. We therefore do not expect the **mean** surface flux and temperature to be effected by the thin magnetic surface layer. Thus the magnetic field is not likely to alter the cooling history of the neutron star. It is, however, important to understand the angular variation of the surface temperature, $T_s(\theta)$. This will, for example, justify using upper limits to **pulsed** thermal radiation from the surfaces of rotating neutron stars, thereby providing more stringent observational constraints on the cooling history. The interesting open problem of the magnetic surface layer is also linked with understanding the binding energy of the surface, and therefore with the neutron star atmosphere and radiative transfer (Jones 1985; Romani 1987).

3. A Crystal With Relativistic Electrons

Moving further into the crust, the next interesting change in the physics takes place as the electrons become relativistic. This happens when the momentum $\hbar k_F$ of an electron on the Fermi surface becomes of the order of mc. Thus, a typical density for the transition is

$$\rho_{rel} \cong 2\ m_N\ n_e = \frac{2m_N}{3\pi^2}(\frac{m\ c}{\hbar})^3 \cong 3 \times 10^6\ gm\ cm^{-3} \tag{12}$$

taking a mass density of two nucleons (mass m_N) per electron. There is a gradual transition to the relativistic regime for electrons. At higher densities, say from

about 10 ρ_{rel}, electrons become ultrarelativistic, with $\varepsilon_F \cong \hbar k_F c$. Their kinetic energies then far exceed the electrostatic potential energy, so that the electrons are nearly free and there is very little screening of the ions by local concentrations of electrostatically attracted electron clouds around them. The electrostatic potential energy of an electron due to the ions of charge Z and inter-ion spacing $r_i \equiv (Z/n_e)^{1/3}$ is

$$U \sim \frac{Ze^2}{r_i} \sim Z^{2/3} e^2 n_e^{1/3} \tag{13}$$

which gives

$$\frac{U}{\varepsilon_F} = \frac{Z^{2/3}}{(3\pi^2)^{1/3}} \frac{e^2}{\hbar c} \ll 1. \tag{14}$$

indicating the relative weakness of electrostatic effects. The perturbative Thomas-Fermi theory, for relativistic electrons, gives the screening lenth λ (eg. Ziman 1972)

$$\lambda^{-2} = \frac{12\pi n_e e^2}{\varepsilon_F} \tag{15}$$

The screening length is roughly the size of the electron cloud around an ion that is held electrostatically and neutralizes the ionic charge, so that at distances less than λ, the ion exerts its bare field, but further than λ the ionic charge is screened. More precisely, the bare Coulomb potential of the ion is replaced with a Yukawa potential

$$U = \frac{Ze^2 e^{-\lambda r}}{r} \tag{16}$$

The comparison of the inter-ion spacing r_i with the screening length tells us that each ion in the lattice forming the neutron star crust feels the **bare** Coulomb potential of its neighbours:

$$[\frac{r_i}{\lambda}]^2 = \frac{12\pi}{(3\pi^2)^{1/3}} Z^{2/3} \frac{e^2}{\hbar c} < 1 \tag{17}$$

The neutron star crust lattice is therefore strongly coupled through the long range unscreened Coulomb interaction. In such a lattice it is very difficult to create or move local defects or dislocations. Stresses introduced locally will quickly extend to the lattice through the strong coupling. A crystal lattice will respond elastically, with a simple Hooke's law proportionality between stress and strain, up to a dimensionless critical strain "angle" θ_c. If this critical value is exceeded the lattice "breaks": the distribution of defects and dislocations changes and new local defects are introduced. For terrestrial crystals, where there is effective screening and weak, short range coupling between atoms, θ_c is typically 10^{-4} 10^{-5}. For a Coulomb crystal, like the neutron star crust, θ_c could be as high as $10^{-2} - 10^{-1}$. There is no calculation of θ_c or of the behaviour of dislocations in the Coulomb crystal. There is, however, an interesting lower limit, $\theta_c > 10^{-3}$, that follows if the 35d. period of

Her X-1 is the precession period of the neutron star reflecting the properties of the star's solid crust (Trümper et al. 1986). This lower limit, is already a factor of 10 larger than terrestrial values, and is a good example of the kind of valuable information on exotic condensed matter that can be obtained from neutron star timing observations. A **global** model of the stars dynamics, with the lattice described as a spring of given rigidity and critical strain, has been employed to address pulsar glitches as well as precession. On this starquake hypothesis for the origin of glitches, the solid crust cannot deform continuously to follow the spin-down of the star and breaks every time critical strains are reached (Ruderman 1969). Starquake models fail to explain large glitches like the ones observed in the Vela pulsar roughly once every two years, with the relative increase in rotation rate of the star, $\frac{\Delta\Omega}{\Omega} \sim 10^{-6}$. Starquakes are still a viable explanation for timing noise and for the smaller glitches with $\frac{\Delta\Omega}{\Omega} \sim 10^{-9}$, possibly operating in conjunction with instabilities in the crust superfluid in the form of suden vortex unpinning. Interesting open problems here are, in addition to the microscopic physics of the Coulomb crystal, the relation between the microscopic physics and the global structure of the star's crust, as well as the interplay between the crystal, and the vortex lines of the superfluid which coexists with the crystal lattice. Future observations of glitches and noise, as well as indications of neutron star precession, will give us further clues. Note that astrophysical evidence can indicate the **extent** as well as the physics of the crust. For a neutron star of known mass, the relative thickness of the crust, which can be inferred from observations of glitches and of precession, distinguishes between different stellar models, that is, ultimately, between different models of the nuclear force. On this note, let us proceed to another unterrestrial peculiarity of the crystal lattice in the neutron star crust, namely its abundance of neutrons.

4. Neutrons In The Crust

At densities above about $4 \times 10^{11}\ gm\ cm^{-3}$, the neutron abundance becomes so high that not all of the neutrons can be accommodated in the nuclei that form the crust lattice (Shapiro et al. 1983). Above this neutron drip density, some neutrons occupy extended Bloch states of the crystal, while some neutrons, along with the protons, are in localized bound states in nuclei. Thus we have a crystal with a conduction band of neutrons, in addition to electrons. This inner crust carries most of the crystal mass and moment of inertia, and covers most of the crust thickness, extending up to densities of $\sim\ 2 \times 10^{14}\ gm\ cm^{-3}$ (Negele 1973). With increasing density and neutronisation, the neutron density at interstitial sites approaches that inside the nuclei, and the lattice spacing decreases until the inner crust melts to a homogeneous medium of neutrons, with roughly 5 % admixture of protons and electrons.

The most important feature of the inner crust is that the neutrons in the continuum states are superfluid, starting from the neutron drip density (For superfluidity in neutron stars see Pines et al. 1985). The neutron-neutron interaction in the ^1S_O channel is attractive in the density range of the crust neutrons, resulting in the formation of Cooper pairs, and condensation into the superfluid phase, with a

gap/ transition temperature of the order of MeV. This transition into the superfluid phase should take place very early in the cooling history of the neutron star. Neutrons in the core regions of the star, from the inner boundary of the crust at $\sim 2 \times 10^{14}\ gm\ cm^{-3}$, all the way to the star's center at $\sim 10^{15}\ gm\ cm^{-3}$, are also believed to be superfluid, this time from neutron-neutron attraction in the $^3P_2$ channel, while protons in the core form a ^1S_O superconductor.

These superfluids can partake in the neutron star's rotation by carrying an array of quantized vortices. The rotation rate of the superfluid is proportional to the density of vortex lines per unit area perpendicular to the rotation axis. To spin down, the superfluid must move its vortices radially outward and decrease their density. Thus the dynamics of the neutron star, whose interior is mostly superfluid, is determined by the motion of quantized vortex lines. This leads to a fundamental distinction between the crust superfluid and the core superfluid, In the crust, the size of a vortex line ($radius \gtrsim 10fm.$), nucleus ($radius\ 7fm.$) and the lattice spacing ($30 - 50\ fm.$) are all commensurate. The difference in superfluid neutron density at interstitial sites and inside the nuclei causes interactions between the vortex lines and the lattice of nuclei, leading to possible pinning of vortex lines by the lattice. This is an extremely dirty, inhomogeneous medium, in contrast to the spatially homogeneous neutron-proton superfluid in the core regions of the neutron star. The dynamics of the crust superfluid is described by a statistical theory of vortex line motion in a random pinning potential to represent the lattice (Alpar et al. 1984). As a result, the crust superfluid has a rather weak dynamical coupling to external torques on the star. The core superfluid, by contrast, is coupled very tightly to the outer crust and external torques, because the homogeneous neutron-proton superfluid has spontaneous magnetization on its vortex lines, which thereby interact electromagnetically with electrons (matter in the normal state) (Sauls this volume). The observed dynamical relaxation of pulsars following glitches reflects the slow relaxation times of the crust superfluid, and the observed changes in spin-down rate give a measure of the crust superfluid's moment of inertia, found to be of order $10^{-2} - 10^{-3}$ of the neutron star's total moment of inertia (Pines and Alpar 1985). Thus, the detailed state of the interior, regarding the presence and extent of a lattice of nuclei, is reflected in observable dynamical behaviour of the neutron star.

5. Timing Observations Against Strange Stars

Let us wind up our menu of selected topics with a simple consequence of pulsar timing observations on the question of strange stars. It has been proposed that the stable state of matter at high density is a mixture of up, down and strange quarks, and furthermore, that the observed objects hitherto believed to be neutron stars could be strange stars as these would not be observationally distinguishable from neutron stars (Witten 1984; Alcock et al. 1986). However, a simple argument shows that at least the glitching radio pulsars are not strange stars (Alpar 1987). To the extent that glitches occur in all radio pulsars, which is statistically plausible and that some radio pulsars are evolutionary descendants of the accretion powered X-ray

sources, all these objects would have to be neutron stars. The argument rests on the observation that the spindown rate $\dot{\Omega}$ changes by a fraction $\Delta\dot{\Omega}/\dot{\Omega} \sim 10^{-3} - 10^{-2}$ at glitches. As no correlated changes in the electromagnetic properties of a pulsar are observed together with a glitch, the glitches must reflect some change in the interior of the star. The fractional change in spindown rate must then indicate the fraction of the total moment of inertia involved in the event. Thus, the star must have some distinct physical component that contains $10^{-3} - 10^{-2}$ of its total moment of inertia. In strange stars, a homogeneous, high density strange matter medium extends all the way to the surface or to the neutron drip density 4×10^{11} $gm\ cm^{-3}$ in which case there is an outer crust like that of a neutron star below this density. This outer crust contains at most about 10^{-5} of the total moment of inertia, and is the only distinct component of the strange star. Thus the glitching pulsars cannot have underlying strange stars, they must be neutron stars. Timing observations serve to protect the very existence of neutron stars!

REFERENCES:

Alcock, C., Farhi, E. and Olinto, A.: 1986, *Phys. Rev. Lett.* **57**, 2088.

Alpar, M.A.: 1987, *Phys. Rev. Lett.* **58**, 2152.

Alpar, M.A., Anderson, P.W., Pines, D. and Shaham, J.: 1984, *Astrophys. J.* **276**, 325.

Hernquist, L.: 1985, *Mon. Not. R. astr. Soc.* **213**, 313.

Jones, P.B.: 1985, *Mon. Not. R. astr. Soc.* **229**, 223.

Negele, J.W. and Vautherin, D.: 1973, *Nucl. Phys. A.*, **207**, 298.

Pines, D. and Alpar, M.A.: 1985, *Nature,* **316**, 27.

Romani, R.W.: 1987, *Astrophys. J.* **313**, 718.

Ruderman, M.: 1969, *Nature,* **223**, 579.

Shapiro, S.L. and Teukolsky, S.A.: 1983, "Black Holes, White Dwarfs and Neutron Stars", Wiley Interscience.

Trümper, J., Kahabka, P., Ögelman, H., Pietsch, W. and Voges, W.: 1986, *Astrophys. J. (Letters)* **300**, L63.

Witten, E.: 1984, *Phys. Rev.*, **D30**,272.

Ziman, J.M.: 1972, "Principles of the Theory of Solids", Cambridge University Press.

VORTEX CREEP DYNAMICS: THEORY AND OBSERVATIONS

M. ALI ALPAR
Physics Department, Research Institute for Basic Sciences
P.O. Box 74, 41470 Gebze-Kocaeli Turkey

DAVID PINES
Physics Department, University of Illinois
110 W. Green St., Urbana, ILL 61801, U.S.A.

1. Introduction

The directly observed part of a neutron star is its outer crust and magnetosphere. Information about the superfluid interior comes from observing its response to sudden perturbations of the crust's rotation. Timing observations of radio pulsars, in particular of glitches (sudden changes) in the rotation rate Ω_c of the crust and its time derivative $\dot{\Omega}_c$ (eg. Lyne and Pritchard 1987 for the newest Crab pulsar glitch), and of the relaxation of these quantities following a glitch, are of unique values as clues to the interior structure of neutron stars. These events are not caused by changes in the external electromagnetic torque on the pulsar, because they are not correlated with sudden changes in the pulse shape, spectrum or polarization of the electromagnetic signal received from the pulsar. Radio pulsars also exhibit timing noise (eg. Cordes and Downs 1985). Some types of timing noise possibly originate in or involve the response of the interior (Cheng 1987), but as a cumulative effect of individually unresolved perturbations to the crust, timing noise does not carry the detailed information that glitches and postglitch relaxation present. Accretion powered neutron stars (X-ray sources in binaries) also show erratic timing behaviour, but in their case it is even more difficult to extract information on the neutron star interior, as the variability probably reflects changes in the accretion process. We shall concentrate on the radio pulsar glitches and particularly on post glitch relaxation, and describe the superfluid interior, in particular the superfluid in the crust regions of the star, from a phenomenological viewpoint. In this picture, the dynamical properties of the crust superfluid, which is proposed to be responsible for the glitches and for postglitch relaxation, are described in terms of the "Thermal creep" of quantized vortex lines (Pines and Alpar 1985 and references therein).

H. Ögelman and E. P. J. van den Heuvel (eds.), Timing Neutron Stars, 441–455.

The fractional change in rotation rate, $\Delta\Omega/\Omega$, is between 10^{-9} and 10^{-6}. The Crab pulsar has exhibited three glitches with $\Delta\Omega/\Omega$, a few times 10^{-9} to 3×10^{-8}, and two old pulsars have shown such small glitches, in the 10^{-9} range. Seven large glitches, each with $\Delta\Omega/\Omega \sim$ a few $\times10^{-6}$ have been observed in the Vela pulsar so far. Four old pulsars have also exhibited glitches in the 10^{-7} - 10^{-6} range. These events, in particular the Vela glitches which take place once every few years, cannot be explained with starquake models. The catastrophic unpinning of pinned vortex lines in the crust superfluid has been proposed as the likely origin of these events (Anderson and Itoh 1975). The mechanism for this instability is not understood though work is in progress. Ovservationally the uncertainty in the exact time of a glitch has come down to as short as one hour. At this resolution, the glitch still still appears as a discontinuous change in the rotation and spindown rates between preglitch and postglitch timing fits. Observations in the near future might catch a glitch during its rise time.

The post glitch relaxation of Ω_c amd $\dot{\Omega}_c$ towards an extrapolation of preglitch timing fits has been observed in detail following several glitches. This relaxation is generally composite, exhibiting several different timescales and different modes of behaviour in time, ranging from simple exponential decay to persistent shifts in the spin-down rate which don't relax for many years. The different modes of post-glitch relaxation are all amenable to analysis within the simple dynamical model of vortex creep. We shall concentrate on this analysis of postglitch relaxation behaviour, rather than the origin of the glitches. Fits to postglitch timing data yield information on the moment of inertia involved in the relaxation process. The observed relaxation times, when evaluated within the vortex creep theory, yield information on the crust superfluid, the superfluid gap and pinning forces and the internal temperature of the neutron star. First, we shall describe the basic features of the vortx creep theory and identify the various modes of observed relaxation with the different regimes of vortex creep. This phenomenological approach yields an evolutionary picture of the nature of post-glitch relaxation as the pulsar ages. We shall then discuss how the uncertainties in the pysics of the crust superfluid effect inferences of the internal temperature and of the superfluid gap and pinning parameters.

The single most basic piece of information provided by glitches and post-glitch relaxation is the fractional change$\Delta\dot{\Omega}_c/\dot{\Omega}_c$ of the spin-down rate. As there is no indication of any change in the external electromagnetic torque on the pulsar, this quantity must reflect the fractional moment of inertia involved in the glitch. In all glitches observed so fra, $\Delta\dot{\Omega}_c/\dot{\Omega}_c$ is positive, that is, the magnitude of the negative spin-down rate $\dot{\Omega}_c$ increases in a glitch. Unlike the case in starquake models, if the glitch arises from catastrophic vortex unpinning, the actual moment of inertia of the star does not decrease. Instead, some part of the star's interior, namely, part of the crust superfluid, decouples from the observed outer crust, so that after the glitch the same external torque is now acting on less moment of inertia; the amount of this decoupled component is given by:

$$\frac{\Delta\dot{\Omega}_c}{\dot{\Omega}_c} = \frac{I_i}{I} = 10^{-2} - 10^{-3} \qquad (1)$$

where I_i is the moment of inertia in the decoupled regions and I the total monent of inertia of the star. All observations so far (a total of 14 glitches from 7 pulsars) (eg. Lyne and Pritchard 1987; Cordes et al. 1987; Manchester et al. 1983; Backus et al. 1982; Newton et al. 1981; Downs 1982; Lyne 1987) yield values of I_i/I in the range 10^{-2} - 10^{-3} . This points to a component of the star that carries less than a hundredth of the moment of inertia. This is precisely the range of fractional moment of inertia in the crust superfluid in most current neutron star models. The crust superfluid is the one interior component which is qualitatively and fundamentally distinct in its dynamical properties from the rest of the star. This qualitative distinction arises from the ingomogeneity that the crust superfluid presents to the motion of quantized vortex lines, which determines its dynamics.

The other basic observation is the slowness of postglitch relaxation. The observed postglitch relaxation times, ranging from a few days to years, are not compatible with viscous relaxation processes of normal fluids and thus form the observational evidence for the existence of superfluid in the neutron star interior. We note that this direct observational evidence at present applies to only $\sim 10^{-2} - 10^{-3}$ of the star in view of the $\Delta\dot{\Omega}_c/\dot{\Omega}_c$ observed. The rest of the star's interior, which, on theoretical grounds, is excected to be mostly superfluid, must then be already rotating rigidly with the observed outer crust on the timescales, > hours, of post-glitch relaxation. Thius implies a very tight dynamical coupling between the neutron star's core and its outer crust (Sauls 1988). The existence of such coupling in spite of the superfluid nature of the core (in fact, because of the presence of a mixed proton-neutron superfluid), is described in Jim Sauls' talk in this volume.

2. Outline of vortex creep theory

The rotation of a superfluid is carried by an array of quantized vortices, each with a quantum of vorticity, κ which is $h/2m_n$ in the case of the neutron superfluid (h is the Planck constant and m_n the neutron mass). Rigid rotation, which minimizes the free energy, cannot be achieved exactly by a superfluid (eg. Feynman 1972). Nevertheless, a superfluid can mimic rigid body rotation very closely by forming an array of quantized vortices. The rotation rate Ω of the superfluid is related to the number n of vortices per unit area through

$$n\kappa = 2\Omega \tag{2}$$

The superfluid spins down if vortices move radially outward from the rotation axis. The equation of motion for Ω is thus:

$$\dot{\Omega} = -\frac{\eta\kappa v_r}{r} \tag{3}$$

where v_r is the velocity of vortex lines in the radially outward direction. Each physical model for the spindown of the superfluid is a model for v_r. In the neutron star crust, the neutron superfluid coexists with a lattice. The lattice presents a very inhomogeneous medium for the motion of vortex lines. The vortex lines have cores made of normal (i.e. non-superfluid) matter. The energy cost of the vortex

core is $\sim \Delta^2/E_F$ per particle in the core, where Δ is the superfluid energy gap and E_F the Fermi energy of the neutrons. These quantities depend on the local density of superfluid neutrons, which is different within the nuclei at the lattice sites and in the interstitial zones. As a result, in the inner crust of the neutron star at densities $10^{13} \leq \rho \leq 2 \times 10^{14}$ gm cm^{-3}, it is energetically favorable for vortex lines to have their cores coincident with the nuclei (Alpar et al. 1984a). This leads to pinning forces. The most general description of this inhomogeneous medium, and the pinning sites it presents to vortex lines is in terms of a random pinning potential, characterized by a typical pinning energy E_p, which is the energy gain at each pinning site, and a typical distance b, the distance between successive pinning sites along a vortex line. This random potential is depicted in Fig. 1a.

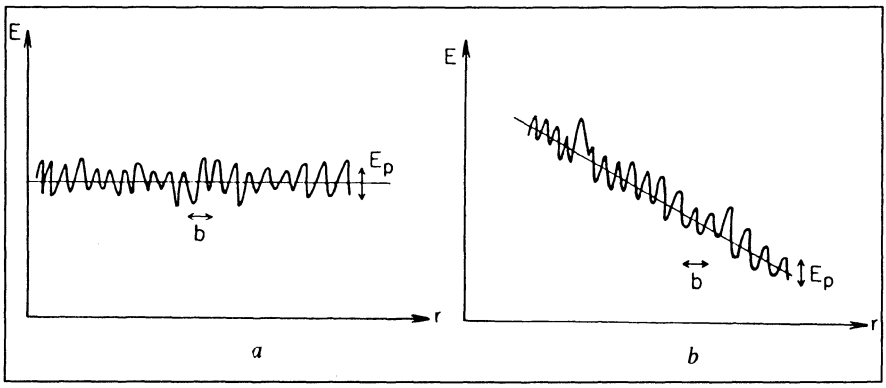

Figure 1: a) The random pinning potential. b) The lag $\Omega - \Omega_c$ biases the random potential. The slope of the average potential is now $\frac{\Delta E}{b} \simeq \rho\kappa\xi(\Omega - \Omega_c)$.

If the star's crust (the lattice) and the superfluid are rotating at the same rate ($\Omega = \Omega_c$) and there are no torques spinning the star down, then there is no bias for a net radially outward flow of vortex lines to spin the superfluid down. At a finite temperature, vortex lines will be climbing over the barriers between pinning sites ("creeping"). In the case of no bias (no external torque) the average creep rate is the same in any direction, so that the expectation value of the radially outward vortex velocity is zero, $< v_r >= 0$.

Now, as the star spins down, vortex pinning will lead to a lag between the superfluid's rotation rate Ω, and that of the crust, Ω_c. The superfluid rotation rate Ω is determined by the distribution of vortex lines: where these have a tendency to pin, their density remains high compared to the density that would give $\Omega = \Omega_c$, the current rotation rate of the of the decelerating crust. The pinned vortex cores themselves are rotating at the rate Ω_c, with the lattice to which they are pinned, while the ambient superfluid rotates at a rate $\Omega > \Omega_c$, set up by the pinned vortex lines. The equation for vortex lines

$$\vec{f_p} = \rho\vec{\kappa} \times (\vec{V_s} - \vec{V_L}) \tag{4}$$

indicates that such a velocity difference between the vortex lines and the superfluid can be sustained only if there is a force on the vortex lines. Here $\vec{f_p}$ is the pinning force exerted by the lattice, per unit length of a line, ρ is the superfluid density and $\vec{\kappa}$ is the vorticity directed along the line, and with magnitude equal to the vortex quantum κ. $\vec{V_s}$ and $\vec{V_L}$ are the velocity of the superfluid and the vortex line, respectively. The pinning force per unit length required by a lag $(\Omega - \Omega_c)$ in rotation rates is thus

$$f_p = \rho\kappa r(\Omega - \Omega_c) \tag{5}$$

where r is the distance from the rotation axis. This corresponds to an energy

$$\Delta E_p = f_p b\xi = \rho\kappa b\xi r(\Omega - \Omega_c) \tag{6}$$

expended at each pinning site. Here b is the distance between pinning sites along the vortex line, and ξ, the coherence length, is the radius of the vortex core. As the star spins down, the tendency of pinned vortices is to move outward, and the pinning force exerted by the lattice is in the radially inward direction. An energy ΔE_p will be gained whenever a vortex line moves outward from a pinning site; if it moves inward, it must face a barrier $E_p + \Delta E_p$. Thus, the pinning forces that sustain the lag $\Omega - \Omega_c$, on the random pinning potential (see Fig. 1b). At a finite temperature T, the probability to tunnel through a pinning barrier will be proportional to $exp - (E_p - \Delta E)/kT$ for motion in the radially outward direction, and to $exp - (E_p + \Delta E_p)/kT$ for radially inward motion. If the microscopic velocity of the vortex line is v_o, the thermal expectation value of the vortex velocity in the radial direction becomes:

$$< v_r >= v_o exp - (\frac{E_p - \Delta E}{kT}) - v_o exp - (\frac{E_p + \Delta E}{kT}) = 2v_o exp - \frac{E_p}{kT} \sinh \frac{\Delta E}{kT} \tag{7}$$

Now, if the lag is so large that ΔE is larger than E_p, vortex lines cannot remain pinned. The lag requires the maximum pinning force available when $\Delta E = E_p$. This defines a critical lag, ω_{cr}:

$$\omega_{cr} = \frac{E_p}{\rho\kappa r b\xi}. \tag{8}$$

Using this definition, we write Eq. (7) as:

$$< v_r >= 2v_o exp - \frac{E_p}{kT} \sinh \left(\frac{E_p}{kT} \frac{(\Omega - \Omega_c)}{\omega_{cr}} \right) \tag{9}$$

3. The equations of motion

Consider a region of pinned superfluid, with rotation rate Ω_i. Substituting the vortex creep rate from Eq. (9) in Eq. (3), we obtain:

$$\dot{\Omega}_i = -\frac{(2\Omega_i)}{r} 2v_o exp - \frac{E_p}{kT} \sinh \left(\frac{E_p}{kT} \frac{(\Omega_i - \Omega_c)}{\omega_{cr}} \right) \tag{10}$$

for the "crust",

$$I_c\dot{\Omega}_c = N_{ext} + \Sigma_i N_{int,i} \tag{11}$$

where N_{ext} is the external torque onthe pulsar and $N_{int,i}$ is the internal torque from region i,

$$N_{int,i} = -I_i\dot{\Omega}_i \tag{12}$$

Each layer i can be treated separately by first neglecting contributions from other internal torques in Eq. (11), since, as the observations indicate,

$$\Sigma_i N_{int,i} = 0(10^{-2})N_{ext}. \tag{13}$$

Thus we replace Eq. (11) with

$$I_c\dot{\Omega}_c = N_{ext} - I_i\dot{\Omega}_i \equiv I\dot{\Omega}_\infty - I_i\dot{\Omega}_i \tag{14}$$

In the last equality we have expressed the external torque N_{ext} in terms of the steady state spindown rate $\dot{\Omega}_\infty$, which obtains when $\dot{\Omega}_c = \dot{\Omega}_i$, with $I \equiv I_i = I_c$ denoting the total moment of inertia. The solutions for $\dot{\Omega}_i$ obtained from (10) and (11) for each separate layer i of the pinned superfluid are then used to construct $\Sigma N_{int,i}$ and thus the expected behaviour of $\dot{\Omega}_c$, including the contribution of all internal torques.

Note that this model has cylindrical symetry. We expect that the equatorial regions of the star, which have the smallest $\omega_{cr} \propto E_p/r$, are involved in unpinning events and their relaxation. The spherical geometry of the star is ignored and it is assumed that thin boundary layers can efficiently patch up the variation of $\Omega_i(r)$ and of the vortex distribution throughout the crust. Operationally, we fit the data with a model consisting of cylindrical pinning layers, and justify these assumptions to the extent that the model fits are successfull.

4. Two Regimes of Vortex Creep

From equations (10) and (11), we form the equation for $\omega = \Omega - \Omega_c$ the lag between the superfluid rotation rate Ω (where we delete the subscript) and that of the crust, Ω_c :

$$\dot{\omega} = -\frac{N_{ext}}{I_c} - \frac{I}{I_c}\frac{4\Omega_o}{r}v_o e^{E_p/kT}\sinh(\frac{\omega}{\bar{\omega}}) \tag{15}$$

where

$$\bar{\omega} \equiv \frac{kT}{E_p}\omega_{cr} \tag{16}$$

We have taken a constant value of Ω, Ω_o, on the right hand side of (15) since variations in Ω are of order ω, and $\omega/\Omega \ll 1$. Eq. (15) can be written as:

$$\dot{\omega} = \frac{I}{I_c}|\dot{\Omega}|_\infty\{1 - \sinh\frac{(\omega/\bar{\omega})}{\eta}\} \tag{17}$$

where the "linearity parameter" η is :

$$\eta \equiv \frac{|\dot{\Omega}|_\infty r}{4\Omega_o v_o} exp \frac{E_p}{kT} \tag{18}$$

In each layer of the pinned superfluid, the value of η is fixed by the pinning energy E_p there and the spindown rate $\dot{\Omega}_\infty = N_{ext}/I$ required by the external torque. Depending on the value of η, Eq. (17) will evolve in one or the other of two different regimes which we shall call the **linear** and the **non-linear** regimes. Each regime is characterized by a different steady state value ω_∞. If the initial conditions are far from the appropriate steady state, there will be rapid transients after which the system settles into an asymptotic evolution to its steady state and spends most of its time close to the steady state. Eq. (17) then has the form:

$$\dot{\omega} = \frac{I}{I_c}|\dot{\Omega}|_\infty \{1 - \frac{\omega}{\bar{\omega}\eta}\} \; if \; n < 1, \; linear \; regime \tag{19}$$

or

$$\dot{\omega} = \frac{I}{I_c}|\dot{\Omega}|_\infty \{1 - \frac{exp(\omega/\bar{\omega})}{2\eta}\} \; if \; n > 1, \; non - linear \; regime \tag{20}$$

The parameter η reflects a comparison between the steady state spindown rate $|\dot{\Omega}|_\infty$ required by the external torque, and the purely thermal rate for vortex line motion through the random potential. It can be written as the ratio of the coresponding timescales,

$$\eta \equiv \frac{t_{tr}}{8t_s} \tag{21}$$

where t_s is the pulsar's characteristic age (spindown time),

$$t_s \equiv \frac{\Omega_o}{2|\dot{\Omega}|_\infty} \tag{22}$$

and t_{tr} is a thermal transit time,

$$t_{tr} \equiv \frac{r}{(v_o exp - E_p/kT)}. \tag{23}$$

If E_p/kT is small enough, thermal creep will be efficient in setting up the equilibrium spindown rate $|\dot{\Omega}|_\infty$ with only a small bias (lag) ω. In the situation, $t_{tr} < t_s$ and $\eta < 1$ the system is in the linear regime. In the opposite situation, $t_{tr} > t_s$, $\eta > 1$, a large bias is required and the system responds non-linearly.

5. The Linear Regime

We write Eq. (19) as:

$$\dot{\omega} = \frac{I}{I_c}(|\dot{\Omega}|_\infty - \frac{\omega}{\tau_\ell}) \tag{24}$$

where the linear regime relaxation time τ_ℓ is defined through:

$$\tau_\ell = \eta \frac{\bar{\omega}}{|\dot{\Omega}|_\infty} = \frac{kT}{E_p} \frac{\omega_{cr} r}{4\Omega_o v_o} exp \frac{E_p}{kT} \tag{25}$$

The steady state lag, ω_∞, which gives $\dot{\omega} = 0$, is:

$$\omega_\infty = |\dot{\Omega}|_\infty \tau_\ell. \tag{26}$$

The solution of Eq. (24) is:

$$\omega(\tau) = \omega_\infty - \delta\omega(0^+) e^{-t/(\tau_\ell I_c/I)} \tag{27}$$

where

$$\delta\omega(0^+) = \omega_\infty - \omega(0^+) \tag{28}$$

In the linear regime, the response of the creep process to a perturbation $\delta\omega(0^+)$ from steady state is linear in the perturbation. This response shows up as:

$$\dot{\Omega}_c = \dot{\Omega}_\infty - \frac{I_p}{I} \frac{\delta\omega(0^+)}{\tau\ell} exp - t/(\tau_\ell I_c/I) \tag{29}$$

in the observed spindown of the crust, as can be obtained from equations (14), (24) and (27). The creep response in the linear regime is a simple exponential decay in time. The relaxation time can be taken to be just τ_ℓ , since $I_c/I \cong 1 - 0(10^{-2})$. I_p denotes the moment of inertia of pinned superfluid. In the steady state, the rate of energy dissipation in I_p, coupled to the crust through Equations (10) and (14) will be,

$$\dot{E}_{diss} = I_p \omega_\infty |\dot{\Omega}|_\infty \tag{30}$$

In the linear regime, this gives

$$\dot{E}_{diss} = I_p |\dot{\Omega}|^2_\infty \tau_\ell \tag{31}$$

This is a very low rate of energy dissipation, compared to that in the non-linear regime, as we shall see below.

6. The Nonlinear Regime

In the non-linear regime, a large bias on thermal creep is needed to make the pinned superfluid spin down at the steady state rate $\dot{\Omega}_\infty$. The evolution of the lag ω is given by Eq. (20). In the steady state, $\dot{\omega} = 0$, we have

$$\omega_\infty = \bar{\omega} ln\ 2\eta = \omega_{cr}(1 - ln\ (4v_o t_s/r)) \tag{32}$$

In most situations, $\eta \gg 1$ and the steady state is then close to the critical lag, $\omega_\infty \cong \omega_{cr}$. When a perturbation $\delta\omega(0^+)$ gives

$$exp\frac{\delta\omega(t)}{\bar{\omega}} \equiv exp\{\frac{\omega_\infty - \omega(t)}{\bar{\omega}}\} = 1 + [exp\frac{\delta\omega(0^+)}{\bar{\omega}} - 1]e^{-t/(\tau_n I)c/I)} \tag{33}$$

where the characteristic relaxation time in the non-linear regime is:

$$\tau_n \equiv \frac{\bar{\omega}}{|\dot{\Omega}|_\infty} = \frac{kT}{E_p}\frac{\omega_{cr}}{|\dot{\Omega}|_\infty} \tag{34}$$

As is the case of linear creep, we have chosen to retain the factor I_c/I in the solution, and defined a τ_n that does not contain I_c/I. This factor can be taken as 1, since $I_c/I = 1 - 0(10^{-2})$. The non-linear relaxation time does not have the intuitive $exp\ E_p/kT$ dependence one expects from thermal relaxation processes. Indeed, the relaxation time is shorter in a **colder** system. This reflects the fact that in the non-linear regime, the thermal processes are strongly driven by the external torque. The colder the system is, the larger the steady state bias required (cf.Fig.1b), and the faster the relaxation processes about this steady state. The response in Eq. (33) has a very non-linear dependence on the initial perturbation. The corresponding response in $\dot{\Omega}_c(t)$ is:

$$\dot{\Omega}(t) = \frac{I}{I_c}\dot{\Omega}_\infty - \frac{I_p}{I_c}\dot{\Omega}_\infty \frac{1}{1 + (e^{t_o/(t_n - 1)e^{-t/(\tau_n I_c/I)}} \tag{35}$$

where we have written the exponential dependence on the initial offset in terms of the "offset time" t_o

$$t_o \equiv \frac{\omega_\infty - \omega(0^+)}{|\dot{\Omega}|_\infty} = \frac{\delta\omega(0^+)}{|\dot{\Omega}|_\infty} \tag{36}$$

The characteristic behaviour of this non-linear response obtains when $t_o \gg \tau_n$, so that

$$\dot{\Omega}_c(t) \cong \dot{\Omega}_\infty + \frac{I_p}{I_c}\dot{\Omega}_\infty \frac{1}{e^{(t-t_o)/\tau_n} + 1} \tag{37}$$

The second term here is a Fermi-function ($(\varepsilon - \mu)kT \rightarrow (t - t_o)/\tau_n$), and $\dot{\Omega}_c$ has the shape shown in Fig.2. The initial perturbation leads to an almost complete stopping of vortex creep. As a result the pinned superfluid does not spin down, and is uncoupled from the external torque. Thus, for a time t_o after the perturbation, the external torque acts on the crust alone. The crust spins down at a rate N_{ext}/I_c, which is $I_p/I_c\dot{\Omega}_\infty$ lower than the steady state rate $\dot{\Omega}_\infty = N_{ext}/I$. This **persistent shift** in $\dot{\Omega}_c$ continues until the offset time t_o. This is the time by which the initial perturbation $\delta\omega(0^+)$ can be remedied by the spindown of the crust alone. At $t \sim t_o$, the lag is back close to ω_∞ and vortex creep starts again. The pinned superfluid recouples with a timescale τ_n about $t = t_o$, and the system returns to steady state, as vortex creep proceeds at a rate giving $\dot{\Omega} = \dot{\Omega}_c = \dot{\Omega}_\infty = N_{ext}/I$. Such persistent

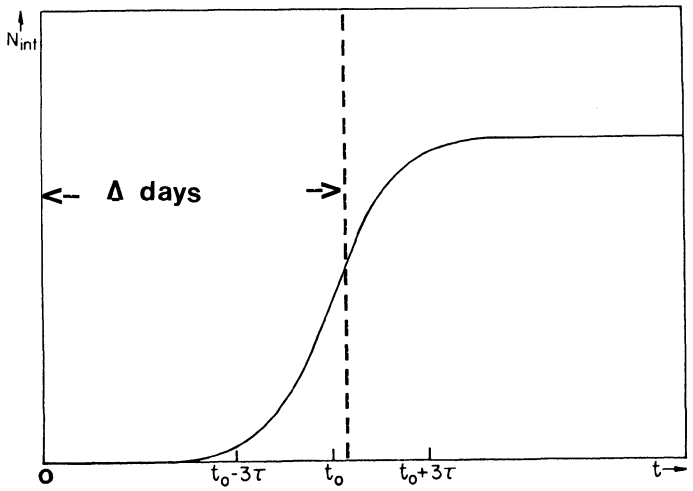

Figure 2: The Fermi function response. At $t = 0$, the time of the glitch, creep is decoupled copmpletely, giving a reduced $\dot{\Omega}_c$. Recoupling starts at $t \simeq t_o$. If the glitch was caught after some Δ days, the observed response (to the right of the dashed line) is quite similar to a simple exponential.

shifts in $\dot{\Omega}_c$ are the most important manifestation of strong non-linear response to perturbations, and indicate the presence of the non-linear regime in the Crab and Vela pulsars in PSR 0355+54 and in PSR 0525+21 (Alpar et al. 1984b; Alpar et al. 1985; Alpar et al. 1988).

The steady state rate of energy dissipation in the non-linear regime is

$$\dot{E}_{diss} = I_p \omega_\infty |\dot{\Omega}|_\infty \cong I_p \omega_{cr} |\dot{\Omega}|_\infty. \tag{38}$$

This is larger than the dissipation rate in the linear regime, by a factor $\omega_{cr}/|\dot{\Omega}|_\infty \tau_\ell$. Let us use the parameters of PSR 0355+54 as an example. The postglich relaxation of this pulsar contains a simple exponential decay with a 44 d time constant, which seems to reflect the linear regime (Lyne 1987). The spindown rate of PSR 0355+54 is $|\dot{\Omega}| \cong 10^{-12} rad/s^2$. We take a typical estimate of ω_{cr}, 10^{-2} (the current observational upper limit is $\omega_{cr} \leq 0.7 rad/s$). We find that typically a region of non-linear creep with $\omega_{cr} \cong 10^{-12}$ dissipates energy at a rate that is some 2500 times higher than in a linear creep region. The energy dissipation by non-linear creep could be large enough to be observable in old pulsars. In these systems, the initial heat content has already been radiated away, so that enerty dissipation in the interior forms the source of any thermal luminosity from the surface. Thus,

$$4\pi R^2 \sigma T_s^4 = I_p \bar{\omega}_{cr} |\dot{\Omega}| \tag{39}$$

can be used to detect, or place upper limits on, the parameter $I_p \bar{\omega}_{cr}$, representing an average over the entire pinned superfluid. This has been used to convert upper

limits on the thermal luminosities of radio pulsars to limits on the pinning parameter $\bar{\omega}_{cr}$. The lowest of these, that for PSR 1929+10, gives $\bar{\omega}_c \lesssim 0.7$ rad s^{-1} if I_p is taken to be 10^{43} gm cm^2. It is encouraging to note that the temperature inferred from Eq. (39) for PSR 0525+21 agrees with the temperature obtained from relaxation times in the post-glitch timing fits, assuming the postglitch relaxation reflects the presence of non-linear creep.

7. Ambiguities in Distinguishing Linear and Nonlinear Response

The behaviour of $\dot{\Omega}_c(t)$ following a glitch is clearly the key to an evaluation of the pulsar's dynamics in the framework of vortex creep theory. In principle, the observation of a postglitch relaxation of the simple exponential form given in Eq. (29) will indicate the presence of a linear creep region, while a Fermi-function response, as in Eqs. (35) or (37), indicates non-linear creep. One can then proceed to extract information on the structure of the star from an appropriate evaluation of the parameters of the timing fit. For example Eq. (25) would be applied to relaxation times of a linear response, while Eq. (34) would be used the non-linear regime.

In practice, the interpretation of postglitch timing data can be ambiguous for several reasons. The postglitch response usually requires more than one component, of the type given in Eq. (29) or Eq. (37), to fit the data. Different combinations of exponentials and/or Fermi functions can produce equally good fits to the data.

In the past, the uncertainties in the glitch date, typically a few weeks, introduced a further ambiguity. When the Fermi-function response is not observed for the initial Δ days, and $\Delta \sim t_o$, what is then observed is similar to an exponential function. For some parts of the pinned superfluid, where no sudden vortex motion occurs at the glitch $\delta\omega(0) = \Delta\Omega_c$, the observed change in $\Omega_c.t_o = \Delta\Omega_c/|\dot{\Omega}|$ for such regions (Alpar et al. 1984a). For the first four Vela pulsar glitches, this $t_o \cong 10$ days, and the uncertainty in the glitch date is of the same order. As there was a long term offset in $\dot{\Omega}_c$, which indicates the presence of non-linear creep, our fits to the first four post-glitch data sets of the Vela pulsar employed non-linear creep response (Fermi-functions) alone (Alpar et al. 1984b). The last three glitches have been caught within a day and the postglitch response contains prompt exponentially relaxing components (Hamilton et al. 1982; McCulloch et al. 1983; Klekociuk et al. 1985). It is likely that detailed data analysis will show that the early response is from a linear rather than non-linear creep region.

Another possible source of ambiguity is that non-linear creep regions can also produce linear response, in the form of an exponential decay in time, **if the initial perturbation is small enough.** If $t_o \ll \tau_n$, Eq. (35) reduces to

$$\dot{\Omega}_c(t) = \dot{\Omega}_\infty - \frac{I_p}{I}\frac{|\dot{\Omega}|_\infty t_o}{\tau_n} e^{-t/(\tau_n I_c/I)} \tag{40}$$

This is formally identical to the linear response in Eq. (29). However, $t_o \ll \tau_n$ is the precondition for Eq. (40) to obtain in the non-linear regime; this response

is smaller, by a factor t_o/τ_n, than the usual magnitude $I_p/I|\dot{\Omega}|_\infty \sim 10^{-2}|\dot{\Omega}|_\infty$ of creep response and will not be part of the **observable** response in most cases.

Interpreting a given postglitch response in terms of linear or non-linear creep is a matter of distinguishing between the different time dependences when several distinct components reflecting the response of different parts of the pinned superfluid are present.

8. Linear vs Non-linear Creep in the Evolution of a Pulsar

If we assume that all neutron stars are structurally similar and contain pinned superfluid regions of similar properties in their crust, the prevalence of linear vs. non-linear creep in a particular pinning layer characterzed by some pinning energy E_p depends on the spindown rate $\dot{\Omega}$ and the temperature T of the pulsar. As a pulsar ages, $|\dot{\Omega}|$ becomes smaller and the temperature also drops. The linear or non-linear nature of vortex creep thus depends on the pulsar's age. One finds that non-linear creep prevails over larger and larger parts of the pinned superfluid and dominates postglitch response as a pulsar ages.

The transition, $\eta = 1$, between the two creep regimes, gives a transition value of E_p/kT, as a function of the pulsar's age, so that in pinning regions with E_p/kT less than the transition value, creep is in the linear regime, while E_p/kT greater than the transition value requires non-linear creep. From Eq. (18), with $\eta = 1$, we obtain:

$$\frac{E_p}{kT}|_{transition} = ln\ (\frac{8t_s v_o}{r}) \cong 35.5 + ln\ t_{s,6} + ln\ (\frac{v_o,7}{r_6}) \qquad (41)$$

where $t_{s,6}$ is the star's characteristic (spin-down) age $\Omega/2|\dot{\Omega}|$ in units of 10^6 years, and typical values $v_o = 10^7$ cm/sec and $r = 10^6$ cm are used for the microscopic velocity v_o of vortex lines and the distance r from the rotation axis. The transition has a **logarithmic** dependence on the star's age. If the temperature remained constant as the star became older, $E_{p,tr}$ would become larger, so that over a given spectrum of pinning energies E_p, a gradually diminishing set of the strongest pinning layers would support non-linear creep. This is a consequence of decreasing external torque on the system: more of the pinning regions are able to meet the demands of the external torque with small biases and linear creep. However, this tendency, only logarithmic in t_s, is overcome by the effect of cooling. The dependence of the transition condition on internal temperature is **linear**, and the temperature in turn has a power-law or algebraic dependence on the $|\dot{\Omega}|$ and the age of the pulsar. This effect dominates and pushes $E_{p,tr}$ to lower values. As the pulsar **cools**, thermal rates become less efficient and strong biases and non-linear response are required over larger and larger portions of the pinned superfluid in order to achieve steady state conditions with the decreasing $|\dot{\Omega}|$.

All pulsars with observed postglitch timing relaxation have exhibited persistent shifts indication non-linear response. Younger pulsars, like Crab and Vela, and 0355+54 also seem to possess linearly responding regions. It is likely that linear response is restricted to smaller portions of the pinned superfluid, until it becomes

unobservable in old pulsars (Alpar et al. 1988). A detailed analysis of existing and future post-glitch data with this evolutionary viewpoint will form a critical test of the vortex creep theory. The linearity parameter η can also be written as:

$$\eta = \frac{\tau_\ell}{\tau - n} \tag{42}$$

using Equations (18), (25) and (34). Vortex creep will operate in the regime with the shortest relaxation time. In a given pinning layer, we note that τ_n depends only linearly on $T/|\dot{\Omega}|$ while τ_ℓ becomes larger exponentially in E_p/kT as the star cools, so that the non-linear regime takes over.

9. Information From Relaxation Times

The observed relaxation times can be evaluated within the vortex creep model to yield information on the interior temperature and/or on pinning energies and the superfluid gap in the neutron star's inner crust. The ambiguities concerning the linear or non-linear nature of the response are likely to be resolved with recent or future data. Here we shall illustrate the way an observed relaxation time can lead to an estimate of the interior temperature or to bounds on pinning parameters, most fundamentally on the value of the superfluid gap in the dense inner crust medium.

A relaxation time from the linear regime is not very useful because of its exponential dependence on E_p/kT. The ubiquitous presence of persistent shifts in postglitch data indicates that non-linear creep is present in all pulsars with observed relaxation, even the youngest ones. The particular data sets from the Vela and the Crab pulsars, which we previously interpreted as non-linear relaxation, may turn out to reflect the linear regime. The old pulsar PSR 0525+21 exhibits a 150d relaxation time that is probably in the non-linear regime. It is likely that more definite examples of non-linear relaxation time depends on ω_{cr}/E_p, and thus, with Eq. (34), can be written as:

$$\tau_n = \frac{kT}{|\dot{\Omega}|}\frac{1}{\rho\kappa r}\frac{1}{(b\xi)} \tag{43}$$

Using an observational limit on T or a theoretical estimate based on the energy dissipation rate, one can obtain the value of $(b\xi)$ from an observed non-linear relaxation time. Alternatively, a **model dependent** estimate of $b\xi$ will lead to an estimate of the internal temperature (the inner crust is part of the isothermal care of the neutron star after about 500 years).

The distance b between successive pinning sites along a vortex line is of order of the lattice spacing b_z only if the pinning energy is large enough to move the nuclei, which constitute pinning sites from their equilibrium lattice sites (Alpar et al. 1984b). If pinning is really strong, the corresponding ω_{cr} is relatively large ($\gtrsim$a few rad s^{-1}). The observational upper limits on $I_p\bar{\omega}_{cr}$ rule out the prevalence of such strong ω_{cr} over most of the pinned superfluid (Alpar et al. 1987). Pinning energies depend roughly on the square of the superfluid gap. Recent calculations have reduced theoretical values of the gap, providing another argument against

strong pinning. If pinning is not strong enough to dislodge nuclei, one has a picture of weak pinning wherein a vortex line pins to those nuclei that happen to be on their way geometrically. In this picture,

$$b \cong b_z^3/\pi\xi^2 \tag{44}$$

giving

$$\tau_n = \frac{kT}{|\dot{\Omega}|}\frac{1}{\rho\kappa r}\frac{\xi}{b_z^3} = \frac{kT}{\Delta}\frac{3\kappa}{k_F^2 b_z^3 r}\frac{1}{|\dot{\Omega}|} \tag{45}$$

Using some typical values of density and lattice spacing, this gives

$$\tau_n(days) \cong 10\frac{kT(keV)}{\Delta(MeV)}\frac{1}{r_6|\dot{\Omega}|_{-10}}(b_z/50fm)^3(k_F/k_{F,O})^2 \tag{46}$$

Where k_F is the Fermi wavenumber of the neutrons, and $k_{F,0}$ that of nuclear matter. We have expressed the coherence length ξ as $2E_F/(\pi k_F \Delta)$. This is of great value as a direct handle on Δ, when T can be estimated independently. Alternatively within the uncertainties of the physics of pinning and the calculations of energy gaps, one can in principle estimate the internal temperature. A detailed re-evaluation of pinning of vortex lines by the lattice or its defects is now in order, as the body of astrophysical data has accumulated to accommodate a systematic phenomenology of postglitch relaxation in terms of vortex creep models.

We have not discussed the model for the glitches in terms of sudden vortex unpinning events the relevance of vortex creep to the understanding of pulsar timing noise or the treatement of precession of the superfluid in terms of vortex creep (Alpar et al. 1987; Cheng et al. 1988; Alpar and Ögelman 1987). These other avenues of research will also yield further information on the neutron star interior as more glitches and postglitch data are collected and to the extent that the present dynamical model in terms of vortex creep continues to pass the test as a systematic reference frame encompassing the different modes of postglitch relaxation. The evaluation from linear to non-linear creep is a particularly important feature that one expects to emerge from the body of data from pulsars of different ages.

ACKNOWLEDEMENTS: We thank K.S. Cheng and J. Shaham for many discussions of vortex creep.

REFERENCES:

Alpar, M.A., Anderson, P.W., Pines, D. and Shaham, J.: 1984a, *Astrophys. J.* **276**, 323.

Alpar, M.A., Anderson, P.W., Pines D. and Shaham, J.: 1984b, *Astrophys. J.* **278**, 791.

Alpar, M.A., Brinkmann, W., Kizilo, Ü., Ögelman, H. and Pines, D.: 1987, *Astron. Astrophys.* **177**, 101.

Alpar, M.A., Cheng, K.S. and Pines, D.: 1988, to be submitted.

Alpar, M.A., Cheng, K.S., Pines, D. and Shaham, J.: 1988, *Mon. Not. R. astr. Soc.* in the press.

Alpar, M.A., Nandkumar, R. and Pines D.: 1985, *Astrophys. J.* **288**, 191.

Alpar, M.A., and Ögelman, H.: 1987, *Astron. Astrophys.* **185**, 196.

Anderson, P.W. and Itoh, N.: 1975, *Nature,* **256**, 25.

Backus, P.R., Taylor J.H. and Damashek, M.A.: 1982, *Astrophys. J. (Letters)* **255**, L63.

Cheng, K.S.: 1987, *Astrophys. J.* **321**, 805.

Cheng, K.S., Alpar, M.A., Pines, D. and Shaham, J.: 1988, *Astrophys. J.* in the press.

Cordes, J.M. and Downs, G.S.: 1985, *Astrophys. J. Suppl. Ser.)* **59**, 343.

Cordes, J.M., Downs, G.S. and Krause-Polstroff: 1987, *Astrophys. J.*

Downs, G.S.: 1982, *Astrophys. J. (Letters)* **257**, L67.

Feynman, R.P.: 1972, **Statistical Mechanics**, Benjamin.

Hamilton, P.A., McCulloch, P.M. and Royle, G.W.R.: 1982, IAU Circ. No. 3729.

Klekociuk, A.R., McCulloch, P.M. and Hamilton, P.A.: 1985, IAU Circ. No. 4089.

Lyne, A.G.: 1987, *Nature,* **326**, 569.

Lyne, A.G. and Pritchard, R.S.: 1987, *Mon. Not. R. astr. Soc.* **229**, 223.

Manchester, R.N., Newton, L.M., Hamilton, P.A. and Goss, W.M.: 1983, *Mon. Not. R. astr. Soc.* **202**, 269.

McCulloch, P.M., Hamilton, P.A., Royle, G.W.R. and Manchester, R.N.: 1983, *Nature,* **302**, 319.

Newton, L.M., Manchester, R.N. and Cooke, D.J.: 1981, *Mon. Not. R. astr. Soc.* **194**, 841.

Pines, D. and Alpar, M.A.: 1985, *Nature,* **316**, 27.

SUPERFLUIDITY IN THE INTERIORS OF NEUTRON STARS

J.A. Sauls
Department of Physics and Astronomy
2145 Sheridan Road
Northwestern University
Evanston, IL 60208
U.S.A.

ABSTRACT. The discoveries of more than 400 neutron stars as radio pulsars continue to provide an intellectual challenge to physicists and astronomers with diverse backgrounds. I review some of the ideas that have been proposed for the structure of neutron star interiors, and concentrate on the theoretical arguments for the existence of superfluidity in neutron stars. I also discuss the implications of neutron superfluidity and proton superconductivity for the rotational dynamics of pulsars, and review arguments that have been proposed for observable effects of superfluidity on the timing history of pulsars and perhaps other neutron stars.

1. INTRODUCTION

The discovery of pulsars, and their subsequent identification as rotating neutron stars, initiated a flurry of activity by theorists to better understand neutron-star structure and matter at extremely high density [see the reviews by Baym and Pethick (1975, 1979)]. Our model of neutron star structure is reminiscent of the interior structure of Earth [Anderson, Alpar, Pines, Shaham (1982)]; a solid outer crust, with various layers, which encloses a much hotter fluid core. This latter component is a conducting fluid, which although not well understood, is the source of a magnetic field. For the purpose of constructing a model for neutron star interiors, perhaps their distinguishing feature is that they are extraordinarily cold; even at interior temperatures of order $10^6 - 10^8$ K quantum statistics plays a crucial role in the thermodynamic and transport properties of nuclear matter. It is because neutron-star matter is cold that many exotic states of matter have been proposed to exist inside these stars. The idea that neutron stars contain a liquid interior of *superfluid neutrons* and *superconducting protons* [Migdal (1959); Ginzburg and Kirzhnits (1964)] was motivated in large part by our understanding of the mechanism for superconductivity in terrestrial materials as a result of the BCS [Bardeen, Cooper, Schrieffer (1957)] theory, and also by the observation of *glitches* in the timing data of Vela pulsar [Radhakrishnan and Manchester (1969); Reichley and Downs (1969)].

In Sec.3 I review the *standard model* for the interior structure of neutron stars, paying special attention to the arguments in support of the idea that neutron stars contain superfluid interiors. One expects the rotational motion of a neutron star with a superfluid core, decelerating under the action of external radiation torques, to be rather different than an otherwise similar star with a normal fluid core of high viscosity. The main features of the rotational equilibrium of the superfluid

H. Ögelman and E. P. J. van den Heuvel (eds.), Timing Neutron Stars, 457–490.

and superconducting interior are discussed in Sec.4-6, while in the remaining sections I discuss the essential features of the rotational dynamics of the superfluid interior. The important differences in the rotational dynamics of a star with a superfluid core compared to a normal-matter core are: (i) the timescales for momentum transfer between the superfluid and the neutron star crust, and (ii) the existence of metastable flow states which are fundamentally related to the phenomenon of persistent superfluid flow, as in liquid HeII, and vortex pinning, as in laboratory superconductors. It is here that an important connection exists between the theory of neutron stars and the timing observations on radio pulsars. In Sec.12-13 I discuss more speculative aspects of the theory and some unanswered questions of importance for our understanding of the evolution of pulsar interiors. I begin by reviewing some concepts from the theory of superfluidity and superconductivity.

2. CONDENSATION

Review articles [*e.g.* Shaham (1980)] that discuss superfluidity in neutron stars often emphasize the importance of the *energy gap* in the superfluid phase. The existence of an energy gap in nuclear matter is important in understanding neutron-star rotational dynamics; however, the essential concept is the phenomenon of *condensation*, by which I mean the *macroscopic occupation* of a single quantum state. In liquid ^4He superfluidity is closely related to Bose-Einstein condensation. The relevant single-particle states are simply $\psi_{\vec{p}} \sim e^{i\vec{p}\cdot\vec{r}}$, and below 2.2 K a finite fraction of the ^4He particles occupy the zero-momentum state, ψ, *i.e.* $|\psi|^2 \sim O(N/V)$. The important feature of condensation, so far as the phenomenon of superfluidity is concerned, is that the amplitude of the condensate,

$$\psi(\vec{R}) = |\psi(\vec{R})|\, e^{i\vartheta(\vec{R})}, \tag{1}$$

is *phase coherent* over the entire fluid. Thus, if the condensate phase is known at point $\vec{R}$, then one can predict the phase a macroscopic distance away, according to $\vartheta(\vec{R}') = \vartheta(\vec{R}) + 2M\vec{v}_s \cdot (\vec{R}' - \vec{R})/\hbar$, where $\vec{v}_s$ is the local velocity of the condensate, *i.e.* the superfluid velocity.

In systems of Fermions, *e.g.* neutrons and protons in the interior of neutron stars, condensation occurs by the formation of *pairs* of Fermions, or *Cooper pairs*. Since Fermions have a spin ($s = \hbar/2$ for neutrons and protons) the amplitude of the condensate depends on the internal arrangement of the constituent spins; in addition the pair may exhibit internal orbital motion. The general form of the Cooper pair amplitude is described by a wave function $\psi_{s_1,s_2}(\vec{R},\vec{r})$, where s_1, s_2 are the spin projections of the Fermions, $\vec{R}$ is the center-of-mass of the pair, and $\vec{r}$ is the orbital coordinate of the pair. The dimension of the pair wave function in neutron matter, the *orbital size* of the Cooper pair, is of order 100 fm, which although small, is nevertheless large compared to the average distance between neutrons in the interior of the star. Even though the size of the pair wave function is measured in hundreds of Fermis, this amplitude is *coherent* over macroscopic distances, in this case throughout the liquid interior of the star. When condensation occurs a macroscopic number of neutrons form pairs in precisely the same two-particle wave

function, independent of their center-of-mass position. Hereafter I use the term 'order parameter' to mean 'Cooper pair amplitude' because this macroscopically occupied state represents a high degree of order, and the symmetry and structure of the Cooper pair amplitude determine the macroscopic magnetic and flow properties of the condensed phase. There is a great variety of phenomena associated with the spin and orbital motion of the Cooper pairs. Since these states may play a role in the theory of the rotational motion of neutron star interiors, it is useful to classify some of the possible internal motions of the pairs and comment briefly on what is known about the order parameters for laboratory superfluids and superconductors.

2.1 *S-wave, spin-singlet pairs*

Since the order parameter represents a bound state of two Fermions it must be anti-symmetric under exchange of the coordinates and spins of the pair,

$$\psi_{s_1,s_2}(\vec{R},\vec{r}) = -\psi_{s_2,s_1}(\vec{R},-\vec{r}). \tag{2}$$

Most laboratory superconductors are described by an order parameter with quantum numbers, $|\vec{S}| = 0$ (*spin singlet*) and $|\vec{l}| = 0$ (*s-wave*), where $\vec{S} = \vec{s}_1 + \vec{s}_2$ is the total spin, and $\vec{l} = \vec{r} \times \frac{\hbar}{i}\vec{\nabla}_r$ is the orbital angular momentum of the pair. The orbital motion is isotropic and the spins of the Fermions are paired into a magnetically inert singlet; thus, the pair amplitude reduces to a single complex scalar amplitude, $\psi(\vec{R}) = \psi_{\uparrow,\downarrow}$, analogous to the order parameter in superfluid ^4He. This is also the form of the order parameter believed to describe the condensate of superfluid neutrons in the inner crust of a neutron star, and the superconducting protons in the liquid interior.

2.2 *P-wave, spin-triplet pairs*

The most remarkable terrestrial superfluids are the phases of liquid ^3He [see Anderson and Brinkman (1978)]. There are three superfluid phases that are stable in different regions of temperature, pressure and magnetic field. This fact alone differentiates liquid ^3He from liquid ^4He and conventional *s-wave* superconductors. It is known that superfluid ^3He is described by a *spin-triplet* ($S = |\vec{s}_1 + \vec{s}_2| = \hbar$), *p-wave* ($l = \hbar$) order parameter. For pairing into states with one unit of orbital angular momentum, ψ is a linear combination of the spherical harmonics, $\{Y_{1,m}(\vec{r})\ ;\ m = \pm 1, 0\}$,

$$\psi_{s_1,s_2}(\vec{R},\vec{r}) = \sum_{m=\pm 1,0} \psi^m_{s_1,s_2}(\vec{R})\ Y_{1,m}(\vec{r}). \tag{3}$$

These odd-parity states, [$Y_{1,m}(\vec{r}) = -Y_{1,m}(-\vec{r})$], imply that the spin-dependent part of the pair amplitude is symmetric under exchange of the two Fermion spins. The ^3He atom has a total spin of $\hbar/2$ due to an unpaired nucleon, and there are three symmetric spin states that can be constructed from two spin-1/2 amplitudes. Thus, the general form of the pair amplitude is

$$|\psi> = \psi_{\uparrow\uparrow}\ |\uparrow\uparrow> + \psi_{\uparrow\downarrow}\ |\uparrow\downarrow + \downarrow\uparrow> + \psi_{\downarrow\downarrow}\ |\downarrow\downarrow> . \tag{4}$$

In contrast to superfluid ^4He, a spin-triplet p-wave superfluid such as ^3He requires up to nine complex amplitudes (3 spin $\times$ 3 orbital). Note that these Cooper pairs are in principle *magnetic*. I list the form of the order parameter for a few specific cases.

2.3 *Superfluid* $^3He - B$

The order parameter is a superposition of all three magnetic states with equal amplitudes and phases,

$$|\psi >= \psi_B(\vec{r}) \{| \uparrow\uparrow> + | \uparrow\downarrow + \downarrow\uparrow> + | \downarrow\downarrow>\}, \tag{5}$$

and the orbital amplitude is such that the *total* angular momentum of the Cooper pairs is zero, $|\vec{J}| = |\vec{l} + \vec{S}| = 0$. The B-phase is a special state which is "isotropic" in that the pair amplitude is invariant under joint rotations of the spin and orbital coordinates.†

2.4 *Superfluid* $^3He - A_1$

The A_1 phase corresponds to pairing in only one component of the spin triplet and is stable only in a magnetic field and a narrow range of temperatures. The order parameter directly reflects the *magnetic polarization* of this superfluid,

$$|\psi >= \psi_{A_1}(\vec{r}) \mid \uparrow\uparrow> . \tag{6}$$

2.5 *Interior superfluid of neutron stars:* $^3P_2$ *phase*

As I discuss below it is plausible that neutron matter in the liquid interior of a neutron star is a Fermion superfluid described by a spin-triplet, p-wave amplitude with total angular momentum $J = 2$ [Hoffberg, Glassgold, Richardson, Ruderman (1971)],

$$|\psi > = \sum_{J_z=0,\pm1,\pm2} \psi_{J_z} \, |J = 2, J_z > . \tag{7}$$

In fact the ground state of the non-rotating $^3P_2$ phase, to use the spectroscopic designation for the pair amplitude, is believed to be a state with $J_z = 0$ with respect to a fixed but arbitrary axis $\hat{z}$ [Sauls and Serene (1978); Vulovic and Sauls (1984)]. Thus, the ground state of the core superfluid in neutron star matter is also described by a single scalar amplitude, ψ_0. This is no longer the case for the equilibrium state of a *rotating* neutron superfluid; a proper description of the *vortices* in the $^3P_2$ phase - which are required for the superfluid to co-rotate with the crust, conducting plasma and magnetic field - requires that all five magnetic sub-states, ψ_{J_z}, be present in the vicinity of the vortices. This fact leads to a novel magnetic structure for the vortex lines inside neutron stars (Sec.9).

---

† This statement is slightly modified when the weak nuclear dipolar interaction is included.

3. PAIRING INSTABILITY AND TRANSITION TEMPERATURES

There is no direct evidence that the interiors of neutron stars are superfluid. However, there are two arguments in favor of this idea. The first is based on the BCS theory of superconductivity, which is arguably the most successful many-body theory of condensed matter. The second reason is the existence of long timescales for the recovery of the angular deceleration of several pulsars following a glitch (Sec.7).

The basic structure of a neutron star with a mass $M = 1.4\ M_{sun}$ is summarized in Fig.1. The radius and central density of the star, which depend on the mass and the equation of state of neutron-rich nuclear matter for densities above that of terrestrial nuclear matter, are both somewhat uncertain. However, all models of neutron stars have a liquid interior, which contains most of the moment of inertia of the star, surrounded by a solid metallic crust of neutron-rich nuclei embedded in a degenerate fluid of electrons. The radial structure of the crust has been studied in detail by numerous authors and is reviewed by Baym and Pethick (1975). Of particular importance is the structure of the inner crust of the neutron star for densities $\rho > 4.3 \times 10^{11}\ g/cm^3$, where the nuclei become so neutron rich that the neutrons begin leaking out of the nuclei to form a background fluid of degenerate neutrons surrounding the nuclear lattice. This crustal region persists to densities near terrestrial nuclear matter density, $\rho \simeq 2 \times 10^{14}\ g/cm^3$, at which point the nuclei dissolve into a dense fluid consisting primarily of neutrons and a small percentage of protons and electrons, all of which are degenerate. Many other exotic states of matter have been proposed to exist in very dense cores of neutron stars, including pion condensates, free quarks and solid neutron matter [see Baym and Pethick (1975)]. However, I do not discuss these more speculative possibilities for the inner core.

Neutron stars are cold (*i.e.* $T \sim 10^8 K \ll T_{\rm Fermi} \sim 10^{12} K$) and the same theoretical arguments that lead to the conclusions that terrestrial matter should be superconducting with transition temperatures $T_c \simeq 10^{-3}\ T_{Fermi}$ also predict that neutron stars should have superfluid interiors. The necessary ingredient for the formation of a condensate of Cooper pairs, and hence a superfluid (or superconductor) is an attractive interaction between two neutrons (or protons) on the Fermi surface with *zero* total momentum. The Fermi sea guarantees the formation of a bound-state, *i.e.* a Cooper pair, no matter how weak the interaction, so long as it is attractive. Of course the strength of the interaction has an important effect on the temperature at which condensation occurs. In neutron-star matter the origin of this attraction is the nucleon-nucleon interaction, which has the contributions,

$$V_{nn} = V_{central}(|\vec{r}|) + V_{so}(|\vec{r}|)\ \vec{S} \cdot \vec{l}, \tag{8}$$

where the *central* part of the potential is attractive at long-range, $r > \frac{1}{2} fm$, due the exchange of pions, and repulsive at short distances due to the exchange of the ω meson; this same vector meson is responsible for the spin-orbit interaction, which is large at short distances [Brown and Jackson (1979)]. A great deal is known about these basic interactions from nucleon-nucleon scattering. In Fig.2 I reproduce the experimentally determined scattering phase shifts of free neutrons [as compiled in Tamagaki (1970)]. A positive phase shift represents an attractive

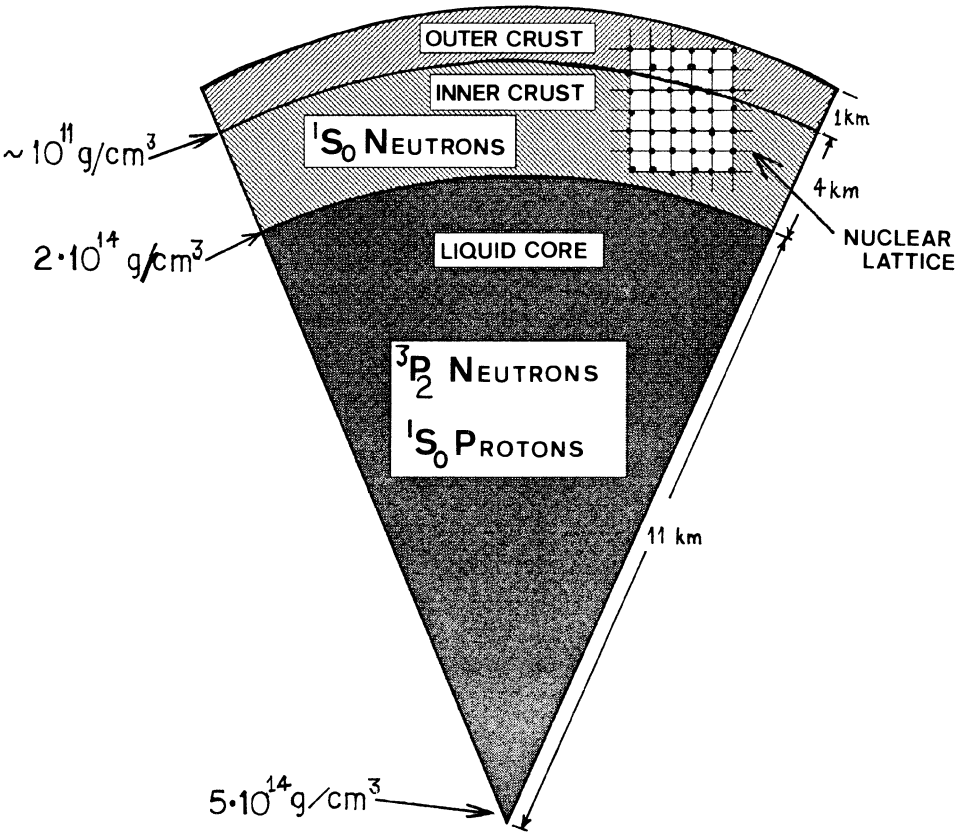

Figure 1. Cross section of a 1.4 M_{Sun} neutron star based on a *stiff* equation of state [Pandharipande, Pines and Smith (1976)]. The density profiles for the superfluid components are based on the transition temperatures of Hoffberg, *et al.* (1971) and Chao, *et al.* (1972).

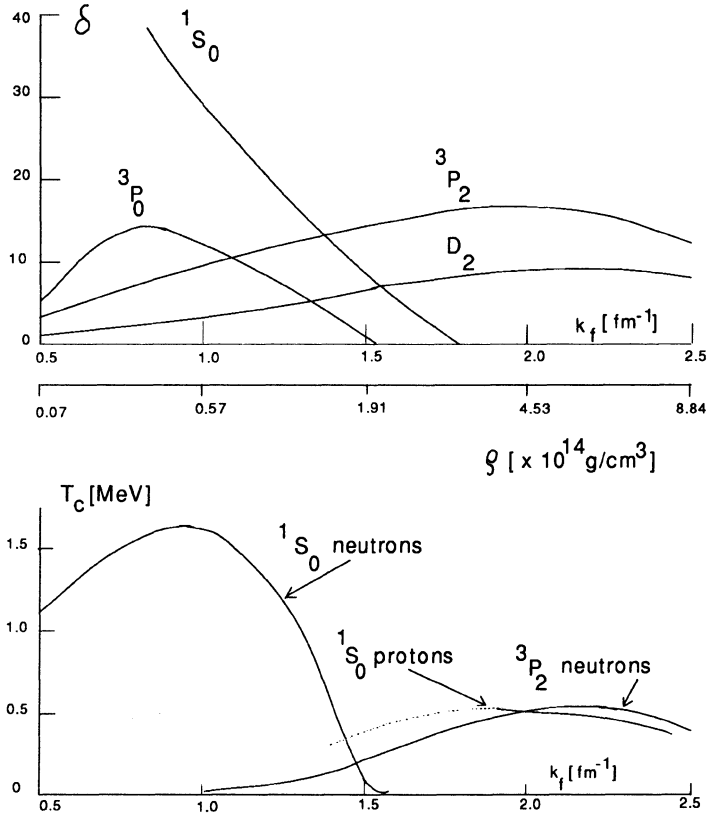

Figure 2. The top figure shows the free nucleon-nucleon scattering phase shifts (in degrees) [from Tamagaki (1971)] for the lowest angular momentum channels. At low density the most attractive interaction is in the singlet, s-wave channel, $^1S_0$, while at high density the dominant attraction is in the $^3P_2$ channnel. The transition temperatures were calculated by Hoffberg, *et al.* (1970) for neutron matter, and by Chao, *et al.* (1972) for proton matter. The cross-over from s-wave pairing to p-wave pairing occurs at approximately 2×10^{14} g/cm^3, which is close to the density of the crust-core interface.

interaction in channels with various angular momentum quantum numbers (S, l, J). The energy dependence (in the center-of-mass frame) is converted to density by setting the center-of-mass energy equal to that of two Fermions on the Fermi surface, *i.e.* $E_{cm} = 4\ E_F(\rho)$. At low density, below approximately $2 \times 10^{14} g/cm^3$, the most attractive channel is the singlet, s-wave channel ($^1S_0$). However, the $^3P_2$ and $^1D_0$ interactions dominate the S-wave interaction at higher density, with the $^3P_2$ channel being the most attractive. Note that the P-wave interactions with $J = 0, 1$ are always repulsive at high density. Based on this data, and calculations of the structure and density profile of a neutron star, Hoffberg,*et al.* (1971) argued that more than one superfluid state was possible inside a neutron star. In the inner crust, $3 \times 10^{11} g/cm^3 < \rho < 2 \times 10^{14} g/cm^3$, a BCS-superfluid of neutron pairs in $^1S_0$ bound states forms, while at higher densities the neutrons condense into a $^3P_2$ state. The lower density protons are predicted to condense into a $^1S_0$ state [Chao, *et al.* (1972)]. Many authors have used this phase shift data, combined with more sophisticated approaches, to estimate the transition temperatures for condensation into these superfluid states. Typical values of the transition temperatures, T_c, for both superfluid states range from 0.1 MeV to 1 MeV, *i.e.* 10^9 K to 10^{10} K, which are low temperatures compared to the Fermi temperatures of neutron-star matter, but quite high temperatures compared to the ambient temperatures for even the youngest neutron star; *e.g.* the interior temperature of the Crab pulsar is estimated to be of order 10^8 K [Alpar, *et al.* (1985)].

A word of caution: transition temperatures are notoriously difficult to calculate accurately. This is clear from the BCS formula for the transition temperature, $T_c = E_F\ e^{1/N(E_F)V_{BCS}}$, which contains in the exponent the strength of the pairing interaction, which itself is a many-body effective interaction between neutron excitations and may differ significantly from the bare interaction. The uncertainty in estimates of T_c is in fact more serious than indicated by this simple formula. The BCS theory is an inadequate theory for predicting whether a given material will be a superconductor, *i.e.* in predicting T_c. Such a theory exists, and was formulated roughly ten years after the BCS theory, but it is applicable only to superconductors in which the pairing interaction between electrons is mediated by the phonons of the (heavier) ionic lattice [for a review see Rainer (1985)]. There is so far no reliable first principles theory of T_c for a self-interacting Fermi superfluid.† However, the *standard model* illustrated in Fig.1 is based on plausible estimates for the pairing channel and transition temperatures, probably the best estimates available given the current state of the art in many-body theory. A better model of neutron star structure will necessarily have to wait until a first-principles theory of the superfluid transition temperature in a self-interacting system is developed. Nevertheless, the *discovery* of superfluidity in liquid ^3He gives us confidence in the BCS pairing theory as a mechanism for superfluidity in neutron stars, simply because the mechanism for pairing in neutron stars is the self-interaction between the nucleons.

† There is a rather lengthy literature on failed attempts to calculate the transition temperature and pairing channel for the superfluid phases liquid ^3He before it was discovered.

Before the discovery of superfluidity in liquid ^3He it had not been demonstrated that superfluidity could arise from the self-interaction between the Fermions.

Although it is difficult to reliably predict T_c for neutron-star matter, it is important to note that the BCS theory is an excellent theory *if* T_c *and the pairing channel* $[S, l, J]$ *are known.* It has the power to reliably predict

- the ground-state order parameter ψ,
- thermodynamic and transport properties of the superfluid phase,
- the hydrodynamic properties of *rotating* superfluids, and
- the structure of vortices, an important consideration for rotating P-wave superfluids.

Extensions of the BCS theory are sufficiently powerful that difficult problems of relevance to the rotational dynamics of superfluid neutron stars are also tractable, including,

- theoretical estimates of the pinning energies of vortex lines on impurities or defects in the stellar crust,
- theory of nucleation and destruction of vorticity at interfaces, *e.g.* the crust-liquid interface, and
- theoretical analysis of the mechanisms and timescales for dissipative motion of vortex flow during deceleration or acceleration events of pulsars.

Below I review some aspects of the theory of superfluidity as it applies to a rotating neutron star, discuss some of the novel features of the *mixture* of core superfluids, and present a mechanism for rapid equilibration of the interior superfluid to a disturbance of the crustal rotation period.

4. SUPERFLUIDITY, CURRENTS, AND QUANTIZED CIRCULATION

I assume for simplicity that the interiors of neutron stars are described by a scalar order parameter, *i.e.* a $^1S_0$ pair amplitude. This is consistent with the standard model for the neutron liquid in the inner crust and the proton superconductor in the core, but not for the neutrons in the core. However, most of the concepts discussed here for the $^1S_0$ superfluid are easily generalized to the $^3P_2$ superfluid in the interior. In Sec.9 and 12 I discuss the important differences between the $^3P_2$ and $^1S_0$ phases that reside in the core and crust, respectively.

The order parameter for the $^1S_0$ superfluid is described by an amplitude and a *phase*,

$$\psi(\vec{R}) = |\psi| \; e^{i\vartheta(\vec{R})}, \tag{9}$$

which have two distinct roles. The amplitude $|\psi|$ is a thermodynamic variable of state, fixed by a free-energy functional which attains its minimum in equilibrium. The free-energy is derivable from the BCS theory, and is most conveniently discussed in the limit $T \sim T_c$, the Ginzburg-Landau (GL) limit where the amplitude $|\psi|$ may be assumed small [Ginzburg and Landau (1950)]. The GL free-energy functional

is a formal expansion of the full BCS free-energy functional in terms of the order parameter ψ,

$$F[\psi,T] = \int d^3R \, \{\alpha \, (T/T_c - 1)|\psi|^2 + \frac{\beta}{2}|\psi|^4 + \frac{\hbar^2}{2\mu^*}|\vec{\nabla}\psi|^2\}. \tag{10}$$

The form of the expansion is required by gauge and rotational invariance of the free energy. In a uniform system the gradient term may be neglected, in which case the minimum of the functional is either the *normal state* with $\psi_{eq} = 0$ for $T > T_c$, or the *condensed state* with $\psi_{eq}^2 = \frac{\alpha}{\beta}(1 - T/T_c)$, and the free energy, $F_{eq} = F[\psi_{eq}, T] = -\text{Volume } [\frac{\alpha^2}{2\beta}](1 - T/T_c)^2$ for $T < T_c$ is the condensation energy associated with pair formation. The coefficients α, β, and μ^* calculated from the BCS theory are determined by T_c and the mass density, and are all positive.

The gradient energy in Eq.(10) is related to the *kinetic energy* of superfluid flow. The connection between superflow and the phase of the order parameter is obtained by considering the transformation property of the order parameter under a Galilean *boost* [Mermin (1978)]. The order parameter represents a bound-state of Cooper pairs, so we require that ψ transform as a two-particle wave function, $\psi \xrightarrow{\vec{u}} \psi \; e^{-i2M\vec{u}\cdot\vec{R}/\hbar}$, where $\vec{u}$ is the boost velocity and M is the bare mass of the Fermion. Thus, the quantity,

$$\vec{v}_s \equiv \frac{\hbar}{2M}\vec{\nabla}\vartheta, \tag{11}$$

transforms as a velocity field under a Galilean boost. That $\vec{v}_s$ implies the existence of a mass current is also evident from the transformation of the free-energy functional, $F \xrightarrow{\vec{u}} F - \int d^3R \, \{ \, \vec{g}\cdot\vec{u} + O(u^2) \, \}$. The mass current density is proportional to the superfluid velocity: $\vec{g} = \rho_s \vec{v}_s$, with a density $\rho_s \propto |\psi|^2$. This result defines the mass current in the rest frame of the *excitations*, *i.e.* the non-condensate fraction with density, $\rho_{ex} = \rho - \rho_s$, where ρ is the total mass density of the fluid.

Many of the hydrodynamic properties of superfluids and superconductors follow directly from the form of the superfluid velocity field. Since $\vec{v}_s$ is the gradient of a scalar field, superflow is purely potential flow; the condensate cannot support a circulation,

$$\vec{\nabla} \times \vec{v}_s = 0, \tag{12}$$

except at singular points within the fluid. This qualification is of crucial importance in the rotating state of a superfluid; the global circulation is given by the integral of $\vec{v}_s$ around a *path* C that encloses the fluid,

$$\oint_C \vec{v}_s \cdot d\vec{l} \; = \; \frac{h}{2M} \, N, \tag{13}$$

where N is an integer. The right side of this equation is determined by the requirement that the order parameter be single-valued, equivalently that the phase change, $\Delta\vartheta_C$, around the path C be an integral multiple of 2π. This quantization

of the circulation leads immediately to the concept of quantized vorticity and the the requirement that quantized vortices be present in a rotating vessel of superfluid [Onsager (1949) and Feynman (1955)]. In particular if $N \neq 0$ then there is necessarily a singularity in the velocity field. For a rectilinear line singularity with $N = 1$, enclosed by a circular path of radius R, we have by inspection,

$$\vec{v}_s = \kappa \frac{\hat{\phi}}{2\pi R}, \tag{14}$$

which is the axial flow field of a vortex with a unit of circulation, $\kappa = \frac{h}{2M_n}$, and a singular vorticity field, $\vec{\nabla} \times \vec{v}_s = \kappa\, \delta^{(2)}(\vec{R})\, \hat{z}$.

5. ROTATING EQUILIBRIUM OF THE CORE OF A NEUTRON STAR

Thermodynamic equilibrium of a rotating vessel - in this case the crust and magnetic field of the neutron star - is determined by the free-energy functional *in the rotating frame*; only in this reference frame is the interaction between the particles of the liquid and the vessel time independent. The general form of this free energy is

$$F' \;=\; F - \vec{\Omega} \cdot \vec{L}, \tag{15}$$

where F is the free-energy functional in the non-rotating frame, $\vec{L}$ is the angular momentum of the fluid, and $\vec{\Omega}$ is the angular velocity of the vessel, *i.e.* the crust of the neutron star.

This functional simplifies in the limit where the order parameter is determined by its local equilibrium value, *i.e.* $\psi = \psi_{eq}\, e^{i\vartheta(\vec{R})}$, which is an excellent approximation in those cases in which one is interested in the *macroscopic* flow state of the fluid. However, the assumption of local equilibrium of the condensate breaks down on short length scales near the singularity of a vortex, but for now it is sufficient to ignore this issue. I also ignore for the moment the fact that the protons are most likely superconducting. The angular momentum then reduces to the two-fluid form,

$$\vec{L} \;=\; \int d^3R\; \vec{R} \times (\rho_n \vec{v}_n + \rho_{ex} \vec{v}_{ex}), \tag{16}$$

and the free-energy reduces to

$$F_n' = F_n + \int d^3R\; \tfrac{1}{2} \rho_n (\vec{v}_n - \vec{\Omega} \times \vec{R})^2, \tag{17}$$

where $\vec{\Omega} \times \vec{R}$ is the velocity of the rigidly rotating crust and co-rotating normal-fluid excitations, and F_n is independent of $\vec{v}_n$. The quantities ρ_n and $\vec{v}_n$ are the superfluid density and velocity of the neutron condensate. An unrestricted minimization of this functional leads to the incorrect conclusion that the superfluid co-rotates perfectly with the crust, *i.e.* $\vec{v}_n = \vec{\Omega} \times \vec{R}$, in conflict with the constraint $\vec{v}_n = \frac{\kappa_n}{2\pi} \vec{\nabla} \vartheta$. In order for the superfluid to carry circulation, and thus to rotate

with the vessel, the condensate must be perforated with vortices, each with a unit of circulation κ_n, whose total circulation adds up to the rigid-body circulation of 2Ω. This latter condition is obtained by averaging the superfluid velocity over an area that contains many vortices, in which case the circulation contained in an area πR^2 of radius R is

$$\overline{\oint_{C_R} \vec{v}_n \cdot d\vec{l}} = (\Omega R)(2\pi R) = N_v \frac{h}{2M_n}, \tag{18}$$

where M is the bare neutron mass and $\kappa_n = \frac{h}{2M_n}$, which yields the Onsager-Feynman formula for the areal density of vortices,

$$\frac{N_v}{\pi R^2} = \frac{4M_n\Omega}{h} \simeq 6.3 \times 10^3 \frac{\text{vortices}}{\text{cm}^2} P^{-1}, \tag{19}$$

where P is the period of rotation of the star in seconds. For Vela pulsar ($P = 0.083$ *sec*) this corresponds to an inter-vortex distance of approximately 4×10^{-3} cm. In Fig.3 a sketch of the equilibrium rotating state of the core superfluid is shown,† as well as that of the superfluid velocity along a line through the center of rotation. The superfluid velocity deviates from the classical rigid-body value of ΩR only near the center of a vortex, where the velocity field of that particular vortex dominates the average field of all other vortices. In Sec.8-11 I discuss the *core* structure of vortices and their specific role in the rotational dynamics of the superfluid.

An important feature to note from Eq.(19) is that the number of vortices is directly proportional to the angular speed of the crust. Thus, if the neutron star experiences a torque which decelerates the crust to lower speed, then a new equilibrium state can be achieved only by the *destruction* of vortices. This process proceeds by the *outward flow* of vortices, and annihilation of vorticity at the interface between the superfluid and the crust. Since the neutron stars that have been observed are rotating with speeds ranging from roughly $1 - 10^3$ rad/sec, and decelerating due to radiation torques acting on the magnetic field and crust of the star, a question of central importance for understanding the dynamics of a decelerating superfluid neutron star is: *what determines the timescale for the equilibration of the vortex density to the rotational speed of the crust?* The answer is that there is a *mutual friction force* between vortices and the non-superfluid component of the star. However, before discussing mutual friction, and the resulting deceleration of the superfluid component of the star, it is worthwhile to discuss the equilibrium rotation of the *superconducting* proton condensate.

6. ROTATIONAL EQUILIBRIUM OF THE SUPERCONDUCTING PROTONS

The important difference between the equilibrium state of the rotating superconductor (protons) and that of the neutral superfluid is that the superconducting

† An accurate representation of the vortex state would show the vortices arranged in a hexagonal array with the area per vortex given in Eq.(19)

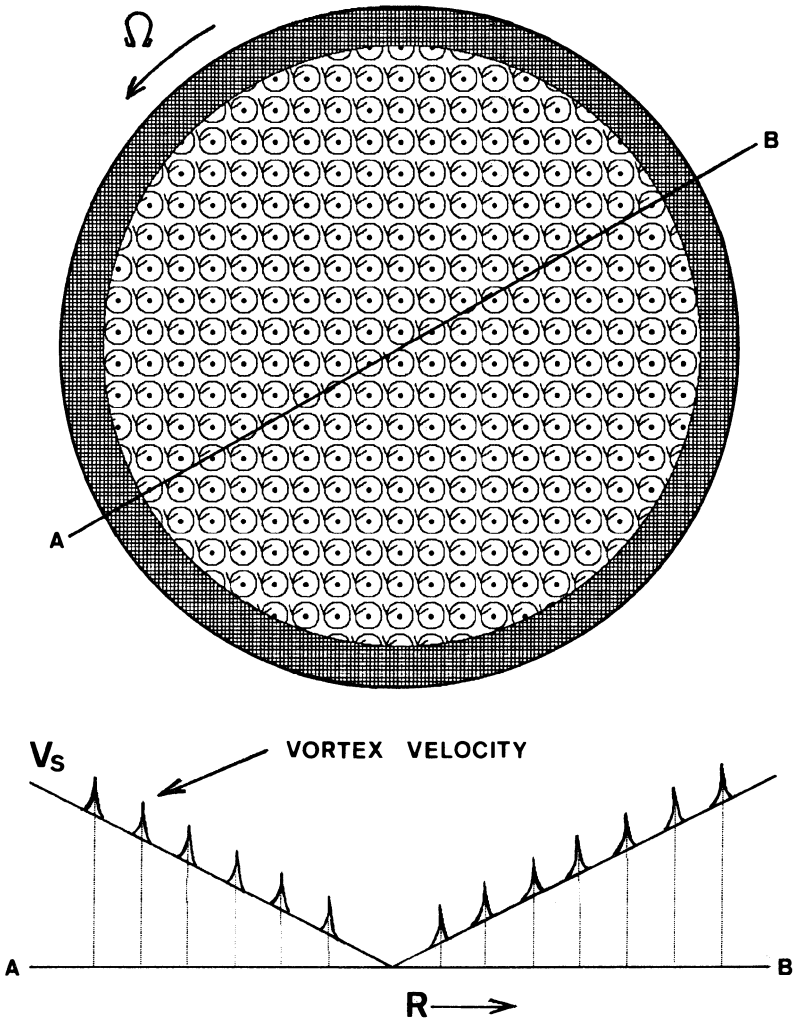

Figure 3. Schematic representation of the *vortex state* in the interior neutron superfluid. The radial dimension of the interior is 10 km; the mean distance between vortices for Vela pulsar, P = 0.083 rad/sec, is 4×10^{-3} cm; and the radial dimension of the vortex core is of order 100 fm.

condensate co-rotates with the crust lattice *without forming vortices.* This fact, first noted by F. London (1950), follows from the hydrodynamic free-energy for the rotating superconductor, which has a similar form to that of the neutral superfluid,

$$F_p' = F_p + \int d^3R \, \{\tfrac{1}{2}\rho_p(\vec{v}_p - \vec{\Omega} \times \vec{R})^2 + \frac{|\vec{b}|^2}{8\pi}\}, \tag{20}$$

where the energy of the self-consistent magnetic field $\vec{b} = \vec{\nabla} \times \vec{A}$ is included, and I temporarily omit the interaction between the neutron and proton condensates (see Sec.10). For the charged system the velocity field is given by

$$\vec{v}_p = \frac{\hbar}{2M_p}\vec{\nabla}\vartheta_p - \frac{e}{M_p c}\vec{A}(\vec{R}), \tag{21}$$

where the appearance of the vector potential $\vec{A}$ is required for gauge invariance of the theory. Minimization of the free energy in the rotating frame again implies that the proton condensate velocity co-rotates with the crust of the neutron star. And in contrast to the neutral superfluid there is *no constraint* on the proton superfluid velocity field that is in conflict with the condition of co-rotation. In fact co-rotation of the bulk of the superconducting condensate is enforced with $\vec{\nabla}\vartheta_p = 0$,† *i.e.*

$$\vec{\nabla} \times \vec{v}_p = 2\vec{\Omega} = -\frac{e}{M_p c}(\vec{\nabla} \times \vec{A}). \tag{22}$$

Thus, the kinetic energy of the superconductor is minimized at the cost of a tiny magnetic field (the London field) distributed uniformly throughout the superconducting interior of the star,

$$\vec{b}_{London} = -\frac{2M_p c}{e}\vec{\Omega}, \tag{23}$$

and directed along the axis of rotation. The source of this field is a thin surface layer (of order 100 fm thick) of superconducting protons slightly out of co-rotation with the crust. Thus, classical rotation of the superconducting component is achieved by introducing a tiny field (of order 10^{-4} Gauss for the Vela) which is an irrelevant magnetic field except that it is responsible for the co-rotation of the proton condensate.

7. MUTUAL FRICTION - COUPLING OF THE CORE SUPERFLUID TO THE CRUST

Figure 4 shows a portion of the timing data for Vela pulsar, including the first four *glitches* [see Downs (1981) for original references]. These glitches are discontinuous spin-up events ($\Delta\Omega \sim 10^{-6}\ \Omega$) of the neutron star, at least within the resolution of several days, accompanied by a discontinuous increase in the angular deceleration

† For clarity I omit the stellar field, which generates proton vortex lines but does not change the substance of this argument.

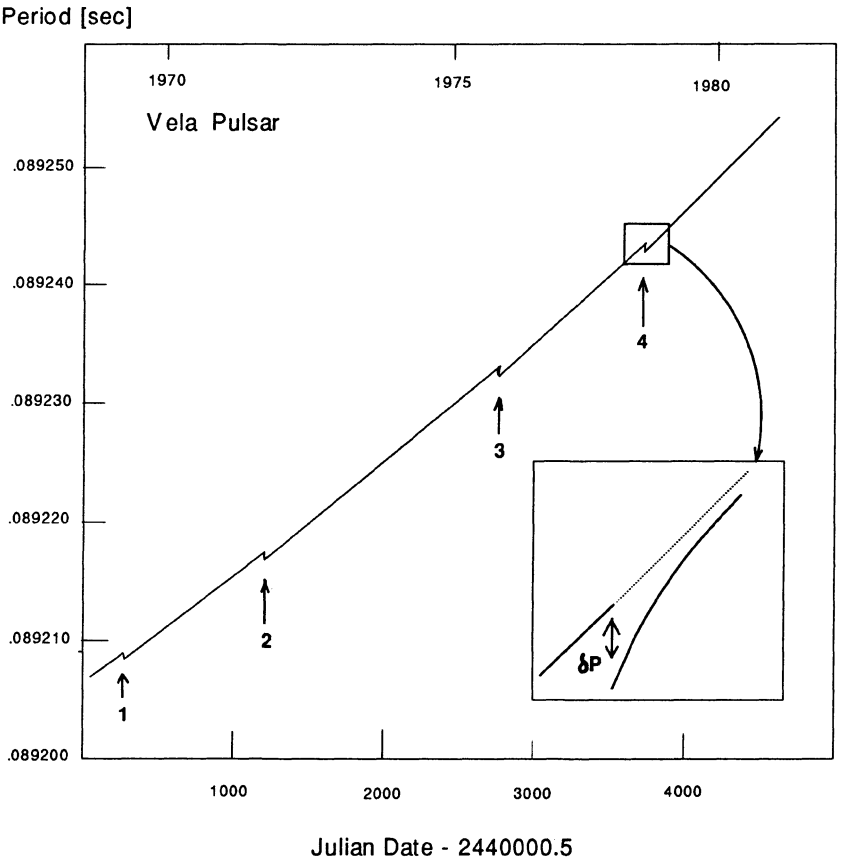

Figure 4. The first four giant glitches of Vela pulsar [from G. Downs (1981)]. The change in period due for each glitch is of order $\Delta P/P \sim 10^{-6}$, and the timescale for the recovery of the glitch is estimated to be of order $\tau \sim 1 - 3$ months; however, the post-glitch behavior of the period is more complicated than simple exponential recovery of the period and spin-down rate.

$\Delta\dot{\Omega} \sim -10^{-2}$. Following each of these glitches is a slow recovery of the angular deceleration back to the pre-glitch spin-down rate. The timescale for the recovery of the glitch is *a macroscopic timescale*, of order a few months or longer in the Vela. To date there have been seven giant glitches of the Vela pulsar occurring every 2 to 4 years since the timing observations began in 1969. The Crab pulsar also shows glitches, a total of 3 glitches of smaller magnitude $\Delta\Omega \sim 10^{-8}\ \Omega$, and the timescale for recovery of glitches in Crab varies from 3 to 60 days, also a macroscopic timescale. Glitch events have been observed in less studied pulsars, and seem to be ubiquitous, at least among relatively young pulsars. The largest glitch observed was in PSR 0355 + 54 with a magnitude of $\Delta\Omega = 4.4 \times 10^{-6}\ \Omega$ [Lyne (1987)].

As a means of defining the *mutual friction* timescale governing the coupling of the neutron superfluid interior to the rotation of the crust, I review the phenomenological two-component model of Baym, *et al.* (1969b) for the rotational dynamics of a neutron star. This model supposes that the relevant structure of a neutron star is a *crust*,† with moment of inertia I_c, containing a liquid interior of moment of inertia I_s. These two components are presumed weakly coupled via a *frictional coupling* of the form,

$$N_{internal} = I_s\dot{\Omega}_s = (\frac{I_c}{I})[\Omega_c - \Omega_s]/\tau, \tag{24}$$

which acts to bring the crust (rotating at Ω_c) and interior fluid (rotating at Ω_s) into co-rotation. The quantity τ that defines this coupling is the mutual friction timescale. The equation determining the rotational motion of the crust is

$$I_c\dot{\Omega}_c = N_{external} - N_{internal}. \tag{25}$$

Implicit in the model is the assumption that the relaxation of the fluid occurs nearly uniformly throughout the interior. Such a bulk mechanism for the coupling is reasonable given that the interior fluid contains a high conductivity plasma of electrons and protons, which are strongly coupled to the the stellar magnetic field, and therefore the crust. The two-component model was proposed in order to explain the response of a neutron star to a glitch, and although it fails to explain the rotational history of the Vela or Crab pulsar quantitatively, it is the link to the tenuous thread of evidence supporting the proposal that neutron stars contain superfluid interiors. To appreciate this point it is important to examine the possible mechanisms for momentum transfer between the neutral liquid interior and the crust.

Easson (1979) has previously analyzed the coupling of the high conductivity plasma of protons and electrons to the magnetic field and crust with a simplified model in which the plasma is confined to slab that is bounded on both sides by a conductor ("the crust"). The plasma and conductor extend to infinity in the radial direction and a magnetic field $\vec{B}$, perpendicular to the slab, penetrates the plasma and conductor. Easson analyzes the solutions to the magnetohydrodynamic equations

† I use the term 'crust' to refer to the solid outer crust, magnetic field and plasma interior of the star together, unless it is necessary to specify the individual constituent.

with the initial condition that the rotation of the 'crust' changes by $\Delta\Omega_c$. Spin-up of the plasma proceeds either by the formation of an Ekman boundary layer, and an associated radial flow of plasma which transports angular momentum, or by the excitation of low frequency hydromagnetic waves. In either case the spin-up time for the plasma is of order a few seconds for typical neutron-star parameters: $\tau_{Ekman} \simeq 30\ T_7\ \Omega_2^{-\frac{1}{2}} R_6\ \rho_{13}^{-\frac{7}{12}}$ sec, and $\Omega_2 = \Omega/(10^2 \mathrm{rad/sec})$, $R_6 = R/10^6 \mathrm{cm}$, $\rho_{13} = \rho/(10^{13} \mathrm{g/cm}^3)$, and $B_{12} = B/(10^{12} \mathrm{G})$. Thus, for the purposes of analyzing the post-glitch response of a neutron star the plasma can be assumed to co-rotate with the solid crust during a glitch. The long timescale for the post-glitch relaxation observed in pulsars is then attributed to the equilibration of the neutral component of the star to the plasma and crust.†

The primary *bulk* scattering mechanism available for the transfer of momentum between the plasma and the neutron liquid interior is the strong interaction. It is straight forward to estimate the timescale for momentum transfer between the neutron liquid and proton component of the plasma for the degenerate Fermi liquid of *non-superfluid* neutrons and *non-superconducting* protons. The timescale is determined primarily by the phase-space for binary collisions between a dilute *gas* of neutron and proton excitations at temperature $T \ll E_F$ [Pines and Nozières (1966)]:

$$\frac{\hbar}{\tau_{np}} \sim E_F \left(\frac{T}{E_F}\right)^2, \tag{26}$$

which corresponds to a microscopic timescale, $\tau_{np} \sim 10^{-11}$ sec at $T = 10^6\ K$. It is because this process leads to rapid equilibration that superfluidity is introduced. In order for the neutrons to be weakly coupled to the crust it is necessary that this strong-interaction scattering process be shut off, that the bulk of the neutron and proton excitations be *frozen out of the star.* This is most easily accomplished if there is an *energy gap*, $\Delta_n \gg T$, below which there are no allowed neutron states. Just such an energy gap appears as a consequence of the BCS pairing theory. In fact the timescale for momentum transfer at interior temperatures of $T \sim 10^6\ K$, when the neutrons and protons are both superfluid (with $\Delta_n \sim \Delta_p \sim 1 Mev$), becomes incredibly long,

$$\frac{\hbar}{\tau_{np}} \sim E_F\ e^{-(\Delta_n + \Delta_p)/T} \Longrightarrow \tau_{np} \rightarrow \text{`}\infty\text{'}\ , \tag{27}$$

far too long to account for the observed post-glitch timescales ranging from weeks to months. Thus, there is necessarily another mechanism responsible for the frictional coupling between the crust and the neutral interior.

---

† The model of Easson (1979) assumes the proton matter is not superconducting. The spin-up of a type II superconductor, in which the field is organized into flux tubes has not been analyzed. However, Alpar, Langer and Sauls (1984) provide some qualitative arguments for the rapid spin-up of the superconducting protons.

8. S-WAVE VORTEX STRUCTURE AND ELECTRON-VORTEX-EXCITATION SCATTERING

I previously represented a vortex in the s-wave neutron superfluid by the velocity field given in Eq.(14), with the *amplitude* of the order parameter given by the equilibrium amplitude, $|\psi(\vec{R})| = \psi_{eq}$; the full order parameter for the vortex being

$$\psi(\vec{R}) = \psi_{eq}\ e^{i\phi}, \tag{28}$$

where the phase, ϕ, is the azimuthal angle in coordinates centered on the vortex. This representation of the vortex is valid only on length scales long compared to the superfluid coherence length, ξ, defined roughly as the distance from the center of the vortex at which the superfluid kinetic energy density, $\frac{1}{2}\ \rho_n {v_n}^2$, becomes equal to the condensation energy density, $\frac{1}{2}\ \alpha\ (1 - T/T_c){\psi_{eq}}^2$. For neutron matter this length scale (for $T \ll T_{cn}$) is of order,

$$\xi \simeq \frac{\hbar v_{Fn}}{\pi \Delta_n} \simeq 10^2\ fm. \tag{29}$$

and defines the radial dimension of the vortex core, inside of which the amplitude collapses to zero. The core is important for the rotational dynamics of the neutron star because it is the point of contact between the conducting plasma in the interior of the star and the neutron matter; at temperatures well below the neutron gap, $T \ll \Delta_n$, all scattering mechanisms involving neutron excitations in the bulk of the interior are frozen out. Scattering of the conducting plasma off the neutral component occurs only in the vicinity of the vortex cores. In fact since the protons are expected to be superconducting, while the electrons are not,† the only significant scattering processes are those involving the neutron vortex cores and the *electronic* component of the plasma. A schematic representation of the momentum transfer process between the electrons and the neutron vortices is shown in Fig.5. The relative velocity between the electron fluid and the vortices, produced for example by a glitch, leads to preferential scattering of electrons from the vortex cores.

The equation of motion for rectilinear vortices moving relative to the background of excitations, in this case the electronic fluid, is well known from the study of superfluid hydrodynamics in liquid helium [see the review by Sonin (1987)]. The momentum transfer to the vortex due to scattering of excitations off the core determines the response of the *superfluid* according to

$$\vec{f}_{ev} = -\rho_{plasma}\ \frac{(\vec{v}_l - \vec{v}_e)}{n_v \tau} = \frac{\hbar}{2M_n}\rho_n(\vec{v}_l - \vec{v}_n) \times \hat{\Omega}, \tag{30}$$

where $\vec{v}_l$ is the velocity of the vortex line, $\vec{v}_e$ is the velocity of the electrons, $\vec{v}_n$ is the velocity of the neutron superfluid, n_v is the areal density of the vortices and

† The superconducting transition for electrons, due to the polarization of the protons, is exceedingly small, $T_{ce} \simeq T_{Fe}\ e^{-1/\lambda}$ with $\lambda \sim \frac{e^2}{\hbar c} \sim 1/137$ [Baym (1975)].

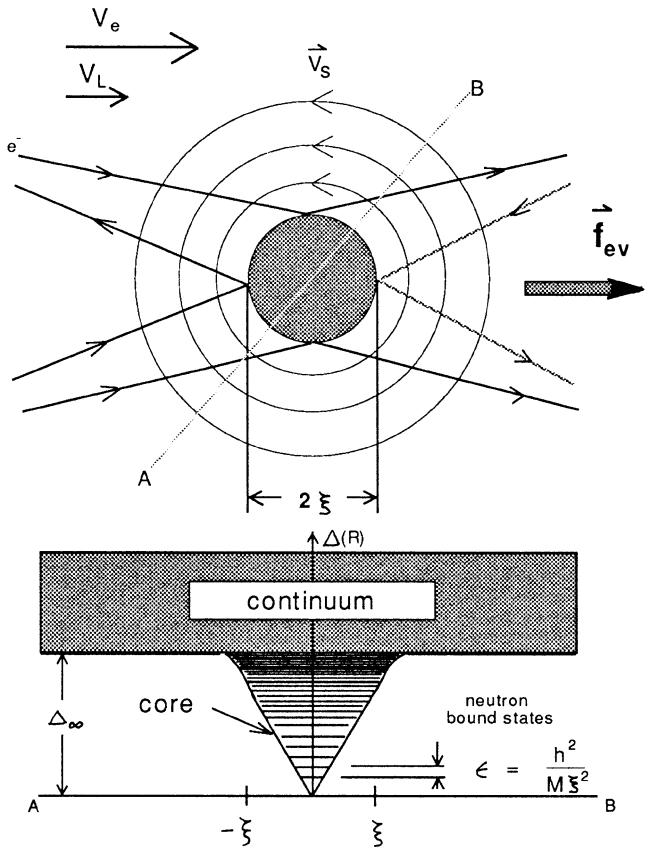

Figure 5. Electron-vortex-core scattering is responsible for the velocity relaxation of the interior superfluid to the crust. The magnitude of the scattering depends on the structure of the vortex core. The mechanism considered by Feibelman (1971) is the magnetic interaction between electrons and neutron *excitations* in the vortex cores. However, the scattering rate is dominated by electrons scattering off the magnetic field of the vortices.

τ is the velocity relaxation time for the relative motion of the vortices and the electrons. This mutual friction timescale has been calculated for several models of the coupling of the plasma to the neutron vortices [Feibelman (1971), Sauls, Stein and Serene (1982), Alpar, Langer and Sauls (1984)], and is simply related to the timescale for the dynamical response of the superfluid neutrons to a change in the motion of the plasma [Alpar and Sauls (1988)], $\tau_d = \tau\ (\rho_s/\rho_{plasma})(\frac{n_v \kappa}{2\Omega}) \sim \tau/x$, where $x \sim 0.05$ is the electron concentration in the interior.

The obvious mechanism of momentum transfer in the interior superfluid is the scattering of electrons, via electromagnetic interactions, off the *low-energy* neutrons that are bound to the vortex core. That such neutron bound states exist in the vicinity of the core is plausible given that the order parameter, and therefore the local gap, is depressed in the center of the vortex core (Fig.5). Even though the neutron gap vanishes inside the core, the lowest energy neutron state is determined by the dimensions of the vortex core; the spatially varying gap acts as a potential for the neutron excitations, and a simple estimate of the energy level spacing for bound states gives,

$$\epsilon = \frac{h^2}{M_n \xi^2} \sim \frac{{\Delta_n}^2}{E_F} \ll \Delta_n. \tag{31}$$

This level spacing determines the probability for a thermally excited neutron excitation in the vortex core,

$$P_{excitation} \sim e^{-\frac{\Delta_n^2}{E_F\, T}}, \tag{32}$$

which although much larger than that for bulk neutron excitations, is still an extremely small number, except in very young neutron stars. The density of excitations is the most sensitive factor determining the scattering rate for electrons interacting via their magnetic moments with these neutron excitations in the vortex cores. Feibelman's (1971) calculation of the scattering rate yields the estimate,

$$\tau \propto \frac{\Delta_n}{T}\, e^{\frac{\Delta_n^2}{E_F\, T}} \sim 10^{20}\ sec, \tag{33}$$

for $\Delta_n = 1\ Mev$ at $T = 10^6\ K$. In all models of neutron stars, except those with high interior temperatures and low neutron gaps (*i.e.* $\Delta_n^2/E_F\, T \sim 1$), electron-vortex-excitation scattering is ineffective, and probably does not explain the observed relaxation timescale following a glitch. The scattering time is so sensitive to the gap and interior temperature that is is difficult to account for the relatively small range of post-glitch relaxation times in pulsars with widely different ages, and presumably different interior temperatures. In any event there is a more efficient mechanism for momentum transfer in the interior that is *not* sensitive to the interior temperature and neutron gap.

9. VORTICES IN THE $^3P_2$ NEUTRON SUPERFLUID

I have so far treated the neutron superfluid interior as if the condensate were simply an s-wave, singlet state described by a single complex order parameter. This simplification is adequate for a description of the hydrodynamic flow far from the

core of a vortex, but fails dramatically at distances of order the coherence length near any vortex in the $^3P_2$ phase. The qualitatively new feature of vortices in the $^3P_2$ phase is that the *condensate* in the core of the vortex is *spin-polarized* [For a more general discussion of vortex states in the $^3P_2$ phase see Muzikar, *et al.* (1980) and Richardson (1972).],

$$\langle S_z \rangle \;=\; |\psi_{\uparrow\uparrow}(R)|^2 \;-\; |\psi_{\downarrow\downarrow}(R)|^2. \tag{34}$$

This can only occur in a *spin-triplet* superfluid, and since the neutrons have a magnetic moment the vortex itself carries a magnetization of order,

$$M_{vortex} \simeq (\gamma_n\, \hbar)\; n_n (\frac{\Delta_n}{E_F})^2 \;\simeq 10^{11}\; Gauss. \tag{35}$$

A sketch of the vortex structure is shown in Fig.6. Magnetic vortices in a neutral superfluid were first proposed for the $^3P_2$ phase of neutron matter [Sauls (1980), Sauls *et al.* (1982)], but have since been observed experimentally in the B-phase of rotating ^3He, with the magnetization predicted by Eq.(35) (of course with the appropriate parameters for ^3He). The experimental observation of this effect in superfluid ^3He gives us considerably more confidence in applying the microscopic theory to the novel phases of superfluid neutron-star matter.

The existence of a magnetic field localized near each neutron vortex is important for the rotational dynamics of the neutron superfluid because this inhomogeneous field scatters electrons. This mechanism for the transfer of momentum between the plasma and the neutron vortices is intrinsically different than Feibelman's mechanism because the vortex magnetization is a property of the *condensate* rather than the excitations. As a result the mutual friction timescale does not depend on the small number of thermally excited neutrons in the vortex cores, and is therefore only weakly dependent on the temperature and density [Sauls *et al.* (1982)],

$$\tau = 1.26 \times 10^8\; \frac{k_f\; x^{2/3} P}{\Delta_n}\; \text{sec}, \tag{36}$$

where k_f is the neutron Fermi wavevector in fm, x is the electron concentration, and P is the rotation period in seconds. For Vela pulsar this result gives a velocity relaxation time of about $\tau \sim 2$ months with typical estimates of the gap and interior density, which is in reasonable agreement with the observed times for Vela. However, this agreement is destroyed by a more efficient scattering mechanism due to the *strong interaction* between the neutron and proton condensates (which is distinct from the strong interaction scattering between neutron and proton excitations). Below I show how the rapid equilibration of the core superfluid comes about and then in Sec.12 return to the question on the origin of the *slow* relaxation timescale observed in pulsars.

10. NEUTRON-PROTON INTERACTIONS AND SUPERFLUID DRAG

There is a larger magnetic field attached to each neutron vortex, which is independent of the spin structure of the order parameter, and leads to a rapid equilibration

of the interior superfluid to the plasma with $\tau \simeq 400\ P$[sec]! Most discussions of the hydrodynamics of neutron star interiors treat the constituents as independent fluids of electrons, protons, and neutrons, at most coupled together by electromagnetic interactions and the strong stellar field. In fact there is an important role played by the strong interaction between the neutrons and protons in the superfluid hydrodynamics of the interior fluid mixture that is distinct from the scattering of neutron and proton excitations.† In a system of interacting Fermions, the elementary excitations are not simply *bare* neutrons or protons, but rather are quasiparticles - bare neutrons (or protons) *dressed* by a polarization cloud of other particles. This polarization cloud is a well-studied many body effect, and is responsible for the *effective mass* of a neutron (or proton) quasiparticle. In an interacting mixture of neutrons and protons the polarization cloud comprises *both neutrons and protons*. Calculations of the neutron and proton effective masses in neutron-star matter have been carried out by several authors (a contribution to the proton effective mass from polarization of the neutron medium is shown in Fig.7). In particular, Sjöberg (1972) has shown that the neutron and proton effective masses, defined as the ratios of their respective Fermi momenta to their Fermi velocities, are given by

$$\begin{aligned} M_n^* &= M_n + \delta M_{nn}^* + \delta M_{np}^* \ , \\ M_p^* &= M_p + \delta M_{pp}^* + \delta M_{pn}^* \ , \end{aligned} \tag{37}$$

where δM_{np}^* (δM_{pn}^*) determines the proton (neutron) contribution to the effective mass of the neutron (proton), and $\frac{\delta M_{pn}^*/M_p}{\delta M_{np}^*/M_n} = \frac{M_p^* n_n}{M_n^* n_p}$. The dilute concentration of protons interact with the neutrons through the long-range attractive part of the nucleon-nucleon interaction and reduce the neutron effective mass. Estimates of the neutron correction to the proton effective mass are $\delta M_{pn}^* \sim 0.5\ M_p$.

The polarization cloud that surrounds a neutron excitation in the two-component mixture of neutrons and protons is modified by the condensation of both the neutrons and protons, and as a result the superfluid mass current of neutrons is also modified; the constitutive relations are,

$$\begin{aligned} \vec{g}_n &= \rho_{nn}\ \vec{v}_n + \rho_{np}\ \vec{v}_p \ , \\ \vec{g}_p &= \rho_{pp}\ \vec{v}_p + \rho_{np}\ \vec{v}_n \ , \end{aligned} \tag{38}$$

where the densities $[\rho_{nn}, \rho_{pp}, \rho_{np}]$ determine the *conserved* neutron and proton currents, $\vec{g}_n$ and $\vec{g}_p$, in terms of the superfluid velocity fields, $\vec{v}_n$, $\vec{v}_p$, given in Eqs.(11) and (21). These equations, first considered by Andreev and Bashkin (1975) for $^3He - ^4He$ mixtures [see also Vardanyan and Sedrakyan (1981), and Alpar, Langer and Sauls (1984)], exhibit the *superfluid drag effect* in which the condensate velocity of one species, *e.g.* the neutrons, induces a particle current of the other species, *e.g.* the protons. This effect is important because the rotation of the star couples directly to the velocity, $\vec{v}_n$, which as I argued earlier is non-zero due to the existence

† I have previously mentioned that the *scattering* between neutron and proton excitations in the bulk is essentially irrelevant.

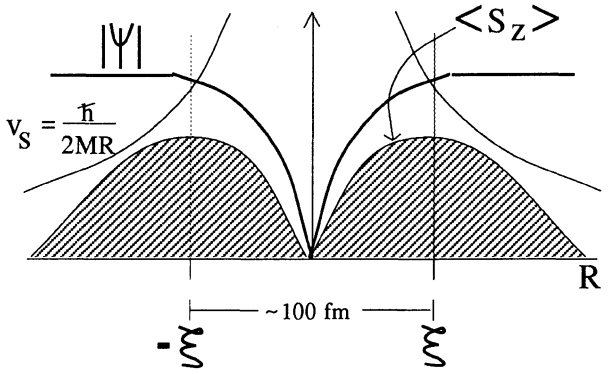

Figure 6. Sketch of the ferromagnetic core of the $^3P_2$ vortex showing the suppression of the overall magnitude of the order parameter, $|\psi|$, the vortex flow field, $v_s = \hbar/2MR$, and the spin polarization of the pairs,$< S_z >$.

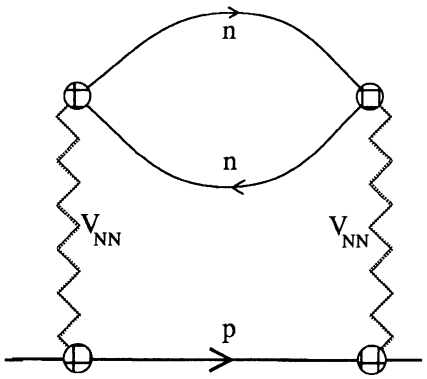

Figure 7. The effective mass of the proton quasiparticle is determined in part by the polarization of the neutron fluid through the nucleon-nucleon interaction. Estimates of this contribution by Sjöberg (1972) give $\delta M^*_{pn} \simeq 0.5 M_p$ for $\rho_{14} = 2$.

of vortices in the neutron condensate. In the reference frame of the rotating star the proton condensate rotates with the crust without the formation of proton vortices, and thus the only contribution to the proton condensate velocity is the London current, $\vec{v}_p = -\frac{e}{M_p c}\vec{A}$, which gives zero contribution to the bulk proton current in the rotating frame except near a neutron vortex line. The resulting superfluid charge current, induced by the neutron vortex lines, is

$$\vec{j} = \frac{c}{4\pi}(\vec{\nabla} \times \vec{b}) = \frac{e}{M_p}[\rho_{pp}\vec{v}_p + \rho_{np}\vec{v}_n], \tag{39}$$

where $\vec{b} = \vec{\nabla} \times A$ is the induced magnetic field. Attached to each neutron vortex is a magnetic flux line with a local magnetic field determined by,

$$\nabla^2\vec{b} + \Lambda_*^{-2}\vec{b} = \frac{4\pi e}{M_p c}\rho_{np}\ \vec{\nabla} \times \vec{v}_n, \tag{40}$$

where the vortex circulation, $\vec{\nabla} \times \vec{v}_n = \kappa_n \delta^{(2)}(\vec{R})\ \hat{z}$, is the source of the flux and $\Lambda_* = [\frac{M_p c^2}{4\pi e^2 \rho_{pp}}]^{\frac{1}{2}}$ is the length scale on which the magnetic field decays away from the center of the vortex. A simple calculation gives the magnitude of the trapped flux,

$$\Phi_* = \oint \vec{A} \cdot d\vec{l} = \phi_0(\frac{M_p}{M_n})(\frac{\rho_{np}}{\rho_{pp}}), \tag{41}$$

in terms of the drag coefficient ρ_{np}, and the conventional flux quantum, $\phi_0 = \frac{hc}{2e} \simeq 2 \times 10^{19}\ \mathrm{G} - \mathrm{fm}^2$.†

The drag coefficient, ρ_{np}, as well as the other superfluid densities, ρ_{pp} and ρ_{nn}, depend on the microscopic interactions between the neutron and proton quasiparticles in the interacting mixture, and have been calculated from the BCS theory generalized to a two-component superfluid mixture [Sauls (1984)]. For low temperatures, $T \ll \Delta_n, \Delta_p$, these coefficients are given simply in terms of the neutron and proton effective masses,

$$\begin{aligned} \rho_{pp} &= \rho_p(\frac{M_p}{M_p^*}), \qquad \rho_{nn} = \rho_n(\frac{M_n}{M_n^*}), \\ \rho_{np} &= \rho_p(\frac{\delta M_{pn}^*}{M_p^*}) = \rho_n(\frac{\delta M_{np}^*}{M_n^*}), \end{aligned} \tag{42}$$

where ρ_n (ρ_p) is total the neutron (proton) mass density.

The radial dimension of the flux tube is given by,

$$\Lambda_* = 29.5\ [\frac{M_p^*}{M_p} x^{-1} \rho_{14}^{-1}]^{\frac{1}{2}}\ \mathrm{fm}, \tag{43}$$

† Note that in the superfluid mixture the flux quantum is *not* simply related to fundamental constants; this is a generic feature of two-component superconducting condensates.

where ρ_{14} is the mass density in units of 10^{14} g/cm^3 and x is the proton concentration. Typical values of these parameters imply that $\Lambda_* \simeq 50$ fm, and thus the magnitude of the vortex field,

$$b_{\rm vortex} = \frac{|\Phi_*|}{2\pi\Lambda_*^2} \simeq 3.8 \times 10^{15}\ [\frac{|\delta M^*_{np}|}{M_p}\rho_{14}]\ \text{Gauss}, \tag{44}$$

is $b_{\rm vortex} \simeq 8 \times 10^{14}$ Gauss, which is roughly three orders of magnitude larger than the spin-polarization induced magnetization discussed in Sec.9.

11. ELECTRON-MAGNETIC-VORTEX SCATTERING

The mutual friction timescale resulting from the scattering of the electrons from the magnetic vortices has been calculated in the Born approximation, by Sauls *et al.* (1982). The electron Fermi energy for densities of order 10^{14}g/cm^3 is approximately 100 Mev, which implies that the electrons form an ultra-relativistic degenerate Fermi liquid. In this limit the Born amplitude for electron scattering from the magnetic field of a single vortex is given by

$$M(\vec{k}, s \to \vec{k}', s') = \frac{ec}{2\epsilon_k}\int \frac{dx^3}{\rm Vol} e^{i(\vec{k}-\vec{k}')\cdot\vec{x}/\hbar}\ (\vec{k}+\vec{k}')\cdot\vec{A}(\vec{x})\ \delta_{s,s'}\ , \tag{45}$$

where $\vec{A}$ generates the vortex magnetic field given by Eq.(44). The Boltzmann equation for the relaxation of the electron distribution function $n_{\vec{k},s}$ following an 'instantaneous' change in the relative velocity of the electron fluid and the vortex array is,

$$\frac{\partial n_{\vec{k},s}}{\partial t} = N_v \sum_{\vec{k}',s'} \frac{2\pi}{\hbar}\delta(\epsilon_k - \epsilon_{k'})|M(\vec{k}, s \to \vec{k}', s')|^2[n_{\vec{k}',s'} - n_{\vec{k},s}], \tag{46}$$

which is simply the total Born scattering rate from N_v vortices calculated from Fermi's rule including the *phase space* restrictions imposed by the degenerate sea of electrons. An analysis of this scattering rate [Alpar, Langer and Sauls (1984)] shows that the velocity relaxation time between the superfluid core of the star and the plasma is given by

$$\frac{1}{\tau} = \frac{3\pi^2}{32}(\frac{\Omega}{k_{Fe}\Lambda_*})(\frac{\rho_c}{\rho})[1 - g(\frac{\xi}{\Lambda_*})], \tag{47}$$

where the dimensionless function $g(x)$ is given in Alpar and Sauls (1988), and determines the correction to the electron-vortex scattering due to the finite dimension of the flux line; for $\xi/\Lambda_* \simeq 1$, $g(1) \simeq 0.13$, and is not sensitive to the precise value of the core radius ξ and magnetic field distribution length Λ_*. At low temperature ($T \ll \Delta_n, \Delta_p$) we find,

$$\tau \simeq\ 400\ (\frac{M_p}{\delta M^*_{pn}})^2\ P\ \text{sec}. \tag{48}$$

which implies rapid equilibration of the neutral superfluid interior of the star.

The original two-component model for the dynamical response of a rotating neutron star proposed by Baym, *et al.* (1969b) explained the long timescale for the recovery of the period of the Vela and Crab pulsars as a very weak coupling between the neutral liquid core and the crust of the star. In fact the *existence* of a neutron superfluid was originally thought to be confirmed by the long timescale for post-glitch relaxation. However, assuming the neutrons and protons are both superconducting then the superfluid drag effect provides an efficient mechanism for the transfer of momentum between the plasma and the neutral superfluid. Equilibration of the core superfluid (actually the establishment of a new steady-state response to the radiation torque) occurs within an hour or so following a glitch. So far the onset of a glitch in either the Crab or Vela has not been observed; typical uncertainties in the onset time of a glitch are a few weeks, although recent glitches in Vela [McCullough, *et al.* (1983)] have an uncertainty of one day. In any event there is as yet no direct observational evidence for a short relaxation timescale, $\tau \sim 10^3$ sec $\sim$ 1hr, involving a major fraction of the moment of inertia of the star. Although Boynton's (1981) analysis of the timing noise from Crab (and also from Her X-1) suggests that a large fraction of the moment of inertia of the star is rigidly coupled to the crust, at least on timescales greater than two days.

12. SUPERFLUIDITY IN THE CRUST, VORTEX PINNING AND GLITCHES

The *origin* of glitches in pulsars is poorly understood. What is clear is that the obvious energy source capable of supplying the enormous energies associated with a glitch, $\Delta E_{rot} = 2\frac{\Delta\Omega}{\Omega}E_{rot} \sim 10^{43}$erg, is the rotational energy of the neutron star. However, the physically appealing 'starquake' model of the Vela glitches [Ruderman (1969), Baym and Pines (1971)] is unable to account for the magnitude and frequency of the glitches in Vela. It is not possible, based on theoretical estimates of the maximum shear stress that the neutron star crust can sustain, to store 10^{43}ergs in elastic energy in the crust in a period of 2 to 4 years between glitches [Baym and Pines (1971); Anderson, *et al.* (1982)].

Metastable states of flow are ubiquitous to superfluids; for example, persistent currents in superfluid helium are a consequence of kinetic energy barriers separating states with different amounts of quantized circulation. That metastability of superflow is a possible explanation for pulsar glitches was suggested by Packard (1972), and a specific model for the source of the metastability was proposed by Anderson and Itoh (1975). This model was motivated by the analogy between the crust of a neutron star and terrestrial *hard* superconductors. The inner crust ($\rho > 5 \times 10^{11}$g/cm^3) is a crystalline lattice of heavy nuclei embedded in a degenerate liquid of superfluid neutrons. In the crust the protons are confined within the nuclei, so that unlike the liquid core, there is no superconducting proton component, and since the neutron superfluid in the crust is a condensate of $^1S_0$ pairs there is no electron-magnetic-vortex scattering process present to couple the neutron superfluid to the plasma. However, the existence of the solid crust is expected to have an important effect on the coupling of the neutron superfluid to the crust. In superfluid helium vortices tend to attach themselves to imperfections on the walls of the vessel. If the vessel is decelerated the vortices may remain *pinned* to

the vessel and a metastable flow is created in which the superfluid is flowing faster than the vessel. Only if the vortices *unpin* and annihilate on the vessel wall will the superfluid spin down. A similar metastability exists in laboratory superconductors; very stable current-carrying states of hard superconductors are maintained by the pinning of flux vortices (which are present because of the supercurrent). However, in superconductors pinning occurs on impurities and defects of the crystal lattice. Degradation of the supercurrent occurs only if vortices are transported by the current. In hard superconductors the decay of supercurrents occurs either gradually as vortices *diffuse* through the array of pinning sites (vortex 'creep') or discontinuously when many vortices unpin and flow unimpeded without re-pinning. These latter events are the laboratory analog of Anderson and Itoh's proposal for the glitch events; as the neutron star slows down the superfluid must expel vortex lines (at a rate of $\dot{N} = 4M_n\dot{\Omega}/h \sim 10^9$ yr^{-1}) in order to achieve equilibrium with the crustal rotation. Pinning of this vorticity in the crust is thus a mechanism for storing superfluid kinetic energy. As the relative velocity between the superfluid and crust builds up, the Magnus force tending to expel the vorticity increases, and eventually overcomes the pinning forces. Unpinning occurs at a critical value of the relative angular speed,

$$|\Omega_s - \Omega_c|_{crit} = \frac{2\pi}{\kappa_n} f_p/(R_p\rho_n) \ , \tag{49}$$

which is determined by balancing the Magnus force per unit length, $f_M = \frac{\kappa_n}{2\pi}\rho_n|\Omega_c - \Omega_n|\ R_p$, and the pinning force per unit length, $f_p = \epsilon_p/d$, where ϵ_p is the pinning energy per site, d is the average spacing between pinning centers on a particular vortex and R_p is the radial distance to the pinned vortices. Estimates of the pinning force [Alpar (1977)] assume that vortices pin to individual nuclei in the crustal lattice, and that the pinning energy per site is equal to the difference between the vortex core energy in the absence of the pinning center and the condensation energy for neutron pairs bound within the nuclei. The basic equation used to estimate the elementary pinning energy is

$$\epsilon_p = \frac{3}{8}[\rho_i \frac{\Delta(\rho_i)^2}{E_f(\rho_i)} - \rho_o \frac{\Delta(\rho_o)^2}{E_f(\rho_o)}]\ V, \tag{50}$$

where ρ_i and ρ_o are the neutron densities inside and outside the nuclei, and V is the volume of intersection between the vortex core and the nucleus. With energy gaps in neutron matter of order an MeV and plausible assumptions about the number of intersecting nuclei per vortex, the pinning force can be calculated and converted into a critical velocity difference for vortex depinning. Typically, $\delta\Omega_{crit} \sim 10$ rad/s, except perhaps in regions of the inner crust where the pinning force may be an order of magnitude or so smaller [Alpar (1977); Anderson, *et al.* (1984)]. In order to account for glitches in terms of vortex depinning every 2-4 years the critical angular velocity difference in some region of the crust must be much smaller than the estimate of 1-10 rad/sec; *i.e.* $\dot{\Omega}_c\Delta t_{glitch} \simeq 10^{-2}$rad/s (Fig.4). The theory of vortex pinning and flux jumps in laboratory superconductors is not well developed;

the elementary pinning energy between a vortex and a small impurity ($R_{imp} \ll \xi$) was only recently calculated correctly [Thuneberg, *et al.* (1984)] and found to be much larger (by a factor ξ/R_{imp}) than the estimate [Eq.(50)] based on minimizing the lost condensation energy of the vortex core and defect. Thus, whether regions of weak pinning in neutron stars are likely due to a low density of lattice defects or impurities, or to exceptionally weak intrinsic pinning is unclear. In fact one of the important assumptions made in estimating the pinning energy of vortices in the crust of a neutron star is that vortex lines pin to the nuclear clusters that constitute the crystalline lattice of nuclei. This intrinsic pinning of vortices to the lattice nuclei is not relevant in most superconductors because of the long coherence length compared to the atomic lattice spacing. Superfluidity in the crust may be in the regime where the coherence length is comparable to the size of the nuclei, in which case intrinsic pinning may be relevant; however, there is no microscopic theory of pinning of vortices to the lattice nuclei in short coherence length superconductors. In any event estimates of the vortex pinning energy in the crust are uncertain, but it is difficult to explain the origin and frequency of the Vela pulsar glitches without regions of very weak pinning compared to the estimate of 0.5 MeV/fm. The problem is all the more difficult because within the vortex unpinning model of Alpar, *et al.* (1981a) the change in the angular acceleration resulting from the glitch implies that the moment of inertia of the star containing vortices that unpin is $\delta I_p/I_c = \delta\dot{\Omega}_c/\dot{\Omega}_c \simeq 10^{-2}$, which translates into roughly 10^{13} vortices simultaneously depinning (on any observable timescale) during a glitch. Such a catastrophic unpinning of vorticity is difficult to explain unless there is a mechanism (as yet unspecified) for amplifying fluctuations in the local vortex density which then drive the local superfluid velocity above the critical velocity for unpinning.

In spite of the difficult problem of explaining the *trigger* for the catastrophic unpinning of vortex lines, Alpar, *et al.* (1982) have analyzed the *response* of the crustal superfluid to the glitch (identified as catastrophic unpinning) in terms of the *vortex creep* model for vorticity flow [Anderson and Kim (1964)], originally invented for understanding the motion of flux in superconductors with defects that pin flux vortices. This model is discussed in detail in this volume by Alpar and Pines; the important point to note here is that vortex creep theory explains the slow relaxation of a pulsar's angular speed back to the pre-glitch spin-down rate in terms of the re-establishment steady-state vortex creep - which requires *repinning* of vortex lines. While it seems plausible that this timescale is long, the microscopic physics of the repinning process is not well understood [see Shaham in this volume].

13. PROTON SUPERCONDUCTIVITY - SOME OPEN PROBLEMS

Laboratory superconductors exhibit striking properties in response to an applied magnetic field. At sufficiently low magnetic field all superconduturs exhibit the Meissner effect, *i.e.* the complete exclusion of magnetic flux. The threshold field for the penetration of flux into a superconductor depends on the microscopic properties of the superconductor, most importantly the ratio of the field penetration length, $\Lambda = \sqrt{Mc^2/4\pi ne^2}$, to the coherence length, ξ, which controls the surface energy of a superconducting-normal domain. For $\Lambda/\xi > \sqrt{2}$ (type II superconductors) the surface energy is negative and flux enters the superconductor without destroying

the superconducting state in the form of flux lines with an elementary unit of flux, $\phi_0 = hc/2e$. The threshold field for flux entry is the lower critical field, $B_{c1} = \frac{hc/2e}{\pi\Lambda^2} ln(\Lambda/\xi)$. Ultimately superconductivity is destroyed when the magnetic field is sufficiently strong, *i.e.* greater than the *upper* critical field, $B_{c2} = \frac{hc/2e}{\pi\xi^2}$. In neutron stars the protons are expected to be type II superconductors with a lower critical field of $B_{c1} \simeq 10^{15}G$ and an upper critical field of roughly $B_{c2} \simeq 10^{17}G$ [Baym, *et al.* (1969a)]. Since the stellar field of most neutron stars is estimated to be less than a few times $10^{12}G$, the thermodynamic state of the core of superconducting protons is the Meissner state with complete flux expulsion. However, for a neutron star 'born' with a stellar field, *e.g.* in a supernova, the timescale for the flux to diffuse through the high-conductivity (σ), degenerate plasma may be as long as $\tau_{diffusion} = 4\pi\sigma R_{star}^2/c^2 \sim 10^{10}$ years. Therefore, Baym, *et al.* (1969a) proposed that superconductivity nucleates in the presence of the field by confining the stellar field into a low density of flux tubes, with an average spacing, $d_f >> \Lambda$. This implies that the bulk of the neutrons are in a field-free environment in the interior.

There are a number interesting unanswered questions regarding the magnetic field structure within the superfluid core. Firstly, there is no detailed theoretical understanding of the non-thermodynamic superconducting transition in the presence of the stellar field, in which the timescale for cooling below T_c is short compared to the flux expulsion timescale $\tau_{diffusion}$. And even if the superconductivity nucleates in the presence of the field, the timescale for the reorganization of the field into quantized flux lines is unknown. Answers to these questions of timescale and flux motion may be relevant to the issue of pulsar 'turn off' if indeed the absence of pulsars with apparent ages greater than a few million years old is due to the decay of their magnetic fields. Recently several authors [Muslimov and Tsygan (1985), Jones (1987)] estimated the Bernoulli and drag forces on proton flux lines and conclude that expulsion of the flux state of the superconductor may occur on the timescale of several million years. However, these authors neglect the tension of flux lines which can act to inhibit flux motion; also the timescale for a flux line to be expelled from the interior is sensitive to the cross-section for electrons scattering off the flux lines.

Finally it is interesting to speculate that the proton flux lines (assuming they have nucleated) may have a role in the *rotational dynamics* of pulsars. In pulsars the magnetic field axis is misaligned with respect to the rotation axis, so that some of the neutron vortices (which control the rotation of the neutron superfluid) must pass through the proton flux lines as the pulsar spins down. The proton flux lines provide a natural collection of extended pinning 'centers' (or rather a 'clothesline') for vortex lines in the core of the star; a simple estimate for the pinning energy of a vortex-flux line intersection due to the proton density perturbation in the center of a flux line is

$$\epsilon_{pin} \sim n \frac{\Delta_p^2}{E_{Fp}^2} \frac{\Delta_n^2}{E_{Fn}} (\xi_n^2 \xi_p) \lesssim 0.1 \text{ MeV/connection}, \tag{51}$$

which suggests that pinning in the superfluid core may be important. In fact there

are additional reasons for looking more carefully at the pinning problem in the core superfluid. (i) The effective pinning energy per vortex line is automatically lower than the simple estimate given for pinning in the crust simply because the mean distance between flux lines (pinning centers) is much larger than the distance between the nuclei, $d_f \simeq \Lambda\sqrt{B_{c1}/B} \simeq 10^2 - 10^3$ fm, which translates into a considerably smaller critical velocity difference for unpinning from the flux lines, $\delta\Omega_{crit} \simeq 10^{-2} - 10^{-3}$rad/sec, which is reasonably close to the velocity difference that can be built up in ~ 2 years as Vela spins down. (ii) Pinning in the crust may be absent or unimportant if intrinsic pinning of vortices to the nuclear lattice is absent (this would be the case if the neutron coherence length overlaps many nuclear clusters) or if the density of crystal defects is low. (ii) Because of the 'anisotropy' of the pinning centers in the interior of the star a relatively small *cone* of neutron vortices would be pinned by the proton flux lines (see Fig.8), thus giving rise to a small effective moment of inertia of pinned vorticity, also consistent with the small discontinuity in the spin-down rate due to the glitch. (iii) A model of the post-glitch response based on pinning in the core superfluid, compared to the pinned crustal superfluid, has the advantage of not depending on the difficult problem of vortex *repinning* to nuclei in the crust simply because there is no way for vortices flowing radially out to avoid the flux lines in the directions perpendicular to the field. In any case the problem of vortex pinning and dynamics needs additional study in order to determine if catastrophic unpinning and vortex creep are plausible models for pulsar glitches and spin-down of the neutron superfluids.

ACKNOWLEDGEMENT

I benefitted greatly from the lectures and conversations with the participants of the school on *Timing Neutron Stars*, and wish to express my thanks to Hakke Ögelman, Ed van den Heuvel and the other organizers for their efforts. I particularly thank Ali Alpar for his many stimulating comments to me on the physics of neutron stars over the years. I also thank Daryl Hess and Taku Tokuyasu for their comments on the manuscript.

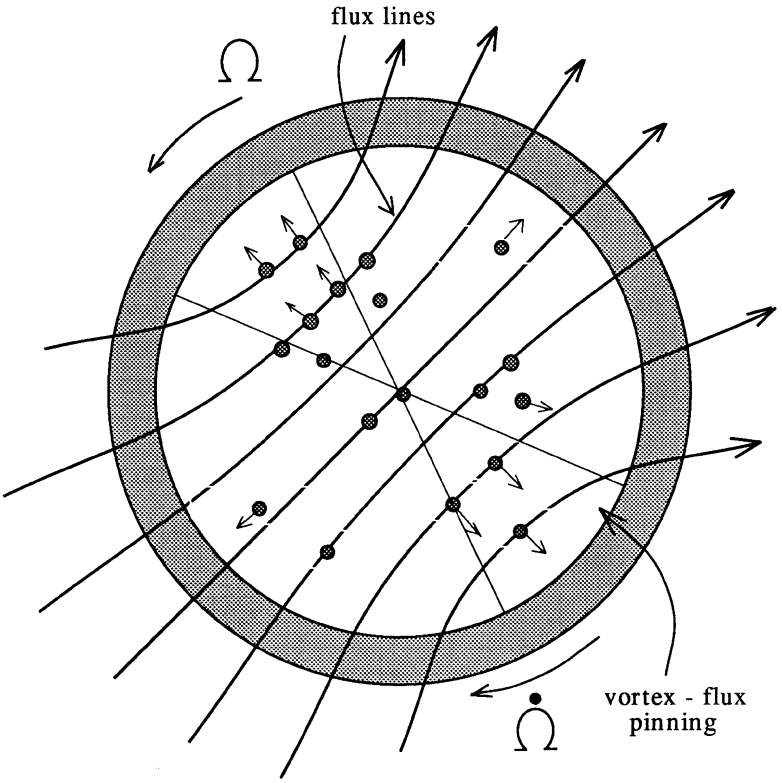

Figure 8. Vortex lines in the core superfluid may pin on the proton flux lines. The region of strongest pinning is the cone where the radial flow of vortex lines is nearly perpendicular to the flux lines.

REFERENCES

Alpar M.A. 1977, Ap.J. **213**, 527.

Alpar M.A., Anderson P.W., Pines D. and Shaham J. 1981a, Ap. J. (Letters), **249**, L33.

Alpar M.A., Anderson P.W., Pines D. and Shaham J. 1981b, Proc. Natl. Acad. Sci., **78**, 5299.

Alpar M.A., Anderson P.W., Pines D. and Shaham J. 1984, Ap. J. **276**, 325.

Alpar M.A., Langer S.A. and Sauls J.A. 1984, Ap.J. **282**, 533.

Alpar M.A., Nandkumar R., and Pines D. 1985, Ap. J. **288**, 191.

Alpar M.A. and Sauls J.A. 1988, Ap. J. **327**, 723.

Anderson P.W. and Itoh N. 1975, Nature, **256**, 25.

Anderson P.W. and Kim Y.B. 1964, Rev. Mod. Phys. **36**, 39.

Anderson P.W. and Brinkman W. 1978, in *The Physics of Liquid and Solid Helium, part II*, ed. by K.H. Bennemann and J.B. Ketterson, p. 177, Wiley, New York.

Anderson P.W., Alpar M.A., Pines D. and Shaham J. 1982, Phil. Mag. A, **45**, 227.

Andreev A.F. and Bashkin E.P. 1975, Zh. Eksp. Teor. Fiz., **69**, 319 [English translation 1976, Soviet Phys. - JETP, **42**, 164].

Bardeen J., Cooper L.N., Schrieffer J.R. 1957, Phys. Rev. **108**, 1175.

Baym G. 1975, in *Quantum Statistics and the Many Body Problem*, ed. by S.B. Trickey, W.P. Kirk, and J.W. Dufty, p.221, Plenum, New York.

Baym G., Pethick C. and Pines D. 1969a, Nature, **224**, 673.

Baym G., Pethick C., Pines D. and Ruderman M. 1969b, Nature, **224**, 872.

Baym G. and Pethick C. 1975, Ann. Rev. of Nucl. Sci. **25**, 27.

Baym G. and Pethick C. 1979, Ann. Astron. Astrophys. **17**, 415.

Baym G. and Pines D., Ann. Phys. **66**, 816.

Boynton P.E. 1981, *Proc. of IAU Symposium 95, "Pulsars"*, ed. R. Wielebinski and W. Siever, p. 279.

Brown G.E. and Jackson A. 1979, *The Nucleon-Nucleon Interaction*, North-Holland, Amsterdam.

Chao N.C., Clark J.W., Yang C.H. 1972, Nucl. Phys. **A179**, 320.

Downs G.S. 1981, Ap. J. **249**, 687.

Easson I. 1979, Ap. J. **228**, 257.

Feibelman P. 1971, Phys. Rev., **D4**, 1589.

Feynman R.P. 1955, in *Progress in Low Temperature Physics*, ed. by C.J. Gorter, Vol. 1, p. 17, North Holland, Amsterdam.

Ginzburg V.L. and Landau L.D. 1950, Zh. Eskp. Teor. Fiz. **20**, 1064.

Ginzburg V.L. and Kirzhnits D.A. 1964, Zh. Eskp. Teor. Fiz. **47**, 2006 [English translation 1965, Sov. Phys. JETP, **20**, 1346].

Hoffberg M., Glassgold A.E., Richardson R.W. and Ruderman M. 1970, Phys. Rev. Lett., **24**, 175.

Jones P.B. 1987, M.N.R.A.S. **228**, 513.

London F. 1950, *Superfluidity*, Vol. 1, Wiley, New York.

Lyne A.G. 1987, Nature **326**, 569.

McCulloch P.M., Hamilton P.A., Royle G.W.R. and Manchester R.N. 1983, Nature **302**, 319.

Mermin, N.D. 1978, in *Quantum Fluids*, ed. by J. Ruvalds and T. Regge (New York: North Holland).

Migdal A.B. 1959, Zh. Eskp. Teor. Fiz. **37**, 249 [English translation 1960,Sov. Phys. JETP, **10**, 176].

Muslimov A.G. and Tsygan A.I. 1985, Astrophys. Space Sci. **115**, 43.

Muzikar P., Sauls J.A. and Serene J.W. 1980, Phys. Rev. **D21**, 1494.

Onsager L. 1949, Nouvo Cimento Suppl., **6**, 249.

Packard R.E. 1972, Phys. Rev. Lett. **28**, 1080.

Pines D. and Nozières P. 1966, *The Theory of Quantum Liquids*, W.A. Benjamin, New York.

Radhakrishman V. and Manchester R.N. 1969, Nature **222**, 228.

Rainer D. 1986, in *Progress in Low Temperature Physics*, vol. X, ed. by D.F. Brewer, p. 371, Elsevier.

Reichley P.E. and Downs G.S. 1969, Nature, **222**, 229.

Richardson R.W. 1972, Phys. Rev. **D5**, 1883.

Ruderman M. 1969, Nature **223**, 597.

Sauls J.A. and Serene J.W. 1978, Phys. Rev. **D17**, 1524.

Sauls J.A. 1980, Ph.D. thesis, SUNY-Stony Brook.

Sauls J.A., Stein D.L. and Serene J.W. 1982, Phys. Rev. **D25**, 967.

Sauls J.A. 1984, unpublished.

Shaham J. 1980, Journ. de Phys., **41**, C2-9.

Sjöberg O. 1976, Nucl. Phys., **A65**, 511.

Sonin E.B. 1987, Rev. Mod. Phys. **59**, 87.

Tamagaki R. 1970, Prog. Theor. Phys. **44**, 905.

Thuneberg E., Kurkij:arvi J. and Rainer D. 1984, Phys. Rev. Lett. **29**, 3913.

Vardanyan G.A. and Sedrakyan D.M. 1981, Zh. Eskp. Teor. Fiz. **81**, 1731 [English translation 1981, Soviet Phys. - JETP, **54**, 919].

Vulovic V.Z. and Sauls J.A. 1984, Phys. Rev. **D29**, 2705.

RADIATION FROM COOLING NEUTRON STARS

JOSEPH VENTURA
Physics Department, University of Crete,
Heraklion, Crete, Greece
and
Max Planck Inst. f. Extraterrestr. Physik,
Garching, F. R. Germany

ABSTRACT. The thermal structure of neutron star envelopes is discussed with emphasis on recent analytic results. The effect of the neutron star magnetic field on the opacities and on heat conduction is further reviewed. We finally discuss the physics of the spectra emitted at the neutron star surface focussing on the expected deviations from the black body spectrum.

1. Introduction

We already learned in this conference (Pines 1989, Müller 1989), that neutron stars are probably formed with very high internal temperatures approaching $10^{11}K$ in the core of a supernova explosion (see also Shapiro et al. 1983). Copious neutrino emission brings the temperature down to $10^9 - 10^{10}K$ within about one day. Neutrino cooling actually continues to dominate over photon cooling until the internal temperature has droped to $\approx 10^8K$ with a corresponding surface temperature of $\approx 10^6K$, attained typically within 10^4 - 10^5 years after formation (Shapiro et al. 1983). It was realised very early (*e.g.* Chiu 1964, Chiu and Salpeter 1964) that the surface temperature of the star may remain above, or at the vicinity of 10^6K, for at least 10^4 years after formation, so that young neutron stars may be detectable through their thermal emission in the soft X-rays (Chiu and Salpeter 1964, Tsuruta and Cameron 1965).

Neutron stars have since been identified by the hundreds as radio pulsars or as accreting X-ray sources. In the mean while, the possibility of detecting weak point sources in the soft X-rays was afforded recently, after the orbiting of the *Einstein* and *EXOSAT* observatories. This new observational capability has spurred recent detailed thermal evolution calculations. These are complex studies sensitive to both the interior structure - thus depending on the nuclear equation of state, superfluidity, pion condensation, etc. - as well as to the properties of the outer

H. Ögelman and E. P. J. van den Heuvel (eds.), Timing Neutron Stars, 491–502.

envelope such as surface gravity, opacities and magnetic field strength (e.g. Maxwell 1979, Nomoto and Tsuruta 1981, 1986, Richardson et al. 1982). Recent reviews of the *Einstein* observations have been given by Helfand (1983) and by Helfand and Becker (1984), while the *EXOSAT* results have been discussed by Alpar *et al.* (1987), Brinkmann and Ögelman (1987) and by Ögelman (1987).

Further progress in the 1980's was achieved by decoupling the internal structure from the properties of the outer envelope (Gudmundsson 1981, Gudmundsson et al. 1982, 1983, Hernquist and Applegate 1984). This is meaningful for two reasons: (*a*) The high interior conductivity renders, as we shall see, the region with densities $\rho \gtrsim 10^{10} g/cm^3$ practically isothermal, so that a relation between the surface effective temperature, T_e, and the interior temperature, T_i, can be established. (*b*) For a significant period of time the interior cools via neutrino emission independently of the properties of the outer layers. While isothermality of the neutron star interior has been questioned in recent studies (see *e.g.* Nomoto and Tsuruta 1986), these considerations would only affect the boundary condition, T_i, on the determination of the thermal structure of the envelope. We shall, therefore, principally review here the properties of the outer envelope, as this allows one some insight on the extensive numerical results on neutron star cooling.

Neutron star cooling may also be influenced by internal heating processes due to friction between the differentially rotating solid crust and the superfluid interior of the star as it spins down (Pines and Alpar 1985, 1989, Ögelman 1987). Current estimates of this reheating, based on the superfluid vortex - creep theory, suggest that this could be important in later stages of neutron star cooling, say 10^6 years after formation (Alpar *et al.* 1987).

2. Outer Envelope of a Neutron Star

While the outer layers may not influence the cooling of the star during the initial, neutrino dominated era, yet their thermal properties will determine in the end the X-ray photon flux and spectrum, which is our only means of detecting these objects.

To briefly summarize some of the cardinal properties of the neutron star surface let us then remember the very high gravitational binding energy per unit mass, $E_G/m = GM/R \simeq .15\, c^2$ (M and R denote the star's mass and radius), the enormous surface gravity $g = .15c^2/R \simeq 10^{14} cm/s^2$, the small scale-heights $h \simeq P/(g\rho)$, and column density $y \simeq P/g$. Thus, following a thin nondegenerate atmosphere with a scaleheight

$$h = \frac{kT}{\mu g m_p} \simeq 6\, 10^{-6}\, R\, T_7/\mu,$$

degeneracy sets in at densities $\rho/\mu_e \gtrsim 10\, T_6^{3/2} g/cm^3$ ($\mu = A/(Z+1)$ and $\mu_e = A/Z$ denote the mean molecular weights, while m_p is the proton mass). The equation of state is then mainly that of the degenerate electrons:

$$P_e = 10^{23} \frac{dynes}{cm^2} \frac{(\rho_6/\mu_e)^{5/3}}{1+(1+(\rho_6/\mu_e)^{2/3})^{1/2}}.$$

Thermal structure. The temperature profile inside the envelope can be obtained by solving the heat diffusion equation, assuming a constant heat flux throughout the layer:

$$Q = \frac{16}{3}\frac{\sigma T^3 dT}{\bar{\kappa}\rho dz} \equiv \frac{4}{3}\sigma\frac{dT^4}{d\tau}. \tag{1}$$

This clearly leads to a temperature profile which is a power-law of the optical depth τ, *i.e.*

$$\frac{T}{T_e} \cong \left(\frac{3}{4}\tau\right)^{1/4} \tag{2}$$

where the effective surface temperature T_e is defined from $Q \equiv \sigma T_e^4$. A precise knowledge of the mean opacity $\bar{\kappa}$ is then needed to relate the temperature to the other thermodynamic quantities, which can then also be expressed as functions of τ, *i.e.* $\rho = \rho(\tau)$, etc. Knowledge of $\bar{\kappa}(\rho, T)$ is also necessary in order to compute the overall depth τ_{tot} of the layer, necessary to establish a relation between the temperatures T_i and T_e.

Opacity. Heat is transported through the layer by radiation or, alternately, by electron conduction - which usually dominates when the electron gas becomes degenerate. Since the two mechanisms operate in parallel the total opacity is simply

$$\kappa^{-1}(\rho, T) = {\kappa_r}^{-1} + {\kappa_c}^{-1} \tag{3}$$

Modern cooling calculations routinely use the Roseland mean of the opacity as tabulated in the Los Alamos Opacity Library (Huebner *et al.* 1977).

Analytic Considerations. These opacities were recently reviewed for the application to neutron star envelopes in (Gudmundsson 1981), where extensive plots are also given. An important feature of these opacities is, that they are well represented by a power law of the form $\bar{\kappa}(\rho, T) \sim \rho^\alpha T^\beta$ over large segments of the (ρ, T) plane, with the powers α, β changing dramatically, when the transport changes from radiative to conductive. For illustrative purposes we shall represent the opacity as

$$\kappa_r = A_r \rho / T^{3.5} + \kappa_{Th}$$

$$\kappa_c = A_c T^2 / \rho^2, \tag{4}$$

where the radiative part is given by a Kramer's-law absorbsion term augmented by the Thomson opacity (see also Hernquist and Applegate *loc. cit.*). The constant coefficients in eq(4) are in CGS units

$$A_r \cong 10^{23}\, Z/{\mu_e}^2$$

$$A_c \cong 1.28\, A\, 10^{-7},$$

where A is the nuclear weight, and Z the atomic number.

The region near the turn of the opacity law from conductive to radiative is of paramount importance in the heat transport problem, contributing most of the resistance to the heat flow. This region is easily determined from eq(4) requiring $\kappa_r = \kappa_c$. We immediately find the condition $\rho = (A_c/A_r)^{1/3}\, T^{5.5/3}$, whence

$$\rho \simeq 11\, \mu_e\, {T_6}^{5.5/3}\, \frac{g}{cm^3}. \tag{5}$$

An accurate knowledge of the opacity law in this region is, therefore, necessary, while details in the opacity outside this "sensitivity strip" of the parameter space will not affect substancially the heat flow. This important result was first demonstrated in the numerical calculations of Gudmundsson *et al.* (1982), but is also reproduced quite accurately through analytic integration of eq(1), using a power law opacity as suggested by eq(4).

Analytic integration has in fact been employed by Hernquist and Applegate (1984) to obtain the thermal structure of neutron star envelopes. Using again eq(4) along with the equation of hydrostatic equilibrium,

$$dP = g\, \rho\, dz = \frac{g}{\kappa}\, d\tau, \tag{6}$$

we readily obtain $\rho^2 \sim T^{6.5}$, or

$$T \sim \rho^{4/13} \tag{6a}$$

for the nondegenerate, radiative segment of the envelope, while the corresponding relation in the degenerate conductive regime becomes

$${T_b}^2 - {T_t}^2 \sim {\rho_t}^{-1/3} \tag{6b}$$

(the indices b, t designate the botom and top of the integration layer). We thus get a sharp and continuing flattening of the temperature profile $T(\rho)$ at high densities.

The temperature at the base of the radiative zone T_r should then give the order of magnitude of the interior temperature T_i. A somewhat more careful statement of eq(6a) includes the constants of proportionality:

$$T/T_e \simeq (\rho/\rho_0)^{4/13},$$

$$\rho_0{}^2 \equiv 1.25 \frac{\mu g m_p}{kT_e} \frac{T_e^{3.5}}{A_r}. \tag{8}$$

Normalizing A_r in accordance with the Los Alamos Opacities we thus find for a pure helium and a pure iron atmosphere respectively,

$$\rho_0 = \left\{ \begin{matrix} 0.1 \\ 0.027 \end{matrix} \right\} T_{e6}{}^{5/4} g/cm^3$$

ρ_0, here represents the density at optical depth $\tau \simeq 1.2$ (Kylafis and Ventura 1988).

Following the curve $T(\rho)$ in the radiative zone up to the density at which the medium becomes conductive, *i.e.* eq(5), we obtain at the base of the radiative zone the values indicated in the accompanying Table.

	He	Fe
T_r/T_e	45	113
τ_r	$5\ 10^6$	$2.2\ 10^8$
$\rho(g/cm^3)$	$2.2\ 10^4$	$1.3\ 10^5$

Thus, an iron neutron star is expected to have its interior about two orders of magnitude hotter than its surface, while this ratio is reduced in the case of a pure helium atmosphere.

3. Effects of Magnetic Fields

Ali Alpar (this conference) already reviewed for us the essencial physics of the magnetic surface of a neutron star. The magnetic field profoundly influences the properties of electronic matter with characteristic energies kT, $\epsilon_F \leq \hbar eB/mc = 116\, keV\, B_{13}$ ($\hbar eB/mc \equiv \hbar\omega_c$ defines the energy required to excite the transverse Landau orbital of an electron, see *e.g.* Canuto and Ventura 1977).

With the electrons frozen in the ground state Landau level, the electron phase space becomes essencially one-dimensional,

$$\epsilon = \hbar^2 k_\parallel{}^2/2m.$$

At $T = 0$, the parallel to the field Fermi momentum is related to the density through the relation

$$n_e = \frac{k_F}{\pi \lambda_\perp^2}, \qquad \left(\lambda_\perp \equiv \left(\frac{\hbar}{m\omega_c} \right)^{1/2} \simeq 8\, 10^{-11} cm\, {B_{13}}^{1/2} \right) \tag{9}$$

Here $\lambda_\perp$ is the typical dimension of the electron's transverse Landau orbital. It is noteworthy that $\lambda_\perp$ becomes less than the atomic Bohr radius for for magnetic fields in excess of $10^9\, G$. We can thus anticipate that the atomic binding energy is strongly increased in the presence of a pulsar magnetic field, a phenomenon which will, of course, leave its mark on the bound-bound and bound-free opacities, as we shall see. By contrast to eq.(9), at $B = 0$ the relation is $n_{e0} = (3\pi^2)^{-1} {k_F}^3$ so that the onset of degeneracy will occur in the presence of an external field at a density, n_e, higher than required in the nonmagnetic case:

$$\frac{n_e}{n_{e0}} = \frac{1}{{k_F}^2 {\lambda_\perp}^2} \simeq \frac{\hbar\omega_c}{kT}. \tag{10}$$

Notice further, that the Fermi temperature and pressure now scale as $T_F \sim \rho^2$, $P_e \sim \rho^3$ rather than the usual $T_F \sim \rho^{2/3}$ and $P_e \sim \rho^{5/3}$. The question we now wish to address is: how these modified properties might change the overall depth τ of the radiative layer.

Magnetic Opacities. In addition to the previously described effects, the coefficient of heat transport is drastically modified in the presence of a strong magnetic field. Let us first consider the radiative opacities. Two propagating polarization normal modes are defined in the presence of an external field having different mean free paths each in the various photon-electron interactions (Lodenquai *et al.* 1972, Gnedin and Sunyaev 1974, Mészáros and Ventura 1979, Nagel and Ventura 1983, Soffel *et al.* 1983). A principal result is that, at frequencies $\omega << \omega_c$, photons having their polarization perpendicular to the **Bk** - plane have a mean free path which is increased relative to the nonmagnetic case by a factor $(\omega_c/\omega)^2$ in both the Thomson and free-free interactions. Since $kT < \hbar\omega_c$ in a magnetic neutron star atmosphere, a thermal plasma would principally cool via these weakly interacting photons reducing its Roseland mean of the opacity according to

$$\frac{\bar{\kappa}_H}{\bar{\kappa}_0} \simeq 41 \left(\frac{kT}{\hbar\omega_c} \right)^2. \tag{11}$$

The conductive opacity is also strongly modified in the degenerate regime. The collision frequency of an electron is found to be an oscillating function of its kinetic energy (Ventura 1973). In the high field limit, ϵ_F, $kT < \hbar\omega_c$, one finds (Yakovlev 1980, 1982, 1984, Hernquist 1984)

$$\frac{\kappa_H}{\kappa_0} \sim \rho^{-2}, \tag{12}$$

in the degenerate case, while in the nondegenerate case the magnetic and nonmagnetic conductive opacities are essentially equal:

$$\kappa_H \simeq \kappa_0 \simeq 10^4 Z \Lambda \frac{T_7^{1/2}}{\rho} cm^2/g, \tag{13}$$

where Z denotes the mean atomic number. At higher densities the electron Fermi energy increases beyond the Landau excitation energy, and the opacity exhibits an oscillatory behaviour, as the value of ϵ_F passes through the excitation energies in the Landau spectrum. Fig. 1. shows a comparison of the opacity law as given in Eq. (14) (solid line) to the magnetic opacities discussed in this Section (broken line) for the case of a pure iron atmosphere at a constant temperature of 10^7 K.

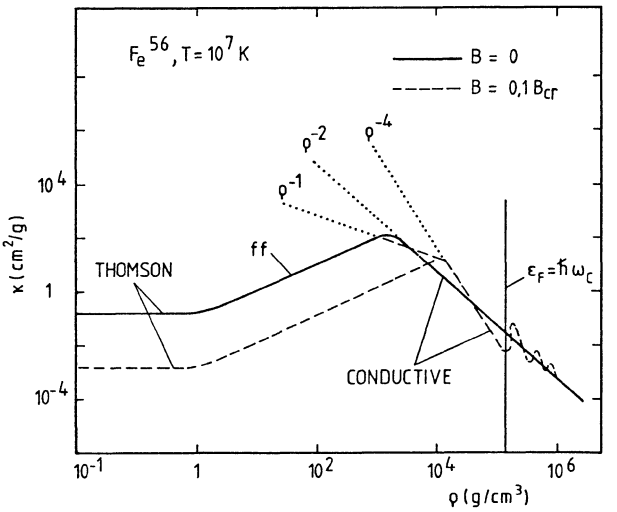

Fig.1. *A comparison between the magnetic (broken line) and the nonmagnetic (solid) opacities.*

The magnetic field value assumed is equal to 0.1 B_{cr}, where the critical value of the magnetic field, B_{cr} is defined from

$$\frac{\hbar e B_{cr}}{mc} \equiv mc^2.$$

Magnetic field values of about 0.1 B_{cr} are suggested from recent observations of cyclotron lines in some X-ray pulsars and in gamma ray bursts (Trümper *et al.* 1978, Mazets *et al.* 1981). Fig. 1 also clearly indicates the density regions, where the opacity is dominated by the Thomson scattering and the free-free processes, as well as the region where electron conduction dominates. In the magnetic case the conduction region has been pushed to higher densities. The magnetic opacity is

seen to decrease with increasing values of the density with a very sharp ρ^{-4} law, and then shows several quantum oscillations around the nonmagnetic value.

Thermal Structure. These different effects represent substantial quantitative as well as qualitative deviations from the nonmagnetic opacity. Recent calculations by Hernquist (1984) incorporating the magnetic opacities have indicated, nevertheless, that due to cancellations, the net change in the overall optical depth is small, which in turn implies that the relation between the interior and surface temperatures remains essentially unaffected. It should be mentioned, however, that the above calculations are limited by the fact that they are one-dimensional in nature. One thus assumes that the transport of heat occurs primarily in the radial directrion, and then computes in a manner similar to the isotropic case, but using coefficients appropriate for the transport parallel (or perpendicular) to the external field. Therefore, one facet of the problem still remaining unexplored is a full, quantitative study of the two-dimensional temperature profile at the surface of a magnetic neutron star.

In the above we have assumed that a one-dimensional magnetic lattice, as first suggested by Ruderman (1971) will probably not form, according to recent improved computations (see *e.g.* Müller 1984, Flowers *et al.* 1977). In the case that such a magnetic solid were to form the outer envelope would end abruptly at the typical density of this solid *i.e.* at about $10^4\ g/cm^3$. Both the luminosity and the spectral character of the emitted radiation would then be affected (see Brinkmann 1980).

4. Emergent Spectrum

Traditionally *Einstein* pulsar observations have been translated into a total flux at the neutron star surface, and thereby a surface temperature, assuming that the emmission follows the Planck law. This assumption can in fact be crucial, given the expected surface temperatures, which range between 10^5 and 10^6, and the fact that instrumental sensitivity combined with interstellar absorption peaks at energies in the range from 0.3 - 5 keV. As these energies may well exceed the Planck peak at $\sim$ 3 kT, one would only be able to observe the high energy tail of the emitted thermal spectrum. Deviations from the black body law may then easily result into an erroneous determination of the effective temperature.

This problem was clearly demonstrated by Romani (1987), whose calculations also show a sensitivity to the assumed chemical composition. Thus the spectrum emitted by a pure helium or pure hydrogen neutron star atmposphere is found to deviate most strongly from the black body law, being much harder as compared to the spectrum emitted by an atmosphere containing heavier elements (see Fig. 2). These calculations are based on a simple numerical code starting with the thermal structure of a grey atmosphere, and correcting the temperature profile until self-consistancy is achieved with the spectral energy density at every depth.

Qualitatively it is, of course, easy to understand this strong dependence on chemical composition. At $10^6\ K$ helium is totally ionized, while even a small ad-

mixture of heavier elements would contribute strong photoabsorption edges in the range 0.3 to 5 *keV*, or close to it. In the fully ionized case the photon extinction coefficient would follow the law

$$\kappa_\omega \simeq \bar{\kappa}_R \frac{1 - e^{-u}}{u^3}, \tag{14}$$

where $\bar{\kappa}_R$ is the Roseland mean of the opacity and $u \equiv \hbar\omega/kT$. The strong u^{-3} dependence is then reflected in the photon mean free path. At high frequencies

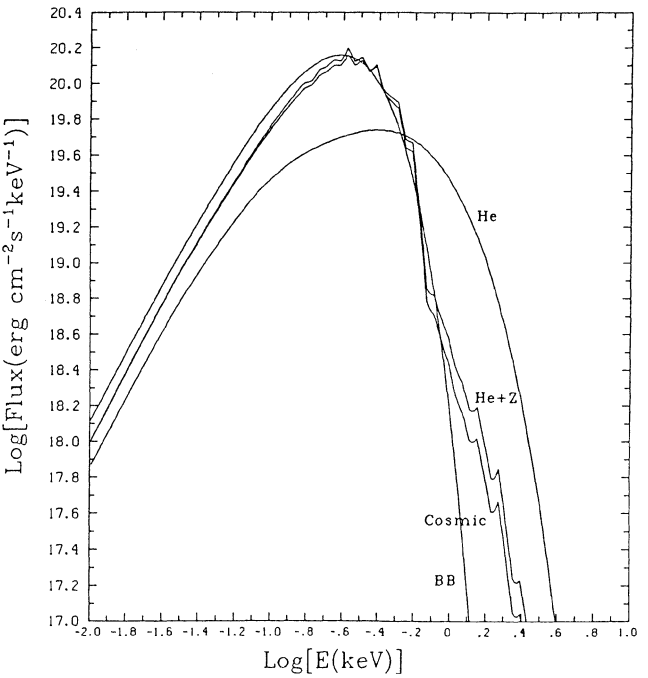

Fig.2. *Calculated spectra from a neutron star model atmosphere at an assumed surface effective temperature of* 10^6 *K. The spectra show a strong dependence on chemical composition. After Romani (1987).*

then, the medium becomes more transparent and one is able to sample deeper and hotter layers in the neutron star's atmosphere. This results naturally in a harder spectrum than given by either the black body or the grey atmosphere law. The presence of heavier elements would of course, change this behaviour due to the presence of the forementioned photoabsorption edges.

Much in the numerical results presented by Romani can thus be understood in a fairly simple framework. This is especially interesting if one is to include the effect of magnetic fields in these calculations, in which case extensive Los Alamos

opacities are not available. It is then of some interest to note that for a magnetic field of $0.1\,B_{cr}$, similar to that measured in the X-ray pulsar Hercules-X1 (Trümper *et al.* 1978), the atomic binding energies are greately enhanced. The binding energies of hydrogen, and the hydrogenic ions of helium and iron are then found at $\sim$ 0.27, 0.67, and 25.8 *keV* respectively (see *e.g.* Wunner, Ruder and Herold 1981; Wunner *et al.* 1981). Magnetic helium would thus no longer be totally ionized at $10^6\,K$ contributing a strong photoabsorption edge precisely within the energy band of high instrumental sensitivity, and, once again, profoundly changing the spectral character.

ACKNOWLEDEMENTS: It is a pleasure to thank Hakki Ögelman and Wolfgang Brinkmann for discussions. My thanks are also extended to Gregor Morfill for the warm hospitality offered me at the Max Planck Institute in Garching.

REFERENCES:

Alpar, M.A., 1989, This Volume.

Alpar, M.A., Brinkmann, W., Kiziloglu, Ü., Ögelman, H. and Pines, D., 1987, *Astron. Astrophys.* **177**, 101.

Brinkmann, W. and Ögelman, H., 1987, *Astron. Astrophys.* **182**, 71.

Brinkmann, W., 1980, *Astron. Astrophys.* **82**, 352.

Chiu, H.Y. 1964, *Ann. Phys.* **26**, 364.

Chiu, H.Y. and Salpeter E. 1964, *Phys. Rev. Lett.* **12**, 413.

Flowers, E.G., Lee, J.-F., Ruderman, M.A., Sutherland, P.G., Hillebrandt, W., Müller, E., 1977, *Astrophys. J.* **215**, 291.

Gnedin, Yu.N. and Sunyaev, R.A. 1974, *Astron. Astrophys.* **36**, 379.

Gudmundsson, E., 1981, *PhD Thesis*, Nordita Report, Unpublished.

Gudmundsson, E.H., Pethick, C.J. and Epstein R.I., 1982, *Astrophys. J. (Letters)* **259**, L19.

Gudmundsson, E.H,, Pethick, C.J. and Epstein R.I., 1982, *Astrophys. J.* **272**, 286.

Helfand, D.J., Channan, C. and Novick R., 1980, *Nature,* **283**, 337.

Helfand D.J., 1983, *in Supernova Remnants and their X-ray Emission, IAU Symposium No. 101*, eds. J. Danziger, P. Gorenstein, Reidel, Dortrecht, p. 471.

Helfand, D.J. and Becker, R.H., 1984, *Nature,* **307**, 215.

Hernquist, L., 1984, *Astrophys. J. Suppl. Ser.)* **56**, 325.

Hernquist, L. and Applegate, J.H., 1984, *Astrophys. J.* **287**, 244.

Hernquist, L., 1984, *Mon. Not. R. astr. Soc.* **213**, 313.

Huebner, W.F., Merts, A.L., Magee, JR., N.H. and Argo, M.F., 1977, Los Alamos Report LA-6760-M.

Lodenquai, J., Canuto, V., Ruderman, M., and Tsuruta, S., 1974, *Astrophys. J.* **190**, 141.

Kylafis, N. and Ventura J., 1988, in preparation.

Maxwell, O.V., 1979, *Astrophys. J.* **231**, 201.

Mazets, E.P., Golentskii, S.V., Aptekar, R.L.,Gur'yan, Yu.A., and Il'inskii, V.N., 1981, *Nature,* **290**, 378.

Mészáros, P. and Ventura, J., 1979, *Phys. Rev.* D **19**, 3565.

Müller E., 1984, *Astron. Astrophys.* **130**, 415.

Müller E. 1989, This Volume

Nagel, W. and Ventura, J. 1983, *Astron. Astrophys.* **118**, 66.

Nomoto, K. and Tsuruta, S. 1986, *Astrophys. J. (Letters)* **305**, L19.

Ögelman, H., 1987, *Europhys. News* **18**,98.

Pines, D. and Alpar, M.A., 1985, *Nature,* **316**, 27.

Pines D. 1989, This Volume.

Pines D. and Alpar, M.A., 1989, This Volume.

Richardson, M.B., Van Horn, H.M., Ratcliff and Malone R.C., 1982, *Astrophys. J.* **255**, 624.

Romani, R.W., 1987, *Astrophys. J.* **313**, 718.

Ruderman, M.A., 1971, *Phys. Rev. Lett.* **27**, 1306.

Shapiro S.L. and Teukolsky S.A., 1983, *Black Holes, White Dwarfs and Neutron Stars*, (Wiley, New York).

Soffel, M., Ventura J., Herold H., Ruder, H. and Nagel W., 1983, *Astron. Astrophys.* **126**, 251.

Trümper, J., Pietsch, W., Repin, C., Voges, W., Staubert, R., Kendziorra, E., 1978, *Astrophys. J. (Letters)* **219**, L105.

Tsuruta, S. and Cameron A.G.W., 1965, *Nature,* **207**, 364.

Tsuruta, S., 1986, *Comments on Astrophys.* **XI**, 151.

Ventura, J., 1973, *Phys. Rev.* A **8**, 3021.

Ventura, J., 1979, *Phys. Rev.* D **19**, 1684.

Wunner, G., Ruder H., and Herold H., 1981, *Astrophys. J.* **247**, 374.

Wunner, G., Ruder H., Herold, H. and Trümper, J., 1981, *Phys. Rev. Lett.* **46**, 1700.

Yakovlev, D.G., 1980, Ioffe Institute Preprint No. 679.

Yakovlev, D.G., 1982, *Soviet Astron.* **26**, 416.

Yakovlev, D.G., 1984, *Astrophys. Sp. Sc.* **98**, 37.

A MODEL OF PULSAR TIMING NOISE

K.S. Cheng[1], M.A. Alpar[2], D. Pines[3] and J. Shaham[4]
[1] Physics Department, University of Wollongong, N.S.W. 2500, Australia
[2] Research Institute for Basic Sciences, P.K. 74, Gebze, Kocaeli 41470, Turkey
[3] Physics Department, University of Illinois, IL 61801, U.S.A.
[4] Physics Department, Columbia Universtiy, N.Y., N.Y 10027, U.S.A.

ABSTRACT. We propose that the pulsar timing noise results from the magnetospheric fluctuations and internal superfluid unpinning. In general, the pulsar timing noise power spectra of frequency derivation contains two components. The high frequency component results from the small scale superfluid unpinning (microglitches) which can happen spontaneously with a characteristic rate inverse proportional to the thermal relaxation time of vortex creep. The low frequency component could be either caused by the sudden change of current braking torque which is induced by the microglitches or some rapid variations in current braking torque due to the fluctuation of the outermagnetosphere gaps.

1. INTRODUCTION

The most remarkable feature of pulsars is the regularity of the pulsations, which are very precise, to 10^{-10}s for most pulsars. The secular decrease of the rotation rate from energy loss is also very regular. Pulsars seemed to be a category of well-behaved stellar objects, until the abrupt increases in fequency (glitches) were found in the Vela pulsar (Radhakrishnan and Manchester 1969; Reichley and Downs 1969) and the Crab uplsar (Boynton et al. 1969). A second kind of irregularity (timing noise) was also recognized in the Crab pulsar by Boynton et al. (1972). They found large phase residuals remaining after the removal of the low-order polynomial that could result from a random walk in the rotation frequency or white noise in the power spectrum of the frequency derivative. A more detailed analysis of the arrival time of the Crab pulsar by Groth (1975) confirmed this conclusion. Cordes and Helfand (1980) examined the timing-noise behaviour of 50 pulsars from the JPL data and showed that the timing noise is a general characteristic feature of pulsars: a study of 11 pulsars indicates that random walks occur in rotational phase in two objects, in frequency in four objects, and in frequency derivative in two objects. Based on such a vast amount of timing-noise data, it is possible to construct a theoretical framework in which to understand the timing-noise behaviour of pulsars.

2. HIGH FREQUENCY TIMING NOISE (MAGNETOSPHERIC FLUCTUATIONS)

2.1 Fluctuations of Outermagnetosphere Gap

We (Cheng 1987a) point out that the pair production mechanism in outermagnetosphere gap models (Cheng, Ho and Ruderman 1986 a,b) can give rise to fluctuations which result in rapid variation of the current braking torque, leading to a random walk in rotation frequency. Basically, we follow the statistical description of torque variation in terms of noise process developed by Lamb, Pines and Shaham (1978 a,b) and assume that each fluctuation in torque is an independent event which occurs at random time t_i with a rate R during a time interval T (the duration of the observing period). The number of events has a

H. Ögelman and E. P. J. van den Heuvel (eds.), Timing Neutron Stars, 503–509.

poisson distribution mean value, RT, and time t_i are uniformly distributed for $O < t_i < T$. Since the time scale ($t_O \sim 2\Omega_C^{-1}$) of the fluctuations is so rapid that it is not difficult to show that it can result in a series of δ-function-like fluctuations in the current braking torque which cause a series of random walk in angular frequency. The random walk strength parameter in frequency can be expressed as

$$S_{FN} = \frac{R<\delta\Omega_i^2>}{(2\pi)^2} \approx \frac{\Omega_c}{8\pi^2} \left(\frac{I_{tot}}{I_c}\right)^2 \left(\frac{\delta N_{JxB}}{N_{tot}}\right)^2 \frac{1}{t_{age}^2} \qquad (1)$$

where Ω_c is stell angular frequency, I_{tot} is the total moment of inertia of the star, I_c is the moment of inertia of the stellar crust. δN_{JxB} is the fluctuation in current braking torque, N_{tot} is the spin down torque and $t_{age} = (\Omega_c/2\dot{\Omega})$ is the apparent age of the pulsar. Here, we have used the fact that the fluctuation so rapid that only the stellar crust can respond to the change of the external torque and the core superfluid sits still. Since S_{FN} is a function of I_{tot}/I_c which depends upon the equation of state, thus S_{FN} can give us a clue about the structure of the neutron star.

2.2 Micro-glitches and the Induced Magnetospheric Fluctuations.

It is possible that the small scale internal superfluid unpinning (micro-glitches) could create some perturbations in the pulsar magnetosphere which result in the sudden chane of current braking torque. The perturbed torque will remain unchanged until the next micro-glitch; hence the step-function-like variations in torque give rise to a random walk in frequency derivative.
We (Cheng 1987b) have shown that the random walk strength of frequency derivatire (S_{SN}) is given by

$$S_{SN} = \frac{\Omega_c^2 f^2 (\Delta\dot{\Omega}/\dot{\Omega})}{16\,\pi^2\, t_{age}^2\, \tau} \left(\frac{\delta N_{JxB}}{N_{tot}}\right)^2 \qquad (2)$$

where $\tau = kT\,\omega_{cr}/E_p\,|\dot{\Omega}|$ is the relaxation time of thermal vortex creep (Alpar et al 1984 a,b) and $f(\Delta\dot{\Omega}_c/\dot{\Omega}_c)$ is the function which describes the response of the magnetosphere to the glitches.

T is the internal temperature of the star, ω_{cr} is the critical relative angular frequency between stellar rotation frequency and superfluid rotation frequency Ω_s which determine the pinning status of the vortex line. E_P is the pinning energy, $|\dot{\Omega}_c|$ is the derivative of the rotation frequency.

3. LOW FREQUENCY TIMING NOISE (MICROGLITCHES)

According to the vortex creep model (Alpar et al. 1984 a,b) the equation of motion of superfluid can be describe by

$$\frac{\partial \omega}{\partial t} = -\dot{\Omega}_s - \frac{\kappa n(r,t)}{r} V_r(r,t) \qquad (3)$$

where $\omega = \Omega_s - \Omega$, $n(r,t) = 1/\kappa\,(2\Omega_s + r\,\partial\omega/\partial r)$ is the vortex lines density and $V_r = V_o \exp - E_p/kT\,(1 - \omega/\omega_{cr})$ is average radial velocity of the vortex lines, $\kappa = h/2m_n$ is the vorticity and $V_o = 10^7$ cm s^{-1} is the microscropic velocity of vortex lines.

3.1 Accumulation and Depleion Regions of Vortex Lines

The steady state solution of equation (3) is

$$\frac{\omega_{cr} - \omega_\infty}{\omega_{cr}} = \frac{kT}{E_p}\,\ell n\left(\frac{V_o}{V_\infty}\right) \qquad (4)$$

The subscript "∞" indicates the steady state value of these quantities. Since $kT/E_p << 1$ ($kT \simeq 100$eV for most pulsars and $E_p \sim 0.1$ MeV), therefore ω_∞ should have a spatial variation similar to ω_{cr}. We can approximate the vortex density

$$n_\infty \simeq \frac{1}{\kappa}\left[2\Omega_c + r\frac{d\omega_\infty}{dr}\right] \simeq \frac{r}{\kappa}\frac{\delta\omega_o}{\delta r_a} \equiv n_a \quad \text{if } r\frac{d\omega_{cr}}{dr} \simeq \frac{r\delta\omega_o}{\delta r_a} >> 2\Omega_c \qquad (5)$$

This is called vortex accumulation region with radial size δr_a and $\delta\omega_o$ is the fluctuation of ω_{cr} due to spatial irregularity is negative and $-d\omega_{cr}/dr > 2\Omega/r$. Then, we cannot to use equation (5). In order to reduce the magnus force which is proportinal to $\omega - \omega_{cr}$, ω will try to be close to ω_{cr} as much as possible, this results in a vortex depletion region where $n_\infty = 1/\kappa\,[2\Omega + r\,d\omega_\infty/dr] \simeq O$. This implies

$$-\frac{d\omega_\infty}{dr} \simeq \frac{\delta\omega_o}{\delta r_d} \simeq \frac{2\Omega_c}{r} \qquad (6)$$

where δr_d is the radial size of the vortex depletion region.

3.2 A Naive Spontaneous Unpinning Scenario

In the accumulation region, the Magnus force on a particular vortex line required to balance the local superfluid velocity set up by a neighbouring vortex is

$$\delta f_m \simeq \rho\kappa^2 n_a^{1/2} \qquad (7)$$

At the same time, the total magnus force in steady state, $f = \rho\kappa r\omega_\infty$ is below the critical value for unpinning, by an amount

$$\delta f \equiv f_p - f = \rho\kappa r(\omega_{cr} - \omega_\infty) = \frac{kT\rho\kappa r\,\omega_{cr}}{E_p}\,\ell n\left(\frac{V_o}{V_\infty}\right) \tag{8}$$

Suppose that a few free vortex lines migrate into the vortex accumulation region. (The source of these vortex lines will be discussed later). They will rotate with the superfluid which is moving faster than crust. These free vortex lines will circulate around the spin axis of the neutron star and drift out slowly, contributing additional local superfluid velocity to pinned vortex lines, an extra force of order of δf_m, given by eq. (7), will be acting at the pinned vortex lines. Furthermore, if $\delta f_m > \delta f$, then some vortex lines will be forced out of their pinning sites. But the accumulation region must be followed by a depletion region, otherwise, the unpinned vortex lines will be immediately repinned. Therefore, only single layer of vortex lines at the boundary between the accumulation region and the depletion region can be ultimately unpinned. Number of unpinned vortex lines in this case will be $N_u = 2\pi r n_a^{1/2}$. The resulting charge of angular velocity of the superfluid in the depletion region is then $\delta\Omega_s = -\kappa N_u/2\pi r_o^2$ and the crust will be suddenly spun-up by an amount

$$\Delta\Omega_c^{th} = \frac{I_d}{I}|\delta\Omega_s| = \frac{\delta\omega_{co}}{2\Omega_c}\,\frac{\omega_{cr}}{E_p}\,kT\,\ell n\left(\frac{V_o}{V_\infty}\right) \tag{9}$$

due to conservation of angular momentum [N.B. the moment of inertia of the vortex depletion region is given by eq. (6)].

3.3 Spectrum

Since the microglitches create a series of δ-function-like variation in rotation frequency, which is equivalent to have a series of random walk in phase, as long as the relaxation time of individual microglitches is much shorter than the observed period. This is first considered by Alpar, Nandkumar and Pines (1986). They show that the spectrum of timing noise due to the microglitches is phase noise and the random walk strength parameter (S_{PN}) is $R\,(2\pi\Delta\Omega_c\tau)^2$. But they treat R (the rate of microglitches) and $\Delta\Omega_c$ (the size of microglitches) as parameters. In our spontaneous unpinning scenario, we need at least one free vortex line to initiate the whole mechanism. Such free vortex lines could be created as the pinned vortex lines creep outward and encounter a spatially irregular region with missing pinning sites.This situation can happen anytime,but the mean time interval for each event must be the relaxation time scale (τ) for excursions from the steady state of thermal creep. Furthermore, $\Delta\Omega_c$ is given by eq.(9) in this particular model.Hence we get

$$S_{PN} = \left[\frac{\pi\,\delta\omega_o\,\omega_{cr}}{E_P}\,\ell n\left(\frac{V_o}{V_\infty}\right)\frac{kT}{\Omega_c}\right]^2 \frac{kT}{E_P}\,\frac{\omega_{cr}}{|\dot{\Omega}|} \tag{10}$$

4. APPLICATION AND DISCUSSION

In order to compare our theoretical results to the observed data, we need to know the internal temperature of pulsars. By using the GPE (Gudmusson, Petlick and Epstein, 1983) model which relate the internal temperature to the surface temperature and assuming the vortex creep is the ultimate heating mechanism of the star, we (Alpar et al. 1986 and Cheng 1987b) can show that T is proportional to $|\Omega|^{0.455}$. Therefore, the random walk parameters can be expressed as

$$S_{PN} \alpha\, |\dot{\Omega}|^{0.365}/\Omega^2\,, \tag{11}$$

$$S_{FN} \alpha\, (|\dot{\Omega}|^2/\Omega)\left(\frac{\delta N_{JxB}}{N_{tot}}\right)^2 \tag{12}$$

and

$$S_{SN} \alpha\, |\dot{\Omega}|^{2.545}\left(\frac{\delta N_{JxB}}{N_{tot}}\right)^2 f^2\left(\frac{\Delta\dot{\Omega}}{\dot{\Omega}}\right) \tag{13}$$

where $(\delta N_{JxB}/N_{tot})^2 \simeq 0.02$ - 0.1 for pulsars with outermagnetosphere gap and $(\delta N_{JxB}/N_{tot}) \simeq 1$ for typical pulsars.

In Table I, we summarise the random walk strength parameters (S_{pn}, S_{fn} and S_{sn}) given by Cordes and Downs (1985) and Boynton and Deeter (1985). We compare our model results of $\Delta\Omega_c/\Omega_c$ (eq. 9) with the observed data in table II. They are pretty consistant with each other. Furthermore, Cordes et al (1987) analyse the 15 years timing data of the Vela pulsar, they find that there are two type of discontinuities in the spin frequency of the Vela pulsar: macrojumps (giant glitches) occur about once every 1000 days with amplitudes $\Delta\Omega_c/\Omega_c \sim 10^{-6}$ while microjumps (microglitches) occur ten times more often and have $\Delta\Omega_c/\Omega_c \sim 10^{-9}$. These results agree with $R \sim 1/\tau$ and equ. (9) very well, if we assume that the spontaneous unpinning happens in weak pinning regions where $\delta\omega_o \simeq \omega_{cr} \simeq 10^{-2}$ rad s^{-1}.

In order to evaluate the theoretical value of S_{fn}, we need to know I_c which depends upon the equation of state. Since the uncertainties of the observed data is large, it is not accurate enough to pinpoint what kind of equation of state give the best fit. Nevertheless, we can still determine that the stiff equations of state (e.g. Pandharipande, Pines and Smith 1976, which give $I_c/I_{tot} \sim 0.15$ - 0.3) are better than the soft equations of state (e.g. Reid potential and BJ which give ~ 0.02 - 0.1) in table III. Although the random walk strength parameter of frequency derivative (Ssn) involves an unknown function f $(\Delta\Omega/\Omega)$ which is still under investigation, we assume that is a constant which turns out to be a good approximation in table IV.

REFERENCES

1. Alpar, M.A., Anderson, P.W., Pines. D., and Shaham, J. 1984a, Ap. J., 276, 325.
2. Alpar, M.A. Anderson, , Pines, D., and Shaham, J., 1984b Ap. J. 278, 791.
3. Alpar, M.A., Nandkumar, R., and Pines, D., 1986, Ap. J. 311, 197.
4. Boynton, P.E., Groth, E.J., Hutchinson, D.P., Nanos, G.P., Partridge, R.B., and Wilkinson, D.T. 1972, ap. J. 175, 217.
5. Boynton, P.G., Groth, E.J., Partridge, R.B., and Wilkinson, D.J 1969, Ap. J. (Letters), 157, L197.
7. Cheng, K.S. 1987a, Ap. J. 321, 799.
8. Cheng, K.S. 1987b Ap. J. 321, 805.
9. Cheng, K.S., Alpar, M.A., Pines D. and Shaham, J., Ap. J. (1988) in press.
10. Cheng, K.S., Ho, C., and Ruderman, M.A., 1986a, Ap. J. 300, 500 (CHR I).
11. Cheng, K.S., Ho, C., and Ruderman, M.A., 1986b, Ap. J. 300, 522 (CHR II).
12. Cordes, J.M. and Helfand, D.J., Ap. J. 239, 640 (1980).
13. Cordes, J.M. and Downs, G.S., ap. J. Suppl. (1985).
14. Cordes,J.M., et al. 1987, Ap. J. submitted.
15. Groth, E.J., Ap. J. Suppl., 29, 453 (1975).
16. Gudmundsson, E.H., Petlick, C.J., and Epstein, R. 1983, Ap. J. 272, 285.
17. Lamb, F.K., Pines, D., and Shaham, J. 1978a, Ap. J. 224, 969.
18. Lamb, F.K., Pines, D., and Shaham, J. 1978b, Ap. J. 225, 582.
19. Pandharipande, V.R., Pines, D., and Smith, R.A. 1976, Ap. J. 208, 550.
20. Pandharipande, V.R., and Smith, R.A. 1975, Nucl. Phys. A, 237, 507.
21. Radhakrishnan, V., and Manchester, R.N. 1969, Nature, 222, 228.
22. Richards, D.W., and Comella, J.M., 1969, Nature, 222, 551.

TABLE I

OBSERVED RANDOM WALK PARAMETERS

Pulsar	S_{SN}^{obs} ($Hz^2\ s^{-3}$)	S_{pN}^{obs} (s^{-1})	S_{FN}^{obs} ($Hz^2\ s^{-1}$)
0329 + 54	$(8.15 \pm 2.0) \times 10^{-43}$	$(1.61 \pm 0.05) \times 10^{-10}$	.....
0355 + 54	$(0.66 \pm 3.6) \times 10^{-41}$	$(2.21 \pm 0.11) \times 10^{-9}$	.....
0525+ 21			$(1\text{-}2.5) \times 10^{-28}$
0531 + 21			$(3.5\text{-}9.7) \times 10^{-23}$
0611 + 22	$(1.31 \pm 0.88) \times 10^{-37}$	.....	.....
0628 - 28	$(0.77 \pm 4.9) \times 10^{-42}$	$(2.19 \pm 0.07) \times 10^{-9}$	.....
0736 - 40	$(2.36 \pm 0.52) \times 10^{-41}$	$(3.61 \pm 0.34) \times 10^{-10}$	.....
0823 + 26	$(2.8 \pm 0.25) \times 10^{-40}$	.....	$(1.28 \pm 2.32) \times 10^{-24}$
0833 - 45	$(1.01 \pm 0.04) \times 10^{-34}$	$(9.12 \pm 1.0) \times 10^{-9}$	.....
1133 + 16	$(-0.11 \pm 3.2) \times 10^{-43}$	$(7.53 \pm 0.51) \times 10^{-11}$	.....
1237 + 25	$(-0.21 \pm 4.01) \times 10^{-43}$	$(1.07 \pm 0.06) \times 10^{-10}$	.....
1642 - 03	$(1.97 \pm 3.39) \times 10^{-40}$	$(7.52 \pm 5.88) \times 10^{-10}$	.....
1706 - 16	$(3.45 \pm 1.50) \times 10^{-41}$	$(2.19 \pm 0.86) \times 10^{-10}$	.....
1749 - 28	$(7.88 \pm 0.72) \times 10^{-41}$	$(8.98 \pm 1.11) \times 10^{-10}$	.....
1818 - 04	$(2.37 \pm 0.69) \times 10^{-40}$	$(2.79 \pm 0.19) \times 10^{-9}$	.....
1911 - 04	$(0.37 \pm 4.79) \times 10^{-42}$	$(2.07 \pm 6.89) \times 10^{-10}$	.....
1929 + 10			$(3.2\text{-}6.3) \times 10^{-27}$
1933 + 16			$(0.2\text{-}1.99) \times 10^{-27}$
2021 + 51	$(2.45 \pm 0.26) \times 10^{-41}$	$(4.12 \pm 0.33) \times 10^{-10}$	.....
2045 - 16	$(1.44 \pm 1.33) \times 10^{-43}$	$(5.9 \pm 0.22) \times 10^{-11}$	.....

Table II

Pulsar	$S_{pN}^{obs}/(S_{pN}^{obs})_{2021}$	T_{in} (10^5 K)	$[\Delta\Omega_c/(\Delta\Omega_c)_{2021}$	$(\frac{\Delta\Omega_c}{(\Delta\Omega_c)_{2021}})^{th}$
0329 + 54	$(3.91 \pm 0.12) \times 10^{-1}$	1.6	$(4.59 \pm 0.07) \times 10^{-1}$	9.0×10^{-1}
0355 + 54	$<(5.39 \pm 2.6) \times 10^{-1}$	9.1	$<(4.77 \pm 0.12) \times 10^{0}$	1.3×10^{0}
0628 - 28	$<(5.34 \pm 0.17) \times 10^{0}$	1.74	$<(1.76 \pm 0.03) \times 10^{0}$	1.71×10^{0}
0736 - 40	$<(8.80 \pm 0.83) \times 10$	2.63	$<(9.17 \pm 0.43) \times 10^{-1}$	7.83×10^{-1}
0833 - 45	$<(2.22 \pm 0.24) \times 10^{-1}$	1.5×10^{2}	$<(2.38 \pm 0.13) \times 10^{1}$	1.1×10^{1}
1133 + 16	$(1.83 \pm 0.13) \times 10^{-1}$	1.36	$(2.82 \pm 0.09) \times 10^{-1}$	1.2×10^{0}
1237 + 25	$(2.61 \pm 0.15) \times 10^{-1}$	0.65	$(2.08 \pm 0.06) \times 10^{-1}$	7.1×10^{-1}
1642 - 03	$(1.83 \pm 1.43) \times 10^{0}$	2.7	$(1.31 \pm 0.51) \times 10^{0}$	0.85×10^{0}
1706 - 16	$(5.30 \pm 0.21) \times 10^{-1}$	2.87	$(7.81 \pm 1.53) \times 10^{-1}$	1.47×10^{0}
1749 - 28	$(2.19 \pm 0.27) \times 10^{0}$	3.8	$(1.80 \pm 0.11) \times 10^{0}$	1.7×10^{0}
1818 - 04	$<(6.80 \pm 0.46) \times 10^{0}$	3.3	$<(2.81 \pm 0.10) \times 10^{0}$	1.57×10^{0}
1911 - 04	$(0.65 \pm 1.68) \times 10^{0}$	2.0	$(0.82 \pm 1.68) \times 10^{0}$	1.3×10^{0}
2021 + 51	$(1.0 \pm 0.08) \times 10^{0}$	2.4	$(1.0 \pm 0.04) \times 10^{0}$	1.0×10^{0}
2045 - 16	$(1.40 \pm 0.05) \times 10^{-1}$	1.4	$(2.54 \pm 0.04) \times 10^{-1}$	2.1×10^{0}

TABLE III

OBSERVED AND THEORETICAL RANDOM WALK PARAMETERS

Pulsar	P (S)	t_{age} (10^6 yr)	(S_{FN}^{obs}) (Hz s^{-1})	$(S_{FN}^{obs})_{soft}$ (Hz^2 s^{-1})	$(S_{FN}^{th})_{soft}$ (Hz^2 s^{-1})
0525 + 21	3.75	1.5	$(1 - 2.5) \times 10^{-28}$	$(0.2 - 1.4) \times 10^{-27}$	$(1.6 - 3.6) \times 10^{-28}$
0531 + 21	0.033	.001	$(3.5 - 9.7) \times 10^{-23}$	$\leq(0.045 - 1.0) \times 10^{-21}$	$\leq(0.8 - 2) \times 10^{-23}$
1929 + 10	0.23	3.11	$(3.2 - 6.3) \times 10^{-27}$	$(0.4 - 8.6) \times 10^{-26}$	$(0.7 - 1.5) \times 10^{-27}$
1933 + 16	0.359	0.95	$(0.2 - 1.99) \times 10^{-27}$	$(0.2 - 5.7) \times 10^{-25}$	$(4.4 - 9.8) \times 10^{-27}$

TABLE IV

COMPARISON OF MODEL WITH OBSERVATIONS OF S_{SN}

Pulsar	$\Omega(s^{-1})$	$\dot{\Omega}_{-14}$	$\ddagger_6$	$S_{SN}^{obs}/(S_{SN}^{obs})_{2021}$	T_5	$S_{SN}^{th}/(S_{SN}^{th})_{2021}$
0329 + 54	8.8	2.46	5.4	$(3.4 \pm 0.1) \times 10^{-2}$	1.6	9.1×10^{-2}
0355 + 54	40	110	0.56	(0.28 ± 1.5)	9.1	1.1×10^{3}
0611 + 22	18.8	330	0.09	$(4.4 \pm 3.7) \times 10^{3}$	15	1.7×10^{4}
0628 - 28	5.1	2.9	2.95	$(0.32 \pm 2.1) \times 10^{-1}$	1.74	0.31
0736 - 40	16.8	7.2	3.7	$(9.8 \pm 1.2) \times 10^{-1}$	2.63	1.12
0823 + 26	11.8	3.8	4.9	$(1.17 \pm 0.11) \times 10^{1}$	1.97	0.22
0833 + 45[a]	70.6	10^4	0.011	$(3.5 \pm 0.1) \times 10^{6}$	150	5.5×10^{6}
1133 + 16	5.3	1.7	5	$(-0.05 \pm 1.3) \times 10^{-2}$	1.36	2.8×10^{-2}
1237 + 25	4.55	0.31	23	$(-0.09 \pm 1.75) \times 10^{-2}$	0.65	1.0×10^{-4}
1642 - 03	16	7.3	3.4	(0.82 ± 1.41)	2.7	0.57
1706 - 16	9.6	9.4	1.6	(6.44 ± 0.63)	2.87	2.28
1749 - 28	11.1	16.2	1.1	(3.3 ± 0.33)	3.8	8.6
1818 - 04	10.5	11	1.5	(9.5 ± 2.9)	3.3	1.6
1911 - 04	2.6	3.7	3.2	$(0.15 \pm 2.0) \times 10^{-1}$	2.0	0.09
2021 + 51	11.9	6.9	2.75	(1 ± 0.10)	2.4	1
2045 - 16	3.2	1.8	2.8	$(6.1 \pm 5.5) \times 10^{-3}$	1.4	3.3×10^{-2}

Soliton Stars and the Cosmic X-ray Background

Hong-Yee Chiu
Goddard Space Flight Center
Greenbelt, MD 20771
U. S. A.

ABSTRACT. Properties and origin of soliton stars are explored. Evolution of soliton stars in early universe is discussed. A large amount of matter in the Universe could be irreversibly locked inside soliton stars. Soliton stars are efficient energy converters. Models based on the simplest soliton structure (with no net quantum numbers) indicate that soliton stars are possible intense X-ray sources at large red shifts.

1. Introduction.

Most X-ray sources can be classified into one of the following types: Stellar coronae and winds, supernova remnants, and accreting objects, a category which includes objects such as binaries, white dwarfs, neutron stars, stellar mass black holes[1]. X-ray emission from active galactic nuclei has been speculated to be the result of accretion of matter onto a giant black hole of mass $\geq 10^6 M_\odot$. While theories are fairly complete regarding galactic sources, there is considerable uncertainty regarding the role played by extremely massive black holes in the X-ray emission mechanism of active galactic nuclei. Theoretical ground for the formation of giant black holes is not as well established as in the case of stellar black holes.

In addition, there are many yet unexplained phenomena in X-ray astronomy, in particular, the existence of a diffuse cosmic X-ray background. Although in the past theoretical work based on condensed objects (white dwarfs, neutron stars, stellar mass black holes as single objects or as members of binary systems) has yielded important information on the nature of X-ray emitters, there are many mysteries in X-ray objects which cannot be explained in terms of these objects. New physics might be needed.

In this paper we report work done along a new path that might resolve some of these problems[2], this is the area of soliton stars. These are giant, non black hole mass configurations that are stable as hot or cold masses. As hot objects they are intense X-ray emitters. They are also very efficient energy converters, capable of converting nearly 100 % of the rest energy of matter coalescing into them.

2. Basic Concepts.

Recently, R. Friedberg, T. D. Lee and Y. Pang[3,4,5,6] proposed a new class

H. Ögelman and E. P. J. van den Heuvel (eds.), Timing Neutron Stars, 511–520.

of astronomical objects which exhibit unusual properties, called soliton stars. While ordinary stars are embedded in an ordinary vacuum we are familiar with, a soliton star is embedded in a degenerate or abnormal vacuum which resulted from a background coherent Higgs boson field. An ordinary vacuum is characterized as the lowest energy state. A free particle in an ordinary vacuum possesses a mass, which exhibit the well known inertial and gravitational properties. However, even ordinary vacuum possesses properties which may be vastly complex. For example, if the electric field energy density $E^2/8\pi$ approaches a critical value $E_c^2/8\pi = mc^2/(\hbar/m_e c)^3$, the dielectric constant of ordinary vacuum deviates from unity and exhibits a nonlinear behavior (and as $E >> E_c$, spontaneous pair creation can take place).

A coherent Higgs boson field behaves as a vacuum state that also represents a (locally) lowest energy state. This vacuum (referred to as 'abnormal' or 'degenerate' vacuum, after Lee[3]) has different properties from those of an ordinary vacuum. At present very little is known about the nature of the Higgs bosons, except that they should be massive, of spin 0, and their expectation values modify the masses of other fields. In this context a degenerate vacuum has the additional property that the masses of particles (which interact with Higgs bosons) may be modified. One may compare this property (to modify masses of particles) as a kind of 'dielectric' properties of the abnormal vacuum.

Consider a degenerate vacuum within an ordinary vacuum. According to Lee[5], the self interaction U due to the Higgs type field is:

$$U = \tfrac{1}{2} m^2\sigma^2(1 - \frac{\sigma}{\sigma_0})^2 \tag{1}$$

(Unless otherwise specified, the constants $\hbar$ and c are set to unity; restoration of $\hbar$ and c is easily accomplished by multiplying the final quantity by appropriate powers of $\hbar$ and c until the desired unit is obtained.) A surface tension is created at the boundary of the degenerate vacuum, resulting in a surface energy E_S given by:

$$E_s = 4\pi s R^2 \tag{2}$$

where s is the surface tension and is given by[3]:

$$s = \tfrac{1}{6} m\sigma_0^2 \left[= \tfrac{1}{6} mc^2 (\sigma_0/\hbar c)^2 \approx 10^{24} (m\sigma_0^2/m_p^3)\ erg\ cm^{-2}\right] \tag{3}$$

with m_p = proton mass. Without an internal pressure, this surface tension will compress the space occupied by the abnormal vacuum until a zero volume is reached. An abnormal vacuum by itself is therefore unstable. However, if there is a gas inside, an internal pressure is present and this pressure will prevent the collapse of the abnormal vacuum. Stability is achieved by the balance of the internal pressure and the surface tension. This stable configuration is represented by a local minumum of the energy surface.

Assuming a relativistic Fermi gas of total particle number N inside the abnormal vacuum, the kinetic energy E_k is obtained in the usual way as:

$$E_k = (3\pi)^{1/3}(\tfrac{3}{4} N)^{4/3}/R \tag{4}$$

An equilibrium configuration is obtained from minimizing the total energy $E = E_s + E_k$, we find:

$$E_k = 2E_s \tag{5}$$

$$E = 3E_s = 12\pi sR^2 \tag{6}$$

In terms of the total particle number N, we find:

$$E \approx s^{1/3} N^{8/9} \tag{7}$$

The mass of the system, M, is given by:

$$M = E/c^2 \tag{8}$$

Note that M is *positive*. However, the actual binding energy of the system, E_b, is the difference between the mass of the system after soliton binding and that before soliton binding. We therefore have,

$$E_b = k N^{8/9} m - Nm \tag{9}$$

where k is a number close to unity. For any reasonably large value of N, such as 10^{57} (roughly the number of particles in the sun), the first term in Eq. (9) is small compared to Nm, therefore E_b is very close to Nm. A soliton star is a very tightly bound system and the source of binding is predominantly the surface tension.

The inclusion of the gravitational energy will add a negative contribution to E. The gravitational energy E_g is:

$$E_g \approx G M^2/R$$

For large enough M, E_g will eventually dominate over the surface energy which is proportional to M and a black hole will result when the relativistic parameter $w = GM/R$ approaches $1/2$. However, a numerical evaluation[5] shows that the mass M for a soliton star black hole is of the order of 10^{14} $M_\odot$, with a radius of the order of a light year. These values are substantially greater than those for ordinary stellar objects (neutron stars). It is these large values of black hole mass and radius that makes soliton stars interesting objects, if they exist.

3. Basic Formulations.

The equations of structure of soliton stars may be obtained from the Einstein field equations, when all relevant quantities such as the energy of the Higgs Boson fields are properly included.

The Einstein field equations are:

$$\mathfrak{G}_{\mu\nu} \equiv \mathfrak{R}_{\mu\nu} - \tfrac{1}{2} g_{\mu\nu} \mathfrak{R} = 8\pi G \mathfrak{T}_{\mu\nu} \tag{10}$$

where $\mathfrak{R}_{\mu\nu}$ is the Ricci curvature tensor and $\mathfrak{R} = g^{\mu\nu}\mathfrak{R}_{\mu\nu}$ is the scalar tensor, $\mathfrak{T}_{\mu\nu}$ is the stress energy tensor, which includes the effects of the Higgs field. In a spherical coordinate system with the line element ds given by:

$$ds^2 = -e^{2u}dt^2 + e^{2v}d\rho^2 + \rho^2(d\alpha^2 + \sin^2\alpha\, d\beta^2) \tag{11}$$

where u, v are time and spatial metric, and ρ, α, β are standard polar coordinate variables, the stress energy tensors are[5]:

$$\mathfrak{T}_t{}^t = W + V - U \tag{12}$$

$$\mathfrak{T}_\rho{}^\rho = T + V - U \tag{13}$$

$$\mathfrak{T}_\alpha{}^\alpha = \mathfrak{T}_\beta{}^\beta = T - V + U \tag{14}$$

where W is the energy density of particles, T is the pressure, V and U are

field quantities associated with the Higgs bosons (V is analogous to the kinetic energy and U is analogous to the potential energy). The expressions for W and T are:

$$W = \frac{2}{8\pi^2}\int d^3p\, n_p\, \epsilon_p \tag{15}$$

$$T = \frac{2}{8\pi^2}\int d^3p\, n_p\, \epsilon_p\, \frac{p^2}{3\,\epsilon_p} \tag{16}$$

The expression for U is given in Eq. (1) and that for V is:

$$V = \tfrac{1}{2}\, e^{-2\bar{v}}\left(\frac{d\sigma}{d\rho}\right)^2 \tag{17}$$

The tensor $\mathcal{G}_{\mu\nu}$ satisfies the Bianchi identity:

$$\mathcal{G}^{\mu}{}_{\nu;\mu} = \emptyset \tag{18}$$

and the subscript $(\nu;\mu)$ denotes covariant differentiation with respect to the coordinate μ. Applying covariant differentiation to the field equation (10), we obtain the conservation law which must be satisfied by the stress energy tensor $\mathfrak{T}_{\mu\nu}$:

$$\mathfrak{T}^{\mu}{}_{\nu;\mu} = \emptyset \tag{19}$$

W and T already satisfy conservation laws like Eq.(19). The conservation law (19) when applied to U and V yields the field equations of σ:

$$e^{-2\bar{v}}\left[\frac{d^2\sigma}{d\rho^2} + \left\{\frac{2}{\rho} + \frac{du}{d\rho} - \frac{d\bar{v}}{d\rho}\right\}\frac{d\sigma}{d\rho}\right] + fS - \frac{dU}{d\sigma} = \emptyset \tag{20}$$

where f is the coupling constant between the fermion and the Higgs boson, so that the interaction between σ and the fermion (whose wave function is ψ) is $f\bar{\psi}\psi$, and S is a quantity related to T, W:

$$S = \frac{2}{8\pi^2}\int d^3p\, n_p\, \epsilon_p^{-1}\,(m - f\sigma) \tag{21}$$

Because of the form of U, a solution of Eq.(20) is

$$\sigma = \sigma_0. \tag{22}$$

Indeed, it has been shown by Lee and Pang[5] that the deviation of σ from σ_0 is extremely small. In addition, the effective mass $m^* = m - f\sigma$ is nearly zero so that the following equality:

$$m - f\sigma_0 = \emptyset \tag{23}$$

is valid to a high degree of accuracy. *This means that the mass of any fermion interacting with the Higgs boson inside a soliton star is always very close to zero.*

Using Eq.(23), the equations of structure of soliton stars become:

$$\rho^2\mathcal{G}^t{}_t = e^{-2\bar{v}} - 1 - 2e^{-2\bar{v}}\rho\frac{d\bar{v}}{d\rho} = -8\pi G\rho^2(W + V + U) \tag{24}$$

$$\rho^2\mathcal{G}^{\rho}{}_{\rho} = e^{-2\bar{v}} - 1 + 2e^{-2\bar{v}}\rho\frac{du}{d\rho} = 8\pi G\rho^2(T + V - U) \tag{25}$$

which can be solved to yield the structure of soliton stars. Details of solutions for completely degenerate fermi gas configurations at zero temperature

have been described by Lee and Pang[5].

Suffice it to say that the solutions show that soliton stars have very large mass, radius, and very large number of particles. Order of magnitude wise, the mass M, the radius R, the particle number N are:

$$M \approx \hbar^2 c^2 / G^2 m \sigma_0^2 \approx 10^{45} (30 m_p/m)(30 m_p/\sigma_0)^2 \ g \tag{26}$$

$$R \approx \hbar^2 / G m \sigma_0^2 \approx 10^{18} (30 m_p/m)(30 m_p/\sigma_0)^2 \ cm \tag{27}$$

$$N \approx (\hbar c)^{9/4} / G^{9/4} m^{3/2} \sigma_0^3 \approx 10^{76} (30 m_p/n)^{3/2} (30 m_p/\sigma_0)^3 \tag{28}$$

Note that M is of the order of 10^{11} solar masses, R is of the order of a light year, and N is two or three orders of magnitude larger than the bayron numbers of a large galaxy.

4. Origin and Early Evolution of Soliton Stars.

To summarize, soliton binding is very different from that in ordinary stars, where gravitational force is the dominant source of binding. Soliton stars are bound by the surface tension found at the interface between the degenerate vacuum and the ordinary vacuum, and the importance of gravitational force is usually secondary (unless the mass of the soliton star is very large). Therefore it is quite inconceivable that soliton stars can be formed in the gravitational collapse process. Most likely, soliton stars are created with the universe during the inflationary epoch. Prior to the inflationary epoch the universe is dominated by a degenerate vacuum state that bears a similarity to the degenerate vacuum state of the soliton stars. During the inflationary phase, the degenerate vacuum state decayed and evolved into the current universe. A theory accounting for the genesis of soliton stars in a second-order transition in the early Universe has been proposed[7], and it has been found that for a large range of parameters, non-topological solitons can be cosmologically significant, contributing a significant fraction of the present mass density of the Universe.

Independent of the origin of soliton stars, the main purpose of this work is to explore the observational consequences of soliton stars, if they exist.

Assuming the existence of soliton stars, we now explore their composition and early evolution properties. As shown by Lee and Pang[5], the mass of particles inside a soliton star would be modified by the Higgs field to be nearly zero. Now consider a hadron, such as a proton, moving from the ordinary vacuum into an the abnormal vacuum, the interior of a soliton star. Upon crossing the boundary into the abnormal vacuum, the effective mass of the proton, m_p^* becomes essentially zero. In a bound system the binding energy is proportional to the mass of the constituent particles; if the mass of the constituent particles vanishes, the binding energy will vanish and the bound state will disappear. An analogy is found in the binding of an electron in an atom: the binding energy of the K-shell electrons is roughly $\frac{1}{2}\alpha^2 m_e c^2$ where α is the fine structure constant and m_e is the electron mass. When m_e vanishes the binding energy also vanishes.

Thus a proton crossing from an ordinary vacuum into an abnormal vacuum will disintegrate into quarks (the most elementary particle known), whose effective mass is also modified by the Higgs field to become very close

to zero. The equilibrium between protons and quarks man be considered as a reversible reaction taking place across the interface:

$$p(outside) \leftrightarrow p'(inside) + \Delta E_b, \quad \Delta E_b \approx m_p c^2 \tag{29}$$

$$p' \leftrightarrow 2u + d - \Delta E_{q'}, \quad \Delta E_{q'} \approx 0, \tag{30}$$

where $\Delta E_{q'}$ is the binding energy of the proton with respect to its quark constituents *inside* a soliton star, and is very close to zero.

The equations that governs the equilibrium between a proton outside a soliton star and quarks inside are:

$$\mu_p + m_p{}^2 = 2\mu_u + \mu_d \tag{31}$$

where μ is the chemical potential for the particle specified. Defining $U_0 \equiv m_p c^2/kT$, the expression for μ for a nondegenerate gas of the particle species a is given by:

$$N_a = N_0 \exp(\mu_a/kT)\, U_0{}^{-3}\, H(U_0) \exp -U_0, \quad N_0 = (m_p c)^3/\pi^2\hbar^3 \tag{32}$$

and $H(s)$ is a function given by:

$$H(s) = \int_0^\infty t^2 \exp -\left(\sqrt{t^2+s^2} - s\right) \cdot dt \tag{33}$$

and we have:

$$H(s) \to 2, \qquad s \to 0,\ T \to \infty \qquad (relativistic)$$

$$H(s) \to \sqrt{\tfrac{\pi}{4}}\, s^{3/2}, \qquad s \to \infty,\ T \to 0 \qquad (nonrelativistic) \tag{34}$$

Eqs.(31) and (32) then yield a relation between the equilibrium compositions of p, u, and d:

$$N_p/N_d{}^3 \approx N_0{}^{-2} \exp(-U_0)\, U_0{}^{7.5} \tag{35}$$

Since the effective mass of the quarks is nearly zero, their number densities are roughly given by black body radiation law, i.e.,

$$N_u \approx 1.8\, N_0\, U_0{}^{-3} \approx 0.3\, aT^4/kT \tag{36}$$

Then we have (the superscript (e) is added here to denote equilibrium composition) :

$$N_p^{(e)} \approx N_0\, U_0{}^{-1.5} \exp -U_0 \tag{37}$$

If the actual proton number density N_p is less than the equilibrium density, $N_p^{(e)}$, then an equilibrium configuration will require all available quarks u and d to revert to protons, and vice versa.

The proton number density in our universe can be obtained from cosmological models. Despite uncertainties in cosmological models, the proton number densities N_p in our universe in relation to the temperature can be estimated to within a factor of 5 from the following equation (which is obtained from a cosmological model that yields the present densities of particles and temperature):

$$N_p \approx 10^{-7}\, T^3, \qquad T \approx 10^{10}\, t^{-1/2} \tag{38}$$

Numerically $N_p^{(e)} > N_p$ at temperatures $> T_r = 4 \cdot 10^{11}$ K. On account of the strong exponential factor of Eq.(37), this crossing temperature is rather insensitive to details of cosmological models. Note that the above treatment

applies to all particle species which are composed of quarks.

We thus conclude that the equilibrium configuration prohibits the entry of hadrons into soliton stars during early epochs when the temperature of the universe is $\gtrsim T_c$. During this stage soliton stars expands with the universe and their interior is composed of quark pairs in equilibrium with radiation. The temperature of soliton stars is essentially the same as the universe. However, at temperatures below T_c, the equilibrium configuration is reversed and protons (and other hadrons) can enter a soliton star. The rest energy of hadrons is converted into thermal energy and the temperature of the soliton star can be different from the universe. In fact, this heating can drastically increase the temperature of soliton stars. It is also conceivable that a large number of baryons in our universe could have been irreversibly locked inside soliton stars and their rest energy is almost totally converted into radiation.

5. Energetics and Radiations.

The effective mass of quarks inside soliton stars is very small. Since the effective mass appears directly in the Dirac equation[5], the 'classical electron radius' of quarks (inside soliton stars) r_q is determined by the effective mass, and could be very large. Indeed, from the mass to particle number ratio of soliton star models it may be concluded that the effective mass m^* is at least 100 times smaller than the electron mass, m_e. This causes the opacity of quark matter inside soliton stars to be very large. In normal stars a very large opacity will reduce luminosity. However, since the effective mass m^* is small, the pair creation temperature $T_p = m^* c^2/k$ is also small and at temperatures $T >> T_p$ the internal energy is chiefly in the form of quark pairs in equilibrium with radiation. The annihilation radiation from the surface within one optical depth may escape and be radiated away, independent of opacity. The energy source of the emitted radiation is contained within the photosphere. This radiation mechanism is very different from that of ordinary stars, where the energy source is in the deep interior and through radiation transfer or convection the thermal energy is brought to the surface and radiated away. This radiation mechanism makes the radiation rate of soliton stars independent of opacity. Indeed, the photosphere literally radiates itself away. As a good approximation, the surface temperature of a soliton star may be assumed to be the same as its interior.

Let T be the temperature of the soliton star, R be its radius, and M be its mass, then the luminosity L (up to the Eddington's limit) is given by:

$$L = 4\pi \sigma T^4 R^2 \tag{39}$$

Since the radiated energy comes from the mass energy of the star, the mass M decreases with time. As mass decreases, the characteristics (such as R and T) also changes with time. An evolutionary sequence can be constructed once the initial conditions are given.

6. Model Calculations.

Lee and Pang's work deals with fermion soliton stars. As discussed previously, soliton stars composed of quarks belong to this category. In realistic models, during evolution protons will enter soliton stars carrying an equal number of electrons. While the mass of the proton is modified by the Higgs field, the mass of the electrons is not modified. Indeed, electrons will become

the most massive particle inside such soliton stars. In fact, since the coupling constant between the electron and the Higgs field is zero, the equations of structure is different from Eqs. (24) and (25). Solutions of completely different character from that of Lee and Pang are obtained[6].

The solutions obtained by Lee and Pang are exactly applicable to soliton stars with an equal number of quarks and antiquarks (with a zero net quantum number) with negligible electron pairs. Their solutions are therefore applicable to soliton stars whose temperatures are less than the electron pair creation temperature ($\approx 7 \cdot 10^9$ K), so that electron pairs will not contribute much to the mass, while the temperature is not so low that the mass associated with electrons are negligible. Figures 1, 2, and 3 show respectively the time evolution of the temperature, the luminosity and the radius. In the solutions shown a scaling factor η is put to unity and the luminosity is set to the Eddington limit. Note that in this idealized model (with no net quantum number) the temperature increases with time while the luminosity decreases with time. As we discussed above, the applicability of this model is possibly limited to early evolution of soliton stars. Nevertheless, it is seen that the temperature of soliton stars is of the order of 1 keV with a luminosity corresponding to the Eddington limit.

Work is in progress to include the effects of electrons inside soliton stars[8].

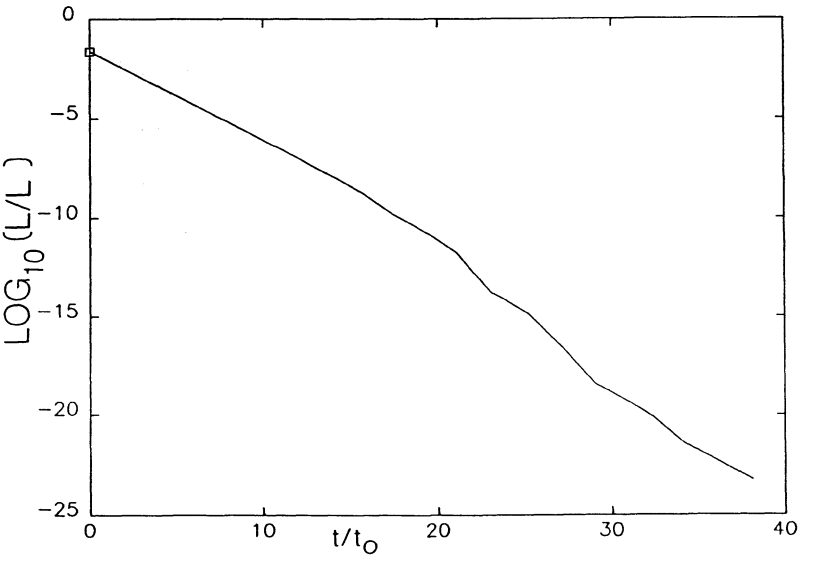

Figure 1. Evolutionary tracks of the luminosity L of soliton stars. Plotted here is $\log_{10}(L)$ vs. time t. The unit of luminosity L is roughly 10^{19} $L_\odot$ and the unit of time is approximately 10^{16} seconds.

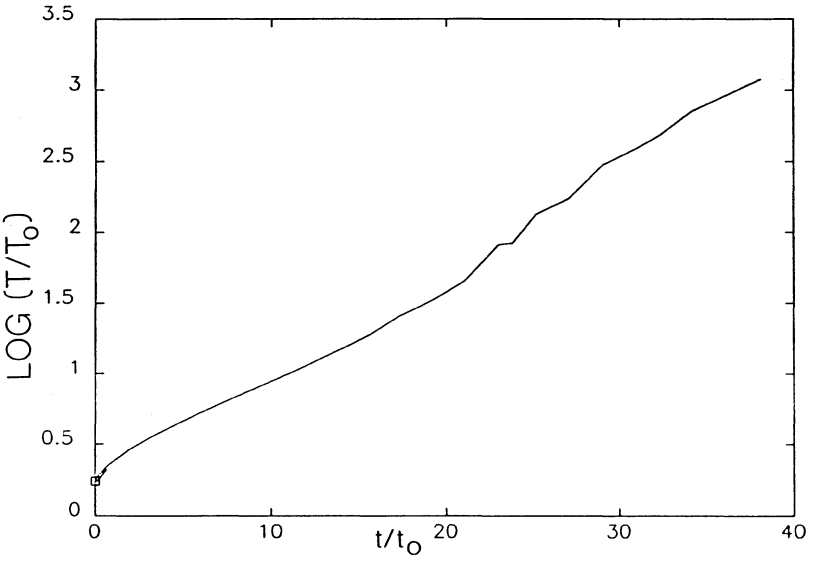

Figure 2. Evolutionary track of the surface temperature. Plotted here is $log_{10}(T/T_0)$ vs. time t, where $T_0 = 2.3 \cdot 10^6$ K and t has the same unit as in Figure 1.

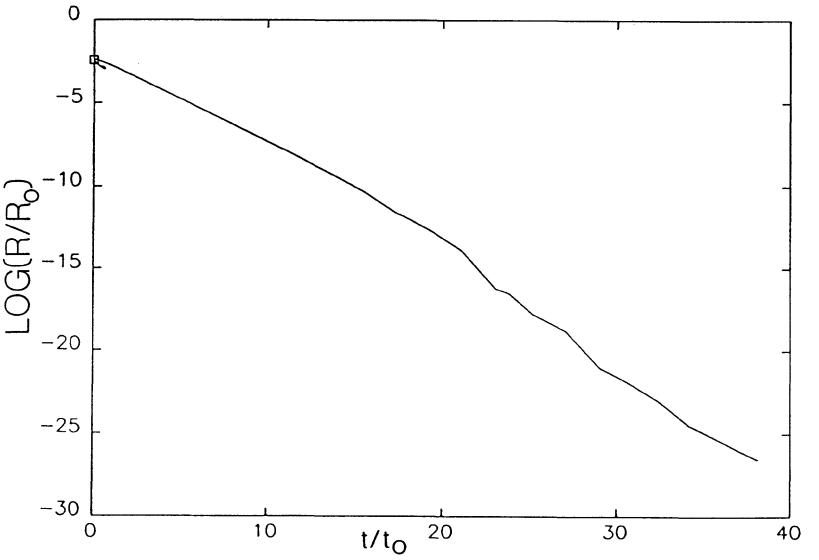

Figure 3. Evolutionary track of the radius R. Plotted here is $log_{10}(R/R_0)$ vs. time t, and $R_0 = 8 \cdot 10^{18}$ cm. t has the same unit as in Figures 1 and 2.

7. Discussions.

In this paper we discussed the possible evolution of soliton stars. The models used do not contain electrons, thus the applicability is limited. However, it seems that the life times of soliton stars as X-ray emitters are rather short, around a few times 10^9 years, thus they would be seen at large red shifts with $Z \approx 4$. It is possible that they might account for the unexplained cosmic X-ray background. Further work on the role played by electrons will be needed to make a more conclusive statement regarding the applicability of soliton stars to the explanation of the cosmic X-ray background.

8. Acknowledgements.

I would like to thank Drs. G. Hasinger and Kent Wood for interesting discussions, Dr. H. Ogelman for a very stimulating environment during this meeting, to the Laboratory for Atmospheres for the general support received, especially that of Drs. E. Maier and M. Geller.

References

1. References to this vast subject may be found elsewhere in this volume, and also in the "Cosmic Neutrinos and Gamma Rays", Ed. M. M. Shapiro and J. P. Wefel.(Reidel, Dordrecht, Holland 1988).
2. H. Y. Chiu, "Massive Quark Soliton Stars", to be published in the Astrophysical J. (1989).
3. T. D. Lee, Phys. Rev. *D 35*, 3637 (1987).
4. R. Friedberg, T. D. Lee and Y. Pang, Phys. Rev. *D 35*, 3658 (1987).
5. T. D. Lee and Y. Pang, Phys. Rev. *D 35*, 3678 (1987).
6. R. Friedberg, T. D. Lee and Y. Pang, Phys. Rev. *D 35*, 3640 (1987).
7. J. A. Frieman, G. B. Gelmini, M. Gleiser, and E. W. Kolb, "Solitogenesis: Primordial Origin of Non-Topological Solitons", to be published in Physical Review Letters (1988).
8. H. Y. Chiu, "Extended Solutions of Soliton Stars" (work in progress).

IV. BIRTH AND EVOLUTION OF NEUTRON STARS

STELLAR EVOLUTION AND THE FORMATION OF NEUTRON STARS IN BINARY SYSTEMS

E.P.J. van den Heuvel
Astronomical Institute
and Center for High-Energy Astrophysics
University of Amsterdam
The Netherlands

ABSTRACT. Mechanisms for the formation of neutron stars in binary systems are reviewed. In close binary systems, stars in the (zero-age) mass range ~ 10 to > 40 $M_\odot$ are expected to leave neutron stars as remnants. In wide binaries and for single stars the lower limit is reduced to about ~ 8 $M_\odot$. The precise value of the lower limit depends on various input parameters, especially on the treatment of convection.

Accretion-induced collapse (AIC) of a white dwarf of suitable mass and chemical composition is a second viable mechanism for the formation of neutron stars in binary systems. Evidence is summarized indicating that in the wide radio pulsar binaries and wide low-mass X-ray binaries the neutron stars may have formed by AIC.

1. INTRODUCTION

We will not extensively review here the evolution of single stars up to their final evolutionary stages, as there are many up to date reviews on the subject (e.g.: Arnett 1978 un; Woosley 1987; Trimble 1982, 1983; van den Heuvel 1987a) to which the reader is referred. Only a brief summary of the evolution of single massive stars is given, in section 2.

Section 3 is devoted to the evolution of binary systems leading to the formation of compact objects, and to the final evolution of X-ray binaries and the formation of binary pulsars. For further reading we refer to Lewin and van den Heuvel (eds. 1983), van den Heuvel and Habets (1985) and van den Heuvel (1986, 1987a,b).

2. THE EVOLUTION OF SINGLE STARS

In order to understand in which mass ranges compact stars (neutron stars or black holes) are expected to be formed, one should consider the evolution of the physical parameters of the stellar core.

Figure 1 depicts the evolutionary tracks of the central density and temperature of stars of various masses (cf. Trimble 1982). We will briefly describe the evolution of stars in the various mass ranges that are relevant for our subject.

H. Ögelman and E. P. J. van den Heuvel (eds.), Timing Neutron Stars, 523–548.

2.1. The carbon flash and carbon deflagation "Supernovae"

Only above ~ 8 $M_\odot$ carbon is ignited sufficiently close to the boundary with the non-degenerate region that the star can avoid the carbon flash.
All evidence suggests that in stars of lower mass in the carbon flash sufficient energy is generated to disrupt the entire star in a so-called carbon-deflagration supernova (Mazurek et al. 1974, 1977). The stellar material is converted into Ni^{56} which decays in 120^d to Fe^{56}. A carbon-deflagration SN may well be identified with a type I SN as both the liberated energy (~ 10^{51} ergs) and expected shape of the lightcurve fit the observations (cf. Chevalier 1981, 1985).

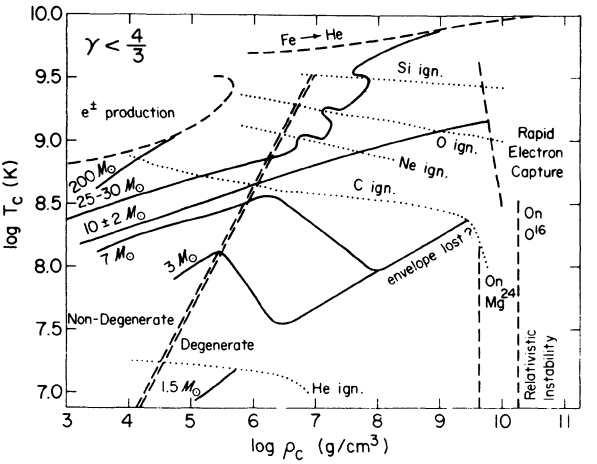

Figure 1. Stellar evolution in the central-temperature - central-density plane after Trimble (1982). Dotted lines show loci of ignition (energy liberated exceeds energy lost by neutrino production, etc.) of helium, carbon, neon, oxygen, and silicon fuels. Double dashed line separates non-degenerate from degenerate conditions. Dashed lines mark off regions of instability due to electron-position pair production and photodisintegration of iron (upper left) and electron capture and relativistic instabilities (far right). Solid lines are the (slightly simplified) evolutionary tracks for stars of 1.5, 3, 7, 8-12, 25-30, and 200 $M_\odot$. Collapse triggered by $e^\pm$ production gives way to collapse triggered by photodisintegration at about 100 $M_\odot$; photodisintegration of iron gives way to electron capture on lighter elements near 12 $M_\odot$.

2.2. Competing effects in the 3 - 8 $M_\odot$ region: mass loss; evidence from white dwarfs in clusters

When they are approaching C-ignition, stars in this mass range are on the Asymptotic Giant Branch (AGB) appearing as bright red giants (Iben and Renzini 1983). Such stars lose much mass in the form of stellar winds. White dwarfs have been found in galactic clusters that still contain stars as massive as 5 - 6 $M_\odot$ (Romanishin and Angel 1979; Koester and Reimers 1985). This indicates that stars as massive as at least 6 $M_\odot$ still terminate life as a white dwarf, i.e. are apparently able to shed their envelopes in the AGB phase before carbon violently ignites. This confines the possible mass range for carbon deflagration "supernovae" of single stars to at most 6 - 8 $M_\odot$. Possibly the peculiar Type I supernovae, which are always found in HII regions, are carbon-deflagration supernovae arising from stars in this mass range.

2.3. The fate of stars more massive than about 8 $M_\odot$

In the mass range between 8 and 10-12 $M_\odot$, C-ignition is non-violent, but the O-Ne-Mg core which is formed degenerates. Here, however, after further fuel ignition the treshold for electron-capture is expected to be crossed (see figure 1). This causes the onset of core collapse, as the removal of electrons causes the pressure of the electron-degenerate gas to drop. At time of the collapse the iron-element core is relatively small ($\sim$ 0.6 $M_\odot$, cf. Mönchmeyer and Müller, this volume).
For stars more massive than $\sim$ 10 - 12 $M_\odot$ an iron core of $M > 1.2\ M_\odot$ is formed which collapses as a consequence of the iron-helium transition (see figure 1 and Mönchmeyer and Müller, this volume).
Thus, for $M > 8\ M_\odot$, stars are expected to leave neutron stars as remnants. At masses $> 100\ M_\odot$ stars are expected to undergo an $e^\pm$ pair-production collapse, which might cause complete disruption of the star (see figure 1).

2.4. The evolution of helium stars

As the evolution of the helium core in post main-sequence stars is practically independent of the presence of a hydrogen-rich envelope, it is, for the study of the final evolution, practical to study only the evolution of this core. The results of recent studies of helium stars by Habets (1985, 1986a) are shown in figures 2 and 3. Figure 2 shows the interior evolution of a helium star of 3.2 $M_\odot$ which corresponds to a hydrogen star of about 12 $M_\odot$. The figure shows that the heavy-element core formed in the star has a mass of 2.2 $M_\odot$ and will therefore certainly collapse to a neutron star.

Figure 3 shows the evolutionary tracks for helium stars with masses 2.0 - 4.0 $M_\odot$ in the radius vs. core-mass diagram. C denotes C-ignition. The figure shows that in all helium stars with masses $> 2.2\ M_\odot$ the heavy-element core becomes larger than the Chandrasekhar mass, such that these stars are expected to leave neutron star remnants. Table 1 summarizes the above described expectations for the types of remnants from main-sequence stars of various masses.

Due to uncertainties in the effects of convection and of semi-convection (see, for example, Castellani et al. 1985) an uncertainty of about 20 per cent in the mass boundaries in table I cannot be excluded.

TABLE 1. Types of final evolutionary products expected as a function of stellar mass.

He core mass	Main-sequence mass	Final product
1.4 - 1.9 $M_\odot$	3 - 8 $M_\odot$	C-flash (disruption?) or CO-white dwarf
1.9 - 2.2 (3.0)$M_\odot$	8 - 10 (12)$M_\odot$	degenerate O-Ne-Mg core
		Ne-ignition/collapse
>2.2 (3.0) $M_\odot$	>10 (12) $M_\odot$	collapse of iron core
>60 $M_\odot$	>100 $M_\odot$	pair-creation instability (No remnant?)

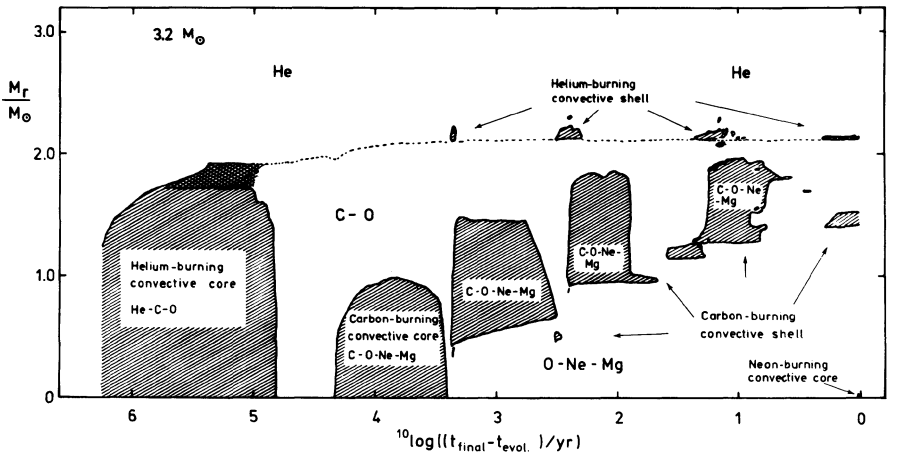

Figure 2. The interior evolution of a helium star of 3.2 $M_\odot$ up to neon ignition, as calculated by Habets (1985, 1986a). Convective regions are hatched, semi convective regions doubly hatched. The dashed and dotted lines indicate the regions of maximum energy generation in the helium burning shell and in the carbon-burning shell, respectively. These dashed and dotted lines are expected to be the boundaries of the C-O and O-Ne-Mg cores, respectively.

3. FORMATION OF NEUTRON STARS IN BINARY SYSTEMS

3.1. Introduction

Before discussing the various ways in which binary systems can evolve to produce neutron stars we briefly review in section 3.2. the observed characteristics of the various types of binary systems that contain neutron stars. In the subsequent section we review the evolution of close binary systems and the types of compact remnants that may be left at the end of the evolution.

3.2. Types of Binaries that contain Compact Stars

Three broad categories of neutron-star binaries are known, as follows.

(i) The Massive X-ray Binaries (MXBs) in which the companion of the neutron star has a mass $M_s > 8 - 10\ M_\odot$. For orbital shapes, sizes and masses, see Rappaport and Joss (1983), Joss and Rappaport (1984) and Ogelman (this volume). In most of these systems the X-ray source shows regular pulsations.

(ii) The Low Mass X-ray Binaries (LMXBs) in which the companion of the neutron star has a mass M_s typically $< 1.2\ M_\odot$ (the only exception is Her X-1 where $M_s \sim 2\ M_\odot$). Orbital periods of a number of characteristic systems are listed in table II. Only in three of these systems the X-ray source shows regular pulsations.

(iii) The eleven binary radio pulsars for which the system parameters are listed in table III. In the two systems with highly eccentric orbits, PSR 1913+16 and PSR 2303+46, the companion of the neutron star is most likely also a neutron star (cf. Srinivasan and Van den Heuvel 1982; Van den Heuvel 1984; Stokes et al. 1985). In other systems the companion is most probably a white dwarf (Van den Heuvel and Taam 1984; Van den Heuvel 1984; Kulkarni 1986).

A few peculiar binary X-ray sources such as SS 433, Cir X-1 and Cyg X-3 cannot be simply classified in the above scheme, but evidence suggests that the first two of these belong to the MXBs (see Margon 1984), and Cyg X-3 ($P = 4.8^h$) may be an LMXB. The special feature distinguishing these systems from the others is: an extremely high mass- transfer rate.

Table II. Some low-mass X-ray binaries with known orbital periods. The five systems in the last part of the table have evolved companions.

Name	P_{orb}	Name	P_{orb}	Remark
1626 – 67	42 min	2129 + 47	5.6 h	
2259 – 59	41 min(:)	1659 – 29	7.1 h	transient
1916 – 05	50 min	0620 – 00	7.8 h	transient, K-type spectrum
1323 – 62	3 h	Sco X-1	0.78 d	Radio source, opposite radio jets
1636 – 53	3.8 h	Her X-1	1.7 d	1.2s pulsar: A-type spectrum
1755 – 31	4.2 h	0921 – 63	9.0 d	F-giant
Cyg X-3	4.8h	Cyg X-2	9.8 d	F-giant
1254 – 69	4.8 h(:)	GX 1 + 4	≥ few months	118s pulsar; M6 IIIe spectrum; radio source
1822 – 37	5.3 h			

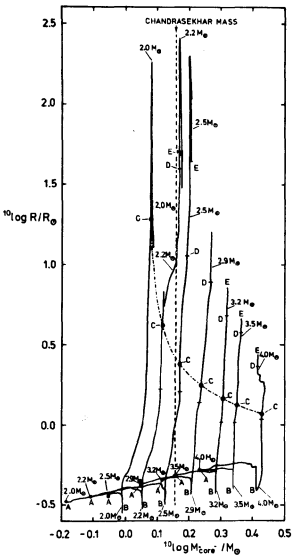

Figure 3. The core-mass vs. radius relation of helium stars in the mass range 2.0 to 4.0 $M_\odot$ undergoing C-ignition and neon ignition as calculated by Habets (1986a); the 2.9 $M_\odot$ helium star was followed till very close close to neon ignition the 2.0 $M_\odot$ helium star was only followed up to the time at which the convective carbon-burning shell reaches the centre. The open circles mark the onset of either central or off centre convective core-carbon burning (at letter C). The dash-dotted curve has been drawn through these circles. The horizontal marking between B and C indicates the point where carbon burning begins in the radiative core.

Table III. Some important properties of the eleven binary radio pulsars and the two single millisecond pulsars together with estimates of their surface magnetic field strengths and of the masses of the companions in the binary systems.

Pulsar PSR	P_p (ms)	log $(P_p/\dot{P}_p)$	log B (G)	P_{orb} (days)	e	most likely comp. mass ($M_\odot$)	glob. clust.	ref.
1937+21	1.55	16.2	8.6	single	-	-	-	1
1957+20	1.60	-	-	0.38	<0.001	0.02	-	2
1855+09	5.4	17.4	8.5	12.33	0.000021	0.2-0.4	-	1
1953+29	6.1	17.3	8.6	117.35	0.00033	0.2-0.4	-	1
1831-00	521.0	>16.7	<10.9	1.81	<0.005	0.06-0.13	-	1
0820+02	864.9	15.9	11.5	1232.40	0.0119	0.2-0.4	-	1
1913+16	59.0	15.9	10.3	0.32	0.6171	1.40	-	1
0655+64	195.6	17.5	10.0	1.03	<0.00005	0.7-1.3	-	1
2303+46	1066.4	15.4	11.3	12.34	0.6584	1.4	-	1
1821-24	3.1	15.3	9.3	single	-	-	M28	3
0021-72A	4.5	-	-	0.2	0.33	0.02	47Tuc	4
0021-72B	6.1	-	-	7-95	-	-	47Tuc	4
1620-26	11.1	-	-	191.4	0.025	0.35	M4	5
2127+12	110.7	-	-	single	-	-	M15	6

Refs.: 1. Taylor and Stinebring (1986); 2. Fruchter et al. (1988); 3. Lyne et al. (1987); 4. Ables et al. (1988); 5. Lyne et al. (1988); 6. Wolszcan et al. (1988).

3.3. Outline of the formation processes of neutron stars in binaries

The neutron stars in X-ray binaries can either have been formed by (i) the direct collapse of the nuclearly exhausted core of an (initially) massive star, or (ii) by the accretion-induced collapse of a white dwarf in an old binary (a similar collapse might also be triggered by the coalescence of two white dwarfs in a very close white dwarf binary, cf. Webbink 1980; 1984; Iben and Tutukov 1984).

The first type of evolution has taken place in the massive X-ray binaries. The reason why these systems were not disrupted by the SN explosion that formed the neutron star, is that at the moment of the explosion the star had already become the less massive component of the system, as a consequence of a preceding stage of large-scale mass transfer (Van den Heuvel and Heise 1972; Tutukov and Yungelson 1973; Van den Heuvel 1974). As was shown by Blaauw (1961), the system is disrupted only if more than half of the system mass is ejected in the explosion, which is not the case here. Figure 4 depicts, as an example, the evolutionary history of a typical B-emission X-ray binary (Habets 1985, 1986b). The various evolutionary stages are described in the figure caption. This type of close binary evolution, in which the mass transfer starts after the end of core-hydrogen burning, but before helium ignition, is called case B (in the terminology of Kippenhahn and Weigert (KW 1967), see below). Basically the formation of the massive X-ray binaries can be understood in terms of so called "conservative" models such as that depicted in figure 4, in which it is assumed that the total mass and total orbital angular momentum of the system is conserved during phases of mass transfer (i.e. between phases B and C in figure 4). We refer to reviews available in the literature (Van den Heuvel 1978, 1981, 1983). The implications of the conservative assumptions for the changes in the orbital parameters are dealt with in section 3.8.

The second neutron-star formation mechanism - by white-dwarf collapse - is expected to have taken place in a number of the low-mass X-ray binaries. This is because in the direct collapse of a nuclearly exhausted stellar core always a considerable amount of mass is ejected (see next section). Taking the effects of the impact of the SN shell onto a low-mass companion in a close system into account it turns out that it may be difficult in this case to keep a low-mass companion star bound (cf. van den Heuvel 1978, 1981). On the other hand, in the collapse of a white dwarf not more than $\sim 0.1\ M_{\odot}$ (the mass equivalent of the binding energy of the neutron star) needs to be ejected, and disruption of the system is in general not expected. We will now consider these two ways for neutron-star formation in binaries in more detail.

3.4. Types of close binary evolution

The type of remnant that is produced by close binary evolution, depends on the initial primary mass, mass ratio and orbital period. Figure 5 depicts the three main types A, B and C of close binary evolution as de fined in KW 1967, as explained in the figure caption.

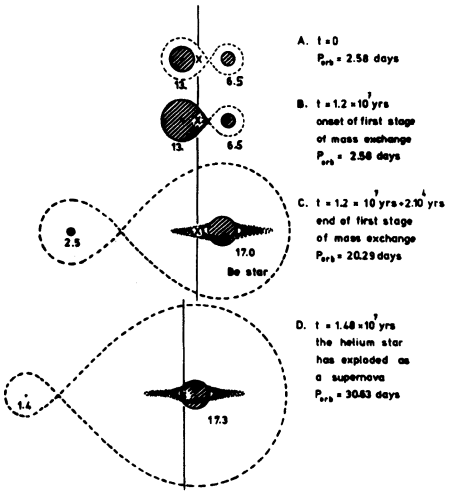

Figure 4. Conservative evolutionary scenario for the formation of a Be-X-ray binary out of a close pair of early B stars with masses of 13.0 $M_\odot$ and 6.5 $M_\odot$. The numbers indicate mass ($M_\odot$). After the end of the mass transfer the Be star presumably has a circumstellar disc or shell of matter associated with the rapid rotation (induced by the previous accretion of matter with high angular momentum; cf. Habets 1986b).

Case B and C are statistically most common among the known unevolved close spectroscopic binaries. Case A is relatively rare.
The critical orbital period which separates the cases A and B, and B and C, respectively, depends on the initial mass of the primary star M_1, and (slightly) on the initial mass ratio. Figure 6 depicts the combinations of orbital period and primary mass for which the cases A,B and C occur, for an initial mass ratio unity as derived from Iben's evolutionary tracks (partly after Webbink 1980).

In what follows we will mainly concentrate on the results of case B evolution, as this case is very common, and its results can be described in fairly simple terms. Later on we will extend the discussions also to case C.

In case B, after the first phase of mass transfer - which takes place on a thermal timescale - only the helium core of the primary star is left. Therefore, whether or not the primary star will terminate its life as a white dwarf or as a neutron star, can be discussed simply in terms of the evolution of helium stars, which has been reviewed in the foregoing section.

The correspondence between helium-core mass and initial (hydrogen-rich) primary mass can be simply expressed by analytic forms such as

$$M_{He} = 0.073 \ (M_1/M_\odot)^{1.42} \qquad (1)$$

(van Beveren 1980; for chemical composition X = 0.70, Z = 0.03).

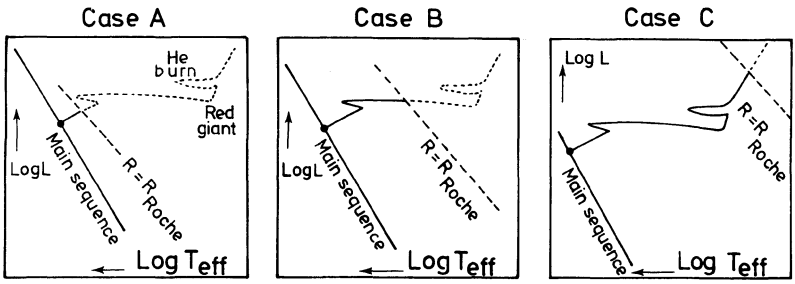

Figure 5. The three basic cases A, B and C of mass exchange in a close-binary system, as defined by Kippenhahn & Weigert (1967), illustrated on the evolutionary track of the primary star in the Hertzsprung-Russell diagram.

3.5. The evolution of helium stars, the occurrence of a second phase of mass transfer, and the lower mass limit for neutron-star formation in a binary

Figure 2 shows that after the end of core carbon burning, several episodes of carbon-shell burning occur around the growing O-Ne-Mg core. The outer radii of helium stars with $M > 3.5\ M_\odot$ never become larger than a few solar radii, before the final core collapse. Therefore, in a binary such stars will not undergo a second phase of mass transfer before they explode as a supernova.

However, for lower masses the outer radii of helium stars may become very large during the late evolutionary stages (Paczynski 1971; Arnett 1978). This can be seen in figure 3, based on the calculations by Habets (1985, 1986a). (The core mass is defined here as the mass inside the helium burning shell). The figure shows that helium stars with $M < 3.5\ M_\odot$ may, in a binary, undergo a second phase of mass transfer (so-called case BB mass transfer, cf. Delgado and Thomas 1979).

As this reduces their mass, this second mass-transfer phase may increase the lower mass limit for neutron-star formation.

Habets' calculations show that the cores of helium stars in binaries with $M_{He} > 2.2\ M_\odot$ will always collapse to neutron stars (also if still a case BB mass transfer occurs). This implies that, in a case B binary, the initial (hydrogen-rich) stellar mass for reaching collapse to a neutron star is $\sim 10\ M_\odot$. For case C and for single stars this limit is lower, since in these stars the helium-core mass can still grow considerably during the later evolutionary stages, as a consequence of hydrogen-shell burning.

3.6. Types of remnants produced, as a function of initial primary mass and orbital period

Figure 6 schematically represents the various types of remnants of primary stars of close binaries that can be produced, as a function of

initial primary mass and orbital period, as based on the results of Habets (1985, 1986a; cf. van den Heuvel 1983, Van den Heuvel and Habets 1985). At the top of the figure also the various types of remnants of single star evolution are indicated: these are practically identical to the remnants of primary stars of case C evolution, with the exception of the O-Ne-Mg white dwarfs, which (probably) do not occur for single stars. The following points can be noticed in the figure.

1. For initial primary masses > 10-12 $M_\odot$ (case B), ≥ 8-9 $M_\odot$ (Case C) or ≥ 8 $M_\odot$ (single stars), respectively, a neutron star is produced, as the mass of the helium core is > 2.2 $M_\odot$.
2. For a range in initial primary masses below these boundaries, in the cases B and C the remnants are white dwarfs consisting of O, Ne and Mg (products of carbon burning). In case B this occurs for initial primary masses approximately in the range 9 (± 1) to 12 (± 2) solar masses. For Case C: in the range ~ 8 $M_\odot$ to ~ 9 $M_\odot$. These white dwarfs are mainly the products of the later evolution of helium stars in the mass range ~ 1.9 - 2.5 $M_\odot$ which lose their envelopes in a second phase - BB or CB - of mass transfer.

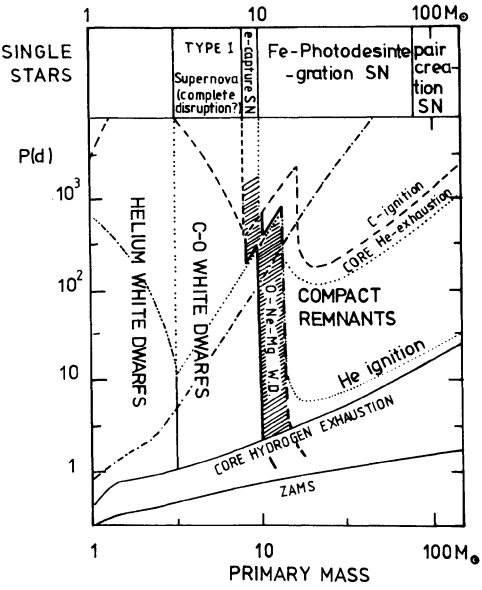

Figure 6. Classification of expected final evolutionary states of primary stars of close binaries as a function of primary mass and initial orbital period (for mass ratio 0.5 and X = 0.70). At the top of the figure the expected final evolution of single stars is indicated. In a subsequent phase of reversed mass-transfer CO white dwarfs may be triggered to explode as a type I supernova (complete disruption, see Nomoto 1982); old CO white dwarfs with a mass close to the Chandrasekhar limit, and O-Ne-Mg white dwarfs may be triggered by accretion to implode to a neutron star.

(The above mass ranges, as depicted in figure 6, are only approximate, as the precise values of the limits depend not solely on the initial primary mass and orbital period, but also on the initial mass ratio and on the convection theory used; the orbital period and mass ratio determine whether or not cases BB or CB of mass transfer will occur, which may slightly modify the precise values of the limiting masses. A full discussion of the various complicating factors is given in chapter IIIc of Habets 1985,1986ab).

The interesting point in figure 6 is especially the mass range in which the remnants are O-Ne-Mg white dwarfs. When single stars produce such cores, these are still surrounded by a helium shell and a hydrogen envelope, which leads these cores to grow to the Chandrasekhar mass and to undergo collapse, leaving a neutron star (cf. Sugimoto and Nomoto 1980; Nomoto, 1984 a,b, 1987 Hillebrandt, 1984; Hillebrandt et al. 1984, and: Müller this volume). In binaries, the mass transfer (case BB or CB) removes these envelopes, such that the cores may stay behind as O-Ne-Mg white dwarfs. In the case of reversed mass transfer in a binary these white dwarfs may be triggered by the accretion to collapse to a neutron star, as was first pointed out by Miyaji et al. (1980) and Sugimoto and Nomoto (1980).

3.7. Conditions for the occurrence of accretion-induced collapse of a white dwarf in a close binary

The reaction of a white dwarf to accretion of matter depends on a number of aspects, such as (Nomoto 1982, 1987):

(i) Composition. C-O white dwarfs will, when their masses increase, evolve to degenerate carbon ignition. This is expected to lead to a nuclear runaway in which part or all of the white dwarf is converted to Ni^{56} (see section 2.1). Under some circumstances (carbon ignition in a shell) a small white dwarf remnant may be left (Taam 1980 a,b; Nomoto 1982; Labay et al. 1983). Many authors believe that this complete or partial nuclear explosion of a C-O white dwarf is to be identified with a type I Supernova (see Chevalier, 1985).
On the other hand, when O-Ne-Mg white dwarfs grow in mass, their core density may grow to the threshold for electron capture, leading to an electron-capture collapse and formation of a neutron star (see section 2.3).

(ii),(iii) Accretion rate and Mass. The accretion rate is probably the most crucial parameter, as it determines whether or not the white dwarf will grow in mass. A full discussion of all the recent work on this subject and the uncertainties involved is given by Habets (1985, 1986a).
Briefly (though roughly) summarized: at low accretion rates ($< 10^{-9}$ $M_\odot$/yr) the thermonuclear (nova-like) flashes in the accreted hydrogen are so violent that most or all of the accreted matter is expected to be ejected. Only for relatively high

accretion rates (> 10^{-9} to 10^{-8} $M_\odot$/yr) the flashes are sufficiently weak that most of the accreted matter can be retained, such that the white dwarf will grow. If it has a suitable composition, it may then collapse to a neutron star. This is most easily achieved for O-Ne-Mg white dwarfs.

3.8. Conservative vs. non-conservative evolution. Reasons for the occurence of common-envelope evolution.

3.8.1. Introduction. So far we have only looked at the final evolutionary states of the primary star after it has lost its hydrogen-rich envelope. We did not look into what happened to the envelope matter, nor what precisely happened with the orbital period. This we will consider here.

Basically two extreme types of assumptions regarding the fate of the exchanged mass and orbital angular momentum can be made: (a) "conservative" evolution, where it is assumed that all mass lost by the one star is captured by the other and also the total orbital angular momentum is conserved, and (b) highly non-conservative evolution, in which all of the envelope mass lost by the star is ejected from the system. We will first consider the implications of the conservative assumptions, and from this derive under which circumstances these assumptions are expected to apply.

3.8.2. Conservative evolution.

(1) Changes in orbit during the mass transfer.

The assumptions of conservation of total mass

$$M_1 + M_2 = M = \text{const.} \qquad (2)$$

and total orbital angular momentum J, given by (for circular orbits):

$$J^2 = \frac{G M_1^2 M_2^2}{M_1 + M_2} a \qquad (3)$$

imply that the orbital radius a changes in the conservative case according to the relation

$$\frac{a}{a_o} = \left(\frac{M_1^o M_2^o}{M_1 M_2}\right)^2 \qquad (4)$$

where sub- and superscripts zero indicate the initial situation. Eq. (4) in combination with (2) implies that if mass is transferred from the more massive to the less massive component, the orbit shrinks whereas in the opposite case the orbit expands.
The Roche-lobe radius is given by

$$r_L/a = 0.49\, q^{2/3}/[0.6q^{2/3} + \ln\,(1+q^{1/3})] \qquad (5)$$

(Eggleton 1983), where $q = M_1/M_2$.

Figure 7 depicts how the Roche-lobe radius of the initially more massive star changes during conservative mass transfer as a function of the mass M_1 of the mass-losing star. Until a mass ratio $M_1/M_2 = 0.85$ is reached (for decreasing M_1) r_L decreases. For $M_1/M_2 < 0.85$ it increases again.

The change in orbital parameters during the mass transfer can, for example, be seen in figure 4, where the conservative mass exchange of a moderately massive close binary system is depicted (between the phases B and C).

(2) Phases in the evolution of a binary system and their timescales.
The large reduction of the Roche-lobe radius of the more massive component during mass transfer from this star to its companion, as depicted in figure 7, leads to a highly unstable situation, for the following reason.
We first consider stars with radiative envelopes. When mass is taken away from the star both its hydrostatic and thermal equilibrium are disturbed. It will immediately - on a dynamical timescale - restore its hydrostatic equilibrium. But, to restore its thermal equilibrium requires roughly a thermal timescale.
Important is here, that the thermal equilibrium radius - i.e. the radius which it reaches after its thermal equilibrium is restored - does not decrease very much when its mass M_1 decreases. This is depicted by the R_e curve in figure 7.

The figure shows that for decreasing M_1 the Roche-lobe radius r_L can only become larger again than the thermal equilibrium radius if M_1 has become considerably smaller than M_2, i.e. when the mass ratio of the system has been reversed.
Since stars with radiative envelopes at first become smaller when mass is taken away from them, but then begin to expand on a thermal timescale to restore their thermal equilibrium, the timescale of the mass transfer in systems with such primary stars is: **the thermal timescale.**
From the above we conclude that the following phases occur in the evolution of a close binary in which the envelope of the primary is in radiative equilibrium (see figure 7, after Paczynski 1970):

a. When neither of the two stars fills its Roche lobe, both stars gradually expand on an **nuclear timescale.**
b. When the primary star begins to overflow its Roche lobe, a phase of rapid mass transfer occurs, on a **thermal timescale,** leading to reversal of the mass ratio.
c. After restoration of the thermal equilibrium, the (now less massive) primary further evolves on a **nuclear timescale.** If it is a helium star, it will not even fill its Roche lobe, unless case BB mass transfer occurs. If it still has a hydrogen-rich envelope and fills its Roche lobe, its radius will gradually expand on a nuclear timescale, leading to stable mass transfer on a **nuclear timescale** since now the Roche lobe expands when the star

loses mass.
The system of figure 4, and the massive ($M_1 > 10\ M_\odot$) close binaries in general, are good examples of the conservative evolution in the above-described way. This can be seen from figure 6, where the convective boundary is indicated by the dashed line.

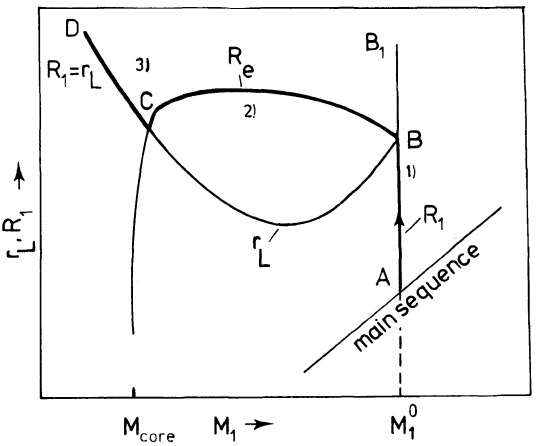

Figure 7. Variation of the thermal-equilibrium radius R_e of the primary component and the radius of its Roche lobe r_L during the mass transfer from the primary to the secondary. Only after the primary has become less massive than the secondary will r_L begin to increase. Consequently, equilibrium is not possible before the primary has lost so much matter that is has become the less massive component (after Paczynski 1970). In stages 1 and 3 the star is expanding on a nuclear timescale, in stage 2 it is transferring mass on a thermal timescale (the envelope of the primary is assumed to be in radiative equilibrium).

3.8.3. Breakdown of the conservative assumptions; the formation of a Common Envelope.

The conservative assumptions are expected to be a good approximation only if:

a. the mass ratio M_2/M_1 is not too different from unity, i.e. > 0.4 - 0.5.

b. the envelope of the mass-losing star is in radiative equilibrium.

If either of these conditions is not fulfilled one expects that the secondary star will be unable to accept most of the matter transferred to it, and will itself rapidly expand to overflow its Roche lobe. The result is that the transferred matter will form a Common Envelope (CE) around the system in which both stars are embedded.

The reasons for the formation of such a common envelope have been described extensively elsewhere and will not be given here (e.g. see Paczynski 1976; Ostriker 1976; Webbink 1980; Van den Heuvel 1976, 1981; 1983; Iben and Tutukov 1984). In the case that the companion has a

convective envelope, the reason is the highly unstable character of such an envelope. If mass is taken away from it, a convective envelope has a tendency to expand on semi-dynamical timescale (a timescale intermediate between the thermal and the dynamical timescale, cf. Paczynski and Sienkiewicz 1971).

4. COMMON-ENVELOPE EVOLUTION: THE FINAL EVOLUTION OF MASSIVE X-RAY BINARIES

4.1. Introduction

The MXBs have very small mass ratios and therefore are typical examples of systems that are bound to undergo CE-evolution. CE evolution is a very complex physical process which requires detailed 2-D or 3-D hydrodynamical calculations. Such calculations, in a somewhat simplified form, were carried out for the MXBs by Taam et al. (1978), Delgado (1980) and by Bodenheimer and Taam (1984), and for the origin of Cataclysmic Variable binaries by Meyer and Meyer-Hofmeister (1979), and Livio and Soker (1984 a,b).

The secondary star which is moving through the envelope of its companion undergoes very large frictional drag, causing its orbit to rapidly shrink. The orbital energy deposited in the envelope may be sufficient to blow off the envelope, such that a very close binary system remains, consisting of the secondary star plus the compact core of the primary. The very short orbital periods of the binary radio pulsars PSR 1913+16 and PSR 0655+64 indicate that these systems must be the result of such a type of evolution. The same holds for the Cataclysmic Variable (CV) binaries, which are expected to be the descendants of wide binaries, consisting of a red giant with a degenerate core together with a red dwarf (cf. Meyer and Meyer-Hofmeister 1979).

4.2. Simplified approach to CE evolution

We will follow here a simplified approach based on rather simple energy considerations (see, e.g., Van den Heuvel 1976; Tutukov and Yungelson 1979; Webbink 1980, 1984; Iben and Tutukov 1984).
We assume that the compact star has a mass M_1 and the massive star consists of a compact core of mass M_{2f} and an extended envelope of mass M_{2e}.

To calculate the maximum orbital period with which the system may terminate its evolution, we assume that all of the loss of orbital energy is used to expell the envelope (i.e. that the loss of orbital energy in the form of radiation is negligible). The numerical computations of Bodenheimer and Taam suggest that this is a good approximation.

The above assumptions lead to the following equation for the relation between the original and final orbital radii a_1 and a_2, respectively (cf. Webbink 1984):

$$\frac{G(M_{2f} + M_{2e})\ M_{2e}}{\lambda a_1 r_L} = \frac{G\ M_1 M_{2f}}{2a_2} - \frac{G(M_{2f} + M_{2e})\ M_1}{2\ a_1} \qquad (6)$$

where $r_L a_1$ denotes the Roche lobe radius of the primary star at the onset of the transfer and λ is a weighting factor (< 1) for the gravitational binding energy of core and envelope. Equation (6) yields

$$\frac{a_2}{a_1} = \frac{M_1\ M_{2f}}{M_{2f} + M_{2e}} \Big/ (M_1 + 2\ M_{2e}/\lambda r_L) \qquad (7)$$

With eq. (7) it is simple to calculate the fate of an X-ray binary such as, for example, Cen X-3. Assume $M_1 = 1.4\ M_\odot$, $M_{2e} = 12\ M_\odot$, $M_{2f} = 4\ M_\odot$. In this case: $r_L = 0.6$. We assume $\lambda = 0.5$ (which is a reasonable approximation since stars are rather strongly centrally condensed). With eq. (7) these values result in $a_2/a_1 = 0.0043$. With $a_1 = 17.8\ R_\odot$ (as for Cen X-3) this yields $a_2 = 0.077\ R_\odot$. This value is so small, that it is deep inside the $4\ M_\odot$ helium core of the companion of Cen X-3 (this core has a radius of $\sim 0.4\ R_\odot$).
We therefore are forced to conclude that in Cen X-3 the neutron star will spiral down completely into the center of the companion star. (The same conclusion was reached by Taam et al. (1978) from 2-D hydrodynamical calculations).

In order to avoid such a complete spiral in, $a_2 r_L$ must be $> 0.5\ R_\odot$ which implies that a_1 should have been 13.5 times larger than that of Cen X-3, implying an original orbital period > 104 days.

We thus conclude that the neutron stars in all the "standard" massive X-ray binaries, (which have orbital periods $\leq$ 42 days) will end up in the center of their companion stars.

Only for very wide systems, such as some of the B-emission X-ray binaries, such a fate can be avoided, and a binary system can remain, consisting of a helium star plus a neutron star, in a circular orbit. This may for example be the case for 4U1145-61 which has an alleged orbital period of 117^d (Bradt and McClintock 1983), and for X Persei, with $P \simeq 587^d$ days. Figure 8 depicts these two types of results from CE evolution of MXBs.

4.3. Constraints on the initial system parameters of PSR 1913+16 and PSR 2303+46

Helium stars more massive than $\sim 3.5\ M_\odot$ do not expand very much during their further evolution, and will finally explode as supernovae.
If, in such an - assumedly symmetric - explosion more than half of the system mass is ejected, the system will be disrupted, producing two runaway pulsars, as depicted in figure 8b. For a neutron star mass of 1.4 $M_\odot$ this occurs for helium star masses $> 4.2\ M_\odot$.

In PSR 1913+16 and PSR 2303+46 the mass of the helium star must thus have been less than $4.2\ M_\odot$, and assuming a spherically symmetric explosion, it is simple, from the presently observed orbital eccentricities of these systems, to calculate the mass of the helium star progenitor of the last-formed neutron star in the system (van den Heuvel 1987a).

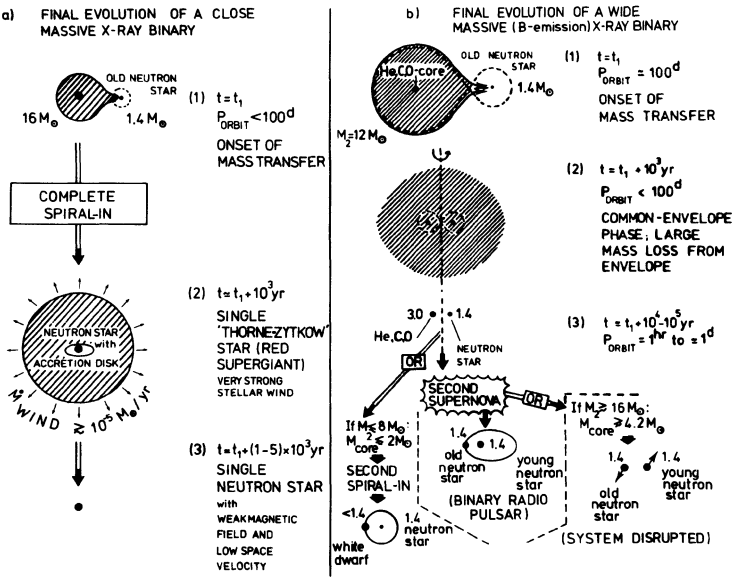

Figure 8. Final evolution of massive X-ray binaries. a. Short-period systems ($P_{orb} < 100^d$) are expected to evolve towards coalescence during the second phase of mass transfer, leading to a so-called 'Thorne-Zytkow' star, a red supergiant with an accreting neutron star in its center. Due to its very large wind mass loss, this star loses its entire mantle within a few million years, leaving a single old neutron star with a low space velocity (the velocity of the original MXB). b. Wide systems ($P > 100^d$) leave very close binaries consisting of the old neutron star plus the core of the companion (Cygnus X-3 may be an example). If M_2 was $< 8\ M_\odot$, no second SN will occur and a close binary radio pulsar with a white dwarf companion in a circular orbit remains. PSR 0655+64 may have formed in this way. If $8 < M_2/M_\odot < 16$, the core explodes as a supernova but has a mass $< 4.2\ M_\odot$ such that a bound binary radio pulsar with an eccentric orbit will remain, consisting of two neutron stars. PSR 1913+16 and PSR 2303+46 must have formed in this way. If $M_2 > 16\ M_\odot$, the core mass is so large that the system is disrupted in the second supernova and two runaway pulsars are formed. (If their orbital period is < 12 hours, systems such as PSR 0655+64 will evolve towards coalescence leading to the formation of a single rapidly rotating pulsar with a low space velocity. This is one possible way to form a single msec pulsar, cf. Bonsema and van den Heuvel 1985; see however, also section 5).

As a result one finds for PSR 1913+16 a mass of the exploding helium star of $M_1^o = 3.16\ M_\odot$, and an orbital period at the time of the explosion of $P_o = 1.45^{hr}$ ($a_o = 1.08\ R_\odot$). For PSR 2303+46 these values

become $M_1^o = 3.29\ M_\odot$ and $P_o = 1.92$ days ($a_o = 10.9\ R_\odot$).
If we assume these M_1^o values to correspond to helium core masses, the progenitors of both stars must have had masses $\sim 12\ M_\odot$.
Adopting this mass and applying eq. (7) with $\lambda = 0.5$ we find $a_1/a_2 = 161.4$ for PSR 1913+16 and $a_1/a_2 = 152.8$ for PSR 2303+46, yielding original orbital separations and periods for these systems of $a_1 = 0.81$ AU, P = 72.3 days for the progenitor of PSR 1913+16 and $a_1 = 7.71$ AU, P = 5.84 yr for the progenitor of PSR 2303+46.

The progenitor of PSR 1913+16 closely resembles one of the wider B-e X-ray binaries, such as 4U1145-61. The progenitor of PSR 2303+46 must have been a system resembling the ζ Aurigae and VV Cephei binaries.

4.4. The progenitor of PSR 0655+64

Like PSR 1913+16 and PSR 1953+29 this pulsar combines a very short pulse period with a relatively weak magnetic field, which strongly suggests that it is "recycled" pulsar, i.e.: that it has been spun up by accretion of matter from its companion (see Van den Heuvel 1984, and Taylor, this volume, for details). The perfect circularity of the orbit indicates that no second supernova explosion took place, and indeed the conpanion has been found to be a white dwarf (Kulkarni 1986).

The evolution of this systems must thus have been very similar to that of PSR 1913+16 and PSR 2303+46, the only difference being that its companion had a lower mass, i.e. below $\sim 8\ M_\odot$.

Figure 8b (left-hand part, after Van den Heuvel and Taam 1984) depicts the evolutionary history of this system.
Assuming a present neutron star mass of $1.4\ M_\odot$, a present companion mass M_{2f} of $0.8\ M_\odot$ and an original companion mass of $5\ M_\odot$, one obtains with eq. (7) an original orbital period and separation of 2.50 yr and 3.43 AU, respectively.

Like the progenitor of PSR 2303+46 this system again shows a close resemblance to the ζ Aurigae binaries.

5. LOW-MASS X-RAY BINARIES

5.1. Mechanisms driving the mass transfer

As the winds from low-mass stars are never very strong (except perhaps when the stars reach the asymptotic red giant branch) in general mass transfer by Roche-lobe overflow is required to power these strong sources.
As the companion is less massive than the neutron star, the mass transfer will be stable as it leads to an increase in orbital separation. (The only exception is Her X-1, where the companion has $M \sim 2\ M_\odot$; here beginning atmospheric Roche-lobe overflow can power the source for several million years before it reaches the Eddington limit, cf. Savonije 1983a).
There are two mechanisms by which Roche-lobe overflow in low-mass systems can be driven (cf. Savonije 1983a):

(i) Angular-momentum losses by gravitational radiation (possibly supplemented by "magnetic braking" (cf. Verbunt and Zwaan 1981)). These losses cause the orbit and the Roche-lobe to gradually shrink, thus inducing the companion to transfer matter.
As the characteristic timescale for orbital decay by gravitational radiation (GR) losses is given by (cf. Savonije 1983a):

$$t_{GR} = \frac{(M_1 + M_2)^{1/3}}{2^{1/3} M_1 M_2} (P/1.6^h)^{8/3} \quad 4.10^7 \text{ yr} \qquad (8)$$

this mechanism will only be of importance in systems with $P_{orb} \leq 10^h$, since only in such systems t_{GR} is smaller than the Hubble time (for $M_1 \simeq M_2 \simeq = 1$, in solar units).
Table II shows that most of the known low-mass systems belong to this category.
The most extensive analysis of the combined effects of GR losses and magnetic braking for the driving of the mass transfer in low-mass systems was given by Rappaport et al. (1983). As an example figure 9 shows the mass transfer rate and the variations of the orbital parameters with time for a system with an initial companion of 1 $M_\odot$, and magnetic braking according to the Verbunt and Zwaan (1981) formulation (cf. Savonije 1983a):

$$dJ_1/dt = - k^2 M_1 R_1^4 (0.5 f^{-2} \quad 10^{-28}) \omega_1^3 \qquad (9)$$

where M_1, R_1, ω_1 denote the mass, radius and rotational (= orbital) angular velocity of the companion, and k its radius of gyration. The constant f has to be determined from observations and is about 1.7.
The M-profile as a function of time in Figure 9 is characteristic for systems in which these angular momentum losses drive the mass transfer. One observes from the figure that although mass loss rates $\geq 0.5 \times 10^{-8}$ $M_\odot$/yr can be reached for a short interval of time ($\leq 2.10^7$ yrs), during most of the time ($\sim 10^9$ yrs) the system has $\dot{M}$ in the range 10^{-10} to 10^{-9} $M_\odot$/yr. It should be noticed that although GR losses are not important for $P \geq 10^h$, magnetic braking may still be important for orbital periods up to about 2-4 days. This does require, however, the low-mass companion to have a radius close to that of its Roche-lobe, implying that it must be an evolved star.

(ii) Internal nuclear evolution of the companion star is the only mechanism that can drive the mass transfer in low-mass systems with $P_{orb} > 0^d.5$ (since unevolved stars with $M < 1.4$ $M_\odot$ cannot overflow their Roche-lobes in such systems). As mentioned in section 3.2, in systems such as Cyg X-2 ($P_{orb} = 9^d.8$), 2S 0921-63 ($P_{orb} = 9^d.0$), and even in Sco X-1 ($P_{orb} = 0^d.78$) the companion stars are evolved low-mass stars.

The evolution of binaries in which the mass-losing star is a low-mass (sub-) giant star was studied by Webbink et al. (1983) and Taam (1983). The luminosity in these low-mass ($M \sim M_\odot$) giants

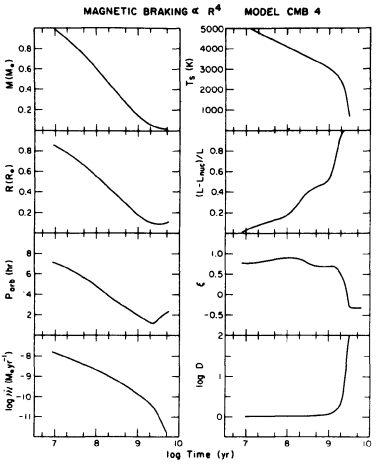

Figure 9. Evolution of close binary with angular momentum losses by gravitational radiation and magnetic braking as calculated by Rappaport et al. (1983). The initial system consisted of a 1 $M_\odot$ main-sequence star and a 1.2 $M_\odot$ compact star with an orbital period of 7.2 hours. Magnetic braking was treated according to the formulation of Verbunt and Zwaan (1981). Plotted are: the evolution with time of the stellar mass, radius, mass-transfer rate, orbital period, as well as some other parameters characterizing the system (C Astrophysical Journal).

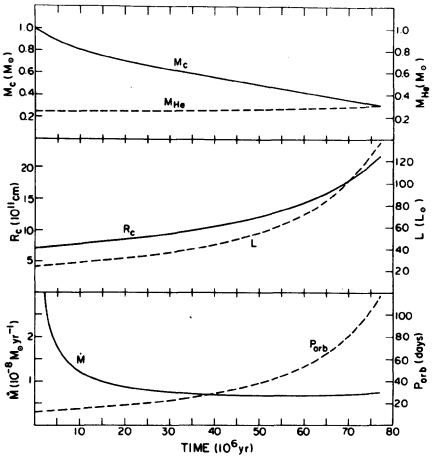

Figure 10. Evolution of a binary with a lower giant-branch secondary component of initial mass 1.0 $M_\odot$ and surface composition X = 0.70, Z = 0.02, as calculated by Joss & Rappaport (1983). Plots as functions of time: upper, total mass (M_c) and core mass of the secondary; middle, radius and intrinsic bolometric luminosity of the secondary; lower, mass accretion rate M onto the neutron star. Mass of the neutron star was taken to be 1.3 $M_\odot$. (C Nature).

is generated in a hydrogen-burning shell which surrounds the degenerate helium core of low mass ($M_{He} \simeq 0.2 - 0.4\ M_\odot$). During the evolution the core mass of the giant grows, and its radius and luminosity gradually increase. It is this increase in radius which, in a binary system, drives the mass transfer. During this transfer the orbit gradually widens, such that at any time the stellar radius just equals the Roche-lobe radius.

Figure 10 represents, as an example, the evolution of a binary with an initial orbital period $P_o = 12.5^d$, an initial mass of the giant of 1 $M_\odot$ and of the neutron star of 1.3 $M_\odot$, calculated by Joss and Rappaport (1983). (Such a system will resemble Cyg X-2 and 2S 0921-63). The figure shows that after a brief initial episode with a mass transfer rate of several times the Eddington limit ($\dot{M}_{Edd} \sim 2.10^{-8}\ M_\odot$/yr) the mass transfer rate settles at a value of $\sim 10^{-8}\ M_\odot$/yr for an interval of about 60 million years. During this time the orbital period gradually increases to $\sim 120^d$. In the end only the helium core remains, as a 0.31 $M_\odot$ helium white dwarf (while at the onset of the mass transfer, M_{He} was 0.24 $M_\odot$). It turns out that for systems of this type the average mass transfer rate depends (for a companion mass $M_\odot$, Z = 0.02), in first approximation only on the initial orbital period, roughly as:

$$\langle \dot{M} \rangle = - 6 \times 10^{-10}\ (P/\text{day})\ M_\odot/\text{yr}. \qquad (10)$$

(for other companion masses and chemical composition the relation becomes slightly different, cf. Webbink et al. 1983).
The evolutionary calculations by Webbink et al. (1983) are applicable only if the initial orbits are relatively wide (P > 2 days). For shorter initial periods, in the range 0.5 to 2 days, the transfer of mass is driven by a combination of magnetic braking and interior nuclear evolution of the companion. Systems like Sco X-1 and several cataclysmic variables fall in this category. Detailed numerical calculations of the evolution of such systems, and of the resulting mass-transfer rates, were carried out by Pylyser and Savonije (1988 a,b). These show that there are two groups of systems: if the initial orbital period is below a certain critical value, the system will evolve to shorter orbital periods (so-called "converging" systems); if it is larger than this critical value, the orbital period will gradually increase ("diverging" systems). The mass transfer rates in these systems tend to be relatively high (10^{-9} to $10^{-8}\ M_\odot$) and do not strongly change in time.

5.2. The nature of the strong sources in the galactic bulge: neutron stars with a low-mass sub-giant companion

There are about 8 strong X-ray sources ($L_x \sim 10^{38}$ ergs/s) in the galactic bulge (together with a few dozen weaker sources, $L_x \sim 10^{36} - 10^{37}$ ergs/s). Similarly, in the bulge of M31 there are a few dozen very strong ($L_x \sim 10^{38}$ ergs/s) sources. The mass transfer rates in these systems are typically of order $10^{-8}\ M_\odot$/yr. The only viable model for

these old-population sources is that of a binary system in which the companion star is an evolved low-mass star ("giant"), for the following reason (as argued by Webbink et al. 1983). If the systems were binaries in which the mass transfer is driven by gravitational radiation losses and/or magnetic braking alone, the systems would, according to figure 9, spend some 50 times longer at accretion rates between 10^{-10} and 10^{-9} $M_\odot$/yr than at rates between (0.5 - 2) x 10^{-8} $M_\odot$/yr. Consequently, in a steady state one would expect in the bulge of the galaxy some 400 sources with X-ray luminosities between 10^{36} and 10^{37} ergs/s, whereas only a few dozens of such systems are observed. Hence, gravitational radiation (in combination with magnetic braking) predicts an $\dot{M}$ -profile as a function of time which disagrees with the observations.

On the other hand, as figure 10 shows, mass transfer from a low-mass sub-giant companion yields a steady high (10^{-8} $M_\odot$/yr) mass transfer rate for the entire system lifetime. Therefore, it does not predict a large population of weaker sources. This is a very strong argument in favour of the low-mass sub-giant model for the bulge sources. Thus, one expects the strong bulge sources to be systems typically resembling Sco X-1, Cygnus X-2 and 2S0921-63.

5.3. Relation between the wide binary radio pulsars with low-mass companions and X-ray binaries with a low-mass giant component; evidence for accretion-induced collapse of old white dwarfs

The orbital characteristics and companion masses of the wide radio pulsar binaries PSR 0820+02, PSR 1953+29, PSR 1855+09 and PSR 1620+26 (see table III) very closely resemble those of systems that result from the evolution of wide low-mass X-ray binaries considered in the foregoing section, as depicted in figure 10. This was noticed by Joss and Rappaport (1983), Savonije (1983b) and Paczynski (1983).

One paradoxical thing with PSR 0820+02 is, however, that its neutron star must be younger than $\sim 10^7 - 10^8$ yrs (since surface magnetic fields of neutron stars decay on a timescale of $< (5 - 10) \times 10^7$ yrs (Lyne 1981; Lyne et al. 1985)), whereas this system itself must be older than 5.10^9 yrs. The latter follows from the fact that the low-mass companion, which must have started out with $M_s < 1.2\ M_\odot$, has already terminated its evolution and has become a helium white dwarf of 0.2 - 0.4 $M_\odot$ (see table III). For stars with $M < 1.2\ M_\odot$, this requires over 5.10^9 yrs. Thus: we have an old binary that contains a young neutron star.

The only way out of this paradox is that the neutron star in this system was formed recently - during the mass-transfer process itself - by the accretion-induced collapse of a white dwarf (Helfand et al. 1983; Van den Heuvel and Taam 1984; Van den Heuvel 1984). (We thus imply that at the onset of the mass transfer it still was a white dwarf). As the mass transfer in this system lasted less than $\sim 10^7$ yrs (see eq. 10)) the neutron star can indeed have formed quite recently and thus still have retained some magnetic field. Since this seems the only possible way out of the above-mentioned paradox, the existence of the PSR 0820+02 system provides strong observational evidence in support of the possibility that neutron stars can be formed in an old stellar population by the

accretion-induced collapse of a white dwarf (as suggested first by Whelan and Iben 1973). [That the mass transfer in this system indeed has terminated only very recently ($< 10^7$ yrs ago) follows from Kulkarni's (1986) discovery of its optical counterpart which is a very hot white dwarf with a cooling age $< 10^7$ yrs.]
Moreover, just these wide systems provide particularly favourable conditions for such a collapse, since, as mentioned in section 3.7, at their accretion rates of $\sim 10^{-8}$ $M_\odot$/yr, the hydrogen accreted by the white dwarfs will burn steadily or in weak flashes, which are unable to cause considerable mass ejection. (For further arguments: see Van den Heuvel and Taam 1984; Van den Heuvel 1984).

Precisely the same arguments as for this system hold for the pulsating wide low-mass X-ray binary GX 1+4. In GX 1+4 the companion still is a low-mass red giant, which also must have an age $> 5.10^9$ yrs. On the other hand its neutron star still has a very strong magnetic field, in the range 10^{12} to 10^{14} Gauss (Makishima et al., 1988). This system is an excellent progenitor for systems like the two wide radio-pulsar binaries (Van den Heuvel 1981; Joss and Rappaport 1983).

For the precise evolutionary history of the other binary radio pulsars with low-mass companions and of the single and binary puslars in globular clusters we refer the reader to Pylyser and Savonije (1988 ab), and Verbunt (this volume). As to the formation of single millisecond pulsars: apart from the possibility mentioned in section 4.3, and from exchange collisions in globular clusters, an exciting and viable possibility is that of "evaporation" of the companion by the large energy flux of the millisecond pulsar itself, which will start as soon as the mass transfer in the System becomes interrupted. In the eclipsing system PSR 1957+20 this evaporation appears to be taking place at present (Fruchter et al. 1988, and this volume). Theoretical models for this "evaporation" were worked out by Ruderman et al. (1988); Kluzniak et al. (1988) Phinney et al. (1988) and van den Heuvel and van Paradijs (1988).

As to the precise evolution of binary radio pulsars and their magnetic fields we refer to earlier reviews (van den Heuvel 1984, 1987b, Taam and van den Heuvel 1986, Van den Heuvel et al. (1986), and to van Paradijs (this volume).

REFERENCES

Ables, J.G., Jacks, C.E., McConnell, D., Hamilton, P.A., McCulloch, P.M. and Hall, P.J. 1988, IAU Circ. Nr. 4602.
Arnett, W.D. 1978, in Physics and Astrophysics of Neutron Stars and Black Holes (R. Giacconi and R. Ruffini, eds.), North-Holland Publ. Co., Amsterdam, pp. 356-436.
Blaauw, A. 1961, Bull. Astron. Inst. Netherlands **15**, 265-290.
Bodenheimer, P. and Taam, R.E. 1984, Astroph. J., **280**, 771.
Bonsema, P.F.A. and Van den Heuvel, E.P.J. 1985, Astron. Astrophys., **46**, L3.
Bradt, H.V.D. and McClintock, J.E. 1983, Ann. Rev. Astron. Astrophys. **21**, 13.
Castellani, V., Chieffi, A., Pulone, L. and Tornambe, A. 1985, Astrophys. J. **294**, L31.
Chevalier, R. 1981, Fundamentals of Cosmic Physics, **7**, 1-58.
Chevalier, R. 1985, in: Supernovae, their progenitors and remnants (G. Srinivasan and V. Radhakrishnan, eds.) Indian Acad. Sci., Bangalore, pp. 65-73.
Delgado, A.J., 1980 Astron. Astrophys. **87**, 343.
Delgado, A.J. and Thomas, H.-C. 1981, Astron. Ap. **96**, 142-145.
Eggleton, P.P. 1983, Astrophys. J. **268**, 368.
Fruchter, A.S., Stinebring, D.R. and Taylor, J.H. 1988, Nature **333**, 237.
Habets, G.M.H.J. 1985, Ph.D. Thesis, University of Amsterdam.
Habets, G.M.H.J., 1986a, Astron. Astrophys. **167**, 61.
Habets, G.M.H.J., 1986b, Astron. Astrophys. **165**, 95.
Helfand, D.J., Ruderman, M.A. and Shaham, J. 1983, Nature **304**, 423.
Hillebrandt, W., 1984, Ann. N.Y. Acad. Sci. **422**, 197.
Hillebrandt, W., Nomoto, K. and Wolff, R.G., 1984, Astron. Astrophys. **133**, 175.
Iben, I. and Renzini, A. 1984, Ann. Rev. Astron. Astrophys. **21**, 271-342.
Iben, I. and Tutukov, A.V. 1984, Astrophys. J. Suppl. Ser. **54**, 335-372.
Joss, P.C. and Rappaport, S.A. 1983, Nature **304**, 419-421.
Joss, P.C. and Rappaport, S.A.: 1984, Ann. Rev. Astron. Astrophys. **22**, 537-592.
Kippenhahn, R. and Weigert, A. 1967, Zeitschr. f. Astrophys. **65**, 251.
Kluzniak, W., Ruderman, M., Shaham, J. and Tavani, M. 1988, Nature (submitted).
Koester, D. and Reimers, D. 1985, Astron. Astrophys. **153**, 260.
Kulkarni, S.R., S. 1986, Astrophys. J. **306**, L85.
Labay, J., Canal, R. and Isern, J. 1983, Astron. Ap. **117**, L1-4.
Lewin, W.H.G. and Van den Heuvel, E.P.J. (eds.), 1983, Accretion-Driven Stellar X-ray Sources, Cambridge University Press.
Livio, M. and Soker, N., 1984a, Mon. N. Roy. Astr. Soc. **208**, 763.
Livio, M. and Soker, N., 1984b, Mon. N. Roy. Astr. Soc. **208**, 783.
Lyne, A.G. 1981, in IAU Symp. nr. 95 "Pulsars", eds. W. Sieber and R. Wielebinski, D. Reidel, Dordrecht, p. 423.
Lyne, A.G., Manchester, R.N., Taylor, J.H. 1985, Mon. Not. Roy. Astron. Soc. **213**, 613.
Makishima, K., Ohashi, T., Sakao, T., Dotani, T., Inoue, H., Koyama, K., Makino, F., Mitsuda, K., Nagase, F., Thomas, H.D., Turner, M.J.L.,

Kii, T., and Tawara, Y. 1988, Nature **333**, 746.
Margon, B. 1984, Ann. Rev. Astron. Astrophys. **22**, 507-536.
Mazurek, T.J., Meier, D.L. and Cameron, A.G.W. 1974. Astrophys. Sp. Sc. **27**, 261.
Mazurek, T.J., Meier, D.L. and Wheeler, J.C. 1977, Astrophys. J. **213**, 518.
Meijer, F. and Meijer-Hofmeister, E. 1979, Astron. Astrophys. **78**, 167.
Miyayi, S., Nomoto, K., Yokoi, K. and Sugimoto, D. 1980, Publ. Astron. Soc. Japan **32**, 303-329.
Nomoto, K. 1982, Astrophys. J. **253**, 798.
Nomoto, K. 1984a, Astrophys. J. **277**, 791.
Nomoto, K. 1984b, in: "Collapse and Numerical Relativity" IAU Toulouse; Reidel, Dordrecht.
Nomoto, K., 1987, in: The Origin and Evolution of Neutron Stars (eds. D.J. Helfand and J.- Huang), Reidel Publ. Co. Dordrecht, P. 281.
Ostriker, J.P. 1976, (private conversation).
Paczynski, B. 1970, in: Mass Loss and Evolution of Close Binaries (K. Gyldenkerne and R. West, eds.), Kopenhagen Univ. Publ. Funds, p. 142.
Paczynski, B. 1971, Acta Astron. **21**, 1-14.
Paczynski, B. 1976, in: Structure and Evolution of Close Binaries (P.P. Eggleton, S. Mitton and J. Whelan, eds.). Reidel, Dordrecht, p. 423.
Paczynski, B. 1983, Nature **304**, 421.
Paczynski, B. and Sienkiewicz, R. 1971, Acta Astr. **21**, 73.
Phinney, E.S., Evans, C.R., Blandford, R.D., Kulkarni, S.R., 1988, Nature (in the press).
Pylyser, E. and Savonije, G.J. 1988a, Astron. Astrophys. (in the press).
Pylyser, E. and Savonije, G.J. 1988b, Astron. Astrophys. (in the press).
Rappaport, S.A. and Joss, P.C. 1983, in: Accretion Driven Stellar X-ray Sources (W. Lewin and E.P.J. van den Heuvel, eds.), Reidel, Dordrecht, pp. 1-39.
Rappaport, S.A., Verbunt, F. and Joss, P.C. 1983, Astrophys. J. **275**, 713.
Romanishin, W. and Angel, J.R.P. 1980, **235**, 992.
Ruderman, M., Shaham, J. and Tavani, M., 1988a, Astrophys. J. (in the press).
Savonije, G.J. 1983a, in: "Accretion-Driven Stellar X-ray Sources", (W.H.G. Lewin and E.P.J. van den Heuvel, eds.), Cambridge University Press, p. 343.
Savonije, G.J. 1983b, Nature **304**, 422-423.
Srinivasan, G. and van den Heuvel, E.P.J. 1987, Astron. Astrophys. **108**, 143.
Stokes, G.H., Taylor, J.H. and Dewey, R.J. 1985, Astrophys. J. **294**, L21.
Sugimoto, D. and Nomoto, K. 1980, Space Science Reviews **25**, 155.
Taam, R.E. 1980a, Astrophys. J. **237**, 142.
Taam, R.E. 1980b, Astrophys. J. **242**, 749.
Taam, R.E. 1983, Astroph. J. **270**, 694.
Taam, R.E., Bodenheimer, P. and Ostriker, J.P. 1978, Astrophys. J. **222**, 269.
Taam, R.E. and Van den Heuvel, E.P.J. 1986, Astroph. J. **305**, 235.
Taylor and Stinebring, 1986, Ann. Rev. Astron. Astrophys. **24**, 285.

Trimble, V. 1982, Reviews of Mod. Phys., **54**, 1183-1224.
Trimble, V. 1983, Reviews of Mod. Phys., **55**, 511.
Tutukov, A.V. and Yungelson, L.R. 1973, Nautsnie Inform. **27**, 58.
Tutukov, A.V. and Yungelson, L.R. 1979, in: Mass Loss and Evolution of O-type Stars (P.S. Conti and C. De Loore, eds.). Reidel, Dordrecht, 401-407.
Van Beveren, D. 1980, Ph.D. Thesis, Free University of Brussels.
Van den Heuvel, E.P.J. 1974, Proc. 16th Solvay Conf. on Physics, Univ. of Brussels Press, p. 119.
Van den Heuvel, E.P.J., 1976, in: Structure and Evolution of Close Binary Systems, (Eggleton et al., eds) Reidel, Dordrecht, pp. 35-61.
Van den Heuvel, E.P.J. 1978, in: Physics and Astrophysics of Neutron Stars and Black Holes (eds. R. Giacconi and R. Ruffini), North Holl. Publ. Co. Amsterdam, p. 828-871.
Van den Heuvel, E.P.J. 1981, in: "Pulsars", W. Sieber and R. Wielebinski (eds.), Reidel, Dordrecht, p. 379.
Van den Heuvel. E.P.J. 1983, in "Accretion-Driven Stellar X-ray Sources" (W.H.G. Lewin and E.P.J. van den Heuvel, eds.), Cambridge University Press, p. 303.
Van den Heuvel, E.P.J. 1984, J. Astroph. Astron. **5**, 209.
Van den Heuvel, E.P.J., 1986, in: Evolution of Galactic X-ray Binaries (W. Brinkmann, W.H.G. Lewin and J. Truemper, eds.), Reidel, Dordrecht.
Van den Heuvel, E.P.J. 1987a, in: High-Energy Phenomena around Collapsed Stars (ed. F. Pacini), Reidel Publ. Comp. Dordrecht, p. 1.
Van den Heuvel, E.P.J. 1987b, in: The Origin and Evolution of Neutron Stars (eds.: D.J. Helfand and J.-H. Huang), Reidel Publ. Comp. Dordrecht, p. 393.
Van den Heuvel, E.P.J. and Habets, G.J. 1985, in: Supernovae, their Progenitors and Remnants (G. Srinivasan and V. Radhakrishnan, eds.), Indian Acad. Sci., Bangalore, 129-154.
Van den Heuvel, E.P.J. and Heise, J. 1972, Nature Phys. Sci. **239**, 67.
Van den Heuvel, E.P.J. and Taam, R.E. 1984, Nature **309**, 235-237.
Van den Heuvel, E.P.J., van Paradijs, J.A. and Taam, R.E. 1986, Nature **322**, 153.
Van den Heuvel, E.P.J. and van Paradijs, J.A. 1988, Nature (in the press).
Verbunt, F. and Zwaan, C. 1981, Astron. Ap. **100**, L7-9.
Webbink, R.F., 1980, IAU Coll. **53**, Univ. of Rochester, p. 426.
Webbink, R.F. 1984, Astroph. J. **277**, 355.
Webbink, R.F., Rappaport, S. and Savonije, G.J. 1983, Astroph. J. **270**, 678.
Whelan, J. and Iben, I.Jr. 1973, Astroph. J. **186**, 1007-1014.
Wolszczan, A., Middleditch, J., Kulkarni, S.R. and Fruchter, A.S. 1988, IAU Circ. nr. 4552.
Woosley, S.E. 1987, in: Nucleosynthesis and Chemical Evolution, 1986 Saas-Fee course (eds. J. Andouze, C. Chiosi and S.E. Woosley), Geneva Observatory Publ.
Woosley, S.E. and Weaver, T.A. 1986, Ann. Rev. Astron. Astrophys. **24**, 205.

Core Collapse With Rotation And Neutron Star Formation

Ralph Mönchmeyer and Ewald Müller
Max-Planck-Institut für Physik und Astrophysik
Institut für Physik
Karl-Schwarzschild-Straße 1
D-8046 Garching b. München, FRG

ABSTRACT:

Numerical simulations of the collapse of non–rotating and rotating cores of massive stars ($M \geq 8\ M_{\odot}$) are presented. After reviewing briefly the underlying physics the numerical results are discussed and possible consequences for neutron star formation are outlined.

1. Introduction

Type II supernovae (SN II) are generally assumed to occur when at the endpoint of the hydrostatic thermonuclear evolution of a massive star ($M \geq 8M_{\odot}$) its Fe-Ni-core collapses, bounces and generates an outgoing shock wave, which eventually leads to explosive mass ejection and the formation of a neutron star.

The numerical simulation of supernova explosions still poses one of the most fascinating and challenging problems in astrophysics inspite of more than twenty years of intense research (for recent reviews see Hillebrandt 1986 and Woosley 1986). Since the pioneering numerical calculations done by Colgate and White (1966) and by Arnett (1967) the simulation programs have been improved considerably both from the physics input as well as from the treatment of hydrodynamics. Nowadays for spherically symmetric simulations a detailed treatment of the neutrino transport, of the weak interaction rates and of the equation of state up to a few times nuclear matter density are necessary ingredients in any state of the art computer program.

Only a few attempts have been made to relax the assumption of spherical symmetry and perform axisymmetric, i.e. two-dimensional supernova simulations, which allow to study effects due to rotation (Müller, Różyczka and Hillebrandt, 1980; Tohline, Schombert and Boss, 1980; Müller and Hillebrandt, 1981) and magnetic fields (Le Blanc and Wilson, 1970; Müller and Hillebrandt, 1979; Ohnishi 1983; Symbalisty 1984).

In the next section the physics of SN II explosions will be briefly reviewed. In section 3 the results of a one-dimensional simulation performed to calibrate our new 2d-hydro-code are discussed and compared with previous collapse simulations. After some general remarks on possible effects of rotation on the dynamics of core

H. Ögelman and E. P. J. van den Heuvel (eds.), Timing Neutron Stars, 549–572.

collapse, we then present in section 4 the results of two rotational core collapse simulations. Finally in section 5 some implications for neutron star formation are pointed out.

2. Type II Supernova Explosions

Supernovae, which can spectroscopically be distinguished into two main classes, namely those of type I showing no hydrogen lines and those of type II possessing strong hydrogen lines in their spectra at maximum light, are the optical manifestation of stellar explosions (see e.g. Wheeler 1987). Observations show that in a supernova event an energy of the order 10^{51} *erg* is released in form of radiation and mass ejection connected with optical peak luminosities of the order 10^{43} erg/s.

In the currently most favoured theoretical model type II supernovae gain their energy from the gravitational binding energy released during the collapse of the Fe-Ni-cores of highly evolved massive stars to neutron star densities (see e.g. Hillebrandt 1986 and references therein). In this model neutrinos carry away an energy of the order 10^{53} *ergs*, a prediction which has been confirmed convincingly by the detection of neutrinos from SN 1987A (see articles in Danziger 1987). According to stellar evolution calculations the progenitor stars of type II supernovae have masses greater than 8 $M_\odot$ on the main sequence (Woosley 1986).

The crucial problem in explaining SN II explosions is to find the mechanism by which a small part ($\approx 1\%$) of the energy liberated during core collapse ($\approx 10^{53} erg$) is transfered to the outer layers of the star, thereby giving rise to the observed explosive mass ejection with velocities up to a few times 10^4 km/sec. In addition the models have to explain the formation of a neutron star of about $1.4 M_\odot$ in at least a fraction of the type II events. The low efficiency of this proposed implosion-explosion mechanism makes it difficult to treat the problem numerically, because (i) the outcome of the calculations is very sensitive to changes in the physical parameters, and (ii) a high degree of numerical accuracy (e.g. energy conservation) is required to simulate the dynamics correctly.

As was first pointed out by Bethe et al. (1979) in all progenitor models considered so far the entropy inside the iron-nickel core at the onset of core collapse is small ($\approx 1\ k_B/nucleon$), which greatly simplifies the qualitative discussion of the dynamics of (spherically symmetric) core collapse.

The collapse of the core is triggered by a combination of electron captures and photodisintegration of nuclei. Whereas the first process is more important for less massive stars ($8 \lesssim M/M_\odot \lesssim 15$), the latter process is the dominant one for the cores of more massive stars ($M \gtrsim 20\ M_\odot$), which have a larger entropy (Woosley 1986).

Because of the low initial entropy the number density of free protons is small in the core. Nevertheless electron capture on free protons provides the dominant process for changing the electron abundance, since electron captures on nuclei are greatly reduced by shell-blocking effects as shown by Fuller, Fowler and Newman (1982). Simulations show that the electron concentration during the early phases of core collapse changes only by about 20%. This holds up to densities of a few times

10^{11} g/cm^3, where the neutrinos are trapped due to coherent scattering off nuclei, or more precisely where the neutrino diffusion time scale becomes longer than the collapse time scale (Mazurek 1975; Sato 1975). As electron captures are the only non-equilibrium processes in the core — the strong and electromagnetic reactions due to the high temperatures ($T \gtrsim 5\ 10^9 K$) are in equilibrium — the entropy will change only a little during this early collapse phase.

After neutrino trapping some entropy will be produced, until equilibrium with respect to the weak interactions (β-equilibrium) is achieved. The equilibrium electron and neutrino number fractions are about $Y_e = 0.32$ and $Y_\nu = 0.08$, respectively. But again the entropy increase is small, less than about 0.5 $k_B/nucleon$. Note that the final lepton fraction implies a Chandrasekhar mass $M_{Ch} = 5.76\ Y_l^2 \approx 0.92\ M_\odot$.

During collapse the equation of state closely resembles a polytropic equation of state $p = K(s)\rho^{\gamma_p}$ with $\gamma_p \lesssim 4/3$ and K depending on the entropy. For constant γ_p and adiabatic hydrodynamics it is well known, that the core splits into an inner core collapsing homologously (i.e. $v \sim r$) with subsonic velocity, and into an outer core falling in with supersonic velocity (Goldreich and Weber, 1980; Yahil and Lattimer, 1982). The mass of the inner core depends on an effective index $\gamma_c \equiv (\partial \ln p/\partial \ln \rho)_{collapse}$, which gives the change of pressure with respect to density along the actual collapse trajectory. It takes into account the reduction in Y_e and effects due to the non-adiabaticity of the collapse (van Riper and Lattimer 1981). Due to electron captures γ_c drops below γ_p, and thus the homologously falling mass is reduced from $\approx 1.2\ M_\odot$ at the onset of collapse to the Chandrasekhar mass ($\approx 0.9\ M_\odot$) corresponding to the final lepton fraction.

As the entropy stays almost constant during collapse the concentration of free nucleons remains small. Consequently leptons dominate the pressure up to nuclear matter density, where a transition to homogeneous nuclear matter occurs. Then the collapse is stopped abruptly, because the adiabatic index changes from values close to 4/3 to about 3. After the central density has exceeded nuclear matter density the inner core comes to rest within about 1 *msec*. Pressure waves, which are created when successive mass shells are stopped, steepen up into a shock wave, which forms near the edge of the inner core at the sonic point separating subsonic from supersonic infall regimes. The shock propagates outwards both in mass and radius. Matter passing through the shock front is compressed and heated to entropies of about 6 to 10 $k_B/nucleon$ due to the dissipation of the kinetic infall energy.

The crucial question to be answered by numerical simulations is whether the shock wave is energetic enough to eject the stellar envelope in a supernova explosion. This is a non-trivial question, although the energy initially put into the shock wave is about $(5 - 8)\ 10^{51}$ *erg*, much more than required to explain the observed energy output of a supernova. While propagating outwards the shock wave is heavily damped by photodisintegration of nuclei ($1.6\ 10^{51}$ *erg*/$0.1\ M_\odot$) and by neutrino losses outside the neutrino sphere. The aim of the numerical simulations is to investigate, whether these energy losses are so severe that the shock stalls. As the energy losses due to photodisintegration are proportional to the difference between the mass of the Fe-Ni-core and that of its unshocked inner part, it is obvious that the best candidates for type II supernovae are stars with small Fe-Ni-cores ($M < 1.3\ M_\odot$) and low initial entropy the latter resulting in a large mass of the homologous core (for more details see e.g. Hillebrandt 1986).

3. Collapse Simulations of Non-Rotating Cores

At present only in a few simulations a prompt explosion has been found, namely for the low mass cores of a 10 $M_\odot$ star (Hillebrandt 1982), and of a 9 $M_\odot$ star (Hillebrandt, Nomoto and Wolff, 1984; see however Baron, Cooperstein and Kahana, 1987). For stars in the mass range 12 $M_\odot$ to 20 $M_\odot$ the core mass ($\approx$ 1.3 $M_\odot$) is probably, and for stars more massive than about 25$M_\odot$ the core mass ($\gtrsim$ 2.0 $M_\odot$) is definitely too large for the prompt explosion mechanism to work successfully (Hillebrandt 1986; Wilson et al., 1986).

Very recently Nomoto and Hashimoto (1987) have evolved a 13 $M_\odot$ star, which develops a low mass iron core of only 1.18 $M_\odot$. This star and also previously the 12 $M_\odot$ and 15 $M_\odot$ stars of Weaver, Woosley and Fuller (1985) have been claimed to explode via the prompt explosion mechanism (Baron, Cooperstein and Kahana, 1985; Baron et al., 1987). Their results may be questioned however, as has been pointed out recently by Glendenning (1988). The supranuclear equation of state employed by them is very soft giving rise to a maximum stable neutron star mass of 1.27 $M_\odot$, which is too small to account for the very accurately measured mass of the binary pulsar PSR 1913+16 (Taylor 1987), and the less accurately known mass of the pulsar 4U0900-40 (Joss and Rappaport, 1984).

However there may exist another, so-called delayed explosion mechanism by which the more massive stars become a supernova (Wilson 1985; Bethe and Wilson, 1985; Wilson et al., 1986). Wilson (1985) has found that a few hundred milliseconds after core bounce the stalled shock wave is revived due to energy transport by neutrinos as the shocked matter is irradiated by a neutrino flux originating from the neutrino sphere. This neutrino flux leads to a slow accumulation of energy behind the stalled shock, and consequently to a gradual heating and expansion, ultimately producing a relatively weak explosion of a few times 10^{50} *erg* only. Up to now these results have not been confirmed by other workers in the field (see e.g. Hillebrandt 1986). Obviously the success or failure of the late time explosion mechanism is very sensitive to details of the neutrino transport scheme (Wilson 1988).

We have also performed a spherically symmetric collapse calculation to calibrate the hydro–code, which necessarily cannot be as sophisticated as genuine 1d–codes. Our explicit axisymmetric code is spatially second–order accurate, and as far as the advection terms are concerned also of second–order accuracy in time. The source terms are second–order accurate in time only in the 1d–runs because of CPU-time considerations; additional equation of state calls are thereby avoided in the 2d–simulations. The code is based on a conservative difference scheme with monotonic advection on a moving (non–equidistant) grid in spherical coordinates. The details of the difference scheme will be published elsewhere (Mönchmeyer and Müller, 1989).

The Newtonian equations of hydrodynamics are integrated using an entropy equation instead of an energy equation. The equation of state of Wolff (see Hillebrandt and Wolff, 1985), which is based on temperature–dependent Hartree–Fock calculations with an effective nucleon–nucleon interaction of Skyrme force type, is used in tabular form. For this equation of state the adiabatic index $\gamma \approx 1.32$ for densities between 10^{10} g/cm^3 and 10^{14} g/cm^3 and for entropies less than 3 $k_B/nucleon$.

The neutrino transport consists of a simple trapping scheme with a trapping density of 3 10^{11} g/cm^3 during the infall epoch. After bounce the trapping density is reduced to 10^{10} g/cm^3 to take into account the change of the hydrodynamical time scale relative to the diffusion time scale.

The results of our 1d–simulation are given in Fig. 1 and in Table 1, respectively. The initial model was the 20 $M_\odot$ star of Weaver, Woosley and Fuller (1985), which has an iron core mass of 1.36 $M_\odot$ and a central entropy of $\approx$ 0.7 $k_B/nucleon$. Comparing our results with those of Hillebrandt and Wolff (1985), we find a good overall agreement (see Table 1). The similarity of the results proves the ability of the 2d–hydro–code to handle the physical processes of core collapse adequately.

Table 1: Comparison of the results of two 1d–simulations. The various quantities are all given at bounce.

	Hillebrandt and Wolff (1985)	this work
$M_{hc}/M_\odot$	0.85	0.90
Y_e^c	0.32	0.33
Y_ν^c	0.09	0.08
$S^c(k_B/nucleon)$	1.10	0.96
ρ^c (g/cm^3)	3.3 10^{14}	3.1 10^{14}
T^c (K)	2.4 10^{11}	2.0 10^{11}
E^i_{shock} (erg)	$\approx$ 8 10^{51}	6 10^{51}

There are small discrepancies in the mass of the homologous core (M_{hc}) and in the central entropy (S^c) at bounce. These are caused by the usage of a trapping scheme instead of an equilibrium neutrino diffusion transport scheme as in the simulation of Hillebrandt and Wolff (1985). However, we get the same total lepton fraction at bounce in the center of the core ($Y_l^c = Y_e^c + Y_\nu^c$), and the differences in the central density ρ^c and temperature T^c are only 10% and 20%, respectively. As we did not include general relativistic effects in our simulation, we obtain a smaller central and average density for the inner core than Hillebrandt and Wolff (1985). This may explain why their initial shock energy is larger than ours.

Due to the improved spatial resolution and the second order accuracy of our hydro–code we are able to resolve the initial rarefaction wave (Fig. 1c) and the subsequent core expansion, which eventually produces a second pressure wave moving outwards (Figs. 1d and 1e). The latter wave finally merges with the already significantly weakened shock wave at a radius of about 110 km and an interior mass of $m(r) = 1.15\ M_\odot$, while another rarefaction wave starts propagating towards the center (Fig. 1e). About 5 $msec$ after bounce only a small amount of mass still has positive velocities ($\lesssim$ 5 10^8 cm/sec), and the shock wave is turning into an accretion shock at a radius of about 140 km and at an interior mass of 1.25 $M_\odot$

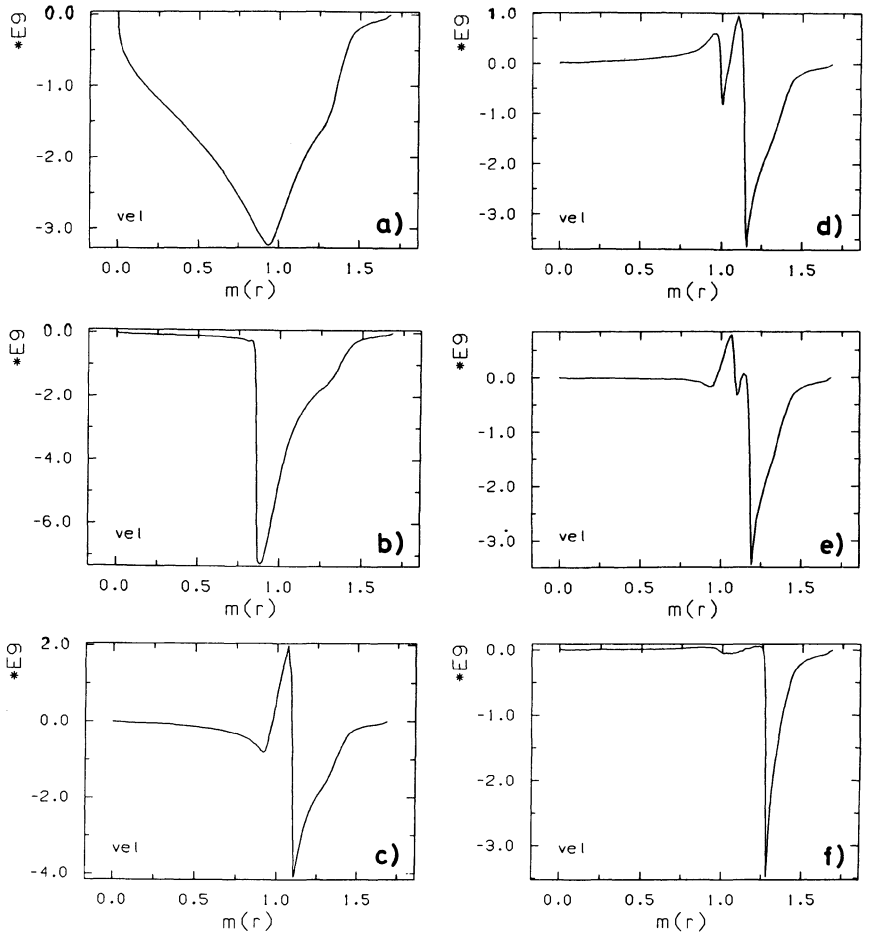

Figure 1: Six snapshots of velocity versus interior mass for the collapse of the 1.36 $M_\odot$ iron core of the 20 $M_\odot$ star of Weaver, Woosley and Fuller (1985). The first snapshot (a) is taken at bounce, i.e. 169 *msec* after the begin of the collapse. The other five snapshots are taken roughly 0.5 *msec* (b), 2 *msec* (c), 3 *msec* (d), 4 *msec* (e), and 8 *msec* (f) after bounce, respectively.

(Fig. 1f). In passing we note that the ability of the hydro–code to resolve the various waves behind the shock is crucial for a correct numerical treatment of the dynamically important core oscillations after bounce in the rotating models. Hillebrandt, Nomoto and Wolff (1984) did not find the rarefaction wave, which may be explained, however, by the enhanced binding of the core in the general relativistic potential.

4. Collapse Simulations of Rotating Cores

4.1 Some General Remarks on the Influence of Rotation

From a variety of studies it is known that rotation has a stabilizing influence on instability modes. A criterion for rigid rotators has been given by Ledoux (1945)

$$\gamma > \gamma_{crit} \text{ , with } \gamma_{crit} = \frac{2}{3} \cdot \frac{2-5\beta}{1-2\beta} \text{ ,}$$

where β is the absolute value of the ratio of rotational to gravitational energy. Computer simulations have shown that this criterion holds for differential rotators, too, and that the stabilizing effect depends mainly on the amount of rotational energy and not so much on its distribution or the density stratification (Ostriker and Tassoul, 1969; Ostriker and Bodenheimer, 1973; Durisen and Imamura, 1981). If the adiabatic index of the collapsing core is very close to the value of 4/3 (see chap. 2), a small amount of rotation may be enough to stop the collapse and lead to the formation of stable rotating configurations with central densities below nuclear matter density (Tohline 1984; Eriguchi and Müller, 1984; Symbalisty 1984).

Due to conservation of angular momentum configurations may form during core collapse, which are unstable against tri–axial deformations on secular or even dynamical time scales (Tohline 1984; Eriguchi and Müller, 1984), if $\beta \geq 0.14$ and $\beta \geq 0.27$, respectively (see e.g. Tassoul 1978). Whether these instabilities indeed do occur is a non–trivial question, if a stiff sub–nuclear equation of state is valid, where the adiabatic index is very close to 4/3. For such an equation of state the core may be stabilized before its rotational energy exceeds the critcal value. If on the other hand side the initial amount of rotation is small enough for the collapse to proceed to nuclear densities, $\beta > 0.14$ may not be reached before bounce.

Due to conservation of angular momentum and due to the resulting increase of the centrifugal forces matter will not fall in on radial trajectories. In addition matter at the equatorial plane will not fall towards the center as fast as matter at the pole. This leads to a progressively flattening of the core and to a change of the collapse time scale in comparison to a spherically symmetric collapse. As basic properties of the collapsing core depend on the size of the collapse time scale relative to the electron capture time scale and the neutrino diffusion time scale, the kinetic infall energy, the final lepton fraction, and the mass of the inner core may change in the presence of rotation.

Before and after bounce one expects the infall velocities at the pole to be larger than those at the equator. The resulting non–spherical density stratification may

modify the neutrino signal in a characteristic way (Janka and Mönchmeyer, 1989). Due to the asymmetric infall of matter the propagation of the shock wave at the pole will differ from the propagation near the equatorial plane. In particular this effect will be evident in the dissipation rates and in the maximum entropy values behind the shock front.

After bounce the rotating core will oscillate with a superposition of various axi–symmetric radial and surface modes. The frequency of these modes is determined by the average density of the inner core. Contrary to a spherically symmetric core, which comes to rest soon after bounce, in a rotating core a certain fraction of its kinetic infall energy will be converted into oscillations, which are damped by non–spherical pressure waves. The oscillations will also contribute to the gravitational wave signal of the bouncing core.

Finally it is very well known that rotation can drive meridional circulations in baroclinic regions (see e.g. Tassoul 1978). For type II supernova models the interesting question arises, whether there exist large scale circulation patterns behind the shock, that extend inwards to regions with high energy neutrinos. In the (neutrino) opaque matter those vortices could transport neutrinos towards the shock front much faster than diffusion (Müller and Hillebrandt, 1981). From 1d–calculations one knows in addition that a negative entropy gradient is established behind the shock after photodisintegration losses have weakened it significantly. This region of decreasing entropy is unstable against convection provided that the stabilizing lepton gradient is not too large (Epstein 1979). Arnett (1985) has first pointed out the possible importance of convection for the type-II supernova mechanism. However, whether convection indeed helps or even harms the propagation of the shock is debated (Burrows 1987; Bethe, Brown and Cooperstein, 1987). Note that for rotating cores mixing of high and low entropy matter may be enhanced, if convectional currents are supported by vortices resulting from rotation in regions, where the surfaces of constant pressure do not coincide with isopycnic surfaces. On the other hand side it has been argued that rotation may have a stabilizing effect on certain types of convective instability modes (see Tassoul 1978). However, especially for centrally condensed and differentially rotating objects the interaction of rotation and convection has not been clarified completely up to now.

4.2 Initial Models

We have computed the collapse of two iron cores, whose initial rotational energies differed by a factor of four. All other model parameters and particularly the form of the angular momentum distribution were identical for these calculations. The results of models with different angular momentum distributions will be published elsewhere (Mönchmeyer, Wolff and Müller, 1989).

Both initial models are based on the 20 $M_\odot$ star of Weaver, Woosley and Fuller (1985). In the simulations we followed the dynamics of the innermost 1.6 $M_\odot$ of this star after adding a certain amount of rotation to the model. Note that the initial models are not relaxed with respect to rotation. But as both cores rotate rather slowly (see below), the deviations from equilibrium are relatively small. Electron captures, neutrino transport and equation of state were treated as in the 1-d calculation.

The choice of the initial angular momentum distribution is one of the most problematic aspects of any 2-d simulation, because there exist no evolutionary calculations of rotating massive stars up to iron core collapse. Therefore the amount as well as the distribution of the initial angular momentum can be chosen arbitrarily within certain limits imposed by stability considerations (see e.g. Tassoul 1978). The initial rotation profiles in our simulations are similar to those used in previous investigations of rotational core collapse (Müller and Hillebrandt, 1981; Symbalisty 1984), where the angular velocity is a function of radius only:

$$\Omega(r) = \Omega_0 \cdot \frac{R^2}{r^2 + R^2} \qquad \text{with} \quad R = 10^8 cm \quad .$$

The interior mass corresponding to R is about 1.31 $M_\odot$, i.e. a large fraction of the Fe–Ni–core approximately rotated as a rigid rotator. The rotational energies and the corresponding values of β of both initial models are given together with the values of Ω_0 in Table 2.

Table 2: Initial models

	Model A	Model B
$\Omega_0(s^{-1})$	4.0	8.0
$E_{rot}(erg)$	2.47 10^{49}	9.87 10^{49}
β	0.005	0.020
N_r	100	50
N_θ	30	20

We used a two–dimensional grid in spherical coordinates, which was equidistantly spaced in angular direction. During collapse the grid was contracted in radial direction to follow on average the collapse of the core. The number of gridpoints in radial direction N_r and per quadrant in angular direction N_θ are given in Table 2.

4.3 Model A

The concept of homology cannot be used for rotating cores. Yet there exists a surface, which separates subsonically from supersonically falling matter. We will speak of the "inner core", when we refer to the matter in the subsonic regions. After bounce this inner core corresponds to the unshocked central part of the iron core.

Up to 170 msec the density stratification of the inner core is comparable to that of the 1–d model. Afterwards the inner core starts to flatten slightly, which first becomes evident in the entropy per unit mass. The aspherical density stratification leads to angular dependent variations in the entropy generation due to electron

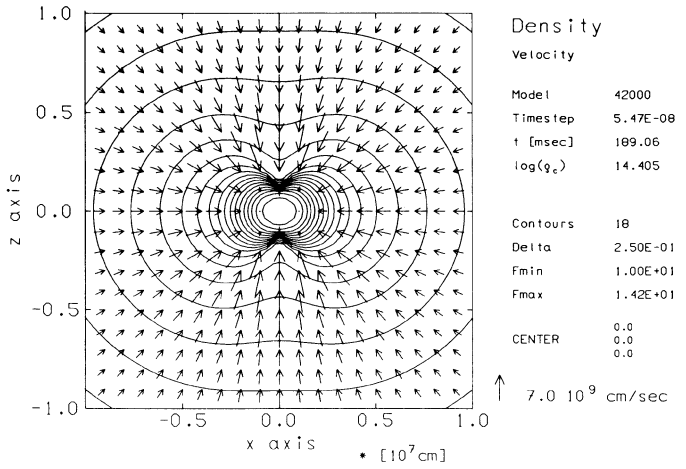

Figure 2: Density profiles and flow pattern for model A at bounce. The axis of rotation is identical with the z–axis. The contours cover a range from Fmin to Fmax with a logarithmic spacing of Delta. The time, the central density and the velocity scale are given in the legend of the figure.

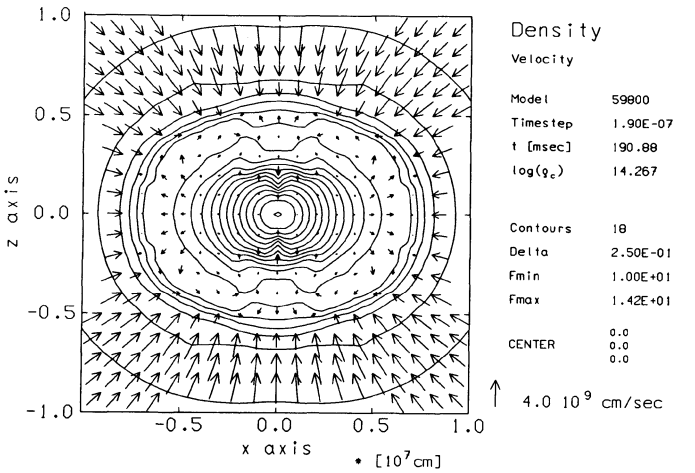

Figure 3: Density profiles and flow pattern for model A about 1.8 *msec* after bounce. The circulation flow between the central "hydrostatic" configuration and the shock is clearly visible.

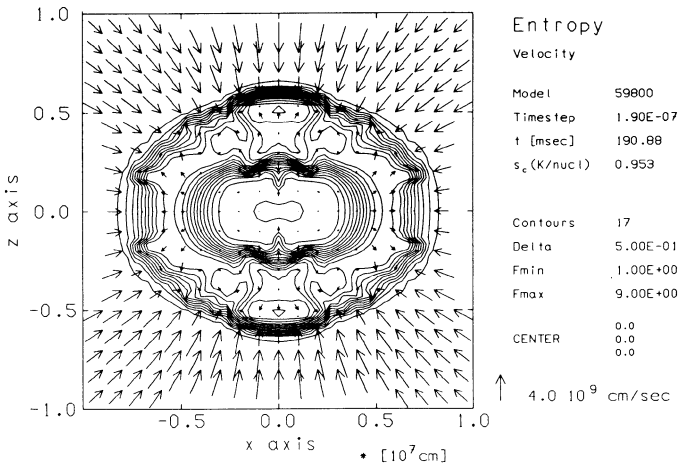

Figure 4: Entropy profiles and flow pattern for model A about 1.8 *msec* after bounce. Blobs of high entropy have formed at the axis. Note that the central region is unshocked.

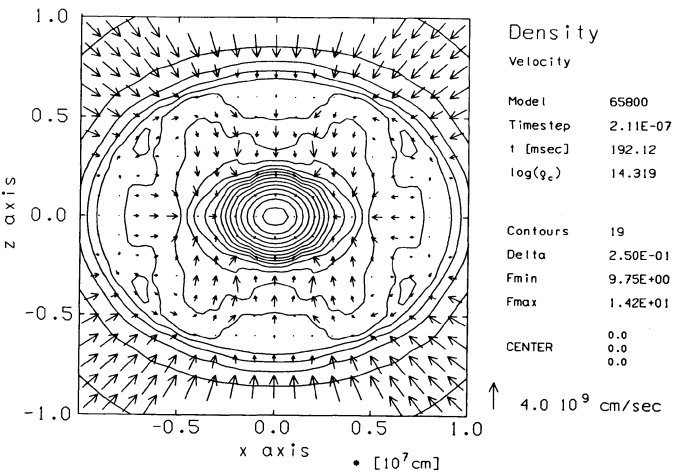

Figure 5: Density profiles and flow pattern for model A about 3 *msec* after bounce, when the inner core re–contracts.

captures, which for $\rho \geq 5\ 10^{10}\ g/cm^3$ are sensitive to density. At 178 *msec* neutrino trapping sets in and β – equilibrium is established about 5 *msec* later when the central density exceeds $8\ 10^{12}\ g/cm^3$.

Significant flattening of the inner core occurs for $t \gtrsim 187$ *msec*. The level surfaces of the angular velocity are no longer spherical in this phase, but have aquired a more cylindrical shape indicating that the inner core has gone through some rearrangement of matter and angular momentum approaching the rotation profile of a barotrope with $\partial\Omega/\partial z = 0$ (see e.g. Tassoul 1978).

At $t \approx 188$ *msec* a growing pressure gradient leads to an efficient deceleration of the collapse of the inner core near the pole. The maximum of the angular velocity is located 15.8 *km* off–center at the axis. There a dip is formed in the density distribution of the inner core (Fig. 2). Such a "bottle neck" structure was not found in the collapse calculations of Müller and Hillebrandt (1981) and of Symbalisty (1984), but is present in the rotating equilibrium configurations calculated by Eriguchi and Müller (1984). Actually the situation near the axis is similar to that of a rotating fluid in a homogeneous acceleration field, where the density stratification is of parabolic shape. This probably explains the appearance of the "bottle-neck", whose exact shape is determined by inhomogeneities in the gravitational acceleration and by the ram pressure of the infalling matter.

Model A bounces at $t = 189$ *msec* at a central density of $2.58\ 10^{14}\ g/cm^3$ and a central entropy of 0.89 $k_B/nucleon$. The angular velocity Ω reaches a maximum value of $1.4\ 10^4\ sec^{-1}$ in the "bottle-neck" and has a value between $(1-2)\ 10^3\ sec^{-1}$ at the surface of the inner core. Despite the fact that the total collapse time up to bounce is stretched by approximately 20 *msec* compared to the 1-d calculation the same final electron ($Y_e = 0.32$) and neutrino ($Y_\nu = 0.08$) concentrations are reached inside the trapping region. This can be explained by the fact that before trapping no significant flattening and deceleration of the core occurs, and that the (averaged) electron capture time scale before trapping $\tau_{EC} = Y_e/\dot{Y}_e \approx 2$ *sec* is long compared to the dynamical time scale.

The mass within the sonic surface at bounce is roughly equal to that of the 1–d models, namely 0.9 $M_\odot$. The kinetic energy, the ratio of rotational to gravitational energy and the rotational energy of the inner core at bounce are $(5-6)\ 10^{51}$ *erg*, 0.065, and $6\ 10^{51}$ *erg*, respectively. For the whole core we find $\beta = 0.078$ and $E_{rot} = 8\ 10^{51}$ *erg*. The axis ratio for the inner core at bounce is $r_{pole}/r_{equator} = 0.53$ and the maximum infall velocities at the pole are a factor of 2.2 larger than in the equatorial plane. The peak value of the infall velocity ($\approx 10^{10}$ *cm/sec*) is reached in the bottle-neck region. This velocity is only slightly smaller than the free fall velocity at that point. This is consistent with the fact that at the axis the pressure gradient in the region of maximum infall velocity is always less than 10% of the gravitational force during the collapse.

After bounce the inner core first expands into polar direction and a strong shock is formed near the axis. Afterwards it expands in angular direction generating a deformed but closed shock surface, which separates from the inner core at 189.8 *msec*. The large infall velocities at the axis cause a very high dissipation rate of kinetic energy. As a result blobs of high entropy are created behind the shock as it propagates outwards. These entropy blobs give rise to buoyancy forces, which support the shock at the axis for about 3 *msec* (Fig. 3 and Fig. 4). A similar effect

has already been seen by Müller and Hillebrandt (1981).

During the first 2 *msec* after bounce a circulation flow from the equatorial plane towards the symmetry axis evolves behind the shock. This circulation is driven by forces resulting from a non–alignment between isobaric and isopycnic surfaces behind the shock. As the angular velocity is approximately constant on cylinders the nonradial flow is also partially caused by a redistribution of angular momentum in the expanding matter behind the shock. A smaller vortex caused by thermodynamical forces is located at the edge of the entropy blobs (Kelvin-Helmholtz-instability) and leads to their "mushroom" shape (Fig. 4).

At 191 *msec* the inner core starts to contract again. As a consequence the large scale circulation splits up into smaller vortices and eventually an overall motion towards the center results (Fig. 5). As in the spherical simulation this rarefaction wave weakens the shock. Note, however, that the main damping effect on the shock propagation in this phase still results from the photodisintegration of nuclei.

The expansion and the subsequent contraction of the core can be interpreted as part of an overall radial oscillation of the inner core with a mean period of 2.5 *msec*. The decrease of both period and amplitude of that oscillation with time can be seen from Fig. 6. The shortening of the period corresponds to an increase of the average density of the inner core as it approaches equilibrium.

At 192.5 *msec* the shock has reached a radius of approximately 100 *km* in the equatorial plane and of about 75 *km* in polar direction. The mass inside the shock front is roughly 1.2 $M_\odot$. The maximum entropy value in the blobs is $\approx$ 9 $k_B/nucleon$, whereas in the equatorial plane the highest value is only $\approx$ 6.5 $k_B/nucleon$. The density in the shock front now becomes smaller than the trapping density. Therefore energy losses due to escaping neutrinos lead to an enhanced weakening of the shock. Consequently the velocity of the shock and the entropy generation in the shock are drastically reduced. Thus the regions of high entropy are left at some distance behind the shock front, and as soon as the neutrino losses become significant the shock propagation stalls and an accretion shock formes.

We did not find any efficient transport of neutrinos to the shock front, because the speed of shock propagation is larger than or of the same order as the circulation velocities behind the shock front before it stalls. On the other hand we may have overestimated the neutrino losses in our crude trapping scheme. However, as the neutrino density gradient and the mass density gradient are very large at the front, it is possible that neutrino diffusion across the front is very effective, too.

The evolution after 194 *msec* is mainly characterized by hydrodynamical processes, which lead to a damping of the oscillations of the inner core and establish an approximate hydrodynamical equilibrium for the mass between the shock and the inner core. The amplitudes and energy of the core oscillations are diminished by pressure waves, which propagate outwards from the edge of the inner core. They finally catch up with the shock, because the sound velocity in the shocked matter is larger than the shock speed at this stage. The second expansion of the inner core generates a further entropy blob at the axis located behind the shock but ahead of the slightly contracted high entropy region created earlier in the evolution. However, due to strong neutrino cooling the shock remains an accretion shock.

Furtheron in the evolution a Rayleigh–Taylor instability sets in at the edge of

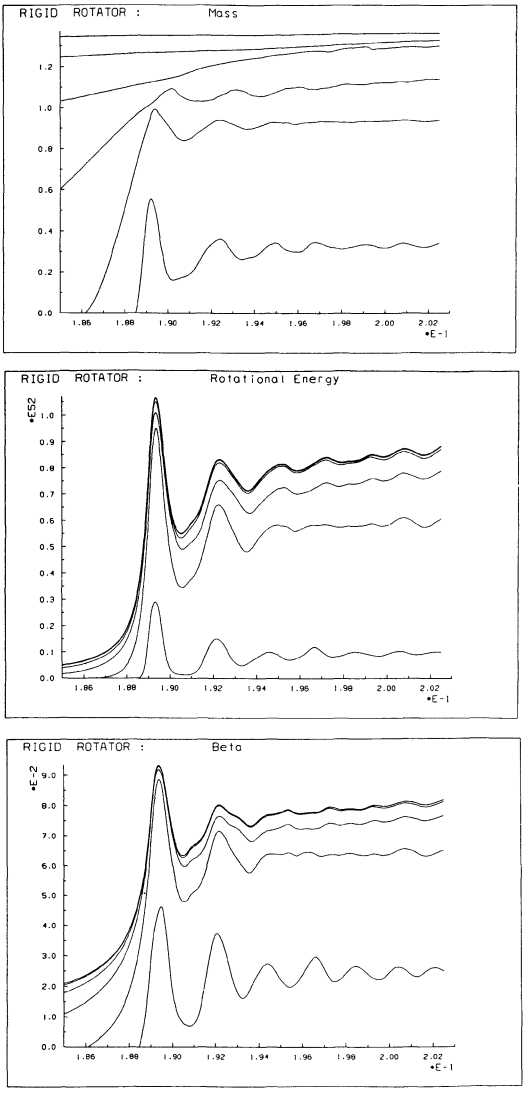

Figure 6: Mass, rotational energy and β versus time for model A integrated over the matter which has a density larger than $10^9, 10^{10}, 10^{11}, 10^{12}, 10^{13}$ and 10^{14} g/cm^3, respectively (counted from top).

the high entropy region (Fig. 7). Small scale vortices first support the development of finger–like structures of a gravity mode, which is characterized by the rise of lighter mass elements of higher entropy and the sinking of heavier elements of lower entropy. Mixing of high with low entropy material then causes the isolation of the outer parts of the fingers and "islands" of high entropy are formed (Fig. 8), which later on begin to dissolve continously. Afterwards a broad layer of matter having a low and almost homogeneous entropy is established behind the shock front, and the shock itself retreats at the axis to a radius of only 70 *km*. There it forms a stationary accretion shock, giving rise again to the previously described bottle neck structure.

The final configuration consists of a compact central object of 1 $M_\odot$ of low entropy, which is surrounded by a region of shocked matter of higher entropy. This shocked mass is separated from a deformed accretion shock by a layer of 40 *km* width, where due to mixing the entropy is approximately constant at a level of 2 $k_B/nucleon$. Only at the axis there still exists a region of very high entropy (Fig. 9 and 10). The shock has reached a radius of 125 *km* in the equatorial plane and is located at a radius of about 60 *km* in the polar direction. Between the inner core and the shock front a large scale meridional circulation is present (Fig. 9a) The mass inside the shock front is 1.31 $M_\odot$ at the end of the computation and the final value of $\beta = 0.09$. Further properties of the final configuration are summarized in Table 3.

Table 3: Properties of the final configuration.

	Model A	Model B
$\rho_c(g/cm^{-3})$	2.1 10^{14}	2.1 10^{13}
$\Omega_{surf}(s^{-1})$	5.0 10^2	1.5 10^2
$\Omega_{max}(s^{-1})$	1.2 10^4	3.0 10^3
$E_{rot}(erg)$	9.0 10^{52}	7.3 10^{51}
$\beta(1.0\ M_\odot)$	0.074	0.098
$\beta(1.3\ M_\odot)$	0.08	0.14
$T_{osc}(msec)$	≤ 2.7	≤ 13.5
$r_{sh}^{pole}(km)$	60	67
$r_{sh}^{eq}(km)$	120	$--$
$M_{sh}/M_\odot$	$\gtrsim 1.30$	$\gtrsim 1.38$

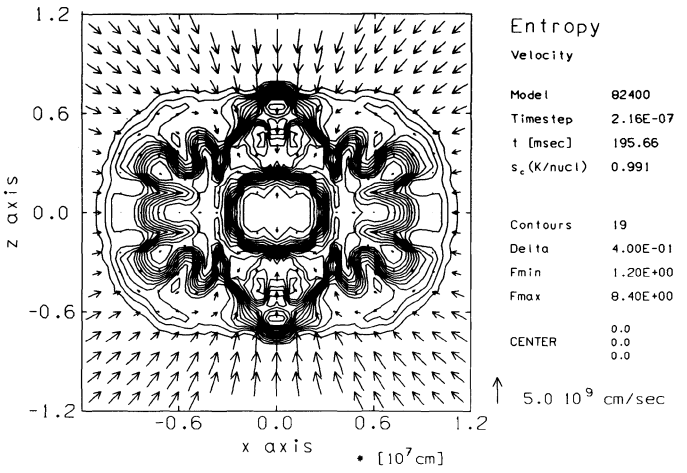

Figure 7: Entropy profiles and flow pattern for model A about 6.5 *msec* after bounce showing the instability at the edge of the high entropy region.

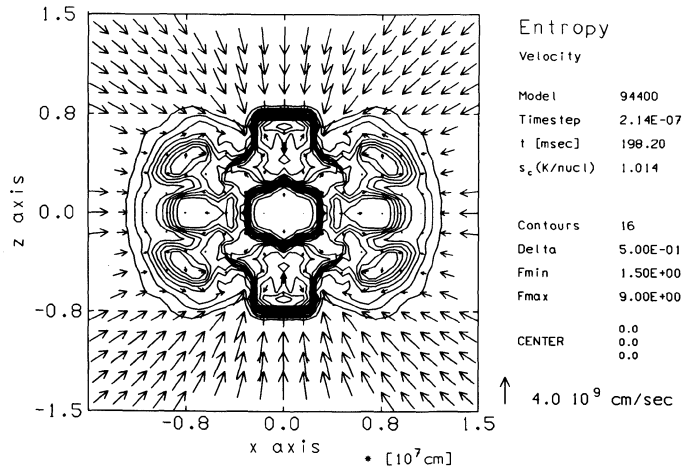

Figure 8: Entropy profiles and flow pattern for model A about 9 *msec* after bounce. The finger-like structures from Fig. 7 have developed into "islands" of higher entropy.

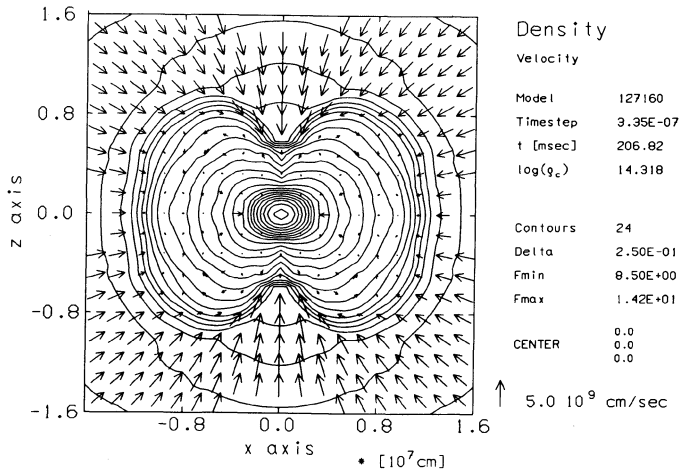

Figure 9: Density profiles and flow pattern for model A at the end of the calculation about 18 *msec* after bounce.

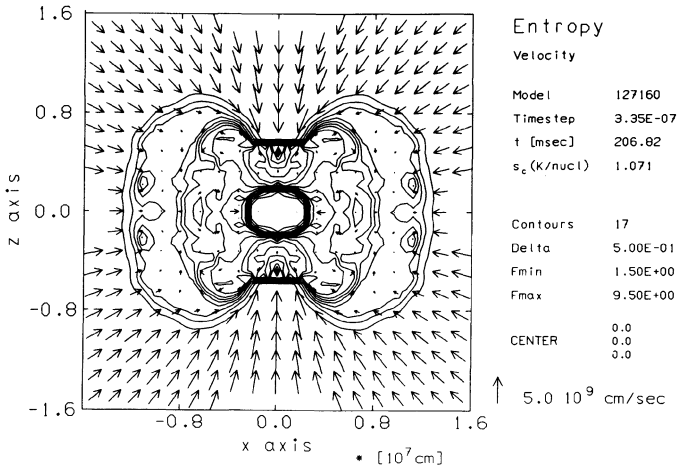

Figure 10: Same as Fig. 9 but showing entropy profiles.

4.4 Model B

The larger initial angular momentum in model B causes the time scale of the infall epoch to be significantly longer than in model A. Appreciable flattening of the inner core occured after $t = 250$ *msec* at a central density of 10^{11} g/cm^3 just prior to the onset of neutrino trapping. About 58 *msec* later a compact inner core of approximately 1.15 $M_\odot$ had formed. The density stratification shows an extended "bottle–neck" around the axis. In this "channel" the infall velocities reach approximately the free fall velocity (Fig. 11).

Model B bounced at 308 *msec* (Fig. 11), the inner core mass being about 1.2 $M_\odot$. The equatorial diameter of the inner core at bounce is approximately 190 *km*, while its polar diameter is only 90 *km*. The central lepton density is again 0.41 with a neutrino number fraction of 0.08. The infall velocities at the pole and at the equator are 5.2 10^9 *cm/sec* and 2 10^9 *cm/sec*, respectively. The central density reaches a peak value of only 3.6 10^{13} g/cm^3, i.e. model B bounced well below nuclear matter density.

A strong shock is created at the polar axis, which is probably not resolved sufficiently, as only 50 radial gridpoints were used in this calculation. The shock forms a region of high entropy ($S_{max} \approx 13$ $k_B/nucleon$ at 326 *msec*) at the bottom of the "bottle–neck channel" (Fig. 12). However, most of the dissipated kinetic energy is immediately carried away by neutrinos, because the density in the polar shock region is below the trapping density. Neutrino cooling together with the high ram pressure of the infalling material prevent the propagation of the shock along the axis. It remains an accretion shock located at a radius of 60 *km* (Fig. 13)

Symbalisty (1984) found for a similar model (with a comparable resolution of 1200 cells per quadrant), that at the axis the shock propagated outwards to a radius of more than 1000 *km* driving a circulation flow behind it, which Symbalisty interprets as a "jet". We cannot exclude that such a phenomenon is possible, because we have no detailed neutrino transport scheme included in our code. However, we have strong doubts, whether high neutrino loss rates and the consequent fatal weakening of the shock can be avoided in the low density regions at the axis outside a radius of about 100 *km*. A simple estimate shows that for our model the escape rate for neutrinos always dominates the production rate due to electron captures and also the supply rate due to diffusion from regions further inside. Furthermore we think that the ram pressure of the infalling matter in the bottle–neck structure present in our model reduces the possibility of a "jet"–like event. However, detailed calculations with an appropriate neutrino transport scheme together with an improved grid resolution are necessary to get a decisive answer.

In the equatorial plane a weaker shock propagated outwards to a radius of about 250 *km*. The ram pressure is relatively small in the equatorial plane, where the infalling matter is significantly decelerated by centrifugal forces. Therefore the propagation of the shock was supported by a rotationally driven expansion of the inner core in the equatorial plane until the central density averaged over some small oscillations reached approximately 2 10^{13} g/cm^3. Just outside the shock radius the infall velocities are only about 1.2 10^9 *cm/sec* in the equatorial plane (Fig. 14).

For $t > 340$ *msec* the evolution is characterized by the formation of a central equilibrium configuration, which grows in mass through accretion of matter. Its equatorial radius is growing too, while the polar radius is almost constant and in-

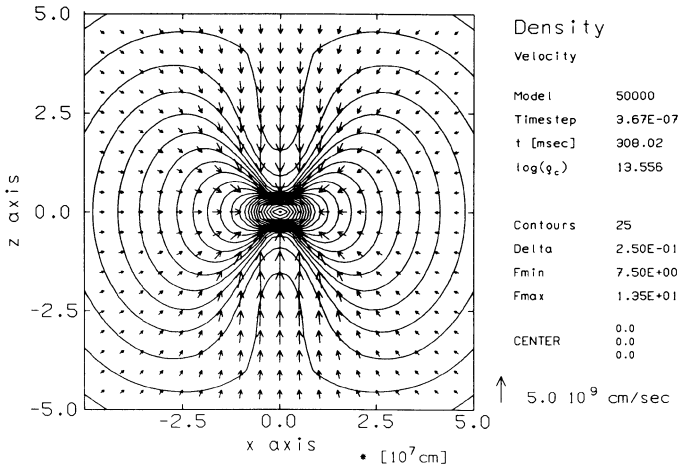

Figure 11: Density profiles and flow pattern for model B at bounce. The central density is only 3.6 10^{13} g/cm^3.

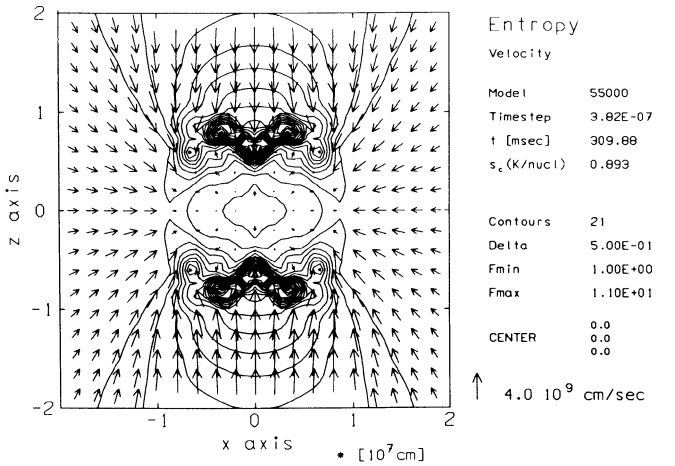

Figure 12: Entropy profiles and flow pattern for model B about 2 *msec* after bounce showing the strong shock on the axis at the bottom of the "bottle-neck channel".

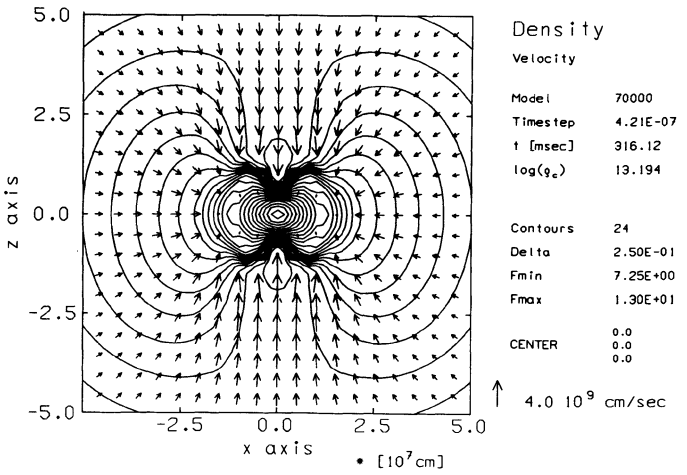

Figure 13: Density profiles and flow pattern for model B about 8 *msec* after bounce.

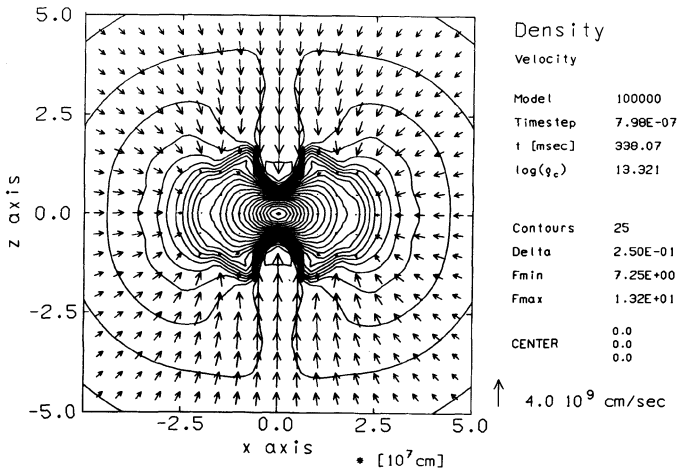

Figure 14: Density profiles and flow pattern for model B about 30 *msec* after bounce.

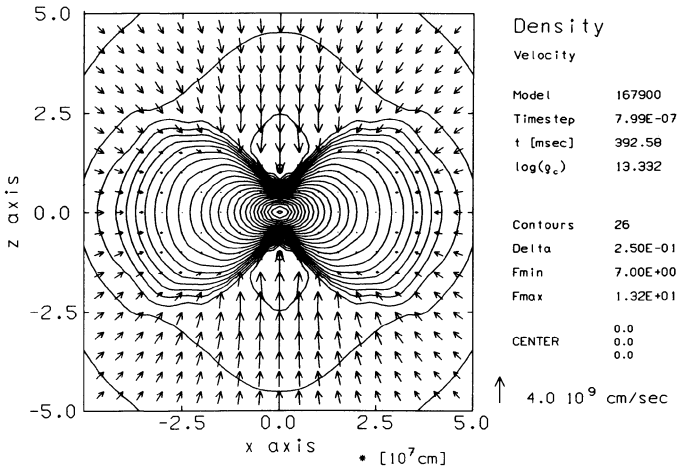

Figure 15: Density profiles and flow pattern for model B about 84 *msec* after bounce showing the highly flattened configuration at the end of the calculation.

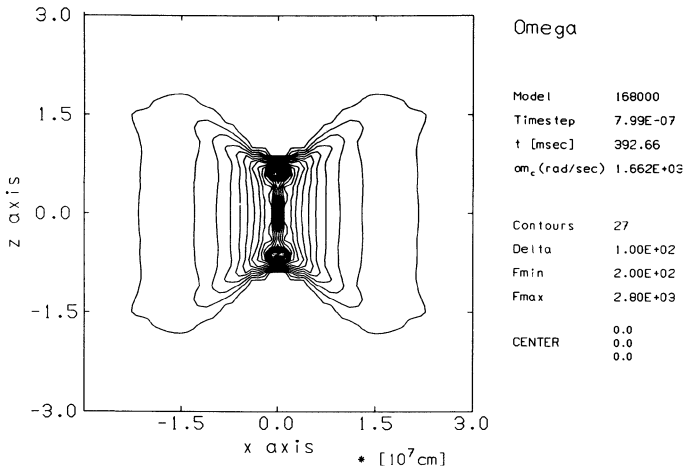

Figure 16: Angular velocity contours for the same model as in Fig. 15.

creases only slightly to 66 km. In addition the bottle–neck structure at the pole continously adjusts to the local ram pressure and the centrifugal forces. Therefore the final configuration at the end of the computation has a rather deformed "butterfly" shape (Fig. 15). This whole evolution is accompanied by small oscillations of the inner core. In the final model the mass of the approximately hydrostatic configuration is about 1.36 $M_\odot$. Further properties of the final configuration are summarized in Table 3. From Fig. 16 one can see that the equilibrium configuration in fact has the property of Ω being constant on cylinders, the angular velocity at the equator of the equilibrium configuration being about 200 sec^{-1}.

5. Implications for Neutron Star Formation

Deriving definite and specific statements about neutron star formation from the collapse simulations of rotating or non–rotating cores of massive stars obviously requires that the examined models are successful in producing a supernova in the first place. This is definitely not the case for the initially slowly rotating model A. For model B on the other hand the question of success or failure of the shock propagation (at the axis) cannot be answered. From our results we are still able to obtain interesting insights into the process of neutron star formation.

First of all model B shows that already a relatively small amount of rotation in combination with a stiff equation of state for sub–nuclear densities ($\gamma \approx 4/3$) leads to a bounce and at least a temporarily halt of the collapse at densities well below nuclear matter density (at $\approx 10^{13}\ g/cm^3$ in model B). Due to centrifugal forces a fast rotating ($\beta \approx 0.14$) central configuration forms, which is almost in hydrostatic equilibrium. For the further evolution of this central equilibrium configuration three points are of importance:

1. As $\beta \approx 0.14$ for the innermost 1.36 $M_\odot$, the central equilibrium configuration is hovering right at the edge of the secular instability limit against tri–axial deformations. What happens when β eventually exceeds the critical value is unclear. One possibility is that the instability leads to a fission of the central configuration. However, we think this evolution is somewhat unlikely. The combined action of shock waves, which are created at the edge of the tri–axial central configuration, and gravitational radiation will cause angular momentum losses, which will probably keep the configuration near the instability point.
2. The inner 1.1 $M_\odot$ of the core will eventually loose its neutrinos due to diffusion, thereby getting neutronized and cooled down. Due to the smaller average densities in model B the neutrino diffusion time scale is smaller than the typical value in 1-d models being of the order of seconds. It is not at all clear, however, whether the corresponding pressure reduction will lead to a second dynamical collapse or whether only a slow quasi–stationary contraction sets in. In both cases the rotational energy will increase, thereby enhancing the chance of tri–axial instabilities.
3. Outside the iron core and the silicon shell a layer of about $1 - 2\ M_\odot$ of oxygen exists (Weaver, Wossley and Fuller, 1985). This potential nuclear fuel may be ignited by either compressional heating while falling onto the central equilibrium

configuration, or by a shock wave resulting from the re–collapse of the central regions after part or all of the oxygen layer has already been accreted. In both cases an energy of the order 10^{51} *erg* will be liberated leading to a supernova explosion (see e.g. Bodenheimer and Woosley, 1983).

Independent which of these scenarios actually occurs the resulting neutron star, if formed at all, will be born as a fast rotator. Model A as well as model B indicate that the expected surface angular velocities of the neutron star will be in the range of 500 $sec^{-1} \lesssim \Omega \lesssim 1000\ sec^{-1}$, which corresponds to periods in the range 6 $msec \lesssim P \lesssim 13\ msec$. These periods are consistent with the idea that the Crab pulsar with its (present!) period of 33 *msec* was formed by the collapse of a rotating core. In addition recent observations suggest that the system 1E1024.0–5732/Wack 2134 contains a 60 *msec* X–ray pulsar and a massive early–type companion (Caraveo, this volume). The mass of the companion implies an age of the binary system of only a few million years indicating that the pulsar was born as a fast rotator and not spun up. This may also be the case for the millisecond pulsars, although the prevailing opinion on these objects is that they are spun–up by accretion (see e.g. van den Heuvel, this volume).

References

Arnett, W.D., 1967, *Astrophys. Space Sci.*, **5**, 180.

Arnett, W.D., 1985, unpublished

Baron, E., Cooperstein, J. and Kahana, S., 1985, *Phys. Rev Lett.*, **55**, 126.

Baron, E., Cooperstein, J. and Kahana, S., 1987, *Astrophys. J.*, **320**, 300.

Baron, E., Bethe, H.A., Brown, G.E., Cooperstein, J. and Kahana, S., 1987, *Phys. Rev. Lett.*, **59**, 736.

Bethe, H.A., Brown, G.E., Applegate, J. and Lattimer,J.M., 1979, *Nucl. Phys.*, **A324**, 487.

Bethe, H.A., Brown, G.E. and Cooperstein, J., 1987, *Astrophys. J.*, **322**, 201.

Bethe, H.A. and Wilson, J.R., 1985, *Astrophys. J.*, **295**, 14.

Bodenheimer, P. and Woosley, S.E., 1983, *Astrophys. J.*, **269**, 281.

Burrows, A., 1987, *Astrophys. J. (Letters)* , **318**, L57.

Colgate, S.A. and White, R.H., 1966, *Astrophys. J.*, **143**, 626.

Danziger, I.J.(ed.), 1987, proceedings of the *ESO Workshop on the SN 1987A*, ESO, Garching b. München, FRG.

Durisen, R.H. and Imamura, J.N., 1981, *Astrophys. J.*, **183**, 215.

Epstein, R.I., 1979, *Mon. Not. Roy. Astron. Soc.*, **188**, 305.

Eriguchi, Y. and Müller, E., 1984, *Astron. Astrophys.*, **147**, 161.

Fuller, G.M., Fowler, W.A. and Newman, M.J., 1982, *Astrophys. J.*, **252**, 715.

Goldreich, P. and Weber S.V., 1980, *Astrophys. J.*, **238**, 991.

Glendenning, N.K., 1988, LBL preprint, submitted to *Phys. Rev. Lett.*

Hillebrandt, W., 1982, *Astron. Astrophys.*, **110**, L3.

Hillebrandt, W., 1986, in NATO ASI on *High Energy Phenomena Around Collapsed Stars*, ed. F.Pacini (Reidel, Dordrecht).

Hillebrandt, W., Nomoto, K. and Wolff, R.G., 1984, *Astron. Astrophys.*, **133**, 175.

Hillebrandt, W. and Wolff, R.G., 1985, in *Nucleosynthesis: Challenges and New Developments*, eds. W.D.Arnett and J.W.Truran, (Univ. Chicago Press).
Janka, H.T. and Mönchmeyer, R., 1989, in preparation.
Joss, P.C. and Rappaport, S.A., 1984, *Ann. Rev. Astron. Astrophys.*, **22**, 537.
Le Blanc, J.M. and Wilson, J.R., 1970, *Astrophys. J.*, **161**, 541.
Ledoux, P., 1945, *Astrophys. J.*, **102**, 143.
Mazurek, T.J., 1975, *Astrophys. Space Sci.*, **35**, 117.
Mönchmeyer, R. and Müller, E., 1989, in preparation.
Mönchmeyer, R., Wolff,R.G. and Müller,E., 1989, in preparation.
Müller, E. and Hillebrandt, W., 1979, *Astron. Astrophys.*, **80**, 147.
Müller, E. and Hillebrandt, W., 1981, *Astron. Astrophys.*, **103**, 358.
Müller, E., Różyczka, M. and Hillebrandt, W., 1980, *Astron. Astrophys.*, **81**, 288.
Nomoto, K. and Hashimoto, M., 1987, *Physics Reports* in press.
Ohnishi, T., 1983, *Tech. Rep. Atom. Energy Kyoto Univ.*, **198**.
Ostriker, J.P. and Bodenheimer, P., 1973, *Astrophys. J.* **180**, 171.
Ostriker, J.P. and Tassoul, J.L., 1969, *Astrophys. J.* **155**, 987.
Sato, K., 1975, *Prog. Theor. Phys.*, **54**, 1352.
Symbalisty, E.M.D., 1984, *Astrophys. J.*, **285**, 729.
Tassoul, J.-L., 1978, *Theory of Rotating Stars*, Princeton Univ. Press.
Taylor, J.H., 1987, in *Proceedings of the 13th Texas Symposium on Relativistic Astrophysics*, (World Scientific Publ. Co. Pte Ltd., Singapore).
Tohline, J.E., 1984, *Astrophys. J.*, **285**, 721.
Tohline, J.E., Schombert, J.M. and Boss, A.P., 1980, *Space Sci. Rev.*, **27**, 555.
van Riper, K.A. and Lattimer,J.A., 1981, *Astrophys. J.*, **249**, 270.
Weaver, T.A., Woosley, S.E. and Fuller, G.M., 1985 in *Numerical Astrophysics*, eds. J. Centrella, J. LeBlanc and R. Bowers, (Jones and Bartlett, Boston).
Wheeler, J.C., 1987, in *Proceedings of the 13th Texas Symposium on Relativistic Astrophysics*, (World Scientific Publ. Co. Pte Ltd., Singapore).
Wilson, J.R., 1985, in *Numerical Astrophysics*, eds. J. Centrella, J. LeBlanc and R. Bowers, (Jones and Bartlett, Boston).
Wilson, J.R., 1988, talk presented at the Aspen Winter Workshop on the Supernova 1987A.
Wilson, J.R., Mayle, R.W., Woosley, S.E. and Weaver, T.A., 1986, in *Proceedings of the 12th Texas Symposium on Relativistic Astrophysics*, Annals N. Y. Acad. Sci.
Woosley, S.E., 1986, in *Nucleosynthesis and Chemical Evolution*, 16th Advanced Course of the Swiss Academy of Astronomy and Astrophysics, ed. B. Hauck and A. Maeder, (Geneva Observatory, Sauverny, Switzerland).
Yahil A. and Lattimer, J.M., 1982, in NATO-ASI on *Supernovae: A Survey of Current Research*, ed. M.J. Rees and R.J. Stoneham, (Reidel, Dordrecht).

NEUTRON STAR EVOLUTION AND THE BIRTH PROPERTIES OF RADIO PULSARS

Rachel J. Dewey
Jet Propulsion Laboratory
4800 Oak Grove Drive
Pasadena, CA 91109
USA

ABSTRACT. Because very few radio pulsars are observed within a few thousand years of their formation our knowledge of their birth properties is intimately connected with our understanding of the evolution of the pulsar population as a whole. The first two sections of this paper outline the most commonly invoked model of pulsar evolution and review the observed properties of the pulsar population in the context of this model. The third section outlines some possible shortcomings of this model, looking particularly at the possible effects of binary evolution, the possiblity that some pulsars are formed in the accretion-induced collapse of white dwarfs, and the possiblity that some pulsars are born as slow rotators.

KEYWORDS: pulsars - stars: evolution - stars: neutron

1. INTRODUCTION: THE STANDARD MODEL

There is a widely accepted model for the birth and evolution of radio pulsars which can be summarized as follows: Pulsars are born in Type II supernovae, when a star of $8\,M_\odot$ or larger explodes. If the star initially had a companion, the explosion disrupts the binary system. The explosion takes place in or close to the plane and the pulsar receives a velocity kick which eventually sends it out of the plane. The star's angular momentum and magnetic flux are approximately conserved in the collapse, so the pulsar's initial period is small (~ 10 ms) and its initial magnetic field is large (10^{12} - 10^{13} G). Because of its high spin rate and high magnetic field, the pulsar's energy loss is large and powers a Crab-like plerion nebula for the first few thousand years of the pulsar's life. In time the pulsar slows down and its magnetic field decays, leading to a decrease in its energy loss rate and radio luminosity. The pulsar spends most of its observable lifetime with a period of several tenths of a second or more and a magnetic field of 10^{11} - 10^{12} G. Finally, after about 10 Myr the pulsar "dies" because the slow spin rate and weakened magnetic field cease to support the production of radio radiation.

The wide acceptance of the model just outlined (hereafter, "the standard model"), is due to its compatibility both with much of the theoretical understanding of neutron stars,

H. Ögelman and E. P. J. van den Heuvel (eds.), Timing Neutron Stars, 573–591.

and with many radio pulsar observations. However, even if many features of this model are correct, it is certainly not a complete model. This paper examines the properties of the pulsar population in the context of this model, and tries to identify some of its shortcomings. I have not attempted anything approaching a complete discussion of either the observational data on pulsars or the wide variety of scenarios for pulsar formation and evolution. A much more complete discussion of the observed pulsar population and models of pulsar evolution is given by Taylor and Stinebring (1986), and much of the background information on pulsar physics and its relation to pulsar observations can be found in Manchester and Taylor (1978). In recent years it has become clear that the formation of pulsars in binary systems can significantly affect their observable properties; models of binary evolution and their relation to pulsar evolution are discussed by, among others, van den Heuvel (1984, 1987, also this volume)[1], Dewey and Cordes (1987) and references therein. Extensive discussions of supernova physics and its relation to the formation of neutron stars can be found in Woosley and Weaver (1986), Burrows (1985), Trimble (1984) and references therein. Further information on almost any issue discussed in this paper can be found in the proceedings of IAU symposium No. 125 (Helfand and Huang 1987).

2. THE RADIO PULSAR POPULATION

The major directly observable properties of pulsar are its period, P, period derivative, $\dot{P}$, flux density, S, dispersion measure, DM, and location in the sky. These, combined with some model-dependent assumptions, provide estimates of other pulsar parameters, including age, distance, magnetic field strength, energy loss rate, and radio luminosity. Relating pulsar observations to models of pulsar birth and evolution is not an entirely straight forward processes. It involves two steps of extrapolation, first from the small fraction of the galactic pulsar population that can be observed to a picture of the entire population, and then from the present properties of this population to their evolution over time. Pulsar searches reach only a small fraction of the galaxy, and a search's abitily to detect a pulsar depends not only on the pulsar's luminosity and distance, but on its period, dispersion measure and location in the sky. This results in complicated selection baises which must be accounted for in statistical analyses of the pulsar population. It is important to remember that, in both obvious and subtle ways, properties typical of the of the observed population may not be typical of of the population as whole. These issues are discussed in more detail by Lyne, Manchester and Taylor (1985) and Narayan (1987). Despite these difficulties, much useful information can be obtained from the properties of the observed pulsar population.

2.1 P, $\dot{P}$ and related quantities

There are presently about 450 known pulsars; these have pulse periods in the range

$$1.55\,\mathrm{ms} < P < 4.3\,\mathrm{s} \quad .$$

[1] At a number of places I refer to work presented at this ASI, assuming that it appears in these proceedings. My apologies if for some reason this is not the case.

The period derivatives of over 350 pulsars have been measured; these have values in the range

$$2 \times 10^{-20}\,\mathrm{s\,s^{-1}} < \dot{P} < 1.5 \times 10^{-12}\,\mathrm{s\,s^{-1}} \quad .$$

The quantities P and $\dot{P}$ provide a direct indication of a pulsar's evolution in time, and in most models are intimately connected with the properties of the neutron star and its past history. A plot of P *vs.* $\dot{P}$ is, therefore, very useful in discussing pulsar evolution. Figure 1 shows such a plot for 364 pulsars with measured values of $\dot{P}$; pulsars associated with supernova remnants are shown stars (*) and binary pulsars by circled dots. There are number of notable features in this plot. First, the large majority of pulsars lie in the region $0.3 \leq P \leq 2\,\mathrm{s}$ and $10^{-17} \leq \dot{P} \leq 3 \times 10^{-14}\,\mathrm{s\,s^{-1}}$. However, pulsars with short periods ($P \leq 100\,\mathrm{ms}$) tend to have either unusually large or unusually small period derivatives while binary pulsars tend to have smaller values of both P and $\dot{P}$ than the population as a whole[2]. Finally, there is a marked absence of pulsars in the lower righthand portion of the diagram. As discussed below, pulsars generally move from the upper left portion of the diagram to the lower right during their lifetimes. The dotted line $\dot{P}/P^3 \approx 2 \times 10^{-17}\,\mathrm{s^{-3}}$ is often refered to as the pulsar "death line"; neutron stars falling below this line apparently no longer function as radio pulsars. The dashed line in the figure, the "spin-up" line, is discussed further in §3.1. In most pulsar models P and $\dot{P}$ are related to a many of the physically interesting properties of the neutron star. The following discussion outlines these relations for the case where pulsar evolution is dominated by the effects of its dipole magnetic field.

The quantity $P/\dot{P}$ gives the timescale on which a pulsar's period changes, and in most models is related directly to the pulsar's age. The characteristic age, defined as

$$\tau = \frac{P}{2\dot{P}} \quad ,$$

is equal to the pulsar's true age if the pulsar's initial period was much smaller than its current period, the effects of magnetic field decay and/or alignment (see below) have been neglible, and the period has evolved solely due to magnetic dipole torques. For most pulsars τ probably provides upper limit to the age: a longer birth period and the effects of field decay or alignment both cause τ to overestimate the true age of the pulsar. The situation is more complicated for "spun-up" pulsars (see §3.1), since the spin-up which decreases P also reduces τ. For such pulsars τ provides a rough upperlimit on the time since spin-up ended, and (barring significant field decay) a rough lower limit on the pulsar's remaining active lifetime. Figure 2a shows lines of τ superimposed on the $P\dot{P}$ diagram.

The rate at which a pulsar loses rotational kinetic energy is given by

$$\dot{E} = \frac{4\pi^2 I \dot{P}}{P^3} \quad ,$$

where I is the pulsar's moment of inertia. This expression is valid regardless of the slowdown mechanism, but is uncertain to the extent that I is uncertain. For a pulsar radius of 10 km and mass of $1.4\,\mathrm{M_\odot}$, $I \approx 10^{45}\,\mathrm{g\,cm^2}$, yielding

$$10^{30}\,\mathrm{erg\,s^{-1}} \lesssim \dot{E} \lesssim 10^{38}\,\mathrm{erg\,s^{-1}}$$

[2] Two recently discovered binaries not shown in Fig. 1, with periods of 1.6 ms (Fruchter *et al.* 1988b), and 11 ms (Lyne *et al.* 1988), confirm the tendency of binaries to have short rotational periods.

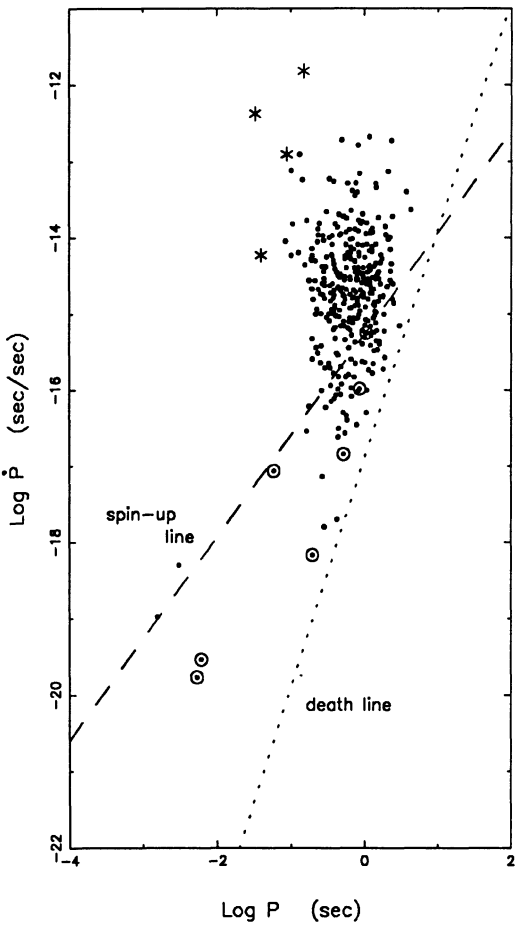

FIGURE 1. P *vs.* $\dot{P}$ for the 364 pulsars with measured values of $\dot{P}$. Binary pulsars are shown by circled dots, and pulsars associated with supernova remnants by stars (*).

for the observed pulsar population. Figure 2b shows lines of constant $\dot{E}$ superimposed on the $P\dot{P}$ diagram. Note that these lines are parallel to the "death-line" shown in Fig 1.

If a pulsar's spindown is due only to torques produced by the rotation of its dipole magnetic field, the strength of this field is given by:

$$B = \left(\frac{3Ic^3}{8\pi^3 R^6 \sin^2\alpha}\right)^{1/2} (P\dot{P})^{1/2} \quad ,$$

where R is the pulsar radius, and α is angle between the magnetic field and spin axes. For

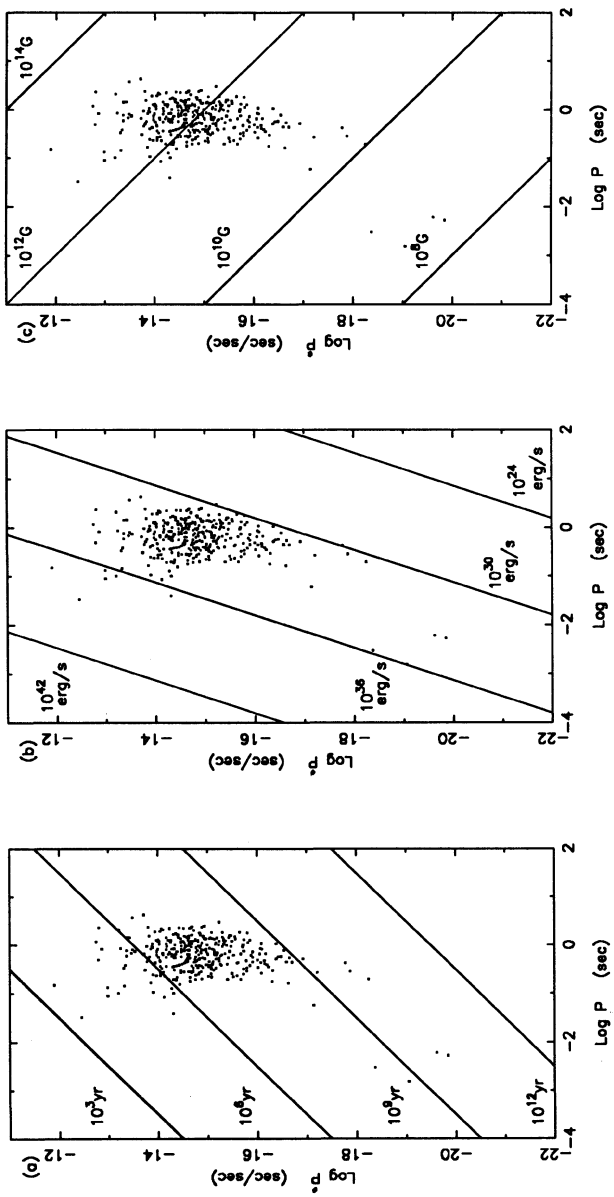

FIGURE 2. Lines of constant charcteristic age (a), energy loss rate (b) and magnetic field (c) superimposed on the $P\dot{P}$ diagram. An expanded plot of P *vs.* $\dot{P}$ is shown in Fig 1.

standard pulsar parameters, and the assumption $\sin\alpha \approx 1$, this relation can be approximated

$$B_{12} \approx \left(P\dot{P}_{-15}\right)^{1/2} \quad ,$$

where B_{12} is measured in units of 10^{12} G, P in seconds and $\dot{P}_{-15}$ in $10^{-15}\,\mathrm{s\,s^{-1}}$. With this relation the magnetic fields of known pulsars lie in the range

$$3 \times 10^8\,\mathrm{G} \lesssim B \lesssim 2 \times 10^{13}\,\mathrm{G} \quad .$$

Figure 2c shows lines of constant B superimposed on the $P\dot{P}$ diagram.

In no realistic pulsar model is the relation between a pulsar magnetic field and slowdown rate as simple as that just described. The actual relation depends on the physics neutron star magnetospheres which is extremely complicated and not yet well understood. The above expressions provide at best an approximate indicator of a pulsars magnetic field; nevertheless they provide the basis for all discussions of pulsar magnetic field strength in this paper.

As can be seen in Figure 2a, as a pulsar ages it moves downward and to the right in the $P\dot{P}$ diagram (from small to large τ). If the magnetic field (as given above) remains constant, this evolutionary track lies along a line of constant $P\dot{P}$ (Fig. 2c). Statistical analyses of the pulsar population (*e.g.* Lyne, Manchester and Taylor 1985) suggest that the tracks are infact steeper than that, in other words that $P\dot{P}$ decreases over a pulsar's lifetime. This decrease is usually attributed to magnetic field decay on a 5 to 10 Myr timescale. In the context of the simple dipole torque model a systematic decrease in $\sin\alpha$ (*i.e.* alignment of the magnetic field and spin axes) on the same time scale would produce the same effect. This possibility is discussed by Lyne and Manchester (1988) and Blair and Candy (1988) (also by Blair in this volume).

Figures 3a and 3b show representative evolutionary tracks for assumed magnetic field decay times of 10 Myr and 2 Myr, respectively. In each case track (A), starts at $P = 10$ ms and $B = 3 \times 10^{13}G$, while track (B) starts at $P = 10$ ms and $B = 3 \times 10^{11}$. In both cases these two tracks bracket a large fraction of the pulsar population. The time it takes a pulsar moving along one of these tracks to reach the death line gives an estimate of that pulsar's observable lifetime. For a 10 Myr field decay time a pulsar moving on track (A) takes 4 Myr to reach the death line, as compared to 40 Myr for a pulsar on track (B). For a 2 Myr decay time the times are 4 Myr and 13 Myr, respectively.

2.2 Dispersion measure, distance and luminosity

Because of the dispersive effects of the ionized interstellar medium, pulsar pulses at high radio frequencies arrive at the earth slightly earlier than those at low frequencies; the extent of this delay provides a direct measurement of the column density of electrons along the line of sight to the pulsar (the pulsar's dispersion measure). This number, when combined with a model of the galactic electron distribution, provides an estimate of the pulsar's distance. The dispersion measures of known pulsars range from $3\,\mathrm{cm^{-3}\,pc}$ to $1140\,\mathrm{cm^{-3}\,pc}$. Using the electron density model of Lyne, Manchester and Taylor (1985)[3] the distances of the known pulsars range from

[3] As a rough rule of thumb a dispersion measure of $30\,\mathrm{cm^{-3}\,pc}$ translates to a distance of 1 kpc.

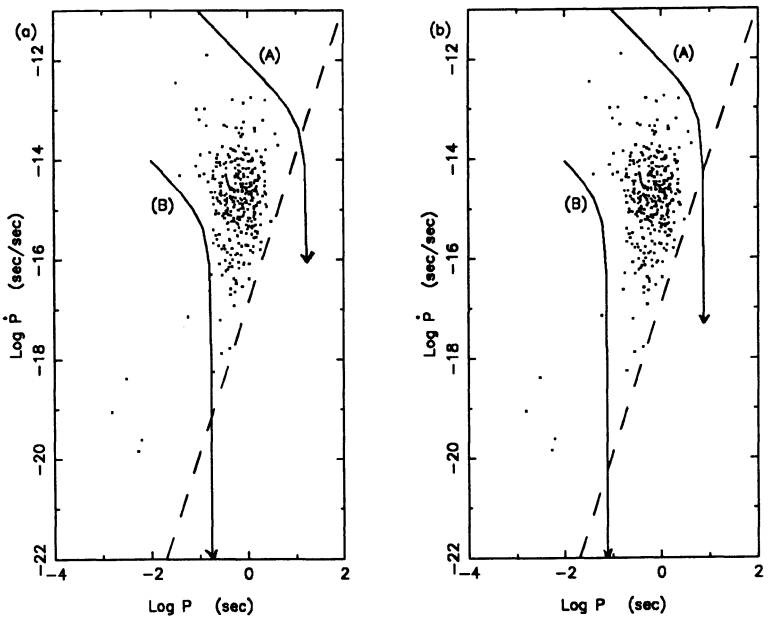

FIGURE 3. Representative evolutionary tracks assuming magnetic field decay times of 10 Myr (a) and 2 Myr (b) superimposed on the $P\dot{P}$ diagram. The dashed lines on each plot represent the "death line".

80 pc to 32 kpc within the Galaxy; over half are less than 3 kpc. There is one known radio pulsar in the Magellanic Clouds.

The observed time-average flux densities of pulsars at 400 MHz, S_{400}, range from about 1 mJy, (the limit of the most sensitive surveys), to 5000 mJy. Pulsars are steep spectrun sources, with $S_\nu \propto \nu^{-2}$ being fairly typical. A pulsar's radio luminosity is usually defined by $L_\nu = S_\nu d^2$, where d is the distance to the pulsar. In standard pulsar units the 400 MHz luminosities, L_{400}, of the known pulsars ranges from 1 to 15000 mJy kpc^2. Translating to more common units, 1 mJy kpc^2 is roughly equivalent to 10^{11} erg s^{-1} Hz^{-1}. Even for the strongest pulsars the total luminosity integrated over the radio band accounts for only a small fraction of the total energy loss.

Its it generally believed that there should be some relation between radio luminosity and P and $\dot{P}$. Gunn and Ostriker (1970) suggested $L \sim B^2$ (*i.e.* $L \sim P\dot{P}$), a model which has been used for many analyses of the pulsar population. However statistical studies of the data (*e.g.* Proszynski and Przybycien 1984, Narayan 1987) suggest that $L \sim \dot{P}^{1/3}P^{-1}$ may be more realistic. Figure 4 shows scatter plots of L_{400} *vs.* $P\dot{P}$ and L_{400} *vs.* $\dot{P}^{1/3}P^{-1}$ for 364 pulsars. The correlation between the logarithms of L and $\dot{P}^{1/3}P^{-1}$ is 0.43 while between L and $P\dot{P}$ it is 0.12. Note, however, the very large scatter even around the $L \sim \dot{P}^{1/3}P^{-1}$ relation.

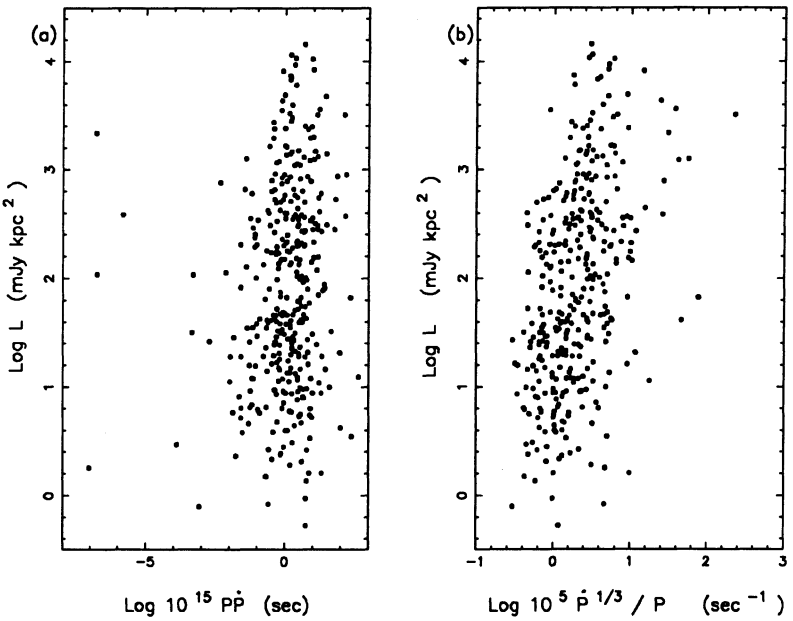

FIGURE 4. Scatter plots of radio luminosity L_{400} against two proposed luminosity laws, $L \sim P\dot{P}$ (a), and $L \sim \dot{P}^{1/3}P^{-1}$ (b).

2.3 Coordinates, velocities and relation to progenitors

Figure 5 shows the location of 442 known pulsars in galactic coordinates. Pulsars are concentrated at low galactic latitudes, and towards the inner portion of the galaxy. This distribution is similar to the distribution of the massive stars assumed to be their progenitors. The major difference is that the scale height of pulsars around the galactic plane ($\approx$ 350 pc) is significantly larger than that of massive stars ($\approx$ 70 pc). However, pulsars are observed to have high velocities, averaging 100 - 200 km s^{-1}, and can easily move a few hundred parsecs in lifetimes of a few million years. The exact origin of the high pulsar velocities is still unclear, but it is probably due in part to the break-up of binary systems (*e.g.* Gott, Gunn and Ostriker 1970, van den Heuvel 1981), and in part to asymmetries in supernova explosions (Dewey and Cordes 1987).

Unlike massive stars, most ($\sim$ 80%) of which are in binary systems, the vast majority ($\gtrsim$ 97%) of observed pulsars are single. It is becoming increasingly clear that the small number of observed binary pulsars is due in part to the insensitivity of many pulsar surveys to short spin periods; Taylor (1987) estimates that about 10% of observable pulsars may be members of binaries. However binary pulsars appear to have significantly longer lifetimes than single pulsars, so it is unlikely that the *birthrate* of binary pulsars is more than at most a few percent of the birthrate of single pulsars. The processes which form pulsars must, therefore, disrupt binary systems very efficiently. As discussed in §3, this observation can be used to constrain

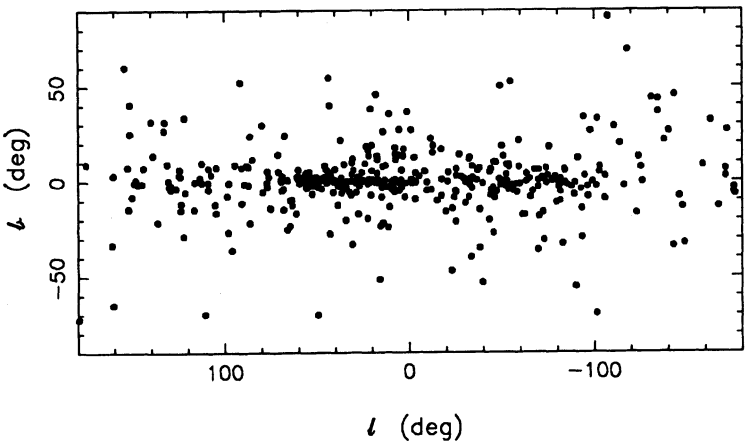

FIGURE 5. The distribution of 442 known pulsars in galactic coordinates. The large concentration at positive longitudes in the inner portion of the Galaxy compared to negative longitudes, is due to the large number of high sensitivity surveys carried out from the northern hemisphere.

possible models of pulsar formation (see also Dewey and Cordes 1987).

If pulsars are formed in Type II supernovae, one expects them to be associated with supernova remnants. There are approximately 450 known pulsars and approximately 150 catalogued galactic supernova remnants, but in only four cases is there a clear association between the two types of objects. The existence of pulsars not associated with supernova remnants is easily understood: the observable lifetimes of pulsars are much longer than those of supernova remanants. The existence of supernova remnants without central pulsars is perhaps more surprising, but there are a number factors which may cause this. First, a third to a half (van den Bergh, McClure and Evans 1987) of the supernovae occuring in the Galaxy are expected to be Type I events, which probably result from the total disruption of an accreting white dwarf (*e.g.* Trimble 1984) and do not produce neutron stars. Some fairly massive stars may also completely disrupt as they explode (Sugimoto and Nomoto 1980) leaving a supernova remnant but no neutron star. Second, some fraction of massive stars probably end thier lives as black holes rather than neutron stars; at present it is unclear what this fraction is, and whether such collapses result in explosions that look like Type II supernovae. Third, some unknown fraction of active pulsars are not beaming towards earth. A beaming fraction, f, of approximately 0.2 (*i.e.* one fifth of active pulsars beam in our direction) is often assumed, but some studies suggest that f may be significantly larger, particularly for short period pulsars (Narayan and Vivekenand 1983, see also Lyne and Manchester 1988). If all young pulsars are surrounded by a Crab-like plerion nebula, these should provide a beaming-independent means of identifying neutron stars in supernova remnants, as well as providing information about the beaming factor

(Becker 1987, Seward 1987, also Helfand in this volume). Finally, most supernova remnants are quite distant, so any pulsars in them are would be hard to detect.

2.4 Young pulsars

The four pulsars associated with galactic supernova remnants are listed in Table 1. Also listed in Table 1 is a pulsar, so far detected only at optical and X-ray wavelenths, associated with the remnant 0540-64.3 in the Large Magellanic Cloud (Seward 1987 and references therein), with properties very similar to the Crab. As would be expected from the standard model these all have short periods, large slowdown rates, small characteristic ages and relatively high magnetic fields. However, given the present parameters of these pulsars, there must have been considerable variation in their properties at birth. For example, PSR1951+32 has the largest characteristic age of these four pulsars, yet has a period only a six milliseconds longer than the Crab, the youngest of the pulsars. PSR1509−58, with a characteristic age only slightly larger than the Crab, has a period five times as long and a magnetic field five times larger.

TABLE 1

Pulsar	Remnant	P (ms)	$\dot{P}$ (10^{-15} s s^{-1})	τ (yr)	B (10^{12} G)
0531+21	Crab nebula	33.	420.	1240	3.7
0540−69	0540-64.3 (LMC)	50.	479.	1670	4.9
0833−45	Vela	89.	125.	11000	3.3
1509−58	MSH15-52	150.	1520.	1560	15.
1951+32	CTB80	40.	5.92	110000	0.5

The Crab pulsar, since its discovery in 1968, has provided the standard picture of a young pulsar, so it useful to look at it in somewhat more detail. It is the only known pulsar connected with a historical (1054AD) supernova. It has the smallest characteristic age of any pulsar and the shortest period of any pulsar not believed to have undergone spin-up. It energy loss rate is more than twenty times higher than that of any other pulsar in the Galaxy; however, nineteen pulsars have higher values of L_{400}. It is one of the few pulsars for which $\ddot{P}$ has been measured (-2.8×10^{-24} s^{-1}). This allows one to compare a pulsar's observed period evolution with that predicted by various theoretical models. The comparison is generally parametized by the "braking index", n, defined by the relation $\dot{P} \propto P^{2-n}$. For the Crab pulsar $n = 2.5$, reasonably close to the value expected for pure magnetic dipole radiation, $n = 3$. A braking index has also been measured for PSR1509-58 which, at $n = 2.8$, is also close to that expected for dipole radiation.

Unlike most radio pulsars, the Crab pulsar emits pulsed radiation throughout most of the observable spectrum: at infra-red, optical, x-ray and γ-ray, as well as radio wavelengths. The luminosity integrated over all bands, $\gtrsim 10^{35}$ erg s^{-1}, is compatible with the pulsar's total energy loss rate. The pulsar is surrounded by a continuum nebula, which also emits from radio to γ-ray wavelengths, with a total luminosity of about 10^{38} erg s^{-1}. Until the discovery of the

pulsar, the source of energy powering the emission from the nebula was unknown; the lifetimes of the electrons producing the high energy radiation are much less than the age of the nebula. Shortly before the discovery of pulsars, Pacini (1967) suggested that a rotating, magnetized neutron star could provide the requisite energy, and infact, the pulsar, losing rotational kinetic energy at a rate of $5 \times 10^{38}\,\mathrm{erg\,s^{-1}}$ easily does so. Though the Crab nebula is brighest such nebula, a number of other radio pulsars (all with large values of $\dot{E}$) are associated to with high energy continuum emission (see Helfand, this volume). Many models suggest that if pulsars resemble the Crab pulsar at birth, they should, when young, be associated with plerion nebulae very similar to the Crab.

2.5 The pulsar birthrate and the deathrate of massive stars

According the standard model, the pulsar birthrate should be equal to the rate at which Type II supernova occur, which in turn should be equal to the death rate of massive stars. Present evidence suggests that any discrepancies in these rates are not serious, though there are large uncertainties in all of them. A number of calculations (*e.g.* Lyne, Manchester and Taylor 1985, Narayan 1987) arrive at a pulsar birthrate of about 1 per 60 yr in the Galaxy. The uncertainty in this rate is about a factor of two in either direction and is due to uncertainties in the beaming factor and in pulsars lifetimes, and to the heavy reliance of the calculations on the small number of low luminosity pulsars nearby enough to be detected.

Current estimates of the supernova rate (*e.g.* Tammann 1982, van den Bergh, McClure and Evans 1987) lie in the range 1 per 30 to 110 yr in the Galaxy, with about half of these being Type II. The birthrate of Crab-like supernova remnants (plerions) appears to be somewhat lower: 1 per 120 to 300 yr (Reynolds and Fix 1987, Srinivasan, Battacharya and Dwarakananth 1984), suggesting that some young pulsars may not be associated with such objects even in their earliest years. The relevant stellar death rate depends on the mass range of pulsar progenitors. To produce one pulsar every 50 yr, standard galactic birthrates (*e.g.* Miller and Scalo 1979) require all stars larger than $9\,M_\odot$ form pulsars, or alternately, all stars in the range 8 - $30\,M_\odot$, or as another alternative, all stars in the range 6 - $11\,M_\odot$. These ranges are based on pulsar and stellar birthrates calculated for the Galaxy as a whole. Blaauw (1986) examines the local pulsar birthrate and local stellar deathrate and concludes that all stars larger than $6\,M_\odot$ must form pulsars. The pulsar birthrate is then compatible with stellar death rates, as long as all (or at least most) stars larger than 6 - $9\,M_\odot$ form pulsars. This is compatible with current theoretical supernova models which suggest that stars larger than about $8\,M_\odot$ are the progenitors of neutron stars (*e.g.* Trimble 1984, Woosley and Weaver 1986).

3. SHORTCOMINGS OF THE STANDARD MODEL

From the evidence discussed above, the standard model outlined in the introduction, appears to be a good first order description of pulsars birth and evolution. However, many questions remain as to just how complete a description it is. This section outlines a number of possible complications to the simple picture described earlier and considers three (the effects of binary evolution, the possibility of formation via white dwarf collapse, and "injection" at long periods) in some detail.

Perhaps the most obvious problem with the standard model is that some pulsars clearly do not fit. These are the millisecond pulsars in the lower left region of the $P\dot{P}$ diagram (Fig. 1) which have very short periods but also very small slowdown rates and very small magnetic fields. Instead of being very young, these pulsars appear to be very old. Though it is conceivable that these pulsars were simply born with low magnetic fields, the absence of a continuum in the $P\dot{P}$ plane from Crab-like pulsars to millisecond pulsars suggests otherwise, as does the high incidence of binaries among short period pulsars. Four of the six known pulsars with periods below 12 ms are members of binary systems, and as discussed below, the anomalous properties of these pulsars appear to be the result of binary evolution. Since a large fraction of pulsar progenitors begin thier lives in binary systems, the possibility that many seemingly ordinary pulsars have been effected by a binary past should be considered. If this is the case, statistical determination of quantities such as the magneitc field and luminosity decay times, pulsar lifetimes, or estimates of the initial pulsar period distribution may be in error.

As mentioned in §2.3 it is possible that not all Type II supernova produce neutron stars. More important for understanding the pulsar population is the possiblity that some pulsars are produced by processes other than Type II supernovae. One alternate process is the accretion induced collapse of a white dwarf, and since white dwarfs are numerous objects, this process could contribute substantially to the pulsar birthrate. If it does, the properties of these pulsars may be significantly different from the properties of pulsars formed in collapse of massive stars, and these differences may be important in understanding the evolution of the pulsar population.

Though it is usually assumed that pulsars are born with fields $\gtrsim 10^{12}$ G, this assumption has been questioned on both theoretical and observational grounds. The recent discovery of 1951+32 (Kulkarni *et al.* 1988) an apparently young pulsar with a magnetic field of 5×10^{11} G brought renewed interest in this possibility and in the model proposed by Blandford, Applegate and Hernquist (1983) that pulsar fields are built up over thousands of years by a dynamo mechanism. Timing measurements should soon indicate if this pulsar's field is infact growing on such timescales (Fruchter *et al.* 1988a), but as yet there is little direct evidence for late turn-on of magnetic fields. The Crab pulsar shows that some pulsars have strong fields within 1000 yr of their birth, and 1951+32 may not be as anomalous as a comparision with the Crab and the other pulsars listed in Table 1 might suggest. In a statistical analysis of the pulsar population, Lyne, Manchester and Taylor (1985) conclude that the mean pulsar magnetic field at birth is 7.5×10^{11} G, only slightly larger than the field of 1951+32. As can be seen in Figure 3, 1951+32 and the rest of the pulsar population (excepting millisecond pulsars) are compatible with a model in which pulsars are born with fields in the range 3×10^{11} G - 3×10^{13} G which decay on times scales of 5 - 10 Myr.

A number of authors have questioned the assumption that all pulsars are born with short spin periods, and suggest that a substantial fraction of pulsars are born with periods of a few hundred milliseconds. This hypothesis is commonly refered to as "injection" (the idea being that pulsars are "injected" into the population at long periods). The best direct evidence for this hypothesis would be the discovery of a long period pulsar in a supernova remnant. As yet none has been found, but, given the small number of pulsar - SNR associations, this does not provide a strong argument against the hypothesis. As discussed in §3.3, evidence for injection (and it is by no means conclusive) comes mainly from statistical analyses of the pulsar population which suggest that there are not enough young pulsars observed to sustain

the population of older pulsars. The scarity of Crab-like supernovae remnants in the Galaxy is also cited as evidence that some pulsars are born rotating slowly (Battacharya and Srinivasan 1987), because, if they are rapidly rotating ($P \lesssim 50\,\mathrm{ms}$), neutron stars with high magnetic fields ($B \gtrsim 10^{12}\,\mathrm{G}$) should power observable plerion nebulae independent of their observability as radio pulsars.

3.1 Binary evolution and spun-up pulsars

Most main sequence stars ($\approx 80\%$) have at least one companion, whose presence may, depending on the system's parameters, have a marked effect on the primary's evolution, and on the observable properties of any neutron star it produces. The formation of pulsars in binary systems is often used to explain the properties of individual pulsars as well as certain characteristics of the pulsar population as a whole; most relevant to the present discussion is the possibility that binary evolution causes pulsars to deviate significantly from a simple "born fast, slowdown, fade and die" life history.

In a binary system of main sequence stars formed at (approximately) the same time, the more massive star (the primary) evolves more quickly than its companion. If the binary is tight enough (a separation of $\lesssim 1000\,\mathrm{R}_\odot$) the primary overflows it Roche lobe as it leaves the main sequence and becomes a red giant. Mass is then either transfered to the companion or lost from the system. If the orginal mass of the primary is large enough ($\gtrsim 8$ - $12\,\mathrm{M}_\odot$, depending on how much mass loss takes place) its core eventually explodes as a supernova, forming a neutron star. If, assuming a circular orbit and a symmetric explosion, half the total pre-explosion mass of the system is ejected, the system becomes unbound. This is the fate of most binary systems, particularly the substantial fraction of wide systems in which mass tranfer does not occur (Dewey and Cordes 1987). However, if the mass ratio of the original binary is close to unity, or if the secondary accretes a significant amount of mass, the system can survive the explosion intact. It is this case that is of interest here.

If binary is disrupted, the neutron star formed in the supernova should look very similar to puslars produced in the explosion of single stars, except, sometimes, for a higher velocity. If the system remains bound it consists of the neutron star remnant of the primary and the secondary which is usually still near the main sequence. To date no radio pulsar with a main sequence companion has been found which may be due simply to the small number statistics of binary pulsars. However, it may be an indication that the presence of a main sequence companion (through the effects, perhaps, of its stellar wind) prevents a neutron star from acting as an observable radio pulsar.

If, during its evolution, the secondary overflows its Roche lobe, mass is transfered to the neutron star, which then probably appears as an X-ray source but not a radio pulsar. This accretion is believed to produce the combination of short period and small slowdown rate seen in millisecond pulsars. Detailed descriptions of this scenario can be found in Alpar *et al.* (1982) and van den Heuvel (1984, 1987). To summarize the argument briefly: angular momentum, as well as mass, is transfered from the evolving star to the neutron star, with the amount of angular momentum depending on the velocity of the matter when it is captured by the neutron star. The point at which capture takes place is determined by the strength of the neutron star's magnetic field: the weaker the field, the closer to the neutron star capture occurs, and the larger

the Keplerian velocity and specific angular momentum of the accreted matter. The neutron star accretes matter and angular momentum until it is co-rotating with the infalling matter at the capture radius, at which point equilibrium is reached. In this model the equilibrium spin period of the pulsar, P_{eq}, is proportional to $B^{6/7}$. Standard pulsar parameters and accretion at the Eddington limit yield

$$P_{eq} \approx 2B_9^{6/7} \quad \text{ms} \quad ,$$

where B_9 is the magnetic field in units of 10^9 G. This can also be written $\dot{P} \approx 10^{-15}P^{4/3}$, which is shown as the "spin-up line" in Figure 1. According to this model, spun-up pulsars should lie near or below the spin-up line as the millisecond and binary pulsars do.

Clearly, to be spun up to millisecond periods, neutron stars must have magnetic fields significantly smallar than the 10^{12} G fields that, according to standard model, they have at birth. This is one of the strongest arguments for magnetic field decay in neutron stars: for the spin-up model to work, the actual magnetic field, not just the spin down torque it produces, must be low. Pulsars with large magnetic fields but small spin-down torques (because, for example, the magnetic field and spin axes are aligned) can not, according to this model, be spun up to millisecond periods.

Assuming magnetic field decay takes place independent of accretion (*e.g.* Taam and van den Heuvel 1986), P_{eq} depends on the time elapsed between the formation of the neturon star and the end of mass transfer, which depends on the mass of the secondary. The less massive the secondary, the smaller P_{eq}. Whether the system remains bound after the secondary has completed its evolution also depends on the secondary's mass. If it is massive enough it will explode as a supernova and form a neutron star. In this case there is a high probability that the system is disrupted, producing two isolated neutron stars, one of which may have undergone spin-up, and one of which is an ordinary young pulsar. If the binary is not disrupted by this explosion, the final system consists of two neutron stars in an eccentric orbit, as seen in PSRs 1913+16 and 2303+46. Slightly less massive secondaries may disrupt completely in a carbon deflagration supernova, leaving the remnant of the primary as an isolated, possibly spun-up neutron star. Many of the less massive secondaries collapse quietly to white dwarfs, leaving the system bound. PSRs 0655+64, 0820+02, and 1855+09 (and probably the other circular binary pulsar systems) are of this type. The discovery of PSR1957+20 (Fruchter *et al.* 1988b, also in this volume) suggests that in some binaries the radiation from the neturon star eventually evaporates the companion (*e.g.* Ruderman, Shaham and Tavani 1988, Phinney *et al.* 1988, see also Ruderman and Shaham in this volume), explaining the existence of isolated millisecond pulsars. It is not yet clear whether this mechanism is important to understanding isolated long period pulsars.

Although spin-up scenarios are most commonly applied to binary pulsars, as just seen, some single pulsars have probably been affected, and it is useful to consider what fraction of the total pulsar population these comprise. Dewey and Cordes (1987) in outling the possible paths of binary evolution find that 2 - 15% of single neutron stars may have undergone spin-up; the relevant paths are ones where a binary system survives the explosion of the primary, but not that of the secondary, and in which the neutron star undergoes accretion during the evolution of the secondary. The fraction 2 - 15% is compatible with the observation that about 25% of the pulsars in Figure 1 lie below the spin-up line. The properties of isolated,

spun-up pulsars, in particular their periods and magnetic fields, should depend strongly on the distribution of companion masses and on the timescale for magnetic field decay, and may be useful in constraining scenarios of pulsar evolution in binary systems.

3.2 White dwarf collapse

The evolution of a binary system whose primary has a mass $\lesssim$ 8 - 12 $M_\odot$ is similar to that outlined above, except that the primary forms a white dwarf rather than a neutron star. If the secondary overflows its Roche lobe during its evolution, the white dwarf may accrete enough matter to be pushed over the Chandrasekhar limit and form a neutron star. It has been suggested that a number of the binary pulsars were formed this way (van den Heuvel 1984, 1987). Since many more stars end their lives as white dwarfs than explode in Type II supernovae, the possibility that accreting white dwarfs eventually form pulsars raises the possibility that a condsiderable fraction of the pulsar population might be formed this way. Such pulsars could be expected to have birth properties significantly different from those formed in Type II supernovae. In particular, they would probably have smaller velocities, and possibly a wider initial z-distribution. It is easy to imagine that their initial period and magnetic field distributions would be different from those of normal pulsars, though the nature of these differences is hard to assess.

Current research (*e.g.* Nomoto 1987, Woosley 1987 and references therein) suggests that only a small fraction of accreting white dwarfs do, in fact, form neutron stars. The best candidates appear to be ONeMg white dwarfs formed from massive (8 - 12 $M_\odot$) stars which have undergone mass loss, and very old CO white dwarfs. Younger CO white dwarfs probably disrupt completely if enough mass is accreted to trigger an explosion; these are believed to be the progenitors of Type I supernovae. The rate of mass transfer may also be a critical factor in determining which white dwarfs (if any) can collapse to form neutron stars. For a large range of accretion rates, nova outbursts on ths surface of the white dwarf prevent a sufficient amount of mass from accreting.

The best constraint on the number of pulsars formed from collapsing white dwarfs may be provided by the scarcity of binary pulsars. It is difficult for collapsing white dwarfs to form single neutron stars, since very little mass is ejected in the process. For the system to become unbound, the secondary must either be massive enough to explode and disrupt the system, or in some way be completey disrupted itself. The number of systems in which the secondary is massive enough to explode, even though the primary formed a white dwarf, is small, but not negligible. The results of Dewey and Cordes (1987) suggest that, if only ONeMg white dwarfs are considered, it would take very favorable circumstances for more than 20% of isolated pulsars to be formed this way, and that the number is probably considerably lower. It seems fairly safe to conclude that though white dwarf accretion may be an important mechanism for forming binary pulsars, it probably does not contribute substanstially to the total pulsar birthrate. However, like the spun-up neturon stars described above, pulsars formed via white dwarf collapse may complicate the models needed to fully understand the pulsar population.

3.3 Injection

The major arguments for injection, the hypothesis that some pulsars are born with, or first become visible with, relatively long periods, comes from statistical analyses of the pulsar population. In one of the first of these, Vivekanand and Narayan (1981), consider the "current" of puslars from short to long periods and find that there are not enough short period pulsars to support the population of longer period pulsars. Lyne, Manchester and Taylor (1985) conclude that injection is not required if $L \sim P\dot{P}$, while Chevalier and Emmering (1986), assuming $L \sim \dot{P}^{1/3}P^{-1}$, conclude that it is. These analyses use as their basic data set pulsars discovered in major surveys carried out prior to 1980, all of which suffered from a bias against short period objects (*e.g.* Dewey *et al.* 1984). This raises the possibility that any shortage of young pulsars is due entirely to selection effects.

Narayan (1987) re-does the pulsar current calculation using a similar data set, but with a careful accounting of search selection effects and again finds a need for injection at periods up to 0.5 s. On the other hand Stollman (1987), also using a similar data set, finds no need for injection. The major differences in these two analyses lie in their assumptions about the evolution of pulsar luminosities and beaming factors. Nayaran uses $L \sim \dot{P}^{1/3}P^{-1}$ and, based on the results of Narayan and Vivekanand (1983), assumes that the beaming factor falls from $f \approx 1$ at $P < .2$ s to $f \approx 0.25$ at $P = 1$ s. Both these assumptions suggest that young pulsars should be easily detectable, being very luminous and sweeping out a large fraction of the sky. Stollman, on the other hand, uses a luminosity relation that flattens at large values of $\dot{P}^{1/3}P^{-1}$, and assumes no evolution in the beaming factor. As of now it is impossible to say which of these models is more realistic. However, it appears that doing so will be necessary before the initial period distribution of pulsars can be accurately assessed.

Two recent pulsar searches (Stokes *et al.* 1985, 1986 and Clifton and Lyne 1986) with good period sensitivity to periods as short as 10 - 20 ms should help resolve some of the problematic issues in injection calculations. The searching strategies of the two surveys differed signifcantly; Stokes *et al.* covered a large area of sky and were sensitive mainly to pulsars within 2 - 3 kpc, while Clifton and Lyne concentrated their efforts on a smaller area of sky looking for distant objects in the galactic plane towards the inner portion of the Galaxy. Stokes *et al.* found 20 new pulsars, all with $P > 100$ ms and $DM < 300\,\mathrm{cm}^{-3}\,\mathrm{pc}$. Period derivatives have now been measured for 17 of these pulsars (Dewey *et al.* 1988) and only two show characteristic ages less than 1 Myr. This search, which covered a region of the Galaxy similar to those probed by previous surveys, did not uncover a previously missing population of young pulsars.

Clifton and Lyne found 40 new pulsars, most with $DM > 300\,\mathrm{cm}^{-3}\,\mathrm{pc}$. These pulsars have significantly shorter periods than the observed pulsar population as a whole. As yet only three of these pulsars have published values of $\dot{P}$, but of these, two have $\tau < 25{,}000$ yr (smaller than all but three previously known pulsars), and the third has $\tau \approx 150{,}000$ yr. These preliminary results suggest that the Clifton and Lyne pulsars may be significantly younger than most previously known pulsars. They may, therefore be the pulsars that injection calculations find to be missing. This interpretation, however, is not entirely obvious. The dispersion measures of these pulsars are considerably larger than those of most previously known pulsars, suggesting that Clifton and Lyne probed a more distant portion of the Galaxy than previous searches. If there was a deficiency of young, short period pulsars amoung the local population (on which

most statistical analyses have been based) it is not clear that the Clifton and Lyne discoveries remove it. These pulsars appear to be highly luminous and should add considerabley to our understanding of the relation between L, P, and $\dot{P}$, though given the undertainties in the electron distribution in the inner galaxy, the translation from dispersion measure to distance must be done with caution. Further study of these pulsars (*e.g.* period derivatives, dispersion independent distances, pulse polarization studies) should significantly improve our understanding of the ages, magnetic fields, luminsosities, and beam shapes of short period pulsars, and in doing so should add valuable data to analyses of pulsar statistics.

A number of explanations have been proposed as to why pulsars might be born as slow rotators (Narayan 1987). One of the more interesting is that the neutron star is not actually born rotating slowly, but is hidden by a binary companion on or near the main sequence see for a substantial time after its formation. Under favorable circumstances the models delineated by Dewey and Cordes (1987) suggest that 5 - 20% of pulsars might be affected, which is compatible with the fraction of injected pulsars (50%) found by Narayan. Narayan also found injection to be more prominent in high magnetic field pulsars, which is consistent with this model: if the pulsar undergoes spin-up, its period, when it first becomes visible, should be directly related to its magnetic field.

4. SUMMARY

Simple models of pulsar birth and evolution, such as that outlined in the introduction, are sometimes refered to as "the standard lies". This is a rather uncharitable description – "the standard half-truths", or even "the standard three-quarter-truths" is probably nearer the mark. The model in which pulsars are born in Type II supernovae, with large magnetic fields and short periods, and in which their later evolution is dominated by the effects of the dipole magnetic field is consistent with much of the observational data on pulsars. However, much work remains to be done on questions such as the initial period distribution, the role of magnetic field decay and alignment, and the effects of binary evolution (to name a few) in order to sort out the lies, the truths and the half-truths.

ACKNOWLEDGEMENTS: I would like to thank Joe Taylor for his pulsar data file which provided the data for all the figures. The preparation of this paper was carried out at the Jet Propulsion Laboratory, California Institute of Technology, under contract with NASA.

REFERENCES

Alpar, M. A., Cheng, A. F., Ruderman, M. A. and Shaham, J. 1982, *Nature* **300**, 728.

Battacharya, D. and Srinivasan, G. 1987, in *High Energy Phenomena Around Collapsed Stars*, ed. F. Pacini, (Dordrecht: Reidel), p.235.

Blair, D. G. and Candy, B. N., 1988, preprint.

Becker, R. H. 1987, in *The Origin and Evolution of Neutron Stars*, ed. D. J. Helfand and J.-H. Huang, (Dordrecht: Reidel), p.91.

Blandford, R. D., Applegate, J. H. and Hernquist, L. 1983, *M. N. R. A. S.* **204**, 1025.

Blaauw, A 1986, in *The Birth and Evolution of Massive Stars and Stellar Groups*, ed. W. Boland and H. van Woerden, (Dordrecht: Reidel), p.211

Burrows A. 1985, *Comments on Astrophys.* **10**, 149.

Chevalier, R. A. and Emmering, R. T. 1986, *Ap. J.* **304**, 140.

Clifton, T. R. and Lyne, A. G. 1986, *Nature* **320**, 43.

Dewey, R. J., Stokes, G. H., Segelstein, D. J., Taylor, J. H. and Weisberg J. M. 1984, in *Millisecond Pulsars* ed. S. P. Reynolds and D. R. Stinebring, (Green Bank: National Radio Astronomy Observatory), p.234.

Dewey, R. J., and Cordes, J. M. 19873, *Ap. J.* **321**, 780.

Dewey, R. J., Taylor, J. H., Maguire, C. M. and Stokes, G. H. 1988, *Ap. J.* , in press.

Fruchter, A. S., Taylor, J. H., Backer, D. C., Clifton, T. R., Foster, R. S. and Wolszczan, A. 1988a, *Nature* **331**, 53.

Fruchter, A. S., Sinebring, D. R. and Taylor, J. H., 1988b, *Nature* , submitted.

Gott, J. R., Gunn, J. E. and Ostriker, J. P. 1970, *Ap. J. Letters* **160**, L91.

Gunn, J. E. and Ostriker, J. P. 1970, *Ap. J.* **160**, 979.

Helfand, D. J. and Huang,J.-H. (eds.) 1987, *The Origin and Evolution of Neutron Stars*, (Dordrecht: Reidel).

Kulkarni, S. R., Clifton, T. R., Backer, D. C., Foster, R. S., Fruchter, A. S. and Taylor, J. H. 1988, *Nature* **331**, 50.

Lyne, A. G., Manchester, R. N. and Taylor J. H. 1985, *M. N. R. A. S.* **213**, 613.

Lyne, A. G., Biggs, J. D., Brinklow, A., Ashworth, M. and McKenna, J. 1988, *Nature* **332**, 45.

Lyne, A. G. and Manchester, R. N. 1988, *M. N. R. A. S.* , in press.

Miller, G. E. and Scalo, J. M. 1979, *Ap. J. Suppl.* **41**, 513.

Manchester, R. N. and Taylor, J. H., *Pulsars* (San Francisco: W. H. Freeman and Co.).

Narayan, R. 1987, *Ap. J.* **319**, 162.

Narayan, R. and Vivekanand, M. 1983, *Astr. Ap.* **122**, 45.

Nomoto, K. 1987, in *The Origin and Evolution of Neutron Stars*, ed. D. J. Helfand and J.-H. Huang, (Dordrecht: Reidel), p.281.

Pacini, F. 1967, *Nature* **216**, 567.

Phinney, E. S., Evans, C. R., Blandfor, R. D. and Kulkarni, S. R. 1988, *Nature* , submitted.

Proszynski, M. and Przybycien, D. 1984, in *Millisecond Pulsars* ed. S. P. Reynolds and D. R. Stinebring, (Green Bank: National Radio Astronomy Observatory), p.151.

Reynolds, S. P. and Fix, J. D. 1987, *Ap. J.* **322**, 673.

Ruderman, M., Shaham, J and Tavani, M. 1988, *Ap. J.* , submitted.

Seward, F. D. 1987, in *The Origin and Evolution of Neutron Stars*, ed. D. J. Helfand and J.-H. Huang, (Dordrecht: Reidel), p.99.

Srinivasan, G., Battacharya, D.and Dwarakananth, K. S. 1984, *J. Astrophys. Astron.* **5**, 403.

Stokes, G. H., Taylor, J. H., Weisberg J. M. and Dewey, R. J., 1985, *Nature* **317**, 787.

Stokes, G. H., Segelstein, D. J., Taylor, J. H., and Dewey, R. J., 1986, *Ap. J.* **311**, 694.

Stollman, G. M. 1987, *Astr. Ap.* **178**, 143.

Sugimoto, D. and Nomoto, K. 1980, *Space Sci. Rev.* **25**, 155.

Taam, R. E. and van den Heuvel, E. P. J. 1985, *Ap. J.* **305**, 235.

Tammann, G. A. 1982, in *Supernovae, A Survey of Current Research*, ed. M. J. Rees and

R. J. Stoneham (Dordrecht: Reidel) p.371.

Taylor, J. H. and Stinebring, D. R. 1986, *Ann. Rev. Astron. Astrophys.* **24**, 285.

Taylor, J. H. 1987, in *The Origin and Evolution of Neutron Stars*, ed. D. J. Helfand and J.-H. Huang, (Dordrecht: Reidel), p.383.

Trimble, V. 1984, *J. Astrophys. Astron.* **5**, 389.

van den Bergh, S,, McClure, R. D., and Evans, R. 1987, *Ap. J.* **323**, 44.

van den Heuvel, E. P. J. 1981, in *IAU Symposium No. 95, Pulsars*, ed. W. Sieber, and R. Wielebinski, (Dordrecht: Reidel), p.379.

————. 1984, *J. Astrophys. Astron.* **5**, 209.

————. 1987, in *The Origin and Evolution of Neutron Stars*, ed. D. J. Helfand and J.-H. Huang, (Dordrecht: Reidel), p.393.

Vivekanand, M and Narayan, R. 1981, *J. Astrophys. Astron.* **2**, 315.

Woosley, S. E. and Weaver, T. A. 1986, *Ann. Rev. Astron. Astrophys.* **24**, 205.

Woosley, S. E. 1987, in *The Origin and Evolution of Neutron Stars*, ed. D. J. Helfand and J.-H. Huang, (Dordrecht: Reidel), p.255.

X-RAY BINARIES AND RADIOPULSARS IN GLOBULAR CLUSTERS

Frank Verbunt
Max Planck Institut für Extraterrestrische Physik
D-8046 Garching bei München
Federal Republic of Germany

Abstract. Globular clusters contain a relatively large number of low-mass X-ray binaries and low-magnetic-field radiopulsars. This can be understood as a consequence of the high number densities of stars in the cores of some globular clusters. Close encounters between neutron stars and main-sequence or (sub)giant stars lead to the formation of low-mass X-ray binaries, some of which may evolve into binary radiopulsars. If the binary is destroyed, the neutron star — rotating rapidly if it has accreted enough matter from its companion — may become a single radiopulsar. Accurate theoretical predictions of the number of low-mass X-ray binaries in globular clusters are not possible, since the number of neutron stars in globular clusters, and the life time of low-mass X-ray binaries are both uncertain by an order of magnitude.

1. Introduction

This article reviews the ideas put forward to explain why there are so many low-mass X-ray binaries in globular clusters: the globular cluster system of our galaxy contains fractions of about 0.0001 of the mass, but about 0.1 of the low-mass X-ray binaries of our galaxy /Katz 1975/. In Section 2 I therefore start with a summary of what we know about low-mass X-ray binaries. The physical processes that may lead to the formation of low-mass X-ray binaries in globular clusters, and the appreciable uncertainties in our understanding of them, are discussed in Section 3. To calculate the numbers of different types of low-mass X-ray binaries that may be formed in globular clusters, we use the stellar number densities as derived from the initial mass function, and taking the effect of mass segregation into account. This account of the formation of low-mass X-ray binaries, and the evolution of some of them into binary or single radiopulsars, is made up in Section 4. A summary of the results and the conclusions that may be drawn are given in Section 5.

Of the earlier reviews of low-mass X-ray binaries in globular clusters some /Grindlay 1987, 1988, Hertz 1984, and Lewin & Joss 1983/ mainly discuss the observations, others /Verbunt & Hut 1987, Verbunt 1988a/ consider the problem more from the theoretical point of view, like this paper. In addition, several papers in these proceedings deal with radiopulsars and X-ray sources in globular clusters.

H. Ögelman and E. P. J. van den Heuvel (eds.), Timing Neutron Stars, 593–608.

2. The nature of low-mass X-ray binaries

Low-mass X-ray binaries come in different varieties, which are easiest discriminated by their orbital periods (Figure 1).

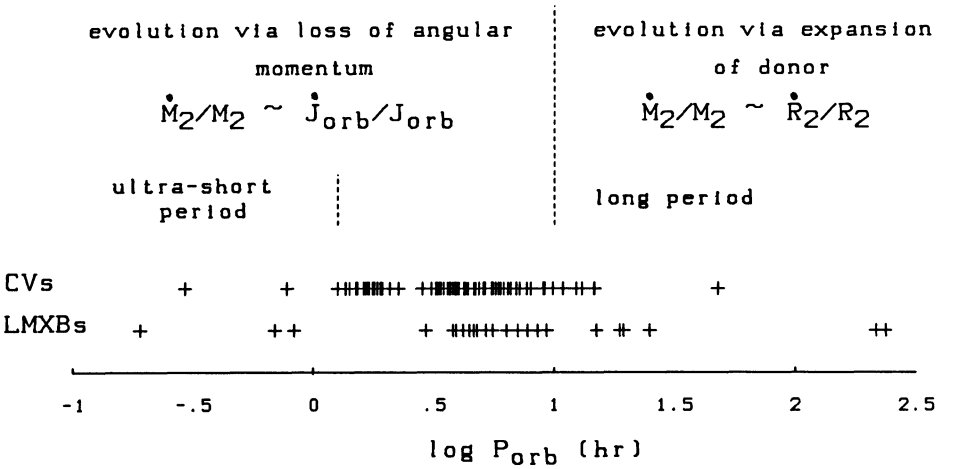

Figure 1. The orbital period distributions of cataclysmic variables and low-mass X-ray binaries. Data mainly from /Ritter 1987/. The systems with orbital periods between about 80 min and 10 hr probably contain stars close to the main-sequence as mass donors. Systems with periods longer than 10 hr contain (sub)giant donor stars. Systems with periods shorter than 80 min contain He rich stars. Mass transfer is driven by loss of angular momentum from the binary for systems with orbital periods less than about 10 hr, and by expansion of the donor radius in systems with orbital periods longer than about 10 hr.

Systems with orbital periods longer than about 10 hr contain low-mass (sub)-giant donor stars. In these systems the mass transfer is driven by the radius expansion of the donor, driven by the nuclear evolution of its core. The mass-transfer rate is roughly given by $\dot{M}_2/M_2 \sim \dot{R}_2/R_2$, where M_2 and R_2 are the mass and radius of the donor star, and the dot indicates the time derivative. Systems with shorter orbital periods evolve via loss of angular momentum from the orbit, which drives the two stars together, and causes mass transfer at a rate of roughly $\dot{M}_2/M_2 \sim \dot{J}_{orb}/J_{orb}$. In systems with orbital periods between about 80 min and 10 hr, the mass donor can be a main-sequence type star, and the loss of angular momentum is caused by gravitational radiation, and probably some additional mechanisms like magnetic braking. In systems with orbital periods less than 80 min the mass donors are thought to be helium rich stars — degenerate or helium burning — and the loss of angular momentum may be due solely to gravitational radiation. The evolution of low-mass X-ray binaries is reviewed in, *e.g.*, /Savonije, 1983, and Verbunt, 1988b/).

3. Capture of neutron stars

To understand the presence of a relatively large number of low-mass X-ray binaries in globular clusters, one must understand how (sub)giants, main-sequence stars, or helium-rich stars can get close to neutron stars. A promising mechanism for this is tidal capture in close encounters between these stars and neutron stars, important in globular clusters thanks to the large number density of stars in the cluster cores /Sutantyo 1975, Fabian, Pringle and Rees 1975/. Another possibility, less important in practice, is the exchange of an ordinary star in a binary with a neutron star /Hills 1976/. We will discuss these possibilities in turn.

3.1 Tidal capture in close encounters between single stars

During a close encounter between two stars, tidal forces will cause a deformation of the stars with respect to their original spherical forms. The energy required for the deformation is taken from the relative kinetic energy of the two stars. If this deformation energy is rapidly dissipated, the two stars may become bound. It is through this process of capture via dissipation of tidal energy that low-mass X-ray binaries may be formed in the core regions of globular clusters /Fabian, Pringle & Rees 1975/.

A simple estimate for the closest approach required can be made as follows (see /Verbunt & Hut 1987/). Consider a neutron star with mass m, which has a velocity at infinity v with respect to a target star with mass M and radius R. The relative kinetic energy of the two stars is given by

$$E_k = \frac{1}{2}\frac{mM}{m+M}v^2 \tag{1}$$

At the distance of closest approach d, the height h and mass m_t of the tidal bulge are roughly given by

$$h \simeq \frac{m}{M}\frac{R^4}{d^3}; \qquad m_t \simeq k\frac{h}{R}M \simeq k(\frac{R}{d})^3 m$$

where k is the apsidal motion constant. The energy E_t of the bulge can be estimated:

$$E_t \simeq m_t\frac{GM}{R^2}h \simeq k\frac{Gm^2}{R}(\frac{R}{d})^6 \tag{2}$$

If a) $E_t > E_k$, and b) the tidal energy is dissipated, a binary is formed. Condition a) can be rewritten:

$$d \lesssim 3R(\frac{k}{0.14}\frac{m}{M}\frac{m+M}{2M_\odot}\frac{R_\odot}{R})^{1/6}(\frac{10km\ s^{-1}}{v})^{1/3} \tag{3}$$

where the normalizations are on values characteristic for globular clusters.

A more accurate semi-analytical estimate of the distance at which capture ensues, must include higher order deformation terms. Due to the strong dependence

on d of the tidal energy in the deformation (see eq.(2)), these more accurate calculations /Giersz 1986; Lee & Ostriker 1986; McMillan, McDermott & Taam 1987/ give almost the same result as the rough estimate above. It is interesting to note that this approach breaks down when the energy in the tidal bulge is larger than its binding energy to the stellar core, as can be the case in close encounters with large giants /McMillan et al. 1987, Bailyn 1988/.

Another way to improved accuracy is the numerical study of close encounters between stars consisting of N particles. In such studies it is found that some mass can be lost from the system /Gingold & Monaghan 1980/, carrying a substantial amount of angular momentum /Benz & Hills 1987/. The occurrence of such effects limits the reliability of the semi-analytical calculations, which do not include mass loss. A neutron star at the very surface of a low-mass main-sequence star exerts a tidal force which is sufficient to disrupt the star completely /Krolik 1984/. Calculations of direct hits between a compact star and a N-particle star suggest that the matter of the disrupted star can form a massive disk around the compact star /Shara & Regev 1986; Soker et al. 1987/.

The calculations so far indicate that capture will occur if the compact star approaches to within 2 to 3 times the radius of the target star. Whether a capture leads to merging of the two stars, possibly in the form of a massive disk around the compact star, or to binary formation, depends on the mass ratio of the two stars, on the closest distance, on the stellar structure of the target star, and on the relative velocity. The number of realistic calculations is too small to enable us to estimate the cross sections for these different possibilities with accuracy. For illustrative purposes, I will assume in this paper that a direct hit — i.e. a closest approach with $d < R$ — leads to merging, and a closest approach between one and three radii — $R < d < 3R$ — to binary formation.

The cross section for closest encounters at distance d is easily derived from conservation of energy and angular momentum in a Keplerian orbit:

$$\sigma = \pi d^2 (1 + \frac{2G(m+M)}{v^2 d}) \simeq \pi d \, \frac{2G(m+M)}{v^2}$$

For number densities n_c and n for the compact and target stars, respectively, the capture rate of compact stars per unit volume can be written:

$$\Gamma = n_c n v \sigma \simeq 6 \times 10^{-11} \frac{n_c}{10^2 pc^{-3}} \frac{n}{10^4 pc^{-3}} \frac{m+M}{M_\odot} \frac{3R}{R_\odot} \frac{10 km\ s^{-1}}{v} \ yr^{-1} pc^{-3} \qquad (4)$$

3.2 Exchange encounters with binaries

If we consider all stars as point sources, a close encounter between a single star and a binary can have three different outcomes: the binary may be dissolved (which may be called ionization), the binary parameters may be changed by the encounter (excitation), or the single star may swap places with one of the binary members (exchange): see Figure 2. Accurate cross sections for these processes are known

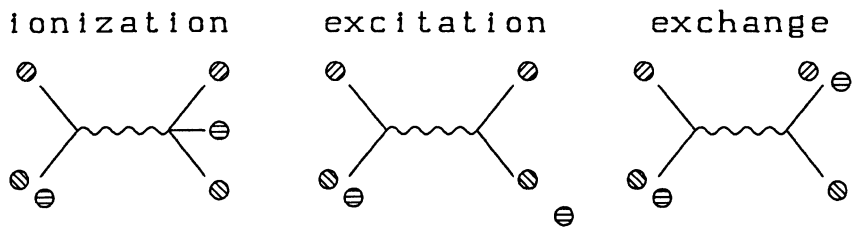

Figure 2. The different possible outcomes of encounters between a single star and a binary, for three point-mass stars. For finite stars, merging between two or all three stars are possible.

only for the case where all three stars have the same mass /Hut & Bahcall 1983; Hut 1984/.

If the finite size of the stars is taken into account, the cross sections for these different processes may be affected by mass loss, and by tidal forces, and direct collisions between stars may lead to merging of two or all three stars. Hitherto, these processes have not been much studied.

Strong interaction between a single star and a binary, will most often occur via the formation of a temporary triple system, the so-called resonance scattering. The rate of resonance scattering, in the case of three equal point masses m, is /Hut & Bahcall 1983/:

$$\Gamma_{bin} \simeq 5 \times 10^{-10} \frac{n_c}{10^2 pc^{-3}} \frac{n_{bin}}{10^2 pc^{-3}} \frac{m}{M_\odot} \frac{a}{1\text{A.U.}} \frac{10 km\ s^{-1}}{v}\ yr^{-1} pc^{-3} \qquad (5)$$

For equal masses, the incoming star will remain in the binary in 2 out of every 3 encounters. If the incoming star is more massive, its chance of ending up in the binary is larger. From Eqs. (4) and (5), one sees that exchange via resonance scattering gains on tidal capture by having a larger cross section (a rather than R), but looses because of the number density of binaries, n_{bin}, is much smaller than the number density n of single stars /Hut & Verbunt 1983/. As a result, the formation of low-mass X-ray binaries via exchange encounters between a neutron star and a binary probably does not compete with direct capture. However, close encounters between field stars and low-mass X-ray binaries may play a role in the formation of single radio pulsars in globular clusters (see Section 4.5).

4. The formation of different types of low-mass X-ray binaries and their evolution

To calculate the formation rate of low-mass X-ray binaries in a globular cluster one must know the number density of neutron stars and of target stars. For the cluster as a whole, these can be derived from the initial mass function (Section 4.1). In the cluster core, where most of the close encounters occur, the more massive stars are over-represented, due to mass segregation (Section 4.2). The relative frequencies of the formation of different types of low-mass X-ray binaries can now be determined, albeit with appreciable uncertainty, and it will be seen that some of these binaries may evolve into binary radiopulsars (Section 4.3). The predicted systems can then be compared with the observed ones (Section 4.4). Finally, I discuss some proposals for the formation of single radiopulsars in globular clusters (Section 4.5).

4.1 The stellar content of a globular cluster

To determine the number of target stars and compact stars in a globular cluster, one may follow the method of /Tinsley 1974/. This method starts from the assumption that the initial mass function can be written as a power law, i.e. initially the number of stars $dN(m)$ in a mass interval dm around mass m can be written as : $dN(m) = C_o m^{-1-x} dm$. From stellar counts of main sequence stars, the normalization constant C_o and the slope x can be found. One then extrapolates this to higher masses to find the number of progenitors of white dwarfs and neutron stars.

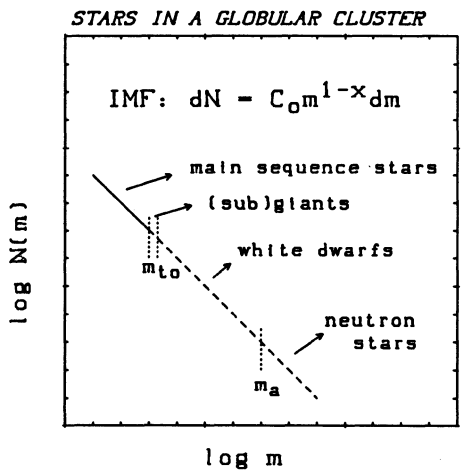

Figure 3. The numbers of different stars in a globular cluster as derived from the initial mass function. The slope x and normalization constant C_o of the initial mass function are determined by study of the main sequence stars, and by extrapolation the number of white dwarf and neutron star progenitors is found. (Neutron star progenitors have a mass higher than $m_a \simeq 6 - 8 M_\odot$.) The (sub)giants all have a mass close to the turnoff mass $m_{to} \simeq 0.8 M_\odot$. For details see text.

The number of stars with original masses between m_1 and m_2 is given by:

$$N(m_1, m_2) = \int_{m_1}^{m_2} C_o m^{-1-x} dm = \frac{C_o}{x}(m_1^{-x} - m_2^{-x}) \qquad (6)$$

If all stars more massive than m_a have evolved into neutron stars, the number of neutron stars formed, follows from Eq.(6) as $N_{ms} \simeq C_o m_a^{-x}/x$. The number of white dwarfs is given by $N_{wd} \simeq C_o(m_{to}^{-x} - m_a^{-x})$, where m_{to} is the maximum mass of main-sequence stars, the turnoff-mass.

m_a is not exactly known, but values between 6 and 8 $M_\odot$ are likely /Blaauw 1985/, possibly dependent on the metallicity. In estimating the number of neutron stars now present in a globular cluster, one encounters two major difficulties. First, neutron star progenitors have masses much higher than the stars in the observed part of the IMF, which have $m \lesssim 0.8 M_\odot$, so that a large and uncertain extrapolation is necessary. Second, the velocities of the radiopulsars in the galactic disk indicate that many neutron stars are born with velocities of $\sim$ 100 km/s, higher than the escape velocity of a globular cluster: the fraction of neutron stars that are born with sufficiently low velocities to remain cluster members is very uncertain. It has been estimated as between 16 and 40 % /Verbunt & Hut 1987; Verbunt 1988a/. These two difficulties lead to an uncertainty in the number of neutron stars in a globular cluster of at least a factor 10.

As far as target stars are concerned, the number of main-sequence stars is reasonably well known, in the better studied clusters. The number of giants can be estimated from evolutionary calculations which give the turnoff mass m_{to}, above which all stars have evolved away from the main sequence, as a function of the cluster age τ /Rood 1972/:

$$log\frac{m_{to}}{M_\odot} = -0.28\ log\frac{\tau}{10^9 yr} + 0.013\ logZ - 0.75\ logY + 0.453$$

Z and Y are the metal and helium contents of the cluster. The derivative from this equation relates a time interval Δt to a mass interval Δm_{to} as: $\Delta m_{to} \simeq -0.28 m_{to} \Delta t/\tau$. From this the number of giants $N_{G,i}$, in an evolutionary stage i with life time Δt_i follows:

$$N_{G,i} = 0.28\ C_o\ \frac{\Delta t_i}{\tau}\ m_{to}^{-x} \tag{7}$$

From Eq.(4) we see that the capture rate involves the product $N_{G,i}R_i$, where R_i is the stellar radius at evolutionary phase i. Using the stellar radius as a function of age, we can calculate the chance for a star to be captured in the different phases of its evolution. The result is shown in Figure 4, for a star of 0.9 $M_\odot$. Similar calculations for stars of 0.8 $M_\odot$ give very similar results /Verbunt & Hut 1987; Verbunt 1988/.

The numbers in this Figure do not take into account the loss of capture efficiency for large giants /Bailyn 1988; see Section 3.1/. The importance of this effect is small, since large giants have only short life times, and do not contribute much to the total capture rate as calculated for Figure 4.

Normalizing on the number of captures by main-sequence stars, one finds for the capture rate by giants $\Gamma_{G,i}$ /Verbunt & Hut 1987/:

$$\frac{\Gamma_{G,i}}{\Gamma_{ms}} \simeq \frac{\Sigma\ N_{G,i}R_i}{N_{ms}R_{ms}} \simeq 0.07 \tag{8}$$

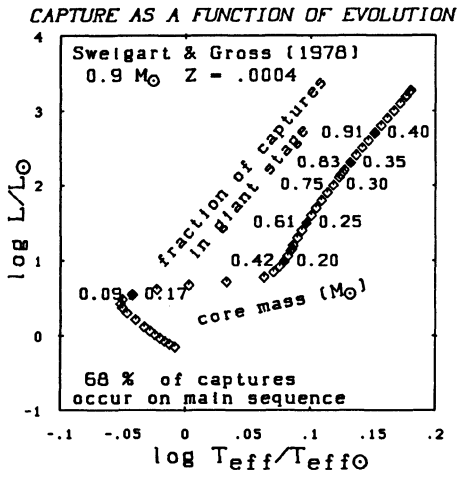

Figure 4. Capture as a function of evolutionary stage for a 0.9 $M_\odot$ star. Parameters for the star are taken from /Sweigart & Gross 1978 and Mengel et al. 1979/. About 68% of all captures occur on the main sequence. Of the remaining captures, about 42 % occurs on the subgiant branch with core mass less than 0.20 $M_\odot$; 58 % on the giant branch. For some stages the cumulative fraction of capture after leaving the main sequence, and the core mass are indicated. Thus 83 % of all captures on the (sub)giant branches occurs before the core mass of the (sub)giant has grown to 0.35 $M_\odot$.

The fraction 0.07 is found with the values of Δt_i and R_i from the evolution calculation for giants RG3 in /Rood 1972/. In Eq. (8) the distortion of the initial mass function due to mass segregation, which is discussed in Section 4.2, is ignored.

4.2 The stellar content of the cluster core

To calculate the total number of captures in a globular cluster, one must integrate Eq.(4) over the cluster volume. In the core region, the stellar number densities are much higher than outside the core, and virtually all captures occur within a few core radii /Verbunt & Meylan 1988/. In a globular cluster the stars with higher masses are concentrated towards the core. This is called mass segregation. The mass segregation enhances the number of neutron stars in the core of ω Cen by a factor of 3, and in the core of 47 Tuc by a factor of 20. As a result, the capture of neutron stars is higher than one would estimate when ignoring mass segregation. Also, captures by more massive stars, in particular giants and massive main-sequence stars, are enhanced by mass segregation. Thus, the number of giants is enhanced by factors of about 2 and 4 in the cores of ω Cen and 47 Tuc, respectively /Verbunt & Meylan 1988/. To estimate the importance of capture by giants in all globular clusters, one would have to know whether ω Cen or 47 Tuc is more representative. However, only a handfull of globular clusters has been studied sufficiently well to make more detailed calculations of mass segregation possible.

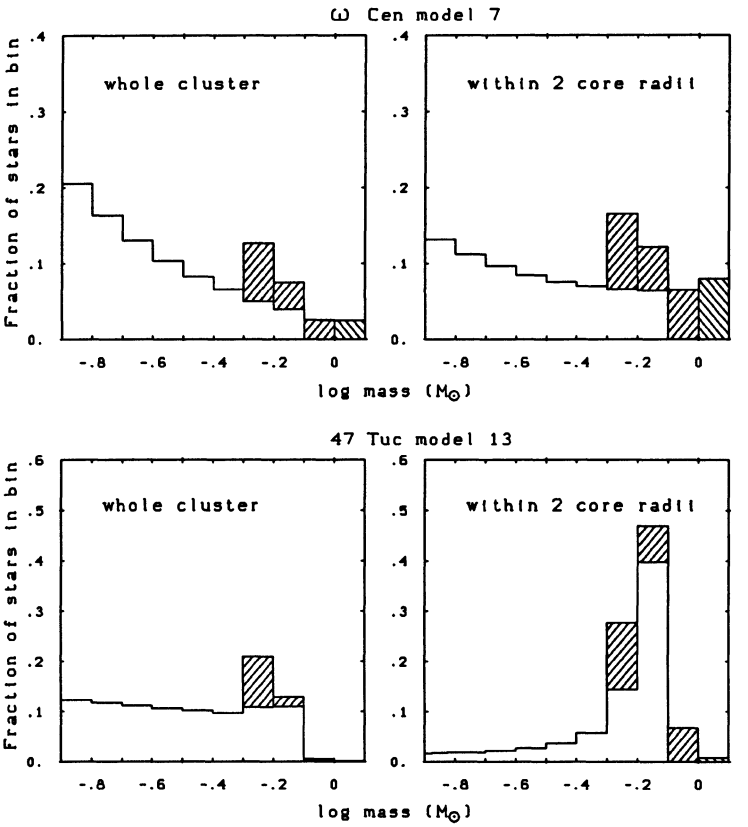

Figure 5. The mass functions for ω Cen (top) and 47 Tuc (bottom) for the cluster as a whole (left) and for the innermost region at $r < 2r_c$ (right). The data for the figure are from Verbunt & Meylan 1988. The hatched blocks indicate the compact stars: the white dwarfs are distributed in three groups with masses around 0.58, 0.74 and 1.1 $M_\odot$, the neutron stars all are 1.4 $M_\odot$. (The mass scale of the graph is not valid for the 1.1 $M_\odot$ white dwarfs or for the neutron stars.) The numbers of neutron stars shown in the Figure are based on the assumption that all neutron stars formed in the cluster still reside there. In reality, a large fraction of them probably was born with a velocity high enough to escape from the cluster. The relative importance of the more massive stars is enhanced in the core due to mass segregation, in particular in the centrally condensed cluster 47 Tuc.

4.3 Formation of different types of binaries

Knowing the number densities of the neutron stars and of the target stars, as well as the capture cross section, we can calculate the relative frequencies of the different types of close encounters. A schematic overview is given in Figure 6.

The most frequent encounters involving a neutron star, are those with main-sequence stars. In 1/3 of these cases, the encounter will be a direct hit, which presumably leads to the complete destruction of the main-sequence star (see Section 3.1). For a short time a massive disk may be formed around the neutron star, but accretion of some of the disk matter will produce enough radiation to blow the rest of the disk mass away. Thus the neutron star may emerge from this encounter virtually unchanged. In the other 2/3 of the encounters between a main-sequence star and a neutron star a binary may be formed with an orbital period in the range of hours (see Figure 1). Loss of angular momentum will cause the binary stars to move together, and the binary shows up as an X-ray source, when mass transfer starts.

Close encounters between a neutron star and a (sub)giant are less frequent. In a moderately concentrated cluster like ω Cen encounters with (sub)giants are about 7 times less frequent than encounters with main-sequence stars, but in the strongly concentrated cluster 47 Tuc they are only 3 times less frequent. Thus the relative importance of encounters with (sub)giants can vary appreciably between clusters. 1/3 of the encounters between a neutron star and a (sub)giant will be direct hits. It has been suggested /Verbunt 1987/ that a direct hit causes the neutron star and the giant core to orbit one another within the giant envelope. In that case, the friction with the giant envelope causes the two stars to spiral together, until the energy released by the friction is sufficient to expell the envelope. At that point the neutron star and white dwarf may have spiralled in to an orbit on the order of 10 min. Such a system can become an X-ray binary, evolving under the influence of gravitational radiation.

In the remaining 2/3 of encounters between a giant and a neutron star, a binary may be formed, in which mass transfer will occur because of the giant expansion (see Section 2). The orbital period depends on the size of the giant at the moment of capture. For a subgiant close to the main sequence P_{orb} is about a day. The mass transfer will stop once the giant envelope is exhausted, and a wide binary with a neutron star and a white dwarf remains. The neutron star rotates rapidly, after having accreted the giant envelope matter, and can show up as a pulsar once mass transfer has stopped. Thus, the capture of a neutron star by a giant eventually leads to a binary radiopulsar. The orbital angular momentum of a binary can be written $J_{orb} = mM\sqrt{Ga/(m+M)}$, where m and M are the masses of the two stars, and a is the semi-major axis. Assuming that the mass transfer from the giant to the neutron star is conservative, i.e. that total mass and angular momentum of the binary are conserved, the ratio of the semi-major axis after and before mass transfer can be calculated, and — using Kepler's law — also the ratio of the orbital periods:

$$\frac{a_f}{a_i} = \frac{(m_i M_i)^2}{(m_f M_f)^2} \qquad \frac{P_{orb,f}}{P_{orb,i}} = \frac{(m_i M_i)^3}{(m_f M_f)^3} \tag{9}$$

Here the indices i and f refer to the initial and final situation, respectively. For example, a neutron star with mass $1.4 M_\odot$ captured by a giant with mass $0.8 M_\odot$, may accrete the $0.6\ M_\odot$ giant envelope, causing a to increase by a factor ~ 8 and P_{orb} by a factor ~ 20.

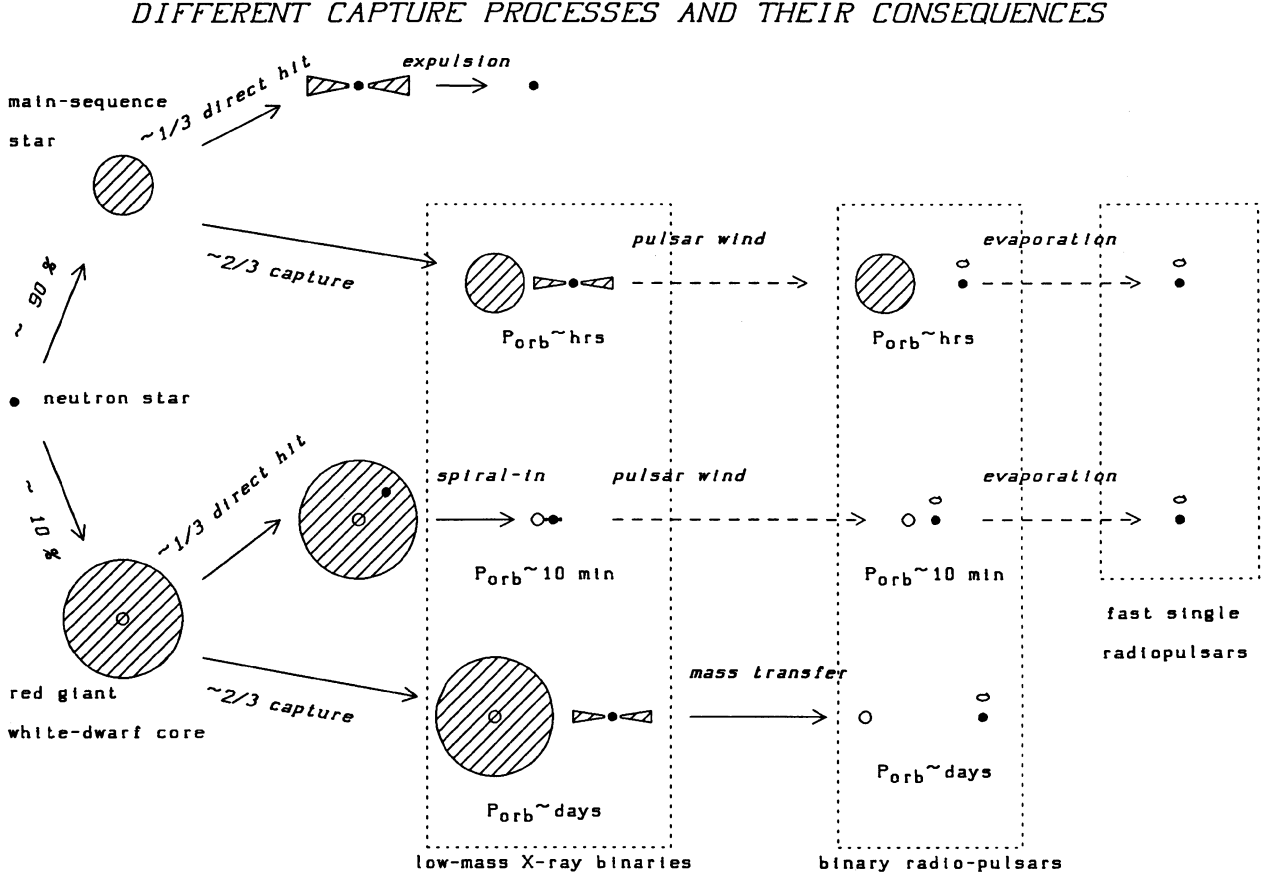

Figure 6. Formation and subsequent evolution of X-ray binaries via tidal capture. Note that the relative importance of the different processes is indicative only, and varies appreciably between clusters.

4.4 Comparison of observed systems with the predictions.

We can now compare these formation and evolution scenarios with the observed systems. The scenarios are summarized in Figure 6, the observations in Table 1.

Table 1. *Parameters for low-mass X-ray binaries (with known orbital periods) and radiopulsars in globular clusters. From left to right the Table gives the position of the source, the pulse period (for radiopulsars), the orbital period, the probable companion mass, the cluster identification, and the reference of the discovery paper. (Notice that the two pulsars in 47 Tuc were discovered after the conference.)*

Globular clusters which contain a bright X-ray source for which no binary parameters are known are: NGC 1851, Liller 1, NGC 6440, NGC 6441, NGC 6712, Terzan 1, Terzan 2 and Terzan 3. For references see /Bradt & McClintock 1983/.

source	P	P_{orb}	e	M_c	cluster	ref
	X-ray binaries with known orbital period					
1820 − 30		864s		$0.05M_\odot$	NGC 6624	1
2127 + 12		0.35d			M 15	2
		radiopulsars				
1821 − 24	3.1ms				M 28	3
0021 − 72A	4.5ms	0.02d	0.33	$0.02\ M_\odot$	47 Tuc	4
0021 − 72B	6.1ms	7-95d			47 Tuc	4
1620 − 26	11.1ms	191.4d	0.025	$0.35M_\odot$	M 4	5
2127 + 12	110.7ms				M 15	6

[1] Stella, Priedhorsky & White 1987 [2] Ilovaisky et al. 1987, Hertz 1987, Naylor et al. 1988 [3] Lyne et al. 1987 [4] Ables et al. 1988 [5] Lyne et al. 1988 [6] Wolszczan et al. 1988

For most X-ray sources in globular clusters the orbital period is not known, hence we do not know via which channel these binaries were formed. Their number is compatible (within the appreciable uncertainty) with the formation rate expected according to Eq.(4): a dense globular cluster can have a stellar number density in the core of about 10^5 pc^{-3}. With a core volume of a few cubic parsec, and the relative numbers of main-sequence and neutron stars as in Figure 5, one finds a formation rate of order 1 every 10^9 yr. The life time of low-mass X-ray binaries is very uncertain. If it is in the range of 10^9 yr, one would expect of order one bright X-ray source in the densest clusters, as observed.

The 11 minute binary in NGC 6624 can be located in Figure 6, as having formed via a collision of a neutron star with a giant, and subsequent spiral-in /Verbunt 1987/. In another scenario suggested for this source, a neutron star was captured by a main-sequence star, and spiral-in occurred once this main-sequence star started to ascend the (sub)giant branch /Bailyn & Grindlay 1987/. However, it is unclear whether mass transfer from a subgiant onto a neutron star leads to spiral in; the

observed wide binary systems indicate that such mass transfer is stable, and that the orbital period increases (see Eq.(9), and /Verbunt & Rappaport 1988/).

The 8.5 hr binary in M 15 has an orbital period which seems too long for a main-sequence mass donor, and too short for a giant mass donor (see Figure 1). It may be that systems with orbital periods around a day, evolve via both radius expansion of the giant and angular momentum loss from the system /Pylyzer & Savonije 1988/. In that case the orbital periods may stay shorter than calculated under neglect of angular momentum losses, and a system like that in M 15 could ensue from capture of a neutron star by a subgiant.

Of the five radiopulsars now known in globular clusters, two are in wide binaries, and from Figure 6 we see that this indicates that they originate from a capture of a neutron star by a giant, followed by mass transfer in a wide binary, until the giants envelope was exhausted. The 1924.3 s binary, with an eccentricity of 0.33 does not fit the current scenarios: if a radiopulsar switches on in an ultra-short period X-ray source, like the one in NGC 6624, one expects the orbit to be circular. This source needs more thinking. Finally, two of the radiopulsars in globular clusters are single. Their possible origin is discussed in the next subsection.

4.5 The formation of single millisecond radiopulsars.

Four different mechanisms have been proposed for the formation of a single millisecond radiopulsar in a globular cluster. The first of these was in fact a prediction: a direct hit of a neutron star on a main-sequence star may lead to the formation of a massive disk around the neutron star. If all the disk mass is accreted, a single millisecond pulsar remains /Krolik 1984/. If this mechanism works, many single radiopulsars are expected in globular clusters. However, it could well be that accretion of a small fraction of the disk matter releases enough radiation to blow the rest of the disk away /Verbunt et al. 1987/. In that case the neutron star will not accrete enough mass to be spun up.

The second possibility is to start from a wide-binary radiopulsar, like the one in M 4, say. This binary can undergo encounters with single stars, and several processes can occur (Figure 2). If the velocity of the third star is sufficiently high, the binary can be ionized /Romani, Kulkarni & Blandford 1987/, and for smaller velocities the third star can change places with the neutron star /Verbunt et al. 1987/. In both cases the neutron star is released, and the radiopulsar has become single. It is not clear whether the cross sections for these processes are sufficiently large to make them likely. Detailed calculations are being made, and should provide an answer /Rappaport, Putney & Verbunt 1988/. An interaction between a third star and the wide binary can also cause an eccentricity to be induced. This can in principle be used to set a limit to the age of the wide binary /Lyne et al. 1988/. Detailed calculations indicate that the small eccentricity of the binary in M 4 is compatible with an age of that binary of $\sim 10^9$ yr /Rappaport, Putney & Verbunt 1988/.

A third possibility involves a low-mass X-ray binary with an orbital period of a few hours. A passing third star can drive the two stars closer together, and cause an onset of runaway mass transfer /Verbunt & Rappaport 1988/. Alternatively,

the third star may collide with the mass donor, and completely destroy it /Verbunt et al. 1987/. These mechanisms lead to a rather smaller predicted number of single radiopulsars than accretion from a massive disk (discussed above as the first possibility).

The fourth possibility is that energy of the millisecond radiopulsar in a close binary hits and destroys it companion. In this case the theoretical prediction /Kluzniak et al. 1989/ just preceded the observation of a radiopulsar in a 9 hr orbit, which is evaporating it companion /Fruchter, Stinebring & Taylor 1988/. If the time scale for the destruction of the companion is very short, one is tempted to use the word vaporization, to convey an impression of the stranger-than-fiction systems that we find in globular clusters.

5. Conclusions.

The presence of relatively large numbers of low-mass X-ray binaries in globular clusters can be understood as a consequence of tidal capture of single neutron stars by main-sequence or giant stars. The absolute numbers of such binaries is very uncertain, due to two major uncertainties: first, the number of single neutron stars in globular clusters is badly known (Section 3.1), and second, the life time of low-mass X-ray binaries in their active state is very uncertain. The combination of these two uncertainties leads to an uncertainty in the predicted number of low-mass X-ray binaries of a factor $\gtrsim 10^2$. Smaller uncertainties arise because of our limited knowledge of the cross sections for the different capture processes (Section 3.1), and because we do not know the degree of mass segregation in many clusters (Section 4.2).

Wide-binary radiopulsars are formed via the evolution of the (sub)giant / neutron star binaries. Single radiopulsars can be formed when a millisecond pulsar in a binary destroys its companion, or when a third star interacts with a binary containing a rapidly rotating neutron star.

References

Ables, J.G., Jacka, C.E., McConnell, D., Hamilton, P.A., McCulloch, P.M. & Hall, P.J. 1988, *IAU Circ.#* 4602.

Bailyn, C.D. 1988, *Nature* **332**, 330.

Bailyn, C.D. & Grindlay, J.E. 1987, *Astrophys. J. (Letters)* **316**, L25.

Benz, W. & Hills, J.G. 1987, *Astrophys. J.* **323**, 614.

Blaauw, A. 1985, in: *Birth and evolution of massive stars and stellar groups*, eds. W. Boland and H. van Woerden, Reidel, Dordrecht, p. 211.

Bradt, H.V.D. & McClintock, J.E. 1983, *Ann. Rev. Astr. Astrophys.* **21**, 13.

Fabian, A.C., Pringle, J.E. & Rees, M.J. 1975, *Mon. Not. R. astr. Soc.* **172**, 15p.

Fruchter, A.S., Stinebring, D.R. & Taylor, J.H. 1988, *Nature* **333**, 237.

Giersz, M. 1986, *Acta Astr.* **36**, 181.

Gingold, R.A. & Monaghan, J.J. 1980, *Mon. Not. R. astr. Soc.* **191**, 897.

Grindlay, J.E. 1987, in: *The origin and evolution of neutron stars*, IAU Symp. # 125 Nanjing P.R. China, eds. D.J. Helfand and J.H. Huang, Reidel, Dordrecht, p.173.

Grindlay, J.E. 1988, in: *The physics of compact objects, theory vs. observation*, eds. N.E. White and L. Fillipov, Pergamon Press, Oxford, in press.

Hertz, P. 1984, in: *X-ray astronomy '84*, Bologna, eds. M. Oda and R. Giacconi, Institute of Space & Aeronautical Sciences, p.85.

Hertz, P. 1987, *Astrophys. J. (Letters)* **315**, L119.

Hills, J.G. 1976, *Mon. Not. R. astr. Soc.* **175**, 1p.

Hut, P. 1984, *Astrophys. J. Suppl. Ser.* **55**, 301.

Hut, P. & Bahcall, J.N. 1983, *Astrophys. J.* **268**, 319.

Hut, P. & Verbunt, F. 1983, *Nature* **301**, 587.

Ilovaisky,S.A., Aurière, M., Chevalier, C., Koch-Miramond, L., Cordoni, J.P. & Angebault, L.P. 1987, *Astron. Astrophys.* **179**, L1.

Katz, J.I. 1975, *Nature* **253**, 698.

Kluzniak, W., Ruderman, M., Shaham, J. & Tavani, M. 1989, these proceedings.

Krolik, J.H. 1984, *Astrophys. J.* **282**, 452.

Lee, H.M. & Ostriker, J.P. 1986, *Astrophys. J.* **310**, 176.

Lewin, W.H.G. & Joss, P.C. 1983, in: *Accretion-driven stellar X-ray sources*, eds. W.H.G. Lewin and E.P.J. van den Heuvel, Cambridge University Press, p. 41.

Lyne, A.G., Brinklow, A., Middleditch, J., Kulkarni, S.R., Backer, D.C. & Clifton, T.R. 1987, *Nature* **328**, 399.

Lyne, A.G., Biggs, J.D., Brinklow, A., Ashworth, M. & McKenna, J. 1988, *Nature* **332**, 45.

McMillan, S.L.W., Mc Dermott, P.N. & Taam, R.E. 1987, *Astrophys. J.* **318**, 261.

Mengel, J.G., Sweigart, A.V., Demarque, P. & Gross, P.G. 1979, *Astrophys. J. Suppl. Ser.* **40**, 733.

Naylor, T., Charles, P.A., Drew, J.E. & Hassall, B.J.M. 1988, *Mon. Not. R. astr. Soc.* in press.

Pylyzer, E. & Savonije, G.J. 1988, *Astron. Astrophys.* **191**, 57.

Rappaport, S., Putney, A. & Verbunt, F. 1988, *Astrophys. J.* in preparation.

Ritter, H. 1987, *Astron. Astrophys. Suppl. Ser.* **70**, 335.

Rood, R.T. 1972, *Astrophys. J.* **177**, 681.

Romani, R.W., Kulkarni, S.R. & Blandford, R.D. 1987, *Nature* **329**, 309.

Savonije, G.J. 1983, in: *Accretion-driven stellar X-ray sources*, eds. W.H.G. Lewin and E.P.J. van den Heuvel, Cambridge University Press, p. 343.

Shara, M. M. & Regev, O. 1986, *Astrophys. J.* **306**, 543.

Soker, N., Regev, O., Livio, M. & Shara,M.M. 1987, *Astrophys. J.* **318**, 760.

Stella, L., Priedhorsky, W. & White, N.E. 1987, *Astrophys. J. (Letters)* **312**, L17.

Sutantyo, W. 1975, *Astron. Astrophys.* **44**, 227.

Sweigart, A.V. & Gross, P.G. 1978, *Astrophys. J. Suppl. Ser.* **36**, 405.

Tinsley, B.M. 1974, *Publ. Astr. Soc. Pac.* **86**, 554.

Verbunt, F. 1987, *Astrophys. J. (Letters)* **312**, L23.

Verbunt, F. 1988a, in: *The physics of compact objects, theory vs. observation*, eds. N.E. White and L. Fillipov, Pergamon Press, Oxford, p.529.

Verbunt, F. 1988b, in: *The physics of neutron stars and black holes*, eds. Y. Tanaka, ISAS, Tokyo, in press.

Verbunt, F. & Hut, P. 1987, in: *The origin and evolution of neutron stars*, IAU Symp. # 125 Nanjing P.R. China, eds. D.J. Helfand and J.H. Huang, Reidel, Dordrecht, p.187.

Verbunt, F. & Meylan, G. 1988, *Astron. Astrophys.* in press.

Verbunt, F. & Rappaport, S.A. 1988, *Astrophys. J.* in press.

Verbunt,F., van den Heuvel, E.P.J., van Paradijs, J. & Rappaport, S.A. 1987, *Nature* **329**, 312.

Wolszczan, A., Middleditch, J., Kulkarni, S.R. & Fruchter, A.S. 1988, *IAU Circ.*# 4552.

The Evolution of Pulsars

D.G. Blair and B.N. Candy
Department of Physics
University of Western Australia
Nedlands WA 6009

ABSTRACT. The relative contributions of field decay and alignment to the evolution of radio pulsars is discussed. Physical arguments are used to demonstrate that geometrical evolution should be expected on a timescale 10^6 - 10^8 yr. An evolutionary model involving alignment and polar cap emission, is shown to give remarkable agreement with a range of measured pulsar properties. Evidence is presented, which suggests that pulsar energy loss is dominated by beams of relativistic particles, and the radio luminosity is shown to be well behaved if the observed data is corrected for beam geometry.

1. INTRODUCTION: ALIGNMENT OR FIELD DECAY

Ostriker and Gunn (1969) in one of the earliest papers on radio pulsars, discussed the possibility that pulsar evolution is dominated either by magnetic field decay, or by alignment or counter alignment. Ohmic field decay could be modelled quite simply, and the relevant timescale obtained from the conductivity of the neutron star interior, which had already been estimated by Canuto (1970) in a study of a relativistic Fermi gas. By contrast, Ostriker and Gunn (1969) emphasised the complexity of the analysis in the case of electromagnetic torques: "from a theoretical point of view, the question of alignment is extremely difficult, depending as it does on details of the electromagnetic field near the star." They also noted that "In any case, the observations indicate that alignment does not occur for at least the first 10^7 years". Here we reassess this conclusion.

In this paper we first review the literature on both field decay and alignment. There now appears to be no strong theoretical grounds for belief in field decay on the required $\sim 10^{6\text{-}7}$ year time scales. In spite of the extreme difficulty of an exact analysis, there are, however, strong grounds for believing that geometrical evolution (alignment or counter alignment) is inevitable in pulsars, and that the timescale will be comparable to the observed spindown time scales. We then go on to review observations which strongly support magnetic alignment, and to discuss the consequences of alignment on population, birthrate and luminosity.

H. Ögelman and E. P. J. van den Heuvel (eds.), Timing Neutron Stars, 609–625.

2. GENERALISED PULSAR MODELS

It is often assumed that magnetic dipole radiation dominates the energy loss from radio pulsars. The surface magnetic field, B, is then related to the observable quantities P and $\dot{P}$ by the relation:

$$B^2 \sin^2\theta = \left(\frac{3\,c^3\,I}{8\,\pi^2\,R^6}\right) P\dot{P}, \qquad (1)$$

where I and R are the pulsar moment of inertia and radius respectively, and θ is the angle between the magnetic dipole and spin axes. This equation can be generalised to

$$\left(\frac{3\,c^3\,I}{8\,\pi^2\,R^6}\right) P\dot{P} = \eta B^2 \sin^2\theta + \xi B^2 \cos\theta + \lambda B^2 \beta^2 \sin^2\theta\,, \qquad (2)$$

where η and ξ are constants which allow for the difference between an idealised vacuum dipole model ($\eta = 1$, $\xi = 0$, $\lambda = 0$) and a real pulsar which generates a dense magnetosphere leading to possible field aligned electric currents ($\xi>0$), non-dipole radiation ($\eta \neq 1$), and relativistic beams ($\lambda > 0$) with beamwidth 2β. The case $\lambda > 0$ has not been previously discussed, and will be discussed in more detail in section 7.

Subsequent to Ostriker and Gunn (1969) the majority of papers on pulsars have made the drastic assumption that the pulsar magnetic field can be inferred from equation (1), with $\theta = 90°$. In general it is useful to distinguish three distinct scenarios:

I	$\eta=1, \xi=0, \lambda=0$ θ = constant	Slowdown dominated by vacuum magnetic dipole torque. Negligible torque from magnetosphere currents. No geometrical evolution.
II	$\eta=0, \xi=1, \lambda=0$ θ increasing	Slowdown dominated by field aligned currents in the magnetosphere. Geometrical evolution - counteralignment (eg Beskin *et al*, 1983).
III	$\eta=1, \xi=0, \lambda=0$ θ decreasing	Slowdown dominated by vacuum dipole torque. Geometrical evolution - alignment (eg Kundt, 1981; Jones, 1976)

It is remarkable that the above scenarios which all involve very different physics have not been distinguished observationally. It is unlikely, however, that any will correctly describe all pulsars. Both η and ξ must be period dependent, since at least in the limit $P \rightarrow \infty$ the magnetosphere density must decay until the system is described by the vacuum solution. This, of course, will only apply to isolated neutron stars after they have died as

radio pulsars. A complete description would require η and ξ as period and field dependent functions, as well as time dependence for B and θ. The third term, involving λ cannot always be zero since some young pulsars (eg. Vela) have beamed luminosity ~ 1% of the spin down power. Since we can only see the electromagnetic component of the beam, it is not unreasonable to suppose that beamed luminosity could dominate the emission of pulsars.

In the meantime, the solution of the alignment question has not been satisfactorily answered either theoretically or experimentally. Major papers on the evolution of pulsars have been based on the unstated assumption that the geometry is stationary in time. In fact, numerous workers have found varying reasons for suspecting that geometrical evolution occurs (see section 5).

3. REVIEW OF MAGNETIC FIELD DECAY MODELS

Our understanding of the decay of neutron star magnetic fields has developed considerably since 1968. The earliest estimates of the ohmic magnetic field decay timescale, τ, assumed a spherical, isotropic star, so that

$$\tau = \frac{4 R^2 \sigma}{\pi c^2} \quad , \qquad (3)$$

where σ is the internal conductivity, and R is the radius of the star (Lamb, 1887). The conductivity was first obtained by using a relativistic electron gas to model the charge carrying component. The resultant conductivity $\sigma \sim 10^{22}$ s^{-1} corresponds to a decay timescale $\tau \sim 10^6$ yr, consistent with the value suggested by the pulsar characteristic age distribution (eg Lyne *et al*, 1975). Baym and Pethick (1969) showed, however, that including the effect of the high level of proton degeneracy in the core led to much higher conductivities $\sigma \sim 10^{29}$ s^{-1}, corresponding to much larger decay timescales ~ 10^{13} yr. Subsequent analyses concentrated on the expected variation of σ within the neutron star. The most detailed study by Ewart *et al* (1975) concluded that even allowing for the lower conductivity of the neutron star crust, significant field decay would not be expected on a 10^7 yr timescale.

Even neglecting the possibility of proton superconductivity in the core, the conductivity of the neutron star interior now appears far too great to allow significant field decay on a 10^7 yr timescale. Several other mechanisms by which the magnetic field of a neutron star might decay have been suggested however.

Flowers and Ruderman (1977) suggest that the internal magnetic field decays to a lower energy state through fluid motions. This process can occur on very short timescales so that some mechanism is required to stabilise the field in the fluid centre. Flowers and Ruderman (1977) suggest that the interior field is stabilised either by a rigid crust which pins the interior field, or by toroidal currents in the crust. In both cases, ohmic decay of crustal fields (allowed because of the lower conductivity in this region) is followed by hydromagnetic decay in the core.

It has also been suggested that flux drift in the superconducting interior might lead to the magnetic field being ejected from the interior on a 10^7 year timescale (eg Jones, 1987). The literature on field decay is summarised in Table 1.

Table I. Field Decay Theory

Authors	σ (s^{-1})	τ (yr)	Assumptions
1. Ohmic decay of internal field			
Pacini (1968,1969)	$\sim 10^{22}$	3×10^6	The charge carrying component
Ostriker and Gunn (1969)	6×10^{22}	4×10^6	is modelled as a relativistic Fermi gas.
Baym and Pethick (1969)	1.5×10^{29}	$\sim 10^{13}$	Proton degeneracy in the core reduces the effect of protons as electron scatterers, thus the conductivity of the interior is increased.
2. Ohmic decay of field in crust			
Solinger (1970)	$\sim 10^{22}$	4×10^6	Conductivity limited by the electron phonon interaction.The results are valid only in the high temperature limit.
3. Ohmic decay of field in neutron star with varying conductivity			
Chanmugam and Gabriel (1971)		$\sim 10^{10}$	
Ewart *et al* (1975)		$> 10^7$ yr	Analysis includes the effects of impurities, lattice defects and the effect of the electron phonon interaction.
4. Other field decay mechanisms			
Flowers and Ruderman (1975)			The interior field decays through interior fluid motions which reduce the magnetic energy.
Jones (1987)			Field decays through flux drift in the superconducting interior

4. REVIEW OF ALIGNMENT/COUNTER ALIGNMENT MODELS

Pulsar electrodynamics is so complex that no models have satisfactorily taken into account all of the perturbations which cause the real pulsar to differ from a dipole magnetised sphere rotating in a vacuum. An accurate model must take into account rotational deformation, magnetic deformation, crustal distortion, cracking and creeping, internal fluid motions and dissipation, magnetic quadrupole components, and radiation torques produced by currents in the magnetosphere. Table II summarises the literature. Each study considers only specific perturbations (given in the last column).

We shall restrict our discussion to the most recent paper in table II, by Good and Ng (1986). This is still restricted to a spherical rigid star, but for the first time takes into account the torques due to current flow in the magnetosphere. Classical electromagnetic torques, magnetospheric torques and near field effects which contribute anomalous torques varying as Ω^2 rather than Ω^3 are included in the analysis. Their main conclusions are the

a. There are several new dipole torque terms which are at present incalculable, and which are of the same order of magnitude as the vacuum dipole torque.

b. The anomalous torques do not effect alignment, but cause rotation about the magnetic axis (this may be consistent with Kundt's (1981) suggestion of an approach to alignment by nutation).

c. In the event of maximal currents along open field lines, the counteraligning torque is roughly 3 times larger than the classical dipole aligning torque.

d. Anomalous spindown torques are negligible,. This implies (within their assumptions) that spindown is described by W^3 torques, which may be described in

$$\Gamma = \Omega^3 B^2 \sin^2 \theta \quad . \qquad (4)$$

In reference to (c) above we note that if $\xi \lesssim 0.3$ the aligning torque exceeds the counter aligning torque. Thus in the case $\xi = 10^{-4}$ this term would be negligible (Kundt, 1981). However if $\xi = 1$ as argued by Beskin *et al* (1983) this term will dominate over the aligning torque.

The overall picture that remains, is that the theoretical solution to the alignment problem is not yet possible. Depending on the magnetosphere structure, and on the stellar structure (including crustal structure and fluid currents in the core) one can expect alignment or counteralignment to occur. There is, however, no reason to expect all torques to cancel. Torque cancellation to even 10% of the maximal value would provide a torque that is significant in evolutionary terms, extending the alignment or counteralignment time scale from a few times 10^6 years to a few times 10^7 years.

We therefore conclude that any evolutionary model which does not contain geometrical evolution cannot correctly describe the properties of the pulsar population. Field decay should be considered as a possibility, with possible time scales in the range 10^7 - 10^{13} years. Alignment or counteralignment should be *expected*, on time scales 10^6 - 10^8 years.

Table II. Magnetic Alignment Theory

Authors	Conclusions
Michel and Goldwire (1970)	Magnetic torques cause the alignment of dipole and spin
Davis and Goldstein (1969)	axes for a dipole magnetised sphere rotating in a vacuum.
Goldreich (1970)	Elastic and viscous damping of the precession angle by energy dissipation in the stellar interior may dominate over magnetic torques.
Chau and Henriksen (1970)	Including the effect of gravitational radiation. Alignment on a braking timescale.
Soper (1972)	Generalises from a dipolar field to an axisymmetric field. Alignment of field and spin axes still takes place on a braking timescale.
Macy (1974)	Whether alignment or counteralignment take place depends of the relative strength of dipole and toroidal field components.
Jones (1976)	Includes the torque produced by current outflow, but this is assumed small compared to the vacuum dipole torque, so that alignment still takes place.
Beskin *et al* (1983)	The torque produced by field aligned currents exceeds the vacuum dipole torque, so that counteralignment takes place.
Good and Ng (1986)	Alignment or counteralignment may take place, depending on the relative magnitude of torques produced by field and currents in the magnetosphere.

5. OBSERVATIONAL STUDIES

It is important to emphasise that the interpretation of almost all the data on pulsars is strongly model dependent. Thus, while a variety of data is available which can be used to distinguish the contributions of alignment and field decay to pulsar evolution, the interpretation of this data requires extreme caution. For example, to identify $(P\dot{P})^{\frac{1}{2}}$ with the pulsar magnetic field (see for example Radhakrishnan (1986)) is clearly wrong in view of the above analysis. The value of $(P\dot{P})^{\frac{1}{2}}$ can, at best provide a rough estimate of B, within the 1-2 orders of magnitude variation possible for sin θ. [Given that pulsar beams are a few degrees wide the value of sin θ cannot become less than 10^{-2} without a pulsar attaining a 100% duty cycle]. It is certainly incorrect to label a $(P\dot{P})^{\frac{1}{2}}$ axis as magnetic field, and in view of the uncertainty of η and ξ it is probably incorrect to interpret this as the transverse magnetic field.

Those properties of radio pulsars which are determined by the transverse magnetic field strength cannot be used to distinguish between alignment and field decay *as both may affect the transverse field in the same way.* The pulsewidth and polarisation gradient, however, are dependent only on the emission geometry and are independent of the strength of the magnetic field, so that they can be used to distinguish between the two models of pulsar evolution. Studies of the dependence of pulsewidth and polarisation-gradient on characteristic age and pulse period have provided strong support for alignment models (Candy and Blair, 1983,1986,1987, 1988; Kuzmin et al, 1983,1984).

Kundt (1981) shows that the distribution of pulsars in the $(P\dot{P})^{\frac{1}{2}}$ versus characteristic age plane is more consistent with alignment than field decay. Essentially his argument is that the number of pulsars located in a strip of constant rotation period decreases with characteristic age, in a manner consistent with an increase in the beaming factor produced by secular alignment.

Statistical studies of the observed pulsewidth distribution have consistently shown that the θ distribution is concentrated at small values (e.g. Wu et al, 1982; Henry & Paik, 1969; Proszynski, 1979; Candy & Blair 1986). This result clearly supports the alignment model, which provides a mechanism for producing this concentration.

Kuzmin et al. (1983, 1984) obtain the size of the emission cone directly from the pulsar period, by assuming $\beta \propto \beta_0 P^{-\gamma}$, where β is the halfwidth of the emission cone. The values of β are then combined with the observed pulsewidth and polarisation gradients to yield values of θ for each pulsar. The resulting θ distribution is concentrated at small values, and θ decreases with increasing characteristic age, strongly favouring the alignment model.

Finally, Candy and Blair (1983,1986,1987) have established that both the polarisation gradient and the mean pulsewidth vary with characteristic age, in good agreement with a model incorporating magnetic alignment and narrowing of the emission cone. We have also demonstrated that these two results are incompatible with magnetic field decay models (Candy and Blair, 1988). This model is discussed in more detail in section 6.

The conclusions of these studies of the observational data which relate to the geometrical evolution/field decay question are summarised in table III.

Table III. Observational Studies

Authors	Conclusions
Manchester & Taylor (1977)	The concentration of interpulse pulsars at short periods can be interpreted as evidence for alignment.
Kundt (1981)	The distribution of pulsars in the $(PP)^{1/2}$ vs characteristic age plane is more consistent with alignment than field decay.
Wu *et al* (1982) Proszynski (1979) Candy and Blair (1986)	The distribution of pulsewidths requires a θ distribution concentrated at small values.
Kuzmin *et al* (1983)	The angle θ is estimated for 300 pulsars from the pulsewidth and period values. θ values are concentrated at small values, and there is an inverse relation between θ and characteristic age.
Candy and Blair (1983)	There is a minimum in the observed mean pulsewidth characteristic age relation, which is consistent with a model incorporating alignment and emission cone narrowing.
Kuzmin *et al* (1984)	The angle θ is obtained with greater accuracy from the pulsar period, pulsewidth and polarisation gradient. The θ values decrease with increasing characteristic age.
Candy and Blair (1986)	There is a maximum in the polarisation gradient characteristic age relation, which is consistent with the combined effects of cone narrowing and alignment.

6. THE CONE NARROWING -ALIGNMENT MODEL

The cone-narrowing-alignment model, described in Candy and Blair (1983, 1986, 1987), assumes a standard polar cap emission cone geometry determined by the opening angle of the first open field lines. The opening half angle of the emission cone is given by:

$$\beta = \beta_o \left(\frac{P}{P_m}\right)^{-\gamma} , \qquad (5)$$

where γ is predicted to be 0.33 (Ostriker and Gunn, 1969) 0.5 (Roberts and Sturrock, 1972), 0.67 (Ruderman and Sutherland, 1975), but is left as a free parameter to be determined by the data.

While the model of Ruderman and Sutherland (1975) has been criticised by Jones (1987) and Aarons *et al* (1983,1985) on the basis of the predicted solid state properties of the neutron star crust, we distrust the solid state modelling of neutron star crusts, and prefer to submit the model to the data on the pulsar population for confirmation or rejection.

We first assume that a vacuum-dipole like torque dominates pulsar alignment, so that:

$$\sin\theta = \sin\theta\,(0)\,\exp^{-t/\tau} , \qquad (6)$$

(eg Davis and Goldstein, 1970: Jones 1976), where the alignment timescale, τ, is left as a free parameter. The assumption of a vacuum dipole torque is tested later against the observed data. If magnetic dipole radiation dominates the pulsar energy loss, then the decline in the angle θ will result in a period evolution equation of the form

$$P = P_m \left(1 - e^{-2t/\tau}\right)^{1/(n-1)} , \qquad (7)$$

where n is the pulsar braking index (for magnetic dipole radiation n =3). Substituting equation 7 in equation 5 allows the evolution of β to be determined explicitly:

$$\beta = \beta_o \left(1 - e^{-2t/\tau}\right)^{-\gamma / (n-1)} . \qquad (8)$$

Equations 6 and 8 then determine the evolution of the pulsar emission geometry. By using these equations it is possible to predict the dependence of the mean pulsewidth, and median polarisation gradient on characteristic age.

The evolution of the mean pulsewidth is obtained, by substituting equations 6 and 8 into the following expression:

$$\bar{W} = \int_{\theta - \beta}^{\theta + \beta} 2 \arccos \left(\frac{\cos\beta - \cos\theta \cos\theta_{obs}}{\sin\theta \sin\theta_{obs}} \right) P(\theta_{obs})\, d\theta_{obs} , \qquad (9)$$

where θ_{obs} is the observer orientation relative to the spin axis, and $P(\theta_{obs})$ is the probability distribution of the observer orientation (for randomly aligned spin axis $P(\theta_{obs}) = \sin\theta_{obs} / 2$).

The median polarisation gradient is approximately given by the polarisation gradient value, corresponding to an observer direction lying halfway between the cone axis and the edge of the emission cone (Candy and Blair, 1986). The evolution of the median polarisation gradient, $(d\psi/d\phi)_m$, is then obtained by substituting equations 6 and 8 into the expression

$$\left(\frac{d\psi}{d\phi}\right)_m = \frac{\sin\theta}{\sin(\beta/2)} . \qquad (10)$$

By averaging over all pulsar ages, the number pulsewidth distribution and number polarisation gradient distributions can also be obtained (see Candy and Blair, 1988). By allowing for variations in the fraction of sky spanned by the emission cone, the number age distribution can also be obtained.

In previous work, we have assumed, following Jones (1976), that the initial orientation of the emission cone, $\theta_o = 90^o$. There is now evidence (Kuz'min *et al*, 1983, 1984) , however, that the θ values of young pulsars are distributed over a wide range, so that small values of θ_o for these pulsars are not precluded. Since Jones (1976) model relies on detailed assumptions about the neutron star interior, and so does not have a strong physical justification, we have generalised the alignment model to include a random distribution of θ_o values, so that:

$$P(\theta_o)\, d\theta_o = \frac{\sin\theta_o}{2}\, d\theta_o . \qquad (11)$$

This refinement does not change the model appreciably, but does lead to numerically different conclusions regarding the beaming factor and birthrate. We favour this model, because it is consistent with a simple scenario for pulsar formation, whereby the pulsar field is a frozen relic of the randomly oriented field of the progenitor star.

We have obtained the best fit parameters corresponding to this generalised model, by fitting to the observed pulsewidth age relation (figure 1 (a)). These parameters are then used to *predict* the median polarisation gradient age relation (figure 1(b)) , the observed pulsewidth distribution (figure 1(c)) the observed polarisation gradient distribution (figure 1(d)), and the observed number age distribution (figure 1(e)).

In fitting to the observed linear polarisation data, the choice of β_o values is not obvious. Analysis of the observed fifty percent intensity pulsewidth data yields a best fit value of β_o = .047, whereas fitting to the ten percent intensity pulsewidth data yields β_o = .085. The value of β_o, which provides the better fit to the linear polarisation data is β_o = .085, which suggests that the 10% pulsewidth data is a better measure of the emssion geometry.

The best fit parameters for the generalised model are summarised in table IV, along with the best fit parameters corresponding to the evolutionary model described in Candy and Blair (1986).

Table IV. Evolutionary Model Parameters

	β_o	θ_o	τ (yr)	γ	n	n'	$\bar{F}$	N_G	Birth Period(yr)
Model 1	.065	90^o	$2x10^7$	0.6	3	-	18	$1.3x10^6$	22-30
Model 2	.047	random	$2x10^7$	0.6	3	-	40	$2.8x10^6$	10-17
Model 3	.047	random	$2x10^7$	0.84	2.1	3.8	40	$2.8x10^6$	10-17

Model 1 - refers to the model developed in Candy and Blair (1983,1986) for θ_o assumed to be 90^o.

Model 2 -assumes that the intitial alignment of the pulsar spin axis is random, so that the angle θ_o has a distribution given by $P(\theta_o) = \sin \theta_o /2$.

Model 3 - (beamed emission) represents an entirely different scenario, that the entire energy loss from the pulsar is in the form of beamed emission. Only a small modification of the parameters is required to retain the model 2, fits to the data.

Figure 1

(a) The mean pulsewidth is plotted against characteristic age using data from the catalogue of Manchester and Taylor (1981). The solid curve shows the prediction of the evolutionary model. The parameters used are n = 3, γ = 0.6, β_o = .047, and a distribution of alignment timescales which is gaussian in the log, with mean (log τ) = 7.3 and σ = 0.7 (Candy and Blair, 1986).

(b) The median polarisation gradient is plotted against characteristic age. The solid curve shows the prediction of the evolutionary model. The model fit uses the best fit parameters obtained in Fig 1(a), except that the value of β_o, is replaced by a larger value β_o = 0.085 obtained by fitting to the ten per cent pulsewidth data (see section 6).

(c) The distribution of the observed angular pulsewidths is compared to the prediction of the evolution model, using the parameters of Fig 1(a).

(d) The observed distribution of polarisation gradients, compared with the model prediction (solid curve), using the same parameters as Fig 1(b).

(e) The number distribution of characteristic age values is compared to the model prediction of Candy and Blair (1988), using the best fit parameters of Fig 1(a).

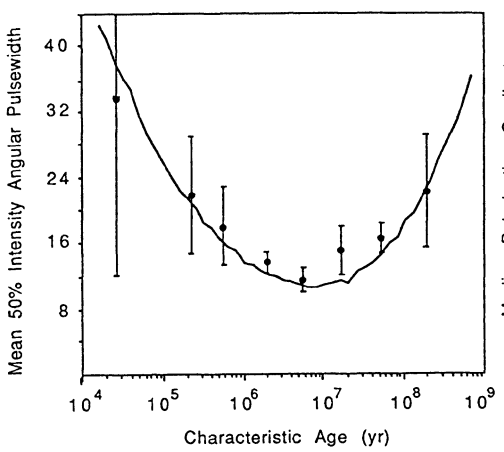
Mean 50% Intensity Angular Pulsewidth
40
32
24
16
8
10^4 10^5 10^6 10^7 10^8 10^9
Characteristic Age (yr)

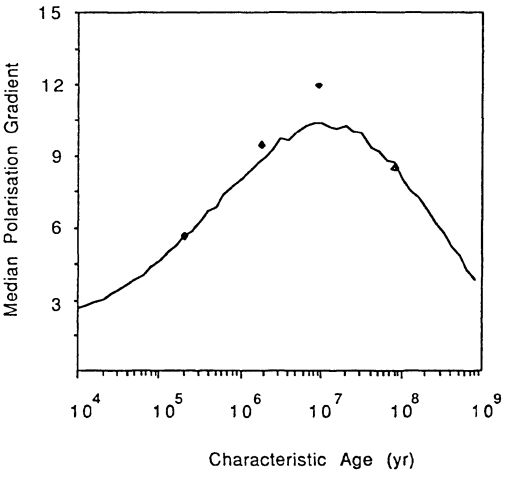
Median Polarisation Gradient
15
12
9
6
3
10^4 10^5 10^6 10^7 10^8 10^9
Characteristic Age (yr)

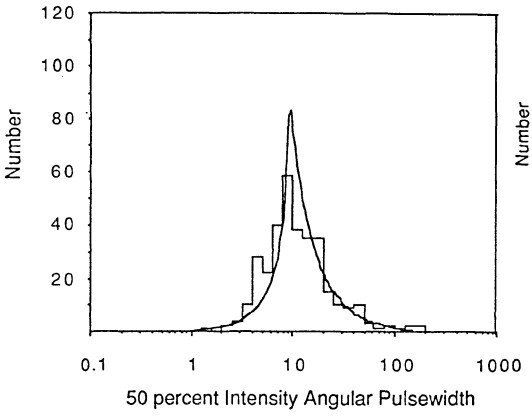
Number
120
100
80
60
40
20
0.1 1 10 100 1000
50 percent Intensity Angular Pulsewidth

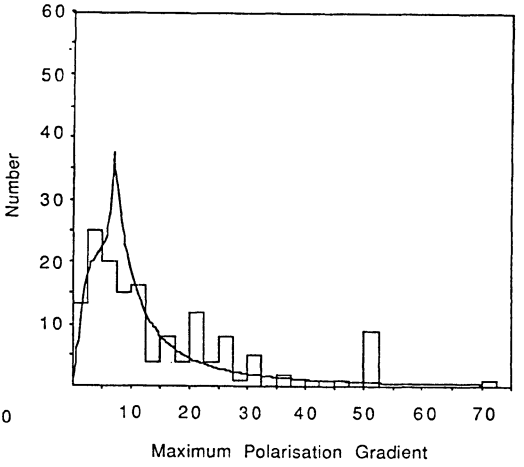
Number
60
50
40
30
20
10
10 20 30 40 50 60 70
Maximum Polarisation Gradient

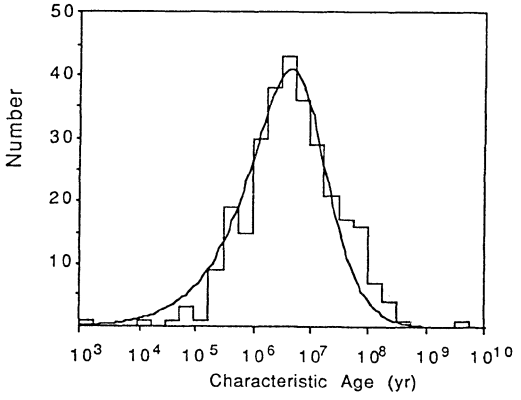
Number
50
40
30
20
10
10^3 10^4 10^5 10^6 10^7 10^8 10^9 10^{10}
Characteristic Age (yr)

Using the best fit parameters for the generalised model, the evolution of the pulsar beaming factor, F, can be obtained. F is defined as the reciprocal of the fraction of the sky spanned by the emission cone and, assuming that each pulsar has one emission cone of halfwdith β and orientation θ, is given by:

$$F = (\sin\theta \sin\beta)^{-1} \quad . \qquad (12)$$

In Figure 2 we show explicitly the evolution with characteristic age of θ. The solution for the time evolution of θ is in reasonable agreement with the results of Kuzmin *et al* (1983,1984) which are based on polarisation data. Although we have used polarisation data to confirm our results, we note that the polarisation data has not been explicitly used in obtaining our best fit parameters. Thus we see broad consistency between independent measures of pulsar evolution.

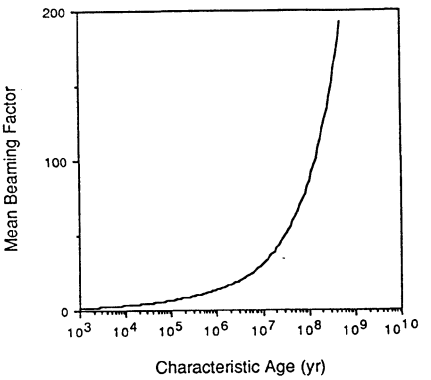

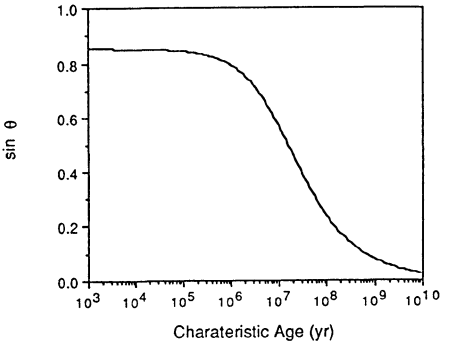

Figure 2 The model predicted value of θ is plotted against characteristic age, using the best fit parameters obtained by fitting to the pulsewidth characteristic age data.

Figure 3 The model predicted value of β is plotted against characteristic age, using the best fit parameters obtained by fitting to the pulsewidth age data.

Figure 4 The beaming factor predicted by the evolutionary model is plotted against characteristic age, using the best fit parameters obtained by fitting to the pulsewidth characteristic age data.

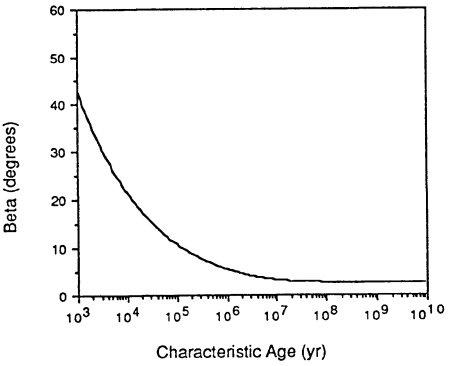

The evolution of β is shown in Figure 3. The model does not uniquely distinguish between γ and n, since the fit is to γ/n-1. Moreover, we shall see in section 8 that $P\dot{P}$ data and luminosity considerations give grounds for using an alternate value of γ.

Finally in Figure 4 we show the evolution with characteristic age of the mean beaming factor F. The value of F rises from 2-6 for young pulsars ($t_c < 10^6$ yr), to ~ 100 for old pulsars ($t_c > 10^8$ yr). The majority of the population ($t_c \sim 10^7$ years) are quite highly beamed, and the mean beaming factor of the population is ~40. We stress again that the broad pulse widths of old pulsars is due to the alignment of spin and cone axes, so that when observed the pulsewidth appear to be magnified.

7. LUMINOSITY AND $\dot{P}\dot{P}$ EVOLUTION

Pulsars are unique among astrophysical systems in that the large majority of their energy output is derived from the kinetic energy of rotation. Thus $(P\dot{P})^{\frac{1}{2}}$ is directly related to the absolute energy loss rate of the system. The apparent decline in $(P\dot{P})^{\frac{1}{2}}$ with increasing characteristic age (see figure 5) has been noted previously, and interpreted as evidence for both field decay (Flowers and Ruderman, 1975) and magnetic alignment (Kundt, 1981). In fact the spin down luminosity $L_S \sim (P\dot{P})\ P^{-4}$, is also very well behaved amongst the population as the binned data, with standard errors emphasises in Figure 6.

The observed luminosity of radio pulsars, L_R, is generally determined just from the observed intensity and distance, and is a very small fraction of L_S in all cases (In the case of the Crab and Vela for which pulsations have been observed from radio to gamma ray frequencies, the observed total pulsed radiation is $\sim 10^{-3}$ of L_S). Data for L_R versus characteristic age as inferred by Lyne *et al* , (1985) strongly contrasts with the spindown luminosity data, showing large scatter, and even when binned shows a scattered non-monotonic dependence on characteristic age. The mean luminosity falls by only 1.5 orders of magnitude over three orders of magnitude of characteristic age (Lyne *et al* , 1985). We now go on to consider this difference in the behaviour of L_R and L_S.

We first point out that the true pulsar radio luminosity L_{RT} can only be roughly inferred from the observed radio flux since only part of the emission cone is sampled. Secondly, if cone narrowing occurs the best estimate for the true luminosity must allow for the smaller emission cones of old pulsars. The radiation from an old pulsar is confined to a narrow conical beam so that total luminosity is far less than inferred from the observed flux density. Thus we propose that the weak dependence of inferred luminosity on characteristic age, is an artifact. A better approximation to the true pulsar luminosity, L_{RT} is obtained by using the relation:

$$L_{RT} = \frac{\beta^2}{2}\ L_R\ , \qquad (13)$$

where we have assumed only one emission cone, and the most probable position of the observer relative to the emission cone representing half the peak value. Using equation 5 the observed radio luminosities can be corrected by the relation

$$L_{RT} = \beta_o{}^2\ P^{-2\gamma}\ L_R\ . \qquad (14)$$

Figure 7 shows the evolution with characteristic age of the corrected radio luminosity given by equation 14, for $\gamma = 1$, while there is still large scatter, the decline appears more consistent with the spindown luminosity data.

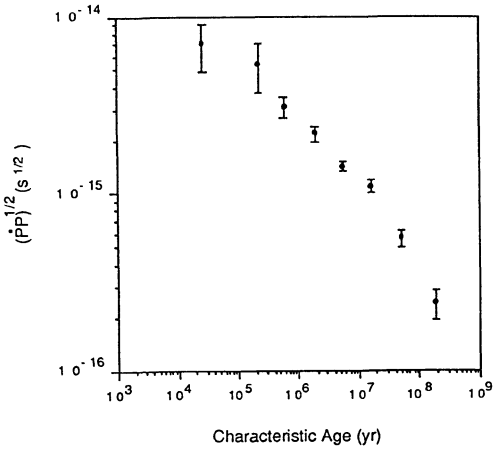

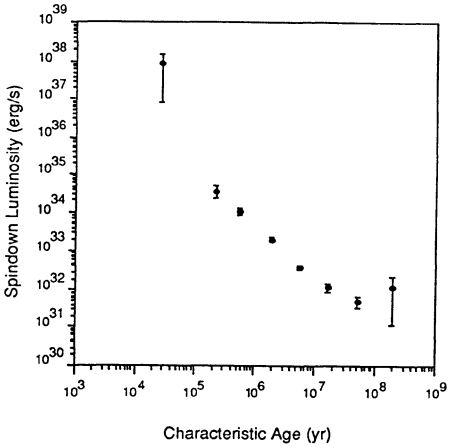

Figure 5 The obsered value of $(\dot{P}P)^{\frac{1}{2}}$ is plotted against characteristic age, using the same data grouping as in figure 1. Error bars in all cases are standard errors of the mean.

Figure 6 The observed spindown luminosity is plotted against characteristic age.

Figure 7 The dependence of the corrected radio luminosity on characteristic age.

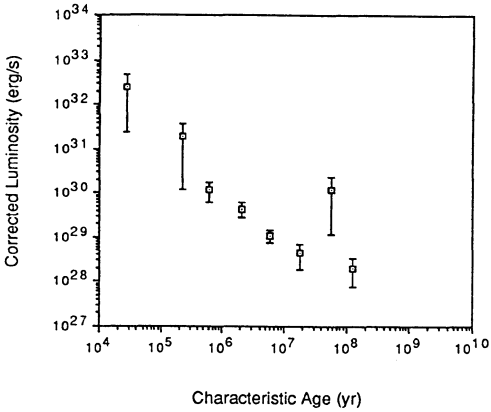

The apparent reduction of pulsar luminosity of 1 - 1.5 orders of magnitude in 3 decades of characteristic age represents *a real reduction of luminosity of at least 3 orders of magnitude*. The weak reduction in flux density with characteristic age means that the observability of pulsars is dominated by geometric evolution, and flux density decline has a relatively weak effect on the number- characteristic age distribution.

Lyne et al. (1985) have shown that L_R can be expressed roughly as $L_R \propto P$, so that:

$$L_R \propto L_S P^3 . \qquad (15)$$

Using equation (13), it then follows that

$$L_{RT} \propto L_S P^2 \qquad (\gamma = 0.5) \qquad (16)$$
$$L_{RT} \propto L_S P \qquad (\gamma = 1.0).$$

Thus for γ values in the range 0.5 - 1, the efficiency for conversion of mechanical energy into radio luminosity still increases with the rotation period, with a power between 1

and 2. Short period pulsars are relatively inefficient radio emitters, but they increase in efficiency as the rotation period increases.

We now consider the idea that in active radio pulsars, low frequency magnetic dipole radiation is completely suppressed, and that the pulsar efficiently converts rotational energy into relativistic particle beams. We assume that the radio beams reflect the geometry of the particle beams as they leave the pulsar, although the particle beam geometry is not preserved, due to deflection in galactic magnetic fields. We also assume that the unseen luminosity of radio pulsars is dominated by these beams. We then ask what effect the evolution of the emission geometry will have on the decelleration torque.

We will assume that the mean angular flux density within the beam *saturates* at a value proportional to $\Omega^{n+1}B^2 \sin^2\theta$. In this circumstance the transverse magnetic field determines the flux density, but the beam geometry determines the total flux, and hence L_S. The assumption of saturation implies that the charged particle current density in the emission region is limited, and independent of the emission geometry. This scenario corresponds to the case $\xi = \eta = 0$, and $\lambda = 1$ in equation (2).

Since the spindown luminosity L_S is now confined to the fraction of space $\beta^2/4\pi$ it follows that:

$$L_S = \Omega^{n+1} \beta^2 B^2 \sin^2\theta \quad . \tag{17}$$

Expressed in terms of the decellerating torque Γ, the above analysis suggests that Γ is not given by the dipole radiation equation:

$$\Gamma = \Omega^n B^2 \sin^2\theta \quad , \tag{18}$$

but rather by

$$\Gamma = \Omega^n \beta^2 B^2 \sin^2\theta \, . \tag{19}$$

Substituting equation 5 then yields

$$\Gamma = \Omega^{(n+2\gamma)} B^2 \sin^2\theta \quad . \tag{20}$$

This dependence of the slowdown rate of pulsars on the beaming of emission, can thus be described in terms of an increase in the braking index, n, defined through the expression

$$\dot{\Omega} = - k \Omega^n \, . \tag{21}$$

from n to $n' = n + 2\gamma$. This increase in the braking index, leads to a new period evolution equation:

$$P = P_m \left(1 - e^{-2t/\tau}\right)^{1/(n'-1)} \quad , \tag{22}$$

(exponential evolution of $\sin\theta$ is still assumed), and a new equation for the evolution of $(P\dot{P})^{\frac{1}{2}}$:

$$(P\dot{P})^{\frac{1}{2}} = k \, e^{-t/\tau} \left(1 - e^{-2t/\tau}\right)^{(3-n')/(2n'-2)} \quad . \tag{23}$$

where $k^2 = 2 P_m^2/(n'-1)\,\tau$.

In figure 8 we show a comparison of this equation with the observed $(\dot{P}\dot{P})^{\frac{1}{2}}$ data: an excellent fit is obtained using the same alignment timescale as was used to fit to the pulsewidth age and number age distributions. In comparison the dipole radiation equation used to obtain the results in Section (6) does not give a good fit as is shown in Figure 8. We take this as strong evidence, that beamed emission better describes the energy loss than our standard scenario.

While this beamed emisison equation of motion produces a large change in the predicted evolution of $(\dot{P}\dot{P})^{\frac{1}{2}}$, the model fitting to the pulsewidth and polarisation data is unaffected. This is because only the ratio $\gamma / (n' - 1)$ is used in the model fitting. It is possible to find values of γ, n and n', which satisfy the fit to the $(\dot{P}\dot{P})^{\frac{1}{2}}$ characteristic age data ($n' = n + 2\gamma = 3.8$), and which also give the same value of $\gamma/(n' - 1)$ that is used in the model fitting to the pulsewidth and polarisation data ($\gamma/(n'-1) = 0.3$). These requirements are satisfied, for $\gamma = 0.84$, and $n = 2.1$ and $n' = 3.8$. The full set of evolutionary pulsar parameters, corresponding to this beamed emission equation of motion, is included in table 4.

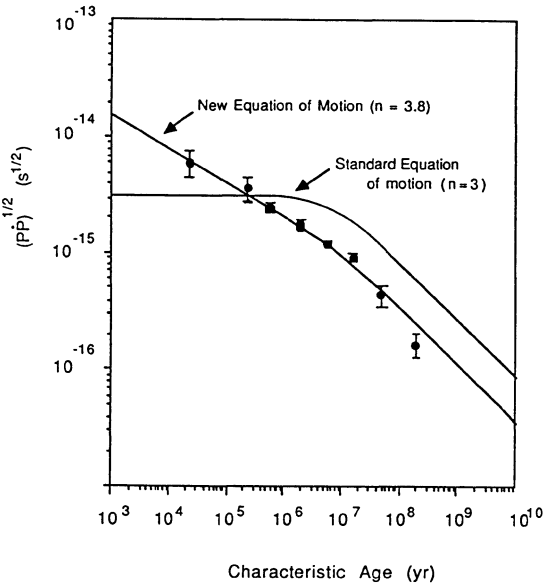

Figure 8

The observed value of $(\dot{P}\dot{P})^{\frac{1}{2}}$ is plotted against characteristic age, also shown is the standard vacuum dipole equation of motion (including a decay in the transverse field) which corresponds to n=3, and the equation of motion corresponding to the domination of the energy loss by relativistic beams so that n = 3.8.

8. CONCLUSION

A single model for pulsar alignment shows a remarkable degree of agreement with observation. It has been shown that geometrical evolution in the form of either alignment or counter alignment should be expected on fundamental grounds, and that models without geometrical evolution are physically extremely unlikely.

A $\beta \propto P^{-\gamma}$ form for the emission cone geometry (which is derived from polar cap models, but not necessarily dependent on a particular emission mechanism), combined with exponential alignment explains

a) the skewness of the pulse width distribution
b) the pulse width characteristic age distribution
c) the number-characteristic age distribution
d) the polarisation gradient characteristic age distribution and
e) the number polarisation gradient distribution.

In addition this model explains the weak dependence of the apparent pulsar luminosity with age, and enables the derivation of a corrected luminosity age relation. Implicit in the model is the assumption that magnetic field decay does not occur. The results obtained here support the views of the workers in table III, who have argued from independent observations that pulsar alignment occurs. The evolution of $(\dot{P}P)^{\frac{1}{2}}$ is consistent with the model if the pulsar equation of motion is assumed to be dominated by beamed energy loss with a saturated flux density, and not by the usual dipole radiation term.

Finally we conclude by emphasising that the assumption found throughout the literature that neutron stars magnetic fields decay on a time scale of 10^6 years should at the least be treated with scepticism, and should not be relied on in constructing evolutionary scenarios for x-ray sources.

ACKNOWLEDGEMENTS

We are glad to acknowledege the hospitality of the Institute of Astronomy, Cambridge, where much of the work in this paper was started. This work was supported in part by the Australian Research Grants Scheme.

REFERENCES

Baym, G. Pethick, C. Pines, P. 1969 *Nature* **224**, 675 .
Beskin, V.S., Gurevich, V.S. and Istomin, Ya.N. 1983. *Astrop.Sp.Sc.* **102**, 301.
Candy, B.N. and Blair, D.G. 1983. *Monthly Notices Roy.Astron.Soc.* **205**, 281.
Candy, B.N. and Blair, D.G. 1986. *Astrop.J.* **307**, 535.
Candy, B.N. and Blair, D.G. 1987. *Astron.Astrop.* **183**, L17.
Candy, B.N. and Blair, D.G. 1988 (In preparation)
Canuto, V. 1970 *Astrop.J.* **159**, 641,
Chanmugam, G. Gabriel G. 1970. *Astron.Astrop.* **11**, 268.
Chau W.Y. and Henriksen, R.N. 1970. *Astrop.J.* **161**, L137.
Davis, L. and Goldstein M. 1970. *Astrop.J.* **159**, L81.
Ewart, G.M. Guyer, R.A. Greenstein, G 1975. *Astrop.J.* **202**, 238.
Flowers, E. & Ruderman M.A. 1977. *Astrop. J.* **215**, 302.
Fokker, A.D. 1987. *Astron. Astrop.* **182**, 41.
Gentile, A.M. 1970 *Astrop. Lett* **5**, 245.
Ghosh, P. , J. *Astron. Astrop.* 1984. **5**, 307.
Goldreich, P. 1970, *Astrop. J.* **160**, 41.
Good, M.L. and Ng, K.K. *Astrop. J.* **299**, 706.
Guseinov, O. Kh, Yusifov, I.M. 1985. *Sov. Astron.* **29 (2)**, 136.
Guseinov, O. Kh, Kasumov, F.K. Yusifov, I.M. 1982. *Sov Astron* **26 (1)**, 31.
Jones, P.B. 1976. *Astrop.J.* **209**, 602.
Jones, P.B. 1976. *Astrop .Sp .Sc* . **45**, 369 .

Jones, P.B. 1987. *Monthly Notices Roy.Astron.Soc.* **228**, 513.
Kundt, W. 1981 *Astron Astrop* **98**, 207.
Kuz'min, A.D. Dagkesamanskaya I.M.1983. *Sov. Astron. Lett* **9 (2)**, 80
Kuz'min, A.D. Dagkesmanskaya, I.M. Pugachev, V.D. 1984. *Sov. Astron. Lett* . **10 (6)**. 357.
Lamb, H. 1887. *Phil.Trans.* **174**, 519.
Lyne A.G. Ritchings, R.T. Smith, F.G. 1975 *Monthly Notices. Roy.Astron.Soc.* **171**, 579.
Lyne, A.G., Manchester, R.N. and Taylor, J.H. 1985 *Monthly Notices. Roy.Astron.Soc.* **213**, 613.
Macy, W.W. 1974. *Astrop.J.* **190**, 153.
Manchester, R.N. and Taylor, J.H. 1977 *Pulsars* (eds Freeman, San Francisco).
Michel, F.C. 1987. *Nature* **310**, 329.
Michel, F.C. Goldwire, H.C. 1970. Astrop. Lett. **5**, 21
Ostriker, J.P. and Gunn, J.E. 1970. *Nature.* **223**, 813.
Pacini, F. 1967. *Nat ure.* **216**, 567.
Pacini, F. 1968*Nature* . **219**, 145.
Proszynski, M. 1979. *Astron. Astrop.* **79**, 8.
Radhakrishnan, (1986) *Highlights of Astronomy*, eds J.P.Swings Reidel, Dordrecht, Holland.
Solinger, A.B. 1970. *Astrop. J.* **161**, 553.
Soper, S.R.K. 1972. *Astrop. Sp .Sc* .**19**, 249
Taam, R.E. Van Den Heuvel, E.P.J. 1985. *Astrop. J.* **305**, 235.
Tamman, G.A. 1982 *Supernovae: A Survey of Current Research* p371-403, eds M.J. Rees and R.J. Stoneham (Reidel, Dordrecht).
Van den Heuvel, E.P.J von Paradijs J.A. Taam, R.E. 1986. *Nature* **322**, 153.

THE ORIGIN OF PULSAR VELOCITIES AND THE VELOCITY MAGNETIC MOMENT CORRELATION

MATTHEW BAILES
Mount Stromlo and Siding Spring Observatories
Institute of Advanced Studies
Australian National University
Private Bag, Woden P.O., A.C.T.,Australia, 2606

ABSTRACT. By considering the evolution of intermediate mass binary systems with periods similar to the Be X-ray binaries we find that if a kick velocity of a few hundred kilometres per second is imparted to neutron stars at birth then at the time of the second supernova explosion most of the binaries are disrupted. In addition the two neutron stars released have quite different properties. The first-born pulsar has a weak field and slow velocity whereas the new pulsar has a large velocity and a strong field. Since the majority of pulsars probably arise from intermediate mass stars, and a large fraction of these are in binaries, the model described above explains the velocity - magnetic moment correlation for radio pulsars and the low fraction of pulsars in binaries.

1. Introduction

Radio pulsars have velocities which range from a few to several hundred kilometres per second. The origin of these velocities is uncertain and there are several theories as to their origin. In a recent study, Dewey and Cordes (1987) found that the velocities are unlikely to arise solely from the break-up of binary systems unless a number of special criteria are met. Their favoured model has a kick velocity being imparted to pulsars at birth of order 100 km s-1. This model is in broader agreement with the fraction of pulsars in binaries and the observed velocity distribution than the no-kick model however it could not produce the velocity magnetic moment correlation observed by Anderson and Lyne (1983) and the number of binary pulsars produced was slightly too high. In this paper we outline a model which explains the velocity magnetic moment correlation in terms of two populations of pulsars. One class consists of the first born pulsars in massive binary systems which are released at the time of the second supernova explosion. The other class consists of pulsars arising from single stars and those which are released from binaries upon formation. In our model all pulsars receive an asymmetric kick upon formation of

H. Ögelman and E. P. J. van den Heuvel (eds.), Timing Neutron Stars, 627–629.

order 200 km s−1.

2. Massive Binary Evolution.

In order to sustain the pulsar population Blaauw (1985) calculated that all stars above 6 solar masses must produce pulsars. The steep IMF of massive stars requires the majority of pulsars to arise from stars less than 20 solar masses at ZAMS. Stars in this mass range are often members of binary systems and the binary frequency, whilst somewhat uncertain, is probably at least 50% and may be higher due to the existence of faint low-mass companions (Abt 1983). During the course of its evolution a massive binary in the above mass range has two supernova explosions separated by about 107 years. If it survives the first explosion it undergoes a common envelope phase at the end of the main sequence lifetime of the initially less massive star. During this phase mass transfer takes place and "spins-up" the first-born neutron star. The magnetic field of the first-born neutron star has decayed by about an order of magnitude since birth. The reduction in spin period is between about 2 and 5 depending on the precise values of the field decay and evolutionary timescales. At the time of the second supernova event we have a circularized orbit with an old, slightly spun-up pulsar orbiting a pre-supernova star.

3. The Velocity Magnetic Moment Correlation.

If the second supernova explosion is symmetric then it can be shown that the velocity of the old neutron star is always greater than that of the new neutron star (Radhakrishnan and Shukre 1985). The old pulsar has a weaker field than the new pulsar, and, if we extrapolate back in time to the magnetic field strength at birth we will miscalculate it due to the spinning up of the neutron star (Radhakrishnan 1984). Pulsars which have been spun-up cannot have their initial fields calculated as if they have been single since birth and if this is assumed the derived field comes out too low. If all explosions were symmetric we would observe the opposite correlation between magnetic field and velocity to that observed for both current and initial fields.

The introduction of a kick velocity of a $\sim$ 200 km s−1 does not improve the correlation unless the binaries are quite wide (periods > few weeks) at the time of the second supernova event. If the majority of pulsars are produced from binaries with periods greater than a hundred days before the second supernova then the fraction of pulsars in binaries is consistent with that observed. The old pulsars are ejected from the binary with velocities of a few tens of km s−1 and weak fields. The new pulsars have strong fields and large velocities due to the impulse they received at birth. The correlation between initial fields and velocity only exists because of the spinning-up of the old pulsars. The pulsars with low velocities once possessed high fields but at the time were still members of binary systems and not observable as radio pulsars due to the presence of their main sequence companions. This is why we don't see any high field, low velocity pulsars. We expect pulsars arising from single stars will form part of the high velocity, high field class due to the kicks they

received at birth, as will pulsars which escape the binary during the first supernova explosion.

Systems such as those which produced the binary pulsars PSR1913+16 and PSR2303+46 were very tight before the second supernova event and are probably the descendents of the massive X-ray binaries. The percentage of observed pulsars which come from such systems can only be small or else the fraction of pulsars in binaries would be much greater.

4. Discussion.

The model relies on two main assumptions, that pulsars receive impulsive kicks at birth, and that a reasonable fraction arise from massive binaries with orbital periods of $\geq$ 100 days. In the past, the main objection to kicks has been the cause of the asymmetric explosion, which produces the kick. Whilst this is still a concern it is difficult to model the observed population without such kicks (Dewey and Cordes 1987). If we accept kicks then wide binaries produce the correct fraction of pulsars in binaries as well as the velocity magnetic moment correlation. The inability of Dewey and Cordes to reproduce the correlation can be understood in terms of their orbital period range prior to the second supernova event. This was constrained to lie between 0.03 and 3 days due to the difficulties of modelling the common-envelope phase. If we relax this constraint then not only can we produce the correlation but we also obtain the correct fraction of pulsars in binaries.

The low velocity pulsars are not observable until several million years after they are formed at which time they possess spin periods of several hundred milliseconds. The existence of a class of pulsars which "switch on" at such periods has been postulated by Vivekanand and Narayan (1981) in order to explain the period distribution of radio pulsars.

A full version of this paper is about to be submitted to a scientific journal.

References.

Abt, H. A. 1983, *Ann. Rev. Astron. Astrophys.***21**, 343.

Anderson, B. and Lyne, A. G. 1983 *Nature* **303**, 597.

Blaauw, A. 1985, *The Birth and Evolution of Massive Stars and Stellar Groups*, ed. W. Boland and H. van Woerden, (Dordrecht: Riedel), p.211

Dewey, R.J. and Cordes, J.M. 1987, *Astrophys. J.* **321**, 780

Radhakrishnan, V. 1984, *In "Millisecond Pulsars"*, eds S.P. Reynolds and D.R. Strineberg, (Green Bank:NRAO Publications), p. 130

Radhakrishnan, V. and Shukre, C. S. 1985. *Proc. of Workshop on Supernovae, their Progenitors and Remnants.* Indian Acad. Sci., Bangalore, India), 155

Vivekanand, M., and Narayan, R. 1981, *J. Astrophys. Astron.*, **2**, 315

THE WHITE DWARF-NEUTRON STAR CONNECTION

R. Canal[1,3], J. Isern[2,3], and J. Labay[1,3]
[1]Departament de Fisica de l'Atmosfera, Astronomia i Astrofisica, Universitat de Barcelona, Barcelona
[2]Centre d'Estudis Avancats de Blanes, C.S.I.C., Girona
[3]Grup d'Astrofisica, Institut d'Estudis Catalans, Barcelona

ABSTRACT. The standard mechanism for neutron star formation is collapse of the cores of massive stars at the end of their thermonuclear evolution. However, this mechanism cannot account for the presence of neutron stars in binary systems where their companions are low-mass stars and no capture process (involving a previously isolated neutron star) can be invoked for the formation of the system. Gravitational collapse of a white dwarf into a neutron star is necessarily involved in those cases. Here we review the physical processes relevant to such collapses, for both C+O white dwarfs and O+Ne+Mg white dwarfs. We examine the various possibilities concerning the physical changes in C+O white dwarf cores with cooling and we stress that all of them equally lead (for a suitable range of parameters) to collapsing structures. We discuss the different calculations done so far and we finally compare the case of C+O white dwarfs with that of O+Ne+Mg white dwarfs.

1. INTRODUCTION

Neutron stars have so far been detected either by their pulsed radio emission or by their X-ray (pulsed or nonpulsed) emission. Most radio pulsars are isolated while all compact X-ray sources are in close binary systems.

The standard mechanism for neutron star formation is gravitational collapse of the Fe-Ni cores of initially massive ($M \geq 10\ M_\odot$) stars, the end products of thermonuclear evolution of their central layers. When those cores reach nuclear matter densities, collapse is halted and several solar masses (the fraction of the star outside the core) are somehow ejected at high velocities in a supernova explosion. The recent detection of the neutrino burst associated with neutron star formation (or at least with core collapse), from SN 1987A, has confirmed this mechanism even if its exact workings have not yet been completely elucidated (see, for instance, Arnett 1987). This process can not only explain the formation of isolated pulsars but also a fraction of neutron stars in binaries: those having massive companions (see van den Heuvel, this volume). The same origin may be advocated for low-mass binaries (those with $M_{tot} \leq 5\ M_\odot$) when the ambient density of stars is high enough (as in globular clusters) to make the capture process (involving a previously for-

H. Ögelman and E. P. J. van den Heuvel (eds.), Timing Neutron Stars, 631–640.

med neutron star) likey. But there is a large variety of systems containing neutron stars that cannot be explained by the standard core collapse of massive stars (see, for instance, Taam and van den Heuvel 1986). Examples of such systems are:

-Wide radio pulsar binaries, such as PSR 0820-02 and PSR 1953+29 (the 6 ms pulsar).
-Millisecond pulsars (not in wide binaries).
-Galactic bulge X-ray sources (including QPO's).
-Type I X-ray burst sources and soft X-ray transients.
-Gamma-ray sources.

Formation of those neutron stars is presently attributed to the gravitational collapse of a white dwarf, growing above Chandrasekhar's limit by mass accretion from the current neutron star's companion in the binary system. This idea was first formulated by Schatzman (1974) and developed by Canal and Schatzman (1976), Canal and Isern (1979), and Canal, Isern, and Labay (1980), who considered C+O white dwarfs. Later, Miyaji et al. (1980) proposed the same mechanism for O+Ne+Mg white dwarfs.

In fact, white dwarf structures are always involved in neutron star formation: the Fe-Ni cores of massive stars are electron-degenerate configurations, growing in mass up to their stability limit from thermonuclear processing of the surrounding, Si-burning shell. Conversely, white dwarf stars are the bare cores of red giants that were not massive enough (after mass loss) to undergo the latest stages of thermonuclear burning (C+O white dwarfs stopped short of C-burning; O+Ne+Mg white dwarfs did the same for Ne-burning). The most important difference between both kinds of neutron star progenitors is that the former ones have no nuclear potential energy left while the latter still possess enough energy to be completely disrupted if it is explosively liberated. The problem with massive star cores is to have them ejecting the surrounding layers with enough energy. The problem with white dwarfs is to avoid their explosive disruption before they become gravitationally unstable.

Mass-accreting white dwarfs have long been associated with explosive phenomena: novae and cataclysmic variables in general, and Type I supernovae. In order for a white dwarf to reach Chandrasekhar's mass, it has to avoid both explosive ejection of the outer, accreted layers, and complete disruption from explosive burning initiated in the central layers. The range of parameters (initial mass, temperature, and chemical composition of the white dwarf; mass-accretion rate, and chemical composition of the accreted matter) allowing mass growth without significant ejection of the infalling material has mostly been explored under the assumptions of spherical symmetry and no kinetic energy deposition (Fujimoto and Taam 1982; MacDonald 1984; Nomoto and Hashimoto 1987). When such hypotheses are relaxed (Sparks and Kutter 1987; Shaviv and Starrfield 1987), the results differ so widely that no firm conclusion can be reached and the corresponding parameters may well presently be regarded as almost free. Explosive ignition of electron-degenerate C+O cores was first studied in the context of the final evolution of red giant stars in the mass range: (4-6) $M_\odot \leq M \leq$ (8-10) $M_\odot$. The approaches developed to that purpose were later applied to the mass-accreting white dwarf case (see Woosley and Weaver 1986, for a review). The problem concer-

ning white dwarf collapse can be summarized as follows:

Collapse *versus* disruption basically means pressure and energy removal by electron captures *versus* expansion driven by the energy released by thermonuclear reactions. White dwarfs close to Chandrasekhar's mass are loosely bound: their internal energy approaches their gravitational energy. Release of the nuclear energy contained in only a fraction of the star's mass will unbind it. On the other hand, Chandrasekhar's mass is proportional to the square of the mass-averaged electron mole number Y_e, that decreases from electron captures. Electron capture rates increase with density. They are also much larger for material in nuclear statistical equilibrium (NSE), for a given Y_e, than for either C+O or O+Ne+Mg at the same density. Thus, the thermal runaway associated with thermonuclear ignition of material in a strongly electron-degenerate plasma induces fast electron captures. But, at the same time, it drives expansion, that decreases density and finally suppresses the captures. Moreover, a Rayleigh-Taylor instability grows, inducing mixing of the high-temperature, incinerated material with the overlying cold, unburnt material. This propagates burning on a hydrodynamical time scale. Collapse thus means that electron captures decrease Chandrasekhar's mass below the actual mass of the star before hydrodynamic expansion suppresses them. Therefore, gravitational collapse is favoured both by high ignition density and by slow propagation of the thermonuclear burning. This, for instance, excludes He white dwarfs as candidates to collapse upon mass accretion: the ignition density for He is so low that electron captures after incineration are rather slow; moreover, overpressures produced by explosive helium burning are large enough (for the same reason: relatively low density) to induce by themselves (before any mixing process) ignition of the contiguous layers. The shock wave generated in the layers first ignited grows into a *detonation* and thus supersonically propagates burning: the star cannot avoid complete disruption.

The way electron captures and burning propagation are coupled makes it necessary to resort to numerical hydrodynamic calculations in order to properly determine the range of conditions at ignition leading either to collapse or to disruption of the star. Here we will review the different calculations of this kind done so far. But first we will examine the physical processes that, in turn, determine both ignition density and burning propagation velocities.

2. PHYSICAL PROCESSES

2.1. Thermonuclear reaction rates

At the high densities prevailing in the central layers of massive white dwarfs ($\rho_c \sim 10^8$–10^{10} g cm^{-3}), thermonuclear reaction rates are strongly enhanced by screening effects (see Itoh et al. 1979). This, of course, lowers ignition density. But if temperatures are low enough (for given densities) the ions start to oscillate around fixed positions, forming a crystal lattice. Nuclear reactions in this *pycnonuclear* regime are slower than in the fluid, *strong-screening* regime (Salpeter and Van Horn 1969) and ignition densities are correspondingly larger (Canal and Schatzman 1976; Canal and Isern 1979). If the central layers of a C+O white

dwarf remain solid (which is equivalent to pycnonuclear regime) through the whole mass-accretion phase up to explosive carbon ignition, densities in the range 9.50×10^{9}-1.39×10^{10} g cm^{-3} can be reached, the exact value depending on mass-accretion rate (Hernanz et al. 1988). Here we assume a C+O mixture with $X_C = X_O = 0.50$, forming a random alloy in solid phase (we will see that this is not necessarily the case). Either pure O or a O+Ne+Mg mixture have even higher ignition densities, but the trigger, there, is electron captures, as we will see later.

2.2. Solidification and chemical composition

It had usually been assumed that C and O (or, by that way, also O, Ne, and Mg) were completely miscible both in fluid and in solid phase. A Monte Carlo numerical experiment by Loumos and Hubbard (1973) seemed well to confirm that a C+O mixture would crystallize without any change in its chemical composition, at a temperature given by the weighted mean of those of pure C and pure O solidification. This was challenged by Stevenson (1980) who, based on a simple model, predicted complete phase separation, with a resulting eutectic in the fluid-solid coexistence curve. He also argued that simulations done in the way Loumos and Hubbard (1973) did theirs were unlikely to reproduce such a behaviour, however real it were. Based on Stevenson's (1980) phase diagram, Mochkovitch (1983) showed how a cooling white dwarf would become chemically separated in two regions: a central, solid, pure O core, and a partially fluid C mantle, in a few times 10^{9} years. The implications for C+O white dwarf collapse were first examined by Canal, Isern, and Labay (1980).

Only recently (Barrat, Baus, and Hansen 1986; Ichimaru, Iyetomi, and Tanaka 1987; Barrat, Hansen, and Mochkovitch 1988) Monte Carlo numerical calculations aimed to explore the behaviour of crystallizing C+O fluid mixtures have been undertaken. Results from the hard-sphere model (Barrat, Baus, and Hansen 1986; see also Ichimaru, Iyetomi, and Tanaka 1987) seemed to confirm the eutectic behaviour. In contrast, the calculations of Barrat, Hansen, and Mochkovitch (1988), using a density functional approach, give a phase diagram of the "spindle" form, with the solid phase being slightly more O-rich than the fluid phase. Since this last calculation still involves fairly arbitrary assumptions, the problem of the chemical separation remains open. A second point arises as to, if C and O were miscible in solid phase, whether they should form a random or a completely ordered solid: a body centered cubic (BCC) lattice with C and O sites forming simple cubic sublattices (Dyson 1971). Schatzman (1983) estimated that such a structure would be the most stable one. The above referred calculations give that this is the case at temperatures below the fluid-solid coexistence line. As we will see, the implications of this last possibility, as for thermonuclear ignition, are similar to those of C-O separation.

If C and O separate when crystallizing, O "flakes" falling to the center of the star and C being progressively confined to the outer layers, no thermonuclear ignition happens in the innermost layers, when the white dwarf is later compressed by mass accretion, until ^{16}O starts to capture electrons, at $\rho \cong 2\times10^{10}$ g cm^{-3}. Explosive ignition is then triggered by the ^{16}C formed from the captures. As we will see, such a high ignition density means that electron captures on the incinerated

material are so fast that they overcome burning propagation for any reasonable estimate of the speed of the latter. The only possibility of avoiding collapse, once chemical separation has proceeded to some extent, is to have off-center C ignition, if the central O core is not large enough (this again depending on mass-accretion rate). That would give Type Ia supernova explosions (Lopez et al. 1986a, b; Canal, Isern, and Lopez 1988). A complete parameter study of the conditions leading either to white dwarf collapse or to SN Ia outburst, for C-O separation, can be found in Hernanz et al. (1988). Note that the results are not affected by possible remelting of the previously solid layers as an outcome of mass accretion, since C and O will not remix.

If an *ordered* crystal is formed (and C is, at most, as abundant as O, which is very likely in view of recent values for the $^{12}C(\alpha,\gamma)^{16}O$ reaction rate), ignition is also delayed up to $\rho \cong 2\times10^{10}$ g cm^{-3} (the threshold for electron captures on ^{16}O). The reason is that no ^{12}C ion has another ^{12}C ion as its nearest neighbour, in solid phase. The only possible nuclear fusion in the pycnonuclear regime (but for crystal defects) is $^{12}C + ^{16}O$, much slower than $^{12}C + ^{12}C$. Ignition is thus triggered by electron captures: they heat up and melt the solid, so allowing $^{12}C + ^{12}C$ reactions (in the strong-screening regime). It is clear that, in this case, a large enough solid core has to remain until the end of the mass-accretion stage, in order to reach the above ignition densities (in contrast with the chemical separation case). C ignition at the edge of the solid core (the bottom of the fluid layers) will happen if it becomes sufficiently small due to partial melting during the accretion stage (Canal, Isern, and Labay 1987).

2.3. Burning propagation

Thermal conduction is the most efficient heat transfer mechanism in a strongly electron-degenerate plasma, as long as it remains hydrodynamically stable. Therefore, burning is propagated by conduction through the solid layers of the star. In a stratified fluid, however, when ignition of the deeper layers induces their expansion the stratification becomes unstable. Ensuing mixing propagates burning on a hydrodynamic time scale (velocities of the order of the local velocity of sound). Conductive burning propagation will nonetheless dominate close to the center of the star even in fluid interiors, due to the growth time for instabilities (see Woosley and Weaver 1986).

Conductive velocities are significantly lower than hydrodynamic burning propagation velocities. The estimates of both do involve a number of approximations, but typically $v_{cond} \cong 10^{-2} v_{turb}$, where v_{turb} stands for the velocity of the hydrodynamic (turbulent) flame front (Woosley and Weaver 1986). This favours electron captures in their competition with hydrodynamic expansion (Canal and Isern 1979; Isern et al. 1983). It adds up to the fact that captures are already very fast due to the high ignition densities associated with the pycnonuclear burning regime, when the star's center has remained solid until ignition.

When burning progresses through solid layers towards the surface of the star, a fluid NSE region grows behind it. The turbulent motions of this zone cannot penetrate the solid layers since the kinetic energy associated with the turbulent eddies is only a small fraction of the solid

"strength" (as measured by the latent heat of melting: see Canal et al. 1986). Thus, the burning front remains conductive all the way up to the edge of the solid core. It must be noted, besides, that ignition densities of the order of 10^{10} g cm^{-3} can be reached, in mass-accreting C+O white dwarfs, even after complete melting of an initially solid, random alloy core (Hernanz et al. 1988). In those cases, collapse is still possible, due to the initial "slowness" of the hydrodynamic motions.

3. DYNAMICAL INSTABILITY

Dynamical instability sets in, for mass-accreting white dwarfs, following incineration of their central layers (Canal and Isern 1979). Reaching Chandraskhar's mass before that (even including general-relativistic effects) would require unrealistically high accretion rates (Canal and Schatzman 1976). Canal and Isern (1979) first calculated the evolution of a C+O white dwarf after central C ignition at $\rho_c \cong 10^{10}$ g cm^{-3}. For their estimate of conductive burning front velocities (similar to that of Buchler, Colgate, and Mazurek 1980), they found dynamical contraction of the star. It was followed up to $\rho_c \cong 5\times10^{11}$ g cm^{-3}, when the white dwarf was fully collapsing. For this calculation, the solid core was assumed to be a random C+O alloy. Similar results have been reported in Isern et al. (1983), Isern, Labay, and Canal (1984), Canal et al. (1986, 1987), and Isern et al. (1987a, b).

Calculations corresponding to the hypothesis of C-O separation have been done in Canal, Isern, and Labay (1980, 1982a, b), Labay et al. (1985), and Canal et al. (1987). In this case, collapse always ensues, following central oxygen ignition triggered by flash of the ^{16}C produced by electron captures on ^{16}O (see also Bravo et al. 1983). This happens for any reasonable choice of burning propagation speed, both in conductive and turbulent regimes. No specific calculations have yet been done for an ordered alloy, but ignition densities being the same as in the precedent case, the outcome should also be equivalent.

More recent calculations, for initially solid cores consisting of a random C+O alloy, are reported in Isern et al. (1988). The cores whose evolution after central carbon flash is followed are the descendants of partially solid white dwarfs in the initial mass range $1.2\ M_\odot \leq M \leq 1.4\ M_\odot$. Their previous evolution upon mass accretion is thoroughly studied in Hernanz et al. (1988). Our aim is to self-consistently calculate the transition from quasistatic to fully dynamic evolution, for the most realistic estimates of both conductive and hydrodynamic burning propagations. It turns out that the range of central ignition densities 9.5×10^{9} g cm$^{-3} \leq \rho_c \leq 1.4\times10^{10}$ g cm^{-3}, for current estimates of conductive burning propagation speed (which is the relevant one close to the center, irrespective of physical state, solid or fluid: see Woosley and Weaver 1986), is a critical one. Close to $\rho_c \cong 10^{10}$ g cm^{-3}, transition from collapse to explosion takes place, the exact value depending not only on the uncertainty range for burning front velocities but also on the type of hydrodynamic code used (variously damped hydrodynamics). Thus, in Isern et al. (1988), with an explicit (undamped) hydrodynamic code, collapse is obtained for $\rho_c \geq 1.1\times10^{10}$ g cm^{-3} and current estimates (Woosley and Weaver 1986) of both conductive and turbulent flame velocities (collapse for $\rho_c = 1.4\times10^{10}$ g cm^{-3} had also been calculated in

Canal et al. 1986, 1987). At slightly lower ignition densities, bifurcation between collapse and explosion (for a given burning propagation speed) is sensitive to the degree of damping of the hydrodynamics introduced by the code (Canal et al., in preparation). In all the collapsing models calculated, there is a large amount of electron captures, due to the high entropy of the core (in contrast with the Fe-Ni cores of massive stars). The high entropy is, indeed, due to the thermonuclear deflagration. Large deleptonization means stallation of the shock wave produced by bounce at nuclear matter densities. Collapse should thus be "quiet", with little ejection of matter (Isern et al. 1988).

Also recently, Nomoto (1986a) has attempted a parameter study of the outcome of thermonuclear deflagration of C+O cores at $\rho_c = 10^{10}$ g cm^{-3}. He parametrizes burning front velocities as a fraction of the local velocity of sound c_s. The reported results are somewhat puzzling: his case D ($v_{burn} \cong 0.01\ c_s$), the closest to the actual conductive burning propagation speed, is clearly wrong by a couple of orders of magnitude. Indeed, c_s being $\cong 10^9$ cm s^{-1} and the star radius being $\cong 10^8$ cm, it is utterly impossible, after 155 s (when $\rho_c \cong 10^{11}$ g cm^{-3}), for the mass of the burned region to be only 0.03 $M_\odot$, as claimed in the paper. Case C ($v_{burn} \cong 0.06\ c_s$) is a bit better: the claim that after $\cong 1.7$ s the burned mass is only 0.13 $M_\odot$ is only wrong by one order of magnitude or so. Case B is *a priori* more believable: v_{burn} is $\cong 0.1\ c_s$, and after 0.6 s (also when $\rho_c \cong 10^{11}$ g cm^{-3}) the deflagration front has reached $M_r \cong 0.9\ M_\odot$. However, this result cannot be reproduced, even by imposing quasistatic evolution and increasing at the same time by one order of magnitude current electron capture rates (Canal et al., in preparation). Only the result that $v_{burn} \cong 0.15\ c_s$ gives an explosion that completely disrupts the star is hardly disputable. Those results are repeated in Nomoto(1986b, c, 1987), in Nomoto and Hashimoto (1987), and in Baron et al. (1987). The above referred case B is also the initial model for the collapse calculation of Baron et al. (1987). This model being characterized by a high entropy, as it is always the case for deflagrating cores, the qualitative conclusions as to the outcome of collapse should nonetheless be right.

O+Ne+Mg white dwarfs are still another candidate to gravitational collapse upon mass accretion (Miyaji et al. 1980). When the star contracts, electron captures on ^{24}Mg first heat up its center. Further contraction leads to electron capture on ^{20}Ne, followed by O ignition. The thermal history of the star's center is affected by the treatment of convective instability adopted. Electron captures on ^{24}Mg produce a Y_e gradient that stabilizes the fluid against convective motions (Miyaji and Nomoto 1987). O ignition is avoided during electron captures on ^{24}Mg at $\rho_c \cong 4\times10^9$ g cm^{-3} (but the effects of thermonuclear reactions involving the final products of the electron captures have not been included). Explosive O ignition finally takes place at $\rho_c \cong 9.5\times10^9$ g cm^{-3}. Collapse is obtained by Miyaji and Nomoto (1987), after artificially suppressing any burning (and they consider not a white dwarf but a red-giant core). We see that the ignition density is only at the lower end of those obtained for partially solid C+O white dwarfs, in the random alloy hypothesis (Hernanz et al. 1988).

4. CONCLUSIONS

A fraction of neutron stars are formed by gravitational collapse of mass-accreting white dwarfs. C+O and O+Ne+Mg white dwarfs are the likely candidates. Concerning C+O white dwarfs, it must be stressed that:

a) Stars that are partially solid at the onset of mass accretion and whose centers remain solid until pycnonuclear carbon ignition (or shortly before ignition in the strong-screening regime) ignite their thermonuclear fuel at $\rho_c \cong 10^{10}$ g cm^{-3} (Hernanz et al. 1988). For current estimates of conductive burning propagation velocities, this leads to collapse to a neutron star, at least for central ignition densities $\geq 10^{10}$ g cm^{-3} (Isern et al. 1988). This happens without assuming any C-O separation when the fluid white dwarf interior crystallizes (not even formation of an ordered alloy).

b) C-O chemical separation in the solid phase is an open possibility. In that case, collapse would always ensue, provided that the initial solid (oxygen) core were larger than 0.4-0.5 $M_\odot$ (off-center carbon ignition would result for smaller cores).

c) If C and O do not chemically separate when crystallizing but an ordered crystal is formed, collapse will again happen if melting induced by accretion has not proceeded too close to the centre before reaching the central density $\rho_c \cong 2\times10^{10}$ g cm^{-3} (the threshold for electron captures on ^{16}O).

Summarizing, C+O white dwarfs can collapse to neutron stars if they are partially solid when mass accretion starts, for any hypothesis made as to the outcome of the crystallization process. The range of parameters (initial masses and internal temperatures, mass-accretion rates) does, of course, depend on such hypothesis. Collapses will be quiet, with little mass ejection, due to the high entropy of the deflagrated cores.

O+Ne+Mg white dwarfs can equally collapse, but depending on the treatment of convection in the presence of a positive gradient of the electron mole number, Y_e, their ignition densities will only be at the lower end of those found for initially cold C+O white dwarfs (whose numbers, in any case, are several orders of magnitude larger).

REFERENCES

Arnett, W.D. 1987, in *The Origin and Evolution of Neutron Stars*, ed D.J. Helfand and J.-H. Huang (Reidel, Dordrecht), p. 273

Baron, E., Cooperstein, J., Kahana, S.H., and Nomoto, K. 1987, *Astrophys. Jour.*, **320**, 304

Barrat, J.L., Baus, M., and Hansen, J.P. 1987, *Phys. Rev. Letters*, **56**, 1063

Barrat, J.L., Hansen, J.P., and Mochkovitch, R. 1988, preprint

Bravo, E., Isern, J., Labay, J., and Canal, R. 1983, *Astron. Astrophys.*, **124**, 39

Buchler, J.R., Colgate, S.A., and Mazurek, T.J. 1980, *Jour. Phys. Suppl.*, No 3, **41**, C2-159

Canal, R., and Schatzman, E. 1976, *Astron. Astrophys.*, **46**, 229
Canal, R., and Isern, J. 1979, in *White Dwarfs and Variable Degenerate Stars*, ed. H.M. Van Horn and V. Weidemann (Univ. of Rochester Press, Rochester), p.52
Canal, R., Isern, J., and Labay, J. 1980, *Astrophys. Jour. (Letters)*, **241**, L33
Canal, R., Hernanz, M., Isern, J., Labay, J., and Mochkovitch, R. 1986, in *Accretion Processes in Astrophysics*, ed. J. Audouze and T. Thanh Van (Eds. Frontieres, Paris), p. 109
Canal, R., Isern, J., Hernanz, M., Labay, J., Bravo, E., and Garcia, D. 1987, in *Advances in Nuclear Astrophysics*, ed. E. Vangioni-Flam, J. Audouze, M. Casse, J.P. Chieze, and J. Tran Thanh Van (Eds. Frontieres, Paris), p. 251
Canal, R., Isern, J., and Labay, J. 1987, *Rev. Mexicana Astron. Astrof.*, **14**, 260
Canal, R., Isern, J., and Lopez, R. 1988, *Astrophys. Jour. (Letters)*, in press
Dyson, F. 1971, *Ann. Phys. (N.Y.)*, **63**, 1
Hernanz, M., Isern, J., Canal, R., Labay, J., and Mochkovitch, R. 1988, *Astrophys. Jour.*, **324**, 331
Ichimaru, S., Iyetomi, H., and Tanaka, S. 1987, *Phys. Rept.*, **149**, 95
Isern, J., Labay, J, Hernanz, M., and Canal, R. 1983, *Astrophys. Jour.*, **273**, 320
Isern, J., Labay, J., and Canal, R. 1984, *Nature*, **309**, 431
Isern, J., Canal, R., Hernanz, M., and Labay, J. 1987a, *Astrophys. Space Sci.*, **131**, 665
Isern, J., Canal, R., Garcia-Berro, E., Hernanz, M., and Labay, J. 1987b, *Rev. Mexicana Astron. Astrof.*, **14**, 260
Isern, J., Canal, R., Garcia, D., Garcia-Berro, E., Hernanz, M., and Labay, J. 1988, *Adv. Space Res.*, in press
Itoh, N., Totsuji, H., Ichimaru, and De Witt, 1979, *Astrophys. Jour.*, **234**, 1079
Fujimoto, M.Y., and Taam, R.E. 1982, *Astrophys. Jour.*, **260**, 249
Labay, J., Canal, R., Garcia-Berro, E., Hernanz, M., and Isern, J. 1985, in *Recent Results on Cataclysmic Variables*, ed. J. Rahe (ESA SP-236)
Lopez, R., Isern, J., Canal, R., and Labay, J. 1986a, *Astron. Astrophys.*, **155**, 1
Lopez, R., Isern, J., Labay, J., and Canal, R. 1986b, *Rev. Mexicana Astron. Astrof.*, **13**, 41
Loumos, G.L., and Hubbard, W.B. 1973, *Astrophys. Jour.*, **180**, 199
MacDonald, J. 1984, *Astrophys. Jour.*, **283**, 241
Miyaji, S., Nomoto, K., Yokoi, K., and Sugimoto, D. 1980, *Pub. Astron. Soc. Japan*, **32**, 303
Miyaji, S., and Nomoto, K. 1987, *Astrophys. Jour.*, **318**, 307
Mochkovitch, R. 1983, *Astron. Astrophys.*, **122**, 212
Nomoto, K. 1986a, in *Accretion Processes in Astrophysics*, ed. J. Audouze and T. Thanh Van (Eds. Frontieres, Paris), p. 137
Nomoto, K. 1986b, *Progr. Part. Nucl. Phys.*, **17**, 249
Nomoto, K. 1986c, *Ann. New York Acad. Sci.*, **470**, 294
Nomoto, K. 1987, in *The Origin and Evolution of Neutron Stars*, ed. D.J. Helfand and J.-H. Huang (Reidel, Dordrecht), p. 281

Nomoto, K., and Hashimoto, M. 1987, *Astrophys. Space Sci.*, **131**, 395
Salpeter, E.E., and Van Horn, H.M. 1969, *Astrophys. Jour.*, **155**, 183
Schatzman, E. 1974, in *The Nuclei of Galaxies, Black Holes, and Collapsed Matter*, Proc. Erice International School of Cosmology and Gravitation
Schatzman, E. 1983, in *Cataclysmic Variables and Related Objects*, ed. M. Livio and G. Shaviv (Reidel, Dordrecht), p. 149
Shaviv, G., and Starrfield, S. 1987, *Astrophys. Jour. (Letters)*, **321**, L51
Sparks, W.M., and Kutter, G.S. 1987, *Astrophys. Jour.*, **321**, 394
Stevenson, D. J. 1980, *Jour. Phys. Suppl.*, No 3, **41**, C2-53
Taam, R.E., and van den Heuvel, E.P.J. 1986, *Astrophys. Jour.*, **305**, 235
Woosley, S.E., and Weaver, T.A. 1986, *Ann. Rev. Astron. Astrophys.*, **24**, 205

PULSAR TURN-ON AND SECONDARY EVAPORATION IN THE PSR 1957 + 20 BINARY

W. Kluzniak, M. Ruderman*, J. Shaham, and M. Tavani
Department of Physics and
Columbia Astrophysics Laboratory
Columbia University
New York, NY 10027

ABSTRACT. A millisecond pulsar spun up in an accreting low mass X-ray binary is expected to turn on suddenly when the mass accretion rate falls below a critical value ($\sim 10^{16}$ gs^{-1}). The consequent energetic radiation from the pulsar can completely evaporate a very light compnion and ultimately result in a solitary millisecond radiopulsar. The secondary's evaporative wind would interact with the pulsar's Khz dipole radiation to form a bow shock and wake that can assymetrically eclipse the radiopulsar's microwave beam. This scenario has been suggested for PSR 1957 + 20.

1. Pulsar Turn On

The discovery by Fruchter, Stinebring, and Taylor (1988) of the millisecond radiopulsar PSR 1957 + 20, seemingly in the process of evaporating its very light ($2 \cdot 10^{-2} M_\odot$) companion, may be an example of a phase in a suggested scenario for the genesis of solitary millisecond pulsars (Ruderman, Shaham, and Tavani 1988, hereafter RST).

When the secondary fed the accretion disk that presumably spun up the millisecond pulsar PSR 1957 + 20 (e.g. Alpar *et al.* 1982) the secondary mass loss rate to the disk ($\dot{M}$) must have been near the neutron star's Eddington limit (10^{18}gs^{-1}). The accretion disk would then have reached almost to the neutron star's 10^6 cm radius surface. Roughly, the disk's inner radius

$$r_A \sim 10^6 \left(\frac{B_{NS}}{6 \cdot 10^8}\right)^{\frac{4}{7}} \left(\frac{\dot{M}}{10^{18}\mathrm{gs}^{-1}}\right)^{-\frac{2}{7}} \mathrm{cm}, \tag{1}$$

with B_{NS} the neutron star surface dipole magnetic field strength, assumed to be near the $6 \cdot 10^8$ G inferred for other millisecond pulsars from their free spindown rates. For spin-up to have been effective the disk radius r_A should have been less than the Keplerian corotation radius around the $P = 1.5$ ms period neutron star:

$$r_A < r_{co} \sim 2 \cdot 10^6 \mathrm{cm}. \tag{2}$$

Because of the star's very rapid spin rate the light cylinder radius (at which a corotating magnetosphere would rotate at the speed of light)

$$r_{lc} = \frac{cP}{2\pi} \sim 5 \cdot 10^6 \mathrm{cm} > r_A, \tag{3}$$

but would have been only several times larger. A disk which satisfied Eqs (1) – (3), presumably present during the spin-up phase of PSR 1957+20, is expected to have been fed by the Roche lobe overlow of its very light companion. This low mass X-ray binary then evolved into a phase where the secondary became smaller than its Roche lobe, probably because the binary separation grew much more rapidly than the secondary's radius (Kluzniak *et al.* 1988; KRST hereafter, Shaham,

* Talk given by M. Ruderman. Research supported in part by NSF grant AST-81-02381.

H. Ögelman and E. P. J. van den Heuvel (eds.), Timing Neutron Stars, 641–645.

these proceedings). As this occured $\dot{M}$, the flow of mass fed into the accretion disk by the secondary would drop even if driven by a wind from the secondary sustained by radiation from the neutron star and/or its accretion disk. As $\dot{M}$ drops, r_A grows as indicated in Eq. (1) until it reaches the $r_{\ell c}$ of Eq. (3). This will be achieved when (RST)

$$\dot{M} \sim \dot{M}_c = 10^{16} \left(\frac{L_p}{10^{37} \text{erg s}^{-1}} \right) \text{gs}^{-1} \tag{3}$$

with

$$L_p = \left(\frac{P}{10^{-3} \text{s}} \right)^{-4} 10^{37} \text{erg s}^{-1}. \tag{4}$$

The luminosity L_p is that for magnetic dipole radiation of a solitary nonaligned neutron star of period P and magnetic dipole field $B_{NS} = 6 \cdot 10^8$ gauss. When $\dot{M}$ drops below $\dot{M}_c$ there can no longer be a stable accretion disk around the neutron star. As long as $r_A < r_{\ell c}$ the accretion disk radius is determined by a balance between magnetic stress at the edge of the corotating dipole magnetic field of the neutron star (which falls with distance as r^{-6}) and the disk stresses (which fall as $r^{-\frac{5}{2}}$ to $r^{-\frac{7}{2}}$): there is always a stable $r = r_A$. When $r_A > r_{\ell c}$, the magnetic stress is that from the dipole's radiation field (which falls only as r^{-2}.). This stress will always dominate that of the disk. The spinning neutron star will then radiate like a solitary pulsar; its emission irradiates the surface of its companion and pushes any plasma emitted by that companion out of the system.

2. Pulsar Emission

If the total spin-down power of PGR 1957 + 20 turns out to be about the same as that of its cousin PGR 1937 + 214 (which has the same ms period) it would emit about $6 \cdot 10^{36} \text{erg s}^{-1}$, but the fractions into various species is somewhat uncertain. Emission is expected in the following forms:

1. ULF Magnetic Dipole Radiation. Expected $L_p \sim 3 \cdot 10^{36} \text{erg s}^{-1}$ of 1.5×10^3 Hz radiation would give a local electromagnetic field at $r > r_{\ell c}$ with

$$B \sim 10^2 \left(\frac{10^{11} \text{cm}}{r} \right) G \tag{5}$$

2. High Energy Photons. The total spin-down power, the maximum magnetosphere potential drop which can be mobilized for particle acceleration, and the maximum total magnetospheric current flow in PSR 1937 + 214 (and presumably PSR 1957 + 20) are the same as those of the Vela radiopulsar. This suggests strong quantitative similarities between magnetospheric processes in PSR 1957 + 20 and those in Vela's outer magnetosphere where the two pulsars can also have similar magnetic field strengths. That region appears to be the source of Vela's non-radio emissions (Cheng, Ho, and Ruderman 1986). If the γ-ray spectrum and intensity from PSR 1957 + 20 is indeed about the same as those from the Vela pulsar, the secondary wind caused by the part of that radiation intercepted by the secondary can be estimated to have a mass flow (RST, KRST)

$$\dot{m}_w \sim 10^{13} - 10^{14} \text{gs}^{-1} \tag{6}$$

This is probably lower than that inferred from the eclipse observations (Fruchter 1988) but cannot yet (April 1988) be excluded.

3. Tev $e^{\pm}$ Wind. The Crab pulsar appears to inject most of its spin-down power into its surrounding nebula as a TeV $e^{\pm}$ wind (Kennel and Coroniti 1984, Ruderman 1987) which manifests itself in nebular expansion acceleration and synchrotron radiation. Vela also has an x-ray synchrotron halo, as do all other radiopulsars with spin-down power $\gtrsim 10^{34}$erg s^{-1} (Helfand 1986) in supernova remnants. The remnant may constrain a radiated magnetic field from the pulsar enough to induce X-ray synchrotron radiation of the $e^{\pm}$ wind. The millisecond pulsar PSR 1937 + 214, alone among solitary pulsars with spin-down power exceeding 10^{34}erg s^{-1}, is not surrounded by an X-ray halo, but it also is not imbedded in a supernova remnant. Presumably, it also does not have the appropriate surrounding magnetic field structure to cause a TeV $e^{\pm}$ wind to lose its energy to synchrotron X-rays. A TeV $e^{\pm}$ wind incident directly into the surface of the secondary would deposit most of its energy at a column density many hundreds of g cm^{-2} below the surface. Its main consequence would be surface heating and radiation back out at an intensity far below the secondary's Eddington limit. Unless converted to another more strongly absorbed form of energy a TeV $e^{\pm}$ wind would not sustain as strong a secondary wind as that inferred from observation.

3. MeV γ-Rays and Secondary Wind from a TeV e^-/e^+ Primary Wind.

An e^-/e^+ plasma, synchrocompton accelerated to TeV energies by the pulsar's coherent magnetic dipole radiation, would not synchrotron radiate away most of its energy in that same dipole radiation field. However, if the TeV e^-/e^+ wind entered into another non-comoving 10^2G field its energy would be synchrotron radiated away as MeV photons. Such a field, for example, could be the degenerate dwarf secondary's own magnetic field. If that star's surface field were to exceed this value, the 10^2G field which would exist further away from the star would cause a TeV $e^{\pm}$ wind to emit synchrotron radiation there. Alternatively, and less hypothetically, an approrpiate 10^2G field would be expected from the reflection of the pulsar's magnetic dipole radiation by the secondary 10^{11} cm away from its source. From Eq. (5) this would give a reflected $B \sim 10^2G$ around the secondary to convert the energy of TeV $e^{\pm}$ to γ-rays in that region with an energy

$$E_\gamma \sim \gamma_\pm^2 \frac{\hbar eB}{mc} \sim \text{MeV}. \tag{7}$$

It has been shown (Ruderman, Shaham, Tavani, Eichler 1988; RST) that incident MeV γ-rays, which deposit their energy to Compton scattered electrons within several g cm^{-2} of the secondary's surface, are particularly effective in sustaining strong evaporative winds. A $3 \cdot 10^{36}$erg s^{-1} TeV $e^{\pm}$ wind from PSR 1957 + 20 would result in $\hat{L} \sim 6 \cdot 10^{32}$erg s^{-1} of MeV γ-rays incident on its companion and an evaporative wind flow from the secondary

$$\dot{m}_w \sim 10^{-17}\hat{L}\,\text{gs}^{-1} = 6 \cdot 10^{15}\text{gs}^{-1}. \tag{8}$$

The wind would be expected to be almost completely ionized and to have a velocity $v_w \sim 3{\cdot}10^7$cm s^{-1} (RTSE).

4. Evaporation of the Secondary

After pulsar turn on and the disappearance of the neutron star's accretion disk, tidal distortion of the more rapidly orbiting disk by the secondary and the tidal bulge's reaction back on the secondary are no longer possible. Consequently, the main mechanism in the binary system for transferring angular momentum to the secondary would be extinguished and the previous expansion rate of the binary would be supressed by a factor of order the ratio of the secondary's radius (R_*) to the binary separation (a). (If evaporation of the secondary is mainly from the hemisphere facing the neutron

star, $\dot{a} \sim R_*\dot{m}_w/m$). As the degenerate secondary's mass (m) drops, its radius grows ($R_* \propto m^{-\frac{1}{3}}$) until $m \sim 10^{-3}M_\odot$. The secondary will expand but not reach it Roche lobe radius. For this phase of secondary radial expansion at approximate fixed binary separation, the evaporative time scale

$$\tau_{evap} \sim \frac{m}{3\dot{m}_w} \sim 10^8 \text{yrs}. \tag{9}$$

This is less than the neutron star spindown lifetime of the solitary millisecond pulsar PSR 1937 + 214 and, we presume, also of its cousin PSR 14957 + 20. Therefore the secondary evaporation could be completed before the pulsar emission drops. When m drops below $10^{-3}M_\odot$ the secondary is planetlike and $R_* \propto m^{\frac{1}{3}}$. In the contracting planetary phase evaporation at the rate in Eq (8), adjusted for a shrinking secondary, would leave no remnant at all after an additional $2 \cdot 10^7$ yrs. (During all of those evaporative phases the radiation temperature of the secondary hemisphere facing the neutron star, which absorbs $\sim 5 \cdot 10^{36}\text{erg s}^{-1}/4\pi a^2$ per unit area, is about $3 \cdot 10^{40}$K. This is enough to evaporate smaller planets no matter what the form of the incident flux.)

An ionized wind from the secondary will meet the strong ultralow frequency $1.5 \cdot 10^3$Hz magnetic dipole radiation from the pulsar to form a bow shock around the secondary as indicated in Figure 1. The stand off radius of the bow shock

$$R_{so} \sim \frac{(\dot{m}_w v_w)^{\frac{1}{2}}}{B} \sim 10^{10}\text{cm}, \tag{10}$$

of order the secondary's stellar radius for $\dot{m}_w$ and B from Eqs. (8) and (5). Near the bow shock the wind plasma can be very overdense for pulsar microwave emission so that the onset of any eclipse of it by the secondary can be sharp. Egress from the clipse involves microwave beam passage through the down stream plasma wake and would be expected to be much more diffusive. Such an assymetry is observed (Fruchter *et al.* 1988).

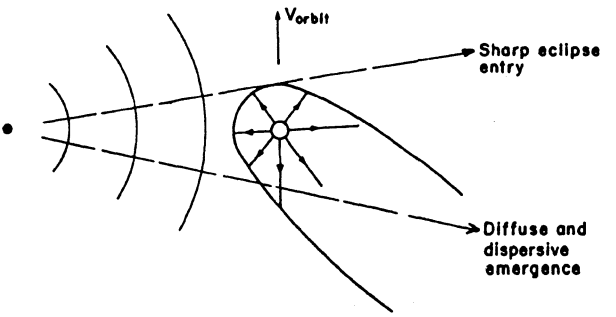

Figure 1. Bow shock and wake from the interaction of a strong secondary plasma wind with the pulsar's Khz magnetic dipole radiation.

The research summarized here was supported in part by NSF grant number AST81-02381.

REFERENCES

Alpar, A., Cheng, A., Ruderman, M. and Shaham, J. 1982,, *Nature*, **300**, 728.

Cheng, K, Ho, C., and Ruderman, M. 1986, *Ap.J.*, **300**, 522.

Fruchter, A., Stinebring, D., and Taylor, J. 1988 *Nature* (in press).

Kłuzniak, W., Rudermann, M. Shaham, J., and Tavani, M 1988 "A Model for the Millisecond Eclipsing Binary Pulsar PSR 1957 + 20," submitted to *Nature*.

Kennel, C and Coroniti, F 1984,, *Ap.J.*, **283**, 710.

Helfand, D. 1984, *Adv. Space Res.*, **3**, No. 10–12 p. 29.

Ruderman, M., Shaham, J. and Tavani, M. 1987, "Rapid Evaporation of Very Light Secondaries in Low Mass X-ray Binaries," *Ap.J.*, in press.

Ruderman, M., Shaham, J. Tavani, M. and Eichler, D. 1987, "Late Evolution of Very Low Mass X-ray Binaries Sustained by Gamma Rays from the Primaries," *Ap.J.*, in press.

Ruderman, M. 1987, "Energetic Radiation from Magnetized Neutron Stars," in *High Energy Phenomena around Collapsed Stars*, F. Pacini, ed. (Reidel).

V. MAGNETOSPHERES, ACCRETION PROCESSES AND COLUMNS

ACCRETION BY MAGNETIC NEUTRON STARS

F. K. Lamb
University of Illinois at Urbana-Champaign
Departments of Physics and Astronomy
1110 West Green Street
Urbana, IL 61801
U.S.A.

ABSTRACT. Many X-ray stars that exhibit periodic and quasi-periodic oscillations in intensity are thought to be magnetic neutron stars accreting matter from a close binary companion. These lectures provide an introduction to some of the concepts needed to understand this process. The capture of material from the wind or from the atmosphere or envelope of a binary companion star is described and the resulting types of accretion flows discusssed. The reasons for the formation of a magnetosphere around the neutron star are explained. The qualitative features of the magnetospheres of accreting neutron stars are then described and compared with the qualitative features of the geomagnetosphere. The conditions for stable flow and for angular and linear momentum conservation are explained in the context of neutron star accretion and applied to obtain rough estimates of the scale of the magnetosphere. Accretion from disk flows is then considered in some detail, including the structure of geometrically-thin Keplerian flows, the interaction of the disk with the magnetosphere, and models of steady disk flows. Accretion torques and the resulting changes in the pulse frequencies of accretion-powered pulsars are considered and the predicted behavior compared with observation. Finally, the beat-frequency magnetospheric model of quasi-periodic intensity oscillations (QPOs) is described and compared with observation.

1. INTRODUCTION

In these lectures I have been asked to provide an introduction to some of the concepts needed to understand accretion by magnetic neutron stars, to describe some of the most interesting aspects of current theoretical models, and to indicate some of the most important unresolved questions. The lectures do not provide a complete and balanced review of the subject but are instead an informal account

H. Ögelman and E. P. J. van den Heuvel (eds.), Timing Neutron Stars, 649–722.

of a variety of problems that have interested me in recent years. Although there has been a substantial amount of work on the problems discussed in these lectures, many important issues remain unresolved. One goal of these lectures is therefore to interest more of you in these problems, with the hope that you may help to solve them. Since the subject of this study institute is "timing neutron stars," I will emphasize aspects of accretion by magnetic neutron stars that can be addressed by timing observations.

Accretion by magnetic neutron stars is still a relatively new topic in astrophysics. Intense study of this process began with the discovery in the early 1970s of periodic oscillations in the intensities of two bright X-ray sources (Schreier *et al.* 1972; Tananbaum *et al.* 1972) and the interpretation of these as strongly magnetic ($B{\sim}10^{12}$ G), rotating neutron stars accreting matter from binary companions (Pringle and Rees 1972; Davidson and Ostriker 1973; Lamb, Pethick, and Pines 1973). About 30 of these accretion-powered pulsars are now known. Most are in high-mass ($M_{\rm tot} \gtrsim 15\,M_\odot$) binary systems located in the disk of the galaxy, although a few have been found in low-mass ($M_{\rm tot} \lesssim 3\,M_\odot$) systems located in the galactic bulge.

Research on accretion by magnetic neutron stars recently received new impetus with the discovery of several types of quasi-periodic intensity oscillations (QPOs) in the most luminous X-ray stars in the galaxy (van der Klis *et al.* 1985; Hasinger *et al.* 1986; Middleditch and Priedhorsky 1986) and the suggestion that the QPOs of one type, the so-called horizontal branch oscillations or HBOs, are produced by interaction of the magnetosphere of a weakly magnetic ($B{\sim}10^8$–10^9 G), rapidly rotating neutron star with inhomogeneities in the Keplerian accretion disk surrounding it (Alpar and Shaham 1985; Lamb *et al.* 1985; Shibazaki and Lamb 1987; Lamb 1988b).

The different types of X-ray intensity variability expected for accreting neutron stars in different galactic locations and different types of binary systems are summarized in Table I. At least some γ-ray burst sources are also thought to be accreting magnetic neutron stars (see Lamb 1988a; Murakami *et al.* 1988; Fenimore *et al.* 1988).

As Ögelman (1989) has discussed, the evidence that accretion-powered pulsars are strongly magnetic accreting neutron stars is compelling. The stability of the X-ray intensity oscillations rules out the possibility that these sources are black holes, while the high spin rates (${\sim}1$–10 Hz) and luminosities (${\sim}10^{37}$–10^{38} ergs s^{-1}) of many are inconsistent with degenerate dwarf models, which have maximum spin rates ${\sim}0.1$ Hz and maximum X-ray luminosities ${\sim}4 \times 10^{36}$ ergs s^{-1}(Kylafis and Lamb 1979). Furthermore, the stellar angular velocity changes inferred from observed changes in oscillation frequency agree quantitatively with the torques expected for accretion by neutron stars with dipole magnetic fields ${\sim}10^{11}$–10^{13} G, but are several orders of magnitude larger than expected for degenerate dwarfs (see Ghosh and Lamb 1979b and references therein). Finally, the X-ray pulse shapes

TABLE I
X-Ray Intensity Variability in Accreting Neutron Stars[a]

Galactic Location	Mass of System	Magnetic Field Strength (G)	Type of X-ray Intensity Variation Expected
Disk	High	10^{12}–10^{13}	Periodic and quasi-periodic oscillations
Bulge	Low	10^{11}–10^{12}	Periodic and quasi-periodic oscillations
Bulge	Low	10^{8}–10^{9}	Quasi-periodic oscillations and bursts
Bulge	Low	$\lesssim 10^{7}$	Small-amplitude variations, flares, and bursts

[a] Based on current ideas of how the various types of X-ray intensity variations are produced. The quasi-periodic oscillations referred to are the so-called horizontal branch oscillations (HBOs) discussed in §6. For the purpose of this table, HBOs are assumed to be a magnetospheric phenomenon. The X-ray bursts referred to are the so-called Type I bursts, which are thought to be caused by thermonuclear flashes in matter that has accreted onto the surface of the neutron star (see Lewin and Joss 1983; Taam 1985).

and spectra agree qualitatively with magnetic neutron star models and indicate surface field strengths as high as 10^{12}–10^{13} G (Kirk and Trümper 1983; Mészáros 1982, 1986). Two accretion-powered pulsars show X-ray spectral features that have been interpreted as lines produced by cyclotron scattering (Trümper *et al.* 1978; Wheaton *et al.* 1979). If they are cyclotron lines, the surface magnetic field strengths in these two stars are $\sim 10^{12}$ gauss.

The evidence that the luminous QPO sources are also accreting neutron stars is strong, although not as compelling as for the accretion-powered pulsars. The evidence that the QPO sources have significant magnetospheres is indirect, but highly suggestive. At present, the most promising model for the HBOs is the beat-frequency modulated accretion (BFMA) model. In this model, interaction of the magnetosphere of the neutron star with the inner edge of the accretion disk causes the accretion rate and hence the stellar luminosity to oscillate at the beat frequency given by the difference between the orbital frequency of inhomogeneities in the inner disk and the rotation frequency of the neutron star. The BFMA model gives oscillation frequencies that agree with observed HBO frequencies for neutron star rotation rates ~ 100 Hz and magnetic field strengths $\sim 10^{9}$ gauss, values expected on the basis of prior evolutionary arguments which suggested that the luminous low-mass X-ray binaries are progenitors of the millisecond rotation-

powered pulsars (see Alpar and Shaham 1985). Magnetic field strengths of this order are also consistent with recent work which suggests that the magnetic dipole moment of a neutron star does not decay below $\sim 10^8$–10^9 G on the relevant evolutionary time scales (Kulkarni 1986; van den Heuvel, van Paradijs, and Taam 1986). The BFMA model appears even more appealing as an explanation for the HBOs following the recent discovery of quasi-periodic oscillations in the intensities of the accretion-powered pulsars Cen X-3 (Tenant 1988a,b; Hasinger 1989) and EXO 2030+375 (Angelini 1988) at frequencies consistent with the BFMA model, and the reported similarities of the power spectra of intensity variations in accretion-powered pulsars and QPO sources (Hasinger 1988, 1989).

In §2 I describe the various mechanisms by which mass can be transferred from the companion star to the neutron star and the properties of the resulting accretion flows. The interaction between the accreting plasma and the neutron star magnetic field and the structures of the quite different magnetospheres that form in different types of accretion flows are discussed in §3. In §4, several aspects of accretion from a Keplerian disk are considered in more detail. Disk accretion is emphasized in these lectures because observations suggest that most accretion-powered pulsars and all QPO sources are accreting from Keplerian or near Keplerian flows. §5 describes how studies of the periodic intensity oscillations of accretion-powered pulsars can provide information on the magnetospheric structure of these stars. In §6 I discuss the physics of disk accretion by a neutron star with a relatively weak magnetic field and outline the beat-frequency model of HBOs. I do not discuss the flow of plasma near the stellar surface or the emission of radiation, nor do I review the very large body of relevant observations. Reviews of these topics may be found in the articles by Giacconi (1975), Mészáros (1982, 1986), White (1982), Bradt and McClintock (1983), Kirk and Trümper (1983), Joss and Rappaport (1984), and van der Klis, van Paradijs, and Lewin (1988).

2. EXTERIOR FLOWS

The character of the accretion flow near the neutron star magnetosphere is determined in part by the flow far from the star, where the effect of the stellar magnetic field is negligible. I refer to the accretion flow in this region as the *exterior flow.* In the present section I summarize the evidence that the neutron star captures matter from a binary companion, describe mechanisms by which the capture can occur, and discuss the basic types of exterior flows that can result (see also Treves, Maraschi, and Abramowicz 1988). It will be helpful, in this discussion, to have in mind the most important macroscopic length scales in binary systems containing magnetic neutron stars. These are listed in Table II, along with their typical values. Note that the radius of the magnetosphere is typically much smaller than the binary separation and the accretion capture radius. Hence the capture process can sometimes be treated, to a first approximation, separately from the loss of

TABLE II
Length Scales in Accreting Neutron Star Binaries[a]

Length	Symbol	Typical value (cm)
Binary separation	a	$\sim 10^{10}$–10^{12}
Accretion capture radius	r_a	$\sim 10^{10}$
Magnetospheric radius	r_m	$\sim 10^{7}$–10^{9}
Neutron star radius	R	$\approx 10^{6}$

[a]The value of the accretion capture radius quoted is for capture from a wind with a velocity $v_w = 10^8\,\mathrm{cm\,s^{-1}}$. The range of magnetospheric radii quoted are for mass accretion rates $\dot{M}$ in the range 10^{17}–$10^{18}\,\mathrm{g\,s^{-1}}$, a neutron star mass $M = 1\,M_\odot$, and a surface dipole magnetic field component in the range 10^{9}–10^{13} G.

matter from the companion star and the interaction with the neutron star magnetosphere. The thermal state of the exterior flow can, however, be strongly affected by the radiation produced near the neutron star.

2.1 Mass Accretion Rates

The most luminous accreting neutron stars have total X-ray luminosities $\sim 10^{35}$–$10^{38}\,\mathrm{ergs\,s^{-1}}$. This X-ray emission is powered largely by release of gravitational binding energy as matter accretes to the surface of the star. The energy released by adding a unit mass to the star is just the chemical potential ϕ_s of the star. Thus, if the mass flux to the stellar surface is $\dot{M}$, the rate of energy release (the so-called accretion luminosity) is

$$L = \dot{M}\phi_s\,. \tag{2.1}$$

In principle, ϕ_s includes the energy released as the structure of the neutron star adjusts to the addition of matter and as the accreted matter is catalyzed to its lowest energy state. In practice, the energy released as the structure of the star readjusts is negligible for cold neutron stars (stars more than a few hours old). The energy released as the accreted matter is catalyzed to its lowest energy state is $\sim$7 MeV per nucleon, which is only a few percent of the $\sim$100–200 MeV per nucleon gravitational binding energy. Thus, the rate of energy release due to nuclear transmutations is small compared to the rate of release of gravitational binding energy, if the nuclear transmutations occur steadily, but may temporarily dominate the rate of release of gravitational binding energy if nuclear transmutations

are inhibited for a time and then occur rapidly, as in the thermonuclear flash model of X-ray bursts (for a recent review of nuclear processes in accreted matter, see Taam 1985).

If the energy released in the readjustment of the star and in nuclear reactions is neglected, the chemical potential ϕ_s of the star is equal to the gravitational potential $\phi_g(r)$ evaluated at the radius of the stellar surface. For current equations of state, general relativistic corrections to the Newtonian expression for ϕ_g can be as large as 10–20 %. If these are also neglected, equation (2.1) becomes

$$L \approx \dot{M}\, GM/R = 1.33 \times 10^{37}\, \dot{M}_{17}\, (M/M_\odot)\, R_6^{-1} \ \mathrm{ergs\,s^{-1}}\,, \qquad (2.2)$$

where M is the mass of the neutron star and R is its radius. Here and below, numerical subscripts on quantities indicate that they are to be evaluated in terms of the corresponding power-of-ten of the cgs unit. Thus, for example, in equation (2.2), $\dot{M}_{17} \equiv \dot{M}/10^{17}\,\mathrm{g\,s^{-1}}$ and $R_6 \equiv R/10^6\,\mathrm{cm}$.

For a neutron star with an extensive magnetosphere, the energy released near the stellar surface completely dominates that released near the magnetospheric boundary, since $\phi_g(r) \propto 1/r$. Near the star, the kinetic energy acquired by the accreting plasma in falling into the deep gravitational potential is converted first into heat and then into radiation (very little is conducted into the star, even if it is cold). The luminosity of the star in the 0.1–100 keV X-ray band depends on the efficiency with which the kinetic energy of the infall is converted into X-rays, but cannot exceed the accretion luminosity. In practice, most of the accretion luminosity emerges as X-radiation, except perhaps in stars that are completely swamped by accreting matter.

The luminosities of the most luminous accreting neutron stars imply mass accretion rates $\sim 10^{-11}$–$10^{-8}\, M_\odot\,\mathrm{yr^{-1}}$. These rates are much larger than a neutron star can capture from the interstellar medium. Such neutron stars must therefore be capturing matter from a binary companion. Direct evidence for the presence of a binary companion in some systems comes from observations of periodic eclipses of the X-ray emission. Other evidence comes from the periodic Doppler shift of the pulsation frequencies of accretion-powered pulsars, 180° out of phase with the Doppler shift of emission from the companion star. In some cases, the heating of one face of the companion star by X-rays from the neutron star can be seen. All three effects have been observed in a few systems. The known binary periods of accretion-powered pulsars range from ~1 hour to ~40 days (see Bradt and McClintock 1983). Those of QPO sources range from ~0.2 hours to ~10 days (Lamb and Priedhorsky 1988).

2.2 Mass Capture

Only neutron stars in close binary systems with a companion star of mass $\gtrsim 15\, M_\odot$ or $\lesssim 2\, M_\odot$ are expected to be observed as X-ray stars, since only companion stars

TABLE III
Mass Transfer Mechanisms in Close Binary Systems

Mass of System	Source of Accreting Matter	Mean Angular Momentum	Peak Angular Momentum
High	Radiation-driven wind	Low	Low to high
	Overflowing atmosphere	High	High
Low	Self-excited wind	Low	Low to high
	Overflowing envelope	High	High

with masses in these ranges provide matter at sufficient rates to power luminous X-ray emission for an appreciable length of time (see Taam 1984; van den Heuvel 1989). Companion stars in the upper mass range transfer matter to the neutron star via a radiation-pressure-driven stellar wind or by having their atmosphere overflow the gravitational potential well confining the star. Under some conditions, massive companions may transfer matter by both mechanisms simultaneously. Companion stars in the lower mass range transfer matter by envelope overflow or, possibly, via a self-excited wind, if their outermost layers are sufficiently heated by absorbing soft X-rays coming from the neutron star. The atmosphere or envelope of the companion star may overflow its gravitational potential well if the star expands as a result of nuclear evolution or mass loss. In short-period systems, mass transfer is driven by loss of orbital angular momentum via gravitational radiation or mass loss. These possible mechanisms of mass transfer are summarized in Table III.

Capture from a wind.—When the companion star loses matter via a wind, some of it will be deflected and focused by the gravity the neutron star, and then compressionally heated, cooled, and captured. In the usual picture of accretion from a homogeneous medium by a star moving at a hypersonic velocity v_0, it is assumed that the particles of accreting matter follow Keplerian orbits. All particles with the same impact parameter then collide at the same point behind the star, where they share their momentum. It is assumed that particles with an impact parameter less than a certain value are accreted, whereas those with larger impact parameters are not. This argument gives a mass accretion rate

$$\dot{M} = \rho_0 v_0 \pi r_a^2 \tag{2.3}$$

where ρ_0 is the mass density far from the neutron star and

$$r_a = \xi 2GM/v_0^2 \approx 10^{10}\,(M/M_\odot)(v_0/10^8\ \mathrm{cm\,s^{-1}})^{-2} \tag{2.4}$$

is the so-called accretion capture radius. Here ξ is a dimensionless number that depends on one's assumptions about the gas dynamics of the capture process but is presumed to be of order unity. For example, if one assumes that the separatrix between the particles that are captured and those that are not occurs where the inward velocity falls below the escape velocity (Hoyle and Lyttleton 1939), $\xi = 1$. Other assumptions lead to other values for ξ. Bondi and Hoyle (1944) have suggested that this picture could be extended to subsonic velocities by using the interpolation formula

$$r_a = \xi 2GM/(v_0^2 + c_s^2), \tag{2.5}$$

where c_s is the sound speed far from the star and ξ is between 1 and 2. From the symmetry of the flow, it is clear that the matter accreted by the star adds no angular momentum. Hence the angular momentum of the star does not change, that is

$$\dot{J}_s \equiv 0. \tag{2.6}$$

Even so, the *spin rate* of the star usually changes, since its moment of inertia usually changes as it accretes matter. The spin-rate change can be either positive or negative, depending on the structure of the star (see §5.2).

Despite the important simplifying assumptions involved, this picture has often been applied to capture of matter by a neutron star immersed in a homogeneous stellar wind, with

$$v_0 = (v_w^2 + v_{\rm orb}^2)^{1/2} \tag{2.7}$$

in terms of the wind velocity v_w at the orbit of the neutron star and the orbital velocity $v_{\rm orb}$ of the neutron star. The results can be very misleading, for several reasons:

- Capture depends in a fundamental way on the physical processes that occur in the region where the streamlines intersect, since unless energy is lost, the matter remains unbound. Yet these physical processes (formation of a shock wave, cooling by radiation, etc.) are not included in the analysis.
- A stellar wind is not a homogeneous medium. At a minimum there are density and velocity gradients on length scales comparable to the distance from the mass-losing star. In fact, there is strong evidence for large velocity and density gradients on much smaller length scales, as discussed below.
- The dimensions of the accreting object (star or magnetosphere) and the boundary conditions imposed on the flow at the object obviously can affect the capture process, but are not considered in the analysis.

In the last decade a so, a variety of efforts have been made to address some of these aspects, first with analytical methods and, more recently, with numerical simulations. Although progress has been made, important issues remain unresolved. Here we briefly summarize the current situation (for a more detailed review, see Ho 1988).

Numerical experiments (Hunt 1971; Shima *et al.* 1985) have shown that the estimates (2.3)–(2.5) for the mass flux and accretion capture radius are correct to within a factor of order unity, for axisymmetric flows. However, the situation for non-axisymmetric flows is much less clear. Density and velocity gradients deform the capture cross section, create circulation in the flow, and lead to accretion of angular momentum by the star.

Quite generally, the time rate of change of the angular momentum $\dot{\mathbf{J}}_s$ of the star is

$$\dot{\mathbf{J}}_s = \mathbf{N}_s \equiv -\int_S (\mathbf{r} \times \mathbf{\Pi}) \cdot \hat{\mathbf{n}}\, dS\,, \tag{2.8}$$

where $\mathbf{N}_s$ is the torque on the star, S is a surface enclosing the star, $\mathbf{\Pi}$ is the momentum flux density tensor, and $\hat{\mathbf{n}}$ is a unit vector normal to the surface and oriented outward. In the following discussion it will be helpful to consider the mean specific angular momentum

$$\ell \equiv \dot{J}_s/\dot{M} \tag{2.9}$$

of the accreting matter.

Early analytical calculations of ℓ_w (Shapiro and Lightman 1976; see also Dodd and McCrea 1952; Illarionov and Sunyaev 1975) considered only a constant velocity wind and the effect of a small density variation of the form

$$\rho(x) = (1 + \epsilon_\rho x/r_a)\rho_0\,, \tag{2.10}$$

where the coordinate x increases in a direction normal to the velocity. The contribution to $\mathbf{\Pi}$ of stresses other than the material stress and the deformation of the accretion capture cross section caused by the density gradient were both neglected. The result was

$$\ell_{w0} \approx \epsilon_\rho r_a v_0\,. \tag{2.11}$$

Shapiro and Lightman estimated that for a constant velocity, homogeneous stellar wind, the size of the density gradient at the orbit of the neutron star is

$$\epsilon_\rho \approx (v_{\rm orb}/v_w)(r_a/a)\,, \tag{2.12}$$

where a is the binary separation. If the mean specific angular momentum of the matter captured from the wind by the neutron star is written as

$$\boldsymbol{\ell}_w = \eta_w r_a^2\, \mathbf{\Omega}_{\rm orb}\,, \tag{2.13}$$

where $\mathbf{\Omega}_{\rm orb}$ is the orbital angular velocity of the system and η_w is a dimensionless number, the estimates of Shapiro and Lightman correspond to η_w positive and of order unity.

Subsequently, Davies and Pringle (1980) analyzed capture of material from a wind by a point mass using the Hoyle-Lyttleton approach and concluded that, to first order in r_a/a, no angular momentum is captured. More recently, Soker and Livio (1984) recalculated ℓ_w following the Hoyle-Lyttleton appproach but assuming a different form for the accretion line and found a small (compared to ℓ_{w0}) but finite value of ℓ_w. Wang (1981) has argued that the zero value of ℓ_w found by Davies and Pringle is a result of their assumption of flow along an accretion line to a point mass. He therefore concluded that if accretion occurs in a column rather than along a line, finite angular momentum capture is possible. Ho (1988) has argued that the Hoyle-Lyttleton approach gives a reasonable estimate of the mass capture rate but that it is unrealistic to expect that it can give accurate estimates of quantities, such as the angular momentum capture rate, that are sensitive to the detailed structure of the accretion flow.

Wang (1981), Anzer, Börner, and Monaghan (1987), and Ho (1988) have recalculated the angular momentum capture rate when there are density and velocity gradients in the upstream flow and only material stresses are included in the integral (2.8). For capture from a spherically symmetric wind leaving the companion star, the expected sizes of the density and velocity gradients are

$$\epsilon_\rho = (v_{\rm orb}/v_w)\,(r_a/a)\,(1+q) \tag{2.14}$$

and

$$\epsilon_v = (v_{\rm orb}/v_w)\,(r_a/a)\,(1-q)\,, \tag{2.15}$$

where $q \equiv (d\ln v_w/d\ln r)$ is to be evaluated at the orbit of the neutron star. For a wind that is still accelerating near the neutron star, $q > 0$, indicating that the acceleration increases ϵ_ρ but decreases ϵ_v. Of course, $q = 0$ for a wind that is coasting. When the effect on the angular momentum capture rate of the deformation of the capture cross section is included, ℓ_w is similar in magnitude *but of opposite sign* to the estimate made by Shapiro and Lightman (1976), that is, η_w in equation (2.13) is of order unity, but negative. Ho (1988) has argued that pressure stresses may make a contribution to ℓ_w that is of the same order as the material stress, for the usual choice of the surface S in the integral (2.8), but found it difficult to estimate the sign of the pressure stress contribution. Under some conditions, viscous shear and magnetic stresses may also be important in equation (2.8). Thus, Ho has concluded that the sign as well as the magnitude of η_w is at present still uncertain.

Numerical simulations of mass capture from a wind have been carried out by several groups. Livio *et al.* (1986a,b) and Soker *et al.* (1986) found that an upstream density gradient led to a finite angular momentum capture rate, based on a series of 3D particle-in-cell claculations. Anzer, Börner, and Monaghan (1987) used a 2D, smoothed-particle code and found that an upstream velocity gradient led to a finite angular momentum capture rate, but could not achieve a steady flow.

Matsuoda, Inoue, and Sawada (1987) studied mass transfer via a thermally-driven wind and found a flow pattern in which the circulation reversed quasi-periodically. Taam and Fryxell (1988) used a 2D piecewise-parabolic method with an upstream density gradient and also found quasi-periodic reversals in the circulation of the flow with attendant oscillations in the accretion rate.

The mean specific angular momentum of the matter captured in most of the numerical experiments is rather uncertain, but appears to be only a small fraction of that expected for $|\eta_w| \approx 1$. In the simulation of Taam and Fryxell (1988), the instantaneous value of η_w is sometimes as large as $\sim$0.2. Ho (1988) has suggested that the fluctuating behavior found in the 2D calculations may be a consequence of the artificially large interaction between the passing wind and the material circulating around the star that is inherent in the 2D approximation. The absence of fluctuations in the 3D calculations could be because the large effective viscosity caused by the relatively coarse zoning of the 3D calculations suppresses this phenomenon, or because the phenomenon is an artifact of the 2D approximation. This issue should be resolved as 3D calculations with finer zoning become possible.

There is evidence that actual winds in binary systems have short-length-scale, large-amplitude fluctuations in density and velocity. For example, the spin-rate changes observed in Vela X-1 by Boynton *et al.* (1984) on time scales of days imply angular momentum capture rates almost 100 times larger than even that predicted by equation (2.13) and of alternating sign. Similar behavior has been observed in 4U1538–52 by Makishima *et al.* (1987).

Ho and Arons (1987) have suggested that large-amplitude fluctuations in the density and velocity of a radiation-driven wind can occur as the result of overstable oscillations produced by the coupling between the mass capture rate and the wind velocity via the effect of X-radiation from the neutron star on the radiation force in the spectral lines. They argue that η_w could be as large as 0.5 for such a flow.

Overflow of atmosphere or envelope.—When the companion star loses matter by overflowing its gravitational potential well, relatively cold plasma from the atmosphere or envelope flows slowly over the gravitational saddle point between the companion star and the neutron star, and is immediately captured by the neutron star. The mass transfer rate is determined by the evolution of the binary system, which can be affected by nuclear burning in the companion star, gravitational radiation of orbital angular momentum, magnetic braking, and tidal coupling between the neutron star and accreting matter and the companion star.

For low-mass systems, the moment arm of matter flowing over the saddle point between the stars is $\sim a$ and the specific angular momentum of the matter captured by the neutron is therefore

$$\ell_o = \eta_o a^2 \, \Omega_{\rm orb} \, , \tag{2.16}$$

where η_o is a dimensionless number of order unity. The precise value of η_o depends

on the mass ratio and other properties of the system. Note that ℓ_o is at least $(a/r_a)^2$ times larger than ℓ_w, for $|\eta_w| \lesssim 1$.

2.3 Disk and Radial Flows

The character of the accretion flow near the neutron star magnetosphere depends strongly on the amount of circulation. I define a *Keplerian disk flow* as one in which the angular velocity Ω at each radius is closely equal to the angular velocity $\Omega_K(r)$ of a circular Keplerian orbit at the same radius. A *radial flow* is one in which the angular velocity is much less. Of course intermediate cases, in which the angular velocity is comparable but not closely equal to $\Omega_K(r)$, are also possible.

Accreting matter with specific angular momentum ℓ relative to the neutron star will orbit it at the radius

$$r_\ell \equiv \ell^2/GM\,. \tag{2.17}$$

Thus, if

$$\ell \leq \ell_{\rm crit} \equiv r_m^2\,\Omega_K(r_m) = (GMr_m)^{1/2}\,, \tag{2.18}$$

then $r_\ell < r_m$ and accreting matter will fall directly onto the magnetosphere. If on the other hand $\ell > \ell_{\rm crit}$, the accreting matter will go into orbit around the magnetosphere, provided that the length scales on which the density and velocity of the matter vary are larger than the critical impact parameter

$$b_{\rm crit} \equiv (1 + r_a/r_m)^{1/2} r_m \tag{2.19}$$

separating orbits that intersect the magnetosphere from those that do not (Ho 1988).

For matter captured from a wind, equation (2.13) for the mean specific angular momentum of the matter gives

$$r_{\ell w} = \eta_w^2 r_a^4 \Omega_{\rm orb}^2/GM \sim \eta_w^2\, 10^5 \ \ {\rm cm}\,, \tag{2.20}$$

where in the last expression on the right we have assumed a wind velocity $v_w = 10^8\,{\rm cm\,s^{-1}}$ and a binary orbital period $P_{\rm orb} = 1$ day. Equation (2.20) shows that η_w must be $\gtrsim 10^2$ in order for an extensive disk to form around the magnetosphere of a strongly magnetic neutron star, which extends to a radius greater than 10^8 cm (cf. Table II). Thus, an extensive disk cannot form if the wind is homogeneous, but may form if the flow has a large circulation, as suggested by the observations of spin-rate changes of wind-fed neutron stars discussed in §2.2.

If no disk forms, the radial component v_r of the inflow velocity will approach the free-fall velocity

$$v_{\rm ff}(r) \equiv (2GM/r)^{1/2} = 0.94 \times 10^9\,(M/M_\odot)^{1/2}\, r_9^{-1/2} \ \ {\rm cm\,s^{-1}} \tag{2.21}$$

near the magnetosphere, and the flow time scale will be comparable to the free-fall time

$$t_{\rm ff}(r) \equiv r/v_{\rm ff}(r) = 1.06\,(M/M_\odot)^{-1/2}\,r_9^{3/2}\ \ {\rm s}\,. \tag{2.22}$$

Assuming that viscous shear stresses in the flow are unimportant, the specific angular momentum of the accreting matter will remain approximately constant as the matter falls toward the neutron star, and the angular velocity of the accreting matter will therefore satisfy $\Omega \approx \ell/r^2$.

If instead a disk forms, outward transport of angular momentum will cause the disk to expand radially. Formation of an extensive disk may significantly affect the mass capture process (see, for example, Ho 1988).

For matter overflowing the gravitational potential well of the companion star,

$$r_{\ell o} = \eta_o^2 a^4 \Omega_{\rm orb}^2/GM \sim 10^{10}\,\eta_o^2 \quad {\rm cm}\,, \tag{2.23}$$

where we have used equation (2.16) and in the last expression on the right we have assumed a binary separation $a = 10^{11}$ cm and a binary orbital period $P_{\rm orb} = 1$ day. Thus, matter supplied by atmospheric or envelope overflow will always form a Keplerian disk around the neutron star magnetosphere (the magnetospheric radius is expected to be $\lesssim 10^9$ cm, even for a stellar magnetic field $\sim 10^{13}$ G).

Figure 1 shows stages in the formation of a Keplerian disk by matter overflowing the gravitational potential lobe of the companion star. The flow around the neutron star is not initially circular but becomes circular within a few orbital periods. The resulting ring then spreads radially inward and outward as the shear stress transports angular momentum outward. The outer radius r_d of the Keplerian flow depends on whether the neutron star is a source or sink of angular momentum and on whether the tidal interaction of the outer part of the disk with the companion star (which can transfer angular momentum from the disk to the orbital motion of the system) is strong or weak. Normally, r_d will exceed the radius r_ℓ. If the tidal coupling of the matter in the outer part of the disk to the orbital motion is just strong enough, the flow may settle down to a steady state in which matter enters the disk from the stream and then spirals slowly inward as its angular momentum is transported outward by shear stresses and tidal coupling to the orbital motion.

3. MAGNETOSPHERES

I use the term *magnetosphere* to refer to the volume around the neutron star in which its magnetic field strongly affects the flow of mass, energy, and angular momentum. This volume can profoundly affect the observed properties of accreting neutron stars. For example, the intensity of the X-radiation seen by a distant observer will oscillate periodically if the stellar magnetic field is not symmetric about the rotation axis, if the field is strong enough to channel the accretion flow,

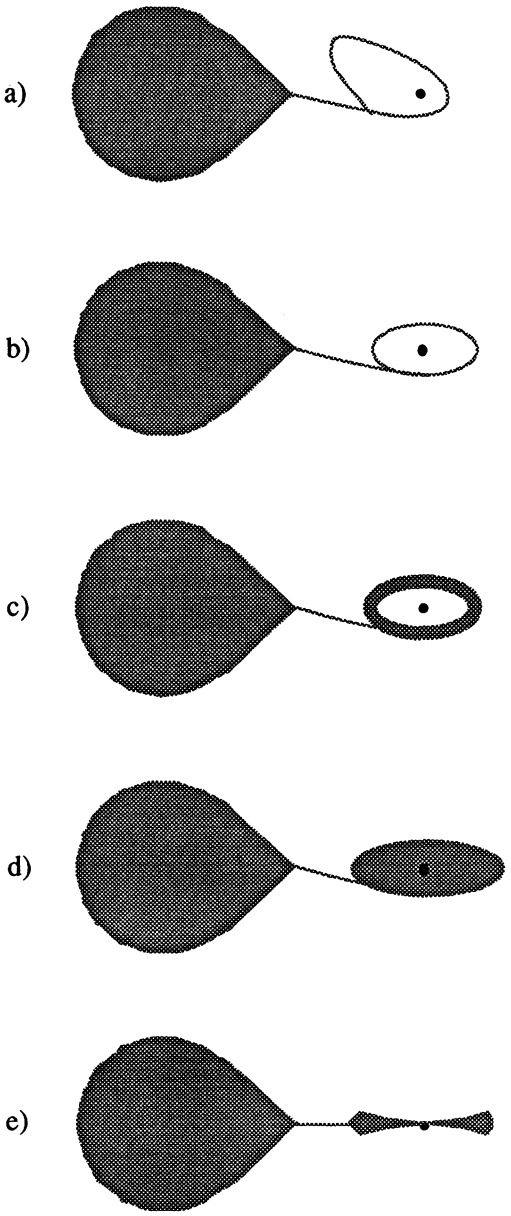

Fig. 1.—Schematic picture of the formation of a Keplerian accretion disk around a neutron star, showing (a) collision of the initial gas stream with itself, (b) formation of a circular ring, (c) spreading of the ring inward and outward, and (d) development of a steady disk flow. Panel (e) shows a side view of the steady flow.

and if the resulting beamed radiation produced near the star can escape without being isotropized. Such periodic intensity oscillations are especially important because they reflect directly the stellar rotation rate.

The very existence of a magnetosphere changes the rotation-rate behavior of an accreting neutron star, by increasing the radius where the accreting plasma couples to the star and changing the nature of the coupling. A magnetosphere also makes possible new, potentially important radiation processes, such as cyclotron emission and scattering. The interaction of the stellar magnetic field with the accretion flow can create large electrical potential drops in the system, which may accelerate charged particles to very high energies, leading to production of TeV γ-rays. The shapes of pulses, the spectra of the radiation, and the time scales of quasi-periodic and random variations in intensity are all affected by the structure of the magnetosphere.

Aside from its astronomical importance, the study of neutron star magnetospheres is also a fascinating physics problem, which provides a check on our understanding of plasma and magnetospheric physics under conditions that differ by many orders of magnitude from those encountered in planetary magnetospheres or terrestrial laboratories.

In the present section I describe the qualitative features of the interaction between the accretion flow and the stellar magnetic field, the characteristic features of accretion flows that lead to formation of a magnetosphere, and the physical principles that determine the scale of the magnetosphere.

3.1 Formation of a Magnetosphere

The structure of the outer magnetosphere depends on the angular velocity of the plasma near the magnetosphere as well as the angular velocity of the neutron star. A useful measure of the dynamical importance of the circulation of the accreting plasma is the dimensionless number (Elsner and Lamb 1977)

$$\omega_p \equiv \Omega(r_m)/\Omega_K(r_m)\,, \tag{3.1}$$

which is less than or equal to 1. Here $\Omega(r_m)$ is the angular velocity of the plasma at the magnetospheric boundary and $\Omega_K(r_m)$ is the Keplerian angular velocity there. Rotation is dynamically unimportant for approximately radial accretion flows (those with $\omega_p \ll 1$) but important for orbital flows (those with $\omega_p \approx 1$). For Keplerian accretion disks, $\omega_p = 1$. In most systems, the angular velocity of the plasma at the magnetospheric boundary appears to be comparable to the Keplerian velocity there, and one has to consider the dynamical effects of this circulation. The radial accretion problem, on the other hand, is defined by the assumption that circulation is dynamically unimportant.

Despite their profound differences, disk and radial accretion flows have several important features in common:

- Both are inward flows controlled primarily by gravity, which causes the plasma streamlines to converge on the neutron star. Because of this convergence, both flows tend to trap the stellar magnetic field and sweep it inward toward the neutron star, at least to a first approximation.
- In both types of flows, the material stress ρv^2 increases more slowly with decreasing radius than does the stress of the stellar magnetic field. In radial flows, for example, the material stress scales approximately as $r^{-5/2}$. In disk flows, the material stress scales approximately as $r^{-5/2}$ in the gas-pressure dominated region and $r^{-3/2}$ in the radiation-pressure dominated region (see §4.1). In contrast, the magnetic stress of a dipolar stellar magnetic field scales approximately as r^{-6}.
- The electrical conductivity of the accreting plasma in both types of flows is very high. Motion across field lines therefore occurs slowly on the time scale of the inflow, and the tendency of the flow to confine the stellar magnetic field in the sectors where it is converging is realized to an important degree.

If the intrinsic (undistorted) magnetic field of the neutron star has non-zero higher multipole moments, the stress of the intrinisic magnetic field of the star will increase even more steeply with decreasing radius than r^{-6}, for radii near the stellar surface. Even if the intrinsic stellar magnetic field is purely dipolar, the confinement of the stellar magnetic field by the flow (screening) and the resulting higher multipole moments created by the electrical currents in the flow and the electrical currents induced in the star will cause the stress of the magnetospheric magnetic field to increase more steeply with decreasing radius than r^{-6}. As a result, even for relatively weak neutron star magnetic fields ($B \sim 10^8$ G) there is a volume around the neutron star in which the magnetic field strongly affects the flow of mass, energy, and angular momentum.

Because the magnetic field of the neutron star is comparatively weak at the radii where matter is captured and because the subsequent flow of the highly conducting matter converges toward the neutron star, a negligible fraction of the magnetic flux threading the star is expected to thread the accreting matter at the time it is captured. This fact and the high electrical conductivity of the accreting plasma means that the plasma does not have ready access to the stellar surface. The flux of mass into the magnetosphere due to microscopic processes, such as collisional diffusion or loss-cone entry, is generally negligible compared to the total mass fluxes inferred from the luminosities of these neutron stars (Elsner and Lamb 1984). Thus, the large inward mass fluxes must be the result of macroscopic processes. An important problem in both disk and radial flow geometries is to understand how plasma eventually reaches the surface of the neutron star.

Fortunately, the radius of the magnetosphere is typically much smaller than the radius at which matter is captured (cf. Table II), so that the structure of the magnetosphere can be discussed, to a first approximation, independently of the capture process. In accretion-powered pulsars (but not in QPO sources) the

magnetospheric radius is estimated to be much larger than the stellar radius, so that the interaction of the flow with the magnetospheric boundary can also be treated, to a first approximation, separately from the interaction of the flow with the stellar surface.

As discussed further below, the material stresses associated with plasma circulation and flow into the magnetosphere dominate thermal pressure in determining the scale and structure of the magnetosphere. Thus, the structure of the magnetosphere depends sensitively on the accretion flow pattern, which is generally quite complex, and can vary greatly from one type of flow to another. The dynamical character of the interaction between the flow and the stellar magnetic field makes it difficult to model.

A quantitative description of the magnetospheres of accreting neutron stars is particularly difficult to construct for the conditions expected in accretion-powered pulsars and QPO sources. In these sources, the magnetic field of the neutron star is thought to be misaligned with its spin axis. As a result, the rotation of the star causes the magnetic field to vary explicitly with time, which imposes an explicit time dependence on the interaction between the star and the flow, even if the flow far from the star is time-independent. In addition, since the magnetic field has no spatial symmetry, the interaction with the flow has no symmetry and hence is three-dimensional. Finally, the actual flow may have large-amplitude fluctuations. Although some attempts to analyze the explicitly time-dependent, three-dimensional case have been made (see, e. g., Anzer and Börner 1980), quantitative models have been developed only for steady radial or axisymmetric flows.

3.2 Comparison with the Geomagnetosphere

Some workers have tried to apply models of the geomagnetosphere directly to accreting magnetic neutron stars. This approach fails because of the profound differences between the magnetospheres of accreting neutron stars and the geomagnetosphere, some of which are indicated in Table IV and Figure 2.

The most important differences between the geomagnetosphere and the magnetospheres of accreting neutron stars can be traced to one or more of the following factors (cf. Table IV):

- The strong gravitational field of the neutron star, which creates a converging flow while the accreting plasma is still far away from the magnetosphere and continues to control the flow of matter into the magnetosphere and toward the stellar surface.
- The highly variable nature of the plasma flow toward the neutron star magnetosphere, which can cause the structure of the magnetosphere to change dramatically with time.

TABLE IV
Magnetospheres of the Earth and Neutron Stars

Aspect	Earth	Neutron Stars
Exterior flow	Always similar (solar wind)	Highly varied ($\neq$ solar wind)
Effect of gravity	Very small	Very large
Mass influx	Very small	Very large
Stresses caused by plasma entry	Small	Large
Plasma density	Low	High
Collison rates	Low	Low to high
Effects of cooling	Small	Very large
Effects of radiation	Very small	Very large
Effects of rotation	Small	Typically large

- The large flux of matter into the neutron star magnetosphere, which stresses the outer magnetosphere and produces a relatively high plasma density throughout.
- The high plasma density near the neutron star, which makes the plasma collisional or quasi-collisional on the scale of the magnetosphere.
- The strong magnetic field of the neutron star, which typically causes charged particles to lose their energy by cyclotron emission in much less than one transit time across the magnetosphere.
- The intense radiation field from near the surface of the neutron star, which cools the plasma in the magnetosphere in much less than an infall time and can produce radiation pressure forces even larger than gravity.
- The typically strong circulation of the accreting plasma and the rapid rotation of the neutron star, which stress the outer magnetosphere and can strongly affect the plasma flow pattern.

The fact that all or almost all of the matter that interacts with a neutron star magnetosphere enters it and the highly variable nature of accretion flows deserve further comment.

Because almost all of the matter that interacts with the geomagnetosphere flows on by (see Fig. 2), the characteristic radius of the nose of the geomagneto-

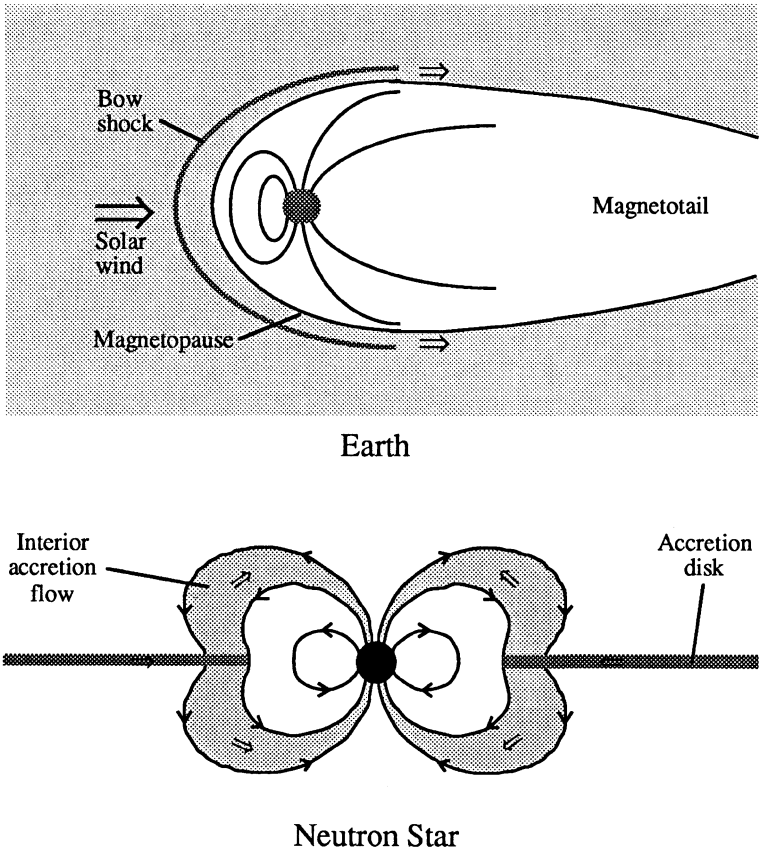

Fig. 2.—Side views of the geomagnetosphere (top) and the magnetosphere of a neutron star accreting from a Keplerian disk (bottom), illustrating the profound differences in the exterior plasma flows and the resulting structures of the two magnetospheres. Almost all of the plasma that interacts with the geomagnetosphere flows on by, whereas essentially all of the plasma that interacts with the magnetosphere of an accreting neutron star enters it. Also, the geomagnetosphere is always immersed in the solar wind, whereas neutron star magnetospheres are immersed in flows that may vary dramatically with time, from nearly radial to Keplerian.

sphere can be estimated simply by balancing a static plasma pressure, set equal to the ram pressure of the solar wind, against the static pressure of the confined magnetic field of the earth. In contrast, essentially all of the matter that interacts with the magnetosphere of an accreting neutron star penetrates it and reaches the stellar surface within one free-fall or transit time (again see Fig. 2). The material stresses associated with the flow of matter into a neutron star magnetosphere are therefore generally as large as the stresses outside, and play an important role in determining the scale and structure of the magnetosphere. As a result, determin-

ing the structure of the magnetosphere of an accreting neutron star is a dynamic rather than a static problem, even to a first approximation.

A further important difference is that the geomagnetosphere is always immersed in a single, albeit somewhat variable, environment, namely the solar wind. In contrast, accreting neutron stars are found in a wide variety of environments, ranging from nearly radial flows to geometrically thin Keplerian disks, none of which are similar to the solar wind. Indeed, as noted in §2.2, even the flow near a given neutron star may change dramatically with time. Thus, one expects large variations in the structure of the magnetosphere from one accreting neutron star to another and in the structure of the magnetosphere of a single neutron star from one time to another.

Although the structure of the magnetosphere of an accreting neutron star is complex, for some purposes it is both useful and sufficient to have an order-of-magnitude estimate of the radius inside which the stellar magnetic field strongly affects the motion of accreting plasma. In the next three sections I review such estimates. Of course the structure of the magnetosphere is not spherical, so that any single length scale can only be a very rough guide to its structure.

3.3 Stable Magnetospheric Flow

To be credible, an estimate of the radius of the magnetosphere of an accreting neutron star must take into account the fact that essentially all of the matter approaching the star flows through the magnetosphere to the stellar surface. For this reason, estimates made by simply balancing the thermal pressure of static plasma outside the magnetosphere against the pressure of a static magnetic field inside are not credible. Indeed, if the plasma were to remain outside the magnetosphere, no plasma could reach the stellar surface and hence, whatever else it might be, such a star could not be a luminous X-ray source. If, as expected, the plasma does *not* remain in a static configuration outside, then the assumption of *static* pressure equilibrium is not consistent.

There is ample evidence that the flow of accreting plasma in accretion-powered pulsars is guided by the stellar magnetic field toward the magnetic poles (see Mészáros 1982, 1986; Kirk and Trümper 1983). This is natural if the accreting plasma has become threaded by the stellar magnetic field. Assuming that threading occurs readily, one can construct a first estimate of the scale of the magnetosphere based on *the* fundamental characteristic of accretion, namely plasma *flow*, and the fact that the stellar magnetic field can control the flow only if it is strong enough (see Lamb, Pethick, and Pines 1973; Elsner and Lamb 1977; Ghosh, Lamb, and Pethick 1977). Two forms of the argument are possible, one global and the other local. Both consider plasma flow inside the magnetosphere (which I call *magnetospheric flow*) and hence can be applied for any exterior flow.

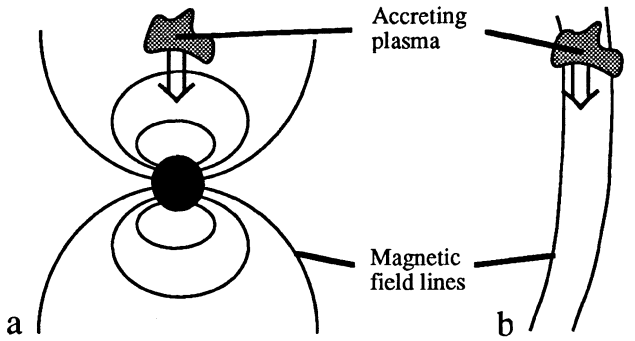

Fig. 3.—Schematic illustration of global (a) and local (b) MHD stability arguments that set an upper bound on the extent of the magnetosphere of an accreting neutron star. Both arguments are based on the fact that the disturbance of the stellar magnetic field by the accreting matter propagates at the Alfvén speed.

Global argument.—The global argument (see Fig. 3a) starts with the fact that the inward falling plasma cannot be deflected by the stellar magnetic field in a time shorter than the time taken by an Alfvén wave propagating in the stellar field to travel from the plasma to the stellar surface and back. Thus, the stellar magnetic field can significantly affect the motion of accreting plasma at radius r only if

$$t_A < t_r\,, \tag{3.2}$$

where

$$t_A = -\int_r^R \frac{dr}{v_A} \tag{3.3}$$

is the time for an Alfvén wave to travel from r to the stellar surface at R and

$$t_r = \int_r^R \frac{dr}{v_r} \tag{3.4}$$

is the time for the flow to travel from r to the stellar surface. The Alfvén velocity in equation (3.3) is given by

$$v_A = \frac{B_p}{\sqrt{4\pi\rho}}\,, \tag{3.5}$$

where B_p is the poloidal component of the stellar magnetic field and ρ is the density of the plasma *on the stellar field lines.*

Both integrals (3.3) and (3.4) are typically dominated by the domain where r is large, since both v_r and v_A are usually smallest there. Thus, $t_r \approx r/v_r(r)$ and $t_A \approx r/v_A(r)$. On substituting these expressions into inequality (3.2), one finds

that an *upper bound* on the radius of the magnetosphere is given implicitly by the inequality

$$\rho(r)\, v_r^2(r) \leq \frac{B_p(r)^2}{4\pi}, \tag{3.6}$$

where ρ is the mass density on the stellar field lines. Note that condition (3.6) does not guarantee that the magnetic stress is large enough to control the flow, if other components of the flow velocity are larger than v_r. Thus, the actual radius of the magnetosphere may be less than the radius given by condition (3.6).

Local argument.—The local form of this argument (see Fig. 3b) may be stated as follows. Field-aligned flow must be sub-Alfvénic in the poloidal field of the star in order to be stable (Lamb and Pethick 1974; Williams 1975; Ghosh, Lamb, and Pethick 1977; Adam 1978). The condition that this be so is

$$\rho(r)\, v_p(r)^2 \leq \frac{B_p(r)^2}{4\pi}, \tag{3.7}$$

where v_p and B_p are the poloidal components of the bulk flow velocity and the magnetospheric magnetic field, respectively.

Inequality (3.7) is typically also hardest to satisfy at large r. For example, if the accreting matter is falling freely inward along the lines of a dipolar field, $\rho v_p^2 \propto r^{-7/2}$, whereas $B_p^2 \propto r^{-6}$. Thus, inequality (3.7) implicitly sets an upper bound on the radius of the magnetosphere on each flux tube.

The global and local arguments agree if $v_r \sim v_p$. The radius defined by these arguments is called the *Alfvén radius* and is usually denoted r_A.

3.4 Disk Flows

The converging streamlines of a Keplerian accretion flow tend to sweep the magnetic field of the accreting star inward. Cross-field motion due to microscopic diffusion is negligible, so that even the relatively slow inward drift of the disk plasma is sufficient to confine much of the magnetic flux of the star to its vicinity. However, the inward flow is typically confined by gravity to a solid angle $\sim 10^{-2}$ ster. As a result, the stellar magnetic field is likely to be much more compressed in the disk plane than in directions away from it, and hence the magnetosphere is not spherical. Instead, the magnetosphere is pinched inward in the disk plane but balloons outward in directions away from the plane. Some lines of the stellar magnetic field may be open.

"Diamagnetic disk" models.—Several authors (Pringle and Rees 1972; Aly 1980; Riffert 1980; Kundt and Robnik 1980; Anzer and Borner 1983; White and Stella 1987) have assumed that a geometrically thin Keplerian disk flow will interact with the magnetic field of the neutron star only by excluding it from the

volume occupied by the disk. In order for this to happen, the disk flow would have to be stable and the plasma in the disk perfectly diamagnetic. Despite the absence of any couple between the disk and the star in this "diamagnetic disk" picture, the disk is usually assumed to have an inner edge, from which matter falls freely to the stellar surface. The radius of the inner edge of the disk is typically calculated by balancing the thermal pressure of the plasma at the midplane of a steady disk flow model against the magnetic pressure of an undistorted dipolar magnetic field (see, for example, Pringle and Rees 1972; White and Stella 1987).

Although the diamagnetic disk picture provides some insight into the topology of the magnetic field near a Keplerian disk flow, it has several major defects as a model for neutron star X-ray sources. First, the very physical processes that cause the plasma in the disk to drift inward by creating a substantial shear stress will also lead to a large magnetic diffusivity. These processes include turbulent motions, and magnetic field amplification and reconnection. Instabilities of the disk-magnetic field interface, such as the Kelvin-Helmholtz instability, will also assist the magnetospheric magnetic field to mix into the disk. Reasonable estimates of the rate at which the magnetospheric magnetic field diffuses into the disk indicate that the field will thread through the disk in a time much shorter than the radial drift time, as discussed below. If these estimates are correct, the assumption of a diamagnetic disk is self-contradictory and such a disk can never form. Even if the threading of the disk plasma by the magnetospheric magnetic field is not complete, the interaction between the disk plasma and the magnetospheric magnetic field will create a couple between the disk and the star that radically changes the character of the flow.

A second defect of the diamagnetic disk picture, if applied consistently, is that plasma in the disk never reaches the stellar surface on time scales of interest (assuming these are much shorter than the time scales on which electrical currents in the neutron star decay). This can be seen by considering the initial value problem of the formation and evolution of a Keplerian disk from a stream of accreting matter approaching the neutron star (cf. Fig. 1). In accordance with the diamagnetic disk picture, we assume that the incoming flow is stable and perfectly diamagnetic, and that the boundary between the Keplerian flow and the magnetic field can be determined by balancing the static thermal pressure of the plasma in the flow against the pressure of the surrounding magnetic field. Because of the extreme weakness of the stellar magnetic field at the radius r_ℓ where the material from the stream first orbits the neutron star, the pressure balance surface is initially far from the center of the plasma ring, as shown in the top panel of Figure 4. As the plasma streaming into the ring diffuses inward and outward, the ring spreads, the pressure at the inner edge of the ring increases, and the inner edge of the pressure balance surface moves inward, as shown in the middle panel of Figure 4.

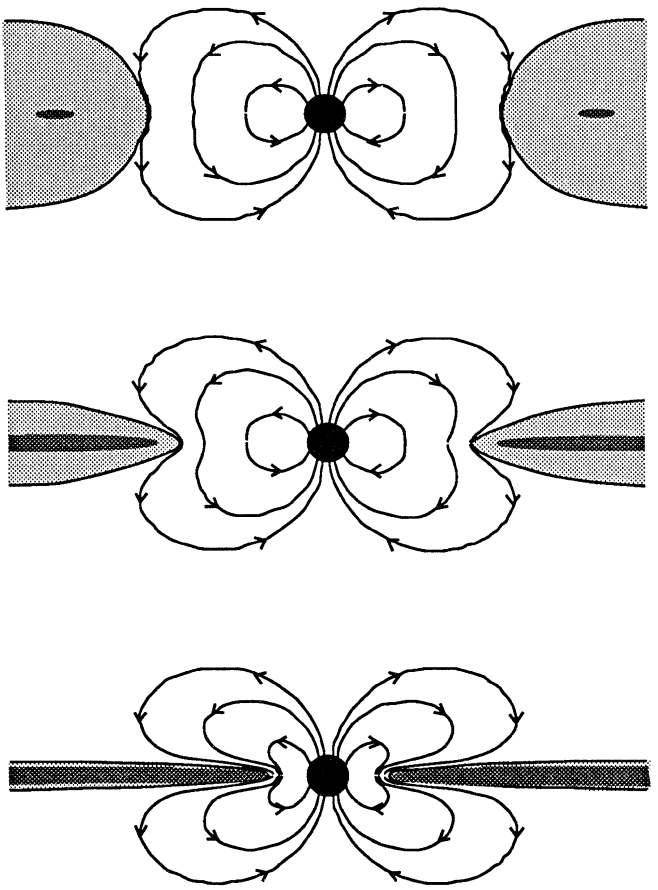

Fig. 4.—Schematic side views of the time evolution of a stable, perfectly diamagnetic Keplerian disk flow around an aligned rotator, showing the initial interaction of the plasma ring with the stellar magnetic field (top), the inward and outward diffusion of the plasma in the ring (middle), which causes the inner edge of the pressure balance surface to move inward, and the gradual accumulation of plasma near the star (bottom), which increasingly pinches the stellar magnetic field between the inner edge of the flow and the star. A steady flow never develops.

Since, in accordance with the diamagnetic disk picture, there is no couple between the magnetic field and the flow, angular momentum can be removed from the Keplerian flow only by internal shear stresses. However, as shown below in §4.1, removal of angular momentum by shear stresses internal to a geometrically thin Keplerian flow can never proceed fast enough to cause the angular velocity of the flow to deviate significantly from the Keplerian value or the radial velocity to approach free-fall. Thus, the plasma in the disk will continue to diffuse slowly

inward indefinitely, maintaining its Keplerian azimuthal velocity. As the density and pressure at the inner edge of the disk increase, the inner edge of the pressure balance surface will continue to move inward, as shown in the bottom panel of Figure 4.

As the pressure of the magnetic field confined between the inner edge of the disk and the star increases, ever increasing plasma pressure is required to move the inner edge of the pressure balance surface further inward. Even if the intrinsic magnetic field of the star is purely dipolar (and it may not be), once the pressure balance surface is within a distance $\sim R$ of the stellar surface, the higher multipole moments of the pinched stellar magnetic field will become very important, causing the magnetic pressure to rise even more steeply as the inner radius of the pressure balance surface decreases. Thus, the structure of the Keplerian flow continues to evolve and is very unlikely to be similar to that in models of steady-state disk flows. Since no plasma ever reaches the neutron star, the mass accretion rate to the stellar surface is zero, there is no energy release at the stellar surface, and the luminosity comes only from the disk.

This discussion shows that attempts to determine the inner radius of the diamagnetic disk, from which matter supposedly "falls" from the disk to the star, by balancing the thermal pressure at the midplane of a steady-state flow model against the magnetic pressure of an undistorted dipolar magnetic field are deeply misleading, for several reasons: (1) The tacit assumption that the pressure at the inner edge of the time-dependent diamagnetic inflow is the same as the pressure in the midplane of a steady-state Keplerian disk flow is unjustified, and is probably wrong. (2) The tacit assumption that the magnetic pressure of the pinched stellar magnetic field is the same as the pressure of an undistorted dipolar field at the same radius is incorrect. (3) The assumption that matter deviates significantly from Keplerian motion at the pressure balance surface violates angular momentum conservation, since by assumption there is no couple between the disk and the star and since the shear stress in a geometrically thin flow is too small to cause any significant deviation from Keplerian motion. On the other hand, if there *is* a significant couple between the disk and the star, then the use of static pressure balance to determine the inner edge of the Keplerian disk flow is unfounded.

The couple between disk and star.—Consider now the physical processes that create a couple between the disk flow and the neutron star. Typical values of the coupling times due to some of these processes, as well as other important time scales in disk accretion, are listed in Table V.

Near the inner edge of the Keplerian flow, the interface between the disk flow and the magnetospheric magnetic field is Kelvin-Helmholtz unstable (Ghosh and Lamb 1978). Penetration of the Keplerian flow by the magnetospheric magnetic field is assured if unstable modes grow to an amplitude comparable to the semi-thickness h of the disk. Modes with wavelengths λ greater than h can achieve

TABLE V
Important Time Scales in Disk Accretion[a]

Time Scale	Symbol	Typical Value (s)
Kelvin-Helmholtz growth time	τ_{KH}	$\sim 10^{-2}$
Magnetic flux reconnection	τ_R	$\sim 10^{-1}$
Keplerian orbital period	τ_K	$\sim 10^{-1}$
Turbulent diffusion through disk	τ_D	~ 1
Radial drift	τ_r	$\sim 10^{3}$
Doubling of spin rate	τ_s	10^{9}–10^{13}

[a]Near the inner edge of the disk. Accretion flow and neutron star parameters are the same as in Table II.

such an amplitude while still in the linear regime. Since the growth times of the Kelvin-Helmholtz modes in the linear regime can be estimated analytically, using the MHD dispersion relation appropriate to the disk-magnetosphere interface, Ghosh and Lamb concentrated on long-wavelength modes. They found that near the inner edge of the disk, the growth time for long-wavelength Kelvin-Helmholtz modes is $\sim 10^{-5}$ times the radial drift time. Thus, there appears to be plenty of time for these modes to grow to sufficiently large amplitude to greatly disturb the disk surface and allow the magnetospheric magnetic field to mix with the disk plasma before the plasma drifts significantly inward. This mixing produces a couple between the disk and the star.

The disk and the star will also be coupled by turbulent diffusion of the magnetospheric field into the disk, as shown in Figure 5. This process is important in the region where the kinetic energy density of convective or turbulent motions in the disk exceeds the energy density of the magnetospheric magnetic field just outside the disk. In this region one expects the magnetospheric magnetic field to be entrained by the convective motions and carried into the disk. In order to make an estimate of the efficiency of this process, Ghosh and Lamb (1978) adopted a mixing length approach, assuming a diffusion coefficient $\sim 0.1\, u_t \ell_t$, where u_t is the turbulent velocity and ℓ_t is the length scale of the largest eddies. They found that the magnetospheric magnetic field would diffuse through the disk in a time $\sim 10^{-3}$ times the radial drift time. Thus, there appears to be ample time for the magnetic field to diffuse into the disk. Once inside the disk, magnetic field lines that were formerly above the disk can reconnect to magnetic field lines that were formerly below the disk, creating an additional couple between the disk and the neutron star.

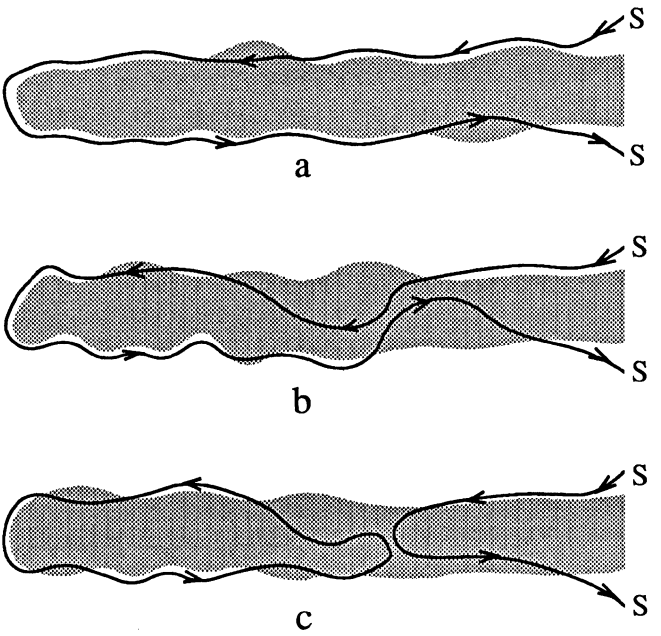

Fig. 5.—Side view of the inner edge of a Keplerian disk flow (shaded) being threaded by the magnetospheric magnetic field via turbulent diffusion and reconnection. Field lines that connect to the neutron star are indicated by the letter S. The stellar magnetic field first diffuses into the disk (a-b) and then reconnects (c), linking magnetic field lines that were formerly above and below the disk through it (right) and creating a magnetic island (left) within the disk. Such an island will subsequently be distorted and subdivided by turbulence, convection, and reconnection within the disk. Afterwards, its orientation could favor reconnection to the magnetospheric magnetic field just outside the disk.

A third process that couples the disk and the star is reconnection of the magnetospheric magnetic field to magnetic fields in the disk (Ghosh and Lamb 1978). The disk flow amplifies and reconnects any seed field in the stream of matter that feeds it, creating closed loops of magnetic flux within the disk. These flux loops are continually distorted by convection and turbulence within the disk, and by reconnection (see Stella and Rosner 1984, and references therein). Even if there were no magnetic field initially threading the disk flow, turbulent diffusion of the magnetospheric magnetic field into the disk flow will create such a field. Once there are magnetic flux loops within the disk, either because magnetic fields were present in the incoming stream or because the magnetospheric magnetic field earlier diffused into the disk, it will be energetically favorable for the magnetospheric field to reconnect to the disk fields. The time scale for this to occur near the inner edge of the disk is $\sim 10^{-3}$ times the radial drift time. In the usual reconnection picture, almost all of the magnetic flux is conserved, but the topology is radically

changed. As a result, field lines that initially formed closed loops in the disk now connect to the star. This produces a couple between the star and the disk flow.

In summary, even if the Keplerian disk flow were not initially coupled to the stellar magnetic field, a significant couple would develop rapidly compared to the radial drift time. Thus, any realistic model of disk accretion by a magnetic neutron star must take into account the coupling between the disk and the star.

Radius of the inner edge of the disk.—As noted above, if the neutron star did not have a magnetic field, or if the magnetic field did not couple the disk and the star, the plasma in the disk would remain in near-Keplerian motion, spiralling slowly inward as the weak shear stresses within the disk slowly transported angular momentum outward. In order for the Keplerian flow to have an inner edge other than at the stellar surface, angular momentum must be extracted from the Keplerian flow by some mechanism other than viscous shear stresses. The interaction with the magnetic field of the neutron star can be such a mechanism.

Consider, for simplicity, a slowly rotating neutron star. The coupling between the star and the disk via the stellar magnetic field increases rapidly as the flow nears the star. This is true even if the stellar magnetic field is dipolar and the flow does not appreciably screen the stellar field, simply because of the steep increase of B^2 with decreasing radius. At a certain distance from the star, the flow of angular momentum out of the disk via magnetic stresses becomes larger than the radially outward flow of angular momentum via the the shear stresses in the disk. The Keplerian disk does not end at this radius, however, because the angular momentum flux out of the disk is still far too small to cause a significant departure from Keplerian motion. The Keplerian disk ends when the magnetic coupling to the star is large enough to remove the angular momentum of the flow in a radial distance Δr small compared to r. This is what marks the end of the Keplerian disk flow and the beginning of the magnetospheric flow.

This analysis shows that the inner radius of the Keplerian disk is determined by conservation of angular momentum (Ghosh and Lamb 1979a). The radius at which the magnetic stress removes the angular momentum of the Keplerian flow in a radial distance Δr ($\ll r$) is given implicitly by the azimuthal stress balance condition

$$\frac{B_p B_\phi}{4\pi} 4\pi r^2 \Delta r \approx \dot{M} r v_K \,, \tag{3.8}$$

where B_p and B_ϕ are the poloidal and toroidal components of the magnetospheric field, Δr is the radial distance over which the magnetospheric field and the disk interact, $\dot{M}$ is the mass flux through the inner disk, and $v_K = r\Omega_K$ is the azimuthal velocity of the flow in terms of the Keplerian angular velocity Ω_K. Equation (3.8) implicitly determines the radius r_0 of the inner edge of the Keplerian disk.

The shape and structure of the magnetosphere is affected by the large material stresses associated with the orbital motion of the disk plasma, the flow of

TABLE VI
Static and Dynamic Stresses in Accretion from a Keplerian Disk[a]

Stress Ratio	Flow in the Disk	Flow in the Magnetosphere
$\rho v_p^2 : P$	$\sim 10^{-4}$	$\sim 10^4$
$\rho v_p v_\phi : P$	~ 1	$\sim 10^3$
$\rho v_\phi^2 : P$	$\sim 10^4$	$\sim 10^4$

[a] Accretion flow and neutron star parameters are the same as in Table II. Here ρ is the mass density of the flow, v_p is the poloidal velocity, v_ϕ is the azimuthal velocity, and P is the thermal pressure.

plasma into the magnetosphere, and the tendency of plasma within the magnetosphere to corotate with the neutron star. The relative sizes of these stresses just outside and just inside the magnetosphere are compared with one another and with the thermal pressure in Table VI. In the disk, the radial ram pressure is typically much less than the thermal pressure. However, the off-diagonal part of the material stress is typically comparable to the thermal pressure, while the diagonal part of the material stress in the azimuthal direction is large compared to the thermal pressure. Just inside the magnetosphere, all the dynamical stresses are much larger than the thermal pressure. The structure of the magnetosphere is clearly a dynamical problem, not a static one.

3.5 Radial Flows

I define an approximately radial accretion flow as one for which $\omega_p \ll 1$. Approximately radial accretion by neutron stars has been the focus of a substantial theoretical effort (Lamb 1975a,b; Elsner 1976; Elsner and Lamb 1976, 1977, 1984; Arons and Lea 1976a,b, 1980; Michel 1977a,b,c; Wang and Welter 1982; Burnard, Lea, and Arons 1983; Wang and Nepveu 1983; Wang, Nepveu, and Robertson 1984; Wang and Robertson 1984), motivated in part by its comparative tractability. Under some conditions, accretion flows near neutron stars that are capturing matter from a stellar wind may be approximately radial, as discussed in §2.3. Investigations of approximately radial flows have usually assumed that the neutron star is rotating sufficiently slowly that centrifugal forces can be neglected. Even though the dynamical effects of the circulation of the accreting plasma are, by definition, negligible in approximately radial flows, the difference between the angular velocity of the neutron star and that of the plasma just outside the magnetosphere may strongly affect the way in which the accreting plasma enters the magnetosphere.

TABLE VII
Important Time Scales in Radial Accretion[a]

Time Scale	Symbol	Typical Value (s)
Compton cooling	t_C	10^{-6}–10^{-2}
Electron-ion energy exchange	t_{ei}	$\sim 10^{-1}$
Free-fall (dynamical)	t_{ff}	$\sim 10^{-1}$
Bremsstrahlung cooling	t_{br}	10^{-1}–1

[a]Near the magnetospheric boundary. Accretion flow and neutron star parameters are the same as in Table II.

Two cooling regimes.—The character of approximately radial accretion flows depends sensitively on whether there is a substantial flow of plasma to the stellar surface at the time in question. If there is little or no flow to the stellar surface, plasma near but outside the magnetosphere cools predominantly via electron-ion energy exchange and bremsstrahlung radiation. If, on the other hand, there *is* a substantial flow of plasma to the stellar surface, the X-rays produced there rapidly cool the electrons in the accreting plasma by the inverse Compton process, and the electrons then rapidly cool the ions by collisional energy exchange.

Whereas cooling by bremsstrahlung emission typically takes much longer than the free-fall time to the stellar surface, inverse Compton cooling of plasma exposed to X-rays from the stellar surface typically takes much less than a free-fall time, as indicated in Table VII. Thus, when X-rays are being emitted, plasma accreting to the stellar surface cools as it falls. For electrons moving in the magnetospheric field, the cyclotron cooling time is shorter still, while ion cyclotron cooling becomes important near the stellar surface. As long as the accreting plasma remains optically thin, cooling occurs so rapidly that neither the electrons nor the ions will mirror in the magnetospheric field.

Evolution of radial flows.—As discussed in §2.3, approximately radial inflow is possible only if matter is captured from a stellar wind. Consider a wave front of plasma falling approximately radially from the accretion capture radius r_a toward the neutron star. At first, the magnetic field ahead of the wave front is very weak, and hence the infalling plasma readily sweeps it inward, toward the star. However, as the wave front compresses the magnetic field, the field becomes increasingly rigid. If, as expected, the plasma approaching the star is highly conducting and therefore cannot readily penetrate the stellar magnetic field, the rising back-pressure of the magnetic field will decelerate the plasma. When this happens, a shock wave forms near the plasma-magnetic field interface (the so-called

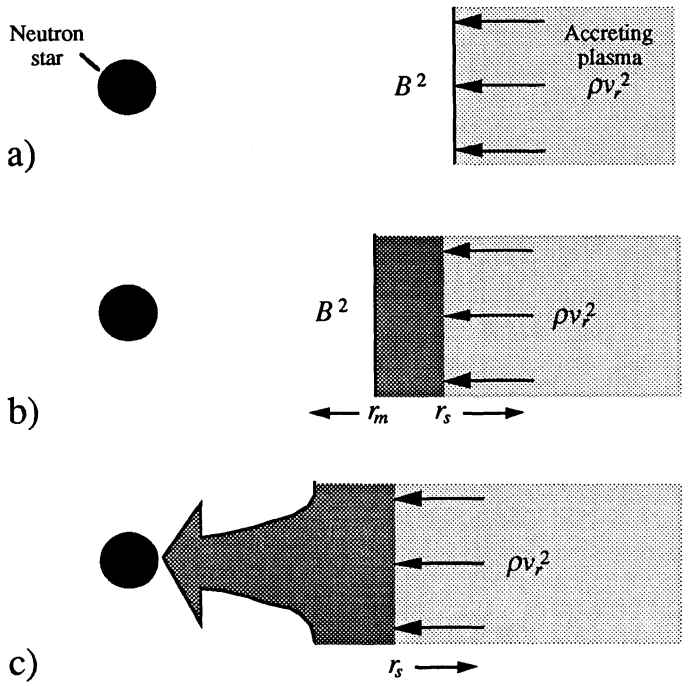

Fig. 6.—Schematic view of stages in the interaction between an initially radial inflow and the magnetic field of the neutron star, showing the initial compression of the stellar magnetic field by the infalling, diamagnetic plasma (a), the accumulation of shock-heated plasma outside the magnetopause (b), and the large-scale change in the structure of the magnetosphere as the plasma cools and the magnetosphere becomes unstable (c). The radius of the magnetopause is denoted by r_m and the radius of the shock front, by r_s.

magnetopause) and begins to propagate upstream through the accreting plasma, heating it and slowing its inward motion (see Fortner, Lamb, and Zylstra 1984). Post-shock electron and ion temperatures may reach $\sim 10^{10}$ K for a shock radius $r_s \sim 10^8$ cm. After the plasma passes through the shock front, its inward motion is slowed further by a gradient in the plasma pressure between the shock front and the magnetic field. Eventually the magnetic field becomes rigid enough to completely halt the inflow of the heated plasma near the initial magnetospheric radius r_{m0}.

This sequence of events is shown schematically in Figures 6a and 6b. In Figure 6a, the plasma is driving the magnetic field inward. As a result, the location of the interface between the plasma and the stellar magnetic field, the so-called magnetopause, is not determined by static pressure balance. As the increasingly compressed stellar magnetic field becomes stiffer, it eventually slows the inflow, and a shock wave forms. A brief interval of quasi-static evolution

follows, as plasma accumulates between the outward-moving shock front at r_s and the inward-moving magnetopause at r_m, as shown in Figure 6b. During this phase little plasma reaches the stellar surface, and the neutron star is not a luminous X-ray source, although some emission of $\sim$100 keV hard X-rays is expected. Even so, the magnetopause continues to move inward as plasma accumulates outside.

As discussed below, very little of the shock-heated plasma is expected to penetrate the stellar magnetic field on a free-fall time, and hence at first very little plasma reaches the stellar surface to produce cooling X-rays. Moreover, thermal conduction can probably be neglected, since even a very small magnetic field in the accreting plasma will suppress it. Thus, the shock-heated plasma is expected to cool primarily via electron-ion energy exchange and bremsstrahlung radiation. Since the bremsstrahlung cooling time is typically longer than the time required for the magnetosphere to assume its equilibrium shape (a time of order the free-fall time, which is greater than or comparable to the time for an Alfvén wave to cross the magnetosphere), there is a brief interval when the shape of the magnetosphere is determined by a quasi-static balance between the pressure of plasma and swept-up magnetic fields outside the magnetosphere and the pressure of the stellar magnetic field inside.

Relative motion between the plasma just outside and just inside the magnetopause will tend to drive the magnetopause Kelvin-Helmholtz unstable, mixing the accreting plasma into the magnetosphere. If a sufficient quantity of plasma enters the magnetosphere and falls to the stellar surface, releasing X-rays, inverse Compton cooling will accelerate the cooling of the plasma near the magnetopause. After approximately one cooling time, the plasma near the magnetopause has become sufficiently dense that the magnetopause tends to become Rayleigh-Taylor unstable. At this point a large-scale flow of plasma into the magnetosphere develops, as shown schematically in Figure 6c. Once this large inward flow toward the stellar surface has begun, the large-scale structure of the magnetosphere is distorted by the stresses associated with the copious flow of plasma into the magnetosphere and static pressure balance is no longer a good guide to the location and shape of the magnetopause. When the increased inflow of plasma approaches the stellar surface, the star begins to emit an increased flux of X-rays, speeding cooling. If the infalling plasma is threaded rapidly by the stellar magnetic field, ordered flow cannot extend outside the Alfvén radius r_A defined in §3.3.

Clearly, the time development of approximately radial accretion flows and the resulting structure of the magnetosphere depend sensitively on whether or not the plasma-field interface is hydromagnetically stable. It is therefore useful to consider models in which the magnetopause is presumed stable separately from those in which it is unstable.

Stable magnetopause.—When the magnetosphere is hydromagnetically stable and in quasi-static equilibrium, the shape of the magnetosphere is determined

by conservation of linear momentum. During this phase, the accreted plasma is separated from the interior of the magnetosphere by a current layer. Electron and proton temperatures $T \sim 10^{10}$ K and particle densities $n \sim 10^{15}$ cm^{-3} are typical of the conditions expected outside the magnetosphere for accretion rates typical of the luminous neutron star X-ray sources. Lower particle densities may be of interest for neutron star models of flaring X-ray and γ-ray sources (Lamb *et al.* 1977). Under these conditions, both the electrons and protons are collisionless, with mean free paths $\gtrsim r_{m0}$.

The current layer separating the accreted plasma from the interior of the magnetosphere is expected to have a thickness $\Delta r_m \sim a_i$, where a_i is the ion Larmor radius in the magnetospheric field. Since a_i is typically $\sim$1 cm, Δr_m is completely negligible compared to r_{m0}, and the gravitational force acting on the plasma in the boundary layer can be neglected in calculating the balance of linear momentum across the magnetopause, which may be expressed as

$$\left(\frac{B_t^2}{8\pi}\right)_{\rm in} = \left(\frac{B_t^2}{8\pi}\right)_{\rm out} + P_{\rm out}\,, \tag{3.9}$$

where B_t is the component of the magnetic field tangential to the boundary and P is the plasma thermal pressure. The subscripts indicate whether the terms are to be evaluated just inside or just outside the magnetopause.

Applying conservation of linear momentum across the initially thin shocked plasma layer (including the effect of the gravitational force on the plasma within the layer), the initial plasma thermal pressure just outside the magnetopause is

$$P_{\rm out} \approx \rho v_r^2\,, \tag{3.10}$$

so that the *initial* radius r_{m0} of the magnetopause is the so-called Chapman-Ferraro radius $r_{\rm CF}$ defined implicitly by (Chapman and Ferraro 1931)

$$\left(\frac{B_t^2}{8\pi}\right) = \rho v_r^2\,. \tag{3.11}$$

For a purely radial inflow, the shape and location of the initial plasma-magnetic field interface $r_{m0}(\theta)$ is given by equation (3.11). As discussed below in §3.7, typical values of $r_{\rm CF}$ are $\sim 10^7$–10^9 cm for accretion-powered pulsars, much greater than the radius $R \approx 10^6$ cm of the neutron star. At these radii, the stellar magnetic field is dominated by its dipole component, and there are point cusps above the magnetic poles.

As accretion continues, plasma accumulates between the shock front and the magnetopause, and hence the radius of the shock front tends to increase. Simultaneously, the shocked plasma cools, the pressure at the magnetopause increases, and

hence r_m decreases. If gravitational forces were absent, the magnetopause would remain stable as the plasma cools, since it is convex toward the plasma. However, gravitational forces *are* present, and hence the boundary becomes Rayleigh-Taylor unstable as soon as the plasma cools sufficiently (see below).

Appreciable entry of plasma by *any* mechanism causes copious emission of X-rays from the stellar surface and extremely rapid cooling of the plasma at the magnetospheric boundary by the inverse Compton process, as discussed above. Thus, in order to compete effectively with the Kelvin-Helmholtz and Rayleigh-Taylor instabilities, other entry mechanisms must create an average inflow velocity comparable to the free-fall velocity at the magnetospheric boundary, since the average inflow velocity produced by hydromagnetic instabilities will be of this order in any case.

What processes might compete with hydromagnetic instabilities? Particles can enter the magnetosphere via loss-cone entry through the polar cusps and microscopic diffusion across the magnetopause. However, these processes are not important for conditions typical of the luminous binary X-ray sources (Elsner and Lamb 1984). According to current theoretical models of magnetic flux reconnection, plasma entry into the magnetosphere via reconnection cannot compete with the Kelvin-Helmholtz and Rayleigh-Taylor instabilities unless the magnetic field within the accreting plasma is comparable in scale and strength to the magnetospheric magnetic field; otherwise magnetic flux linkage will not proceed fast enough nor go deep enough into the magnetosphere for reconnection to be competitive. Among other things, this requires that the strength of the magnetic field in the plasma accreting onto a given neutron star have a particular value at the capture radius, otherwise the magnetic field at the magnetopause will either be too weak or too small-scale for entry via flux reconnection to compete with entry via the Kelvin-Helmholtz and Rayleigh-Taylor instabilities. Given the available evidence concerning magnetic fields and plasma flow patterns in neutron star binaries, it appears very unlikely that plasma entry into the magnetosphere via flux reconnection can be competitive (Elsner and Lamb 1984).

In summary, the plasma entry mechanisms that operate when the magnetopause is hydromagnetically stable cannot compete with plasma entry via hydromagnetic instabilities, except perhaps in very exceptional circumstances.

Unstable magnetopause.—Consider now the mixing of plasma into the magnetosphere produced by the Rayleigh-Taylor and Kelvin-Helmholtz instabilities.

Although there is general agreement on the conditions under which the magnetospheric boundary is Rayleigh-Taylor unstable, the wavelengths of the modes that are most important for transporting plasma into the magnetosphere when this happens remain uncertain. Lamb (1975a,b), Elsner (1976), and Elsner and Lamb (1976, 1977) emphasized the likely importance of relatively long-wavelength modes and rapid diffusion of plasma onto magnetospheric magnetic field lines,

whereas Arons and Lea (1976a,b, 1980) assumed that only short-wavelength modes can exist and that the plasma would diffuse only slowly onto field lines. In evaluating the results of a numerical study, Wang and Nepveu (1983) conjectured that mass transport into the magnetosphere via long-wavelength modes is favored, both because the growth of long-wavelength modes tends to saturate more slowly than that of shorter wavelength modes and because there are numerous effects, including rotation, viscosity, and magnetic shear, that preferentially stabilize shorter-wavelength modes. However, in a later numerical study, Wang, Nepveu, and Robertson (1984) found that the shortest wavelengths consistent with the effective viscosity of the plasma flow were likely to be the most important (these could, however, be comparable to r_m, if the pressure scale-height in the shocked plasma is $\sim r_m$).

If the most important nonlinear modes turn out to have wavelengths that are a substantial fraction of r_m, the problem of flow into the magnetosphere becomes much more complex than assumed by Arons and Lea, because tangential pressure gradients and inertial stresses will distort the shape of the outer magnetosphere, while the magnetopause itself (here defined as the region that contains screening currents and in which the magnetic field transfers momentum to the inflowing plasma) may broaden to an appreciable fraction of r_m. If relatively long-wavelength modes are the most important for plasma flow into the magnetosphere, there are a number of important and interesting observational consequences. For example, in persistent X-ray sources in which plasma enters the magnetosphere predominantly as a result of the Rayleigh-Taylor instability, one may expect intensity fluctuations of relatively large amplitude. Mass transport into the magnetosphere by relatively long-wavelength modes also implies relatively large fluctuations in the corresponding accretion torque, with important observational consequences. Finally, the growth of such modes will produce plasma sheets or filaments that have a much greater chance of surviving intact deep into the magnetosphere, where their breakup would lead to plasma inflow over a substantial fraction of the stellar surface and hence to the formation of complex pulse waveforms at keV energies (Elsner and Lamb 1976).

The possibility that the Rayleigh-Taylor instability occurs preferentially near the polar cusps is of interest because X-ray emission from X-ray pulsars is localized on the stellar surface, as indicated by the pulsed emission. Even though the cusp region is inherently more stable than the equatorial magnetopause, most of the accreting plasma might still enter the magnetosphere there if the luminosity is low and the cusps are preferentially illuminated by X-rays from the stellar surface. However, entry near the cusps cannot be the dominant entry process if the star has a persistent luminosity greater than $\sim 10^{36}\,\mathrm{ergs\,s^{-1}}$ and, as in the presently known pulsing sources, a substantial fraction of the magnetopause is illuminated (Elsner and Lamb 1984). Under these conditions, plasma near the magnetopause cools in a time much shorter than the free-fall time there, and

hence there is no time for an extensive plasma atmosphere to accumulate outside the magnetosphere. Instead, plasma everywhere outside the magnetosphere will fall into it via Rayleigh-Taylor instability of the magnetopause before it has time to flow a significant distance around the magnetosphere. Plasma above the cusp axis, which is stable, can enter the magnetosphere by flowing a short distance sideways to a point where the magnetopause is unstable.

For approximately spherically-symmetric radial accretion by neutron stars with moderate rotation rates, the relative motion of the magnetosphere and the surrounding plasma suppresses the Rayleigh-Taylor instability. Burnard, Lea, and Arons (1983) have studied such stars and conclude that the accreting plasma is mixed into the magnetosphere by the Kelvin-Helmholtz instability. Wang and Welter (1982) concluded that even a very weak magnetic field within the plasma may suppress this instability, and suggested that mixing of moving plasma into the magnetosphere is not the result solely of the Kelvin-Helmholtz instability. In a later numerical study of the nonlinear development of the Kelvin-Helmholtz instability, Wang and Robertson (1984) found that the tendency for neighboring vortices to coalesce causes the longest wavelength modes to dominate the mixing process. They also found that a component of the magnetic field parallel to the flow does have a stabilizing effect. Wang and Robertson concluded that the width of the Kelvin-Helmholtz mixing layer is likely to grow until it is comparable to the scale-height of the plasma outside the magnetopause, or until it becomes comparable to the scale-length over which the field-line orientation changes near the magnetospheric boundary.

3.6 Effects of Stellar Rotation

As just noted, even if the accretion flow outside the magnetosphere is almost purely radial, the shear produced at the magnetospheric boundary by stellar rotation can play an important role in mixing the accreting plasma into the magnetosphere (see Burnard, Lea, and Arons 1983; Wang and Robertson 1984).

An important radius for rotating stars is the so-called *centrifugal radius*

$$r_c = (GM/\Omega_s)^{1/3} = 1.5 \times 10^8 \, P^{2/3} (M/M_\odot)^{1/3} \quad \mathrm{cm}\,, \tag{3.12}$$

where the centrifugal force acting on matter corotating with the star just balances gravity. Here P is the stellar rotation period in seconds.

Accretion-powered pulsars are frequently characterized as short period ($P < 10\,\mathrm{s}$), intermediate ($10\,\mathrm{s} \leq P \leq 100\,\mathrm{s}$), or long-period ($P > 100\,\mathrm{s}$) rotators. However, the influence of an accreting star's rotation on the *dynamics of the flow* depends on the mass accretion rate and the stellar magnetic moment as well as the spin period. For matter that has been brought into corotation with the star,

centrifugal forces become important when r_c approaches r_m or, equivalently, the so-called *fastness parameter* (Elsner and Lamb 1977; Ghosh and Lamb 1979a)

$$\omega_s \equiv \Omega_s/\Omega_K(r_m) \tag{3.13}$$

approaches 1. Here the magnetospheric radius r_m is to be interpreted as the angular momentum balance radius r_0, for Keplerian accretion flows, or the Chapman-Ferraro radius $r_{\rm CF}$, for approximately radial flows. The star's rotation is dynamically unimportant for $\omega_s \ll 1$. Note that $\omega_s = (r_m/r_c)^{3/2}$. Values of ω_s inferred from observation range from $\sim 10^{-3}$ to ~ 1.

3.7 Scale of the Magnetosphere

The various order-of-magnitude estimates of the scale of the magnetosphere discussed in the preceding sections, and the types of flows to which they are applicable and inapplicable, can be summarized as follows.

Stable magnetospheric flow.—An estimate of the radius inside which ordered, field-aligned flow is possible can be made based on the MHD stability arguments summarized in §3.3. As explained there, field-aligned flow is stable inside the Alfvén radius r_A, given implicitly by the condition

$$\frac{B_p^2}{4\pi} = \rho v_p^2 . \tag{3.14}$$

This condition recognizes the fundamental characteristic of accretion, namely inward flow of matter, and can be applied when the flow outside the magnetosphere is radial, Keplerian, or anything in between.

As an example of the application of condition (3.14), suppose we assume as a rough approximation that (1) the poloidal component of the magnetic field in the outer magnetosphere is given approximately by

$$B_p(r) = \mu/r^3 , \tag{3.15}$$

where μ is the stellar dipole moment, (2) the inward poloidal velocity v_p of the accreting plasma at radius r is approximately equal to the free-fall velocity $v_{\rm ff}(r)$ there, and (3) the mass density ρ at radius r in the outer magnetosphere is equal to the mass density

$$\rho_{\rm ff}(r) \equiv \dot{M}/4\pi r^2 v_{\rm ff}(r) \tag{3.16}$$

that would be there if the flow were spherically-symmetric inflow at the free-fall velocity. Then $\rho v_p^2 \propto r^{-5/2}$ whereas $B_p^2 \propto r^{-6}$, and the Alfvén radius is

$$r_{A_1} \approx \left(\frac{\mu^4}{GM\dot{M}^2}\right)^{1/7} \approx \left(\frac{\mu^4 GM}{L^2 R^2}\right)^{1/7} = 4 \times 10^8 \left[\frac{\mu_{30}^4}{L_{37}^2 R_6^2}\left(\frac{M}{M_\odot}\right)\right]^{1/7} \text{cm} . \tag{3.17}$$

In the last two expressions on the right we have used equation (2.2) and in the last expression μ_{30} is the magnetic moment in units of 10^{30} gauss cm^3, L_{37} is the accretion luminosity in units of 10^{37} ergs s^{-1}, and R_6 is the neutron star radius in units of 10^6 cm.

As a second example of the application of condition (3.14), suppose that (1) the poloidal component of the magnetic field in the outer magnetosphere is approximately dipolar, (2) the flow in the outer magnetosphere is field-aligned, so that

$$\rho v_p / B_p = \text{const.} \tag{3.18}$$

on each flux tube, (3) the inward poloidal velocity v_p of the accreting plasma at r is again approximately equal to the free-fall velocity $v_{\rm ff}(r)$, and (4) the accreting plasma falls on an area A at the stellar surface, which is a fraction $f \equiv A/4\pi R^2$ of the whole surface. Then $\rho v_p^2 \propto r^{-7/2}$ while B_p^2 is again $\propto r^{-6}$. The resulting estimate of the Alfvén radius is

$$r_{A_2} \approx \left(\frac{\mu^4 f^2}{GM\dot{M}^2R^2}\right)^{1/5} \approx \left(\frac{GM\mu^4 f^2}{L^2R^4}\right)^{1/5} \approx 7\times 10^8 \left[\frac{\mu_{30}^4 f_{-2}^2}{L_{37}^2 R_6^4}\left(\frac{M}{M_\odot}\right)\right]^{1/5} \text{cm}\,, \tag{3.19}$$

where $f_{-2} \equiv f/10^2$. Equation (3.19) is particularly useful for setting an upper bound on the size of the magnetosphere if observational data provide an estimate of f (see, for example, Tuohy *et al.* 1981).

Note that if $f \approx R/r_{A_2}$, as expected on dimensional grounds if threading occurs readily (Lamb, Pethick, and Pines 1973), the estimate r_{A_2} is the same as the estimate r_{A_1}.

Angular momentum conservation.—For Keplerian disk flows, the radius at which the Keplerian disk ends is determined by angular momentum conservation, as explained in §3.4. The radius r_0 of the inner edge of the Keplerian disk is given implicitly by

$$\gamma B_p^2 r^2 = \dot{M} v_K\,, \tag{3.20}$$

where

$$\gamma \equiv (B_\phi/B_p)(\Delta r/r) \tag{3.21}$$

in terms of the mean azimuthal magnetic pitch B_ϕ/B_p in the region of radial width Δr at the inner edge of the Keplerian disk where the stellar magnetic field strongly interacts with the flow, and $v_K = (GM/r)^{1/2}$ is the Keplerian azimuthal velocity.

As an example of how condition (3.20) can be applied, suppose all important length scales in the inner part of the Keplerian disk flow are approximately proportional to r. This is in fact the case for the standard "α-model" of geometrically thin Keplerian disk flows around neutron stars, in the so-called gas-pressure-dominated (GPD) region, which extends outward from a transition radius

$r_t \sim 10^7$ cm (see Treves, Maraschi, and Abramowicz 1988 and §4.1). Then, since the stellar magnetic field has no length scale either, the interaction between the Keplerian flow and the stellar magnetic field has no length scale. As a result, the mean azimuthal magnetic pitch B_ϕ/B_p in the interaction region must be independent of r, while the width Δr of the interaction region must scale approximately as r. Thus, γ is independent of r, and

$$r_0 \approx \left(\frac{\gamma^2\mu^4}{GM\dot{M}^2}\right)^{1/7} \approx \left(\frac{\gamma^2\mu^4 GM}{L^2R^2}\right)^{1/7} = 4\times 10^8\,\gamma^{2/7}\left[\frac{\mu_{30}^4}{L_{37}^2R_6^2}\left(\frac{M}{M_\odot}\right)\right]^{1/7}\ \mathrm{cm}\,. \tag{3.22}$$

What is a reasonable estimate for γ? The width Δr of the region where the stellar magnetic field strongly interacts with the Keplerian flow is limited by the fact that $B_p^2 r^2 \propto r^{-4}$ whereas $\dot{M}v_K \propto r^{-1/2}$. Thus, from the steep dependence of B_p on r alone, one would expect $\Delta r \approx 0.3r$. The actual width may be smaller, due to toroidal screening currents generated in the flow both in the disk plane and above and below it. It seems unlikly that Δr can be less than $\sim 0.01\,r$. The mean aximuthal magnetic pitch B_ϕ/B_p is limited to values $\sim$1–3 by the expansion of the magnetosphere that occurs when the magnetospheric magnetic field is sheared, as discussed in more detail in §4.2. Thus, $\gamma^{2/7}$ is probably in the range 0.3–0.7. With these assumptions, one finds $r_0 \propto \dot{M}^{-2/7}$.

To get some idea of the sensitivity of the scaling of r_0 with $\dot{M}$ and other parameters, consider a second example. In the inner, radiation-pressure-dominated (RPD) region of a standard α-disk, the disk thickness is approximately independent of radius (again see Treves, Maraschi, and Abramowicz 1988 and §4.1). Suppose that as a result, the width Δr of the interaction region is approximately independent of r and equal to a fraction of the disk thickness h. Assuming that the mean azimuthal magnetic pitch B_ϕ/B_p in the interaction region is also independent of r, this gives $\gamma \approx f\,(h/r)$, where $f \equiv (\Delta r/h)(B_\phi/B_p)$, and

$$r_0 \approx \left(\frac{f^2h^2\mu^4}{GM\dot{M}^2}\right)^{1/9} \approx \left(\frac{f^2h^2\mu^4 GM}{L^2R^2}\right)^{1/9}\,. \tag{3.23}$$

With these assumptions, $r_0 \propto \dot{M}^{-2/9}$.

Note that in these two examples, the exponent of $\dot{M}$ varies from about 0.2 to about 0.3. Obviously, more complicated estimates of the radius r_0 of the inner edge of the Keplerian flow can be made, based on more detailed modeling of the structure of the inner disk and of the disk-magnetosphere interaction, as described in §4. Most lead to scalings not very different from the estimate (3.22). However, *an important complication arises for neutron stars rotating sufficiently rapidly that the corotation radius r_c is not large compared to r_0*. For such stars, other lengths (such as $r_0 - r_c$) enter the problem, and may cause the scaling of r_0 to deviate significantly from the slow-rotator scaling (3.22).

TABLE VIII
Physical Principles and Characteristic Radii

Physical Principle	Relevant Condition	Characteristic Radius
MHD stability of field-aligned flow	$B_p^2/8\pi = \rho v_p^2$	Maximum radius r_A of stable magnetospheric flow
Angular momentum conservation	$\gamma B_p^2 r^2 = \dot{M} v_K$	Inner disk radius r_0 for Keplerian disk flows
Linear momentum conservation	$B_t^2/8\pi = \rho v_r^2$	Initial magnetopause radius r_{CF} for nearly radial flows

Linear momentum conservation.—For radial flows, the initial shape and location of the magnetopause is determined by linear momentum conservation, as explained in §3.5. The initial radius r_{CF} of the magnetopause is given implicitly by

$$\left(\frac{B_t^2}{8\pi}\right) = \rho v_r^2 . \tag{3.24}$$

However, once the magnetopause becomes unstable and there is a large flux of matter into the magnetosphere, material stresses will distort the magnetopause and hence condition (3.24) will give only a rough estimate of the location of the magnetospheric boundary.

As an example of the application of condition (3.24), suppose that (1) the magnetic field in the outer magnetosphere is approximately dipolar and (2) the accreting plasma is falling freely toward the neutron star. Then the Chapman-Ferraro radius is

$$r_{CF} \approx \left(\frac{\mu^4}{GM\dot{M}^2}\right)^{1/7} \approx \left(\frac{\mu^4 GM}{L^2 R^2}\right)^{1/7} = 4 \times 10^8 \left[\frac{\mu_{30}^4}{L_{37}^2 R_6^2}\left(\frac{M}{M_\odot}\right)\right]^{1/7} \text{ cm} . \tag{3.25}$$

For easy reference, the physical principles discussed here and the characteristic radii that they give are listed in Table VIII.

4. DISK ACCRETION BY MAGNETIC STARS

In considering disk accretion by magnetic neutron stars, one could address the observed X-ray pulsing behavior directly by trying to model an oblique rotator, and there have been some attempts to do this (see, e. g., Anzer and Borner 1980).

However, two features make the oblique rotator much more difficult to handle than the aligned rotator. First, the rotation of the star imposes an explicit time-dependence on the flow. Second, the oblique rotator has no symmetry, so one is forced to attempt three-dimensional modeling. Even when the rotation axes of the disk and star are parallel, the magnetic field in the disk plane is not axisymmetric, the magnetic stresses acting on the disk plasma are explicitly time dependent, and magnetic pressure gradients affect the azimuthal, as well as the radial, motion. These difficulties have so far prevented detailed quantitative calculations of accretion by oblique rotators.

In contrast to the oblique rotator, the aligned rotator allows the possibility of a stationary flow and, if the flow is axisymmetric, two-dimensional modeling. Moreover, solutions for the poloidal magnetic field around a perfectly conducting rigid plate with a circular hole and a magnetic dipole centered in the hole have a topology near the inner edge of the plate that is the same as that of the aligned rotator, for magnetic field inclination angles $\lesssim 60°$ (Aly 1980; Arons 1987). For these reasons, I consider only axisymmetric disk accretion by an aligned rotator in the discussion that follows.

4.1 Flow Outside the Magnetosphere

In an extensive Keplerian accretion disk, the properties of the flow well inside the outer radius r_d are relatively insensitive to the properties of the stream of matter flowing into the disk, since the radial diffusion of the plasma causes it to "forget" many of the details of the flow at the outer boundary. Most discussions of disk accretion by magnetic neutron stars therefore assume that the flow near the magnetosphere is steady and Keplerian.

The α-model of accretion disks.—At present there is no truly satisfactory theory of Keplerian disk flows. The diverse time scales and complexity of such flows is too great for current supercomputers and analytical methods. As a result, almost all modeling is based on relatively simple, semi-analytical solutions for geometrically-thin Keplerian flows. The most widely used model of such flows is the so-called *α-model* (Shakura and Sunyaev 1973). The key assumptions of the α-model are as follows (see Pringle 1981; Treves, Maraschi, and Abramowicz 1988):

- The accretion disk flow is steady.
- The flow is axially symmetric about the neutron star, and hence $\partial/\partial\phi \equiv 0$.
- The flow is symmetric with respect to the plane $z = 0$, and hence the vertical structure of the flow depends only on $|z|$.
- The flow is geometrically thin, i. e., its semi-thickness h at radius r is small compared to r.

- The shear stress is related to the thermal pressure ρc_s^2 by

$$-\eta r \frac{\partial \Omega}{\partial r} \equiv \alpha \rho c_s^2 , \tag{4.1}$$

  where η is the effective dynamic viscosity, which is thought to be due to turbulence and/or magnetic field amplification and dissipation in the disk (the kinetic viscosity is negligible). The dimensionless quantity α, which is assumed constant in space and time, is a free parameter of the model (however, the model is self-consistent only if $\alpha \lesssim 1$).
- The azimuthal motion is closely Keplerian, i.e., v_ϕ at radius r is very close to v_K.
- The velocity field satisfies $|v_z| \ll |v_r| \ll |v_\phi|$, and $v_r \ll c_s$.
- The radial pressure gradient and heat flux are negligible.
- The vertical optical depth to absorption or scattering is greater than 1.

The discussion that follows includes references to the radial drift time scale $t_r \equiv |r/v_r|$ and the hydrodynamic time scale $t_H \equiv h/c_s$.

Vertical structure.—Plasma in the α-disk is confined vertically by gravity. Since $|v_r|$ and $|v_z|$ are small compared to c_s, the disk plasma is in hydrostatic equilibrium in the z-direction. Thus,

$$-\rho\, g_z \approx -\partial p/\partial z , \tag{4.2}$$

where g_z is the z-component of the gravitational acceleration. The left side of equation (4.2) is $\sim \rho (h/r)(v_K^2/r)$ while the right side is $\sim \rho c_s^2/h$. Hence equation (4.2) implies

$$h \approx (c_s/v_K)\, r . \tag{4.3}$$

At all but the smallest radii, estimates of the vertical heat flux carried by radiation lead to temperatures sufficiently small that $c_s \ll v_K$, so that the initial assumption that the flow is geometrically thin turns out to be self-consistent.

Radial drift velocity.—The inward radial velocity of the flow in the disk can be estimated from angular momentum conservation, since matter in the disk can fall inward only as it loses its angular momentum, which is carried outward by the viscous shear stress. The net transport of angular momentum through the disk is given by the difference between transport inward by the material stress, $\sigma_m \approx \rho v_r v_\phi$, and transport outward by the shear stress, $\sigma_v \approx \eta r \partial \Omega/\partial r$. Thus, for a steady flow, angular momentum conservation implies

$$4\pi \eta h r^3 \frac{\partial \Omega}{\partial r} + \dot{M} r^2 \Omega = \dot{J}_s , \tag{4.4}$$

where the first term on the left side describes the outward transport of angular momentum by the shear stress and the second, the inward transport by the material stress. $\dot{J}_s \equiv \dot{M} \ell_0$ is the net inward flux of angular momentum in terms of the

TABLE IX
Radial Structure of the α-Disk

Name	Dominant Pressure	Dominant Opacity
Outer disk	Gas pressure	Absorption
Middle disk	Gas Pressure	Electron scattering
Inner disk	Radiation pressure	Electron scattering

mass inflow rate $\dot{M}$ and the characteristic specific angular momentum ℓ_0 carried by the flow.

At radii r much greater than the radius r_0 of the inner edge of the disk, both terms on the left side of equation (4.4) scale approximately as $r^{1/2}$. Hence, at sufficiently large radii, the two terms on the left side are each much larger than the term on the right side, and equation (4.4) becomes

$$-\alpha\rho c_s^2 - \rho v_r v_\phi \approx 0\,. \tag{4.5}$$

Therefore, the radial drift velocity v_r at large radii is

$$v_r \approx -\alpha(c_s^2/v_K^2)\,v_K \approx -\alpha(h/r)^2\,v_K\,, \tag{4.6}$$

where in the last expression on the right we have used equation (4.3). This gives the estimate

$$t_r \approx (v_K^2/\alpha c_s^2)\,t_H \gg t_H \tag{4.7}$$

for the radial drift time. The mass flux $\dot{M}$ and the net flux of angular momentum $\dot{J}_s$ are not determined by the model. They are usually presumed to be fixed by the boundary conditions at the outer and inner edges of the disk flow.

Radial structure.—The α-disk has three distinct regions, which are listed in Table IX. The transition between the middle, gas-pressure-dominated (GPD) region and the inner, radiation-pressure-dominated (RPD) region occurs very graadually near the transition radius

$$r_t \sim 10^7\,\alpha^{2/21}(M/M_\odot)^{23/21}\,(\dot{M}/\dot{M}_E)^{16/21}\quad \mathrm{cm}\,, \tag{4.8}$$

where $\dot{M}_E$ is the mass flux that would produce an Eddington accretion luminosity (see Treves, Maraschi, and Abramowicz 1988). Thus, the magnetospheres of neutron stars with strong magnetic fields, such as the accretion-powered pulsars, are immersed in the GPD region, whereas the magnetospheres of stars with weak fields, like those thought to be present in the QPO sources, are immersed in the RPD region.

The structure and behavior of the α-disk in the GPD region is comparatively well understood. Cooling is efficient in this region, so that the disk is quite thin ($h/r \sim 10^{-2}$–10^{-3}). The structure and behavior of Keplerian flows in the RPD region is much less clear. Cooling is less efficient in the RPD region. As a result, the structure of this region calculated from the α-model is thermally unstable if the shear stress is proportional to the total pressure. No consistent, stable flow model is currently available for this case. In fact, calculations of the stress produced by amplification and dissipation of small-scale magnetic fields in the disk give a stress that is proportional to the gas pressure alone (Stella and Rosner 1984). If the shear stress in the RPD region *is* proportional to the gas pressure alone, stable flows can be constructed. However, at present the structure of the RPD region remains uncertain. If the mass flux through the disk approaches $\dot{M}_E$, the radiation pressure in the RPD region becomes so great that the inner disk expands vertically and can no longer be treated as geometrically thin (see Treves, Maraschi, and Abramowicz 1988).

Effect of disk-star coupling.—Using their model of disk accretion by magnetic stars, Ghosh and Lamb (1979a) calculated the effect on the structure of the disk flow of the interaction with the magnetospheric magnetic field, when the inner edge of the disk is in the GPD region, and found that it is relatively small, except when the neutron star is rotating rapidly. Most other authors have simply assumed that the interaction with the neutron star magnetic field leaves the disk structure unaltered from that around a nonmagnetic star, but this is certainly not a safe assumption in general.

4.2 Disk-Magnetosphere Interaction

In this section I discuss the consequences of the coupling between the disk flow and the stellar magnetic field described in §3.4. In the following discussion, I assume that (1) the neutron star has a dipole magnetic field, (2) the star is rotating with angular velocity Ω_s about its dipole axis, (3) the rotation axis is perpendicular to the plane of the disk, and (4) the flow is steady and has axial symmetry everywhere. I use a cylindrical polar co-ordinate system (ϖ,ϕ,z) centered on the neutron star and oriented such that the polar (z-) axis lies along the rotation axes of the star and disk.

The matter in the neutron star and the disk has a high electrical conductivity. Therefore, as this matter moves in directions perpendicular to the magnetic field, it creates a $\mathbf{v} \times \mathbf{B}$ polarization electric field. The potential difference V across the system created by the cross-field motion of disk plasma could be as large as

$$V = 300 \frac{1}{c} \int \mathbf{v} \times \mathbf{B} \cdot d\boldsymbol{\ell} \approx E_r \, \Delta r \sim 10^{13} \text{ volts}. \tag{4.9}$$

The presence of such large potential differences may play a role in creating the TeV γ-rays reported from some accretion-powered pulsars (see Katz and Smith 1988 and references therein).

If there is sufficient plasma between the star and the disk, the electrical potential difference can drive appreciable magnetospheric electrical currents around the system. The resulting $\mathbf{j} \times \mathbf{B}$ forces act on the matter in the star, the magnetosphere, and the disk to reduce their relative motion. The character of this electrodynamic interaction depends on the distribution of electrical resistance along the current paths. Ghosh and Lamb (1979a) examined this question and concluded that the conductivity along field lines in the magnetosphere is likely to be high but that cross-field currents are more likely to flow in the disk and the star. They therefore arrived at a system of field-aligned currents that is not unlike the polar-cap ionospheric current system that is thought to couple the rotation of Jupiter's ionosphere to its magnetospheric sheath (see Kennel and Coroniti 1975, 1977).

An example of this type of current system is shown in Figure 7. The azimuthal motion of the disk plasma relative to the star generates electric fields that drive field-aligned currents within the magnetosphere and cross-field currents within the star and the disk. The poloidal components of the magnetospheric currents create a toroidal magnetic field, which acts to synchronize the orbital motion of the disk plasma and the rotation of the star. In an analogous manner, the radial inward motion of the plasma across the poloidal component of the magnetic field within the disk generates a toroidal electric field that drives toroidal currents, partially screening the disk from the stellar magnetic field and pinching the magnetic field lines inward in the disk plane. The toroidal components of the field-aligned currents within the magnetosphere also contribute to the total poloidal magnetic field.

Despite its high electrical conductivity, the plasma between the disk and the star cannot support arbitrarily large electrical currents. Since the plasma in this region is essentially electrically neutral, the currents driven by electric fields are conduction currents. Such currents drive instabilities that dissipate them if the magnitude of the relative velocity between the oppositely charged species exceeds the local sound speed (see Spicer 1982). How significant is this limitation on the strength of the electrodynamic coupling beween the disk and the star, for accretion-powered pulsars and QPO sources?

This question was examined by Ghosh and Lamb (1979a) and has recently been reconsidered by Zylstra (1988), based on new observational evidence concerning the plasma density surrounding neutron star X-ray sources. Zylstra estimated the magnetic field gradient $(\Delta B/\Delta r)_{max}$ that could be supported by the maximum stable current density. The undistorted stellar magnetic field near the inner edge of the disk is expected to be approximately dipolar in both pulsars and QPO sources, corresponding to stellar dipole magnetic moments $\sim 10^{30}$ G cm^3 and

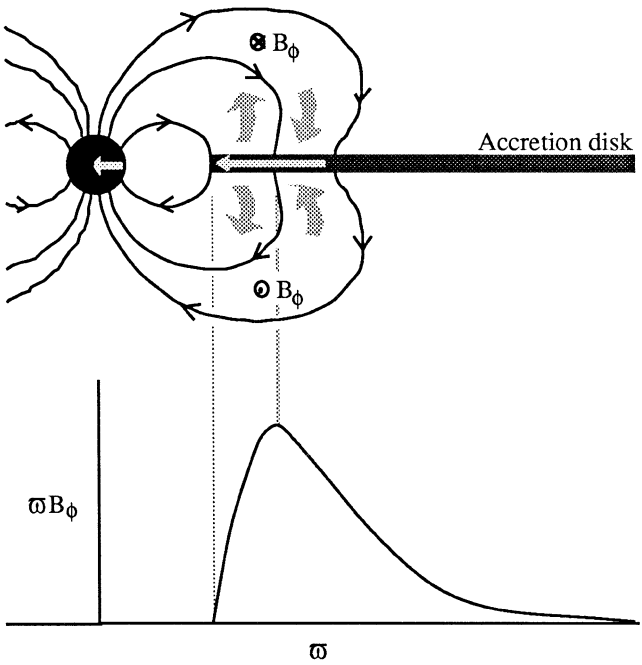

Fig. 7.—Side view of an aligned rotator (top) interacting with disk plasma that has an angular velocity greater than the star. The azimuthal motion of the plasma in the disk plane into the page generates a radial electric field within the disk that drives field-aligned currents within the magnetosphere and cross-field currents within the disk and the neutron star. The poloidal components of the magnetospheric currents create a toroidal magnetic field that points into the page above the disk and out of the page below. The resulting torque density ϖB_ϕ on the star (bottom) acts to try to spin up the star. The density of the poloidal field-aligned current within the magnetosphere vanishes on the poloidal flux surface where the torque density is a maximum. The toroidal components of the currents within the disk and the field-aligned currents within the magnetosphere create a poloidal magnetic field that points radially inward above the disk and radially outward below it, pinching the total poloidal field inward in the disk plane.

$\sim 10^{27}$ G cm^3, respectively. Spectral and temporal evidence indicates that the magnetospheres of the neutron stars in the QPO sources are surrounded by a dense central corona with an electron number density of at least $10^{16} - 10^{18}$ cm^{-3} within $\sim 10^7 - 10^8$ cm from the neutron star. The evidence concerning the plasma density near the inner edge of Keplerian disks in accretion-powered pulsars is not as clear. However, observations of Her X-1 indicate the presence of a central corona with an electron number density $\gtrsim 10^{12}$ cm^{-3} within $\sim 10^9$–10^{10} cm of the neutron star. Plasma with a comparable density is probably present between the disk and the star in other accretion-powered pulsars. Coronal temperatures are expected to be ~ 10 keV.

Based on this evidence, Zylstra (1988) estimated that electrical currents flowing between the disk and the star could support magnetic field gradients at radius r as large as

$$(\Delta B/\Delta r)_{max} \sim 10^4\text{–}10^8\, n_{12} r_8^4 (B_0/r)\,, \tag{4.10}$$

where B_0 is the magnitude of the undistorted dipole field at r. The smaller estimate is for QPO sources while the larger estimate is for pulsars. These estimates indicate that in both types of source, electrical currents flowing in the space between the disk and the star could support very large magnetic field gradients. Of course, magnetic field gradients are also limited by other effects, such as magnetohydrodynamic instabilities, so that gradients as large as those that could be supported by the plasma between the disk and the star are unlikely to arise.

The electrodynamic coupling between the star and the disk has been studied in more detail by Zylstra, Lamb, and Aly (1988), who used a special iterative scheme to calculate numerically the two-dimensional structure of a magnetosphere interacting with an accretion disk. The magnetospheric magnetic field was assumed to be in force-free equilibrium. Several distributions of the poloidal magnetic flux on the disk were explored. Given the symmetry of the problem, the poloidal flux distribution can be written in terms of a poloidal flux function ψ, which is constant on a given magnetic fieldline. Distributions of ψ at the disk plane were chosen to model strong and weak screening by toroidal electrical currents in the disk. One of the poloidal flux distributions Zylstra *et al.* explored is shown in Figure 8a. The effect of the azimuthal electrical currents can be judged by comparing the screened field with the unscreened field.

Various models of the interaction of the azimuthal motion of the disk plasma with the magnetic field were explored by specifying different distributions of the *torque density* $n \equiv \varpi B_\phi$ on the disk plane. In axisymmetric systems, the torque density is a function only of the poloidal magnetic flux function ψ. In their calculations, Zylstra *et al.* specified only the *shape* of the torque density function (TDF). The magnitude of the TDF was determined as part of the calculation. Given the distribution of ψ on the disk, knowledge of the TDF specifies the distribution of B_ϕ on the disk.

The sign of $n(\psi)$ is expected to reflect the sign of the difference between the orbital angular velocity of the disk flow and the rotational angular velocity of the star. The magnitude of $n(\psi)$ depends on the effective electrical conductivity of the disk, magnetosphere, and star, and the largest twists that the magnetic field can support in equilibrium. Figure 8b shows two of the TDFs Zylstra, Lamb, and Aly considered, corresponding to the interaction between the Keplerian disk flow and the star that is expected for slow rotators (curve SR) and fast rotators (curve FR). For the FR curve, the corotation radius (at which n vanishes) is only slightly larger than the radius of the inner edge of the disk.

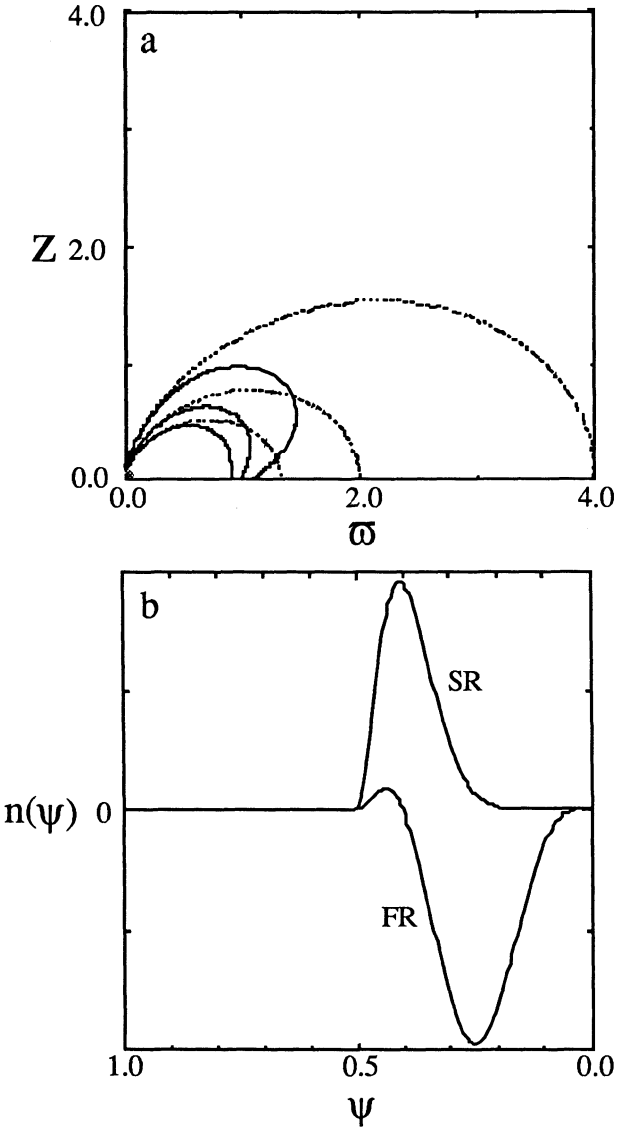

Fig. 8.—(a) Side view of the star, accretion disk, and magnetosphere, showing constant-flux surfaces of the undistorted dipolar magnetic field of the star (dashed curves) and the magnetospheric field produced by the currents in the star and the accretion disk (solid curves). The small, shaded quadrant in the lower left shows the size of the star. (b) Torque density functions $n(\psi)$ corresponding to a slow rotator (SR) and a fast rotator (FR). Note that the flux function ψ increases to the left. The equator of the star is at $\psi = 1.0$ while the inner edge of the disk is at $\psi = 0.5$. The fast rotator curve models a star with a spin rate such that the corotation point in the disk is at $\psi \approx 0.6$.

Zylstra *et al.* find that as the magnetospheric field is twisted, the surfaces of constant poloidal flux expand outward away from the disk and star. As a result of this expansion of the field above and below the disk, the poloidal component of the magnetic field develops an inward pinch in the disk plane as the twist increases, even if the poloidal flux distribution on the disk is unscreened (i.e., the same as for an undistorted dipolar magnetic field). The expansion of the magnetic field is not uniform throughout the inner magnetosphere. Rather, the expansion is large for some field lines but relatively modest for others. This is illustrated in Figure 9, which shows the structure of the untwisted field and the maximally expanded field for a solution sequence based on the FR torque density function shown in Figure 8b. In this sequence, the stellar radius R is 0.875 times the radius ϖ_0 of the inner edge of the disk. As a result of the expansion of the magnetosphere, the magnitude of B_ϕ on and near the surfaces of the disk first increases and then decreases, while the magnitude of B_ϕ in regions far from the disk increases monotonically.

Zylstra, Lamb, and Aly also find that the structure of the magnetospheric field is relatively insensitive to the ratio of the stellar radius to the inner radius of the disk. Thus, for example, the maximum magnetic pitch $|B_\phi/B_\theta|_{max}$ at the surface of the disk depends only weakly on the ratio R/ϖ_0. It is 0.12 for $R/\varpi_0 = 0.875$ and 0.13 for $R/\varpi_0 = 0.100$. The appropriately scaled torque on the star also depends only weakly on the ratio R/ϖ_0. The reason is that the magnetic field is twisted primarily near the inner edge of the disk rather than near the star.

4.3 Steady Flow Models

Based on concepts similar to those just described, Ghosh and Lamb (1978, 1979a,b; hereafter GL) developed a quantitative model of disk accretion by an aligned rotator by solving the two-dimensional, non-ideal hydromagnetic equations assuming that the effective conductivity of the disk flow is relatively low as a result of the magnetic field diffusion processes discussed in section §3.4.

GL showed that the solutions exhibit boundary layer behavior at the radius determined implicitly by the angular momentum conservation condition (3.8) and that if the stellar magnetic field threads the disk, a steady flow is possible only if the effective electrical conductivity $\sigma_{\rm eff}$ for radial currents in the disk has the value

$$\sigma_{\rm crit} = \frac{c^2}{4\pi}\left|\frac{\gamma_\phi}{rh(\Omega - \Omega_s)}\right| . \tag{4.11}$$

GL argued that magnetic flux reconnection in the disk flow is inherently a self-adjusting process that might give an effective conductivity equal to $\sigma_{\rm crit}$. They

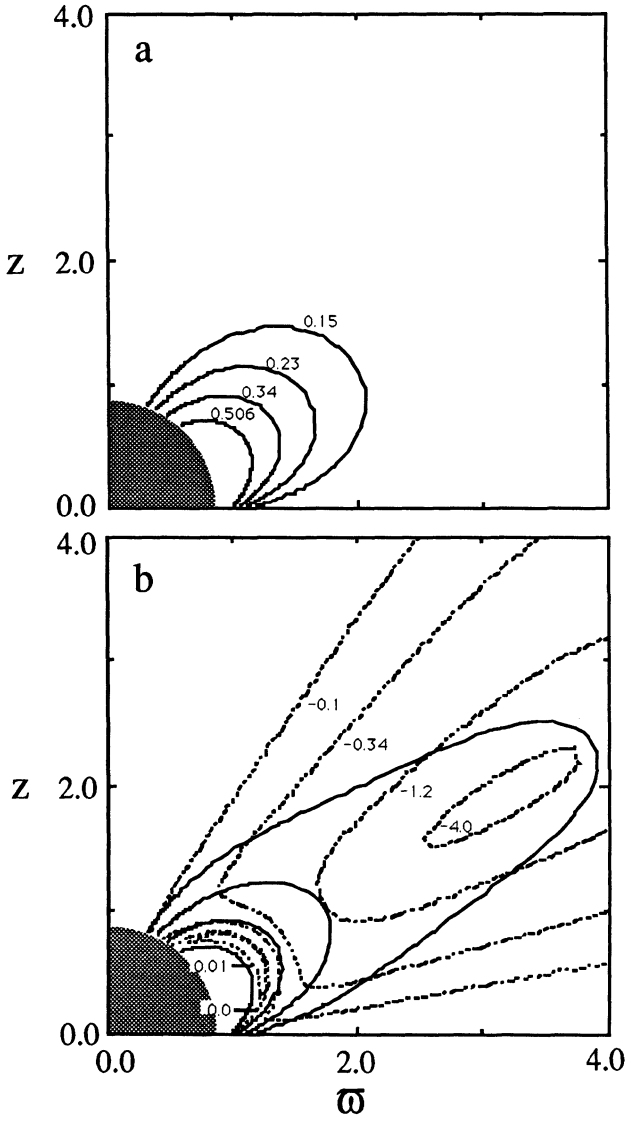

Fig. 9.—Side view of the star, accretion disk, and magnetosphere, showing the structure of the magnetosphere when the currents in the disk strongly screen a relatively weak stellar magnetic field. The radius of the star is 0.85 times the radius of the inner edge of the disk (the star is indicated by the shaded quadrant in the lower left). (a) Selected surfaces of constant poloidal magnetic flux when the field is not sheared. The poloidal flux surfaces are labelled with the value of the poloidal magnetic flux function ψ. (b) The same surfaces (solid curves) and surfaces of constant magnetic pitch (dashed curves) when the field is maximally expanded.

therefore adopted $\sigma_{\rm eff} = \sigma_{\rm crit}$ as a working hypothesis, assuming for simplicity that the conductivity tensor is isotropic.

GL also assumed that azimuthal currents in the disk plane and the magnetosphere screen the poloidal component of the stellar magnetic field on the radial length scale

$$\Delta\varpi \approx \frac{c^2}{4\pi\sigma_{\rm eff} v_{\varpi 0}}, \tag{4.12}$$

where $v_{\varpi 0}$ is the radial velocity of plasma in the boundary layer. From the radial component of the momentum equation, GL found

$$v_{\varpi 0} \approx (\Delta\varpi/\varpi)^{1/2} v_{\rm ff}(\varpi_0). \tag{4.13}$$

Equations (4.11) to (4.13), together with the angular momentum conservation condition (3.8), are sufficient to estimate ϖ_0, giving a result very close to the result (3.22). GL adopted the simple result (3.22) on the grounds that the uncertainties in the model are larger than the very small deviation from (3.22) given by the model. The boundary layer in the GL model is relatively narrow, with $\Delta\varpi \approx 0.03\,\varpi_0$, and hence $\gamma^{2/7} \approx 0.5$. The character of this steady flow solution may be summarized as follows.

The region where the stellar magnetic field threads the disk constitutes a *transition region* between undisturbed disk flow far from the star and the flow inside the magnetosphere. The interaction between the *azimuthal* motion of the flow in the transition region and the stellar magnetic field generates radial currents that tend to twist the field, as described in §4.2, creating an azimuthal field component. The interaction between the *radial* motion of the matter in the transition region and the magnetic field generates azimuthal currents which tend to confine the poloidal field, creating a radial field component.

The transition region divides naturally into two zones: a broad outer zone, where the motion is Keplerian, and a narrrow inner zone, where the angular velocity falls sharply from the local Keplerian value to the stellar angular velocity at the radius $\varpi_{\rm co}$. GL defined the radius ϖ_0 of the boundary between these two zones as the radius where $\partial\Omega/\partial\varpi = 0$. Thus, at $\varpi = \varpi_0$, the shear stress vanishes.

In the *inner transition zone*, between $\varpi_{\rm co}$ and ϖ_0, the interaction of the azimuthal flow with the magnetic field significantly reduces the azimuthal velocity. This zone is like a boundary layer, in that the velocity and magnetic fields change there on the length scale $\Delta\varpi \ll \varpi_0$. The angular velocity of the inflowing plasma is reduced from the Keplerian value just outside ϖ_0 to the corotational value at $\varpi_{\rm co}$ by the magnetic stress, while azimuthal currents screen the poloidal field, typically by a factor $\sim$5. As a result, centrifugal support is lost and the plasma begins to fall rapidly toward the neutron star.

In the *outer transition zone*, outside ϖ_0, the flow is very similar to that of an undisturbed disk, except that angular momentum is removed from the disk

plasma not only by the "viscous" shear stress but also by the twisted lines of the stellar magnetic field, while the total energy dissipation rate is augmented by resistive dissipation of the electrical currents flowing in the disk. GL found that the couple between the outer transition zone and the star is a substantial fraction of the total couple. Since the couple falls off gradually, the outer boundary of the outer transition zone is purely conventional.

The field lines that thread the boundary layer form an *accretion bundle*, defined as the field lines along which matter accretes to the surface of the star. The motion of the plasma in the accretion bundle at the disk plane and just above and below it has a significant cross-field component. Therefore the field lines in this region are only approximate streamlines of the flow. As matter falls closer to the star, the cross-field motion is diminished by the increasing stress exerted by the magnetic field, while the field-aligned motion is accelerated by the component of the gravitational force that is along the field line. As a result, the motion of the accreting plasma can approach free fall. GL showed that in their model, the magnetospheric flow is sub-Alfvénic in the magnetospheric field even if it is free fall, and hence is MHD stable.

5. PERIODIC INTENSITY OSCILLATIONS

If the magnetic field of the neutron star is strong enough to force the accreting plasma to flow toward the magnetic poles, the radiation produced near the star will be anisotropic. If in addition the magnetic axis is not aligned with the spin axis, a distant observer will see periodic oscillations in the X-ray intensity with a frequency equal to the rotation frequency of the star. Thus, the X-ray oscillation frequency reveals the neutron star spin rate. Changes in the spin rate produced by accretion torques can therefore be studied by pulse timing measurements. Such measurements are important because they can be made very accurately and offer the possibility of direct, quantitative comparisons with theoretical predictions. These comparisons provide insights about the physics of the accretion flow near the magnetosphere and the internal properties of neutron stars. Thus, for example, observations of long-term changes in the stellar rotation rate provide information about the time-averaged circulation of the accreting plasma, the strength of the dipole component of the stellar magnetic field, and the size of the star's moment of inertia, while measurements of short-term fluctuations probe the stability of the accretion flow and the internal dynamical properties of the neutron star (Lamb, Pines, and Shaham 1978).

In the present section I describe how the accretion torque N_s acting on a magnetic neutron star accreting matter from a disk can be calculated and summarize the results of the calculation for the two-dimensional, steady flow solutions discussed in §4.3. Finally, I briefly compare the theoretical predictions with current observations.

5.1 Accretion Torques

Early work.—The accretion torque produced by capture from a wind was first considered by Davidson and Ostriker (1973). They considered only material stress, tacitly assuming that all other stresses can be neglected and that the capture cross section remains unchanged. Davidson and Ostriker argued that the variation in wind density across the capture cross section causes the accreted matter to have a mean specific angular momentum of order ℓ_{w0}. However, as discussed in §2.2, the presence of a density gradient deforms the capture cross section in such a way that the mean specific angular momentum of the captured matter actually has the opposite sign, if only the material stress is included. Moreover, other stresses may make important contributions to the accretion torque. Since at present the sign as well as the magnitude of the specific angular momentum of matter captured even from an isotropic stellar wind is uncertain, little can be said about the accretion torque produced by such a flow.

The accretion torque produced by a Keplerian disk flow was considered by Pringle and Rees (1972). They estimated the torque by considering only the contribution of the material stress at the inner edge of the disk, tacitly assuming that all other stresses are negligible. Pringle and Rees found a torque of order

$$N_0 \equiv \dot{M}(GMr_0)^{1/2}\,, \tag{5.1}$$

where r_0 is the radius of the inner edge of the disk. They estimated r_0 by balancing the static pressure of an undistorted dipole magnetic field against the thermal pressure of the gas at the midplane of an unperturbed steady disk flow, a procedure that we have argued in §3.4 is not meaningful for disk flows interacting with a stellar magnetic field.

Lamb, Pethick, and Pines (1973) wrote down the general equation for the angular momentum flux onto the star and noted that not only material, but also magnetic and viscous stresses could make important contributions to the torque on the star. They pointed out that for slow rotators accreting from a disk, the angular velocity of the flow necessarily passes through a maximum at a radius near the inner edge of the disk, and noted that at this radius the shear stress vanishes. By placing the surface S of the integral (2.8) at the radius r_0 of the angular velocity inflection point and noting that the magnetic couple to the region of the disk beyond this point can only increase the torque by an amount of order unity, they showed that the torque on a slow rotator accreting from a disk is approximately equal to N_0. In evaluating N_0, Lamb, Pethick, and Pines based their estimate of r_0 on MHD stability arguments like those outlined in §3.3, but used a flow velocity larger than that later found by GL. Compared with the angular momentum conservation condition, which we have argued in §3.4 is a more accurate way of estimating r_0, their argument somewhat underestimates r_0 and hence also the torque.

Ghosh, Lamb, and Pethick (1977) sought to make the torque argument of Lamb, Pethick, and Pines more precise for steady, axisymmetric flows. These authors showed that if the width Δr of the region where the magnetic field couples to the disk is small compared to r, then the accretion torque is closely equal to N_0, for all ω_s for which there is a steady accretion flow. Thus, for disks rotating in the same sense as the star, a narrow transition region would imply a spin-up torque approximately equal to N_0, even on fast rotators. This result strongly suggested that the transition region for disk flows is in fact broad, since otherwise the torque on Her X-1, which is 30–40 times smaller than N_0, would be extremely difficult to understand.

GL showed that in their model of disk accretion, the couple between the disk and the star via the stellar field lines that interact with the Keplerian flow in the outer transition zone is comparable to that of the material falling onto the star from the inner transition zone. The interaction in the outer transition zone increases the spin-up torque on slow rotators, but reduces the spin-up torque on moderately fast rotators. For very fast rotators, the torque produced by the interaction with the outer transition zone can exceed that of the matter falling onto the star, causing the net torque to become negative, braking the star's rotation. This result does not contradict the lower bound on the torque found earlier by Ghosh, Lamb, and Pethick, because the transition region in the GL model is broad rather than narrow.

General framework.—The accretion torque produced by flow of matter onto a neutron star is given by the integral (2.8) of the angular momentum flux density over any surface S that encloses the star, if we neglect the very short time required for the stress to be communicated from the surface S to the star. For a time-independent, axisymmetric flow, this integral may be written in the form (Lamb 1977)

$$N = \int_S \left(-\rho \varpi^2 \Omega \mathbf{v}_p + \varpi \frac{B_\phi \mathbf{B}_p}{4\pi} + \eta \varpi^2 \nabla \Omega \right) \cdot \hat{\mathbf{n}} \, dS \,, \tag{5.2}$$

where again ϖ is the cylindrical radius. Equation (5.2) displays explicitly the various stresses that contribute to the torque. Here Ω and v_p are the angular and poloidal velocities of the flow, B_ϕ and B_p are the poloidal and azimuthal components of the magnetic field, η is the effective dynamic viscosity, and $\hat{\mathbf{n}}$ is a unit vector normal to S and oriented outward. The three terms on the right side of equation (5.2) represent, in turn, the contributions of the material, magnetic, and viscous stresses to the accretion torque. The relative sizes of these three contributions depend on the location and shape of the surface used to evaluate the integral. However, for any surface S close to the surface of the neutron star, the angular momentum flux is carried almost entirely by the magnetic stress.

In evaluating expression (5.2), it is convenient to choose for S a surface composed of three parts: (1) an approximately cylindrical surface S_1, which coincides

with the poloidal magnetic flux surface that leaves the disk at the radius ϖ_0 where the angular velocity goes through its maximum, and which extends slightly above and below the disk flow, (2) a surface S_2 consisting of two circular, approximately horizontal surfaces having a circular hole of radius ϖ_0 at the center, which connect to the top and bottom of S_1 at ϖ_0 and extend outward just above and below the flow to large ϖ, and (3) a surface S_3 composed of two separate, hemispherical surfaces that meet the sheets of S_2 at large ϖ and close the surface S above and below the star.

The total torque on the star is the sum

$$N_s = N_1 + N_2 + N_3 \tag{5.3}$$

of the torque contributions from each of the three surfaces S_1, S_2, and S_3. The contribution N_1 is the torque that is eventually communicated to the star by the magnetic field lines that interact with the flow in the inner transition zone, while the contribution N_2 is the torque that is communicated to the star by the magnetic field lines that interact with the flow in the outer transition zone. The contribution N_3 is negligible, since the magnetic stress falls off much more rapidly than r^3.

The torque contribution N_1 is given by the material stress on S_1, since both the viscous and the magnetic stresses on S_1 are negligible, owing to the way in which this surface was chosen. The angular velocity Ω_0 of the plasma at ϖ_0 must lie between the angular velocity $\Omega_K(\varpi_0)$ and the stellar angular velocity Ω_s. Thus, for a fast rotator, $\Omega_0 \approx \Omega_K(\varpi_0)$. Even for a slow rotator, Ω_0 will be a substantial fraction ($\sim$0.5) of $\Omega_K(\varpi_0)$. Thus,

$$N_1 \approx -\int_S \rho v_r \cdot \varpi_0^2\, \Omega_K(\varpi_0) \cdot 2\pi\varpi_0 \cdot 2h \approx N_0\,. \tag{5.4}$$

The torque contribution N_2 is given by the magnetic stress on S_2, since the material stress on S_2 is zero (no matter crosses it) while the viscous stress is expected to be quite small. Thus

$$N_2 \approx \int_{S_2} (\varpi B_z B_\phi/4\pi)\, dS\,. \tag{5.5}$$

Specific example.—Using their flow model to evaluate equation (5.5), GL found that N_s could be written

$$N_s \approx n(\omega_s)\, N_0\,, \tag{5.6}$$

where n is a dimensionless function that depends primarily on the fastness parameter ω_s, as indicated by the explicit dependence on ω_s displayed in equation (5.6).

For stars rotating slowly in the same sense as the disk flow ($\omega_s \ll 1$), GL found $n(\omega_s) \approx 1.4$. They also found that the dimensionless torque function n decreases with increasing ω_s, vanishing at a certain critical fastness ω_c and becoming negative for $\omega_s > \omega_c$. Finally, for ω_s greater than a certain maximum fastness $\omega_{\max}$ (typically ≈ 0.95) GL could find no stationary solutions to the two-dimensional flow equations, and hence could not calculate the torque on the star using the approach described here. A simple expression for $n(\omega_s)$ that agrees approximately with their numerical results over the whole range of ω_s from 0 to $\omega_{\max}$ is

$$n(\omega_s) \approx 1.4 \left(\frac{1 - \omega_s/\omega_c}{1 - \omega_s} \right) . \tag{5.7}$$

GL found $\omega_c \sim 0.35$ from their model, but stressed that the actual value was relatively uncertain. Subsequent work (see below) suggests that a larger value, perhaps ~0.8–0.9, is probably more realistic.

The behavior of n as a function of ω_s can be understood as follows. The accretion torque is the sum of the torque N_1 produced by accretion of the angular momentum of the matter that falls onto the star and the torque N_2 contributed by the twisted field lines from the star that interact with the disk in the outer transition zone. N_1 always acts to spin up a star rotating in the same sense as the disk flow, whereas N_2 can have either sign, since the azimuthal pitch of the stellar field lines that interact with the Keplerian flow in the outer transition zone must change sign at the corotation radius ϖ_c, where the angular velocity of the disk plasma is the same as that of the star. The contribution to the torque from the field lines threading the disk between ϖ_0 and ϖ_c is positive whereas the contribution from the field lines threading the disk outside ϖ_c is negative. For slow rotators, $\varpi_0 \ll \varpi_c$, the positive contribution to N_2 dominates the negative, and hence N_2 adds a further spin-up torque, approximately equal to $0.4\,N_0$, to the spin-up torque N_0 contributed by the term N_1. For moderately fast rotators, $\varpi_0 \approx \varpi_c$, the negative contribution to N_2 dominates, and N_2 contributes a spin-down torque that partly cancels N_1. For very fast rotators, the spin-down torque contributed by N_2 dominates the spin-up torque contributed by N_1 and there is a net spin-down torque on the star.

The maximum strength of the net spin-down torque depends sensitively on the azimuthal magnetic pitch B_ϕ/B_p in the outer transition zone. In calculating the azimuthal pitch caused by interaction of the magnetosphere with the Keplerian disk flow in the outer transition zone, GL estimated the rate at which B_ϕ is generated by shearing the polodial field as $\gamma_a|\Omega_K - \Omega_s|$, where γ_a is a numerical factor of order unity. However, as pointed out by Lamb (1978, 1984), this expression implies that the azimuthal magnetic field is created by shearing the azimuthal component of the magnetic field, even though GL explicitly state that the azimuthal field is generated by shearing the poloidal component. As a result

of this inconsistency, GL found

$$|B_\phi| = \left(\frac{\gamma_a}{\xi}\right) 2h(4\pi\rho)^{1/2}|\Omega_K - \Omega_s|\,, \tag{5.8}$$

where ξ is a numerical factor of order 0.1–1 that characterizes the magnetic field reconnection rate, which was assumed to be $\xi v_A/2h$. When this inconsistency is corrected, the azimuthal magnetic field is instead (Zylstra 1988)

$$|B_\phi| = \left(\frac{\gamma_a}{\xi}\right) \left[2h(4\pi\rho)^{1/2}\right]^{1/2} |\Omega_{\rm K} - \Omega_s|^{1/2}|B_z|^{1/2}\,. \tag{5.9}$$

Use of this correct expression leads to much smaller pitches in the outer transition zone (Lamb 1978, 1984; Wang 1987). Although the spin-down torque on fast rotators is therefore less than estimated by GL (corresponding to an increase in ω_c), the magnitude of the spin-down torque on fast rotators can still be several times larger than the magnitude of the spin-up torque on slow rotators (Wang 1987).

Unfortunately, the incorrect expression (5.8) for B_ϕ introduced another inconsistency. GL assumed correctly that the azimuthal current created in the disk by the inward motion of the disk plasma across field lines screens the polodial magnetic field. However, GL used equation (5.8) to evaluate γ_ϕ in equation (4.11) for the effective electrical conductivity, which was then used to calculate the azimuthal screening current, $j_\phi = -\sigma_{\rm eff} v_r B_z/c$, from which the net poloidal magnetic field was calculated. The resulting azimuthal "screening" current actually amplifies the stellar magnetic field, rather than canceling it, causing an increase in $|B_p|$ with increasing radius (Zylstra 1985, 1988; Campbell 1987). This error in the sign of the azimuthal current was not noticed by GL because of a compensating sign error in their expression for the poloidal magnetic field generated by the azimuthal current. When the correct expression (5.9) is used for B_ϕ, the azimuthal currents in the disk indeed screen the stellar magnetic field, as required by the nature of the flow. Although important in principle, this correction does not change the general conclusions of GL concerning the qualitative character of the accretion torque, because of the compensating nature of their two errors.

Arons and several collaborators (see Arons *et al.* 1984; Arons 1987) have suggested that interaction of the stellar magnetic field with the disk flow will cause plasma to be mixed with the field via the Kelvin-Helmholtz instability, loading the field lines that pass near the surface of the disk with plasma. Then, if the magnetic stress on this plasma is great enough to accelerate it to a slightly super-Keplerian velocity, the plasma will flow outward along the top and bottom surfaces of the disk from some radius $\varpi_{\rm wind}$ ($> \varpi_0$), opening up the loaded field lines and carrying away angular momentum from the system. This has been proposed as a mechanism for creating a spin-down torque on the neutron star.

Several points are worth noting about this suggestion. First, it is not clear that an ordered poloidal field will persist in the disk once the stellar field has been opened up, since the field lines carrying the outflowing plasma are then no longer connected to the neutron star. Of course, a disordered magnetic field that extends above the disk might still generate outflow. Second, the angular momentum carried outward by the flow is, in the first instance, removed from the disk, not the star. As mentioned several times previously, loss of angular momentum from the disk, even a relatively large loss, will not cause the plasma in the disk to depart significantly from Keplerian motion, unless the loss is so great that it removes all the angular momentum of the plasma in a radial distance small compared to r. In the picture in question, the magnetic stress that creates the outflow is being generated by the orbital motion at a slightly smaller radius, so it seems unlikely that all the angular momentum of the flow can be removed in a short distance by this mechanism. As long as the plasma at ϖ_0 has a near-Keplerian azimuthal velocity, the term N_1 in the sum (5.3) will contribute a strong spin-up torque, comparable to N_0.

Could this strong spin-up torque nevertheless be overwhelmed by a strong spin-down torque N_2, transmitted from the region of outflowing plasma to adjacent field lines that thread the surface S_2 and connect to the star? This seems unlikely. The spin-up torque N_1 is the maximum torque that can be transmitted to the star by a substantial fraction ($\sim$0.3–0.8) of the star's poloidal magnetic flux. However, only the much smaller fraction of the star's poloidal magnetic flux that threads the disk between ϖ_0 and $\varpi_{\rm wind}$ can contribute to N_2. (If this fraction is not much less than unity, the outflow from the disk plays no significant role and the model reduces to the GL model.) Suppose that the term N_2 does contribute a spin-down torque. In order for it to be larger in magnitude than the spin-up torque contributed by the term N_1, the small fraction of the star's poloidal magnetic flux that contributes to N_2 would have to transmit a torque greater than the maximum torque that can be transmitted by the much larger fraction of the star's poloidal magnetic flux that contributes to N_1.

5.2 Response of the Star

Changes in the spin rate and rotational energy of the neutron star can be related to ℓ, the angular momentum added to the star per unit mass of accreted matter (Ghosh, Lamb, and Pethick 1977). For simplicity, in this section I assume that the star responds as a rigid body (but see Lamb, Pines, and Shaham 1978).

The rate of change of the angular momentum of the star is

$$\dot{J}_s \equiv \frac{d}{dt}(I\Omega_s) = \dot{M}\ell, \tag{5.10}$$

where I is the moment of inertia of the star and Ω_s is its angular velocity. It follows that the rate of change of Ω_s is

$$\dot{\Omega}_s = (\zeta - 1)(d\ln I/d\ln M)(\dot{M}/M)\Omega_s\,, \tag{5.11}$$

where $J_s = I\Omega_s$, R_g is the radius of gyration of the star, and

$$\zeta \equiv \frac{\ell}{R_g^2\Omega_s}\left(\frac{d\ln M}{d\ln I}\right) = \frac{\ell}{\Omega_s}\frac{dM}{dI} \tag{5.12}$$

is a dimensionless parameter that compares the angular momentum added to the star by accretion of the mass dM with the specific angular momentum required to maintain the star at the same angular velocity, after the moment of inertia I has been changed by adding the mass dM to the star. In contrast, the rate of change of the rotational energy $E_{\rm rot}$ of the star is

$$\dot{E}_{\rm rot} \equiv \frac{1}{2}\frac{d}{dt}\left(I\Omega_s^2\right) = 2(\zeta - \tfrac{1}{2})(d\ln I/d\ln M)(\dot{M}/M)E_{\rm rot}\,. \tag{5.13}$$

For $\zeta < 1$, the star loses rotational energy and spins down, whereas for $\zeta > 1$, it gains rotational energy and spins up. For $\frac{1}{2} < \zeta < 1$, *the star gains rotational energy but spins down.*

For neutron stars with masses in the range 0.2–1.6 $M_\odot$, the structure factor $d\ln I/d\ln M$ is positive and $\sim$1. For such intermediate-mass stars, $\zeta \approx \ell/R_g^2\Omega_s \gg 1$, unless ℓ is less than or comparable to the small quantity $R_g^2\Omega_s$. In the following, I assume $\zeta \gg 1$. The first term on the right side of equations (5.11) and (5.13) is then the dominant one.

5.3 Changes in Pulse Frequency

Note first that a slowly rotating ($\omega_s \ll 1$) star rotating in the same sense as the circulation of the accretion flow and with a magnetosphere of appreciable size will be rapidly spun-up by accretion, *even if the angular velocity Ω of the flow outside the magnetosphere is less than the angular velocity Ω_s of the star.* To see this, note that the contribution of material stresses to ℓ gives

$$\zeta \approx r_m^2\Omega/R_g^2\Omega_s\,. \tag{5.14}$$

Thus for $r_m \gg R$, one can have $\zeta \gg 1$ even if $\Omega \ll \Omega_s$. The reason is that the much larger moment arm of the matter at r_m gives it a much greater specific angular momentum than that of the matter in the star, even though its angular velocity is much less. Thus, when it is added to the star, the star spins up.

For approximately radial flows, the rate of change of the pulse period can be written in the form (Ghosh and Lamb 1979b)

$$-\dot{P} = f_1(MR/I)\,\ell(L,\ldots)\,P^2 L\,, \tag{5.15}$$

where the function f_1 depends on MR/I and the mean specific angular momentum ℓ of the flow generally depends on L and other properties of the source, as indicated by the notation $f_1(MR/I)$ and $\ell(L,\ldots)$. Given the equation of state, R and I are functions only of M, so that f_1 actually depends only on the mass of the neutron star. Note that equation (5.15) does not depend on the stellar magnetic moment μ or spin period P, because the magntosphere plays no role in determining ℓ. Given the present uncertainty about ℓ_w, the mean angular momentum of matter captured from a stellar wind, little more can be said about the changes in pulse frequency to be expected for radial flows.

For disk flows, Lamb, Pethick, and Pines (1973) used their expression for the accretion torque to write an equation of the form

$$-\dot{P}/P = f_2(\mu, M)\,PL^{6/7} \tag{5.16}$$

for the rate of change of the pulse period of a slow rotator rotating in the same sense as the disk flow. Note that given the two intrinsic properties μ and M of the star, equation (5.16) gives a single curve in the $(\dot{P}/P,\ PL^{6/7})$-plane. If M and μ are allowed to vary, equation (5.16) generates a two-parameter family of curves.

In the more complete theory of GL, which allows one to calculate the accretion torque for finite values of the fastness ω_s, the equation that corresponds to equation (5.16) can be written in the form

$$-\dot{P}/P = n(\omega_s)\,f_2(\mu, M)\,PL^{6/7}\,, \tag{5.17}$$

which depends on the fastness parameter ω_s as well as μ and M. The reason is that ω_s measures the dynamical effect of stellar rotation on the flow near the inner edge of the disk. For example, the ratio of the centrifugal force to the gravitational force for matter corotating with the star near the inner edge of the disk is just ω_s. Similarly, the ratio of the radius ϖ_0 of the inner edge of the disk to the radius ϖ_c of the corotation point in the disk, which is a measure of the relative size of the magnetic braking torque, is just $\omega_s^{2/3}$. Thus, one expects the spin-up rate to vary with ω_s on quite general grounds, although the particular functional form of the variation necessarily depends on details of the model. Equation (5.16) is independent of ω_s because it is the slow rotation limit ($\omega_s \to 0$) of equation (5.17).

An important general point made by Ghosh and Lamb (1979b) is that in comparing theories of the rate of change of the pulse period produced by disk flows with observations, one should plot $\log(-\dot{P})$ vs. $\log PL^{3/7}$, rather than $\log(-\dot{P}/P)$

vs. $\log PL^{6/7}$. The reason is that otherwise the dependence of the right side of equation (5.17) on ω_s introduces uneccessary scatter in the plot. One can see this by noting that since

$$\omega_s = f_3(\mu, M)/PL^{3/7} \tag{5.18}$$

the right side of equation (5.17) is not simply a function of μ, M, and $PL^{6/7}$, but also depends on $PL^{3/7}$. Therefore, plotting $\log(-\dot{P}/P)$ vs. $\log PL^{6/7}$ will cause neutron stars that are identical except for their spin periods and/or luminosities to scatter over the plane, rather than falling on a single curve. Stated differently, fast rotators occur everywhere in the $(\dot{P}/P,\ PL^{6/7})$-plane.

One can recover a two-parameter family of curves by multiplying both sides of equation (5.17) by P, with the result

$$-\dot{P} = n(\omega_s)\, f_2(\mu, M)\, (PL^{3/7})^2 = f_2(\mu, M)\, f_4(PL^{3/7})\,, \tag{5.19}$$

which depends on P and L only through the combination $PL^{3/7}$. Thus, given the two intrinsic properties μ and M of the star, $\dot{P}$ depends only on the single parameter $PL^{3/7}$. Therefore, measurements of P, $\dot{P}$, and L for neutron stars that have different spin periods and/or different luminosities but are otherwise identical, or measurements of the P, $\dot{P}$, and L of a given neutron star made at different times, when its period and luminosity have different values, will fall on a single curve in a plot of $\log(-\dot{P})$ vs. $\log PL^{3/7}$. In such a plot, the slow rotation limit ($\omega_s \to 0$) corresponds to large $PL^{3/7}$ (cf. eq. [5.18]). Thus, surfaces of constant fastness are vertical lines. As a result, fast and slow rotators are separated in a systematic way, with fast rotators to the left and slow rotators to the right. In the slow-rotation limit, $\log(-\dot{P})$ is a straight line of slope +2.

The dependence of the $\dot{P}$ equation (5.19) on both P and L can produce complex spin-rate behavior (see Elsner, Ghosh, and Lamb 1978). However, the behavior of the spin rate is quite simple in two special cases of astrophysical interest, namely: (1) a star of given spin period that accretes matter at a time-varying rate and (2) a star whose spin changes as it accretes matter at a constant rate.

Consider first the pulse period behavior of a star rotating in the same sense as the disk flow and accreting at a constant rate $\dot{M}$. Such a star can experience either spin up or spin down, depending on its spin period. If P is large, ω_s is small compared to unity, and the star experiences a strong spin-up torque, causing P to decrease. As P falls, ω_s increases, and the spin-up torque decreases, vanishing at the critical spin period $P_c(\dot{M})$ at which $\omega_s = \omega_c$. If on the other hand P is small but still greater than $P_{\min}(\dot{M})$, at which $\omega_s = \omega_{\max}$, the star experiences a spin-down torque. As P increases, ω_s decreases, and the magnitude of the spin-down torque diminishes, vanishing at the critical spin period $P_c(\dot{M})$. Thus, the spin period of such a star will approach the critical period P_c that corresponds

to its accretion rate, and will then maintain that period. For P less than $P_{\min}$, accretion, if it occurs at all, is not steady.

The behavior of a star of given spin period accreting at a time-varying rate is somewhat different. If $\dot{M}$ is sufficiently large, ω_s is small compared to unity, and the star is a slow rotator. The star therefore experiences a strong spin-up torque. As $\dot{M}$ decreases, ω_s increases, and the spin-up torque falls, vanishing at the critical accretion rate $\dot{M}_c(P)$, at which $\omega_s = \omega_c$. For accretion rates less than $\dot{M}_c(P)$, the star experiences a spin-down torque, which increases steadily in magnitude with decreasing $\dot{M}$until $\dot{M}$ reaches the minimum accretion rate $\dot{M}_{\min}$ consistent with steady accretion. At this accretion rate, $\omega_s = \omega_{\max}$. If accretion continues at all for accretion rates less than $\dot{M}_{\min}$, it is not steady.

5.4 Comparisons with Observation

Starting with the earliest theoretical work, the qualitative agreement between the predicted and measured changes of the spin rates of accretion-powered pulsars has been cited as evidence that these sources are neutron stars. Thus, Pringle and Rees (1972) noted the agreement of their torque estimate with the observed spin-up rate of Cen X-3, assuming it was a neutron star. Lamb, Pethick, and Pines (1973) considered both white dwarfs and neutron stars, and argued on the basis of the observed spin-up rates of Cen X-3 and Her X-1 that both are neutron stars and not white dwarfs.

Elsner and Lamb (1976) compared the slow-rotator spin-up equation of Lamb, Pethick, and Pines with the more detailed $\dot{P}$ observations then available and concluded that agreement was satisfactory for Cen X-3 but not for Her X-1, which has a mean rate of change of its spin period about 30–40 times smaller than expected for a slow rotator. They argued strongly that the then newly-discovered long-period sources are neutron stars. Elsner and Lamb also emphasized the importance of the predicted spin-up time scale for slow rotators as a discriminant between neutron stars and white dwarfs, pointed out that the torque on fast rotators should be smaller, and suggested that this might explain the slow rate of change of the spin period of Her X-1. Rappaport and Joss (1977) and Mason (1977) compared the larger quantity of $\dot{P}$ data available by the time they did their studies with the accretion torque theory of Lamb, Pethick, and Pines, plotting the left side of equation (5.16) against the right side. The results of both studies indicated that the theory agrees qualitatively with observation, and that the sources considered by these authors are neutron stars accreting from Keplerian or near-Keplerian flows. Ghosh and Lamb (1979b) applied their model of disk accretion to nine pulsing X-ray stars and showed that the model was consistent with the available $\dot{P}$ data. Elsner, Ghosh, and Lamb (1980) pointed out that bright transient pulsars provide the best opportunity to test accretion torque theories.

Recently, Parmar *et al.* (1988) have analyzed EXOSAT pulse period and luminosity data from an outburst of the transient X-ray source EXO 2030+375. This source has a pulse period of 42 s and a binary period ~50 days. During the outburst, the luminosity declined steadily by an order of magnitude, providing the first opportunity for a quantitative test of accretion torque models along the lines suggested by Elsner, Ghosh, and Lamb. Parmar *et al.* find that the dependence of P on L is consistent with the GL torque theory, including a negative torque at low luminosities. At high luminosities, a fit to a power-law gives $-\dot{P} \propto L^{1.16\pm0.12}$, within 2.5σ of the expected relationship $-\dot{P} \propto L^{6/7} \propto L^{0.86}$. Recently, Angelini (1988) has reported the discovery of quasi-periodic oscillations in this source and a broad feature in the power spectrum that she interprets as evidence of the Kepler frequency at the inner edge of the accretion disk. If Ω_s and $\Omega_K(\varpi_0)$ are both known, ω_s is determined. The observed spin-rate changes can then be compared with the torque curve $n(\omega_s)$. Angelini concludes that the results are in satisfactory agreement with the GL theory. Future close studies of bright, transient pulsing sources will provide more stringent tests of accretion torque theory and guidance concerning the physics of the inner disk and the outer magnetosphere.

6. QUASI-PERIODIC INTENSITY OSCILLATIONS

During the last few years, relatively narrow peaks at frequencies ~1-60 Hz have been discovered in power density spectra of X-ray intensity time series from about ten luminous compact X-ray sources. Peaks at frequencies ~10^{-3} to 10^{-1} Hz have been reported in several other compact X-ray sources. The sources displaying these quasi-periodic oscillations in intensity (QPOs) are thought to be low-mass binary systems in which a neutron star is accreting matter from a companion star via an accretion disk (for recent reviews of QPO observations and theory, see Lamb 1988b; Stella 1988; van der Klis, van Paradijs, and Lewin 1988; Lamb and Priedhorsky 1988).

These discoveries have created excitement partly because the low-mass X-ray binaries have previously provided so few clues about their nature. The QPOs are thought to be produced near the neutron star and hence to provide direct evidence of what is happening there. Studying QPO phenomena may therefore lead to a much better understanding of the properties of the neutron stars and accretion flows in these systems. One particular type of QPO appears to be a magnetospheric phenomenon.

6.1 Types of QPOs

The intense observational studies that followed the initial discovery of QPOs in luminous low-mass X-ray binaries have revealed a variety of power spectra, X-ray spectra, and QPO behavior. As a result of these studies, it seems clear now

that there are two or three distinct types of QPOs in low-mass X-ray binaries. The types are defined by the properties of the QPO and the X-ray spectrum of the source at the time the QPO is observed.

A key discriminant is the X-ray spectrum of the source. It has recently been shown (see Hasinger 1988a; Schulz 1989) that the luminous low-mass X-ray binaries have three distinct spectral states, now called the *horizontal branch* (HB), the *normal branch* (NB), and the *flaring branch* (FB). The shape of power density spectra of the X-ray intensity time series is also a powerful discriminant, as shown schematically for the horizontal and normal branches in Figure 10. A steep red noise (SRN) component dominates both HB and NB power spectra at frequencies below ~0.01 Hz. However, in all other respects HB and NB power spectra are qualitatively different. HB power spectra show a distinct red noise (RN) component, which dominates the continuum power density in the range 0.1–20 Hz but which falls off approximately exponentially above ~20 Hz. In NB power spectra, this component appears to be weak or absent, except in Sco X-1, which has a red-noise-like component that extends up to ~65 Hz, with a total integrated power equivalent to an rms variation in intensity of ~4%.

The centroid frequencies of horizontal branch oscillations (HBOs) are ~20–60 Hz, whereas the centroid frequencies of normal branch oscillations (NBOs) are ~5–8 Hz. The flaring branch oscillations (FBOs) in Sco X-1 have frequencies ranging from ~6 Hz at the lower left of the flaring branch to ~20 Hz part way up the flaring branch. Table X summarizes the properties that are currently associated with the horizontal, normal, and flaring branches. A question mark indicates uncertainty, either because the property is at present uncertain or because it is well-determined for too few sources to be confident that the results are characteristic of the given spectral state.

This summary of the observations indicates that any model of the horizontal branch oscillations should explain the following key properties:

- The frequency ranges of the oscillations, typically ~20–60 Hz.
- The amplitudes of the oscillations, typically ~3%–7%.
- The FWHMs of the oscillation peaks, typically ~0.2–0.6 times the QPO frequency.
- The modest power at overtones of the oscillation frequency, which is typically < 20% of the power at the fundamental (overtones are sometimes seen, however).
- The strong, positive correlation of the oscillation frequency with source intensity.
- The presence of a substantial red noise component in the power spectrum, with a total power that varies with the total power in the oscillation peak.
- The lag of the oscillations at higher X-ray energies, typically by ~1 ms.

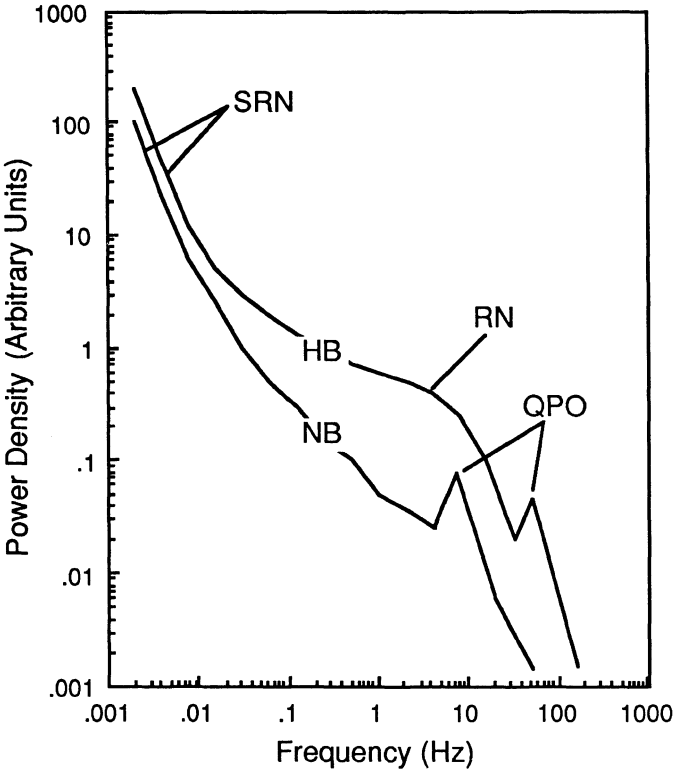

Fig. 10.—Schematic representation of typical horizontal branch (HB) and normal branch (NB) power spectra. Note the QPO peaks at 6 Hz in the NB state and at 50 Hz in the HB state, the strong red noise (RN) in the HB state, and the steep red noise (SRN) in both states. See Hasinger (1988a).

- The hardness of the oscillation photons, which are harder than typical photons from the source.
- The weakness of periodic intensity oscillations, which have been shown to have amplitudes <10–30 % in many sources and <1 % in GX 5–1, Sco X-1, and Cyg X-2 (see Lamb 1988b).

Any model should also be consistent with the luminosities of the HBO sources, which are all near the Eddington limit, and with their X-ray spectra.

6.2 Beat-Frequency Modulated Accretion Model

The so-called *beat-frequency modulated accretion* (BFMA) model was proposed as an explanation for what are now known to be horizontal branch oscillations (Alpar and Shaham 1985; Lamb *et al.* 1985; Shibazaki and Lamb 1987). This

TABLE X
Observed Properties of QPO Sources[a]

Source Property	Branch of X-Ray Color-Color Plot		
	Horizontal	Normal	Flaring
QPO frequency (Hz)	~20–60	~5–8	~6–20?
Red noise (RN)	Strong	Weak	?
Steep red noise (SRN)	Present	Present	Strong
QPO frequency–X-ray intensity correlation	Strong, positive	Weak, negative in Sco X-1	Strong, positive in Sco X-1
Energy spectrum of QPO photons	Relatively hard	Concave upward	Relatively hard?
Magnitude and sign of QPO phase shift	~0.2–4 ms hard lag	~80 ms hard lag	?

[a]See Hasinger (1988a).

model assumes that the X-ray source is a weakly magnetic neutron star accreting matter from a binary companion via a Keplerian disk. The key ideas of the BFMA model are as follows:

- The relatively weak magnetic field of the neutron star disrupts the Keplerian flow at a radius r_0 only slightly greater than the radius of the neutron star.
- The plasma density and magnetic field strength in the boundary layer at r_0 vary with azimuth due to fragmentation and/or instabilities.
- The resulting density and magnetic field variations and fluctuations orbit within the boundary layer at the local Kepler frequency.
- The interaction of these variations and fluctuations with the rotating magnetic field of the neutron star causes the accretion rate from the disk to the star to vary at the local pattern frequency, which is the beat frequency

$$\omega_B \equiv \Omega_0 - \Omega_s \,. \tag{6.1}$$

  Here Ω_0 is the mean angular frequency of matter in the boundary layer at the inner edge of the disk and Ω_s is the angular frequency of the neutron star (see Fig. 11).
- The resulting quasi-periodic modulation of the accretion rate causes quasi-periodic modulation of the luminosity of the neutron star and hence quasi-periodic modulation of the X-ray intensity seen at infinity.

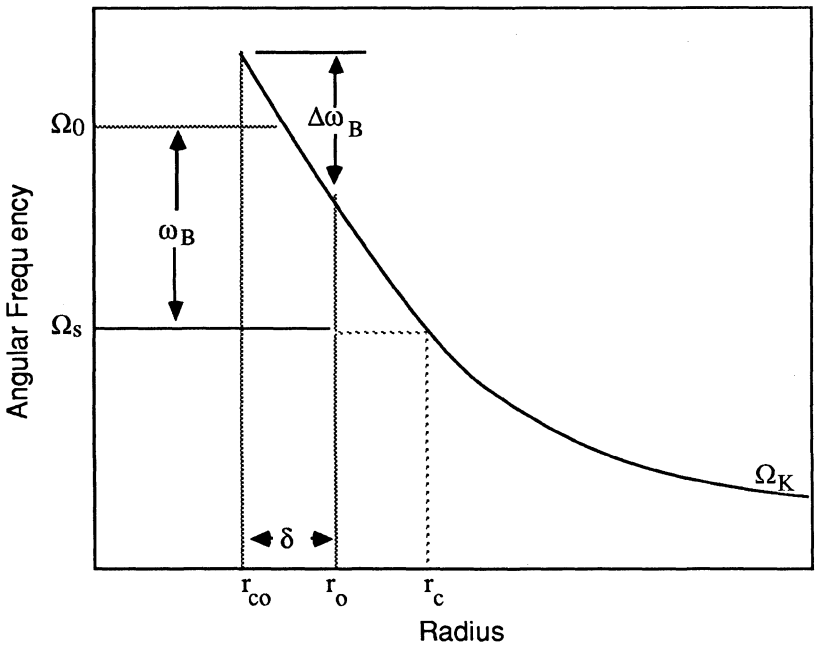

Fig. 11.—Frequency-radius relation in the inner disk ($r > r_c$) and boundary layer ($r_{co} < r < r_c$), showing the relationship of the mean beat-frequency $\omega_B = \Omega_0 - \Omega_s$ to the mean orbital frequency Ω_0 in the boundary layer and the stellar rotation frequency Ω_s. Also indicated is the spread $\Delta\omega_B$ in the beat frequencies of plasma orbiting within the boundary layer.

In this model, the interaction of density and magnetic field inhomogeneities orbiting in the boundary layer with the rotating magnetospheric field pattern causes the accretion rate to the neutron star surface to be modulated at the beat frequency, creating a quasi-periodic modulation of the luminosity of the star.

One strength of the beat-frequency model is that it provides a clear conceptual framework and makes possible quantitative predictions of the oscillation frequency, frequency range, and frequency-intensity correlation via equation (6.1). Moreover, the predicted oscillation frequency agrees with observed HBO frequencies for neutron star rotation rates $\sim$100 Hz and magnetic field strengths $\sim 10^9$ G, values expected on the basis of prior evolutionary arguments which suggest that the luminous low-mass X-ray binaries are progenitors of the 100 Hz rotation-powered pulsars. The narrowness of the oscillation peaks is explained by the narrowness of the boundary layer at r_0, while the hardness of the HBO photons is accounted for by the fact that they are emitted near the surface of the neutron star. The relatively strong red noise present in HB power spectra is a direct consequence of the density fluctuations in the boundary layer that make Ω_0, and

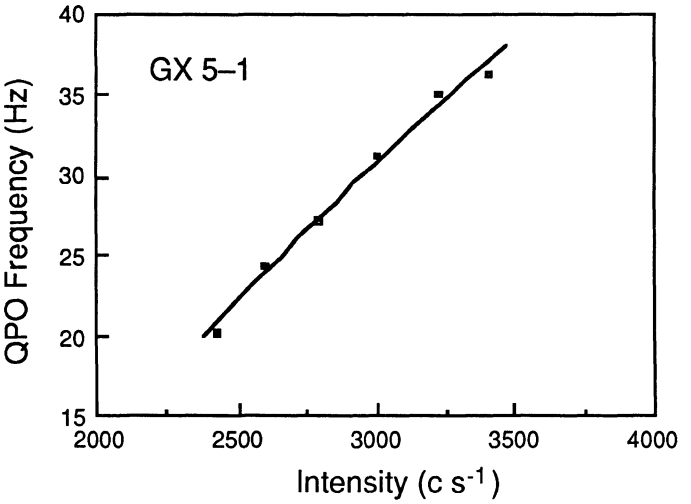

Fig. 12.—QPO frequency-intensity correlation observed in GX 5–1 on the horizontal branch (data points) and predicted by the simplest version of the beat-frequency model (curve).

hence the beat frequency, visible.

The beat frequency increases steeply with increasing accretion rate through the boundary layer, due to the decrease in r_0 and the resulting increase in Ω_0. Generally speaking, one expects the X-ray intensity to reflect the accretion luminosity and hence the accretion rate through the boundary layer. However, if mass leaves the system after passing through the boundary layer, or if there are changes in the geometry of the emission region, the shape of the X-ray spectrum, or the amount of obscuration, then the intensity I observed in a given X-ray energy range may not be strictly proportional to $\dot{M}$ (Lamb *et al.* 1985).

Suppose $I \propto \dot{M}^{\beta}$, for example. Then if r_0 is $\propto \dot{M}^{\gamma}$, the fundamental oscillation frequency will vary with I as

$$f_{QPO} = f_0 - f_s = aI^{\gamma/\beta} - f_s\,, \tag{6.2}$$

where $f_0 \equiv \Omega_0/2\pi$ is the mean circular frequency of material orbiting in the boundary layer, $f_s \equiv \Omega_s/2\pi$ is the circular frequency of the neutron star rotation, and a is a constant. The logarithmic derivative of the QPO frequency with respect to I is then

$$a \equiv \frac{\partial \ln f_{QPO}}{\partial \ln I} \approx \left(\frac{\gamma\beta}{1 - f_s/f_0}\right) = \left(\frac{\gamma\beta}{1 - \omega_s}\right)\,. \tag{6.3}$$

Figure 12 shows that the simplest choices, namely $\beta = 1$ and $\gamma = 0.3$, adequately describe the HBO frequency–intensity relation in GX 5–1. If the beat-frequency model proves correct, fits such as this one can be used to constrain the structure of the inner disk and the outer magnetosphere.

6.3 Amplitudes of Periodic Intensity Oscillations

If the magnetic field of the neutron star is strong enough to create a corotating magnetosphere near the star, as in the beat-frequency model of HBOs, one expects plasma to be directed preferentially toward the magnetic poles, creating an anisotropic radiation pattern. If in addition the magnetic axis is not aligned with the spin axis, an observer should see periodic oscillations in the X-ray intensity at the rotation frequency of the star, as explained at the beginning of §5. However, as noted in §6.1, careful observations have shown that the amplitudes of such oscillations, if present, must be very small. Thus, an important question is whether magnetospheric models are consistent with the observed upper limits on the amplitudes of periodic oscillations.

The expectation that QPO sources with magnetospheres will show at least moderate-amplitude periodic oscillations is based on experience with canonical accretion-powered pulsars. However, experience with accretion-powered pulsars may be very misleading in the case of the luminous low-mass X-ray binaries, where the dimension of the magnetosphere, the pattern of the accretion flow, and the transport of radiation differ in crucial ways from similar processes in accretion-powered pulsars. In fact, if the beat-frequency model of HBOs is correct, the intensity variation at the neutron star rotation frequency should be very weak (see Lamb *et al.* 1985; Lamb 1988b):

- For the $\sim 10^{38}$ ergs s^{-1} luminosities observed in the HBO sources and the $\sim 10^9$ G field strengths expected in the beat-frequency model, the magnetosphere is small, the radiation back-pressure is very large, and channeling of the accretion flow by the stellar magnetic field is likely to be only partially effective.
- As a result of weak channeling, accreting matter is expected to fall over a large fraction of the stellar surface, creating a relatively broad radiation pattern and relatively weak beaming.
- The radiation back-pressure may cause accreting matter to fall intermittently onto different parts of the stellar surface, producing phase as well as amplitude modulation. If so, the peak in the power spectrum at the stellar rotation frequency will be significantly broadened.
- Because the beaming of the radiation produced near the stellar surface is relatively weak, gravitational lensing can be effective in reducing the amplitude of the oscillations seen by a distant observer, if the star is not rotating too rapidly.
- Multiple scattering of X-ray photons by the relatively dense and widely distributed plasma within the magnetosphere will further broaden and weaken the beaming of the emerging X-rays. As a result, the radiation escaping from the magnetosphere is expected to be much more isotropic in these

stars than in canonical accretion-powered pulsars.

- Because these neutron star sources are older, the magnetic axis of the neutron star may be more aligned with its rotation axis than in canonical accretion-powered pulsars.
- The relatively thick accretion disk expected around the small magnetosphere restricts the path for relatively unimpeded propagation of X-rays to directions near the rotation axis, where the intensity modulation caused by beaming and rotation is inherently weak.
- If there is a central corona of optical depth ~5–10, as indicated by models of the HBO hard lags and horizontal branch X-ray spectra, scattering by the corona will reduce still further the amplitude of intensity oscillations at the rotation frequency of the neutron star.
- Detection of periodic oscillations in the HBO sources is made still more difficult by the substantial orbital Doppler shifts expected and the fact that the orbital period, the semi-major axis of the orbit, and the orbital phase of the neutron star are frequently unknown..

To amplify the next-to-last point, even if the stellar rotation frequency is as low as 30 Hz and the beam pattern is purely sinusoidal, the amplitude of intensity oscillations outside such a corona will be only $\sim 10^{-2}$ times the amplitude at the magnetospheric boundary. If instead the stellar rotation frequency is ~100 Hz and the radiation pattern has multiple lobes, the amplitude outside the corona could be a fraction $\sim 10^{-4}$ or less of the amplitude at the magnetospheric boundary. The presence of a central corona does *not* affect the amplitude of the intensity oscillations produced by the luminosity oscillations at the beat frequency, as long as the time for photons to escape from the corona is short compared to the oscillation period. For the central coronae expected in the luminous QPO sources, this is the case.

Although periodic intensity oscillations at the spin frequencies of the QPO sources are expected to be very difficult to detect, detection will be crucial in resolving two key questions regarding these sources, namely their magnetic field strengths and spin frequencies. Until periodic oscillations are found, the magnetic fields and spin rates of these neutron stars, and the validity of the beat frequency model, will remain in doubt.

It is a pleasure to thank J.-J. Aly, B. Fortner, G. S. Miller, W. C. Priedhorsky, N. Shibazaki, and G. Zylstra for many fruitful discussions of topics related to the subject of these lectures. I am also grateful to H. Ögelman and E.P.J. van den Heuvel for their kind hospitality at the Advanced Study Institute in Çeşme-İzmir. This research was supported in part by NASA grant NSG-7653 and NSF grant PHY 86-00377 at Illinois.

REFERENCES

Adam, J. A. 1978, *J. Plasma Phys.*, **19**, 77.

Alpar, M. A., and Shaham, J. 1985, *Nature*, **316**, 239.

Aly, J.-J. 1980, *Astron. Ap.*, **86**, 192.

Angelini, L. 1988, Talk presented at the Workshop on Quasi-Periodic Oscillations, La Cienega, New Mexico, October 2–7, 1988.

Anzer, U., and Börner, G. 1980, *Astron. Ap.*, **83**, 133.

_____. 1983, *Astron. Ap.*, **122**, 73.

Anzer, U., Börner, G., and Monaghan, J. J. 1987, *Astron. Ap.*, **176**, 235.

Arons, J. 1987, in *The Origin and Evolution of Neutron Stars, IAU Symposium No. 125*, ed. D. J. Helfand and J.-H. Huang (Dordrecht: Reidel), p. 207.

Arons, J., *et al.* 1984, in *High Energy Transients in Astrophysics, AIP Conf. Proc. No. 115*, ed. S. E. Woosley (New York: American Institute of Physics), p. 215.

Arons, J., and Lea, S. M. 1976a, *Astrophys. J.*, **207**, 914.

_____. 1976b, *Astrophys. J.*, **210**, 792.

_____. 1980, *Astrophys. J.*, **235**, 1016.

Bondi, H., and Hoyle, F. 1944, *Mon. Not. R. astr. Soc.*, **104**, 273.

Boynton, P. E., *et al.* 1984, *Astrophys. J.*, **238**, L35.

Bradt, H., and McClintock, J. E. 1983, *Ann. Rev. Astron. Astrophys.*, **21**, 13.

Burnard, D. J., Lea, S. M., and Arons, J. 1983, *Astrophys. J.*, **266**, 175.

Campbell, C. G. 1987, *Mon. Not. R. astr. Soc.*, **229**, 405.

Chapman, S., and Ferraro, V.C.A. 1931, *Terr. Mag.*, **36**, 171.

Davidson, K., and Ostriker, J. P. 1973, *Astrophys. J.*, **179**, 585.

Davies, R. E., and Pringle, J. E. 1980, *Mon. Not. R. astr. Soc.*, **191**, 599.

Dodd, K. N., and McCrea, W. H. 1952, *Mon. Not. R. astr. Soc.*, **112**, 205.

Elsner, R. F. 1976, Ph.D. thesis, University of Illinois at Urbana-Champaign.

Elsner, R. F., Ghosh, P., and Lamb, F. K. 1978, *Astrophys. J.*, **241**, L155.

Elsner, R. F., and Lamb, F. K. 1976, *Nature*, **262**, 356.

_____. 1977, *Astrophys. J.*, **215**, 897.

_____. 1984, *Astrophys. J.*, **278**, 326.

Fenimore, E. E., *et al.* 1988, *Astrophys. J.*, submitted.

Fortner, B., Lamb, F. K., and Zylstra, G. 1984, in *Numerical Astrophysics*, ed. J. M. Centrella, J. M. LeBlanc, and R. L. Bowers (Boston: Jones and Bartlett), p. 128.

Ghosh, P., and Lamb, F. K. 1978, *Astrophys. J.*, **223**, L83 (GL).

_____. 1979a, *Astrophys. J.*, **232**, 259 (GL).

_____. 1979b, *Astrophys. J.*, **234**, 296 (GL).

Ghosh, P., Lamb, F. K., and Pethick, C. J. 1977, *Astrophys. J.*, **217**, 578.

Giacconi, R. 1975, in *Proc. 8th Texas Symp. on Relativistic Astrophysics* (*Ann. NY Acad. Sci.*, **262**, 312).

Hasinger, G., *et al.* 1986, *Nature*, **319**, 469.

Hasinger, G. 1989, This volume.
_____. 1988, Talk presented at the Workshop on Quasi-Periodic Oscillations, La Cienega, New mexico, October 2–7, 1988.
Ho, C. 1988, *Mon. Not. R. astr. Soc.*, **232**, 91.
Ho, C., and Arons, J. 1987, *Astrophys. J.*, **321**, 404.
Hoyle, F., and Lyttleton, R. A. 1939, *Proc. Cam. Phil. Soc.*, **35**, 405.
Hunt, R. 1971, *Mon. Not. R. astr. Soc.*, **154**, 141.
Illarionov, A. F., and Sunyaev, R. A. 1975, *Astron. Astrophys.*, **39**, 185.
Joss, P. C., and Rappaport, S. A. 1984, *Ann. Rev. Astron. Astrophys.*, **22**, 537.
Katz, J. I., and Smith, I. A. 1988, *Astrophys. J.*, **326**, 733.
Kennel, C. F., and Coroniti, F. V. 1975, in *The Magnetospheres of the Earth and Jupiter*, ed. V. Formisano (Dordrecht: Reidel), p. 451.
_____. 1977, *Ann. Rev. Astron. Astrophys.*, **15**, 389.
Kirk, J. G., and Trümper, J. E. 1983, in *Accretion-Driven Stellar X-Ray Sources*, ed. W.H.G. Lewin and E.P.J. van den Heuvel (Cambridge: Cambridge University Press), p. 261.
Kulkarni, S. R. 1986, *Ap. J. (Letters)*, **306**, L85.
Kundt, W., and Robnik, M. 1980, *Astron. Ap.*, **91**, 305.
Kylafis, N. D., and Lamb, D. Q. 1979, *Astrophys. J.*, **228**, L105.
Lamb, D. Q. 1988a, in *Nuclear Spectroscopy of Astrophysical Sources, AIP Conf. Proc.*, ed. N. Gehrels and G. Share (New York: American Institute of Physics), in press.
Lamb, F. K. 1975a, in *X-Rays in Space*, ed. D. Venkatesan (Calgary: University of Calgary), p. 613.
_____. 1975b, in *Proc. 7th Texas Symposium on Relativistic Astrophysics* (*Ann. NY Acad. Sci.*, **262**, 331).
_____. 1977, in *Proc. 8th Texas Symposium on Relativistic Astrophysics* (*Ann. NY Acad. Sci.*, **302**, 482).
_____. 1984, Lecture series presented at the Workshop on Astrophysical Magnetospheres, Taos, New Mexico, August 1984.
_____. 1988b, in *Physics of Compact Objects: Theory versus Observations*, ed. L. Filipov and N. White (Oxford: Pergamon), in press.
Lamb, F. K., *et al.* 1977, *Astrophys. J.*, **217**, 197.
Lamb, F. K., and Pethick, C. J. 1974, in *Astrophysics and Gravitation, Proc. 16th Internat. Solvay Congress* (Brussels: L'Université de Bruxelles), p. 135.
Lamb, F. K., Pethick, C. J., and Pines, D. 1973, *Astrophys. J.*, **184**, 271.
Lamb, F. K., Pines, D., and Shaham, J. 1978, *Astrophys. J.*, **224**, 969.
Lamb, F. K., and Priedhorsky, W. C. 1988, *Rev. Mod. Phys.*, in preparation.
Lamb, F. K., *et al.* 1985, *Nature*, **317**, 681.
Lewin, W.H.G., and Joss, P. 1983, in *Accretion-Driven Stellar X-Ray Sources*, ed. W.H.G. Lewin and E.P.J. van den Heuvel (Cambridge: Cambridge University Press), p. 41.

Livio, M., *et al.* 1986a, *Mon. Not. R. astr. Soc.*, **218**, 593.
Livio, M., *et al.* 1986b, *Mon. Not. R. astr. Soc.*, **222**, 235.
Makishima, K., *et al.* 1987, *Astrophys. J.*, **314**, 619.
Mason, K. O. 1977, *Mon. Not. R. astr. Soc.*, **178**, 81P.
Matsuda, T., Inoue, M., and Sawada, K. 1987, *Mon. Not. R. astr. Soc.*, **226**, 785.
Mészáros, P. 1982, in *Accreting Neutron Stars*, ed. W. Brinkmann and J. Trümper (Garching, FRG: Max-Planck-Institut fur Physik und Astrophysik), p. 253.
_____. 1986, in *Plasma Penetration into Magnetospheres*, ed. N. Kylafis *et al.* (Iraklion, Crete: Crete University Press), p. 143.
Michel, F. C. 1977a, *Astrophys. J.*, **213**, 836.
_____. 1977b, *Astrophys. J.*, **214**, 261.
_____. 1977c, *Astrophys. J.*, **216**, 838.
Middleditch, J., and Priedhorsky, W. C. 1986, *Astrophys. J.*, **306**, 230.
Murakami, T., *et al.* 1988, *Nature*, in press.
Ögelman, H. 1989, This volume.
Parmar, A. N., *et al.* 1988, *Astrophys. J.*, in press.
Pringle, J. E. 1981, *Ann. Rev. Astron. Astrophys.*, **19**, 137.
Pringle, J. E., and Rees, M. J. 1972, *Astron. Astrophys.*, **21**, 1.
Rappaport, S., and Joss, P. C. 1977, *Nature*, **266**, 683.
Riffert, H. 1980, *Astrophys. Space Sci.*, **71**, 195.
Schreier,E. J., *et al.* 1972, *Astrophys. J.*, **172**, L79.
Schulz, N. S. 1989, This volume.
Shakura, N. I., and Sunyaev, R. A. 1976, *Mon. Not. R. astr. Soc.*, **175**, 613.
Shapiro, S. L., and Lightman, A. P. 1976, *Astrophys. J.*, **204**, 555.
Shibazaki, N., and Lamb, F. K. 1987, *Astrophys. J.*, **318**, 767.
Shima, E., *et al.* 1985, *Mon. Not. R. astr. Soc.*, **217**, 367.
Soker, N., and Livio, M. 1984, *Mon. Not. R. astr. Soc.*, **211**, 927.
Soker, N., *et al.* 1986, *Mon. Not. R. astr. Soc.*, **221**, 445.
Spicer, D. S. 1982, *Space Sci. Rev.*, **31**, 351.
Stella, L. 1988, in *Physics of Compact Objects: Theory versus Observations*, ed. L. Filipov and N. White (Oxford: Pergamon), in press.
Stella, L., and Rosner, R. 1984, *Astrophys. J.*, **277**, 312.
Taam, R. E. 1984, in *High Energy Transients in Astrophysics, AIP Conf. Proc. No. 115*, ed. S. E. Woosley (New York: American Institute of Physics), p. 1.
_____. 1985, *Ann. Rev. Nucl. Part. Sci.*, **35**, 1.
Taam, R. E., and Fryxell, B. A. 1988, *Astrophys. J.*, **327**, L73.
Tananbaum, H. *et al.* 1972, *Astrophys. J.*, **174**, L143.
Tenant, A. 1988a, Result reported by A. Fabian at the Symposium in Honor of Minoru Oda, Tokyo, February 1988.
_____. 1988b, Talk presented at the Workshop on Quasi-Periodic Oscillations, La Cienega, New Mexico, October 2–7, 1988.

Treves, A., Maraschi, L., and Abramowicz, M. 1988, *Pub. Astron. Soc. Pacific*, in press.
Trümper, J., *et al.* 1978, *Astrophys. J.*, **219**, 105.
Tuohy, I. R., *et al.* 1981, *Astrophys. J.*, **245**, 183.
van den Heuvel, E.P.J. 1989, This volume.
van den Heuvel, E.P.J., van Paradijs, J., and Taam, R. E. 1986, *Nature*, **322**, 153.
van der Klis, M., *et al.* 1985, *Nature*, **316**, 225.
van der Klis, M., van Paradijs, J., and Lewin, W.H.G. 1988, *Space Sci. Rev.*, in press.
Wang, Y.-M. 1981, *Astron. Astrophys.*, **102**, 36.
_____. 1987, *Astron. Astrophys.*, **183**, 257.
Wang, Y.-M., and Nepveu, M. 1983, *Astron. Astrophys.*, **118**, 267.
Wang, Y.-M., Nepveu, M., and Robertson, J. A. 1984, *Astron. Astrophys.*, **135**, 66.
Wang, Y.-M., and Robertson, J. A. 1984, *Astron. Astrophys.*, **139**, 93.
Wang, Y.-M., and Welter, G. M. 1982, *Astron. Astrophys.*, **113**, 113.
Wheaton, W. A., *et al.* 1979, *Nature*, **282**, 240.
White, N. E. 1982, in *Accreting Neutron Stars*, ed. W. Brinkmann and J. Trümper (Garching, FRG: Max-Planck-Institut fur Physik und Astrophysik), p. 29.
White, N. E., and Stella, L. 1987, *Mon. Not. R. astr. Soc.*, **231**, 325.
Williams, D. J. 1975, *Mon. Not. R. astr. Soc.*, **171**, 537.
Zylstra, G. 1988, Ph.D. thesis, University of Illinois at Urbana-Champaign.
Zylstra, G., Lamb, F. K., and Aly, J.-J. 1988, in preparation.

SELF-CONSISTENT MODELLING OF PULSAR MAGNETOSPHERES

H. Herold[1,2], T. Ertl[2], B. Finkbeiner[2], H. Ruder[2]

[1]Institut für Theoretische Physik der Universität Zürich
Schönberggasse 9
CH-8001 Zürich
Switzerland

[2]Lehrstuhl für Theoretische Astrophysik der Universität Tübingen
Auf der Morgenstelle 12
D-7400 Tübingen 1
F.R.G.

ABSTRACT. The magnetosphere of a rapidly rotating, strongly magnetized neutron star with aligned magnetic and rotational axes (parallel rotator) is modelled numerically. Including the radiation of the particles accelerated to relativistic energies as an efficient damping mechanism, we obtain a quasi-stationary self-consistent solution to this classical problem. The numerical simulation, which was started from the well-known vacuum solution, yields a global magnetospheric structure that can be characterized by two regions of oppositely charged particles, which eventually produce a relativistic pulsar wind, separated by a vacuum gap of considerable extent.

1. INTRODUCTION

The problem — fundamental to the physics of pulsars — of determining the global structure of the magnetospheres of rapidly rotating strongly magnetized neutron stars has not yet been solved self-consistently (for a review cf. Michel 1982), but it must be solved before any conclusive interpretation can be given to the large amount of detailed experimental data on pulsar radiation (cf. e.g. the contribution by D. Backer in these proceedings). Apart from this reason, it is " ... *just intolerable that we should not know how a rotating magnetized neutron star comes to terms with its environment* " (Mestel 1981).

We concentrate here on the self-consistent modelling of the magnetosphere of an aligned rotator, where the rotation axis is parallel to the magnetic axis of the neutron star. In this case, the homopolar induction, which should be responsible for populating the magnetosphere with charged particles pulled out from the neutron star surface via field emission (Goldreich and Julian 1969), can be studied in purity, whereas electromagnetic wave effects are neglected. The main questions

H. Ögelman and E. P. J. van den Heuvel (eds.), Timing Neutron Stars, 723–729.

to be answered are the following: What is the global structure of the electric and the magnetic field? How are the charge and current density distributed that produce these fields (together with the star)? Which particle populations exist in the magnetosphere?

2. BASIC EQUATIONS

2.1. Maxwell and Vlasov Equations

In the stationary axially symmetric case the electromagnetic fields $\mathbf{E}$ and $\mathbf{B}$ in the pulsar magnetosphere can be described (in cylindrical coordinates ρ, φ, z) by the electrostatic potential $\Phi(\rho, z)$, the magnetic flux function $\Psi(\rho, z)$ and the poloidal magnetic field $B_\varphi(\rho, z)$: $\mathbf{E} = -\nabla\Phi$ and $\mathbf{B} = (1/\rho)\nabla\Psi \times \mathbf{e}_\varphi + B_\varphi \mathbf{e}_\varphi$. The charge density ρ_e and the current density $\mathbf{j}$ determine the electric potential via the Poisson equation and the magnetic field via Ampere's law, which here read in suitable units such that all quantities are dimensionless:

$$\Delta\Phi = -\rho_e\,; \qquad \left(\Delta - \frac{2}{\rho}\frac{\partial}{\partial\rho}\right)\Psi = -\rho\, j_\varphi \tag{1a}$$

$$\frac{\partial}{\partial z}(\rho B_\varphi) = -\rho\, j_\rho\,; \qquad \frac{\partial}{\partial z}(\rho B_\varphi) = -\rho\, j_z \tag{1b}$$

The magnetosphere is formed by a collisionless plasma, in which the particles are expected to be extremely relativistic due to the huge electric and magnetic fields (the homopolar induction voltage between pole and equator of the neutron star is typically of the order 10^{17}–10^{18}V). The charge and current densities are derived from the zeroth and first momentum of the particle distribution function

$$\rho_e = \int f(\mathbf{r}, \mathbf{p})\, d^3p\,; \qquad \mathbf{j} = \int \mathbf{v}\, f(\mathbf{r}, \mathbf{p})\, d^3p\,, \tag{2}$$

where the distribution function $f(\mathbf{r}, \mathbf{p})$ is determined by the Vlasov equation

$$\mathbf{v}\frac{\partial f}{\partial \mathbf{r}} + \frac{\partial}{\partial \mathbf{p}}\left[(\mathbf{E} + \mathbf{v} \times \mathbf{B} + \begin{matrix}\text{radiation}\\ \text{damping}\end{matrix})f\right] = 0\,. \tag{3}$$

The velocity $\mathbf{v}$ is given by $\mathbf{v} = \mathbf{p}/\sqrt{(\varepsilon^2 + \mathbf{p}^2)}$, where the dimensionless parameter ε is defined by

$$\varepsilon = \frac{2mc^2}{eB_0 a^2 \Omega}\,, \tag{4}$$

i.e. by the ratio between rest mass energy and homopolar induction energy (B_0 is the polar magnetic field strength, a is the radius and Ω is the angular velocity of the neutron star). Because typical values for ε are extremely small ($\varepsilon \sim -10^{-12}$ for electrons, $\varepsilon \sim 10^{-9}$ for protons), the particles are expected to become extremely relativistic, since their maximum Lorentz factors should be comparable with $1/|\varepsilon|$,

at least if the radiation reaction during phases of acceleration can be neglected. Although this is not the case, as will be discussed in the following, it is nevertheless convenient to use a scaled Lorentz factor $\Gamma = \varepsilon\,\gamma$ that never exceeds unity.

2.2. Particle Motion in the Limit of Strong Radiation Damping

Studying the trajectories of particles in realistic pulsar vacuum fields, one can get an idea of how strongly the radiation reaction does affect the particle motion.

The Lorentz-Dirac equation of motion in the Landau approximation (cf. Landau and Lifshitz 1975) can be written (for $|\varepsilon| \ll 1$) as

$$\dot{\mathbf{v}} = \frac{1}{\Gamma}\mathbf{F}\,; \quad \dot{\Gamma} = \mathbf{E}\cdot\mathbf{v} - D_0\Gamma^2\mathbf{F}^2 \tag{5a}$$

with

$$\mathbf{F} = \mathbf{E} + \mathbf{v}\times\mathbf{B} - \mathbf{v}(\mathbf{E}\cdot\mathbf{v})\,. \tag{5b}$$

The dimensionless damping constant D_0, which is defined by

$$D_0 = \frac{e^2}{6\pi\epsilon_0}\,\frac{\Omega}{mc^3\varepsilon^3}\,, \tag{6}$$

characterizes the strength of the radiation reaction. For typical pulsar parameters, its value is of the order of $D_0 \sim -10^{14}$ for electrons, and $D_0 \sim 10$ for protons. Thus, at least for the electrons, the radiation reaction force dominates the particle motion. Large values of $|D_0|$ imply that the factor of D_0 in (5a) always remains very small; this leads us to the assumption, which was confirmed by numerical integration of eqs. (5) (cf. Herold et al. 1985, Herold et al. 1986), that during the motion the condition $\mathbf{F} \approx 0$ is fulfilled, which means that the radiation reaction is locally minimized along the trajectory. This is a condition for the velocity and yields, for given $\mathbf{E}$ and $\mathbf{B}$ fields

$$\mathbf{v} = \frac{1}{\mathbf{B}^2 + P^2}\left[\mathbf{E}\times\mathbf{B} + \frac{1}{P}(\mathbf{E}\cdot\mathbf{B})\mathbf{B} + P\mathbf{E}\right] \tag{7a}$$

with

$$P^2 = \frac{1}{2}(\mathbf{E}^2 - \mathbf{B}^2) + \frac{1}{2}\left[(\mathbf{E}^2 - \mathbf{B}^2)^2 + 4(\mathbf{E}\cdot\mathbf{B})^2\right]^{\frac{1}{2}}. \tag{7b}$$

Thereby, we have obtained a local velocity field $\mathbf{v} = \mathbf{v}(\mathbf{E},\mathbf{B})$ and thus a fluid-like picture for the particle motions in the magnetosphere. The main characteristics of this "damping-free" motion is that the particles try to come to rest in surfaces where $\mathbf{E}\cdot\mathbf{B} = 0$.

3. NUMERICAL APPROACH AND RESULTS

Based on these results, the task to determine a self-consistent solution is simpler than before, but still difficult due to the great non-linearity of the problem. Our approach is based on the idea to start from the vacuum solution and to fill up the magnetosphere with the particles that are pulled out from the neutron star

surface. This is not a real time-dependent calculation, since we assume that the electric field is always described by an electrostatic potential, but for transporting the charge with the velocity (7) we need to solve the time-dependent continuity equation

$$\dot{\rho}_e + \mathrm{div}(\rho_e \mathbf{v}) = 0 \tag{8}$$

and therefore $\dot{\mathbf{E}}$ cannot be omitted in Ampere's law. Thus eqs. (1b) have to be replaced by

$$\left(\Delta - \frac{2}{\rho}\frac{\partial}{\partial\rho}\right)(\rho B_\varphi) = \rho\left(\frac{\partial j_z}{\partial\rho} - \frac{\partial j_\rho}{\partial z}\right). \tag{9}$$

[Actually, for each particle species the corresponding continuity equation is solved as the velocity (7a) depends on the particle charge: the sign of the quantity P ($P = \mathbf{E}\cdot\mathbf{v}$) from (7b) has to be identical to the charge sign. The charge and the current density, which enter Maxwell's equations, are calculated by summation over both particle species.]

In summary, we solve at each time step the elliptic equations (1a) with Dirichlet boundary conditions for Φ and Ψ on the star — we assume a homogeneously magnetized neutron star — (the change of Φ at infinity has to be derived from Ampere's law) and equation (9) with the Neumann boundary condition $\partial(\rho B_\varphi)/\partial r = \rho j_\vartheta$ on the star's surface, where the simple emission law $j = \sigma E_\parallel$ is assumed. The three elliptic equations are solved by successive over-relaxation (SOR) in a vectorizable checkerboard scheme. For the continuity equations an explicit discretization in time with 2-dimensional Flux Corrected Transport is used in order to preserve steep gradients in the charge density. A more detailed description of our numerical methods is given in Ertl (1988).

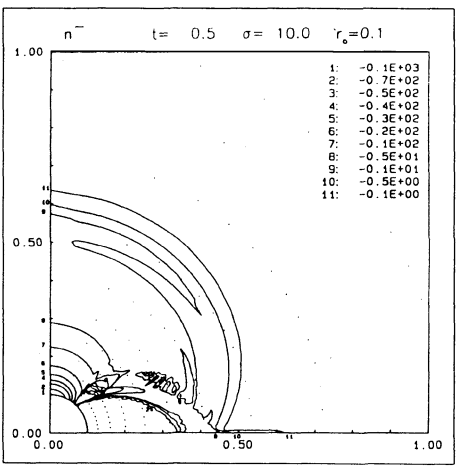

Fig.1: Initial phase: density of the negative particles

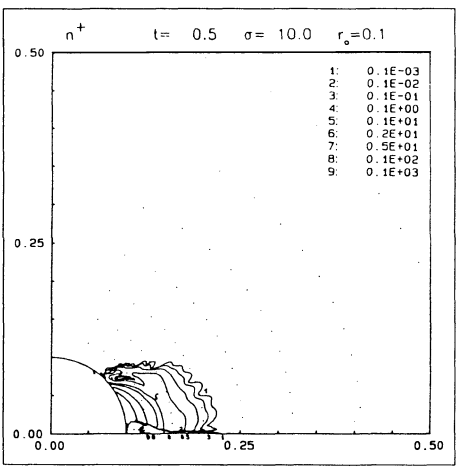

Fig.2: Initial phase: density of the positive particles

The results described in the following were obtained for a rapid rotator with $r_0 = (\Omega a)/c = 0.1$ as ratio of stellar radius and light cylinder radius (cf. also Ertl et al. 1987). We start with the vacuum fields of an uncharged aligned rotator, i.e. an electric quadrupole field and a magnetic dipole field resulting in $\mathbf{E} \cdot \mathbf{B} \leq 0$ everywhere. Therefore, only negative particles can be emitted and then transported along the magnetic field lines towards the equator where they accumulate. This causes a change in the electric field such that the $\mathbf{E} \cdot \mathbf{B} = 0$ surface rises from the equator towards the polar field line forcing the negative particles to follow it. As soon as $\mathbf{E} \cdot \mathbf{B} > 0$ at some part of the star's surface positive particles can enter the magnetosphere.

Figs. 1 and 2 show a snapshot of this initial phase at $t = 0.5$ (one revolution of the star corresponds to $t = 2\pi$). The cloud of positive particles has evolved to a sizable extent, although the negative charge density still dominates. After about one revolution the magnetosphere has developed a structure which already resembles the final situation. This quasi-stationary end phase is depicted (after 35 revolutions) in Figs. 3 – 6, where the charge densities and the contour lines of the electrostatic potential and of $\mathbf{E} \cdot \mathbf{B}$ are shown. One recognizes two regions of charged particles (the negative ones in a cone around the polar field line, the positive ones around the equatorial plane) separated by a vacuum gap in between. (Vacuum gaps in non-selfconsistent models are not new; for a more recent model with such a feature, cf. Mestel et al. 1985.) In this vacuum gap the parallel electric field $E_{\|} = (\mathbf{E} \cdot \mathbf{B})/|\mathbf{B}|$ is greatly different from zero (s. Fig. 6), whereas in the regions populated with plasma the electric field, which is now totally unsimilar to the initial quadrupole (s. Fig. 5), has evolved as to achieve $\mathbf{E} \cdot \mathbf{B} \sim 0$ there. The poloidal magnetic field does not change very much, it remains essentially dipolar. The neutron star is now positively charged, and the positive and the negative currents out of the star exactly match each other.

From the velocity fields — which are not shown here — one can conclude that the positive particles corotate with the star (to a very good approximation) as long as they are inside the light cylinder, but close to the light cylinder they lose corotation and stream through a sort of nozzle into the outer parts of the magnetosphere forming a radial wind. The velocity of the negative particles is dominantly poloidal and, thus, also a negatively charged wind builds up.

There are still some wave-like fluctuations, especially inside the negative zone, which seem to originate from the tendency of the system to make $\mathbf{E} \cdot \mathbf{B}$ small (or even zero) in the plasma regions. This also explains the strange folded structure of the $\mathbf{E} \cdot \mathbf{B} = 0$ surface and might be an indication that the magnetosphere wants to form an extended region with $\mathbf{E} \cdot \mathbf{B} = 0$; however, this is difficult to achieve with a relativistic particle population. Whether for this end a cool non-relativistic plasma population is necessary or whether such fluctuations are a physically real part of a quasi-stationary configuration is an open question. Globally, our solution represents a stationary structure; for instance, the charges of the star and of the magnetosphere remain, in the end phase, constant with great accuracy.

For the first time in pulsar magnetospheric theory it seems that a stationary self-consistent solution for the aligned rotator has been found by a quasi-time-dependent simulation. Detailed diagnostic investigations of this solution, such as the calculation of the radiation of the accelerated particles, as well as studies of

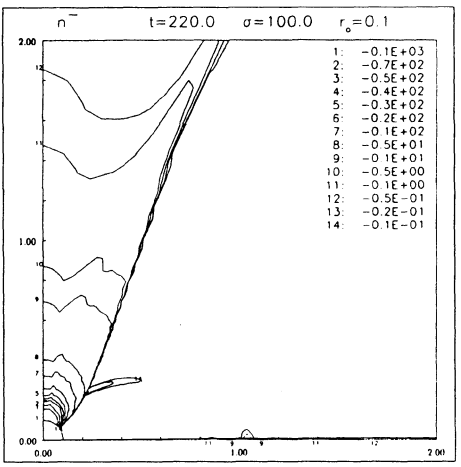

Fig.3: Quasi-stationary end phase: density of the negative particles

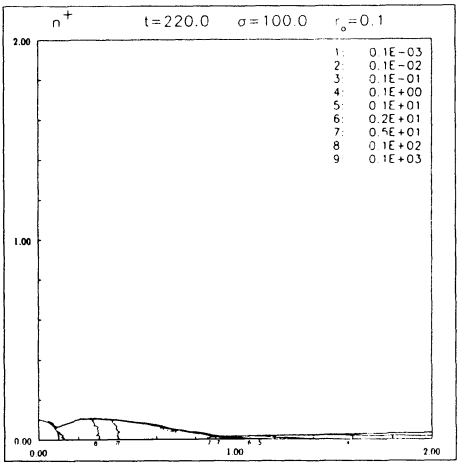

Fig.4: Quasi-stationary end phase: density of the positive particles

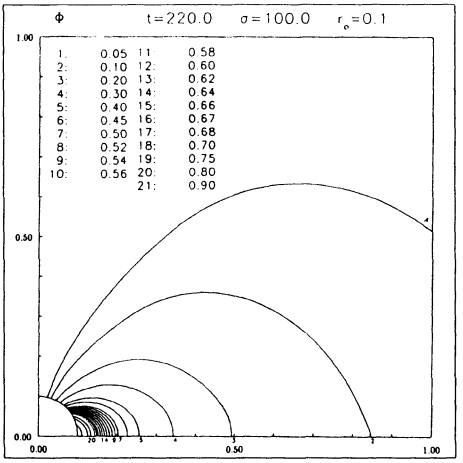

Fig.5: Quasi-stationary end phase: contour lines of the electrostatic potential Φ

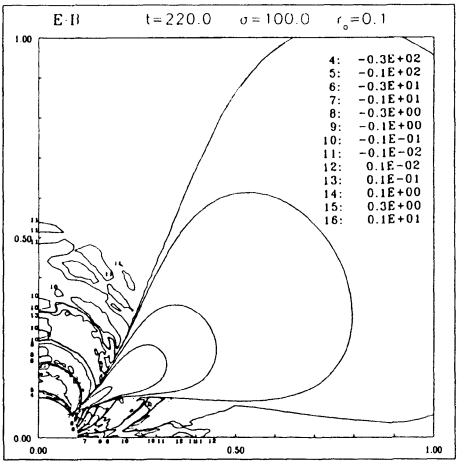

Fig.6: Quasi-stationary end phase: contour lines of $\mathbf{E} \cdot \mathbf{B}$

the parameter dependence (rotation frequeny Ω, emissivity σ of the neutron star) are tasks for the future.

REFERENCES

Backer, D.: 1989, in these proceedings

Ertl, T.: 1988, Thesis, Universität Tübingen

Ertl, T., Herold, H., Finkbeiner, B., Ruder, H.: 1987, *Mitt. Astron. Ges.* **70**, 372

Goldreich, P., Julian, W.H.: 1969, *Astrophys. J.* **157**, 869

Herold, H., Ertl, T., Ruder, H.: 1985, *Mitt. Astron. Ges.* **63**, 174

Herold, H., Ertl, T., Ruder, H.: 1986, Proceedings of the 8th EPS Conference on Computational Physics — Computing in Plasma Physics, Eibsee, *Europhysics Conference Abstracts* **10D**, 3

Landau, L.D., Lifshitz, E.M.: 1975, *The Classical Theory of Fields*, Pergamon Press, Oxford

Mestel, L.: 1981, in *"Pulsars", IAU Symp.* **95**, Reidel, Dordrecht, p. 37

Mestel, L., Robertson, J.A., Wang. Y.-M., Westfold, K.C.: 1985, *Mon. Not. R. Astr. Soc.* **217**, 443

Michel, F.C.: 1982, *Rev. Mod. Phys.* **54**, 1

SMEARING OF X-RAY OSCILLATIONS BY ELECTRON SCATTERING

Nikolaos D. Kylafis
University of Crete
Physics Department
714 09 Iraklion, Crete
GREECE

E. S. Phinney
Theoretical Astrophysics
Caltech 130-33
Pasadena, CA 91125
U.S.A.

ABSTRACT We discuss the effects that electron scattering has on the oscillations of an X-ray source. We consider a point source at the center of a spherical cloud of radius R and optical depth to electron scattering τ. The emission pattern of the source and its time variability are assumed to be either isotropic with intensity varying sinusoidally in time, or in the form of a δ-function beam rotating uniformly about a fixed axis and having intensity constant in time. More complicated source emissions and variabilities can be studied by superposing the above forms. We present approximate analytic expressions of the variability observed at infinity and compare them with accurate Monte Carlo results. Our calculations reveal the conditions under which quasi-periodic oscillations (QPO) *can* be observed from X-ray sources while coherent oscillations at the rotation frequency of the neutron star are completely smeared out.

1. INTRODUCTION

Consider a point X-ray source at the center of a scattering cloud. Photons that are emitted at a given time from the source *do not* reach an observer at infinity simultaneously. This is because not all photons spend the same amount of time in the scattering cloud. Some escape unscattered, some are scattered once before escape, some twice, and so on. On the average, the more scatterings a photon suffers, the more its escape from the cloud is delayed.

If the source emits isotropically with an intensity which varies sinusoidally in

H. Ögelman and E. P. J. van den Heuvel (eds.), Timing Neutron Stars, 731–737.

time, then a photon emitted at, say, time t_1 may suffer many scatterings, while another photon emitted at a later time t_2 may suffer fewer scatterings and reach the observer at the same time as the first photon. Thus, different photon travel times in the cloud may result in smearing of the oscillations of the source.

If the source emission is in the form of a pencil beam rotating about a fixed axis and having constant intensity, then electron scattering introduces an additional effect that can reduce the amplitude of the oscillations observed at infinity. This is the isotropization of the radiation field. If the optical depth to electron scattering in the cloud is small, the photons escape unscattered and the observer sees the source once per rotation period. However, if the optical depth is large, the direction into which a photon escapes is essentially independent of the direction into which it was emitted, because of the large number of scatterings that it suffered in the cloud. In this case, an observer at infinity sees hardly any variation at all. It should be stressed that the isotropization of the radiation field of the beam by electron scattering is important for moderate and large optical depths even if the time delay in the cloud due to random walk is negligible.

One motivation for this work has been the following: Quasi Periodic Oscillations (QPO) have been observed from several bright low-mass X-ray binaries (for reviews see Shaham 1989; Lamb and Priedhorsky 1988; Lewin, van Paradijs and van der Klis 1988). These sources *do not* show periodic oscillations at the rotation frequency of the neutron star (exception Cen X-3). In the context of the so-called Beat Frequency Modulated Accretion (BFMA) model (Alpar and Shaham 1985; Lamb *et al.*1985; Lamb 1986; Shibazaki and Lamb 1987; Lamb 1988) something must wash out the periodic oscillations (caused by emission in the form of a beam) and leave essentially unaffected the QPO (caused by modulated accretion). As we demonstrate below, electron scattering *can* do just that.

Previous work on the subject includes that of Hertz, Joss, and Rappaport (1978), Chang and Kylafis (1983), Wang and Schlickeiser (1987), Brainerd and Lamb (1987), Kylafis and Klimis (1987).

In §2 we give a semi-quantitative discussion of the problem, in §3 we present the basic formalism, in §4 we derive the basic results, and in §5 we conclude with a summary.

2. SEMI-QUANTITATIVE DISCUSSION

Consider a point X-ray source at the center of a uniform, spherical cloud of radius R and optical depth to electron scattering $\tau \gtrsim 3$. We will examine two emission patterns of the source.

2.1 Isotropic Emission

Let the X-ray source emit isotropically with an intensity which is varying sinusoidally in time with period P. The mean time $\langle t \rangle$ that a photon spends in the

cloud due to random walk is

$$\langle t \rangle \;=\; \langle n \rangle \frac{l}{c} \;\approx\; 0.5\tau \frac{R}{c}\;, \tag{1}$$

where $\langle n \rangle \approx 0.5\tau^2$ is the mean number of scatterings suffered by a photon before escape (Lightman, Lamb and Rybicki 1981), $l \equiv R/\tau$ is the mean free path, and c is the speed of light. Let A_0 be the amplitude of oscillations at the source and A_∞ the corresponding amplitude seen by a distant observer. It is clear that if $\langle t \rangle \ll P$, the effect of electron scattering on the smearing of the oscillations is negligible and one has

$$\frac{A_\infty}{A_0} \;\approx\; 1\;. \tag{2}$$

However, if $\langle t \rangle \gg P$, we expect that only the photons that did not scatter at all will retain memory of the oscillations. In this case, one can write

$$\frac{A_\infty}{A_0} \;\approx\; e^{-\tau}\;. \tag{3}$$

2.2 Beam Emission

Let the source emit in the form of a δ-function beam of constant intensity I_0. If $\hat{\mathbf{n}}$ is the direction of the beam and $\hat{\mathbf{n}}'$ is the direction to the observer, then the intensity seen by the observer is (Brainerd and Lamb 1987)

$$\frac{I_\infty}{I_0} \;=\; \frac{1}{4\pi}\left(1 + \frac{2}{1+\tau}\hat{\mathbf{n}}\cdot\hat{\mathbf{n}}'\right)\;. \tag{4}$$

Thus, if for simplicity we consider a beam rotating with period P in the xy-plane and take $\hat{\mathbf{n}}'$ along the x-axis, the observed amplitude is

$$A_\infty \;=\; \frac{2}{1+\tau}\;, \tag{5}$$

plus a δ-function contribution $e^{-\tau}\delta(\hat{\mathbf{n}} - \hat{\mathbf{n}}')$ from the unscattered photons. If it happens that $\langle t \rangle \gtrsim P$, then A_∞ is reduced further.

3. FORMALISM

Consider a point source at the center of a scattering cloud emitting *isotropically* with an intensity $I(t)$. Our purpose is to compute the intensity $I_\infty(t)$ observed at infinity.

Let P_n be the probability that a photon emitted by the source escapes after n scatterings and let $\phi_n(t, t_0)$ be the distribution of escape times for photons that are emitted at time t_0 and scattered n times. The P_n and ϕ_n obey the normalization conditions

$$\sum_{n\,=\,0}^{\infty} P_n \;=\; 1, \qquad \int_{t_0}^{\infty} \phi_n(t, t_0)\,dt \;=\; 1\;. \tag{6}$$

Then, the probability that a photon that was emitted at time t_0 will escape at time t is

$$G(t,t_0) = \sum_{n=0}^{\infty} P_n \phi_n(t,t_0) , \tag{7}$$

which is the Green's function and is properly normalized. Therefore, if $I(t)$ is the intrinsic variability of the source, the variability observed at infinity can be written formally as

$$I_\infty(t) = \int_{-\infty}^{t} G(t,t_0)\ I(t_0)\ dt_0 . \tag{8}$$

4. RESULTS

Using the above formalism we have derived approximate analytic expressions for the amplitude of the oscillations observed at infinity for the two emission patterns.

4.1 Isotropic Emission

Let the intensity $I(t)$ at the source be

$$\frac{I(t)}{I_0} = 1 + A_0 \cos \omega t . \tag{9}$$

Then, from equation (8) we have

$$\frac{I_\infty(t)}{I_0} = 1 + A_0 \int_{-\infty}^{t} \cos \omega t_0\ G(t-t_0)\ dt_0 , \tag{10}$$

or equivalently

$$\frac{I_\infty(t)}{I_0} = 1 + A_0\ Re\left\{ e^{i\omega t} \int_0^\infty e^{-i\omega(t-t_0)}\ G(t-t_0)\ dt \right\} . \tag{11}$$

For a point source, at the center of a uniform spherical cloud of optical depth to electron scattering $\tau \gtrsim 3$, the probabilities P_n are given by (Lightman, Lamb, and Rybicki 1981)

$$P_n = \frac{1}{3\tau^2} \frac{1}{2\pi i} \int_{-i\infty}^{i\infty} \frac{\sqrt{s}\ e^{s\xi}}{\sinh \sqrt{s}} ds , \tag{12}$$

where $\xi \equiv n/3\tau^2$. For the probabilities $\phi_n(t,t_0)$ we make the approximation (see Kylafis and Klimis 1987 for a justification)

$$\phi_n(t,t_0) = \delta_{n,c(t-t_0)/l} = \delta_{n,c\tau(t-t_0)/R} . \tag{13}$$

Then, using equation (7) we get

$$G(t,t_0) = \frac{1}{3\tau R/c} \frac{1}{2\pi i} \int_{-i\infty}^{i\infty} \frac{\sqrt{s}\ e^{s\varsigma}}{\sinh \sqrt{s}} ds , \tag{14}$$

where $\varsigma \equiv (t - t_0)/(3\tau R/c)$. From equation (14) we conclude that $G(t, t_0)$ has the form of an inverse Laplace transform. In other words,

$$\int_0^\infty e^{-p\varsigma} G(\varsigma) d\varsigma \;=\; \frac{1}{3\tau R/c} \frac{\sqrt{p}}{\sinh\sqrt{p}} \,. \tag{15}$$

Setting $p\varsigma \equiv i\omega(t - t_0)$ in equation (15) we get the desired Fourier transform,

$$\int_0^\infty e^{-i\omega(t-t_0)} G(t - t_0) dt \;=\; \frac{\sqrt{i\omega 3\tau R/c}}{\sinh\sqrt{i\omega 3\tau R/c}} \,. \tag{16}$$

Combining equations (11) and (16) we get

$$\frac{A_\infty}{A_0} \;=\; \frac{\sqrt{2}x}{\sqrt{\sinh^2 x \cos^2 x \;+\; \cosh^2 x \sin^2 x}} + e^{-\tau} \;\approx\; 2\sqrt{2}xe^{-x} \;+\; e^{-\tau} \,, \tag{17}$$

where $x \equiv \sqrt{(3/2)\omega\tau R/c}$ and the last term in equation (17) has been added by hand to account for the unscattered photons. The approximate equality is better than 6% for $x > 1.3$.

In order to check the accuracy of our analytic expression (17), we also calculated the amplitude A_∞ by Monte Carlo simulation. In the Figure presented here we show for the case of $\tau = 7$ the amplitude of the Fourier transform of the Green's function (which can be shown to be equivalent to A_∞/A_0) as a function of the frequency f of the source variability. The frequency f is measured in units of $(1/200)(c\tau/R)$, where $c\tau/R$ is the Nyquist frequency. The crosses correspond to the analytic expression (17) and the circles to the Monte Carlo result. It is seen that expression (17) is quite accurate.

4.2 Beam Emission

Consider a δ-function beam of constant intensity I_0 in the xy-plane rotating about the z-axis with angular frequency ω. The direction of the observer is also in the xy-plane.

It was demonstrated by Kylafis and Klimis (1987) that, to a first approximation, one can take the amplitude observed at infinity to be

$$(A_\infty)_{beam} \;=\; \left(\frac{A_\infty}{A_0}\right)_{isotropic} \frac{2}{1+\tau} \,, \tag{18}$$

where the first factor is due to the travel time of the photons in the cloud and is given by equation (17) and the second is due to the isotropization of the radiation field by electron scattering (see eq. 5).

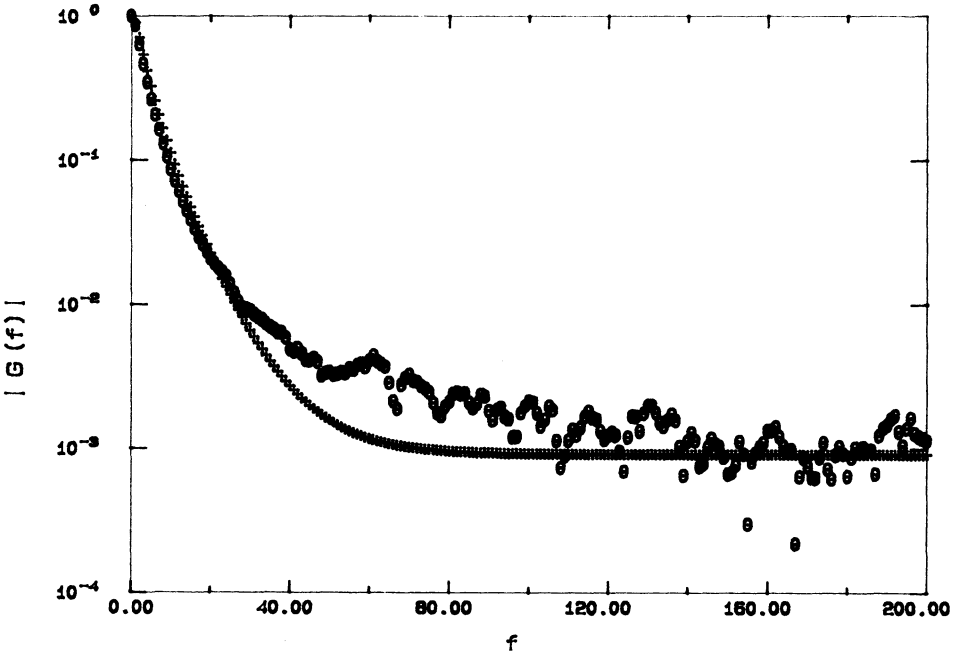

Figure. Comparison of analytic solution (17) and Monte Carlo simulation result for the reduction in apparent amplitude of variability of a source in a uniform scattering sphere of optical depth $\tau = 7$.

5. SUMMARY

We have derived approximate analytic expressions for the smearing of X-ray oscillations by electron scattering. Comparing equations (17) and (18), we conclude that it is possible to smear out the oscillations caused by beaming while leaving the oscillations caused by luminosity variation essentially unaffected.

A uniform, spherical scattering cloud is certainly not a realistic representation of the distribution of plasma around a source exhibiting QPO, but the analytic results presented here help one draw semi-quantitative conclusions for more realistic distributions of plasma. A more sophisticated formalism for treating problems of this sort, and results for more realistic scattering clouds will be presented in a forthcoming paper (Phinney and Kylafis, in preparation). This work has been supported in part by NSF grants AST84–51725 and PHY82–17853.

6. REFERENCES

Alpar, M. A., and Shaham, J. 1985, *Nature*, **316**, 239.

Brainerd, J., and Lamb, F. K. 1987, *Ap. J. (Letters)*, **317**, L33.
Chang, K. M., and Kylafis, N. D. 1983, *Ap. J.*, **265**, 1005.
Hertz, P., Joss, P. C., and Rappaport, S. 1978, *Ap. J.*, **224**, 614.
Kylafis, N. D., and Klimis, G. S. 1987, *Ap. J.*, **323**, 678.
Lamb, F. K. 1986, in *The Evolution of Galactic X-ray Binaries* eds. J. Trümper, W. H. G. Lewin, and W. Brinkmann, NATO ASI Series C: Math. & Phys. Sci., **167**, 151 (Dordrecht:Reidel).
Lamb, F. K. 1988, preprint.
Lamb, F. K., Shibazaki, N., Alpar, M. A., and Shaham, J. 1985, *Nature*, **317**, 681.
Lamb, F. K., and Priedhorsky, W. C. 1988, *Rev. Mod. Phys.*, in preparation.
Lewin, W. H. G., van Paradijs, J., and van der Klis M. 1988, *Space Sci. Rev.*, in press.
Lightman, A. P., Lamb, D. Q., and Rybicki, G. B. 1981, *Ap. J.*, **248**, 738.
Shaham, J. 1989, these proceedings.
Shibazaki, N., and Lamb, F. K. 1987, *Ap. J.*, **318**, 767.
Wang, Y. -M., and Schlickeiser, R. 1987, *Ap. J.*, **313**, 200.

Iterative Scattering Approach to Radiative Transfer

T . Maile [1], H. Herold [1,3], A. Rebetzky [1,2], H. Ruder [1], K. Wolf [1]

[1] *Lehrstuhl für Theoretische Astrophysik der Universität Tübingen, D-7400 Tübingen, FRG*
[2] *Max-Planck-Institut für Extraterrestrische Physik, D-8046 Garching, FRG*
[3] *Institut für Theoretische Physik der Universität Zürich, CH-8001 Zürich, Switzerland*

Abstract. A solution of the coherent radiative transfer problem in two-dimensional geometries by an Iterative-Scattering-Algorithm (ISA) is presented. The method is efficient for optically thin media and can reasonably be applied up to an optical depth where the diffusion approximation becomes valid. We treat a simplified model of an X-ray pulsar accretion column and compare the results obtained by the ISA with both, Monte-Carlo computations and diffusion approximation.

1. Introduction

For accretion columns of magnetized neutron stars in X-ray binaries solutions of the radiative transfer problem have been given in the diffusion approximation by several authors (Nagel 1981, Silant'ev 1982, Kaminker, Pavlov and Shibanov 1983, Soffel et al. 1984, Rebetzky et al. 1988). However, in the low energy range where a large amount of thermal radiation is emitted the plasma is optically thin and the diffusion approximation becomes inaccurate. Therefore, the problem remains how to compute correct angle-dependent fluxes in this energy range, especially for those energies, where the zero-scattering approximation - only valid in optically very thin media - is inappropriate. The algorithm presented here was intended to bridge this gap and gives a full solution of the time-independent radiative transfer equation.

For the numerical treatment we developed a computer code for two-dimensional geometries, which was implemented on CRAY-2 and CONVEX supercomputers. As a first test of the ISA we have solved the radiative transfer equation for a cylindrical column homogeneously filled with an electron plasma and with an isotropically radiating base (hot spot). Furthermore, we simplified our model of an "accretion column" by using an isotropic cross-section for the photon-electron scattering. The reasonable agreement that we have obtained between solutions of the diffusion approximation and the ISA method for our test model for $\tau_\perp \gtrsim 2$ has confirmed our expectation that the ISA scheme can sucessfully be applied for realistic models of X-ray pulsars.

H. Ögelman and E. P. J. van den Heuvel (eds.), Timing Neutron Stars, 739–742.

2. The method of successive approximations

The time-independent equation of coherent radiative transfer for the specific intensity $I(\mathbf{r},\mathbf{k})$ (at point $\mathbf{r}$ and into direction $\mathbf{k}$) of unpolarized radiation in a homogeneous medium can be written as an integral equation

$$I(\mathbf{r},\mathbf{k}) = I_s(\mathbf{r}-s_0\mathbf{k},\mathbf{k})\exp\{-\kappa(\mathbf{k})s_0\} + \int_0^{s_0} ds \int_{4\pi} d^2k'\,\sigma^{\mathrm{scatt}}(\mathbf{k}'\to\mathbf{k})\,I(\mathbf{r}-s\mathbf{k},\mathbf{k}')\exp\{-\kappa(\mathbf{k})s\}. \quad (1)$$

The scattering and extinction coefficients are denoted by σ^{scatt} and κ, which are, if absorption can be neglected, related by

$$\kappa(\mathbf{k}) = \int_{4\pi} d^2k'\sigma^{\mathrm{scatt}}(\mathbf{k}\to\mathbf{k}'). \quad (2)$$

The parameter s varies from values 0 to s_0 along the path of integration. Here, for simplicity we consider a purely scattering atmosphere which represents no restriction for the validity of the ISA method. A solution of eq. (1) can be given as an absolutely and uniformly convergent series, each term obtained by an iterative procedure:

$$I = I^{(0)} + I^{(1)} + I^{(2)} + \cdots . \quad (3)$$

The zeroth iteration is given by the first term of the r.h.s. of eq. (1)

$$I^{(0)}(\mathbf{r},\mathbf{k}) = I_s(\mathbf{r}-s_0\mathbf{k},\mathbf{k})\exp\{-\kappa(\mathbf{k})s_0\} \quad (4)$$

corresponding to photons which reach the point $\mathbf{r}$ unscattered. All higher iterations are obtained by the recursive formula

$$I^{(n)}(\mathbf{r},\mathbf{k}) = \int_0^{s_0} ds \int_{4\pi} d^2k'\sigma^{\mathrm{scatt}}(\mathbf{k}'\to\mathbf{k})I^{(n-1)}(\mathbf{r}-s\mathbf{k},\mathbf{k}')\exp\{-\kappa(\mathbf{k})s\}. \quad (5)$$

Here, $I^{(n)}$ is the intensity of n-times scattered photons, which have been scattered into direction $\mathbf{k}$ in the last scattering process.

3. Results and discussion

Based on the method described above our numerical ISA code was developed. As a first test we have computed a simplified model of an "accretion column", which was assumed to be cylindrical of radius $R = 1$ km and height $H = 2$ km, homogeneously filled with a non-moving accretion plasma. The boundary conditions correspond to an isotropically radiating hot spot at the bottom of the cylinder and to free escape at the top and the mantle of the cylinder. Furthermore, we have used an isotropic scattering coefficient with value $\sigma^{\mathrm{scatt}} = n_e\sigma_{\mathrm{Th}}/4\pi$, where σ_{Th} is the Thomson cross section and n_e the electron number density of the plasma.

Fig. 1 shows the escape probabilities of photons versus the number of scatterings for a column with transverse optical depth of $\tau_\perp = 2$. The ratio $I^{(n)}/I^{(n-1)}$ is converging asymptotically to a constant value q. The dashed line indicates the geometric sequence $I^{(0)}\,q^n$, which represents an upper limit for the escape probabilities .

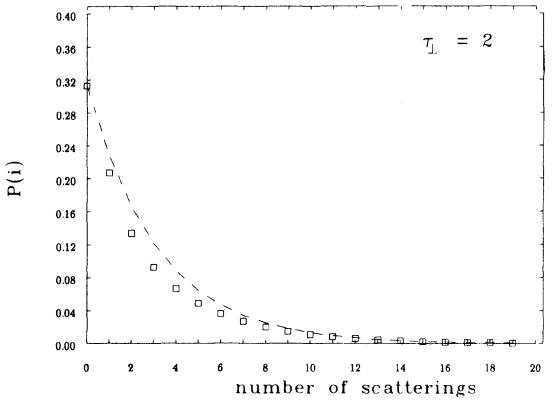

Fig. 1: Photon escape probability p(i) versus the number of scatterings for a column with a transverse optical depth of $\tau_\perp = 2$.

A comparison between the escape probabilities computed by the ISA and a Monte-Carlo simulation is presented in Fig. 2. The results are in good agreement. For each number of scatterings there exists an optical depth where the corresponding escape propability reaches its maximum.

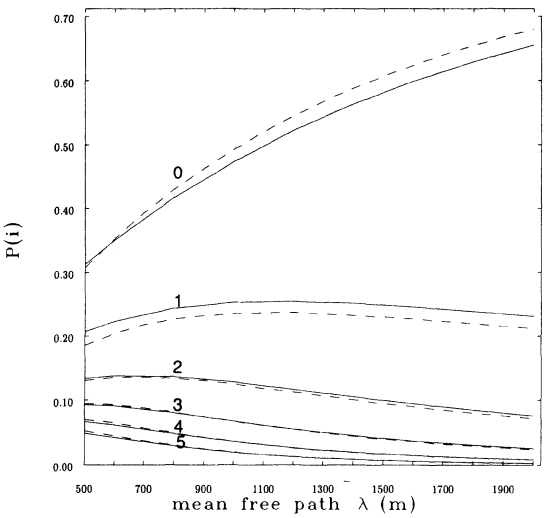

Fig. 2: Photon escape probabilities p(i) as a function of the mean free path $\lambda = R/\tau_\perp$. Solid lines refer to the ISA method, dashed lines to a Monte-Carlo simulation. The various curves correspond to different numbers i of scatterings.

As one might expect the radiation field obtained by the ISA differs considerably from the diffusion solution at the mantle of the cylinder. This is shown in Fig. 3

where lines of constant photon densities inside the cylinder are plotted. Note that even for a transverse optical depth of $\tau_\perp = 2$ the diffusion approximation and the ISA almost yield the same results close to the center of the column.

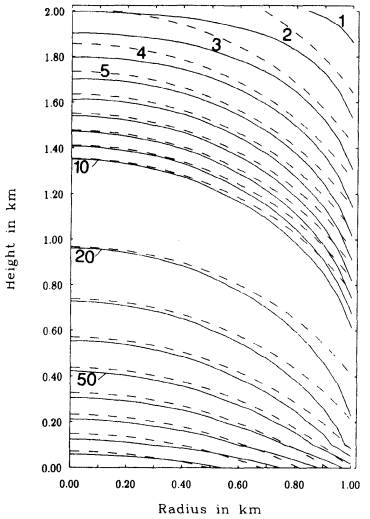

Fig. 3: Lines of constant photon densities in percent of the maximum photon density. Solid lines are calculated with the ISA, dashed lines with the diffusion approximation. The transverse optical depth is $\tau_\perp = 2$.

References

Gnedin, Yu.N., Pavlov, G.G.: 1974, *Sov. Phys. JETP* **38**, 903

Kaminker, A.D., Pavlov, G.G., Shibanov, Yu.A.: 1982, *Ap. Space Sci.* **86**, 249

Maile, T., Herold, H., Rebetzky, A., Ruder H., Wolf, K.: 1987, *Mitt. Astron. Ges.* **70**, 377

Mészáros, P., Bonazzola, S.: 1981, *Astrophys. J.* **251**, 695

Nagel, W.: 1981, *Astrophys. J.* **251**, 278

Pomraning, G.C.: 1973, *The Equations of Radiation Hydrodynamics*, Pergamon Press, Oxford

Rebetzky, A., Herold H., Maile, T., Ruder, H., Wolf, K.: 1988, *Astron. Astrophys.*, in press

Silant'ev, N.A.: 1982, *Ap. Space Sci.* **82**, 363

Soffel, M., Herold, H., Ruder, H., Ventura J.: 1984, *Astron. Astrophys.* **144**, 485

Radiative transfer in optically thick plasmas of accretion columns

A. Rebetzky [1,2], H. Herold [1,3] , T. Maile [1], H. Ruder [1], K. Wolf [1]
[1] *Lehrstuhl für Theoretische Astrophysik, Universität Tübingen, 7400 Tübingen, FRG*
[2] *Max-Planck-Institut für extraterrestrische Physik,8046 Garching, FRG*
[3] *Institut für Theoretische Physik, Universität Zürich, Switzerland*

Abstract. A self-consistent time-independent model of accretion columns of strongly magnetized neutron stars is presented. The problem of coupled frequency-dependent radiative transfer and hydrodynamics is briefly described. By numerically solving the equations we find an upper limit for the mass accretion rate, beyond which there are no stationary solutions. Furthermore, it turns out that effects of aberration and Doppler shift strongly affect the resulting spectra and beaming characteristics.

1. Introduction

Radiative transfer and hydrodynamics in accretion columns of neutron stars are two coupled problems, which should be solved simultaneously. For optically thin plasmas radiative transfer is decoupled from hydrodynamics. We show that in optically thick plasmas the radiative transfer is strongly affected by advection and adiabatic compression.

For high accretion rates the radiation pressure is the main reason for the deceleration of the plasma. This radiation pressure becomes stronger with increasing accretion rate. There is a maximal accretion rate $\dot{M}_{\max}$ beyond which no stationary solutions exist.

For a grey atmosphere the problem of radiation hydrodynamics has been treated by several authors (Davidson, 1973; Basko and Sunyaev, 1975; Wang and Frank, 1981; Herold et al.,1986a). But in the case of a strongly magnetized neutron star, the cross sections are strongly frequency dependent (Kirk, 1980; Gnedin et al.,1978; Herold et al., 1981; Soffel et al., 1983; Herold et al., 1986b), so that the use of a grey atmosphere cannot be justified. One has to solve the frequency–dependent radiative transfer problem together with the momentum equation of the plasma. We developed a method which allows us to solve the complicated system of integro–differential equations self-consistently.

In chapter 2 we summarize the main ideas of the diffusion approximation of the radiative transfer equation in non–uniformly moving, anisotropic media. In chapter 3 we present a self-consistent model of an accretion column.

H. Ögelman and E. P. J. van den Heuvel (eds.), Timing Neutron Stars, 743–747.

2. The diffusion approximation

The numerical treatment of radiative transfer in optically thick media by solving the angle–dependent equation of radiative transfer is extremely computer time consuming. One has to make a reasonable approximation, namely the diffusion approximation. The diffusion equation has a further advantage : it is easier to include the inhomogeneous velocity distribution of the plasma to connect it to hydrodynamics. For a detailed derivation see Rebetzky et al., (1988). The resulting equation is

$$-\nabla(\hat{D}\nabla I_0^{(0)}) + \frac{\partial}{\partial z}\left(\beta I_0^{(0)}\right) - \frac{1}{3}\frac{\partial \beta}{\partial z}\nu_0 \frac{\partial I_0^{(0)}}{\partial \nu_0} = \kappa_a (I^b - I_0^{(0)}) \quad , \tag{1}$$

where we introduced the diffusion tensor

$$\hat{D} = \frac{1}{4\pi}\int_{4\pi} d^2\hat{k}_0\, \hat{\mathrm{k}}_0 \frac{1}{\sigma_{s0}(\hat{\mathrm{k}}_0)} \hat{\mathrm{k}}_0 \quad . \tag{2}$$

In these equations $I_0^{(0)}(\hat{\mathrm{k}}_0, \nu_0)$ is the isotropic part (superscript (0)) of the specific intensity in the comoving plasma frame (all quantities in this frame are denoted by a subscript '0') in the direction $\hat{\mathrm{k}}_0$ at the frequency ν_0, σ_{s0} is the scattering coefficient and κ_a the angle-averaged absorption coefficient, and β is the velocity of the plasma (only along the magnetic field lines) in units of the velocity of light. How is eq.(1) coupled to hydrodynamics ?

To give an answer we have to consider the energy–stress tensor $T_{\mu\nu}$ and transform it into a moving frame by a Lorentz transformation. Neglecting gravitational forces and gas pressure, we obtain two coupled energy equations for the stationary case :

$$\nabla(\mathrm{v}(\frac{1}{2}\rho v^2 + p_{\mathrm{rad}})) = p_{\mathrm{rad}}(\nabla \mathrm{v}) \tag{3}$$

$$\nabla(\mathbf{F}_{\mathrm{rad}} + u_{\mathrm{rad}}\mathrm{v}) = -p_{\mathrm{rad}}(\nabla \mathrm{v}) \tag{4}$$

In this equation $\mathbf{F}_{\mathrm{rad}}$, u_{rad} and p_{rad} are the radiation flux, the radiation energy density and the radiation pressure, respectively. The second of these energy equations describes the diffusive radiative transfer with an adiabatic compression term on the r.h.s.. The momentum equation reads (with $p_{\mathrm{rad}} = \frac{1}{3}u_{\mathrm{rad}}$):

$$\rho v \frac{\partial v}{\partial z} = -\frac{1}{3}\frac{\partial u_{\mathrm{rad}}}{\partial z} \tag{5}$$

Additionally we use $\rho v = \mathrm{const}$ which follows from the continuity equation. The equations (3) to (5) describe the frequency–integrated radiation hydrodynamics in accretion columns. Equation (4) is formally identical with the frequency–dependent diffusion equation (1), and equation (3) is a direct consequence of equation (5). So we can use eq.(1) together with eq.(5) to solve the coupled problem of radiative transfer and hydrodynamics.

3. Self-consistent solutions

We have solved the problem of frequency-dependent radiation hydrodynamics with the following fixed parameters: radius of the accretion column $R_{\rm col} = 1$ km, temperature of the infalling plasma $T = 10^8$ K, radius of the neutron star $R_{ns} = 10$ km, magnetic field strength corresponding to $\hbar\omega_c = 50$ keV. The most interesting adjustable parameter is the mass accretion rate $\dot{M}$.
For our calculations we choose a mass accretion rate of $\dot{M} = 1.06 \cdot 10^{-9}$ $M_\odot$/yr, corresponding to a mass flow $\rho v = 2.2 \cdot 10^6$ g s^{-1} cm^{-2}.

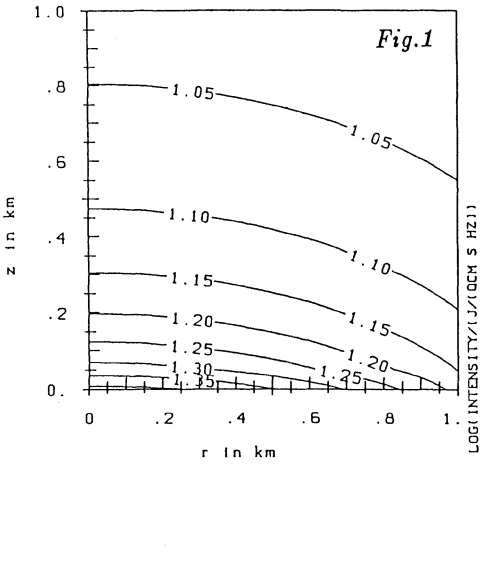

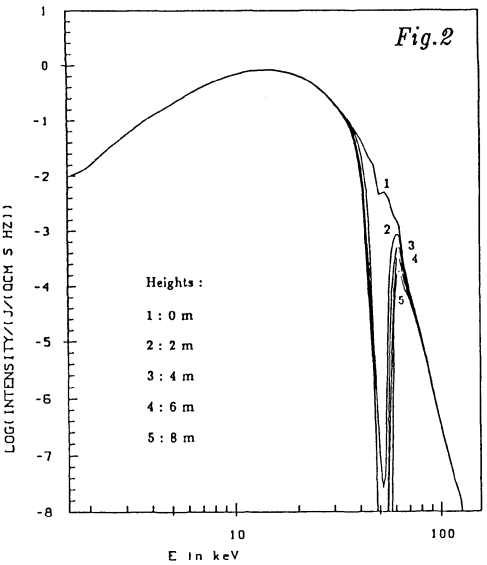

Fig. 1: Self-consistent mass density profile in the cylinder in units of the infalling mass density $\rho_0 = 1.48 \cdot 10^{-4}$ *g cm*$^{-3}$
Fig. 2: Self-consistent spectra in the plasma frame in several heights (see in the figure)

Fig. 1 shows the self-consistent density field as lines of constant mass density in units of the free-fall density. The highest density can be found in the center of the column. In Fig. 2 the spectrum in the plasma frame at the mantle of the column is plotted. Note that this intensity is a quantity in the plasma frame and not observable. In the vicinity of the cyclotron frequency, photons can only be found in very small heights above the surface. The reason for that is the strong advection effect which becomes dramatic, if $\tau|\beta| > 1$ where τ is the optical depth and β the velocity of the plasma in units of c. In the case of a strongly magnetized neutron star with $\hbar\omega_c = 50$ keV the advection effect is expected to be important between $\hbar\omega \approx 30$ keV and $\hbar\omega \approx 100$ keV. We conclude that resonant photons can only escape from the accretion column in very small heights, because they are pressed down onto the star's surface. The term proportional to $\nu_0 \, \partial I_0^{(0)}/\partial\nu_0$ causes a transport of photons in frequency space. Photons gain energy by adiabatic

compression.
We have found an upper limit for the accretion rate, beyond which there are no stationary solutions for the coupled problem of radiative transfer and hydrodynamics. For first results what may then happen see Wolf et al. (1987). The numerical value for this maximum accretion rate is $\sim 1.2 \cdot 10^{-9}$ $M_\odot$/yr corresponding to a total luminosity of 10^{30} W (one column).
As we have already mentioned, the plotted intensities in Fig. 2 are not observable. The intensity has to be transformed into the observers frame (see Pomraning, 1974)

$$I(\nu, \hat{\mathrm{k}}) = \left(\frac{\nu}{\nu_0}\right)^3 \cdot I_0(\nu_0, \hat{\mathrm{k}}_0) \tag{6}$$

where ν and ν_0 are the photon frequencies in the observers frame and the plasma frame, respectively (see eq. (7) for the frequency transformation law).

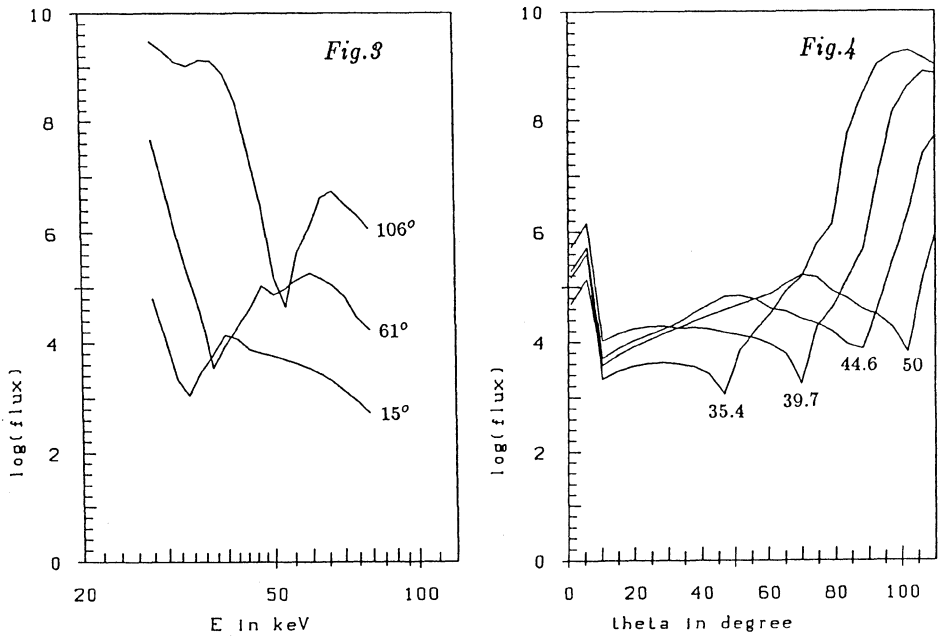

Fig. 3: Photonflux in the observers frame in the vicinity of the cyclotron line
Fig. 4: Angle-dependent flux for several energies (in keV)

Fig. 3 shows the resulting flux integrated over the cylinder for several angles ϑ (ϑ is the angle between the z-axis and the line of sight). For small values of ϑ the cyclotron line is redshifted by about 15 keV ! For a given height in the cylinder the dependence of the cyclotron resonance on the angle ϑ is given by

$$E_c = \hbar\omega_c = \hbar\omega_{c0}(\gamma(1 - \beta\cos\vartheta))^{-1} \tag{7}$$

E_c is a function of β and thus of the height in the cylinder. Integrating over all heights leads to a smearing of the line feature. Finally, in Fig. 4 the angle–dependent flux is plotted for some energies in the optically thick region around the cyclotron resonance. A large amount of the photons is emitted into angles $\vartheta > 90°$. The reason for that is the strong aberration (a photon escaping with $\vartheta = 90°$ from the plasma frame is emitted with $\vartheta = 120°$!) combined with the Doppler shift. These photons produce a luminous area on the neutron star's surface close to the column. Most of the photons in the optically thick energy range cannot be seen directly from the column but from this illuminated area around it! This will have a strong influence on the pulse shapes, which will be discussed in a future paper.

References

Basko, M.M., Sunyaev, R.A.: 1975, *Astron. Astrophys.* **42**, 311

Davidson, K.: 1973, *Nature Phys. Sci.* **246**, 1

Gnedin, Yu.N., Pavlov, G.G., Shibanov, Yu.A.: 1978, *Pis'ma Astron. Zh.* **4**, 214

Herold, H., Ruder, H., Wunner, G.: 1981, *Plasma Phys.* **23**, 775

Herold, H., Wolf, K., Ruder, H.: 1986a, *Mitt. Astron. Ges.* **65**, 214

Herold, H., Maile, T., Ruder, H.: 1986b, *Mitt. Astron. Ges.* **65**, 215

Kirk, J.G.: 1980, *Plasma Phys.* **22**, 639

Pomraning, G.C.: 1973, *The Equations of Radiation Hydrodynamics*, Pergamon Press, Oxford

Rebetzky, A., Herold, H., Maile, T., Ruder, H., Wolf, K. : 1988, *Astron. Astrophys.*, in press

Soffel, M., Ventura, J., Herold, H., Ruder, H., Nagel, W. : 1983, *Astron. Astrophys.* **126**, 251

Wang, Y.M., Frank, J.: 1981, *Astron. Astrophys.* **93**, 255

Wolf, K, Herold, H, Maile, T, Rebetzky, A, Ruder, H. : 1987, *Mitt. Astron. Ges.* **70**, 381

A model for spherically symmetric accretion onto neutron stars

V. DEMMEL, G. MORFILL, AND H. ATMANSPACHER

Max-Planck-Institut für extraterrestrische Physik, 8046 Garching, FRG

Abstract: We present a phenomenological model of spherically accreting neutron stars at high mass accretion rates. The radiation and the optically thick plasma are described as two interacting fluids. The time evolution of the regarded system is calculated by a discrete time iteration map. It is shown, that the neutron star in our model may well exceed the Eddington luminosity.

1. Introduction

The problem of accretion onto neutron stars in case of high mass transfer rates from the companion star is described in a radiation – hydrodynamical framework. In order to get information about the observational variable (the X – ray flux), one has to solve the equations for the infalling plasma simultaneously with the transport equation for the radiation through this medium (see e.g. Rebetzky in this volume). The numerical integration of this coupled time dependent nonlinear differential equation system is not yet possible. Reducing the degrees of freedom of the two interacting systems, plasma and radiation, assuming preferred directions of motion of the particles and the photons, one is able to solve the equations of the problem numerically. For solutions of the spherically symmetric problem see e.g. Klein et al. 1980, Maraschi et al. 1978, Burger and Katz 1980, 1983.

The qualitative results from these calculations were predicted by Zel'dovich in 1964. He rederived a simple argument for the luminosity of shells in sphericallly symmetric stars first used by Eddington in 1921. In the case of an accreting neutron star (NS) there exists an upper limit on the luminosity. As the mass accretion rate $\dot{M}$ increases, so does the radiation pressure slowing down the infalling plasma. The energy gain from the conversion of kinetic energy into radiation reaches an upper limit. The associated luminosity is called the Eddington luminosity L_E:

$$L_E = 1.37 \times 10^{38} \frac{\text{erg}}{\text{s}}$$

H. Ögelman and E. P. J. van den Heuvel (eds.), Timing Neutron Stars, 749–756.

From this we may define an "Eddington mass accretion rate" $\dot{M}_E$:

$$\dot{M}_E = \frac{L_E}{(GM/R)} = 9.47 \times 10^{17} \frac{g}{s}$$

To obtain this value a NS with a radius $R = 10$km, and with a mass $M = 1.4M_\odot$ is assumed. The accreting gas is assumed to be fully ionized hydrogen, and the interaction between the photons and the plasma is described by Thomson scattering.

In this paper we describe an accretion model intended for high mass accretion rates only (i.e. the plasma has to be optically thick).

A phenomenological description is given in 2.1, the evolution of the system is calculated with discrete time step difference equations in 2.2., and for the parameters given in 2.3 we evaluate the dependence of luminosity on the mass accretion rate in 3.

2. The model

2.1 Phenomenological description

In our model we assume that the radiation pressure is highest at the NS surface, where the accreting gas impacts. In an optically thick situation, we treat radiation and plasma as two vertically adjacent fluids in the gravitational field of the NS. The radiation pressure decelerates the plasma at a certain distance above the NS surface, depending on the mass accretion rate. The decelerated accretion flow forms a dense layer. Since this layer has a greater density than the radiation gas, such a situation is *Rayleigh - Taylor* unstable. As a consequence, we can assume that the matter will fall down on the surface in large, optically thick clumps. The radiation, which is produced on the surface during the impact of these clumps, will leave it in "bubbles" of high energy density. These radiation bubbles are able to push the plasma above them out, producing "channels" in the accreting material. When there are several bubbles around, there is a certain probability, that part of the radiation can escape through existing channels. To illustrate how all these processes work together, fig. 1 shows a schematic picture of an accreting neutron star.

2.2 The evolution equations

The time dependent accretion problem can now be formulated in a much simpler way. As the radiation and the plasma are bound in bubbles and clumps in the vicinity of the surface of the star, the interaction between these two systems is reduced to a geometrical problem: We divide the surface of the unstable region, which forms a shell around the star, into zones which either contain channels or clumps. We then assume the following scenario:

- Clumps will only be formed in the unstable layer where there are no channels.
- Every clump which falls down, creates a radiation bubble.
- Part of the bubbles will produce new channels in the accreting plasma, the other part will escape through existing ones.

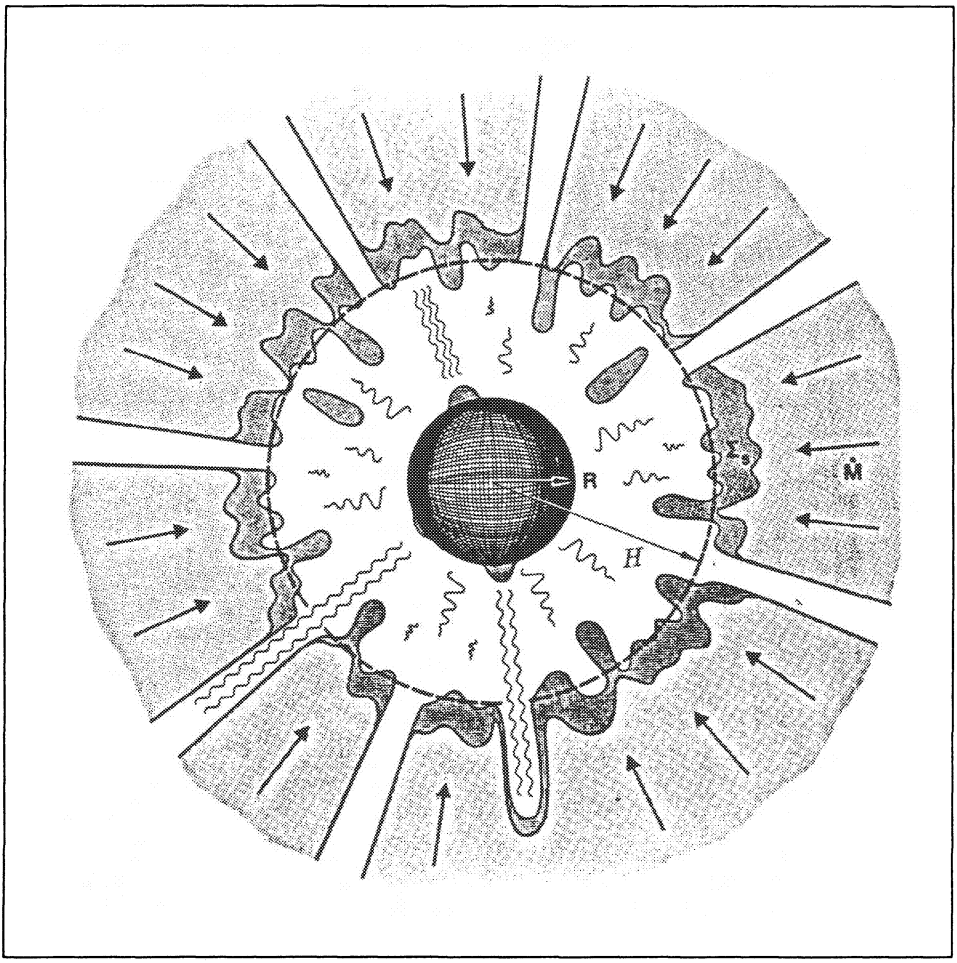

Figure 1: An anisotropically accreting NS, as it is described in the text. The infalling plasma is stopped and compressed at a certain height H above the NS. Clumps are formed, which fall down and convert their energy into radiation bubbles. These either push the plasma outwards creating new channels or escape through existing ones.

The evolution of the whole system is then described by a deterministic differential equation system with the clumps $K(t)$, the bubbles $B(t)$, and the channels $C(t)$ as variables ($K(t) \equiv B(t)$):

$$\begin{aligned} \dot{K}(t) &= f_1(C(t), K(t)) \\ \dot{C}(t) &= f_2(K(t-\tau_1), C(t)) \\ C(t) &= f_3(C(t-\tau_2), C(t-2\tau_2), \ldots) \end{aligned} \tag{2.1}$$

In these equations the functions f_i describe how the variables are coupled. The timescale τ_1 includes the time for creation of the clumps, their free fall time to the surface, and the time the bubbles need to expand to the unstable region. The timescale τ_2 is the mean life time of a channel.

How can one find the f_i? To simplify the derivation, we make the following assumptions:

(1) We discretise the evolution equations and use the smaller of the timescale τ_1 and τ_2 as the time step for this discretisation.

(2) The bubbles and the clumps are assumed to cover an area of the same size at the height of the unstable layer.

(3) The clumps and bubbles (and therefore the channels too) are randomly distributed on the unstable surface.

(4) The bubbles push the accreting material, which lays directly above them, out (i.e. there is no compression of the plasma around a channel).

(5) The clumps are formed spontaneously at the beginning of each timestep.

(6) The life time of the channels will not be extended by bubbles which escape through them.

As a consequence of (1) the system of differential equations will read as follows:

$$\begin{aligned} K_{i+1} &= f_1(C_i, K_i) \\ C_{i+1} &= f_2(K_i, C_i) \\ C_i &= f_3(C_{i-1}, C_{i-2}, \ldots) \end{aligned} \tag{2.2}$$

The surface area of the unstable region is $A = 4\pi(R+H)^2$, where $R+H$ is the distance from the NS center. If a is the cross sectional area of a clump, the maximum number of clumps which can be formed in a time step i, is $N = \frac{A}{a}$. This number will be reduced by the number of channels C_i which are present at this timestep. Because of (2) and (5) the clumps K_{i+1} formed at the time step $i+1$ are given by:

$$K_{i+1} = N(1 - C_i \frac{a}{A}) \tag{2.3}$$

Using (3), the probability that a bubble blows a channel is given by $P_i = (1-\alpha\frac{a}{A})^{C_i}$. The factor α takes into account, that a bubble which is formed sufficiently close to an existing channel, will escape through it. Hence

$$C_{i+1} = K_{i+1} P_i \tag{2.4}$$

Because the lifetime τ_2 of a channel is not equal to the time step we use for the iteration, we have to take into account more than one channel generation (i.e. we have to sum over channels present at previous times).

Using all these arguments we finally end up with the following one dimensional iteration map:

$$C_{i+1} = N(1 - \sum_{j \geq 0} C_{i-j} \frac{a}{A})(1 - \alpha \frac{a}{A})^{\sum_j C_{i-j}} \tag{2.5}$$

The summation over j includes a certain number of previous channel generations, which is given by $n = \frac{\tau_2}{\tau_1}$.

The number of channels varies from timestep to timestep, and can be calculated by iterating this map starting with an initial condition $0 \leq C_0 \leq N$.

Because the map (2.5) does not consider processes of stimulated clump production it describes a regular (nonchaotic) behaviour of its temporal evolution. Fig. 2 shows four different time series with varying numbers of clump generations $j + 1$.

Stimulated clump production occurs in the following way (see chapt. 4): Bubbles which do not escape through existing channels produce their own channels, and in doing so will compress the plasma near these newly formed channels. In these regions the rate of clump production is higher than elsewhere, leading to stimulated Rayleigh – Taylor instabilities. For $n \leq 3$ the number of channels vary (after a certain relaxation time) between their maximum value and zero. That means, that during one time step matter is accreted, and in the following one no accretion occurs because the bubbles are pushing the matter away. Because it needs a time τ_2 to fill up the shell of plasma at the height H again, the NS does not radiate during this phase. For $n > 3$ the oscillations are damped out, and the number of channels reaches a stationary solution.

2.3 The physical parameters

In order to make our model quantitative, we have to calculate and estimate the following parameters:

(1) Size and mass of the clumps.

(2) Distance of the unstable region from the neutron star surface H.

(3) Energy content of the bubbles.

(4) Time scales τ_1 and τ_2.

(5) Height over the neutron star surface R_1, where radiation and plasma are decoupling.

To determine (1) we use the dispersion relation of the *Rayleigh – Taylor* instability (see e.g. Chandrasekhar 1961), setting the diffusion time of the photons equal to the instability growth time scale. This gives us the unstable wavelength which is growing fastest. We take that wavelength as the uniform size of a clump. The density of the unstable region is a factor β higher than the assumed free fall density at this height. A clump falling from H to the NS surface converts all its gravitational energy into radiation. The radiation pressure decelerates the accretion flow and, as mentioned earlier, bubbles may push channels into the plasma loosing all their energy in doing so (this defines the height H). Therefore only the bubbles which escape through existing channels contribute to the luminosity of the star.

The time scale τ_1 is found by using the *RT* instability, the free fall time of a clump from H to the NS surface, and the time the bubbles need to come up to the height

H. The lifetime of a channel is assumed to be the free fall time of the plasma from the distance R_1 to the distance H.

The decoupling distance R_1 is defined by the condition that the optical depth from R_1 to infinity is smaller than 0.5.

Our goal is to express all the physical quantities as a function of only one free parameter: the mass accretion rate $\dot{M}$. This is done by invoking the conservation laws (see Morfill et al. 1988 for further details).

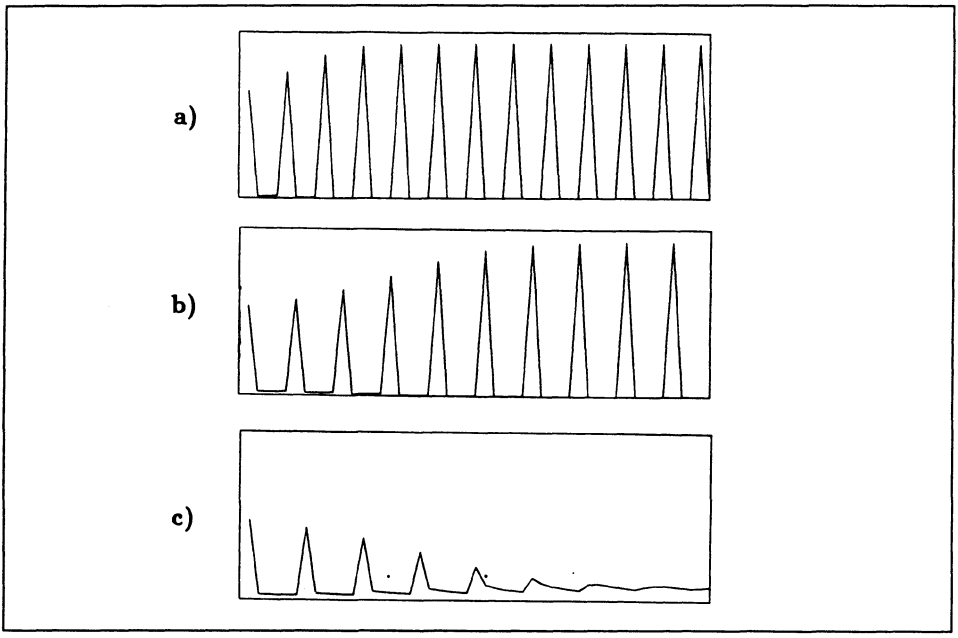

Figure 2: Time series of the iteration map derived in the text. The ordinate is the number of channels at a certain time i, while the abscissa represents the time axis. The two different time scales are chosen, so that $\tau_2 = n\tau_1$ (a): $n = 3$, b): $n = 4$, c): $n = 5$, d): $n = 6$)

3. Results

Because there are only two regular modes in the time behaviour of the discrete evolution equation (oscillation and stationarity), we can calculate time averages very easily. If we use the number of channels (or clumps), we are able to determine the total luminosity of the NS by adding up all the energy of the freely escaping radiation bubbles per time unit (see fig.3).

The main result of our model is the possibility, that the luminosity of the NS may exceed the Eddington limit for mass accretion rates $\dot{M}_E \geq 2.6$. The clumpiness of the accretion flow due to instability processes allows the system to release radiation in a more effective way than the simple models (see introduction) predict.

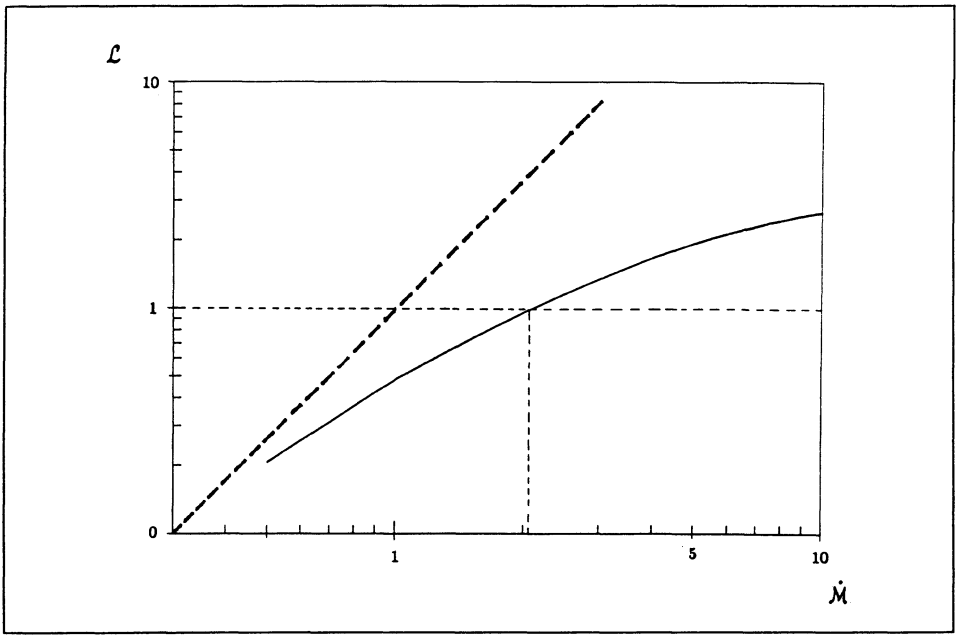

Figure 3: The luminosity of the NS in units of the Eddington luminosity as a function of the mass accretion rate in units of the Eddington mass accretion rate. The dotted line shows the luminosity of the NS if no interaction of the photons and the plasma is assumed $\mathcal{L} \propto \dot{M}$ (this is only true for $\dot{M} \ll 1$).

4. Future work

As mentioned earlier we have not investigated the stimulated production of clumps. This process leads to a back reaction of clump formation at a given time on that occuring some time later (delayed effect). Before trying to derive the coresponding evolutionary equation system, we first simulate our model on a computer. Our goal is to investigate whether such a description leads to a chaotic variation of the luminosity, as it was seen in accreting system like Her X-1 (see H. Atmanspacher et al. in this book)

References

Atmanspacher, H., H.Scheingraber, and W.Voges *in this volume*

Burger, H.L., and J.I.Katz 1980, *Ap.J.* **236**,921

Burger, H.L., and J.I.Katz 1983, *Ap.J.* **265**,393

Chandrasekhar, S. 1961, *Hydrodynamic and Hydromagnetic Stability* (Clarendon Press, Oxford)

Klein, R.I., H.S.Stockman, and R.A.Chevalier 1980, *Ap.J.* **237**,237

Maraschi, L., C.Reina, and A.Treves 1978, *Astron. Astrophys.***66**,99

Morfill, G., V.Demmel, and H.Atmanspacher *to be published*

Rebetzky, A. *in this volume*

Zel'dovich, Ya.B., and I.D.Novikov 1964, *Dokl. Akad. Nauk. SSSR* **158**,811